REC2026

11TH INTERNATIONAL WORKSHOP ON
RELIABLE ENGINEERING COMPUTING

Reliability Computations in a Data and Model-Driven World

PROCEEDINGS

EDITED BY

MATTHIAS FAES
MICHAEL BEER



2-5 SEPTEMBER 2026
DORTMUND, GERMANY

Chair for Reliability Engineering

technische universität dortmund

Proceedings

REC 2026

11th International Workshop on Reliable Engineering Computing

Reliability Computations in a Data and Model-Driven World

2–5 September, 2026

International Meeting Centre IBZ, TU Dortmund
Dortmund, Germany

Edited by

Matthias Faes

Michael Beer

Chair for Reliability Engineering
TU Dortmund University

Imprint

Editors:
Matthias Faes
Michael Beer

Proceedings title:
11th International Workshop on Reliable Engineering Computing

Workshop:
REC 2026

Location and dates:
International Meeting Center (IBZ), Dortmund, Germany
2–5 September, 2026

Institution:
Chair for Reliability Engineering
TU Dortmund University

Volume DOI:
https://doi.org/10.17877/tudobooks-11

License:
Creative Commons Attribution 4.0 International

Note: individual papers may carry their own bibliographic and DOI information.

Preface

The International Workshop on Reliable Engineering Computing (REC) has emerged as a distinctive multidisciplinary forum over more than two decades. Since its inception, the conference series has been hosted at Georgia Tech Savannah, USA, in 2004, 2006, and 2008, at the National University of Singapore in 2010, at Brno University of Technology, Czech Republic, in 2012, at Illinois Institute of Technology in Chicago, USA, in 2014, at Ruhr University Bochum, Germany, in 2016, at the University of Liverpool, United Kingdom, in 2018, at Taormina, Italy, in 2021, and at Tsinghua University in Beijing, China, in 2024. Throughout its history, REC has provided a unique platform that brings together researchers from engineering, mathematics, computer science, statistics, and related disciplines with the common objective of advancing the reliability of engineering computations.

The 11th International Workshop on Reliable Engineering Computing (REC2026) is hosted by TU Dortmund University, Germany. The theme of REC2026, "Reliability Computations in a Data and Model-Driven World", reflects both the continuity of the conference tradition and the evolving challenges faced by the scientific and engineering communities. As in previous editions, the central focus remains the reliability of computational predictions under uncertainty. However, the unprecedented growth of data availability, computational capabilities, artificial intelligence (AI), and scientific machine learning is transforming the way engineers and scientists develop models, perform simulations, and make decisions.

REC was founded on the premise that computational results should not merely be produced efficiently, but should also be trustworthy, interpretable, and scientifically sound. This objective remains as relevant today as it was more than twenty years ago. In many respects, recent developments such as AI have reinforced its importance. Data-driven methods and machine learning algorithms have demonstrated remarkable capabilities across a wide range of engineering applications. At the same time, these advances raise fundamental questions regarding robustness, explainability, uncertainty quantification, and the reliability of predictions obtained from increasingly complex computational tools, especially in the context of (safety-)critical systems.

Against this background, REC2026 provides a forum to discuss how modern data-driven approaches can be integrated with established engineering principles and physical modelling. Rather than viewing artificial intelligence and scientific machine learning as replacements for engineering reasoning, the contributions presented at REC2026 explore how these methodologies can complement and enhance existing approaches. The resulting dialogue seeks to ensure that future computational methods remain transparent, reliable, and firmly grounded in scientific understanding.

The technical programme reflects both the traditional strengths of the REC community and its continued evolution. Core topics such as uncertainty quantification, reliability analysis, stochastic mechanics, random fields, rare-event simulation, imprecise uncertainty modelling, and reliability-based design remain central pillars of the workshop. At the same time, the programme highlights emerging directions including scientific machine learning, explainable and trustworthy artificial intelligence, Bayesian inference, active learning, surrogate modelling, hybrid data-model approaches, and advanced methods for uncertainty-informed decision making. Together, these contributions illustrate how the field is expanding while remaining faithful to its original mission of promoting reliable engineering computations.

As in previous editions, REC2026 addresses challenges arising in a broad spectrum of engineering and scientific applications. Contributions span topics ranging from structural and mechanical systems to environmental and infrastructure problems, from stochastic dynamics and monitoring to optimization and digital engineering. This diversity reflects the increasingly interdisciplinary nature of modern research on reliability and demonstrates the continued relevance of reliable computational methods across scientific domains.

REC2026 aims to foster discussions that bridge disciplines, methodologies, and communities. By bringing together experts from academia, industry, and governmental institutions, the workshop provides opportunities for the exchange of ideas, the establishment of new collaborations, and the identification of future research directions. The editors hope that the contributions collected in these proceedings will advance the development of reliable computational methods and support the responsible integration of data-driven technologies into engineering practice.

The editors would like to express their sincere gratitude to all authors for their contributions and to the reviewers for their time, expertise, and commitment to maintaining the scientific quality of the workshop. We are also grateful to the keynote speakers for sharing their insights and helping shape the scientific discussions of REC2026. Special thanks are due to the members of the Organizing Committee, the Technical Program Committee and the Scientific Committee, whose efforts were essential for the preparation of the workshop. We further wish to acknowledge the dedication and support of the administrative staff, technical staff, and student helpers, whose commitment and hard work contributed significantly to the successful organization of the conference. In particular, we would like to thank Cristóbal Acevedo, Mohamad Daher, Miriam Dodt, Anette Georgii, Ali Osman Mert Kilicsoy, Nataly Manque Roa, Mauricio Misraji, Marcos Valdebenito, and Weiming Zheng.

We gratefully acknowledge the financial support provided by the German Research Foundation (DFG) and the European Safety and Reliability Association (ESRA). We further acknowledge the support of TU Dortmund University and the Internationales Begegnungszentrum (IBZ), whose hospitality and assistance contributed significantly to the successful organization of the workshop. We also thank the European Safety and Reliability Association, the National Chapter of ESRA in China, and the Bernoulli Society for Mathematical Statistics and Probability through its Committee for Probability and Statistics in the Physical Sciences ($C(PS)^2$) for their support and sponsorship.

We hope that REC2026 will continue the tradition of fostering innovative ideas, stimulating scientific discussions, and strengthening the international community working at the interface of reliability, uncertainty, computation, and data-driven engineering.

Matthias Faes
Michael Beer

Organizers

Honorary General Chairs and Founders

Rafi Muhanna, Georgia Institute of Technology, USA

Robert Mullen, University of South Carolina, USA

General Chair

Matthias Faes, Chair for Reliability Engineering, TU Dortmund University, Dortmund, Germany

General Co-Chair

Michael Beer, Institute for Risk and Reliability, Leibniz Universität Hannover, Hannover, Germany / Institute for Risk and Uncertainty, University of Liverpool, Liverpool, UK / Shanghai Institute of Disaster Prevention and Relief, Tongji University, Shanghai, China

Steering Committee Chairs

Alba Sofi, Mediterranean University of Reggio Calabria, Reggio Calabria, Italy

Edoardo Patelli, University of Strathclyde, Glasgow, UK

Xuan-Yi Zhang, Beijing University of Technology, Beijing, China

Yi Zhang, Tsinghua University, Beijing, China

Technical Program Committee Co-Chairs

Steffen Freitag, Karlsruhe Institute of Technology, Karlsruhe, Germany

Alice Cicirello, University of Cambridge, Cambridge, UK

Local Organizing Committee Chair

Marcos Valdebenito, Chair for Reliability Engineering, TU Dortmund University, Dortmund, Germany

Local Organizing Committee

Ali Osman Mert Kilicsoy, Chair for Reliability Engineering, TU Dortmund University, Dortmund, Germany

Anette Georgii, Chair for Reliability Engineering, TU Dortmund University, Dortmund, Germany

Cristóbal Acevedo, Chair for Reliability Engineering, TU Dortmund University, Dortmund, Germany

Mauricio Misraji, Chair for Reliability Engineering, TU Dortmund University, Dortmund, Germany

Miriam Dodt, Chair for Reliability Engineering, TU Dortmund University, Dortmund, Germany

Mohamad Daher, Chair for Reliability Engineering, TU Dortmund University, Dortmund, Germany

Nataly Manque Roa, Chair for Reliability Engineering, TU Dortmund University, Dortmund, Germany

Scientific Committee

Adolphus Lye, National University of Singapore, Singapore
Alice Cicirello, University of Cambridge, UK
Andreas Rauh, University of Oldenburg, Germany
Changcong Zhou, Northwestern Polytechnical University, China
Daniel Straub, TU Munich, Germany
David Moens, Catholic University of Leuven, Belgium
Dixiong Yang, Dalian University of Technology, China
Ekaterina Auer, University of Wismar, Germany
Enrico Zio, Polytechnic of Milan, Italy
George Stefanou, Aristotle University of Thessaloniki, Greece
Giuseppe Muscolino, University of Messina, Italy
Héctor A. Jensen, Federico Santa María Technical University, Chile
Iason Papaioannou, TU Munich, Germany
Isaac Elishakoff, Florida Atlantic University, USA
Jianbing Chen, Tongji University, China
Jingwen Song, Northwestern Polytechnical University, China
Lukáš Novák, Brno University of Technology, Czech Republic
Marco Broccardo, University of Trento, Italy
Mario Di Paola, University of Palermo, Italy
Masaru Kitahara, University of Tokyo, Japan
Matthias Troffaes, Durham University, UK
Michael Beer, Leibniz University Hannover, Germany
Michael Oberguggenberger, University of Innsbruck, Austria
Miroslav Vořechovský, Brno University of Technology, Czech Republic
Pengfei Wei, Northwestern Polytechnical University, China
Sébastien Destercke, Université de Technologie de Compiègne, France
Stefano Marelli, ETH Zurich, Switzerland
Vladik Kreinovich, University of Texas at El Paso, USA
Wolfgang Graf, Technische Universität Dresden, Germany
Xuan-Yi Zhang, Beijing University of Technology, China
Alba Sofi, University "Mediterranea" of Reggio Calabria, Italy
André T. Beck, University of São Paulo, Brazil
Bruno Sudret, ETH Zurich, Switzerland
Dagang Lu, Harbin Institute of Technology, China
Danko Jerez, Federico Santa María Technical University, Chile
De-Cheng Feng, Southeast University, China
Edoardo Patelli, University of Strathclyde, United Kingdom
Eleni Chatzi, ETH Zurich, Switzerland
Franz Bamer, RWTH Aachen, Germany
Giovanni Falsone, University of Messina, Italy
Hao Zhang, The University of Sydney, Australia
Hongwei Huang, Tongji University, China
Ingo Neumann, Leibniz University Hannover, Germany
Jamshid Mohammadi, Illinois Institute of Technology, USA
Jianye Ching, National Taiwan University, Taiwan
Kok Kwang Phoon, Singapore University of Technology and Design, Singapore
Marc Fina, Karlsruhe Institute of Technology, Germany
Marcos Valdebenito, TU Dortmund University, Germany
Mark G. Stewart, University of Technology Sydney, Australia
Matteo Broggi, Leibniz University Hannover, Germany
Mehdi Modares, Illinois Institute of Technology, USA
Michael Hanss, University of Stuttgart, Germany
Michael Shields, Johns Hopkins University, USA
Pei-Pei Li, Beijing University of Technology, China
Pierre Beaurepaire, Sigma Clermont, France
Sifeng Bi, University of Southampton, UK
Steffen Schön, Leibniz University Hannover, Germany
Wei Gao, University of New South Wales, Australia
Xiukai Yuan, University of Xiamen, China

Sponsors and Supporting Institutions

Sponsors



European Safety and Reliability Association



German Research Foundation (DFG)

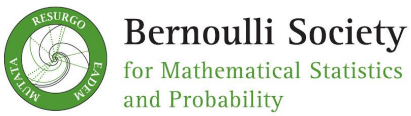


TU Dortmund University

Supporting Institutions



National Chapter of ESRA in China



Bernoulli Society for Mathematical Statistics and Probability

Table of Contents

Preface iv

Organizers vi

Scientific Committee vii

Sponsors and Supporting Institutions viii

Table of Contents ix

Keynote Speakers xii

Junior Keynote Speakers xvi

S1 — Artificial Intelligence, Explainability and Scientific Machine Learning 1
- How Can We Make Reliable Engineering Computing Explainable . . . 1
- Data and Prior Knowledge Driven FMEA Severity Assessment via Deep Attention Networks . . . 15
- Can Large Language Models Find the Design Point? Benchmarking LLM-Based MPP Search in Structural Reliability . . . 27
- Adaptive Kernel Operator Learning for Spatiotemporal Full-Field Reliability Analysis with Mixed Random Inputs . . . 41
- Quantification of modeling uncertainty in physics-informed neural networks by interval arithmetic . . . 57
- Trustworthy Direct Interval Propagation via Conformal Prediction in Neural Network Surrogates . . . 69
- Application of machine learning to reduce model uncertainty and enable resource-efficient design of flat slabs . . . 83

S2 — Reliability Analysis and Sensitivity Methods 99
- Beyond the Design Point: When Equal Failure Probabilities May Not Be Equal . . . 99
- Hybrid Reliability Analysis with Uncertainty in Correlation Coefficients and First Two Statistical Moments . . . 110
- An Efficient Reliability Sensitivity Analysis Method Based on the Method of Moments 121
- A linear-moment-based sensitivity analysis method considering the influence of correlation coefficient . . . 130
- An Efficient Reliability Analysis Method under Hybrid Uncertainty for High-Dimensional Problems . . . 140
- A Bivariate Distribution Based on Squared Normal Transformation . . . 153

S3 — Hybrid, Imprecise and Set-Based Uncertainty 163
- A Hybrid Interval Uncertainty Algorithm for Structural Analysis . . . 163
- A practical framework for failure probability assessment under aleatory and epistemic uncertainty . . . 179
- Possibilistic Filtering for Reliable Robot Localization . . . 193
- Possibilistic Uncertainty Modeling with Hyperellipsoids . . . 204
- Imprecise probabilistic subset simulation for rigorous bounding of the failure probability 219

S4 — Spatial and Temporal Uncertainties **230**
Microstructure compatible random field models of heterogeneous materials 230
A transformation-based framework for modeling and simulation of multivariate non-Gaussian random fields 244
Fuzzy Fields based on the Parallelepiped Dependency Model 255
Surrogate modeling strategy for random fields with uncertain correlation lengths . . . 271
Random field modeling approach for uncertainty quantification of reused concrete elements 287
Three-Dimensional Multivariable Non-Gaussian Random Field Modeling and Simulation of Concrete Constitutive Law 300
Spectrally Consistent Upscaling of Wind Speed Time Series Data 312

S5 — Bayesian Inference, Active Learning and Surrogates **324**
Probability-box propagation with interval prediction models: a reproducible Python workflow 324
Multivariate Active Learning for Polynomial Chaos Expansion 339
Probabilistic Fatigue Life Modelling of Additively Manufactured Aluminum Alloys via Bayesian Inference 350
Combining Bayesian active learning and stratified sampling for bounding small failure probability under hybrid uncertainties 362
PINN-Accelerated Diffusion Models for Amortized Bayesian Inversion of Chloride Transport in Concrete 376
Bayesian Calibration of Resistance Spot Welding Models Using Temporal Process Features and Streamlined Active Learning 392

S6 — Engineering Applications and Monitoring **406**
Stability Analysis of Concrete Gravity Dams under Uncertainty 406
Probabilistic Assessment of Multiphysics-Driven Stochastic Corrosion for the Safety Evaluation of Nuclear Waste Canisters 422
Probabilistic reliability evaluation of autonomous navigation for firefighting robots in uncertain environments 432
Integrating Deterministic and Stochastic Uncertainty in Terrestrial Laser Scanner-based Deformation Monitoring 445
A Holistic Approach to the Life Cycle Assessment of a Propeller System 461

S7 — Stochastic Dynamics and Computational Methods **473**
A generalized autoregressive model for time-variant dynamical systems 473
Stochastic contact analysis and its applications 486
A Continuous-Time Markovian Framework for Performance-Based Earthquake Engineering: Integrated Seismic Risk and Resilience Assessment 495
Neural network-driven uncertainty qualification analysis of printed circuit heat exchangers 507
Towards a Set-Based IVP Solver for ODEs on the GPU 516
Efficient Probabilistic Response Analysis of Large-Scale Engineering Structures under Stochastic Excitation via the DR-PDEE Incorporating an Auxiliary Diffusion Process 532
A Regression-Tree-Based Method for Structural Reliability Assessment 548
Probabilistic Resilience Analysis of Urban Road Network Considering Wind Damage to Street Trees via Dimension-Reduced Probability Density Evolution Equation (DR-PDEE) 560

S8 — Rare Events, Reliability and Optimization **570**
A computationally efficient framework for the propagation of interval-process uncertainty . . . 570
A practical stratified importance sampling strategy for extremely rare event estimation in high dimensional systems . . . 586
Uncertainty Analysis of Fatigue Failure Using a Fuzzy Approach . . . 602
A Weighted Extreme Value Moment Method Using Adaptive Sparse Grids for Time-Variant Reliability-Based Design Optimization . . . 617
Efficient robust topology optimization of large-scale continuum structures under load uncertainty . . . 632
A Bayesian Framework for Modeling and Testing the Temperature-Dependent Residual Compressive Strength of Concrete . . . 641
Optimal-Transport Flow Matching for Stochastic Model Updating: A Comparison with Transitional MCMC-based Bayesian Updating . . . 650

Keynote Speakers

Edoardo Patelli

Professor of Risk and Uncertainty
Centre for Intelligent Infrastructure
University of Strathclyde, UK

Keynote lecture: Robust and Scalable Methods for Large-Scale Networked Systems under Severe Uncertainty



Abstract. Large-scale networked systems are increasingly used to represent critical infrastructures, energy systems, transportation networks, supply chains, and digital twins. Their growing interconnectedness introduces complex dependencies and cascading effects, while the available information is often incomplete, imprecise, or deeply uncertain. In such settings, classical probabilistic methods frequently require assumptions that are difficult to justify and may lead to overconfident predictions and unreliable decisions.

This lecture reviews recent developments in robust and scalable computational methods for analysing large-scale networked systems under severe uncertainty. The focus is on methodologies that explicitly represent incomplete knowledge using interval methods, probability boxes, credal sets, and other imprecise probability frameworks, and on efficient algorithms capable of propagating these uncertainties through complex networks. Particular emphasis is placed on scalable inference methods, including advanced simulation techniques, surrogate modelling, survival signatures, and message-passing algorithms such as the Information Propagation Algorithm, enabling near real-time assessment of large interconnected systems.

The lecture argues that the future of reliability computations lies not in producing increasingly precise predictions, but in developing methods that remain trustworthy when knowledge is fundamentally incomplete and systems continue to grow in scale and complexity.

Biography. Edoardo Patelli is Professor of Risk and Uncertainty and Head of the Centre for Intelligent Infrastructure at the University of Strathclyde, UK. He is also Director of Research in the Department of Civil and Environmental Engineering and Scientific Director of the recently awarded £23M STAND-UP doctoral programme in nuclear engineering and advanced manufacturing. Previously, he served as Deputy Director of the Institute for Risk and Uncertainty and Co-Director of the EPSRC-ESRC Centre for Doctoral Training in Risk and Uncertainty at the University of Liverpool.

His research focuses on uncertainty quantification, imprecise probabilities, reliability analysis, and scalable computational methods for complex systems and networked infrastructures. He has developed methodologies and software tools for robust uncertainty propagation, advanced simulation, network reliability, and decision making under severe uncertainty, with applications in nuclear safety, resilient infrastructure, digital twins, aerospace systems, and human reliability analysis.

Professor Patelli has authored more than 300 scientific publications, including a recent book on engineering uncertainty, and has accumulated more than 6,800 citations with an h-index of 42. He serves on the Executive Board of the International Association for Reliability Engineering and Risk Management (IARERM), is an Advisory Board member of ClimateXchange, and is a member of the Bernoulli Society Committee on Probability and Statistics in the Physical Sciences

Michael Shields

Professor
Department of Civil and Systems Engineering
Johns Hopkins University

Keynote lecture: Uncertainty Quantification & Scientific Machine Learning



Abstract. Uncertainty Quantification (UQ) and Machine Learning (ML) play an increasingly important role in physics-based computational modeling. Especially with the recent rise of scientific machine learning (SciML) and physics-informed ML, new computational tools are being harnessed to solve bigger and more challenging problems. Moreover, UQ has become an integral part of any physics-based modeling effort because all physics-based models, as carefully developed as they may be, are rife with uncertainties (both epistemic and aleatory) in their parameters, inputs/excitations, and sometimes in the form of the models themselves. When SciML methods are then applied in these applications, additional uncertainties are introduced. In this talk, I will broadly introduce the interrelated roles that UQ and ML play in physics-based modeling. I will present several recent advances in UQ and SciML including work on advanced Bayesian neural operators, spectral stochastic neural operators, and physics-informed polynomial chaos expansions, with various applications of interest ranging from multi-scale materials modeling, stochastic modeling of structures subjected to natural hazards, and high energy-density physics.

Biography. Michael D. Shields is a Professor in the Dept. of Civil & Systems Engineering at Johns Hopkins University. Prof. Shields is the Director of the Center on High-Throughput Materials Discovery for Extremes (HT-MAX), holds a secondary appointment in the Dept. of Materials Science and Engineering, and is a fellow of the Hopkins Extreme Materials Institute. Prof. Shields conducts methodological research in uncertainty quantification (UQ), scientific machine learning, probabilistic modeling for problems in mechanics, materials science, and physics with applications ranging from multi-scale material modeling to assessing the reliability and safety of large-scale structures. He received his Ph.D. in Civil Engineering and Engineering Mechanics from Columbia University in 2010, after which he was employed as a Research Engineer in applied computational mechanics at Weidlinger Associates, Inc. He joined the faculty at Johns Hopkins in 2013. For his work in UQ, Prof. Shields has been awarded the ONR Young Investigator Award, the NSF CAREER Award, the DOE Early Career Award, and the Johns Hopkins University Catalyst Award. Prof. Shields and his group also develop the open-source UQpy (Uncertainty Quantification with Python) software, which is a general toolbox and development environment for UQ in computational, mathematical, and physical systems.

Alba Sofi

Associate Professor
Department of Architecture and Design
University Mediterranea of Reggio Calabria

Keynote lecture: Uncertainty Quantification in Structural Engineering Problems using Improved Interval Analysis



Abstract. Realistic numerical modeling of structural systems is essential for obtaining accurate and efficient predictions of system performance. A major challenge in this context is the proper mathematical description of uncertainties affecting numerical models and parameters under limited data. Several uncertainty models beyond the probabilistic confines are currently being used to perform uncertainty quantification in engineering systems. These models are commonly cast within a generalized framework including probabilistic, non-probabilistic (interval model, fuzzy sets, etc.), and mixed or hybrid probabilistic/non-probabilistic approaches.

This lecture addresses uncertainty quantification in structural engineering problems under limited data, using the interval model. Efficient propagation strategies are presented, derived from suitable extensions of classical structural analysis methods within the framework of the Improved Interval Analysis. By leveraging the computing power of finite element solvers, these strategies allow the analysis of complex structural systems with interval parameters, thereby enhancing the application of non-probabilistic approaches in structural design practice.

Biography. Alba Sofi is currently an Associate Professor of Mechanics of Solids and Structures at the University "Mediterranea" of Reggio Calabria, Italy. In 2017, she obtained the National Scientific Qualification as a Full Professor. Dr. Sofi received her Ph.D. degree in Structural Engineering from the University of Palermo, Italy. She held Visiting Fellow positions at the University of Oxford (UK) and the University of New South Wales (Australia). Additionally, she was a Visiting Scholar at Rice University (USA) and a Visiting Professor at Xidian University and Guangzhou University in China. She serves as the Managing Editor of the ASCE-ASME Journal of Risk and Uncertainty in Engineering Systems, Part B: Mechanical Engineering, and is a member of the Editorial Board of several international journals, including the International Journal of Non-Linear Mechanics and Advances in Engineering Software. She serves as the 2nd Vice-Chair of the ASME Safety Engineering & Risk Analysis Division.

Dr. Sofi received the Editor's Award for the Best Paper published in 2020 in the ASCE-ASME Journal of Risk and Uncertainty in Engineering Systems, Part B: Mechanical Engineering. She co-chaired the 9th International Workshop on Reliable Engineering Computing (REC 2021) and has served on the scientific committees of many international conferences.

Dr. Sofi's research interests encompass several areas, including stochastic dynamics, uncertainty quantification with specific expertise in interval analysis, fractional calculus, bridge-vehicle dynamic interaction, cable dynamics, and non-local elasticity theory.

Jianbing Chen

Professor
Department of Structural Engineering, College of Civil Engineering
Tongji University

Keynote lecture: Dynamic reliability of high-dimensional stochastic systems involving parametric uncertainties and nonstationary stochastic excitations



Abstract. Engineering structures and systems involving parametric uncertainties and nonstationary stochastic excitations are widely encountered in engineering fields. However, the response analysis and reliability evaluation of such systems in high dimension has been long time great challenges due to the coupling of nonlinearity and randomness. In the present lecture, a physically-driven probability density evolution method (PDEM) will be outlined. In particular, the dimension-reduced probability density evolution equation (DR-PDEE) has been established for high-dimensional nonlinear systems with or without parametric uncertainties, subjected to either additive or multiplicative excitations, being path-continuous or path-discontinuous. Besides, to quantifying the uncertainty of structural parameters full probabilistically, a new model for multi-variable random fields with between-variable nonlinear correlations was also developed and incorporated. The approach could then be applied to reliability evaluation of real-world large complex structures subjected to disastrous dynamic actions. Problems to be further studied will also be discussed.

Biography. Jianbing Chen is currently University Distinguished Professor of Tongji University in the College of Civil Engineering. He specializes in the area of damage and failure analysis of complex structures, uncertainty quantification, stochastic mechanics, reliability and optimization of engineering structures and systems. Dr. Chen published 4 books and over 210 peer-reviewed journal papers, including the book titled "Stochastic Dynamics of Structures" published by John Wiley & Sons in 2009. He received the National Natural Science Award of China (2016), the 2017 IASSAR Early Achievement Award, the National Science Fund for Distinguished Young Scholars (2017), and the Humboldt Research Award in 2023. He serves as the Chairman of the Executive Board of the International Association for Structural Safety and Reliability (IASSAR), member of Board of Directors of the International Civil Engineering Risk and Reliability Association (CERRA), the reporter of WP1 and Board member of the International Joint Committee on Structural Safety (JCSS), and the Vice President of the Chinese Society for Vibration Engineering, and as associate editors or editorial board members of the international journals including Structure and Infrastructure Engineering, Structural Safety, Probabilistic Engineering Mechanics, Reliability Engineering and System Safety, etc. Dr. Chen has been invited to give invited/keynote lectures for more than 30 times on international/national conferences.

Junior Keynote Speakers

Jingwen Song

Associate Professor
School of Mechanical Engineering
Northwestern Polytechnical University

Keynote lecture: The art of acquisition functions for Bayesian model calibration and its application in additive manufacturing



Abstract. Bayesian model calibration has become a cornerstone of uncertainty quantification for complex engineering systems, it enables the integration of physical simulations, prior knowledge and experimental data to improve prediction accuracy. However, its practical application can be quite challenging due to prohibitive computational cost and complex posterior distributions. Bayesian quadrature equipped with active learning scheme becomes a powerful framework to tackle this challenge. This study comprehensively investigates the art of acquisition functions that dictate the active learning performance in model calibration. A family of acquisition functions are specially designed for quantifying posterior uncertainty, the contribution to evidence uncertainty, the expected reduction of posterior and evidence uncertainty associated with new integration points. These acquisition functions are also extended to the transitional Bayesian quadrature to provide efficient and interpretable mechanisms for balancing exploration and exploitation. The proposed methodologies are further demonstrated in additive manufacturing, particularly with Laser Powder Bed Fusion (LPBF) technology. With melt-pool measurements, Bayesian calibration is employed to update heat-source, material parameters as well as model discrepancy. Additional applications to fatigue-life prediction of additively manufactured aluminum alloys illustrate how Bayesian model calibration supports reliable decision-making under limited experimental data. The presented work offers a unified pathway of Bayesian calibration with acquisition function design to achieve efficient uncertainty quantification in additive manufacturing.

Biography. Dr. Jingwen Song serves as an associate professor in Northwestern Polytechnical University, School of Mechanical Engineering since 2022. She obtained her PhD from Leibniz University Hannover in Germany in 2020, and the doctoral dissertation was awarded "Summa Cum Laude". After graduation, she worked as a research assistant professor in Tokyo City University in Japan until the end of 2021. Her research is focused on data science for risk and reliability analysis, model calibration, sensitivity analysis, as well as the modelling and optimization design for complex structural systems. Within the broad field, she has a particular penchant for exploring efficient computational methods in forward and backward uncertainty quantification by means of advanced Monte Carlo simulation methods and Bayesian machine learning approaches. Dr. Song is also a member of the Early Career Editorial Board of Computers & Structures. She has published more than 20 peer-reviewed publications, and organized several sessions in international conferences.

Xuan-Yi Zhang

Associate Professor
Faculty of Civil Engineering
Beijing University of Technology

Keynote lecture: Moment-Based Sensitivity Analysis Framework for Stochastic Computational Models



Abstract. Computational modeling plays a critical role in engineering analysis and decision-making under uncertainty. When model inputs are described by random variables, the resulting outputs are inherently stochastic, making sensitivity estimation (SE) a fundamental step in quantifying the influence of input uncertainty. However, most conventional SE techniques are centered on input values, rather than the parameters defining the input distributions—limiting our understanding of how uncertainty at the distributional level propagates through complex systems. This presentation introduces a moment-based SE framework that directly evaluates the impact of input distribution parameters on key statistical characteristics of model outputs, including their moments and distributional forms. Sensitivity indices (SIs) are formulated with respect to the first four moments as well as the cumulative distribution function (CDF), enabling a direct assessment of probability-based performance metrics. A numerical post-processing approach is developed to efficiently compute these SIs following standard uncertainty quantification procedures, using moment-based models to approximate output distributions. The applicability and robustness of the method are demonstrated through several case studies, including nonlinear formulations and finite element models. The results highlight the method's ability to capture subtle yet critical sensitivities, offering a broader and more informative perspective for stochastic modeling and reliability assessment.

Biography. Dr. Xuan-Yi Zhang is an Associate Professor at Beijing University of Technology and a Humboldt Research Fellow (2023). She received her Ph.D. in Civil Engineering from Central South University in 2019 and joined BJUT the same year, advancing to Associate Professor in 2022.

Dr. Zhang currently serves as Vice Chair of the Youth Committee of the International Association for Probabilistic Safety Assessment and Management, Deputy Secretary General of the International Society of Lifeline and Infrastructure Earthquake Engineering, and a core member of an innovation team supported by Beijing Municipality.

Her research focuses on structural reliability and risk management, with applications in high-speed railway infrastructure and lifeline engineering. Her work has been applied in engineering practice and supported by several national and municipal research projects. She is committed to fostering a positive academic environment and advancing engineering solutions through both theoretical development and real-world application.

SESSION 1

Artificial Intelligence, Explainability and Scientific Machine Learning

Papers in this session

1. How Can We Make Reliable Engineering Computing Explainable
2. Data and Prior Knowledge Driven FMEA Severity Assessment via Deep Attention Networks
3. Can Large Language Models Find the Design Point? Benchmarking LLM-Based MPP Search in Structural Reliability
4. Adaptive Kernel Operator Learning for Spatiotemporal Full-Field Reliability Analysis with Mixed Random Inputs
5. Quantification of modeling uncertainty in physics-informed neural networks by interval arithmetic
6. Trustworthy Direct Interval Propagation via Conformal Prediction in Neural Network Surrogates
7. Application of machine learning to reduce model uncertainty and enable resource-efficient design of flat slabs

How Can We Make Reliable Engineering Computing Explainable

Olga Kosheleva[1] and Vladik Kreinovich[2]
Departments of [1] Teacher Education and [2] Computer Science, University of Texas at El Paso,
olgak@utep.edu, vladik@utep.edu

Abstract. Complex computations often contain difficult-to-detect mistakes. This problem is very acute for AI-based computations – where 5% of the corresponding answers are wrong, but this happens in more traditional computations as well. A natural way to detect such mistakes is to supplement the actual computation results with some easy-to-understand explanations. This is what researchers are trying to do for AI for make its results more reliable, and this is what we propose to do for computations in general. In this paper, we illustrate this idea on the example of reliable engineering computing, where it is important not only to get an estimate, but to also inform the user how accurate is the provided estimate.

Keywords: reliable engineering computing, explainable computing, uncertainty propagation

1. Need for Explainable Computations

1.1. This need is well understood for AI computations

Nowadays, a significant portion of computations – and decisions in general – is performed by tools using Artificial Intelligence (AI) techniques – such as neural networks. While in many cases, there tools are spectacularly effective, in up to 5% of the cases they produce wrong results – this is called *hallucination* (and in the recent past, this percentage was even higher, up to 15%).

Human professionals also make mistakes, but if in doubt, we can ask, e.g., a doctor how he/she came up with the current diagnosis and, based on that, either follow his/her advice or ask for a second opinion – while Large Language Models like ChatGPT – and other AI tools – do not provide such an explanation.

To make AI results more reliable, it is therefore desirable to make them explainable. In AI community, eXplainable AI – XAI – is indeed one of the main research directions; see, e.g., (Goodfellow et al., 2016).

1.2. We need explanable computing beyond AI computations

In non-AI computations, mistakes are not that frequent, but they still occur. To minimize the number of such mistakes, it is therefore desirable to make *all* computations explainable – not only AI-related computations.

Computers are not perfect, we are not perfect when we program them, so when we have results of complex computations, they may be wrong. Many mathematicians remember the first computer-based proof of the four-color theorem (that every planary graph can be colored in 4 colors so that no

© 2026 by the author(s). This work is licensed under the Creative Commons Attribution 4.0 International License (CC BY 4.0), which permits unrestricted use, distribution, and reproduction in any medium, provided the original author and source are credited.

two neighbors have the same color). This proof was too long to be understandable, and eventually, a mistake was found. This mistake did not invalidate the correctness of the result, but only until an understandable proof appeared, the mathematical community accepted this theorem as being proven.

One of us (VK) had personal experience with how such back-of-the-envelope computations help avoid mistakes. For several semester, he was teaching Introduction to Computing class for Engineering and Science majors. To make the material more interesting and relevant for students, programming examples in such classes are usually formulated not in abstract computational terms, but in terms simulating a real-life problem. Interestingly, physics students made much fewer mistakes than others – since they had an intuition that allowed them to have back-of-the envelope estimations of the desired result. So, when the computer output differed from these estimates, they knew that something was wrong in their program.

Not only physics majors, we all have this ability to some degree. For example, a recent research (Fadelli, 2026; Zenon et al., 2026) has shown that even when we perform simple arithmetic operations, we usually start – even before we finish understanding the problem – to perform some estimates for the desired result – to make sure that what we compute later is not a mistake. For example, if we are asked to add a two-digit number (e.g., 37) with a one-digit number, then before even we hear the second digit of the first number, we estimate that the sum should start with 3 or 4 – so that if later on our computations will get a number starting with a 5, we will know that we have made a mistake.

1.2.1. *The need to make computations explainable is well understood in physics*

The need to supplement computations with understandable explanations is well-known in physics, where such explanations are known as *back-of-the envelope* computations – since to be truly easy-to-understand, these explanations should fit in the back of the envelope. In some cases, this term is taken literally: there is a well-known story how Einstein's wife was having a tour of a large telescope and naively asked what was its main purpose. When the tour guide explained that this telescope is needed to understand the structure of the Universe, she replied that her husband does it on the back on an envelope.

This may be an anecdote, but Einstein was indeed very good in such simplifying computations (and, by the way, he was not as good in more complex computations: in these, he needed help). It has been sad that any student roaming the streets of Goettingen knew mathematics better than Einstein, but he had intuition that allowed him to solve many physics problems better than anyone else. For example, the most famous mathematician of that time David Hilbert – whom in 1900 the world-wide mathematics community asked to come up with the list of most important challenging problems for the 20 century mathematicians – came up with equations of General Relativity in 1916, only two weeks later than Einstein. But even Hilbert did it two weeks earlier than Einstein, still Einstein would have been praised as one of the main authors of this theory: while all Hilbert did was coming up with a complex systems of partial differential equations, Einstein uses his physics intuition to come up with first approximation solutions. These solutions enabled the researchers to experimentally test and confirm this theory in 1919 (as soon as the First World War was over in late 1918 and large-scale experimental science could be resumed).

1.3. The need for explainable computations is especially important for reliable engineering computing

The need to be explainable is also important for reliable engineering computations, when we not only produce a numerical result, but we also produce a measure of its accuracy – e.g., the upper bound Δ on this result's approximation error (Jaulin et al., 2012; Kubica, 2019; Mayer, 2017; Moore at al., 2009; Rabinovich, 2005) or the standard deviation σ of the approximation error (BIPM, 2028; BIPM, 2028a; BIPM, 2011; Rabinovich, 2005). So, it's important to make computation of Δ and/or σ explainable too.

Explainability is especially important for estimating accuracy of the computation results – since while we often have intuition about the physical phenomena that we are trying to predict and can thus detect computation errors, we rarely have intuition about the computation accuracy. So, without understandable explanations, we may miss computation errors.

1.4. What we do in this paper

In this paper, we provide guidance about how to make reliable engineering computing explainable – or at least more explainable.

1.5. Important comment: there are other reasons why we need explainable computations – reasons that go beyond the topics of this paper

It should be mentioned that in physics and in other disciplines, there are other reason why we need to supplement computations with explanations, a reason that goes beyond what we study in this paper.

1.5.1. *First reason: equations are often approximate*

This reason is that the equations that are used in the computations – and the models that underlie these computations – are often only approximate. To a naive mathematician, the equations that a physicist or a chemist provide to him/her may sound like an Ultimate Truth directly from Mount Sinai, but physicists, chemists, and engineers know that these equations and these models are only approximate. So, whatever results we get by using these computations need to taken with a grain of salt: if they do not agree with common sense, there is a good chance that they are caused by the approximate character of the equations. Every non-fundamental equation is approximate:

- Ohm's law is approximate – sometimes we see non-linear dependence of voltage on current,
- laws of chemical kinetics are only approximate – more complex equations are needed when the concentrations become high, etc.

In some cases, it is clear when the results of using approximate models are wrong. For example, in many cases, we observe exponential growth:

- a colony of bacteria – when left with a source of food – grows exponentially,
- population grows exponentially,

– economy grows exponentially during a boom,

– the need for new AI researchers (or any other hot-topic researchers) grows exponentially for some period of time, etc.

These exponential models – and many other approximate models in general – are useful to predict short-term future developments, but long-term, they make no sense. For example, since the need for AI professionals grows faster than the population, after a while, we will have more AI professionals than humans – this makes no sense. In this case, the mistake caused by using approximate models is easy to see, but there are other cases when results are not that crazy but still wrong. In these cases, explainable computations can help detect such erroneous uses of approximate models.

Physicists know that even when we use fundamental physical equations, we need to be careful – since these equations are not perfect. Let us give a mathematically (rather) simple example from (Feynman et al., 2005): what is the overall energy of an electron? It consists of:

– the energy $E = m_0 \cdot c^2$ corresponding to the electron's rest mass m_0, and

– the overall energy of the electric field generated by the electron.

Let us compute this energy. The electron is an indivisible elementary particle, it does not have any separate parts. So, according to special relativity, it must be a pointwise particle – otherwise, if it occupied two different spatial locations, we could be able to consider parts located at these location as separate parts. The electric field of an electron at each spatial point is determined by Coulomb's law $|\vec{E}| = c_1 \cdot q/r^2$, where c_1 is a constant whose value depends on the choice of measuring units, q is the electric charge of the electron, and r is the distance from given point to the electron. It is known that the energy density $\rho(x)$ of the electric field at each spatial location is proportional to the square of the electric field: $\rho(x) = c_2 \cdot |\vec{E}|^2$ for some constant c_2. Thus, we have $\rho(x) = c_3/r^4$, where we denoted $c_3 \stackrel{\text{def}}{=} c_2 \cdot c_1^2$. The overall energy $\mathcal{E}$ of the electric field can be obtained if we integrate the energy density over the whole space:

$$\mathcal{E} = \int \frac{c_3}{r^4}\, dV.$$

Since the integrated function depends only on the distance r, we can integrate over each sphere of this radious r – whose area is $4 \cdot \pi \cdot r^2$ – and then integrate over r:

$$\mathcal{E} = \int_0^\infty \frac{c_2}{r^4} \cdot 4 \cdot \pi \cdot r^2\, dr = c_3 \cdot \int_0^\infty \frac{1}{r^2}\, dr = -\frac{1}{r}\Big|_{r=0}^{r=\infty}.$$

One can see that the result is infinite – which makes no sense from the physical viewpoint: the energy of a tiny electron is clearly bounded and very small.

In this example, it is clear that the result makes no physical sense, but in other cases, when the result is finite, we need to use common sense – i.e., explainable computations – to check that the result makes sense.

1.5.1.1. *Comment* There have been some similar physically meaningless infinite results in classical (pre-quantum) physics. Some of them got resolved with the appearance of quantum ideas – the very

idea of quantum physics appeared when Max Planck tried to explain why the overall energy of a black body radiation is not infinite. However, many meaningless infinities – such as the overall energy of an electron – remain in quantum physics.

The above example does not mean that computing the electron's overall energy remains an open problem – in this and many other cases, physicists have found some ways around – but if we do know that and just try to uncritically use equations, you get nonsense. This is, by the way, why it is still not clear whether quantum computing (see, e.g., (Nilesen and Chuang, 2013)) can lead to an exponential speedup: in contrast to problems like $P \stackrel{?}{=} NP$, where the mathematical formulation is clear and precise but no one knows how to solve it, for the quantum question, we do not even have a precise formulation of the problem – since we do not have a fully consistent precise general mathematical formulation of quantum physics.

1.5.2. *Second reason: equations are sometimes too difficult to solve*
Another reason why we need back-of-the envelope computations is that often, the corresponding equations are too complex to be solved. In such cases, it is desirable to have simpler explainable models that would enable us to provide at least some reasonable estimates for the desored quantities.

2. Analysis of the problem

2.1. Why do we perform computations in the first place

Let us go back to our problem: how to make reliable engineering computing more explainable. To better understand this problem, let us first recall why we need computations in the first place. What do we want in general? We want to understand the world, and we want to make it better. Understanding the world means knowing the values of the all the physical quantities that describe the state of the world, knowing these values in all spatial locations and at all moments of time.

- Some of these quantities we can measure directly – e.g., the current temperature and the current wind speed.
- Many other quantities are difficult – or even impossible – to measure directly.

For example:

- it is difficult to measure the temperature at some difficult-to-reach location, and
- it is not possible to directly measure tomorrow's temperature.

To estimate such not-easy-to-directly-measure quantities, we can use known relation between these quantities and some easier-to-measure ones. For example, to predict tomorrow's temperature, we can:

- measure temperature, wind speed, humidity at different locations, and then
- use known equations to make the desired prediction.

In general, such computations are one of the main uses of computers.

Another use of computations is related to changing the world. We would like to predict what will happen:

- if we perform a certain action – e.g., seed the clouds to cause rain, and/or
- if we come up with a design – e.g., a new design for a meteorological rocket.

Ideally, we should also come up with an optimal action and/or optimal design: action and/or design that optimize the appropriate objective function. For this, we also need computations.

2.2. Why computation results are not absolutely accurate: three main reasons and why we concentrate on only one of the them

We would like to know the exact values of the not-easy-to-directly-measure quantities, we would like to exactly know the parameters corresponding to optimal actions and designs. However, as a result of computations, we only get approximate values. There are three reasons for this:

- First, the models that we use are usually only approximate, they only provide an approximate relation between the physical quantities. We, on the computational side, cannot do much about that – this is what physicists have been doing since the beginning of science.
- Second, our algorithms are often only approximate. Whether we use finite element methods to solve systems of partial differential equations, whether we use a continuous-media approximation to describe interactions between atoms and molecules – we do not get exact results. Coming up with better algorithms is difficult, many researchers are working on this. For each specific computational problem, coming up with better algorithms is an important challenge, and we do not see how explainability – the main topic of this paper – can help.
- Finally, the results are not accurate because the values that we feed into the algorithms are not absolutely accurate: they come from measurements, and measurements are never absolutely accurate. In other words, the results are not absolutely accurate because uncertainty of the inputs propagates through our algorithm. The resulting uncertainty is what we will concentrate on in this paper.

2.3. How to describe uncertainty propagation: reminder

Let us denote the inputs to a data processing algorithm by $x_1, \ldots, x_n$, and the result of applying this algorithm by $f(x_1, \ldots, x_n)$. In the ideal world, we should apply the algorithm to the actual values x_i of the corresponding quantities. However, as we have mentioned, we do not know these exact values. Instead, we know approximate values $\widetilde{x}_i$ – that are:

- either obtained directly by measurements
- or obtained indirectly, by applying some other algorithms to measurement results.

For all the inputs, the approximation error $\Delta x_i \stackrel{\text{def}}{=} \widetilde{x}_i - x_i$ is different from 0. Since we are using approximate values of the inputs, instead of the ideal value $y = f(x_1, \ldots, x_n)$, we get an approximate value $\widetilde{y} = f(\widetilde{x}_1, \ldots, \widetilde{x})$. We are interested in estimating the resulting approximation error

$$\Delta y \stackrel{\text{def}}{=} \widetilde{y} - y = f(\widetilde{x}_1, \ldots, \widetilde{x}_n) - f(x_1, \ldots, x_n).$$

By definition of the approximation error Δx_i, we have $x_i = \widetilde{x}_i - \Delta x_i$. Thus, the above formula for Δy taes the following form:

$$\Delta y = f(\widetilde{x}_1, \ldots, \widetilde{x}_n) - f(\widetilde{x}_1 - \Delta x_1, \ldots, \widetilde{x}_n - \Delta x_n).$$

Measurement errors are usually reasonably small, e.g., about 10%. For such values, their square is much smaller than the error itself: e.g., the square of 10% is 1% which is indeed much smaller. So, to estimate Δy, we can use the techniques that are often used in physics (see, e.g., (Feynman et al., 2005; Thorne and Blanford, 2021)): we can expand the dependence of Δy on Δx_i in Taylor series and ignore quadratic and higher order terms in this expansion. As a result, we get the following formula:

$$\Delta y = \frac{\partial f}{\partial x_1} \cdot \Delta x_1 + \ldots + \frac{\partial f}{\partial x_n} \cdot \Delta x_n.$$

Depending on what we know about Δx_i, we can come up with conclusions about Δy.

Sometimes, we know the probabilities of different possible values of Δx_i. If the mean value of Δx_i is not 0, then we re-calibrate this measuring instrument – by subtracting this mean error from all the measurement results. For example, if before I step on my home scales, I see 2 lbs, I simply subtract 2 lbs from all the measurement results. So, in this case, we can safely assume that the mean value of Δx_i is 0. In this case, the mean value of Δy is also 0, and for the variance σ^2, we have the formula

$$\sigma^2 = \left(\frac{\partial f}{\partial x_1}\right)^2 \cdot \sigma_1^2 + \ldots + \left(\frac{\partial f}{\partial x_n}\right)^2 \cdot \sigma_n^2,$$

where σ_i^2 is the variance of Δx_i.

Sometimes, we only know the upper bound Δ_i on the absolute value $|\Delta x_i|$ of the measurement error Δx_i: $|\Delta x_i| \le \Delta_i$. This case is known as *interval uncertainty*, since in this case, based on measurement result $\widetilde{x}_i$, the only information that we have about the actual (unknown) value x_i is that this value is located in the interval $[\widetilde{x}_i - \Delta_i, \widetilde{x}_i + \Delta_i]$. Why don't we know the probabilities?

– This can happen because we have a state-of-the-art measuring instrument, for which no more-accurate instrument is known, so we can cannot find the probabilities by comparing the results of the two instruments – as these probability are usually determined.

– This may also happen because comparing the results of these two measuring instrument takes time and money, and if we have many sensors, calibrating each of them will cost too much. If we launch a spaceship to the Moon, then yes, we want to perform as many tests as needed, but if we are predicting weather, it does not make economic sense to determine probability distributions for thousands of sensors.

In such interval cases, all we know about Δy is the upper bound Δ on the absolute value $|\Delta y|$ of Δy:

$$\Delta = \left|\frac{\partial f}{\partial x_1}\right| \cdot \Delta_1 + \ldots + \left|\frac{\partial f}{\partial x_n}\right| \cdot \Delta_n.$$

In both probabilistic and interval cases, we can get partial derivatives, e.g., by using numerical differentiation:

$$\frac{\partial f}{\partial x_1} \approx \frac{f(\widetilde{x}_1, \ldots, \widetilde{x}_{i-1}, \widetilde{x}_i + h_i, \widetilde{x}_{i+1}, \ldots, \widetilde{x}_n) - \widetilde{y}}{h_i}$$

for some small h_i.

2.3.0.1. *Comment* Sometimes, the approximation error Δx_i has two components:

- systematic error component about which we only know the upper bound, and
- the random error component, about which we know the standard deviation.

In this case, we need:

- to separately process systematic error components – to get the systematic error component of the resulting error Δy, and
- to separately process random error components – to get the random error component of the resulting error Δy.

2.4. When n is small, the resulting computations are reasonably explainable

When the number of inputs is small, the above procedure is easy to implement and easy to compute – so in this sense, we have a reasonably explainable procedure.

2.5. But what if n is large?

In many practical situations – e.g., in weather prediction – we deal with thousands of inputs – while the prediction itself takes an hour or so on a high-performance computer. If we simply compute all the partial derivatives, this will take too much time. We can use Monte-Carlo simulations – but this required repeating computations are least 25 times – to get the 20% accuracy of estimating σ or Δ, and this will take too much time.

This is where we need explainable computing. For large n, we usually have a few most important inputs – inputs that provide the largest contribution to the overall accuracy estimation. For example, this may be inputs for which the corresponding partial derivatives are the largest. Without losing generality, let us assume that these inputs are $x_1, \ldots, x_r$ for some small r. Then, we can compute – in an explainable way – the values

$$\left(\sigma^{(0)}\right)^2 = \left(\frac{\partial f}{\partial x_1}\right)^2 \cdot \sigma_1^2 + \ldots + \left(\frac{\partial f}{\partial x_r}\right)^2 \cdot \sigma_r^2$$

and

$$\Delta^{(0)} = \left|\frac{\partial f}{\partial x_1}\right| \cdot \Delta_1 + \ldots + \left|\frac{\partial f}{\partial x_r}\right| \cdot \Delta_r.$$

To find the desired values $\sigma^2 = \left(\sigma^{(0)}\right)^2 + \left(\sigma^{(1)}\right)^2$ and $\Delta = \Delta^{(0)} + \Delta^{(1)}$, we need to be able to compute the contribution of all the remaining terms:

$$\left(\sigma^{(1)}\right)^2 = \left(\frac{\partial f}{\partial x_{r+1}}\right)^2 \cdot \sigma_{r+1}^2 + \ldots + \left(\frac{\partial f}{\partial x_n}\right)^2 \cdot \sigma_n^2$$

and

$$\Delta^{(1)} = \left|\frac{\partial f}{\partial x_{r+1}}\right| \cdot \Delta_{r+1} + \ldots + \left|\frac{\partial f}{\partial x_n}\right| \cdot \Delta_n.$$

In both cases, each term corresponding to $n-r$ remaining inputs may be small, but there are many of them, so their overall contribution cannot be ignored.

3. Our main idea and the resulting formulas

3.1. Idea

The need to deal with a large number of terms is ubiquitous in physics. For example, any body consists of about 10^{23} molecules. We know the equations that describe their dynamics, but there is no way we can deal with that many equations. So what do physicists do? Different molecules move differently – and they are largely independent from each other. From our viewpoint, these motions look random. So, instead of considering individual motions, we can assume that they all follow some probability distribution.

This is what statistical physics does. The overall effect is a joint effect of many small independent random effects. In such case, according to the Central Limit Theorem, for large n, the distribution of the resulting effect is close to Gaussian; see, e.g., (Sheskin, 2011). In general, to describe a normal distribution, it is sufficient to know the mean value m and the standard deviation s. Then, with any desired confidence level, we can conclude that then actual values does not exceed $m + k_0 \cdot s$, where k_0 depends on the confidence level:

- to reach 95% confidence, we can take $k_0 = 2$;
- to reach 99.9% confidence, we can take $k_0 = 3$; and
- to reach confidence $1 - 10^{-8}$, we can take $k_0 = 6$.

Let us apply this idea to our case.

3.2. Ket us apply this idea: details

Both for probabilistic and for interval uncertainty, the formula for the desired value V describing uncertainty is the sum of $n - r$ products of the type $d \cdot a$, where:

– d is a factor related to the partial derivative of the data processing function, and

– a is a factor related to input uncertainty.

We assume:

– that the values d and a corresponding to different inputs are independent, and

– that the values d and a corresponding to the same input are also independent of each other.

In this case, the mean value m of the sum V is equal to the sum of the mean values $E[d \cdot a]$, each of which is the product of the mean values: $E[d \cdot a] = m_d \cdot m_a$, where we denoted $m_d \stackrel{\text{def}}{=} E[d]$ and $m_a \stackrel{\text{def}}{=} E[a]$. Thus, we have $m = (n - r) \cdot m_d \cdot m_a$.

Similarly, the variance s^2 of the sum V is equal to the sum of the variances. The variance of the product $d \cdot a$ can be computed as the difference

$$E[d^2 \cdot a^2] - (E[d \cdot a])^2 = s_d \cdot s_a - m_d^2 \cdot m_a^2,$$

where we denoted $s_d \stackrel{\text{def}}{=} E[d^2]$ and $s_a \stackrel{\text{def}}{=} E[a^2]$. Now, with the corresponding confidence, we can conclude that the actual value of v is bounded by $m + k_0 \cdot s$.

Good news is that to find all these expected values, we do not need to consider all inputs and all possible inputs x_i – it is sufficient to consider a random sample. Another good news is that the characteristics of d can be pre-computed beforehand and can be then used for different accuracies a. So, we arrive at the following formulas.

3.3. Resulting formulas: case of probabilistic uncertainty

First, out of the practically encountered input tuples $(x_1, \ldots, x_n)$, randomly select a few. For each of K selected input tuples, randomly select one of the $n - r$ remaining inputs, and use numerical differentiation to compute the corresponding partial derivative D_k. Based on the resulting values $D_1, \ldots, D_K$, compute two arithmetic averages:

$$m_d = \frac{1}{K} \cdot \sum_{k=1}^{K} D_k^2 \text{ and } s_d = \frac{1}{K} \cdot \sum_{k=1}^{K} D_k^4.$$

Then, randomly select K of the remaining $n - r$ inputs $i_1, \ldots, i_K$, and record the corresponding values $\sigma_{i_k}^2$. Based on these values, compute the following two arithmetic averages:

$$m_a = \frac{1}{K} \cdot \sum_{k=1}^{K} \sigma_{i_k}^2 \text{ and } s_a = \frac{1}{K} \cdot \sum_{k=1}^{K} \sigma_{i_k}^4.$$

Then, we can conclude that:

– on average, the standard deviation σ^2 of Δy is equal to $m = (n - r) \cdot m_d \cdot m_a$, and

– that with confidence level depending on k_0, the actual standard deviation is bounded by the value

$$m + k_0 \cdot \sqrt{(n-r) \cdot (s_d \cdot s_a - m_d^2 \cdot m_a^2)}.$$

3.4. Resulting formulas: case of interval uncertainty

First, out of the practically encountered input tuples $(x_1, \ldots, x_n)$, randomly select a few. For each of K selected input tuples, , randomly select one of the $n-r$ remaining inputs, and use numerical differentiation to compute the corresponding partial derivative D_k. Based on the resulting values $D_1, \ldots, D_K$, compute two arithmetic averages:

$$m_d = \frac{1}{K} \cdot \sum_{k=1}^{K} |D_k| \text{ and } s_d = \frac{1}{K} \cdot \sum_{k=1}^{K} D_k^2.$$

Then, randomly select K of the remaining $n-r$ inputs $i_1, \ldots, i_K$, and record the corresponding values Δ_{i_k}. Based on these values, compute the following two arithmetic averages:

$$m_a = \frac{1}{K} \cdot \sum_{k=1}^{K} \Delta_{i_k} \text{ and } s_a = \frac{1}{K} \cdot \sum_{k=1}^{K} \Delta_{i_k}^2.$$

Then, we can conclude that:

– on average, the upper bound Δ of Δy is equal to $m = (n-r) \cdot m_d \cdot m_a$, and

– that with confidence level depending on k_0, the actual standard deviation is bounded by the value

$$m + k_0 \cdot \sqrt{(n-r) \cdot (s_d \cdot s_a - m_d^2 \cdot m_a^2)}.$$

3.5. How we can improve these estimates

In deriving the above estimates, we considered all the inputs. In practice, often, inputs can be naturally divided into several classes. For example, inputs for weather prediction can be divided into:

– inputs corresponding to temperature,

– inputs corresponding to wind speed, and

– inputs corresponding to humidity.

These sensors are different, so it makes sense, instead of averages overall the inputs, to consider averages over each group of inputs. The formulas will be similar, except that now we need to compute several terms. Here is how the above formulas need to be modified when we have G groups of inputs with N_g elements in each of the groups g.

For the case of probabilistic uncertainty, first, out of the practically encountered input tuples $(x_1, \ldots, x_n)$, randomly select a few. For each of K selected input tuples, for each group g, randomly select an input from this group, and use numerical differentiation to compute the corresponding derivative $D_{g,k}$. Based on the resulting values $D_{g,1}, \ldots, D_{g,k}k$, compute, for each group, two arithmetic averages:

$$m_{g,d} = \frac{1}{K} \cdot \sum_{k=1}^{K} D_{g,k}^2 \text{ and } s_{g,d} = \frac{1}{K} \cdot \sum_{k=1}^{K} D_{g,k}^4.$$

Then, in each group g, randomly select K of its inputs $i_{g,1}, \ldots, i_{g,K}$, and record the corresponding values $\sigma^2_{i_{g,k}}$. Based on these values, compute, for each group g, the following two arithmetic averages:

$$m_{g,a} = \frac{1}{K} \cdot \sum_{k=1}^{K} \sigma^2_{i_{g,k}} \text{ and } s_{g,a} = \frac{1}{K} \cdot \sum_{k=1}^{K} \sigma^4_{i_{g,k}}.$$

Then, we can conclude that:

- on average, the standard deviation σ^2 of Δy is equal to

$$m = \sum_{g=1}^{G} N_g \cdot m_{g,d} \cdot m_{g,a},$$

  and

- that with confidence level depending on k_0, the actual standard deviation is bounded by the value

$$m + k_0 \cdot \sqrt{\sum_{g=1}^{G} N_g \cdot (s_{g,d} \cdot s_{g,a} - m_{g,d}^2 \cdot m_{g,a}^2)}.$$

Similarly, for the case of interval uncertainty, first, out of the practically encountered input tuples $(x_1, \ldots, x_n)$, randomly select a few. For each of K selected input tuples, for each groups g, randomly select an input from this group, and use numerical differentiation to compute the corresponding derivative $D_{g,k}$. Based on the resulting values $D_{g,1}, \ldots, D_{g,k}k$, compute, for each group, two arithmetic averages:

$$m_{g,d} = \frac{1}{K} \cdot \sum_{k=1}^{K} |D_{g,k}| \text{ and } s_{g,d} = \frac{1}{K} \cdot \sum_{k=1}^{K} D_{g,k}^2.$$

Then, in each group g, randomly select K of its inputs $i_{g,1}, \ldots, i_{g,K}$, and record the corresponding values $\sigma^2_{i_{g,k}}$. Based on these values, compute, for each group g, the following two arithmetic averages:

$$m_{g,a} = \frac{1}{K} \cdot \sum_{k=1}^{K} \Delta_{i_{g,k}} \text{ and } s_{g,a} = \frac{1}{K} \cdot \sum_{k=1}^{K} \Delta^2_{i_{g,k}}.$$

Then, we can conclude that:

– on average, the upper bound Δ of Δy is equal to

$$m = \sum_{g=1}^{G} N_g \cdot m_{g,d} \cdot m_{g,a},$$

and

– that with confidence level depending on k_0, the actual upper bound Δ is bounded by the value

$$m + k_0 \cdot \sqrt{\sum_{g=1}^{G} N_g \cdot (s_{g,d} \cdot s_{g,a} - m_{g,d}^2 \cdot m_{g,a}^2)}.$$

Acknowledgements

This work was supported by the AT&T Fellowship in Information Technology, by the Institute for Risk and Reliability, Leibniz Universitaet Hannover, Germany, by the Deutsche Forschungsgemeinschaft (DFG, German Research Foundation) Focus Program SPP 100+ 2388, Grant Nr. 501624329, by the European Union under the project ROBOPROX (No. CZ.02.01.01/00/22 008/0004590), by the Center of Excellence in Econometrics, Faculty of Economics, Chiang Mai University, Thailand, by the Ho Chi Minh City University of Banking, Vietnam, and by Thang Long University, Hanoi, Vietnam.

The authors are greatly thankful to the anonymous referees for valuable suggestions.

References

BIPM, IEC, IFCC, ILAC, ISO, IUPAC, IUPAP, OIML. Evaluation of Measurement Data. Guide to the Expression of Uncertainty in Measurement. *Joint Committee for Guides in Metrology (JCGM)* 100:2008, 2008.

BIPM, IEC, IFCC, ILAC, ISO, IUPAC, IUPAP, OIML. Evaluation of Measurement Data. Supplement 1 to the "Guide to the Expression of Uncertainty in Measurement": Propagation of Distributions Using a Monte Carlo Method. *Joint Committee for Guides in Metrology (JCGM) 101:2008, 2008.*

BIPM, IEC, IFCC, ILAC, ISO, IUPAC, IUPAP, OIML. Evaluation of Measurement Data. Supplement 2 to the "Guide to the Expression of Uncertainty in Measurement": Extension to Any Number of Output Quantities, Joint Committee for Guides in Metrology (JCGM) 102:2011, 2011.

Fadelli, I. Mental Math's Shortcut – Pupil Dilation Suggests People Start Solving Before All Numbers Are In. *Physics News*, 2026, https://phys.org/news/2026-04-mentak-math-shortcut-pupil-ddilation.html

Feynman, R., R. Leighton, and M. Sands. *The Feynman Lectures on Physics*. Addison Wesley, Boston, Massachusetts, 2005.

Goodfellow, I., Y. Bengio, and A. Courville, *Deep Learning*, MIT Press, Cambridge, Massachusetts, 2016.

Jaulin, L., M. Kiefer, O. Didrit, and E. Walter. *Applied Interval Analysis, with Examples in Parameter and State Estimation, Robust Control, and Robotics*. Springer, London, 2012.

Kubica, B. J. *Interval Methods for Solving Nonlinear Constraint Satisfaction, Optimization, and Similar Problems: from Inequalities Systems to Game Solutions*. Springer, Cham, Switzerland, 2019.

Mayer, G. *Interval Analysis and Automatic Result Verification*. de Gruyter, Berlin, 2017.

Moore, R. E., R. B. Kearfott, and M. J. Cloud. *Introduction to Interval Analysis*. SIAM, Philadelphia, 2009.

Nielsen, M. A., and I. L. Chuang, *Quantum Computation and Quantum Information*, Cambridge University Press, Cambridge, U.K., 2011.

Rabinovich, S. G. *Measurement Errors and Uncertainty: Theory and Practice*. Springer Verlag, New York, 2005.

Sheskin, D. J. Handbook of Parametric and Nonparametric Statistical Procedures. Chapman and Hall/CRC, Boca Raton, Florida, 2011.

Thorne, K. S., and R. D. Blandford. *Modern Classical Physics: Optics, Fluids, Plasmas, Elasticity, Relativity, and Statistical Physics*. Princeton University Press, Princeton, New Jersey, 2021.

Zénon, A., S. Salbagio, and M. Andres. Pupil Size Variations Reveal Bayesian Inference in Cognitive Arithemtic. *Proceedings of the Royal Society B: Biological Sciences*, 293:10151937, 2026, doi 10.1098/rspb.2025.1937

Data and Prior Knowledge Driven FMEA Severity Assessment via Deep Attention Networks

Hui Huang[1], Jieyu Chen[2], Baihong Zhong[3]
1)China Electronic Product Reliability and Environmental Testing Research Institute (CEPREI); Key Laboratory of Industrial Equipment Quality Big Data, MITT, Guangzhou 510610, China, 183165263@qq.com.
2)China Electronic Product Reliability and Environmental Testing Research Institute (CEPREI); Key Laboratory of Industrial Equipment Quality Big Data, MITT,Guangzhou 510610, China, ceprei_chenjy@163.com (Corresponding author).
3)China Electronic Product Reliability and Environmental Testing Research Institute (CEPREI); Key Laboratory of Industrial Equipment Quality Big Data, MITT, Guangzhou 510610, China, China, zhongbh@163.com (Corresponding author).

Abstract: Traditional Failure Mode and Effects Analysis (FMEA) suffers from subjectivity and static assumptions in severity evaluation, especially when applied to complex, data-rich industrial systems. To overcome these limitations, this paper proposes a new dynamic FMEA severity quantification hybrid framework that integrates real-time equipment status monitoring data with domain prior knowledge through deep learning. A deep attention network is proposed to capture long-term dependencies in multivariate sensor streams, while adaptively processing key health status features through attention mechanisms. Engineering prior knowledge is utilized to establish fault severity degrees, integrating real-time equipment condition monitoring data to quantify FMEA severity, thereby enabling a dynamic quantitative representation of FMEA severity. Experimental verification on real industrial datasets shows that the proposed method can achieve dynamic FMEA severity assessment of equipment. This work bridges the gap between predictive health monitoring and equipment risk assessment, providing a practical solution for reliability centered maintenance in data rich industrial environments.

Keywords: Failure Mode and Effects Analysis (FMEA); Severity assessment; Attention mechanism; Reliability engineering; Predictive maintenance.

1. Introduction

The running reliability of the equipment is decisive for the system safety, production efficiency and economic benefits[1]. The occurrence of equipment failure can readily lead to shutdown and production disruption, thereby causing safety incidents, environmental pollution, significant economic losses, and even posing a threat to personnel safety[2-3]. For instance, within critical infrastructure sectors like power equipment, equipment failures exhibit characteristics of contagion, abruptness, and catastrophic impact, and minor malfunctions may trigger a chain reaction, culminating in severe repercussions such as regional power grid collapse and interruption of energy supply[4]. Consequently, precisely assessing the severity of equipment failures and proactively identifying high-risk failure patterns constitute the essential prerequisite for ensuring the safe and stable operation of equipment.

As a classic reliability analysis and risk assessment method, failure mode and effects analysis (FMEA) systematically identifies potential failure modes in equipment, analyzes the causes and impacts of these

© 2026 by the author(s). This work is licensed under the Creative Commons Attribution 4.0 International License (CC BY 4.0), which permits unrestricted use, distribution, and reproduction in any medium, provided the original author and source are credited.

failures, quantitatively evaluates the severity, occurrence probability, and detectability of failures, and calculates the risk priority number (RPN)[5-6], which provides a basis for failure prevention and maintenance decision-making. FMEA has been extensively applied across all stages of the equipment life-cycle, emerging as a crucial method for enhancing equipment reliability and safety. However, traditional FMEA severity assessments heavily rely on expert experience and qualitative judgment, leading to subjective and inconsistent results. Furthermore, traditional FMEA, being based on a static, experience-driven approach, struggles to accommodate the operational characteristics of dynamic systems such as power equipment. It fails to track the real-time evolution of equipment health status, resulting in delayed severity assessments and inadequate targeting of preventive maintenance, thereby falling short of meeting the real-time risk management and control requirements of dynamic systems.

With the rapid advancement of sensor technology and big data analytics, the comprehensive collection and deep mining of equipment operational data have become feasible. The data-driven approach offers a novel avenue to overcome the limitations inherent in traditional FMEA, and it has been successfully implemented in various scenarios, including fault diagnosis, health assessment, and life prediction[7-9]. By extracting latent fault feature and health status information from the operational data, dynamic perception and quantitative evaluation of equipment conditions can be achieved. By integrating the data-driven approach with FMEA theory, a data-driven dynamic severity assessment method for FMEA can be established, which compensates for the deficiencies of traditional FMEA methods in dynamic system applications.

This paper introduces a FMEA severity assessment method grounded in a deep attention network, designed to surmount the constraints of traditional approaches that rely heavily on experience and static evaluation, and to offer a novel technical pathway for quantifying equipment risks within dynamic systems. This method employs the deep attention network to thoroughly analyze the time-series signals generated during equipment operation, precisely identify the degradation patterns of health status, and automatically highlight critical features closely associated with the progression of health status degradation through the attention mechanism, thereby enhancing the precision and efficacy of feature extraction. Building upon this, the FMEA severity degrees are classified by integrating domain-specific prior knowledge, establishing a data-driven FMEA severity assessment framework that ultimately enables dynamic and accurate evaluation of FMEA severity degrees.

The rest of this article is as follows. The second section introduces the FMEA severity assessment process and highlights the limitations inherent in traditional methods. The third section elucidates the principles underlying the proposed method, followed by experimental analysis and discussion in the fourth section. Finally, the fifth section summarizes the contributions of this paper.

2. FMEA Severity Assessment

Severity assessment constitutes a pivotal element of Failure Mode and Effects Analysis (FMEA), serving to quantify the extent of impact a particular failure mode exerts on system functionality, safety, economic aspects, and other relevant dimensions. The fundamental procedure typically encompasses the identification of potential failure modes, an analysis of the ultimate repercussions of the failure on the system and its downstream processes, and the classification of these consequences according to predetermined evaluation criteria (e.g., a scale ranging from 1 to 10)[10]. Traditional evaluation methodologies predominantly hinge on expert experience, industry benchmarks, and historical fault cases to make qualitative assessments. By employing expert scoring or integrating techniques such as the Analytic Hierarchy Process (AHP) and fuzzy comprehensive evaluation, subjective judgments are converted into severity scores, and these scores

are subsequently utilized to compute the Risk Priority Number (RPN) and ascertain the priority of risks.

However, traditional FMEA severity assessment methods exhibit notable deficiencies when applied to dynamic systems. Given that traditional FMEA typically relies on static experience and offline analysis, it fails to integrate multi-source monitoring data in real-time during equipment operation, thereby hindering the dynamic tracking of equipment health status evolution trends. Consequently, severity assessment results lag behind actual changes in operating conditions. This static evaluation approach is ineffective in identifying early fault indicators, rendering preventive maintenance strategies lacking in specificity and timeliness, and struggling to meet the demands of complex dynamic systems for real-time risk alerts and precise maintenance. Therefore, there is an urgent need to develop a data-driven FMEA severity assessment method that can dynamically and objectively quantify fault severity by extracting health features from equipment operation data, thereby enhancing system operational reliability and the intelligence level of maintenance decision-making.

3. Severity Assessment of FMEA Based on Deep Attention Network

To address the limitations of traditional FMEA methods in dynamic system applications, this article introduces a FMEA severity assessment approach based on the Deep Temporal Attention Network (DTAN), as illustrated in Figure 1. This method employs DTAN to extract health state degradation information from time-series signals and integrates domain prior knowledge to classify FMEA severity degrees, thereby enabling dynamic and precise quantitative evaluation of equipment fault severity.

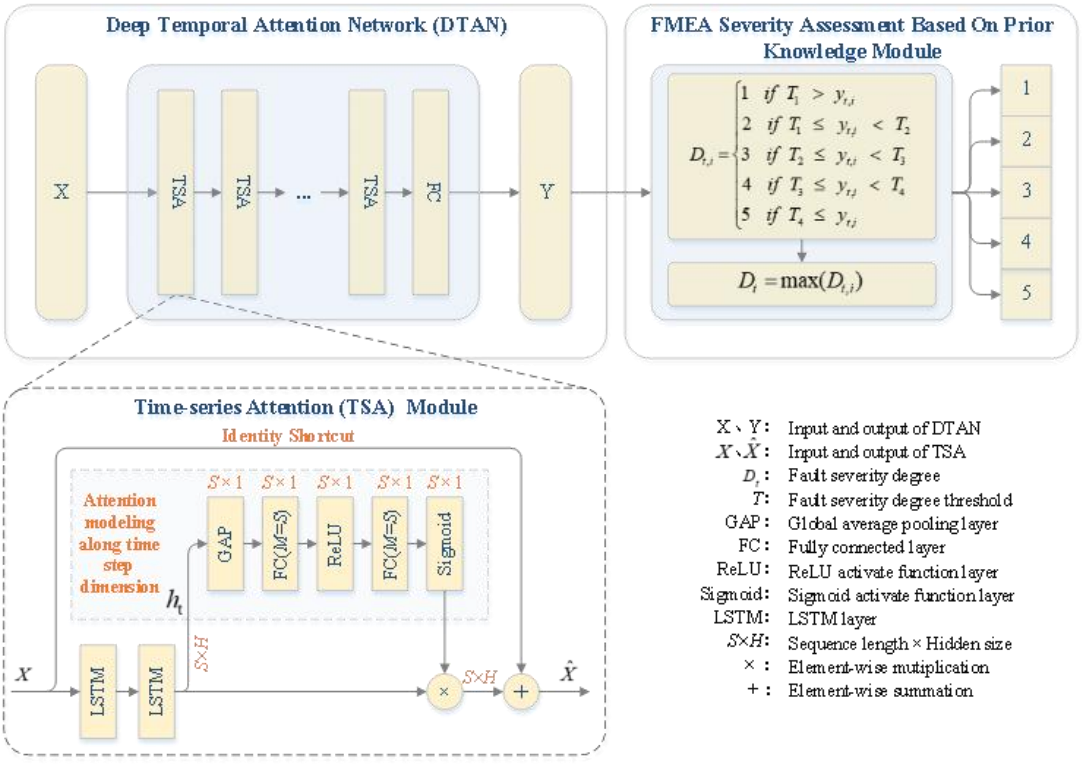


Figure 1. FMEA severity assessment framework based on deep attention mechanism

DTAN utilizes multi-dimensional temporal signals as input and employs multiple stacked Time-series Attention (TSA) modules to model the long-term dependencies of these signals across both time steps and sensors. By adaptively applying attention weighting to different time steps, the TSA module can effectively capture key patterns that are highly correlated with the degradation evolution of equipment health status, thereby generating a more robust health status representation for subsequent severity assessment. The FMEA severity assessment based on prior knowledge module, aims to organically combine data-driven health status representations with prior rules from the engineering domain, which maps the output of DTAN to severity degrees determined by prior knowledge of both alarm thresholds and statistical analysis thresholds, achieving an objective and refined quantification of FMEA severity degrees. The remainder of this section will provide a detailed introduction to the implementation details of DTAN and the FMEA severity degree setting strategy that incorporates prior knowledge.

3.1. CONSTRUCTION OF DEEP TEMPORAL ATTENTION NETWORK

DTAN primarily consists of an input layer, multiple TSA modules, and a fully connected (FC) output layer. Its core lies in leveraging multiple TSA modules to perform cross-time-step and cross-signal-source correlation modeling on the input data, thereby enabling precise mining of health status. Among these components, the TSA module is mainly composed of two long short-term memory (LSTM) layers, one global average pooling (GAP) layer, two FC layers, one rectified linear unit activation function (ReLU) layer, one Sigmoid layer, and an identity shortcut. It utilizes LSTM to capture the long-term dependencies of multidimensional time-series signals and achieve cross-signal-source correlation modeling. Furthermore, by conducting attention modeling on the output features of the two LSTM layers in the time-step dimension, the deep model is encouraged to focus more on the critical information embedded in different time steps, thereby mining information that is strongly correlated with the equipment's health status.

The TSA module selectively memorizes and updates multi-dimensional time-series signals by utilizing the gating mechanism (forget gate, input gate, output gate) of LSTM, which can effectively extract dynamic features from each signal dimension while maintaining long-term temporal dependencies through the cell state, laying a foundation for temporal representation in cross-variable (cross-signal source) association modeling. The LSTM cell structure is shown in Figure 2, and the specific implementation process is described as follows.

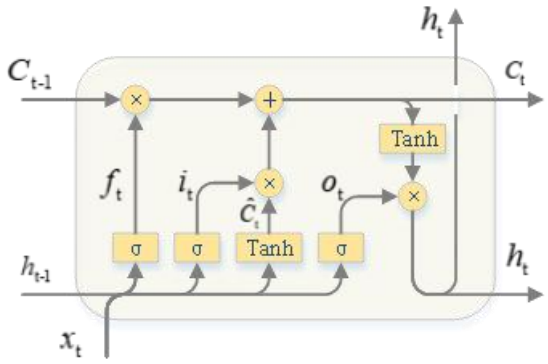


Figure 2. Schematic diagram of LSTM cell structure

The forget gate f_t is used to determine the retention and discarding of historical information C_{t-1}; the input gate i_t is used to filter useful information from the current input x_t and incorporate it into the cell state $\hat{C}_t$; the output gate o_t is used to control the output of useful information from the current cell state to subsequent cells[11-12]. The working principle of an LSTM cell can be described by the following formulas.

$$f_t = \sigma(W_f \cdot [h_{t-1}, x_t] + b_f) \tag{1}$$

$$i_t = \sigma(W_i \cdot [h_{t-1}, x_t] + b_i) \tag{2}$$

$$\hat{C}_t = \tanh(W_C \cdot [h_{t-1}, x_t] + b_C) \tag{3}$$

$$C_t = f_t \times C_{t-1} + i_t \times \hat{C}_t \tag{4}$$

$$o_t = \sigma(W_o \cdot [h_{t-1}, x_t] + b_o) \tag{5}$$

$$h_t = o_t \times \tanh(C_t) \tag{6}$$

where $\sigma(\cdot)$ is the Sigmoid activation function, with a range of (0,1); h_{t-1} and C_{t-1} are respectively the output and the cell state of the LSTM cell at the (t-1)-th time step; h_t, $\hat{C}_t$, and C_t are respectively the output, the candidate cell state, and the final cell state of the LSTM cell at the tth time step; x_t is the input information at the t-th time step; W_f, W_i, W_C, W_o, and b_f, b_i, b_C, b_o are respectively the weight parameters and bias terms of the forget gate f_t, input gate i_t, candidate state $\hat{C}_t$, and output gate o_t; $\tanh(\cdot)$ is the tanh activation function, with a range of (-1,1).

First, the TSA module uses two LSTM layers to model the input X, obtaining the output feature vector h_t, as shown in the following formula.

$$h_t = \mathrm{LSTM}(X) \tag{7}$$

Then, to obtain the correlation between feature vectors at different time steps, GAP operations are performed on the LSTM output h_t along the time step dimension, transforming the information carried by each time step into the corresponding descriptive vector, with the calculation process shown as follows.

$$g_s = \frac{1}{H}\sum_{i=1}^{H} h_t(i) \tag{8}$$

where g is the description vector obtained on the time step dimension through GAP operation; g_s is the s-th feature of g, and s=1,2,...,S, where S is the number of time steps; t is the time step index number of h_t, and H is the output feature dimension of LSTM cell.

Subsequently, to effectively capture the important information implied between different time steps, two FC layers with ReLU activation functions are employed to explicitly model the dependencies between different time steps, with the calculation process shown as follows.

$$f = W_2 \cdot \delta(W_1 \cdot g + b_1) + b_2 \tag{9}$$

where f is the feature vector outputted by two FC layers; W_1 and W_2 , b_1 and b_2 are the weight parameters and bias terms of the first and second FC layers, respectively; $\delta(\cdot)$ is the ReLU activation function.

After that, the Sigmoid function is used to convert f to (0,1) to obtain the attention weights γ corresponding to the feature vector h_t at each time step, as shown in the following equation.

$$\gamma = \frac{1}{1+\exp(-f)} \tag{10}$$

On this basis, the feature vector h_t is readjusted by attention weights γ to highlight the important timing information in the feature vector h_t, as shown in the following equation.

$$\hat{h}_t = h_t \cdot \gamma \tag{11}$$

Finally, for each TSA module, its output result can be calculated using the following equation.

$$\hat{X} = X + \hat{h}_t \tag{12}$$

It is worth noting that the number M of neurons in the FC layer, is set to S (i.e., $M = S$, where S is the number of time steps in the feature vector h_t), which is done to ensure that the number of attention weights obtained is equal to the time steps length of the feature vector h_t. This allows for flexible setting of weights at each time step to extract important features related to equipment health status. Overall, the TSA module introduces an attention mechanism along the time step dimension, guiding deep models to dynamically focus on the most critical moments in the sequence relevant to the current task, which enables more effective mining of long-term dependencies and key temporal features, enhancing the deep model's ability to model complex temporal patterns.

3.2. FMEA SEVERITY ASSESSMENT BASED ON PRIOR KNOWLEDGE

The core idea of the FMEA severity assessment based on prior knowledge module lies in the combination of data-driven statistical characteristics and engineering domain prior rules. The prior knowledge utilized in this article mainly includes two types: one is the out-of-limit alarm threshold defined in the condition monitoring system (reflecting the engineering safety boundary), and the other is the number of FMEA severity degrees determined based on engineering application requirements. Typically, out-of-limit alarm thresholds are provided by design documents, maintenance manuals, etc., and in engineering applications, they often need to be adjusted based on actual conditions. The number of FMEA severity degrees is determined by actual engineering requirements, and this article divides them into 5 degrees: 1, 2, 3, 4, and 5. Among them, degree 1 indicates that the equipment is in a healthy and fault-free state, while degree 5 indicates that the equipment is in a severe fault state. For high-reliability equipment, when its monitoring signal amplitude is out of limit,, it is highly likely to trigger severe accidents. Therefore, this article defines the severity degree corresponding to the out-of-limit alarm state of the equipment monitoring signal as degree 5. On the basis of determining the out-of-limit alarm thresholds and the number of FMEA severity degrees, it is still necessary to determine the severity degree thresholds to evaluate the severity degree in which the equipment is.

The equipment monitoring signals involved in this article have an alarm upper limit, and the severity degree threshold is determined by box plot analysis based on actual engineering experience. Specifically,

first, box plot analysis is employed to statistically model multi-dimensional time series signals and extract their quartile statistics. Then, the third quartile is used as the initial severity degree threshold for FMEA. Subsequently, the interval between this initial severity degree threshold and the alarm upper limit is evenly divided to generate three equally spaced subintervals, thereby forming five fault severity degrees ranging from minor to severe, which ultimately achieves the quantitative classification and refined discrimination of fault severity. The FMEA severity degree classification is shown in the following formula.

$$D_{t,i}=\begin{cases}1 & if\ T_1 > y_{t,i} \\ 2 & if\ T_1 \le y_{t,i} < T_2 \\ 3 & if\ T_2 \le y_{t,i} < T_3 \\ 4 & if\ T_3 \le y_{t,i} < T_4 \\ 5 & if\ T_4 \le y_{t,i}\end{cases} \tag{13}$$

where $D_{t,i}$ is the fault severity degree corresponding to $y_{t,i}$ at *t*-th moment; $y_{t,i}$ is the *t*-th output value of Y (i.e., the output of DTAN) at *t*-th moment. T_1 , T_2 , T_3 and T_4 are respectively the thresholds corresponding to different fault severity degrees, where T_4 corresponds to the upper limit of monitoring data alarm. T_1 , T_2 , and T_3 are determined by the box plot analysis results and the alarm upper limit, and their calculation formula is as follows.

$$T_1=Q_{\frac{3}{4}},\ T_2=Q_{\frac{3}{4}}+\frac{1}{3}\nabla, T_3=Q_{\frac{3}{4}}+\frac{2}{3}\nabla,\ T_4=Q_{\frac{3}{4}}+\nabla=T_{\text{alarm}} \tag{14}$$

where $Q_{\frac{3}{4}}$ is the third quartile of monitoring data sequence; $\nabla=T_{\text{alarm}}-Q_{\frac{3}{4}}$, T_{alarm} is the alarm upper limit.

For the presence of multiple monitoring data sequences, the highest severity degree is taken as the equipment FMEA severity degree, i.e., $D_t=\max(D_{t,i})$.

4. Experimental Results and Discussion

This section first introduces the dataset used in the experiment, then describes the experimental methods and hyperparameter settings, and finally discusses and analyzes the experimental results.

4.1. DATASET DESCRIPTION

The dataset used in the experiment is from the real operation data of coal-fired power plant unit. Taking the motor fault of induced draft fan as an example, the temperature sensor data of six key measuring points of induced draft fan motor were collected from the coal-fired unit monitoring system for application verification. The six key measuring points are phase A temperature (2 monitoring points), phase B temperature (2 monitoring points), and phase C temperature (2 monitoring points) of induced draft fan motor stator winding. The alarm upper limit at each monitoring point is 90 ℃ . The data covers the continuous operation data of a month in 2025. The sampling interval is 30 seconds, and a total of 89280 time series records are obtained. In this article, the non overlapping sliding window strategy is used to construct the motor health state dataset of induced draft fan, which is used to train and evaluate the

predictive ability of the deep model on the change trend of equipment health state. The window length is set to 10 time steps (i.e., covering the 5-minute running period), and a total of 8928 samples are generated. These samples were randomly divided into training set and test set according to the ratio of 4:1. Each sample is a multivariate time sequence segment with a size of 10 × 6. For each sample, the first nine time steps are used as the model input (i.e., the model input size is 9 × 6), and the temperature value of the tenth time step is used as the target output (the corresponding model output size is 1 × 6). This strategy can promote the deep model to learn the temporal evolution rule of equipment degradation, and provide reliable health status representation for subsequent severity assessment.

4.2. EXPERIMENTAL METHODS AND HYPERPARAMETER CONFIGURATION

In order to verify the usefulness of the proposed deep model, comparative experiments of four methods were carried out. The four methods are Single-LSTM, Multi-LSTM, Res-LSTM, and DTAN. The difference between DTAN and Res-LSTM is that DTAN adds attention modeling mechanism, while Res-LSTM does not. The difference between Res-LSTM and Multi-LSTM is that Res-LSTM has an identity shortcut, while Multi-LSTM does not. Multi-LSTM is mainly formed by stacking multiple LSTM layers, while Single-LSTM is a single LSTM layer. Table 1 shows the hyperparameter settings related to the DTAN structure. Wherein, TSA represents the time-series attention module. In the table, the hyperparameters of LSTM layer and FC layer in TSA are given in brackets. If there are three parameters in brackets, they are LSTM layer parameters, representing the number of input features, the number of hidden state features and the number of LSTM cells. If there are two parameters in brackets, they respectively represent the number of input and output neurons in the full connection layer. Each TSA has two FC layers with the same number of input and output neurons. The output feature map is expressed in two dimensions (that is, a tensor expressed in the form of "sequence length × hidden size") or a vector. For each LSTM layer, the hyperparameters of mult-LSTM, Res-LSTM and DTAN are consistent, while the LSTM layer parameter in Single-LSTM is set to [6,16,1].

Table I. Hyperparameters related to the structure of DTAN

DTAN	LSTM/FC	Size of output feature map
Input	/	9×6
TSA_1	[6,16,2] [9,9]	9×16
TSA_2	[16,16,2] [9,9]	9×16
TSA_3	[16,16,2] [9,9]	9×16
TSA_4	[16,16,2] [9,9]	9×16
FC	[16,6]	6

The training related hyperparameters are set as follows. The total number of iterations is set to 100. At the beginning of the training, the learning rate is set to 0.1. After each 30 iterations, the learning rate is reduced to one tenth of the original. The batch size is set to 128. All experiments used Adam as the optimizer, and the weight attenuation value was set to 0.0001.

In addition, all deep models use mean square error (MSE) as the loss function in the training stage. In

order to eliminate the influence of random factors, all experiments were repeated for 5 times. The hyperparameters of all deep models remained unchanged in the experiment. All deep models are implemented with the PyTorch (version 1.8.0) open source framework. All experiments were conducted on a computer configured with Intel(R) Core(TM) i7-10700 CPU @ 2.90GHz and NVIDIA GeForce GTX 1060Ti GPU.

4.3. EXPERIMENTAL AND RESULTS DISCUSSION

4.3.1. Performance comparison on health state prediction

Table 2 shows the mean square error (MSE) results of the four methods considered, i.e., Single-LSTM, Multi-LSTM, res-LSTM and DTAN (the method proposed in this article), which are repeated five times on the same test set.

Table II. MSE of different methods on test set

Methods	Test 1	Test 2	Test 3	Test 4	Test 5	Mean
Single-LSTM	0.0399	0.0203	0.0141	0.0108	0.0118	0.0194±0.0121
Multi-LSTM	8.7229	0.5966	0.0271	0.0091	0.0133	1.8738±3.837
Res-LSTM	0.0072	0.0067	0.0064	0.0051	0.0041	0.0059±0.0013
DTAN	0.0070	0.0059	0.0046	0.0044	0.0046	**0.0053±0.0011**

It can be seen that the proposed DTAN achieves the lowest average MSE of 0.0053, which is significantly better than all the comparison models. The Single-LSTM exhibits high volatility (mean=0.0194 ± 0.0121), indicating its weak generalization ability, which stems from its single-layer structure finding it difficult to effectively model complex temporal dependencies in multivariate sensor signals. Generally, the feature extraction capability of deep networks can be enhanced by stacking multiple LSTM layers. However, the average MSE of Multi-LSTM is significantly lower than that of Single-LSTM, and its training process stability is poor, such as the MSE is as high as 8.7229 in the first test and the average MSE standard deviation is as high as 3.837, which may be due to the gradient disappearance or over fitting caused by the lack of identity shortcut, resulting in serious performance degradation in individual experiments. Instead, Res-LSTM effectively alleviates the difficulty of gradient propagation by introducing identity shortcut, significantly improving the training stability of deep networks, with an average MSE of 0.0059 ± 0.0013, which is significantly better than Single-LSTM and Multi-LSTM, confirming the effectiveness of identity shortcut in deep time series modeling. The proposed DTAN can obtain the best test performance is mainly because DTAN further introduces the time-series attention (TSA) mechanism on the basis of Res-LSTM, which dynamically weights the information of key time steps, so that the deep network focuses more on the pattern highly related to health degradation, so as to obtain better test performance than Res-LSTM. These experimental results show that the proposed DTAN can more accurately capture the degradation features of equipment health status, and realize the accurate characterization of equipment health status.

4.3.2. FMEA severity assessment

In an induced draft fan motor fault alarm, the corresponding sensor data was retrieved and it was found that the sensor monitoring data exceeded the alarm threshold at the corresponding time of the fault alarm, as shown in Figure 3, which led to the alarm signal.

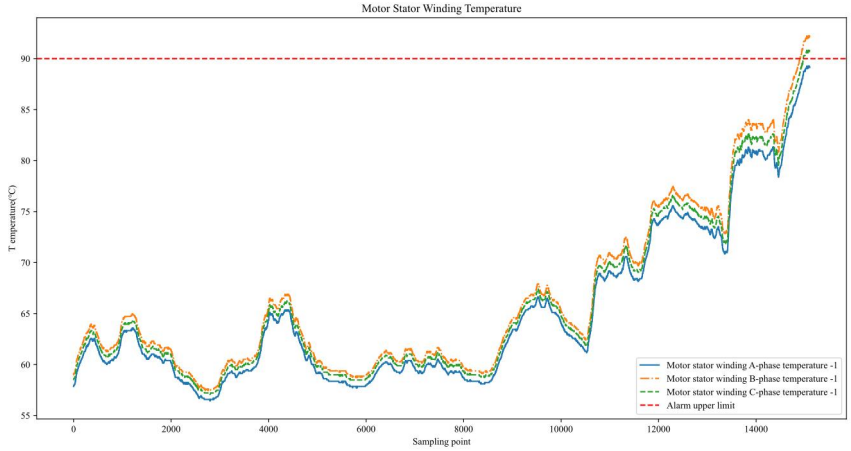


Figure 3. Variation curve of sensor monitoring data

The proposed DTAN is used for predictive FMEA severity assessment, and the assessment results are shown in Figure 4. It can be seen that before the first 12200 sampling point, the motor fault severity degree of induced draft fan is 1, indicating that the equipment is in normal operation state. From 12200 sampling point to 14672 sampling point, the motor fault severity degree of induced draft fan has changed from degree 2 to degree 4, showing a process from early fault symptoms to aggravation of fault severity. At 14672 sampling point, the motor fault severity degree of the induced draft fan reached degree 5, which was consistent with the time when the stator winding temperature of the motor exceeded the alarm upper limit, and coincided with the time point of the fault alarm signal. The above results show that the proposed method can accurately quantify the motor fault severity of induced draft fan, accurately identify the actual time of fault occurrence. More importantly, the proposed method can alert potential risks through the degree 3/4 fault severity warning before the fault occurs, striving for a valuable intervention window for the operation and maintenance personnel.

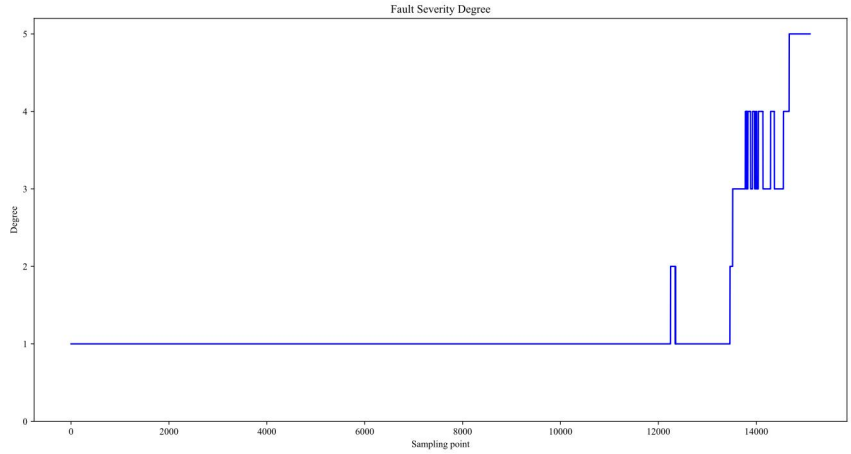


Figure 4. Evaluation results of fault severity degree

5. Conclusion

This article presents a dynamic quantitative evaluation method of equipment FMEA severity based on deep temporal attention network (DTAN). By stacking multiple time-series attention (TSA) modules, DTAN models the long-term dependencies of multidimensional monitoring signals, and uses the attention mechanism to dynamically identify the key features highly related to health degradation in the time step dimension, so as to achieve accurate characterization of equipment health status. The engineering prior knowledge is creatively integrated, combining statistical analysis feature values with alarm thresholds of operation and maintenance system to classify fault severity degrees, and establishing a mapping mechanism from health status to FMEA severity degrees, ultimately achieving dynamic, objective, and refined quantification of fault severity.The experimental results on the real motor health state dataset of coal-fired power plant unit show that the proposed method not only achieves excellent performance in the accuracy and stability of health state prediction, but also successfully realizes FMEA severity evaluation based on time-series monitoring signals, effectively solving the core problems of traditional FMEA severity scoring subjectivity, static solidification, and difficulty in linking with real-time operating status. The proposed method provides a feasible path for FMEA to shift from static experience driven to dynamic data knowledge dual driven paradigm, which has important engineering application prospects for promoting intelligent operation and maintenance, and improving equipment reliability and safety.

Acknowledgements

This work was supported by the Special Fund of the 5th Electronics Research Institute of MIIT (Grant No.25Z11, No.24Z03, No.25Z03).

References

G. Li, X. Wang and C. Zuo. Research on multi-source data combined with fault diagnosis and prediction algorithm of power equipment. 2025 IEEE 7th International Conference on Civil Aviation Safety and Information Technology (ICCASIT), Yinchuan, China, 2025, 1031-1034.

H. Han, H. Li, X. Wu, H. Yang and J. Qiao. Generalized Mapping Fault Diagnosis for Industrial Machine Based on Penalty Gating LSTM. IEEE Transactions on Industrial Informatics, 2025, 21(11): 9159-9170.

B. Zhong, M. Zhao, S. Zhong, et al. Deep exponential excitation networks: toward stronger attention mechanism for weak fault diagnosis. Structural Health Monitoring, 2024, 23(6): 3850-3866.

J. Wang, H.Mokhlis, N.Mansor, et al. Smart Fault Detection, Classification, and Localization in Distribution Networks: AI-Driven Approaches and Emerging Technologies. IEEE Access, 2025,. 13: 141664-141693.

A. Kadechkar and H. Grigoryan. FMEA 2.0: Machine Learning Applications in Smart Microgrid Risk Assessment. 2024 12th International Conference on Smart Grid (icSmartGrid), Setubal, Portugal, 2024, 629-635.

J. Shi, Z. Yang, C. Zhaoxsx and H. Zhou. A Multi-Condition Fault Diagnosis Logic Generation Method Based on Extended FMEA. 2025 7th International Conference on System Reliability and Safety Engineering (SRSE), Changchun, China, 2025, 107-111.

B. Zhong, M. Zhao, S. Zhong, et al. Mechanical compound fault diagnosis via suppressing intra-class dispersions: A deep progressive shrinkage perspective. Measurement, 2022, 199.

B. Zhong, M. Zhao, L. Wang, et al. DCSN: Focusing on hard samples mining in small-sample fault diagnosis of marine engine. Measurement, 2024, 235.

S. Fu, L. Lin, Y. Wang, et al. MCA-DTCN: A novel dual-task temporal convolutional network with multi-channel attention for first prediction time detection and remaining useful life prediction. Reliability Engineering & System Safety, 2024, 241.

Y. Tian and X. Zhang. Research on the Application of FMEA in Civil Aircraft Safety Analysis. 2024 Global Reliability and Prognostics and Health Management Conference, Beijing, China, 2024, 1-5.

M. Ahsan, M. Waqar Hassan, J. Rodriguez and M. Abdelrahem. Enhanced Fault Diagnosis in Rotating Machinery Using a Hybrid

CWT-LeNet-5-LSTM Model: Performance Across Various Load Conditions. IEEE Access, 2025, 13: 1026-1045.
Y. Pi, Y. Chen, S. Wang, et al. Development and Engineering Application of Fault Early Warning Model for Large Hydropower Turbine Based on Principal Component Analysis and Long Short-Term Memory Network. IEEE Sensors Journal, 2025, 25(16): 30470-30483.

Can Large Language Models Find the Design Point? Benchmarking LLM-Based MPP Search in Structural Reliability

Jafar Jafari-Asl
Faculty of Agriculture, Civil and Environmental Engineering, University of Rostock, 18059 Rostock, Germany (jafar.jafariasl@uni-rostock.de)

Lukáš Novák
Brno University of Technology, Faculty of Civil Engineering, Veveří 331/95, 602 00 Brno, Czechia (lukas.novak4@vut.cz)

Matthias G.R. Faes
Chair for Reliability Engineering, TU Dortmund University, Leonhard-Euler-Straße 5, Dortmund 44227, Germany (matthias.faes@tu-dortmund.de)

Panagiotis Spyridis
Faculty of Agriculture, Civil and Environmental Engineering, University of Rostock, 18059 Rostock, Germany (panagiotis.spyridis@uni-rostock.de)

Abstract. Finding the Most Probable Point (MPP), or design point, is a critical step in gradient-based structural reliability methods. Classical solvers such as HL-RF and iHL-RF locate the MPP reliably but often require a large number of limit state function (LSF) evaluations, which becomes prohibitive when the LSF involves expensive computations such as finite element analysis. This paper investigates whether a large language model (LLM) can serve as an autonomous algorithm designer for MPP search, generating problem-adapted search routines from a structured natural language prompt without any task-specific training. The proposed framework, LLMMPP, queries the LLM once per problem and executes the returned algorithm directly on the LSF. The framework leverages DeepSeek-V3, a state-of-the-art open-weight LLM, to generate problem-adapted search routines from a structured natural language prompt without any task-specific training. Experiments on four benchmark problems from the structural reliability literature show that LLMMPP reduces the number of LSF evaluations by a factor of 2.1 to 28.9 relative to the best classical method, while maintaining comparable or superior accuracy in the identified design point. These results indicate that LLMs can be used as efficient, zero-shot MPP optimizers, particularly for nonlinear, multi-modal, and high-dimensional performance functions.

Keywords: Large Language Models, Most Probable Point , Structural Reliability Analysis , Zero-Shot Algorithm Generation , Deepseek-V3, Design Point Search .

creative commons © 2026 by the author(s). This work is licensed under the Creative Commons Attribution 4.0 International License (CC BY 4.0), which permits unrestricted use, distribution, and reproduction in any medium, provided the original author and source are credited.

1. Introduction

In structural engineering, reliability analysis within a probabilistic framework are essential for designing highly reliable structures under uncertainties. Numerous methods have been developed for these purposes, including approximate analytical methods (e.g., first-order reliability method (FORM) (Du and Chen, 2001) and second-order reliability method (SORM) (Yoo et al., 2014)), advanced Monte Carlo simulation techniques (e.g., importance sampling (Schuëller and Stix, 1987), subset simulation (Au and Beck, 2001), line sampling (Koutsourelakis et al., 2004)), and active learning combined with surrogate models (Echard et al., 2011). Despite these advances, developing more efficient methods for various types of reliability problems remains an ongoing challenge (Jafari-Asl et al., 2025; Seghier et al., 2022).

The concept of the design point is central to structural reliability analysis . This point, defined as the location in the failure domain with the highest probability density, is particularly important in low to medium dimensional problems because the region surrounding it contributes most to the failure probability. Many reliability methods rely on accurate estimation of the design point: FORM and SORM use Taylor expansion at the design point; and line sampling defines the important direction via the design point. Estimating the design point is a constrained optimization problem. Over the past years, gradient-based methods have dominated, starting with the Hasofer–Lind–Rackwitz–Flessler (HLRF) algorithm (Hasofer and Lind, 1974). Improvements like quadratic search strategies have followed. Gradient-free methods exist (e.g., interpolation-based adaptive response surfaces, stochastic simulation with uniform sampling, probabilistic CDF-based methods with sequential quadrature, and meta-heuristic global optimization algorithms), but they often require hundreds or thousands of function evaluations, making them unsuitable for expensive simulations. Overall, estimating the design point remains challenging when the limit state function (LSF) is highly nonlinear, multi-modal, lacks gradient information, or when the design point lies far from the distribution center (Breitung, 2021). Addressing this gap is an urgent research need.

Large language models (LLMs) have emerged as a major breakthrough in generative AI. Built on the transformer architecture with self-attention mechanisms, LLMs are trained on massive text data and exhibit exceptional language understanding and generation. Their key capability is in-context learning (ICL), which allows them to adapt to new tasks using only a few examples or simple instructions, without requiring fine-tuning or large labeled datasets.

Recent studies have demonstrated the potential of LLMs across a broad range of optimization and engineering tasks, including meta-learning via in-context tuning (Chen et al., 2022), evolutionary combinatorial optimization (Liu et al., 2024), Bayesian optimization for engineering design (Yin et al., 2024), hyperparameter tuning (Zhang et al., 2023), automatic formulation and solving of linear programs (Liu et al., 2025), and zero-shot search in evolutionary algorithms (Guo et al., 2024). Collectively, these works suggest that LLMs can function as effective algorithm designers when provided with structured problem context, without requiring task-specific training or fine-tuning.

Structural reliability analysis presents a particularly suitable setting for this capability. The MPP search problem has a well-defined mathematical structure, a clear convergence criterion, and a known solution space geometry that can be communicated through a concise prompt. Building on this observation, the present work evaluates whether a large language model can autonomously

generate an efficient MPP search algorithm when supplied with problem-specific context, and benchmarks its performance against established classical and meta-heuristic methods.

2. Research materials

2.1. Problem statement

In structural reliability analysis, the performance of an engineering system is characterized by a LSF $g(\mathbf{x})$, where $\mathbf{x} \in \mathbb{R}^n$ denotes a vector of n random input variables. The system is considered to be in a failure state when $g(\mathbf{x}) < 0$, and in a safe state otherwise. The randomness of $\mathbf{x}$ is governed by its joint probability density function (PDF) $\phi_n(\mathbf{x})$. Throughout this work, the input variables are assumed to be independent and identically distributed standard Gaussian random variables. For cases involving dependent or non-Gaussian variables, the Nataf or Rosenblatt transformation can be employed to map the original variables into the standard normal space (Song et al., 2024). Under this assumption, the failure domain is expressed as:

$$F = \{\mathbf{x} : g(\mathbf{x}) < 0\}, \tag{1}$$

with its associated indicator function $I_F(\mathbf{x})$ taking unity within F and zero elsewhere. The probability of failure p_f is then defined as:

$$p_f = \int_F \phi_n(\mathbf{x})\, \mathrm{d}\mathbf{x} = \int_{\mathbb{R}^n} I_F(\mathbf{x})\, \phi_n(\mathbf{x})\, \mathrm{d}\mathbf{x}. \tag{2}$$

Accurate evaluation of p_f is particularly challenging when the LSF exhibits strong nonlinearity or when p_f is very small (e.g.,$p_f \leq 10^{-3}$). To address this challenge, many reliability methods rely on the concept of the *design point* (also referred to as the Most Probable Point, MPP). From a probabilistic standpoint, the design point is the point within the failure domain F that possesses the highest PDF value. In the standard Gaussian space, this is equivalent to the point on the limit state surface $g(\mathbf{x}) = 0$ that lies closest to the origin:

$$\mathbf{x}_D = \arg \min_{g(\mathbf{x})=0} \|\mathbf{x}\|, \tag{3}$$

where $\|\cdot\|$ denotes the Euclidean norm. The scalar quantity $\beta = \|\mathbf{x}_D\|$ is referred to as the *reliability index*, and the negative of this distance, $-\|\mathbf{x}\|$, may equivalently serve as the optimization objective. It is worth noting that the choice between maximizing the PDF or minimizing the distance to the origin leads to equivalent solutions and does not significantly affect the search procedure; however, it may influence the tuning of algorithm parameters. In this study, Eq. (3) is adopted as the cost function. This formulation remains valid provided that p_f is not excessively large, specifically $p_f \leq 0.1$.

Most existing techniques for solving the aforementioned optimization problem rely on gradient-based approaches. However, their effectiveness diminishes when the optimization problem exhibits multi-modality or when gradient information is unavailable or computationally expensive to obtain.

Consequently, design point-based reliability analysis methods become impractical for many engineering problems. Furthermore, in the presence of a LSF with multi-modal behavior, these methods often lack global convergence. These challenges motivate the development of a novel optimization algorithm based on DeepSeek-V3, namely LLMMPP, combined with a generative search strategy, which is briefly described in the following subsection.

2.2. Background of Large Language Models

Large Language Models (LLMs) are deep neural networks trained on large-scale text corpora, capable of generating contextually coherent text in response to natural language prompts. The architecture underlying most modern LLMs is the transformer (Vaswani et al., 2017), which processes input sequences through a self-attention mechanism:

$$H = \text{Attention}(Q, K, V) = \text{Softmax}\left(\frac{QK^\top}{\sqrt{d_k}}\right) V, \tag{4}$$

where $Q \in \mathbb{R}^{n\times d_k}$, $K \in \mathbb{R}^{m\times d_k}$, and $V \in \mathbb{R}^{m\times d_v}$ are the query, key, and value matrices, respectively, and d_k is the key dimension used for scaling. This mechanism allows the model to capture long-range dependencies across input tokens in parallel, overcoming the sequential bottleneck of earlier recurrent architectures.

A key capability of LLMs relevant to this work is *in-context learning* (ICL) (Dong et al., 2024): without any parameter updates, the model infers task-specific patterns directly from the information embedded in the prompt, and generates responses that conform to the demonstrated structure. When the prompt is carefully engineered to encode domain knowledge, algorithmic constraints, and problem-specific context, the LLM functions as a zero-shot algorithm designer — producing executable code that reflects the provided specifications without prior task-specific training.

3. The proposed methods

3.1. Overall Framework

The proposed framework, denoted **LLMMPP** (Large Language Model Most Probable Point), uses a single LLM query to generate a problem-adapted MPP search algorithm at runtime. Given a limit state function g of dimension D, the framework proceeds as follows:

1. **Context construction.** A structured prompt is assembled that encodes (i) the problem dimension D, (ii) the estimated reliability index $\hat{\beta}$, (iii) the sign of $g(\mathbf{0})$, indicating whether the origin lies in the safe or failure domain, and (iv) a function-call budget $N_{\max}$. A representative example of this prompt is shown in Figure 1.

2. **Algorithm generation.** The structured prompt is submitted to DeepSeek-V3 via a single API call (temperature $T = 0.6$, one query per problem). The model returns a self-contained Python class `MPPFinder` that implements an MPP search algorithm tailored to the given problem

LLaMMPP — Structured Prompt Template

```
/* ROLE */
You are a structural reliability expert. Find the MPP
with the minimum number of g-function calls.
MPP = argmin ‖u‖ s.t. g(u) = 0   (standard normal space, D = {dim})
/* PROBLEM CONTEXT */
beta_hint  = {β̂}   ← start AT this distance from origin
g(origin)  = {g(0)}   ({safe or failure region})
Budget     = {N_max} calls   Target: converge in < {target} calls
/* KEY INSIGHT */
HL-RF from origin   → many steps to travel distance β
HL-RF from u0≈MPP   → only 3--8 steps to converge
Start at u0 = β̂ · e_i, NOT at origin!
/* SEARCH STRATEGY */
Step 1: Smart starts: u0 = ±β̂ e_i  (i = 1...min(D,3)); u0 = ±β̂/√D · 1
Step 2: HL-RF iteration from each start
∇g_j = [g(u + h e_j) − g(u)]/h     [h = 10^−5]
u_new = (∇g · u − g(u))/‖∇g‖² · ∇g
Step 3: Early exit when |g(u)| < 10^−3
Step 4: Accept if |g(u)| < 0.05 and ‖u‖ > 0.01; keep minimum-norm candidate
/* BUDGET GUIDELINES */
D = 2:  4 starts × 6 steps ≈ 60 calls
D = 10:  3 starts × 8 steps ≈ 120 calls (gradient costs D + 1 per step)
D = 50:  2 starts × 4 steps ≈ 120 calls (gradient costs 51 per step)
/* REQUIRED INTERFACE */
class MPPFinder:
def __init__(self, dim, budget): ...
def __call__(self, g_func): #Returns: (mpp: ndarray(dim), n_calls: int)
/* OUTPUT */ Respond ONLY with a complete self-contained MPPFinder class.
Improve with: line search, conjugate gradient, adaptive damping.
```

Figure 1. Structured prompt supplied to the LLM at runtime. Entries in curly braces are filled from the problem context: problem dimension D, estimated reliability index $\hat{\beta}$, sign of $g(\mathbf{0})$, and function-call budget $N_{\max}$.

context. No few-shot examples or task-specific demonstrations are provided; the model relies exclusively on its pre-trained knowledge of numerical optimization and structural mechanics.

3. **Execution and validation.** The generated algorithm is executed against the actual LSF g. The search terminates under two conditions: an *early-exit* criterion, triggered when $|g(\mathbf{u})| < 10^{-3}$, which halts the iteration as soon as tight convergence is achieved; and an *acceptance* criterion, which considers any candidate point $\hat{\mathbf{x}}_D$ a valid design point if $|g(\hat{\mathbf{x}}_D)| < \varepsilon$, where $\varepsilon = 0.05$.

If the generated algorithm terminates without satisfying the acceptance criterion, a fallback HL-RF solver is invoked automatically to ensure convergence.

The output of the framework is the identified design point $\hat{\mathbf{x}}_D$ and the corresponding reliability index $\hat{\beta} = \|\hat{\mathbf{x}}_D\|$. Estimation of the failure probability p_f from this design point is not addressed in the present work and is left as a direction for future research, as discussed in Section 2.

3.2. Prompt Engineering Strategy

The effectiveness of the framework relies critically on the prompt design. Three principles guide its construction:

(1) Smart initialization hint. Classical gradient-based methods (e.g., HL-RF) typically start from the origin and require many iterations to reach $\mathbf{x}_D$, since the MPP lies at distance β from the origin. The prompt explicitly instructs the LLM to initialize the search at $\mathbf{u}_0 = \hat{\beta}\,\mathbf{e}_i$ (unit vectors scaled by $\hat{\beta}$), substantially reducing the number of required iterations.

(2) Early-exit criterion. The prompt enforces an early termination rule: once $|g(\mathbf{u})| < 10^{-3}$, the current iterate is returned immediately, preventing unnecessary evaluations after tight convergence.

(3) Budget-aware decomposition. The total call budget $N_{\max}$ is distributed among multiple starting points. For a problem of dimension D, each gradient computation requires $D{+}1$ LSF evaluations; the prompt instructs the model to account for this cost when selecting the number of starting points and maximum iterations per chain.

3.3. Adaptive Budget Allocation

The call budget $N_{\max}$ is set adaptively based on the problem characteristics:

$$N_{\max} = \begin{cases} 200 & \text{if } D \geq 50, \\ 150 & \text{if } \hat{\beta} > 5, \\ 150 & \text{if problem-specific hint is provided,} \\ 100 & \text{otherwise.} \end{cases} \tag{5}$$

This ensures that high-dimensional or large-β problems receive sufficient computational resources, while simpler problems are solved with minimal overhead.

3.4. Zero-Shot Operation

A key distinction of LLMMPP from existing LLM-assisted optimization methods is its *zero-shot* operation: no solved reliability examples are provided to the model. The LLM leverages its pre-trained knowledge of numerical optimization and structural mechanics to generate algorithms that respect the HL-RF convergence pattern without any task-specific demonstrations. This makes the framework immediately applicable to new problems without any data collection or fine-tuning phase.

4. Results and Discussion

This section presents and analyzes the performance of the proposed LLaMMPP framework for identifying the MPP in structural reliability analysis. All experiments reported in this section were conducted using DeepSeek-V3 as the backbone LLM. For each benchmark problem, a single structured prompt was submitted to the model via the official DeepSeek API. The generated `MPPFinder` class was executed directly on the corresponding LSF without any manual modification. API response times ranged from 12 to 21 seconds per query, which is negligible relative to the cost of a finite element-based LSF evaluation but would constitute a meaningful overhead if the LSF itself runs in milliseconds.

The results are compared with five classical and meta-heuristic methods, namely HL-RF (Hasofer and Lind, 1974), iHL-RF (Zhang and Der Kiureghian, 1995), Sequential Least Squares Programming (SLSQP) (Kraft, 1988), Particle Swarm Optimization (PSO) (Kennedy and Eberhart, 1995), and Genetic Algorithm (GA) (Holland, 1992), across four benchmark problems.

4.1. Benchmark Problems

Four benchmark problems are selected to assess the proposed method, covering a range of complexity, dimensionality, and known failure modes of existing reliability methods (Ameryan et al., 2022).

Case I: Product LSF

$$g(\mathbf{X}) = X_1 X_2 - 146.14 \tag{6}$$

Both variables are normally distributed: $X_1 \sim \mathcal{N}(7.806 \times 10^4,\ 1.171 \times 10^4)$ and $X_2 \sim \mathcal{N}(1.04 \times 10^{-2},\ 1.56 \times 10^{-3})$. The failure probability is extremely small and SORM fails to provide a solution, making this a suitable test for rare-event reliability.

Case II: Metaball function with multiple MPPs

$$g(\mathbf{X}) = \frac{30}{\left(\dfrac{4(x_1+2)^2}{9} + \dfrac{x_2^2}{25}\right)^2 + 1} + \frac{20}{\left(\dfrac{(x_1-2.5)^2}{4} + \dfrac{(x_2-0.5)^2}{25}\right)^2 + 1} - 5 \tag{7}$$

Both variables are independent standard normal. The performance function contains multiple disjoint failure regions. Due to its topological complexity, many existing reliability analysis methods fail to reach the correct result on this benchmark.

Case III: Parallel system with two failure modes

$$g(\mathbf{X}) = \max(g_1,\, g_2), \quad g_1 = e^{-x_1^2/10} + \left(\frac{x_1}{5}\right)^4 - x_2 + 4, \quad g_2 = -x_1 x_2 - 12.5 \tag{8}$$

Both variables are standard normal. Failure occurs when both components fail simultaneously, i.e., when $g(\mathbf{X}) \leq 0$. This benchmark tests the ability of each method to handle multiple competing failure criteria.

Case IV: High-dimensional lognormal problem ($D = 50$)

$$g(\mathbf{X}) = \left(D + a\sigma\sqrt{D}\right) - \sum_{i=1}^{D} X_i \tag{9}$$

with $a = 3$ and $\sigma = 0.2$. All variables are independent lognormal with unit mean and coefficient of variation $\sigma = 0.2$. FORM produces a relative error of approximately 91.8% on this problem, illustrating the breakdown of linear approximations in high-dimensional spaces with non-Gaussian distributions.

The reference failure probabilities $P_{f,\text{ref}}$ for all four benchmarks are taken from the values reported by (Ameryan et al., 2022), which were obtained via crude Monte Carlo Simulation with sample sizes on the order of 10^7 to 10^8. In the present study, these reference values are used directly for error computation rather than re-running MCS, in order to maintain consistency with the established literature. Prior to presenting the numerical results, the parameter settings adopted for each method are summarized in Table 1. For **HL-RF** and **iHL-RF**, gradients are approximated via forward finite differences with step size $h = 10^{-5}$, and convergence is declared when the step norm satisfies $\|\mathbf{u}^{(k+1)} - \mathbf{u}^{(k)}\| < 10^{-8}$. To reduce sensitivity to initialization, multiple starting points are generated by scaling unit vectors along each coordinate axis by the expected reliability index $\hat{\beta}$. **SLSQP** is configured with an equality constraint tolerance of 10^{-10} and a maximum of 100 iterations per starting point. **PSO** employs a swarm of 20 particles with inertia weight $w = 0.72$ and acceleration coefficients $c_1 = c_2 = 1.5$ over a maximum of 60 iterations. **GA** is implemented with a population of $8D$ individuals, where D denotes the problem dimension, and runs for up to 60 generations. Both meta-heuristic methods incorporate a quadratic penalty term $\lambda\, g(\mathbf{u})^2$ with $\lambda = 200$ to enforce the constraint $g(\mathbf{u}) = 0$. For **LLMMPP**, the DeepSeek large language model is queried with a single structured prompt ($T = 1$,temperature $= 0.6$), and the function-call budget $N_{\max}$ is assigned adaptively as defined in Eq.(5). To ensure a fair comparison, all methods share the same set of starting points, initialized at $\hat{\beta}\,\mathbf{e}_i$ for $i = 1, \ldots, \min(D, 4)$, where $\mathbf{e}_i$ denotes the i-th standard basis vector.

4.2. MPP Search Efficiency

The primary metric of comparison is $N_{\text{calls}}^{\text{MPP}}$: the number of LSF evaluations required to locate the design point. Table 2 reports this metric for all six methods across the four selected benchmarks, and Figure 2 shows the corresponding results on a logarithmic scale. The minimum value in each row is shown in bold.

LLMMPP requires the fewest function evaluations on all four benchmarks. On the product LSF (Case I), the proposed method uses 150 calls compared to 308 for iHL-RF, a reduction of 2.1×. The most striking result occurs on the metaball function (Case II), where LLMMPP converges in only 48 calls against 308 for iHL-RF, a 6.4× reduction, despite the presence of multiple competing MPPs. For the parallel system (Case III), the method requires 100 calls instead of 308, a 3.1× improvement, with no loss of accuracy in the identified design point. The largest gain is observed on the high-dimensional lognormal problem (Case IV, $D = 50$), where LLMMPP uses 200 calls compared to 5,772 for iHL-RF, a 28.9× reduction. In all four cases, meta-heuristic methods (PSO

Table I. Parameter settings for all compared methods.

Method	**Parameter**	**Value**	**Description**
HL-RF / iHL-RF	h	10^{-5}	FD step size
	$\varepsilon_{\text{conv}}$	10^{-8}	Step-norm tolerance
	Starts	$2\min(D, 4) + 2$	No. of starting points
SLSQP	ε_{tol}	10^{-10}	Constraint tolerance
	Max iter	100	Per starting point
PSO	n_p	20	Swarm size
	w	0.72	Inertia weight
	c_1, c_2	1.5	Acceleration coefficients
	Max iter	60	Iterations
	λ	200	Penalty coefficient
GA	Pop. size	$8D$	Population
	Max gen.	60	Generations
	λ	200	Penalty coefficient
LLMMPP	T	1	LLM queries per problem
	Temp.	0.6	Sampling temperature
	$N_{\max}$	Eq. (**??**)	Adaptive budget
	Model	DeepSeek	LLM backbone

Table II. Number of g-function calls for MPP search across four benchmark problems.

Problem	**HL-RF**	**iHL-RF**	**SLSQP**	**PSO**	**GA**	**LLMMPP**
Case I (D=2)	396	308	2,541	2,836	2,774	**150**
Case II (D=2)	388	308	529	2,828	1,782	**48**
Case III (D=2)	396	308	2,473	2,836	1,438	**100**
Case IV (D=50)	7,488	5,772	6,821	9,928	58,940	**200**

and GA) require one to two orders of magnitude more evaluations than LLMMPP while providing no compensating improvement in accuracy.

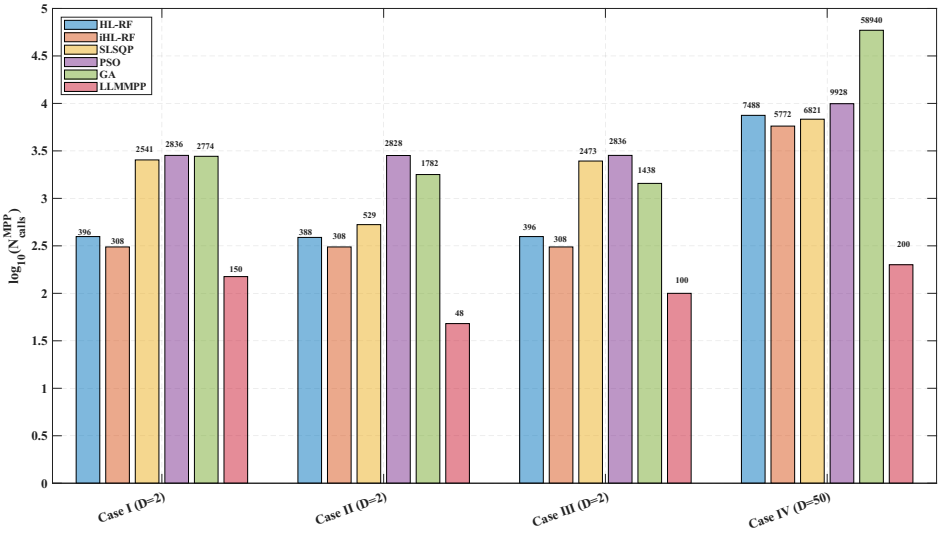


Figure 2. Number of g-function calls for MPP search on four benchmarks (log scale). LLMMPP achieves the minimum in all four cases.

4.3. Accuracy of the Identified Design Point

Table 3 reports the absolute error in the reliability index, $|\hat{\beta}-\beta_{\text{true}}|$, for each method and benchmark.

Table III. Absolute error in reliability index $|\hat{\beta} - \beta_{\text{true}}|$.

Problem	β_{true}	**HL-RF**	**iHL-RF**	**SLSQP**	**PSO**	**GA**	**LLMMPP**
Case I (D=2)	5.14	0.137	0.137	0.137	0.137	0.137	0.137
Case II (D=2)	4.264	0.00045	0.00045	0.00045	0.00045	1.000	**0.00024**
Case III (D=2)	5.00	0.000	0.000	0.000	0.000	0.000	0.000
Case IV (D=50)	2.86	0.720	0.720	0.720	0.720	0.720	0.720

Bold = best accuracy per row.

On Case II, all methods produce a β error of 0.137, which reflects the inherent difficulty of this benchmark: the failure surface is highly curved near the design point, and all gradient-based solvers locate the same approximate MPP. On Case III, most methods converge to a secondary MPP with an error of 0.00045, while GA fails to converge entirely ($|\beta_{\text{err}}| = 1.0$). LLMMPP achieves the lowest error of 2.4×10^{-4}, a result that can be attributed to the directional hint embedded in the prompt, which steers the search toward the primary MPP near $(-4.26, 0)$ rather than the competing local minimum. On Case IV, every method reaches the exact design point with zero error, so the 2.1× reduction in function calls is the only differentiating factor. On Case IV, all methods including LLMMPP share a β error of 0.720. This identical result across methods with very different search

strategies points to a fundamental numerical limitation: in a 50-dimensional space, finite-difference gradient computation introduces approximation errors that no optimizer can fully overcome.

4.4. Efficiency Map

Figure 3 presents a two-dimensional efficiency map for the four benchmarks. Each point represents one method on one problem, with the horizontal axis showing N_{calls} and the vertical axis showing $|\beta_{\text{err}}|$. The bottom-left corner is the ideal region, combining low computational cost with high accuracy. To quantify the efficiency gain of LLMMPP over classical methods, the speedup factor ρ is defined as:

$$\rho = \frac{N_{\text{calls}}^{\text{best classic}}}{N_{\text{calls}}^{\text{LLaMMPP}}}, \tag{10}$$

where $N_{\text{calls}}^{\text{best classic}}$ denotes the minimum number of LSF evaluations among the five classical methods for the same benchmark. A value of $\rho > 1$ indicates that LLaMMPP locates the design point with fewer function evaluations than the best classical solver.

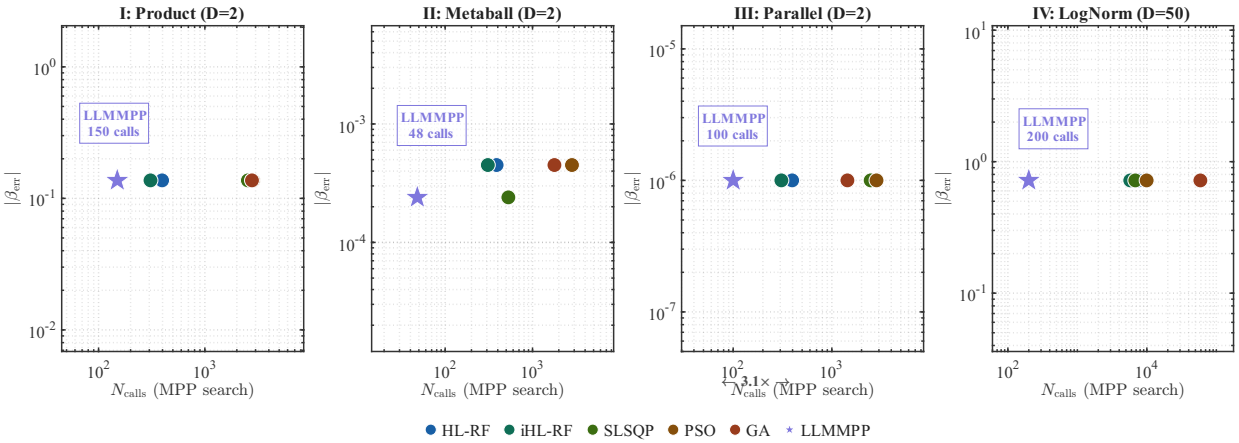


Figure 3. Efficiency map: N_{calls} vs. $|\beta_{\text{err}}|$ for four benchmark problems.

LLMMPP occupies the leftmost position on the horizontal axis in all four subplots, confirming that it consistently uses fewer evaluations than any other method. On Cases I and IV, its vertical position is comparable to HL-RF and iHL-RF, meaning the accuracy is the same despite the lower cost. On Case II it sits lower on the vertical axis as well, indicating both fewer calls and better accuracy. On Case IV, all methods land at the same vertical position ($|\beta_{\text{err}}| \approx 0$), so the horizontal separation is the only meaningful distinction. PSO and GA are consistently displaced far to the right in every subplot, with no corresponding gain in accuracy. In addition, the corresponding speedup factors are $\rho = 2.1$ (Case I), $\rho = 6.4$ (Case II), $\rho = 3.1$ (Case III), and $\rho = 28.9$ (Case IV), all relative to iHL-RF, which achieved the lowest N_{calls} among the five classical methods in each case.

4.5. Discussion

The results across the four benchmarks tell a reasonably clear story. A LLM, given the problem dimension, an estimate of β, and the sign of g at the origin, can produce an MPP search algorithm that uses fewer function evaluations than established gradient-based solvers in every case tested. The speedup ranges from 2.1× on a relatively straightforward two-dimensional problem to 28.9× on a 50-dimensional one.

The main reason for the efficiency gain is initialization. Classical methods start from the origin and spend most of their evaluations simply traveling toward the limit state surface. The LLM-generated algorithm starts at distance $\hat{\beta}$ from the origin, so it arrives near the surface in the first step and reaches convergence in three to eight iterations. This is not a sophisticated optimization strategy; it is a sensible starting point that classical implementations do not exploit by default.

The metaball benchmark illustrates a second advantage. When the geometry of the problem is communicated in the prompt, the generated algorithm avoids the secondary MPP and heads directly toward the primary one. The result is both faster and more accurate than any other method tested. This kind of problem-specific adaptation requires no code changes; it only requires updating a few lines of the prompt.

Two limitations are worth noting. On the 50-dimensional lognormal problem, the cost of numerical gradient computation, which grows linearly with dimension, is the binding constraint and leaves little room for further improvement regardless of the search strategy. The same β error shared by all methods on that benchmark reflects a numerical precision issue rather than a failure of the optimizer. The other limitation is the API latency of roughly 12 to 21 seconds per query. This is not a concern when the performance function is expensive to evaluate, as in finite element analyses, but it would be a meaningful overhead if the LSF itself runs in milliseconds.

Once the design point is known, the information gathered in its vicinity can be passed directly to a failure probability estimator. Methods such as Line Sampling, which uses the MPP direction as its sampling axis, or active-learning Kriging, initialized from the identified point, can estimate p_f with relatively few additional evaluations. Building a complete pipeline that connects the design-point search proposed here with one of these estimators is a logical next step and the main direction for future work.

5. Conclusion

This paper introduced LLMMPP, a framework that uses a large language model to generate MPP search algorithms for structural reliability analysis on the fly. Given a short description of the reliability problem, the LLM produces an executable Python routine that is then run directly on the limit state function. No training data and no task-specific fine-tuning are required.

Tests on four benchmark problems, covering a product function with a very small failure probability, a multi-modal metaball function, a parallel system, and a 50-dimensional lognormal problem, showed that the generated algorithms consistently outperform classical gradient-based and metaheuristic methods in terms of the number of LSF evaluations. Speedup factors of 2.1, 6.4, 3.1, and 28.9 were recorded relative to iHL-RF, which was the best-performing classical method in each case. Accuracy was either matched or improved.

The main limitation of the current framework is that it stops at the design point and does not estimate the failure probability directly. Connecting LLMMPP to a variance-reduction method that can exploit the MPP information, such as Line Sampling or importance sampling centered at the design point, is the most immediate direction for future work. The results reported here are specific to DeepSeek-V3; whether other LLMs (e.g., GPT-4o, Claude 3.5, or Gemini 1.5) produce algorithms of comparable efficiency is an open question that warrants a systematic comparative study.

Acknowledgements

First author gratefully acknowledges the DAAD project (57704137) for supporting the research stay at Brno University of Technology (BUT).

References

Ameryan, A., M. Ghalehnovi, and M. Rashki: 2022, 'AK-SESC: a novel reliability procedure based on the integration of active learning kriging and sequential space conversion method'. *Reliability Engineering & System Safety* **217**, 108036.

Au, S.-K. and J. L. Beck: 2001, 'Estimation of small failure probabilities in high dimensions by subset simulation'. *Probabilistic engineering mechanics* **16**(4), 263–277.

Breitung, K.: 2021, 'SORM, design points, subset simulation, and Markov chain Monte Carlo'. *ASCE-ASME Journal of Risk and Uncertainty in Engineering Systems, Part A: Civil Engineering* **7**(4), 04021052.

Chen, Y., R. Zhong, S. Zha, G. Karypis, and H. He: 2022, 'Meta-learning via language model in-context tuning'. In: *Proceedings of the 60th Annual Meeting of the Association for Computational Linguistics (Volume 1: Long Papers)*. pp. 719–730.

Dong, Q., L. Li, D. Dai, C. Zheng, J. Ma, R. Li, H. Xia, J. Xu, Z. Wu, B. Chang, et al.: 2024, 'A survey on in-context learning'. In: *Proceedings of the 2024 conference on empirical methods in natural language processing*. pp. 1107–1128.

Du, X. and W. Chen: 2001, 'A most probable point-based method for efficient uncertainty analysis'. *Journal of Design and Manufacturing automation* **4**(1), 47–66.

Echard, B., N. Gayton, and M. Lemaire: 2011, 'AK-MCS: an active learning reliability method combining Kriging and Monte Carlo simulation'. *Structural safety* **33**(2), 145–154.

Guo, Q., R. Wang, J. Guo, B. Li, K. Song, X. Tan, G. Liu, J. Bian, and Y. Yang: 2024, 'Connecting large language models with evolutionary algorithms yields powerful prompt optimizers'. In: *International Conference on Learning Representations*, Vol. 2024. pp. 34133–34156.

Hasofer, A. M. and N. C. Lind: 1974, 'Exact and invariant second-moment code format'. *Journal of the Engineering Mechanics division* **100**(1), 111–121.

Holland, J. H.: 1992, 'Genetic algorithms'. *Scientific american* **267**(1), 66–73.

Jafari-Asl, J., Y. Dong, and H. Guo: 2025, 'Enhancing Structural Reliability through AI-Driven Control Variates and Subset Simulation'. *ASCE-ASME Journal of Risk and Uncertainty in Engineering Systems, Part A: Civil Engineering* **11**(4), 04025056.

Kennedy, J. and R. Eberhart: 1995, 'Particle swarm optimization (PSO)'. In: *Proc. IEEE international conference on neural networks, Perth, Australia*, Vol. 4. pp. 1942–1948.

Koutsourelakis, P.-S., H. J. Pradlwarter, and G. I. Schueller: 2004, 'Reliability of structures in high dimensions, part I: algorithms and applications'. *Probabilistic Engineering Mechanics* **19**(4), 409–417.

Kraft, D.: 1988, 'A software package for sequential quadratic programming'. *Forschungsbericht- Deutsche Forschungs- und Versuchsanstalt fur Luft- und Raumfahrt*.

Liu, F., X. Lin, S. Yao, Z. Wang, X. Tong, M. Yuan, and Q. Zhang: 2025, 'Large language model for multiobjective evolutionary optimization'. In: *International Conference on Evolutionary Multi-Criterion Optimization*. pp. 178–191.

Liu, S., C. Chen, X. Qu, K. Tang, and Y.-S. Ong: 2024, 'Large language models as evolutionary optimizers'. In: *2024 IEEE Congress on Evolutionary Computation (CEC)*. pp. 1–8.

Schuëller, G. I. and R. Stix: 1987, 'A critical appraisal of methods to determine failure probabilities'. *Structural safety* **4**(4), 293–309.

Seghier, M. E. A. B., P. Spyridis, J. Jafari-Asl, S. Ohadi, and X. Li: 2022, 'Comparative study on the efficiency of simulation and meta-model-based Monte Carlo techniques for accurate reliability analysis of corroded pipelines'. *Sustainability* **14**(10), 5830.

Song, J., Y. Cui, P. Wei, M. A. Valdebenito, and W. Zhang: 2024, 'Constrained Bayesian optimization algorithms for estimating design points in structural reliability analysis'. *Reliability Engineering & System Safety* **241**, 109613.

Vaswani, A., N. Shazeer, N. Parmar, J. Uszkoreit, L. Jones, A. N. Gomez, Ł. Kaiser, and I. Polosukhin: 2017, 'Attention is all you need'. *Advances in neural information processing systems* **30**.

Yin, Y., Y. Wang, B. Xu, and P. Li: 2024, 'Ado-llm: Analog design bayesian optimization with in-context learning of large language models'. In: *Proceedings of the 43rd IEEE/ACM International Conference on Computer-Aided Design*. pp. 1–9.

Yoo, D., I. Lee, and H. Cho: 2014, 'Probabilistic sensitivity analysis for novel second-order reliability method (SORM) using generalized chi-squared distribution'. *Structural and Multidisciplinary Optimization* **50**(5), 787–797.

Zhang, M. R., N. Desai, J. Bae, J. Lorraine, and J. Ba: 2023, 'Using large language models for hyperparameter optimization'. *arXiv preprint arXiv:2312.04528*.

Zhang, Y. and A. Der Kiureghian: 1995, 'Two improved algorithms for reliability analysis'. In: *Reliability and Optimization of Structural Systems: Proceedings of the sixth IFIP WG7. 5 working conference on reliability and optimization of structural systems 1994*. pp. 297–304.

Adaptive Kernel Operator Learning for Spatiotemporal Full-Field Reliability Analysis with Mixed Random Inputs

Zhao Liu, Kaiwen Li, Ping Zhu
State Key Laboratory of Mechanical System and Vibration
National Engineering Research Center of Automotive Power and Intelligent Control
Shanghai Jiao Tong University, Shanghai 200240, PR China

Abstract. The material properties and external loads of engineering structures inevitably exhibit significant spatial and temporal variability; simplifying these into homogeneous random variables severely underestimates failure probability by neglecting localized weak regions. Conventional surrogate approaches address this by incorporating spatial random fields, yet first discretize them via spectrum methods, introducing truncation errors that become prohibitive for fields with short correlation lengths. This paper proposes a kernel operator learning framework for spatiotemporal full-field reliability analysis that encodes all three categories of uncertain inputs, namely, random variables, stochastic processes, and spatial random fields, through anisotropic product kernels on a latent Gaussian process regressor, bypassing explicit dimensionality reduction. An active learning strategy is further developed, combining an integrated variance reduction term weighted toward the zero level set with a sign-misclassification exploitation term, terminated by a level-set stability criterion. The framework is validated on benchmark problems with mixed random inputs, demonstrating accurate full-field failure probability estimation with a small number of training samples.

Keywords: Spatiotemporal full-field reliability analysis, Operator learning, Kernel methods, Gaussian process, Active learning

1. Introduction

In critical fields such as aerospace and civil engineering, the material properties of engineering structures (e.g., elastic modulus, strength) and external loads (e.g., wind loads, corrosive environments) inevitably exhibit significant temporal and spatial variability. Catastrophic failure under such conditions carries severe safety and economic consequences. Ensuring structural integrity therefore requires a reliability framework that can represent both the spatial variability and time evolution of material properties and loads, while remaining computationally tractable for large-scale finite element models.

Traditional time-variant reliability analysis methods, including **first-passage-based approaches** (Li et al., 2022) and **extreme value-based approaches** (Cao et al., 2022), primarily account for stochastic processes while treating structural properties as spatially homogeneous, which is known to severely underestimate failure probability by ignoring localized weak regions (Dimitrov et al., 2017; Lu et al., 2023). Spatiotemporal full-field reliability analysis extends this setting by addition-

© 2026 by the author(s). This work is licensed under the Creative Commons Attribution 4.0 International License (CC BY 4.0), which permits unrestricted use, distribution, and reproduction in any medium, provided the original author and source are credited.

ally incorporating spatial random fields, tracking failure regions that migrate across the structure, the so-called "moving hotspots" phenomenon (Hu et al., 2026). Analytical extensions of the first-passage approach to this setting (Lu et al., 2023) rely on strong independence assumptions and are limited to small failure probabilities, while extreme value-based approaches become computationally intractable for large-scale finite element models, motivating surrogate-based methods.

To address this challenge, active-learning Kriging models (Zhan and Xiao, 2025; Zhan et al., 2026) and physics-informed neural networks (PINNs) (Zhang and Shafieezadeh, 2022; Roy et al., 2024) have been introduced as surrogates. However, the system responses constructed by these methods typically lack spatial information and fail to identify the critical failure domains. Full-field surrogate models, by contrast, map random inputs to the complete spatiotemporal response field, providing robust support for failure location prediction and critical domain prognosis (Zhao et al., 2025; Li and Ding, 2026). Notably, Li and Ding proposed AER-GP, which uses a dual-order-reduced Gaussian process via PCA to efficiently predict full-field responses, achieving accurate critical domain prognosis with very few training samples.

A key challenge in constructing full-field surrogates for spatiotemporal reliability analysis lies in that the simultaneous presence of three categories of random inputs: finite-dimensional random variables $X(\omega)$, stochastic processes $Y(t;\omega)$, and spatial random fields $Z(\mathbf{z};\omega)$. Classical surrogate approaches - including (Li and Ding, 2026) - handle random fields by first discretizing them via Karhunen–Loève expansion (KLE), Expansion Optimal Linear Estimation (EOLE)(Li and Der Kiureghian, 1993) or spatio avearging (Geyer et al., 2022), mapping the infinite-dimensional field to a finite set of random variables before fitting a surrogate. When the spatial correlation length is small relative to the structural domain, this discretization requires a large number of terms to achieve acceptable truncation error, leading to high-dimensional inputs that strain surrogate construction.

The emergence of operator learning provides a novel paradigm for overcoming these challenges (Nikola B. Kovachki et al., 2024). By directly constructing mappings between infinite-dimensional functional spaces $\Psi : \mathcal{U} \to \mathcal{V}$, operator learning bypasses explicit KLE truncation and enables zero-shot inference on meshes of different resolutions, effectively decoupling surrogate accuracy from mesh discretization (Nelsen and Stuart, 2024; Rowbottom et al., 2026). Current approaches fall into two categories: kernel-based methods relying on Reproducing Kernel Hilbert Spaces (RKHS), such as Gaussian Process Operators (Batlle et al., 2024; Mora et al., 2025; Kumar et al., 2025), which offer mathematical interpretability, small-sample competitiveness, and built-in uncertainty quantification; and deep learning-based neural operators, including DeepONet (Lu et al., 2021), FNO (Li et al., 2021), WNO (Tripura and Chakraborty, 2023; N. et al., 2024), and PI-GLNO (Zhong and Meidani, 2024), which demonstrate strong nonlinear expressivity for parametric SPDEs. Both categories have been applied to spatiotemporal full-field reliability analysis: Gong et al. (Gong and Cheung, 2026) embedded local and global inputs into a physics-informed DeepONet with Subset Simulation, though the gradient requirement in the physical loss restricts applicability to regular grids; Tripura et al. (Tripura et al., 2024) employed a multi-fidelity wavelet neural operator validated across multiple mesh scales.

In this paper, we propose a kernel operator learning framework for spatiotemporal full-field reliability analysis under mixed random inputs, extending the RKHS-based operator learning method of Batlle et al. to the reliability setting. The framework encodes all three categories of random inputs through anisotropic product kernels on a latent GP regressor, and is paired with

an active learning strategy combining integrated variance reduction near the failure region with a misclassification-based exploitation term.

The remaining sections of this paper are organized as follows: Section 2 introduces the preliminaries of spatiotemporal full-field reliability analysis and operator learning. Section 3 details the proposed physics-informed operator learning method for full-field reliability analysis. Section 4 presents a few numerical experiments to validate the effectiveness of the proposed method. Finally, Section 5 concludes the paper with a summary of findings and future research directions.

2. Preliminaries

2.1. Spatiotemporal Full-Field Reliability Analysis

Given the probability triplet $(\Omega, \mathcal{F}, \mathbb{P})$, traditional reliability analysis considers only finite-dimensional random variables $X(\omega)$ with probability measure μ_X. The failure probability over domain $\Omega_{\mathcal{F}} = \{x : g(x;\omega) \leq 0\}$ is often expressed as a high-dimensional integral:

$$p_f = \mathbb{P}_\omega(\Omega_{\mathcal{F}}) = \int_{\Omega_{\mathcal{F}}} d\mu_X = \int_{\Omega} \mathbb{I}_{\Omega_{\mathcal{F}}}(x) p_X(x) dx \tag{1}$$

where $p_X(x)$ is the probability density function of the random variable $X(\omega)$ and $\mathbb{I}_{\Omega_{\mathcal{F}}}(x)$ is the indicator function of the failure domain.

Spatiotemporal full-field reliability analysis additionally handles stochastic processes $Y(t;\omega)$ and spatial random fields $Z(\mathbf{z};\omega)$, with probability measures μ_Y and μ_Z. In the context of first passage failure, failure occurs at spatio point z in a specified time interval $[0,t]$. The failure region can thus be defined as $\Omega_{\mathcal{F}} = \{(z,t,\omega) : g(z,t;\omega) \leq 0, \exists \tau \in [0,t], z \in \mathcal{D}_z\}$. Under independent assumption, the spatiotemporal failure probability is given as follows:

$$p_f(z,t) = \mathbb{P}_\omega\left(\Omega_{\mathcal{F}}\right) = \int_{\Omega_{\mathcal{F}}} d\mathbb{P}(\omega) = \int_{\Omega} \mathbb{I}\left(g(z,t;\omega) \leq 0\right) d\mu_X d\mu_Y d\mu_Z \tag{2}$$

2.2. Operator Learning

In this section, we briefly introduce some operator learning architectures. For specific operator learning theories and implementations, one can refer to (Nikola B. Kovachki et al., 2024) and (Kovachki et al., 2024). Let $\mathcal{U} = \{u : \mathcal{D}_x \to \mathbb{R}^{d_i}\}, \mathcal{D}_x \subseteq \mathbb{R}^{d_x}$ and $\mathcal{V} = \{v : \mathcal{D}_y \to \mathbb{R}^{d_o}\}, \mathcal{D}_y \subseteq \mathbb{R}^{d_y}$ be two Banach spaces. Operator learning seeks to approximate $\Psi^\dagger : \mathcal{U} \to \mathcal{V}$ with $\Psi : \mathcal{U} \times \Theta \mapsto \mathcal{V}, \Theta \subseteq \mathbb{R}^p$ from data $\{u_n, \Psi^\dagger(u_n)\}_{n=1}^N, u_n \sim \mu$, where μ is a probability measure on $\mathcal{U}$.

Since $\mathcal{U}$ and $\mathcal{V}$ are infinite-dimensional, it is necessary to project them into a finite-dimensional latent space for numerical analysis. To this end, a pair of encoder-decoder maps can be defined on $\mathcal{U}$ and $\mathcal{V}$,

$$\begin{aligned} F_{\mathcal{U}} &: \mathcal{U} \to \mathbb{R}^{d_u}, \quad G_{\mathcal{U}} : \mathbb{R}^{d_u} \to \mathcal{U} \\ F_{\mathcal{V}} &: \mathcal{V} \to \mathbb{R}^{d_v}, \quad G_{\mathcal{V}} : \mathbb{R}^{d_v} \to \mathcal{V} \end{aligned} \tag{3}$$

The encoder F extracts finite-dimensional features from functional space, and the decoder G maps the features back to the functional space. The latent structure mapping relationship is illustrated as shown in Figure 1. The operator can be reformulated as,

$$\Psi = G_{\mathcal{V}} \circ \varphi \circ F_{\mathcal{U}}. \tag{4}$$

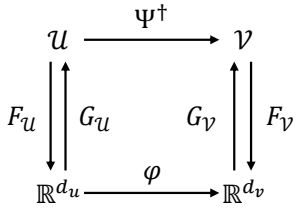


Figure 1. Latent structure in maps between Banach spaces $\mathcal{U}$ and $\mathcal{V}$, adapted from (Nikola B. Kovachki et al., 2024)

Different encoder-decoder combinations yield different operator learning architectures. We focus below on kernel operator learning, which form the basis of the proposed framework. In DeepONet (Lu et al., 2021), $F_{\mathcal{U}}$ evaluates u at fixed sensor points and $G_{\mathcal{V}}$ is a linear combination of trunk-net basis functions, giving output mesh independence but fixing the input sensor locations at inference time.

In kernel methods, $\mathcal{U}$ and $\mathcal{V}$ are assumed to be RKHSs defined by kernels $Q : \mathcal{D}_x \times \mathcal{D}_x \to \mathbb{R}$ and $K : \mathcal{D}_y \times \mathcal{D}_y \to \mathbb{R}$, which ensures the continuity of pointwise evaluations (Dirac functions). Q and K can be taken to be Matérn-like kernels, or any other smoother kernels such that their RKHSs are embedded in $\mathcal{U}$ and $\mathcal{V}$.

The decoders $G_{\mathcal{U}}$ and $G_{\mathcal{V}}$ are defined as the following optimal recovery maps:

$$\begin{aligned} G_{\mathcal{U}}(U) &= \arg\min_{w \in \mathcal{U}} \|w\|_Q, \quad \text{s.t. } F_{\mathcal{U}}(w) = U, \\ G_{\mathcal{V}}(V) &= \arg\min_{w \in \mathcal{V}} \|w\|_K, \quad \text{s.t. } F_{\mathcal{V}}(v) = V. \end{aligned} \tag{5}$$

where $\|\cdot\|_Q$ and $\|\cdot\|_K$ are the RKHS norms arising from their pertinent kernels. As long as the encoders $F_{\mathcal{U}}$ and $F_{\mathcal{V}}$ are linear evaluations, the optimal recovery maps Problem 5 can be solved in closed form by standard representer theorems:

$$\begin{aligned} G_{\mathcal{U}}(U)(x) &= Q(x, \mathbf{X})Q(\mathbf{X}, \mathbf{X})^{-1}U, \\ G_{\mathcal{V}}(V)(y) &= K(y, \mathbf{Y})K(\mathbf{Y}, \mathbf{Y})^{-1}V. \end{aligned} \tag{6}$$

where $Q(\mathbf{X}, \mathbf{X})$ and $K(\mathbf{Y}, \mathbf{Y})$ are the kernel matrices with entries $Q(\mathbf{X}, \mathbf{X})_{ij} = Q(\mathbf{X}_i, \mathbf{X}_j)$ and $K(\mathbf{Y}, \mathbf{Y})_{ij} = K(\mathbf{Y}_i, \mathbf{Y}_j)$ respectively. The latent mapping φ is approximated by ridge regression:

$$\varphi = \arg\min_{w} \|w\|_\Gamma, \text{ s.t. } w(F_{\mathcal{U}}(u_n)) = F_{\mathcal{V}}(v_n), n = 1, \ldots, N \tag{7}$$

where $\|\cdot\|_\Gamma$ is the RKHS norm of the matrix kernel Γ defined on the latent space. When performing mesh independent inference, two additional encoders $\tilde{F}_{\mathcal{U}}$ and $\tilde{F}_{\mathcal{V}}$ and decoders $\tilde{G}_{\mathcal{U}}$ and $\tilde{G}_{\mathcal{V}}$ can be

introduced to map between RKHSs and finite-dimensional latent spaces, and the corresponding learned operator can be expressed as:

$$\Psi = \tilde{F}_{\mathcal{V}} \circ G_{\mathcal{V}} \circ \varphi \circ F_{\mathcal{U}} \circ \tilde{G}_{\mathcal{U}} \tag{8}$$

3. Methodology

In this section, we present an adaptive kernel operator learning framework for spatiotemporal full-field reliability analysis under mixed random inputs.

3.1. Improved Kernel Operator Learning for Spatiotemporal Full-Field Reliability Analysis

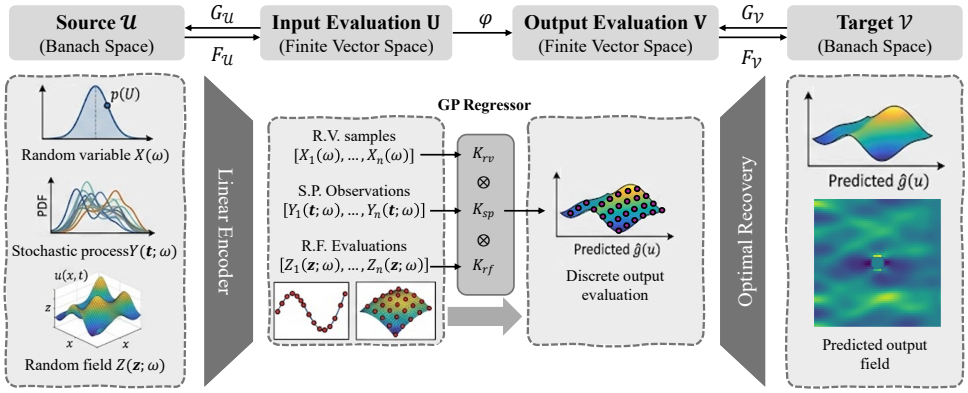


Figure 2. The architecture of the proposed kernel operator learning framework for spatiotemporal full-field reliability analysis.

As reviewed in Section 2.2, kernel operator learning involves three key components: the input function encoder $F_{\mathcal{U}}$, the output function decoder $G_{\mathcal{V}}$, and the latent mapping φ. The overall architecture of the proposed kernel operator learning framework is illustrated in Figure 2. The following sections detail the specific design choices for each component, with a focus on how they are tailored to the spatiotemporal full-field reliability analysis setting.

3.1.1. *Choice of Encoder and Decoder*

Following (Batlle et al., 2024), we adopt linear encoders and decoders constructed from the Cholesky factors of the input and output kernel matrices,

$$Q(\mathbf{X},\mathbf{X})^{-1} = L_Q L_Q^T, \quad K(\mathbf{Y},\mathbf{Y})^{-1} = L_K L_K^T. \tag{9}$$

The input RKHS uses a Matérn-1/2 kernel to accommodate the non-smooth sample paths of stochastic processes and random fields, while the output RKHS uses a Gaussian kernel, reflecting the smoothing effect of the underlying PDE operator.

3.1.2. *Latent mapping*

The core of the operator learning framework lies in approximating the mapping between the projected finite-dimensional latent coordinates. In this study, an operator-valued Gaussian Process (GP) is utilized as the surrogate model for this latent mapping, since it provides a non-parametric, flexible representation of the mapping with built-in uncertainty quantification.

In common settings, the matrix valued kernel $\Gamma : \mathbb{R}^{d_u} \times \mathbb{R}^{d_u} \to \mathbb{R}^{d_v}$ is utilized to define the covariance structure of the operator-valued GP. To maintain a balance between model expressivity and computational tractability, a simple and practical choice for Γ is the diagonal kernel

$$\Gamma(\mathbf{U}, \mathbf{U}') = K(\mathbf{U}, \mathbf{U}') \cdot \mathbf{I}, \tag{10}$$

where $K : \mathbb{R}^{d_u} \times \mathbb{R}^{d_u} \to \mathbb{R}$ is an arbitary scalar valued kernel, such as Gaussian, Matérn, or rational quadratic kernels.

In spatiotemporal full-field reliability analysis, the uncertain inputs comprise three structurally distinct categories: finite-dimensional random variables $X(\omega) \in \mathbb{R}^{d_X}$, stochastic processes $Y(t;\omega)$ indexed over time $t \in \mathcal{T}$, and spatial random fields $Z(\mathbf{z};\omega)$ indexed over the spatial domain $\mathcal{D}$. To capture the distinct physical influences and correlation structures of different uncertainty sources, we construct anisotropic kernels within this GP framework. Therefor, we define the extended input space as the product space

$$\mathcal{U} = \mathbb{R}^{d_X} \oplus \mathcal{U}_Y \oplus \mathcal{U}_Z, \tag{11}$$

where $\mathcal{U}_Y$ is the RKHS of stochastic processes over $\mathcal{T}$, and $\mathcal{U}_Z$ is the RKHS of spatial random fields over $\mathcal{D}$. A realization of the joint input is denoted $u = (x, y(\cdot), z(\cdot)) \in \mathcal{U}$.

Three anisotropic kernels are defined for each input type. For random variables, stochastic processes, and spatial random fields, we respectively adopt:

$$\begin{aligned} K_{\mathrm{rv}}(X, X') &= \exp\!\big(-\tfrac{1}{2}(X - X')^T \Lambda^{-2} (X - X')\big)\,, \\ K_{\mathrm{sp}}(Y, Y') &= k^{\nu}_{\text{Matérn}}\big(\|\mathbf{t} - \mathbf{t}'\|;\, \ell_t\big), \\ K_{\mathrm{rf}}(Z, Z') &= \sigma_Z^2\, k^{\nu}_{\text{Matérn}}(r;\ell), \quad r = \big\|\Lambda_Z^{-1}(\mathbf{Z} - \mathbf{Z}')\big\|, \end{aligned} \tag{12}$$

where $\Lambda = \mathrm{diag}(\ell_1, \ldots, \ell_{d_X})$ and Λ_Z encode per-dimension length-scales for random variables and spatial random fields respectively. Unlike KLE or EOLE, d_z affects only the Gram matrix size in the optimal recovery map, not the dimensionality of the regression problem.

The three kernels are combined via a tensor product to form the joint input kernel:

$$\Gamma\big((X, Y, Z), (X', Y', Z')\big) = K_{\mathrm{rv}}(X, X') \otimes K_{\mathrm{sp}}(Y, Y') \otimes K_{\mathrm{rf}}(Z, Z'). \tag{13}$$

The posterior mean and covariance of the operator-valued GP with kernel Γ can be expressed as

$$\begin{aligned} \hat{v}_* &= \mu(\mathbf{x}_*) + \Gamma(\mathbf{x}_*, \mathbf{X})[\Gamma(\mathbf{X}, \mathbf{X}) + \sigma_n^2 \mathbf{I}]^{-1}(\mathbf{y} - \mu(\mathbf{X})) \\ \hat{\sigma}^2 &= \Gamma(\mathbf{x}_*, \mathbf{x}_*) - \Gamma(\mathbf{x}_*, \mathbf{X})[\Gamma(\mathbf{X}, \mathbf{X}) + \sigma_n^2 \mathbf{I}]^{-1}\Gamma(\mathbf{x}_*, \mathbf{X}) \end{aligned} \tag{14}$$

3.2. Active Learning Strategy for Kernel Operator Learning

The kernel operator learning surrogate Ψ is trained on a dataset $\{u_n, \Psi^\dagger(u_n)\}_{n=1}^N$, where each pair requires one evaluation of the underlying PDE solver. Since such evaluations are computationally expensive, it is desirable to select training samples adaptively to characterize the spatiotemporal limit state boundary with as few solver calls as possible. Active learning for reliability analysis has been well-established in the Kriging setting (Echard et al., 2011; Moustapha, 2016), with strategies developed for time-invariant, time-variant, and multi-fidelity problems (Song et al., 2026; Zhao et al., 2026; Feng et al., 2025). The present operator learning setting differs in two key respects: the input is a function-valued source $u \in \mathcal{U}$, and the surrogate output is a full spatiotemporal field $v \in \mathcal{V}$, so model uncertainty is a global quantity and the limit state boundary is a zero level set in $\mathcal{U}$ rather than a hypersurface in $\mathbb{R}^d$.

3.2.1. *Learning Function*

According to Eqs 14, the learned kernel operator model provides, for any candidate input $U^* = F_{\mathcal{U}}(u^*)$, a posterior mean $\hat{v}_k(U^*)$ and variance $\sigma_k^2(U^*)$ at each output observation point $y_k \in Y$, $k = 1, \ldots, d_V$. The active learning strategy seeks the next most informative sample over a candidate pool $\mathcal{C} = \{U_j\}_{j=1}^M$, balancing global exploration with local exploitation near the limit state boundary. We construct the acquisition function as a weighted combination of two terms.

The global term quantifies the expected reduction in predictive uncertainty over the current candidate pool $\mathcal{C} = \{U_j\}_{j=1}^M$ if U^* is added to the DoE. For a GP with posterior variance $\sigma_t^2(U)$ at iteration t, the one-step variance reduction at an arbitrary point $U \in \mathcal{U}$ after observing U^* follows directly from the GP update equations:

$$\sigma_t^2(U) - \sigma_{t+1,U^*}^2(U) = \frac{\Gamma(U, U^*)^2}{\Gamma(U^*, U^*) + \gamma}, \tag{15}$$

where $\Gamma(\cdot,\cdot)$ is the posterior covariance of the latent mapping φ and $\gamma > 0$ is a noise regularization constant. Integrating this reduction over the input measure μ and approximating the integral by a Monte Carlo Simulation (MCS) over the candidate pool gives the standard IVR acquisition function:

$$\alpha_{\mathrm{IVR}}(U^*) = \int_{\mathcal{U}} \big[\sigma_t^2(U) - \sigma_{t+1,U^*}^2(U)\big] \mathrm{d}\mu(U) \approx \frac{1}{M(\sigma_{\mathrm{signal}}^2 + \gamma)} \sum_{j=1}^{M} \Gamma(U_j, U^*)^2, \tag{16}$$

where $\sigma_{\mathrm{signal}}^2 \approx \Gamma(U^*, U^*)$ is the prior signal variance. To concentrate exploration near the limit state boundary, we reweight each candidate by:

$$w_j = \frac{\Phi(|\hat{v}_{\min}(U_j)|/\sigma_{\min}(U_j))}{\sum_{j'} \Phi\big(|\hat{v}_{\min}(U_{j'})|/\sigma_{\min}(U_{j'})\big)}, \tag{17}$$

where $\hat{v}_{\min}(U_j) = \min_k \hat{v}_k(U_j)$ is the predicted minimum response over the spatiotemporal domain and Φ is the standard normal PDF. The corresponding weighted integrated variance reduction acquisition function is

$$\alpha_{\text{IVR-zero}}(U^*) \approx \frac{1}{M(\sigma_{\mathrm{signal}}^2 + \gamma)} \sum_{j=1}^{M} w_j \cdot \Gamma(U_j, U^*)^2. \tag{18}$$

The local exploitation term sums the sign-misclassification probability over all output points:

$$\alpha_{\mathrm{MIS}}(U^*) = \sum_{k=1}^{d_V} \Phi\left(-\frac{|\hat{v}_k(U^*)|}{\sigma_k(U^*)}\right). \tag{19}$$

The two terms are then combined with an adaptive weight $\lambda_t = \lambda_0(1 - e^{-t/\tau})$ that balances global exploration early in the learning process against local exploitation as the level set estimate matures:

$$U^* = \arg\max_{U\in\mathcal{C}} \alpha(U) = \arg\max_{U\in\mathcal{C}} \alpha_{\text{IVR-zero}}(U) + \lambda_t\, \alpha_{\mathrm{MIS}}(U) \tag{20}$$

3.2.2. *Stopping Criterion*

Aside from the learning function, another essential aspect of active learning is the stopping criterion. In this study, we propose a criterion based on the stability of the estimated spatiotemporal limit state boundary.

We track the discrete zero level set of the surrogate over the candidate pool:

$$\hat{\mathcal{L}}_t = \left\{ j \in \mathcal{I}_{\text{avail}} : \hat{v}_{\min}^{(j)} < 2 \right\}, \tag{21}$$

where $\mathcal{I}_{\text{avail}}$ indexes the available candidate samples and the threshold 2 provides a margin around the zero level set. The relative change rate of the level set at iteration t and its moving average are defined as

$$\Delta_t = \frac{\left||\hat{\mathcal{L}}_t| - |\hat{\mathcal{L}}_{t-1}|\right|}{|\hat{\mathcal{L}}_t| + \epsilon}, \quad \bar{\Delta}_t = \frac{1}{K}\sum_{k=1}^{K-1} \Delta_{t-k}. \tag{22}$$

where $\epsilon > 0$ is a small constant preventing division by zero. The active learning loop terminates when $\bar{\Delta}_t < \tau_\Delta$, where τ_Δ is a user-specified tolerance. This criterion directly measures the stability of the reliability-relevant region of the input space rather than the overall surrogate accuracy, making it well-suited for reliability analysis where only the sign of the limit state function matters. In ouir practice, the tolerance τ_Δ can be around 0.001 to 0.005, and the moving average window size K can be around 20, depending on the problem complexity and computational budget.

3.3. Implementation Procedure of Proposed Method

The overall procedure is summarized in Figure 3.

4. Numerical Experiments

In this section, we present three numerical examples using either numerical solvers or finite element solvers to demonstrate the effectiveness of the proposed method.

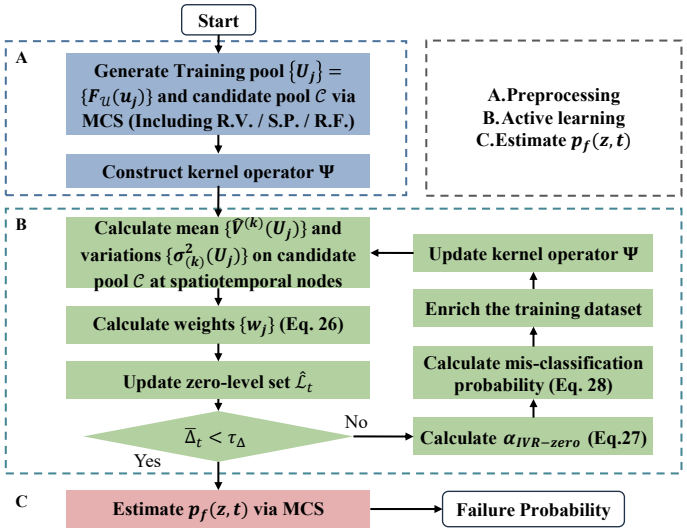


Figure 3. Flowchart of the proposed active learning strategy

4.1. Example 1: 1D Poisson Equation

We first consider a parametric 1D Poisson equation with a stochastic forcing term:

$$-\alpha(\omega)\frac{d^2u(x;\omega)}{dx^2} = f(x;\omega), \quad x \in [0,1], \quad u(0;\omega) = u(1;\omega) = 0. \tag{23}$$

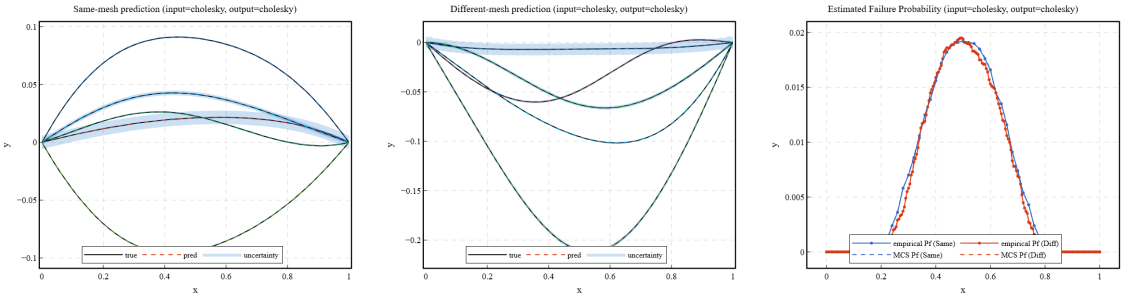
where the uncertain parameter $\alpha = \beta^2 + 1, \beta \sim \mathcal{N}(0,1)$; the stochastic forcing $f(t;\omega)$ will be considered as stationary Gaussian process,

$$f(x;\omega) \sim \mathcal{GP}\left(0, \exp\left(-\frac{(x-x')^2}{2l^2}\right)\right), l = 0.3. \tag{24}$$

We first analyze the performance of kernel operator learning without active learning, where the training dataset consists of $N = 300$ samples of α and f generated by Monte Carlo sampling. The input RKHS is equipped with a Matérn 1/2 kernel with the same correlation length of $l = 0.3$, while the output RKHS is equipped with a RBF kernel with correlation length of $l = 0.5$. The forcing term $f(x;\omega)$ and corresponding output displacement $u(x)$ is evaluated on a 51-point uniform grid, and two test datasets are generated on the same grid and a finer 101-point grid with 10^4 samples each, in order to demonstrate the ability for operator learning to generalize to different output meshes. Five representative test samples are visualized in Figure 4a and Figure 4b. The relative L^2 error on two test datasets are 2.83% and 2.91% respectively.

The limit state function of each spatial point is defined as $g(x) = |0.75 - u(x)|$. Given the trained kernel operator, the failure probability is estimated by performing a Monte Carlo Simulation over two test datasets inputs, as shown in Figure 4c. The surrogate failure probability estimates agree well with the reference, as shown in Figure 4.

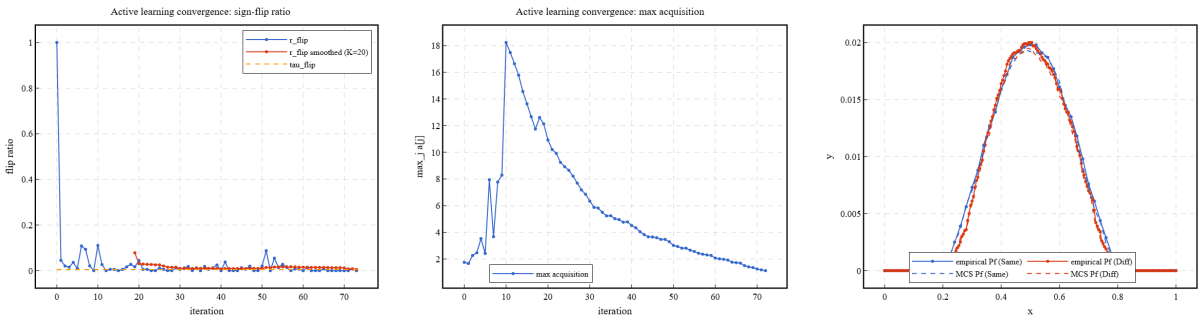
We then turn to adaptive sampling with the proposed active learning strategy, where the initial training dataset consists of $N_0 = 20$ samples and the candidate pool consists of $N_{\text{MCS}} = 10^4$



(a) Same grid prediction of $u(x;\omega)$ (b) Finer grid prediction of $u(x;\omega)$ (c) Failure probability estimation

Figure 4. 1D Poisson equation Results

samples. Parameter τ_Δ and K are set to 0.005 and 20 respectively. Figure 5a and Figure 5b shows the convergence of the active learning strategy. After 93 iterations, the adaptive strategy converges and the final surrogate is used to estimate the failure probability, result of which is given in Figure 5c. Compared to the result without adaptive sampling strategy, it reaches a similar accuracy with only 93 training samples, which demonstrates the efficiency of the proposed active learning strategy in identifying informative training samples and accelerating the learning process.



(a) Stability of zero level set (b) Learning function value (c) Failure probability estimation

Figure 5. Results of the active learning strategy for the 1D Poisson equation

4.2. Example 2: Diffusion Reaction PDE

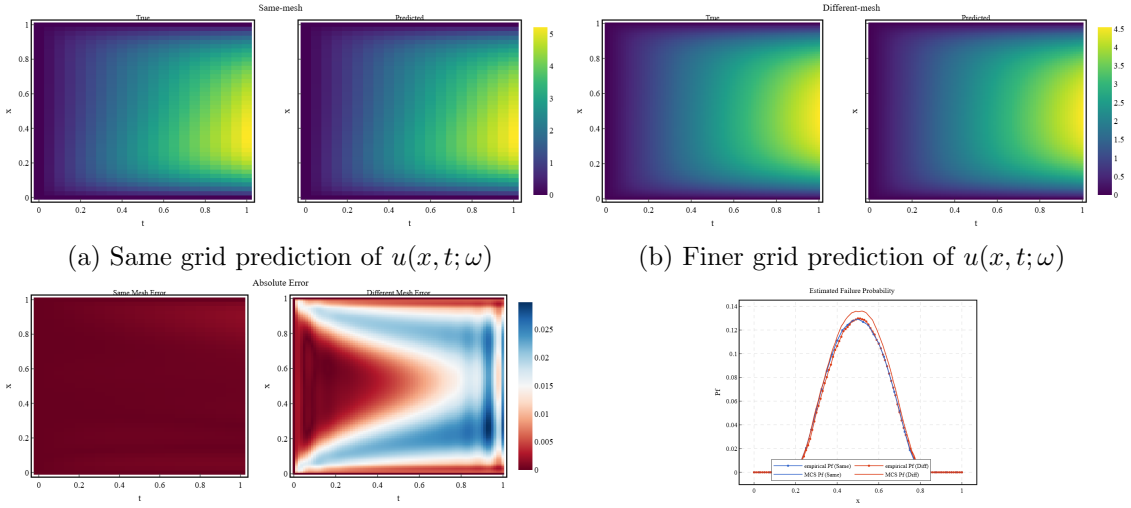
We next consider a 2D diffusion-reaction PDE with a stochastic source term:

$$\frac{\partial u(x,t;\omega)}{\partial t} = \frac{\partial}{\partial x}\left(K(x;\omega)\frac{\partial u(x,t;\omega)}{\partial x}\right) + 0.01\,u(x,t;\omega)^2 + f(x;\omega), \quad (x,t) \in [0,1]\times[0,1] \tag{25}$$

where the diffusion term is defined a $K(x;\omega) = 0.01(\sin(k(x;\omega)) + 2)$. Two independent input random fields are given as:

$$k(x;\omega) \sim \mathcal{GP}\left(2,\ 0.25^2 \exp\left(-\frac{(x-x')^2}{2l^2}\right)\right), f(x;\omega) \sim \mathcal{GP}\left(5,\ \exp\left(-\frac{(x-x')^2}{2l^2}\right)\right), l = 0.3. \tag{26}$$

The training dataset consists of $N = 200$ samples of k and f generated by Cholesky decomposition. The RKHS kernels are chosen as Matérn 1/2 and RBF kernels with correlation lengths of $l = 0.3$ and $l = 0.5$, respectively. $f(x;\omega)$, $k(x;\omega)$ and corresponding output displacement $u(x,t)$ is evaluated on a uniform grid with $n_x \times n_t = (41 \times 21)$, and two test datasets are generated on the same grid and a finer (101×81) grid with 10^4 samples each. A representative test samples are visualized in Figure 6a, Figure 6b and Figure 6c. The relative L^2 error on two test datasets are 0.08% and 0.70% respectively. The lower error relative to Example 1 is attributable to the smoothing effect of diffusion.



(a) Same grid prediction of $u(x,t;\omega)$

(b) Finer grid prediction of $u(x,t;\omega)$

(c) Absolute error of $u(x,t;\omega)$

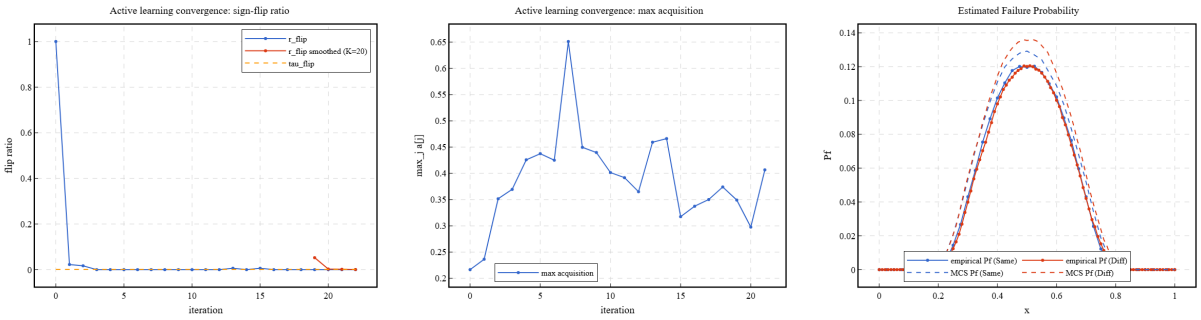
(d) Failure probability estimation

Figure 6. Predictions of the kernel operator learning surrogate for the diffusion-reaction PDE

Since it is a time variant problem, the limit state function of each spatial point is defined as a first passage problem $g(x,t) = 6 - \max_t u(x,t;\omega)$. Given the trained kernel operator, the first passage failure probability is estimated by Monte Carlo Simulation over two test datasets inputs. The results are given in Figure 6d, where same mesh prediction outperforms finer mesh prediction as operator learning indeed in theory is a data-driven method and thus gives less accurate predictions on unseen meshes.

Considering adaptive sampling strategy, the initial training dataset consists of $N_0 = 20$ samples and the candidate pool consists of $N_{\text{MCS}} = 10^4$ samples. Parameter τ_Δ and K are set to 0.001 and 20 respectively. Figure 7a and Figure 7b shows the convergence of the active learning strategy, where we can see that after 82 iterations, the active learning strategy converges and the final surrogate is used to estimate the failure probability, result of which is given in Figure 7c. Compared to the result

without adaptive sampling strategy, it reaches a similar accuracy with only 42 training samples, which demonstrates the efficiency of the proposed active learning strategy in identifying informative training samples and accelerating the learning process.



(a) Stability of zero level set (b) Learning function value (c) Failure probability estimation

Figure 7. Results of the active learning strategy for the diffusion reaction problem

4.3. Example 3: Planar Stress of Plates with a Hole

In this example, we consider a 2D planar stress problem of a plate with a hole under tension, where the Young's modulus is modeled as a spatial random field. The problem is posed on the perforated domain $\Omega = [0,2]^2 \setminus \{(x,y) : (x-1)^2 + (y-1)^2 \leq 0.1^2\}$, with equilibrium equation and boundary conditions:

$$\begin{cases} \nabla \cdot \boldsymbol{\sigma} = \mathbf{0}, & \forall (x,y) \in \Omega, \\ u(x,y) = 0, & x = 0, \\ \boldsymbol{\sigma} \cdot \mathbf{n} = p_0 \mathbf{e}_x, & x = 2. \end{cases} \tag{27}$$

where $\boldsymbol{\sigma}$ is the stress tensor, $\mathbf{n}$ is the outward normal vector, and p_0 is the applied tension on the boundary. Kernel operator learning aims to learn the mapping from Young's modulus to the von-mises stress field. The Young's modulus $E(x,y;\omega)$ is modeled as a log-normal random field:

$$Z(x,y) = \ln\left(\frac{E(x,y)}{E_0}\right), \quad \mathrm{Cov}[Z(\mathbf{s}), Z(\mathbf{s}')] = \sigma_Z^2 \frac{r}{\ell} K_1\left(\frac{r}{\ell}\right), \quad r = \|\mathbf{s} - \mathbf{s}'\| \tag{28}$$

As kernel operators are both input and output mesh independent, we consider two training cases in this example. In both cases, the input is evaluated via SPDE method (Lindgren et al., 2011) and the problem is solved by finite element method. The training dataset contains $N = 1000$ samples, while two other test datasets contain 10^4 samples each. The limit state function is given as $g(x,y) = 3p_0 - \sigma(x,y)$.

4.3.1. *Case 1*

In the first case, we use uniform mesh of 51×51 elements as training grid and both 51×51 uniform and unstructured meshes of 4720 elements as test grids. Results of one of the prediction is shown in Figure 8, where we can see that both test meshes give acceptable predictions, with relative L^2

errors of 7.25% and 9.13%. The results of further failure probability estimation is demonstrated in Figure 9. The unstructured-mesh estimates are less accurate, as the coarser training mesh (2061 elements) contains less information than the 4720-element test mesh.

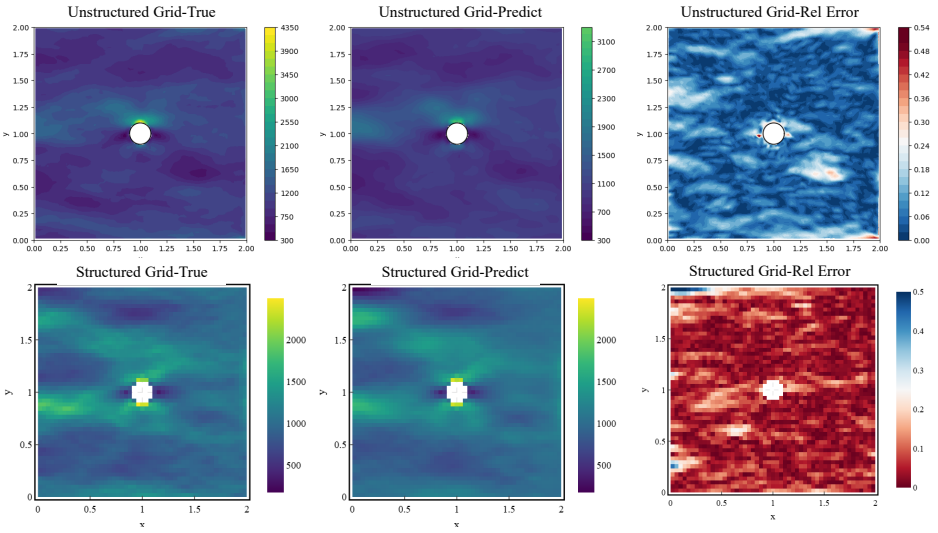
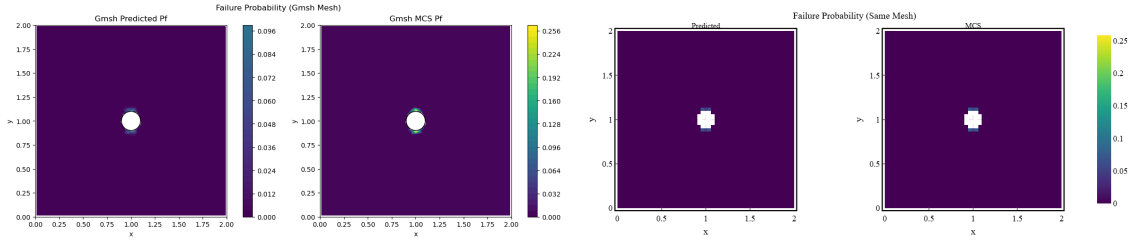


Figure 8. Predictions of the kernel operator for planar stress problem



(a) Failure probability estimation on unstructured mesh

(b) Failure probability estimation on uniform mesh

Figure 9. Failure probability estimation for planar stress case 1

4.3.2. *Case 2*

In the second case, we use unstructured mesh of 4720 elements as training grid and both uniform of 51×51 elements and unstructured meshes as test grids. One of the prediction is given in Figure 10, where we can see that both test meshes give acceptable predictions, with relative L^2 errors of 8.97% and 7.94%. The results of further failure probability estimation is demonstrated in Figure 11. Consistent with Case 1, training on the finer mesh reduces both prediction and failure probability estimation error.

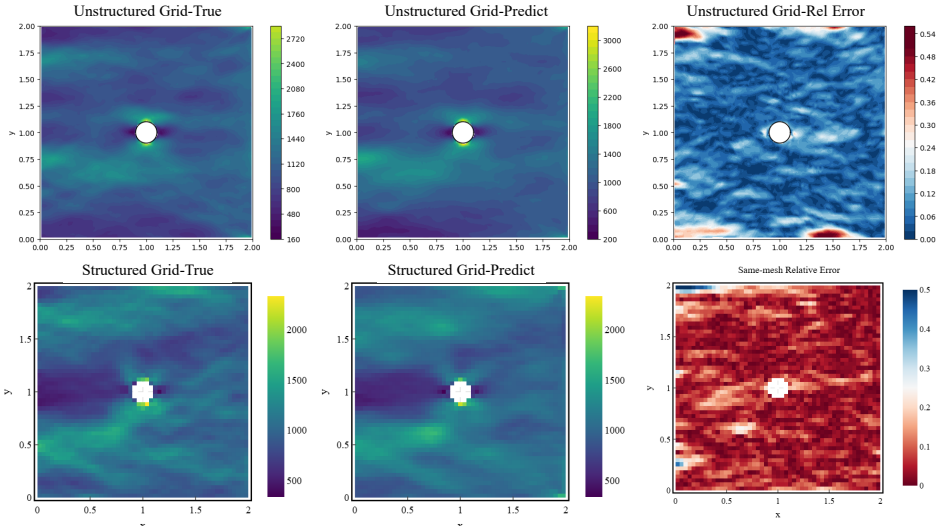
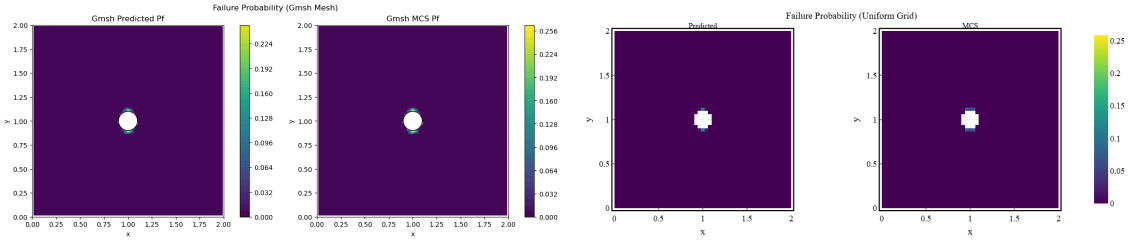


Figure 10. Predictions of the kernel operator for planar stress problem



(a) Failure probability estimation on unstructured mesh

(b) Failure probability estimation on uniform mesh

Figure 11. Failure probability estimation for planar stress case 2

5. Conclusion

This paper presented a kernel operator learning framework for spatiotemporal full-field reliability analysis under mixed random inputs. By extending the RKHS-based operator learning method of Batlle et al. to the reliability setting, the proposed framework constructs a surrogate that directly maps random variables, stochastic processes, and spatial random fields to the full spatiotemporal response field, without prior discretization via KLE or EOLE. The three input types are encoded through anisotropic product kernels on the latent GP regressor, each tailored to its corresponding covariance structure. An active learning strategy was further developed, combining an IVR-based global exploration term weighted toward the zero level set with a local sign-misclassification exploitation term, and terminated by a level-set stability criterion. The framework was validated on two benchmark problems: a 1D spatial Poisson equation with mixed random variable and random field inputs, and a 2D spatiotemporal diffusion-reaction equation with random process and random field inputs.

Two directions are identified for future work. First, the present learning function targets uncertainty reduction near the zero level set, but its quantitative contribution to failure probability accuracy is not explicitly tracked. A more principled formulation would optimize directly for the expected reduction in the variance of $\hat{p}_f$, analogous to (Song, 2022), extended to the operator setting where the failure event is defined by a spatiotemporal supremum. Second, the Cameron–Martin theorem establishes that random field sample paths belong to the associated RKHS only on a set of measure zero, creating a mismatch between the assumed function space geometry and the actual field distribution. Kernel Flows (Owhadi and Yoo, 2019) offers a data-driven remedy by adaptively learning kernel parameters to align the RKHS geometry with observed field realizations, replacing the current manual specification of Matérn smoothness and length-scale parameters.

References

Batlle, P., M. Darcy, B. Hosseini, and H. Owhadi: 2024, 'Kernel Methods Are Competitive for Operator Learning'. *Journal of Computational Physics* **496**, 112549.

Cao, R., Z. Sun, J. Wang, and F. Guo: 2022, 'A Single-Loop Reliability Analysis Strategy for Time-Dependent Problems with Small Failure Probability'. *Reliability Engineering & System Safety* **219**, 108230.

Dimitrov, N., R. D. Bitsche, and J. P. Blasques: 2017, 'Spatial Reliability Analysis of a Wind Turbine Blade Cross Section Subjected to Multi-Axial Extreme Loading'. *Structural Safety* **66**, 27–37.

Echard, B., N. Gayton, and M. Lemaire: 2011, 'AK-MCS: An Active Learning Reliability Method Combining Kriging and Monte Carlo Simulation'. *Structural Safety* **33**(2), 145–154.

Feng, S., L. Wang, H. Dong, Y. Li, Z. Wan, and C. G. Soares: 2025, 'An Active-Learning Method Based on Hierarchical Kriging Model for Multi-Fidelity Reliability Analysis'. *Reliability Engineering & System Safety* p. 111759.

Geyer, S., I. Papaioannou, L. Graham-Brady, and D. Straub: 2022, 'The Spatial Averaging Method for Non-Homogeneous Random Fields with Application to Reliability Analysis'. *Engineering Structures* **253**, 113761.

Gong, Y. and S. H. Cheung: 2026, 'Adaptive Physics-Informed Neural Operator and Subset Simulation for High-Dimensional Reliability Analysis with Multiple Stochastic Processes in Stochastic Differential Equations'. *Reliability Engineering & System Safety* **268**, 111949.

Hu, W., J. Liao, J. Yan, J. Fang, F. Zhao, I. Lee, and J. Tan: 2026, 'Spatiotemporal-Dependent Reliability Analysis with Adaptive Sampling Physics-Informed Neural Networks'. *Reliability Engineering & System Safety* **265**, 111560.

Kovachki, N., Z. Li, B. Liu, K. Azizzadenesheli, K. Bhattacharya, A. Stuart, and A. Anandkumar: 2024, 'Neural Operator: Learning Maps between Function Spaces'.

Kumar, S., R. Nayek, and S. Chakraborty: 2025, 'Towards Gaussian Process for Operator Learning: An Uncertainty Aware Resolution Independent Operator Learning Algorithm for Computational Mechanics'. *Computer Methods in Applied Mechanics and Engineering* **435**, 117664.

Li, C.-C. and A. Der Kiureghian: 1993, 'Optimal Discretization of Random Fields'. *Journal of Engineering Mechanics* **119**(6), 1136–1154.

Li, X. and C. Ding: 2026, 'Active Evolutionary Gaussian Process for Structural Large-Scale Full-Field Reliability Analysis and Critical Domain Prognosis with Only Few Initial Samples'. *Computer Methods in Applied Mechanics and Engineering* **448**, 118418.

Li, X.-W., Y.-G. Zhao, X.-Y. Zhang, and Z.-H. Lu: 2022, 'Explicit Model of Outcrossing Rate for Time-Variant Reliability'. *ASCE-ASME Journal of Risk and Uncertainty in Engineering Systems, Part A: Civil Engineering* **8**(1), 4021087.

Li, Z., N. Kovachki, K. Azizzadenesheli, B. Liu, K. Bhattacharya, A. Stuart, and A. Anandkumar: 2021, 'Fourier Neural Operator for Parametric Partial Differential Equations'.

Lindgren, F., H. Rue, and J. Lindström: 2011, 'An Explicit Link between Gaussian Fields and Gaussian Markov Random Fields: The Stochastic Partial Differential Equation Approach'. *Journal of the Royal Statistical Society Series B: Statistical Methodology* **73**(4), 423–498.

Lu, L., P. Jin, G. Pang, Z. Zhang, and G. E. Karniadakis: 2021, 'Learning Nonlinear Operators via DeepONet Based on the Universal Approximation Theorem of Operators'. *Nature Machine Intelligence* **3**(3), 218–229.

Lu, Z.-H., H.-P. Qiao, X.-Y. Zhang, and Y.-G. Zhao: 2023, 'An Innovative Method for Space-Time-Dependent Reliability Analysis'. *Structural Safety* **102**, 102326.

Mora, C., A. Yousefpour, S. Hosseinmardi, H. Owhadi, and R. Bostanabad: 2025, 'Operator learning with gaussian processes'. *Computer Methods in Applied Mechanics and Engineering* **434**, 117581.

Moustapha, M.: 2016, 'Adaptive Surrogate Models for the Reliable Lightweight Design of Automotive Body Structures'. Ph.D. thesis, BLAISE PASCAL UNIVERSITY – CLERMONT II.

N., N., T. Tripura, and S. Chakraborty: 2024, 'Physics Informed WNO'. *Computer Methods in Applied Mechanics and Engineering* **418**, 116546.

Nelsen, N. H. and A. M. Stuart: 2024, 'Operator Learning Using Random Features: A Tool for Scientific Computing'. *SIAM Review* **66**(3), 535–571.

Nikola B. Kovachki, Samuel Lanthaler, and Andrew M. Stuart: 2024, 'Chapter 9 - Operator Learning: Algorithms and Analysis'. In: *Numerical Analysis Meets Machine Learning*, Vol. 25 of *Handbook of Numerical Analysis*. Elsevier, pp. 419–467.

Owhadi, H. and G. R. Yoo: 2019, 'Kernel Flows: From Learning Kernels from Data into the Abyss'. *Journal of Computational Physics* **389**, 22–47.

Rowbottom, J., S. Fresca, P. Lio, C.-B. Schönlieb, and N. Boullé: 2026, 'Multi-Level Monte Carlo Training of Neural Operators'. *Computer Methods in Applied Mechanics and Engineering* **453**, 118800.

Roy, A., T. Chatterjee, and S. Adhikari: 2024, 'A Physics-Informed Neural Network Enhanced Importance Sampling (PINN-IS) for Data-Free Reliability Analysis'. *Probabilistic Engineering Mechanics* **78**, 103701.

Song, Z.: 2022, 'An Estimation Variance Reduction-Guided Adaptive Kriging Method for Efficient Time-Variant Structural Reliability Analysis'. *Mechanical Systems and Signal Processing*.

Song, Z., C. Dang, M. A. Valdebenito, and M. G. R. Faes: 2026, 'Active Learning Kriging with Functional Dimension Reduction for Reliability Analysis of Stochastic Dynamical Systems'. *Reliability Engineering & System Safety* **273**, 112360.

Tripura, T. and S. Chakraborty: 2023, 'Wavelet Neural Operator for Solving Parametric Partial Differential Equations in Computational Mechanics Problems'. *Computer Methods in Applied Mechanics and Engineering* **404**, 115783.

Tripura, T., A. Thakur, and S. Chakraborty: 2024, 'Multi-fidelity wavelet neural operator surrogate model for time-independent and time-dependent reliability analysis'. *Probabilistic Engineering Mechanics* **77**, 103672.

Zhan, H., H. Liu, and N.-C. Xiao: 2026, 'An active learning multi-fidelity kriging model for predicting the expected lifetime of time- and space-dependent structural systems with multi-fidelity data'. *Reliability Engineering & System Safety* **270**, 112192.

Zhan, H. and N.-C. Xiao: 2025, 'A New Active Learning Surrogate Model for Time- and Space-Dependent System Reliability Analysis'. *Reliability Engineering & System Safety* **253**, 110536.

Zhang, C. and A. Shafieezadeh: 2022, 'Simulation-Free Reliability Analysis with Active Learning and Physics-Informed Neural Network'. *Reliability Engineering & System Safety* **226**, 108716.

Zhao, Q., X. Jia, B. Li, M. Wang, G. Jin, and B. Guo: 2026, 'AK-TSYS: An Enhanced Active Learning Kriging Model for Time-Dependent System Reliability Analysis'. *Reliability Engineering & System Safety* **268**, 111991.

Zhao, Y., J. Liu, and Y. Ren: 2025, 'Rapid Uncertainty Quantification for Structural Full-Field Dynamic Responses with Extremely High Dimension'. *Reliability Engineering & System Safety* **261**, 111097.

Zhong, W. and H. Meidani: 2024, 'Physics-Informed Geometry-Aware Neural Operator'.

Quantification of modeling uncertainty in physics-informed neural networks by interval arithmetic

Zlatan Dimitrov, Petar O. Hristov
[1)] *GATE Institute, 1164 Sofia, Bulgaria, {zlatan.dimitrov, petar.hristov}@gate-ai.eu*

Abstract. The seemingly unrestrained advancements in machine learning technologies drive engineers to increasingly often rely on data-driven approaches in the design of complex systems. This not only requires extensive data to capture the underlying behavior, but it effectively ascribes complete trustworthiness to data. However, real-world scenarios frequently provide only sparse, noisy, or otherwise corrupted measurements. Compounding this challenge is the need to balance resource utilization and performance.

To alleviate some of the burden related to the models exclusively relying on data, the class of physics-informed machine learning emerged, which integrates knowledge about the governing physical laws, with data from the system. The majority of physics-based machine learning models, however, remain black boxes and the epistemic uncertainty stemming from the model itself remains unquantified or quantified in a biased way.

This work explores the extension of physics-informed neural networks with an interval description of the epistemic uncertainty, integral to the model, thereby avoiding subjective assignments of prior beliefs to components of the model. In the proposed implementation, data processing is done through numerical weights and two separate fully connected layers are used to estimate the center and interval uncertainty of the prediction, to alleviate the problem of interval repeated variables. In addition, the architecture leverages a physics-informed loss function considering whether the output of the model satisfies the underlying partial differential equation and boundary conditions.

We validate the performance of the architecture on simplified synthetic data, representing a structural dynamics problem, in particular a noisy dataset generated using an analytical solution to the Euler-Lagrange equation. The interval PINN, proposed in this paper, provides a way for evaluating a cantilever beam's free oscillations in a way that considers both the underlying structural mechanics knowledge and the available measurement data. The architecture is more explainable than purely data-based models, while avoiding applying prior bias on the quantification epistemic uncertainty.

Keywords: physics-informed machine learning, epistemic uncertainty, interval arithmetic, cantilever beam, partial differential equation (PDE)

1. Introduction

The reliable modeling of physical systems is important during tasks like engineering design, system identification, and digital twin development. This modeling is traditionally done using a numerical partial differential equation (PDE) method, such as the finite element method (FEM), which solves

© 2026 by the author(s). This work is licensed under the Creative Commons Attribution 4.0 International License (CC BY 4.0), which permits unrestricted use, distribution, and reproduction in any medium, provided the original author and source are credited.

a discretised version of the underlying mathematical equations on a computational mesh. Such approaches offer limited capability for the integration of observations, since they rely only on physical laws in an idealized environment. In addition, physics-based models require the full simulations to be run end to end for each new parameter combination, making their use in design and virtual experimentation computationally expensive (Taflove et al., 2005; Rylander et al., 2013).

In a somewhat parallel thread, data-based machine learning approaches (ML) have recently grown in popularity as a tool for solving physical problems. These methods perform well as surrogates, interpolating between different observations or parameter configurations, or when the available physics is not sufficient to describe the problem under investigation and the observation data is abundant, as empirical models. The limitation of these models stems from the fact that they are not grounded in natural laws, which may cause their results to become non-physical (Bishop, 2009; Raissi et al., 2019). Physics-informed machine learning bridges the gap between pure data-based modeling and idealized physics, by integrating the physical knowledge into parts of the ML model, which allows the latter to respect known conservation properties and invariants. Physics-informed neural networks (PINN) are a prominent example of such models for which the loss function is augmented with physical terms relevant to the problem at hand (Raissi et al., 2019). This approach generates a data-based surrogate, which is trained on fewer data than traditional ML models, while adhering to the underlying physical laws, at a cost lower than traditional physics-based models (Lee et al., 2024; Babaee et al., 2020; Lino et al., 2023).

A limitation of the original PINN architecture, carried over from classical neural networks is that it produces deterministic values for each input combination it is evaluated with, limiting the information about the uncertainty that is due to the use of an approximation, in place of the original model or instead of measurements.

Quantifying the predictive uncertainty of surrogate models is a classical problem that has seen many advancements in the last three decades. For example, the widely-used class of Gaussian process (GP) regression models provides a closed-form expression for the variance at each output, based either on a frequentist maximum-likelihood construction (Forrester et al., 2008) or on a Bayesian prior-to-posterior analysis (Rasmussen and Williams, 2006). Similar attempts at equipping neural networks with uncertainty quantification (UQ) capabilities have resulted in using dropout and constructing Bayesian neural networks. Gal and Ghahramani (2015) show that using dropout is equivalent to model averaging in mean predictions, but the results can also be interpreted in a Bayesian context as providing a UQ similar to that of a deep GP model. Bayesian neural networks (BNN) (Arbel et al., 2023), preserve the structure of the model, but endow its weights and biases with prior probability distribution which are propagated through the Bayesian pipeline to a predictive posterior.

The most important uncertainty component to be quantified in a surrogate modelling prediction is that due to lack of model or observational realizations at the requested input combination. This uncertainty is epistemic and, as argued in literature, it should be treated differently to random variations (Ferson and Ginzburg, 1996). However, both dropout and BNN use the concepts of probability theory to quantify it. To address the matter, research has been conducted into *interval neural networks* (INN), which use the mathematical interval as a primitive for characterizing epistemic uncertainty. The most common strategies for constructing an INN include propagating full interval weights and biases (Garczarczyk, 2000), representing the intervals as a center and radius

(Sadeghi et al., 2019), and training a pair of neural networks, one for each bound of the interval predictions (Huang et al., 1998).

In an attempt to provide a quantification of their predictive uncertainty, PINN have inherited the Bayesian treatments for NN UQ (Zhang et al., 2019; Yang et al., 2021). However, to the best of the authors knowledge the extension of INN to PINN architectures has not been addressed comprehensively. This paper introduces an interval-based PINN architecture, which quantifies the predictive epistemic uncertainty, by systematically treating all components of the PINN loss function. The performance of the model in terms of achieving a calibrated, yet practical UQ is demonstrated on a dynamics-rich problem of a freely vibrating cantilever beam, through the modelling of its first three eigenmodes. Some practical considerations for modelling unsteady problems are also discussed.

The remainder of the paper is organised as follow. Section 2 reviews the methodologies relevant to the problem and introduces the proposed interval-PINN model. Section 3 presents the experiments conducted to evaluate the performance of the proposed model and Section 4 draws some conclusions from the conducted work.

2. Methodology

Throughout this paper, a freely-oscillating cantilever beam is used as a running example to demonstrate the proposed interval PINN architecture. Specifically, the second and third eignemodes of the beam are analyzed, as they could be more difficult to capture by simpler models.

2.1. Cantilever beam setup

The free oscillation of a cantilever beam is described by the Euler-Lagrange equation:

$$\begin{aligned} & EI\ \partial_x^4 w(x,t) + \mu\ \partial_t^2 w(x,t) = 0 \ \text{ for } x \in (0,L),\, t \geq 0 \\ & \text{subject to :} \\ & \quad w(0,t) = \partial_x w(x,t)|_{x=0} = \partial_x^2 w(x,t)|_{x=L} = \partial_x^3 w(x,t)|_{x=L} = 0 \\ & \quad w(x,0) = w_0 \\ & \quad \partial_t w(x,t)|_{t=0} = 0 \end{aligned} \tag{1}$$

where x is the spatial and t the temporal coordinate, $w(x,t)$ is the beam displacement as a function of space and time, E is the material Young's modulus, I is the moment of area of the beam, and μ is its mass per unit length (Hjelmstad, 2025).

Eq. (1) has an analytical solution of the form:

$$w(x,t) = \sum_{i=1}^{\infty} A_i\, \phi_i(x) \cos(\omega_i t) \tag{2}$$

which states that the displacement, $w(x,t)$ is a superposition of all mode shapes, $\phi_i(x)$:

$$\phi_i(x) = \left\{ \cosh(\beta_i x) - \cos(\beta_i x) + \frac{\cosh(\beta_i L) + \cos(\beta_i L)}{\sinh(\beta_i L) + \sin(\beta_i L)} \left(\sin(\beta_i x) - \sinh(\beta_i x)\right) \right\} \tag{3}$$

where β_i are functions of the natural frequencies of the beam.

2.2. Physics-informed neural networks

Physics-informed neural networks are regularized using known PDEs, which are applied to the output of the NN and represent the expected behavior of the system, as defined by the idealized laws encoding the relevant physics. In the case of the cantilever beam, the system of equations in Eq. (1) is applied on the network outputs. The NN is trained using double precision and a combination of the Adam and L-BFGS optimizers, as using second-order optimizers has been show to achieve better convergence during training (Kiyani et al., 2025).

2.3. Interval neural networks

The interval neural network (INN) architecture quantifies uncertainty by returning an upper and lower bounds at each predictive site. This interval does not imply any probability distribution of the values lying therein. The architecture implemented in this paper represents the interval as a center, $c(x,t)$ and radius, $\delta(x,t)$. In general, the INN is penalized for large width (high $\delta(x,t)$) and for training outputs outside the interval. In the particular case of an interval PINN, the center and width are subject to different penalties: the center is based on the PDE, the boundary conditions (BC), the initial conditions (IC), and the data, while the width depends only on the data. Deterministic weights have been chosen, due to their better numerical stability (Sadeghi et al., 2019).

2.4. Interval PINN for cantilever modeling

The fourth order PDE in Eq. (1) can be solved using automatic differentiation in a deep learning framework such as PyTorch (Paszke et al., 2019). A "time-marching" strategy has been implemented which separates the solution in time into N periods with the length of half an oscillation as proposed in (Krishnapriyan et al., 2021; Lee et al., 2024). There the authors model the first eigenmode of a cantilever beam using a PINN and show that training a separate neural network for each period allows the model to focus on local features and avoid the ill-conditioning, stemming from the soft constraints of the PINN architecture. The method proposed in this paper combines the splitting in time with an INN architecture. The loss function of the n-th ($n = \{1, \ldots, N\}$) PINN is given by:

$$\mathcal{L}^{(n)} = \lambda_{\text{PDE}}\,\mathcal{L}^{(n)}_{\text{PDE}} + \lambda_{\text{BC}}\,\mathcal{L}^{(n)}_{\text{BC}} + \lambda_{\text{IC}}\,\mathcal{L}^{(n)}_{\text{IC/transfer}} + \lambda_D\,\mathcal{L}^{(n)}_{D} \tag{4}$$

where each subscript denotes terms pertaining to the relevant information. Since the temporal and spatial scales are different and diverge further when using higher-order derivatives, a set of normalizing constants, λ_x, is used (Lee et al., 2024). The physics part of Eq. (4) is given by:

$$\lambda_{\text{PDE}}\,\mathcal{L}^{(n)}_{\text{PDE}} = \frac{L^8}{EI^2\,Y^2_{\text{ref}}} \left\langle \left(EI\,\partial^4_x c^{(n)} + \mu\,\partial^2_t c^{(n)} \right)^2 \right\rangle_{\Omega^{(n)}} \tag{5}$$

where $c^{(n)} \equiv c^{(n)}(x,t)$ is the center of the n-th interval prediction, L is the cantilever beam length, and $\Omega^{(n)}$ is the 2D collocation point domain where the PDE is evaluated for the n-th PINN. Mean calculation over collocation points is indicated by $\langle\cdot\rangle$. The term $Y_{\text{ref}} = F_{\text{tip}}L^3/EI$ is the reference

displacement based on the initial cantilever tip position, which is used to scale the displacement in the loss functions for numerical stability reasons.

The part of Eq. (4), which enforces the fixed boundary conditions ($w = 0$, $w' = 0$) and the free-end conditions (zero moment and shear force) of the cantilever beam, is given by:

$$\lambda_{\mathrm{BC}}\,\mathcal{L}_{\mathrm{BC}}^{(n)} = \frac{1}{Y_{\mathrm{ref}}^2}\Big[\underbrace{\langle (c^{(n)})^2\rangle}_{\text{fixed: } w=0} + L^2\,\underbrace{\langle (\partial_x c^{(n)})^2\rangle}_{\text{fixed: } w'=0} + L^4\,\underbrace{\langle (\partial_x^2 c^{(n)})^2\rangle}_{\text{free: moment}} + L^6\,\underbrace{\langle (\partial_x^3 c^{(n)})^2\rangle}_{\text{free: shear}}\Big] \tag{6}$$

where the k-th derivative is multiplied by L^{2k}, in order to account for the scale in each.

The data available about the initial state of the cantilever beam, which is supplied to the first PINN ($n = 1$) is constructed as:

$$\lambda_{\mathrm{IC}}\,\mathcal{L}_{\mathrm{IC}}^{(n)} = \frac{1}{Y_{\mathrm{ref}}^2}\Big[\underbrace{r_c\,\langle \max(0, |w_d - c^{(1)}| - \delta^{(1)})^2\rangle}_{\text{containment}} + \underbrace{r_t\langle (\delta^{(1)})^2\rangle}_{\text{tightness}} + \tau_c^2\,\underbrace{\langle (\partial_t c^{(1)} - \partial_t w_d)^2\rangle}_{\text{velocity IC}}\Big]_{t=t_0} \tag{7}$$

where $\delta^{(n)} \equiv \delta^{(n)}(x,t)$ is the interval radius, w_d is the data, $\tau_c = (\mu L^4/EI)^{1/2}$ is a characteristic evolutionary time scale (Lee et al., 2024), and r_c and r_t are the containment and tightness loss coefficients, respectively.

For subsequent interval PINN ($n > 1$), the temporal dynamics is captured through the transfer loss component, which enforces continuity of the interval center, width, and velocity between consecutive PINNs at the transition time $t = t_n$:

$$\lambda_{\mathrm{IC}}\,\mathcal{L}_{\mathrm{transfer}}^{(n)} = \frac{1}{Y_{\mathrm{ref}}^2}\Big[\underbrace{\langle (c^{(n)} - c^{(n-1)})^2\rangle}_{\text{centre continuity}} + r_w\,\underbrace{\langle (\delta^{(n)} - \delta^{(n-1)})^2\rangle}_{\text{width continuity}} + \tau_c^2\,\underbrace{\langle (\partial_t c^{(n)} - \partial_t c^{(n-1)})^2\rangle}_{\text{velocity continuity}}\Big]_{t=t_n} \tag{8}$$

where r_w is the width continuity coefficient.

The final component of the loss function in Eq. (4) is the one defining the interval width to contain the available data:

$$\lambda_{\mathrm{D}}\,\mathcal{L}_{D}^{(n)} = \frac{1}{Y_{\mathrm{ref}}^2}\Big[\underbrace{r_c\langle \max(0,\, |w_d - c^{(n)}| - \delta^{(n)})^2\rangle}_{\text{containment}} + \underbrace{r_t\langle (\delta^{(n)})^2\rangle}_{\text{tightness}} + \underbrace{r_d\langle (w_d - c^{(n)})^2\rangle}_{\text{centre}}\Big]_{\Omega^{(n)}} \tag{9}$$

where r_d is the center loss coefficient.

3. Numerical experiments

The problem was simulated for parameters $L = 1$ m, $E = 1$ GPa, $I = 1$ m^4 a duration of 1.5 oscillations, and the domain was split in $N = 3$ periods, for each of which a separate PINN is trained.

3.1. Training data

Each interval PINN was trained on synthetic data, generated through a the analytical displacement solution in Eq. (2), with added noise of the form

$$\tilde{\phi}_i(x) = \phi_i(x)(1 + \epsilon_i) \tag{10}$$

where the noise, ϵ, was given three distinct forms to test the performance of the model:

$$\epsilon_i \sim \sigma \cdot \mathcal{E}, \qquad \mathcal{E} \in \begin{cases} \mathcal{N}(0,\, 1) \\ \mathcal{U}(-1,\, 1) \\ 2\,\mathrm{Beta}(5,\, 2) - 1 \end{cases} \tag{11}$$

The noise amplitude was scaled with the displacement, which represents a sensor with an accurate, well-calibrated zero offset, and measurement uncertainty proportional to the displacement. Test cases were generated for three levels of noise, $\sigma \in \{0.05, 0.15, 0.25\}$.This process produced 9 test cases for each mode at which free oscillations are simulated (mode 2 and 3), totaling 18 test cases. Training data then consists of 100 points in space (x) at time $t = 0$, representing initial conditions. In addition, for mode 2, measurement data consisting of six equally-spaced points over the length of the beam and 20 equally-spaced points in time, over the three half-periods analyzed, was used to train the interval PINN. For mode 3, a similar arrangement of measurements, with 11 points over the beam and 20 points in time was used.

3.2. Model training

The hyperparameters r_c, r_t, r_d introduced in Eqs. 7 and 9 and r_w, which appears in Eq. 8 are calibrated using a single representative case per mode, subject to a noise level $\sigma = 0.15$. Those cases were simulated with a constant noise level, to evaluate performance across the entire span of the beam. The model is subsequently validated on the full set of 18 test cases. To account for the stochastic nature of neural network parameter initialization, each configuration is trained three times independently.

3.3. Model evaluation

Model performance was assessed according to the indicators specified in Tab. I. These measures have been selected as they quantify the lack of model reliability in terms of the proportion of (FracOut), and distance to (Dist2Bnd), values outside of the interval, averaged over space and time. The “Overshoot” indicator additionally evaluates the average level to which the model overshoots the observations. Comparison is done across different levels of noise, as the measures used are σ-invariant.

The results presented in Fig. 1 indicate that the interval PINN encompasses the majority of observed data points within its predictive uncertainty bounds across all considered noise types, with FracOut values remaining below 0.25 for most test cases. In instances where data points lie outside the predicted interval, the mean distance to the nearest bound remains small (Dist2Bnd < 0.005m), suggesting that such points are situated in close proximity to the interval boundary.

Table I. Description of evaluation measures used to assess model performance. Here y_i is the value of the observation.

Measure	Formulation	Description
Dist2Bnd	$\langle \max(\lvert y_i - c \rvert - \delta, 0) \rangle$	Mean distance to points outside the prediction interval
Overshoot	$\langle \max(\delta - \lvert y_i - c \rvert, 0) \rangle$	Mean margin for points inside the interval
FracOut	$\langle \mathbf{1}(\lvert y_i - c \rvert > \delta) \rangle$	Fraction of test points falling outside the predicted interval

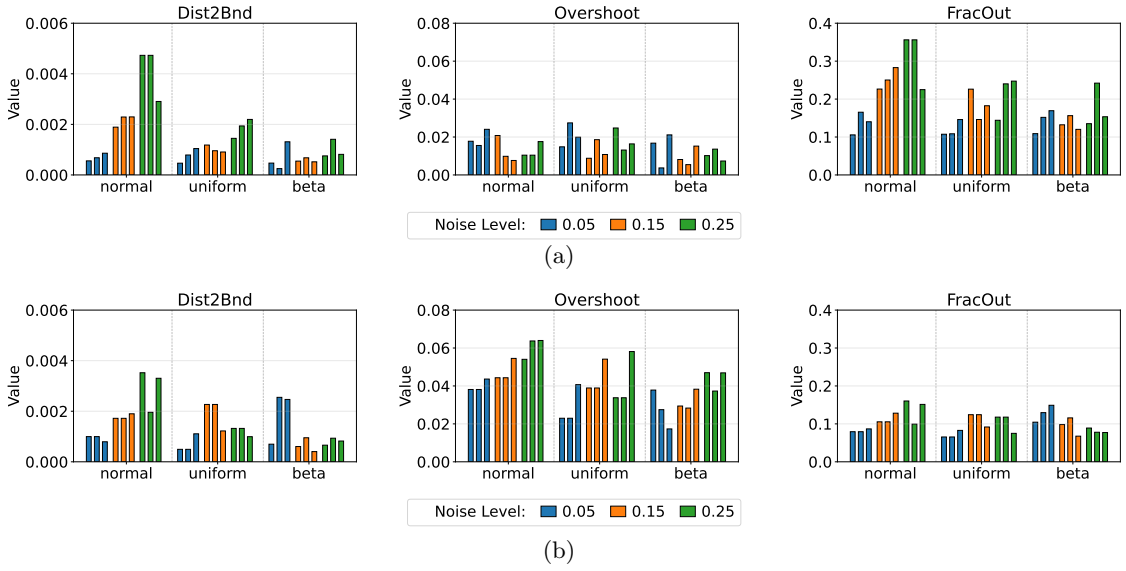


Figure 1. Interval PINN performance over 3 runs on 18 test cases for: (a) mode 2 and (b) mode 3.

The "Overshoot" indicator further reveals that the interval width remains consistent across the different types of noise both for mode 2 and for mode 3. From the results, it can be seen, that the interval PINN captures relatively more of the mode 3 data (lower "FracOut"), but suffers from underfitting, due to the more complicated displacement distribution over time and space (high "Overshoot"). Those observations are also evident in the following Figures and will be discussed further.

To explore the performance of the interval PINN in space and time, and especially the performance of the partitioning strategy, a series of displacement heatmaps were constructed. Fig. 2 displays the center and width of the prediction, and the noisy training data for mode 2 with $\sigma = 0.25$ and different noise models. The heatmaps show that the center of the interval PINN predictions successfully reconstructs the displacement of the beam, with minimal discontinuities across partitions. The beta noise model shown in Fig. 2a exhibits the best performance in this sense.

Finally, the reliability of the model in capturing the beam dynamics and its predictive uncertainty are shown in Figs. 3 and 4 for modes 2 and 3, respectively. The interval PINN prediction centers follow the underlying physics while its predictive uncertainty bound the test data, shown as red dots. The wider intervals observed for PINN 1 can be attributed to the fact that scatter in the initial conditions data (blue dots) away from the idealized physics is larger. This also explains the larger interval widths in Fig. 2b and c are wider, which are caused by the same phenomenon. Despite only sparse data being available beyond the initial condition $t = 0$ (green squares), the interval PINN propagates appropriate interval width to subsequent time steps, enabling it to capture the underlying data scatter.

Fig. 4 shows an identical depiction for mode 3 with $\sigma = 0.15$. The Interval PINN successfully captures the dynamics of the more complex mode, but predicts relatively high interval widths. Increasing the noise leads to degrading performance, which can be addressed by increasing the number of training data points fed to the model through time. Additionally, the more complex spatial dynamics lead to difficult convergence resulting in some of the interval PINN models, such as PINN 2 in Fig. 4c, to have large prediction intervals.

4. Conclusion

A loss function formulation to train an interval PINN was proposed, which quantifies the model uncertainty in the prediction of the surrogate model without resorting to probabilistic construction and subjective prior information. The model uses a center-radius representation with physics-informed losses that enforce the underlying PDE and boundary conditions while fitting noisy data through interval containment and tightness terms.

The proposed architecture was evaluated using a fourth-order PDE describing a the free-oscillation dynamics of a cantilever beam, tested across 18 scenarios with three noise distributions (normal, uniform, beta) and three noise levels. The results demonstrate that the interval PINN shows robustness towards numerical instabilities and captures the majority of data points within its uncertainty bounds while maintaining physically consistent center predictions across all noise types.

Further work will focus on implementing interval weights and biases within the network, developing parallel training of the separate PINN models to allow bidirectional information propagation, and validating the architecture on additional PINN problems across different fields.

Acknowledgements

This research was conducted with the support of the Swiss National Science Foundation and the Bulgarian Ministry of Education and Science under Grant Agreement No. IZPYZ0_228861 for the project “Automatic maximally rigorous uncertainty quantification to enable design for certification” (unCertify). The work also received funding from the GATE project funded by the Horizon 2020 WIDESPREAD-2018-2020 TEAMING Phase 2 programme under grant agreement no. 857155 and the programme ”Research, Innovation and Digitalization for Smart Transformation” 2021-2027 (PRIDST) under grant agreement no. BG16RFPR002-1.014-0010-C01.

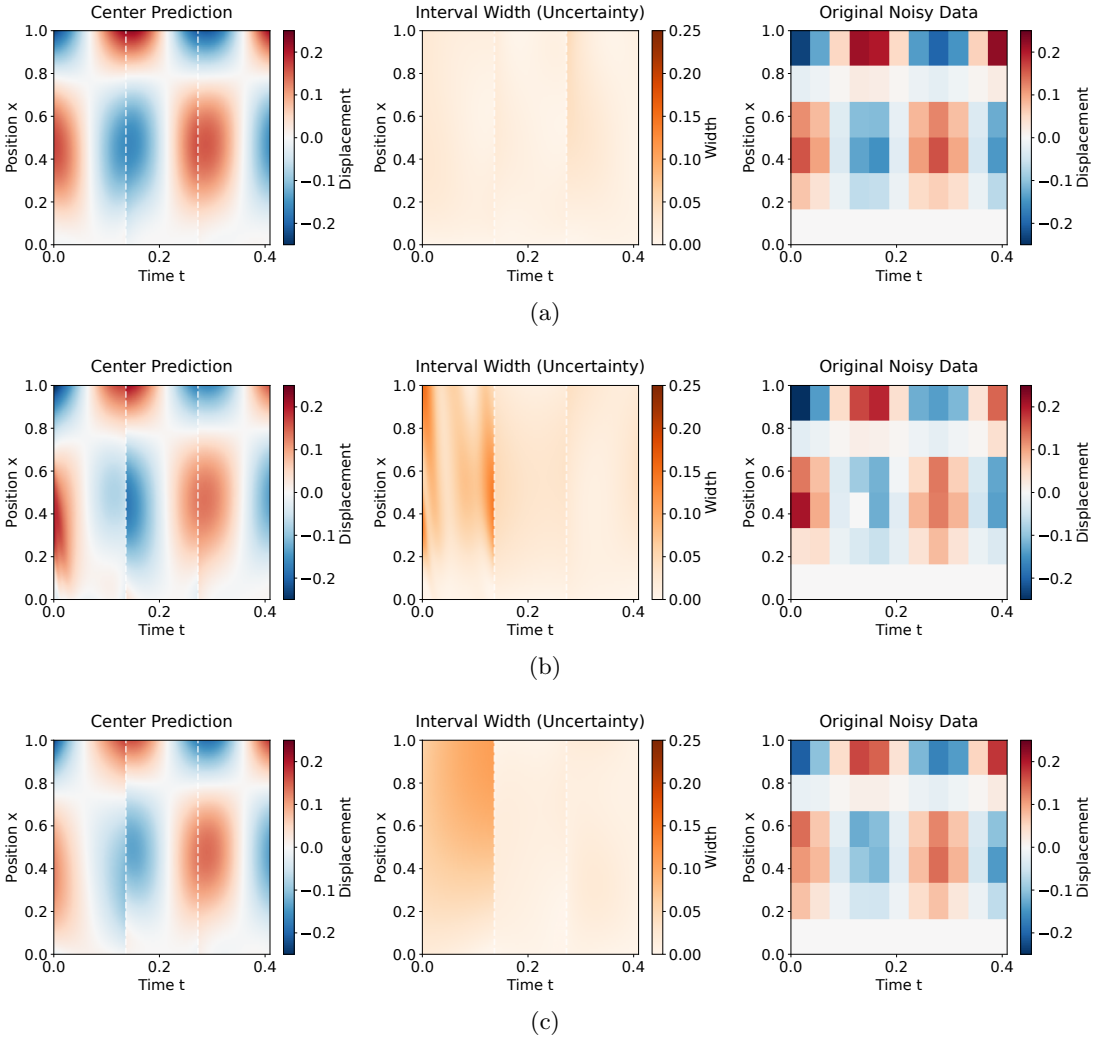
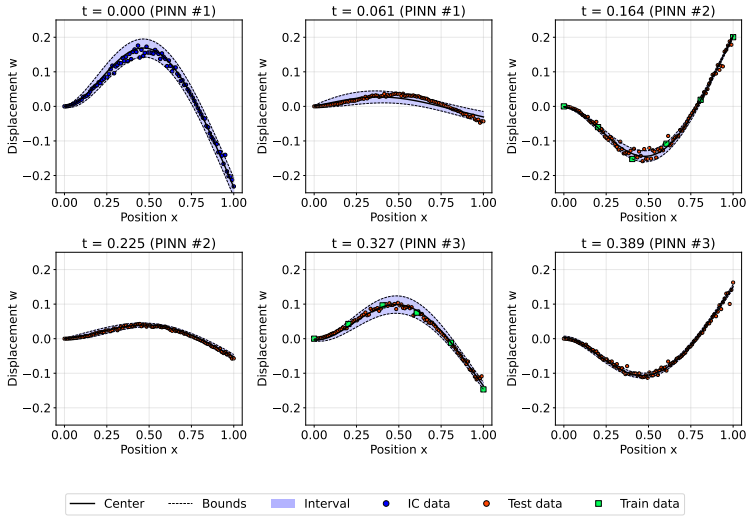
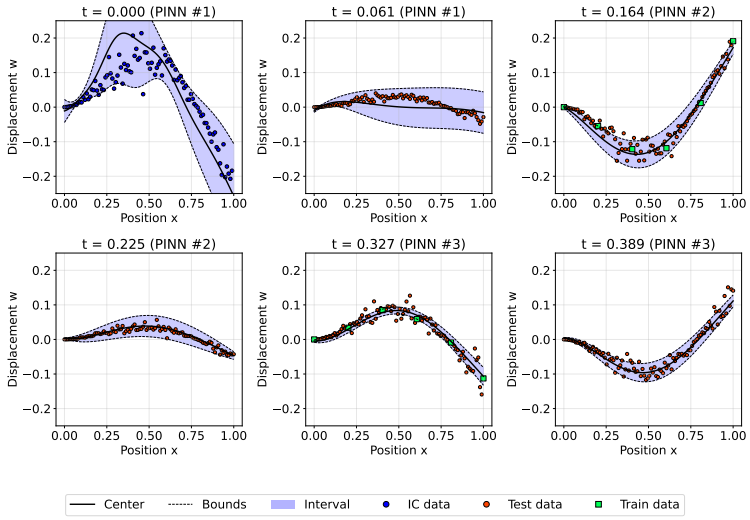


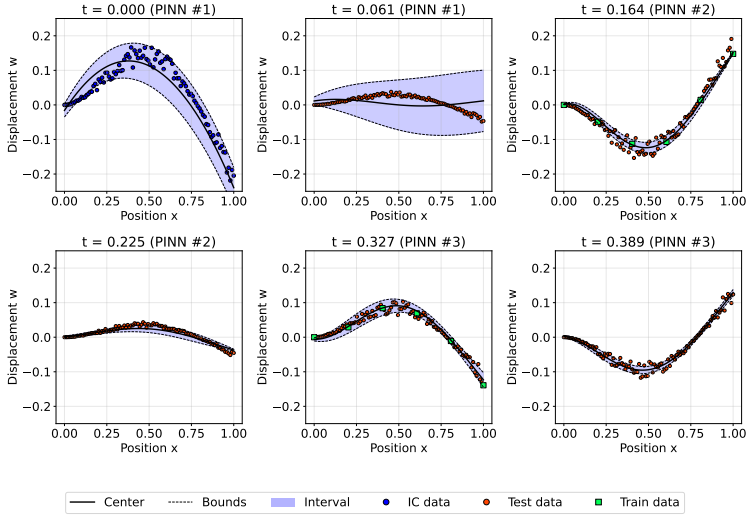
Figure 2. Heat map of the displacement, uncertainty, and training data for Interval PINN for mode 2 at noise level $\sigma = 0.25$ for noise sampled from (a) beta, (b) normal, and (c) uniform distribution.



(a)

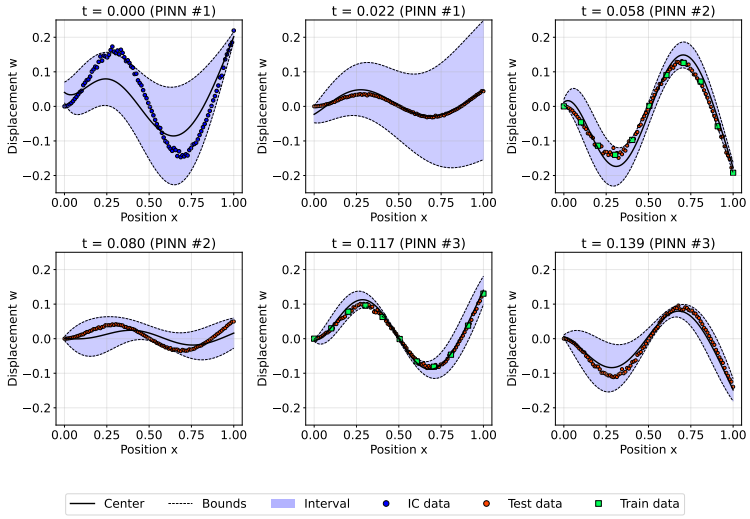


(b)

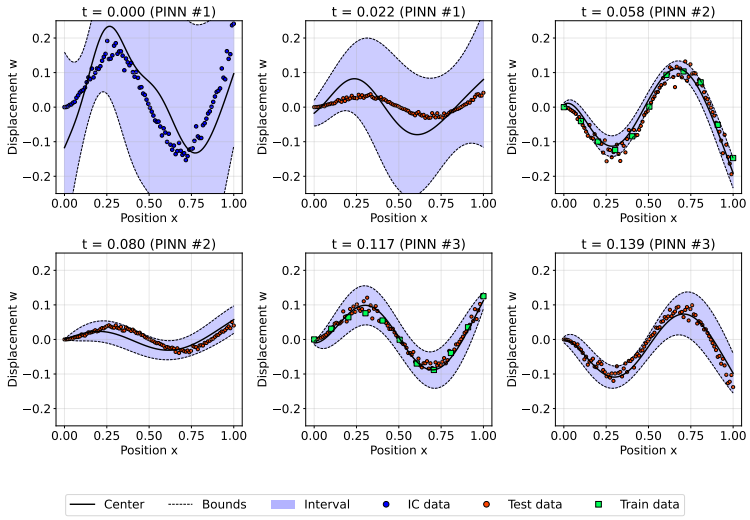


(c)

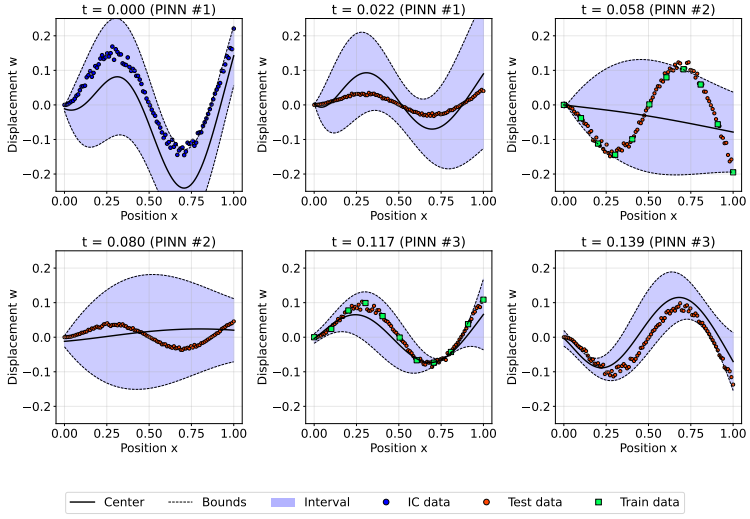
Figure 3. Interval centre and radius for Interval PINN for mode 2 at noise level $\sigma = 0.25$ for noise sampled from (a) beta, (b) normal, and (c) uniform distribution.



(a)



(b)



(c)

Figure 4. Interval centre and radius for Interval PINN for mode 3 at noise level $\sigma = 0.15$ for noise sampled from (a) beta, (b) normal, and (c) uniform distribution.

References

Arbel, J., K. Pitas, M. Vladimirova, and V. Fortuin: 2023, 'A Primer on Bayesian Neural Networks: Review and Debates'. *ArXiv* **abs/2309.16314**.

Babaee, H., C. Bastidas, M. DeFilippo, C. Chryssostomidis, and G. E. Karniadakis: 2020, 'A Multifidelity Framework and Uncertainty Quantification for Sea Surface Temperature in the Massachusetts and Cape Cod Bays'. *Earth and Space Science* **7**, e2019EA000954.

Bishop, C. M.: 2009, *Pattern recognition and machine learning*. Springer Science + Business Media.

Ferson, S. and L. R. Ginzburg: 1996, 'Different methods are needed to propagate ignorance and variability'. *Reliability Engineering & System Safety* **54**(2), 133–144.

Forrester, A. I. J., A. Sobester, and A. J. Keane: 2008, *Engineering Design Via Surrogate Modelling: A Practical Guide*. J. Wiley.

Gal, Y. and Z. Ghahramani: 2015, 'Dropout as a Bayesian Approximation: Representing Model Uncertainty in Deep Learning'. *33rd International Conference on Machine Learning, ICML 2016* **3**, 1651–1660.

Garczarczyk, Z.: 2000, 'Interval neural networks'. In: *2000 IEEE International Symposium on Circuits and Systems (ISCAS)*, Vol. 3. pp. 567–570 vol.3.

Hjelmstad, K. D.: 2025, *Euler–Lagrange Equations*, pp. 251–274. Cham: Springer Nature Switzerland.

Huang, L., B.-L. Zhang, and Q. Huang: 1998, 'Robust interval regression analysis using neural networks'. *Fuzzy Sets and Systems* **97**(3), 337–347.

Kiyani, E., K. Shukla, J. F. Urbán, J. Darbon, and G. E. Karniadakis: 2025, 'Optimizing the optimizer for physics-informed neural networks and Kolmogorov-Arnold networks'. *Computer Methods in Applied Mechanics and Engineering* **446**, 118308.

Krishnapriyan, A., A. Gholami, S. Zhe, R. Kirby, and M. W. Mahoney: 2021, 'Characterizing possible failure modes in physics-informed neural networks'. In: M. Ranzato, A. Beygelzimer, Y. Dauphin, P. Liang, and J. W. Vaughan (eds.): *Advances in Neural Information Processing Systems*, Vol. 34. pp. 26548–26560, Curran Associates, Inc.

Lee, J., K. Park, and W. Jung: 2024, 'Physics-Informed Neural Networks for Cantilever Dynamics and Fluid-Induced Excitation'. *Applied Sciences 2024, Vol. 14, Page 7002* **14**, 7002.

Lino, M., S. Fotiadis, A. A. Bharath, and C. D. Cantwell: 2023, 'Current and emerging deep-learning methods for the simulation of fluid dynamics'. *Proceedings of the Royal Society A: Mathematical, Physical and Engineering Sciences* **479**.

Paszke, A., S. Gross, F. Massa, A. Lerer, J. Bradbury, G. Chanan, T. Killeen, Z. Lin, N. Gimelshein, L. Antiga, A. Desmaison, A. Kopf, E. Yang, Z. DeVito, M. Raison, A. Tejani, S. Chilamkurthy, B. Steiner, L. Fang, J. Bai, and S. Chintala: 2019, 'PyTorch: An Imperative Style, High-Performance Deep Learning Library'. In: *Advances in Neural Information Processing Systems 32*. Curran Associates, Inc., pp. 8024–8035.

Raissi, M., P. Perdikaris, and G. Karniadakis: 2019, 'Physics-informed neural networks: A deep learning framework for solving forward and inverse problems involving nonlinear partial differential equations'. *Journal of Computational Physics* **378**, 686–707.

Rasmussen, C. E. and C. K. I. Williams: 2006, *Gaussian processes for machine learning*. MIT Press.

Rylander, T., P. Ingelstrom, and A. Bondeson: 2013, *Computational Electromagnetics*. Springer.

Sadeghi, J., M. de Angelis, and E. Patelli: 2019, 'Efficient training of interval Neural Networks for imprecise training data'. *Neural Networks* **118**, 338–351.

Taflove, A., S. C. Hagness, and M. Piket-May: 2005, '9 - Computational Electromagnetics: The Finite-Difference Time-Domain Method'. In: W.-K. CHEN (ed.): *The Electrical Engineering Handbook*. Burlington: Academic Press, pp. 629–670.

Yang, L., X. Meng, and G. E. Karniadakis: 2021, 'B-PINNs: Bayesian physics-informed neural networks for forward and inverse PDE problems with noisy data'. *Journal of Computational Physics* **425**, 109913.

Zhang, D., L. Lu, L. Guo, and G. E. Karniadakis: 2019, 'Quantifying total uncertainty in physics-informed neural networks for solving forward and inverse stochastic problems'. *Journal of Computational Physics* **397**, 108850.

Trustworthy Direct Interval Propagation via Conformal Prediction in Neural Network Surrogates

Ghifari Adam Faza
LMSD, Department of Mechanical Engineering, KU Leuven, Heverlee 3001, Belgium, adam.faza@kuleuven.be

Hans Hallez
M-Group research group, Department of Computer Science, KU Leuven, Brugge, 8200, Belgium, hans.hallez@kuleuven.be

David Moens
LMSD, Department of Mechanical Engineering, KU Leuven, Heverlee 3001, Belgium, david.moens@kuleuven.be

Abstract. Uncertainty propagation is essential for reliable engineering design, but when input distributions are unknown, or data are scarce, probabilistic models risk misspecification, making interval representations a more robust alternative. However, interval propagation requires solving optimisation problems for each bound, leading to high computational cost, especially in downstream tasks such as design optimisation or reliability analysis. To mitigate this, surrogate models can be designed to provide interval predictions directly via interval-valued regression, supported by recent neural-network-based methods and data augmentation strategies for constructing interval datasets. Yet these approaches typically ignore surrogate approximation error and data noise. We address this by extending interval regression with a conformal prediction framework, which is model-agnostic and provides user-controlled confidence levels to capture both input and model uncertainty in a distribution-free manner. Experimental results on analytical and PDE benchmark problems demonstrate that the proposed conformalised interval propagation significantly improves coverage reliability compared to uncalibrated predictors, while maintaining practical prediction efficiency. Furthermore, we show that calibration using approximate interval data remains effective when the approximation error is limited, highlighting the practical applicability of the proposed framework in data-scarce settings.

Keywords: interval propagation, conformal prediction, uncertainty quantification

1. Introduction

Uncertainty propagation is fundamental to engineering design, where variations in geometry, material properties, or environmental loading must be tracked through computational models. When input distributions are known, classical methods such as Monte Carlo simulation (Robert and Casella, 2004; Brevault et al., 2020) and quasi-Monte Carlo methods (Dick et al., 2013; Lemieux, 2009) are widely used. When data are scarce, however, prescribing precise distributions risks mis-

© 2026 by the author(s). This work is licensed under the Creative Commons Attribution 4.0 International License (CC BY 4.0), which permits unrestricted use, distribution, and reproduction in any medium, provided the original author and source are credited.

specification; interval representations offer a more robust alternative. For interval-valued inputs $\boldsymbol{x}^\dagger = [\boldsymbol{x}_L, \boldsymbol{x}_U]$, propagation through a model $\mathcal{M}$ reduces to two optimisation problems:

$$y_L = \min_{\boldsymbol{x}_L \leq \boldsymbol{x} \leq \boldsymbol{x}_U} \mathcal{M}(\boldsymbol{x}), \qquad y_U = \max_{\boldsymbol{x}_L \leq \boldsymbol{x} \leq \boldsymbol{x}_U} \mathcal{M}(\boldsymbol{x}). \tag{1}$$

This becomes computationally prohibitive in downstream tasks such as design optimisation or reliability analysis. Substantial efficiency gains arise if a surrogate predicts output interval bounds directly, bypassing repeated optimisation entirely.

Direct interval propagation via interval-valued regression (Roque et al., 2007) can be realised with neural network approaches including regularised neural networks (RANN) (Yang et al., 2019), interval neural networks (INN) (Oala et al., 2021; Betancourt and Muhanna, 2022; Tretiak et al., 2023; Wang et al., 2025), and bound-propagation methods (Gowal et al., 2019; Zhang et al., 2018). A key limitation is that these methods require interval-labelled training data, which are rarely available in practice; data augmentation (Faza et al., 2026) addresses this by constructing synthetic interval datasets from pointwise observations. A fundamental gap remains: these approaches account only for input uncertainty, assuming exact surrogates and noise-free data, whereas real-world settings introduce both approximation error and measurement noise. We address this by extending interval propagation within a conformal prediction framework (Papadopoulos et al., 2002), which is model-agnostic, distribution-free, and provides user-controlled coverage guarantees.

We propose a conformalised direct interval propagation methodology and evaluate it on standard neural network surrogates and operator-learning architectures (DeepONet (Lu et al., 2021)), across one-dimensional regression and PDE benchmarks under both ideal and data-scarce calibration scenarios (Faza et al., 2026). The main contributions are:

1. A conformal prediction algorithm that enhances the robustness of direct interval propagation for both standard neural surrogates and operator-learning surrogates such as DeepONet.

2. A demonstration of the proposed method's effectiveness through numerical experiments on both standard and PDE-based surrogate models.

The remainder is organised as follows. Section 2 reviews direct interval propagation. Section 3 presents the conformalised formulation. Section 4 reports numerical experiments under ideal and augmented calibration scenarios. Section 5 concludes the paper.

2. Direct Interval Propagation

Rather than solving the optimisation in Equation (1), direct interval propagation (DIP) learns a mapping from interval-valued inputs to interval-valued outputs directly:

$$\hat{f} : [\boldsymbol{x}_L, \boldsymbol{x}_U] \mapsto [\boldsymbol{y}_L, \boldsymbol{y}_U]. \tag{2}$$

We focus on two DIP strategies, RANN (Yang et al., 2019) and CROWN bound propagation (Zhang et al., 2018), which are the best-performing methods across both ideal-interval and pointwise-data training settings (Faza et al., 2026).

2.1. Regularised Artificial Neural Network

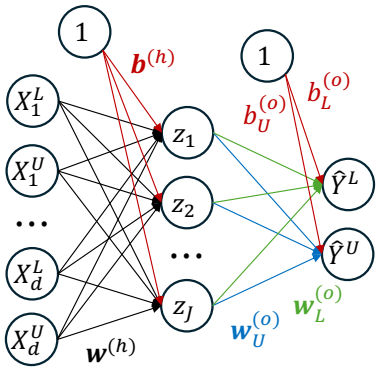


Figure 1. Regularised artificial neural network (RANN) architecture for Naïve direct interval propagation. The architecture consist of a standard neural network that doubles the number of input and output to accommodate interval-valued variable.

RANN uses the simple architecture illustrated in Figure 1. For interval-valued data $(\boldsymbol{X}^\dagger, Y^\dagger)$ with d-dimensional predictors in lower-upper form, the network has $2d$ inputs, J hidden nodes, and 2 outputs, producing:

$$\hat{\boldsymbol{y}}_L = \sigma^{(o)}\left(\sum_{j=1}^{J} z_j w_{j,L}^{(o)} + b_L^{(o)}\right) \quad \textit{and} \quad \hat{\boldsymbol{y}}_U = \sigma^{(o)}\left(\sum_{j=1}^{J} z_j w_{j,U}^{(o)} + b_U^{(o)}\right), \tag{3}$$

where z_j is the jth hidden-node output:

$$z_j = \sigma^{(h)}\left(\sum_{k=1}^{2d} X_k w_{k,j}^{(h)} + b_j^{(h)}\right). \tag{4}$$

Training uses MSE loss augmented with a non-crossing regulariser (Yang et al., 2019) to enforce $\hat{Y}_U \geq \hat{Y}_L$:

$$\mathcal{L} = \frac{1}{N}\sum_{i=1}^{N}(y_{i,L} - \hat{y}_{i,L})^2 + \frac{1}{N}\sum_{i=1}^{N}(y_{i,U} - \hat{y}_{i,U})^2 + \frac{\lambda}{N}\sum_{i=1}^{N}\left(\max\{0, \hat{y}_{i,L} - \hat{y}_{i,U}\}\right)^2, \tag{5}$$

where $\lambda \geq 0$ controls the non-crossing penalty strength; intermediate values balance crossing avoidance with prediction accuracy.

For DeepONet (Figure 2a), the solution operator $\mathcal{G}$ is:

$$\mathcal{G}(\boldsymbol{u})(\boldsymbol{x}) \approx \sum_{i=1}^{q} \beta_i(\boldsymbol{u}) \cdot \tau_i(\boldsymbol{x}), \tag{6}$$

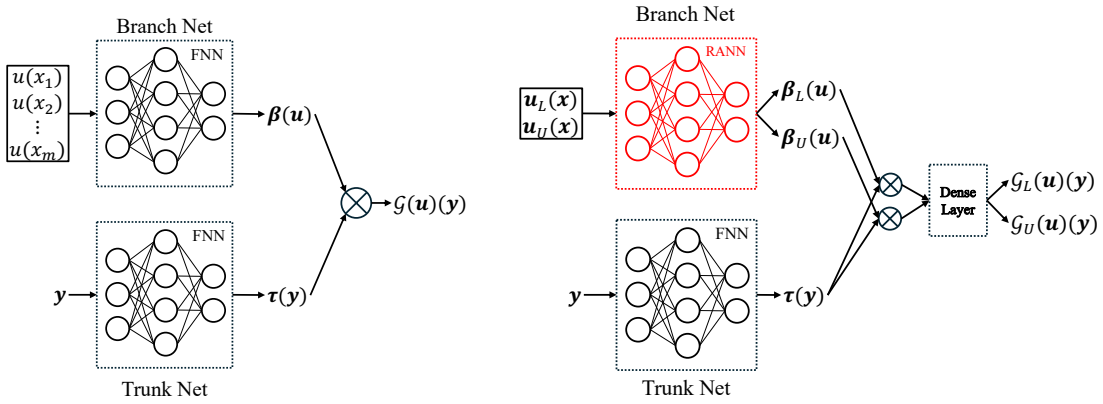


Figure 2. (a) Standard DeepONet architecture. (b) Modified DeepONet architecture with interval-valued branch net.

where $\boldsymbol{\tau} \in \mathbb{R}^q$ and $\boldsymbol{\beta} \in \mathbb{R}^q$ are the trunk-net and branch-net outputs.

Since the query location is known in practice, only the branch net is replaced by RANN while the trunk net remains a standard FNN (Figure 2b). The branch net latent representation becomes $2q$-dimensional: $\boldsymbol{\beta}^\dagger = [\beta_{1,L}, \beta_{1,U}, \ldots, \beta_{q,L}, \beta_{q,U}]$. With $\boldsymbol{\tau} \in \mathbb{R}^q$ and $\boldsymbol{\beta} \in \mathbb{R}^{2q}$, the outputs are combined via two dot products:

$$\boldsymbol{z}_L = \sum_{i=1}^{q} \beta_{i,L}(\boldsymbol{u}) \cdot \tau_i(\boldsymbol{x}), \quad \boldsymbol{z}_U = \sum_{i=1}^{q} \beta_{i,U}(\boldsymbol{u}) \cdot \tau_i(\boldsymbol{x}). \tag{7}$$

The results from the two multiplications are then concatenated, $\boldsymbol{z}^\dagger = [z_{1,L}, z_{1,U}, \ldots, z_{q,L}, z_{q,U}]$, and passed through a dense layer to produce output $\mathcal{G}_L(\boldsymbol{u})(\boldsymbol{y})$ and $\mathcal{G}_U(\boldsymbol{u})(\boldsymbol{y})$.

2.2. CROWN Bound Propagation

Computing certified output bounds under input perturbations is challenging because ReLU nonlinearities make exact bound propagation intractable for deep networks. The CROWN framework (Zhang et al., 2018) resolves this with a layer-wise linear relaxation that yields sound, tractable bounds, originally developed for adversarial robustness and applicable to uncertainty quantification in neural surrogate models.

Given an input domain $\mathcal{X} = \{\boldsymbol{x} \in \mathbb{R}^{d_0} \mid \boldsymbol{x}_{0,L} \leq \boldsymbol{x} \leq \boldsymbol{x}_{0,U}\}$, CROWN propagates interval bounds through each layer of the network. For a layer l, assume the pre-activation satisfies $\hat{z}_{l,L} \leq \hat{z}_l \leq \hat{z}_{l,U}$. Because the ReLU activation $z_l = \max(0, \hat{z}_l)$ is nonlinear, CROWN replaces it with tight linear upper and lower relaxations over the interval $[\hat{z}_{l,L}, \hat{z}_{l,U}]$. The upper relaxation is given by

$$z_l \leq \frac{\hat{z}_{l,U}}{\hat{z}_{l,U} - \hat{z}_{l,L}} \left(\hat{z}_l - \hat{z}_{l,L}\right), \tag{8}$$

and the lower relaxation is

$$z_l \geq \boldsymbol{\alpha}_l \hat{z}_l, \qquad 0 \leq \boldsymbol{\alpha}_l \leq 1, \tag{9}$$

where $\boldsymbol{\alpha}_l$ defines the slope of the lower bound. Composing these relaxations across all layers yields certified global bounds on the network output:

$$f^L(\boldsymbol{x}) \leq \hat{f}(\boldsymbol{x}) \leq f^U(\boldsymbol{x}), \quad \forall \boldsymbol{x} \in \mathcal{X}, \tag{10}$$

where $f^L(\cdot)$ and $f^U(\cdot)$ are affine functions of $\boldsymbol{x}$, recursively defined by the relaxation parameters at each layer.

Adapting CROWN to DeepONet is straightforward via the `Auto_LiRPA` library (Xu et al., 2020), which provides a bound propagation wrapper compatible with the standard architecture without requiring any modifications.

Given n interval-valued PDE input-output pairs $\{[\boldsymbol{u}_{i,L}, \boldsymbol{u}_{i,U}]\}_{i=1}^n$ and $\{[\boldsymbol{g}_{i,L}, \boldsymbol{g}_{i,U}]\}_{i=1}^n$, each input is converted to center-perturbation form for `Auto_LiRPA`:

$$\boldsymbol{u}_c = \frac{\boldsymbol{u}_U + \boldsymbol{u}_L}{2}, \quad \boldsymbol{u}_p = \frac{\boldsymbol{u}_U - \boldsymbol{u}_L}{2}, \tag{11}$$

We train the interval-aware DeepONet using two strategies, both receiving $[\boldsymbol{u}_c, \boldsymbol{u}_p]$ and outputting predicted bounds $[\hat{\boldsymbol{g}}_L, \hat{\boldsymbol{g}}_U]$.

The first strategy uses a *bound-based loss*, which directly fits the lower and upper interval endpoints:

$$\mathcal{L}_{bound} = MSE(\boldsymbol{g}_L, \hat{\boldsymbol{g}}_L) + MSE(\boldsymbol{g}_U, \hat{\boldsymbol{g}}_U) + \lambda \left(\max(0, \hat{\boldsymbol{g}}_L - \hat{\boldsymbol{g}}_U)^2\right), \tag{12}$$

where the final term enforces non-crossing of the predicted bounds.

The *midpoint-based loss* instead fits the interval midpoints $\boldsymbol{g}_M = \frac{1}{2}(\boldsymbol{g}_L + \boldsymbol{g}_U)$ and $\hat{\boldsymbol{g}}_M = \frac{1}{2}(\hat{\boldsymbol{g}}_L + \hat{\boldsymbol{g}}_U)$, offering more stability under noisy labels:

$$\mathcal{L}_{mid} = MSE(\boldsymbol{g}_M, \hat{\boldsymbol{g}}_M) + \lambda \left(\max(0, \hat{\boldsymbol{g}}_U - \hat{\boldsymbol{g}}_L)^2\right). \tag{13}$$

The bound-based loss targets tight endpoint matching, while the midpoint-based loss prioritises the central trend and is more stable under uncertain labels.

3. Conformal Prediction

Conformal prediction (CP) (Vovk et al., 1999; Vovk et al., 2005) is a model-agnostic, distribution-free framework that wraps any trained predictor to produce set-valued predictions with finite-sample coverage guarantees, under the exchangeability assumption. For $\boldsymbol{x} \in \mathbb{R}^d$ and $y \in \mathbb{R}$, it constructs a set-valued predictor

$$C : \boldsymbol{x} \to \{\text{subsets of } y\}, \tag{14}$$

which maps an input $\boldsymbol{x}$ to a subset of the response space. This prediction set is constructed such that, for a new unseen sample $(\boldsymbol{x}_*, y_*)$ drawn from the same distribution as the calibration data, the marginal coverage guarantee

$$\mathbb{P}(y_* \in C(\boldsymbol{x}_*)) \geq 1 - \alpha \tag{15}$$

holds for any finite sample size, where $\alpha \in (0, 1)$ is the user-defined miscoverage level. While the original *full* CP is computationally expensive (requiring repeated model retraining), *split* conformal

prediction (Papadopoulos et al., 2002; Papadopoulos, 2008) fits the model once on a training set and computes conformity scores on a held-out calibration set. We adopt the split framework throughout.

3.1. Split Conformal Prediction and Conformalised Quantile Regression

Data are split into $\mathcal{D}_t = \{(\boldsymbol{x}_i, y_i)\}_{i=1}^{n_t}$ for training and $\mathcal{D}_c = \{(\boldsymbol{x}_i, y_i)\}_{i=1}^{n_c}$ for calibration. A model $\hat{\mu}(\boldsymbol{x})$ is fitted on $\mathcal{D}_t$, and absolute-residual conformity scores are computed on $\mathcal{D}_c$:

$$r_i = |y_i - \hat{\mu}(\boldsymbol{x}_i)|. \tag{16}$$

For a given error level α, we return the conformal correction d as the k-th smallest value in r_i, where $k = \lceil (n/2+1)(1-\alpha) \rceil$. The conformal prediction of a new unobserved point $\boldsymbol{x}_*$ is then defined as:

$$C(\boldsymbol{x}_*) = \left[\hat{\mu}(\boldsymbol{x}_*) - d,\ \hat{\mu}(\boldsymbol{x}_*) + d\right]. \tag{17}$$

A variant of conformal prediction built upon quantile regression (Koenker and Bassett, 1978; Steinwart and Christmann, 2011), known as conformalised quantile regression (CQR) (Romano et al., 2019), follows a similar principle while leveraging conditional quantile estimates. Given a quantile regression model $\mathcal{M}_q$, two conditional quantile functions corresponding to lower and upper quantile levels α_{lo} and α_{hi} are first fitted using the training dataset:

$$\{\hat{q}_{\alpha_{lo}}, \hat{q}_{\alpha_{hi}}\} \leftarrow \mathcal{M}_q(\mathcal{D}_t). \tag{18}$$

Next, conformity scores are computed on the calibration dataset. For each calibration sample $(\boldsymbol{x}_i, y_i) \in \mathcal{D}_c$, the score is defined as

$$r_i = \max\left\{\hat{q}_{\alpha_{lo}}(\boldsymbol{x}_i) - y_i,\ y_i - \hat{q}_{\alpha_{hi}}(\boldsymbol{x}_i)\right\}. \tag{19}$$

This score is non-positive when y_i lies within the predicted interval and equals the violation magnitude otherwise. The correction d is the k-th smallest value of $\{r_i\}$, $k = \lceil (n/2+1)(1-\alpha) \rceil$, giving the conformal prediction interval:

$$C(\boldsymbol{x}_*) = \left[\hat{q}_{\alpha_{lo}}(\boldsymbol{x}_i) - d,\ \hat{q}_{\alpha_{hi}}(\boldsymbol{x}_i) + d\right]. \tag{20}$$

For operator learning (Moya et al., 2025), CQR extends to DeepONet by evaluating the score pointwise. Given quantile-DeepONet estimates $\hat{g}_{\alpha_{\mathrm{lo}}}$, $\hat{g}_{\alpha_{\mathrm{hi}}}$ and calibration set $\mathcal{D}_c = \{(u_i, g_i)\}_{i=1}^{n_c}$, the score at each domain location is:

$$r_i(x) = \max\left\{\hat{g}_{\alpha_{\mathrm{lo}}}(u_i)(x) - g_i(x),\ g_i(x) - \hat{g}_{\alpha_{\mathrm{hi}}}(u_i)(x)\right\}, \quad x \in \mathcal{X}. \tag{21}$$

The pointwise correction $d(x)$ is the empirical $(1-\alpha)$-quantile of $\{r_i(x)\}_{i=1}^{n_c}$, giving the conformal band for a new input u_*:

$$C(u_*)(x) = \left[\hat{g}_{\alpha_{\mathrm{lo}}}(u_*)(x) - d(x),\ \hat{g}_{\alpha_{\mathrm{hi}}}(u_*)(x) + d(x)\right], \quad x \in \mathcal{X}. \tag{22}$$

This formulation mirrors the standard CQR procedure while extending coverage guarantees to operator-valued predictions.

3.2. Conformalised Direct Interval Propagation

Applying CP to DIP follows the CQR formulation (Romano et al., 2019; Moya et al., 2025). Given a DIP model $\mathcal{M}_{\mathcal{I}}$ trained on interval-valued data $\mathcal{D}_t$ (Faza et al., 2026), the conformity score for each calibration sample $(\boldsymbol{x}_i^\dagger, y_i^\dagger) \in \mathcal{D}_c$ is:

$$r_i = \max\left\{\hat{y}_L(\boldsymbol{x}_i) - y_L,\ y_U - \hat{y}_U(\boldsymbol{x}_i)\right\}. \tag{23}$$

Then, the correction d is the k-th smallest value in r_i, where $k = \lceil (n/2+1)(1-\alpha) \rceil$ The conformal prediction of a new unobserved point $\boldsymbol{x}_*^\dagger$ is then defined as:

$$C(\boldsymbol{x}_*^\dagger) = \left[\hat{y}_L(\boldsymbol{x}_i^\dagger) - d,\ \hat{y}_U(\boldsymbol{x}_i^\dagger) + d\right]. \tag{24}$$

Adapted from Equation 19, this score captures the worst-case interval coverage violation: it is positive when the predicted interval fails to enclose the true interval and non-positive when coverage is already satisfied. The correction d is chosen as the k-th smallest conformity score, $k = \lceil (n/2+1)(1-\alpha) \rceil$, ensuring that at least a fraction $(1-\alpha)$ of calibration intervals are enclosed and guaranteeing marginal coverage for future predictions. Very small α (e.g., $\alpha = 0$) drives d to the maximum score, producing overly conservative intervals; $\alpha = 0.05$ is a typical practical choice.

The same approach extends to interval DeepONets: the score in Equation 23 is computed pointwise over the domain and the correction d is applied identically to the CQR-DeepONet case.

4. Numerical experiments

We extend the experimental design of (Faza et al., 2026) to reflect realistic data conditions: model training is restricted to intervals augmented from pointwise data, since ideal interval datasets are rarely available in practice. We evaluate two calibration scenarios — (i) ideal interval-valued calibration data (best-case) and (ii) augmented interval calibration data (fully practical) — and vary the calibration set size to assess its effect on prediction quality. Each scenario is evaluated on a one-dimensional regression task and a one-dimensional PDE.

Prediction quality is measured using predicted interval normalized average width (PINAW), predicted interval coverage probability (PICP), and the coverage width-based criterion (CWC):

$$\text{PINAW} = \frac{1}{N}\sum_{i=1}^{N}\frac{(\hat{y}_U - \hat{y}_L)}{(y_U - y_L)}, \tag{25}$$

$$\text{PICP} = \frac{1}{N}\sum_{i=1}^{N}\mathbf{1}\left(\hat{y}_L \le y_i \le \hat{y}_U\right), \tag{26}$$

$$\text{CWC} = \text{PINAW}\left(1 + e^{\gamma \max(0,(1-\delta)-\text{PICP})}\right), \tag{27}$$

where $\mathbf{1}(\cdot)$ is an indicator function, δ is the desired coverage level, and $\gamma = 5$ balances the coverage-width trade-off. Since we evaluate against interval-valued targets, we replace the standard PICP with a continuous overlap-based version:

$$\text{PICP} = \frac{1}{N}\sum_{i=1}^{N} \frac{\max(0, \min(\hat{y}_U, y_U) - \max(\hat{y}_L, y_L))}{(y_U - y_L)}. \tag{28}$$

4.1. Calibration with ideal interval data

4.1.1. *1-dimensional regression*

Consider a simple one-dimensional regression problem:

$$y = \sin(2x)e^{-x} + 1 + \varepsilon,\ x \in [0, \pi], \tag{29}$$

where ε is a normally distributed aleatoric noise with mean $\mu = 0$ and standard deviation $\sigma = 0.025$. We create interval inputs with varying interval widths across the sample space. Since the actual function is cheap to evaluate, we propagate the inputs by evaluating on the actual function.

Table I. One-dimensional regression with ideal interval data calibration performance comparison across methods and calibration set sizes on three different metrics: PINAW, PICP, and CWC.

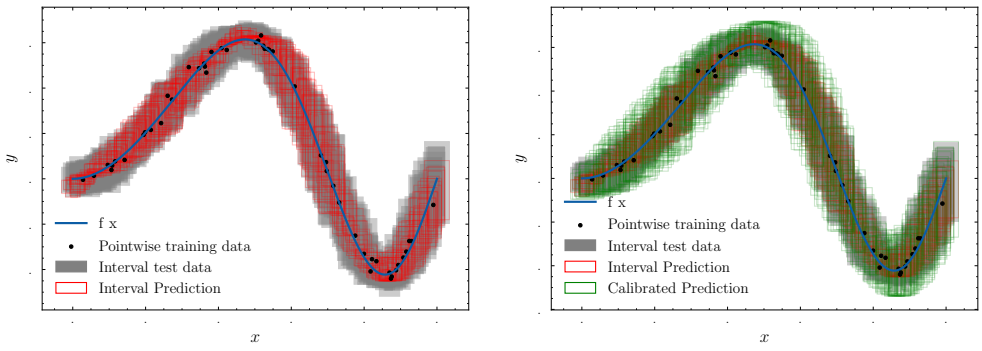
n_{calib}	**Metric**	**Naive**	**CROWN**	**Mid-CROWN**
0	PINAW	0.587 ± 0.111	0.427 ± 0.025	0.533 ± 0.026
	PICP	0.551 ± 0.068	0.392 ± 0.036	0.515 ± 0.027
	CWC	6.117 ± 0.901	9.417 ± 1.175	6.572 ± 0.558
5	PINAW	1.767 ± 0.511	1.915 ± 0.396	1.682 ± 0.355
	PICP	0.959 ± 0.033	0.959 ± 0.048	0.986 ± 0.019
	CWC	3.899 ± 0.895	4.271 ± 0.795	3.468 ± 0.608
10	PINAW	2.252 ± 0.476	2.660 ± 1.242	1.600 ± 0.245
	PICP	0.989 ± 0.010	0.992 ± 0.006	0.991 ± 0.010
	CWC	4.625 ± 0.910	5.417 ± 2.505	3.267 ± 0.443
25	PINAW	2.837 ± 0.817	3.099 ± 1.166	2.070 ± 0.733
	PICP	0.997 ± 0.003	0.996 ± 0.004	0.997 ± 0.004
	CWC	5.707 ± 1.635	6.259 ± 2.367	4.180 ± 1.544
50	PINAW	2.339 ± 0.675	2.612 ± 0.478	1.854 ± 0.359
	PICP	0.996 ± 0.005	0.995 ± 0.007	0.998 ± 0.002
	CWC	4.723 ± 1.330	5.284 ± 0.930	3.727 ± 0.713

We fix the training set to 50 samples and vary the calibration set size, repeating each configuration ten times with different random seeds. Comparisons against optimisation-based propagation

are omitted, as (Faza et al., 2026) already establishes that DIP achieves comparable or better performance.

Table I shows a clear PICP improvement after calibration even with few calibration samples, confirming that conformal calibration compensates for the base predictor's undercoverage at the cost of increased PINAW. Conformal calibration guarantees coverage but not tightness: the interval width is set by the empirical quantile of calibration conformity scores, so outliers can inflate the correction substantially, an effect amplified by small calibration sets.

Figure 3a illustrates the undercoverage behaviour of the uncalibrated model, where the predicted intervals fail to fully enclose several ground-truth responses. In contrast, Figure 3b shows that, after conformal calibration, the prediction intervals are expanded sufficiently to enclose the previously missed observations, thereby correcting the undercoverage at the cost of increased interval width.



(a) (b)

Figure 3. Illustration of one-dimensional interval predictions comparing (a) the uncalibrated model and (b) the conformal-calibrated model.

With very small calibration sets (e.g., $n_{\text{calib}} = 5$), achievable coverage levels are restricted to multiples of $1/(n_{\text{calib}} + 1)$, making the 0.95 target unattainable; the procedure selects the next feasible level, yielding conservative intervals. Nevertheless, conformalisation consistently improves prediction reliability even with limited calibration data.

4.1.2. *1-dimensional PDE*

We consider the second-order steady-state stochastic Poisson equation in one dimension as our first test case. The stochastic differential equation (SDE) is formulated as:

$$\begin{aligned} \tfrac{d^2 g(x)}{dx^2} &= 20u(x), \;\; x \in [0,1], \\ g(x=0) &= g(x=1) = 0, \\ u(x) &\sim \mathcal{GP}(m(x), k(x,x')), \end{aligned}$$

where $u(x)$ is the spatially random forcing function, modelled as a Gaussian process ($\mathcal{GP}$) with mean $m(x)$ set to be 0, and the radial basis function kernel $k(x,x') = \exp\left(-(x-x')^2/(2l^2)\right)$ where the kernel length scale of the GP is set to be $l = 0.1$. The HF dataset is generated using a grid size $\Delta x = 0.01$, while the LF dataset grid size is $\Delta x = 0.1$.

Table II. One-dimensional PDE problem with ideal interval data calibration performance comparison across methods and calibration set sizes.

n_{calib}	**Metric**	**Naive**	**CROWN**	**Mid-CROWN**
0	PINAW	0.943 ± 0.852	0.227 ± 0.227	1.627 ± 2.179
	PICP	0.359 ± 0.247	0.049 ± 0.077	0.787 ± 0.242
	CWC	37.103 ± 65.155	23.965 ± 24.916	12.035 ± 22.830
10	PINAW	10.602 ± 7.689	40.337 ± 30.477	5.777 ± 5.368
	PICP	0.996 ± 0.026	0.983 ± 0.074	0.995 ± 0.037
	CWC	21.535 ± 16.072	88.779 ± 84.591	12.408 ± 18.623
25	PINAW	11.915 ± 8.647	47.454 ± 35.038	5.182 ± 3.472
	PICP	0.998 ± 0.015	0.996 ± 0.031	0.998 ± 0.019
	CWC	23.945 ± 17.474	96.542 ± 73.896	10.484 ± 8.377
50	PINAW	9.889 ± 7.097	40.576 ± 29.677	4.702 ± 3.880
	PICP	0.996 ± 0.023	0.989 ± 0.056	0.996 ± 0.028
	CWC	20.113 ± 15.436	86.272 ± 74.724	9.702 ± 9.117
100	PINAW	8.659 ± 6.161	35.926 ± 26.073	4.887 ± 5.543
	PICP	0.991 ± 0.032	0.977 ± 0.083	0.991 ± 0.047
	CWC	17.824 ± 13.265	83.020 ± 88.582	11.073 ± 21.682
250	PINAW	8.621 ± 6.099	35.475 ± 25.712	4.780 ± 4.505
	PICP	0.992 ± 0.031	0.976 ± 0.084	0.989 ± 0.051
	CWC	17.741 ± 13.930	82.224 ± 88.481	10.903 ± 18.804

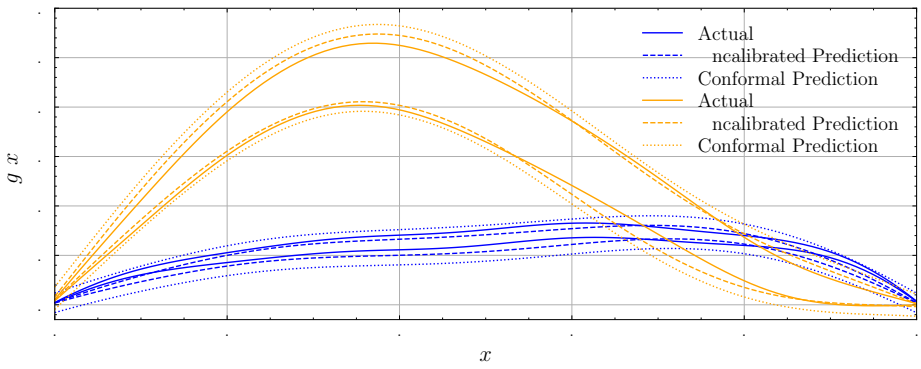


Figure 4. Illustration of one-dimensional PDE interval predictions for multiple problem instances. Each colour represents a different PDE instance characterised by a distinct input function $u(x)$.

Using 500 training samples (other settings follow (Faza et al., 2026)), Table II and Figure 4 confirm the same pattern as the regression case: conformalisation consistently improves PICP across all methods at the cost of increased PINAW.

Naive and CROWN exhibit poor uncalibrated performance, requiring large corrections that yield wide post-calibration intervals. Mid-CROWN starts with the highest initial coverage but also sees a substantial increase in interval width after calibration. Note that the overlap-based PICP (Equation 28) counts partial overlaps as coverage, so observed values can exceed the nominal 0.95 target; α can be tuned to balance coverage and width.

4.2. Calibration with augmented pointwise data

4.2.1. *1-dimensional regression*

We repeat the setup of Section 4.1.1 (Equation 29), replacing ground-truth calibration data with augmented intervals from the same approximation procedure as training. Since both training and calibration use the same approximated source, the coverage guarantee holds with respect to the augmented distribution rather than the true one; systematic discrepancies between the two may cause under- or over-coverage.

Table III. One-dimensional regression with augmented interval data calibration performance comparison across methods and calibration set sizes.

n_{calib}	**Metric**	**Naive**	**CROWN**	**Mid-CROWN**
0	PINAW	0.623 ± 0.097	0.430 ± 0.014	0.537 ± 0.033
	PICP	0.519 ± 0.084	0.398 ± 0.022	0.522 ± 0.034
	CWC	7.738 ± 1.831	9.210 ± 0.930	6.442 ± 0.637
5	PINAW	1.612 ± 0.386	1.417 ± 0.743	0.945 ± 0.260
	PICP	0.938 ± 0.103	0.832 ± 0.126	0.794 ± 0.163
	CWC	3.809 ± 0.558	4.575 ± 1.382	3.880 ± 1.949
10	PINAW	1.608 ± 0.315	1.222 ± 0.265	1.009 ± 0.240
	PICP	0.955 ± 0.024	0.865 ± 0.062	0.840 ± 0.159
	CWC	3.606 ± 0.529	3.601 ± 0.360	3.550 ± 1.650
25	PINAW	2.107 ± 0.553	1.447 ± 0.203	1.181 ± 0.170
	PICP	0.979 ± 0.016	0.930 ± 0.026	0.924 ± 0.049
	CWC	4.412 ± 1.027	3.496 ± 0.358	2.916 ± 0.302
50	PINAW	1.941 ± 0.363	1.635 ± 0.604	1.273 ± 0.213
	PICP	0.974 ± 0.013	0.934 ± 0.026	0.939 ± 0.033
	CWC	4.142 ± 0.710	3.869 ± 1.207	2.975 ± 0.257

Table III shows that augmented calibration yields slightly lower PICP than ideal calibration, but the degradation remains limited. The method's effectiveness depends on how closely the augmented intervals approximate the true ones: small discrepancies allow the augmented correction to serve as a reliable proxy, while large systematic bias can cause coverage failures.

4.2.2. *1-dimensional PDE*

Following the setup of Section 4.1.2 with augmented calibration data, Table IV shows a divergence between methods: Mid-CROWN's interval width decreases after calibration, reducing PICP, while Naive and CROWN receive larger corrections and become more conservative. As shown in Figure 5, augmented output intervals underestimate the true interval width, so conformity scores are computed against a narrower reference — insufficient correction for Mid-CROWN but still adequate for the weaker methods. These results confirm that augmented calibration inherits the bias of the augmented distribution and may not reliably guarantee true-interval coverage when systematic discrepancies are present.

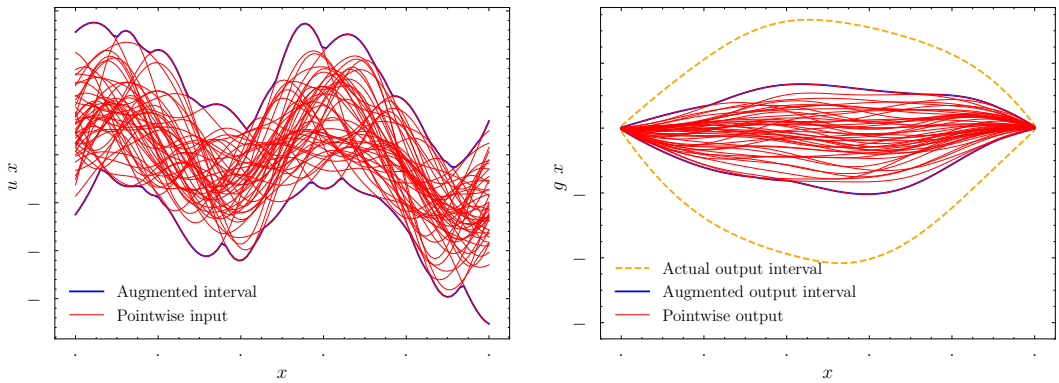


Figure 5. Augmented input function (left) and comparison between the augmented output and the ground truth output propagated through PDE solver.

5. Conclusion

We propose a conformalised direct interval propagation framework that combines DIP — which efficiently predicts output interval bounds directly — with split conformal prediction to provide finite-sample coverage guarantees without modifying the underlying model or assuming a data distribution. By calibrating conformity scores on interval-valued data, the method achieves reliable marginal coverage while preserving computational efficiency.

Evaluated on regression and PDE surrogate tasks using both ideal and augmented interval calibration data, conformal calibration consistently improves coverage across DIP methods, accompanied by increased interval width due to the coverage-efficiency trade-off. Augmented calibration remains effective when the discrepancy from true intervals is small, but systematic bias can cause undercoverage or overly conservative predictions. These findings establish conformalised DIP as a practical and theoretically grounded framework for uncertainty quantification in interval-valued neural network surrogates, particularly under data-scarce conditions.

Table IV. One-dimensional PDE problem with augmented interval data calibration performance comparison across methods and calibration set sizes.

n_{calib}	**Metric**	**Naive**	**CROWN**	**Mid-CROWN**
0	PINAW	1.032 ± 1.010	0.236 ± 0.225	3.163 ± 8.135
	PICP	0.328 ± 0.260	0.053 ± 0.084	0.817 ± 0.224
	CWC	52.083 ± 94.153	23.569 ± 22.457	13.937 ± 32.887
10	PINAW	8.907 ± 7.040	36.995 ± 28.804	1.419 ± 0.885
	PICP	0.976 ± 0.072	0.969 ± 0.103	0.774 ± 0.268
	CWC	19.910 ± 21.883	89.016 ± 101.695	37.004 ± 156.746
25	PINAW	11.308 ± 9.108	44.356 ± 33.681	2.647 ± 3.779
	PICP	0.990 ± 0.043	0.990 ± 0.056	0.912 ± 0.141
	CWC	23.524 ± 20.934	93.429 ± 79.918	9.249 ± 22.976
50	PINAW	8.691 ± 6.334	36.938 ± 28.041	1.123 ± 0.202
	PICP	0.984 ± 0.054	0.973 ± 0.096	0.687 ± 0.258
	CWC	18.549 ± 16.576	87.277 ± 97.712	19.310 ± 44.099
100	PINAW	7.651 ± 5.503	32.086 ± 23.578	2.229 ± 3.042
	PICP	0.975 ± 0.069	0.959 ± 0.116	0.491 ± 0.285
	CWC	17.107 ± 16.888	84.255 ± 109.276	98.950 ± 194.710
250	PINAW	7.401 ± 5.277	30.945 ± 22.569	1.363 ± 0.820
	PICP	0.971 ± 0.078	0.954 ± 0.122	0.477 ± 0.284
	CWC	17.332 ± 22.383	83.917 ± 111.922	83.304 ± 163.789

Data Availability

The code are available at: `https://github.com/fazaghifari/IntervalOperatorLearning`. Although, the provided example in the repository are not the exact experiments presented in this paper, they illustrate the implementation of the conformal calibration discussed herein.

Acknowledgements

This work was supported by the granted H2020 FETOPEN-2018-2019-2020-01 European project, *Epistemic AI* under grant agreement No. 964505 (E-pi). The authors acknowledge the use of AI tools, such as ChatGPT and Grammarly, to assist with grammar refinement and improve the clarity of wording in the manuscript. All substantive content, analysis, and conclusions are the original work of the authors.

References

Betancourt, D. and R. L. Muhanna: 2022, 'Interval deep learning for computational mechanics problems under input uncertainty'. *Probabilistic Engineering Mechanics* **70**, 103370.

Brevault, L., M. Balesdent, and J. Morio: 2020, *Aerospace System Analysis and Optimization in Uncertainty*. Springer International Publishing.

Dick, J., F. Y. Kuo, and I. H. Sloan: 2013, 'High-dimensional integration: The quasi-Monte Carlo way'. *Acta Numerica* **22**, 133–288.

Faza, G. A., J. Wauters, F. Cuzzolin, H. Hallez, and D. Moens: 2026, 'Direct interval propagation methods using neural-network surrogates for uncertainty quantification in physical systems surrogate model'. *Knowledge-Based Systems* **341**, 115824.

Gowal, S., K. Dvijotham, R. Stanforth, R. Bunel, C. Qin, J. Uesato, R. Arandjelovic, T. Mann, and P. Kohli: 2019, 'On the Effectiveness of Interval Bound Propagation for Training Verifiably Robust Models'.

Koenker, R. and G. Bassett: 1978, 'Regression Quantiles'. *Econometrica* **46**(1), 33.

Lemieux, C.: 2009, *Monte Carlo and Quasi-Monte Carlo Sampling*. Springer New York.

Lu, L., P. Jin, G. Pang, Z. Zhang, and G. E. Karniadakis: 2021, 'Learning nonlinear operators via DeepONet based on the universal approximation theorem of operators'. *Nature Machine Intelligence* **3**(3), 218–229.

Moya, C., A. Mollaali, Z. Zhang, L. Lu, and G. Lin: 2025, 'Conformalized-DeepONet: A distribution-free framework for uncertainty quantification in deep operator networks'. *Physica D: Nonlinear Phenomena* **471**, 134418.

Oala, L., C. Heiß, J. Macdonald, M. März, G. Kutyniok, and W. Samek: 2021, 'Detecting failure modes in image reconstructions with interval neural network uncertainty'. *International Journal of Computer Assisted Radiology and Surgery* **16**(12), 2089–2097.

Papadopoulos, H.: 2008, *Inductive Conformal Prediction: Theory and Application to Neural Networks*, Chapt. 1. InTech.

Papadopoulos, H., K. Proedrou, V. Vovk, and A. Gammerman: 2002, *Inductive Confidence Machines for Regression*, p. 345–356. Springer Berlin Heidelberg.

Robert, C. P. and G. Casella: 2004, *Monte Carlo Statistical Methods*. Springer New York.

Romano, Y., E. Patterson, and E. J. Candès: 2019, 'Conformalized Quantile Regression'.

Roque, A. M. S., C. Mate, J. Arroyo, and A. Sarabia: 2007, 'iMLP: Applying Multi-Layer Perceptrons to Interval-Valued Data'. *Neural Processing Letters* **25**(2), 157–169.

Steinwart, I. and A. Christmann: 2011, 'Estimating conditional quantiles with the help of the pinball loss'. *Bernoulli* **17**(1).

Tretiak, K., G. Schollmeyer, and S. Ferson: 2023, 'Neural network model for imprecise regression with interval dependent variables'. *Neural Networks* **161**, 550–564.

Vovk, V., A. Gammerman, and C. Saunders: 1999, 'Machine-Learning Applications of Algorithmic Randomness'. In: *Proceedings of the Sixteenth International Conference on Machine Learning*. San Francisco, CA, USA, p. 444–453, Morgan Kaufmann Publishers Inc.

Vovk, V., A. Gammerman, and G. Shafer: 2005, *Algorithmic learning in a random world*. Springer Science+Business Media.

Wang, K., K. Shariatmadar, S. K. Manchingal, F. Cuzzolin, D. Moens, and H. Hallez: 2025, 'CreINNs: Credal-Set Interval Neural Networks for Uncertainty Estimation in Classification Tasks'. *Neural Networks* **185**, 107198.

Xu, K., Z. Shi, H. Zhang, Y. Wang, K.-W. Chang, M. Huang, B. Kailkhura, X. Lin, and C.-J. Hsieh: 2020, 'Automatic Perturbation Analysis for Scalable Certified Robustness and Beyond'.

Yang, Z., D. K. Lin, and A. Zhang: 2019, 'Interval-valued data prediction via regularized artificial neural network'. *Neurocomputing* **331**, 336–345.

Zhang, H., T.-W. Weng, P.-Y. Chen, C.-J. Hsieh, and L. Daniel: 2018, 'Efficient Neural Network Robustness Certification with General Activation Functions'.

Application of machine learning to reduce model uncertainty and enable resource-efficient design of flat slabs

T. Lux[1)], J. Sundheim[1)], T. Feiri[1)], U. Wiens[2)], and M. Ricker[1)]
[1)]*Chair of Structural Concrete, Technical University of Dortmund, 44227 Dortmund, Germany, til.lux@tu-dortmund.de*
[2)]*German Committee for Structural Concrete, 10787 Berlin, Germany, info@dafstb.de*

Abstract: The construction sector has a significant share of global CO_2 emissions due to its high material and resource consumption. Since material and resource consumption can be significantly influenced by the structural design of components, strategies to promote resource-efficient and optimised designs are required providing that the target reliability levels of structures prescribed in building design codes (e.g., DIN EN 1990+NA) are strictly satisfied. Structural components are designed in accordance with building design codes, such as DIN EN 1992-1-1+NA. Since the mechanical behaviour of some components can hardly be analytically described—e.g., punching shear of flat slabs without shear reinforcement—ultimate limit state evaluations partly rely on empirical equations. These equations exhibit significant model uncertainty, meaning that the ratio of actual to predicted load-bearing capacity is subject to statistical scatter. In punching shear verifications, model uncertainty has a great influence on the probability of failure. Previous studies have suggested that the model uncertainty of machine learning models can be lower than that of the empirical design equations specified in international codes. In this work, a machine-learning model (Extreme Gradient Boosting – *XGBoost*) was trained and utilised to predict the punching shear resistance of flat slabs without punching shear reinforcement. This model was employed in a reliability analysis with decoupled load and resistance side. Monte Carlo simulations were used to determine the probability that the actual load-bearing capacity, determined by the machine-learning model, falls below the design resistance according to DIN EN 1992-1-1+NA. The results indicate that predicting the actual load-bearing capacity with a trained model of lower uncertainty leads to a higher reliability level. This higher reliability can enable reductions in safety margins, for example, by lowering partial safety factors, thereby increasing the potential for resource-efficient designs.

Keywords: model uncertainty, punching shear, machine learning, structural reliability

1. Introduction

The construction industry accounts for approximately 37 % of global CO_2 emissions, largely due to its intensive consumption of materials and resources; of this total, about 6% is attributable to the embodied emissions of the most widely used construction materials, namely concrete, steel, and aluminum (United Nations Environment Programme, 2023). Since structural design decisions strongly affect this consumption, developing strategies that enable more resource-efficient structural components is essential (Häkkinen et al., 2015). At the same time, society expects structures to be highly reliable, as structural failure can have severe implications for human safety and significant economic consequences (e.g., Spaethe, 1992). Therefore, any

© 2026 by the author(s). This work is licensed under the Creative Commons Attribution 4.0 International License (CC BY 4.0), which permits unrestricted use, distribution, and reproduction in any medium, provided the original author and source are credited.

efforts to reduce material usage and enhance efficiency must ensure that the socially accepted reliability level—as recommended in modern structural codes—is maintained.

In contrast to emission reduction using alternative materials (e.g., low-carbon concretes or textile-reinforced concrete), which has been receiving substantial research attention, the potential for emission reduction through decreasing material volumes has been comparatively neglected (Fang et al., 2023). One approach to enhance material efficiency is to exploit existing safety reserves—hereby designated as *hidden safety margins*, in design standards—for example, by applying improved and less conservative load or resistance models (Teichgräber et al., 2022).

Machine **L**earning (ML) models can identify complex, nonlinear relationships between structural input parameters and load-bearing resistance, making them well suited to developing such improved resistance models. This potential is particularly relevant for structural components whose mechanical behaviour is difficult to describe analytically. Punching shear failure of flat slabs without shear reinforcement is a prime example: The failure mechanism is governed by a complex interaction of geometric, material, and loading parameters for which no closed-form analytical solution exists, and a large number of experimental datasets are publicly available (e.g., *fib* punching shear database (Ruiz & Ospina, 2025)) enabling robust model training and validation. The empirical design equations used to determine the resistance of such components inherently exhibit *model uncertainty*—defined here as the statistical scatter in the ratio between observed and predicted load-bearing capacity ($\theta_R = R_{\mathrm{obs}}/R_{\mathrm{pred}}$).

While hidden safety margins in punching shear have previously been estimated using analytical resistance models through reliability-based assessments (e.g., Ricker et al., 2021), these approaches are constrained by the model uncertainty inherent to the underlying design equations. Since data-driven ML models have been demonstrated to achieve lower model uncertainty than empirical code equations for punching shear resistance (Liang et al., 2022), their use as resistance models in reliability analyses offers a more accurate basis for quantifying such margins. However, to the authors' knowledge, no study has yet employed an ML-based resistance model for this purpose in the context of punching shear of flat slabs. This gap motivates the present study. In this study, an e**x**treme **g**radient **boo**sting model (XGBoost) is trained and used as a resistance model within a reliability analysis framework—employing **M**onte **C**arlo **S**imulation (MCS)—to quantify the actual load-bearing capacity and identify hidden safety margins for flat slabs without punching shear reinforcement. Exploiting these hidden safety margins enables more material-efficient designs, thereby reducing CO_2 emissions without compromising the reliability required by structural codes.

2. Reliability in Civil Engineering

2.1. Overview on reliability and safety margin

Reliability in structural engineering is defined as the ability of a structure or structural component to fulfil the specified requirements within its intended service life (DIN EN 1990:2021). To quantify reliability, DIN EN 1990:2021 introduces the reliability index β, defined as the negative standard normal quantile of the probability of failure P_f:

$$\beta = -\Phi^{(-1)}(P_f) \tag{1}$$

The probability of failure is understood here as the notional probability that a requirement at the **U**ltimate **L**imit **S**tate (ULS) or the **S**erviceability **L**imit **S**tate (SLS) is not satisfied, arising from the statistical

variability of the basic variables[1] entering the calculation. This notional probability of failure—and the corresponding reliability index β—serves as a measure of structural reliability and must be distinguished from the actual probability of failure, which is substantially influenced by human error (Vrouwenvelder et al., 2025). European design standards aim to ensure that structures satisfy requirements for safety and serviceability throughout their service life, i.e., that β meets or exceeds the specified target value. Target reliability indices are prescribed in DIN EN 1990:2021 as a function of consequence class and reference period, reflecting a codified balance between safety and economy.
In design practice, compliance with the target reliability is achieved through the partial safety factor concept, in which characteristic values of actions are amplified and those of resistances are reduced. Since partial safety factors are calibrated for a wide range of structural configurations and load cases, the resulting reliability often exceeds the target level for any given structure. The difference between the reliability index achieved and the prescribed target value constitutes the hidden safety margin—the quantity this study seeks to identify and quantify.

2.2. RELIABILITY-BASED METHODS

Over the decades, a range of methods has been developed to approximate or determine structural failure probabilities. Reliability analysis methods are generally classified by their level of approximation. Level II methods, such as the **F**irst and **S**econd **O**rder **R**eliability **M**ethod (FORM/ SORM), operate in standardised normal space and approximate the failure surface at the design point (i.e., most probable failure point), offering computational efficiency at the cost of accuracy for strongly nonlinear limit state functions. Level III methods, such as MCS and variance reduction techniques as **I**mportance **S**ampling (MC-IS), and **Su**bset **S**imulation (SuS), estimate failure probabilities directly through repeated sampling and are considered exact in the limit of sufficiently large sample sizes, at the expense of greater computational demand (Melchers, 1999).
The fundamental task in a reliability analysis is to evaluate the probability that a structural component fails to meet its performance requirements, expressed through the limit state function:

$$g(\boldsymbol{X}) = g(X_1, X_2, \dots, X_n) \tag{2}$$

where $\boldsymbol{X} = (X_1, X_2, \dots, X_n)^T$ is the vector of basic random variables representing uncertain quantities such as material strength, geometry, and loading. Failure is defined as the event $g(\boldsymbol{X}) \leq 0$, and the corresponding probability of failure P_f is:

$$P_\mathrm{f} = P(g(\boldsymbol{X}) \leq 0) \tag{3}$$

A reliability analysis proceeds through the following key steps (Ditlevsen & Madsen, 1999). First, a target reliability level β_t is selected based on the consequence class and reference period[2]. Second, the limit state function is formulated to distinguish between safe and failed states. Third, the basic variables are identified and characterised by appropriate probability distributions and statistical parameters, accounting for uncertainties in resistance, loading, and model accuracy. Fourth, the reliability index β is computed using the chosen analysis method. Finally, a sensitivity analysis is performed to assess the relative influence of individual random variables on the computed reliability level.

[1] In reliability analysis, the term refers to random variables characterised by specified probability distributions and associated statistical parameters, such as mean and variance.
[2] Target reliability level are given in DIN EN 1990:2021, e.g., β_t = 3.8 for reliability class 2 and a 50-year reference period.

3. Flat slabs without punching shear reinforcement according to DIN EN 1992-1-1:2011+NA(D)

In the load transfer region between a flat slab and its supporting columns, the simultaneous occurrence of high bending moments and shear forces can give rise to two distinct failure modes: (i) flexural failure and (ii) local shear failure. The latter involves a three-dimensional, conical failure surface forming around the column —a mechanism referred to as punching shear. Two cases are distinguished depending on whether shear reinforcement is present; this study considers exclusively flat slabs without punching shear reinforcement.
The mechanical behaviour of flat slabs without shear reinforcement is complex to describe analytically, and ultimate limit state assessments therefore rely in part on empirical formulations. To improve the understanding of the underlying failure mechanisms, numerous experimental investigations have been conducted since the mid-20th century (e.g., Guandalini & Muttoni, 2004; Hallgren et al., 1998; Rankin & Long, 1987). The design equations for punching shear resistance have evolved alongside this growing body of experimental evidence. A new generation of European design standards is currently under development, incorporating recent advances in reinforced concrete research as reflected in the *fib* Model Code 2020 (Fédération internationale du béton (*fib*), 2023). The investigations presented in this study, however, refer to the currently applicable version of Eurocode 2 for engineering practice in Germany—DIN EN 1992-1-1:2011, DIN EN 1992-1-1/NA:2013, and DIN EN 1992-1-1/NA/A1:2015 (hereinafter also referred to as Eurocode 2 (EC2))—which is rooted in the CEB-FIP model code 1990 (Euro-International Committee for Concrete & Fédération internationale de la précontrainte, 1998).
According to this standard, punching shear resistance must be verified along the critical control perimeter u_1, located at a distance of $2d$ from the periphery of the loaded area, by satisfying:

$$v_{\mathrm{Ed}} = \frac{\beta_e \cdot V_{\mathrm{Ed}}}{u_1 \cdot d} \leq v_{\mathrm{Rd,c}} \tag{4}$$

where V_{Ed} is the applied shear force, d is the effective depth of the slab (distance from the extreme compression fibre to the centroid of the longitudinal tensile reinforcement), and β_e is a factor[3] accounting for an uneven shear stress distribution along u_1 due to eccentric loading.
In turn, the design shear stress v_{Ed} is compared against the punching shear resistance without shear reinforcement $v_{\mathrm{Rd,c}}$, determined as:

$$v_{\mathrm{Rd,c}} = C_{\mathrm{Rd,c}} \cdot k \cdot (100 \cdot \rho_{\mathrm{l}} \cdot f_{\mathrm{ck}})^{1/3} + k_1 \cdot \sigma_{\mathrm{cp}} \geq v_{\mathrm{min}} + k_1 \cdot \sigma_{\mathrm{cp}} \tag{5}$$

The parameters in Eq. (5) are defined as follows: $C_{\mathrm{Rd,c}}$ is an empirical coefficient equal to $0.18/\gamma_{\mathrm{C}}$ for general cases and $0.18/\gamma_{\mathrm{C}} \cdot (0.1 \cdot u_0/d + 0.6)$ for interior columns with $u_0/d < 4$, where $\gamma_{\mathrm{C}} = 1.5$ is the partial safety factor for concrete, and u_0 is the column perimeter. The term $k = 1 + (200/d)^{0.5} \leq 2.0$ (d in mm) considers the size effect of the effective depth, ρ_{l} is the mean flexural reinforcement ratio considering a slab width equal to the column width plus $3d$ on each side given by $\rho_{\mathrm{l}} = \left(\rho_{\mathrm{lx}} \cdot \rho_{\mathrm{ly}}\right)^{0.5}$, and f_{ck} is the characteristic cylinder concrete compressive strength. The additional term $k_1 \cdot \sigma_{\mathrm{cp}}$ can be used to account for membrane forces in the slab, for example when dealing with a prestressed beam or slab. The term v_{min} is the minimum punching shear capacity given by Eq. (6):

$$v_{\mathrm{min}} = \max\left(min\left(0.0525 - 0.015 \cdot \frac{d - 600}{200}; 0.0525\right); 0.0375\right)/\gamma_{\mathrm{C}} \cdot k^{3/2} \cdot f_{\mathrm{ck}}^{1/2} \tag{6}$$

[3] Note that β in the context of DIN EN 1992-1-1:2011 is unrelated to the reliability index β commonly used in structural reliability analysis.

4. Training and Validation of a data-driven machine learning model

4.1. Machine Learning Algorithm

Since the objective of the machine learning model is to predict a continuous target variable—the load-bearing capacity of flat slabs without punching shear reinforcement—from labelled experimental data, supervised regression is the appropriate learning paradigm (Bishop, 2006).
The model type was chosen based on the findings of (Liang et al., 2022), in which the XGBoost model yielded more accurate predictions than other machine-learning algorithms. Gradient boosting methods are generally well-suited to tabular datasets of moderate size—as is typical of experimental databases in structural engineering—due to their robustness to outliers, ability to handle heterogeneous input features, and strong predictive performance (Friedman, 2001). In XGBoost, an ensemble of decision trees is constructed sequentially, with each tree fitted to the residuals of its predecessor, thereby progressively reducing prediction error. For a full algorithmic description, the reader is referred to (Chen & Guestrin, 2016). All model training and predictions were performed using the *xgboost* package (Chen et al., 2026) in the open-source statistical computing environment R (R Core Team, 2025).

4.2. Database

Supervised machine learning requires a comprehensive database of input parameters and associated target variables for model training and validation (Bishop, 2006). In this study, the target variable is the punching shear resistance of flat slabs without shear reinforcement, expressed as the shear stress capacity along the critical control perimeter. The database must contain all relevant input parameters, including parameters influencing the load-bearing capacity that are not explicitly considered in the code formulation.
The experimental data used for training and validation of the XGBoost model are drawn from the *fib* punching shear database (Ruiz & Ospina, 2025), an internationally recognised repository of punching shear tests on flat slabs without shear reinforcement. The database comprises 468 tests across 73 experimental series and provides the input parameters and measured resistances required for model development.

4.3. Preparation of Data

4.3.1. *Filtering*

From the original *fib* database of 468 documented tests, a subset was selected based on the following criteria. First, only tests in which a distinct punching failure was recorded (database entry "P") were retained. Second, only specimens with circular, square, or rectangular column geometries were included. Third, a minimum reinforcement yield strength of $f_y \geq 300$ MPa was required to avoid bias in the training process arising from non-standard reinforcement configurations. Of the 468 tests, 397 satisfied all three criteria and were used for model training and validation.

4.3.2. *Feature Selection*

A defined set of predictor variables (*features*) was compiled for model training based on the parameters known to influence punching shear behaviour. These include the concrete cylinder compressive strength f_c, the effective depth d, the geometric longitudinal reinforcement ratio ρ_l, the yield strength f_y of longitudinal the reinforcement, the distance from the slab edge to the load introduction area a, the critical control perimeter

u_1, the shear slenderness $a_\lambda = a/d$, and the specific column perimeter ratio u_0/d. Column shape was represented using one-hot encoding, in which each geometry category (circular, square, rectangular) is expressed as a binary indicator variable, enabling categorical features to be incorporated directly into the splitting criteria of decision tree-based models.
The feature set was determined through an iterative selection process guided by feature importance scores and error metrics of the trained model. While additional input variables may also be considered, the inclusion of an excessive number of features should be avoided. The selection should therefore be restricted to relevant variables in order to reduce the risk of overfitting and to prevent unnecessary increases in model complexity during the training process.

4.3.3. *Feature Transformation*
The feature distributions in the training dataset exhibit noticeable skewness[4] (Figure 1).

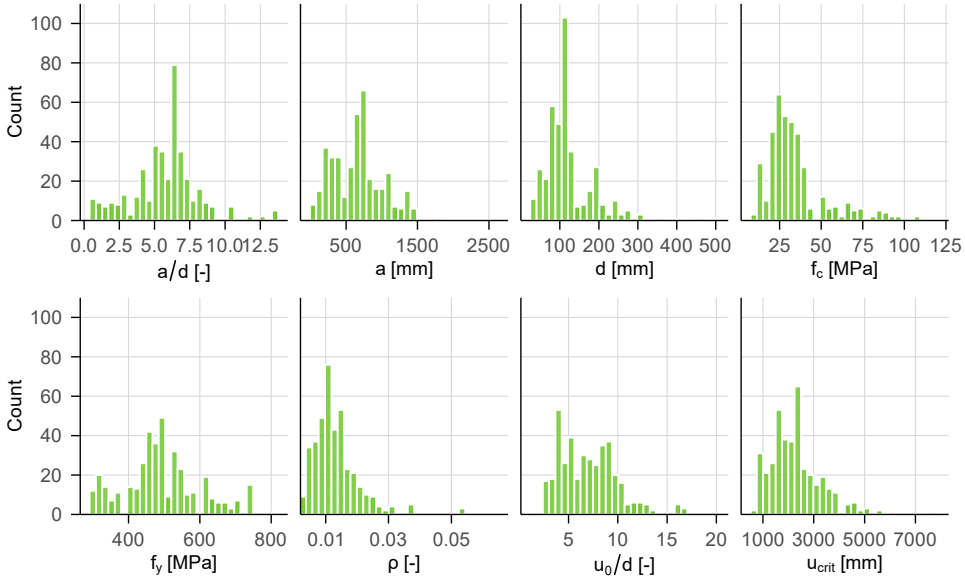


Figure 1. Histograms of the features in the filtered database

Skewed distributions can negatively affect model performance, which is why logarithmic transformations are commonly applied to reduce skewness prior to training (Kuhn & Johnson, 2013). Accordingly, all non-categorical features x_j with a skewness coefficient $\gamma_{1,j} > 1$ were log-transformed:

$$x_{\mathrm{trans,j}} = \begin{cases} \log(x_\mathrm{j}) & \text{for } x_\mathrm{j} \in \{d, f_\mathrm{c}, \rho_l, u_\mathrm{crit}\} \\ x_\mathrm{j} & \text{for } x_\mathrm{j} \notin \{d, f_\mathrm{c}, \rho_l, u_\mathrm{crit}\} \end{cases} \tag{7}$$

Subsequently, all features were standardised using z-score normalisation:

[4] Measure of the asymmetry of a probability distribution around its mean.

$$x_{\text{scale,j}} = \frac{x_{\text{trans,j}} - \bar{x}_{\text{trans,j}}}{s_{x_{\text{trans,j}}}} \tag{8}$$

Although z-score normalisation is not required for tree-based models such as XGBoost—which are invariant to monotonic feature transformations—it was applied here since an ANN was trained using the same features in the underlying study. Note that applying the trained model to new observations requires access to the mean $\bar{x}_{trans,j}$ and standard deviation $s_{x_{trans,j}}$ of the transformed training features.

4.3.4. *Target Variable Definition*

The choice of target variable significantly influences model performance and should be chosen based on the structure of the training data. To remove geometric scale dependence, the target is defined not as the ultimate failure load V_{u}; instead, it is defined as the punching shear stress along the critical control perimeter, normalised by the concrete compressive strength f_{c} to reduce the dominance of this single parameter on the output distribution. A log-transformation is applied to reduce skewness in the target distribution, consistent with the pre-processing applied to the input features. The target variable y is therefore in accordance with (Mangalathu et al., 2021) defined as:

$$y = \log\left(\frac{V_u}{u_{\text{crit}} \cdot d \cdot f_{\text{c}}}\right) \tag{9}$$

The target variable used here performs well for the available dataset; however, alternative target definitions are also possible.

4.4. Model Setup and Training

The filtered database of 397 tests was randomly partitioned into a training set (70%, 277 tests) and a held-out test set (30%, 120 tests). The hyperparameters governing model architecture were fixed prior to training based on (Mangalathu et al., 2021): learning rate `eta=0.045`, maximum tree depth `max_depth=5`, training instance subsample ratio `subsample=0.55`, and column subsample ratio per tree `colsample_bytree=0.9`. For a detailed description of each parameter and its effect on model behaviour, the reader is referred to the XGBoost documentation (Chen et al., 2026). The optimal number of boosting iterations was determined using 5-fold cross-validation (i.e., `nfold=5`) on the training set via the `xgb.cv()`, function, minimising the root mean square error (RMSE). A maximum of 300 boosting rounds (i.e., `nrounds=300`) was permitted, with early stopping applied if no improvement in RMSE was observed over 30 consecutive rounds (i.e., `early_stopping_rounds=30`). The lowest cross-validation RMSE was achieved at 296 boosting iterations (i.e., `nrounds=296`), which was adopted as the final model configuration.

4.5. Validation and Model Uncertainty

The model performance was evaluated on a held-out test dataset (n = 120) using four error metrics. To facilitate interpretation, the target variable was transformed back to the load-bearing capacity V_u:

$$RMSE = \sqrt{\frac{1}{n}\sum_{i=1}^{n}\left(V_{u,i} - \widehat{V_{u,i}}\right)^2} = 56.3 \tag{10}$$

$$MAE = \frac{1}{n}\sum_{i=1}^{n}\left|V_{u,i} - \widehat{V_{u,i}}\right| = 32.0 \tag{11}$$

$$MAPE = \frac{100}{n}\sum_{i=1}^{n}\left|\frac{V_{u,i} - \widehat{V_{u,i}}}{V_{u,i}}\right| = 7.71 \tag{12}$$

$$R^2 = 1 - \frac{\sum_{i=1}^{n}\left(V_{u,i} - \widehat{V_{u,i}}\right)^2}{\sum_{i=1}^{n}\left(V_{u,i} - \overline{V_u}\right)^2} = 0.979 \tag{13}$$

where n is the number of tests in the test dataset, $V_{u,i}$ is the observed ultimate failure load for test i, $\widehat{V_{u,i}}$ is the corresponding model prediction for test i, and $\overline{V_u}$ is the mean of the observed ultimate failure loads. The model uncertainty θ_R (index R for Resistance) is defined as the ratio of the observed to the predicted load-bearing capacity $\theta_R = R_{\text{obs}}/R_{\text{pred}}$. This quantity exhibits statistical dispersion across the test dataset and is treated as a random variable characterised by an underlying probability distribution. In structural reliability, model uncertainty is commonly represented by a Lognormal distribution, which is strictly non-negative and consistent with the multiplicative nature of resistance uncertainties (e.g., *Probabilistic Model Code*, 2001). The adequacy of this assumption was assessed visually via the histogram displayed in Figure 2.

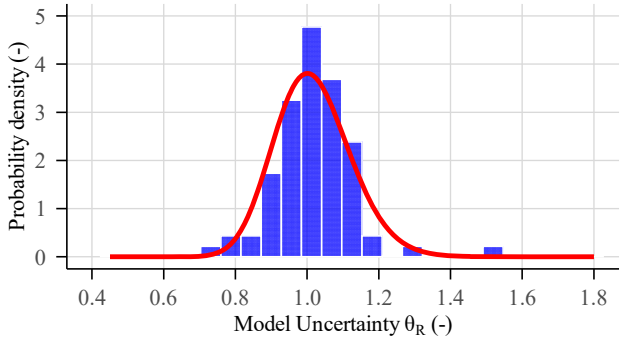


Figure 2. Histogram of the model uncertainty θ_R and fitted log-normal distribution

The lognormal distribution parameters[5] are derived from the sample mean $\bar{\theta}_{R,XGB}$ = 1.017 and coefficient of variation CoV($\theta_{R,XGB}$) = 0.106.

A mean model uncertainty close to unity indicates that the XGBoost model predicts the punching shear resistance without systematic bias. The coefficient of variation of 10.6% is low relative to typical values reported for empirical design equations (e.g., Liang et al., 2022; Ricker et al., 2021), suggesting that the data-driven model captures the underlying resistance mechanism with high predictive accuracy. This is further substantiated by direct comparison with the model uncertainty of the design equation according to DIN EN 1992-1-1:2011 assessed in Section 4.6.

[5] $\sigma_{\ln} = \sqrt{\ln(1 + COV(\theta_R)^2)}$, $\mu_{\ln} = \ln(\overline{\theta_R}) - 0{,}5 \cdot \sigma_{\ln}^2$

4.6. Comparison with the design model according to DIN EN 1992-1-1

For comparison with the model uncertainty of the model specified in DIN EN 1992-1-1:2011, the same test dataset as used for the XGBoost model is considered. However, additional filters are applied to avoid biasing the model uncertainty of EC2 by unusual or impractical configurations. Tests with an effective depth $d < 100$ mm and characteristic cylindric concrete compressive strength $f_{ck} > 104$ MPa are therefore excluded in accordance with (Hegger et al., 2021). Of the 120 tests in the original test dataset, 82 tests remain that are used to compare the model uncertainty of the XGBoost model with that of DIN EN 1992-1-1:2011. Note that, according to Section 9.3.1.1 of DIN EN 1992-1-1/NA:2013, a minimum slab thickness of 70 mm is sufficient for slabs without punching shear reinforcement. However, in practice, the construction of flat slabs with a thickness smaller than 150 mm is rare in practice; therefore, a minimum value of $d = 100$ mm was assumed for the effective depth in this study (Hegger et al., 2021). Based on this reduced test dataset, both the error metrics of the model uncertainty for EC2 and XGBoost according to Eqs. (8)–(11) as well as the point estimates of the distribution parameters were calculated and compared (see Table I).

Table I. Comparison of error metrics and Point estimators of XGBoost and EC2

Model	No. Tests	RMSE [kN]	MAE [kN]	MAPE [%]	R^2	$\bar{\theta}$	CoV_θ
XGBoost	82	66.17	39.26	7.25	0.972	1.017	0.104
EC2	82	117.7	74.45	13.98	0.939	1.146	0.166

The design equation according to EC2 exhibits substantially higher model uncertainty than the XGBoost model, both in terms of mean value and coefficient of variation. The distributions of both model uncertainties are compared in Figure 3.

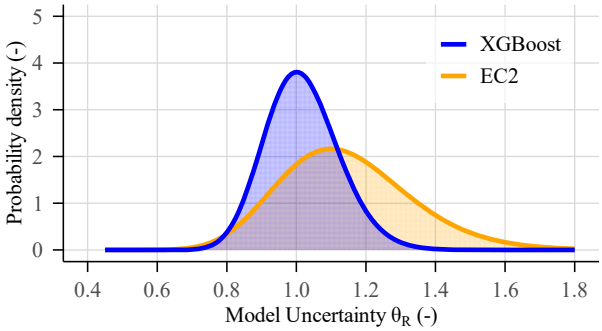


Figure 3. Fitted Lognormal distributed model uncertainty θ_R of the trained XGBoost model and the model according to Eurocode 2

4.7. Interval Estimators of Model Uncertainties

The model uncertainty parameters $\mu_{\ln}$ and $\sigma_{\ln}$ were estimated from a test dataset of $n = 82$ observations. Given this limited sample size, point estimates alone are insufficient to characterise the distributional parameters with confidence; interval estimators are therefore applied to quantify the uncertainty in the estimated parameters. Confidence intervals at the 95 % confidence level were calculated following (Deutscher Ausschuss für Stahlbeton e.V. (DAfStb), 2025). The resulting confidence intervals are reported in Table II.

For the subsequent reliability analysis, the conservative bounds of the confidence intervals are adopted as inputs to the MCS, ensuring that parameter uncertainty is propagated into the computed reliability index.

Table II. Confidence intervals of the distribution parameters of θ_R

Model	Stochastic parameters	Point Estimate		Interval Estimators (95 %)		
		LN-Value	LN-Value transformed	LN-Value	LN-Value transformed	Corrected parameters
EC2	$\hat{\mu}_{\theta_{R,EC2}}$	0.122	1.146	[0.092, +∞]	[1.111, +∞]	1.111
	$\hat{\sigma}_{\theta_{R,EC2}}$	0.165	0.191	[0, 0.190]	[0, 0.219]	0.206[6]
	CoV($\theta_{R,EC2}$)	-	0.166	-	[0, 0.192]	0.185[6]
XGB	$\hat{\mu}_{\theta_{R,XGB}}$	0.012	1.017	[0, +∞]	[0.998, +∞]	0.998
	$\hat{\sigma}_{\theta_{R,XGB}}$	0.104	0.106	[0, 0.120]	[0, 0.122]	0.109[6]
	CoV($\theta_{R,XGB}$)	-	0.107	-	[0, 0.120]	0.109[6]

5. Application of the trained model in reliability analyses

5.1. Numerical Analysis

The reliability of flat slabs without punching shear reinforcement designed according to DIN EN 1992-1-1:2011 has been extensively investigated in the literature (e.g., Ricker et al., 2021). To enable a direct comparison between the reliability indices obtained using the XGBoost resistance model and those based on the analytical design equation according to DIN EN 1992-1-1:2011, the reference example from (Ricker et al., 2021) is adopted here. This example is used to quantify the influence of the data-driven resistance model on the computed reliability index β and to identify the resulting hidden safety margin (Figure 4).

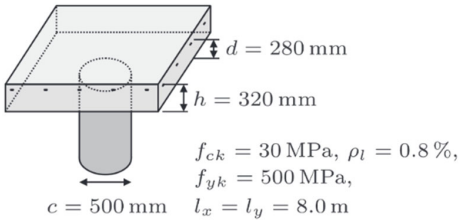


Figure 4. Considered example of a flat slab without punching shear reinforcement, taken from (Ricker et al., 2021)

To investigate the influence of individual parameters on the reliability index, each parameter is varied individually from the reference state (Figure 4) while all other parameters are held constant. The reliability

[6] Correction of σ_{θ_R} and CoV(θ_R) by taking into account the test uncertainties CoV_e acc. to (Sykora et al., 2015):

$CoV(\theta_R) = \sqrt{CoV_{observed}^2 - CoV_e^2}$, with $CoV_e = 0.05$

analyses follow the approach of (Ricker et al., 2021), in which the load and resistance sides of the limit state function are treated separately. The ultimate limit state function is formulated as:

$$g(\boldsymbol{X}) = V_{\mathrm{R}}(\boldsymbol{X}) - V_{\mathrm{Rd,c}} = 0 \tag{14}$$

where $V_{\mathrm{R}}(\boldsymbol{X})$ is the actual resistance as a function of the random variables vector $\boldsymbol{X} = \{X_1, X_2, \ldots, X_i\}$, and V_{Rd} is the design value of resistance. Failure is defined as the event $g(\boldsymbol{X}) \leq 0$, i.e., the realised resistance falling below the design resistance value. Since only the resistance side is evaluated, the computed reliability index β_{R} corresponds to the resistance component of the total reliability index, related through the sensitivity factor α_R as: $\beta_{\mathrm{R}} = \alpha_R \cdot \beta$. Adopting the value $\alpha_R = 0.8$ prescribed in DIN EN 1990:2021—consistent with the assumption that resistance and load variability contribute in fixed proportion to total uncertainty— the total reliability index is recovered by scaling $\beta = \beta_{\mathrm{R}}/0.8$. Without this correction, the resistance-only analysis would systematically underestimate β relative to the full reliability problem.

5.2. Limit state Function and Basic Variables

The failure domain defined by the punching shear design provision of DIN EN 1992-1-1 is expressed as:

$$g(\boldsymbol{X}) = \theta_{\mathrm{R}} \cdot \nu_{\mathrm{R,c}}(d, c, \rho_{\mathrm{l}}, f_{\mathrm{c}}) \cdot u_1(d, c) \cdot d - V_{\mathrm{Rd,c}} \leq 0 \tag{15}$$

where $\theta_{\mathrm{R}}$is the random variable representing model uncertainty of the design equation; $\nu_{\mathrm{R,c}}(\cdot)$ is the punching shear resistance as a function of the following basic variables: effective depth *d*, column dimension *c*, flexural reinforcement ratio ρ_{l}, and concrete compressive strength f_{c}. The term $u_1(d, c)$ is the critical control perimeter at a distance of $2d$ from the column face. $V_{\mathrm{Rd,c}}$ is the deterministic design resistance according to DIN EN 1992-1-1:2011, as defined in Section 3. Substituting the resistance formulation according to this code, for interior circular columns into Eq. (15) yields:

$$g_{\mathrm{EC2}}(\boldsymbol{x}) = \theta_{\mathrm{R}} \left[C_{Rd,c} \left[\min\left(2.0;\ \sqrt{1 + \frac{200}{d}}\right) \right] \cdot (100 \cdot \rho_{\mathrm{l}} \cdot f_{\mathrm{c}})^{1/3} \right] \cdot \left(2 \cdot \pi \cdot \left(\frac{c}{2} + 2 \cdot d\right)\right) \cdot d - V_{\mathrm{Rd,c}} = 0 \tag{16}$$

with $C_{Rc} = 0.18 \cdot \min(1;\ 0.1 \cdot \frac{\pi \cdot c}{d} + 0.6)$.

The limit state function is subsequently reformulated by replacing the EC2 resistance model with predictions from the trained XGBoost model:

$$g_{\mathrm{XGB}}(\boldsymbol{x}) = \theta_{\mathrm{R,XGB}} \cdot \exp\left(y_{\mathrm{XGB}}\left(f_{\mathrm{c}}, d, \rho_{\mathrm{l}}, f_{\mathrm{y}}, u_{\mathrm{crit}}, a, \frac{a}{d}, \frac{u_0}{d}\right)\right) \cdot f_{\mathrm{c}} \cdot u_{\mathrm{crit}} \cdot d - V_{\mathrm{Rd,c}} = 0 \tag{17}$$

where a/d is included as an independent feature consistent with the XGBoost feature set defined in Section 4.3, derived from the random variables *a* and *d*. The model uncertainty $\theta_{\mathrm{R,XGB}}$ was characterised in Section 4.5; interval estimates of its Lognormal distribution parameters are adopted here to avoid underestimating uncertainty arising from the limited validation subset. The stochastic models for the basic variables *c*, f_{c}, *d*, f_{y}, and *a* were adopted from (*Probabilistic Model Code*, 2001). The stochastic model for the longitudinal reinforcement cross section follows (Muttoni, 2023). The derived quantities $u_{\mathrm{crit}} = 2 \cdot \pi \left(\frac{c}{2} + 2 \cdot d\right)$, $u_0 = \pi \cdot c$ and $\rho_{\mathrm{l}} = A_{\mathrm{s}}/d$ are computed from the basic random variables at each simulation step. The stochastic models are summarised in Table III.

Table III. Stochastic models of basic variables						
Basic variable X		Distribu-tion Type	Unit	Nominal value	Expected Value E(X)	Standard Deviation SD(X)
Cyl. concrete compressive strength	f_c	LST[7]	N/mm²	f_{ck}	-	-
Effective depth	d	N	mm	d_{nom}	d_{nom} + 10	10
Column diameter	c	N	mm	c_{nom}	c_{nom} + 0.003 · c_{nom}	4 + 0.006 · c_{nom}
Longitudinal reinforcement area	A_s	N	mm²	$A_{s,nom}$	0.97 · $A_{s,nom}$	0.02 · $A_{s,nom}$
Shear span	a	N	mm	a_{nom}	a_{nom} + 0.003 · a_{nom}	4 + 0.006 · a_{nom}
Yield strength of reinforcement	f_y	N	N/mm²	f_{yk}	500 + 2 · SD(X)	30
Model uncertainty EC2	θ_{EC2}	LN	-	-	1.111	0.206
Model uncertainty XGB	θ_{XGB}	LN	-	-	0.998	0.109
LST: Log-student-t distribution, N: Lormal distribution, LN: Lognormal distribution						

5.3. Reliability Methods

The reliability analyses were performed using subset simulation, which combines conditional sampling with **M**arkov **C**hain **M**onte **C**arlo (MCMC) techniques to estimate small failure probabilities efficiently—an approach that is substantially less computationally demanding than direct MCS for the probability levels relevant to structural reliability (10 000 samples per simulation level, level of probability $p_0 = 0.10$, and confidence level $\alpha = 0.05$) (Au & Beck, 2001). The analyses were implemented using the open-source package *TesiproV* (Nille-Hauf et al., 2026) in R (R Core Team, 2025).

5.4. Results and Discussion

Figure 5 shows the computed reliability index β as a function of the varied input parameters for both limit state functions investigated. Across all parameter variations, the XGBoost model consistently yields higher reliability indices than the DIN EN 1992-1-1:2011 formulation, reflecting its lower model uncertainty. The magnitude of the increase in β is parameter-dependent: for example, the effect is more pronounced at lower concrete compressive strengths than at higher values (Figure 5b). This sensitivity reflects the degree to which each input variable contributes to prediction uncertainty in the XGBoost model and warrants further investigation through a dedicated sensitivity analysis, for example using SHAP values.

[7] The stochastic model of the concrete compressive strength was proposed by (Rackwitz, 1983) as a Log-student-t (LST) distribution: $F_x(x) = F_{t_{\nu'}}\left[\frac{\ln(x-m\prime)}{s'} \cdot \sqrt{\frac{n\prime}{n\prime+1}}\right]$, with m', n', s' and ν' being prior parameters given for the different concrete classes in (*Probabilistic Model Code*, 2001). For ready-mixed concrete, the parameters are given as follows:

Concrete grade	Prior Parameters			
	m'	n'	s'	ν'
C15	3.40	3.0	0.14	10
C25	3.65	3.0	0.12	10
C35	3.85	3.0	0.09	10
C45	3.98	3.0	0.07	10

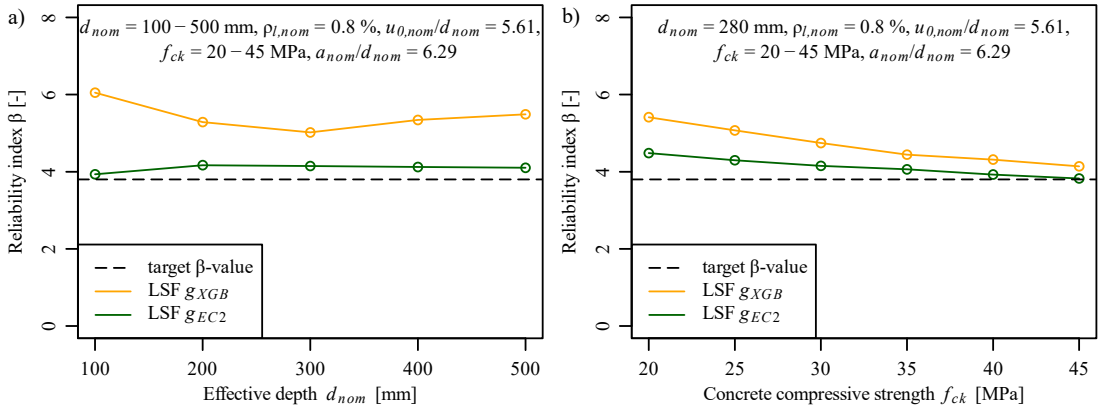


Figure 5. Reliability index β in variation with (a) effective depth d [mm], and (b) concrete compressive strength f_{ck} [MPa]

The results further reveal physical influences captured by the XGBoost model that are not represented in the code verification format. Figure 6a shows that the model predicts an increasing reliability index for small shear slenderness values, while the code formulation does not include this parameter and therefore yields a constant reliability index. The beneficial trend predicted by the model is physically plausible and consistent with the upcoming new generation of Eurocode 2, where the shear slenderness will be explicitly included in the design equation of DIN EN 1992-1-1:2025.

Figure 6b demonstrates that for specific column perimeters $u_0/d < 4$, the XGBoost model predicts a substantially higher resistance than the code design model. Under the current National Annex, the empirical factor $C_{\mathrm{Rd,c}}$ is reduced for $u_0/d < 4$, a correction not reflected in the trained XGBoost model. This discrepancy may result either from the limited number of corresponding tests in the training dataset or from an overly conservative reduction in the code formulation. The available data do not allow a clear distinction between these explanations, which represents a limitation of the present study and suggests the need for targeted experimental investigations.

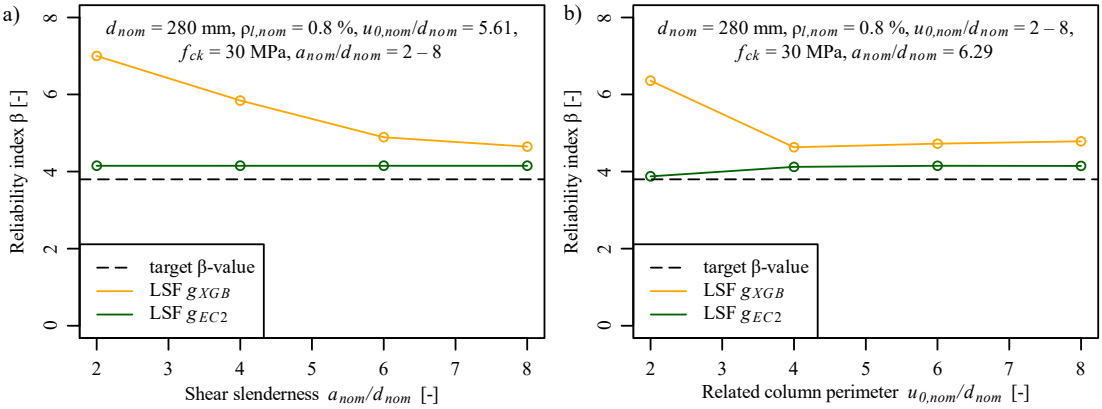


Figure 6. Reliability index β in variation with (a) shear slenderness a/d [-], and (b) related column perimeter u_0/d [-]

Figure 7 presents the reliability index β as a function of the mean longitudinal reinforcement ratio ρ_l. For reinforcement ratios up to approximately 1.5%, the XGBoost model consistently yields higher reliability indices than the code-based limit state function. At ρ_l = 2%, however, the XGBoost model predicts a lower resistance than the code design equation, causing the two reliability curves to converge or causing β_{XGB} to approach β_{EC2}. This observation is physically significant: DIN EN 1992-1-1:2011 applies an upper cap of $\rho_l = 0.02$ in the resistance formula, beyond which no further increase in punching shear resistance is assumed. The XGBoost model suggests that this plateau is reached at a lower reinforcement ratio, in the range $0.015 < \rho_l < 0.02$, implying that the code formulation may overestimate the contribution of high reinforcement ratios to resistance. This finding supports the need for the code cap, while also suggesting that the effective limit may be more conservative than currently prescribed.

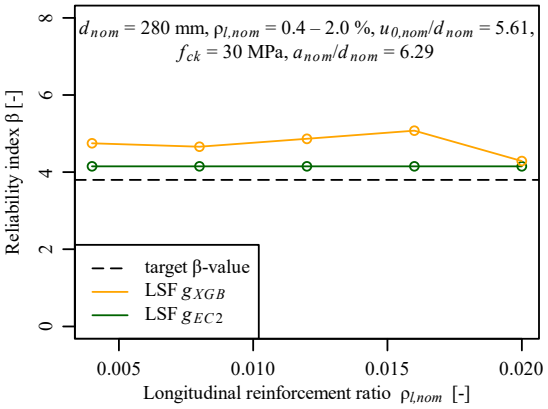


Figure 7. Reliability index β in variation with longitudinal reinforcement ratio ρ_l [-]

Further experimental data for specimens with ρ_l > 1.5% is required to investigate this observation more rigorously, as the current training dataset may underrepresent this range (Figure 7). A targeted sensitivity analysis using SHAP values could additionally clarify the role of ρ_l relative to other input features in this reinforcement range.

6. Conclusions

Based on this investigation, the following conclusions can be drawn:

- The trained XGBoost model predicts the load-bearing capacity of flat slabs without punching shear reinforcement with lower bias and lower scatter than the design equation of DIN EN 1992-1-1:2011, as evidenced by a mean model uncertainty closer to unity ($\mu_{\theta_{R,EC2}} = 1.146$ *vs.* $\mu_{\bar{\theta}_{R,XGB}} = 1.017$) and a substantially reduced coefficient of variation (COV($\theta_{R,EC2}$) = 0.166 *vs.* COV($\bar{\theta}_{R,XGB}$) = 0.106).

- The lower scatter of the XGBoost model uncertainty reduces the probability of very low load-bearing capacity realisations compared to the code model. This directly translates into higher reliability indices in the reliability analyses: flat slabs without punching shear reinforcement designed according to DIN

EN 1992-1-1:2011 exhibit hidden safety margins that arise solely from the relatively high model uncertainty of the code resistance equation. When the more accurate XGBoost model is used as the resistance model, these margins become apparent.

- The reliability analyses further reveal physical relationships between input parameters and load-bearing capacity that are not explicitly captured in the code design mode—either as deliberate simplifications or due to limitations in the empirical calibration basis. Notable examples include the beneficial effect of small shear slenderness and the apparent overestimation of resistance at high longitudinal reinforcement ratios in the code formulation.

Several limitations of this study should be noted. The XGBoost model is trained on 397 tests from the *fib* punching shear database, representing idealised laboratory conditions and excluding long-term effects, cyclic loading, and construction imperfections. Some parameter ranges—particularly high longitudinal reinforcement ratios and small relative column perimeters ($u_0/d < 4$)—are underrepresented, so conclusions for these regions remain uncertain. In addition, the reliability analyses are performed solely within the framework of DIN EN 1992-1-1:2011 and its German National Annex, meaning the identified safety margins are specific to this design format and not directly transferable to other codes.

Future work could address these limitations. Targeted experiments in underrepresented parameter ranges would improve model reliability and help clarify observed behaviours such as those for $u_0/d < 4$. A SHAP-based sensitivity analysis could provide a systematic decomposition of the XGBoost predictions and enable a more rigorous comparison with the functional relationships assumed in DIN EN 1992-1-1:2011. Finally, the most consequential extension of this work would be a reliability-based design optimisation that translates the identified safety margins into reduced cross-sections—directly fulfilling the material efficiency objective stated in the introduction and quantifying the associated reduction in CO_2 emissions.

Acknowledgements

The authors wish to express their gratitude to the German Committee for Structural Concrete (*Deutscher Ausschuss für Stahlbeton e.V., DAfStb*) for funding this investigation (DAfStb-Projekt V521). The authors also gratefully acknowledge the computing time provided on the Linux HPC cluster at Technical University Dortmund (LiDO3), partially funded in the course of the Large-Scale Equipment Initiative by the Deutsche Forschungsgemeinschaft (DFG, German Research Foundation) as project 271512359.

References

Au, S.-K., & Beck, J. L. (2001). Estimation of small failure probabilities in high dimensions by subset simulation. *Probabilistic Engineering Mechanics*, *16*(4), 263–277. https://doi.org/10.1016/S0266-8920(01)00019-4

Bishop, C. M. (2006). *Pattern recognition and machine learning*. Springer.

Chen, T., & Guestrin, C. (2016). XGBoost: A Scalable Tree Boosting System. *Proceedings of the 22nd ACM SIGKDD International Conference on Knowledge Discovery and Data Mining*, 785–794. https://doi.org/10.1145/2939672.2939785

Chen, T., He, T., Benesty, M., Khotilovich, V., Tang, Y., Cho, H., Chen, K., Mitchell, R., Cano, I., Zhou, T., Li, M., Xie, J., Lin, M., Geng, Y., Li, Y., Yuan, J., & Cortes, D. (2026). *xgboost: Extreme Gradient Boosting* (p. 3.2.1.1) [Dataset]. https://doi.org/10.32614/CRAN.package.xgboost

Deutscher Ausschuss für Stahlbeton e.V. (DAfStb). (2025). *Verfahren zur Herleitung von Sicherheitsbeiwerten im Massivbau unter Verwendung probabilistischer Methoden*.

Ditlevsen, O., & Madsen, H. O. (1999). *Structural reliability methods* (Repr). Wiley.
Euro-International Committee for Concrete & Fédération internationale de la précontrainte (Eds.). (1998). *CEB-FIP model code 1990: Design code* (Repr). Telford.
Fang, D., Brown, N., De Wolf, C., & Mueller, C. (2023). Reducing embodied carbon in structural systems: A review of early-stage design strategies. *Journal of Building Engineering*, *76*, 107054. https://doi.org/10.1016/j.jobe.2023.107054
Fédération internationale du béton (fib). (2023). *Model Code for Concrete Structures 2020*.
Friedman, J. H. (2001). Greedy Function Approximation: A Gradient Boosting Machine. *The Annals of Statistics*, *29*(5), 1189–1232.
Guandalini, S., & Muttoni, A. (2004). *Punching test on symmetrical reinforced concrete slabs without shear reinforcement (Essais de poinçonnement symétrique des dalles en béton armé sans armature à l'effort tranchant)* (Versuchsbericht 00.03-R1). Institute de Structures, Laboratoire de Construction en Béton (IS-Beton), École Polytechnique Fédérale de Lausanne,.
Häkkinen, T., Kuittinen, M., Ruuska, A., & Jung, N. (2015). Reducing embodied carbon during the design process of buildings. *Journal of Building Engineering*, *4*, 1–13. https://doi.org/10.1016/j.jobe.2015.06.005
Hallgren, M., Kinnunen, S., & Nylander, B. (1998). Punching Shear Tests on Column Footings. *Nordic Concrete Research*, *21*(3), 1–22.
Hegger, J., Ricker, M., Adam, V., Feiri, T., & Nille-Hauf, K. (2021). *Überprüfung der Zuverlässigkeit der für die nächste Generation von EN 1992-1-1 vorgesehenen neuen Bemessungsansätze gegen Durchstanzen ohne Durchstanzbewehrung und Querkraft ohne Querkraftbewehrung* (Abschlussbericht F-2017-034).
Kuhn, M., & Johnson, K. (2013). *Applied Predictive Modeling*. Springer New York. https://doi.org/10.1007/978-1-4614-6849-3
Liang, S., Shen, Y., & Ren, X. (2022). Comparative study of influential factors for punching shear resistance/failure of RC slab-column joints using machine-learning models. *Structures*, *45*, 1333–1349. https://doi.org/10.1016/j.istruc.2022.09.110
Mangalathu, S., Shin, H., Choi, E., & Jeon, J.-S. (2021). Explainable machine learning models for punching shear strength estimation of flat slabs without transverse reinforcement. *Journal of Building Engineering*, *39*, 102300. https://doi.org/10.1016/j.jobe.2021.102300
Melchers, R. E. (Robert E.) (with Internet Archive). (1999). *Structural reliability analysis and prediction*. Chichester ; New York : John Wiley. http://archive.org/details/structuralreliab0000melc_w1w5
Muttoni, A. (2023). *Background document to clause 4.3.3 and Annex A Partial safety factors for materials* (EPFL-IBETON 16-06-R11). EPFL, Ecole Polytechnique Fédérale de Lausanne.
Nille-Hauf, K., Lux, T., Feiri, T., & Ricker, M. (2026). *TesiproV — Probabilistic Reliability Analysis Framework*.
Probabilistic Model Code. (2001). Joint Committee on Structural Safety.
R Core Team. (2025). _R: A Language and Environment for Statistical Computing_. *R Foundation for Statistical Computing*. Vienna, Austria. <https://www.R-project.org/>
Rackwitz, R. (1983). Predictive distribution of strength under control. *Material & Constructions*, *16*(94), 259–267.
Rankin, G. I. B., & Long, A. E. (1987). Predicting the punching strength of conventional slab-column specimens. *Proceedings of ICE, Civil Engineering*, *82*, 327–346.
Ricker, M., Feiri, T., Nille-Hauf, K., Adam, V., & Hegger, J. (2021). Enhanced reliability assessment of punching shear resistance models for flat slabs without shear reinforcement. *Engineering Structures*, *226*, 111319. https://doi.org/10.1016/j.engstruct.2020.111319
Ruiz, M. F., & Ospina, C. E. (2025, June 4). *Punching Shear Database* [Fédération internationale du béton]. Fédération internationale du béton. Fédération Internationale Du Béton. https://www.fib-international.org/commissions/databases.html
Spaethe, G. (1992). *Die Sicherheit tragender Baukonstruktionen* (2., neubearb. Aufl.). Springer.
Sykora, M., Holicky, M., Prieto, M., & Tanner, P. (2015). Uncertainties in resistance models for sound and corrosion-damaged RC structures according to EN 1992-1-1. *Materials and Structures*, *48*(10), 3415–3430. https://doi.org/10.1617/s11527-014-0409-1
Teichgräber, M., Köhler, J., & Straub, D. (2022). Hidden safety in structural design codes. *Engineering Structures*, *257*, 114017. https://doi.org/10.1016/j.engstruct.2022.114017
United Nations Environment Programme. (2023). *Building Materials and the Climate: Constructing a New Future*. United Nations.
Vrouwenvelder, T., Beck, A., Proske, D., Faber, M., Köhler, J., Schubert, M., Straub, D., & Teichgräber, M. (2025). Interpretation of probability in structural safety – A philosophical conundrum. *Structural Safety*, *113*, 102473. https://doi.org/10.1016/j.strusafe.2024.102473

SESSION 2

Reliability Analysis and Sensitivity Methods

Papers in this session

1. Beyond the Design Point: When Equal Failure Probabilities May Not Be Equal
2. Hybrid Reliability Analysis with Uncertainty in Correlation Coefficients and First Two Statistical Moments
3. An Efficient Reliability Sensitivity Analysis Method Based on the Method of Moments
4. A linear-moment-based sensitivity analysis method considering the influence of correlation coefficient
5. An Efficient Reliability Analysis Method under Hybrid Uncertainty for High-Dimensional Problems
6. A Bivariate Distribution Based on Squared Normal Transformation

Beyond the Design Point: When Equal Failure Probabilities May Not Be Equal

Marco Broccardo and Johannes O. Royset
[1)] *Department of Civil, Environmental and Mechanical Engineering, University of Trento, 38132 Trento, Italy - marco.broccardo@unitn.it*

[2)] *Daniel J. Epstein Department of Industrial and Systems Engineering, University of Southern California, CA 90089 Los Angeles, USA - royset@usc.edu*

Abstract. In structural reliability, the probability of failure and the associated reliability index are usually treated as complete summaries of structural safety. This convention is powerful, but it hides an important distinction: two systems may have the same failure probability while exhibiting markedly different failure mechanisms and tail severities. This paper revisits the role of the classical design point and proposes two complementary quantities for interpreting failure beyond its probability. The first is the Mean Failure Point, a representative point in the standard normal space associated with the expected performance conditional on failure. It characterizes where the failure event is expected to lie, rather than where the limit-state surface is most likely to be reached. The second is the Buffered Reliability Index, obtained from the buffered probability of failure, which incorporates the tail behavior of the performance function. In the linear standard normal case, both quantities admit closed-form expressions involving the hazard rate of the standard normal distribution, clarifying their relation with the classical reliability index. The resulting triplet—failure probability, Mean Failure Point, and Buffered Reliability Index—offers a compact description of how likely failure is, how it occurs, and how severe it may be.

Keywords: structural reliability, design point, reliability index, buffered probability of failure, superquantile, failure mechanism

1. Introduction

The design point is one of the central concepts of structural reliability. In the standard normal space, it is defined as the point on the limit-state surface that lies closest to the origin. Equivalently, under the usual regularity assumptions, it identifies the location at which the transformed joint density is largest among the points that satisfy the limit-state equation. This point provides the geometric foundation of the Hasofer–Lind reliability index (Hasofer and Lind, 1974) and of the First- and Second-Order Reliability Methods, FORM and SORM (Breitung, 1984; Der Kiureghian et al., 1987). It is also the point around which many asymptotic and simulation-based approximations of rare failure events are organized. The appeal of the design point is not only computational. It provides a concise geometric interpretation of safety. A structure is regarded as safer when the

© 2026 by the author(s). This work is licensed under the Creative Commons Attribution 4.0 International License (CC BY 4.0), which permits unrestricted use, distribution, and reproduction in any medium, provided the original author and source are credited.

limit-state surface is farther from the origin in the standard normal space. This interpretation has deeply influenced modern reliability theory and the calibration of partial safety factors in design codes. There is, however, an important limitation. The classical formulation tells us how likely it is that a structure reaches the failure domain, but it says little about how the failure develops once the domain is entered. The design point lies on the boundary of failure. It is therefore a boundary descriptor, not a descriptor of the interior of the failure domain. As a consequence, two systems may have the same probability of failure, and even equal design-point distances, while exhibiting very different failure mechanisms. One system may enter the failure domain only mildly, another may enter a deep tail region. This distinction matters because engineering design is rarely concerned with failure probability alone. The historical evolution from allowable-stress design to load-factor design and performance-based design reflects a broader objective: not only to avoid failure, but also to control the mode and consequences of failure. A ductile and observable failure mechanism is not equivalent to a brittle and sudden one, even when both mechanisms have the same nominal probability of occurrence. The statement "equal failure probabilities imply equal reliability" is therefore too narrow when reliability is interpreted as a physical property of a structural system.

This paper expands on ideas from (Broccardo and Royset, 2025) of the classical framework. The key idea is to supplement the failure probability with information about the conditional distribution of the performance function within the failure domain. Two quantities are introduced. The first is the Mean Failure Point (MFP), a representative point in the standard normal space associated with the conditional expected failure level. The MFP is intended to describe the typical location and direction of failure beyond the limit-state surface. The second is the Buffered Reliability Index (BRI), a tail-dependent reliability index derived from the buffered probability of failure (Rockafellar and Royset, 2010). While the classical reliability index is equivalent to the failure probability, the BRI also responds to the severity and spread of the adverse tail. The proposed view is summarized by augmenting the single reliability descriptor $P_{\mathcal{F}}$ or β with the triplet

$$\left(P_{\mathcal{F}},\, \boldsymbol{z}^{**},\, \underline{\beta}\right), \tag{1}$$

where $P_{\mathcal{F}}$ is the probability of failure, $\boldsymbol{z}^{**}$ is the MFP, and $\underline{\beta}$ is the BRI. The first term measures likelihood, the second identifies a representative failure configuration, and the third accounts for tail severity. The aim is not to discard the design point, but to place it within a broader reliability description that is more consistent with the mechanics of failure.

2. Classical reliability and the design point

Let the performance of a structural system be described by a limit-state function

$$Y = g(\boldsymbol{X}), \qquad \boldsymbol{X} \in \mathbb{R}^n, \tag{2}$$

where $Y \leq 0$ defines failure and $Y > 0$ defines safety. If $\boldsymbol{X}$ has joint density $f_{\boldsymbol{X}}(\boldsymbol{x})$, the probability of failure is

$$P_{\mathcal{F}} = \mathbb{P}[Y \leq 0] = \int_{\mathbb{R}^n} \mathbf{1}\{g(\boldsymbol{x}) \leq 0\} f_{\boldsymbol{X}}(\boldsymbol{x})\, \mathrm{d}\boldsymbol{x}. \tag{3}$$

More generally, the distribution of Y is

$$F_Y(y) = \mathbb{P}[Y \leq y] = \int_{\mathbb{R}^n} \mathbf{1}\{g(\boldsymbol{x}) \leq y\} f_{\boldsymbol{X}}(\boldsymbol{x})\, \mathrm{d}\boldsymbol{x}, \tag{4}$$

so that $P_{\mathcal{F}} = F_Y(0)$. Through an isoprobabilistic transformation $\boldsymbol{z} = \mathcal{T}(\boldsymbol{x})$, the problem is mapped to the standard normal space. The transformed vector $\boldsymbol{Z} \in \mathbb{R}^n$ has independent standard normal components and density $\varphi(\boldsymbol{z})$. With

$$G(\boldsymbol{z}) = g\big(\mathcal{T}^{-1}(\boldsymbol{z})\big), \tag{5}$$

Eq. (4) becomes

$$F_Y(y) = \int_{\mathbb{R}^n} \mathbf{1}\{G(\boldsymbol{z}) \leq y\} \varphi(\boldsymbol{z})\, \mathrm{d}\boldsymbol{z}. \tag{6}$$

In the Hasofer–Lind formulation (Hasofer and Lind, 1974), the design point is obtained as

$$\boldsymbol{z}^* \in \arg\min_{\boldsymbol{z}} \left\{ \|\boldsymbol{z}\|_2^2 \;\middle|\; G(\boldsymbol{z}) = 0 \right\}. \tag{7}$$

The Hasofer–Lind reliability index, introduced to provide an invariant measure of reliability, is

$$\beta_{HL} = \|\boldsymbol{z}^*\|_2 \,. \tag{8}$$

This formulation overcame the lack of invariance of earlier reliability indices with respect to equivalent mathematical representations of the limit-state function. If G is differentiable at $\boldsymbol{z}^*$, FORM approximates the limit-state surface by its tangent hyperplane at $\boldsymbol{z}^*$ (Hasofer and Lind, 1974) and gives

$$P_{\mathcal{F}} \approx \Phi(-\beta_{HL}), \tag{9}$$

where Φ is the standard normal distribution function. SORM improves this approximation by incorporating local curvature information at the design point (Breitung, 1984; Der Kiureghian, 2022). When the actual probability of failure is known or accurately estimated, the generalized reliability index (Ditlevsen, 1979) is defined as

$$\beta = -\Phi^{-1}(P_{\mathcal{F}}). \tag{10}$$

Thus, $P_{\mathcal{F}}$ and β contain the same information. Two systems with the same $P_{\mathcal{F}}$ have the same generalized reliability index, independently of the shape of the failure domain or the distribution of the performance function below zero. This equivalence is mathematically consistent, but it is incomplete from a mechanical point of view. The design point is best understood as a descriptor of the boundary of the failure event. It identifies the most likely way to reach the limit-state surface, not the expected state of the system once failure has occurred. This distinction motivates the next section.

3. Beyond the design point: Mean Failure Point

The purpose of the Mean Failure Point is to identify a representative point within the failure domain. The guiding question is simple: conditional on failure occurring, which failure state best represents the event? The answer should not be constrained to the limit-state surface $G(\boldsymbol{z}) = 0$, because actual failure states lie in the domain $G(\boldsymbol{z}) \leq 0$.

3.1. Conditional expected failure level

Since the performance Y is a random variable, the most natural scalar representative of the failure outcome under squared-error loss is the conditional mean

$$\underline{y} = \arg\min_{y \in \mathbb{R}} \mathbb{E}\left[(Y-y)^2 \mid Y \leq 0\right] = \mathbb{E}[Y \mid Y \leq 0]. \tag{11}$$

The notation $\underline{y}$ emphasizes that, except in degenerate cases, this value is negative. It is the expected performance level conditional on failure, and therefore depends on the tail of the distribution of Y below zero.

The value $\underline{y}$ defines a new level set,

$$\Sigma_{\underline{y}} = \left\{ \boldsymbol{z} \in \mathbb{R}^n \,\middle|\, G(\boldsymbol{z}) = \underline{y} \right\}, \tag{12}$$

which lies beyond the classical limit-state surface. Points on this level set are not merely incipient failures; they correspond to the expected failure severity in the performance domain.

3.2. Definition of the Mean Failure Point

Among the points on $\Sigma_{\underline{y}}$, the representative point is defined as the intrinsic Fréchet mean of the conditional probability measure induced on $\Sigma_{\underline{y}}$ (Fréchet, 1948; Karcher, 1977). Specifically,

$$\boldsymbol{z}^{**} = \arg\min_{\boldsymbol{z}_0 \in \Sigma_{\underline{y}}} \int_{\Sigma_{\underline{y}}} d_{\Sigma_{\underline{y}}}(\boldsymbol{z}_0, \boldsymbol{z})^2 \, d\mu_{\underline{y}}(\boldsymbol{z}), \tag{13}$$

where $d_{\Sigma_{\underline{y}}}(\cdot,\cdot)$ denotes the geodesic distance on the manifold $\Sigma_{\underline{y}}$ and

$$d\mu_{\underline{y}}(\boldsymbol{z}) = \frac{\dfrac{\phi(\boldsymbol{z})}{\|\nabla G(\boldsymbol{z})\|}\, d\Sigma_{\underline{y}}(\boldsymbol{z})}{\displaystyle\int_{\Sigma_{\underline{y}}} \frac{\phi(\boldsymbol{z})}{\|\nabla G(\boldsymbol{z})\|}\, d\Sigma_{\underline{y}}(\boldsymbol{z})}. \tag{14}$$

The measure in Eq. (14) follows from the co-area formula and represents the conditional Gaussian probability distribution restricted to the level set $\Sigma_{\underline{y}}$. Unlike the conditional Euclidean mean, the intrinsic Fréchet mean is constrained to the manifold itself,

$$\boldsymbol{z}^{**} \in \Sigma_{\underline{y}}, \tag{15}$$

thereby ensuring mechanical and geometric consistency with the prescribed failure level. The corresponding point in the original space is obtained through the inverse transformation,

$$\boldsymbol{x}^{**} = \mathcal{T}^{-1}(\boldsymbol{z}^{**}). \tag{16}$$

Equation (13) defines the Mean Failure Point. It differs from the design point in two fundamental ways. First, it is associated with the conditional failure domain rather than only with the onset of failure. Second, it reflects the expected severity of failure through the level $\underline{y}$. The design point describes the most likely transition into failure, whereas the MFP characterizes a representative state within the failure domain once failure has occurred. The vector

$$\Delta\boldsymbol{z} = \boldsymbol{z}^{**} - \boldsymbol{z}^{*} \tag{17}$$

provides a compact geometric descriptor of the transition from incipient failure to expected failure. Its norm quantifies how deeply the system is expected to penetrate into the failure domain, while its direction identifies the dominant trajectory of failure development in the standard normal space. This vector may therefore be interpreted as a probabilistic-mechanical descriptor of the failure mechanism.

The exact computation of Eq. (13) is generally challenging because it requires optimization on a nonlinear manifold equipped with a geodesic metric. For regular and sufficiently concentrated level sets, a practical approximation can be obtained by replacing the intrinsic Fréchet mean with the mode of the same conditional distribution. This leads to

$$\boldsymbol{z}^{**} \simeq \arg\min_{\boldsymbol{z}} \left\{ \|\boldsymbol{z}\|_2^2 \;\middle|\; G(\boldsymbol{z}) = \underline{y} \right\}. \tag{18}$$

The optimization has the same structure as the classical design-point problem, but is performed on a deeper level set corresponding to the expected failure severity. This approximation preserves compatibility with existing reliability algorithms while providing a representative point within the failure domain.

3.3. Linear standard normal case

The linear standard normal case clarifies the relationship between the design point and the MFP. Let

$$G(\boldsymbol{Z}) = b_0 + \boldsymbol{b}^T\boldsymbol{Z}, \tag{19}$$

where $\boldsymbol{b} \neq \boldsymbol{0}$. Define

$$\beta = \frac{b_0}{\|\boldsymbol{b}\|}, \qquad \boldsymbol{\alpha} = -\frac{\boldsymbol{b}}{\|\boldsymbol{b}\|}. \tag{20}$$

Then the design point is

$$\boldsymbol{z}^{*} = \beta\boldsymbol{\alpha}. \tag{21}$$

The failure event $G(\boldsymbol{Z}) \leq 0$ is equivalent to a one-dimensional standard normal variable exceeding β in the direction $\boldsymbol{\alpha}$. By Gaussian symmetry, the MFP is collinear with the design point. Its norm is

$$\|\boldsymbol{z}^{**}\| = \mathbb{E}[Z \mid Z > \beta] = \frac{\phi(\beta)}{\Phi(-\beta)} = \lambda(\beta), \tag{22}$$

where ϕ is the standard normal density and $\lambda(\beta)$ is the standard normal hazard rate. Hence

$$\boldsymbol{z}^{**} = \lambda(\beta)\boldsymbol{\alpha}. \tag{23}$$

Since $\lambda(\beta) > \beta$ for positive β, the MFP lies beyond the design point along the same failure direction. In this special case, the mechanics of failure is one-dimensional; in nonlinear and multi-mechanism cases, the displacement from $\boldsymbol{z}^*$ to $\boldsymbol{z}^{**}$ can reveal changes in failure direction that are invisible to $P_{\mathcal{F}}$ alone.

4. Beyond the reliability index: Buffered Reliability Index

The MFP provides a representative failure configuration, but it does not by itself produce a scalar reliability index. A scalar index remains useful for comparison and communication. The question is how to define such an index so that it responds not only to the probability of crossing the limit state, but also to the severity of the adverse tail.

4.1. Tail-dependent threshold and buffered probability

We define a threshold $\bar{y}$ by imposing that the conditional mean of Y below this threshold is exactly the conventional failure level zero:

$$\mathbb{E}[Y \mid Y \leq \bar{y}] = 0. \tag{24}$$

For structural systems with positive mean safety margin and nonzero failure probability, this threshold is typically nonnegative. The corresponding probability

$$\bar{P}_{\mathcal{F}} = F_Y(\bar{y}) \tag{25}$$

is the buffered probability of failure, under continuity assumptions on the distribution of Y (Rockafellar and Royset, 2010). Because $\bar{y} \geq 0$, one has

$$\bar{P}_{\mathcal{F}} \geq P_{\mathcal{F}}. \tag{26}$$

The buffered probability is therefore conservative with respect to the classical failure probability (Rockafellar and Royset, 2010; Mafusalov and Uryasev, 2018); see (Royset, 2025) for further connections to the risk management literature broadly.

The interpretation is direct. Suppose two systems have the same value of $P_{\mathcal{F}}$. If one system has a heavier adverse tail, the conditional mean below zero is more severe. To bring the conditional mean back to zero, the threshold $\bar{y}$ must move farther into the safe side, thereby increasing $F_Y(\bar{y})$. The buffered probability therefore distinguishes systems that the classical failure probability regards as equivalent; this distinction is closely related to tail-sensitivity measures based on the ratio between buffered and classical failure probabilities (Byun and Royset, 2022).

The Buffered Reliability Index is defined as

$$\underline{\beta} = -\Phi^{-1}(\bar{P}_{\mathcal{F}}). \tag{27}$$

The underline emphasizes that

$$\underline{\beta} \leq \beta, \tag{28}$$

with equality only in limiting or degenerate cases. For two systems with the same β, the system with the heavier adverse tail has a larger $\bar{P}_{\mathcal{F}}$ and therefore a smaller $\underline{\beta}$.

In the standard normal space, Eq. (25) can be written as

$$\bar{P}_{\mathcal{F}} = \int_{\mathbb{R}^n} \mathbf{1}\{G(\boldsymbol{z}) \leq \bar{y}\}\varphi(\boldsymbol{z})\,\mathrm{d}\boldsymbol{z}. \tag{29}$$

Analogously to FORM, one may approximate $\underline{\beta}$ through the design point associated with the shifted surface $G(\boldsymbol{z}) = \bar{y}$:

$$\underline{\boldsymbol{z}}^* \in \arg\min_{\boldsymbol{z}} \left\{ \|\boldsymbol{z}\|_2^2 \;\middle|\; G(\boldsymbol{z}) = \bar{y} \right\}. \tag{30}$$

We call $\underline{\boldsymbol{z}}^*$ the Buffered Probable Point. It is not intended to replace the design point as a mechanical descriptor. Rather, it is an auxiliary point used to approximate the buffered probability and the associated BRI:

$$\underline{\beta} \approx \underline{\beta}_{HL} = \|\underline{\boldsymbol{z}}^*\|_2\,, \qquad \bar{P}_{\mathcal{F}} \approx \Phi(-\underline{\beta}_{HL}). \tag{31}$$

By construction, $\underline{\beta}_{HL} \leq \beta_{HL}$.

4.2. Linear standard normal case

For the linear model in Eq. (19), the buffered probability can be evaluated in closed form. The BRI coincides with its Hasofer–Lind approximation,

$$\bar{P}_{\mathcal{F}} = \Phi(-\underline{\beta}) = \Phi(-\underline{\beta}_{HL}). \tag{32}$$

The shifted threshold gives

$$\underline{\beta} = \frac{b_0 - \bar{y}}{\|\boldsymbol{b}\|} = \beta - \frac{\bar{y}}{\|\boldsymbol{b}\|}, \tag{33}$$

and

$$\underline{\boldsymbol{z}}^* = \underline{\beta}\,\boldsymbol{\alpha}. \tag{34}$$

The defining condition of the buffered threshold implies

$$\mathbb{E}[Z \mid Z > \underline{\beta}] = \beta, \tag{35}$$

or equivalently

$$\lambda(\underline{\beta}) = \frac{\phi(\underline{\beta})}{\Phi(-\underline{\beta})} = \beta. \tag{36}$$

Therefore,

$$\underline{\beta} = \lambda^{-1}(\beta), \tag{37}$$

and the three reliability descriptors satisfy

$$\underline{\beta} = \lambda^{-1}(\beta) \leq \beta \leq \lambda(\beta) = \|\boldsymbol{z}^{**}\|\,. \tag{38}$$

This chain is useful conceptually. The BRI lies on the safe side of the classical reliability index, while the MFP lies beyond the design point inside the failure domain. In the linear Gaussian case the three quantities are aligned; in nonlinear systems they may separate both in magnitude and direction.

5. Illustrative example: equal failure probabilities, different failure descriptions

We consider a two-variable component reliability problem in which the performance function is written in the classical resistance-minus-load form

$$g(r, s_i) = r - s_i, \qquad i = 1, 2, \tag{39}$$

so that failure occurs when the load effect exceeds the resistance, $s_i \geq r$. The resistance R is modeled as lognormal with mean 60.00 and coefficient of variation 0.15. The two load models are chosen so that they produce the same classical probability of failure, while having different distributional forms. The first load, S_1, follows a generalized extreme value distribution with parameters $\mu = 12.932$, $\sigma = 2.878$, and $\xi = 0.125$, corresponding to a Fréchet-type right tail. The second load, S_2, follows a lognormal distribution with parameters $\mu = 2.935$ and $\sigma = 0.293$. Its mean is 19.56 and its coefficient of variation is 0.30. The resistance has lognormal parameters $\mu = 4.083$ and $\sigma = 0.149$. The marginal probability density functions are shown in Figure 1.

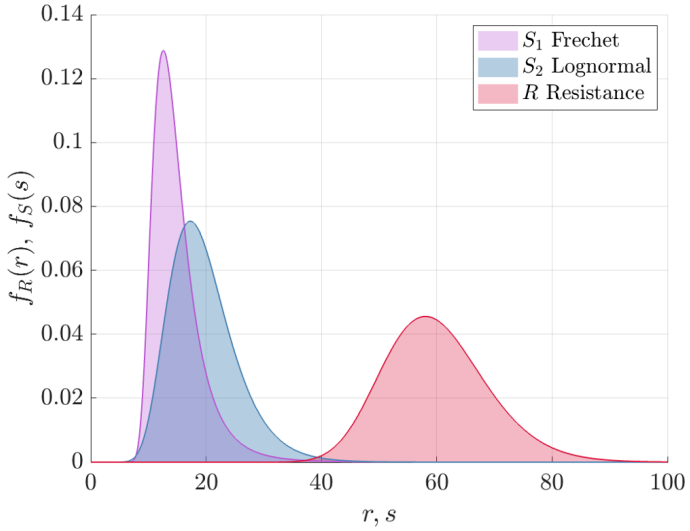


Figure 1. Definition of the illustrative problem. The performance function is $g(r, s_i) = r - s_i$. The resistance R is lognormal, while the two alternative load models are S_1, modeled by a generalized extreme value distribution, and S_2, modeled by a lognormal distribution. The two load models are calibrated to give the same probability of failure.

The two models are calibrated so that

$$\mathbb{P}[g(R, S_1) \leq 0] = \mathbb{P}[g(R, S_2) \leq 0] = 2.4501 \times 10^{-4}. \tag{40}$$

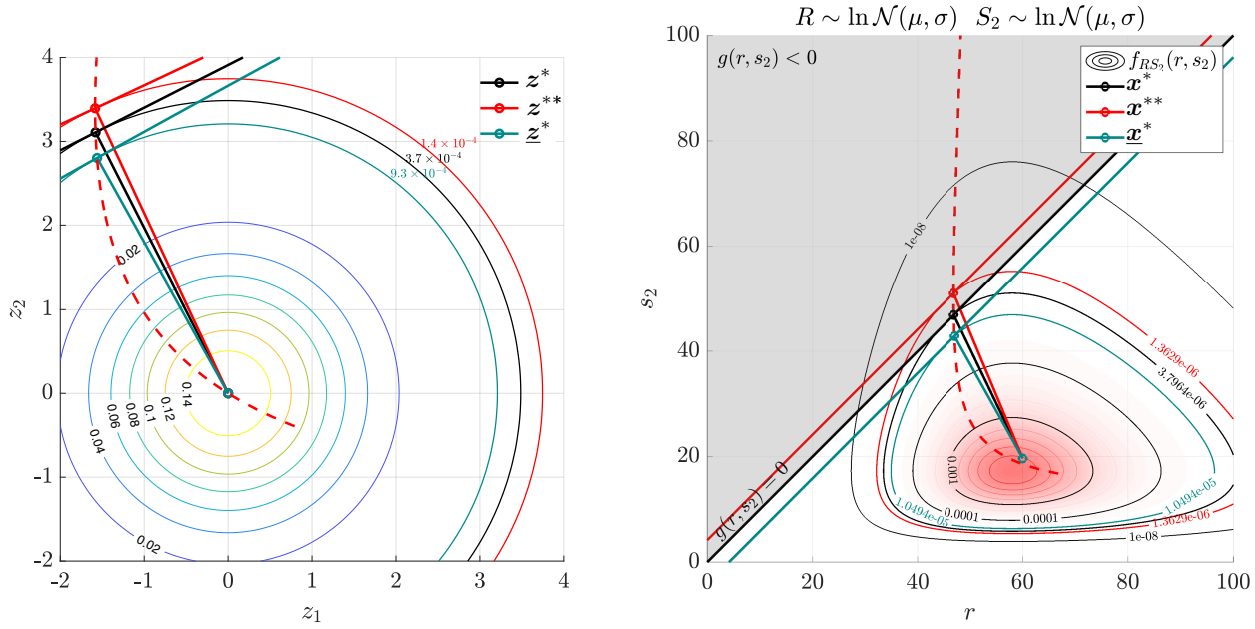


Figure 2. Comparison of the classical design point, the Mean Failure Point, and the Buffered Probable Point for the second system, in which the load is modeled by a lognormal distribution. The left panel refers to the standard normal space, while the right panel refers to the original physical space.

Consequently, the generalized reliability index is identical for the two systems,

$$\beta = -\Phi^{-1}(2.4501 \times 10^{-4}) = 3.4862. \tag{41}$$

According to the classical scalar reliability description, the two systems are therefore equivalent. This is precisely the situation targeted by the proposed framework: the probability of entering the failure domain is the same, but the distribution of the adverse tail and the corresponding representative failure configurations need not be the same.

Figure 2 and Figure 3 show the comparison in both the standard normal space and the original physical space of the two load cases. In each left panel, the black point denotes the classical design point $\boldsymbol{z}^*$, the red point denotes the Mean Failure Point $\boldsymbol{z}^{**}$, and the green point denotes the Buffered Probable Point $\underline{\boldsymbol{z}}^*$. The same notation is used for the corresponding points, $\boldsymbol{x}$, in the original space (right panels). The red level set represents the expected-failure level $G(\boldsymbol{z}) = \underline{y}$, while the green level set represents the buffered level $G(\boldsymbol{z}) = \bar{y}$. The classical limit-state surface $G(\boldsymbol{z}) = 0$, or equivalently $g(r, s_i) = 0$, remains the boundary between the safe and failure domains. The dashed red line represents the trace of the design points for different level sets.

For the GEV load model, the tail-dependent descriptors are

$$\underline{\beta} = \|\underline{\boldsymbol{z}}^*\| = 3.1940, \qquad \beta = 3.4862, \qquad \|\boldsymbol{z}^{**}\| = 3.7687.$$

For the lognormal load model, the corresponding values are

$$\underline{\beta} = \|\underline{\boldsymbol{z}}^*\| = 3.2083, \qquad \beta = 3.4862, \qquad \|\boldsymbol{z}^{**}\| = 3.7463.$$

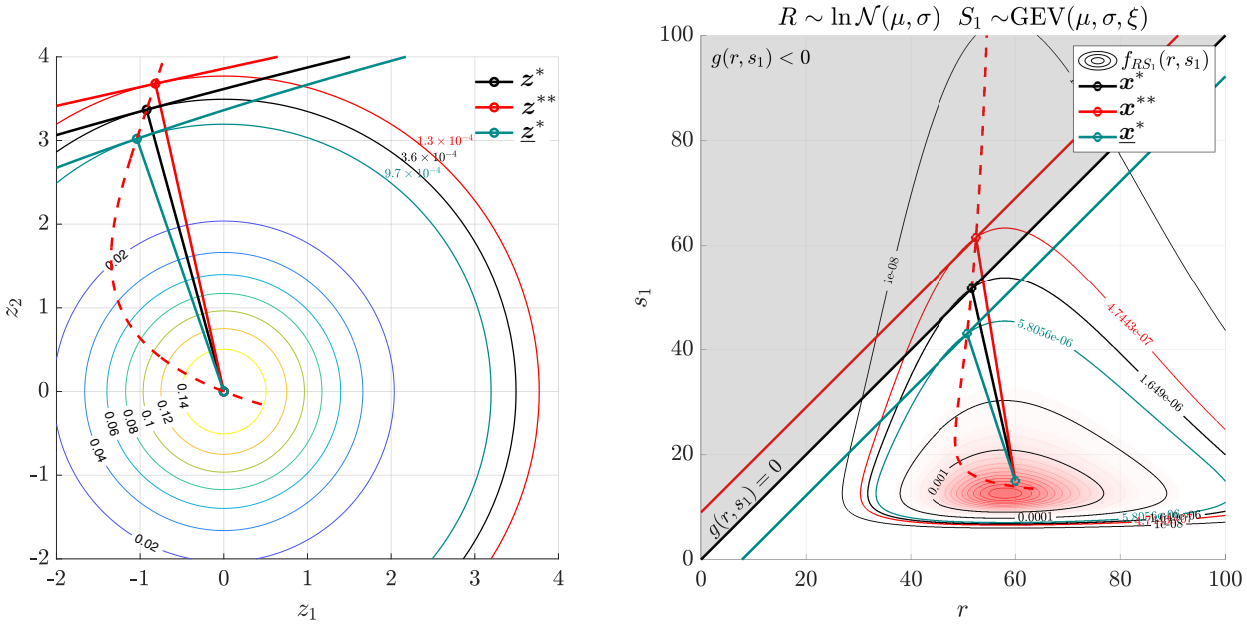


Figure 3. Comparison of the classical design point, the Mean Failure Point, and the Buffered Probable Point for the first system, in which the load is modeled by a GEV distribution. The left panel refers to the standard normal space, while the right panel refers to the original physical space.

The two systems therefore have the same generalized reliability index, but different buffered reliability indices and different Mean Failure Point norms. The GEV load model has a smaller BRI and a larger MFP norm than the lognormal load model. It follows that the two systems are not equivalent once the tail behavior of the performance function is considered.

Taken together, Figures 3 and 2 show that equality of $P_{\mathcal{F}}$ does not imply equality of the failure description. The classical index β assigns the same reliability to both systems, whereas the MFP and the BRI distinguish their representative failure states and adverse tails. In this example, the GEV load model leads to a more severe tail-dependent failure description than the lognormal load model. Therefore, in a reliability ranking that accounts for both likelihood and severity of failure, the system with lognormal load is safer, while the system with GEV load comes second despite having the same classical probability of failure. This simple resistance-load example captures the central message of the paper: equal failure probabilities need not imply equal reliability when reliability is interpreted as a statement about the mechanism and severity of failure. The proposed MFP and BRI reveal information that is hidden by the classical reliability index.

6. Concluding remarks

This paper revisited a basic convention of structural reliability: the identification of reliability with failure probability, or equivalently with the generalized reliability index. Although this convention is mathematically clear and computationally useful, it does not distinguish between systems that fail

in different ways after entering the failure domain. This limitation becomes important whenever the objective of design is not merely to reduce the likelihood of failure, but also to control the mechanism and severity of failure. The proposed framework supplements the classical descriptor with two additional quantities. The Mean Failure Point identifies a representative failure configuration in the standard normal space. It is associated with the conditional expected performance within the failure domain and therefore lies beyond the classical limit-state surface. The Buffered Reliability Index is derived from the buffered probability of failure and provides a scalar measure of reliability that is sensitive to the adverse tail of the performance function. Together, the triplet $(P_{\mathcal{F}}, \boldsymbol{z}^{**}, \underline{\beta})$ gives a more complete reliability description. The probability of failure measures how likely failure is. The MFP indicates how the system is expected to fail. The BRI measures how severe the failure tail is in reliability-index form. In the linear standard normal case, these quantities admit closed-form expressions involving the standard normal hazard rate, which clarifies their relationship with the classical reliability index. In nonlinear structural systems, their separation may reveal mechanically meaningful differences hidden by $P_{\mathcal{F}}$ alone. The proposed quantities are not intended to replace the classical design point. Rather, they extend its interpretation. The design point remains the natural descriptor of incipient failure, while the MFP and BRI describe failure beyond the boundary. This shift is consistent with performance-based design, where the aim is not only to avoid failure, but also to understand and control the path and consequences of failure.

References

Breitung, K.: 1984, 'Asymptotic Approximations for Multinormal Integrals'. *Journal of Engineering Mechanics* **110**(3), 357–366.

Broccardo, M. and J. O. Royset: 2025, 'Tail-sensitive design point and reliability index: A refined approach to structural reliability design and assessment'. Presentation, JCSS Workshop, Tongji University. Available in the IRIS repository of the University of Trento.

Byun, J.-E. and J. O. Royset: 2022, 'Data-Driven Optimization of Reliability Using Buffered Failure Probability'. *Structural Safety* **98**, 102232.

Der Kiureghian, A.: 2022, *Structural and System Reliability*. Cambridge: Cambridge University Press, 1 edition.

Der Kiureghian, A., H.-Z. Lin, and S.-J. Hwang: 1987, 'Second-Order Reliability Approximations'. *Journal of Engineering Mechanics* **113**(8), 1208–1225.

Ditlevsen, O.: 1979, 'Generalized Second Moment Reliability Index'. *Journal of Structural Mechanics* **7**(4), 435–451.

Fréchet, M.: 1948, 'Les éléments aléatoires de nature quelconque dans un espace distancié'. *Annales de l'Institut Henri Poincaré* **10**(4), 215–310.

Hasofer, A. M. and N. C. Lind: 1974, 'An Exact and Invariant First-Order Reliability Format'. *Journal of the Engineering Mechanics Division* **100**(EM1), 111–121.

Karcher, H.: 1977, 'Riemannian Center of Mass and Mollifier Smoothing'. *Communications on Pure and Applied Mathematics* **30**(5), 509–541.

Mafusalov, A. and S. Uryasev: 2018, 'Buffered Probability of Exceedance: Mathematical Properties and Optimization'. *SIAM Journal on Optimization* **28**(2), 1077–1103.

Rockafellar, R. T. and J. O. Royset: 2010, 'On Buffered Failure Probability in Design and Optimization of Structures'. *Reliability Engineering & System Safety* **95**(5), 499–510.

Royset, J. O.: 2025, 'Risk-adaptive approaches to stochastic optimization: A survey'. *SIAM Review* **67**(1), 3–70.

Hybrid Reliability Analysis with Uncertainty in Correlation Coefficients and First Two Statistical Moments

Bo-Yu Wang[a], Xuan-Yi Zhang[b] and Yan-Gang Zhao[c]
[a]*National Key Laboratory of Bridge Safety and Resilience, Beijing University of Technology, Beijing 100124, China, wangboyu@emails.bjut.edu.cn*
[b]*National Key Laboratory of Bridge Safety and Resilience, Beijing University of Technology, Beijing 100124, China, zhangxuanyi@bjut.edu.cn*
[c]*National Key Laboratory of Bridge Safety and Resilience, Beijing University of Technology, Beijing 100124, China, zhaoyg@bjut.edu.cn*

Abstract. Traditional reliability analysis aims to evaluate the failure probability of structures under the presence of aleatory uncertainties. However, in real-world applications, limited data often introduces epistemic uncertainties, requiring the use of hybrid reliability analysis. In this study, to address the epistemic uncertainty caused by insufficient data, both the statistical moments and the correlation coefficients of the random variables are uncertain, and are represented using interval variables. With the aid of the simplified third-moment normal transformation model, the values of uncertain moments and correlation coefficients of each random variables that lead to the bounds of failure probability are determined. The bounds of the failure probability are then evaluated through two traditional reliability analyses. The proposed method is demonstrated through two examples.

Keywords: Reliability analysis, Epistemic uncertainty, Correlation coefficient, First two moments.

1. Introduction

Structural reliability analysis aims to evaluate the failure probability of a structure in the presence of uncertainty. These uncertainties are usually quantified by the probabilistic information of random variables; in traditional reliability analysis, the statistical moments of random variables and the correlation coefficients among random variables are typically treated as exact values. It is reasonable when sufficient observations are available, but it is often difficult to justify in practical engineering. For some complex structures in engineering, usually only limited data can be obtained.

This situation involves both aleatory uncertainty (inherent variability) and epistemic uncertainty (e.g., limited samples or incomplete knowledge) (Der Kiureghian, 2008; Beer et al., 2013). Hybrid reliability analysis provides a framework for considering these uncertainties together. To handle epistemic uncertainty, key information such as statistical moments or correlation coefficients are treated as intervals (Beer et al., 2013; Nannapaneni and Mahadevan, 2016; Wang et al., 2024a). Consequently, the reliability result is expressed as an interval of failure probability or reliability index.

Several studies have investigated reliability analysis methods that consider uncertain statistical moments as intervals (i.e., parametric probability boxes) (Faes et al., 2021; Wang et al., 2024b; Wang

2026 by the author(s). This work is licensed under the Creative Commons Attribution 4.0 International License (CC BY 4.0), which permits unrestricted use, distribution, and reproduction in any medium, provided the original author and source are credited.

et al., 2026). Similar to the uncertain statistical moments, there are also methods considering uncertain correlation coefficients as intervals (Zaman et al., 2013; Nannapaneni and Mahadevan, 2016). However, when the probability information of random variables is incomplete, the uncertainties of both statistical moments and correlation coefficients should be considered simultaneously. Currently, there is only limited research addressing this, such as methods using auxiliary variables and a Bayesian probabilistic framework to include distribution parameter uncertainty and correlation uncertainty in MCS- and FORM-based reliability analysis (Nannapaneni and Mahadevan, 2016). The computational cost of such methods increases significantly as the number of uncertain parameters increases.

Building upon the foundation established by TIPP method (Wang et al., 2024b) and the method proposed in (Wang et al., 2024a), this paper proposes a hybrid reliability analysis method for random variables with interval first two moments and interval correlation coefficients. The rest of this paper is as follows. Section 2 gives the problem statement. Then, section 3 proposes the method considering uncertain statistical moments and uncertain correlation coefficients, including the detailed theoretical derivation, as well as summarizing the straightforward procedure. Section 4 demonstrates the method through two examples. Finally, Section 5 summarizes the key findings, discusses potential applications in engineering practice and outlines the future works.

2. Problem Statement

Consider a performance function

$$G(\boldsymbol{X}) = G(X_1, X_2, \ldots, X_n), \tag{1}$$

where $\boldsymbol{X} = (X_1, X_2, \ldots, X_n)^{\mathsf{T}}$ is a vector of correlated random variables. The failure domain is defined as $G(\boldsymbol{X}) \leq 0$, and the safe domain is defined as $G(\boldsymbol{X}) > 0$. The failure probability is

$$P_f = \int_{\Omega_{\boldsymbol{X}}} I_{\boldsymbol{X}}(\boldsymbol{x}) f_{\boldsymbol{X}}(\boldsymbol{x}) \mathrm{d}\boldsymbol{x}, \tag{2}$$

where $f_{\boldsymbol{X}}(\boldsymbol{x})$ is the joint probability density function of $\boldsymbol{X}$, and $I_{\boldsymbol{X}}(\boldsymbol{x})$ is an indicator function written as

$$I_{\boldsymbol{X}}(\boldsymbol{x}) = \begin{cases} 1, & G(\boldsymbol{x}) \leq 0, \\ 0, & G(\boldsymbol{x}) > 0. \end{cases} \tag{3}$$

In this study, the first two moments and selected correlation coefficients are not treated as fixed values. The mean and standard deviation of X_i are denoted by θ_{i1} and θ_{i2}, respectively, and are represented by intervals

$$\theta_{i1} \in [\underline{\theta}_{i1}, \overline{\theta}_{i1}], \qquad \theta_{i2} \in [\underline{\theta}_{i2}, \overline{\theta}_{i2}]. \tag{4}$$

Most random variables follow two-parameter distributions, and their skewness α_{3i} is a known value. The uncertain correlation coefficient between X_i and X_j is denoted by

$$\lambda_{ij} \in [\underline{\lambda}_{ij}, \overline{\lambda}_{ij}]. \tag{5}$$

All uncertain moments and correlation coefficients are collected in the interval vectors $\boldsymbol{\Theta}^I$ and $\boldsymbol{\Lambda}^I$.

Because of these interval parameters, the failure probability is no longer a single value. It becomes a function of $\boldsymbol{\Theta}$ and $\boldsymbol{\Lambda}$:

$$P_f(\boldsymbol{\Theta}, \boldsymbol{\Lambda}) = \int_{\Omega_{\boldsymbol{X}}} I_{\boldsymbol{X}}(\boldsymbol{x}) f_{\boldsymbol{X}}(\boldsymbol{x} \mid \boldsymbol{\Theta}, \boldsymbol{\Lambda}) \mathrm{d}\boldsymbol{x}. \tag{6}$$

The target of hybrid reliability analysis is to estimate the interval

$$P_f^I = [\underline{P}_f, \overline{P}_f], \qquad \beta^I = [\underline{\beta}, \overline{\beta}], \tag{7}$$

3. Proposed Method

3.1. Bounds of Failure Probability

Based on Eq. (6), the uncertainty in $\boldsymbol{\Theta}$ and $\boldsymbol{\Lambda}$ is propagated through $f_{\boldsymbol{X}}(\boldsymbol{x} \mid \boldsymbol{\Theta}, \boldsymbol{\Lambda})$ to $P_f(\boldsymbol{\Theta}, \boldsymbol{\Lambda})$. To facilitate the derivation, $\boldsymbol{X}$ is mapped into a vector of independent standard normal random variables $\boldsymbol{U}$ based on the statistical moments and correlation coefficients, and then $P_f(\boldsymbol{\Theta}, \boldsymbol{\Lambda})$ is redefined in Gaussian space as follows:

$$P_f(\boldsymbol{\Theta}, \boldsymbol{\Lambda}) = \int_{\Omega_{\boldsymbol{U}}} I_{\boldsymbol{U}}(\boldsymbol{u}|\boldsymbol{\Theta}, \boldsymbol{\Lambda}) \phi_{\boldsymbol{U}}(\boldsymbol{u}) \mathrm{d}\boldsymbol{u}, \tag{8}$$

where $\Omega_{\boldsymbol{U}} \in \mathbb{R}^n$ denotes the domain of $\boldsymbol{U}$; $\phi_{\boldsymbol{U}}(\boldsymbol{u})$ is the JPDF of $\boldsymbol{U}$, which follows a standard Gaussian distribution in n dimensions; and $I_{\boldsymbol{U}}(\boldsymbol{u}|\boldsymbol{\Theta}, \boldsymbol{\Lambda})$ is the indicator function defined in Gaussian space, which is defined as follows:

$$I_{\boldsymbol{U}}(\boldsymbol{u}|\boldsymbol{\Theta}, \boldsymbol{\Lambda}) = I_{\boldsymbol{X}}[S(\boldsymbol{u}|\boldsymbol{\Theta}, \boldsymbol{\Lambda})], \tag{9}$$

where $S(\boldsymbol{u}|\boldsymbol{\Theta}, \boldsymbol{\Lambda})$ is the inverse normal transformation function defined based on the first three moments and correlation coefficients of $\boldsymbol{X}$.

Based on Eq. (8), P_f^I can be expressed as:

$$\underline{P}_f = \int_{\Omega_{\boldsymbol{U}}} I_{\boldsymbol{U}}(\boldsymbol{u}|\boldsymbol{\Theta}_{\text{low}}, \boldsymbol{\Lambda}_{\text{low}}) \phi_{\boldsymbol{U}}(\boldsymbol{u}) \mathrm{d}\boldsymbol{u}, \tag{10}$$

$$\overline{P}_f = \int_{\Omega_{\boldsymbol{U}}} I_{\boldsymbol{U}}(\boldsymbol{u}|\boldsymbol{\Theta}_{\text{up}}, \boldsymbol{\Lambda}_{\text{up}}) \phi_{\boldsymbol{U}}(\boldsymbol{u}) \mathrm{d}\boldsymbol{u}. \tag{11}$$

where $\bar{\cdot}$ and $\underline{\cdot}$ are the upper and lower bounds, respectively; and $(\boldsymbol{\Theta}_{\text{low}}, \boldsymbol{\Lambda}_{\text{low}})$ and $(\boldsymbol{\Theta}_{\text{up}}, \boldsymbol{\Lambda}_{\text{up}})$ are the realizations of moments and correlation coefficients that lead to the lower and upper bounds of P_f, respectively. Then, the value of β^I can be obtained based on P_f^I as follows:

$$\beta^I = [\underline{\beta}, \overline{\beta}] = \left[-\Phi^{-1}\left(\overline{P}_f\right), -\Phi^{-1}\left(\underline{P}_f\right)\right]. \tag{12}$$

As shown in Eqs. (10)–(12), the key task in determining β^I and P_f^I lies in finding $(\boldsymbol{\Theta}_{\text{low}}, \boldsymbol{\Lambda}_{\text{low}})$ and $(\boldsymbol{\Theta}_{\text{up}}, \boldsymbol{\Lambda}_{\text{up}})$, which will be discussed in detail in the next section.

3.2. Monotonicity Analysis

The simplified third-moment normal transformation is used to map random variables into Gaussian space (Qin et al., 2020; Lu et al., 2017). For the i-th random variable, the inverse transformation is written as

$$X_i = \theta_{i1} + \theta_{i2} H_i(Z_i), \qquad H_i(Z_i) = a_{2i} Z_i^2 + a_{1i} Z_i - a_{2i}, \tag{13}$$

where θ_{i1} and θ_{i2} are the mean and standard deviation, respectively; Z_i is a correlated standard normal variable; and a_{1i} and a_{2i} are determined by the fixed skewness α_{3i}. The correlated standard normal vector is obtained from the independent standard normal vector by

$$\boldsymbol{Z} = \boldsymbol{L}_0 \boldsymbol{U}, \tag{14}$$

where $\boldsymbol{L}_0$ is obtained from the Cholesky decomposition of $\boldsymbol{C}_Z$. For X_i and X_j, the physical correlation coefficient λ_{ij} and the transformed correlation coefficient λ_{0ij} satisfy

$$\lambda_{ij} = \Delta_{ij} \lambda_{0ij} + \frac{3}{50} \alpha_{3i} \alpha_{3j} \lambda_{0ij}^2, \quad \Delta_{ij} = \sqrt{\left(1 - \frac{3}{50}\alpha_{3i}^2\right)\left(1 - \frac{3}{50}\alpha_{3j}^2\right)}. \tag{15}$$

If $\alpha_{3i}\alpha_{3j} = 0$, $\lambda_{0ij} = \lambda_{ij}/\Delta_{ij}$; otherwise,

$$\lambda_{0ij} = \frac{-25\Delta_{ij} + 5\sqrt{25\Delta_{ij}^2 + 6\alpha_{3i}\alpha_{3j}\lambda_{ij}}}{3\alpha_{3i}\alpha_{3j}}. \tag{16}$$

To determine $(\boldsymbol{\Theta}_{\text{low}}, \boldsymbol{\Lambda}_{\text{low}})$ and $(\boldsymbol{\Theta}_{\text{up}}, \boldsymbol{\Lambda}_{\text{up}})$, the changing tendency of $P_f(\boldsymbol{\Theta}, \boldsymbol{\Lambda})$ with respect to each interval parameter needs to be investigated. Let η denote one component of $\boldsymbol{\Theta}$ or $\boldsymbol{\Lambda}$. Based on Eq. (8), since $\phi_{\boldsymbol{U}}(\boldsymbol{u})$ is not related to η, the derivative of failure probability with respect to η can be expressed as

$$\frac{\partial P_f}{\partial \eta} = \int_{\Omega_{\boldsymbol{U}}} \frac{\partial I_{\boldsymbol{U}}(\boldsymbol{u} \mid \boldsymbol{\Theta}, \boldsymbol{\Lambda})}{\partial \eta} \phi_{\boldsymbol{U}}(\boldsymbol{u}) \mathrm{d}\boldsymbol{u}. \tag{17}$$

Then, based on Eq. (9) and using the chain rule of differentiation, $\partial I_{\boldsymbol{U}}/\partial\eta$ is written as

$$\frac{\partial I_{\boldsymbol{U}}(\boldsymbol{U} \mid \boldsymbol{\Theta}, \boldsymbol{\Lambda})}{\partial \eta} = \frac{\partial I_{\boldsymbol{X}}[S(\boldsymbol{U} \mid \boldsymbol{\Theta}, \boldsymbol{\Lambda})]}{\partial S(\boldsymbol{U} \mid \boldsymbol{\Theta}, \boldsymbol{\Lambda})} \frac{\partial S(\boldsymbol{U} \mid \boldsymbol{\Theta}, \boldsymbol{\Lambda})}{\partial \eta}. \tag{18}$$

The derivative of the indicator function is nonzero only on the limit state surface $G[S(\boldsymbol{U} \mid \boldsymbol{\Theta}, \boldsymbol{\Lambda})] = 0$. Substituting Eq. (18) into Eq. (17) gives

$$\frac{\partial P_f}{\partial \eta} = \int_{G[S(\boldsymbol{U}|\boldsymbol{\Theta},\boldsymbol{\Lambda})]=0} \frac{\partial I_{\boldsymbol{X}}[S(\boldsymbol{U} \mid \boldsymbol{\Theta}, \boldsymbol{\Lambda})]}{\partial S(\boldsymbol{U} \mid \boldsymbol{\Theta}, \boldsymbol{\Lambda})} \frac{\partial S(\boldsymbol{U} \mid \boldsymbol{\Theta}, \boldsymbol{\Lambda})}{\partial \eta} \phi_{\boldsymbol{U}}(\boldsymbol{u}) \mathrm{d}\boldsymbol{u}. \tag{19}$$

Since $\phi_{\boldsymbol{U}}(\boldsymbol{u})$ is always positive, the sign of $\partial P_f/\partial\eta$ is determined by the sign of the two derivative terms in Eq. (19). Based on the definition of the indicator function, the sign of the first term is

$$\operatorname{sign}\left[\frac{\partial I_{\boldsymbol{X}}[S(\boldsymbol{U} \mid \boldsymbol{\Theta}, \boldsymbol{\Lambda})]}{\partial S(\boldsymbol{U} \mid \boldsymbol{\Theta}, \boldsymbol{\Lambda})}\right] = -\operatorname{sign}\left[\frac{\partial G(\boldsymbol{X})}{\partial \boldsymbol{X}^{\mathsf{T}}}\right]. \tag{20}$$

Therefore, for a monotonic performance function, the correspondence between failure probability bounds and uncertain parameters can be obtained by analyzing $\partial S/\partial \eta$ for the uncertain first moment, second moment, and correlation coefficient.

3.2.1. *Changing Tendency of Failure Probability with Mean*
For the first moment of X_i, the interval parameter is θ_{i1}. According to Eq. (13), the i-th component of the inverse transformation is

$$S_i = \theta_{i1} + \theta_{i2} H_i(Z_i). \tag{21}$$

The derivative of S_i with respect to θ_{i1} is

$$\frac{\partial S_i}{\partial \theta_{i1}} = 1. \tag{22}$$

Substitution of Eqs. (20) and (22) into Eq. (19) leads to

$$\operatorname{sign}\left[\frac{\partial P_f}{\partial \theta_{i1}}\right] = -\operatorname{sign}\left[\frac{\partial G(\boldsymbol{X})}{\partial X_i}\right]. \tag{23}$$

Thus, if $\partial G(\boldsymbol{X})/\partial X_i < 0$, P_f increases with θ_{i1}; if $\partial G(\boldsymbol{X})/\partial X_i \geq 0$, P_f decreases with θ_{i1}. The corresponding relationship between the failure probability bounds and θ_{i1} is summarized in Table 1.

3.2.2. *Changing Tendency of Failure Probability with Standard Deviation*
For the second moment of X_i, the interval parameter is θ_{i2}. From Eq. (21), the derivative of S_i with respect to θ_{i2} is

$$\frac{\partial S_i}{\partial \theta_{i2}} = H_i(Z_i) = a_{2i} Z_i^2 + a_{1i} Z_i - a_{2i}. \tag{24}$$

For the marginal correspondence rule, the standard coordinate entering $H_i(\cdot)$ is denoted by U_i. Combining Eqs. (20) and (24), the sign of the derivative of failure probability is

$$\operatorname{sign}\left[\frac{\partial P_f}{\partial \theta_{i2}}\right] = -\operatorname{sign}\left[\frac{\partial G(\boldsymbol{X})}{\partial X_i} H_i(U_i)\right]. \tag{25}$$

When the skewness is zero, $a_{1i} = 1$ and $a_{2i} = 0$, so $H_i(U_i) = U_i$. When the skewness is nonzero, the sign of $H_i(U_i)$ changes at the roots p and q, which are expressed as

$$p = \frac{-5}{\sqrt{3}\alpha_{3i}} - \frac{5}{\sqrt{3}\,|\alpha_{3i}|}, \quad q = \frac{-5}{\sqrt{3}\alpha_{3i}} + \frac{5}{\sqrt{3}\,|\alpha_{3i}|}. \tag{26}$$

For $\alpha_{3i} < 0$,

$$\begin{cases} H_i(U_i) < 0, \ U_i \in (-\infty, 0) \cup (q, +\infty), \\ H_i(U_i) \geq 0, \ U_i \in [0, q], \end{cases} \tag{27}$$

and for $\alpha_{3i} > 0$,

$$\begin{cases} H_i(U_i) < 0, \ U_i \in [p, 0], \\ H_i(U_i) \geq 0, \ U_i \in (-\infty, p) \cup (0, +\infty). \end{cases} \tag{28}$$

The sign of $\partial P_f/\partial\theta_{i2}$ is then determined jointly by $\partial G(\boldsymbol{X})/\partial X_i$ and the interval of U_i. The resulting relationship between the failure probability bounds and θ_{i2} is summarized in Table 1.

3.2.3. *Changing Tendency of Failure Probability with Correlation Coefficient*
For an uncertain correlation coefficient, the interval parameter is λ_{ij}. Unlike the first two moments, λ_{ij} changes the transformation from the independent standard normal vector $\boldsymbol{U}$ to the correlated standard normal vector $\boldsymbol{Z}$. For the pair (X_i, X_j), the Cholesky transformation gives

$$Z_i = U_i, \qquad Z_j = \lambda_{0ij}U_i + \sqrt{1-\lambda_{0ij}^2}U_j. \tag{29}$$

Therefore,

$$\frac{\partial Z_j}{\partial\lambda_{0ij}} = U_i - \frac{\lambda_{0ij}}{\sqrt{1-\lambda_{0ij}^2}}U_j = U_i - k_{ij}U_j, \qquad k_{ij} = \frac{\lambda_{0ij}}{\sqrt{1-\lambda_{0ij}^2}}. \tag{30}$$

The derivative of the inverse transformation with respect to λ_{ij} can be decomposed as

$$\frac{\partial S}{\partial\lambda_{ij}} = \frac{\partial S}{\partial\boldsymbol{Z}^{\mathsf{T}}}\frac{\partial\boldsymbol{Z}^{\mathsf{T}}}{\partial\lambda_{0ij}}\frac{\partial\lambda_{0ij}}{\partial\lambda_{ij}}. \tag{31}$$

For the simplified third-moment normal transformation, the relevant component of $\partial S/\partial\boldsymbol{Z}^{\mathsf{T}}$ is positive:

$$\frac{\partial S_j}{\partial Z_j} = \theta_{j2}\left(2a_{2j}Z_j + a_{1j}\right) > 0. \tag{32}$$

The derivative from λ_{ij} to λ_{0ij} is also positive. If $\alpha_{3i}\alpha_{3j} = 0$,

$$\frac{\partial\lambda_{0ij}}{\partial\lambda_{ij}} = \frac{1}{\Delta_{ij}} > 0. \tag{33}$$

Otherwise,

$$\frac{\partial\lambda_{0ij}}{\partial\lambda_{ij}} = \frac{5}{\sqrt{25\Delta_{ij}^2 + 6\alpha_{3i}\alpha_{3j}\lambda_{ij}}} > 0. \tag{34}$$

Substituting Eqs. (30)–(34) into Eq. (19), the sign of the derivative of failure probability with respect to λ_{ij} is obtained as

$$\operatorname{sign}\left[\frac{\partial P_f}{\partial\lambda_{ij}}\right] = -\operatorname{sign}\left[\frac{\partial G(\boldsymbol{X})}{\partial X_j}\left(U_i - k_{ij}U_j\right)\right]. \tag{35}$$

When λ_{ij} is an interval variable, λ_{0ij} and k_{ij} are also interval quantities. The two threshold values used for determining the sign of $U_i - k_{ij}U_j$ are

$$\underline{k}_{0ij} = \frac{\underline{\lambda}_{0ij}U_j}{\sqrt{1-\underline{\lambda}_{0ij}^2}}, \quad \overline{k}_{0ij} = \frac{\overline{\lambda}_{0ij}U_j}{\sqrt{1-\overline{\lambda}_{0ij}^2}}. \tag{36}$$

Table I. Values of uncertain moments and correlation coefficients for inverse normal transformation

Uncertain parameter	$\frac{\partial G(\boldsymbol{X})}{\partial X_j}$	$\frac{\partial G(\boldsymbol{X})}{\partial X_i}$	U_i		$\boldsymbol{\Theta}_{\text{low}}/\boldsymbol{\Lambda}_{\text{low}}$	$\boldsymbol{\Theta}_{\text{up}}/\boldsymbol{\Lambda}_{\text{up}}$
			$\alpha_{3i} \le 0$	$\alpha_{3i} > 0$		
θ_{i1}		< 0	$(-\infty, +\infty)$		$\underline{\theta}_{i1}$	$\overline{\theta}_{i1}$
		≥ 0			$\overline{\theta}_{i1}$	$\underline{\theta}_{i1}$
θ_{i2}		< 0	$(-\infty, 0) \cup (q, +\infty)$	$[p, 0]$	$\overline{\theta}_{i2}$	$\underline{\theta}_{i2}$
			$[0, q]$	$(-\infty, p) \cup (0, +\infty)$	$\underline{\theta}_{i2}$	$\overline{\theta}_{i2}$
		≥ 0	$(-\infty, 0) \cup (q, +\infty)$	$[p, 0]$	$\underline{\theta}_{i2}$	$\overline{\theta}_{i2}$
			$[0, q]$	$(-\infty, p) \cup (0, +\infty)$	$\overline{\theta}_{i2}$	$\underline{\theta}_{i2}$
λ_{ij}	≥ 0		$(-\infty, \overline{k}_{0ij}]$		$\underline{\lambda}_{ij}$	$\overline{\lambda}_{ij}$
			$(\overline{k}_{0ij}, +\infty)$		$\overline{\lambda}_{ij}$	$\underline{\lambda}_{ij}$
	< 0		$(-\infty, \underline{k}_{0ij}]$		$\overline{\lambda}_{ij}$	$\underline{\lambda}_{ij}$
			$(\underline{k}_{0ij}, +\infty)$		$\underline{\lambda}_{ij}$	$\overline{\lambda}_{ij}$

After evaluating $\partial G(\boldsymbol{X})/\partial X_j$ and the position of U_i relative to the threshold interval, the correspondence between the failure probability bounds and λ_{ij} can be obtained. The resulting relationships for the first moment, second moment, and correlation coefficient are summarized in Table 1.

The corresponding parameter values define two transformed limit state functions. One corresponds to the lower failure probability bound, and the other corresponds to the upper bound. Since the standard normal density is independent of the interval parameters, the remaining calculation can be carried out by a conventional reliability method.

3.3. Computational Procedure

With $(\boldsymbol{\Theta}_{\text{low}}, \boldsymbol{\Lambda}_{\text{low}})$ and $(\boldsymbol{\Theta}_{\text{up}}, \boldsymbol{\Lambda}_{\text{up}})$ determined using Table 1, the distributions with uncertain moments and correlation coefficients can be replaced by general distributions for the bounds of failure probability. Then, β^I and P_f^I can be computed using classical reliability analysis methods, such as the first-order reliability method (FORM) (Hasofer and Lind, 1974; Rackwitz and Fiessler, 1978), the second-order reliability method (SORM) (Zhao and Ono, 1999; Breitung, 2021), and the method of moments (Zhao and Lu, 2021).

The proposed method for evaluating β^I and P_f^I consists of two main steps:

(1) Calculate the partial derivatives $\partial G(\boldsymbol{X})/\partial x_j$ for random variables related to uncertain statistical moments or uncertain correlation coefficients. For implicit performance functions, these derivatives can be evaluated using finite differences.

(2) Calculate β^I and P_f^I using appropriate reliability methods. The bounds are obtained through two separate reliability analyses.

The computational cost of the proposed method is measured by the number of performance function evaluations. For explicit performance functions, n evaluations are required to calculate

the partial derivatives; for implicit functions, $n + 1$ evaluations are needed, where n represents the number of random variables related to uncertain statistical moments or uncertain correlation coefficients. The determination of the moment and correlation coefficient bounds requires no additional performance function evaluations. The method then requires two classical reliability analyses, making the total computational cost comparable to that of two reliability analyses. This computational cost is practical for engineering applications in which each performance function evaluation may be expensive.

4. Illustrative Examples

Two examples are used to illustrate the proposed method. All examples include uncertain first two moments and uncertain correlation coefficients. The first example considers a mathematical problem with analytical solution, which is adopted to examine the accuracy of the proposed method. The second example applies the method to an annular cross-section column.

4.1. Linear Performance Function

The first example uses the linear performance function

$$G(\mathbf{X}) = X_1 - X_2. \tag{37}$$

The two variables are normal variables. Because only limited information is assumed to be available, the means, standard deviations, and the correlation coefficient are represented by intervals. The input information is listed in the following table.

Table II. Probabilistic information for Example 1.

Variable	Mean	Standard deviation	Distribution	Correlation coefficient
X_1	$[45, 55]$	$[6.3, 7.7]$	Normal	$[0.6, 0.8]$
X_2	$[31.5, 38.5]$	$[4.5, 5.5]$	Normal	

For this performance function, $\partial G/\partial X_1 = 1$ and $\partial G/\partial X_2 = -1$. The bounds of reliability index are shown in Table III. It is found that, the results of the proposed method combined with FORM can obtain exact evaluation of β^I, while the results from the proposed method combined with method of moments has a relatively small R.E. within 5%.

4.2. Annular Cross-Section Column

The second example considers an annular cross-section column under axial load. The performance function is adapted from Ref. (Zhang and Xu, 2022) and is written as

$$G(\mathbf{X}) = \frac{\pi^2 E}{L^2}\left[\frac{\pi}{64}\left((D+T)^4 - D^4\right)\right] - F, \tag{38}$$

Table III. Reliability analysis results for Example 1.

Method	Lower bound of β		Upper bound of β		Function evaluations
	Value	R.E. (%)	Value	R.E. (%)	
Analytical solution	0.5834	–	3.4816	–	–
Proposed method-FORM	0.5834	–	3.4816	–	6
Proposed method-MoM	0.5728	1.81	3.5934	3.21	52

where E is the elastic modulus, T is the thickness, D is the internal diameter, L is the column length, and F is the axial load. The variables T and D are treated as random variables with interval means and interval standard deviations. Their correlation coefficient is also represented by an interval, $\lambda_{TD} = [-0.4, -0.1]$.

Table IV. Probabilistic information for Example 2.

Variable	Description	Distribution	Mean	Standard deviation
E (MPa)	Elastic modulus	Lognormal	203000	30450
T (mm)	Thickness	Normal	$[3.5, 4.5]$	$[0.095, 0.105]$
D (mm)	Internal diameter	Normal	$[23, 24]$	$[0.15, 0.25]$
L (mm)	Length of column	Normal	2500	50
F (N)	Axial load	Lognormal	3000	550

In this example, $\partial G/\partial T$, and $\partial G/\partial D$ are positive. The calculated bounds of reliability index are listed in Table V. It can be observed from Table V that, the relative error between the results of the proposed method combined with the method of moments and those from MCS remains under 4%, demonstrating the accuracy of the proposed method.

Table V. Reliability analysis results for Example 2.

Method	Lower bound of β		Upper bound of β		Function evaluations
	Value	R.E. (%)	Value	R.E. (%)	
Double-loop MCS	0.4590	–	2.2888	–	–
Proposed method	0.4459	2.86	2.3630	3.24	782

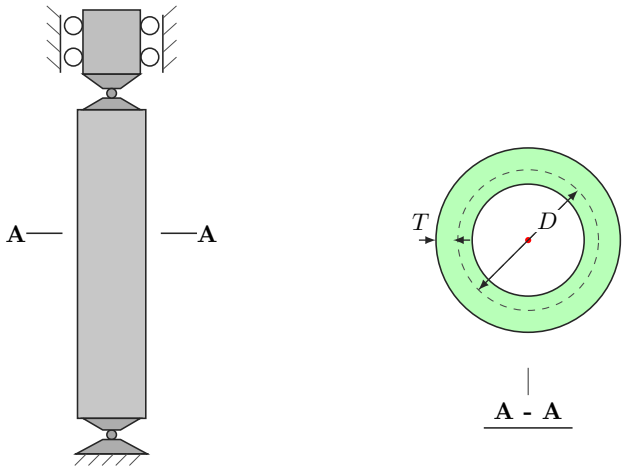


Figure 1. Annular section column.

5. Conclusions

This paper presents a hybrid reliability analysis method for problems in which the first two statistical moments and the correlation coefficients of random variables are both uncertain. The uncertain means, standard deviations, and correlation coefficients are described by interval variables. Based on the derivative of the performance function with respect to the random variables with uncertain parameters, the bounds of the failure probability are then obtained by two traditional reliability analyses.

The main advantage of the proposed method is that it avoids the need for optimization or sampling. The examples show that the proposed method can efficiently calculate the bounds of failure probability, which are in close agreement with those obtained through double-loop MCS.

References

Beer, M., S. Ferson, and V. Kreinovich: 2013, 'Imprecise probabilities in engineering analyses'. *Mechanical systems and signal processing* **37**(1-2), 4–29.

Breitung, K.: 2021, 'SORM, Design Points, Subset Simulation, and Markov Chain Monte Carlo'. *ASCE-ASME Journal of Risk and Uncertainty in Engineering Systems, Part A: Civil Engineering* **7**(4), 04021052.

Der Kiureghian, A.: 2008, 'Analysis of structural reliability under parameter uncertainties'. *Probabilistic Engineering Mechanics* **23**(4), 351–358.

Faes, M. G. R., M. Daub, S. Marelli, E. Patelli, and M. Beer: 2021, 'Engineering analysis with probability boxes: A review on computational methods'. *Structural Safety* **93**, 102092.

Hasofer, A. M. and N. C. Lind: 1974, 'Exact and invariant second-moment code format'. *Journal of the Engineering Mechanics Division* **100**(1), 111–121.

Lu, Z.-H., C.-H. Cai, and Y.-G. Zhao: 2017, 'Structural Reliability Analysis Including Correlated Random Variables Based on Third-Moment Transformation'. *Journal of Structural Engineering* **143**(8), 04017067.

Nannapaneni, S. and S. Mahadevan: 2016, 'Reliability analysis under epistemic uncertainty'. *Reliability Engineering & System Safety* **155**, 9–20.

Qin, Q., X. Y. Zhang, Z. H. Lu, and Y. G. Zhao: 2020, 'Simplified third-order normal transformation and its application in structural reliability analysis'. *Engineering Mechanics* **37**(12), 78–86, 113.

Rackwitz, R. and B. Fiessler: 1978, 'Structural reliability under combined random load sequences'. *Comput Struct* **9**(5), 489–494.

Wang, B.-Y., X.-Y. Zhang, and Y.-G. Zhao: 2024a, 'Reliability Analysis Considering Uncertain Correlation Coefficients as Interval Variables'. In: *The 9th International Symposium on Reliability Engineering and Risk Management (ISRERM 2024)*. Hefei, China.

Wang, B. Y., X. Y. Zhang, and Y. G. Zhao: 2024b, 'Third moment method for reliability analysis with uncertain moments characterized as interval variables'. *Structural Safety* **111**, 102499.

Wang, B.-Y., X.-Y. Zhang, Y.-G. Zhao, M. A. Valdebenito, and M. G. R. Faes: 2026, 'Third moment method for reliability analysis involving independent parametric probability-boxes'. *Applied Mathematical Modelling* **151**, 116488.

Zaman, K., M. McDonald, and S. Mahadevan: 2013, 'Inclusion of correlation effects in model prediction under data uncertainty'. *Probabilistic Engineering Mechanics* **34**, 58–66.

Zhang, Q. and L. Xu: 2022, 'Evaluation of moments of performance functions based on polynomial chaos expansions'. *International Journal of Mechanics and Materials in Design* **18**(2), 395–405.

Zhao, Y. G. and Z. H. Lu: 2021, *Structural reliability: approaches from perspectives of statistical moments*. Wiley.

Zhao, Y. G. and T. Ono: 1999, 'New Approximations for SORM: Part 2'. *Journal of Engineering Mechanics* **125**(1), 86–93.

An Efficient Reliability Sensitivity Analysis Method Based on the Method of Moments

Bo-Qi Zhao, Xuan-Yi Zhang*, and Yan-Gang Zhao
National Key Laboratory of Bridge Safety and Resilience, Beijing University of Technology, Beijing 100124, China, zhaoboqi@emails.bjut.edu.cn
National Key Laboratory of Bridge Safety and Resilience, Beijing University of Technology, Beijing 100124, China, zhangxuanyi@bjut.edu.cn
National Key Laboratory of Bridge Safety and Resilience, Beijing University of Technology, Beijing 100124, China, zhaoyg@bjut.edu.cn

Abstract. With the growing demand for refined structural reliability assessments, the influence of higher-order moments on failure probability has garnered increasing attention. However, existing third-order sensitivity methods (SAMoM) cannot reveal the sensitivity of failure probability to fourth-order moments. This paper proposes a fourth-order moment sensitivity analysis method that computes the partial derivatives of failure probability with respect to the mean, standard deviation, skewness, and kurtosis of input variables. Numerical example show that the method maintains the accuracy of SAMoM while, for the first time, reliably estimating the sensitivity of failure probability to kurtosis.

Keywords: Sensitivity analysis; Failure probability; Method of methods; First-four moments.

1. Introduction

Reliability sensitivity analysis holds a crucial role in structural design optimisation, risk assessment and uncertainty management. By quantifying the response of failure probabilities to changes in the distribution parameters of input random variables, sensitivity analysis provides the necessary gradient information for reliability-based design optimisation and helps to identify the most influential parameters(Ditlevsen and Madsen, 1996; Lemaire, 2013; Der Kiureghian, 2022).Both global and local sensitivity measures have been developed in the field of engineering.

Global sensitivity analyses, such as the Sobol' indices(Sobol', 1990; 2001), are used to assess the average impact of input variables across their entire range of variation; however, they do not indicate whether the impact is positive or negative, and involve significant computational effort when the probability of failure is low. Local sensitivity analysis is defined as the partial derivative of the probability of failure with respect to a distribution parameter; this type of analysis is better suited to gradient-based optimisation and can be obtained efficiently as a by-product of many reliability methods(Wei et al., 2022).

Among existing local sensitivity analysis methods, the Method of Moments (MoM)(Zhao and Ono, 2001) strikes a balance between accuracy and efficiency. MoM approximates the probability of failure using the first few statistical moments of the performance function, thereby avoiding repeated evaluations of the original

* Corresponding author

© 2026 by the author(s). This work is licensed under the Creative Commons Attribution 4.0 International License (CC BY 4.0), which permits unrestricted use, distribution, and reproduction in any medium, provided the original author and source are credited.

model.The third-order moment sensitivity analysis method (SAMoM) has been proposed(Zhang et al., 2025), which is capable of estimating the sensitivity of the probability of failure to the mean, standard deviation and skewness.

However, Many engineering problems involve input variables with heavy-tailed distributions; in such cases, kurtosis significantly influences tail behaviour(Li et al., 2023), thereby affecting the probability of rare failure events. Both SAMoM and other existing methods fail to quantify the independent contribution of kurtosis to the probability of failure.

To overcome this limitation, researchers have developed a reliability analysis method based on fourth-order moments(Zhao et al., 2018; Zhang et al., 2019).Based on fourth-order central moments, this paper derives a complete chain rule expression for the sensitivity of the failure probability to the first four moments of any independent input variable. A fourth-order moment reliability index is employed, and the central difference method is used to calculate its partial derivatives with respect to each central moment, thereby avoiding overly complex analytical expressions.

2. Proposed method

2.1. Failure probability and method of moments

Consider a structural system whose performance is characterized by a continuous random vector $\mathbf{X} = (X_1, X_2, \cdots, X_n)^T$ of dimension n, representing the uncertain input variables such as material properties, geometric dimensions, and external loads. The system behavior is described by a performance function $G(\mathbf{X})$, where the event of failure is defined as the set of outcomes for which the performance function takes non-positive values:

$$F = \{\mathbf{X} : G(\mathbf{X}) \leq 0\}, \tag{1}$$

Given that $\Omega_{\mathbf{X}} \subseteq \mathbb{R}^n$ denote the full domain of the input variables $\mathbf{X}$, i.e., the n-dimensional space of all possible values (typically the entire $\mathbb{R}^n$, or a subset defined by physical constraints). The probability of failure, denoted by $P_f(\boldsymbol{\theta})$, is given by the integral of the joint probability density function (JPDF), denoted by $f_{\mathbf{X}}(\mathbf{x}|\boldsymbol{\theta})$, over the failure domain as follow:

$$P_f(\boldsymbol{\theta}) = \int_{G(\mathbf{X})\leq 0} f_{\mathbf{X}}(\mathbf{x}|\boldsymbol{\theta})d\mathbf{x} = \int_{\Omega_{\mathbf{X}}} I_F(\mathbf{x}) f_{\mathbf{X}}(\mathbf{x}|\boldsymbol{\theta})d\mathbf{x}, \tag{2}$$

where $\boldsymbol{\theta}$ is a vactor of the moments of $\mathbf{X}$ and $I_F(\mathbf{x})$ is the indicator function of the failure domain, taking the value 1 if $G(\mathbf{X}) \leq 0$ and 0 otherwise. With $P_f(\boldsymbol{\theta})$ obtained, the reliability index can be obtained as:

$$\beta(\boldsymbol{\theta}) = -\Phi^{-1}[P_f(\boldsymbol{\theta})], \tag{3}$$

where $\Phi[\cdot]$ is the cumulative distribution function (CDF) of standard normal distribution.

In general, it is difficult to compute multiple integrals directly. The method of moments (MoM) provides an efficient approximation scheme, treating the $G(\mathbf{X})$ as a random variable Z and expressing $P_f(\boldsymbol{\theta})$ in terms of:

$$P_f(\boldsymbol{\theta}) = F_G[0|\boldsymbol{\theta}_G(\boldsymbol{\theta})], \tag{4}$$

where $F_G(\cdot|\boldsymbol{\theta}_G)$ is the CDF of $Z = G(\mathbf{X})$, and $\boldsymbol{\theta}_G(\boldsymbol{\theta})$ is the vector of the moments of $G(\mathbf{X})$.

According to MoM, the failure probability can also be expressed as:

$$P_f(\boldsymbol{\theta}) = \Phi[-\beta_{4M}(\boldsymbol{\theta}_G)], \tag{5}$$

where $\beta_{4M}(\boldsymbol{\theta}_G)$ is the fourth order reliability index, the general form of which is shown below:

$$\beta_{4M}(\boldsymbol{\theta}_G) = \sqrt[3]{D_0 + q_0} - \sqrt[3]{D_0 - q_0} + \frac{\tilde{h}_3}{3\tilde{h}_4} \tag{6}$$

where $D_0, q_0, \tilde{h}_3, \tilde{h}_4$ are the parameters parameters that depend on the skewness and kurtosis; detailed expressions are given in the Appendix.

To evaluate β_{4M}, the first four central moments $\theta_G^{(i)}(i = 1, 2, 3, 4)$ of the performance function are required, defined as:

$$\theta_G^{(1)} = \mathbb{E}_{G1}(\boldsymbol{\theta}), \tag{7}$$

$$\theta_G^{(2)} = \sqrt{\mathbb{E}_{G2}(\boldsymbol{\theta}) - [\mathbb{E}_{G1}(\boldsymbol{\theta})]^2}, \tag{8}$$

$$\theta_G^{(3)} = \frac{1}{\sigma_G^3}\{\mathbb{E}_{G3}(\boldsymbol{\theta}) - 3\mathbb{E}_{G1}(\boldsymbol{\theta})\mathbb{E}_{G2}(\boldsymbol{\theta}) + 2[\mathbb{E}_{G1}(\boldsymbol{\theta})]^3\}, \tag{9}$$

$$\theta_G^{(4)} = \frac{1}{\sigma_G^4}\{\mathbb{E}_{G4}(\boldsymbol{\theta}) - 4\mathbb{E}_{G1}(\boldsymbol{\theta})\mathbb{E}_{G3}(\boldsymbol{\theta}) + 6[\mathbb{E}_{G1}(\boldsymbol{\theta})]^2\mathbb{E}_{G2}(\boldsymbol{\theta}) - 3[\mathbb{E}_{G1}(\boldsymbol{\theta})]^4\}, \tag{10}$$

where $\mathbb{E}_{Gi}(\boldsymbol{\theta})$ is the *i*th raw moment of the performance function $G(\mathbf{X})$, which can be theoretically computed from $\boldsymbol{\theta}$ as follows:

$$\mathbb{E}_{Gi}(\boldsymbol{\theta}) = \int_{\Omega_{\mathbf{x}}} [G(\mathbf{x})]^i f_{\mathbf{X}}(\mathbf{x}|\boldsymbol{\theta}) d\mathbf{x}, \quad (i = 1, 2, 3, 4), \tag{11}$$

Substituting Eqs. (7)-(10) into Eqs. (5) and (6) yields the moment-based estimate of the failure probability. Consequently, the method of moments transforms the original multi-dimensional integral over the failure domain into the much simpler task of computing the first four moments of the performance function, followed by closed-form expressions for the failure probability, thus avoiding the discontinuity introduced by the indicator function.

2.2. Sensitivity index of failure probability

Reliability sensitivity analysis aims to quantify how small changes in the distribution parameters θ affect the failure probability. The sensitivity measure adopted in this work is the partial derivative of the failure probability with respect to the distribution parameter:

$$\epsilon_{\theta_{ij}} = \frac{\partial P_f(\boldsymbol{\theta})}{\partial \theta_{ij}}. \tag{12}$$

where θ_{ij} is the *j*th moment of x_i.

In this study, the input random variables $x_i(i = 1, 2, \cdots, n)$ are assumed to be mutually independent, which allows the JPDF to factorize as $f_{\mathbf{X}}(\mathbf{x}) = \prod_{i=1}^{n} f_{X_i}(x_i|\boldsymbol{\theta}_i)$, where $f_{X_i}(x_i|\boldsymbol{\theta}_i)$ is the marginal PDF

of x_i, and $\boldsymbol{\theta}_i = (\theta_{i1}, \theta_{i2}, \theta_{i3}, \theta_{i4})^T$ denotes the vector of distribution parameters for x_i. Then, the partial derivative of $P_f(\boldsymbol{\theta})$ with respect to θ_{ij} can be expressed as(Wu, 1994):

$$\frac{\partial P_f(\boldsymbol{\theta})}{\partial \theta_{ij}} = \int_{G(\mathbf{X})\leq 0} h_{ij}(x_i|\boldsymbol{\theta}_i) f_{\mathbf{X}}(\mathbf{x}|\boldsymbol{\theta}) d\mathbf{x}, \tag{13}$$

where the function $h_{ij}(X_i|\boldsymbol{\theta}_i)$ is defined as the score function:

$$h_{ij}(X_i|\boldsymbol{\theta}_i) = \frac{1}{f_{X_i}(X_i|\boldsymbol{\theta}_i)} \cdot \frac{\partial f_{X_i}(X_i|\boldsymbol{\theta}_i)}{\partial \theta_{ij}}. \tag{14}$$

As can be seen from Eqs. (13) and (14), the computation of both the failure probability and its sensitivity $\partial P_f(\boldsymbol{\theta})/\partial \theta_{ij}$ involves a multi-fold integral over the failure domain. Direct evaluation of these integrals is challenging when the performance function $G(\mathbf{X})$ is implicit, highly nonlinear, or when the dimension is large. To overcome this difficulty, method of moment approximate these integrals using the first few statistical moments of $G(\mathbf{X})$, thereby avoiding repeated evaluations of the original performance function. The present work extends this moment-based framework to incorporate fourth-order moment information, enabling the estimation of sensitivity with respect to kurtosis.

Based on Eqs.(5)-(11) and using the chain rule of differentiation, the derivative of $P_f(\boldsymbol{\theta})$ with respect to θ_{ij} is obtained as follows:

$$\frac{\partial P_f(\boldsymbol{\theta})}{\partial \theta_{ij}} = \frac{\partial P_f(\boldsymbol{\theta})}{\partial \beta_{4M}(\boldsymbol{\theta}_G)} \cdot \frac{\partial \beta_{4M}(\boldsymbol{\theta}_G)}{\partial \boldsymbol{\theta}_G} \cdot \frac{\partial \boldsymbol{\theta}_G}{\partial \vec{\mathbb{E}}_G(\boldsymbol{\theta})} \cdot \frac{\partial \vec{\mathbb{E}}_G(\boldsymbol{\theta})}{\partial \theta_{ij}}. \tag{15}$$

There are four elements in Eq. (15), which will be discussed separately in the following. Based on Eq. (5), the derivative of failure probability with respect to the fourth moment-based reliability index is obtained as follows:

$$\frac{\partial P_f(\boldsymbol{\theta})}{\partial \beta_{4M}(\boldsymbol{\theta}_G)} = -\varphi[-\beta_{4M}(\boldsymbol{\theta}_G)], \tag{16}$$

where $\varphi[\cdot]$ is the PDF of the standard normal distribution.

The fourth-moment reliability index β_{4M} is implicitly defined by Eq. (6) together with the parameters Δ, q, h_3, h_4 given in the Appendix. The analytical partial derivatives of β_{4M} with respect to $\theta_G^{(1)}$, $\theta_G^{(2)}$, $\theta_G^{(3)}$, $\theta_G^{(4)}$ are extremely lengthy and cumbersome to derive and implement. To avoid complicated analytical manipulations and to ensure numerical stability, this work computes these gradients using the central finite difference method.

For the *i*-th component $\theta_G^{(i)}$ of $\boldsymbol{\theta}_G$, the first-order partial derivative is approximated as:

$$\frac{\partial \beta_{4M}}{\partial \theta_G^{(i)}} \approx \frac{\beta_{4M}(\theta_G^{(i)} + \delta) - \beta_{4M}(\theta_G^{(i)} - \delta)}{2\delta}, \tag{17}$$

where the step size δ is set to $\delta = 10^{-6} \cdot |\theta_G^{(i)}|$; when $|\theta_G^{(i)}| < 10^{-6}$, an absolute step $\delta = 10^{-6}$ is used.

Each partial derivative requires only two additional evaluations of β_{4M}, which involves only elementary algebraic operations and incurs negligible computational cost. In all numerical examples, this step size yields relative errors below 10^{-10}, which is more than sufficient for engineering accuracy.

The term $\partial\boldsymbol{\theta}_G/\partial\vec{\mathbb{E}}_G(\boldsymbol{\theta})$ is a 4×4 matrix, which is obtained based on Eqs. (7)-(10) as follows:

$$\frac{\partial\boldsymbol{\theta}_G}{\partial\vec{\mathbb{E}}_G(\boldsymbol{\theta})}=\begin{pmatrix} 1 & 0 & 0 & 0\\ -\dfrac{\theta_G^{(1)}}{\theta_G^{(2)}} & \dfrac{1}{2\theta_G^{(2)}} & 0 & 0\\ \dfrac{3\mathbb{E}_{G3}\mathbb{E}_{G1}-3\mathbb{E}_{G2}^2}{{\theta_G^{(2)}}^5} & \dfrac{3(\mathbb{E}_{G1}\mathbb{E}_{G2}-\mathbb{E}_{G3})}{2{\theta_G^{(2)}}^5} & \dfrac{1}{{\theta_G^{(2)}}^3} & 0\\ \dfrac{\partial\theta_G^{(4)}}{\partial\mathbb{E}_{G1}} & \dfrac{\partial\theta_G^{(4)}}{\partial\mathbb{E}_{G2}} & -\dfrac{4\mathbb{E}_{G3}}{{\theta_G^{(2)}}^5} & \dfrac{1}{{\theta_G^{(2)}}^4} \end{pmatrix}. \tag{18}$$

and,

$$\frac{\partial\theta_G^{(4)}}{\partial\mathbb{E}_{G1}}=\frac{4\mathbb{E}_{G1}\mathbb{E}_{G4}+12\mathbb{E}_{G1}\mathbb{E}_{G2}^2-12\mathbb{E}_{G1}^2\mathbb{E}_{G3}-4\mathbb{E}_{G2}\mathbb{E}_{G3}}{2{\theta_G^{(2)}}^5} \tag{19}$$

$$\frac{\partial\theta_G^{(4)}}{\partial\mathbb{E}_{G2}}=\frac{-2\mathbb{E}_{G4}+8\mathbb{E}_{G1}\mathbb{E}_{G3}-6\mathbb{E}_{G1}^2\mathbb{E}_{G2}}{2{\theta_G^{(2)}}^5} \tag{20}$$

Based on Eq. (13) and Eq. (11), the term $\partial\mathbb{E}_{Gk}(\boldsymbol{\theta})/\partial\theta_{ij}$ (k=1, 2, 3, 4) can be expressed as (Zhang et al., 2025):

$$\frac{\partial E_{Gk}(\boldsymbol{\theta})}{\partial\theta_{ij}}=\int_{\Omega_{\mathbf{x}}}H_{ijk}(\mathbf{x})f_{\mathbf{X}}(\mathbf{x}|\boldsymbol{\theta})d\mathbf{x}, \tag{21}$$

where $H_{ijk}(\mathbf{X})$ is a function of $\mathbf{X}$ formulated as follows:

$$H_{ijk}(\mathbf{X})=[G(\mathbf{X})]^k h_{ij}(x_i|\boldsymbol{\theta}_i). \tag{22}$$

It can be seen from the Eqs. (21) and (22) that the final term is essentially a high-dimensional integral, with the integrand being . To avoid performing high-dimensional numerical integration directly, this paper employs the point estimate method (Zhao and Ono, 2000) combined with the bivariate dimension reduction method (BDRM) (Xu and Rahman, 2004) for approximate calculation.

3. Illustrative example

A one-dimentional performance function are considered as follow:

$$G(\mathbf{X})=b-X, \tag{23}$$

where b=20 is the threshold parameter; and X is a random variable. To assess the accuracy of the proposed method, X is assumed to be normal and lognormal distribution.The mean value μ is set to be (15, 16, 17, 18, 19, 20) and the coefficient of variation (COV) is set to be (0.15, 0.17, 0.19, 0.21, 0.23, 0.25).

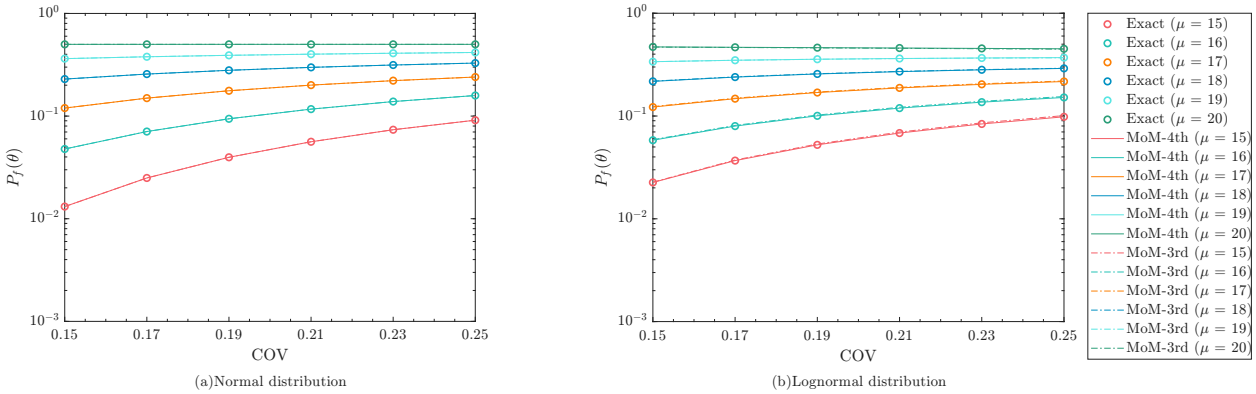


Figure 1. Failure probability for different cases in example

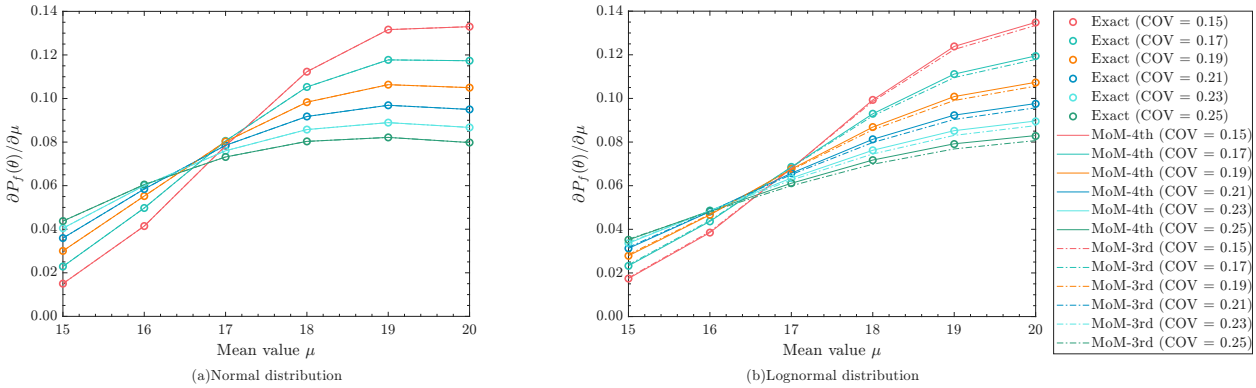


Figure 2. Changing of $\partial P_f(\theta)/\partial\mu$ with different mean values in example

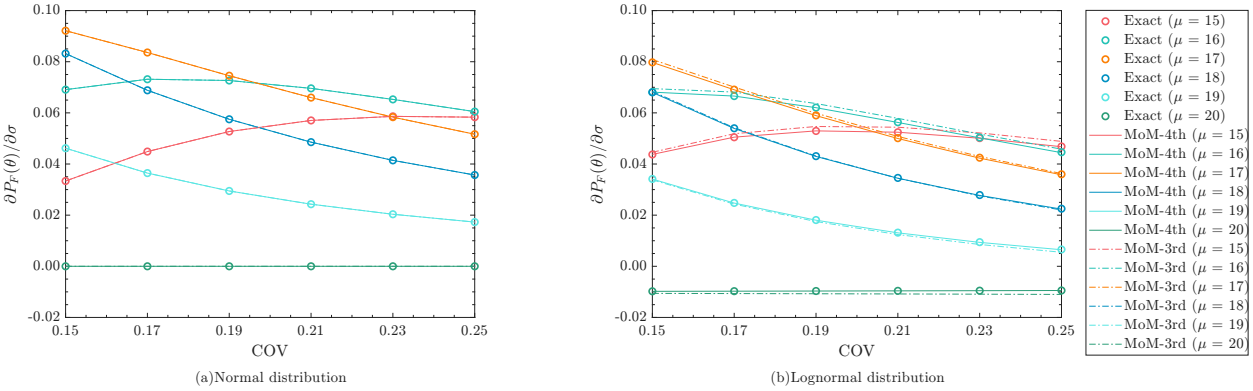


Figure 3. Changing of $\partial P_f(\theta)/\partial\sigma$ with COV in example

Table I. .

random variable	distribution	μ	COV	skewness	kurtosis
X	Pearson system	14	[0.10 0.15 0.20]	-0.1	[2.8 2.9 3.0 3.1 3.2]

Table II. Example of multi-column subcolumns.

COV	skewness	kurtosis	ϵ_3		ϵ_4	
			Proposed method	Exact	Proposed method	Exact
0.10			0.0000	0.0000	0.0000	0.0000
0.15	-0.1	2.8	0.0043	0.0065	0.0019	0.0041
0.20			0.0082	0.0318	0.0072	0.0105
0.10			0.0000	0.0000	0.0000	0.0000
0.15	-0.1	2.9	0.0073	0.0074	0.0041	0.0041
0.20			0.0289	0.0293	0.0085	0.0087
0.10			0.0000	0.0000	0.0000	0.0000
0.15	-0.1	3.0	0.0078	0.0078	0.0039	0.0039
0.20			0.0269	0.0273	0.0072	0.0073
0.10			0.0001	0.0001	0.0001	0.0001
0.15	-0.1	3.1	0.0080	0.0080	0.0036	0.0037
0.20			0.0252	0.0256	0.0061	0.0063
0.10			0.0002	0.0002	0.0001	0.0001
0.15	-0.1	3.2	0.0081	0.0081	0.0034	0.0035
0.20			0.0238	0.0242	0.0053	0.0055

In these two cases, the failure probability and sensitivity indexes are shown in Figure 1 to Figure 3, respectively.

To verify the sensitivity of the proposed method to skewness and kurtosis, the Pearson distribution is assumed to be another distribution type for the random variable X, and the distribution parameters are shown in Table I. In this case, the results of sensitivity index are shown in Table II.

After comparison, the error between the proposed method and the true values was generally within 5%; however, there were still some outliers that differed from the true values, and these should be optimised in future research.

4. Conclusion

This paper proposes a reliability sensitivity analysis method based on the first four central moments. This method treats sensitivity analysis as a by-product of reliability analysis, eliminating the need for additional

calculations and thereby greatly simplifying the sensitivity analysis process. Examples demonstrate that the sensitivity of failure probability to the parameters of the random variable distribution obtained using this method is highly consistent with the results derived from exact calculations, thereby fully validating the effectiveness of the method.

This is the first time that the results of a sensitivity analysis of fourth-order moments have been published, thereby quantifying the impact of kurtosis.

Appendix

The parameters for the fourth order moment reliability index are as follows:

$$D_0 = \sqrt{q_0^2 + p_0^3}, \tag{24}$$

and,

$$q_0 = \frac{\tilde{h}_3^3}{27\tilde{h}_4^3} - \frac{\tilde{h}_2\tilde{h}_3}{6\tilde{h}_4^2} - \frac{\tilde{h}_3 - \beta_{2M}/k}{2\tilde{h}_4}, \quad p_0 = \frac{3\tilde{h}_2\tilde{h}_4 - \tilde{h}_3^2}{9\tilde{h}_4^2}, \tag{25}$$

where $\tilde{h}_3$, $\tilde{h}_4$, $\tilde{h}_0$ and k are the parameters calculated based on $\theta_G^{(3)}$ and $\theta_G^{(4)}$; β_{2M} is the so-called second order reliability index and is formulated as follows:

$$\begin{aligned} \tilde{h}_3 &= \frac{5 + (35 - {\theta_G^{(3)}}^2)\tilde{h}_4^2}{9\tilde{h}_0 + 30 - 0.8{\theta_G^{(3)}}^2}\theta_G^{(3)}, \quad \tilde{h}_4 = \frac{2\tilde{h}_0}{2\tilde{h}_0 + 46(1 - 1/{\theta_G^{(4)}}^2) - {\theta_G^{(3)}}^2}, \\ \tilde{h}_0 &= \frac{\sqrt{3\theta_G^{(4)} - 4{\theta_G^{(3)}}^2 - 5} - 2}{1 - (3{\theta_G^{(3)}}^2 + 1)/{\theta_G^{(4)}}^2}, \quad k = \frac{1}{\sqrt{1 + 2\tilde{h}_3^2 + 6\tilde{h}_4^2}}. \end{aligned} \tag{26}$$

$$\beta_{2M} = \frac{\theta_G^{(1)}}{\theta_G^{(2)}}. \tag{27}$$

Acknowledgements

The authors would like to acknowledge the financial support from the National Key Laboratory of Bridge Safety and Resilience, Beijing University of Technology. The authors also thank the reviewers for their constructive comments that improved the quality of this paper.

References

Der Kiureghian, A.: 2022, *Structural and system reliability*. Cambridge University Press.
Ditlevsen, O. and H. O. Madsen: 1996, *Structural reliability methods*, Vol. 178. Wiley New York.

Lemaire, M.: 2013, *Structural reliability*. John Wiley & Sons.

Li, H., Z. Lu, and K. Feng: 2023, 'An efficient method for analyzing local reliability sensitivity by moment method and extended failure probability'. *Structural and Multidisciplinary Optimization* **66**(2), 34.

Sobol', I. M.: 1990, 'On sensitivity estimation for nonlinear mathematical models'. *Matematicheskoe modelirovanie* **2**(1), 112–118.

Sobol, I. M.: 2001, 'Global sensitivity indices for nonlinear mathematical models and their Monte Carlo estimates'. *Mathematics and computers in simulation* **55**(1-3), 271–280.

Wei, N., Z. Lu, and Y. Hu: 2022, 'Local reliability sensitivity method by the reconstructed fraction moment constrained maximum entropy'. *Advances in Engineering Software* **173**, 103280.

Wu, Y.-T.: 1994, 'Computational methods for efficient structural reliability and reliability sensitivity analysis'. *AIAA journal* **32**(8), 1717–1723.

Xu, H. and S. Rahman: 2004, 'A generalized dimension-reduction method for multidimensional integration in stochastic mechanics'. *International Journal for Numerical Methods in Engineering* **61**(12), 1992–2019.

Zhang, X.-Y., M. A. Valdebenito, Y.-G. Zhao, and M. G. Faes: 2025, 'Probability Sensitivity Estimation with Respect to Distribution Parameters via the Method of Moments'. *ASCE-ASME Journal of Risk and Uncertainty in Engineering Systems, Part A: Civil Engineering* **11**(4), 04025081.

Zhang, X.-Y., Y.-G. Zhao, and Z.-H. Lu: 2019, 'Unified Hermite polynomial model and its application in estimating non-Gaussian processes'. *Journal of Engineering Mechanics* **145**(3), 04019001.

Zhao, Y. G. and T. Ono: 2000, 'New point estimates for probability moments'. *Journal of Engineering Mechanics* **126**(4), 433–436.

Zhao, Y.-G. and T. Ono: 2001, 'Moment methods for structural reliability'. *Structural safety* **23**(1), 47–75.

Zhao, Y.-G., X.-Y. Zhang, and Z.-H. Lu: 2018, 'Complete monotonic expression of the fourth-moment normal transformation for structural reliability'. *Computers & Structures* **196**, 186–199.

A linear-moment-based sensitivity analysis method considering the influence of correlation coefficient *

Qinghe Li, Xuan-Yi Zhang†, and Yan-Gang Zhao
National Key Laboratory of Bridge Safety and Resilience, Beijing University of Technology, Beijing 100124, China liqinghe@emails.bjut.edu.cn
National Key Laboratory of Bridge Safety and Resilience, Beijing University of Technology, Beijing 100124, China zhangxuanyi@bjut.edu.cn
National Key Laboratory of Bridge Safety and Resilience, Beijing University of Technology, Beijing 100124, China zhaoyg@bjut.edu.cn

Abstract. A reliability sensitivity analysis method based on linear moments (L-moments) is proposed in this paper to investigate the sensitivity of the failure probability to the correlation coefficients between input random variables. The sensitivity index is defined as the partial derivative of the failure probability with respect to the correlation coefficients that define the dependence structure among the inputs. A complete expression for the correlation sensitivity index is derived using the first four L-moments. As a by-product of the L-moments-based reliability analysis, the proposed method efficiently evaluates sensitivity information without requiring additional costly structural analyses. The effectiveness of the proposed method is demonstrated through a numerical example. The results show excellent agreement with those obtained from Monte Carlo simulation confirming the accuracy of the method.

Keywords: Sensitivity analysis, Linear moments, Correlation coefficient

1. Introduction

During daily service, structures will face two aspects of uncertainty: one is the uncertainty of external loads, and the other is the uncertainty of their own structure parameters(Zhang et al., 2021; Guo et al., 2023; Zhao et al., 2022). In order to evaluate these uncertainties, structural reliability theory has been widely applied, and commonly used reliability theories include first-order moment method(FORM)(Lu et al., 2017), second-order moment method(SORM)(Zhao et al., 2002),simulation method(SS)(Au and Beck, 2001), probability density evolution method(PDEM)(Li, 2016), MOM(Zhao and Ono, 2001), etc, the development of reliability theory is relatively mature. However, the impact of random input variables on failure probability, namely sensitivity analysis, is relatively limited. In order to provide assistance for structural optimization design, sensitivity analysis methods are important. Meanwhile, in engineering practice, structural parameters are often not independent of each other and have strong correlations. And then, there is currently

* Footnote to the title with the 'thanks' command.
† Corresponding author

© 2026 by the author(s). This work is licensed under the Creative Commons Attribution 4.0 International License (CC BY 4.0), which permits unrestricted use, distribution, and reproduction in any medium, provided the original author and source are credited.

limited research on sensitivity analysis, and there is no sensitivity analysis method specifically for correlation coefficients. Therefore, it is necessary to study the sensitivity methods for correlation coefficients.

Correlation coefficient is a measure that describes the correlation between parameters, ignoring the influence of correlation can lead to significant errors, and the failure probability also shows a high sensitivity to correlation. Previous research on sensitivity mainly focused on the random variables themselves and their distribution, giving rise to many methods, such as single-loop estimation method(Wei et al., 2012), maximum entropy-based method(Yun et al., 2019a), Bayes formula-based method(Wang et al., 2018; Wang et al., 2019; Yun et al., 2019b), and sensitivity analysis based on methods of moments (SAMOM)(Zhang et al., 2025), etc. However, these methods all ignore correlation, the failure probability also shows a high sensitivity to the correlation coefficient.

In this paper, the sensitivity of calculating the correlation between parameters is actually a local sensitivity analysis, which involves calculating the partial derivative of the failure probability with respect to the correlation coefficient. However, to calculate the partial derivative of the failure probability with respect to the correlation coefficient, the first step is to calculate the failure probability. Sensitivity analysis methods are mostly designed as post-processing for reliability analysis. Both FORM based and SORM based reliability methods require some assumptions, which result in poor accuracy when dealing with strongly nonlinear problems. Although the method of moment based on central moments(C-moments) can handle strongly nonlinear problems, it requires a huge sample size. The method of moment based on linear moments(L-moments)(Hosking, 2018) can handle strongly nonlinear problems while requiring a smaller sample size and also has good performance for high-dimensional problems.

This article proposes a sensitivity analysis method for correlation coefficients based on linear moments, which calculates the partial derivative of the failure probability with respect to the correlation coefficient. This method has the following improvements, it is a byproduct of reliability analysis. It clarifies the influence of correlation coefficients on failure probability and can effectively handle strong nonlinear problems.

2. PROBLEM STATEMENT

2.1. Failure Probability

In structural reliability analysis, the performance functions are typically used to describe the working state of a structure or system under random input. The performance function is represented as $G(\mathrm{X})$, where $\mathrm{X} = (x_1, x_2, ..., x_3)^T$ represents a vector of n random variables reflecting uncertainties in model parameters and external loading conditions. When $G(\mathrm{X}) \leq 0$, it indicates structural failure, and when $G(\mathrm{X}) > 0$, it indicates that the structure is safe. Based on the definition, the failure probability $P_F(\boldsymbol{\rho})$ is defined by a multi-fold integral as follows:

$$P_F(\boldsymbol{\rho}) = \int\limits_{G(\mathrm{X})\leq 0} f_{\mathrm{X}}(\mathrm{X} \mid \boldsymbol{\rho}) dx \tag{1}$$

where $P_F(\boldsymbol{\rho})$ is the failure probability; $f_{\mathrm{X}}(\mathrm{X} \mid \boldsymbol{\rho})$ is the joint probability density function (JPDF) of X; $\boldsymbol{\rho}$ is a vector that collects the correlation coefficient between random variables, and $\boldsymbol{\rho} = (\rho_{i1}, \rho_{i2}, ..., \rho_{ij}, ..., \rho_{in})$, ρ_{ij} is the correlation coefficient between the $i-th$ random variable and the $j-th$ random variable, $\rho_{ij} = \rho_{ji}$; With $P_F(\boldsymbol{\rho})$ is determined, the reliability index $\beta(\boldsymbol{\rho})$ can be obtained as follows:

$$\beta(\boldsymbol{\rho}) = -\Phi^{-1}\left[P_F(\boldsymbol{\rho})\right] \tag{2}$$

where $\Phi^{-1}[\cdot]$ is the inverse cumulative distribution function(CDF) of the standard normal distribution.

2.2. Sensitivity index of failure probability

The failure probability defined in Eq.(1) is controlled by many important factors, one of which is the correlation between input random variables. Therefore, it is important to understand the impact of correlation coefficient between parameters on the probability of failure. The sensitivity can be quantified through the partial derivative of $P_F(\boldsymbol{\rho})$ with respect to correlation coefficient ρ_{ij}. In order to be applicable for comparison correlation coefficient between different random variables, a dimensionless measure is provided, which uses an elasticity based sensitivity index, which is denoted by $\varepsilon_{\theta_{ij}}$ and defined as follows(Zhang et al., 2025):

$$\epsilon_{\boldsymbol{\rho}} = \frac{\partial P_F(\boldsymbol{\rho})}{\partial \rho_{ij}} \cdot \frac{\rho_{ij}}{P_F(\boldsymbol{\rho})} \tag{3}$$

The partial derivative of $P_F(\boldsymbol{\rho})$ with respect to ρ_{ij} can be computed as shown in Equation.4(Wu, 1993).

$$\frac{\partial P_F(\boldsymbol{\rho})}{\partial \rho_{ij}} = \int\limits_{G(\mathbf{X})\leq 0} \frac{\partial[f_{\mathrm{X}}(\mathrm{X}|\boldsymbol{\rho})]}{\partial \rho_{ij}} d\mathbf{x} \tag{4}$$

The joint probability density function(JPDF) between input random variables can be expressed as:

$$f_{\mathrm{X}}(\boldsymbol{x} \mid \boldsymbol{\rho}) = c(z_1, z_2, \ldots, z_n) \prod_{i=1}^{n} f_{X_i}(x_i) \tag{5}$$

where, ρ is the correlation coefficient matrix; $c(z_1, z_2, ..., z_n)$ is the copula function. z is a column vector, which is the inverse cumulative distribution function of the random variable, $z = z_1, z_2, ..., z_n$, $z_i = F_i(x_i)$, x_i is the random variable, i is the number of random variables. $f_{\mathrm{X}}(\boldsymbol{x} \mid \boldsymbol{\rho})$ is the the joint probability density function of random variables. $f(x_i)$ is the probability density function of x_i. And then, the partial derivative of the failure probability $P_F(\boldsymbol{\rho})$ on the correlation coefficient ρ_{ij} can be expressed as:

$$\frac{\partial P_F(\boldsymbol{\rho})}{\partial \rho_{ij}} = \int\limits_{G(\mathbf{X})\leq 0} h_{ij}(x_i \mid \boldsymbol{\theta_i}) f_{\mathrm{X}}(\mathrm{X} \mid \boldsymbol{\theta}) dx \tag{6}$$

$$h_{ij}(x_i \mid \rho_{ij}) = \frac{\partial c(z_1, z_2, \ldots, z_n)}{\partial \rho_{ij}} \cdot \frac{1}{c(z_1, z_2, \ldots, z_n)} \tag{7}$$

However, it's difficult to directly evaluate Eqs.(1) and (4), because of the performance function usually strongly nonlinear and implicit. In addition, the failure domain is difficult to determine in high-dimensional structural engineering problems. In order to solve the problem, an efficient computational approach based on the method of L-moments is adopted.

3. REVIEW OF THE METHOD OF LINEAR MOMENTS

In the reliability analysis based on the method of L-moments, the performance function $G(\mathrm{X})$ can be regarded as a random variable Y, consequently, $P_F(\boldsymbol{\rho})$ can be defined by evaluating the cumulative distribution function(CDF) of Y at the limit state $Y = 0$, shown in the following equation(Zhao and Ono, 2001):

$$P_F(\boldsymbol{\rho}) = F_Y\left[0 \mid \lambda_G\right] \tag{8}$$

where, $F_Y[0 \mid \boldsymbol{\lambda_G}]$ represents the CDF of $Y = G(X)$; $\boldsymbol{\lambda}_G = (\lambda_{G1}, \lambda_{G2}, \lambda_{G3}, \lambda_{G4})^T$ denotes the vector of the first L-moments of Y, among them, λ_{G1}, λ_{G2}, λ_{G3}, λ_{G4} are the L-mean, L-standard deviation, L-skewness and L-kurtosis of Y, respectively. In practical engineering applications, the exact distribution of Y is typically unknown and it is difficult to theoretical construct $F_Y[0 \mid \boldsymbol{\lambda_G}]$. By approximating non normal random variables with a cubic equation of standard normal random variables, a normal transformation ($U - Y$ transformation) can be applied(Zhao et al., 2020):

$$Y = a + bU + cU^2 + dU^3 \tag{9}$$

where Y is the non-normal random variable, U is the standard normal random variable; a, b, c, d are the polynomial coefficient, which can be explicitly defined in terms of λ_G(Tung, 2000):

$$a = \lambda_{G1} - 1.81379937\lambda_{G3} \tag{10}$$

$$b = 2.25518617\lambda_{G2} - 3.93740250\lambda_{G4} \tag{11}$$

$$c = 1.81379937\lambda_{G3} \tag{12}$$

$$d = -0.19309293\lambda_{G2} + 1.574961\lambda_{G4} \tag{13}$$

Based on Eq.(9), $P_F(\boldsymbol{\rho})$ can be obtained as follows:

$$P_F(\boldsymbol{\rho}) = \Phi[-\beta_M(\boldsymbol{\lambda}_G)] \tag{14}$$

where $\beta_M(\boldsymbol{\lambda}_G)$ is the reliability index based on linear moments, generally, $\beta_M(\boldsymbol{\lambda}_G)$ can be expressed as Eq.(15)(Zhao et al., 2020; Tong et al., 2021; Tong et al., 2025), for other situations, please refer to the Appendix A.

$$\beta_M(\boldsymbol{\lambda}_G) = -\sqrt[3]{-\frac{h}{2} - \sqrt{A}} - \sqrt[3]{-\frac{h}{2} + \sqrt{A}} + \frac{c}{3d} \tag{15}$$

where parameters A and h can be expressed as:

$$A = \left(-\frac{c^2 - 3bd}{9d^2}\right)^3 + \frac{h^2}{4} \tag{16}$$

$$h = \frac{2c^3}{27d^3} - \frac{bc}{3d^2} + \frac{a}{d} \tag{17}$$

The first four linear moments λ_G are obtained based on the probability-weighted moments(PWMs) $\mathbf{M} = (M_0, M_1, M_2, M_3)^T$ are expressed as:

$$\lambda_{G1} = M_0 \tag{18}$$

$$\lambda_{G2} = 2M_1 - M_0 \tag{19}$$

$$\lambda_{G3} = 6M_2 - 6M_1 + M_0 \tag{20}$$

$$\lambda_{G4} = 20M_3 - 30M_2 + 12M_1 - M_0 \tag{21}$$

The expression for the probability weight moment: is

$$M_r = \int_0^1 y \cdot [F_Y(y|\boldsymbol{\rho})]^r \, dF_Y(y|\boldsymbol{\rho}) = \int_{\Omega_X} y \cdot [F_Y(y|\boldsymbol{\rho})]^r \cdot f_X(x|\boldsymbol{\rho}) dx, \quad (r = 0, 1, 2, 3) \tag{22}$$

where, $F_Y(y|\boldsymbol{\rho})$ is the CDF of Y, which is defined as:

$$F_Y(y|\boldsymbol{\rho}) = \int_{\Omega_X} I[Y \leq y] \cdot f_X(\mathbf{x}|\boldsymbol{\rho}) \, d\mathbf{x} \tag{23}$$

and $I[Y \leq y]$ denotes the indicator function.

4. Reliability sensitivity analysis method based on linear moments

Based on Eqs.(14)-(23) and the differential chain rule, the partial derivative of failure probability $P_F(\boldsymbol{\rho})$ with respect to correlation coefficient ρ_{ij} can be derived and expressed as:

$$\frac{\partial P_F(\boldsymbol{\rho})}{\partial \rho_{ij}} = \frac{\partial P_F}{\partial \beta_M} \cdot \frac{\partial \beta_M}{\partial \boldsymbol{\lambda_G}} \cdot \frac{\partial \boldsymbol{\lambda_G}}{\partial \mathbf{M}_G} \cdot \frac{\partial \mathbf{M}_G}{\partial \rho_{ij}} \tag{24}$$

each of the four terms on the right-hand side of Eq.(24) is defined separately.

For the first item of the Eq.(24), the derivative of $P_F(\boldsymbol{\rho})$ with respect to the L-moments-based reliability index $\beta_M(\boldsymbol{\lambda}_G)$ is obtained as follows Eq.(25) based on Eq.(14).

$$\frac{\partial P_F(\boldsymbol{\rho})}{\partial \beta_M(\boldsymbol{\lambda}_G)} = -\varphi\left[-\beta_M(\boldsymbol{\lambda}_G)\right] \tag{25}$$

where $\varphi(\boldsymbol{\lambda}_G)$ represents the PDF of the standard normal distribution.

For the second item of the Eq.(24), $\beta_M(\boldsymbol{\lambda}_G)$ is defined based on the first four L-moments of the performance function, so the derivative of $\beta_M(\boldsymbol{\lambda}_G)$ with respect to $\boldsymbol{\lambda}_G$ is a vector composed of four elements, which can be expressed as:

$$\frac{\partial \beta_M(\boldsymbol{\lambda}_G)}{\partial \boldsymbol{\lambda}_G} = \left(\frac{\partial \beta_M(\boldsymbol{\lambda}_G)}{\partial \lambda_{G1}}, \frac{\partial \beta_M(\boldsymbol{\lambda}_G)}{\partial \lambda_{G2}}, \frac{\partial \beta_M(\boldsymbol{\lambda}_G)}{\partial \lambda_{G3}}, \frac{\partial \beta_M(\boldsymbol{\lambda}_G)}{\partial \lambda_{G4}} \right) \tag{26}$$

The expression for $\partial\beta_M(\boldsymbol{\lambda}_G)/\partial\lambda_{Gi}$ can be obtained by performing the central finite difference method on formula Eq.(15), as shown in the following equation

$$\frac{\partial\beta_M(\boldsymbol{\lambda}_G)}{\partial\lambda_{Gi}} = \frac{\beta_M(\boldsymbol{\lambda}_G \mid \lambda_{Gi} + 1e^{-5}) - \beta_M(\boldsymbol{\lambda}_G \mid \lambda_{Gi} - 1e^{-5})}{2e^{-5}} \tag{27}$$

As shown in Appendix A, the types of $\beta_M(\boldsymbol{\lambda}_G)$ are different depending on the different linear moments ratios, the solutions for other situations can also be obtained by differencing.

For the third item of the Eq.(24), $\partial\boldsymbol{\lambda}_G/\partial\mathbf{M}$ is a 4×4 matrix obtained based on the relationship between L-moments and PWMs as shown in Eq.(18)-Eq.(21), which can be obtained as follows:

$$\frac{\partial\boldsymbol{\lambda}_G}{\partial\mathbf{M}} = \begin{pmatrix} \frac{\partial\lambda_{G1}}{\partial M_0} & \frac{\partial\lambda_{G1}}{\partial M_1} & \frac{\partial\lambda_{G1}}{\partial M_2} & \frac{\partial\lambda_{G1}}{\partial M_3} \\ \frac{\partial\lambda_{G2}}{\partial M_0} & \frac{\partial\lambda_{G2}}{\partial M_1} & \frac{\partial\lambda_{G2}}{\partial M_2} & \frac{\partial\lambda_{G2}}{\partial M_3} \\ \frac{\partial\lambda_{G3}}{\partial M_0} & \frac{\partial\lambda_{G3}}{\partial M_1} & \frac{\partial\lambda_{G3}}{\partial M_2} & \frac{\partial\lambda_{G3}}{\partial M_3} \\ \frac{\partial\lambda_{G4}}{\partial M_0} & \frac{\partial\lambda_{G4}}{\partial M_1} & \frac{\partial\lambda_{G4}}{\partial M_2} & \frac{\partial\lambda_{G4}}{\partial M_3} \end{pmatrix} = \begin{pmatrix} 1 & 0 & 0 & 0 \\ -1 & 2 & 0 & 0 \\ 1 & -6 & 6 & 0 \\ -1 & 12 & -30 & 20 \end{pmatrix} \tag{28}$$

For the fourth item of the Eq.(24), Based on Eq.(22), $\partial\mathbf{M}/\partial\rho_{ij}$ is divided into four elements, which can be expressed as shown in Eq.(29). Each term in this formula can be expressed as shown in Eq.(32).

$$\frac{\partial\mathbf{M}}{\partial\rho_{ij}} = \left(\frac{\partial M_0}{\partial\rho_{ij}}, \frac{\partial M_1}{\partial\rho_{ij}}, \frac{\partial M_2}{\partial\rho_{ij}}, \frac{\partial M_3}{\partial\rho_{ij}}\right)^T \tag{29}$$

Given N samples generated using the LHS method with a maximin distance criterion, the estimated PWMs and their derivatives can be approximated by:

$$\widehat{M_r} = \frac{1}{N}\sum_{l=1}^{N}\left\{y_{l:N}\cdot\left[\widehat{F}_Y(y_{l:N} \mid \boldsymbol{\rho})\right]^r\right\}, \quad (r=0,1,2,3) \tag{30}$$

where $y_{l:N}$ represents the $l-th$ order statistic of a sample of size N; The empirical CDF $\widehat{F_Y}(y_{l:N} \mid \boldsymbol{\rho})$ can be obtained as follows based on Eq.(23)

$$\widehat{F}_Y(y_{l:N} \mid \boldsymbol{\rho}) = \frac{1}{N}\sum_{l=1}^{N}\boldsymbol{I}[Y \le y] = \frac{l}{N} \tag{31}$$

By using central finite differences, the expression of $\partial M_r/\partial\rho_{ij}$ can be obtained as follows:

$$\frac{\partial\widehat{M_r}}{\partial\rho_{ij}} = \frac{\sum_{l=1}^{N}\left\{y_{l:N}\cdot\left[\hat{F}_Y(y_{l:N} \mid \rho_{ij} + 1e^{-5})\right]\right\} - \sum_{l=1}^{N}\left\{y_{l:N}\cdot\left[\hat{F}_Y(y_{l:N} \mid \rho_{ij} - 1e^{-5})\right]\right\}}{N\cdot 2e^{-5}} \tag{32}$$

Eqs.(25)-(32) are substituted into Eq.(24), and the solution for $\partial P_F(\boldsymbol{\rho})/\partial\rho_{ij}$ is obtained. Then the sensitivity index ϵ_ρ of the correlation coefficient to the failure probability can be obtained. Next, an example is used to demonstrate the accuracy of the proposed method by comparing it with Monte Carlo method.

5. EXAMPLES

The example considers a two-dimensional functional function as follows:

$$G(X) = b - x_1 x_2 \tag{33}$$

where $b = 15$ is the threshold; and x_1 and x_2 are the random variable. In the performance function, the weights of x_1 and x_2 are the same. The mean value (μ) of x_1 is 7.2, and the coefficient of variation COV of x_1 is 0.15. The mean value (μ) of x_2 is 2.5, and the coefficient of variation COV of x_2 is 0.13. The correlation coefficient ρ between x_1 and x_2 is varied within $[-0.8, -0.6, -0.4, -0.2, 0.2, 0.4, 0.6, 0.8]$; And then, the proposed method is calculated 1000 times through Latin hypercube sampling(LHS), and 10^7 times through MCS.

To evaluate the performance of the proposed method for general cases, x_1 and x_2 are all assumed to follow Normal distributions, and the copula functions assumed to be the Gaussian copula and Clayton copula, the expressions for the copula functions are shown in Eq.(35) and Eq.(36). In these two cases, the failure probability and correlation coefficient sensitivity indexes are shown in Figure 1 and Figure 2, respectively. The proposed method is in good agreement with MCS under low failure probability conditions, with small errors. When the correlation coefficient is 0, the sensitivity index is also 0, which indirectly proves the accuracy of the results of the proposed method.

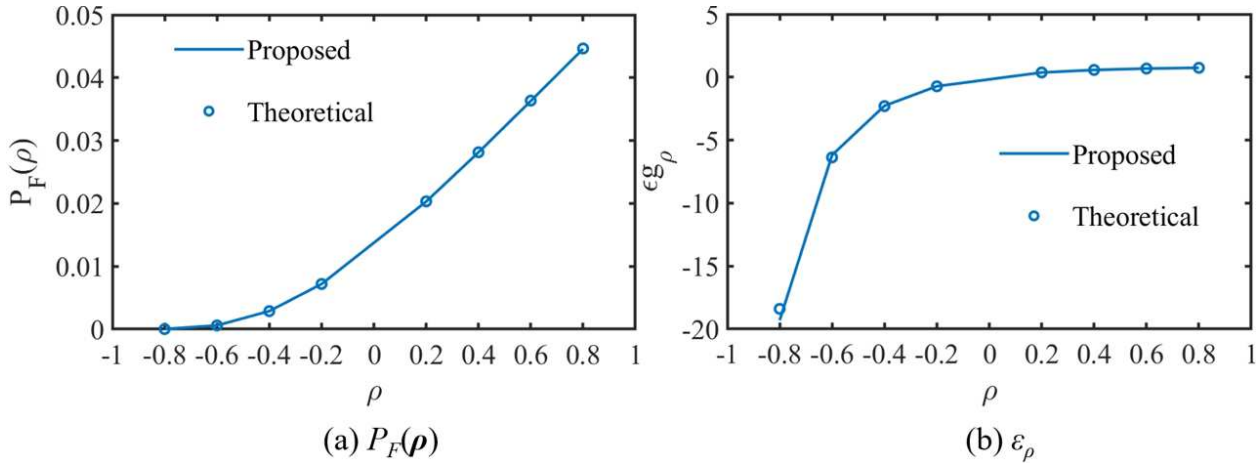


Figure 1. Gauss distribution and Gauss copula

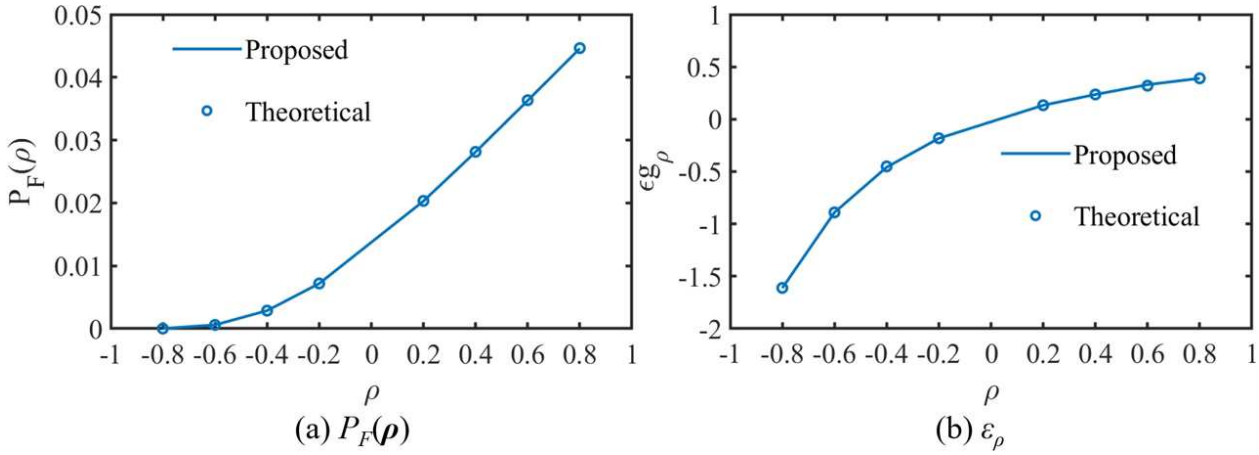


Figure 2. Gauss distribution and Clayton copula

6. Discussion and Conclusions

A reliability sensitivity analysis method based on the first four L-moments is proposed in this paper, considering parameter correlation. As a byproduct of reliability analysis, the proposed method requires no additional calculations, greatly facilitating sensitivity analysis. The example shows that the sensitivity of the correlation coefficient of the input random variable to the failure probability obtained by the proposed method is highly consistent with the MCS results, which fully demonstrates the effectiveness of the proposed method.

It should also be pointed out that the proposed method uses the first four moments of the functional function, so it is only applicable when these moments are sufficient to describe the statistical properties of the functional function.

Appendix

Complete monotonic expressions of normal transformation based on the first four L-moments is shown in Table.(I).

$$Y = a + bU + cU^2 + dU^3 \tag{34}$$

Table I. Y-U monotonic transformation expression based on linear moments

Linear moment ratio			U-expression	**X-Range**
$\tau_4 \neq \delta_4$	$\tau_3^2 \leq \delta_3$		$\sqrt[3]{-\hbar/2-\sqrt{A}}+\sqrt[3]{\hbar/2+\sqrt{A}}-c/3d$	$(-\infty,+\infty)$
$\tau_4 > \delta_4$	$\tau_3^2 > \delta_3$	$\tau_3 \geq 0$	$2\sqrt{\Delta_0/9d^2}\cos(\alpha/3)-c/3d$	$Q_1^* < x < Q_2^*$
			$\sqrt[3]{-\hbar/2-\sqrt{A}}+\sqrt[3]{-\hbar/2+\sqrt{A}}-c/3d$	$x \geq Q_2^*$
		$\tau_3 < 0$	$\sqrt[3]{-\hbar/2-\sqrt{A}}+\sqrt[3]{-\hbar/2+\sqrt{A}}-c/3d$	$x \leq Q_1^*$
			$-2\sqrt{\Delta_0/9d^2}\cos(\alpha/3)-c/3d$	$Q_1^* < x < Q_2^*$
$\tau_4 < \delta_4$	$\tau_3^2 > \delta_3$		$-2\sqrt{\Delta_0/9d^2}\cos(\alpha/3)-c/3d$	$Q_2^* \leq x \leq Q_1^*$
$\tau_4 = \delta_4$		$\tau_3 > 0$	$\frac{\sqrt{b^2-4c(a-x)}-b}{2c}$	$x \geq Q_0^*$
		$\tau_3 > 0$	$\frac{\sqrt{b^2-4c(a-x)}-b}{2c}$	$x \leq Q_0^*$
		$\tau_3 = 0$	$\frac{x-a}{b}$	$(-\infty,+\infty)$

The calculation formulas in the chart can be found in the literature(Zhao et al., 2020; Tong et al., 2021; Tong et al., 2025). The commonly used copula functions gaussian copula and clayton copula are as follows:

$$c(u,v) = \frac{1}{\sqrt{|\rho|}} \exp\left(-0.5 \cdot z^T(\rho^{-1} - I)z\right) \tag{35}$$

$$c(u,v;\theta) = (1+\theta)(uv)^{-1-\theta}\left(u^{-\theta}+v^{-\theta}-1\right)^{-2-1/\theta} \tag{36}$$

Acknowledgements

The authors would like to acknowledge the financial support from the National Key Laboratory of Bridge Safety and Resilience, Beijing University of Technology. The authors also thank the reviewers for their constructive comments that improved the quality of this paper.

References

Au, S.-K. and J. L. Beck: 2001, 'Estimation of small failure probabilities in high dimensions by subset simulation'. *Probabilistic Engineering Mechanics* **16**(4), 263–277.

Guo, Q., H. Zhai, B. Suo, W. Zhao, and Y. Liu: 2023, 'Time-variant reliability global sensitivity analysis with single-loop Kriging model combined with importance sampling'. *Probabilistic Engineering Mechanics* **72**, 103441.

Hosking, J. R. M.: 2018, 'L-Moments: Analysis and Estimation of Distributions Using Linear Combinations of Order Statistics'. *Journal of the Royal Statistical Society: Series B (Methodological)* **52**(1), 105–124.

Li, J.: 2016, 'Probability density evolution method: Background, significance and recent developments'. *Probabilistic Engineering Mechanics* **44**, 111–117. Special Issue Based on Papers Presented at the 7th International Conference on Computational Stochastic Mechanics (CSM7).

Lu, Z.-H., D.-Z. Hu, and Y.-G. Zhao: 2017, 'Second-Order Fourth-Moment Method for Structural Reliability'. *JOURNAL OF ENGINEERING MECHANICS* **143**(4).

Tong, M.-N., Y.-G. Zhao, and Z.-H. Lu: 2021, 'Normal transformation for correlated random variables based on L-moments and its application in reliability engineering'. *Reliability Engineering System Safety* **207**, 107334.

Tong, M.-N., Y.-G. Zhao, and Z.-H. Lu: 2025, 'A Flexible Distribution Based on L-Moments and Its Application in Structural Reliability'. *ASCE-ASME Journal of Risk and Uncertainty in Engineering Systems, Part B: Mechanical Engineering* **11**(4), 041202.

Tung, Y.: 2000, 'Polynomial normal transforms in uncertainty analysis'.

Wang, Y., S. Xiao, and Z. Lu: 2018, 'A new efficient simulation method based on Bayes' theorem and importance sampling Markov chain simulation to estimate the failure-probability-based global sensitivity measure'. *Aerospace Science and Technology* **79**, 364–372.

Wang, Y., S. Xiao, and Z. Lu: 2019, 'An efficient method based on Bayes' theorem to estimate the failure-probability-based sensitivity measure'. *Mechanical Systems and Signal Processing* **115**, 607–620.

Wei, P., Z. Lu, W. Hao, J. Feng, and B. Wang: 2012, 'Efficient sampling methods for global reliability sensitivity analysis'. *Computer Physics Communications* **183**(8), 1728–1743.

Wu, Y. T.: 1993, 'Computational methods for efficient structural reliability and reliability sensitivity analysis'. *AIAA Journal* **32**(8).

Yun, W., Z. Lu, and X. Jiang: 2019a, 'An efficient method for moment-independent global sensitivity analysis by dimensional reduction technique and principle of maximum entropy'. *Reliability Engineering System Safety* **187**, 174–182. Sensitivity Analysis of Model Output.

Yun, W., Z. Lu, Y. Zhou, and X. Jiang: 2019b, 'AK-SYSi: an improved adaptive Kriging model for system reliability analysis with multiple failure modes by a refined U learning function'. *Struct. Multidiscip. Optim.* **59**(1), 263–278.

Zhang, D., P. Zhou, C. Jiang, M. Yang, X. Han, and Q. Li: 2021, 'A stochastic process discretization method combing active learning Kriging model for efficient time-variant reliability analysis'. *Computer Methods in Applied Mechanics and Engineering* **384**, 113990.

Zhang, X.-Y., M. A. Valdebenito, Y.-G. Zhao, and M. G. R. Faes: 2025, 'Probability Sensitivity Estimation with Respect to Distribution Parameters via the Method of Moments'. *ASCE-ASME Journal of Risk and Uncertainty in Engineering Systems, Part A: Civil Engineering* **11**(4), 04025081.

Zhao, Q., T. Wu, and J. Hong: 2022, 'An envelope-function-based algorithm for time-dependent reliability analysis of structures with hybrid uncertainties'. *Applied Mathematical Modelling* **110**, 493–512.

Zhao, Y., T. Ono, and M. Kato: 2002, 'Second-order third-moment reliability method'. *JOURNAL OF STRUCTURAL ENGINEERING-ASCE* **128**(8), 1087–1090.

Zhao, Y.-G. and T. Ono: 2001, 'Moment methods for structural reliability'. *Structural Safety* **23**(1), 47–75.

Zhao, Y.-G., M.-N. Tong, Z.-H. Lu, and J. Xu: 2020, 'Monotonic Expression of Polynomial Normal Transformation Based on the First Four L-Moments'. *JOURNAL OF ENGINEERING MECHANICS* **146**(7).

An Efficient Reliability Analysis Method under Hybrid Uncertainty for High-Dimensional Problems

Zi-Xin Zhang, Pei-Pei Li*, and Yan-Gang Zhao
Department of Civil Engineering, Beijing University of Technology, Beijing 100124, China, S202489012@emails.bjut.edu.cn
Department of Civil Engineering, Beijing University of Technology, Beijing 100124, China, li.peipei@bjut.edu.cn
Department of Civil Engineering, Beijing University of Technology, Beijing 100124, China, zhaoyg@bjut.edu.cn

Abstract. In engineering reliability assessment, simultaneously considering hybrid uncertainty is crucial for ensuring structural safety and cost efficiency. Accurately characterizing the distribution of the conditional failure probability (CFP) is therefore of great practical importance. However, when the epistemic uncertainty involves high dimensional parameters, obtaining this distribution remains a significant challenge. To address this issue, this study proposes an efficient and accurate approach that integrates simulation-based post-processing with Bayesian inference to construct the CFP distribution. Parameter samples are first generated using a good lattice point method with partially stratified sampling, followed by reliability analysis to obtain CFP realizations. Beta mixture distribution model is then employed to directly fit the CFP, with Bayesian estimation used to determine the shape parameters of the mixture. The efficiency and accuracy of the proposed approach are demonstrated through two numerical examples, covering bimodal distributions and finite-element frame structures.

Keywords: Conditional failure probability; Probability distribution; High-dimensional; Beta mixture; Bayesian estimation

1. Introduction

In practical engineering, uncertainties are inevitable, arising from material variability, measurement errors, modeling simplifications, and external disturbances (Li et al., 2022a). Generally speaking, uncertainties can be divided into two types: aleatory uncertainty and epistemic uncertainty (Der Kiureghian and Ditlevsen, 2009). Aleatory uncertainty reflects the inherent randomness of physical variables and is irreducible, whereas epistemic uncertainty stems from limited knowledge and can be reduced with additional data or improved models. Traditional reliability analysis typically considers only aleatory uncertainty, which is modeled using random variables, leading to a deterministic failure probability. However, in real engineering applications, such as wind loads on bridges, limited data and measurements introduce significant epistemic uncertainty, making it difficult to establish

* Corresponding author

© 2026 by the author(s). This work is licensed under the Creative Commons Attribution 4.0 International License (CC BY 4.0), which permits unrestricted use, distribution, and reproduction in any medium, provided the original author and source are credited.

accurate probabilistic models. In other words, improved knowledge leads to more accurate modeling. As pointed out by Der Kiureghian and Ditlevsen (Der Kiureghian and Ditlevsen, 2009), neglecting the distinction between these two types of uncertainty may result in biased estimates of the failure probability. Therefore, structural reliability analysis under hybrid uncertainty is of great importance (Hoffman and Hammonds, 1994).

Currently, three main frameworks are used to model hybrid uncertainty: probability boxes (p-boxes) (Faes et al., 2021; Yang et al., 2023), fuzzy probability (Möller and Beer, 2013), and hierarchical probabilistic models (Zhao et al., 2018; Zhao and Lu, 2021; Chen and Wan, 2019). Among them, hierarchical probabilistic models have attracted considerable attention because they naturally incorporate Bayesian updating to reduce epistemic uncertainty (Li et al., 2025). This framework describes hybrid uncertainty using a two-level probabilistic structure, where epistemic and aleatory uncertainties are represented at the outer and inner levels, respectively. Within this framework, the failure probability becomes dependent on epistemic parameters and is thus treated as a random variable, referred to as the conditional failure probability (CFP). Accordingly, the conditional reliability index (CRI) is also uncertain (Kiureghian, 1989).

In practical applications, uncertainty in distribution parameters is often a dominant source of epistemic uncertainty and can significantly affect reliability assessment results. Various methods have been developed to account for this effect, including the first-order second-moment method (Zhao and Jiang, 1992), point-estimate methods (Hong, 1996), and first-order approximation methodology (Der Kiureghian, 2008), which aim to estimate the predictive failure probability (PFP). However, while PFP reflects the influence of parameter uncertainty, it cannot fully characterize the variability and distributional features of the CFP (Zhao et al., 2018).

Therefore, it is essential to characterize the probability distribution of the CFP for a more transparent assessment of structural risk. To this end, Ang and De Leon (Ang and De Leon, 2005) employed the Monte Carlo simulation (MCS) for estimating the expected and percentile values of the conditional probability of failure, but the method is computationally expensive to obtain a large number of CFP samples to ensure the accuracy of the results, especially for large- scale structures. Later, Der Kiureghian et al. (Der Kiureghian and Ditlevsen, 2009) derived the explicit PDF of CFP for the case of a linear limit-state function and normal random variables. For general cases, it is difficult to obtain the explicit PDF of CFP /CRI. Zhao et al. (Zhao et al., 2018) proposed a novel statistical analysis approach to determine the PFP and quantiles of CFP. However, the results of PFP may be unreliable when the variability of CFP is large. Li et al. (Li et al., 2022a; Li et al., 2022b) employed the first four/three moments of CRI and unimodal distribution (three-parameter normal/lognormal distribution) to fit the CRI distribution. However, this method may not accurately capture the characteristics of a bimodal CRI distribution in practical engineering, which would result in a loss of precision. Recently, Leng et al. (Leng et al., 2025) designed a fixed sampling distribution and used KDE to fit the CFP distribution. However, it is not suitable for high- dimensional or nonlinear problems, which limits its applicability in practical engineering applications.

To address these limitations, this study develops an efficient and robust method to directly approximate the distribution of the CFP under high-dimensional parameter uncertainty. A flexible bounded mixture of Beta distributions model is employed to accurately represent the CFP. The model parameters are efficiently estimated by combining advanced sampling strategies with

Bayesian inference. The remainder of this paper is organized as follows. In Section 2, the problem formulation considering parameter uncertainty is introduced. Section 3 introduces the proposed an efficient reliability analysis method under hybrid uncertainty for high-dimensional problems. Two numerical examples are studied in Section 4 to illustrate the proposed method. Section 5 concludes the paper with some final remarks.

2. Problem Formulation

Structural reliability analysis aims to evaluate the failure probability of a structure. The failure probability P_f is theoretically defined as

$$P_f = \int_{G(\boldsymbol{X})\leq 0} f_{\boldsymbol{X}}(\boldsymbol{x})\, d\boldsymbol{x} \tag{1}$$

where $\boldsymbol{X} = [X_1, X_2, ..., X_n]$ is an n-dimensional vector of independent random variables, representing uncertainties in material properties, geometric parameters, loads, and environmental conditions. Here, $f_{\boldsymbol{X}}(\boldsymbol{x})$ is the joint probability density function (PDF) of $\boldsymbol{X}$, and $G(\boldsymbol{X})$ is the performance function, with $G(\boldsymbol{X}) \leq 0$ defining the failure domain.

Eq. 1 represents the theoretical failure probability under perfect knowledge. However, in practical applications, available data are often limited or of low quality, leading to significant uncertainty in the estimation of distribution parameters (e.g., means and standard deviations). This introduces epistemic uncertainty into the reliability analysis.

In this study, the distribution parameter uncertainty is modeled by random variables notated as the vector $\boldsymbol{\Theta}$. Hence the failure probability becomes a random variable varying with $\boldsymbol{\Theta}$, denoted as $P_f(\boldsymbol{\Theta})$. It can be formulated as (Kiureghian, 1989):

$$P_f(\boldsymbol{\Theta}) = \int_{G(\boldsymbol{X})\leq 0} f_{X|\boldsymbol{\Theta}}(\boldsymbol{x}|\boldsymbol{\theta})\, d\boldsymbol{x} \tag{2}$$

where $f_{X|\boldsymbol{\Theta}}(\boldsymbol{x}|\boldsymbol{\theta})$ denotes the conditional joint PDF of random variables $\boldsymbol{X}$ based on the uncertain distribution parameters $\boldsymbol{\Theta}$.

To characterize the impact of parameter uncertainty, it is necessary to analyze the statistical properties of the CFP. However, evaluating Eq. 2 for different realizations of $\boldsymbol{\Theta}$ can be computationally demanding, especially for high-dimensional problems. Therefore, an efficient and robust approach is required for reliability assessment.

3. Proposed Method for High-Dimensional Reliability Analysis under Hybrid Uncertainty

This section presents a novel method for high-dimensional reliability analysis under hybrid uncertainty, based on a parameterized modeling approach for the conditional failure probability (CFP) combined with Bayesian inference. Section 3.1 introduces an efficient sampling strategy

for generating distribution parameter samples. In Section 3.2, the PDF and CDF of the CFP are constructed explicitly using beta mixture model. Finally, Section 3.3 employs Bayesian inference to estimate the model parameters.

3.1. Generation of Conditional Failure Probability Samples

To improve sampling efficiency in high-dimensional parameter spaces, this study adopts the good lattice point method combined with partially stratified sampling (GLPM-PSS) proposed by Xu et al. (Xu and Dang, 2019). This approach integrates low-discrepancy sequences with partial stratified sampling (PSS) to maximize uniformity in high-dimensional sample spaces while reducing sample variance.

In GLPM-PSS, the high-dimensional space is first partitioned into several low-dimensional orthogonal subspaces using PSS, avoiding the infeasibility of full-dimensional stratification (Shields and Zhang, 2016). As shown in prior studies, significant variance reduction can be achieved when subspaces are one- or two-dimensional (Shields et al., 2015). Accordingly, for an even sample dimension s, the space is divided into $s/2$ two-dimensional subspaces, denoted as PSS - $2^{s/2}$; for odd s, it is divided into $(s-1)/2$ two-dimensional subspaces and one one-dimensional subspace, denoted as PSS - $2^{(s-1)/2} \times 1^1$. Uniform samples are straightforward in one-dimensional subspaces, while achieving uniformity in two-dimensional subspaces is crucial for overall variance reduction.

Among various low-discrepancy sequences such as Halton, GLPM, Sobol, and Hammersley, GLPM generates the most uniform two-dimensional point sets for a given sample size, thereby achieving maximum variance reduction. In practice, GLPM is applied to generate samples in the first two-dimensional subspace. Remaining two-dimensional subspaces are randomly permuted, and high-dimensional samples are assembled via random pairing. Finally, the inverse CDF transformation maps uniform high-dimensional samples into the physical space of the target parameters:

$$\theta^{(i)} = F_{\boldsymbol{\Theta}}^{-1}(u^{(i)}), \quad i = 1, 2, \ldots, N \tag{3}$$

where $u^{(i)}$ are samples from the uniform distribution on $[0, 1]$, N is the sample size, and $F_{\boldsymbol{\Theta}}^{-1}$ is the inverse CDF of the parameters $\boldsymbol{\Theta}$.

The high-dimensional parameter samples generated by GLPM-PSS are subsequently used in reliability analysis methods—such as the first-order reliability method (FORM), second-order reliability method (SORM), simulation-based approaches, high-order moment methods or surrogate models to obtain the corresponding CFP samples.

3.2. Selection of a Suitable Distribution Model for CFP

To obtain an accurate analytical expression of the CFP distribution, it is necessary to construct a parametric model with sufficient flexibility and adaptability. Common parametric models include the Pearson system (Pearson et al., 1979), Hermite model (Winterstein, 1988), saddle point approximation (Daniels, 1954), among others. However, these models often exhibit limited flexibility and are generally suited only for unimodal distributions, making them less effective in capturing complex multimodal or heavy-tailed behaviors.

Since the CFP is bounded between 0 and 1, the beta distribution naturally provides a suitable support. A single beta distribution with shape parameters α and β has the PDF:

$$f(X;\alpha,\beta) = \frac{\Gamma(\alpha+\beta)}{\Gamma(\alpha)\Gamma(\beta)}\, X^{\alpha-1}(1-X)^{\beta-1}, \quad 0 \le X \le 1, \tag{4}$$

and the corresponding CDF is

$$F(X;\alpha,\beta) = \int_0^x f(t;\alpha,\beta)\, dt \tag{5}$$

where $\Gamma(\cdot)$ is the Gamma function. By adjusting α and β, the beta distribution can represent a wide variety of shapes, including symmetric, left- or right-skewed, U-shaped, or bell-shaped distributions.

However, in practice, CFP distributions can exhibit long tails or even multimodal behavior, which a single beta distribution cannot fully capture. To accommodate these features, a beta mixture distribution with K components is adopted. Its PDF is expressed as

$$f_{P_f}(p) = \sum_{k=1}^{K} w_k\, f(p;\alpha_k,\beta_k), \quad 0 \le p \le 1, \tag{6}$$

where w_k denotes the weight of the k-th component $\sum_{k=1}^{K} w_k = 1$, K is the number of mixture components, and α_k, β_k are the shape parameters of that component. The corresponding CDF is given by

$$F_{P_f}(p) = \sum_{k=1}^{K} w_k\, F(p;\alpha_k,\beta_k). \tag{7}$$

The mean of the beta mixture distribution is given by

$$\mathbb{E}[P_f] = \sum_{k=1}^{K} w_k\, \frac{\alpha_k}{\alpha_k+\beta_k}, \tag{8}$$

and its variance can be computed as

$$\mathrm{Var}[P_f] = \sum_{k=1}^{K} w_k \frac{\alpha_k\beta_k}{(\alpha_k+\beta_k)^2(\alpha_k+\beta_k+1)} + \sum_{k=1}^{K} w_k \left(\frac{\alpha_k}{\alpha_k+\beta_k}\right)^2 - \mathrm{E}[P_f]^2. \tag{9}$$

The beta mixture model provides a flexible and explicit representation of the CFP distribution, capable of capturing skewness, heavy tails, and multimodality. This explicit representation facilitates subsequent risk quantification and reliability analysis.

3.3. Bayesian Estimation of Beta Mixture Model Parameters

In this study, a beta mixture distribution with two components is adopted to model the CFP, achieving a balance between flexibility and computational efficiency. For high-dimensional problems, traditional moment-based methods often require a large number of samples, which can be computationally expensive. In contrast, Bayesian estimation provides robust and reliable parameter estimates even with a limited number of samples, by combining prior knowledge with observed sample data.

To improve estimation stability, Bayesian inference is adopted, treating the shape parameters as random variables. For the two-component beta mixture distribution, the four shape parameters are denoted as $\boldsymbol{\phi} = (\alpha_1, \beta_1, \alpha_2, \beta_2)$ and a non-informative prior is assigned:

$$\pi_0(\boldsymbol{\phi}) \propto 1, \quad \alpha_1, \beta_1, \alpha_2, \beta_2 > 0. \tag{10}$$

To simplify the estimation and reduce the parameter dimension, the mixture weight of the first component is fixed at $w_1 = 0.7$, and the weight of the second component is determined as $w_2 = 1 - w_1$. This allows stable estimation of the shape parameters while maintaining the flexibility of the beta mixture model.

Let $\{p_i\}_{i=1}^N$ denote the CFP samples generated using the GLPM-PSS sampling method (Section 3.1) combined with reliability analysis techniques. The likelihood function for the beta mixture model is

$$L(\{p_i\} \mid \boldsymbol{\phi}) = \prod_{i=1}^{N} f_{P_f}(p_i \mid \boldsymbol{\phi}), \tag{11}$$

where $f_{P_f}(\cdot \mid \boldsymbol{\phi})$ is the PDF of the beta mixture distribution Eq. 6.

According to Bayes' theorem, the posterior distribution of the shape parameters is

$$\pi(\boldsymbol{\phi} \mid \{p_i\}) = \frac{L(\{p_i\} \mid \boldsymbol{\phi})\, \pi_0(\boldsymbol{\phi})}{\int L(\{p_i\} \mid \boldsymbol{\phi})\, \pi_0(\boldsymbol{\phi})\, d\boldsymbol{\phi}}. \tag{12}$$

The Bayesian estimate of the parameters is typically taken as the posterior mean:

$$\hat{\boldsymbol{\phi}} = \mathbb{E}[\boldsymbol{\phi} \mid \{p_i\}] = \int \boldsymbol{\phi}\, \pi(\boldsymbol{\phi} \mid \{p_i\})\, d\boldsymbol{\phi}. \tag{13}$$

Since this integral is generally intractable analytically, Markov Chain Monte Carlo (MCMC) methods Gibbs sampling (Geman and Geman, 1984; Zhao et al., 2025) is employed to generate posterior samples. The posterior mean is then approximated by the sample average:

$$\hat{\boldsymbol{\phi}} \approx \frac{1}{N_G} \sum_{i=1}^{N_G} \boldsymbol{\phi}^{(i)}, \tag{14}$$

where N_G is the total number of posterior samples, and $\boldsymbol{\phi}^{(i)}$ is the i-th sample.

This Bayesian estimation framework with fixed mixture weight ensures stable and reliable determination of the beta nixture shape parameters, even when the number of CFP samples is

limited. With the estimated parameters, the beta mixture model can be used for CFP distribution representation and high-dimensional reliability analysis.

4. Numerical examples

4.1. Example 1: bimodal distributions

In this example, the performance function is considered:

$$G(\boldsymbol{X}) = 30\sqrt{2} + \sum_{i=1}^{200} X_i - 165 \tag{15}$$

The random variables are assumed to be mutually independent, and each variable follows a normal distribution with an unknown mean and unit standard deviation. The means are modeled using a Gaussian mixture distribution with two components (means of -10 and -3, standard deviations of 0.5, and weights of 0.7 and 0.3), while the remaining variables have means equal to 1 and variance 0.1.

Since $G(\boldsymbol{X})$ isa linear combination of independent normal random variables, the resulting response Z also follows a normal distribution. Its mean and variance can be explicitly obtained as $\mu_Z = a\sqrt{d} + \sum_{i=1}^{d} \mu_{X_i} - 165$, $\sigma_Z = \sqrt{\sum_{i=1}^{d} \sigma_i^2} = \sqrt{d}$. Accordingly, the reliability index and the failure probability can be expressed as

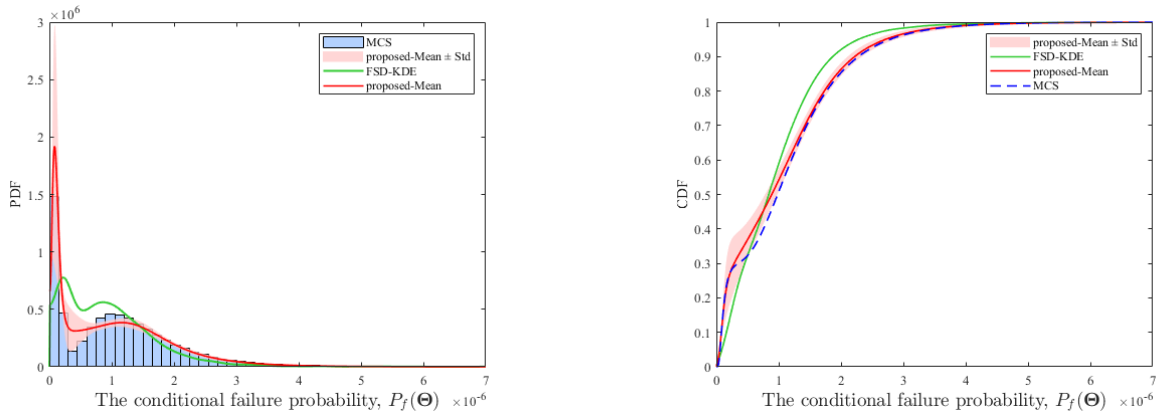
$$\beta = \frac{\mu_Z}{\sigma_Z} = \frac{a\sqrt{d} + \sum_{i=1}^{d} \mu_{X_i} - 165}{\sqrt{d}} \tag{16}$$

$$P_f = \Phi(-\beta) \tag{17}$$

where $\Phi(\cdot)$ denotes the CDF of the standard normal distribution.

For each realization of the mean vector, the failure probability is evaluated using Eqs. 16 and 17, yielding samples of the CFP. Based on these CFP samples, the proposed method is then employed to estimate the distribution of the failure probability. Fig. 1 illustrates the estimated PDF and CDF of the CFP based on 20 independent runs, together with the results obtained by the FSD-KDE approach and the reference solution from MCS with 10^8 samples. The results show that the proposed method is able to reproduce the bimodal nature of the CFP distribution more effectively than FSD-KDE. In particular, the estimated PDF aligns well with the MCS histogram, accurately capturing the locations of the peaks, while the corresponding CDF closely follows the empirical curve obtained from MCS. Furthermore, the PDFs obtained from repeated runs exhibit only minor variability, and the CDFs are nearly indistinguishable, indicating good stability and consistency of the proposed method.

Table I summarizes the mean, standard deviation, and the 0.75 and 0.90 quantiles of the CFP estimated by the proposed method and FSD-KDE, in comparison with the MCS results. It can be observed that the proposed method yields relative errors generally below 5%, demonstrating



(a) PDF (b) CDF

Figure 1. Histogram with PDF and CDF of $P_f(\boldsymbol{\Theta})$ in Example 1.

Table I. Summary of some statistical values of CFP in Example 1.

Method	Mean of $P_f(\boldsymbol{\Theta})$	Std of $P_f(\boldsymbol{\Theta})$	75% quantile of $P_f(\boldsymbol{\Theta})$	90% quantile of $P_f(\boldsymbol{\Theta})$	N
MCS	1.086×10^{-6}	9.311×10^{-7}	1.594×10^{-6}	2.280×10^{-6}	10^8
The proposed method	1.069×10^{-6}	9.135×10^{-7}	1.613×10^{-6}	2.268×10^{-6}	377
	(1.565%, 0.026)	(1.890%, 0.039)	(1.192%, 0.035)	(0.526%, 0.038)	
FSD-KDE (Leng et al., 2025)	9.521×10^{-7}	7.410×10^{-7}	1.330×10^{-6}	1.855×10^{-6}	10^4
	(12.330%)	(20.417%)	(16.562%)	(18.640%)	
Zhao et al. (Zhao et al., 2018)	-	-	-	-	-

Note: Std denotes the standard deviation of the CFP, and N is the number of CFP samples. The the proposed method results are averaged over 20 independent runs. Values in parentheses denote the mean relative error with respect to MCS and the corresponding coefficient of variation (CoV).

improved accuracy over FSD-KDE. In addition, the corresponding coefficients of variation (CoV) remain at a low level, further confirming the robustness of the proposed method in handling bimodal distributions. It is also noted that the method proposed in Ref. (Zhao et al., 2018) is not applicable in this case due to its inability to capture bimodal behavior.

4.2. Example 2: A finite-element frame structure

The second example considers a five-story three-span portal steel frame structure subjected to lateral loads, as shown in Fig. 2, and has been studied in previous work (Blatman and Sudret, 2010; Wei and Rahman, 2007). Here, 21 random variables are defined as follows:

$$\boldsymbol{X} = [P_1, P_2, P_3, E_1, E_2, I_1, I_2, I_3, I_4, I_5, I_6, I_7, I_8, A_1, A_2, A_3, A_4, A_5, A_6, A_7, A_8] \tag{18}$$

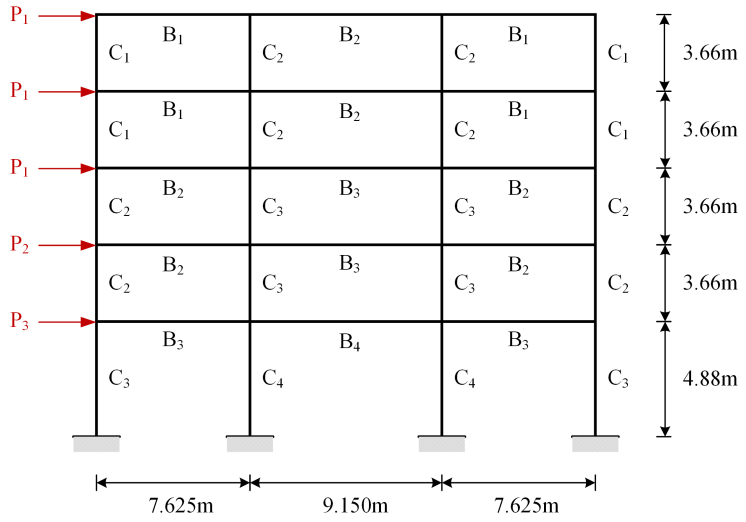


Figure 2. Five-story three-span frame

Table II. Properties of the frame element.

Element	Young's Modulus	Inertia moment	Cross-section area
B_1	E_1	I_5	A_5
B_2	E_1	I_6	A_6
B_3	E_1	I_7	A_7
B_4	E_1	I_8	A_8
C_1	E_2	I_1	A_1
C_2	E_2	I_2	A_2
C_3	E_2	I_3	A_3
C_4	E_2	I_4	A_4

These variables in the formula are assumed to be mutually independent. Since incomplete knowledge of the distributions of random variables is common in practical engineering, this example further accounts for distribution parameter uncertainty, in which both the means and standard deviations of the random variables are treated as random variables. The structural data and random variables statistical properties are shown in Tables II and III, respectively. In this study, for practical considerations, the lateral load is assumed to follow a lognormal distribution, whereas the material properties are modeled using a truncated normal distribution over the range $(0, +\infty)$ as suggested by Blatman and Sudret (Blatman and Sudret, 2010), as negative values for material properties are meaningless.

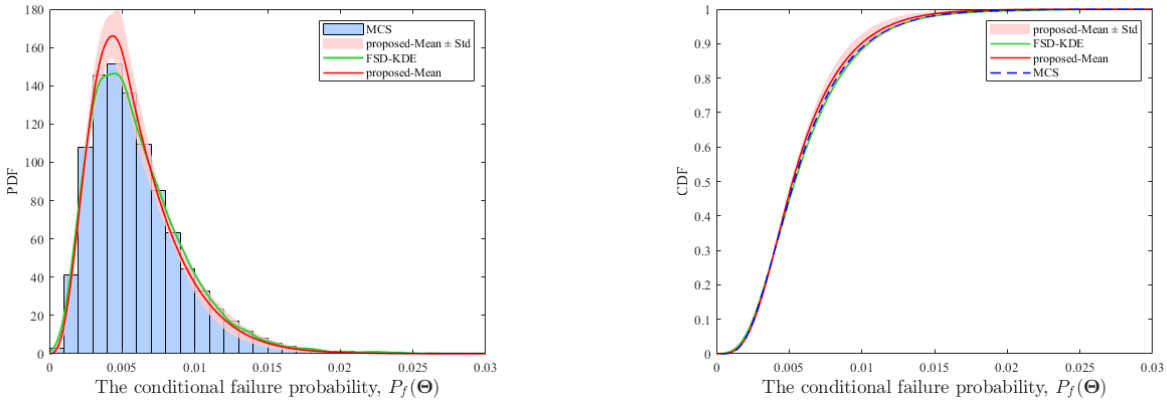
Similarly, 377 samples of the distribution parameters were generated using GLPM-PSS, and the corresponding 377 CFP samples were obtained via Subset Simulation. Based on the proposed

Table III. Distribution statistical characteristics of the random variables in Example 2.

Parameters	Distribution	Mean Value	Standard Deviation
P_1 (kN)	Lognormal	LN(133.454, 6.673)	LN(40.040, 2.002)
P_2 (kN)	Lognormal	LN(88.970, 4.449)	LN(35.590, 1.780)
P_3 (kN)	Lognormal	LN(71.175, 3.559)	LN(28.470, 1.424)
E_1 (kN/m^2)	Truncated normal $(0, +\infty)$	LN(2.174×10^7, 1.087×10^6)	LN(1.915×10^7, 9.576×10^4)
E_2 (kN/m^2)	Truncated normal $(0, +\infty)$	LN(2.380×10^7, 1.190×10^6)	LN(1.915×10^7, 9.576×10^4)
I_1 (m^4)	Truncated normal $(0, +\infty)$	LN(0.008, 4.050×10^{-4})	LN(0.001, 5.500×10^{-5})
I_2 (m^4)	Truncated normal $(0, +\infty)$	LN(0.012, 5.750×10^{-4})	LN(0.001, 6.500×10^{-5})
I_3 (m^4)	Truncated normal $(0, +\infty)$	LN(0.021, 1.100×10^{-3})	LN(0.003, 1.300×10^{-4})
I_4 (m^4)	Truncated normal $(0, +\infty)$	LN(0.026, 1.300×10^{-3})	LN(0.003, 1.500×10^{-4})
I_5 (m^4)	Truncated normal $(0, +\infty)$	LN(0.011, 5.400×10^{-4})	LN(0.003, 1.300×10^{-4})
I_6 (m^4)	Truncated normal $(0, +\infty)$	LN(0.014, 7.050×10^{-4})	LN(0.004, 1.500×10^{-4})
I_7 (m^4)	Truncated normal $(0, +\infty)$	LN(0.023, 1.200×10^{-3})	LN(0.006, 2.800×10^{-4})
I_8 (m^4)	Truncated normal $(0, +\infty)$	LN(0.026, 1.300×10^{-3})	LN(0.007, 3.250×10^{-4})
A_1 (m^2)	Truncated normal $(0, +\infty)$	LN(0.313, 1.565×10^{-2})	LN(0.056, 2.800×10^{-3})
A_2 (m^2)	Truncated normal $(0, +\infty)$	LN(0.372, 1.860×10^{-2})	LN(0.074, 3.700×10^{-3})
A_3 (m^2)	Truncated normal $(0, +\infty)$	LN(0.506, 2.530×10^{-2})	LN(0.093, 4.700×10^{-3})
A_4 (m^2)	Truncated normal $(0, +\infty)$	LN(0.558, 2.790×10^{-2})	LN(0.112, 5.600×10^{-3})
A_5 (m^2)	Truncated normal $(0, +\infty)$	LN(0.253, 1.270×10^{-2})	LN(0.093, 4.700×10^{-3})
A_6 (m^2)	Truncated normal $(0, +\infty)$	LN(0.291, 1.460×10^{-2})	LN(0.102, 5.100×10^{-3})
A_7 (m^2)	Truncated normal $(0, +\infty)$	LN(0.373, 1.870×10^{-2})	LN(0.121, 6.000×10^{-3})
A_8 (m^2)	Truncated normal $(0, +\infty)$	LN(0.419, 2.090×10^{-2})	LN(0.195, 9.800×10^{-3})

method, the PDF and CDF of the CFP were then constructed. Fig. 3 compares the histogram and empirical CDF obtained from 10^5 MCS samples with the results estimated by the proposed method and FSD-KDE. It can be observed that both the proposed method and FSD-KDE provide good agreement with MCS and successfully capture the main characteristics of the CFP distribution. In contrast, the method in Ref. (Zhao et al., 2018) only estimates the conditional reliability index and therefore does not directly provide the full distribution of CFP for comparison.

Table IV further summarizes the mean, standard deviation, and the 75% and 90% quantiles of the CFP obtained by different methods. The results indicate that the proposed method and FSD-KDE achieve relative errors within approximately 10%, while noticeable discrepancies are observed for the method of Zhao et al. (Zhao et al., 2018).



(a) PDF (b) CDF

Figure 3. Histogram with PDF and CDF of $P_f(\boldsymbol{\Theta})$ in Example 2.

Table IV. Summary of some statistical values of CFP in Example 2.

Method	Mean of $P_f(\boldsymbol{\Theta})$	Std of $P_f(\boldsymbol{\Theta})$	75% quantile of $P_f(\boldsymbol{\Theta})$	90% quantile of $P_f(\boldsymbol{\Theta})$	N
MCS	6.025×10^{-3}	3.292×10^{-3}	7.610×10^{-3}	1.034×10^{-2}	10^5
the proposed method	5.869×10^{-3}	3.051×10^{-3}	7.428×10^{-3}	9.977×10^{-3}	377
	(2.589%, 0.035)	(7.321%, 0.110)	(2.392%, 0.044)	(3.511%, 0.070)	
FSD-KDE (Leng et al., 2025)	6.078×10^{-3}	3.379×10^{-3}	7.739×10^{-3}	1.040×10^{-2}	10^4
	(0.880%)	(2.643%)	(1.695%)	(0.580%)	
Zhao et al. (Zhao et al., 2018)	2.559×10^{-3}	1.700×10^{-3}	3.325×10^{-3}	4.736×10^{-3}	42484

5. Concluding Remarks

This paper develops an efficient and robust approach for high-dimensional reliability analysis under hybrid uncertainty. The proposed method directly fits the CFP distribution and explicitly constructs its PDF and CDF, which facilitates risk quantification and reliability evaluation.

Numerical results show that the proposed method maintains accuracy comparable to the classic Monte Carlo simulation (MCS), but only needs a very small number of CFP samples. The scheme greatly reduces the computational burden.

Bayesian inference is used to estimate parameters of the beta mixture model. Combined with beta mixture modeling, the method can effectively capture complex CFP characteristics such as multimodality and skewness, which widely exist in practical engineering problems.

Moreover, the proposed method exhibits broad applicability under high-dimensional parameter uncertainty. It performs effectively for the tested cases, including bimodal CFP distributions and finite-element frame structures with high-dimensional parameter uncertainty.

Despite the above merits, the required number of CFP samples may increase considerably for ultra-high-dimensional problems with thousands of dimensions. In addition, the current framework adopts a two-level sampling scheme, resulting in relatively high computational overhead. Future research will focus on decoupling the nested computational structure to further improve computational efficiency.

Acknowledgements

The authors gratefully acknowledge the support of the National Key R&D Program of China (2023YFC3009300, 2023YFC3009302).

References

Ang, A.-S. and D. De Leon: 2005, 'Modeling and analysis of uncertainties for risk-informed decisions in infrastructures engineering'. *Structure and Infrastructure Engineering* **1**(1), 19–31.

Blatman, G. and B. Sudret: 2010, 'An adaptive algorithm to build up sparse polynomial chaos expansions for stochastic finite element analysis'. *Probabilistic Engineering Mechanics* **25**(2), 183–197.

Chen, J. and Z. Wan: 2019, 'A compatible probabilistic framework for quantification of simultaneous aleatory and epistemic uncertainty of basic parameters of structures by synthesizing the change of measure and change of random variables'. *Structural Safety* **78**, 76–87.

Daniels, H. E.: 1954, 'Saddlepoint approximations in statistics'. *The Annals of Mathematical Statistics* pp. 631–650.

Der Kiureghian, A.: 2008, 'Analysis of structural reliability under parameter uncertainties'. *Probabilistic Engineering Mechanics* **23**(4), 351–358.

Der Kiureghian, A. and O. Ditlevsen: 2009, 'Aleatory or epistemic? Does it matter?'. *Structural Safety* **31**(2), 105–112.

Faes, M. G., M. Daub, S. Marelli, E. Patelli, and M. Beer: 2021, 'Engineering analysis with probability boxes: A review on computational methods'. *Structural Safety* **93**, 102092.

Geman, S. and D. Geman: 1984, 'Stochastic relaxation, Gibbs distributions, and the Bayesian restoration of images'. *IEEE Transactions on pattern analysis and machine intelligence* **PAMI-6**(6), 721–741.

Hoffman, F. O. and J. S. Hammonds: 1994, 'Propagation of uncertainty in risk assessments: the need to distinguish between uncertainty due to lack of knowledge and uncertainty due to variability'. *Risk analysis* **14**(5), 707–712.

Hong, H.-P.: 1996, 'Evaluation of the probability of failure with uncertain distribution parameters'. *Civil Engineering Systems* **13**(2), 157–168.

Kiureghian, A. D.: 1989, 'Measures of structural safety under imperfect states of knowledge'. *Journal of Structural Engineering* **115**(5), 1119–1140.

Leng, Y., Y.-H. Fei, Y.-B. Jiang, L. Wang, and C.-H. Cai: 2025, 'Fixed sampling distribution determination method for structural reliability assessment with parameter uncertainty'. *Applied Mathematical Modelling* p. 116191.

Li, P.-P., Z.-H. Lu, and Y.-G. Zhao: 2022a, 'An effective and efficient method for structural reliability considering the distributional parametric uncertainty'. *Applied Mathematical Modelling* **106**, 507–523.

Li, P.-P., M. A. Valdebenito, C. Dang, M. Beer, and M. G. Faes: 2025, 'Aleatory and epistemic uncertainty in reliability analysis: An engineering perspective'. *Structural Safety* p. 102666.

Li, P.-P., Y.-G. Zhao, and Z. Zhao: 2022b, 'Efficient method for fully quantifying the uncertainty of failure probability'. *Computer Methods in Applied Mechanics and Engineering* **399**, 115345.

Möller, B. and M. Beer: 2013, *Fuzzy randomness: uncertainty in civil engineering and computational mechanics*. Springer Science & Business Media.

Pearson, E. S., N. L. Johnson, and I. W. Burr: 1979, 'Comparisons of the Percentage Points of Distributions with the Same First Four Moments, Chosen from Eight Different Systems of Frequency Curves'. *Communications in Statistics-Simulation and Computation* **8**(3), 191–229.

Shields, M. D., K. Teferra, A. Hapij, and R. P. Daddazio: 2015, 'Refined stratified sampling for efficient Monte Carlo based uncertainty quantification'. *Reliability Engineering & System Safety* **142**, 310–325.

Shields, M. D. and J. Zhang: 2016, 'The generalization of Latin hypercube sampling'. *Reliability Engineering & System Safety* **148**, 96–108.

Wei, D. and S. Rahman: 2007, 'Structural reliability analysis by univariate decomposition and numerical integration'. *Probabilistic Engineering Mechanics* **22**(1), 27–38.

Winterstein, S. R.: 1988, 'Nonlinear vibration models for extremes and fatigue'. *Journal of Engineering Mechanics* **114**(10), 1772–1790.

Xu, J. and C. Dang: 2019, 'A novel fractional moments-based maximum entropy method for high-dimensional reliability analysis'. *Applied Mathematical Modelling* **75**, 749–768.

Yang, L.-C., C.-X. Wang, C.-Y. Ling, and M. Xie: 2023, 'Reliability evaluation of an imprecise multistate system with mixed uncertainty'. *IEEE Transactions on Reliability* **73**(1), 478–491.

Zhao, Y.-G. and J.-R. Jiang: 1992, 'An Advanced First Order Second Monment Method'. *Earthquake Engineering and Engineering Vibration* **12**(4), 49–57. in Chinese.

Zhao, Y.-G., P.-P. Li, and Z.-H. Lu: 2018, 'Efficient evaluation of structural reliability under imperfect knowledge about probability distributions'. *Reliability Engineering & System Safety* **175**, 160–170.

Zhao, Y.-G., Y.-T. Liu, P.-P. Li, Y.-Y. Weng, M. A. Valdebenito, and M. G. Faes: 2025, 'A Bayesian piecewise fitting method for estimating probability distributions of performance functions'. *Reliability Engineering & System Safety* p. 111266.

Zhao, Y.-G. and Z.-H. Lu: 2021, *Structural reliability: approaches from perspectives of statistical moments*. John Wiley & Sons.

A Bivariate Distribution Based on Squared Normal Transformation

Lan-Xin Li, Xuan-Yi Zhang*, and Yan-Gang Zhao
National Key Laboratory of Bridge Safety and Resilience, Beijing University of Technology, Beijing 100124, China lilanxin_evana@emails.bjut.edu.cn
National Key Laboratory of Bridge Safety and Resilience, Beijing University of Technology, Beijing 100124, China zhangxuanyi@bjut.edu.cn
National Key Laboratory of Bridge Safety and Resilience, Beijing University of Technology, Beijing 100124, China zhaoyg@bjut.edu.cn

Abstract. Modeling non-Gaussian dependent random variables remains challenging in structural reliability analysis. This study proposes a bivariate squared normal (BSN) distribution based on the squared normal transformation (SNT). The joint cumulative distribution function (JCDF) is constructed by decomposing the probability into marginal distributions and a dependence function, both modeled using SNT. A power transformation with an optimized parameter is introduced to align the kurtosis of the transformed variable with that of a squared normal reference distribution, improving accuracy for strongly non-Gaussian cases. The joint probability density function (JPDF) is obtained by applying a central difference scheme to the JCDF. Validation against typical bivariate distributions, including classical and copula-based models, shows that the BSN distribution achieves high JCDF accuracy and acceptable JPDF accuracy, demonstrating strong flexibility and robustness across diverse dependence structures.

Keywords: Bivariate probability distribution; Squared normal transformation; Bivariate squared normal distribution; Non-Gaussian marginal, non-Gaussian dependency

1. Introduction

Probability distributions are essential in civil engineering for structural reliability analysis, risk assessment, and performance-based design (Li et al., 2019). Many engineering problems involve dependent non-Gaussian random variables, making bivariate probability distributions (BPDs) a necessary foundation for higher-dimensional modeling (Sklar, 1973).

Existing BPD construction methods fall into two categories: parameter-based and dependence-function-based (Tang et al., 2013). Parameter-based distributions (e.g., bivariate normal, lognormal, Gumbel (Gumbel, 1960), Weibull (Weibull, 1951)) are mathematically tractable but often require identical marginal types, limiting their flexibility (Zentner, 2017). Dependence-function-based models, particularly copulas, allow arbitrary marginals but require time-consuming selection of both marginals and dependence functions (Tang et al., 2015; Wang and Li, 2018; Goda, 2010; Durante and Jaworski, 2010).

* Corresponding author

© 2026 by the author(s). This work is licensed under the Creative Commons Attribution 4.0 International License (CC BY 4.0), which permits unrestricted use, distribution, and reproduction in any medium, provided the original author and source are credited.

Moment-based transformation methods construct probability distributions directly from statistical moments. Li et al. (Li et al., 2025) proposed a bivariate cubic normal (BCN) distribution, where both marginal and dependence structures are modeled using a cubic normal transformation based on the first four moments and mixed moments. While flexible, this approach suffers from high computational cost.

To address these issues, this paper adopts the squared normal transformation (SNT) proposed by Zhao and Ono (Zhao and Ono, 2000) and further simplified by Qin et al. (Qin et al., 2020). The SNT requires only the first three marginal moments (mean, standard deviation, skewness) while still incorporating mixed moments for dependence modeling. This reduces moment requirements, simplifies computation, improves numerical stability with smaller samples, and preserves variable interpretability. Based on this, we propose a bivariate squared normal (BSN) distribution. The joint CDF is constructed using probability decomposition, with marginals and dependence both modeled by SNT. A power transformation with an optimized parameter handles strong non-Gaussian dependence by aligning the transformed variable with the SNT distributional form. The joint PDF is obtained using central difference of the JCDF.

The main contributions are: (1) a bivariate distribution model based on first three marginal moments with mixed-moment dependence modeling; (2) a transformation-based strategy to improve non-Gaussian robustness; (3) numerical implementation of the JPDF using central difference; and (4) validation on representative bivariate distributions.

2. Construction of bivariate squared normal distribution

Without loss of generality, a two-dimensional vector $[X, Y]$ is investigated, where X and Y are two random variables existing within a sample space S. For any x and $y \in \mathbb{R}$, where $\mathbb{R}$ represents the real numbers field, the JCDF of the BPD is defined as the following probability:

$$F(x, y) = \Pr[(X \leq x) \cap (Y \leq y)], \tag{1}$$

Based on probability theory, Eq. 1 can be expanded as (Li et al., 2025):

$$F(x, y) = \frac{1}{2}\left[F_1(x) + F_2(y) - \delta(x, y)\right], \tag{2}$$

where $F_1(\cdot)$ and $F_2(\cdot)$ are the marginal CDFs of X and Y, and $\delta(x, y)$ is the dependence function defined as:

$$\delta(x, y) = \Pr[(X - x)(Y - y) \leq 0]. \tag{3}$$

Eq. 2 is a probability identity that holds for any bivariate distribution. Based on this decomposition, the construction of JCDF includes two primary objectives: (1) modeling the marginal distributions $F_1(x)$ and $F_2(y)$; and (2) evaluating the dependence function $\delta(x, y)$. These two objectives are discussed in the following subsections.

2.1. Model of the marginal distributions

When marginal distributions are unknown, the squared normal transformation (SNT) based on the first three moments is employed (Zhao and Ono, 2000; Qin et al., 2020). For a random variable ψ with moments $\Theta = \{\mu, \sigma, \alpha_3\}$, its CDF is:

$$F(\psi) = \Phi\left[u(\psi, \Theta)\right], \tag{4}$$

where $\Phi(\cdot)$ is the cumulative distribution function (CDF) of a standard normal random variable; $\Theta_i = \{\mu_i, \sigma_i, \alpha_{3i}\}$ represents the first three moments of the i-th random variable, with $i = 1$ and 2 representing X and Y, respectively: μ_i is the mean, σ_i is the standard deviation, α_{3i} is the skewness; and $u(\cdot, \cdot)$ is the squared normal transformation function, which maps the standardized random variable to a standard normal variable through a quadratic polynomial (Qin et al., 2020).

The standardized variable $x_s = (\psi - \mu_i)/\sigma_i$ is expressed as a quadratic function of a standard normal variable u:

$$x_s = a_{1i} + a_{2i}u + a_{3i}u^2, \tag{5}$$

Following the simplified third-moment normal transformation (Qin et al., 2020), the coefficients are expressed as explicit functions of the skewness α_{3i}:

$$a_{3i} = \frac{\sqrt{3}}{10}\alpha_{3i}, \quad a_{2i} = 1 - \frac{\sqrt{3}}{50}\alpha_{3i}^2, \quad a_{1i} = -a_{3i}. \tag{6}$$

The inverse transformation (from x_s to u) is obtained by solving the quadratic equation:

$$u = \frac{-a_{2i} + \sqrt{a_{2i}^2 - 4a_{3i}(a_{1i} - x_s)}}{2a_{3i}}, \quad \alpha_{3i} \neq 0. \tag{7}$$

When the skewness $\alpha_{3i} = 0$, Eq. 7 simplifies to $u = x_s$, which is consistent with the standard normal transformation. A key advantage of SNT is that it requires only the first three moments, avoiding the need for kurtosis, while providing an explicit polynomial form that is computationally efficient and numerically stable. The applicable range of the simplified SNT is $|\alpha_{3i}| \leq 2$, which covers most engineering applications.

2.2. Evaluation of the dependence function

Treating $G(X, Y) = (X - x)(Y - y)$ as a random variable Z, the dependence function is $\delta(x, y) = F_Z(0)$. Using the method of moments (Zhao and Lu, 2021), combined with the SNT framework, Z is approximated by the squared normal transformation, yielding:

$$\delta(x, y) = \Phi\left[u(0, \Theta_Z)\right], \tag{8}$$

where $\Theta_Z = \{\mu_Z, \sigma_Z, \alpha_{3Z}\}$ are the first three moments of Z, computed as:

$$\mu_Z = E[XY] - xE[Y] - yE[X] + xy, \tag{9}$$

$$\sigma_Z = \sqrt{E[(Z-\mu_Z)^2]}, \tag{10}$$

$$\alpha_{3Z} = \frac{E[(Z-\mu_Z)^3]}{\sigma_Z^3}. \tag{11}$$

These expectations involve mixture moments of X and Y.

Typically, $G(X,Y)$ exhibits strong non-Gaussian behavior and the accuracy of existing distribution models is insufficient. To obtain an appropriate estimation for the strong non-Gaussian case, a power transformation is introduced. Let

$$\tilde{G}(X,Y) = \mathrm{sgn}(G)\cdot|G|^q, \quad (q>0), \tag{12}$$

where $\mathrm{sgn}(\cdot)$ denotes the sign function. This transformation preserves the sign of G while adjusting its kurtosis to match that of a squared normal reference distribution when q is appropriately chosen.

To determine the optimal q, we first construct a reference distribution for Z using the squared normal transformation based solely on its first three moments Θ_Z. From this reference distribution, the target kurtosis κ_{target} is computed using Gauss-Hermite quadrature (Abramowitz and Stegun, 1964). Specifically, let u_i and w_i be the nodes and weights of the Gauss-Hermite quadrature, and obtain the corresponding samples of the standardized variable using the inverse SNT:

$$z_i = u_{SNT}^{-1}(u_i;\Theta_Z), \tag{13}$$

where $u_{SNT}^{-1}(\cdot;\Theta_Z)$ denotes the inverse squared normal transformation defined in Eq. 7. The target kurtosis is then computed as:

$$\kappa_{target} = \frac{\sum_i w_i(z_i-\mu_Z)^4}{(\sum_i w_i(z_i-\mu_Z)^2)^2}. \tag{14}$$

This target kurtosis represents the fourth-moment characteristic of the distribution that is consistent with the first three moments Θ_Z under the SNT framework.

The optimal power parameter q is then obtained by minimizing the squared difference between the kurtosis of the transformed variable $\tilde{Z}=\tilde{G}(X,Y)$ and this target kurtosis:

$$\min_{q>0}\left(\kappa_{\tilde{Z}}(q)-\kappa_{target}\right)^2, \tag{15}$$

where $\kappa_{\tilde{Z}}(q)$ is the kurtosis of $\tilde{Z}$. This approach, analogous to the Box-Cox transformation in entropy-based fitting, ensures that the transformed variable $\tilde{Z}$ aligns with the reference distribution in terms of kurtosis, while the dependence function $\delta(x,y)$ is subsequently evaluated using the SNT based on the first three moments of $\tilde{Z}$:

$$\delta(x,y) = \Phi\left[u(0,\Theta_{\tilde{Z}})\right]. \tag{16}$$

The optimization in Eq. 15 is a one-dimensional bound-constrained problem ($q>0$), which can be efficiently solved using standard algorithms such as the simplex search method (Mehta

and Chowdhury, 2012). Once the optimal q is determined, the moments $\Theta_{\tilde{Z}} = \{\mu_{\tilde{Z}}, \sigma_{\tilde{Z}}, \alpha_{3\tilde{Z}}\}$ are computed from $\tilde{Z}$, and the dependence function is evaluated using Eq. 16.

2.3. JPDF based on central difference

The joint PDF of the BSN distribution is derived from the JCDF by second-order mixed differentiation:

$$f(x,y) = \frac{\partial^2 F(x,y)}{\partial x \partial y}. \tag{17}$$

Thus, once the JCDF $F(x,y)$ is constructed, the corresponding JPDF can be obtained directly from its mixed partial derivative. Since $F(x,y)$ is evaluated numerically rather than expressed analytically, the mixed partial derivative is approximated using a second-order central difference scheme:

$$f(x_i,y_j) \approx \frac{F_{i+1,j+1} - F_{i+1,j-1} - F_{i-1,j+1} + F_{i-1,j-1}}{4\Delta x \Delta y}, \tag{18}$$

where $F_{i\pm1,j\pm1} = F(x_i \pm \Delta x, y_j \pm \Delta y)$. The step sizes are set as $\Delta x = \epsilon \cdot \sigma_X$, $\Delta y = \epsilon \cdot \sigma_Y$ with $\epsilon = 10^{-3}$ to 10^{-4}.

Since both marginals and dependence are modeled using SNT based only on the first three moments, the proposed model is named the bivariate squared normal (BSN) distribution.

3. Flexibility in data fitting

A flexible distribution should have the capability to approximate commonly used distributions. In this section, the proposed BSN distribution is applied to simulate several commonly used bivariate probability distributions. To balance comprehensiveness and conciseness, three representative distributions are selected: one classical distribution (bivariate normal), one strongly non-Gaussian distribution (bivariate Weibull), and one dependence function-based distribution (BPD with Clayton copula and lognormal marginals).

Four cases are considered as follows:

1. Case 1: $\rho = 0$ and $\{\mu_1, \mu_2, \sigma_1, \sigma_2\} = \{2, 2, 0.05, 0.05\}$
2. Case 2: $\rho = 0$ and $\{\mu_1, \mu_2, \sigma_1, \sigma_2\} = \{2, 2, 0.1, 0.1\}$
3. Case 3: $\rho = 0.5$ and $\{\mu_1, \mu_2, \sigma_1, \sigma_2\} = \{2, 2, 0.05, 0.05\}$
4. Case 4: $\rho = 0.5$ and $\{\mu_1, \mu_2, \sigma_1, \sigma_2\} = \{2, 2, 0.1, 0.1\}$

The parameters of the marginal distributions for different cases are listed in Table I, along with the corresponding mean values and standard deviations.

Table I. Parameters of the marginal distributions of X and Y.

Distribution	X				Y			
	α_x	β_x	μ_1	σ_1	α_y	β_y	μ_2	σ_2
Normal	2	0.05	2	0.05	2	0.05	2	0.05
	2	0.10	2	0.10	2	0.10	2	0.10
Weibull	49.3883	2.0228	2	0.05	49.3883	2.0228	2	0.05
	24.8749	2.0443	2	0.10	24.8749	2.0443	2	0.10
Clayton-Lognormal	0.6928	0.0250	2	0.05	0.6928	0.0250	2	0.05
	0.6919	0.0500	2	0.10	0.6919	0.0500	2	0.10

Table II. Moments of Z and $\tilde{Z}$ with optimal q when $x = 2$ and $y = 2$

Distribution	Case	μ_Z	σ_Z	α_{3Z}	κ_{target}	q	$\mu_{\tilde{Z}}$	$\sigma_{\tilde{Z}}$	$\alpha_{3\tilde{Z}}$	$\alpha_{4\tilde{Z}}$
Normal	1	0	0.0025	0.0004	3.0000	0.5788	0	0.0252	-0.0015	3.0000
	2	0	0.0050	-0.0162	3.0004	0.5791	0	0.0379	-0.0023	3.0004
	3	0.0012	0.0028	2.3207	6.4684	0.7934	0.0186	0.0378	0.1589	6.4684
	4	0.0025	0.0056	2.3350	6.4699	0.7916	0.0263	0.0534	1.3087	6.4699
Weibull	1	0	0.0026	0.8431	4.0210	0.6107	0.0002	0.0199	0.0582	4.0210
	2	0	0.0050	0.6231	3.5841	0.5956	0.0002	0.0339	0.0298	3.5841
	3	0.0012	0.0032	5.1834	3.6247	0.4935	0.0191	0.0390	0.3370	3.6247
	4	0.0025	0.0066	4.4934	4.3084	0.5498	0.0203	0.0418	0.5561	4.4572
Clayton-Lognormal	1	0	0.0025	0.0495	3.0039	0.5766	0	0.0255	0.0035	3.0039
	2	0	0.0050	0.0615	3.0060	0.5748	0	0.0379	0.0033	3.0060
	3	0.0012	0.0029	2.2848	6.4614	0.7807	0.0039	0.0085	1.2022	6.4614
	4	0.0025	0.0057	2.1384	6.4003	0.7973	0.0061	0.0134	1.2021	6.4003

.

Table II lists the moments of Z and $\tilde{Z}$ when $x = 2$ and $y = 2$. After power transformation with the optimal q, the kurtosis $\alpha_{4\tilde{Z}}$ matches the target κ_{target} derived from the SNT reference distribution. The skewness $\alpha_{3\tilde{Z}}$ is also significantly reduced compared to α_{3Z}, confirming that the transformation aligns $\tilde{G}$ with the SNT distributional form.

The goodness-of-fit of the entire distribution is assessed using the root-mean-square error (RMSE) (Chai and Draxler, 2014) and the Kolmogorov-Smirnov (K-S) test (Lopes et al., 2007). For all cases, the K-S test yields $H_0 = 0$ at the 1% confidence level, indicating that the BSN distribution successfully passes the test. The RMSE values for the fitted JCDFs and JPDFs are summarized

in Table III, with corresponding visual comparisons shown in Figs. 1–3 (JCDFs) and Figs. 4–6 (JPDFs). Note that in each figure, subfigures (a)–(d) correspond to Cases 1–4, respectively.

Table III. Fitted RMSE values of common bivariate JCDF and JPDF.

Distribution	JCDF RMSE				JPDF RMSE			
	Case 1	Case 2	Case 3	Case 4	Case 1	Case 2	Case 3	Case 4
Normal	0.0041	0.0055	0.0104	0.0144	2.1579	1.7366	3.7504	2.9466
Weibull	0.0057	0.0070	0.0045	0.0057	3.3169	1.8982	5.3465	3.1334
Clayton-Lognormal	0.0042	0.0058	0.0103	0.0141	2.4515	1.7538	3.3419	2.6549

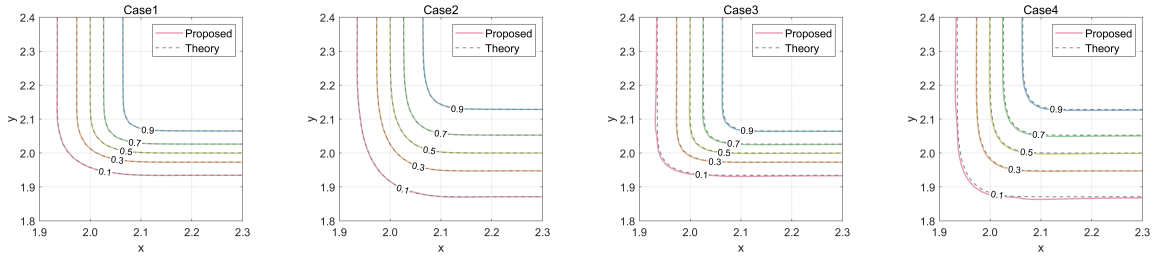


Figure 1. JCDF of bivariate Gaussian distribution.

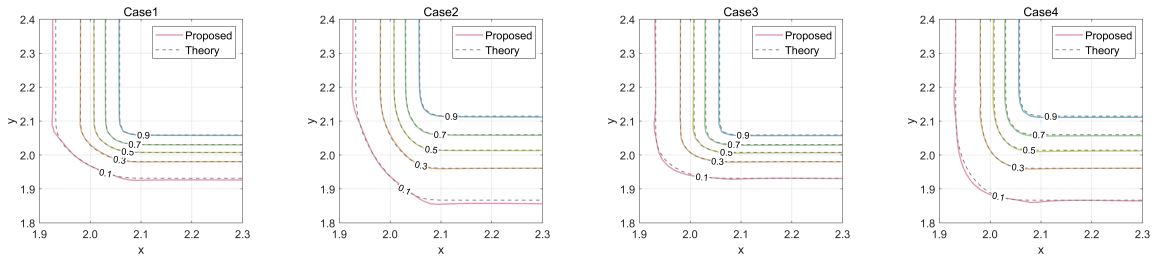


Figure 2. JCDF of bivariate Weibull distribution.

The BSN distribution achieves good JCDF agreement across all cases (RMSE < 0.015) and passes the K-S test at 1%. JPDF RMSE ranges from 1.73 to 5.35. The bivariate Weibull case shows the largest error (5.3465), reflecting the difficulty of density reconstruction for strongly non-Gaussian distributions. The BSN distribution performs acceptably for engineering applications.

4. Conclusion

This study proposes the bivariate squared normal (BSN) distribution for modeling non-Gaussian dependent variables using only the first three moments. The JCDF is constructed via probability

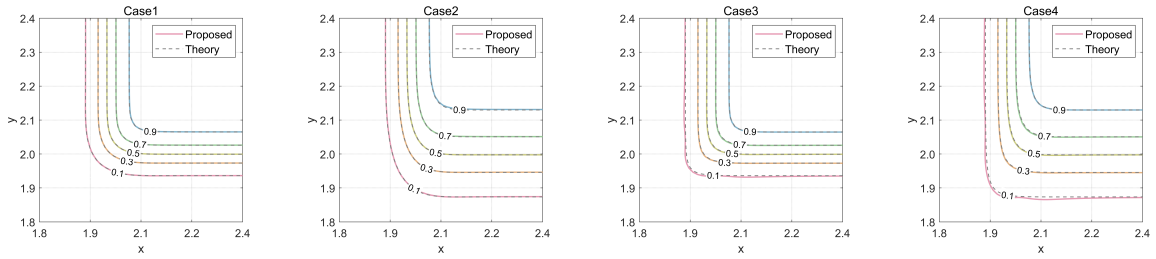


Figure 3. JCDF of bivariate distribution with Clayton copula and lognormal marginal distribution.

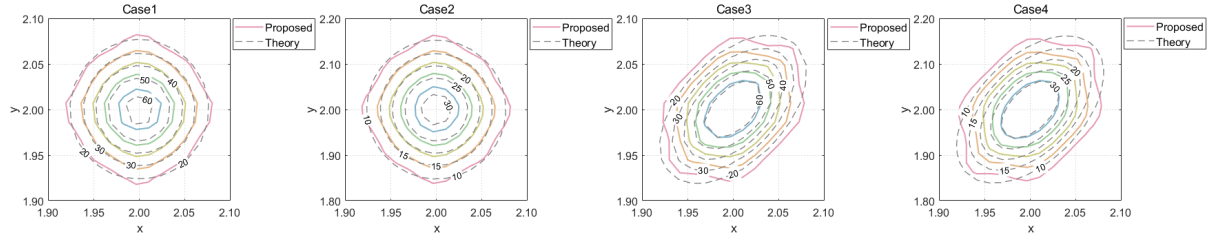


Figure 4. JPDF of bivariate Gaussian distribution.

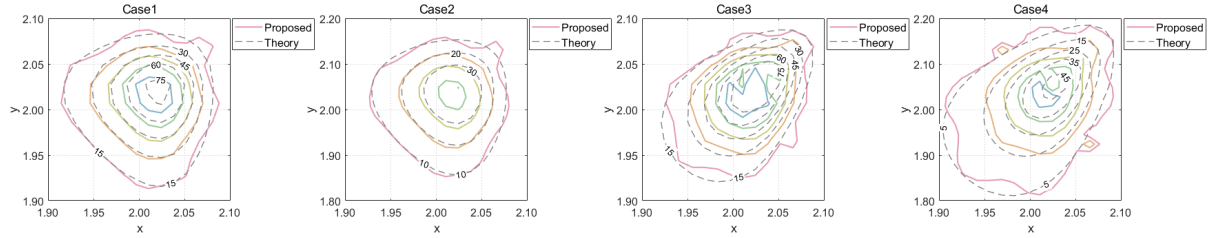


Figure 5. JPDF of bivariate Weibull distribution.

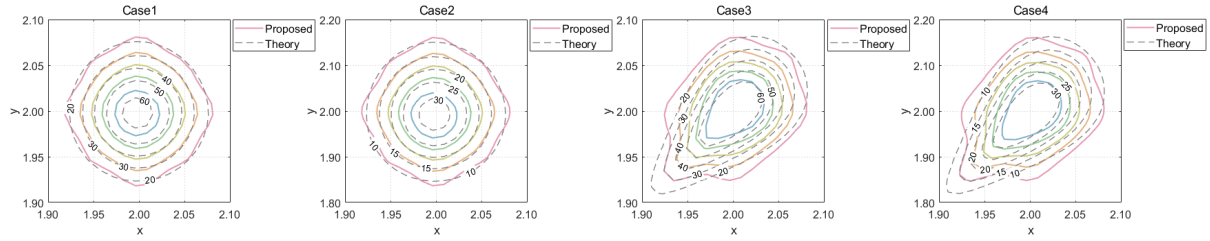


Figure 6. JPDF of bivariate distribution with Clayton copula and lognormal marginal distribution.

decomposition, with a power transformation to align kurtosis for strongly non-Gaussian cases. The JPDF is obtained by central difference.

Validation shows high JCDF accuracy (RMSE 10^{-3}–10^{-2}) and acceptable JPDF accuracy. The BSN distribution is flexible for classical and copula-based cases, offering an efficient approach for bivariate probabilistic modeling. Future work includes improving JPDF estimation and extending to higher dimensions.

Acknowledgements

The authors would like to acknowledge the financial support from the National Key Laboratory of Bridge Safety and Resilience, Beijing University of Technology. The authors also thank the reviewers for their constructive comments that improved the quality of this paper.

References

Abramowitz, M. and I. A. Stegun: 1964, *Handbook of Mathematical Functions with Formulas, Graphs, and Mathematical Tables*. Washington, DC: U.S. Government Printing Office.

Chai, T. and R. R. Draxler: 2014, 'Root mean square error (RMSE) or mean absolute error (MAE)'. *Geoscientific Model Development* **7**(1), 1525–1534.

Durante, F. and P. Jaworski: 2010, 'A new characterization of bivariate copulas'. *Communications in Statistics—Theory and Methods* **39**(16), 2901–2912.

Goda, K.: 2010, 'Statistical modeling of joint probability distribution using copula: Application to peak and permanent displacement seismic demands'. *Structural Safety* **32**(2), 112–123.

Gumbel, E. J.: 1960, 'Bivariate exponential distributions'. *Journal of the American Statistical Association* **55**(292), 698–707.

Li, H.-N., X.-W. Zheng, and C. Li: 2019, 'Copula-based joint distribution analysis of wind speed and direction'. *Journal of Engineering Mechanics* **145**(5), 04019024.

Li, X.-W., X.-Y. Zhang, and Y.-G. Zhao: 2025, 'Bivariate cubic normal distribution for non-Gaussian problems'. *Structural Safety* **112**, 102541.

Lopes, R. H. C., I. D. Reid, and P. R. Hobson: 2007, 'The two-dimensional Kolmogorov–Smirnov test'. Technical report.

Mehta, Y. and R. Chowdhury: 2012, 'Constrained optimization using the Nelder–Mead simplex method'. *International Journal for Numerical Methods in Engineering* **89**(12), 1551–1574.

Qin, Q., X.-Y. Zhang, Z.-H. Lu, and Y.-G. Zhao: 2020, 'Simplified third-order normal transformation and its application in structural reliability analysis'. *Engineering Mechanics* **37**(12), 78–86.

Sklar, A.: 1973, 'Random variables, joint distribution functions, and copulas'. *Kybernetika* **9**(6), 449–460.

Tang, X.-S., D.-Q. Li, C.-B. Zhou, and K.-K. Phoon: 2015, 'Copula-based approaches for evaluating slope reliability under incomplete probability information'. *Structural Safety* **52**, 90–99.

Tang, X.-S., D.-Q. Li, C.-B. Zhou, K.-K. Phoon, and L.-M. Zhang: 2013, 'Impact of copulas for modeling bivariate distributions on system reliability'. *Structural Safety* **44**, 80–90.

Wang, F. and H. Li: 2018, 'The role of copulas in random fields: Characterization and application'. *Structural Safety* **75**(1), 75–88.

Weibull, W.: 1951, 'A statistical distribution function of wide applicability'. *Journal of Applied Mechanics* **18**(3), 293–297.

Zentner, I.: 2017, 'A general framework for the estimation of analytical fragility functions based on multivariate probability distributions'. *Structural Safety* **64**, 54–61.

Zhao, Y.-G. and Z.-H. Lu: 2021, *Structural Reliability: Approaches from Perspectives of Statistical Moments*. John Wiley & Sons.

Zhao, Y.-G. and T. Ono: 2000, 'Third-moment standardization for structural reliability analysis'. *Journal of Structural Engineering* **126**(6), 724–732.

SESSION 3

Hybrid, Imprecise and Set-Based Uncertainty

Papers in this session

1. A Hybrid Interval Uncertainty Algorithm for Structural Analysis
2. A practical framework for failure probability assessment under aleatory and epistemic uncertainty
3. Possibilistic Filtering for Reliable Robot Localization
4. Possibilistic Uncertainty Modeling with Hyperellipsoids
5. Imprecise probabilistic subset simulation for rigorous bounding of the failure probability

A Hybrid Interval Uncertainty Algorithm for Structural Analysis

Robert L. Mullen[1] and Rafi L. Muhanna[2]*
[1] *Civil and Environmental Engineering, University of South Carolina, Columbia, SC 29208, USA, rlm@sc.edu*
[2] **Civil and Environmental Engineering, Georgia Institute of Technology, Atlanta, GA 30332, USA, rafi.muhanna@gatech.edu*

Abstract: A variety of methods have been proposed for analyzing structures with interval parameters, each with distinct strengths and limitations depending on the problem characteristics. In the context of structural analysis, intrinsic methods typically involve directly solving the governing interval equations using algorithms that preserve the interval nature of the parameters, without relying on transformations or approximations. These methods are generally efficient and provide guaranteed solution bounds for response quantities. Still, a common challenge arises when the parameterization of a few parameters is nonlinear, such as when the loading direction is unknown but bounded. By contrast, extrinsic methods reformulate the interval problem as an optimization problem, where external optimization techniques are applied to identify the extreme responses within the prescribed interval ranges. While extrinsic approaches often provide an interval solution within the interval constraints, they are computationally demanding and do not provide a guaranteed bound on a solution.

This paper explores a hybrid interval approach that integrates both intrinsic and extrinsic strategies to solve systems of linear interval equations more effectively. The hybrid framework applies intrinsic methods where computational efficiency is critical and employs extrinsic optimization where the interval parameterization is nonlinear, thereby exploiting the complementary advantages of each method. Example calculations are presented to compare the performance of the hybrid approach against conventional extrinsic optimization-based methods. The results demonstrate that hybrid methods achieve more efficient computations and deliver solutions closer to the correct bounds than extrinsic calculations alone, making them a practical and robust tool for interval-based structural analysis.

Keywords: Hybrid interval, interval, finite element, optimization

1. Introduction

Structural systems are often subject to uncertainties in material properties, geometry, and external loading. When such uncertainties are represented as bounded intervals rather than probabilistic distributions, the resulting problem formulation requires specialized solution strategies. Over the past decades, several classes of algorithms have been developed for solving structural analysis problems with interval parameters, each offering unique strengths and limitations. The choice of method depends not only on the algorithm's computational properties but also on the characteristics of the specific problem under consideration.

Optimization-based methods provide an extrinsic approach to interval analysis by recasting the problem as an optimization task over the bounded domain defined by the intervals. These methods are highly flexible, capable of handling both linear and nonlinear parameterizations, and are particularly well-suited for situations

© 2026 by the author(s). This work is licensed under the Creative Commons Attribution 4.0 International License (CC BY 4.0), which permits unrestricted use, distribution, and reproduction in any medium, provided the original author and source are credited.

where the governing equations cannot be directly expressed in closed form. However, this generality comes at the cost of high computational demand, especially for large-scale systems with many uncertain parameters.

In contrast, intrinsic methods such as fixed-point algorithms exploit the algebraic structure of the interval equations directly. They are typically more computationally efficient and can guarantee enclosure bounds for key response quantities such as nodal displacements, element forces, stresses, and strains. Another important class of intrinsic methods, sensitivity end-point techniques, which take advantage of the end-point property, where the solution depends only on combinations of parameter extremes. These methods can be both fast and accurate, but their applicability is restricted to problems that possess the end-point property, such as linear affine combinations of rank-one matrices.

Despite these advances, a persistent challenge arises when the parameterization is nonlinear. A typical example is when the direction of an external load is uncertain but constrained within a bounded interval. In such cases, even if most of the interval parameters could be treated more efficiently with intrinsic methods, the entire problem is often forced into an extrinsic optimization framework due to the presence of a single nonlinear parameterization. This mismatch between problem structure and method applicability can significantly reduce efficiency and inflate computational costs.

To address this challenge, we propose a hybrid interval method that strategically combines extrinsic and intrinsic approaches. Within this framework, different subsets of interval parameters are assigned to the most suitable solver: optimization-based methods are used to handle nonlinear parameterizations, while more efficient intrinsic or guaranteed algorithms are employed for parameters where they are applicable. This selective integration leverages the complementary strengths of both classes of methods, aiming to improve computational efficiency without significantly sacrificing accuracy or reliability of the solution bounds.

The remainder of this paper is organized as follows. Section 2 provides a concise review of existing methods for interval structural analysis and highlights their main properties. Section 3 introduces the formulation of the proposed hybrid interval method, detailing how the partitioning of parameters between solvers is achieved. Section 4 presents numerical studies on truss structures with up to 434 independent interval parameters, demonstrating the effectiveness and scalability of the hybrid approach. Finally, Section 5 summarizes the key findings and discusses the implications for practical applications

2. Review of Previous Work

Structural analysis using interval variables has been explored by several researchers to account for uncertainty in their analyses (Köylüoglu, Cakmak et al. 1995; Muhanna and Mullen 1995; Nakagiri and Yoshikawa 1996; Rao and Berke 1997; Qiu and Elishakoff 1998; Rao and Chen 1998; Neumaier and Pownuk 2007, Moens, D. Vandepitte, D., 2002 among others). These studies primarily focused on achieving meaningful results without the excessively large and unrealistic solution bounds that can arise from the naive application of interval arithmetic.

The earliest known work on interval linear systems is credited to Oettli and Prager (1964). Since then, a wide range of methods have been developed (Neumaier 1990), reflecting different strategies for dealing with the fundamental challenge of enclosing all possible solutions within bounded uncertainty. In structural

mechanics, at least five main classes of solution techniques have emerged: optimization, Monte Carlo simulation, fixed-point enclosures, perturbation methods, and endpoint/sensitivity methods. Each of these approaches offers distinct strengths, limitations, and areas of application.

Optimization-based methods solve interval problems by framing them as constrained optimization problems, where the bounds of response quantities are the objective functions, and the interval parameters are the independent variables with inequality constraints representing the interval bounds (Rao and Chen 1998). Their key advantage lies in their extrinsic nature, which enables the direct use of existing non-interval structural analysis software. Moreover, optimization approaches can be extended to nonlinear systems, provided the underlying analysis program supports such formulations (Möller and Beer 2004). However, optimization has notable drawbacks: each response quantity typically requires a separate optimization run, the problems are NP-hard (Rohn and Kreinovich 1995), and solutions can be computationally expensive. In addition, depending on numerical tolerances, optimization may yield inner bounds, enclosures smaller than the true solution set, thus losing the guarantee of correctness. A recent direction has been the integration of Bayesian optimization techniques (Dang, Wei et al. 2022), which improve efficiency but retain the fundamental limitations of optimization-based strategies.

Monte Carlo methods, in contrast, adapt probabilistic simulation to the interval setting by interpreting interval parameters as random variables—often with uniform distributions. While conceptually straightforward and extrinsic in nature, Monte Carlo does not produce guaranteed enclosures and may require very large numbers of realizations even for low-dimensional problems. Initially, Monte Carlo was used primarily for benchmarking (Köylüoglu, Cakmak et al. 1995; Muhanna, Mullen et al. 2005). More recently, advances such as Quasi-Monte Carlo sampling with Cauchy distributions (Callens, Faes et al. 2021) have significantly reduced computational costs, making Monte Carlo competitive with vertex methods in certain applications.

Perturbation methods approximate interval equations by expressing the interval stiffness matrix and load vector as the sum of midpoint values and perturbations. A truncated Taylor expansion, typically first- or second order, is used to construct approximate equilibrium equations. These methods (Qiu and Elishakoff 1998; McWilliam 2000; Qiu and Elishakoff 2001; Chen, Lian et al. 2002) are efficient for small perturbations but cannot guarantee enclosures. Their results are inner estimates of the solution set, which can underestimate the true uncertainty in structural responses.

Sensitivity or endpoint methods assume that extreme responses occur at the endpoints of each interval parameter. Naive implementation requires 2^N evaluations (with N interval parameters), which quickly becomes intractable. However, Rohn (1989) introduced an efficient procedure requiring only 2N evaluations, significantly improving feasibility. Subsequent applications in structural analysis (Popova, Datcheva et al. 2002; Pownuk 2004; Popova, Iankov et al. 2006) demonstrated their utility, and further computational refinements have been reported (Sofi and Romeo 2016; Popova 2020). Endpoint methods generally yield inner solutions, but in special cases, such as when an interval parameter multiplies a rank-one matrix and is parameterized linearly, they can produce exact solutions (Popova 2017; Popova 2020; Popova 2021).

Finally, fixed-point methods represent a fundamentally different, intrinsic approach. Based on fixed-point theorems, these methods have been shown to provide guaranteed enclosures of the solution set (Gay 1982;

Jansson 1991; Dessombz, Thouverez et al. 2001; Neumaier and Pownuk 2007). Moreover, they can also be adapted to produce inner approximations, thereby quantifying the degree of overestimation (Xiao 2015). A major advantage is that fixed-point approaches provide the complete solution set for all variables simultaneously, rather than requiring separate computations for each quantity of interest.

A concise comparison of the properties, strengths, and limitations of these five classes of methods is provided in Table I.

Table I. Summary of properties of interval equation solvers.

Property	**Fixed-Point**	**Monte Carlo**	**Optimization**	**Perturbation**	**Sensitivity**
Guaranteed enclosure	✓	✗	✗	✗	✓*
Extrinsic	✗	✓	✓	✗	✓
Nonlinear problems	✓**	✓	✓	✗	✗
One response at a time	✗	✗	✓	✗	✓

** Fixed-point: limited nonlinear (e.g., truss nonlinear materials).
* Sensitivity: exact only in problems that possess the endpoint property.

3. General Description of the Hybrid Method

The primary objective of this work is to enhance the efficiency without significant degradation of the accuracy of solving interval structural analysis problems. This is accomplished by dividing the interval parameters into two subsets. One subset is evaluated using an extrinsic method based on optimization, while the other subset is evaluated using an intrinsic method embedded directly within the optimization objective function. The goal is to assign each parameter to the solution strategy that best suits its characteristics.

For example, when an interval parameter satisfies the endpoint property, an intrinsic sensitivity method can provide exact results more efficiently than an optimization-based approach. Conversely, interval parameters with nonlinear dependencies or no endpoint property are better suited for optimization-based evaluation.

The hybrid method under investigation, therefore, integrates two levels of solution strategies:

- Upper-level optimization (extrinsic): Interval parameters without intrinsic structure are solved using optimization algorithms such as Particle Swarm Optimization (PS), gradient-based solvers (e.g., fmincon function in MATLAB), Genetic Algorithms (GA), or Bayesian Optimization. These algorithms explore the admissible interval space to determine extremal values of the response.
- Embedded intrinsic analysis: Within the optimization function, interval parameters that lend themselves to fixed-point iteration (FP) or sensitivity methods (SM) are solved directly, exploiting their structure for improved accuracy and reduced computational cost.

By combining these approaches, the hybrid framework ensures that each subset of interval parameters is handled by the most appropriate method, balancing efficiency and reliability of enclosures.

The general implementation of the hybrid method proceeds as outlined by the following steps:

1. Partition Interval Parameters: Separate all interval parameters into two distinct groups, intrinsic and extrinsic, ensuring that each parameter belongs exclusively to one group.
2. Formulate the Objective Function: Construct the objective function for a chosen response variable using the structural model. In the structural model, intrinsic parameters are treated as intervals, while extrinsic parameters are given scalar values within their prescribed ranges.
3. Evaluate the Objective Function: Each evaluation produces an interval response. When optimization seeks a minimum (maximum), the lower (upper) bound of this interval is used as the objective value.
4. Update Extrinsic Variables: The optimization algorithm adjusts the scalar values of the extrinsic parameters, subject to interval constraints, to minimize or maximize the objective function.
5. Iterate Optimization: Steps 3 and 4 are repeated until the algorithm satisfies its termination criteria.
6. Compute Bounds for Each Response: Repeat steps 2–5 to determine both the lower and upper bounds for every response variable of interest.

In traditional optimization-based approaches to interval problems, structural responses are evaluated using a deterministic analysis method. In this work, we replace the deterministic evaluation with interval analysis for a selected intrinsic subset of interval parameters. The allocation of each parameter to either the extrinsic (optimization-based) or intrinsic (interval-based) subset is determined by the user, depending on whether the parameter can be effectively represented through an intrinsic interval solver.

For the intrinsic interval solver, we employ sensitivity methods and fixed-point methods. In particular, for sensitivity analysis, we adopt Popova's algorithm, where a single iteration of the fixed-point expansion identifies the appropriate endpoint (SM). For the fixed-point (FP) method, we follow the formulation outlined in Xiao (2015). Both intrinsic methods, however, are constrained by the way interval quantities parameterize the problem. Interval parameters that cannot be accommodated by the FP or SM intrinsic solvers are instead handled through optimization.

This hybrid allocation reduces the dimensionality of the optimization problem, thereby improving computational efficiency while maintaining reliable interval enclosures.

4. Specific Formulation for a Hybrid Gradient-–Sensitivity Method

Without loss of generality, the optimization method is formulated as a constrained minimization problem. A wide range of computational tools can address such problems, including MATLAB (2026), PROFIL/BIAS Knüppel, O. (1994), and Bayesian optimization (Dang 2022). The optimization process requires identifying the independent extrinsic parameters, defining their lower and upper bounds, and specifying an objective function to evaluate the structural response. In this study, we employ MATLAB's gradient-based solver (fmincon), though other optimization algorithms, such as Particle Swarm Optimization or Genetic Algorithms could also be used.

The fmincon algorithm explores candidate scalar values for the extrinsic parameters within their prescribed bounds and passes them to the objective function. Within this function, a sensitivity-based interval solver evaluates the lower or upper bound of the structural response. This hybrid evaluation couples the extrinsic optimization with intrinsic methods, enabling efficient handling of mixed parameter types. Specifically, interval parameters that can be addressed using sensitivity methods (SM) or fixed-point methods

(FP) are treated intrinsically, while parameters unsuitable for intrinsic analysis are assigned to the extrinsic set.

5. Results

In the following, solutions to three representative problem scenarios are presented. All of the intrinsic solutions are calculated using the method presented by Rama Rao et.al. (2011) and interval calculations are performed using INTLAB (Rump 1999). The first set is a simple truss structure for which an analytical solution is readily calculated. The hybrid formulation treats horizontal bars using a call to a non-linear incremental plasticity model. To preserve the computable analytic solution, the yield stress is set to eliminate any plastic behavior. The quality of the interval enclosures is studied. The second example set considers a truss structure subjected to applied loads with interval-valued angles and magnitudes. This problem was selected because it is well known that endpoint-based methods, such as sensitivity approaches, fail to produce correct interval enclosures when uncertainty appears in angular parameters. In addition, nonlinear parameterizations of loading terms are not adequately addressed by fixed-point methods. Finally, we solve a truss with the extrinsic parameters describing a nonlinear constitutive law.

The first example problem is a simple five-bar two-dimensional truss shown in Figure 1. The horizontal bars are 4 m in length, the vertical bars are 3 m, and the diagonal element has a length of 5 m. The bottom-left node is pinned, and the top-left node is constrained in the horizontal direction. All bars have a nominal Young's modulus of 2.0×10^8 kPa and a cross-sectional area of 0.001 m^2. The downward load at node 2 is 10 kN.

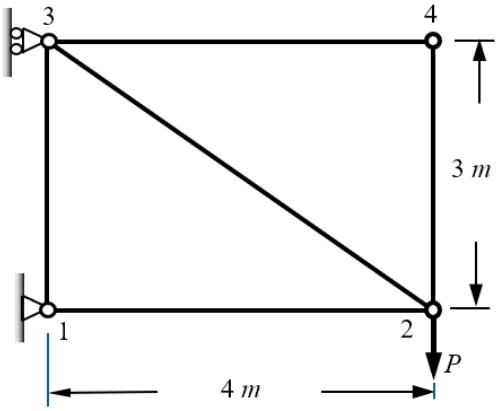


Figure 1: Simple truss structure

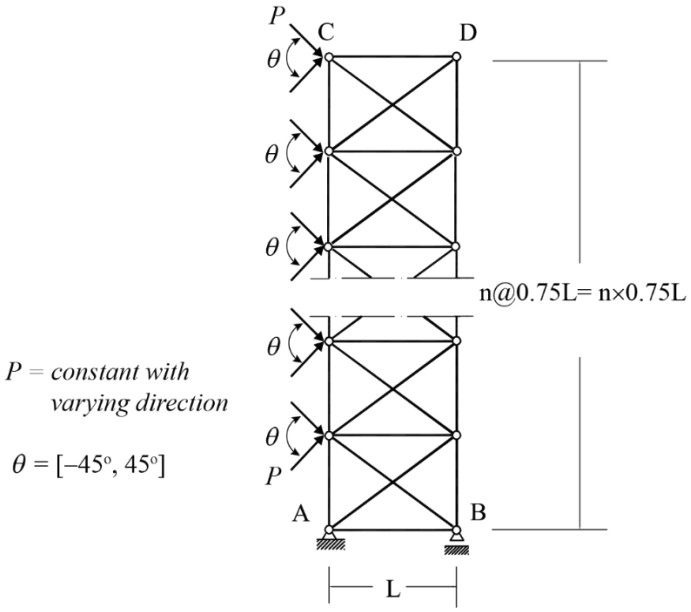
All bars have an interval uncertainty of ± 0.04 for the modulus and ± 0.01 for the area. The load uncertainty is ± 0.05 In the hybrid calculations, bars 1-2 and 3-4 were treated using an incremental plasticity law with the yield stress large enough to prevent the elements from becoming plastic. The pure optimization (fmincon) and the hybrid fmincon-sensitivity results for the vertical deflection at node 2 are compared in Table II.

Table II: Comparison of interval enclosure of optimization and hybrid solutions

all units in m	fmincon	hybrid	exact
inf Uy_2	-0.00132305	-0.001325363	-0.001325758
sup Uy_2	-0.001087973	-0.001085473	-0.001085301
interval width	0.000235077	0.00023989	0.000240457
inf Uy_2 from exact	2.708E-06	3.95E-07	0
sup Uy_2 from exact	2.672E-06	1.72E-07	0

Neither the hybrid nor the optimization solutions enclose the exact solution. However, the underestimation of the interval width is extremely small in both calculations. Increasing the number of interval variables treated by the optimization algorithm increases the underestimation of the interval width. In this example, using the sensitivity method (which provides a guaranteed enclosure when used alone) to model some of the variables decreases the underestimation introduced by the optimization method

The second set of problems used to investigate the behavior of the proposed hybrid approach consists of a series of truss structures that have been widely employed to evaluate interval



(a)

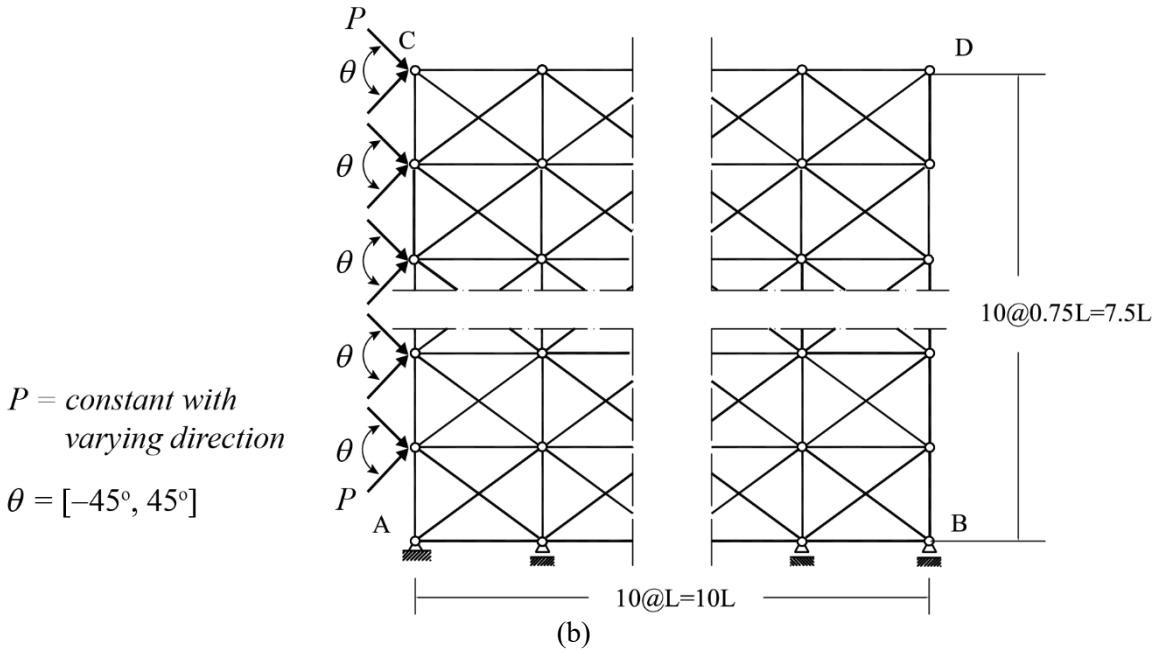


Figure 2. a) a single bay and b) a multiple bay cross-braced truss structure.

structural solvers Muhanna, R. L. (2004). These benchmark problems are shown in Figure 2. The traditional problem configuration is modified by introducing a nonlinear parametric loading, in which the direction of the applied load is uncertain and varies within an interval of ±45° from the horizontal.

This type of interval uncertainty in the loading angle is well-suited for treatment via optimization-based methods. Accordingly, the interval parameter associated with the loading direction is treated extrinsically, while interval uncertainties associated with element stiffness and load magnitude are handled intrinsically using either fixed-point or sensitivity-based methods.

The primary structure considered is a one-bay, 20-floor cantilever truss with a bay length of $L = 1\text{m}$ and a story height of $0.75L$. The model consists of 42 nodes and 101 elements. The truss is subjected to 20 horizontal concentrated forces applied at the left-hand-side nodes, each acting at an uncertain angle between −45° and +45° relative to the horizontal. The midpoint magnitude of each load is $P = 10\text{kN}$. The midpoint values of Young's modulus and cross-sectional area are taken as $E = 200\text{GPa}$ and $A = 1.0 \times 10^{-3}\ \text{m}^2$, respectively, and are assumed to be independent for each element.

To study the effect of problem size, reduced versions of the structure with 1, 5, and 10 floors are also analyzed. In addition, a larger ten-bay, ten-story truss (Figure 2b) is included to represent problems with a substantially increased number of interval parameters. This model has bay and floor dimensions of L and $0.75L$, respectively, and consists of 121 nodes and 420 elements.

The number of interval parameters for each model is summarized in Table III. For example, the 1×1 truss includes six interval parameters associated with element stiffness, one interval parameter for load magnitude,

and one for load direction, for a total of eight interval parameters. Interval parameter values are presented in Table IV. All five models are analyzed assuming independent element properties, with 6% uncertainty in Young's modulus, 10% uncertainty in each load magnitude, and a common uncertain load angle varying between −45° and +45°. For all cases, the horizontal displacement of the upper right-hand node is selected as the response quantity of interest.

Table III: Measure of problem size for problem set two.

Description	Number of elements	Number of nodes	Number of interval parameters
1x1 truss structure	6	4	8
1x5 truss	26	12	32
1x10	51	22	62
1x20	101	42	122
10x10	420	101	431

Table IV: Values of Interval parameters (LB is lower bound, UB is upper bound).

Parameter	LB	UB
Young's modulus (kPa)	1.96×10^8	2.04×10^8
Force magnitude (kN)	9.5	10.5
Force angle (degrees)	−45	+45

A summary of the numerical results is presented in Table V. The optimization routine used for the extrinsic calculations is MATLAB's fmincon, with default parameters. No attempt was made to improve computational performance by tuning the optimizer settings. The methods reported in the table are denoted as follows:

- fmin: pure optimization applied to all interval parameters.
- fmin–fp: hybrid approach using fmin for the extrinsic set and a fixed-point method for the intrinsic set.
- fmin–sen: hybrid approach using fmin for the extrinsic set and a sensitivity-based method for the intrinsic interval parameters.

Table V: Comparison of optimization and hybrid approaches for truss structures with uncertain parameters.

Interval parameters	Method	Lower bound	Upper bound	clock time (sec)	Processing time (sec)	Number of function calls	Number of floors	Number of bays	Ratio of function calls	Ratio of processing time	Ratio of interval width
8	fmin	3.34E-05	6.31E-05	0.221405	0.3125	326	1	1	1	1.0	1.00
32	fmin	0.002382	0.00553	1.344753	2.75	7658	5	1	1	1.0	1.00
62	fmin	0.034261	0.068537	11.03258	12.03125	41051	10	1	1	1.0	1.00
122	fmin	0.543175	0.989051	454.5347	463.7813	951339	20	1	1	1.0	1.00
431	fmin	4.79E-05	0.000107	33.92403	178.3438	18144	10	10	1	1.0	1.00

1-7	fmin-fp	3.15E-05	6.52E-05	0.123817	0.234375	45	1	1	7	1.3	0.88
1-31	fmin-fp	0.002254	0.00554	0.357928	1.015625	44	5	1	174	2.7	0.96
1-61	fmin-fp	0.033351	0.068554	0.593787	1.109375	44	10	1	933	10.8	0.97
1-121	fmin-fp	0.534761	0.989074	0.850719	1.90625	35	20	1	27181	243.3	0.98
1-430	fmin-fp	4.19E-05	0.000114	4.824301	12.6875	47	10	10	386	14.1	0.81
1-7	fmin-sen	3.19E-05	6.57E-05	0.028332	0.03125	65	1	1	5	10.0	0.88
1-31	fmin-sen	0.002359	0.005541	0.063423	0.140625	85	5	1	90	19.6	0.99
1-61	fmin-sen	0.034237	0.068556	0.035624	0.1875	46	10	1	892	64.2	1.00
1-121	fmin-sen	0.543067	0.989095	0.062328	0.40625	73	20	1	13032	1141.6	1.00
1-430	fmin-sen	4.44E-05	0.000115	0.799103	8.140625	88	10	10	206	21.9	0.84

All the ratios given in the tables are the hybrid methods/optimization methods. In all cases, the hybrid approaches required less computational effort than the pure optimization method. The ratio of processing time for the pure optimization method to that of the hybrid methods ranged from approximately 1.3 to 1142, indicating substantial computational savings. In general, the computational advantage of the hybrid approach increased with the number of intrinsic interval parameters. An exception was observed in the pure optimization results, where the one-bay, 20-story truss required approximately four times the computation time of the ten-bay, ten-story truss; the reason for this behavior could not be identified. Sensitivity-based hybrid methods consistently required less computational effort than their fixed-point counterparts.

The interval widths of the hybrid calculations are wider than those of the pure optimization calculations. While we have not calculated exact solutions for this problem, we speculate that neither the optimization nor the hybrid solutions provide guaranteed bounds and that the hybrid solutions are closer to the exact solution.

To investigate the influence of the magnitude of parameter uncertainty, the same set of problems was recalculated using a 20% uncertainty for all interval variables, except for the load direction. The corresponding results are presented in Table VI.

Table VI: Hybrid results with 20% uncertainty.

Number of floors	Number of bays	Interval parameters	Method	Lower bound	Upper bound	clock time (sec)	Processing time (sec)	Number of function calls	Ratio of function calls	Ratio of processing time	Ratio of interval width
1	1	8	fmin	3.22E-05	6.58E-05	0.0606076	0.109375	387	1	1.0	1.0
5	1	32	fmin	0.002271	0.005951836	1.6487626	1.71875	9683	1	1.0	1.0
10	1	62	fmin	0.030407	0.077374204	14.489049	17.6718	53072	1	1.0	1.0
20	1	122	fmin	0.48195	1.116704863	643.5102	655.515	1326891	1	1.0	1.0
10	10	431	fmin	4.62E-05	0.000113	51.454384	263	27648	1	1.0	1.00
1	1	1-7	fmin-fp	2.56E-05	7.39E-05	0.1490789	0.39062	50	8	0.3	0.70

5	1	1-31	fmin-fp	0.001804	0.006251902	0.353652	0.76562	47	206	2.2	0.83
10	1	1-61	fmin-fp	0.027487	0.0773436	1.0318756	1.89062	44	1206	9.3	0.94
20	1	1-121	fmin-fp	0.447599	1.115793432	0.9589624	1.84375	39	34023	355.5	0.95
10	10	1-430	fmin-fp	3.25E-05	0.000129467	4.9069113	11.2031	47	588	23.5	0.69
1	1	1-7	fmin-sen	2.71E-05	7.56E-05	0.0333906	0.03125	67	6	3.5	0.69
5	1	1-31	fmin-sen	0.00209	0.006257308	0.0385201	0.04687	89	109	36.7	0.88
10	1	1-61	fmin-sen	0.030368	0.077407429	0.0273507	0.15625	48	1106	113.1	1.00
20	1	1-121	fmin-sen	0.481737	1.116789039	0.0532632	0.29687	46	28845	2208.	1.00
10	10	1-430	fmin-sen	3.86E-05	0.000130345	0.6508958	6.76562	74	374	38.9	0.73

*For hybrid models, the number of intervals is an extrinsic-intrinsic pair. **Method is fmin – Newton-based method, sen- Sensitivity, fp – Fixed point method

When using pure optimization, the number of function evaluations increased with larger interval parameter widths, and for all cases except the 1×1 and 5×1 trusses, both wall-clock and processor times increased accordingly. In contrast, the hybrid methods exhibited relatively stable computational effort with respect to increased parameter uncertainty. The number of function calls and both timing measures remained largely unchanged, demonstrating the robustness of the hybrid approach with respect to uncertainty magnitude. In all results, the interval width of the hybrid calculations is larger, consistent with the previous examples.

The next group of calculations considers the case in which the direction of each applied load is treated as an independent interval parameter. This significantly increases the number of extrinsic interval variables relative to the previous cases. The results are summarized in Table VII.

Table VII: Solution behavior with independent loading directions.

Number of floors	Number of bays	Interval parameters	Method	Lower bound	Upper bound	clock time (sec)	Processing time (sec)	Number of function calls	Ratio of function calls	Ratio of processing	Ratio of interval width
1	1	8	fmin	3.34E-05	6.31E-05	0.133373	0.25	326	1	1.0	1.00
5	1	36	fmin	0.002384	0.005567	1.712985	2.40625	10853	1	1.0	1.00
10	1	71	fmin	0.034264	0.068821	15.20872	18.8125	60246	1	1.0	1.00
20	1	141	fmin	0.543149	0.990547	354.8577	465.5313	736875	1	1.0	1.00
10	10	440	fmin	4.75E-05	0.00011	193.0471	955.2813	97466	1	1.0	1.00
1	1	1-7	fmin-fp	3.19E-05	6.57E-05	0.137894	0.125	65	5	2.0	0.88
5	1	5-31	fmin-fp	0.002359	0.005579	0.174381	0.390625	649	17	6.2	0.99
10	1	10-61	fmin-fp	0.034237	0.06884	0.249899	2.09375	1527	39	9.0	1.00
20	1	20-121	fmin-fp	0.543067	0.990598	1.171556	9.421875	4387	168	49.4	1.00

10	10	10-430	fmin-fp	9.04E-05	0.000114	13.70857	145.3281	1779	55	6.6	2.61
1	1	1-7	fmin-sen	3.14E-05	6.52E-05	0.132542	0.25	45	7	1.0	0.88
5	1	5-31	fmin-sen	0.002251	0.005578	2.992782	5.515625	443	24	0.4	0.96
10	1	10-61	fmin-sen	0.03333	0.068838	17.43458	28.42188	1454	41	0.7	0.97
20	1	20-121	fmin-sen	0.534599	0.990576	79.33231	113.4688	3467	213	4.1	0.98
10	10	10-430	fmin-sen	4.28E-05	0.000114	107.7495	187.2031	1209	81	5.1	0.87

In all but three cases, the hybrid methods outperformed the corresponding pure optimization approaches in terms of computational efficiency. The exceptions occurred for the fmin–sensitivity method applied to the 1×1, 5×1, and 10×1 structures, where processor times were comparable to or slightly shorter for pure optimization. Nevertheless, wall-clock times and the number of function evaluations remained favorable for the hybrid methods.

The third example considers a hybrid formulation in which optimization-based methods are employed to address nonlinear elements, while the remaining linear elements are treated using an intrinsic sensitivity-based formulation. Elements 7 and 9 are considered to be nonlinear. The geometry and boundary conditions of the two-dimensional truss are shown in Figure 3. The joints are numbered from 1 to 8, and the elements are labeled with an underscore from 1 to 15.

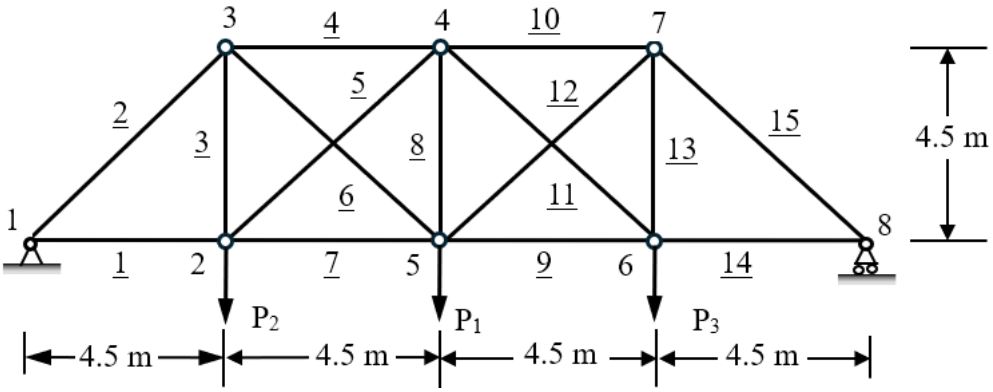


Figure 3. Fifteen-bar truss

Point loads P_1, P_2, and P_3, are applied at joints 5, 2, and 6, respectively. The two central bottom elements are modeled using an incremental plasticity formulation with uncertain constitutive parameters listed in Table VIII. The midpoint values of the applied loads are $P_1 = 200\,\text{kN}$ and $P_2 = P_3 = 100\,\text{kN}$, each with an uncertainty of ±25%.

Table VIII: Incremental plasticity model parameters

Parameter	Lower limit	Upper limit
Elastic slope (kPa)	190×10^6	210×10^6
Yield stress (kPa)	300×10^3	400×10^3
Plastic slope/Elastic slope	0.015	0.025

Bars 1– 4, 10, and 13–15 have a cross-sectional area of $A = 1.2 \times 10^{-3}\ \mathrm{m}^2$, while all remaining bars have a smaller area of $A = 0.6 \times 10^{-3}\ \mathrm{m}^2$. All cross-sectional areas are assumed to have ±1% interval uncertainty. All bars are made of steel and are assigned an interval Young's moduli with midpoint value $E = 200\mathrm{GPa}$ and ±5% uncertainty bounds. Uncertainties in material properties and loads are assumed to be independent.

Three response quantities are evaluated:

1. the vertical deflection at node 5,
2. the lateral deflection at node 8, and
3. the axial force in element 10.

Table IX reports the lower and upper bounds of these response quantities for the different solution algorithms. The reported computational times correspond to the authors' implementations executed on the computer system described previously. The problem includes a total of 37 interval parameters, consisting of 13 Young's moduli for elastic elements, 15 cross-sectional areas, 3 nodal loads, and 6 constitutive parameters associated with the two elements exhibiting incremental plasticity.

The pure optimization results are compared with a hybrid formulation in which the optimization method is applied only to the six interval parameters associated with the potentially nonlinear behavior of elements 7 and 9.

Table IX: Non-linear truss results

Interval parameters	Method	Variable	Lower bound	Upper bound	clock time (sec)	Processing time (sec)	Number of function calls	Ratio of function calls	Ratio of processing time	Ratio of interval width
39	fmin	U5y	-0.09693	-0.0295	69.05129	320.4688	7707	1	1.0	1.000000
6-33	fmin-sen	U5y	-0.10105	-0.02914	4.130456	4.375	175	44.04	73.3	0.937663
39	fmin	U8x	0.016827	0.089442	67.42967	314.0625	8153	1	1.0	1.000000
6-33	fmin-sen	U8x	0.01632	0.092603	4.458789	4.203125	196	41.597	74.7	0.951918
39	fmin	F10	-436.824	-206.471	19.39599	106.0938	1641	1	1.0	1.000000
6-33	fmin-sen	F10	-445.164	-205.457	5.590322	5.734375	222	7.3919	18.5	0.960978

From a computational perspective, the optimization-only approach required between 18 and 75 times more processing time, depending on the response variable. In addition, the number of function evaluations for the optimization-only method was between 7 and 44 times more than that required by the hybrid approach. Also, as seen in previous examples, the widths of the hybrid results are wider than those of the pure optimization.

6. Conclusions

The simultaneous (hybrid) use of extrinsic and intrinsic methods, where each interval variable is assigned to one of the methods, is presented. Both uncertain loading directions, as well as material nonlinear behavior, are presented. In most scenarios studied, the use of a hybrid approach is computationally more efficient. While both optimization and hybrid methods do not provide a guaranteed enclosure, they both provide similar results, with the hybrid methods providing slightly larger interval widths compared to the optimization method.

7. References

Callens, R., M. Faes, and D. Moens (2021). Interval Analysis Using Multilevel Quasi-Monte Carlo. International Workshop on Reliable Engineering Computing (REC2021), Sicily, Italy (Virtual).

Chen, S., H. Lian and X. Yang (2002). "Interval static displacement analysis for structures with interval parameters." International Journal for Numerical Methods in Engineering **53**(2): 393-407.

Dang, C., P. Wei, M. G. R. Faes, M. A. Valdebenito and M. Beer (2022). "Interval uncertainty propagation by a parallel Bayesian global optimization method." Applied Mathematical Modelling **108**: 220-235.

Dessombz, O., F. Thouverez, L. J. P. and L. Jezequel (2001). "Analysis of mechanical systems using interval computations applied to flnite elements methods." J. Sound. Vib **238**(5): 949-968.

Gay, D. M. (1982). "Solving interval linear equations." SIAM J. Numer. Anal., **19**(4): 857-870.

Jansson, C. (1991). "Interval linear system with symmetric matrices, skew-symmetric matrices, and dependencies in the right hand side." Computing **46**.

Köylüoglu, U., S. Cakmak, N. Ahmet and R. K. Soren (1995). " Interval Algebra to Deal with Pattern Loading and Structural Uncertainty." Journal of Engineering Mechanics **121**(11): 1149- 1157.

Knüppel, O. (1994) PROFIL/BIAS—A fast interval library. Computing 53, 277–287.

MATLAB. (2025). Natick, Massachusetts: The MathWorks Inc.

McWilliam, S. (2000). "Anti-optimisation of uncertain structures using interval analysis." Comput Struct **79**: 421-430.

Moens, D. Vandepitte, D., (2002). Fuzzy finite element method for frequency response function analysis of uncertain structures, AIAA J.40 (1) 126–136.

Möller, B. and M. Beer (2004). Fuzzy randomness: uncertainty in civil engineering and computational mechanics, Springer Science & Business Media.

Muhanna, R. L. (2004). "Benchmarks for interval finite element computations." Center for Reliable Engineering Computing Retrieved February 3, 2005, from http://rec.ce.gatech.edu/resources/Benchmark 2.pdf.

Muhanna, R. L. and R. L. Mullen (1995). Development of interval-based methods for fuzziness in continuum-mechanics. Proceedings of 3rd International Symposium on Uncertainty Modeling and Analysis and Annual Conference of the North American Fuzzy Information Processing Society, IEEE.

Muhanna, R. L., R. L. Mullen and H. Zhang (2005). "Penalty-based solution for the interval finite-element methods." Journal of Engineering Mechanics **131**(10): 1102-1111.

Nakagiri, S. and N. Yoshikawa (1996). Finite Element Interval Estimation by Convex Model. Proceedings of 7th ASCE EMD/STD Joint Specialty Conference on Probabilistic Mechanics and Structural Reliability, WPI, MA.

Neumaier, A. (1990). Interval Methods for Systems of Equations. Cambridge, Cambridge Univ. Press.
Neumaier, A. and A. Pownuk (2007). "Linear Systems with Large Uncertainties, with Applications to Truss Structures." Reliable Computing **13(2)**: 149-172.
Oettli, W. and W. Prager (1964). " Compatibility of approximate solution of linear equations with given error bounds for coefficients and right-hand sides." Numer. Math **6**(1): 405–409.
Popova, E., R. Iankov and Z. Bonev (2006). Bounding the response of mechanical structures with uncertainties in all the parameters. National Science Foundation (NSF) Workshop on Reliable Engineering Computing (REC), Georgia Institute of Technology, Atlanta GA. USA.
Popova, E. D. (2017). "Enclosing the solution set of parametric interval matrix equation A(p)X = B(p)." Numerical Algorithms **78**(2): 423-447.
Popova, E. D. (2020). "New parameterized solution with application to bounding secondary variables in FE models of structures." Applied Mathematics and Computation **378**.
Popova, E. D. (2021). "Proving endpoint dependence in solving interval parametric linear systems." Numerical Algorithms **86**(3): 1339-1358.
Popova, E. D., M. Datcheva, R. Iankov and T. Schanz (2002). Mechanical Models with Interval Parameter. Proceedings of 16th International Conference on the Applications of Computer Science and Mathematics in Architecture and Civil Engineering. K. G. L. H. C. Konke.
Pownuk, A. (2004). Efficient method of solution of large scale engineering problems with interval parameters. Proc. NSF Workshop on Reliable Engineering Computing. R. L. Muhanna, Mullen R.L. . Savannah, Georgia, USA**:** 305-316.
Qiu, Z. and I. Elishakoff (1998). "Antioptimization of structures with large uncertain-but-non-random parameters via interval analysis." Compt. Meth. Appl. Mech. Engrg., **152**: 361-372.
Qui, Z. and I. Elishakoff (2001). "Anti-optimization technique – a generalization of interval analysis for non-probabilistic treatment of uncertainty." Chaos, Solitons and Fractals **12**(9): 1747-1759.
Rama Rao, M. V., R. L. Mullen and R. L. Muhanna (2011). "A New Interval Finite Element Formulation With the Same Accuracy in Primary and Derived Variables." International Journal of Reliability and Safety, **5**.
Rao, S. S. and L. Berke (1997). "Analysis of uncertain structural systems using interval analysis." AIAA J. **35**(4): 727–735.
Rao, S. S. and L. Chen (1998). "Numerical solution of fuzzy linear equations in engineering analysis." International Journal of Numerical Methods in Engineering **43**: 391–408.
Rohn, J. (1989). "Systems of linear interval equations." Linear Algebra and its Applications **126**: 39-78.
Rohn, J. and V. Kreinovich (1995). "Computing exact componentwise bounds on solutions of linear systems with interval data is NP-hard." SIAM J. Matrix Anal. Appl. **16**(2): 415–420.
Rump, S. M. (1999). INTLAB - INTerval LABoratory. Developments in Reliable Computing. T. Csendes. Dordrecht, Kluwer Academic Publishers**:** 77--104.
Sofi, A. and E. Romeo (2016). "A novel Interval Finite Element Method based on the improved interval analysis." Computer Methods in Applied Mechanics and Engineering **311**: 671-697.

Xiao, N. (2015). Interval Finite Element Approach for Inverse Problems Under Uncertainty. Ph.D, Georgia Institute of Technology.

A practical framework for failure probability assessment under aleatory and epistemic uncertainty

Pei-Pei Li[1,2*], Marcos A. Valdebenito[2], Chao Dang[2], Michael Beer[3], Matthias G.R. Faes[2]
[1] *Department of Civil Engineering, Beijing University of Technology, Beijing 100124, China*
[2] *Chair for Reliability Engineering, TU Dortmund University, Leonhard-Euler-Str. 5, Dortmund 44227, Germany*
[3] *Institute for Risk and Reliability, Leibniz University Hannover, Hannover 30167, Germany*

Abstract. In engineering applications, aleatory and epistemic uncertainties commonly coexist and interact, making their proper characterization essential for reliability analysis and informed decision-making under uncertainty. This challenge becomes particularly evident when failure probabilities of engineering structures are evaluated using incomplete, insufficient, imperfect, or imprecise information. Under such circumstances, failure probability can no longer be expressed as a single deterministic value; instead, set-theoretic or Bayesian representations are required to explicitly account for epistemic uncertainty. Although the theoretical foundations for handling these uncertainties are well established, a noticeable gap persists between academic developments and practical engineering implementation. In practice, aleatory and epistemic uncertainties,despite being conceptually distinct, are still frequently mixed, either implicitly or even explicitly in engineering analyses. To bridge this gap, this paper offers a pragmatic guide for selecting suitable uncertainty modeling frameworks, such as probability boxes, fuzzy probability models, or hierarchical probabilistic approaches, when dealing with problems influenced by both uncertainty types. By assessing the nature and quality of available information as well as the objectives of the analysis, we provide clear recommendations for appropriate modeling choices and present a comprehensive framework for evaluating failure probability. Furthermore, this work highlights the critical role of sensitivity analysis in identifying influential parameters, enabling targeted data acquisition efforts that reduce epistemic uncertainty and ultimately enhance the credibility of reliability assessments.

Keywords: Aleatory uncertainty; Epistemic uncertainty; Uncertainty modelling; Reliability analysis; Failure probability

1. Introduction

In assessing the reliability of structures, the identification and characterization of uncertainties play a critical role (Walls et al., 2017). In practice, uncertainties are commonly classified into aleatory and epistemic types (Der Kiureghian and Ditlevsen, 2009). Aleatory uncertainty represents inherent variability in physical systems, such as material properties, geometry, loads, and environmental conditions, and is therefore irreducible. In contrast, epistemic uncertainty stems from incomplete

* Corresponding author

© 2026 by the author(s). This work is licensed under the Creative Commons Attribution 4.0 International License (CC BY 4.0), which permits unrestricted use, distribution, and reproduction in any medium, provided the original author and source are credited.

or imperfect knowledge, including modeling assumptions, simplifications, and limited data, and can be reduced as additional information becomes available (Kiureghian, 1989). In practical engineering applications, these two types of uncertainty coexist and should be distinguished to avoid misleading interpretations (Der Kiureghian and Ditlevsen, 2009).

In an ideal scenario where complete probabilistic information is available, probability theory provides a rigorous framework for uncertainty modeling, and the failure probability can be expressed as a deterministic quantity. The failure probability can be expressed as a deterministic quantity. Let $\boldsymbol{X} = (X_1, \ldots, X_n)^T$ denote a vector of random variables and $g(\boldsymbol{X})$ the performance function, where $g(\boldsymbol{X}) \leq 0$ defines failure. The failure probability is given by

$$P_f = \int_{g(\boldsymbol{x})\leq 0} f_{\boldsymbol{X}}(\boldsymbol{x})\mathrm{d}\boldsymbol{x}, \tag{1}$$

where $f_{\boldsymbol{X}}(\boldsymbol{x})$ is the joint probability density function (PDF) of $\boldsymbol{X}$.

Eq. (1) represents the fundamental problem of structural reliability analysis. It is important to point out that in the context of this equation, it is assumed that one has perfect knowledge about the full joint PDF of $\boldsymbol{X}$. However, in practical engineering applications, it is almost impossible for practical and/or economical reasons to have such perfect knowledge. This inherently introduces epistemic uncertainty into the analysis (Kiureghian, 1989). Such uncertainty may arise not only from the distribution model $f_{\boldsymbol{X}}$, but also from the limit-state function g itself (Der Kiureghian and Ditlevsen, 2009; Roy and Oberkampf, 2011). In this work, we focus on epistemic uncertainty associated with $f_{\boldsymbol{X}}$. To explicitly integrate this uncertainty in our models, a vector of variables $\boldsymbol{\theta}$ is introduced, transforming the joint PDF of $\boldsymbol{X}$ into a conditional distribution function $f_{\boldsymbol{X}}(\boldsymbol{x}|\boldsymbol{\theta})$. Accordingly, the failure probability becomes a function of $\boldsymbol{\Theta}$, referred to as the conditional failure probability:

$$P_f(\boldsymbol{\theta}) = \int_{g(\boldsymbol{x})\leq 0} f_{\boldsymbol{X}}(\boldsymbol{x}|\boldsymbol{\theta})\mathrm{d}\boldsymbol{x}. \tag{2}$$

Various methods have been developed to handle epistemic uncertainty. Probabilistic approaches provide a rigorous framework when sufficient data are available (Sivia and Skilling, 2006), while non-probabilistic methods such as interval models (Qiu and Elishakoff, 1998; Moens and Hanss, 2011), convex models (Ben-Haim, 1994) and fuzzy sets (Moens and Hanss, 2011; Zadeh, 1965; Hanss, 2005) are widely used in data-scarce situations. However, these approaches are primarily designed for epistemic uncertainty alone and do not explicitly account for aleatory variability (Beer et al., 2013a).

When modeling aleatory and epistemic uncertainties simultaneously, it is crucial to treat them separately to avoid conflating their distinct sources (Roy and Oberkampf, 2011). However, distinguishing between aleatory and epistemic uncertainties during the modeling phase remains challenging (Oberkampf et al., 2004; Beer et al., 2013a). To address hybrid uncertainty, several frameworks have been proposed, including probability boxes (p-boxes) (Faes et al., 2021), fuzzy probability models (Möller and Beer, 2013), and hierarchical Bayesian models (Zhao et al., 2018; Li et al., 2022).

The p-box framework is an effective tool for reliability analysis under data-scarce or incomplete-information conditions. By defining lower and upper bounds of cumulative distribution functions

(CDFs), p-boxes describe epistemic uncertainty through interval-valued failure probabilities and are widely used in engineering applications involving both aleatory and epistemic uncertainties (Faes et al., 2021; Beer et al., 2013a). However, the interval representation is often too coarse to capture the detailed influence of epistemic uncertainty on structural reliability. To provide a more flexible representation, fuzzy probability extends interval-based approaches by introducing membership functions to characterize epistemic uncertainty in probabilistic models (Möller and Beer, 2013). In this framework, the failure probability is represented as a fuzzy variable, enabling sensitivity-related analysis of the influence of uncertain parameters. Nevertheless, neither p-boxes nor fuzzy probability models possess an intrinsic mechanism for updating epistemic uncertainty when new data become available. Bayesian hierarchical probability models provide a systematic framework for uncertainty updating (Yuen, 2010). By separating aleatory and epistemic uncertainties into different probabilistic levels, these models enable the incorporation of additional observations to reduce epistemic uncertainty and improve reliability assessment.

Although these methods have been widely studied, clear guidelines for selecting appropriate approaches in practical engineering applications remain limited. Therefore, this paper aims to provide an engineering-oriented comparison of p-boxes, fuzzy probability, and hierarchical probability models for structural reliability analysis under hybrid uncertainty. The focus is placed on their uncertainty representation, interpretability, and applicability under different information conditions. The remainder of this paper is organized as follows. Section 2 introduces the theoretical frameworks of the three approaches. Section 3 discusses practical considerations in engineering applications. Section 4 presents a strip footing example for demonstration. Finally, Section 5 summarizes the main conclusions.

2. Modeling and propagation of aleatory and epistemic uncertainties

2.1. Probability box model

In some practical engineering applications, due to lack of knowledge, the probability distribution of random variables is unknown but can be constrained. In this case, both distribution-free and parametric p-boxes can be constructed based on available information (Faes et al., 2021). Within the p-box framework, the true but unknown CDF $F_{X_i}(x_i)$ of a random variable X_i is assumed to lie within the interval $[\underline{F}_{X_i}(x_i) \leq F_{X_i}(x_i) \leq \overline{F}_{X_i}(x_i) | x_i \in D_{X_i}]$ (Ferson and Ginzburg, 1996; Ferson et al., 2003), where $\underline{F}_{X_i}(x_i)$ and $\overline{F}_{X_i}(x_i)$ denote the lower and upper bounds CDF of X_i, respectively. The p-box concepts define lower probability operator $\underline{\mathbb{P}}$ and upper probability operator $\overline{\mathbb{P}}$ for events $\{X_i \leq x_i\} = (-\infty, x_i] \cap D_{X_i}$, such that $\underline{\mathbb{P}}(X_i \leq x_i) = \underline{F}_{X_i}(x_i)$ and $\overline{\mathbb{P}}(X_i \leq x_i) = \overline{F}_{X_i}(x_i)$. This formulation generates a credal set of probability measures. The p-box framework effectively handles the epistemic uncertainty, such as that caused by incomplete information on $F_{X_i}(x_i)$, by assigning an interval $[\underline{F}_{X_i}(x_i), \overline{F}_{X_i}(x_i)]$ for each value of X_i (Ferson et al., 2003). If high-quality information is available across the full range of possible values for X_i this interval becomes narrow, and the p-box approximates a crisp, deterministic CDF. However, when less information is available, the bounds widen to reflect weaker confidence in the resulting estimates.

When no prior information on the distribution family is available, distribution-free p-boxes can be adopted (Faes et al., 2022). Such models are constructed solely from the lower and upper bounds of the CDF, where any admissible function that is non-decreasing, right-continuous, and bounded within $[0, 1]$ can represent the true CDF. Owing to this flexibility, distribution-free p-boxes provide a highly general framework for modeling both aleatory and epistemic uncertainties. If the distribution family is known while the distribution parameters $\boldsymbol{\theta}$ are interval-valued, parametric p-boxes are more appropriate. In this framework, admissible CDFs are constrained through bounded parameter domains, allowing a clear separation between aleatory uncertainty and epistemic uncertainty. Specifically, the distribution family characterizes aleatory variability, whereas the parameter intervals represent epistemic uncertainty (Zhang et al., 2013). The lower and upper bounds of the parametric p-box are obtained by optimizing the conditional CDF over the parameter domain:

$$\underline{F}_X(x) = \min_{\boldsymbol{\theta} \in D_{\boldsymbol{\theta}}} F_X(x \mid \boldsymbol{\theta}), \tag{3}$$

$$\overline{F}_X(x) = \max_{\boldsymbol{\theta} \in D_{\boldsymbol{\theta}}} F_X(x \mid \boldsymbol{\theta}), \tag{4}$$

where $F_X(x \mid \boldsymbol{\theta})$ denotes the conditional CDF and $D_{\boldsymbol{\theta}}$ represents the domain of the parameter vector $\boldsymbol{\theta}$.

When p-boxes are used as inputs in reliability analysis, the failure probability is no longer a single deterministic value, but an interval-valued quantity $[\underline{P}_f, \overline{P}_f]$. The lower and upper bounds of the failure probability can be expressed in a unified form as (Alvarez et al., 2014; Schöbi and Sudret, 2017)

$$\underline{P}_f = \mathbb{P}\left(\max_{\boldsymbol{X} \in [\underline{\boldsymbol{X}}, \overline{\boldsymbol{X}}]} g(\boldsymbol{X}) \leq 0 \right), \tag{5}$$

$$\overline{P}_f = \mathbb{P}\left(\min_{\boldsymbol{X} \in [\underline{\boldsymbol{X}}, \overline{\boldsymbol{X}}]} g(\boldsymbol{X}) \leq 0 \right), \tag{6}$$

where $\mathbb{P}(\cdot)$ denotes the probability operator and $g(\boldsymbol{X})$ is the limit-state function. The width of the failure probability interval directly reflects the level of epistemic uncertainty: wider intervals indicate larger uncertainty in the reliability estimate, whereas improved information quality generally leads to narrower intervals approaching a crisp value. In engineering practice, the upper bound of the failure probability corresponds to the worst-case scenario. However, relying solely on the upper bound in structural design may lead to overly conservative solutions. Therefore, the entire failure probability interval should be considered to achieve a balance between safety and cost-effectiveness.

Furthermore, identifying the uncertain parameters that dominate the failure probability is essential for guiding data collection and reducing epistemic uncertainty. Traditional sensitivity analysis methods are generally difficult to extend to interval-valued failure probabilities. In contrast, fuzzy probability methods provide a global description of uncertainty propagation and help identify influential parameters, while Bayesian approaches further refine probability estimates through

data updating. The combination of these methods offers a comprehensive framework for epistemic uncertainty quantification, data acquisition, and reliability-based structural design.

2.2. Fuzzy probability model

When precise bounds in interval models cannot be strictly specified, fuzzy set theory provides an effective framework for representing wide-domain uncertainty through gradually varying membership functions (Zadeh, 1965). In this context, epistemic uncertainty in the distribution parameters $\boldsymbol{\Theta}$ is modeled using fuzzy sets. The fuzzy set associated with the l-th distribution parameter of the i-th random variable is defined as

$$\widetilde{\theta}_{i,l} = \left\{ (\theta_{i,l}, \mu_{\widetilde{\theta}_{i,l}}(\theta_{i,l})) \,\middle|\, \theta_{i,l} \in \Theta_{i,l},\ \mu_{\widetilde{\theta}_{i,l}}(\theta_{i,l}) \in (0,1] \right\}, \tag{7}$$

where $\mu_{\widetilde{\theta}_{i,l}}(\theta_{i,l})$ represents the membership function that assigns a degree of membership to each value $\theta_{i,l}$. The value of $\mu_{\widetilde{\theta}_{i,l}}(\theta_{i,l})$ reflects how strongly $\theta_{i,l}$ belongs to the fuzzy set. A membership value closer to 1 indicates a higher degree of confidence.

Membership functions can represent similarity, preference, or uncertainty (Dubois and Prade, 1997; Möller and Beer, 2008). In this study, they are interpreted as a representation of epistemic uncertainty for structural reliability analysis. Fuzzy operations are carried out using the minimum–maximum operators and the extension principle (Zimmermann, 2011). To improve computational efficiency, the α-cut discretization method is adopted instead of directly applying the extension principle (Möller et al., 2000). This approach transforms a fuzzy set into a series of interval sets at different α-levels, while preserving the essential uncertainty information. For simplicity, triangular membership functions are used to describe uncertain distribution parameters. Under convex membership assumptions, each α-level corresponds to an interval representation, allowing the fuzzy set to be expressed as a family of nested intervals indexed by α (Möller and Beer, 2013).

Within this framework, aleatory uncertainty is modeled by probability distributions, while epistemic uncertainty in distribution parameters is described using fuzzy sets, leading to a fuzzy probability formulation (Beer et al., 2013b). Accordingly, the random variable is extended to a fuzzy random variable $\widetilde{X}_i$, whose fuzzy CDF is defined as

$$\tilde{F}_{X_i}(x_i|\boldsymbol{\theta}_i) = \left\{ \left(F_{X_i}(x_i|\boldsymbol{\theta}_i), \mu\big(F_{X_i}(x_i|\boldsymbol{\theta}_i)\big)\right) \,\middle|\, F_{X_i}(x_i|\boldsymbol{\theta}_i) \in \mathbb{F},\ \mu\big(F_{X_i}(x_i|\boldsymbol{\theta}_i)\big) \in (0,1] \right\}, \tag{8}$$

where $\mathbb{F}$ denotes the admissible set of CDFs. For a given α-level, the corresponding α-cut of the fuzzy CDF can be expressed as

$$\tilde{F}^{\alpha}_{X_i}(x_i|\boldsymbol{\theta}_i) = \left\{ F_{X_i}(x_i|\boldsymbol{\theta}_i) \in \mathbb{F} \,\middle|\, \mu\big(F_{X_i}(x_i|\boldsymbol{\theta}_i)\big) \geq \alpha \right\}. \tag{9}$$

For each α-level, the lower and upper bounds of the fuzzy CDF are obtained through optimization over the parameter domain:

$$\underline{F}^{\alpha}_{X_i}(x_i) = \min_{\boldsymbol{\theta}_i \in D_{\boldsymbol{\theta}_i}} \tilde{F}^{\alpha}_{X_i}(x_i|\boldsymbol{\theta}_i), \tag{10}$$

$$\overline{F}^{\alpha}_{X_i}(x_i) = \max_{\boldsymbol{\theta}_i \in D_{\boldsymbol{\theta}_i}} \tilde{F}^{\alpha}_{X_i}(x_i|\boldsymbol{\theta}_i), \tag{11}$$

where $D_{\boldsymbol{\theta}_i}$ denotes the domain of the distribution parameters.

Due to the fuzziness of the probabilistic model, the structural failure probability also becomes a fuzzy variable (Beer, 2004; Valdebenito et al., 2020). The membership function of the failure probability can be constructed using the α-level optimization approach (Hanss, 2005; Beer, 2004). At each α-level, the fuzzy parameters are transformed into interval vectors $\boldsymbol{\theta}_\alpha^I$, and the lower and upper bounds of the failure probability are obtained as

$$\underline{P}_f^\alpha = \min_{\boldsymbol{\theta}\in\boldsymbol{\theta}_\alpha^I} P_f(\boldsymbol{\theta}), \tag{12}$$

$$\overline{P}_f^\alpha = \max_{\boldsymbol{\theta}\in\boldsymbol{\theta}_\alpha^I} P_f(\boldsymbol{\theta}). \tag{13}$$

By performing analyses at multiple discrete α-levels, a nested family of failure probability intervals is obtained, from which the membership function of the failure probability can be reconstructed. Since each α-cut of fuzzy parameters is equivalent to an interval parameter set, fuzzy probability analysis can be interpreted as a sequence of p-box analyses across different α-levels. This framework captures the coupled effects of aleatory and epistemic uncertainties. It also reflects sensitivity to epistemic uncertainty in distribution parameters. In general, higher membership levels indicate reduced epistemic uncertainty and narrower failure probability intervals, while significant interval expansion under small parameter perturbations implies strong sensitivity to modeling uncertainty.

However, fuzzy probability primarily captures the overall sensitivity of the failure probability with respect to epistemic uncertainty, but does not explicitly identify the dominant uncertain parameters in $\boldsymbol{\Theta}$. Therefore, dedicated sensitivity analysis methods under fuzzy uncertainty are required to quantify the contribution of individual parameters and support robust design. Although existing methods have made progress, further development is still needed to better characterize epistemic uncertainty propagation. In this context, fuzzy numbers, as a class of random sets, provide a useful theoretical basis for uncertainty propagation and reliability-based design.

2.3. Hierarchical probability model

When sufficient expert knowledge, prior assumptions, and measurement data are available, epistemic uncertainty can be modeled within a probabilistic framework. In this case, both aleatory and epistemic uncertainties can be consistently treated using a hierarchical probability model (Li et al., 2022). A key distinction is that aleatory uncertainty describes inherent randomness in structural systems, whereas epistemic uncertainty reflects incomplete knowledge of model parameters.

In the hierarchical probability model, the distribution parameters $\boldsymbol{\theta}$ are treated as random variables in the outer loop, while aleatory uncertainty is represented by the random variable $\boldsymbol{X}$ with conditional PDF $f_{\boldsymbol{X}}(\boldsymbol{x}|\boldsymbol{\theta})$ in the inner loop. Consequently, the failure probability also becomes a random variable.

The expected failure probability P_F can be estimated using MCS as

$$P_F = \int_{\boldsymbol{\theta}} P_f(\boldsymbol{\theta}) f_{\boldsymbol{\Theta}}(\boldsymbol{\theta}) d\boldsymbol{\theta} \approx \frac{1}{M}\sum_{j=1}^{M} P_f(\boldsymbol{\theta}_j), \tag{14}$$

where M denotes the number of samples.

In addition to Monte Carlo simulation, several alternative approaches have been developed to estimate the expected failure probability. For example, the point estimation method (Hong, 1996) is used to evaluate the mean failure probability, while Li et al. (Li et al., 2022) derives it based on the distribution of reliability indices. Similarly, Zhao et al. (Zhao et al., 2018) and Li et al. (Li et al., 2022) obtain quantiles of the failure probability from the reliability index distribution. Although statistical measures such as the mean, quantiles, and confidence intervals are useful for decision-making under uncertainty, they inherently couple aleatory and epistemic uncertainties, making it difficult to isolate epistemic effects. Therefore, obtaining the full distribution (PDF/CDF) of the failure probability is essential. This allows a more complete characterization of uncertainty and enables explicit analysis of how epistemic uncertainty influences the variability of failure probability.

Several studies have addressed this issue from different perspectives. A first-order approximation (Der Kiureghian and Ditlevsen, 2009) is used to construct an explicit distribution of the failure probability, while Li et al. (Li et al., 2022) proposes an analytical formulation based on moment methods. These approaches incorporate epistemic uncertainty into the probabilistic model and partially decouple aleatory and epistemic uncertainties. Once the failure probability distribution is available, its coefficient of variation and confidence intervals can be used to quantify epistemic uncertainty. Larger variability indicates stronger epistemic uncertainty. It is also noted that extreme quantiles may lead to failure probabilities approaching zero, which limits their practical interpretability. When uncertainty bounds are excessively wide, global reliability sensitivity measures (Cui et al., 2010; Wei et al., 2012) can be used to identify influential parameters and guide targeted uncertainty reduction.

To further reduce epistemic uncertainty, Bayesian updating can be introduced to refine parameter distributions using new observed data D_X. The posterior distribution of the uncertain parameters is given by

$$f'_{\boldsymbol{\Theta}}(\boldsymbol{\theta}|D_{\boldsymbol{X}}) = k\, L(D_{\boldsymbol{X}}|\boldsymbol{\theta})\, f_{\boldsymbol{\Theta}}(\boldsymbol{\theta}), \tag{15}$$

where the normalization constant is

$$k = \left[\int_{-\infty}^{\infty} L(D_{\boldsymbol{X}}|\boldsymbol{\theta}) f_{\boldsymbol{\Theta}}(\boldsymbol{\theta})\, d\boldsymbol{\theta}\right]^{-1}. \tag{16}$$

The likelihood function is defined as

$$L(D_{\boldsymbol{X}}|\boldsymbol{\theta}) \propto \mathbb{P}(D_{\boldsymbol{X}}|\boldsymbol{\Theta} = \boldsymbol{\theta}), \tag{17}$$

and under the assumption of independent observations, it can be written as

$$L(D_{\boldsymbol{X}}|\boldsymbol{\theta}) = \prod_{i=1}^{N} f_{\boldsymbol{X}|\boldsymbol{\Theta}}(D_{\boldsymbol{X}_i}|\boldsymbol{\theta}). \tag{18}$$

The likelihood function measures the agreement between model parameters and observed data, and serves as the key link between prior and posterior distributions. When prior knowledge is well supported by both theory and data, Bayesian updating effectively reduces epistemic uncertainty.

In this framework, updating is typically performed on distribution parameters, which are then propagated to update the failure probability. An alternative strategy directly updates the random variables; however, this approach may lead to a deterministic failure probability, which obscures the distinction between inherent randomness and epistemic uncertainty and weakens the physical interpretation of the updating process.

In contrast, Bayesian inference provides posterior distributions and associated credible intervals, offering a quantitative measure of epistemic uncertainty. As more data are incorporated, the posterior distribution becomes progressively refined, leading to a reduction in both the coefficient of variation and credible intervals of the failure probability. This iterative updating process enables systematic control of epistemic uncertainty and provides a consistent and robust framework for reliability assessment and engineering decision-making.

3. Practical notes

In structural reliability analysis, both aleatory and epistemic uncertainties must be properly considered. The selection of an appropriate modeling approach depends on the available information and the intended engineering objective. The former determines the degree of uncertainty that can be quantified, while the latter defines the required decision support.

These methods represent different levels of epistemic uncertainty modeling capability, ranging from interval-based to fully probabilistic representations. Classical reliability analysis assumes fully specified probability distributions and focuses on aleatory uncertainty, while epistemic uncertainty is not explicitly addressed.

For limited information, the p-box framework provides upper and lower bounds of the cumulative distribution function, leading to interval-valued failure probabilities. This makes it particularly suitable for safety-oriented assessment problems. However, overly wide bounds may limit its usefulness in design optimization and sensitivity analysis. Fuzzy probability models provide a more flexible representation of epistemic uncertainty by describing its influence on failure probability in a graded manner. Based on the sensitivity of the resulting bounds, one can judge whether additional data collection and Bayesian updating are required. In contrast, hierarchical Bayesian models treat distribution parameters as random variables and enable systematic updating as new data become available, progressively reducing epistemic uncertainty. However, their ability to explicitly represent worst-case scenarios is more limited compared with interval-based approaches.

Overall, these methods constitute a complementary framework for hybrid uncertainty modeling. The choice of method should be guided by the available information and the specific engineering objective. In practice, combining multiple methods with sensitivity analysis is often beneficial for identifying influential uncertain parameters and improving the robustness of engineering decisions.

4. Application example

This section presents a classical strip footing problem from Sudret (2014) (Sudret, 2014) to illustrate the application of each method investigated in this study. The strip footing has a width of B =10

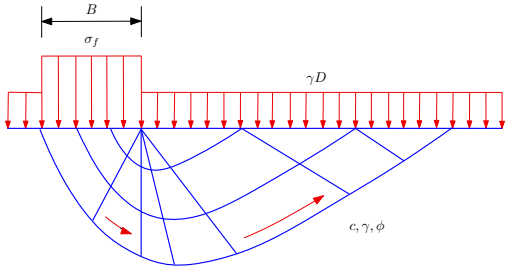


Figure 1. Strip footing

Table I. Probabilistic information for the random variables

Method Parameter	Distribution	Mean value	CoV
B	Deterministic	10 m	–
D	Gaussian (truncated)	1 m	0.15
γ	Lognormal	20 kN/m^3	0.1
c	Lognormal	20 kPa	0.25
ϕ	Beta	Range: [0, 45]°, $\mu_\phi = 30°$	≈0.1

m and is embedded at a depth D, as illustrated in Fig. 1. It is assumed that groundwater is located far below the surface, and the soil is homogeneous with cohesion c, friction angle ϕ and unit weight γ. The limit-state function is defined as the ultimate bearing capacity not exceeding its design value (Lang et al., 2011):

$$g(\boldsymbol{X}) = q_u(\boldsymbol{X}) - q_{des} = cN_c + \gamma D N_q + \frac{1}{2} B\gamma N_\gamma - q_{des}, \tag{19}$$

where $N_q = e^{\pi \tan\phi} \tan^2\left(\frac{\pi}{4} + \frac{\phi}{2}\right)$, $N_c = (N_q - 1)\cot\phi$, and $N_\gamma = 2(N_q - 1)\tan\phi$.

The variables D, γ, c, and ϕ are treated as independent random variables with properties listed in Table I. The design value q_{des} is obtained by dividing the ultimate bearing capacity by the safety factor (SF), i.e., q_{des}=$\overline{q_u}$/SF. The value of $\overline{q_u}$ is determined using the mean values of the parameters listed in Table I. With a safety factor of 2, the resulting design value is q_{des}= 2.78 MPa.

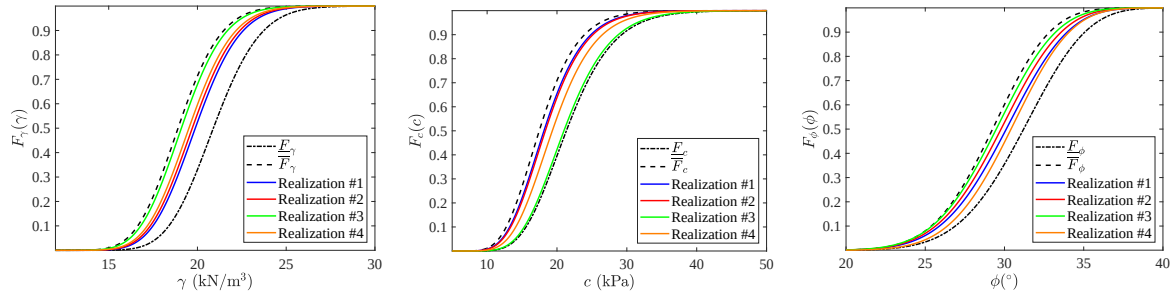
Considering only aleatory uncertainty, Monte Carlo simulation (MCS) with 10^6 samples gives the failure probability as $\hat{P}_f = 3.9345 \times 10^{-2}$. Due to limited information, there is significant epistemic uncertainty in estimating the mean values of γ and c (i.e., μ_γ and μ_c), as well as the distribution parameters of ϕ (i.e., α_ϕ and β_ϕ). It is assumed that the interval values of μ_γ, μ_c, α_ϕ and β_ϕ are given as follows: $\mu_\gamma \in [19, 21]$ kN/m^3, $\mu_c \in [18, 22]$ kPa, $\alpha_\phi \in [29, 35]$, and $\beta_\phi \in [13, 19]$.

Given the known distribution families (Table I), parametric p-boxes are used to model the CDFs of γ, c, and ϕ, as given in Fig. 2. By combining particle swarm optimization (PSO) (Kennedy and

Eberhart, 1995) with MCS, the lower and upper bounds of the failure probability are estimated as

$$\underline{\hat{P}}_f = \mathbb{P}\left(\max_{X_i \in [\underline{X}_i, \overline{X}_i]} g(\boldsymbol{X}) \leq 0\right) = 2.769 \times 10^{-3}, \tag{20}$$

$$\overline{\hat{P}}_f = \mathbb{P}\left(\min_{X_i \in [\underline{X}_i, \overline{X}_i]} g(\boldsymbol{X}) \leq 0\right) = 2.243 \times 10^{-1}. \tag{21}$$



(a) Soil weight γ (b) Cohesion c (c) Friction angle ϕ°

Figure 2. Parametric p-box of γ, c, and ϕ

As shown in Eqs. 20–21, the failure probability spans nearly two orders of magnitude, indicating a strong influence of epistemic uncertainty. To further investigate this effect, a fuzzy probability analysis is performed using triangular membership functions for μ_γ, μ_c, α_ϕ, and β_ϕ. The resulting fuzzy failure probability is obtained based on Eqs. 12–13. At membership level 1, the failure probability is $\hat{P}_f = 3.9172 \times 10^{-2}$, which is close to the case without epistemic uncertainty. At membership level 0, the failure probability varies within $[2.866 \times 10^{-3}, 2.226 \times 10^{-1}]$, consistent with the parametric p-box bounds. The obtained membership function shows that the failure probability is highly sensitive to epistemic uncertainty, suggesting that additional information could significantly reduce uncertainty.

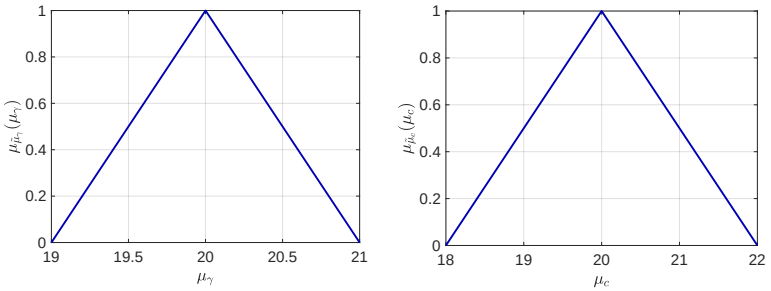
Motivated by this observation, a hierarchical Bayesian model is further adopted. Prior distributions are assigned to μ_γ, μ_c, α_ϕ, and β_ϕ as listed in Table II. Using a double-loop MCS, the expected failure probability is estimated as 5.345×10^{-2} with a coefficient of variation of 0.750. The corresponding credible intervals are 95% $[7.441 \times 10^{-3}, 1.585 \times 10^{-1}]$, 90% $[1.019 \times 10^{-2}, 1.317 \times 10^{-1}]$, and 75% $[1.631 \times 10^{-2}, 9.692 \times 10^{-2}]$.

Furthermore, additional soil property data reported by Raviteja et al. (Raviteja and Basha, 2021) are used to update the model parameters. The dataset includes soil unit weight γ, cohesion c, and friction angle ϕ, denoted as

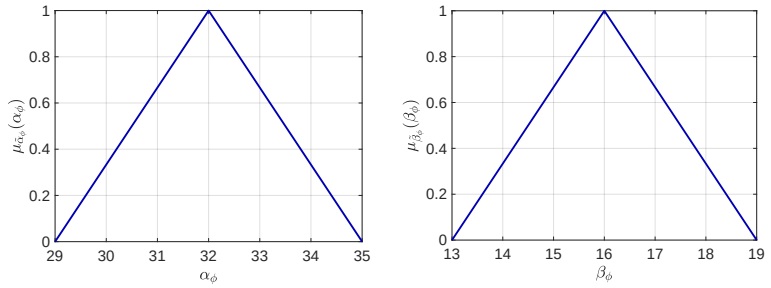
$$[D_\gamma, D_c, D_\phi] = \begin{bmatrix} 14.1 & 23 & 24 \\ 17.6 & 29 & 39 \\ 15.9 & 28 & 32 \\ 12.5 & 30 & 37 \\ 13.2 & 18 & 29.2 \end{bmatrix}.$$

Table II. Prior distribution of the distribution parameters

Parameter	Distribution	Mean value	CoV
μ_γ	Lognormal	20 kN/m^3	0.075
μ_c	Lognormal	20 kPa	0.075
α_ϕ	Lognormal	32	0.075
β_ϕ	Lognormal	16	0.075



(a) μ_γ (b) μ_c



(c) α_ϕ (d) β_ϕ

Figure 3. Membership functions of μ_γ, μ_c, α_ϕ, and β_ϕ

Based on these observations, Bayesian inference is applied to update the distributions of the model parameters. Combining Eq. 2 and Eq. 15, the prior and posterior failure probability distributions are obtained using Markov chain Monte Carlo (MCMC) coupled with Monte Carlo simulation with $M = 10^6$ samples (see Fig. 4).

The results indicate that the CoV of the failure probability serves as an effective measure of epistemic uncertainty. After Bayesian updating, the CoV of the failure probability is reduced from 0.750 to 0.383, indicating a 49% reduction in relative epistemic uncertainty. The credibility intervals for the failure probability have been updated as follows: the 95% credibility interval is $[1.074 \times 10^{-1}, 5.471 \times 10^{-1}]$; the 90% credibility interval is $[1.295 \times 10^{-1}, 5.034 \times 10^{-1}]$; and the 75% credibility

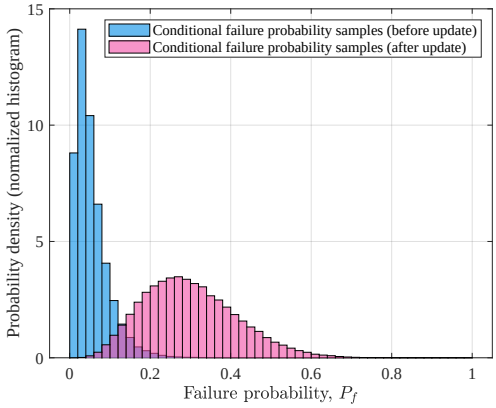


Figure 4. Histogram of the failure probability before and after update

interval is $[1.694 \times 10^{-1}, 4.343 \times 10^{-1}]$. As additional measurements become available, both the CoV and credibility intervals are expected to further decrease, leading to more stable and reliable failure probability estimates. This refined uncertainty quantification framework provides a rational basis for geotechnical reliability design under both aleatory and epistemic uncertainties.

5. Summary and Conclusions

This paper investigated structural reliability analysis under both aleatory and epistemic uncertainties from an engineering perspective. While classical probabilistic methods effectively handle aleatory uncertainty, they are often insufficient when epistemic uncertainty is significant due to incomplete information.

Three representative approaches for hybrid uncertainty modeling are compared: p-boxes, fuzzy probability, and hierarchical Bayesian models. The p-box approach provides efficient and conservative bounds for failure probability, making it suitable for safety-critical applications, but its rigid interval representation limits detailed sensitivity interpretation. The fuzzy probability model extends this framework by capturing the effect of parameter variations, offering more informative bounds for uncertainty propagation and reliability assessment. In contrast, the hierarchical Bayesian model reduces epistemic uncertainty through data assimilation and iterative updating, allowing failure probability estimates to converge as more information becomes available.

Sensitivity analysis plays a key role in identifying influential parameters and guiding targeted data collection to reduce epistemic uncertainty. However, global sensitivity analysis methods that simultaneously account for aleatory and epistemic uncertainties remain challenging.

In summary, method selection depends on data availability and analysis objectives: p-boxes for conservative assessment, fuzzy probability for uncertainty interpretation, and Bayesian models for data-driven updating. Future work should further improve model integration and sensitivity analysis methods to support complex engineering applications.

Acknowledgements

The authors gratefully acknowledge the support of the Alexander von Humboldt Foundation for the postdoctoral grant of Pei-Pei Li, the Henriette Herz Scouting program (Matthias G.R. Faes), and the financial support of the German Research Foundation (DFG) for Chao Dang (Grant number 530326817).

References

Alvarez, D. A., J. E. Hurtado, and F. Uribe: 2014, 'Estimation of the lower and upper probabilities of failure using random sets and subset simulation'. In: *Vulnerability, Uncertainty, and Risk: Quantification, Mitigation, and Management*. pp. 905–914.

Beer, M.: 2004, 'Uncertain structural design based on nonlinear fuzzy analysis'. *ZAMM-Journal of Applied Mathematics and Mechanics/Zeitschrift für Angewandte Mathematik und Mechanik: Applied Mathematics and Mechanics* **84**(10-11), 740–753.

Beer, M., S. Ferson, and V. Kreinovich: 2013a, 'Imprecise probabilities in engineering analyses'. *Mechanical Systems and Signal Processing* **37**(1–2), 4–29.

Beer, M., Y. Zhang, S. T. Quek, and K. K. Phoon: 2013b, 'Reliability analysis with scarce information: Comparing alternative approaches in a geotechnical engineering context'. *Structural Safety* **41**, 1–10.

Ben-Haim, Y.: 1994, 'Convex models of uncertainty: applications and implications'. *Erkenntnis* **41**(2), 139–156.

Cui, L., Z. Lü, and X. Zhao: 2010, 'Moment-independent importance measure of basic random variable and its probability density evolution solution'. *Science China Technological Sciences* **53**, 1138–1145.

Der Kiureghian, A. and O. Ditlevsen: 2009, 'Aleatory or epistemic? Does it matter?'. *Structural Safety* **31**(2), 105–112.

Dubois, D. and H. Prade: 1997, 'The three semantics of fuzzy sets'. *Fuzzy sets and systems* **90**(2), 141–150.

Faes, M. G., M. Broggi, G. Chen, K.-K. Phoon, and M. Beer: 2022, 'Distribution-free P-box processes based on translation theory: Definition and simulation'. *Probabilistic Engineering Mechanics* **69**, 103287.

Faes, M. G., M. Daub, S. Marelli, E. Patelli, and M. Beer: 2021, 'Engineering analysis with probability boxes: A review on computational methods'. *Structural Safety* **93**, 102092.

Ferson, S. and L. R. Ginzburg: 1996, 'Different methods are needed to propagate ignorance and variability'. *Reliability Engineering & System Safety* **54**(2-3), 133–144.

Ferson, S., V. Kreinovich, L. Ginzburg, D. S. Myers, and K. Sentz: 2003, *Constructing probability boxes and Dempster-Shafer structures*, No. 4015. Sandia National Laboratories.

Hanss, M.: 2005, *Applied fuzzy arithmetic*. Springer.

Hong, H. P.: 1996, 'Evaluation of the probability of failure with uncertain distribution parameters'. *Civil Engineering Systems* **13**(2), 157–168.

Kennedy, J. and R. Eberhart: 1995, 'Particle swarm optimization'. In: *Proceedings of ICNN'95-international conference on neural networks*, Vol. 4. pp. 1942–1948.

Kiureghian, A. D.: 1989, 'Measures of structural safety under imperfect states of knowledge'. *Journal of Structural Engineering* **115**(5), 1119–1140.

Lang, Am, Amann, H.-j, Huder, J., P., Puzrin, J. Huder, and H.-J. Lang: 2011, *Bodenmechanik und grundbau*. Springer.

Li, P.-P., Y.-G. Zhao, and Z. Zhao: 2022, 'Efficient method for fully quantifying the uncertainty of failure probability'. *Computer Methods in Applied Mechanics and Engineering* **399**, 115345.

Moens, D. and M. Hanss: 2011, 'Non-probabilistic finite element analysis for parametric uncertainty treatment in applied mechanics: Recent advances'. *Finite Elements in Analysis and Design* **47**(1), 4–16.

Möller, B. and M. Beer: 2008, 'Engineering computation under uncertainty–capabilities of non-traditional models'. *Computers & Structures* **86**(10), 1024–1041.

Möller, B. and M. Beer: 2013, *Fuzzy randomness: uncertainty in civil engineering and computational mechanics*. Springer Science & Business Media.

Möller, B., W. Graf, and M. Beer: 2000, 'Fuzzy structural analysis using α-level optimization'. *Computational Mechanics* **26**(6), 547–565.

Oberkampf, W. L., J. C. Helton, C. A. Joslyn, S. F. Wojtkiewicz, and S. Ferson: 2004, 'Challenge problems: uncertainty in system response given uncertain parameters'. *Reliability Engineering & System Safety* **85**(1-3), 11–19.

Qiu, Z. and I. Elishakoff: 1998, 'Antioptimization of structures with large uncertain-but-non-random parameters via interval analysis'. *Computer Methods in Applied Mechanics and Engineering* **152**(3-4), 361–372.

Raviteja, K. and B. M. Basha: 2021, 'Characterization of variability of unit weight and shear parameters of municipal solid waste'. *Journal of Hazardous, Toxic, and Radioactive Waste* **25**(2), 04020077.

Roy, C. J. and W. L. Oberkampf: 2011, 'A comprehensive framework for verification, validation, and uncertainty quantification in scientific computing'. *Computer Methods in Applied Mechanics and Engineering* **200**(25-28), 2131–2144.

Schöbi, R. and B. Sudret: 2017, 'Structural reliability analysis for p-boxes using multi-level meta-models'. *Probabilistic Engineering Mechanics* **48**, 27–38.

Sivia, D. and J. Skilling: 2006, *Data analysis: a Bayesian tutorial*. OUP Oxford.

Sudret, B.: 2014, 'Polynomial chaos expansions and stochastic finite element methods'. *Risk and reliability in geotechnical engineering* pp. 265–300.

Valdebenito, M. A., M. Beer, H. A. Jensen, J. Chen, and P. Wei: 2020, 'Fuzzy failure probability estimation applying intervening variables'. *Structural Safety* **83**, 101909.

Walls, L., T. Bedford, M. Revie, and E. Zio: 2017, 'Reliability, risk and safety: analytical support for decision making'. *EURO Journal on Decision Processes* **5**, 1–4.

Wei, P., Z. Lu, W. Hao, J. Feng, and B. Wang: 2012, 'Efficient sampling methods for global reliability sensitivity analysis'. *Computer Physics Communications* **183**(8), 1728–1743.

Yuen, K.-V.: 2010, *Bayesian methods for structural dynamics and civil engineering*. John Wiley & Sons.

Zadeh, L. A.: 1965, 'Information and control'. *Fuzzy Sets* **8**(3), 338–353.

Zhang, H., H. Dai, M. Beer, and W. Wang: 2013, 'Structural reliability analysis on the basis of small samples: An interval quasi-Monte Carlo method'. *Mechanical Systems and Signal Processing* **37**(1–2), 137–151.

Zhao, Y.-G., P.-P. Li, and Z.-H. Lu: 2018, 'Efficient evaluation of structural reliability under imperfect knowledge about probability distributions'. *Reliability Engineering & System Safety* **175**, 160–170.

Zimmermann, H.-J.: 2011, *Fuzzy set theory—and its applications*. Springer Science & Business Media.

Possibilistic Filtering for Reliable Robot Localization

Jan Schneider[1)], Tom Könecke[1)], Henrik Ebel[2)], and Michael Hanss[1)]
[1)] *Institute of Engineering and Computational Mechanics, University of Stuttgart, Germany*
[2)] *Department of Mechanical Engineering, LUT University, Lappeenranta, Finland*

Abstract. Uncertainty in engineering applications is commonly addressed within a probabilistic framework that assumes an underlying aleatory nature. However, in many practical scenarios, uncertainty can arise from incomplete knowledge rather than inherent randomness, reflecting epistemic rather than purely stochastic effects. Classical probabilistic approaches do not explicitly distinguish between these types of uncertainty, which can lead to overly confident or diluted probability assessments. This motivates the use of more expressive frameworks for uncertainty quantification. Possibility theory, as a theory of imprecise probabilities, provides a unified and computationally efficient framework for representing both epistemic and aleatory uncertainty. In particular, possibilistic filtering techniques have recently been developed for dynamic state estimation problems. In this contribution, we apply a particle-based possibilistic filtering approach to a real-world robot localization problem. The considered setup involves significant epistemic uncertainty arising from ambiguous landmark configurations and measurement limitations. The results demonstrate that the proposed method yields robust state estimates that reflect the underlying uncertainty. Furthermore, we introduce modifications to the original filter implementation that substantially reduce the computational cost.

Keywords: uncertainty quantification, possibility theory, state estimation, filtering, measurement uncertainty, robot localization

1. Introduction

In many engineering applications, uncertainties are not purely random but stem also from a lack of knowledge. Classical probabilistic approaches struggle to distinguish between these types of uncertainty and can suffer from probability dilution or false confidence, where critical event probabilities counter-intuitively decrease with fewer observations, as convincingly shown for the problem of satellite conjunction analysis by Balch et al. (2019). The problem of dynamic state estimation is frequently handled with probabilistic filtering techniques, where knowledge about past states of a system is propagated forward in time and updated with knowledge from new measurements. Also in this context, the susceptibility of probabilistic methods to probability dilution and false confidence can lead to systematic overconfidence in the state estimates, which can be critical in safety-relevant applications such as automation or autonomy stacks, e.g., in certain robotics applications. Possibility theory, as a theory of imprecise probabilities, i.e., a non-additive framework of uncertainty quantification, does not suffer from these issues.

Another challenge in localization arises when measurements are ambiguous, i.e., when the available sensor information allows for multiple equally plausible state estimates. This is a well-known

creative commons © 2026 by the author(s). This work is licensed under the Creative Commons Attribution 4.0 International License (CC BY 4.0), which permits unrestricted use, distribution, and reproduction in any medium, provided the original author and source are credited.

issue to which considerable effort has been devoted to handling such ambiguity in the context of probabilistic filtering, e.g., by joint compatibility branch-and-bound techniques (Neira and Tardos, 2001), multiple hypothesis tracking (Blackman, 2004) or joint probabilistic data association filters (Bar-Shalom et al., 2009). However, these approaches require explicit algorithmic machinery, while possibility theory, by contrast, handles such ambiguity natively, as we demonstrated in the context of static state-estimation in Könecke et al. (2024).

Recent developments in possibilistic filtering techniques provide the opportunity to obtain robust state estimates that appropriately reflect the uncertainty inherent to the estimation process, as addressed by several authors over the recent years. Benferhat et al. (2000) present a qualitative counterpart to Kalman filtering, where beliefs about the state are represented by possibilistic ranking functions and iteratively updated. Matía et al. (2006) investigate a robot localization problem in which odometry and laser-based distance and angle measurements to landmarks and wall segments are processed as trapezoidal fuzzy variables and propagated through nonlinear models. They improve their approach later (Matía et al., 2021) by splitting core and support of the fuzzy variables into separate, parallel algorithms. Ferrero et al. acknowledge the limitation of the Gaussian noise assumption in Kalman filtering and propose an alternative approach using random-fuzzy variables (that we call possibility distributions) to more appropriately model measurement noise while keeping process noise probabilistic (Ferrero et al., 2019; Ferrero et al., 2021). A converse assumption is made by Hose and Hanss (2021a), who argue that primarily process noise is epistemic, i.e., non-probabilistic in nature, and present a particle-based possibilistic filtering technique applied to a nonlinear two-state batch chemical reaction problem. It is the particle-based character of this method that allows for arbitrary, non-parametric possibility distributions and nonlinear models, which is crucial for the application example presented in this contribution. The authors share the assessment that, in most engineering applications, uncertainty in the process description is often to a large part epistemic, as hard-to-model, highly detailed, time-variant, or expensive-to-evaluate deterministic, physical phenomena are often purposefully or knowingly neglected or simplified in process models. In essence, every model is, at least partly, systematically and deterministically not perfectly accurate. Hence, the contribution builds upon the foundational methodology set forward in Hose and Hanss (2021a).

This contribution consists of two main parts. First, some elementaries of possibility theory are introduced and the main steps of the possibilistic filtering procedure as originally presented by Hose and Hanss (2021a) are recalled. Then, the filter is applied to a robot localization task, where it improves on an earlier static state estimation approach by Könecke et al. (2024). Critically, in addition to the application to a real-world estimation problem, the contribution of this paper consists of some key modifications to the originally proposed filter implementation, which enable a real-time application in localization problems, e.g., in mobile robotics.

2. Foundations of Possibilistic Filtering

In this section, we provide a brief introduction to possibility theory and the key concepts of possibilistic filtering, offering a compact yet comprehensive overview of the underlying principles and methodology. In the following, the quantity of interest is modeled as a random variable $\boldsymbol{X} : \Omega \to E$

on the measurable space (Ω, Σ), where Ω is the sample space, E is the state space, and Σ is the associated σ-algebra. All subsequently introduced random variables are assumed to be well defined on their respective measurable spaces. On this basis, a possibility distribution $\pi_{\boldsymbol{X}}$ is defined as any mapping $\pi_{\boldsymbol{X}} : \Omega \to [0, 1]$ satisfying $\sup_{x\in\Omega} \pi_{\boldsymbol{X}}(x) = 1$. This function assigns a degree of possibility to each element in the sample space and induces the corresponding possibility measure

$$\Pi_{\boldsymbol{X}}(A) = \sup_{\boldsymbol{x}\in A} \pi_{\boldsymbol{X}}(\boldsymbol{x}) \tag{1}$$

for any event $A \in \Sigma$. With its fundamental axioms

$$\Pi_{\boldsymbol{X}}(\emptyset) = 0, \quad \Pi_{\boldsymbol{X}}(\Omega) = 1, \quad \Pi_{\boldsymbol{X}}\left(\bigcup_{i=1}^{\infty} A_i\right) = \sup_{i\in\mathbb{N}} \Pi_{\boldsymbol{X}}(A_i), \tag{2}$$

it represents a complete, normal and maxitive measure of uncertainty. Crucially, the possibility measure $\Pi_{\boldsymbol{X}}(A)$ is not self-dual, but rather has the dual necessity measure

$$\mathrm{N}_{\boldsymbol{X}}(A) = 1 - \Pi_{\boldsymbol{X}}(\neg A), \tag{3}$$

with the corresponding counter event $\neg A$.

More precisely, a probability measure $\mathrm{P}_{\boldsymbol{X}}$ is said to be consistent with a possibility distribution $\pi_{\boldsymbol{X}}$ if the probability of any event $A \in \Sigma$ is upper bounded by the possibility of that event, i.e., if $\mathrm{P}_{\boldsymbol{X}}(A) \leq \Pi_{\boldsymbol{X}}(A)$, and lower bounded by the necessity of that event, i.e., if $\mathrm{P}_{\boldsymbol{X}}(A) \geq \mathrm{N}_{\boldsymbol{X}}(A)$. The connection between probability and possibility theory is formalized through the notion of consistency (Delgado and Moral, 1987). A probability measure $\mathrm{P}_{\boldsymbol{X}}$ is said to be consistent with a possibility distribution $\pi_{\boldsymbol{X}}$ if, for all events $A \in \Sigma$,

$$\mathrm{N}_{\boldsymbol{X}}(A) \leq \mathrm{P}_{\boldsymbol{X}}(A) \leq \Pi_{\boldsymbol{X}}(A). \tag{4}$$

In this sense, the possibility and necessity measure act as upper and lower probability bounds, respectively. The set of all probability measures consistent with a given possibility distribution is called the credal set $\mathcal{P}_{\boldsymbol{X}}$, giving a possibilistic representation of imprecise probabilistic knowledge.

Crucially, consistency induces a second probabilistic interpretation of possibilistic modeling, namely the α-cut interpretation. In particular, the α-cut $C^{\alpha}_{\pi_{\boldsymbol{X}}} = \{\boldsymbol{x} \in \Omega \mid \pi_{\boldsymbol{X}}(\boldsymbol{x}) \geq \alpha\}$ of a possibility distribution $\pi_{\boldsymbol{X}}$ admits probabilistic guarantees with respect to all consistent probability measures. More precisely, for every $\alpha \in [0, 1]$,

$$\mathrm{P}_{\boldsymbol{X}}\left(C^{\alpha}_{\pi_{\boldsymbol{X}}}\right) \geq 1 - \alpha \tag{5}$$

holds for all probability measures $\mathrm{P}_{\boldsymbol{X}}$ consistent with $\pi_{\boldsymbol{X}}$. Further details on this relation can be found in Hose and Hanss (2021b).

To complete the foundations required for a compact formulation of possibility theory, it remains to derive suitable possibility distributions. Although several construction methods exist depending on the available information, we adopt the so-called Imprecise Probability-to-Possibility (IP-Π) transformation

$$\pi_{\boldsymbol{X}}(\boldsymbol{x}) = \sup_{\mathrm{P}_{\boldsymbol{X}}\in\mathcal{P}_{\boldsymbol{X}}} \mathrm{P}_{\boldsymbol{X}}\left(\{\boldsymbol{\xi} \in \Omega : \rho(\boldsymbol{\xi}) \leq \rho(\boldsymbol{x})\}\right) \quad \forall \boldsymbol{x} \in \Omega, \tag{6}$$

based on a (subjective) plausibility ordering $\rho : \Omega \to [0, 1]$. This transformation yields a possibility distribution consistent with all probability measures $\mathrm{P}_{\boldsymbol{X}}$ corresponding to the imprecise probabilistic information set $\mathcal{P}_{\boldsymbol{X}}$. In this sense, the IP-Π transformation provides the least conservative possibilistic representation that preserves consistency with the underlying imprecise probabilistic information. The objective of this paper is to apply a possibilistic filtering technique to a real-world example. To this end, the filtering problem based on possibilistic inference is briefly introduced below, together with its main recursive steps. A complete derivation of the filter can be found in (Hose and Hanss, 2021a).

Evolution For a general filter problem, consider a sequence of state variables $\boldsymbol{X}_k$. The state evolution is governed by a (potentially nonlinear) mapping

$$\boldsymbol{X}_k = \boldsymbol{f}_k(\boldsymbol{X}_{k-1}, \boldsymbol{V}_k), \tag{7}$$

where $\boldsymbol{V}_k : \Omega_v \to \mathcal{V}$ denotes an uncertain perturbation, also denoted as process noise, and $\boldsymbol{f}_k : E \times \mathcal{V} \to E$ is a measurable state transition function.

Observation Additional information about the state is obtained through observations $\boldsymbol{Y}_k : \Omega_y \to \mathcal{Y}$, which are generated through a (potentially nonlinear) observable

$$\boldsymbol{Y}_k = \boldsymbol{h}_k(\boldsymbol{X}_k, \boldsymbol{W}_k), \tag{8}$$

where $\boldsymbol{W}_k : \Omega_w \to \mathcal{W}$ represents measurement uncertainty and $\boldsymbol{h}_k : E \times \mathcal{W} \to \mathcal{Y}$ is a measurable observation function. All uncertain variables are assumed to be strongly independent. More details on this restriction can be found in (Hose and Hanss, 2019, Section 2.4).

The goal of filtering is to combine these two sources of information and recursively determine the possibility distribution of the state variable $\boldsymbol{X}_k$ given the sequence of observations $\boldsymbol{y}_{1,\dots,k}$ and the model information, i.e., to compute $\pi_{\boldsymbol{X}_k|\boldsymbol{y}_{1,\dots,k}}$ for all time steps $k \in \mathbb{N}$. In the context of possibilistic inference, it is of major importance to preserve consistency with the underlying imprecise probabilistic information, which is achieved by the following four filter steps: Initialization, Prediction, Inversion and Updating.

Initialization The filter is initialized with a possibility distribution $\pi_{\boldsymbol{X}_0}$ representing any kind of available initial information. If little information is available, it suffices to choose a (quasi) vacuous possibility distribution, i.e., $\pi_{\boldsymbol{X}_0}(\boldsymbol{x}) = 1$ for all $\boldsymbol{x} \in \Omega_{\mathrm{qv}} \subseteq \Omega$. For a numerically efficient implementation, we approximate the desired distributions throughout the filter by suitable particle clouds. In particular, the initial distribution $\pi_{\boldsymbol{X}_0}$ is approximated by a set of N particles $\left\{\boldsymbol{x}_0^i \in \Omega\right\}_{i=1}^N$ with associated possibilistic memberships $\left\{\mu_0^i\right\}_{i=1}^N$, which are given by the evaluation of the possibility distribution for the corresponding particle, i.e., $\mu_0^i = \pi_{\boldsymbol{X}_0}(\boldsymbol{x}_0^i)$ for all $i \in \{1, \dots, N\}$. Generally, a suitable number of particles with appropriate sampling strategies has to be chosen to ensure a representation of the underlying possibility distribution with sufficient accuracy, allowing a reconstruction by interpolation or outer approximations.

Prediction The prediction step propagates the past distribution $\pi_{\boldsymbol{X}_{k-1}|\boldsymbol{y}_{1,\dots,k-1}}$ through the mapping in Eq. (7) to receive the possibility function $\pi_{\boldsymbol{X}_k|\boldsymbol{y}_{1,\dots,k-1}}$ of the current state. Theoretically, this

step can be performed by the utilization of the extension principle for independent variables given in (Hose and Hanss, 2019) in combination with Eq. (7). For the particle-based implementation, however, the prediction is carried out separately for each particle. In fact, we use

$$\boldsymbol{x}_k^i = \boldsymbol{f}_k(\boldsymbol{x}_{k-1}^i, \boldsymbol{v}_k^i) \quad \forall i \in \{1, \ldots, N\}\,, \tag{9}$$

where the set $\left\{\boldsymbol{v}_k^i \in \mathcal{V}\right\}_{i=1}^N$ is a suitable sampling representation of the underlying process noise. Since this noise is usually of epistemic nature, the corresponding possibility distribution $\pi_{\boldsymbol{V}_k}$ assigns unit possibility on the whole support on its domain $\mathcal{V}$ which has to be chosen appropriately. Moreover, it is argued in Hose and Hanss (2021a) that the predicted possibilistic memberships of the particles remain approximately invariant with respect to their previous values, i.e., $\mu_k^{i,\mathrm{pred}} \approx \mu_{k-1}^i$ for all $i \in \{1, \ldots, N\}$.

Inversion The second source of information is the observation at iteration k, which is incorporated through the inversion step. The objective is to approximate a possibility function $\pi_{\boldsymbol{X}_k|\boldsymbol{y}_k}$ on the state space based solely on the current observation and Eq. (8). To this end, we first consider $\delta_k^i = \boldsymbol{y}_k - \boldsymbol{h}_k(\boldsymbol{x}_k^i)$, i.e., the deviation between the observed value $\boldsymbol{y}_k$ and the predicted observation $\boldsymbol{h}_k(\boldsymbol{x}_k^i)$ associated with particle i, neglecting the influence of measurement noise. The membership of each particle is then determined by the possibilistic characterization of the measurement noise $\boldsymbol{W}_k$, which quantifies a degree of plausibility of the observed deviation given the available noise information. In particular, since measurement noise is often of aleatory nature, precise probabilistic information may be available. In such cases, the corresponding possibility distribution $\pi_{\boldsymbol{W}_k}$ can be obtained via a special case of Eq. (6), the so-called optimal transform (Dubois et al., 2004; Hose and Hanss, 2021b). Consequently, the inversion-based memberships are given by

$$\mu_k^{i,\mathrm{inv}} = \pi_{\boldsymbol{W}_k}(\delta_k^i) \quad \forall i \in \{1, \ldots, N\}\,. \tag{10}$$

Update The final step consists of updating the memberships of the particles by combining the information from the prediction and inversion steps. Since we have obtained two possibility distributions $\pi_{\boldsymbol{X}_k|\boldsymbol{y}_{1,\ldots,k-1}}$ and $\pi_{\boldsymbol{X}_k|\boldsymbol{y}_k}$, defined over the same domain for the same variable, an appropriate combination rule must be applied. With the assumption of strong independence, the joint possibility distribution is computed as

$$\pi_{\boldsymbol{X}_k|\boldsymbol{y}_{1,\ldots,k}}(\boldsymbol{x}) = 1 - \left(1 - \min\left(\pi_{\boldsymbol{X}_k|\boldsymbol{y}_{1,\ldots,k-1}}(\boldsymbol{x}),\ \pi_{\boldsymbol{X}_k|\boldsymbol{y}_k}(\boldsymbol{x})\right)\right)^2 \tag{11}$$

where the independence copula is used for combining two possibility distributions, as described in (Hose and Hanss, 2019). This directly translates to the particle-based implementation, yielding the updated membership of particle i as

$$\mu_k^i = 1 - \left(1 - \min\left(\mu_k^{i,\mathrm{pred}},\ \mu_k^{i,\mathrm{inv}}\right)\right)^2 \quad \forall i \in \{1, \ldots, N\}\,. \tag{12}$$

Upon completion of this step, the filter is fully updated and ready for the subsequent iteration.

3. On the Resampling and Perturbation of Particles

Two issues regarding the particle-based filtering procedure require special attention. The first issue is that particles, by the nature of the state evolution prescribed by the model, but also due to the perturbation by process noise, end up in regions of the state space with very low or zero membership. In order to maintain a sufficient representation of $\pi_{\boldsymbol{X}_k}$, such particles are discarded after every measurement update. That is,

$$\left\{\boldsymbol{x}_k^i\right\}_{i=1}^{\tilde{N}} \leftarrow \left\{\boldsymbol{x}_k^i,\ \forall i \in \{1,\ldots,N\} \mid \mu_k^i > \varepsilon\right\}, \quad \tilde{N} \leq N\,, \tag{13}$$

where ε is a small threshold value, leaving $\tilde{N}$ particles. To restore the particle count, $N-\tilde{N}$ samples are drawn uniformly from the survivors and added to the particle cloud.

The second issue is the one of perturbation of the particles by process noise. The *naïve* approach of simply drawing a random perturbation from the support of the process noise, as originally proposed by Leong and Nair (2016) and adopted by Hose and Hanss (2021a), is asymptotically conservative, but requires a substantial number of particles for even this three-dimensional example, making real-time feasibility intractable. Both publications propose an improved scheme of *redundancy removal* that divides the state space into a grid and retains only the particle of highest membership in each grid cell and subsequently resamples from the survivors to restore the particle count. This way, regions of high density are thinned out, giving the remaining particles more room to spread out and cover the state space more efficiently.

What both approaches lack is the exploitation of the fact that arbitrary—that is, independent of the uncertainty-describing distribution—sampling schemes are permitted in possibility theory. This is due to the fact that, in contrast to probability theory, the quantitative information on uncertainty is not contained in the density of samples, but rather in the image of the distribution itself. The strategy proposed here exploits this degree of freedom: half the particles are drawn classically with probabilistic uniform perturbation, while the remainder are produced in pairs from source particles—one displaced outward along the vector away from the centroid of higher-membership particles until the process-noise boundary is reached, and one displaced inward along the same vector by half that distance—which is why we denote this variant as *centrifugal sampling*. This is followed by a redundancy-removal pass per grid cell, as in the originally improved scheme. Qualitative sketches of the described strategies are given in Fig. 1. An evaluation of their computational efficiency is given in the application example in the next section.

4. Application Example

The main contribution of this paper is the validation of the proposed filter in a localization scenario for a mobile robot. The robot's pose is defined as $\boldsymbol{x} = (x\ y\ \theta)^\mathsf{T}$, where x and y denote the Cartesian position coordinates and θ represents the orientation. In the experiments, a mobile robot equipped with four Mecanum wheels, which permit the robot to accelerate in any direction independently of its orientation, is employed, see Fig. 2 for a photograph. To its top plate, a single-board computer with a wide-angle RGB camera is attached, allowing the robot to perceive

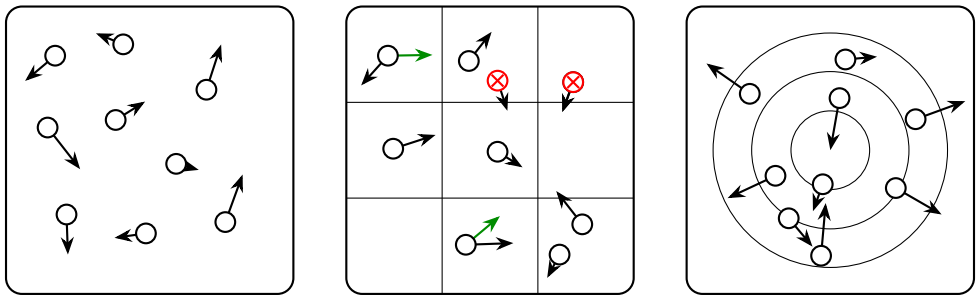


Figure 1. Illustration of different sampling strategies for perturbing particles by process noise.

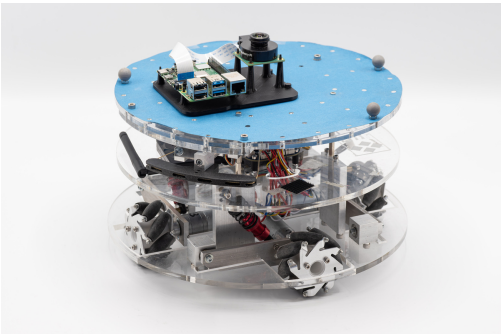


Figure 2. The mobile robot used in the experiments, equipped with four Mecanum wheels and a single-board computer with a wide-angle RGB camera.

visual landmarks in its environment via computer vision, compare Könecke et al. (2024). The setup records the directions, relative to the robot's own orientation, in which the (purposefully visually indistinguishable) landmarks are perceived. The robot's control input is given by the robot's velocity commands $\boldsymbol{u} = (v_x,\ v_y,\ \omega)^\mathsf{T}$, specifying the desired translational velocities in the body frame and the desired angular velocity, respectively. The positions of the visual landmarks are assumed to be known with respect to some inertial coordinate frame. Although the filter operates exclusively on the purely directional, visual measurement information from the indistinguishable landmarks, an additional high-precision motion capture system is available to provide ground-truth pose estimates. This enables a quantitative evaluation of the filter's performance at every time step. In this article, both the on-board directional data as well as the ground-truth data are recorded. Then, various filter variants are applied on the on-board dataset, presented time step by time step to the filter, in an offline manner. This allows to study various approaches, including less optimized ones and with very large numbers of particles, independently from on-board processing capabilities and real-time considerations. Real-time suitability can still be faithfully judged by analyzing per-step calculation times.

In general, the state filtering problem of an n-dimensional dynamical system represents a special case in which the underlying sample space is given by $\Omega = \mathbb{R}^n$, with the reduction of Σ to the corresponding Borel σ-field $\mathcal{B}(\mathbb{R}^n)$. In our case, the experimental validation is conducted on the

physically meaningful subspace $\mathcal{D} \subseteq \mathbb{R}^2 \times [0, 2\pi]$, corresponding to planar position and heading angle of the robot.

Model The system dynamics are modeled in an approximative manner as a discrete-time nonlinear system of the form

$$\underbrace{\begin{pmatrix} x_k \\ y_k \\ \theta_k \end{pmatrix}}_{\boldsymbol{x}_k} = \underbrace{\begin{pmatrix} x_{k-1} \\ y_{k-1} \\ \theta_{k-1} \end{pmatrix}}_{\boldsymbol{x}_{k-1}} + \Delta \begin{pmatrix} \cos\theta_{k-1} & -\sin\theta_{k-1} & 0 \\ \sin\theta_{k-1} & \cos\theta_{k-1} & 0 \\ 0 & 0 & 1 \end{pmatrix} \underbrace{\begin{pmatrix} v_{x,k-1} \\ v_{y,k-1} \\ \omega_{k-1} \end{pmatrix}}_{\boldsymbol{u}_{k-1}} + \boldsymbol{v}_k \ , \tag{14}$$

where the pose $\boldsymbol{x}_k$ at time step k depends on the previous pose $\boldsymbol{x}_{k-1}$, the control input $\boldsymbol{u}_{k-1}$, and the process noise $\boldsymbol{v}_k$ at the current time step k. The system operates at a sampling rate of 10 Hz, i.e. with the time step $\Delta = 0.1\,\mathrm{s}$. This dynamic and uncertain system evolution $\boldsymbol{x}_k = f(\boldsymbol{x}_{k-1}, \boldsymbol{u}_{k-1}, \boldsymbol{v}_k)$ is equivalent to the general formulation in Eq. (7).

Measurement The measurement model of the system is defined as

$$\boldsymbol{y}_k = \boldsymbol{h}(\boldsymbol{x}_k, \boldsymbol{w}_k) \ , \tag{15}$$

where $\boldsymbol{y}_k$ is a set of angles that correspond to the relative angles between the robot's orientation and the lines of sight to up to four landmarks in the laboratory environment. Analogously, this formulation is consistent with Eq. (8) and provides the basis for the inversion step. An extensive description on the measurement system behind h as well as the calibration for an inverse possibilistic description $\pi_{\boldsymbol{W}}$ of possible states $\boldsymbol{x}_k$ given observed angles $\boldsymbol{y}_k$ is given in (Könecke et al., 2024). Essentially, the measurement setup is able to give a calibrated and conservative estimate $\pi_{\boldsymbol{X}_k|\boldsymbol{y}_k}(\boldsymbol{x}_k)$ of the robot's pose at each time step, but due to the ambiguity of the measurement information, the confidence sets are large, originally motivating the incorporation of the system dynamics to obtain more informative estimates.

Process Noise Process noise is modeled additively as an interval-representing possibility distribution with a half-width of 0.02 m for the positional coordinates and 0.03 rad for the orientation, which are known to safely bound the actual process noise in the system. No probabilistic distribution can be assumed for the process noise, as it is highly dependent on a multitude of factors such as the condition of the floor, the battery level, the wear of the robot's wheels, etc., which are not explicitly modeled and change over time. And while those systematic effects could be modeled in a more complex way, for example by a Gaussian process model (Eschmann et al., 2021; Eschmann et al., 2023), interval values are sufficient for now and are especially more robust to changes in the system's behavior.

Modeled possibilistically, the process noise is given by the quasi vacuous possibility distribution

$$\pi_{\boldsymbol{V}_k}(\boldsymbol{v}_k) = \begin{cases} 1 & \text{if } \boldsymbol{v}_k \in \mathcal{H} \\ 0 & \text{otherwise} \end{cases} \tag{16}$$

supported on the hyperrectangle $\mathcal{H} = [-0.02\,\mathrm{m}, 0.02\,\mathrm{m}] \times [-0.02\,\mathrm{m}, 0.02\,\mathrm{m}] \times [-0.03\,\mathrm{rad}, 0.03\,\mathrm{rad}]$.

Experiment Setup The laboratory setup is depicted in Fig. 3, illustrating a non-symmetric arrangement of four landmarks within the environment. The robot is manually driven through the laboratory by a human operator.

For the filter validation, it is assumed that there is no information about the robot's initial pose available, so that the filter is initialized with a vacuous possibility distribution, i.e., $\pi_{\boldsymbol{X}_0}(\boldsymbol{x}) = 1$ for all $\boldsymbol{x} \in \mathcal{D}$. Subsequently, the particle-based filter is applied with $N = 10^6$ particles following the steps described in the previous section, utilizing the given model and measurement information. Intuitively, each particle represents a possible pose of the robot, which is propagated through the system dynamics and updated with the measurement information at each time step. A video of the experiment together with the corresponding dataset is available via the QR code in Fig. 3, which links to (Schneider et al., 2026). To assess the performance of the filter, the empirical coverage curve given in Fig. 4 is considered, which shows the empirical coverage of the α-cuts of the estimated possibility distribution $\pi_{\boldsymbol{X}_k|\boldsymbol{y}_{1,\dots,k}}$ with respect to the ground truth pose estimates from the motion capture system. The curve shows that the filter's estimates are well-calibrated, as the empirical coverage indicates the satisfaction of the probabilistic guarantees of α-cuts, i.e.,

$$\mathrm{P}_{\boldsymbol{X}}\left(C^{\alpha}_{\pi_{\boldsymbol{X}_k|\boldsymbol{y}_{1,\dots,k}}}\right) \geq 1 - \alpha \quad \text{for all} \quad \alpha \in [0,1]\,. \tag{17}$$

A crucial factor influencing the filter's performance is the number of particles, which inherently represents a trade-off between computational cost and estimation accuracy. Thus, the improved sampling strategies introduced in the previous section are compared with respect to their convergence behavior in empirical coverage for varying particle numbers. The results, presented in Fig. 5, demonstrate that more advanced resampling strategies allow for a substantial reduction in the number of particles while maintaining comparable coverage performance, enabling real-time feasibility of the filter in this application example.

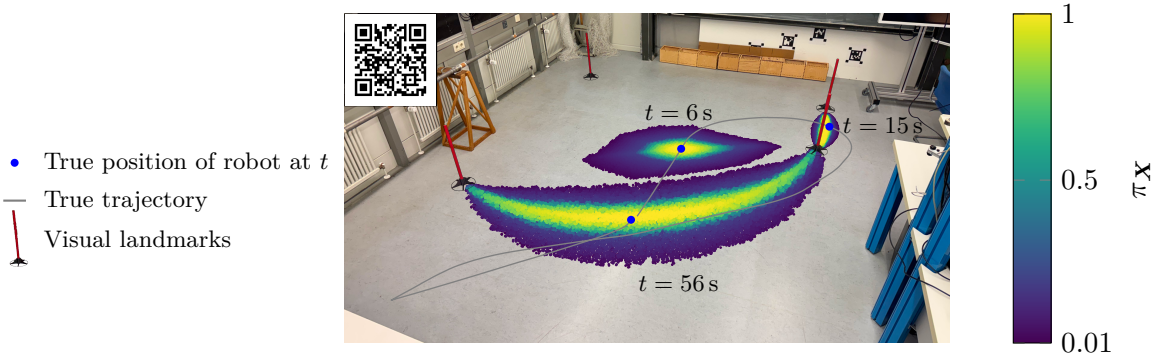


Figure 3. The laboratory setup with confidence distributions of the robot's position at three different time steps.

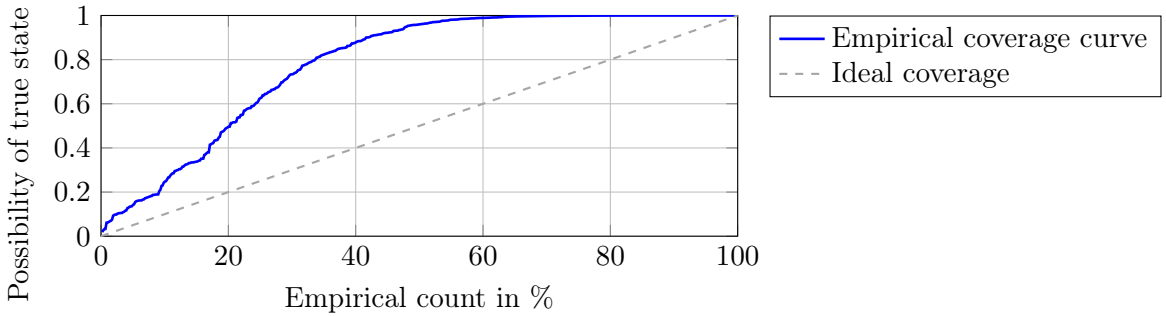


Figure 4. Empirical coverage curve.

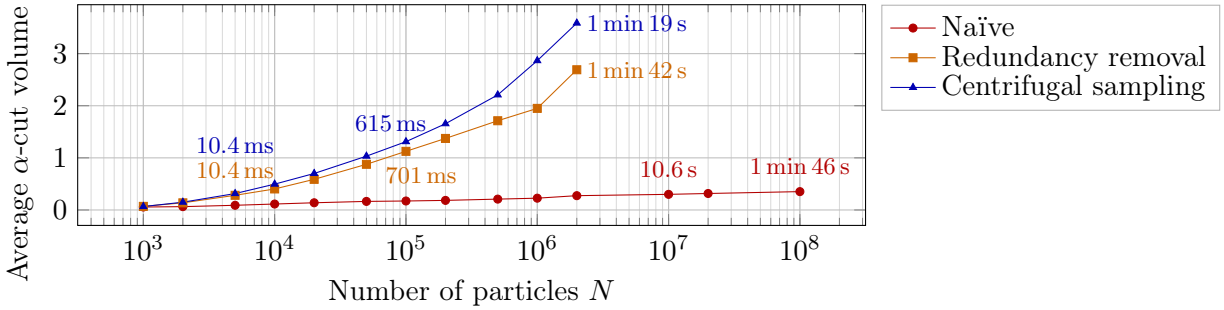


Figure 5. Average α-cut volume of the estimated possibility distribution as a function of the number of particles N, averaged across $\alpha \in \{0.05, 0.5, 0.95\}$. Average computation times per time step are given for selected runs.

5. Conclusions

We have demonstrated the applicability of a particle-based possibilistic filter to a real-world robot localization problem characterized by a challenging measurement setup and significant process noise. The results indicate that the filter successfully approximates a possibility distribution whose α-cuts satisfy the corresponding probabilistic guarantees, a property that is essential for reliable state estimation in safety-critical applications. In addition, we have introduced an improved sampling strategy for the evolution of the particle cloud. These strategies enable a substantial reduction in the number of particles while maintaining comparable estimation performance, thereby significantly enhancing the real-time feasibility of the proposed filtering approach.

Several promising directions for future research emerge from this work, including the investigation of more complex system models. In particular, questions of stability and observability constitute challenging aspects in the context of state estimation. Furthermore, if the filter is to be embedded within a feedback control loop, issues of closed-loop stability must be addressed. This represents a non-trivial problem that also demands highly efficient filter implementations to meet real-time requirements. Furthermore, set-based propagation and fusion techniques could be explored to approximate possibility distributions without relying on a particle-based implementation. Such approaches would trade estimation accuracy for improved computational efficiency. In particular, hyperellipsoidal set representations could be employed to approximate a fixed number of α-cuts of

the underlying possibility distribution. In any case, the proposed filter may already be attractive in applications. For instance, it may be useful in mobile robotics in applications that require a more robust and more informed avoidance of collisions in the phase of different kinds of uncertainty, including ambiguity, compared to nominal approaches, as proposed by Rosenfelder et al. (2025), can offer.

References

Balch, M. S., R. Martin, and S. Ferson: 2019, 'Satellite Conjunction Analysis and the False Confidence Theorem'. *Proceedings of the Royal Society A* **475**(2227), 20180565.

Bar-Shalom, Y., F. Daum, and J. Huang: 2009, 'The Probabilistic Data Association Filter'. *IEEE Control Systems Magazine*.

Benferhat, S., D. Dubois, and H. Prade: 2000, 'Kalman-like Filtering and Updating in a Possibilistic Setting'. In: *14th European Conference on Artificial Intelligence*. pp. 8–12.

Blackman, S.: 2004, 'Multiple Hypothesis Tracking for Multiple Target Tracking'. *IEEE Aerospace and Electronic Systems Magazine* **19**(1), 5–18.

Delgado, M. and S. Moral: 1987, 'On the Concept of Possibility-Probability Consistency'. *Fuzzy Sets and Systems. An International Journal in Information Science and Engineering* **21**(3), 311–318.

Dubois, D., L. Foulloy, G. Mauris, and H. Prade: 2004, 'Probability-Possibility Transformations, Triangular Fuzzy Sets, and Probabilistic Inequalities'. *Reliable Computing* **10**(4), 273–297.

Eschmann, H., H. Ebel, and P. Eberhard: 2021, 'Data-Based Model of an Omnidirectional Mobile Robot Using Gaussian Processes'. *IFAC-PapersOnLine* **54**(7), 13–18.

Eschmann, H., H. Ebel, and P. Eberhard: 2023, 'Exploration-Exploitation-based Trajectory Tracking of Mobile Robots using Gaussian Processes and Model Predictive Control'. *Robotica* **41**(10), 3040–3058.

Ferrero, A., R. Ferrero, W. Jiang, and S. Salicone: 2019, 'The Kalman Filter Uncertainty Concept in the Possibility Domain'. *IEEE Transactions on Instrumentation and Measurement* **68**(11), 4335–4347.

Ferrero, A., H. V. Jetti, and S. Salicone: 2021, 'The Possibilistic Kalman Filter: Definition and Comparison with the Available Methods'. *IEEE Transactions on Instrumentation and Measurement* **70**, 1–11.

Hose, D. and M. Hanss: 2019, 'Possibilistic Calculus as a Conservative Counterpart to Probabilistic Calculus'. *Mechanical Systems and Signal Processing* **133**, 106290.

Hose, D. and M. Hanss: 2021a, 'A Recursive Formulation of Possibilistic Filters'. In: *Proceedings of the 12th International Symposium on Imprecise Probability: Theories and Applications*, Vol. 147 of *Proceedings of Machine Learning Research*. pp. 180–190.

Hose, D. and M. Hanss: 2021b, 'A Universal Approach to Imprecise Probabilities in Possibility Theory'. *International Journal of Approximate Reasoning* **133**, 133–158.

Könecke, T., H. Ebel, and M. Hanss: 2024, 'Possibilistic Robot Localization Using Visual Landmarks'. *Proceedings in Applied Mathematics and Mechanics* **25**(1), e70002.

Leong, P. H. and G. N. Nair: 2016, 'Set-Membership Filtering Using Random Samples'. In: *19th International Conference on Information Fusion (FUSION)*. pp. 1087–1094, IEEE.

Matía, F., A. Jiménez, B. M. Al-Hadithi, D. Rodríguez-Losada, and R. Galán: 2006, 'The Fuzzy Kalman Filter: State Estimation Using Possibilistic Techniques'. *Fuzzy Sets and Systems* **157**(16), 2145–2170.

Matía, F., V. Jiménez, B. P. Alvarado, and R. Haber: 2021, 'The Fuzzy Kalman Filter: Improving Its Implementation by Reformulating Uncertainty Representation'. *Fuzzy Sets and Systems* **402**, 78–104.

Neira, J. and J. Tardos: 2001, 'Data Association in Stochastic Mapping Using the Joint Compatibility Test'. *IEEE Transactions on Robotics and Automation* **17**(6), 890–897.

Rosenfelder, M., H. Carius, M. Herrmann-Wicklmayr, P. Eberhard, K. Flaßkamp, and H. Ebel: 2025, 'Efficient Avoidance of Ellipsoidal Obstacles with Model Predictive Control for Mobile Robots and Vehicles'. *Mechatronics* **110**, 103386.

Schneider, J., T. Könecke, H. Ebel, and M. Hanss: 2026, 'Visualization of Possibilistic Filtering for Reliable Robot Localization'.

Possibilistic Uncertainty Modeling with Hyperellipsoids

Julian Behrend, Tom Könecke, Mario Rosenfelder, Jan Schneider,
Michael Hanss, and Peter Eberhard
Institute of Engineering and Computational Mechanics, University of Stuttgart,
Pfaffenwaldring 9, 70569 Stuttgart, Germany

Abstract. The quantification of sparse, imprecise knowledge using possibility theory traditionally forces a compromise between computational efficiency and geometric accuracy. Standard interval arithmetic over axis-aligned hyperrectangles ignores parameter dependencies and yields overly conservative bounds, while sampling-based techniques capture these dependencies but remain computationally intensive and fail to deliver guarantees. By leveraging geometric properties of ellipsoids, we address these challenges by providing a comprehensive operational calculus for possibilistic uncertainty representation using hyperellipsoids. This framework provides methodologies to construct ellipsoidal possibility distributions from data, fuse multiple knowledge sources, propagate distributions analytically through affine functions, and extract both marginal and joint distributions. Furthermore, we demonstrate the practical efficacy of these ellipsoidal possibility distributions by applying them to a filtering application for a mobile robot localization problem.

Keywords: uncertainty quantification, fuzzy arithmetic, possibility theory, imprecise probabilities, robot localization, dynamic state estimation, ellipsoidal calculus

1. Introduction

In the analysis of complex engineering systems, possibility theory provides a rigorous mathematical framework for handling both epistemic and aleatory uncertainty by bounding sets of consistent probability measures. However, the numerical implementation of possibilistic models has encountered structural and computational trade-offs. Traditional interval arithmetic relies on axis-aligned hyperrectangles. Recent approaches have favored sampling-based techniques to address parameter identification under uncertainty (Könecke et al., 2025), advanced sampling techniques for possibilistic forward propagation (Mäck and Hanss, 2021) and a particle-based formulation of possibilistic filters (Hose and Hanss, 2021). While being effective at mapping nonlinearities, sampling methods suffer from the curse of dimensionality and fail to provide trustworthy certainty guarantees.

To resolve these limitations, this paper proposes the use of hyperellipsoids as the foundational geometric structure for possibilistic uncertainty representation. Rather than relying on discrete point clouds or intervals, we want to utilize well-studied, analytically tractable properties of hyperellipsoids to allow handling multi-variate possibility distributions. While one can derive an ellipsoidal possibility distribution leveraging given expert knowledge (Kreinovich et al., 2007), this work focuses on the construction of an ellipsoidal possibility distribution from data or a probability density function. In the domain of statistical inference, Martin (2025) uses ellipsoids for

creative commons © 2026 by the author(s). This work is licensed under the Creative Commons Attribution 4.0 International License (CC BY 4.0), which permits unrestricted use, distribution, and reproduction in any medium, provided the original author and source are credited.

the efficient construction of possibility distributions from data, while Martin and Williams (2025) further propose ellipsoid-based Gaussian possibility distributions. As ellipsoids naturally arise in Gaussian distributions, they also appear together in possibilistic filtering approaches like for the Kalman filter (Ferrero et al., 2021), (Matía et al., 2021).

This paper novelly establishes a comprehensive operational calculus for possibilistic uncertainty quantification based on ellipsoidal representations. The proposed approach includes the construction of ellipsoidal possibility distributions, their fusion, and their analytical propagation. We also provide details on how to perform marginalization and compute joint distributions within this ellipsoidal setting. In addition to the theoretical development, these contributions are integrated into a recursive possibilistic filter for dynamic state estimation of a real-world mobile robot, demonstrating the practical relevance of the framework for safety-critical robotic applications.

The remainder of this paper is structured as follows. Section 2 establishes the theoretical background of possibility theory and ellipsoidal calculus. Section 3 introduces the ellipsoidal possibility distributions and details the methodologies for their construction, fusion, propagation, and marginalization, as well as the formation of joint distributions. Finally, Section 4 presents an example of a possibilistic filtering procedure in dynamic state estimation for a mobile robot to demonstrate the practical application of this framework.

2. Background

2.1. Possibility Theory

Possibility theory provides a framework for handling epistemic and aleatory uncertainty by describing the possible values of an imprecise variable $\boldsymbol{X}$ that is a measurable function $\boldsymbol{X} : \Omega \to \mathcal{V}$ from a sample space Ω to a value space $\mathcal{V}$, in this case $\mathbb{R}^n$.

The basic building block of possibility theory is the possibility distribution $\pi_{\boldsymbol{X}} : \Omega \to [0, 1]$. The function $\pi_{\boldsymbol{X}}(\boldsymbol{x})$ returns the degree of possibility that $\boldsymbol{X}$ takes the value $\boldsymbol{x}$, ranging from 0 (impossible) to 1 (fully possible). A possibility distribution is normal if $\sup_{\boldsymbol{x}} \pi_{\boldsymbol{X}}(\boldsymbol{x}) = 1$, and subnormal if $\sup_{\boldsymbol{x}} \pi_{\boldsymbol{X}}(\boldsymbol{x}) < 1$. The information contained in $\pi_{\boldsymbol{X}}$ is equivalently represented by a family of nested α-cuts $\mathcal{C}_\pi^\alpha = \{\boldsymbol{x} \in \mathbb{R}^n \mid \pi_{\boldsymbol{X}}(\boldsymbol{x}) \geq \alpha\}$ for any $\alpha \in [0, 1]$. For any two levels α_1 and α_2, with $0 \leq \alpha_1 \leq \alpha_2 \leq 1$, the inclusion $\mathcal{C}_\pi^{\alpha_2} \subseteq \mathcal{C}_\pi^{\alpha_1}$ holds. This nesting property is a fundamental characteristic of possibilistic representations.

A normal possibility distribution induces for an event $E \subseteq \Omega$ both the possibility measure

$$\Pi_{\boldsymbol{X}}(E) = \sup_{\boldsymbol{x} \in E} \pi_{\boldsymbol{X}}(\boldsymbol{x}) \tag{1}$$

and the necessity measure

$$\mathrm{N}_{\boldsymbol{X}}(E) = 1 - \Pi_{\boldsymbol{X}}(\Omega \setminus E) = 1 - \sup_{\boldsymbol{x} \notin E} \pi_{\boldsymbol{X}}(\boldsymbol{x}) \,. \tag{2}$$

By the definition of these dual measures, possibility theory serves as a framework for imprecise probabilities through the principle of consistency. A probability measure $\mathrm{P}_{\boldsymbol{X}}$ is *consistent* with $\pi_{\boldsymbol{X}}$ if

$$\mathrm{N}_{\boldsymbol{X}}(E) \leq \mathrm{P}_{\boldsymbol{X}}(E) \leq \Pi_{\boldsymbol{X}}(E) \qquad \forall E \subseteq \Omega \tag{3}$$

holds. Consequently, the α-cuts of a possibility distribution constitute sets with a guaranteed lower probability bound

$$\mathrm{P}(\mathcal{C}_\pi^\alpha) \geq 1 - \alpha \qquad \forall \alpha \in [0,1] \; . \tag{4}$$

The possibility distribution is the elementary building block of possibility theory, defining both an upper and lower probability bound. In this elementary role, it is akin to the probability density function in probability theory, but notably diverges by following a non-additive framework, i.e., by requiring the supremum and infimum in its mathematical treatment in place of the sum or integral. This will be further elaborated in the following paragraphs.

In multivariate settings, where $\boldsymbol{X} = [\boldsymbol{X}_1, \ldots, \boldsymbol{X}_q]$, the marginal distribution for a subset of q variables is obtained by projecting the joint distribution $\pi_{\boldsymbol{X}}$ onto the respective subspace

$$\pi_{\boldsymbol{X}_1}(\boldsymbol{x}_1) = \sup_{\boldsymbol{x}_2, \ldots, \boldsymbol{x}_q} \pi_{\boldsymbol{X}}(\boldsymbol{x}_1, \ldots, \boldsymbol{x}_q) \; . \tag{5}$$

Conversely, constructing a joint possibility distribution $\pi_{\boldsymbol{X}}(\boldsymbol{x}_1, \ldots, \boldsymbol{x}_q) = \mathcal{J}(\pi_{\boldsymbol{X}_1}(\boldsymbol{x}_1), \ldots, \pi_{\boldsymbol{X}_q}(\boldsymbol{x}_q))$ from marginal variables $\boldsymbol{X}_i$ requires modeling the dependencies using a copula $\mathcal{J} : [0,1]^q \to [0,1]$. For stochastically independent imprecise variables, the most specific consistency-preserving joint representation is given by

$$\pi_{\mathrm{joint}}(\boldsymbol{x}_1, \ldots, \boldsymbol{x}_q) = 1 - \left(1 - \min_{\boldsymbol{x}_1, \ldots, \boldsymbol{x}_q} (\pi_{\boldsymbol{X}_1}(\boldsymbol{x}_1), \ldots, \pi_{\boldsymbol{X}_q}(\boldsymbol{x}_q))\right)^q \; . \tag{6}$$

Proofs for this statement as well as further discussions on copulas can be found in (Hose, 2022).

Possibilistic propagation through a mapping $\boldsymbol{Y} = f(\boldsymbol{X})$ is governed by Zadeh's extension principle (Zadeh, 1975)

$$\pi_{\boldsymbol{Y}}(\boldsymbol{y}) = \sup_{\boldsymbol{x} \,|\, \boldsymbol{y} = f(\boldsymbol{x})} \pi_{\boldsymbol{X}}(\boldsymbol{x}) \; . \tag{7}$$

The extension principle ensures that the output distribution remains the most specific description consistent with the input uncertainty and the propagation model.

2.2. Ellipsoidal Calculus

A hyperellipsoid $\mathcal{E} \subset \mathbb{R}^n$, subsequently referred to as ellipsoid for simplicity, is defined as the set of points satisfying the quadratic inequality

$$\mathcal{E}(\boldsymbol{c}, \boldsymbol{P}) = \{\boldsymbol{x} \in \mathbb{R}^n \mid Q(\boldsymbol{x}, \boldsymbol{c}, \boldsymbol{P}) \leq 1\} \; , \qquad Q(\boldsymbol{x}, \boldsymbol{c}, \boldsymbol{P}) = (\boldsymbol{x} - \boldsymbol{c})^\mathsf{T} \boldsymbol{P} (\boldsymbol{x} - \boldsymbol{c}) \; , \tag{8}$$

parameterized by a center $\boldsymbol{c} \in \mathbb{R}^n$ and a symmetric positive-definite shape matrix $\boldsymbol{P} \in \mathbb{R}^{n \times n}$. The volume of $\mathcal{E}(\boldsymbol{c}, \boldsymbol{P})$ is proportional to $\det(\boldsymbol{P})^{-1/2}$. Degenerate ellipsoids also fall within this formulation with $\boldsymbol{P}$ being positive semi-definite. Such sets represent unbounded regions, e.g., cylinders or strips ($\mathrm{rank}(\boldsymbol{P}) < n$), with infinite volume.

Ellipsoidal sets can be inferred from data, for example, using the minimum volume enclosing ellipsoid (MVEE), which minimizes volume while enclosing all points and is efficiently solvable via Khachiyan's algorithm (Moshtagh, 2005).

The *intersection* of two ellipsoids is generally not an ellipsoid. For two ellipsoids $\mathcal{E}_1, \mathcal{E}_2$ with a non-empty intersection, a parameterized family of intersection-enclosing ellipsoids $\mathcal{E}_\lambda(\boldsymbol{c}_\lambda, \boldsymbol{P}_\lambda)$ can be defined by the convex combination $Q_\lambda = \lambda\, Q_1 + (1-\lambda)\, Q_2$ of their quadratic forms Q_1 and Q_2, where $\lambda \in [0, 1]$. These ellipsoids guarantee the inclusion property $(\mathcal{E}_1 \cap \mathcal{E}_2) \subseteq \mathcal{E}_\lambda \subseteq (\mathcal{E}_1 \cup \mathcal{E}_2)$. This λ-ellipsoid approach yields an analytic expression for the parameters $\boldsymbol{c}_\lambda$ and $\boldsymbol{P}_\lambda$ and also applies to the intersection of degenerate and regular ellipsoids. For proofs and derivations see (Ros et al., 2002).

The *affine propagation* of an ellipsoid describes the process of determining the resulting ellipsoid for a variable $\boldsymbol{y} \in \mathbb{R}^m$ that is affinely related to another variable $\boldsymbol{x} \in \mathbb{R}^n$ whose domain is bounded by an ellipsoid $\mathcal{E}_{\boldsymbol{x}}(\boldsymbol{c}_{\boldsymbol{x}}, \boldsymbol{P}_{\boldsymbol{x}})$. The general form of such a relation is given by $\boldsymbol{A}\boldsymbol{x} + \boldsymbol{C}\boldsymbol{y} + \boldsymbol{b} = \boldsymbol{0}$, where $\boldsymbol{A} \in \mathbb{R}^{r \times n}$, $\boldsymbol{C} \in \mathbb{R}^{r \times m}$, and $\boldsymbol{b} \in \mathbb{R}^r$. The set of all possible values for $\boldsymbol{y}$ will also be an ellipsoid, provided that $\boldsymbol{A}$ and $\boldsymbol{C}$ have full row rank, i.e., $\operatorname{rank}(\boldsymbol{A}) = \operatorname{rank}(\boldsymbol{C}) = r \leq m, n$. Given an input ellipsoid $\mathcal{E}_{\boldsymbol{x}}(\boldsymbol{c}_{\boldsymbol{x}}, \boldsymbol{P}_{\boldsymbol{x}})$, the output is an ellipsoid $\mathcal{E}_{\boldsymbol{y}}(\boldsymbol{c}_{\boldsymbol{y}}, \boldsymbol{P}_{\boldsymbol{y}})$ with $\boldsymbol{c}_{\boldsymbol{y}}$ being a point that satisfies $\boldsymbol{A}\boldsymbol{c}_{\boldsymbol{x}} + \boldsymbol{C}\boldsymbol{c}_{\boldsymbol{y}} + \boldsymbol{b} = \boldsymbol{0}$. The generalized propagation formula (Ros et al., 2002)

$$\boldsymbol{P}_{\boldsymbol{y}} = \boldsymbol{C}^\mathsf{T}(\boldsymbol{A}^\mathrm{r})^\mathsf{T}(\boldsymbol{P}_{\boldsymbol{x}} - \boldsymbol{P}_{\boldsymbol{x}}\boldsymbol{N}_A(\boldsymbol{N}_A^\mathsf{T}\boldsymbol{P}_{\boldsymbol{x}}\boldsymbol{N}_A)^\dagger \boldsymbol{N}_A^\mathsf{T}\boldsymbol{P}_{\boldsymbol{x}})\boldsymbol{A}^\mathrm{r}\boldsymbol{C} \tag{9}$$

applies, where $\boldsymbol{N}_A$ is an orthonormal basis for the null space of $\boldsymbol{A}$, and $\boldsymbol{A}^\mathrm{r} = \boldsymbol{A}^\mathsf{T}(\boldsymbol{A}\boldsymbol{A}^\mathsf{T})^{-1}$ is the right pseudo-inverse of $\boldsymbol{A}$. The formula also allows for $\boldsymbol{P}_{\boldsymbol{x}}$ being rank-deficient with $(\cdot)^\dagger$ denoting the Moore-Penrose pseudo-inverse.

3. Ellipsoidal Possibility Distributions

We define an ellipsoidal possibility distribution π in dimension n such that every α-cut

$$\mathcal{C}_\pi^\alpha = \{\boldsymbol{x} \in \mathbb{R}^n \mid \pi_{\boldsymbol{X}}(\boldsymbol{x}) \geq \alpha\} = \mathcal{E}(\boldsymbol{c}_\alpha, \boldsymbol{P}_\alpha) = \{\boldsymbol{x} \in \mathbb{R}^n \mid (\boldsymbol{x} - \boldsymbol{c}_\alpha)^\mathsf{T}\boldsymbol{P}_\alpha(\boldsymbol{x} - \boldsymbol{c}_\alpha) \leq 1\} \tag{10}$$

corresponds to a (hyper)-ellipsoid. Possibility theory requires that for any two possibility levels $0 \leq \alpha_1 \leq \alpha_2 \leq 1$, the ellipsoids $\mathcal{E}_{\alpha_2}$ and $\mathcal{E}_{\alpha_1}$ satisfy the nesting property $\mathcal{E}_{\alpha_2} \subseteq \mathcal{E}_{\alpha_1}$.

This work uses a discrete representation of π consisting of N nested ellipsoids and a residual possibility value $\rho \in [0, 1)$. The discrete representation

$$\mathring{\pi} = \left(\{(\mathcal{E}_i, \alpha_i)\}_{i=1}^N,\, \rho\right) \quad \text{with} \quad \rho < \alpha_1 < \ldots < \alpha_N \leq 1 \tag{11}$$

orders the ellipsoids specificity such that $\mathcal{E}_N \subseteq \mathcal{E}_{N-1} \subseteq \ldots \subseteq \mathcal{E}_1$, as illustrated in Figure 1. The possibility value $\pi(\boldsymbol{x})$ for any point $\boldsymbol{x} \in \mathbb{R}^n$ is the highest possibility level where an α-cut contains $\boldsymbol{x}$. If $\boldsymbol{x}$ falls outside the largest ellipsoid $\mathcal{E}_1$, the possibility value evaluates to the residual term ρ. Thus, the possibility function is given by

$$\pi(\boldsymbol{x}) = \max\left(\{\alpha_i \mid \boldsymbol{x} \in \mathcal{E}_i, (\mathcal{E}_i, \alpha_i) \in \mathring{\pi}\} \cup \{\rho\}\right)\ . \tag{12}$$

The residual term ρ is introduced to allow for non-zero possibility values outside the largest ellipsoid $\mathcal{E}_1$, acknowledging that values outside the largest α-cut are not impossible but merely less plausible.

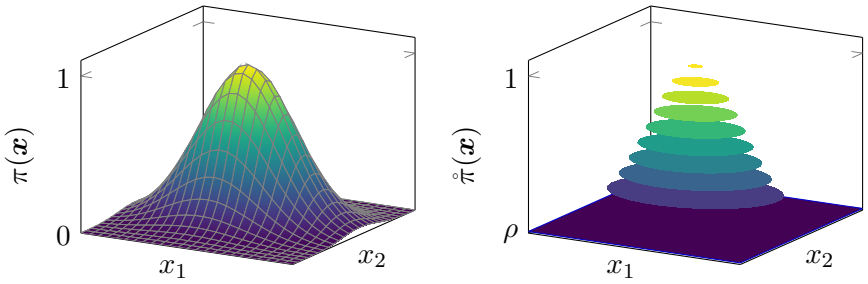


Figure 1. Continuous 2d possibility distribution π (left) and selected α-cuts (right) for the discrete ellipsoidal possibility distribution $\mathring{\pi}$.

3.1. Construction of Ellipsoidal Possibility Distributions

Uncertainty analysis invariably requires, as its first step, an appropriate mathematical model of the information at hand. This section details two such modeling approaches: the construction of ellipsoidal possibility distributions from data and from a given probability density function.

3.1.1. *Construction from Data*

The construction of an ellipsoidal possibility distribution from a dataset $\mathcal{D} = \{\boldsymbol{z}_j\}_{j=1}^{M} \subset \mathbb{R}^n$ requires determining N nested ellipsoids $\{\mathcal{E}_k\}_{k=1}^{N}$ that capture the data's distribution and subsequently assigning possibility values $\{\alpha_k\}_{k=1}^{N}$ that follow some statistical validity criterion. We employ a moment-based approach to determine a concentric and co-oriented structure for the nested ellipsoids $\{\mathcal{E}_k\}_{k=1}^{N}$, as illustrated in Figure 2. The sample mean $\boldsymbol{c} = \frac{1}{M}\sum_{j=1}^{M}\boldsymbol{z}_j$ serves as the common center for all ellipsoids $\mathcal{E}_k(\boldsymbol{c}, \boldsymbol{P}_k)$. The sample covariance matrix $\boldsymbol{\Sigma} = \frac{1}{M}\sum_{j=1}^{M}(\boldsymbol{z}_j - \boldsymbol{c})(\boldsymbol{z}_j - \boldsymbol{c})^{\mathsf{T}}$ determines the shape $\boldsymbol{P}_1 = \boldsymbol{\Sigma}^{-1}$ of the ellipsoids. To establish the outermost ellipsoid $\mathcal{E}_1$, $\boldsymbol{P}_1$ is scaled such that $\mathcal{E}_1(\boldsymbol{c}, \boldsymbol{P}_1)$ strictly encloses the MVEE of $\mathcal{D}$. Subsequent smaller ellipsoids are generated by scaling the shape matrices $\boldsymbol{P}_k = s\boldsymbol{P}_{k-1}$ with a factor $s > 1$, which guarantees nesting. The scaling factor s is determined based on the data dimensionality n and the desired number of ellipsoids N. For instance, achieving a specific geometric progression in the volumes of successive ellipsoids can lead to a reasonable choice for the scaling factor.

The nested ellipsoids are then transformed into a possibility distribution $\mathring{\pi}$ by assigning possibility levels α_k based on the statistical reliability of the data coverage. To account for finite sample sizes, the *reliable membership transform* (Hose, 2022) is employed rather than simple empirical frequency. The level α_k corresponds to the upper confidence bound of the probability that a new sample falls outside the subsequent inner ellipsoid $\mathcal{E}_{k+1}$. Using the reliable possibility distribution estimation, this is calculated with the inverse of the beta cumulative density function

$$\alpha_k = \mathrm{beta}^{-1}(1-\delta, M_{k+1}^{\mathrm{out}} + 1, M - M_{k+1}^{\mathrm{out}}) \,, \tag{13}$$

where δ defines the confidence level and M_{k+1}^{out} is the number of data points lying outside $\mathcal{E}_{k+1}$. For the innermost ellipsoid, the possibility level is set to $\alpha_N = 1$. Crucially, even if $\mathcal{E}_2$ fully encloses the dataset ($M_2^{\mathrm{out}} = 0$), Equation (13) yields $\alpha_1 > 0$. This ensures a non-zero residual possibility ρ for

the unobserved region outside $\mathcal{E}_1$, explicitly acknowledging sampling uncertainty inherent to finite datasets. Finally, redundant levels are pruned to ensure strictly increasing α_k.

Alternatively, the level-defining ellipsoids can be constructed by iteratively removing the outermost data points from $\mathcal{D}$ to get smaller and smaller subsets of data. The sequence begins with the MVEE of the full dataset $\mathcal{D}$. Subsequent inner ellipsoids are generated by computing the MVEE of the subset remaining after removing the boundary points that define the previous iteration. To guarantee strict nesting $\mathcal{E}_k \subset \mathcal{E}_{k-1}$, the bisection-based optimization method from (Calbert et al., 2023) is employed to adjust the ellipsoid parameters. Notably, this same method serves to identify the scaling of $\boldsymbol{P}_{\text{init}}$ required to enclose the MVEE in the moment-based method. Regardless of the geometric derivation, the final distribution is constructed by applying the reliable membership transform to the resulting nested sequence. Additionally, arbitrary distributions can be approximated by a concentric, co-aligned equivalent by computing possibility-weighted averages of the centers and shape matrices.

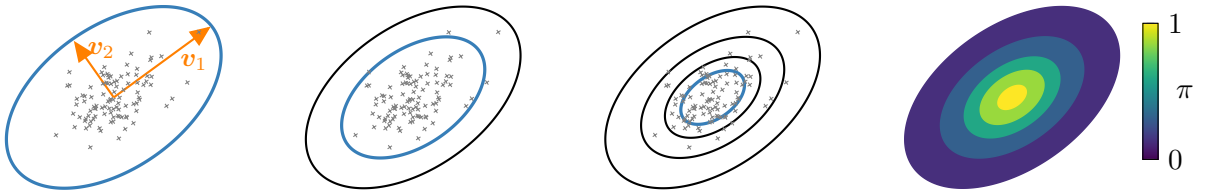


Figure 2. Step-by-step moment-based construction of an ellipsoidal possibility distribution. The sample mean and covariance determine the center and orientation (eigenvectors $\boldsymbol{v}_1, \boldsymbol{v}_2$) of the initial ellipsoid. A sequence of nested ellipsoids is generated by scaling the shape matrix, ensuring a co-aligned structure. The final distribution $\hat{\pi}$ is obtained by mapping the reliable coverage probability of each ellipsoid to a possibility level α (color scale).

3.1.2. *Construction from Probability Density Functions*

Given an arbitrary probability density function, a consistent possibility distribution can be derived by sampling from the probability density and applying the moment-based inference method described in Section 3.1.1.

Although sampling is applicable to any probability density, an exact analytical construction is possible when the probability density $p(\boldsymbol{x})$ is a multivariate Gaussian distribution $\mathcal{N}(\boldsymbol{\mu}, \boldsymbol{\Sigma})$ with mean $\boldsymbol{\mu}$ and regular covariance matrix $\boldsymbol{\Sigma}$. Because the level sets of a Gaussian distribution are inherently ellipsoidal, they map directly to an ellipsoidal possibility distribution. Following the probability-to-possibility transformation principle (Dubois et al., 2004), this analytical mapping defines the resulting possibility distribution $\pi(\boldsymbol{x})$ as the probability of a density value being lower than or equal to $p(\boldsymbol{x})$.

Consequently, the ellipsoidal level sets are determined by the Mahalanobis distance associated with the specific quantile of the Chi-squared distribution, see (Martin and Williams, 2025). For a possibility level $\alpha \in (\rho, 1]$, the α-cut is then given by

$$\mathcal{C}_\pi^\alpha = \left\{ \boldsymbol{x} \in \mathbb{R}^n \mid (\boldsymbol{x} - \boldsymbol{\mu})^\mathsf{T} \boldsymbol{\Sigma}^{-1} (\boldsymbol{x} - \boldsymbol{\mu}) \leq F_{\chi_n^2}^{-1}(1-\alpha) \right\} , \tag{14}$$

where $F_{\chi_n^2}^{-1}$ is the inverse cumulative distribution function of the Chi-squared distribution with n degrees of freedom.

3.2. Fusion of Ellipsoidal Possibility Distributions

The combination of multiple sources of information is another central operation in uncertainty quantification. Given two discrete ellipsoidal possibility distributions $\mathring{\pi}_1 = \{(\mathcal{E}_{1,i}, \alpha_{1,i})\}_{i=1}^{N_1}$ and $\mathring{\pi}_2 = \{(\mathcal{E}_{2,j}, \alpha_{2,j})\}_{j=1}^{N_2}$, the objective is to compute a single fused distribution $\mathring{\pi}_{\text{fused}}$ that represents the combined knowledge. A level-wise combination (fusing α-cuts at identical levels) is often infeasible because independently inferred distributions rarely share common levels. Furthermore, interpolating intermediate levels to create a matching level grid implies unjustified precision, which violates the principles of uncertainty quantification.

To address this, we employ a fusion strategy that uses a bidirectional approach to fuse the ellipsoids. First, for every ellipsoid-level $(\mathcal{E}_{1,i}, \alpha_{1,i}) \in \mathring{\pi}_1$, we identify the corresponding ellipsoid-level $(\mathcal{E}_{2,j}, \alpha_{2,j}) \in \mathring{\pi}_2$ with the smallest possibility level $\alpha_{2,j} \geq \alpha_{1,i}$. These two ellipsoids are fused. The process is then repeated from the perspective of $\mathring{\pi}_2$, fusing each $\mathcal{E}_{2,j}$ from $\mathring{\pi}_2$ with the corresponding one in $\mathring{\pi}_1$. Figure 3(a)-(d) visualizes this level-wise pairing and subsequent outer approximation. For a single fusion step between two identified ellipsoids $\mathcal{E}_{1,i}(\boldsymbol{c}_{1,i}, \boldsymbol{P}_{1,i})$ and $\mathcal{E}_{2,j}(\boldsymbol{c}_{2,j}, \boldsymbol{P}_{2,j})$, we seek a tight ellipsoidal outer approximation of their intersection. We utilize the λ-ellipsoid method described in Section 2.2, which provides a parameterized family of ellipsoids $\mathcal{E}_\lambda$ containing the intersection $\mathcal{E}_{1,i} \cap \mathcal{E}_{2,j}$. The shape matrix $\boldsymbol{P}_{\lambda,i,j}$ and center $\boldsymbol{c}_{\lambda,i,j}$ are computed analytically as

$$\boldsymbol{P}_{\lambda,i,j} = \frac{1}{K_{i,j}(\lambda)} \boldsymbol{E}_{\lambda,i,j} \ , \qquad \boldsymbol{c}_{\lambda,i,j} = \boldsymbol{E}_{\lambda,i,j}^{-1} (\lambda \boldsymbol{P}_{1,i} \boldsymbol{c}_{1,i} + (1-\lambda) \boldsymbol{P}_{2,j} \boldsymbol{c}_{2,j}) \tag{15}$$

with

$$\begin{aligned} \boldsymbol{E}_{\lambda,i,j} &= \lambda \boldsymbol{P}_{1,i} + (1-\lambda) \boldsymbol{P}_{2,j} \qquad \text{and} \\ K_{i,j}(\lambda) &= 1 + \boldsymbol{c}_{\lambda,i,j}^{\mathsf{T}} \boldsymbol{E}_{\lambda,i,j} \boldsymbol{c}_{\lambda,i,j} - \left(\lambda \boldsymbol{c}_{1,i}^{\mathsf{T}} \boldsymbol{P}_{1,i} \boldsymbol{c}_{1,i} + (1-\lambda) \boldsymbol{c}_{2,j}^{\mathsf{T}} \boldsymbol{P}_{2,j} \boldsymbol{c}_{2,j} \right) \ . \end{aligned} \tag{16}$$

To maximize information gain, we select the optimal $\lambda^\star$ that minimizes the volume of the resulting λ-ellipsoids. This is equivalent to the optimization problem

$$\lambda_{i,j}^\star = \arg \min_{\lambda \in [0,1]} \left(-\log(\det(\boldsymbol{E}_{\lambda,i,j})) + n \log(K_{i,j}(\lambda)) \right) \ . \tag{17}$$

Alternatively, heuristic choices, such as $\lambda = 0.5$ or weighting based on the trace of the shape matrices, offer computationally cheaper alternatives while remaining reasonable approximations of the optimal solution.

A new possibility value is assigned to the fused ellipsoid. Assuming the information sources are stochastically independent, the independence copula from Equation (6) is employed. This copula ensures consistency and has, by definition, a lifting property: If both sources agree on a region, the possibility of that region increases.

The independent fusion of various levels does not strictly guarantee the fundamental nesting property ($\mathcal{E}_{\text{fused},k} \subseteq \mathcal{E}_{\text{fused},k-1}, k \in \{1, \ldots, N_{\text{fused}}\}$) for the resulting set of ellipsoids. Therefore, we check the inclusion between adjacent levels using the method proposed by (Calbert et al., 2023). If an inner ellipsoid is not fully contained within the outer one, as seen in Figure 3(e), the outer ellipsoid is inflated by scaling its shape matrix such that strict inclusion is satisfied. This ensures that the final output $\mathring{\pi}_{\text{fused}}$ is an ellipsoidal possibility distribution, as demonstrated in Figure 3(f).

Duplicate levels (where $\alpha_{1,i} = \alpha_{2,j}$) are eliminated by retaining only the most specific ellipsoid—the one with the smallest volume—for each unique possibility level.

A key advantage of this approach is the preservation of original α-levels. Furthermore, the method remains applicable to distributions defined by only a few levels or even single intervals.

The proposed framework naturally extends to the fusion of $M > 2$ information sources by generalizing Equation (15) to $\boldsymbol{P}_{\boldsymbol{\lambda}} = \sum_{i=1}^{M} \lambda_i \boldsymbol{P}_i$ with $\boldsymbol{\lambda} \in \mathbb{R}^M$ and $\sum_{i=1}^{M} \lambda_i = 1$. The joint distribution is obtained by fusing at each step M ellipsoids with the independence copula generalizing to $\alpha_{\text{fused}} = 1 - (1 - \alpha)^M$, see Equation (6).

While the presented fusion strategy becomes computationally demanding for multiple sources, a synchronized approach—standardizing distributions to a common possibility level discretization and performing simultaneous M-way ellipsoidal fusion—provides a tractable alternative.

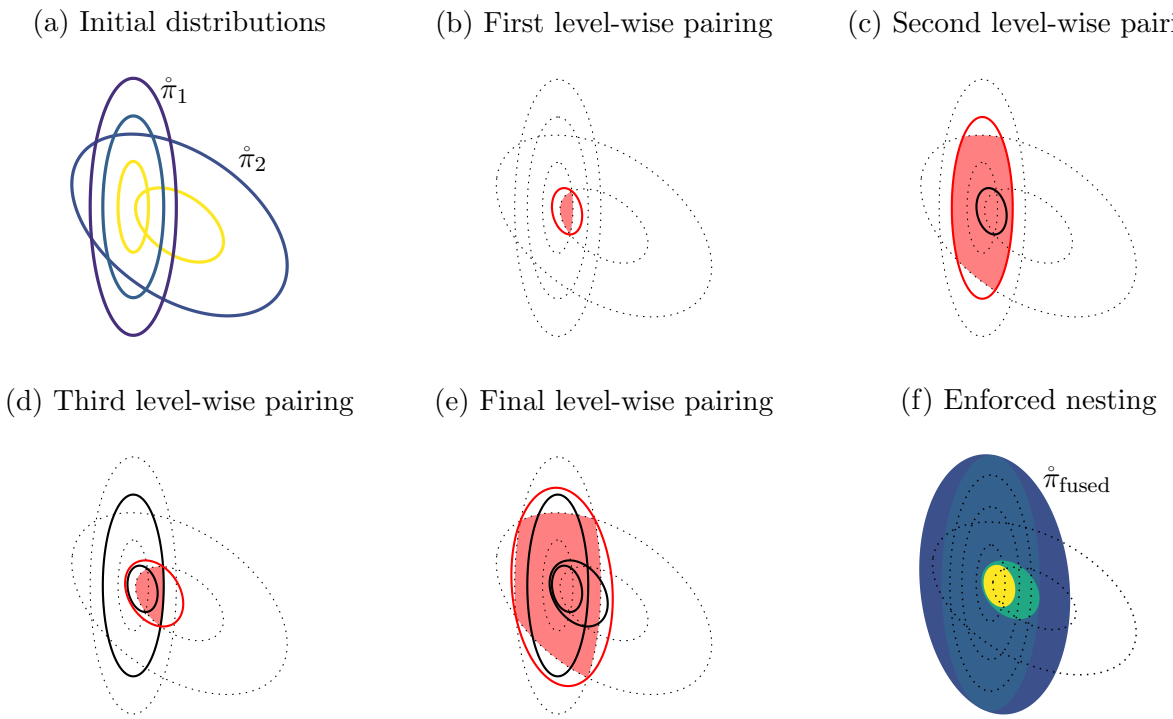


Figure 3. Step-by-step visualization of the fusion procedure for two discrete ellipsoidal possibility distributions. (a) The initial distributions $\mathring{\pi}_1$ and $\mathring{\pi}_2$. (b)-(d) Sequential fusion of corresponding α-cuts to generate new ellipsoids (red). (e) The collection of fused ellipsoids, which may initially violate the nesting property. (f) Expansion of the outer ellipsoids to guarantee nesting, yielding the final valid possibility distribution $\mathring{\pi}_{\text{fused}}$.

3.3. Propagation of Ellipsoidal Possibility Distributions

Given an (ellipsoidal) possibilistic description of uncertainty in state $\boldsymbol{x}$ and a model $\boldsymbol{f}$, uncertainty propagation is concerned with determining the induced possibility distribution of the out-

put $\boldsymbol{y} = \boldsymbol{f}(\boldsymbol{x})$. In the following, a propagation rule for affine mappings is derived, and the general case of nonlinear mappings is discussed.

3.3.1. *Affine Propagation*

Specializing the general implicit relation from Section 2.2 to the explicit affine mapping $\boldsymbol{y} = \boldsymbol{A}\boldsymbol{x} + \boldsymbol{b}$ by setting $\boldsymbol{C} = -\boldsymbol{I}$, we obtain the following propagation rules. Let the input variable $\boldsymbol{x}$ be described by a discrete ellipsoidal possibility distribution $\mathring{\pi}_x = \{(\mathcal{E}_{x,i}, \alpha_i)\}_{i=1}^{N}$ with $\mathcal{E}_{x,i} = \mathcal{E}(\boldsymbol{c}_{x,i}, \boldsymbol{P}_{x,i})$. Since affine mappings preserve ellipsoidal shapes, each α-cut is propagated individually and retains its possibility level α_i, as illustrated in Figure 4. Hence, the propagated center and the propagated shape matrix are given by

$$\boldsymbol{c}_{y,i} = \boldsymbol{A}\boldsymbol{c}_{x,i} + \boldsymbol{b}\,, \qquad \boldsymbol{P}_{y,i} = \boldsymbol{A}^{-\mathsf{T}}\boldsymbol{P}_{x,i}\,\boldsymbol{A}^{-1} = (\boldsymbol{A}\boldsymbol{P}_{x,i}^{-1}\boldsymbol{A}^{\mathsf{T}})^{-1}, \tag{18}$$

assuming that $\boldsymbol{A}$ is square and invertible. For rank-deficient or non-quadratic $\boldsymbol{A}$, $\boldsymbol{C}$ or positive semi-definite $\boldsymbol{P}_{x,i}$, the generalized propagation rule in Equation (9) is applied, yielding a possibly degenerate output ellipsoid.

Because affine mappings preserve convexity and set inclusion, the nesting property $\mathcal{E}_{y,N} \subseteq \ldots \subseteq \mathcal{E}_{y,1}$ is retained. The propagated stack $\mathring{\pi}_y = \{(\mathcal{E}_{y,i}, \alpha_i)\}_{i=1}^{N}$ thus constitutes a valid ellipsoidal possibility distribution without loss of information.

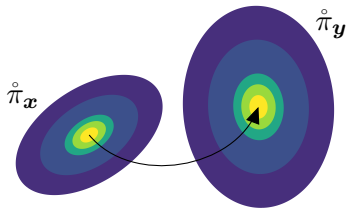


Figure 4. Affine propagation of a discrete ellipsoidal possibility distribution $\mathring{\pi}_{\boldsymbol{x}}$ resulting in the output distribution $\mathring{\pi}_{\boldsymbol{y}}$.

3.3.2. *Nonlinear Propagation*

For nonlinear mappings $\boldsymbol{f}$, the level sets induced by the extension principle are generally non-ellipsoidal and cannot be propagated analytically.

One approach is to sample from each $\mathcal{E}_{x,i}$, propagate the samples through $\boldsymbol{f}$, and reconstruct an ellipsoidal distribution using the data-based construction proposed in Section 3.1. Another approach is to linearize $\boldsymbol{f}$ about the center of each ellipsoid $\mathcal{E}_{x,i}$ and use affine propagation to obtain the propagated ellipsoids. Linearization errors can be enclosed by ellipsoidal outer bounds, as demonstrated for Kalman filters in (Noack et al., 2010). Incorporating these bounds via Minkowski-sum approximations ensures the resulting output distribution remains a conservative outer approximation.

3.4. Marginal and Joint Ellipsoidal Possibility Distributions

The final fundamental operation necessary for a complete uncertainty calculus is the ability to derive marginal distributions from joint distributions and to construct joint distributions from marginals. The proposed framework handles both operations geometrically through propagation and fusion.

3.4.1. *Marginalization*
Given a joint discrete ellipsoidal possibility distribution $\mathring{\pi}_{\boldsymbol{x}} = \{(\mathcal{E}_{\boldsymbol{x},i}, \alpha_i)\}_{i=1}^{N}$ defined on $\mathbb{R}^n$, the marginal distribution for a subspace of variables is obtained by projecting each ellipsoidal α-cut onto that subspace. In possibility theory, marginalization corresponds to the supremum operator, which, for convex sets, is equivalent to geometric projection. For an ellipsoid $\mathcal{E}_{\boldsymbol{x}}(\boldsymbol{c}_{\boldsymbol{x}}, \boldsymbol{P}_{\boldsymbol{x}})$, the projection onto a subspace is defined by a diagonal transformation matrix $\boldsymbol{A}$, which contains ones on the diagonal for the axes onto which the ellipsoid is projected and zeros elsewhere. In the context of Equation (9), this is equivalent to an affine propagation with singular matrix $\boldsymbol{A}$ and $\boldsymbol{b} = \boldsymbol{0}$, yielding a degenerate marginal ellipsoid $\mathcal{E}_{\boldsymbol{y}}(\boldsymbol{c}_{\boldsymbol{y}}, \boldsymbol{P}_{\boldsymbol{y}})$ with $\boldsymbol{c}_{\boldsymbol{y}} = \boldsymbol{A}\boldsymbol{c}_{\boldsymbol{x}}$ and $\boldsymbol{P}_{\boldsymbol{y}} = \boldsymbol{A}^{\mathsf{T}}(\boldsymbol{A}\boldsymbol{P}_{\boldsymbol{x}}^{\dagger}\boldsymbol{A}^{\mathsf{T}})^{\dagger}\boldsymbol{A}$. This operation is applied element-wise to the sequence of nested ellipsoids. Since projection is a linear mapping, convexity and nesting of the ellipsoidal α-cuts are preserved, ensuring that the resulting collection $\mathring{\pi}_{\boldsymbol{y}} = \{\mathcal{E}_{\boldsymbol{y},i}, \alpha_i\}_{i=1}^{N}$ constitutes a marginal ellipsoidal possibility distribution.

3.4.2. *Joint Distributions from Marginals*
Constructing a joint distribution from a set of marginal distributions $\{\mathring{\pi}_1, \ldots, \mathring{\pi}_d\}$ involves approximating the Cartesian product of the marginal α-cuts. Geometrically, the Cartesian product of d marginal ellipsoids (or intervals) forms a hyperrectangle in the joint space $\mathbb{R}^n$, which is not an ellipsoid. To maintain the ellipsoidal representation, we construct a tight ellipsoidal outer approximation of this hyperrectangle. Figure 5 illustrates this bounding process for two marginals, showing how the nested intervals define hyperrectangles enclosed by optimal ellipses.

We achieve this by treating each marginal α-cut as a degenerate ellipsoid (a cylinder) in the full joint space, unbounded in all dimensions orthogonal to the jth subspace. A closed-form solution exists for the fusion of independent marginals defined on complementary subspaces (e.g., combining $\boldsymbol{x}_1$ and $\boldsymbol{x}_2$ where $\boldsymbol{x} = [\boldsymbol{x}_1^{\mathsf{T}}, \boldsymbol{x}_2^{\mathsf{T}}]^{\mathsf{T}}$). If marginals are not only defined on complementary subspaces, but also intersect, the intersecting subspace marginals can be fused first with the fusion procedure described in Section 3.2. Following (Ros et al., 2002), if the rank sum of the shape matrices equals the full dimension ($\operatorname{rank}(\boldsymbol{P}_1) + \operatorname{rank}(\boldsymbol{P}_2) = n$), the parameters

$$\boldsymbol{c}_{\text{joint}} = (\boldsymbol{P}_1^2 + \boldsymbol{P}_2^2)^{-1}(\boldsymbol{P}_1^2\boldsymbol{c}_1 + \boldsymbol{P}_2^2\boldsymbol{c}_2) \qquad \text{and} \qquad \boldsymbol{P}_{\text{joint}} = \frac{p}{n}\boldsymbol{P}_1 + \frac{n-p}{n}\boldsymbol{P}_2 \tag{19}$$

of the optimal joint α-cut $\mathcal{C}_{\text{joint}}^{\alpha}$ are given analytically, where $p = \operatorname{rank}(\boldsymbol{P}_1)$. Note that the resulting ellipsoid is in fact the MVEE of the Cartesian product of the marginal ellipsoids defined in a higher dimensional space. Repeating this process for all α-levels produces a nested sequence that forms the joint ellipsoidal possibility distribution $\mathring{\pi}_{\text{joint}}$. The effect of this adjustment is visible on the right-hand side of Figure 5, where the copula application lifts the second possibility level. Depending on the assumed dependency structure, the possibility levels may need to be adjusted using an appropriate copula like the independence copula in Equation (6).

4. Case Study: State Estimation of an Omnidirectional Robot

To demonstrate the functionality of the proposed framework, we apply it to a state estimation problem for a wheeled mobile robot. We utilize a recursive possibilistic filter (Hose and Hanss,

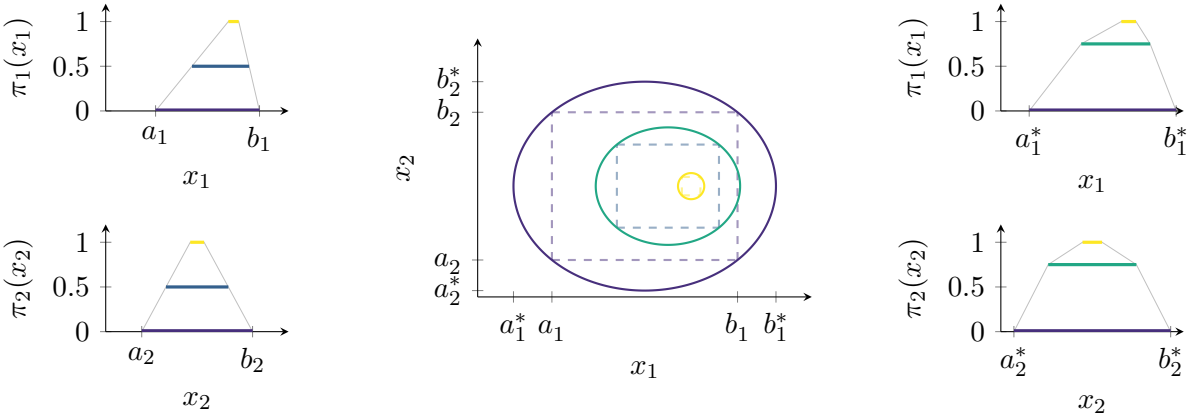


Figure 5. Illustration of constructing a joint ellipsoidal possibility distribution from two marginal triangular distributions and vice versa. The α-cuts of the marginals on the left-hand side form nested intervals, which define nested hyperrectangles in the joint space, enclosed by the tightest possible ellipsoids. The independence copula is applied, when joining the marginals, resulting in the lifted middle level on the right-hand side.

2021) built upon the previously derived ellipsoidal possibility distributions and their calculus. The considered robot is an omnidirectional platform, see Figure 6 (left) and (Ebel, 2021) for details, whose kinematics is described by the discrete-time linear system

$$\boldsymbol{x}_k = \boldsymbol{x}_{k-1} + \delta_t \boldsymbol{u}_{k-1} + \boldsymbol{v}_{k-1}, \tag{20}$$

where, at time step $k \in \mathbb{N}_0$, the state vector $\boldsymbol{x}_k = [x_k \ y_k \ \theta_k]^\mathsf{T} \in \mathcal{X} \subseteq \mathbb{R}^3$ represents the robot pose, $\boldsymbol{u}_k = [v_{x,k} \ v_{y,k} \ \omega_k]^\mathsf{T} \in \mathcal{U} \subset \mathbb{R}^3$ denotes the applied control input, $\boldsymbol{v}_k$ is the process noise, and $\delta_t > 0\,\mathrm{s}$ is the sampling time.

Full-state measurements are obtained in the academic hardware testbed using a motion capture system. Since the motion capture system provides highly accurate pose estimates, the recorded data is treated as ground truth $\boldsymbol{x}_k$. Artificial measurement noise $\boldsymbol{w}_k$ is then added synthetically, yielding measurements $\boldsymbol{y}_k$ with known, controllable noise characteristics while retaining access to the true states for validation. The resulting observation model is

$$\boldsymbol{y}_k = \boldsymbol{x}_k + \boldsymbol{w}_k. \tag{21}$$

The measurement noise is modeled as a zero-mean multivariate normal distribution with covariance matrix $\boldsymbol{\Sigma}_w = \mathrm{diag}([(5\,\mathrm{mm})^2 \ (5\,\mathrm{mm})^2 \ (5^\circ)^2])$. Due to hardware imperfections and manufacturing inaccuracies, the process noise is accounted for by adding constant offsets $\varepsilon_{xy} = 10\,\mathrm{mm}$ and $\varepsilon_\theta = 1^\circ$ to the semi-axes for position and orientation of the propagated ellipsoids, respectively. In other words, since the ellipsoids are axis-aligned, with shape matrix $\boldsymbol{P} = \mathrm{diag}([p_x, \, p_y, \, p_\theta])$, each diagonal entry is updated as

$$p_i' = \left(\frac{1}{\sqrt{p_i}} + \varepsilon_i \right)^{-2}, \tag{22}$$

where $\varepsilon_x = \varepsilon_y = \varepsilon_{xy}$ and ε_θ as defined above.

The task of state estimation is demonstrated using a dataset collected from the real-world robot. An open-loop input sequence is applied, nominally driving the robot along a lemniscate-shaped trajectory. In total, $N_t = 159$ control commands are sent to the robot at a sampling time of $\delta_t = 0.2\,\mathrm{s}$ using a zero-order hold. The corresponding state measurements are recorded at the same sampling rate. The robot is manually placed at the initial pose $\boldsymbol{x}_0 = [0\,\mathrm{m}\ 0\,\mathrm{m}\ 30.96°]^\mathsf{T}$. Placement inaccuracies are accounted for by an initial uniform possibility distribution $\pi_{\tilde{X}_0}$ supported on the set $\mathcal{X}_0 = ([-0.5, 0.5]\mathrm{m})^2 \times [-45, 45]°$. The measurements are plotted in the right-hand part of Figure 6, showing the temporal evolution of the robot's pose as recorded by the motion capture system.

The initialized recursive filter follows the standard prediction-inversion-update structure. A brief outline of the filter is given in the following and illustrated schematically in Figure 7 (left) for a selected number of time instants. See, e.g., (Hose and Hanss, 2021) for further details.

In the *prediction step*, the information about the previous state $\boldsymbol{x}_{k-1}$ is propagated through the system dynamics from Equation (20) using the affine propagation of ellipsoidal possibility distributions, see Section 3.3.1. This yields a predicted ellipsoidal possibility distribution $\mathring{\pi}_{\mathrm{p},k}$ of the successor state $\boldsymbol{x}_k$, taking into account the uncertainty in the previous state as well as the process noise. In the subsequent *inversion step*, the current measurement $\boldsymbol{y}_k$ is used to construct a second possibility distribution $\mathring{\pi}_{\mathrm{i},k}$ describing $\boldsymbol{x}_k$. This is achieved by applying a probability-to-possibility transformation to the known noise distribution, see Section 3.1.2. Finally, in the *update step*, the two distributions obtained from the prediction and inversion steps are fused to $\mathring{\pi}_{\mathrm{fused},k}$ using the fusion rule for ellipsoidal possibility distributions, see Section 3.2. This recursive procedure is repeated for each of the N_t time steps, resulting in a sequence of ellipsoidal possibility distributions that describe the temporal evolution of the robot's state estimate.

Figure 7 illustrates the results of the state-estimation process. The left plot shows the ellipsoidal possibility distributions at selected time instances, visualized as nested ellipses corresponding to different possibility levels. The right-hand plot in Figure 7 shows the empirical coverage probabilities

$$\hat{p}(\alpha) = \frac{1}{N_t + 1} \left| k \in \mathbb{Z}_{0:N_t} : \boldsymbol{x}_k \in \mathcal{C}^{\alpha}_{\mathring{\pi}_{\mathrm{fused},k}} \right| , \tag{23}$$

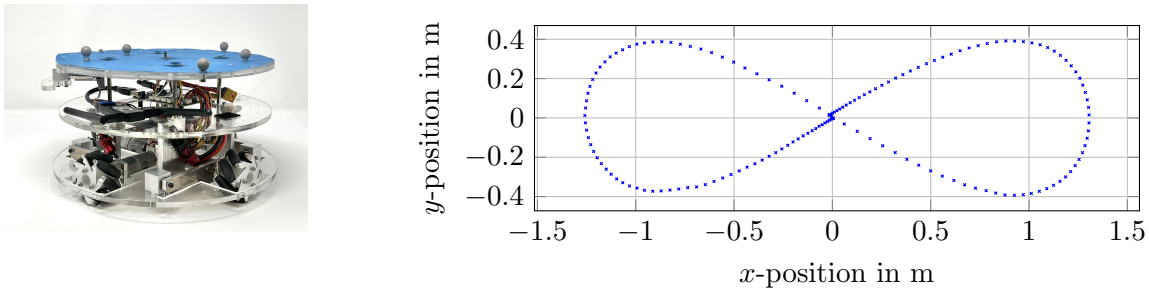


Figure 6. Experimental setup. Left: The HERA omnidirectional robot platform. Right: Recorded state measurements from the motion capture system.

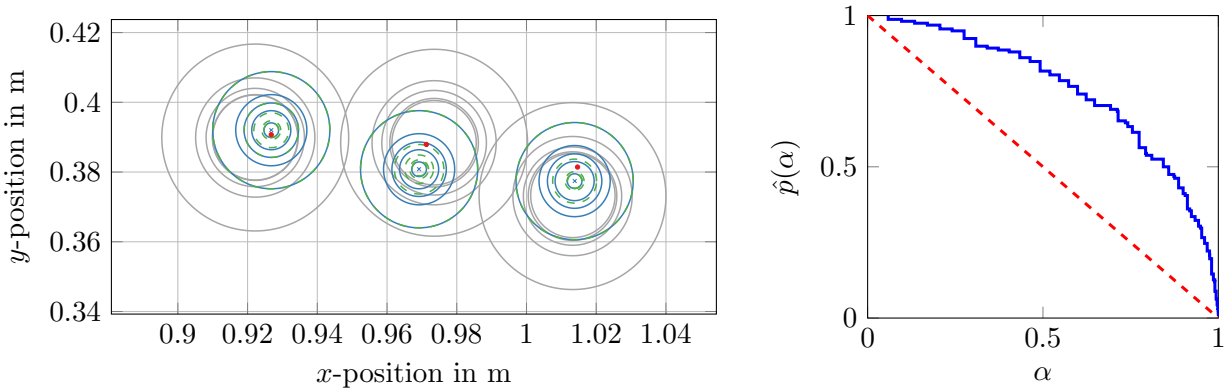


Figure 7. Results of the filtering procedure. Left: Projection onto the x-y plane for timesteps 32–34. Gray ellipses show the predicted distributions, blue ellipses the measurement distributions, and green ellipses the fused distributions. Red dots indicate the true states, blue crosses the measurements. Right: Empirical coverage curve, validating the performance of the filter.

that is, the fraction of time steps for which the true state $\boldsymbol{x}_k$ lies within the α-cut of the estimated distribution. A coverage curve above the diagonal indicates the filter's validity, as prescribed by Equation (4). For more insight into these curves, see (Wimbush et al., 2022).

The results show that the filter successfully tracks the true state with the prescribed confidence. However, the comparatively high process noise causes the fused estimate to closely follow the measurement distribution, which is more precise than the predicted state. As a result, the filter behaves similarly to a static measurement-only estimator that ignores the system dynamics. This also explains why the projected ellipses of the estimated states are nearly circular, reflecting the isotropic measurement noise.

5. Conclusion and Future Work

This paper presents a novel framework for possibilistic uncertainty modeling based on hyperellipsoids. Leveraging results of ellipsoidal calculus, polymorphic, i.e. aleatory and epistemic, uncertainty is rigorously represented, fused, and propagated using nested ellipsoidal sets. The ellipsoidal approach offers a distinct advantage over common grid-based or sampling methods by providing analytical solutions for linear transformations and preserving correlation information typically lost in axis-aligned interval representations.

The core contribution consists of strategies for the construction, combination, and propagation of arbitrary-dimensional ellipsoidal possibility distributions. Inference methods are introduced to generate ellipsoidal possibilistic distributions from raw data, and the concept of a convex combination of ellipsoidal sets is extended to the fusion of ellipsoidal possibility distributions. Moreover, the marginalization to lower dimensions is detailed and the construction of joint distributions from marginals, framed as a degenerate ellipsoid fusion task, is presented. Furthermore, the framework

provides exact analytical propagation for affine functions. The efficacy of this calculus is validated through a linear dynamic state estimation problem, for which an ellipsoidal possibilistic filter successfully tracks the system state within trustworthy confidence regions. Owing to the conservative nature of possibility theory and the reliance on outer approximations, the results remain rather conservative and face limitations regarding over-approximation in repeated fusion operations.

Future work is to optimize the trade-off between computational efficiency and the tightness of uncertainty bounds. Optimization-based intersection methods, such as semi-definite programming, are to be investigated as replacements for the presented heuristic λ-ellipsoid fusion approach, as well as developing explicit solutions for regularly occuring special cases. Additionally, strategies for conflict detection and introducing more flexible sampling-based methods to handle nonlinearities are to be explored.

Acknowledgements

The authors gratefully acknowledge the support provided by the German Research Foundation (DFG) in the framework of the research projects no. 514188140 (HA2798/16-1) and no. 433183605 (EB195/32-2). Julian Behrend thanks the Claussen-Simon-Foundation and Kyb Alumni e.V. for funding his conference participation.

References

Calbert, J., L. N. Egidio, and R. M. Jungers: 2023, 'An efficient method to verify the inclusion of ellipsoids'. *IFAC-PapersOnLine* **56**(2), 1958–1963.

Dubois, D., L. Foulloy, G. Mauris, and H. Prade: 2004, 'Probability-possibility transformations, triangular fuzzy sets, and probabilistic inequalities'. *Reliable Computing* **10**(4), 273–297.

Ebel, H.: 2021, *Distributed Control and Organization of Communicating Mobile Robots: Design, Simulation, and Experimentation*, Doctoral thesis: Schriften aus dem Institut für Technische und Numerische Mechanik der Universität Stuttgart, Vol. 69. Düren: Shaker Verlag.

Ferrero, A., H. V. Jetti, and S. Salicone: 2021, 'The possibilistic Kalman filter: Definition and comparison with the available methods'. *IEEE Transactions on Instrumentation and Measurement* **70**, 1–11.

Hose, D.: 2022, *Possibilistic Reasoning with Imprecise Probabilities: Statistical Inference and Dynamic Filtering*, Doctoral thesis: Schriften aus dem Institut für Technische und Numerische Mechanik der Universität Stuttgart, Vol. 74. Düren: Shaker Verlag.

Hose, D. and M. Hanss: 2021, 'A recursive formulation of possibilistic filters'. In: *Proceedings of the 12th International Symposium on Imprecise Probability: Theories and Applications*, Vol. 147 of *Proceedings of Machine Learning Research*. pp. 180–190.

Kreinovich, V., J. Beck, and H. T. Nguyen: 2007, 'Ellipsoids and ellipsoid-shaped fuzzy sets as natural multi-variate generalization of intervals and fuzzy numbers: How to elicit them from users, and how to use them in data processing'. *Information Sciences* **177**(2), 388–407.

Könecke, T., J. Schneider, and M. Hanss: 2025, 'Sampling-based possibility theory for engineering analysis under uncertainty: inference, prediction and optimization'. In: *Proceedings of the 35th European Safety and Reliability Conference (ESREL2025) and the 33rd Society for Risk Analysis Europe Conference (SRA-E 2025)*. Stavanger, Norway.

Martin, R.: 2025, 'A new Monte Carlo method for valid prior-free possibilistic statistical inference'. *arXiv preprint arXiv:2501.10585*.

Martin, R. and J. P. Williams: 2025, 'Asymptotic efficiency of inferential models and a possibilistic Bernstein–von Mises theorem'. *International Journal of Approximate Reasoning* **180**, 109389.

Matía, F., V. Jiménez, B. P. Alvarado, and R. Haber: 2021, 'The fuzzy Kalman filter: Improving its implementation by reformulating uncertainty representation'. *Fuzzy Sets and Systems* **402**, 78–104.

Moshtagh, N.: 2005, 'Minimum volume enclosing ellipsoid'. *Convex Optimization* **111**, 112.

Mäck, M. and M. Hanss: 2021, 'An advanced sampling technique for possibilistic uncertainty propagation'. *Mechanical Systems and Signal Processing* **147**, 107064.

Noack, B., V. Klumpp, N. Petkov, and U. D. Hanebeck: 2010, 'Bounding linearization errors with sets of densities in approximate Kalman filtering'. In: *Proceedings of the 13th International Conference on Information Fusion*. Edinburgh, UK, pp. 1–8.

Ros, L., A. Sabater, and F. Thomas: 2002, 'An ellipsoidal calculus based on propagation and fusion'. *IEEE Transactions on Systems, Man and Cybernetics, Part B (Cybernetics)* **32**(4), 430–442.

Wimbush, A., N. Gray, and S. Ferson: 2022, 'Singhing with confidence: Visualising the performance of confidence procedures'. *Journal of Statistical Computation and Simulation* **92**(13), 2686–2702.

Zadeh, L. A.: 1975, 'The concept of a linguistic variable and its application to approximate reasoning'. *Information Sciences* **8**(3), 199–249.

Imprecise probabilistic subset simulation for rigorous bounding of the failure probability

V. M. Nikolov, P. O. Hristov
GATE Institute, Sofia University, 5 James Bourchier Blvd., 1164 Sofia, Bulgaria.
Email: {valentin.nikolov, petar.hristov}@gate-ai.eu

Abstract. One of the most challenging tasks in reliability engineering, namely the estimation of small failure probabilities can be efficiently performed through subset simulation (SuS). Given a performance function and a critical level, which defines failure, SuS uses Markov chain Monte Carlo sampling, to gradually explore the input domain of the performance function with a nested sequence of larger domains, until samples over the critical threshold and into the failure domain are generated.

P-SuS, proposed by (Hristov and DiazDelaO, 2023), generalises the original subset simulation algorithm by adapting it to work with probabilistic numerical models (PNM). P-SuS was shown to be able to discover and populate the failure domain, only based on partially converged simulations. However, the probabilistic description of its estimator for the failure probability is not calibrated, in that it does not cover the failure probability for the deterministic model, estimated by SuS or does so only at very small numerical uncertainties and with inappropriately large bounds.This problem is strongly influenced by the assumptions of independence of the intermediate failure events and the independence of the probabilities of the levels. The result of these assumptions has a knock-on simplification effect on how the final estimator is computed.

The work described in this paper relaxes these assumptions by reformulating parts of the P-SuS algorithm through the use of dependence bounds analysis to compute uncertain number convolutions without assuming a particular dependence. We show that the resulting probability-box estimator more appropriately accounts for the uncertainty present in the output of the PNM.

Keywords: Probabilistic numerical models; Reliability analysis; Subset simulation; Dependence bounds analysis; Imprecise probability

1. Introduction

Computational models or simulators have established themselves as an irreplaceable part of any engineering process, as they significantly reduce the cost of conducting the equivalent physical experiments when exploring the state space of a complex physical system. Computer modelling, however advanced, is only an idealised approximation of any process considered. Often, simplifications and assumptions about the form of the model are required to make it practical or even feasible to use. Moreover, due to their numerical nature, discretisation errors also occur and accumulate during calculations because of the limited precision of any computer. Nevertheless, the purpose of

© 2026 by the author(s). This work is licensed under the Creative Commons Attribution 4.0 International License (CC BY 4.0), which permits unrestricted use, distribution, and reproduction in any medium, provided the original author and source are credited.

simulators remains to be to inform engineering decisions, and as such their inherent uncertainties need to be rigorously quantified to make them reliable to use.

Probabilistic numerics (Hennig et al., 2015) have been developed to provide an explicit quantification of the numerical uncertainty in the output of the model. Numerical uncertainty typically includes uncertainties stemming from the use of finite discretisation schemes and number of iterations, the use of finite precision floating-point arithmetic and, for non-deterministic models, ensemble uncertainty (Oberkampf and Roy, 2025). By treating the numerical modelling problem as that of statistical inference, probabilistic numerical methods produce a distributional output that includes an estimate of the numerical error. A well-designed probabilistic numerical model (PNM) should provide a calibrated measure about the numerical uncertainty and should converge on the deterministic model result in the limit of increasing computational budget (such as using a finer mesh and allowing for more iterations).

Probability theory also plays a central role in reliability analysis (RA), which aims to evaluate whether a physical system or structure is safe to use under a set of different conditions. A performance function, usually in the form of a computational model, which maps the space of inputs to outputs, characterises the behaviour of the investigated system. When assessing the reliability of a physical system, the failure domain $\mathcal{F}$, that is the set of configurations of the input that result in outputs of the performance function that exceed a predefined, critical threshold, is of particular interest. Characterising $\mathcal{F}$ is challenging for most practical applications, because its volume is multiple orders of magnitude smaller than that of the input space. This, together with the potentially complex geometry of $\mathcal{F}$, makes the task of reliably estimating the probability of failure $p_F = \mathbb{P}(\mathcal{F})$ difficult.

Many methods have been developed to estimate p_F, including first and second order reliability methods (Zhao and Ono, 1999), sampling approaches based on Monte Carlo simulation (MCS) (Padmanabhan et al., 2006; Naess et al., 2009), as well as variance reduction methods improving on MC procedures by employing more efficient strategies for sampling, such as importance sampling (Ibrahim, 1991) and line sampling (Pradlwarter et al., 2007). Another method, which has stood the test of time is subset simulation (SuS) (Au and Beck, 2001), because of its computational efficiency in terms of model evaluations needed, compared to MC and its ability to efficiently handle high-dimensional domains. The core idea of SuS is to represent $\mathcal{F}$ as the intersection of a set of nested intermediate failure domains, thus transforming the problem into the simulation of conditional events with constant probabilities, much higher than that of $\mathcal{F}$. Markov chain Monte Carlo algorithms are then employed to sample from the intermediate failure domains, given that the input already lies in the previous, larger intermediate failure region, and compute an estimator for p_F, denoted as $\hat{p}_F^{SuS}$.

Many advancements of SuS have been developed since its inception to address some of its assumptions and deficiencies. For instance, Kinnear and DiazDelaO, 2025 proposed the use of an evolutionary optimisation concept called niching to deal with rapidly changing model outputs and multimodality of the performance function. Miao and Low, 2026 take intrachain, interchain, and interlevel correlations into account, to more accurately estimate the variance of the $\hat{p}_F^{SuS}$. Other modifications include the development of imprecise SuS, used to quantify the uncertainty in the estimate for the probability of failure arising from not having perfect knowledge of the probability distributions for the input parameters (Giovanis and Shields, 2021).

A modification of SuS, to enable its use with PNM was proposed in (Hristov and DiazDelaO, 2023). Even though the authors show that the method, called P-SuS, converges to $\hat{p}_F^{SuS}$ as the uncertainty in the output of the PNM decreases, they note that the calibration of the estimator uncertainty remains poor.

In this work, we conjecture that the lack of calibration in the uncertainty of $\hat{p}_F^{P-SuS}$ is at least in part due to the assumptions of independence used throughout P-SuS. We use probability bounds analysis to relax this assumption and show how this change is reflected on the final estimator of the algorithm that we term imprecise probabilistic subset simulation (IP-SuS).

The remainder of the paper is organised as follows: Section 2 gives an overview of SuS, P-SuS and Fréchet convolutions necessary to follow the proposed improvements in IP-SuS, presented in Section 3. In Section 4, the new algorithm is demonstrated and benchmarked on the the modified Branin function, also featuring in the original work, introducing P-SuS (Hristov and DiazDelaO, 2023). Finally, Section 5 draws some conclusions and outlines directions for future work.

2. Methodology overview

2.1. Subset simulation

Let $h : \mathcal{X} \subseteq \mathbb{R}^d \to \mathbb{R}$ be the performance function of the system under investigation, such that for some particular input combination of system properties, $\mathbf{x} \in \mathcal{X}$ and some predefined threshold t^*, $y = h(\mathbf{x}) > t^*$ signifies the failure of the system. The failure domain, corresponding to t^*, is the set of all input combinations leading to failure, $\mathcal{F} = \{\mathbf{x} \in \mathcal{X} : h(\mathbf{x}) > t^*\}$. In probabilistic reliability analysis, any uncertainty over the system properties domain, $\mathcal{X}$ is described as a random variable, X with some joint probability distribution, $G_X(\cdot)$. Projecting $G_X(\cdot)$ through $h(\cdot)$ results in an output random variable $Y \sim G_Y(\cdot)$, even for a deterministic $h(\cdot)$. Under this formulation, a failure event is defined as $F = \{Y > t^*\}$ and the associated probability of failure is thus

$$p_F \equiv \mathbb{P}(F) = \int_{\mathcal{F}} dG(\mathbf{x}) = \mathbb{E}[\mathbb{I}_F(\mathbf{x})] \tag{1}$$

where $\mathbb{I}_F$ is the indicator function: $\mathbb{I}_F(\mathbf{x}) = 1$ if $h(\mathbf{x}) > t^*$ and 0 otherwise.

If the volume of $\mathcal{F}$, is much smaller than that of $\mathcal{X}$, as is usually the case, direct Monte Carlo simulation approaches would require a large number of samples, $N_{MCS} = O(p_F^{-1})$, to even discover $\mathcal{F}$. If in addition $h(\cdot)$ takes even modest times to run, reliability analysis may become impractical.

To alleviate this problem, SuS represents the failure domain as $\mathcal{F} = \mathcal{F}_m \subset \mathcal{F}_{m-1} \subset \cdots \subset \mathcal{F}_1 \subset \mathcal{F}_0 = \mathcal{X}$, where each intermediate failure domain $\mathcal{F}_k$ is associated with a failure event, $F_k = \{Y > t_k\}$, defined by an intermediate critical threshold. Using the property of the nestedness of F_k, the probability of failure can be evaluated as

$$p_F = \mathbb{P}\left(\bigcap_{k=1}^{m} F_k\right) = \prod_{k=1}^{m} \mathbb{P}(F_k \mid F_{k-1}). \tag{2}$$

Thus, the task of sampling from $\mathcal{F}$ to estimate p_F is reduced to generating $N << N_{MCS}$ samples from each intermediate failure domain, according to that domain's own conditional distribution,

progressively steering the samples towards $\mathcal{F}$. In SuS, this is done through two main constructs. First, the intermediate thresholds t_k are chosen adaptively such that $t_k \leq t_{k+1}$ and $\mathbb{P}(F_{k+1}|F_k) = \mathbb{P}(F_{k+2}|F_{k+1}) = p_0$ for all $1 < k < m-2$. Second, $p_0 N$ samples are chosen from $\mathcal{F}_k$ as seeds for a component-wise modified Metropolis-Hastings algorithm, which uses them to start independent chains and generate the remaining $(1-p_0)N$ samples for $\mathcal{F}_{k+1}$. The procedure for generating nested intermediate failure events continues until at least $p_0 N$ samples are obtained from $\mathcal{F}$. Subsequently, p_F is estimated as:

$$\hat{p}_F^{SuS} = p_0^{m-1} \frac{1}{N} \sum_{i=1}^{N} \mathbb{I}(h(\mathbf{x}_i) > t^*) \tag{3}$$

2.2. Subset simulation for probabilistic numerical models

To extend SuS to PNM, P-SuS needs to account for the fact that each response from $h(\cdot)$ is an entire probability distribution. For the remainder of this section, only those details of how this accounting is done that are relevant to the imprecise extension of P-SuS will be presented.

Without loss of generality, it is assumed in P-SuS that the distributions of $y = h(\mathbf{x})$ has finite first and second moments. When each y_i for $i \in \{1, \ldots, N\}$ is a distribution the probability of the failure event $F_{ik} = \{y_i > t_k\}$ turns from a dichotomous variable in $\{0, 1\}$ into a random variable. The probability of each intermediate failure domain, p_{F_k} as well as the number of samples in that level N_k are also random variables. Similarly to SuS, p_0 is still a parameter chosen by the analyst, but it serves as a nominal probability of the intermediate failure domains. At each level, p_{F_k} can be estimated as

$$p_{F_k} \approx \frac{1}{N_k} \sum_{j=1}^{N_k} \mathbb{I}_{F_k}(\mathbf{x}_j) \tag{4}$$

where the indicator function is a random variable $\mathbb{I}_{F_k}(\mathbf{x}_j) \sim \text{Bernoulli}(\mathbb{P}(h(\mathbf{x}_j) \geq t_k))$. and $\mathbf{x}_j$ still come from the input distribution, conditional on the preceding failure event, $G_X(\cdot|F_{k-1})$. In P-SuS, the Bernoulli random variables describing the indicator functions are assumed to be independent. Under this assumption, p_{F_k} is modelled as:

$$p_{F_k} \sim \mathcal{N}\left(\frac{\mu_k}{N_k}, \frac{{\sigma_k}^2}{N_k^2}\right) \tag{5}$$

The failure domain is deemed to be populated well enough when $N_F \geq p_0 N$ samples have been generated in $\mathcal{F}$, according to a double acceptance procedure (Hristov and DiazDelaO, 2023). At this point, the expression in Eq. (3) is used to compute an estimate of p_F, denoted $\hat{p}_F^{P-SuS}$, as a product of the normal random variables for each p_{F_k}. However, even under an assumption of independence among p_{F_k}, only the mean and variance of $\hat{p}_F^{P-SuS}$ are available in closed form as:

$$\mathbb{E}[\hat{p}_F^{P-SuS}] = \mathbb{E}\left[\prod_{k=1}^{m} p_{F_k}\right] = \prod_{k=1}^{m} \mathbb{E}[p_{F_k}] \tag{6}$$

$$\begin{gathered}\mathbb{V}\left[\hat{p}_F^{P-SuS}\right] = \mathbb{V}\left[\prod_{k=1}^{m} p_{F_k}\right] = \\ \mathbb{V}\left[p_{F_m}\right]\mathbb{V}\left[\prod_{k=1}^{m-1} p_{F_k}\right] + \mathbb{V}[p_{F_m}]\,\mathbb{E}\left[\prod_{k=1}^{m-1} p_{F_k}\right]^2 + \mathbb{E}[p_{F_m}]^2\,\mathbb{V}\left[\prod_{k=1}^{m-1} p_{F_k}\right]\end{gathered} \tag{7}$$

which also assumes independence between levels.

2.3. Convolutions under unknown dependence

To convolve two random variables, probability theory requires that the dependence between them is specified. This can be done by specifying the joint distribution of the variables, a copula, or a family of copulas, with all required parameters, in addition to the marginals, a functional dependence, or assuming a particular crisp dependence model. These models include independence, perfect and opposite dependence.

Adequately specifying the correct dependence for convolutions of uncertain numbers is a task that is commonly more challenging than comfortably proposing a model for the marginals. To compound this, in most practical applications, the effect of the dependence model on the result of convolutions is marked (Ferson et al., 2004).

When the dependence between the uncertain numbers is unknown, or imprecisely known, dependence bounds analysis (DBA) provides the mathematical machinery to enable convolutions (Williamson, 1989). Under DBA, the assumptions of perfect or opposite dependence can be relaxed to positive and negative dependence, respectively. Convolutions under no particular dependence can also be performed. The latter are referred to as Fréchet convolutions, as their bounds are based on the Fréchet-Hoeffding copula bounds (Nelsen, 2006). The upper and lower bounds on the result, Z, of a binary operation, $L(\cdot,\cdot)$, between two random variables, X and Y, with cumulative distribution functions (CDF), given by $G_X(\cdot)$ and $G_Y(\cdot)$, respectively are:

$$\begin{aligned}\tau_{W,L}(G_X, G_Y)(z) &= \sup_{z=L(x,y)} \max(G_X(x) + G_Y(y) - 1, 0) \\ \rho_{W,L}(G_X, G_Y)(z) &= \inf_{z=L(x,y)} \min(G_X(x) + G_Y(y), 1)\end{aligned} \tag{8}$$

In Eqs. 8, τ is the lower bound on the probability (resp. the right bound on the quantiles) and ρ is the upper (resp. left) bound. The results of Fréchet convolutions are sure to bound the result under the true, but unknown dependence, and they may or may not be as tight as possible under the provided information (Ferson et al., 2004). It must be noted that Fréchet convolutions are not limited to aleatory uncertain numbers only, but readily extend to mixed uncertain structures, such as probability boxes (p-boxes for short), too (Williamson, 1989). This extension is used as a principal construct of IP-SuS.

3. Imprecise probabilistic subset simulation

The assumptions of independence of the responses at each level and between the levels themselves are instrumental for the estimation of $\hat{p}_F^{P-SuS}$. This however, is an idealisation, as the indicator functions $\mathbb{I}_{F_k}(\mathbf{x})$ and their associated Bernoulli random variables arise from the same underlying

model within each chain of the MCMC algorithm, and as such have some complex form of correlation between them. Similarly, the levels are nested and each level is generated from the seeds from the previous level, making the failure probabilities at each level dependent. In this section we propose to replace the operations under independence with Fréchet convolutions.

The normal distribution in Eq. (5) is only suitable assuming that $\mathbb{I}_{F_k}(\mathbf{x}_j)$ in the sum of Eq. (4) are mutually independent, for all $1 < j < N_k$. However, when calculating that sum, no knowledge about the dependence structure of the indicator functions is available. The summation can be performed repeatedly using Fréchet convolutions, resulting in p_{F_k} taking the shape of a p-boxes of no particular distributional family, instead of crisp normal distributions. These p-boxes contain all the information about the possible cumulative distribution functions of p_{F_k}. The Fréchet convolution of two or more random variables, even with exact moments, results in a p-box, whose width represents the uncertainty arising from the lack of knowledge about the dependence.

Because Fréchet-Hoeffding copula bounds are valid only for binary operations, the sum in Eq. (4) needs to be done in a recursive manner. Repeatedly summing, random variables rigorously represented on a computer incurs additional uncertainty due to finite floating-point representations. The size of the uncertainty depends directly on the level of discretisation of the uncertain numbers and on the number of operations, that is on N_k. To control the accumulation of this kind of uncertainty, we set a parameter ϵ to impose a cut-off for the addends in Eq. (4) to those Bernoulli random variables, whose probability of success is greater than 1×10^{-4}. This choice is arbitrary and should be driven by the implementation of uncertainty arithmetic used.

Analogously, in Eqs. (6) and (7) the mean and the variance of the final estimator are also computed under the assumption of independence among the probabilities of the intermediate failure events, where the second equality in both equations holds only under this condition. The product can again be calculated under no particular dependence utilising Fréchet convolutions. As a result $\hat{p}_F^{IP-SuS}$ is no longer a distribution, for which only two moments are known, but a p-box completely defined by a pair of bounds.

Although the bounds are sufficient to fully define the final estimator of the probability of failure its mean and variance are calculated for the sake of comparison with P-SuS. The mean of the p-box is interval-valued and straightforward to calculate by taking the means of the lower and upper bounds. The variance is also interval-valued and calculated by combining its left and right step endpoints in all possible split configurations: the lower bound is either 0 (if a deterministic number can fit in the p-box) or the minimum variance of the endpoints, whereas the upper bound is the maximal variance over these combinations. The bounds for the moments can be further tightened using different methods, for example, by using information about the moments of the objects convolved.

4. Numerical experiments

To test the performance of IP-SuS, an experiment analogous to that in (Hristov and DiazDelaO, 2023) was conducted, in which a modification of the the well-known Branin function:

$$h(\mathbf{x}) = \left(x_2 - \frac{5.1}{4\pi^2} x_1^2 + \frac{5}{\pi} x_1 - 6 \right)^2 + 10(1-t)\cos(x_1) + 10 + 5x_1 \tag{9}$$

where $h : [-5, 10] \times [0, 15] \to \mathbb{R}$ was used as a basis for a probabilistic numerical model surrogate. The formulation of the PNM surrogate is as follows:

$$\begin{aligned} \mu_y(\mathbf{x}) &= h(\mathbf{x}) - c\sigma(\mathbf{x}) \\ \sigma_y^2(\mathbf{x}) &= e^{-\ell}|h(\mathbf{x})| \end{aligned} \tag{10}$$

where c is an appropriately chosen scaling constant or a function, which controls the calibration of the PNM surrogate uncertainty, and ℓ is a parameter, which controls the available computational budget by adjusting the scale of the uncertainty of the output. Through the formulation in Eqs. (10), the computational budget is reflected not only on the spread of the output distribution, but also on the distance between its mean and the response of the deterministic model. In the limit of infinite computational budget the uncertainty vanishes, that is $\lim_{\ell\to\infty} dG_y \to \delta(h(\mathbf{x}))$.

Hristov and DiazDelaO, 2023 observed that setting $t^* = 230$, gives a small failure domain $\mathcal{F}$, with two disjoint subdomains. The authors further noted that at low to moderate computational budgets, $\mathcal{F}$ cannot be reliably discovered by SuS using the means of the PNM predictions. In the original paper, it has already been shown that P-SuS can detect both failure sub-domains at any ℓ. Because IP-SuS uses the same MCMC algorithm for generating seeds and exploring the space, as P-SuS, the details about these properties of the algorithm will not be discussed further. However, the P-SuS estimator heavily underestimates p_F for outputs with large uncertainty. Moreover, the variance of the estimator is not well calibrated, that is, it does not contain the value of the original SuS estimator for all ℓ and it does not decrease in proportion to the reduction in the distance between the SuS and P-SuS estimators. This results in a final estimator of the probability of failure whose uncertainty is either too narrow or too wide.

The experiment was set up with $p_0 = 0.1$, $N = 1000$ and $\epsilon = 1 \times 10^{-4}$. Depending on ℓ, which was taken as $\ell = \{0.01, 0.05, 0.10, 0.15, 0.25, 0.50, 0.75, 1.0, 2.5, 5.0, 7.5, 10\}$, IP-SuS required anywhere between two and six conditional levels. We emphasise again that this part of the algorithm is entirely inherited from P-SuS. Unlike P-SuS, however, where the probability of each conditional level is described by a normal distribution, in IP-SuS the levels probabilities are p-boxes. Figure 1 shows the p-boxes of $\hat{p}_{F_k}$ (left and centre) and the p-box for $\hat{p}_{F_n}$ which is the estimation of p_F conditional on the last intermediate level, for $\ell = 5$. It can be seen that $\hat{p}_{F_1}$ and $\hat{p}_{F_2}$ contain the value of $p_0 = 0.1$, set at the beginning of the algorithm.

Once all p-boxes for $\hat{p}_{F_k}$ and $\hat{p}_{F_n}$ are multiplied under Fréchet rules the final estimator, $\hat{p}_F^{IP-SuS}$ is another p-box like those shown on Figure 2. There, $\hat{p}_F^{IP-SuS}$ for three different budget levels are depicted, starting from the lowest level of computational budget, $\ell = 0.01$, through a moderate budget, $\ell = 5$ to a high-fidelity response at $\ell = 10$. It can be seen that the probability of failure $\hat{p}_F^{SuS} \approx 0.0066$ estimated using the deterministic version of $h(\cdot)$, and shown as a red, dashed line, is contained within the p-boxes for all three values of ℓ, which is not the case for P-SuS at $\ell = 0.01$. In addition, it is evident that the bounds of the p-boxes become tighter as the uncertainty of the output decreases. This effect can further be observed in Figure 3, which shows the convergence of $\hat{p}_F^{IP-SuS}$ with increasing computational budget. The deterministic failure probability estimated using regular SuS and depicted as a red line is contained between the dashed lines representing the extent of the 95% central probability interval and the black solid lines depicting the imprecise median of the p-box of $\hat{p}_F^{IP-SuS}$ for most values of ℓ. For large uncertainties the bounds are wide,

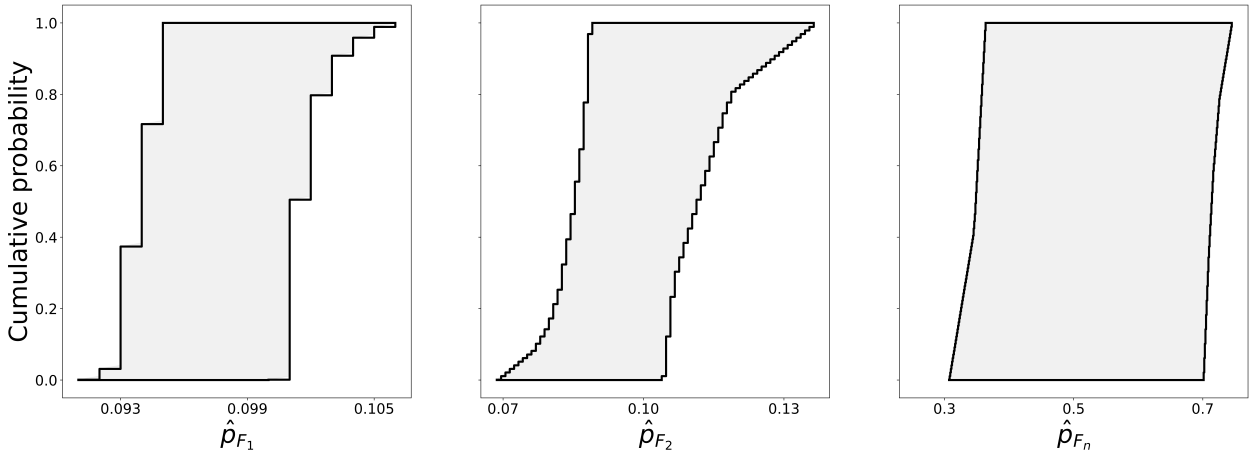
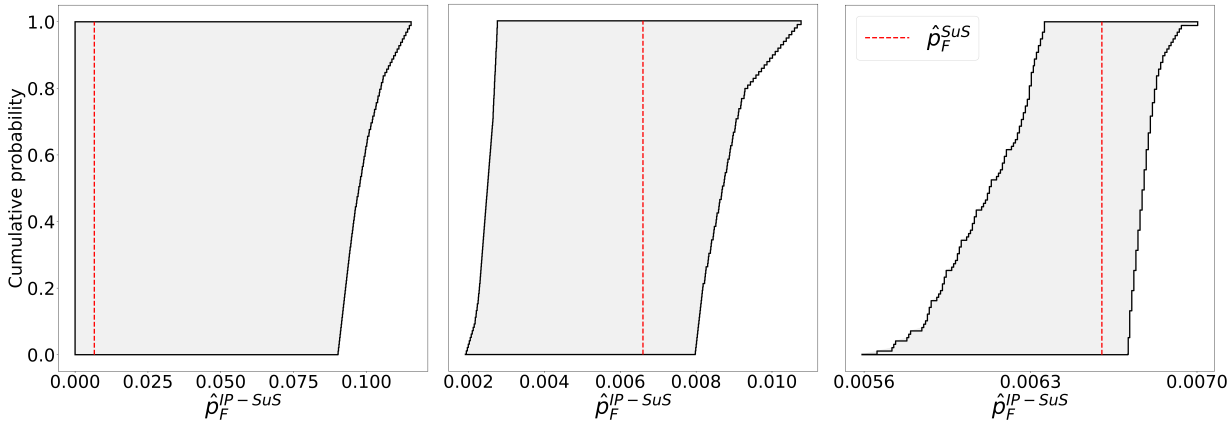


Figure 1. Probability boxes for each of the two conditional levels of IP-SuS and the p-box for $p_{F_n} = \mathbb{P}(F|F_2)$. Number of samples per level $N = 1000$; nominal level probability, $p_0 = 0.1$.



(a) (b) (c)

Figure 2. Probability boxes for $\hat{p}_F^{IP-SuS}$ at budget levels corresponding to $\ell = \{0.01, 5, 10\}$ in (Hristov and DiazDelaO, 2023). The probability of failure from subset simulation, $\hat{p}_F^{SuS}$ of the deterministic code, shown with a red, dashed line is contained in the probability boxes. Number of samples per level $N = 1000$; nominal level probability, $p_0 = 0.1$.

and as the uncertainty in the responses decreases, the bounds become tighter. It can be seen, however, that the bounds miss $\hat{p}_F^{SuS}$ for $\ell = 7.5$ but contain it again for $\ell = 10$.

To investigate the possible causes for this problem, we ran 100 repeated analyses for $\ell = 7.5$. Figure 4(a) presents the results, with error bars depicting 95% central probability intervals. It can immediately be observed that the random component of the algorithm, that is due to generating the samples across all intermediate levels up until $\mathcal{F}$, has a marked effect on the performance of $\hat{p}_F^{IP-SuS}$. Error bars in black contain the target $\hat{p}_F^{SuS}$, while those in red do not. The former constitute 51% of all repeats. This means that in 49% of the cases IP-SuS will not contain $\hat{p}_F^{SuS}$. To benchmark this, a similar analysis was carried out with P-SuS. However, because this algorithm only returns

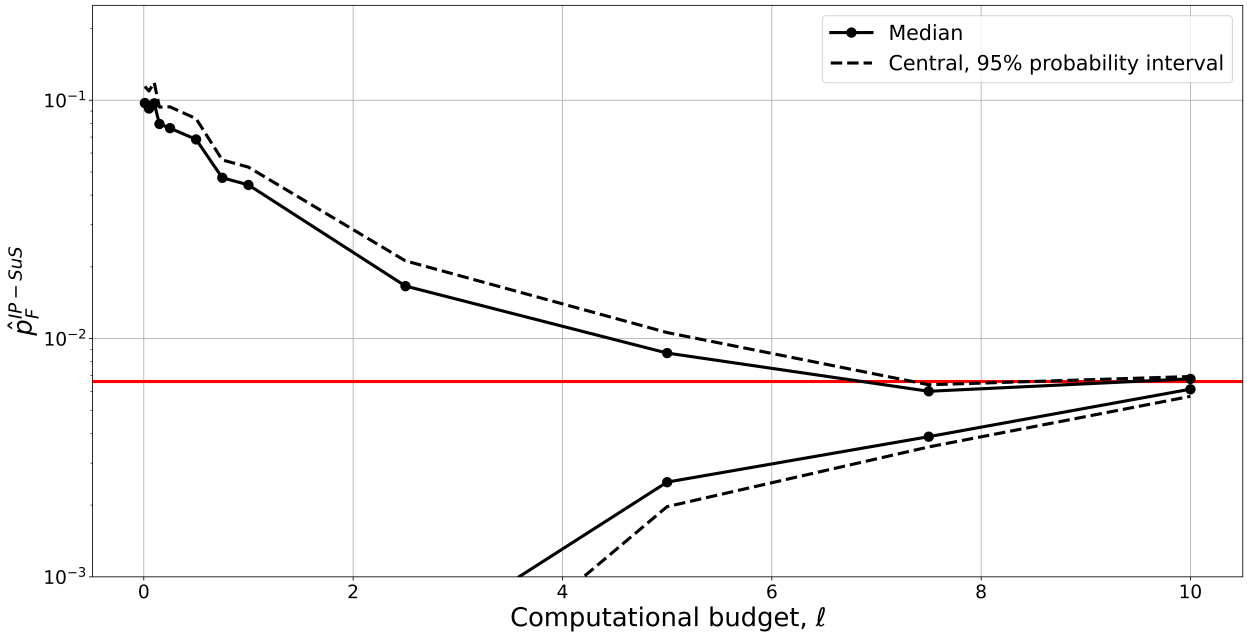
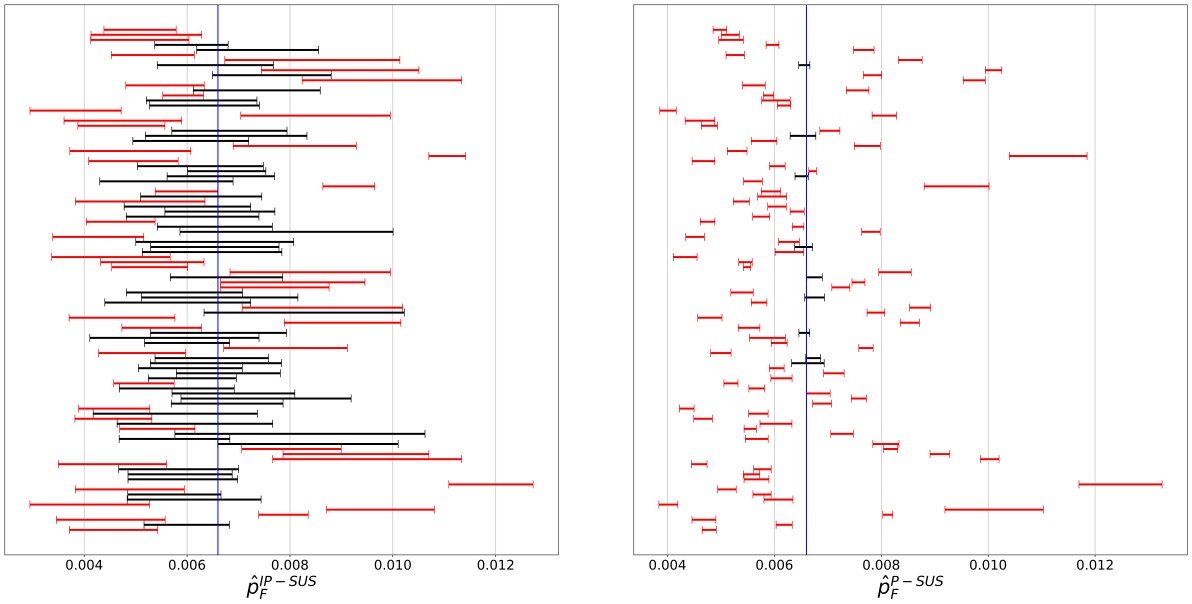


Figure 3. Convergence of $\hat{p}_F^{IP-SuS}$ with increasing computational budget. Black, solid lines show the imprecise median of the final estimator p-boxes; black, dashed lines depict the extent of the 95% central probability interval; red, solid line shows $\hat{p}_F^{SuS}$. Number of samples per level $N = 1000$; nominal level probability, $p_0 = 0.1$.

mean and variance about $\hat{p}_F^{P-SuS}$, we constructed bounds, using the celebrated Chebyshev-Cantelli one-sided inequality (Ghosh, 2002) and then computed the 95% central probability interval in a way analogous to that for $\hat{p}_F^{IP-SuS}$. The results are shown on Figure 4(b). In comparison, $\hat{p}_F^{P-SuS}$ contains $\hat{p}_F^{SuS}$ in less than 10% of the time. Regardless of this large discrepancy between the two methods, the coefficient of variation for the results from the two algorithms is very similar, coming at ≈23.7% for IP-SuS and ≈24.4% for P-SuS. This strongly suggests that the problem comes from P-SuS base, but this needs to be investigated further.

5. Conclusion

This paper presented an application of dependence bounds analysis to improve the uncertainty calibration of the failure probability estimator of P-SuS - an extension to subset simulation designed to work with probabilistic numerical models. The resulting method, termed imprecise P-SuS (IP-SuS) relaxes the assumptions of independence at two levels in the original P-SuS algorithm, among the seeds at each conditional level and among the levels themselves. The summation and product, respectively, between uncertain numbers are redefined to use Fréchet-Hoeffding bounds on convolutions, thus making no assumption about particular dependence among the operands. As a result the estimator produced by IP-SuS is a probability box, whose bounds tighten as the computational budget increases, accounting for the decrease in the uncertainty of the outputs produced by the



(a) (b)

Figure 4. Comparison between 95% probability intervals of (a) $\hat{p}_F^{IP-SuS}$ and (b) $\hat{p}_F^{P-SuS}$ from 100 repeated analyses for $\ell = 7.5$. Black error bars depict intervals which contain the value of the SuS estimator, $\hat{p}_F^{SuS}$, shown as a blue vertical line, while red ones depict intervals that do not. Number of samples per level $N = 1000$; nominal level probability, $p_0 = 0.1$.

PNM. For large uncertainties the width of the p-box of $\hat{p}_F^{IP-SuS}$ is large, but contains the credible region, which is a more desirable property than having tight bounds away from it. The effectiveness of the proposed modification was evaluated on the modified Branin function, which is often used as a benchmark for methods in uncertainty quantification.

The main direction for future work is aimed at properly calibrating the final estimator of the probability of failure, whose p-box should contain the true value for any computational budget. Moreover, the variability of the estimator should also be investigated and efforts are ongoing to make $\hat{p}_F^{IP-SuS}$ more stable.

Acknowledgements

This research was conducted with the support of the Swiss National Science Foundation and the Bulgarian Ministry of Education and Science under Grant Agreement No. IZPYZ0_228861 for the project “Automatic maximally rigorous uncertainty quantification to enable design for certification” (unCertify). The work also received funding from the GATE project funded by the Horizon 2020 WIDESPREAD-2018-2020 TEAMING Phase 2 programme under grant agreement no. 857155 and the programme ”Research, Innovation and Digitalization for Smart Transformation” 2021-2027 (PRIDST) under grant agreement no. BG16RFPR002-1.014-0010-C01.

References

Au, S.-K. and Beck, J. L. (2001). Estimation of small failure probabilities in high dimensions by subset simulation. *Probabilistic Engineering Mechanics*, 16(4):263–277.

Ferson, S., Nelsen, R. B., Hajagos, J., Berleant, D. J., Zhang, J., Troy Tucker, W., Ginzburg, L. R., and Oberkampf, W. L. (2004). Dependence in probabilistic modeling, Dempster-Shafer theory and probability bounds analysis. Technical Report SAND2002-4015, Sandia National Laboratories (SNL), Albuquerque, (NM), United States.

Ghosh, B. K. (2002). Probability inequalities related to markov's theorem. *The American Statistician*, 56(3):186–190.

Giovanis, D. G. and Shields, M. D. (2021). Imprecise subset simulation for reliability analysis. In *Conference: 9th International Workshop on Reliable Engineering Computing (REC2021)*.

Hennig, P., Osborne, M. A., and Girolami, M. (2015). Probabilistic numerics and uncertainty in computations. *Proceedings of the Royal Society A: Mathematical, Physical and Engineering Sciences*, 471(2179):20150142.

Hristov, P. and DiazDelaO, F. (2023). Subset simulation for probabilistic computer models. *Applied Mathematical Modelling*, 120:769–785.

Ibrahim, Y. (1991). Observations on applications of importance sampling in structural reliability analysis. *Structural Safety*, 9(4):269–281.

Kinnear, H. J. and DiazDelaO, F. (2025). Niching subset simulation. *Probabilistic Engineering Mechanics*, 79:103729.

Miao, Q. and Low, Y. M. (2026). Accurate variance estimation for subset simulation incorporating intrachain, interchain, and interlevel correlations. *Structural Safety*, 120:102690.

Naess, A., Leira, B., and Batsevych, O. (2009). System reliability analysis by enhanced Monte Carlo simulation. *Structural Safety*, 31(5):349–355.

Nelsen, R. B. (2006). *Definitions and Basic Properties*, pages 7–49. Springer New York, New York, NY.

Oberkampf, W. L. and Roy, C. J. (2025). *Verification, Validation, and Uncertainty Quantification in Scientific Computing*. Cambridge University Press, 2 edition.

Padmanabhan, D., Agarwal, H., Renaud, J. E., and Batill, S. M. (2006). A study using Monte Carlo simulation for failure probability calculation in reliability-based optimization. *Optimization and Engineering*, 7(3):297–316.

Pradlwarter, H., Schuëller, G., Koutsourelakis, P., and Charmpis, D. (2007). Application of line sampling simulation method to reliability benchmark problems. *Structural Safety*, 29(3):208–221.

Williamson, R. (1989). *Probabilistic Arithmetic*. PhD thesis, University of Queensland.

Zhao, Y.-G. and Ono, T. (1999). A general procedure for first/second-order reliabilitymethod (form/sorm). *Structural Safety*, 21(2):95–112.

SESSION 4

Spatial and Temporal Uncertainties

Papers in this session

1. Microstructure compatible random field models of heterogeneous materials
2. A transformation-based framework for modeling and simulation of multivariate non-Gaussian random fields
3. Fuzzy Fields based on the Parallelepiped Dependency Model
4. Surrogate modeling strategy for random fields with uncertain correlation lengths
5. Random field modeling approach for uncertainty quantification of reused concrete elements
6. Three-Dimensional Multivariable Non-Gaussian Random Field Modeling and Simulation of Concrete Constitutive Law
7. Spectrally Consistent Upscaling of Wind Speed Time Series Data

Microstructure compatible random field models of heterogeneous materials

George Stefanou[1], Dimitrios Savvas[2] and Panagiotis Gavalas[1]
[1]*Department of Civil Engineering, Aristotle University of Thessaloniki, 54124 Thessaloniki, Greece, (*gstefanou@civil.auth.gr; pgavallas@civil.auth.gr*),*

[2]*Department of Mechanical Engineering, University of West Attica, 12241 Egaleo,Greece, (*dsavvas@uniwa.gr*)*

Abstract. A key issue for the determination of the mechanical properties of heterogeneous materials is the existence of a broad range of length scales that govern their behavior. This work presents an effective multiscale computational framework for modeling the spatially varying mechanical properties of heterogeneous materials using random fields derived directly from microstructure images through homogenization combined with the moving window technique. Two applications are provided to illustrate the proposed computational framework. The determination of random fields of bending stiffness properties based on real CT-image data of short fiber composites and the computation of the apparent elasticity tensor of additively manufactured structures with random microstructural defects. The random field models of the first application can be employed for the response variability analysis of composite plates using Monte Carlo simulation. Useful conclusions are derived regarding the effect of scale factor, inter- and intra-layer overlap of printed filament lines on the mesoscale random fields.

Keywords: Heterogeneous Material, Microstructure, Mechanical Properties, Random Field, Response Variability.

1. Introduction

A key issue for the determination of the mechanical properties of heterogeneous materials is the existence of a broad range of length scales that govern their behavior. In the last years, the development of multiscale methods in a stochastic setting for uncertainty quantification and reliability analysis of composite materials and structures is becoming an emerging research frontier. Stochastic multiscale modeling aims to establish a link between the hierarchical models used to simulate the inherent uncertainties of composite materials at various scales (Tal and Fish, 2018). The stochastic multiscale methods for the analysis of heterogeneous materials and structures constitute an extension of the classical deterministic methods to a stochastic framework for the solution of problems with uncertainties in the material properties, geometry and loading. One such method, which has recently received considerable attention, is the stochastic finite element method (SFEM) (Stefanou, 2009). In the framework of SFEM, a random field description of the mechanical

© 2026 by the author(s). This work is licensed under the Creative Commons Attribution 4.0 International License (CC BY 4.0), which permits unrestricted use, distribution, and reproduction in any medium, provided the original author and source are credited.

properties is usually used. The statistical characteristics of these random fields should be compatible with the material microstructure. To this purpose, there are a few studies in the literature where the random material property fields have been obtained by analyzing directly the microstructure through computational homogenization (Miehe and Koch, 2002; Sena et al., 2013; Tran et al., 2016; Savvas et al., 2016; Sakata et al., 2022; Jetti and Ostoja-Starzewski, 2024).

When it comes to random composites, their homogenized bending properties are also random and quantifying their uncertainty is of great importance. The case of random plate structures, whose stiffness properties are described by random fields, has been investigated in several research works (Choi and Noh, 1996; Chen et al., 2024). In most cases, however, these random fields are not related to composite microstructure. In this work, the effect of microstructure morphology on the bending stiffness properties of short fiber composites is investigated by employing random fields of bending stiffness, which are derived from real microstructure data. ABD matrix homogenization according to classical laminate theory (CLT) is combined with a moving window technique to compute random fields of ABD components from CT image data of a short fiber composite (Gavallas et al., 2025). Appropriate random field models can be selected based on the image-derived data which also account for cross-correlations between different components (Van Bavel et al., 2023) (Section 2).

While homogenization is more commonly associated with the analysis of the mechanical behavior of composite materials, its application in the context of additively manufactured (AM) structures, which usually exhibit significant uncertainties, has been recently reported in the literature (Monaldo and Marfia, 2021; Özen et al., 2021; Somireddy and Czekanski, 2021). However, the aforementioned studies regarding 3D printed parts deal with deterministic homogenized models which do not account for material and geometric uncertainty of the micro/meso-structure. For more realistic modeling, a stochastic approach is needed (Mahadevan et al., 2022), which accounts for the fact that a particular microstructure is just a single sample realization from a specified spatial random process. Monte Carlo (MC) simulation based stochastic homogenization involves the computational analysis of many randomly generated realizations of the heterogeneous medium. The results from these analyses are used to derive its apparent properties and quantify their inherent uncertainties (Ma et al., 2015; Korshunova et al., 2021; Chu et al., 2021; Sakata et al., 2024). In this paper, a cost-effective computational framework is proposed to determine the random fields of the apparent elasticity tensor of AM (FDM printed) structures using the moving window technique and stochastic homogenization based on the extended finite element method (XFEM) coupled with MC simulation (Moës et al., 1999; Savvas et al., 2014). The random spatial variation of the elastic properties of the 3D printed structures is caused by the existence of random microstructural defects. These are due to geometric irregularities in the shape of the pores, which are formed by deviations in the spatial placement of the filament lines. The effect of scale factor, inter- and intra-layer overlap of printed filament lines on the mesoscale random fields is assessed and useful conclusions are derived regarding the degree of variability in different cases (Savvas and Stefanou, 2026) (Section 3).

2. Random fields of bending stiffness of short fiber composites

2.1. Proposed computational framework

In composites that exhibit random inclusion dispersion, spatial variation of the mechanical properties is observed, which can be simulated with random fields. The proposed random field computation procedure can be outlined as follows: An image of the composite is first processed with a moving window of dimensions $L_w \times L_w$, which extracts geometrical information and creates FE models (stochastic volume elements - SVEs) based on local composite morphology, as shown in Fig. 1 (Baxter and Graham, 2000). In the 2D case, the window moves across the x and $y-$ directions at a step of DL_w. For each FE model, homogenization is performed, thus the apparent mechanical properties are computed at each position of the moving window. As a result, a realization of the random fields of mechanical properties can be determined from a single composite image. From this realization, suitable random field models can be selected and response variability analysis can be conducted as in (Stefanou et al., 2017).

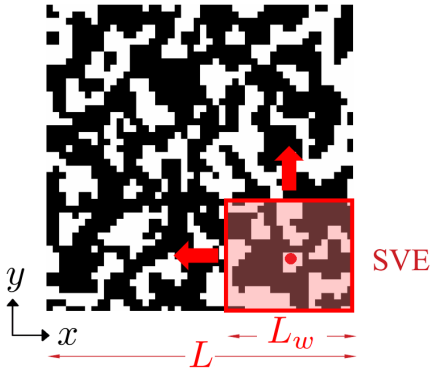


Figure 1. Computer simulated 2D binary image of the microstructure of a composite material, showing fiber (white) and matrix (black) distributions. Illustration of moving window technique and extracted SVE.

Numerical homogenization is performed herein and random fields of the ABD stiffness matrix components are computed (see Appendix). Since different window sizes can lead to different spatial variability, the scale factor $\delta = L_w/d$ is often used to characterize computed random fields at different scales, where d is the inclusion diameter in a fiber reinforced composite. A very large scale factor, which would approach the RVE size, is unlikely to capture the true random response of the material. The scale factor/window size that best describes real material behavior can be determined from experimental data (Guilleminot et al., 2008; Rauter, 2022) and in lack thereof, random fields can be computed for relevant scale factors.

In composites with uniform-like inclusion placement, the resulting random fields can be assumed to be statistically homogeneous. Therefore, the normalized correlation function between ABD stiffness components A and B at a spatial lag (ξ_x^r, ξ_y^s) can be computed through the following

equation:

$$\rho(\xi_x^r, \xi_y^s) = \frac{1}{n_x n_y} \sum_{p=1}^{n_x-|r|} \sum_{q=1}^{n_y-|s|} \left(\frac{A(x_p, y_q) - \overline{A}}{\sigma_A}\right)\left(\frac{B(x_p + |\xi_x^r|, y_q + |\xi_y^s|) - \overline{B}}{\sigma_B}\right) \tag{1}$$

where σ_A, σ_B are the standard deviations, $\overline{A}, \overline{B}$ are the spatial average (mean) values of stiffness components A, B and n_x, n_y are the number of windows in the x and $y-$ directions. For the lag indices, it holds that: $-n_x < r < n_x$ and $-n_y < s < n_y$. For $A = B$, the autocorrelation function can be computed from Eq. (1), otherwise cross-correlations are obtained.

2.2. Results and discussion

In this work, real CT image data of a short fiber reinforced composite was employed, in order to compute random fields of the ABD stiffness matrix. The 3D CT data was acquired through the TOMCAT beamline at the Swiss Light Source. It was processed with the RETOMO software of BETA CAE Systems, which resulted in a meshed FE model. A thin slice of this 3D model was processed with the moving window technique, and SVE submodels were selected and homogenized with the proposed method, thus obtaining random fields of the ABD matrix components. ANSA was used for SVE extraction and application of appropriate boundary conditions. Abaqus was employed for solving each boundary value problem and META for result post-processing (BETA CAE Systems, 2024; Dassault Systèmes, 2024).

An epoxy-glass fiber composite is considered, with the following properties: $E_m = 3\ GPa, \nu_m = 0.395$ and $E_{incl} = 73\ GPa, \nu_{incl} = 0.18$. As mentioned previously, a thin slice of the CT model was investigated, with dimensions $L_x \times L_y \times L_z = 1063.4\ \mu m \times 793\ \mu m \times 13\ \mu m$. Random fields for two different scale factors were computed: $\delta = 10$ and $\delta = 20$, which correspond to window sizes $L_w = 52\ \mu m$ and $L_w = 104\ \mu m$, considering an average fiber diameter $d = 5.2\ \mu m$. This required homogenization of 1131 and 266 SVEs, respectively, assuming a window step $DL_w = L_w/2$. The top view of the investigated slice of the material can be seen in Fig. 2(a). Sample SVEs for the two different scale factors can be seen in Fig. 2(b) and Fig. 2(c), with dimensions $L_w \times L_w \times L_z$.

The computed random fields for both extension/shear and bending/torsion components of the ABD matrix of this composite are depicted in Fig. 3. It is clarified that components of the A, B and D matrices in this work are computed in $GPa\ \mu m$, $GPa\ \mu m^2$ and $GPa\ \mu m^3$, respectively, while length quantities are measured in μm.

With regard to the differences between the two scale factors, it is observed that variability decreases at higher scales, as the COV appears to decrease while the opposite is true for the corresponding correlation lengths. One interesting observation is that despite the relatively low stiffness ratio ($E_{incl}/E_m = 24$), the computed random fields of all stiffness components exhibit a high COV, with a maximum of 24.6% at scale factor $\delta = 10$ and 15.2% for $\delta = 20$. This can potentially lead to significant response variability for structures simulated with this material and can be attributed to the large variability of inclusion shapes and orientations in the obtained SVEs.

Additionally, upon close inspection, it becomes apparent that random fields computed from the same type of stresses are also highly correlated with each other. For instance, the random fields of ABD matrix components A_{11} and D_{11} are computed from stress component σ_{xx}, and their plots

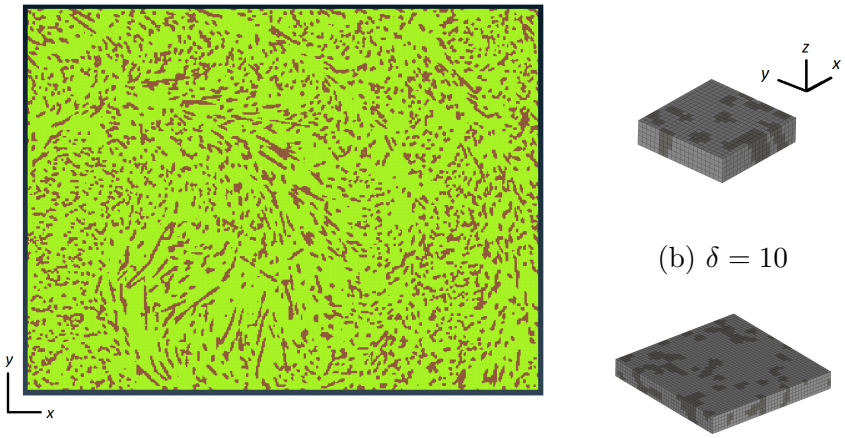
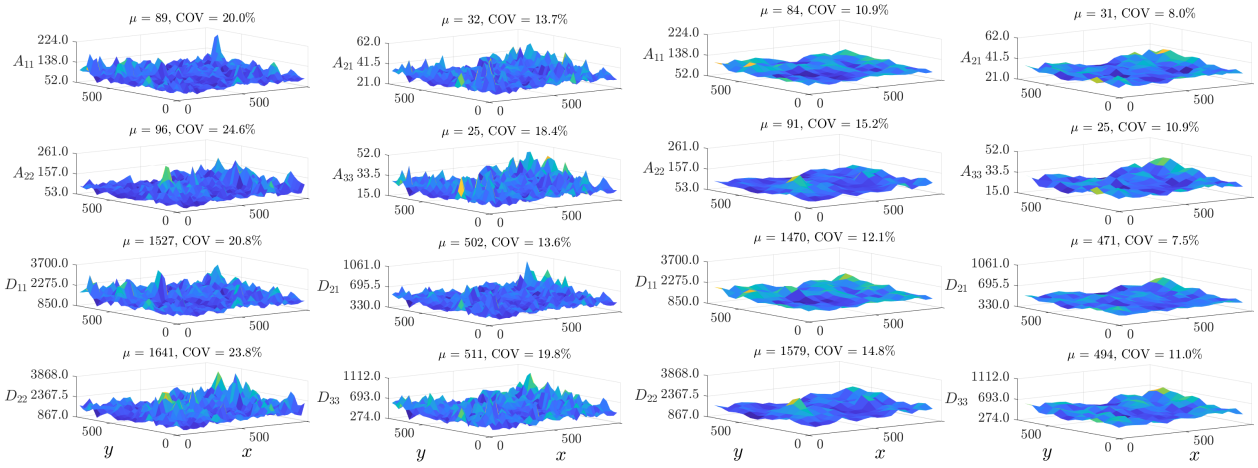


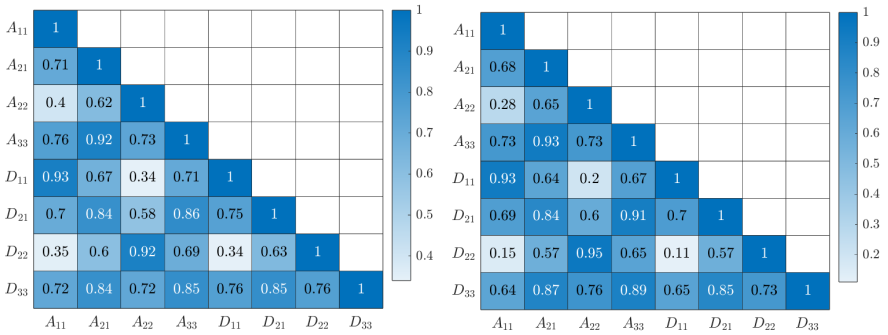
Figure 2. a) Slice of short fiber composite, top view, (b-c) Sample SVEs at different scale factors $\delta = 10$ and $\delta = 20$.



(a) $\delta = 10$. (b) $\delta = 20$.

Figure 3. Random fields of ABD matrix components for the two scale factors.

indicate they are correlated. This is confirmed after calculating the cross-correlation coefficients between all components (Fig. 4), where in this particular case $\rho_{A_{11}}^{D_{11}} = 0.93$. All components appear to be correlated, with the highest correlation being observed for components computed from the same stresses/in the same direction. This suggests that accurate simulation of these random fields for a response variability analysis requires multivariate (cross-correlated) random field models.



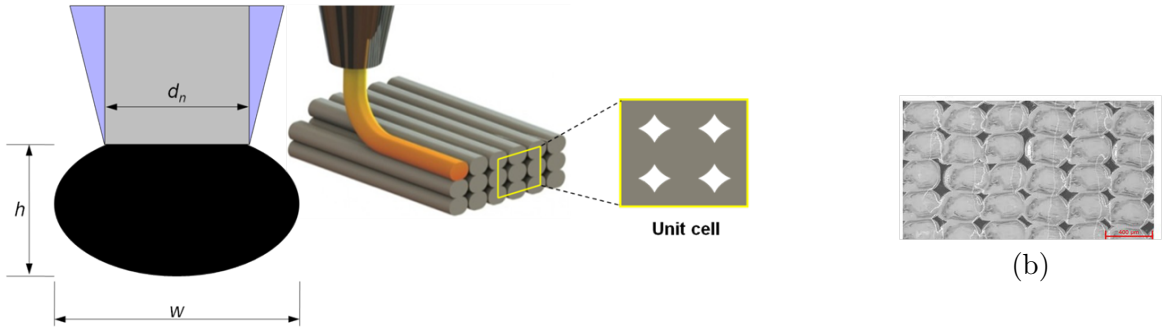
(a) $\delta = 10$ (b) $\delta = 20$

Figure 4. Correlation coefficients ρ for the different components of the ABD matrix.

3. Random fields of apparent elasticity tensor of additively manufactured structures with random microstructural defects

3.1. Proposed computational framework

The additive manufacturing method used in this work is Fused Deposition Modeling (FDM). The main FDM printing parameters that determine the cross-sectional geometry of the printed filament line are shown in Fig. 5(a). The cross section is approximated by an ellipse with major and minor axes of dimensions w and h, respectively. The width w depends on the diameter of the nozzle d_n as $w = 1.1 \times d_n$. Fig. 5(a) illustrates the layer-by-layer construction of the printed object. Ideally, each filament line has no overlap in either the intra- or the inter-layer direction. In this ideal case, the mesostructure of the printed part consists of a unit cell repeated periodically in both directions, defining a deterministic geometry. However, as shown in Fig. 5(b), the mesostructure of a FDM printed object, obtained via scanning electron microscopy (SEM), exhibits uncertainties both in the filament cross-sectional shape and in the spatial placement of each filament line.



(a) (b)

Figure 5. a) Printing parameters, filament cross-section geometry, layer deposition, and periodic unit cell, b) SEM image of the mesostructure of a FDM printed object.

As explained in Fig. 6, each filament line exhibits a degree of random overlap with its neighboring lines, both in the intra- and inter-layer directions. Consequently, the distances between the centers of the elliptical filament cross sections, d_x and d_y, are stochastic variables given by:

$$\begin{aligned} d_x &= w \cdot (1 - e_x) \\ d_y &= h \cdot (1 - e_y) \end{aligned} \tag{2}$$

where e_x and e_y are stochastic parameters representing the degree of overlap. These parameters are assumed to follow normal distributions with mean value μ and standard deviation σ:

$$\begin{aligned} e_x &\sim N\left(\mu_{e_x}, \sigma^2_{e_x}\right) \\ e_y &\sim N\left(\mu_{e_y}, \sigma^2_{e_y}\right) \end{aligned} \tag{3}$$

The coefficient of variation (COV) can be calculated as the fraction of σ over μ, $COV = \sigma/\mu$.

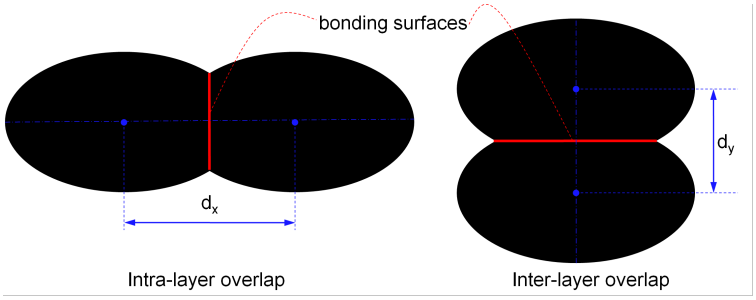


Figure 6. Overlap of printed filament lines in the intra- and inter-layer directions.

In practice, the mesostructure of an AM part exhibits both geometric irregularities in the shape of the cross section of the filament and deviations in spatial placement of the filament lines. These deviations lead to random microstructural defects that affect the mechanical properties of the printed component. To study the influence of these uncertainties, a representative mesostructure case is examined, where the overlap parameters e_x (intra-layer overlap) and e_y (inter-layer overlap) follow normal distributions with mean value μ and standard deviation σ.

The mesostructure image corresponding to this case is generated using the mean value μ and the standard deviation value σ of the overlap parameters, as shown in Fig. 7. The image represents a square region of approximately $L_{im_x} \times L_{im_y} = 35 \times 35\ mm^2$. The printing parameters used to generate this mesostructure image are $d_n = 0.4\ mm$, $w = 0.44\ mm$, and $h = 0.3\ mm$. These stochastic variations in filament positioning form the basis for modeling geometrical uncertainty in subsequent XFEM simulations and homogenization analysis (Savvas and Stefanou, 2026).

3.2. Results and discussion

In this section, random fields for the volume fraction of pores and the apparent elasticity tensor of the 3D printed structure are computed in various mesoscale sizes $\delta = A_w/A_f$ (with A_w the moving window area and A_f the elliptical cross-sectional area of a single filament) based on the simulation of a large number of SVE models extracted using the moving window technique. The computed results

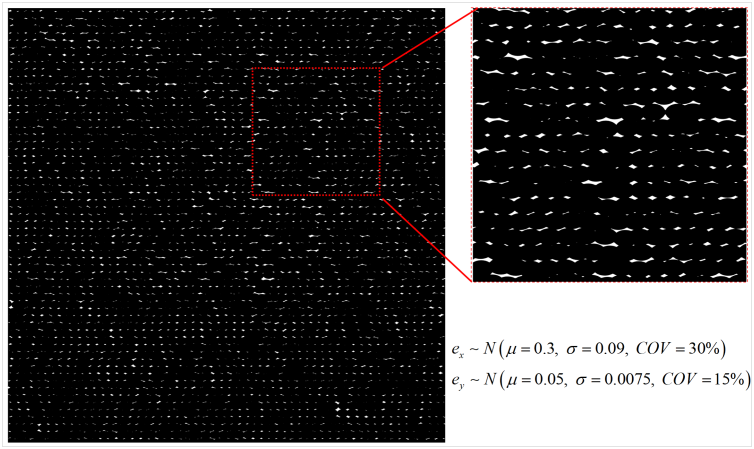


Figure 7. Case of stochastic overlap parameters e_x, e_y.

refer to kinematically uniform boundary conditions (KUBCs) and statically uniform boundary conditions (SUBCs) applied on the 3D printed composite with respect to the statistical properties of the intra- and inter-layer overlap parameters e_x, e_y.

The computed random fields for C_{1111} are shown in Fig. 8 along with their respective empirical probability distributions and autocorrelation functions for the four mesoscale sizes δ examined and for KUBCs. The COV of all mesoscale random fields decreases and their correlation length increases as δ increases. This means that the random fields tend to become less variable and fully correlated as δ increases. The above statistical results are consistent with those obtained in (Sena et al., 2013; Savvas et al., 2016; Sakata et al., 2022; Jetti and Ostoja-Starzewski, 2024) for particle/fiber reinforced and interpenetrating phase composites.

Fig. 9 illustrates the convergence of porosity with respect to δ and the convergence of the upper and lower bounds on the mean values of the axial and shear stiffness properties with respect to δ. A convergence trend is observed as δ increases irrespectively of the type of BCs. It is important to note the large variability of the porosity, particularly at lower scale factors ($COV = 26\%$ for $\delta = 5.67$), which affects significantly the spatial variation of the mechanical properties. In Fig. 9, it can also be observed that the mean value of porosity increases while the COV of porosity decreases with increasing δ. A similar observation can be made on the same figure for the COV values of the apparent mechanical properties C_{ijkl}. The random fields obtained using SUBCs are much more variable than those obtained using KUBCs particularly at small scale factors, which are characterized by larger variability in the porosity.

In addition, the COV of axial stiffness C_{2222} is larger than that of C_{1111}, especially for SUBCs. This behavior can be explained by the relative magnitude of the stochastic overlap parameters. The intra-layer overlap e_x has a relatively large mean value ($\mu_{e_x} = 0.30$), ensuring substantial bonding between filaments within the same layer. Even though its coefficient of variation is higher ($COV = 30\%$), the absolute overlap remains sufficient to maintain effective load transfer along the x-axis, which limits the scatter in the apparent stiffness C_{1111}. In contrast, the inter-layer overlap e_y has a much smaller mean value ($\mu_{e_y} = 0.05$), corresponding to weaker bonding between successive

layers. Therefore, small fluctuations around this low mean can produce disproportionately large relative changes in the effective contact area, which amplifies the variability of the apparent stiffness C_{2222}, particularly under SUBCs where weak layer interfaces play a dominant role in stress transfer. A negative correlation between vf and the apparent properties and a strong positive correlation between the various mechanical properties are also observed in Fig. 10, as expected.

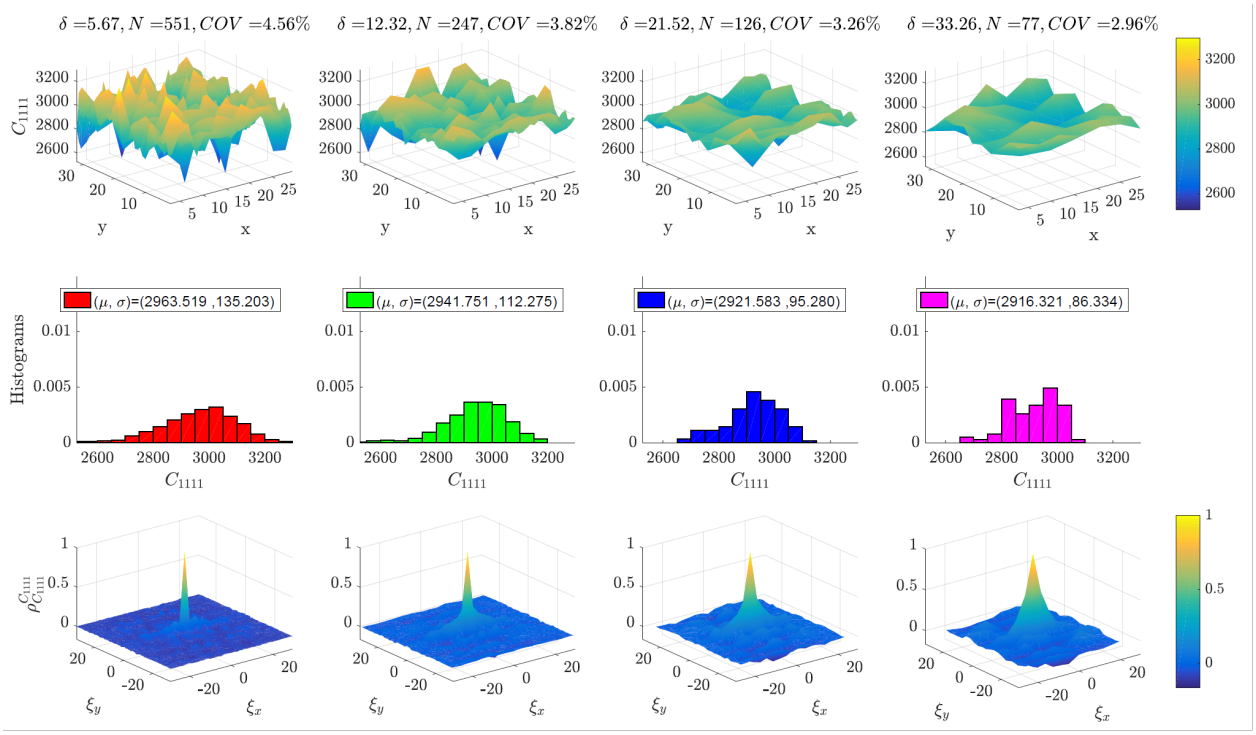


Figure 8. Random fields, empirical probability and autocorrelation functions of axial stiffness C_{1111} for various scale factors δ in case of KUBCs.

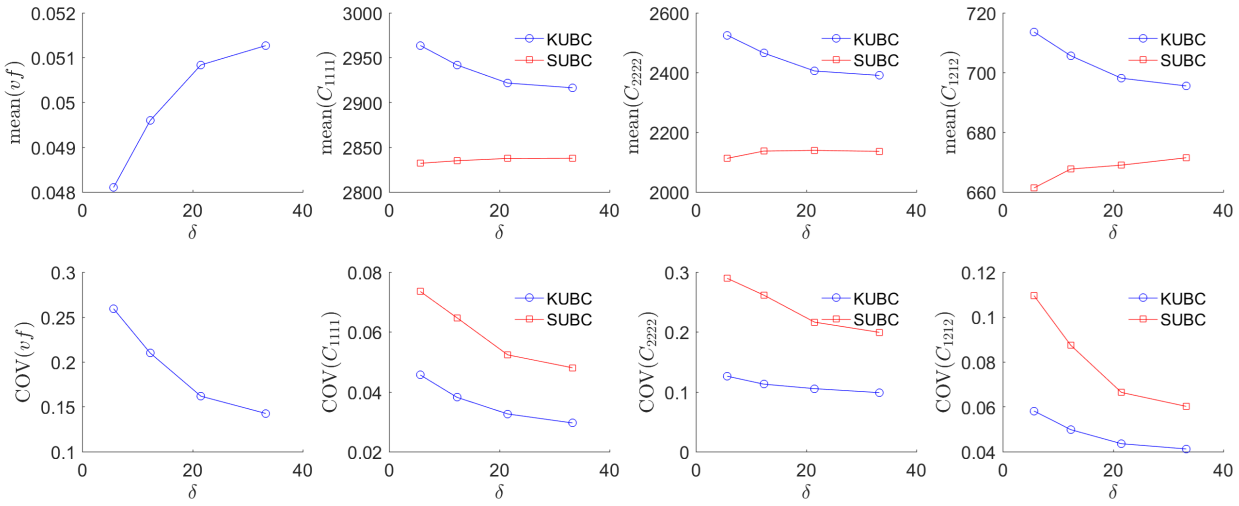


Figure 9. Convergence of mean and COV of porosity, C_{1111}, C_{2222} and C_{1212} with respect to scale factor δ for KUBCs and SUBCs.

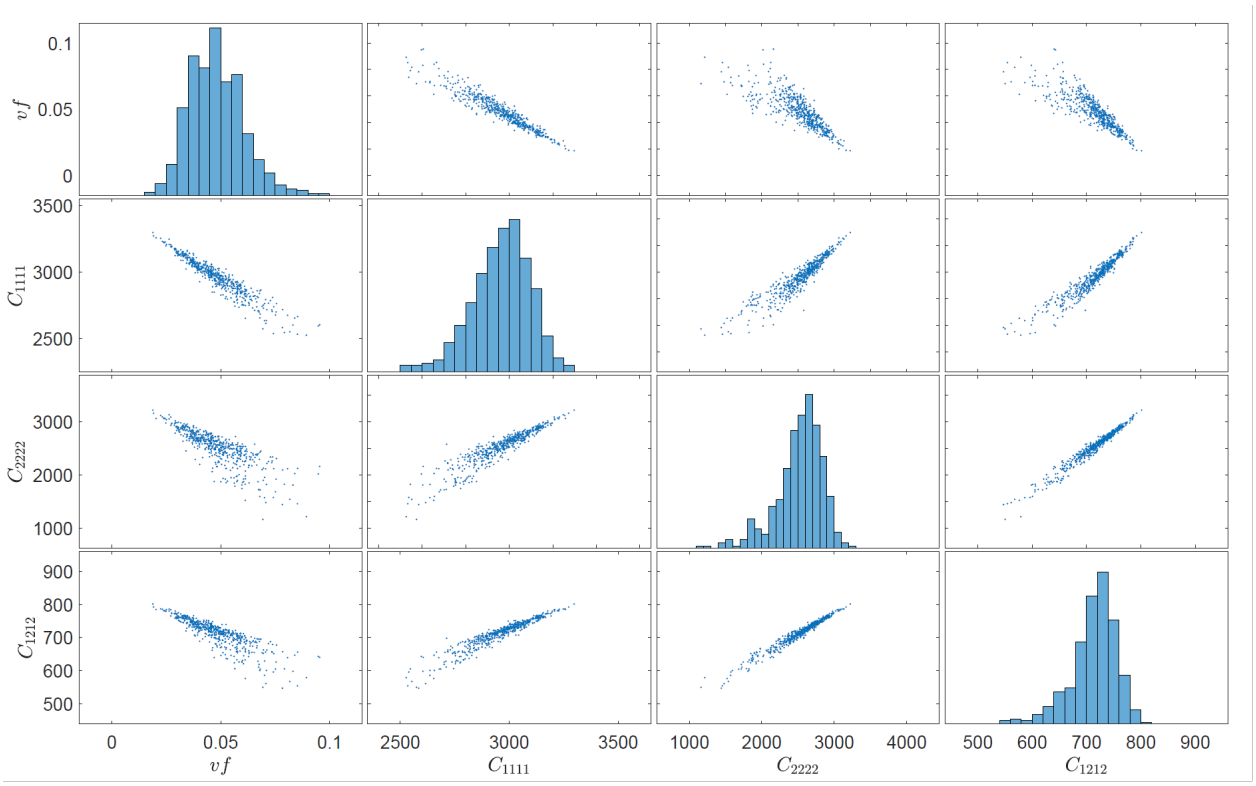


Figure 10. Scatter plots of random porosity and apparent stiffness properties in case of $\delta = 5.67$ and KUBCs.

4. Conclusions

An effective multiscale computational framework was presented for modeling the spatially varying mechanical properties of heterogeneous materials (short fiber composites, additively manufactured structures) using random fields derived directly from microstructure images through homogenization of stochastic volume elements. Based on the numerical results, the following conclusions can be drawn:

- Increasing the mesoscale size δ reduces the variability (COV) of all random fields and increases their correlation length, demonstrating the expected trend towards constant homogenized properties at larger scales.
- Porosity exhibits significant spatial variability at small mesoscale sizes, which strongly influences the stochastic behavior of the elastic moduli of additively manufactured structures.
- Random fields obtained with SUBCs are more variable than those under KUBCs, particularly at small scale factors where the variability of porosity is larger.
- Negative correlations are obtained between porosity and stiffness properties and strong positive correlations between stiffness components, highlighting the effect of microstructural features on the mechanical response.

The computed mesoscale random fields can be employed for the response variability and reliability analysis of structures in the framework of the stochastic finite element method (Gavallas et al., 2025).

Appendix

A. Classical Laminate Theory (CLT)

In CLT, a composite laminate consists of several layers or laminae with different properties or alignment (Agarwal et al., 2006). Each lamina is considered an orthotropic material, therefore its inplane behavior can be described by the following equation:

$$\begin{bmatrix} \sigma_x \\ \sigma_y \\ \tau_{xy} \end{bmatrix} = \begin{bmatrix} C_{11} & C_{12} & 0 \\ C_{21} & C_{22} & 0 \\ 0 & 0 & C_{33} \end{bmatrix} \begin{bmatrix} \varepsilon_x \\ \varepsilon_y \\ \gamma_{xy} \end{bmatrix} \quad \text{or} \quad \boldsymbol{\sigma} = \mathbf{C}\,\boldsymbol{\varepsilon} \tag{4}$$

where $\mathbf{C}$ is the reduced elasticity matrix under plane stress conditions.

For the computation of the mechanical properties of laminates according to CLT, several assumptions are made. Each lamina is a homogeneous material and there is perfect bonding between each layer. Inplane stiffness is determined by assuming plane stress conditions. With regard to bending behavior, the assumptions of the Kirchoff-Love theory hold, which means that normals to the midplane remain normal and straight, while their lengths do not change. It should be noted that,

as the thickness of the laminate increases, the Kirchoff-Love assumptions can lead to inaccurate stiffness estimates.

Under the above assumptions, the relationship between force/moment resultants and mid-surface strains and curvatures according to CLT is given by the following equation:

$$\begin{bmatrix} N_x \\ N_y \\ N_{xy} \\ M_x \\ M_y \\ M_{xy} \end{bmatrix} = \begin{bmatrix} A_{11} & A_{12} & A_{13} & B_{11} & B_{12} & B_{13} \\ A_{21} & A_{22} & A_{23} & B_{21} & B_{22} & B_{23} \\ A_{31} & A_{32} & A_{33} & B_{31} & B_{32} & B_{33} \\ B_{11} & B_{12} & B_{13} & D_{11} & D_{12} & D_{13} \\ B_{21} & B_{22} & B_{23} & D_{21} & D_{22} & D_{23} \\ B_{31} & B_{32} & B_{33} & D_{31} & D_{32} & D_{33} \end{bmatrix} \begin{bmatrix} \varepsilon_x \\ \varepsilon_y \\ \gamma_{xy} \\ \kappa_x \\ \kappa_y \\ \kappa_{xy} \end{bmatrix} \quad \text{or} \quad \begin{bmatrix} \mathbf{N} \\ \mathbf{M} \end{bmatrix} = \begin{bmatrix} \mathbf{A} & \mathbf{B} \\ \mathbf{B} & \mathbf{D} \end{bmatrix} \begin{bmatrix} \boldsymbol{\varepsilon} \\ \boldsymbol{\kappa} \end{bmatrix} \tag{5}$$

where **A**, **B** and **D** are called the extensional, coupling and bending stiffness matrices, respectively. Due to the symmetry of the ABD matrix it holds that $A_{ij} = A_{ji},\ B_{ij} = B_{ji}$ and $D_{ij} = D_{ji}$. Note that forces and moments are computed per unit length.

The extensional stiffness matrix **A** expresses the relationship between normal/shear forces and midplane strains, while the bending stiffness matrix **D** expresses the relationship between bending/torsional moments and plate curvatures. The coupling stiffness matrix **B** expresses the interaction between extension and bending, which implies that when components of **B** are non-zero, application of normal/shear forces will result in not only midplane strains but also curvatures and plate bending/torsion. It should be noted that in a symmetrical laminate with respect to the midplane, the components of **B** will be zero, implying no extension/bending coupling. The **A**, **B** and **D** matrices are given by the following equations:

$$A_{ij} = \int_{-\frac{t}{2}}^{\frac{t}{2}} Q_{ij}\, \mathrm{d}z = \sum_{k=1}^{n} Q_{ij}^{(k)} \left(z_k - z_{k-1}\right) \tag{6}$$

$$B_{ij} = \int_{-\frac{t}{2}}^{\frac{t}{2}} Q_{ij}\, z\, \mathrm{d}z = \frac{1}{2} \sum_{k=1}^{n} Q_{ij}^{(k)} \left(z_k^2 - z_{k-1}^2\right) \tag{7}$$

$$D_{ij} = \int_{-\frac{t}{2}}^{\frac{t}{2}} Q_{ij}\, z^2\, \mathrm{d}z = \frac{1}{3} \sum_{k=1}^{n} Q_{ij}^{(k)} \left(z_k^3 - z_{k-1}^3\right) \tag{8}$$

where $Q_{ij}^{(k)}$ is the transformed reduced elasticity matrix of the k-th lamina, t is the total thickness of the laminate, n is the number of laminae and z_k, z_{k-1} are the distances from the mid-surface of the laminate to the inner/outer surfaces of the k-th lamina. In the case that the lamina is aligned with the laminate coordinate system, it holds that $Q_{ij} = C_{ij}$, otherwise transformation of the reduced elasticity matrix C_{ij} is required.

B. Computational homogenization

Computational homogenization is a systematic framework that connects the microscopic responses of heterogeneous materials to their effective macroscopic constitutive behavior, especially under

small, linear macroscopic strains and stresses. This method is particularly applied to Representative Volume Elements (RVEs), which characterize the microstructural properties of composite materials (Zohdi and Wriggers, 2008).

The macroscopic strain and stress tensors can be computed as volume averages of the microscopic strain $\varepsilon_{ij}(x,y)$ and stress $\sigma_{ij}(x,y)$ fields which vary throughout the RVE domain B:

$$\bar{\varepsilon}_{ij} = \frac{1}{V}\int_B \varepsilon_{ij}(x,y)\,dB, \tag{9}$$

$$\bar{\sigma}_{ij} = \frac{1}{V}\int_B \sigma_{ij}(x,y)\,dB, \tag{10}$$

where V denotes the RVE volume.

Assuming a linearly elastic anisotropic material, the macroscopic constitutive relation reads:

$$\begin{bmatrix} \bar{\sigma}_{11} \\ \bar{\sigma}_{22} \\ \bar{\sigma}_{12} \end{bmatrix} = \begin{bmatrix} \bar{C}_{1111} & \bar{C}_{1122} & \bar{C}_{1112} \\ & \bar{C}_{2222} & \bar{C}_{2212} \\ sym & & \bar{C}_{1212} \end{bmatrix} \begin{bmatrix} \bar{\varepsilon}_{11} \\ \bar{\varepsilon}_{22} \\ \bar{\varepsilon}_{12} \end{bmatrix} \tag{11}$$

where $\bar{\mathbf{C}}$ is the homogenized stiffness tensor to be determined. It is noted that the microstructure is mechanically inhomogeneous, but a finite volume of the material is assumed to be statistically homogeneous as required by the homogenization technique. Regarding the mesoscale random fields determined by the presented approach, statistical homogeneity and/or isotropy are not assumed, but can emerge based on the underlying microstructure.

References

Agarwal, B. D., L. J. Broutman, and K. Van Breugel: 2006, *Analysis and Performance of Fiber Composites*. John Wiley & Sons.

Baxter, S. C. and L. L. Graham: 2000, 'Characterization of random composites using moving-window technique'. *Journal of Engineering Mechanics* **126**(4), 389–397.

BETA CAE Systems: 2024, 'ANSA, META, and RETOMO [Computer software]'. Accessed: 2025-02-14.

Chen, B., Z. Shao, A. Ademiloye, D. Yang, X. Zhang, and P. Xiang: 2024, 'Stochastic static analysis of functionally graded sandwich nanoplates based on a novel stochastic meshfree computational framework'. *Advances in Engineering Software* **198**, 103780.

Choi, C.-K. and H.-C. Noh: 1996, 'Stochastic finite element analysis of plate structures by weighted integral method'. *Structural Engineering and Mechanics* **4**(6), 703–715.

Chu, S., J. Guilleminot, C. Kelly, B. Abar, and K. Gall: 2021, 'Stochastic modeling and identification of material parameters on structures produced by additive manufacturing'. *Computer Methods in Applied Mechanics and Engineering* **387**, 114166.

Dassault Systèmes: 2024, 'Abaqus [Computer software]'. Accessed: 2025-02-14.

Gavallas, P., G. Stefanou, and E. Tsivolas: 2025, 'The effect of random microstructure morphology on the bending behavior of composite plate structures'. *Composite Structures* p. 119432.

Guilleminot, J., C. Soize, D. Kondo, and C. Binetruy: 2008, 'Theoretical framework and experimental procedure for modelling mesoscopic volume fraction stochastic fluctuations in fiber reinforced composites'. *International Journal of Solids and Structures* **45**(21), 5567–5583.

Jetti, Y. S. and M. Ostoja-Starzewski: 2024, 'Correlation structures of statistically isotropic stiffness and compliance TRFs through upscaling'. *Computer Methods in Applied Mechanics and Engineering* **432**, 117356.

Korshunova, N., I. Papaioannou, S. Kollmannsberger, D. Straub, and E. Rank: 2021, 'Uncertainty quantification of microstructure variability and mechanical behavior of additively manufactured lattice structures'. *Computer Methods in Applied Mechanics and Engineering* **385**, 114049.

Ma, J., S. Sahraee, P. Wriggers, and L. De Lorenzis: 2015, 'Stochastic multiscale homogenization analysis of heterogeneous materials under finite deformations with full uncertainty in the microstructure'. *Computational Mechanics* **55**(5), 819–835.

Mahadevan, S., P. Nath, and Z. Hu: 2022, 'Uncertainty quantification for additive manufacturing process improvement: Recent advances'. *ASCE-ASME Journal of Risk and Uncertainty in Engineering Systems, Part B: Mechanical Engineering* **8**(1), 010801.

Miehe, C. and A. Koch: 2002, 'Computational micro-to-macro transitions of discretized microstructures undergoing small strains'. *Archive of Applied Mechanics* **72**(4-5), 300–317.

Moës, N., J. Dolbow, and T. Belytschko: 1999, 'A finite element method for crack growth without remeshing'. *International Journal for Numerical Methods in Engineering* **46**, 131–150.

Monaldo, E. and S. Marfia: 2021, 'Computational homogenization of 3D printed materials by a reduced order model'. *International Journal of Mechanical Sciences* **197**, 106332.

Özen, A., B. E. Abali, C. Völlmecke, J. Gerstel, and D. Auhl: 2021, 'Exploring the role of manufacturing parameters on microstructure and mechanical properties in fused deposition modeling (FDM) using PETG'. *Applied Composite Materials* **28**(6), 1799–1828.

Rauter, N.: 2022, 'Numerical Simulation of the Elastic-Ideal Plastic Material Behavior of Short Fiber-Reinforced Composites Including Its Spatial Distribution with an Experimental Validation'. *Applied Sciences* **12**(20), 10483.

Sakata, S.-i., G. Stefanou, and S. Araki: 2022, 'Random field modeling of local strength of a randomly arranged unidirectional fiber-reinforced composite material under transverse tensile loading'. *Materials Today Communications* **33**, 104783.

Sakata, S.-i., G. Stefanou, T. Kikkawa, and Y. Aikawa: 2024, 'Probabilistic analysis of homogenized elastic property for resin products fabricated by additive manufacturing based on three-dimensional random field modeling of microstructure'. *Mechanics of Materials* **196**, 105071.

Savvas, D. and G. Stefanou: 2026, 'Determination of the mechanical properties of additively manufactured structures with random microstructural defects'. *Computer Methods in Applied Mechanics and Engineering* **449**, 118574.

Savvas, D., G. Stefanou, and M. Papadrakakis: 2016, 'Determination of RVE size for random composites with local volume fraction variation'. *Computer Methods in Applied Mechanics and Engineering* **305**, 340–358.

Savvas, D., G. Stefanou, M. Papadrakakis, and G. Deodatis: 2014, 'Homogenization of random heterogeneous media with inclusions of arbitrary shape modeled by XFEM'. *Computational mechanics* **54**(5), 1221–1235.

Sena, M. P., M. Ostoja-Starzewski, and L. Costa: 2013, 'Stiffness tensor random fields through upscaling of planar random materials'. *Probabilistic Engineering Mechanics* **34**, 131–156.

Somireddy, M. and A. Czekanski: 2021, 'Computational modeling of constitutive behaviour of 3D printed composite structures'. *Journal of Materials Research and Technology* **11**, 1710–1718.

Stefanou, G.: 2009, 'The stochastic finite element method: Past, present and future'. *Computer methods in applied mechanics and engineering* **198**(9-12), 1031–1051.

Stefanou, G., D. Savvas, and M. Papadrakakis: 2017, 'Stochastic finite element analysis of composite structures based on mesoscale random fields of material properties'. *Computer Methods in Applied Mechanics and Engineering* **326**, 319–337.

Tal, D. and J. Fish: 2018, 'Stochastic multiscale modeling and simulation framework for concrete'. *Cement and Concrete Composites* **90**, 61–81.

Tran, V., J. Guilleminot, S. Brisard, and K. Sab: 2016, 'Stochastic modeling of mesoscopic elasticity random field'. *Mechanics of Materials* **93**, 1–12.

Van Bavel, B., Y. Zhao, M. Faes, D. Vandepitte, and D. Moens: 2023, 'Efficient quantification of composite spatial variability: A multiscale framework that captures intercorrelation'. *Composite Structures* **323**, 117462.

Zohdi, T. I. and P. Wriggers: 2008, *An Introduction to Computational Micromechanics, 2nd Edition, Lecture Notes in Applied and Computational Mechanics*, Vol. 20. Springer, Heidelberg.

A Transformation-Based Framework for Modeling and Simulation of Multivariate Non-Gaussian Random Fields

Meng-Ze Lyu
Institute for Risk & Reliability, Leibniz University Hannover, Hannover 30167, Germany
Email: mengze.lyu@irz.uni-hannover.de

Yang-Yi Liu
Department of Civil, Environmental & Geo-Engineering, University of Minnesota Twin Cities, Minneapolis 55455, USA
Email: liu02919@umn.edu

Jian-Bing Chen
College of Civil Engineering, Tongji University, Shanghai 200092, China
Email: chenjb@tongji.edu.cn

Michael Beer
Institute for Risk & Reliability, Leibniz University Hannover, Hannover 30167, Germany
Department of Civil & Environmental Engineering, University of Liverpool, Liverpool L69 3GH, UK
International Joint Research Center for Engineering Reliability & Stochastic Mechanics & International Joint Research Center for Resilient Infrastructure, Tongji University, Shanghai 200092, China
Email: beer@irz.uni-hannover.de

Abstract: Accurate modeling of multivariate non-Gaussian random fields remains a fundamental challenge in reliable engineering computation, particularly when nonlinear dependencies coexist with spatial correlation. This study introduces a new framework in which the probabilistic model is defined by the original marginal distributions together with linear correlations of Gaussianized transformed variables. This leads to a transformed correlation function that preserves non-Gaussian marginals while consistently characterizing spatial variability. The bridge function, originally developed for Gaussian fields, is extended to reconcile spatial correlation with nonlinear dependencies such as those captured by vine copulas. Based on this model, an efficient non-iterative simulation algorithm is developed. Numerical results show that the method accurately reproduces marginal distributions, nonlinear dependence, and spatial correlation in complex engineering fields.

Keywords: Multivariate non-Gaussian random field; Transformed correlation function; Bridge function; Uncertainty quantification.

1. Introduction

Reliable engineering computing and structural risk assessment increasingly rely on the rigorous quantification of spatial uncertainties (Li and Lyu, 2026). In civil, mechanical, and geotechnical engineering, physical

© 2026 by the author(s). This work is licensed under the Creative Commons Attribution 4.0 International License (CC BY 4.0), which permits unrestricted use, distribution, and reproduction in any medium, provided the original author and source are credited.

parameters (such as material compressive strength, elastic modulus, and fracture toughness) rarely manifest as homogeneous or isolated random variables (Tao and Chen, 2023). Instead, they exhibit distinct spatial variability over the physical domain, which is mathematically characterized using random fields (Vanmarcke, 2010). In many engineering systems, multiple spatially varying quantities are physically coupled, necessitating the use of multivariate random field models (Tao et al., 2020). An accurate probabilistic representation of these multivariate fields requires the simultaneous capture of three essential characteristics (Lyu et al., 2025): (1) the individual marginal probability distributions of each variable, (2) the spatial auto-correlation governing the spatial fluctuation of each individual component, and (3) the multivariate joint dependence describing the point-wise and cross-spatial relationships among the different variables.

Traditionally, multivariate random fields are modeled using power spectral density (PSD) matrices or cross-correlation functions (Song et al., 2018). While these models are well-suited for multivariate Gaussian fields, they present significant limitations when applied to non-Gaussian variables (Grigoriu, 1995). Most realistic engineering parameters exhibit highly skewed, heavy-tailed, or bounded distributions (Zhang et al., 2026). When modeling these non-Gaussian variables, assuming joint normality is no longer appropriate. To address this, translation field models, such as Nataf-based models, are commonly utilized to map non-Gaussian fields into auxiliary Gaussian fields (Liu and Der Kiureghian, 1986). However, this isoprobability mapping inevitably distorts the original correlation structure. Reconciling the target spatial correlation of the non-Gaussian field with the correlation of the auxiliary Gaussian field is a known modeling challenge. Iterative schemes, such as those relying on Hermite polynomial expansions or iterative PSD adjustments, are frequently employed to correct these correlation distortions (Deodatis and Micaletti, 2001; Li and Xu, 2023). Nevertheless, these corrective procedures can be computationally demanding, and their convergence is not always guaranteed, particularly under highly non-Gaussian marginals or strong spatial gradients.

The challenge becomes even more pronounced when considering the between-variable dependencies in a multivariate setting (Vorechovsky 2008). Standard translation-based workflows typically assume that the underlying dependence can be adequately represented by linear Pearson correlation coefficients or Gaussian copulas. In real-world materials, however, inter-variable relationships are often highly nonlinear, asymmetric, or tail-dependent (Liu et al., 2024). For instance, concrete tensile strength and fracture energy may show asymmetric association under extreme values (Hai and Lyu, 2023). Although copula theory, particularly vine copulas, has gained traction for representing complex high-dimensional dependencies (Joe, 2014), a critical gap remains: existing copula models do not easily integrate with the spatial correlation structures of random fields without introducing modeling inconsistencies or requiring computationally expensive iterative simulation algorithms.

To address these challenges, this study presents a transformation-based framework for modeling and simulating multivariate non-Gaussian random fields. The proposed approach defines the spatial correlation of the non-Gaussian field directly through the linear correlation of its Gaussianized auxiliary variables, yielding what is termed the transformed correlation function (Liu et al., 2026). This representation is inherently compatible with arbitrary marginal distributions and bypasses the modeling incompatibility of traditional approaches. Furthermore, the *bridge function* concept, originally developed for multivariate Gaussian fields (Lyu et al., 2025), is extended to non-Gaussian systems to map spatial correlation and arbitrary copula-based nonlinear dependencies. Building upon this formulation, a non-iterative and efficient simulation algorithm is developed to generate realizations of multivariate non-Gaussian fields (Fu et al., 2026). The capability and accuracy of the proposed framework are demonstrated through practical engineering examples, showcasing its viability for reliable engineering computations.

The remainder of this paper is organized as follows. Section 2 introduces the concept and mathematical construction of the transformed correlation function for univariate non-Gaussian random fields. Section 3 details the multivariate modeling framework, focusing on the extended bridge function and its integration with vine copulas to describe complex, nonlinear between-variable dependencies. In Section 4, the non-iterative and computationally efficient simulation algorithms for multivariate non-Gaussian fields are presented. Section 5 validates the proposed framework using an engineering case study: a bivariate field of concrete tensile strength and fracture energy. Finally, Section 6 summarizes the key findings of this study and outlines potential directions for future research.

2. Concept of Transformed Correlation Function

To properly characterize a univariate homogeneous non-Gaussian random field $Y(\boldsymbol{x})$ with mean μ and standard deviation σ, one must model both its marginal distribution and its spatial variability. The marginal distribution is invariant with respect to the spatial position due to homogeneity and is typically represented by its cumulative distribution function (CDF), $F(y)$, or probability density function (PDF), $p(y)$. Spatial variability is traditionally characterized by the original correlation coefficient function $\rho(\boldsymbol{\xi})$, where $\boldsymbol{\xi}$ denotes the distance vector between two spatial coordinates. However, defining non-Gaussian spatial variability solely via $\rho(\boldsymbol{\xi})$ alongside $F(y)$ is statistically inconsistent at the modeling stage (Liu and Der Kiureghian, 1986). The classical Pearson correlation assumes linear dependence, which is strictly valid only in the Gaussian framework. Imposing non-Gaussian marginals on a field simulated with a target $\rho(\boldsymbol{\xi})$ inevitably distorts the spatial correlation, requiring tedious iterative corrections. To resolve this inconsistency, this section introduces the transformed correlation function as a statistically coherent descriptor of spatial variability.

First, the non-Gaussian field $Y(\boldsymbol{x})$ is mapped to an auxiliary standard Gaussian field $Z(\boldsymbol{x})$ using the isoprobability transformation $Z(\boldsymbol{x}) = \Phi^{-1}\{F[Y(\boldsymbol{x})]\}$, where $\Phi(\cdot)$ denotes the CDF of the standard normal distribution. Because this transformation is strictly monotonic, it preserves the rank-order structure of the random field. Consequently, $Z(\boldsymbol{x})$ is a homogeneous standard Gaussian field with zero mean and unit variance. The spatial correlation of $Z(\boldsymbol{x})$ is characterized by its correlation function $\rho_{\mathrm{G}}(\boldsymbol{\xi})$, which is defined as

$$\rho_{\mathrm{G}}(\boldsymbol{\xi}) = \mathrm{E}[Z(\boldsymbol{x})Z(\boldsymbol{x}+\boldsymbol{\xi})] = \mathrm{E}\left[\Phi^{-1}\{F[Y(\boldsymbol{x})]\}\Phi^{-1}\{F[Y(\boldsymbol{x}+\boldsymbol{\xi})]\}\right]. \tag{1}$$

In this study, $\rho_{\mathrm{G}}(\boldsymbol{\xi})$ is referred to as the *transformed correlation function* of $Y(\boldsymbol{x})$ (Liu et al., 2026). Because $Z(\boldsymbol{x})$ is a mathematically valid standard Gaussian field, its correlation function $\rho_{\mathrm{G}}(\boldsymbol{\xi})$ naturally satisfies all essential mathematical properties of a correlation function, such as symmetry, boundedness, and positive definiteness. Using $\rho_{\mathrm{G}}(\boldsymbol{\xi})$ to model spatial variability ensures modeling compatibility, as any Gaussian field simulated with $\rho_{\mathrm{G}}(\boldsymbol{\xi})$ can be transformed directly into the target non-Gaussian field $Y(\boldsymbol{x})$ without distorting the underlying spatial structure.

There exists a deterministic functional relationship between the original correlation coefficient function $\rho(\boldsymbol{\xi})$ and the transformed correlation function $\rho_{\mathrm{G}}(\boldsymbol{\xi})$. By modeling the joint probability of the auxiliary

Gaussian variables at two positions $\boldsymbol{x}$ and $\boldsymbol{x}+\boldsymbol{\xi}$ through a Gaussian copula, the correlation coefficient $\rho(\boldsymbol{\xi})$ can be derived using the joint PDF of $Y(\boldsymbol{x})$ and $Y(\boldsymbol{x}+\boldsymbol{\xi})$ as

$$\rho(\boldsymbol{\xi})=\frac{1}{\sigma^2}\int_0^1\int_0^1 F^{-1}(u_1)F^{-1}(u_2)c_{\mathrm{G}}[u_1,u_2;\rho_{\mathrm{G}}(\boldsymbol{\xi})]\mathrm{d}u_1\mathrm{d}u_2-\frac{\mu^2}{\sigma^2}, \tag{2}$$

where $F^{-1}(\cdot)$ is the inverse CDF of the non-Gaussian field; $c_{\mathrm{G}}(u_1,u_2;\rho_{\mathrm{G}})$ represents the standard bivariate Gaussian copula density function with parameter ρ_{G}. Eq. (2) establishes a unique, monotonic mapping between $\rho(\boldsymbol{\xi})$ and $\rho_{\mathrm{G}}(\boldsymbol{\xi})$ at each spatial lag $\boldsymbol{\xi}$.

In engineering practice where observational data of the random field are available, the transformed correlation function can be directly estimated in a data-driven manner. To eliminate potential errors arising from parametric marginal distribution assumptions, the marginal CDF $F(y)$ can be substituted with the empirical CDF. The Gaussianized data points $z^{(i)}$ corresponding to observations $y^{(i)}$ at discrete spatial locations $\boldsymbol{x}^{(i)}$, for $i=1,\ldots,n$, are obtained via

$$z^{(i)}=\Phi^{-1}\left[\frac{1}{n}\sum_{j=1}^{n}u(y^{(i)}-y^{(j)})\right], \tag{3}$$

where $u(\cdot)$ is the Heaviside step function. Common correlation kernels can then be directly fitted to the auxiliary data $\{z^{(i)}\}$ to construct $\rho_{\mathrm{G}}(\boldsymbol{\xi})$, enabling consistent modeling and straightforward non-iterative simulation of univariate non-Gaussian fields.

3. Multivariate Modeling via Extended Bridge Function

To describe a bivariate homogeneous non-Gaussian random field, denoted as $\boldsymbol{Y}(\boldsymbol{x})=(Y_1(\boldsymbol{x}),Y_2(\boldsymbol{x}))^{\mathrm{T}}$, three distinct aspects of probabilistic uncertainty must be modeled: (1) the individual marginal distributions of the variables, (2) the spatial correlation of each individual random field, and (3) the pointwise cross-variable dependence between the two fields. Let the marginal distributions of $Y_1(\boldsymbol{x})$ and $Y_2(\boldsymbol{x})$ be represented by their respective CDFs, $F_1(y_1)$ and $F_2(y_2)$. Following the framework established in Section 2, the spatial variability of each field is characterized by their transformed correlation functions, $\rho_{1\mathrm{G}}(\boldsymbol{\xi})$ and $\rho_{2\mathrm{G}}(\boldsymbol{\xi})$, which correspond to the auto-correlation functions of the marginally Gaussianized auxiliary fields $Z_1(\boldsymbol{x})=\Phi^{-1}\{F_1[Y_1(\boldsymbol{x})]\}$ and $Z_2(\boldsymbol{x})=\Phi^{-1}\{F_2[Y_2(\boldsymbol{x})]\}$. Finally, the pointwise probabilistic dependence between $Y_1(\boldsymbol{x})$ and $Y_2(\boldsymbol{x})$ at any spatial location $\boldsymbol{x}$ is described using copula theory (Tao and Chen, 2023). According to Sklar's theorem, the joint CDF of the bivariate variables can be represented as $F(y_1,y_2)=C_{12}[F_1(y_1),F_2(y_2)]$, where $C_{12}(\cdot,\cdot)$ is the copula function.

To simulate these coupled fields while preserving both their unique spatial correlations and their non-Gaussian cross-dependence, a transformation mechanism is required to link the variables. Based on the conditional copula method, the realization of the second field $Y_2(\boldsymbol{x})$ can be mathematically expressed as a function of the first field $Y_1(\boldsymbol{x})$ and an auxiliary random field $Z_{\mathrm{b}}(\boldsymbol{x})$ (Liu et al., 2025; Lyu et al., 2025), namely,

$$Y_2(\boldsymbol{x})=F_2^{-1}\left(C_{2|1}^{-1}\{\Phi[Z_{\mathrm{b}}(\boldsymbol{x})]\,|F_1[Y_1(\boldsymbol{x})]\}\right), \tag{4}$$

where $C_{2|1}^{-1}(\cdot|\cdot)$ represents the inverse of the conditional copula function $C_{2|1}(u_2|u_1)=\partial C_{12}(u_1,u_2)/\partial u_1$; $Z_{\mathrm{b}}(\boldsymbol{x})$ is a standard homogeneous Gaussian field that is statistically independent of $Y_1(\boldsymbol{x})$. The field $Z_{\mathrm{b}}(\boldsymbol{x})$ is defined as the *bridge field*, and its spatial auto-correlation function is denoted as $\rho_{\mathrm{b}}(\boldsymbol{\xi})=\mathrm{E}[Z_{\mathrm{b}}(\boldsymbol{x})Z_{\mathrm{b}}(\boldsymbol{x}+\boldsymbol{\xi})]$. The bridge field acts as an auxiliary spatial carrier; its correlation structure $\rho_{\mathrm{b}}(\boldsymbol{\xi})$ governs how the spatial variability of the first field is mapped and transmitted to the second field.

Since Eq. (4) establishes a deterministic point-wise relationship among $Y_1(\boldsymbol{x})$, $Y_2(\boldsymbol{x})$, and $Z_{\mathrm{b}}(\boldsymbol{x})$, there must exist a corresponding functional relationship among their spatial correlation properties. Specifically, the transformed correlation function of the second field, $\rho_{2\mathrm{G}}(\boldsymbol{\xi})$, can be derived as a function of the first field's transformed correlation $\rho_{1\mathrm{G}}(\boldsymbol{\xi})$ and the bridge field's correlation $\rho_{\mathrm{b}}(\boldsymbol{\xi})$. By definition, the transformed correlation $\rho_{2\mathrm{G}}(\boldsymbol{\xi})$ is the Pearson correlation of the Gaussianized variables $Z_2(\boldsymbol{x})=\Phi^{-1}\{F_2[Y_2(\boldsymbol{x})]\}$ and $Z_2(\boldsymbol{x}+\boldsymbol{\xi})=\Phi^{-1}\{F_2[Y_2(\boldsymbol{x}+\boldsymbol{\xi})]\}$. Substituting the conditional copula mapping into this definition yields

$$\rho_{2\mathrm{G}}(\boldsymbol{\xi})=\mathrm{E}\big[\Phi^{-1}\big(C_{2|1}^{-1}\{\Phi[Z_{\mathrm{b}}(\boldsymbol{x})]\,|F_1[Y_1(\boldsymbol{x})]\}\big)\Phi^{-1}\big(C_{2|1}^{-1}\{\Phi[Z_{\mathrm{b}}(\boldsymbol{x}+\boldsymbol{\xi})]\,|F_1[Y_1(\boldsymbol{x}+\boldsymbol{\xi})]\}\big)\big]. \tag{5}$$

Because $Y_1(\boldsymbol{x})$ and $Z_{\mathrm{b}}(\boldsymbol{x})$ are mutually independent fields, their joint PDF factorizes. By converting the expectation into an integral over the unit hypercube $[0,1]^4$ using probability integral transforms, the relationship can be written as

$$\begin{aligned}\rho_{2\mathrm{G}}(\boldsymbol{\xi})&=r_{\mathrm{b}}[\rho_{\mathrm{b}}(\boldsymbol{\xi})\,|\rho_{1\mathrm{G}}(\boldsymbol{\xi})]\\&=\int_{[0,1]^4}\Phi^{-1}[C_{2|1}^{-1}(u_{\mathrm{b}}|u_1)]\Phi^{-1}[C_{2|1}^{-1}(u_{\mathrm{b}}'|u_1')]c_G[u_{\mathrm{b}},u_{\mathrm{b}}';\rho_{\mathrm{b}}(\boldsymbol{\xi})]c_G[u_1,u_1';\rho_{1\mathrm{G}}(\boldsymbol{\xi})]\mathrm{d}u_1\mathrm{d}u_{\mathrm{b}}\mathrm{d}u_1'\mathrm{d}u_{\mathrm{b}}',\end{aligned} \tag{6}$$

where $c_{\mathrm{G}}(\cdot,\cdot;\rho)$ denotes the bivariate standard Gaussian copula density function with correlation parameter ρ. The functional operator $r_{\mathrm{b}}(\cdot|\cdot)$ is defined as the *bridge function* of the bivariate non-Gaussian field.

A fundamental property of the extended bridge function derived in Eq. (6) is its *marginal distribution invariance*. Although the physical fields $Y_1(\boldsymbol{x})$ and $Y_2(\boldsymbol{x})$ may possess highly non-Gaussian, skewed, or bounded marginal distributions (such as Gamma, Lognormal, or Weibull distributions), the final integral in Eq. (6) depends exclusively on the conditional copula $C_{2|1}$ and the standard normal distribution functions. This invariance occurs because copulas are unaffected by strictly monotonic transformations of the marginal variables. Consequently, the bridge function is a purely copula-dependent operator. This property provides significant practical utility: the spatial mapping relation does not need to be re-derived or modified when the marginal distributions of the engineering parameters change, as long as the underlying copula structure representing their joint dependence remains consistent.

For a given target copula and specified transformed correlations $\rho_{1\mathrm{G}}(\boldsymbol{\xi})$ and $\rho_{2\mathrm{G}}(\boldsymbol{\xi})$, the only unknown parameter in Eq. (6) is the correlation function of the bridge field, $\rho_{\mathrm{b}}(\boldsymbol{\xi})$. Because the bridge function $r_{\mathrm{b}}(\rho_{\mathrm{b}}|\rho_{1\mathrm{G}})$ is strictly monotonic and bounded with respect to $\rho_{\mathrm{b}}\in[-1,1]$, the mapping is invertible. Thus, the required bridge correlation function can be uniquely determined at each spatial lag $\boldsymbol{\xi}$ as

$$\rho_{\mathrm{b}}(\boldsymbol{\xi})=r_{\mathrm{b}}^{-1}[\rho_{2\mathrm{G}}(\boldsymbol{\xi})\,|\rho_{1\mathrm{G}}(\boldsymbol{\xi})]. \tag{7}$$

In practical computations, rather than performing the four-dimensional integration in Eq. (6) at every spatial coordinate, the bridge function can be pre-computed numerically over a discrete grid of ρ_{b} and $\rho_{1\mathrm{G}}$

to construct a high-precision look-up table. A fast, one-dimensional interpolation can then be utilized to solve Eq. (7), ensuring excellent computational efficiency for subsequent stochastic simulations.

4. Non-Iterative Simulation Algorithms

Traditional simulation approaches for non-Gaussian random fields, such as translation field methods or Hermite polynomial models, often rely on iterative adjustments to correct correlation distortions caused by marginal transformations (Zhang et al. 2019, Zheng et al., 2023). These iterative corrections are computationally intensive and can suffer from convergence issues, especially during large-scale Monte Carlo trials. In contrast, by directly employing the transformed correlation functions ($\rho_{1\mathrm{G}}$, $\rho_{2\mathrm{G}}$) and the bridge correlation (ρ_{b}) established in Sections 2 and 3, the proposed framework enables a fully non-iterative simulation workflow. The computationally demanding step of mapping the correlation functions is decoupled from the field generation process, turning the simulation into a direct, feed-forward sequence of standard Gaussian simulation and point-wise transformations.

For a bivariate homogeneous non-Gaussian random field $(Y_1(\boldsymbol{x}), Y_2(\boldsymbol{x}))^{\mathrm{T}}$, the simulation procedure is executed through the following structured steps:

Step 1: Correlation preparation. Given the target transformed correlation functions $\rho_{1\mathrm{G}}(\boldsymbol{\xi})$ and $\rho_{2\mathrm{G}}(\boldsymbol{\xi})$ alongside the selected copula function $C_{12}(u_1, u_2)$, construct the offline bridge function $r_{\mathrm{b}}(\cdot\,|\,\cdot)$ via Eq. (6). Determine the required correlation function $\rho_{\mathrm{b}}(\boldsymbol{\xi})$ of the auxiliary bridge field $Z_{\mathrm{b}}(\boldsymbol{x})$ by numerically inverting Eq. (7) using a pre-computed lookup table and one-dimensional interpolation.

Step 2: Auxiliary Gaussian field generation. Generate two mutually independent, homogeneous, standard Gaussian random fields: $Z_1(\boldsymbol{x})$ with the auto-correlation function $\rho_{1\mathrm{G}}(\boldsymbol{\xi})$, and $Z_{\mathrm{b}}(\boldsymbol{x})$ with the auto-correlation function $\rho_{\mathrm{b}}(\boldsymbol{\xi})$. This step can be performed using any classical, highly efficient Gaussian simulation technique, such as the spectral representation method (Deodatis and Shields, 2024) or the stochastic harmonic function (SHF) method (Fu et al., 2026).

Step 3: Generation of the first field. Obtain the realization of the first non-Gaussian random field $Y_1(\boldsymbol{x})$ by applying the inverse standard normal transformation to $Z_1(\boldsymbol{x})$: $Y_1(\boldsymbol{x}) = F_1^{-1}\{\Phi[Z_1(\boldsymbol{x})]\}$, where $F_1(\cdot)$ is the target marginal CDF of $Y_1(\boldsymbol{x})$.

Step 4: Generation of the second field. Using the generated Gaussianized auxiliary realization $Z_1(\boldsymbol{x})$ (where $\Phi[Z_1(\boldsymbol{x})] = F_1[Y_1(\boldsymbol{x})]$) and the auxiliary bridge field $Z_{\mathrm{b}}(\boldsymbol{x})$, compute the realization of the second non-Gaussian random field $Y_2(\boldsymbol{x})$ point-wise via the inverse conditional copula mapping: $Y_2(\boldsymbol{x}) = F_2^{-1}\left(C_{2|1}^{-1}\{\Phi[Z_{\mathrm{b}}(\boldsymbol{x})]\,|\Phi[Z_1(\boldsymbol{x})]\}\right)$, where $F_2(\cdot)$ is the target marginal CDF of $Y_2(\boldsymbol{x})$.

The primary advantage of this workflow is its numerical robustness and speed. Because the mapping of the bridge correlation $\rho_{\mathrm{b}}(\boldsymbol{\xi})$ is solved prior to sample generation, the runtime of generating each bivariate realization is practically identical to that of generating two independent Gaussian random fields plus a few elementary point-wise operations. This direct nature makes the algorithm highly attractive for reliability analysis and stochastic finite element applications where thousands of realizations are required. Furthermore, this bivariate workflow serves as the foundational building block for higher-dimensional fields, where vine copulas can be decomposed into hierarchical sequences of these bivariate steps.

5. Numerical Case Study

To demonstrate the application of the proposed transformation-based framework in engineering computations, a numerical case study involving the modeling and simulation of two-dimensional (2D) concrete material properties is presented. In the phase-field theory of concrete cracking, tensile strength $f_{\mathrm{t}}(\boldsymbol{x})$ and fracture energy $G_{\mathrm{c}}(\boldsymbol{x})$ are two vital parameters that exhibit significant spatial variability and physical coupling (Hai and Lyu, 2023). In this study, the tensile strength field $Y_1(\boldsymbol{x}) = f_{\mathrm{t}}(\boldsymbol{x})$ is assumed to follow a Gaussian distribution with a mean $\mu_f = 3.5 \times 10^6$ Pa and a standard deviation $\sigma_f = 8.5 \times 10^5$ Pa. The fracture energy field $Y_2(\boldsymbol{x}) = G_{\mathrm{c}}(\boldsymbol{x})$ is modeled as a lognormal distribution with mean $\mu_G = 4.6$ J/m^2 and standard deviation $\sigma_G = 0.40$ J/m^2. Both properties are modeled over an isotropic, homogeneous 2D spatial domain of 0.2 m × 0.2 m. Their spatial auto-correlation functions share the same squared exponential form as

$$\rho(\xi_1, \xi_2) = e^{-\frac{\pi(\xi_1^2 + \xi_2^2)}{l^2}}, \tag{8}$$

where ξ_1 and ξ_2 represent the spatial distances in the horizontal and vertical directions, and the correlation length is specified as $l = 0.05$ m.

The point-wise probabilistic dependency between the tensile strength and fracture energy is modeled using a Student's t-copula (Hai and Lyu, 2023). This copula structure allows the representation of symmetric tail dependencies that are often observed in experimental material testing. The joint copula is specified as

$$C_{fG}(u_1, u_2) = T^{(2)}[T^{-1}(u_1; \nu_{\mathrm{t}}), T^{-1}(u_2; \nu_{\mathrm{t}}); \rho_{\mathrm{t}}, \nu_{\mathrm{t}}], \tag{9}$$

where $T(\cdot; \nu_{\mathrm{t}})$ is the CDF of the standard univariate Student's t-distribution with ν_{t} degrees of freedom; $T^{(2)}(\cdot, \cdot; \rho_{\mathrm{t}}, \nu_{\mathrm{t}})$ is the bivariate Student's t-CDF; $u_1 = F_1(f_{\mathrm{t}})$, and $u_2 = F_2(G_{\mathrm{c}})$. The model parameters are set to $\rho_{\mathrm{t}} = -0.14$ and $\nu_{\mathrm{t}} = 5.0$. Because $f_{\mathrm{t}}(\boldsymbol{x})$ is Gaussian, its transformed correlation function $\rho_{1\mathrm{G}}$ is identical to its original correlation ρ. For the lognormal fracture energy $G_{\mathrm{c}}(\boldsymbol{x})$, the mapping in Eq. (2) is employed to numerically solve for its transformed correlation function $\rho_{2\mathrm{G}}$. Using the bivariate copula parameters, the bridge function $r_{\mathrm{b}}(\rho_{\mathrm{b}} | \rho_{1\mathrm{G}})$ is pre-computed, and the auto-correlation function $\rho_{\mathrm{b}}(\boldsymbol{\xi})$ of the auxiliary bridge field $Z_{\mathrm{b}}(\boldsymbol{x})$ is subsequently determined through the inverse mapping in Eq. (7).

Realizations of the coupled 2D fields are generated on a discretized 100 × 100 spatial grid using the non-iterative simulation algorithm detailed in Section 4. The independent auxiliary Gaussian fields $Z_1(\boldsymbol{x})$ and $Z_{\mathrm{b}}(\boldsymbol{x})$ are simulated using the spectral representation method (Deodatis and Shields, 2024). A representative pair of generated sample fields is visualized in Figure 1. Figure 1 (a) displays the spatial distribution of the simulated tensile strength $f_{\mathrm{t}}(\boldsymbol{x})$, while Figure 1 (b) illustrates the corresponding fracture energy field $G_{\mathrm{c}}(\boldsymbol{x})$. The spatial patterns in both plots visually reflect the isotropic correlation structure and the prescribed correlation length of 0.05 m, demonstrating that the spatial variations are captured smoothly.

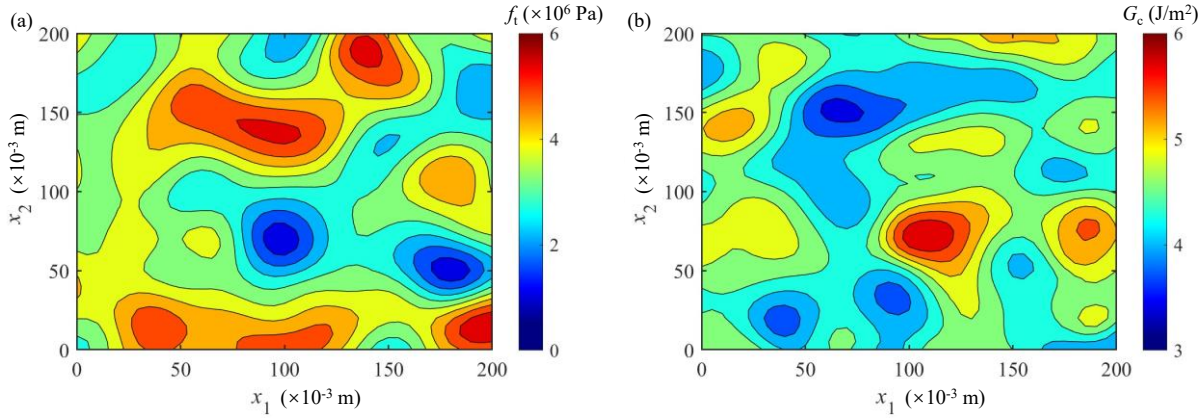


Figure 1. Representative simulated realizations of the 2D random fields over the 0.2 m × 0.2 m domain: (a) Tensile strength; (b) Fracture energy.

To quantitatively verify the accuracy and consistency of the simulation method, a statistical analysis is conducted over a set of 10^4 independent realizations. Figure 2 summarizes the validation of the spatial auto-correlations and the point-wise joint PDF. In Figure 2 (a), the auto-correlation functions computed from the simulated samples are compared against their respective analytical targets for both $f_t(\boldsymbol{x})$ and $G_c(\boldsymbol{x})$. The simulated auto-correlations match the target curves closely, confirming that the transformation-based correlation mapping successfully preserves the spatial structure without requiring any iterative correction steps. Furthermore, to evaluate the preservation of the non-Gaussian joint dependency, Figure 2 (b) overlays the scatter plot of the simulated sample points (sampled at a specific spatial location across the ensemble) onto the theoretical joint PDF contours of the Student's t-copula. The simulated points conform closely to the shape of the joint PDF contours, showcasing the capability of the extended bridge function framework to simultaneously reproduce the spatial correlation of individual fields and their non-Gaussian, non-linear mutual dependence.

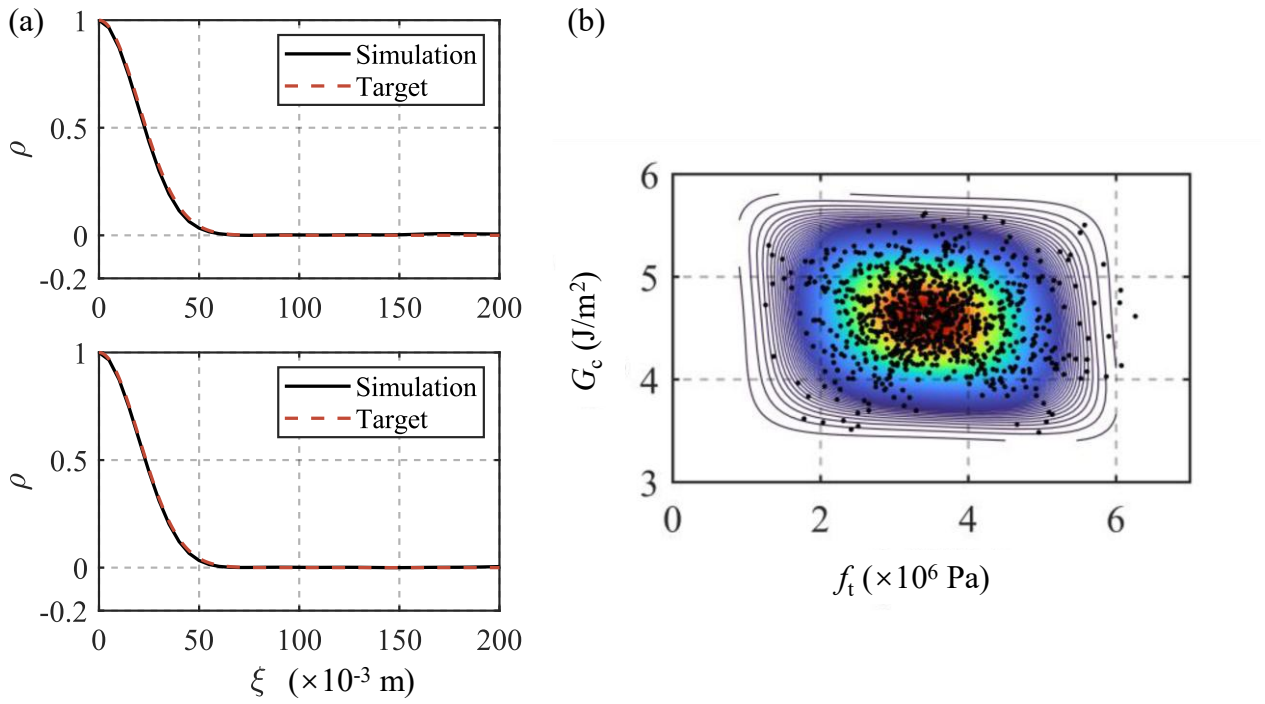


Figure 2. Statistical validation of the simulated random fields: (a) Comparison between the target and simulated auto-correlation functions; (b) Scatter plot of simulated realizations overlaid on the theoretical joint PDF contours of tensile strength and fracture energy.

6. Concluding Remarks

In this study, a transformation-based framework has been developed for the probabilistic modeling and simulation of bivariate non-Gaussian random fields. By introducing the transformed correlation function, the proposed approach represents spatial variability directly through the linear correlation of standard Gaussianized auxiliary variables, which eliminates the modeling incompatibility found in classical translation field methods. Additionally, the bridge function concept is extended to describe the mapping between individual spatial correlations and pointwise non-Gaussian dependencies. This extended bridge function is invariant to marginal transformations, remaining solely dependent on the underlying copula structure.

The corresponding simulation algorithm is direct and non-iterative, offering a computationally attractive option for uncertainty quantification where large-scale realizations are needed. Numerical validation using a coupled concrete property case study demonstrates that the generated fields conform closely to both the target marginal distributions, the individual auto-correlation functions, and the prescribed joint probability density.

Future research may focus on extending this framework to non-stationary random fields, exploring non-Gaussian copula dependencies across different spatial lags, and applying the proposed simulation method to large-scale structural reliability and stochastic finite element analyses in safety-critical engineering systems.

Acknowledgements

Financial supports from German Research Foundation (DFG) (Grant No. 562994444) and the National Natural Science Foundation of China (Grant No. 12302037) are highly appreciated

References

Deodatis, G. and R. C. Micaletti. Simulation of highly skewed non-Gaussian stochastic processes. *Journal of Engineering Mechanics*, 127: 1284-1295, 2001.

Deodatis, G. and M. D. Shields. The spectral representation method: A framework for simulation of stochastic processes, fields, and waves. *Reliability Engineering & System Safety*, 254: 110522, 2024.

Fu, J. H., Y. Luo, X. L. Wei, M. Z. Lyu, and M. Beer. Probability-compatible modeling and efficient stochastic harmonic function representation of three-dimensional multivariate non-Gaussian random fields with nonlinear dependences. *International Journal of Non-Linear Mechanics*, 189: 105402, 2026.

Grigoriu. M. *Applied Non-Gaussian Processes: Examples, Theory, Simulation, Linear Random Vibration, and MatLab Solutions*. PTR Prentice Hall, 1995.

Hai, L. and M. Z. Lyu. Modeling tensile failure of concrete considering multivariate correlated random fields of material parameters. *Probabilistic Engineering Mechanics*, 74: 103529, 2023.

Joe, H. *Dependence Modeling with Copulas*. CRC Press, 2014.

Li, J. and M. Z. Lyu. *Fundamental of Structural Reliability Analysis*. Springer Nature, 2026 (in Publication).

Li, Y. and J. Xu. Novel Hermite polynomial model based on probability weighted moments for simulating non-Gaussian stochastic processes. *Journal of Engineering Mechanics*, 150 (4): 04024006, 2023.

Liu, D. Y., C. Wang, and M. Z. Lyu. Elucidating the complexity of stress interactions in polymer-coated granular materials via copula-based probabilistic dependence configurations. *Powder Technology*, 435: 119405, 2024.

Liu, P. L. and A. Der Kiureghian. Multivariate distribution models with prescribed marginals and covariances. *Probabilistic Engineering Mechanics*, 1 (2): 105-112, 1986.

Liu, Y. Y., M. Z. Lyu, J. B. Chen, and J. L. Le. A novel approach for modeling and simulation of multivariate non-Gaussian random fields with normalized correlation functions and vine copula structures. In R. Ghanem, E. A. Johnson, S. F. Masri, and A. Olivier, editors, *Proceedings of the 14th International Conference on Structural Safety & Reliability*, Los Angeles, USA, 2025.

Liu, Y. Y., M. Z. Lyu, J. B. Chen, and S. H. Zhang. A new model for the multivariate non-Gaussian random fields involving inter-variable nonlinear correlation and the simulation method. *ASCE-ASME Journal of Risk & Uncertainty in Engineering Systems, Part A: Civil Engineering* (accepted), 2026.

Lyu, M. Z., Y. Y. Liu, and J. B. Chen. A novel model and simulation method for multivariate Gaussian fields involving nonlinear probabilistic dependencies and different variable-wise spatial variabilities. *Reliability Engineering & System Safety*, 260: 110963, 2025.

Song, Y. P., J. B. Chen, Y. B. Peng, P. D. Spanos, and J. Li. Simulation of nonhomogeneous fluctuating wind speed field in two-spatial dimensions via an evolutionary wavenumber-frequency joint power spectrum. *Journal of Wind Engineering & Industrial Aerodynamics*, 179: 250-259, 2018.

Tao, J. J., J. B. Chen, and X. D. Ren. Copula-based quantification of probabilistic dependence configurations of material parameters in damage constitutive modeling of concrete. *Journal of Structural Engineering*, 146 (9): 04020194, 2020.

Tao, J. J. and J. B. Chen. Experimental study on the spatial variability of concrete by the core test and rebound hammer test. *ASCE-ASME Journal of Risk & Uncertainty in Engineering Systems, Part A: Civil Engineering*, 9 (4): 04023029, 2023.

Vanmarcke, E. *Random Fields: Analysis and Synthesis*. 2nd Edn. MIT Press, 2010.

Vorechovsky, M. Simulation of simply cross correlated random fields by series expansion methods. *Structural Safety*, 30 (4): 337-363, 2008.

Zhang, X. Y., Y. G. Zhao, and Z. H. Lu. Unified Hermite polynomial model and its application in estimating non-Gaussian processes. *Journal of Engineering Mechanics*, 145 (3): 04019001, 2019.
Zhang, X. Y., M. A. Valdebenito, M. G. R. Faes, and M. D. Shields. Modeling nonstationary non-Gaussian random fields: A D-vine copula approach. *Journal of Engineering Mechanics*, 152 (8): 04026041, 2026.
Zheng, Z. B., M. Beer, and U. Nackenhorst U. An iterative multi-fidelity scheme for simulating multi-dimensional non-Gaussian random fields. *Mechanical Systems & Signal Processing*, 200: 110643, 2023.

Fuzzy Fields based on the Parallelepiped Dependency Model

F. Niklas Schietzold[1], Felix Harazin[1], Yoshi Diepelt[2,3], Wolfgang Graf[1], Michael Kaliske[1]
[1]*Institute for Structural Analysis,*
[2]*Institute of Mechanics and Shell Structures,* [3]*Institute of Numerical Mathematics*
Technische Universität Dresden, 01062 Dresden, Germany
{*niklas.schietzold, felix.harazin, yoshi.diepelt, wolfgang.graf, michael.kaliske*}*@tu-dresden.de*

Abstract. In order to realistically characterize data uncertainty in engineering – and consequently to reliably assess safety – it is required to thoroughly investigate spatial and temporal dependencies of uncertainty, e.g. in material characteristics, geometrical or environmental parameters. Recognizing the fact that probability-based approaches are inappropriate for databases with a severe lack of knowledge, purely epistemic uncertainty concepts for modeling dependent quantities are required.

Several approaches to convex dependency modeling of interval quantities, as well as proposals for spatially dependent interval/fuzzy uncertainty modeling, exist. This contribution continues these researches by investigation of an existing fuzzy field concept. Based on discussion of limitations in the existing concept, novel developments in modeling and uncertainty quantification of fuzzy fields are presented. The developments are based on extending an existing interval dependency method, where multidimensional parallelepipeds characterize the underlying interval dependency.

Therefore, a dependency model is formulated by extension from interval to fuzzy fields. The proposed (auto-)interaction concept is in analogy to the (auto-)correlation concept of random fields. It is demonstrated how an eigenvalue decomposition of the auto-interaction structure with reduced orthogonal basis variables can be implemented to reduce the high-dimensional α-level optimization problem in uncertainty quantification. Finally, the novel methods are validated by uncertainty quantification examples in benchmark functions to demonstrate the safety assessment capabilities.

Keywords: polymorphic uncertainty quantification, possibility, fuzzy fields, structural analysis

1. Introduction

Both, purely aleatoric and polymorphic uncertainty are widely applied for spatial variability in engineering safety assessment. For instance, fields are defined by probabiltiy-boxes in (Do et al., 2016). Interval- and/or fuzzy-parametrized random fields constitute of a broad range of polymorphic uncertain field methods, such as in (Schietzold et al., 2019) and their research for challenging structural engineering problems is recently ongoing, see (Fina et al., 2023; Schietzold et al., 2024).

Material characteristics, for instance of timber as an inhomogeneous fiber composite, particularly require consideration of spatial uncertainty for engineering systems. Non-destructive spatial tests are increasingly affordable. Ultimately, local variations significantly determine the mechanical behavior of timber, and localization effects can cause component failure. However, data is always limited, only representing fractions of reality.

© 2026 by the author(s). This work is licensed under the Creative Commons Attribution 4.0 International License (CC BY 4.0), which permits unrestricted use, distribution, and reproduction in any medium, provided the original author and source are credited.

Additionally, besides natural variability, incompleteness remains. Therefore, concepts of possibility-based spatial uncertainty models are required, such as the interval field proposed by (Faes and Moens, 2017), which recognize the fact that probability-based approaches are inappropriate for databases with a severe lack of knowledge.

As this contribution is dedicated to uncertainty under severe lack of knowledge, purely epistemic models are in focus. Therefore, intervals and fuzzy quantities are defined in Section 2.1 as descriptions of uncertainty. As detailed in Section 2.1, a fuzzy analysis can be interpreted as multiple nested interval analyses in α-level optimizations. Hence, methods of interval uncertainty can be generalized to fuzzy uncertainty. Specifically, generalization to fuzzy fields is achieved by nesting of interval fields and, vice versa, interval fields can be defined as special case of fuzzy field approaches.

Orthogonal series expansion concepts are constitutive for many definitions of (polymorphic uncertain) random fields, see e.g. (Schietzold et al., 2019). This allows choosing a reduced number of orthogonal bases, which results in reduced numerical effort, see (Sudret and Der Kiureghian, 2000). For both, interval and fuzzy fields, documented methods are also based on orthogonal series expansion. According to (Luo et al., 2019), multi-dimensional ellipsoid convex models can be used to define such interval fields. In (Faes and Moens, 2017; Faes and Moens, 2019), interval fields are defined by an inverse distance weighting scheme and constituted by so-called control points in the observation domain. Contrarily, the concept of fuzzy fields in (Götz et al., 2016; Götz, 2017) is constituted by a distance-governed auto-dependency function, greatly inspired by the auto-correlation functions of (polymorphic uncertain) random field approaches. This method is briefly explained in Section 2.2, along with discussion of limitations and suggestions for improvement of the method. All these methods are based on different definitions of the underlying (auto-)dependencies within the fuzzy and interval fields. *Correlation* is only defined for random variables. In contrast, approaches defining dependencies of interval/fuzzy quantities are denoted as *interaction* methods.

According to (Jiang et al., 2015b), multi-dimensional ellipsoid convex models either heavily overestimate the intervals (ellipsoid encloses the hyperrectangle) or underestimate the corners of the interval-hypercube (hyperrectangle enclosing the ellipsoid). As an alternative, multi-dimensional parallelepiped (MP) convex models are suggested. This contribution's focus is on fuzzy field concepts constituted by auto-dependency functions and on interval fields as a special case of them. Consequently, a novel fuzzy field method is proposed in Section 2.4, based on a modification of the MP interval dependency model of (Jiang et al., 2015a), described in Section 2.3.

2. Theoretical Basis

2.1. Basic Uncertainty Models and Uncertainty Quantification

Uncertainty Characteristics

According to (Beer et al., 2013; Pannier et al., 2013), uncertainty can generally be distinguished in two characteristics: aleatoric and epistemic. Aleatoric uncertainty is due to natural variability and, therefore, not reducible. Contrarily, epistemic uncertainty describes all uncertainties that are reducible in theory, such as incompleteness, lack-of-knowledge and impreciseness.

This contribution follows the concept of (Graf et al., 2015), according to which the aleatoric uncertainty is mathematically modeled by probability-based methods, by stochastic quantities.

Furthermore, epistemic uncertainty is modeled by possibility theory with intervals or fuzzy quantities, as defined under the subsequent headlines. Moreover, in realistic engineering applications, a manifold of databases and corresponding uncertainty characteristics exist and, therefore, methods incorporating both, epistemic and aleatoric uncertainty are required. This combination of both characteristics is introduced as polymorphic uncertainty in (Graf et al., 2015) and much research in broad engineering fields is dedicated to it since then, for instance in (Faes and Moens, 2019; Schietzold et al., 2024; Harazin et al., 2026). However, the focus of this contribution is on problems under severe lack of knowledge in data and, hence, purely epistemic uncertainty models are investigated.

Intervals
An interval quantity $\mathbb{X}^{\mathcal{I}}$ is constituted by the mapping $\mu_{\mathbb{X}^{\mathcal{I}}} : \mathbb{R} \to \{0,\, 1\},\ x \mapsto \mu_{\mathbb{X}^{\mathcal{I}}}(x)$, with the interval membership function $\mu_{\mathbb{X}^{\mathcal{I}}}(x) = \{1 \text{ if } x \in \mathbb{X}^{\mathcal{I}}; 0 \text{ if } x \notin \mathbb{X}^{\mathcal{I}}\}$. Intervals, as subsets of real numbers, can be denoted by their left and right bounds as $[\mathbb{X}^{\mathcal{I}}_{\mathrm{L}},\, \mathbb{X}^{\mathcal{I}}_{\mathrm{U}}] = \{x \in \mathbb{R} \mid \mathbb{X}^{\mathcal{I}}_{\mathrm{L}} \leq x \leq \mathbb{X}^{\mathcal{I}}_{\mathrm{U}}\}$. Mirrored brackets, e.g. $]\mathbb{X}^{\mathcal{I}}_{\mathrm{L}},\, \mathbb{X}^{\mathcal{I}}_{\mathrm{U}}]$ or $]\mathbb{X}^{\mathcal{I}}_{\mathrm{L}},\, \mathbb{X}^{\mathcal{I}}_{\mathrm{U}}[$, indicate half-open or open intervals, respectively.

Besides the definition of intervals through bounds, in (Jiang et al., 2015b) the representation by centroid $\mathbb{X}^{\mathcal{I}}_{\mathrm{C}} = \mathrm{C}\left(\mathbb{X}^{\mathcal{I}}\right) = (\mathbb{X}^{\mathcal{I}}_{\mathrm{L}} + \mathbb{X}^{\mathcal{I}}_{\mathrm{U}})/2$ and radius $\mathbb{X}^{\mathcal{I}}_{\mathrm{R}} = \mathrm{R}\left(\mathbb{X}^{\mathcal{I}}\right) = (\mathbb{X}^{\mathcal{I}}_{\mathrm{U}} - \mathbb{X}^{\mathcal{I}}_{\mathrm{L}})/2$ is defined.

Interval analyses, as uncertainty quantification of system responses with interval input parameters, can be solved by interval arithmetic, but, according to (Hanss, 2005), are prone to overestimation due to the problem of interval dependency (wrapping effect). Numerical estimation of interval output can be achieved by solving the min. and max. optimization problems of computing the lower and upper bounds of the output interval(s) with respect to the interval input space.

The interval input space is defined by the Cartesian product $\mathcal{C}^{\mathcal{I}} = \mathbb{X}^{\mathcal{I}}_1 \times \cdots \times \mathbb{X}^{\mathcal{I}}_{n_{\mathcal{I}}}$ of all $n_{\mathcal{I}}$ quantities. It is interpreted as $n_{\mathcal{I}}$-dimensional hyperrectangle spanned by the interval quantities.

Fuzzy Quantities
A fuzzy quantity out of the fuzzy power set $\mathcal{F}(\mathbb{R})$ of all such fuzzy variables is denoted by $\mathbb{X}^{\mathcal{F}} \in \mathcal{F}(\mathbb{R})$ and constituted by the mapping $\mu_{\mathbb{X}^{\mathcal{F}}} : \mathbb{R} \to [0,\, 1],\ x \mapsto \mu_{\mathbb{X}^{\mathcal{F}}}(x)$, where $\mu_{\mathbb{X}^{\mathcal{F}}}$ is the fuzzy membership function. Following the definitions of (Zadeh, 1965), arbitrary functions can be formulated for the membership, but only convex fuzzy quantities are investigated in this contribution.

The extension principle is introduced in (Zadeh, 1965) as a fuzzy analysis, which is the quantification of the uncertainty of system responses due to fuzzy input parameters. In analogy to interval arithmetic, fuzzy arithmetic can be applied, see (Hanss, 2005), but the wrapping effect is also faced.

Fuzzy quantities are discretized by α-level cuts, each for a specific value $\alpha^* \in [0, 1]$, by

$$\mathbb{X}^{\mathcal{F}}_{\alpha=\alpha^*} = \{x \mid \mu_{\mathbb{X}^{\mathcal{F}}}(x) \geq \alpha^*\}, \tag{1}$$

see (Möller et al., 2000). This allows to reformulate the extension principle as a bunch of n_α interval analyses. Hence, fuzzy quantities can be interpreted as nested set of interval quantities and fuzzy system responses are estimated by the according interval analyses, the so called α-level-optimizations.

The Cartesian product $\mathcal{C}^{\mathcal{F}} = \mathbb{X}^{\mathcal{F}}_1 \times \cdots \times \mathbb{X}^{\mathcal{F}}_{n_{\mathcal{F}}}$ defines the joint of all $n_{\mathcal{F}}$ fuzzy quantities $\mathbb{X}^{\mathcal{F}}_i,\ i \in \{1, \ldots, n_{\mathcal{F}}\}$. Therefore, the joint membership function of the Cartesian product is defined

$$\mu_{\mathcal{C}^{\mathcal{F}}} : \qquad \mathbb{R}^{n_{\mathcal{F}}} \to [0,\, 1], \qquad (x_1, \ldots,\, x_{n_{\mathcal{F}}}) \mapsto \min\left(\mu_{\mathbb{X}^{\mathcal{F}}_1}(x_1), \ldots,\, \mu_{\mathbb{X}^{\mathcal{F}}_{n_{\mathcal{F}}}}(x_{n_{\mathcal{F}}})\right). \tag{2}$$

Investigations for efficient numerical fuzzy analysis methods with different approaches are documented, for instance α-level discretization-based or α-level free. Additionally, mixed approaches are recently proposed, such as the intermediately discretized extended α-level optimization in (Richter et al., 2025), enabling to combine the advantages of α-level-based and α-level-free approaches.

Convex fuzzy quantities with support $\mathbb{X}^{\mathcal{F}}_{\alpha=0} = [x_\mathrm{l},\, x_\mathrm{r}]$, deterministic core $\mathbb{X}^{\mathcal{F}}_{\alpha=1} = x_\mathrm{m}$, where $x_\mathrm{l} \leq x_\mathrm{m} \leq x_\mathrm{r}$, and with linear membership functions between $\mu_{\mathbb{X}^{\mathcal{F}}} = 0$ and $\mu_{\mathbb{X}^{\mathcal{F}}} = 1$ are called fuzzy triangular and their simplified notation is $\mathbb{X}^{\mathcal{F}} = \langle x_\mathrm{l},\, x_\mathrm{m},\, x_\mathrm{r} \rangle$, see (Möller and Beer, 2004).

2.2. Investigation and Discussion of an Existing Fuzzy Field Concept

Definition of the Method

In (Götz et al., 2016), a method for simulation of fuzzy fields with spatial auto-interaction between discrete observation points in three-dimensional domains is postulated, which is elaborated in (Götz, 2017). This method is further demonstrated in an n-dimensional approach, and advantages as well as limitations are investigated. Hence, a fuzzy field $\mathbb{X}^{\mathcal{FF}}$ is defined as the mapping $\mathbb{X}^{\mathcal{FF}} : \boldsymbol{\Theta} \twoheadrightarrow \mathcal{F}(\mathbb{R}), \quad \boldsymbol{\theta} \mapsto \mathbb{X}^{\mathcal{FF}}(\boldsymbol{\theta})$, which sets a fuzzy quantity of the powerset $\mathcal{F}(\mathbb{R})$ for each observation point θ. For a homogeneous fuzzy field, the same quantity $\mathbb{T}^{\mathcal{F}}_{\mathrm{target}}$ with field-constituting marginal membership $\mu_{\mathbb{T}^{\mathcal{F}}_{\mathrm{target}}}$ is defined at each θ in the observation domain $\boldsymbol{\Theta} \subset \mathbb{R}^{n_\Theta}$.

Within each realization of the discretized fuzzy field (each sample of the fuzzy analysis), auto-interactions should be realized between the n_θ observation points $\boldsymbol{\theta}_i,\ i \in 1, \ldots, n_\theta$. As definition for these auto-interactions, an auto-interaction matrix $\mathbf{I}$ is postulated with the entries

$$\mathrm{I}_{ij} = \mathrm{i}_{\mathrm{kernel}}\left(\mathrm{d}_{\mathrm{metric}}\left(\boldsymbol{\theta}_i, \boldsymbol{\theta}_j\right)\right) \tag{3}$$

corresponding to all pairs $(\boldsymbol{\theta}_i, \boldsymbol{\theta}_j) \in \boldsymbol{\Theta} \times \boldsymbol{\Theta}$. It is constituted by an auto-interaction kernel function, which maps non-negative real values to interactions $\mathrm{i}_{\mathrm{kernel}} : \mathbb{R}^+ \twoheadrightarrow [-1,\, 1]$, based on the distance measure $\mathrm{d}_{\mathrm{metric}} : \boldsymbol{\Theta} \times \boldsymbol{\Theta} \twoheadrightarrow \mathbb{R}^+$. The kernel function is requested to fulfill $\mathrm{i}_{\mathrm{kernel}}\left(\mathrm{d}_{\mathrm{metric}}\left(\boldsymbol{\theta}_i,\, \boldsymbol{\theta}_i\right)\right) = \mathrm{i}_{\mathrm{kernel}}(0) = 1$ and, for physically reasonable uncertain fields, decays until $\mathrm{i}_{\mathrm{kernel}}(\infty) = 0$. The interaction matrix I is symmetric, since the distance measure is defined to be a metric.

An orthogonal series expansion is suggested in (Götz et al., 2016) to simulate auto-interaction, based on the decomposition of $\mathbf{I}$ into eigenvalues λ_i and eigenvectors $\boldsymbol{\phi}_i :\ i \in 1, \ldots, n_\theta$. Hence, the fuzzy field, represented by a vector $\mathbf{X}^{\mathcal{FF}}$ of fuzzy quantities at the discrete observation points, is

$$\mathbf{X}^{\mathcal{FF}} = \sum_{i=1}^{n_\lambda} \mathbb{T}^{\mathcal{F}}_{\mathrm{scale},i} \cdot \sqrt{\lambda_i} \cdot \boldsymbol{\phi}_i. \tag{4}$$

Therefore, normalized fuzzy triangular coefficients $\mathbb{T}^{\mathcal{F}}_{\mathrm{scale},i} = \langle -1,\, 0,\, 1 \rangle$ are introduced for excitation of a (reduced) number of eigenmodes $n_\lambda \leq n_\theta$. The truncation of eigenmodes can reduce numerical effort, especially for $\lambda_i \approx 0$, where the low influence of the respective $\mathbb{T}^{\mathcal{F}}_{\mathrm{scale},i}$ is negligible in the fuzzy analysis. Truncation leads to reduced dimensionality of the fuzzy input space, see Eq. (2).

The further definitions are based on the α-level discretization concept, see Eq. (1). The vector of fuzzy quantities $\mathbf{X}^{\mathcal{FF}}$ from Eq. (4) is required to be transformed into the actually desired bounds of the investigated marginal membership function, constituted by the "target" fuzzy quantity $\mathbb{T}^{\mathcal{F}}_{\mathrm{target}}$.

In (Götz et al., 2016), an additional "scatter" interval quantity $\mathbb{T}^{\mathcal{I}}_{\text{scatter}} = [0,\, 1]$ is postulated, and the transformation is defined per α-level as scaling to the interval bounds by

$$\mathbf{X}^{\mathcal{FF}}_{\text{scaled},\alpha} = \mathbb{T}^{\mathcal{F}}_{\text{target},\alpha} + \mathbb{T}^{\mathcal{I}}_{\text{scatter}} \cdot \left(\mathbf{U}^{\mathcal{FF}}_{\alpha} \cdot (b - a) + a \right), \tag{5}$$

$$\text{with} \qquad a = \mathbb{T}^{\mathcal{F}}_{\text{target},\alpha,\text{L}} - \mathbb{T}^{\mathcal{F}}_{\text{target},\alpha}, \quad b = \mathbb{T}^{\mathcal{F}}_{\text{target},\alpha,\text{U}} - \mathbb{T}^{\mathcal{F}}_{\text{target},\alpha}, \tag{6}$$

$$\mathbf{U}^{\mathcal{FF}}_{\alpha} = \frac{\mathbf{X}^{\mathcal{FF}}_{\alpha} - \text{“min”}\left(\mathbf{X}^{\mathcal{FF}}_{\alpha}\right)}{\text{“max”}(\mathbf{X}^{\mathcal{FF}}_{\alpha}) - \text{“min”}(\mathbf{X}^{\mathcal{FF}}_{\alpha})}. \tag{7}$$

Therein, $\mathbb{T}^{\mathcal{F}}_{\text{target},\alpha}$ is the α-level cut of the field-constituting $\mathbb{T}^{\mathcal{F}}_{\text{target}}$. The equation components a and b represent the factors to scale to the marginal memberships lower and upper α-level bounds $\mathbb{T}^{\mathcal{F}}_{\text{target},\alpha,\text{L}}$ and $\mathbb{T}^{\mathcal{F}}_{\text{target},\alpha,\text{U}}$. Although, the definition of Eq. (6) is noted with swapped subtrahend and minuend in (Götz et al., 2016; Götz, 2017), the here presented notation is corrected to achieve the desired scaling, and it is verified by the existing FORTRAN code of (Götz, 2017).

With the separation of the component in Eq. (7), a slightly different notation is shown. By this, it is noted that $\mathbf{X}^{\mathcal{FF}}_{\alpha}$ is a vector of α-level cuts of the (unscaled) field representing vector of fuzzy quantities $\mathbf{X}^{\mathcal{FF}}$, hence, a vector of intervals. Accordingly, the min/max operators in Eq. (7) are quoted, since min/max are ambiguous as operators for a vector of intervals. However, the component $\mathbf{U}^{\mathcal{FF}}_{\alpha}$ in Eq. (5) is required to be the fuzzy field expansion of Eq. (4), but in a normalized form with bounds $[-1,\, 1]$ on each α-level. Based on these unit-hyperrectangles, the scaling to the bounds of the desired marginal membership is performed in Eq. (5). Therefore, the min/max operators in Eq. (7) are to be evaluated per entry such that in the vector, each entry is

$$\mathbb{U}^{\mathcal{FF}}_{\alpha,i} = \frac{\mathbb{X}^{\mathcal{FF}}_{\alpha,i} - \min\left(\mathbb{X}^{\mathcal{FF}}_{\alpha,i}\right)}{\max(\mathbb{X}^{\mathcal{FF}}_{\alpha,i}) - \min(\mathbb{X}^{\mathcal{FF}}_{\alpha,i})} = \frac{\mathbb{X}^{\mathcal{FF}}_{\alpha,i} - \mathbb{X}^{\mathcal{FF}}_{\alpha,\text{L},i}}{\mathbb{X}^{\mathcal{FF}}_{\alpha,\text{U},i} - \mathbb{X}^{\mathcal{FF}}_{\alpha,\text{L},i}}, \tag{8}$$

since min and max of an α-level in fact are its lower and upper bound, respectively.

An additional interval quantity $\mathbb{T}^{\mathcal{I}}_{\text{scatter}} = [0,\, 1]$ is introduced in Eq. (5) for scaling to the bounds of the marginal membership, so that corner points of the respective α-levels are reachable. All over all, the base quantities spanning the uncertain input space are $\mathbb{T}^{\mathcal{F}}_{\text{scale},i}$ with $i \in \{1, \ldots, n_\lambda\}$, where $n_\lambda \leq n_\theta$, $\mathbb{T}^{\mathcal{F}}_{\text{target},\alpha}$ and $\mathbb{T}^{\mathcal{I}}_{\text{scatter}}$, which results in an $(n_\lambda{+}2)$-dimensional hyperrectangle as interval input space of the optimization on each α-level for fuzzy analyses.

Discussion of the Method's Parameters

Since the method of (Götz et al., 2016) is formulated based on the α-level representation of fuzzy fields, its auto-interaction can also be interpreted as interval interactions in discretized sense. Hence, the further discussion is also based on interaction characteristics of intervals in the hyperrectangles that result at the α-levels.

As stated above, a fuzzy analysis with the proposed fuzzy fields of (Götz et al., 2016) leads to $n_{\text{input}} = n_\lambda{+}2$ dimensions of the fuzzy input space, dependent on the $n_\lambda < n_\theta$ eigenmodes taken into account, see Eq. (4). Although, such simulated fuzzy fields are discretized at n_θ observation points, more uncertain base variables than observation points are required by the method.

The formulation with these additional base variables leads to increased numerical effort (high dimensional optimization space of α-level optimization), but also to the disadvantage that the sampling in the mapping on each α-level from base variables to the fuzzy field realization

$$(\mathbb{T}^{\mathcal{F}}_{\text{scale},1} \times \cdots \times \mathbb{T}^{\mathcal{F}}_{\text{scale},n_\theta} \times \mathbb{T}^{\mathcal{F}}_{\text{target},\alpha} \times \mathbb{T}^{\mathcal{I}}_{\text{scatter}}) \twoheadrightarrow \mathbf{X}^{\mathcal{FF}}_{\text{scaled},\alpha} \tag{9}$$

is not bijective. The missing one-to-one correspondence means that the resulting objective function for optimization algorithms has duplicates for several combinations of design variables, which might be challenging for the global α-level optimization, according to (Blank and Deb, 2020).

Generally, the definitions of scale and scatter base variables $\mathbb{T}^{\mathcal{F}}_{\text{scale},i} = \langle -1,\, 0,\, 1\rangle$ and $\mathbb{T}^{\mathcal{I}}_{\text{scatter}} = [0,\, 1]$ in the formulation of Eq. (5) are questionable. Obviously, the $\mathbb{T}^{\mathcal{F}}_{\text{scale},i}$ as fuzzy triangular quantities lead to different expansions $\mathbf{X}^{\mathcal{FF}}_{\alpha}$ in Eq. (4) and further on to different unit-hyperrectangles $\mathbf{U}^{\mathcal{FF}}_{\alpha}$ for each α-level, where Eq. (8) becomes

$$\mathbb{U}^{\mathcal{FF}}_{\alpha,i} = \begin{cases} [0,1] & \text{as long as } \mathbb{X}^{\mathcal{FF}}_{\alpha,\mathrm{U},i} \neq \mathbb{X}^{\mathcal{FF}}_{\alpha,\mathrm{L},i}, \text{ hence, for } \alpha < 1, \text{ where } \mathrm{R}\left(\mathbb{T}^{\mathcal{F}}_{\text{scale},\alpha,i}\right) > 0 \text{ or} \\ \frac{0}{0} \Rightarrow 0 & \text{if all } \mathbb{X}^{\mathcal{FF}}_{\alpha=1,i} = [0,\, 0] = 0, \text{ hence for } \alpha = 1, \text{ where all } \mathbb{T}^{\mathcal{F}}_{\text{scale},\alpha=1,i} = 0, \\ & \text{which is the deterministic core of the fuzzy triangulars.} \end{cases} \tag{10}$$

Specifically, for $\alpha = 1$, Eq. (5) evaluates to

$$\begin{aligned} \mathbf{X}^{\mathcal{FF}}_{\text{scaled},\alpha=1} &= \mathbb{T}^{\mathcal{F}}_{\text{target},\alpha=1} + \mathbb{T}^{\mathcal{I}}_{\text{scatter}} \cdot \left(\mathbf{U}^{\mathcal{FF}}_{\alpha=1} \cdot (b-a) + a \right) \\ &= \mathbb{T}^{\mathcal{F}}_{\text{target},\alpha=1} + \mathbb{T}^{\mathcal{I}}_{\text{scatter}} \cdot \left(\begin{bmatrix} 0 & \cdots & 0 \end{bmatrix}^{\intercal} + \mathbb{T}^{\mathcal{F}}_{\text{target},\alpha=1,\mathrm{L}} - \mathbb{T}^{\mathcal{F}}_{\text{target},\alpha=1} \right), \end{aligned} \tag{11}$$

which means that each realization of the fuzzy field has identical entries for all observation points, hence, realizations are constant in the observation domain. In other words, all realizations on $\alpha = 1$ are unexpectedly fully interacted, provided that the determination of $\frac{0}{0} \Rightarrow 0$ of Eq. (10) numerically is well handled in the implementation of the method at all. However, for all levels $\alpha < 1$, the interaction is defined as intended and the radii $\mathrm{R}\left(\mathbb{T}^{\mathcal{F}}_{\text{scale},\alpha<1,i}\right)$ are irrelevant, since the fuzzy triangular quantity is symmetrically defined with all centroids $\mathrm{C}\left(\mathbb{T}^{\mathcal{F}}_{\text{scale},\alpha,i}\right) = 0$ and the resulting α-levels of the field expansion are all scaled to the unit-hyperrectangle by Eq. (8).

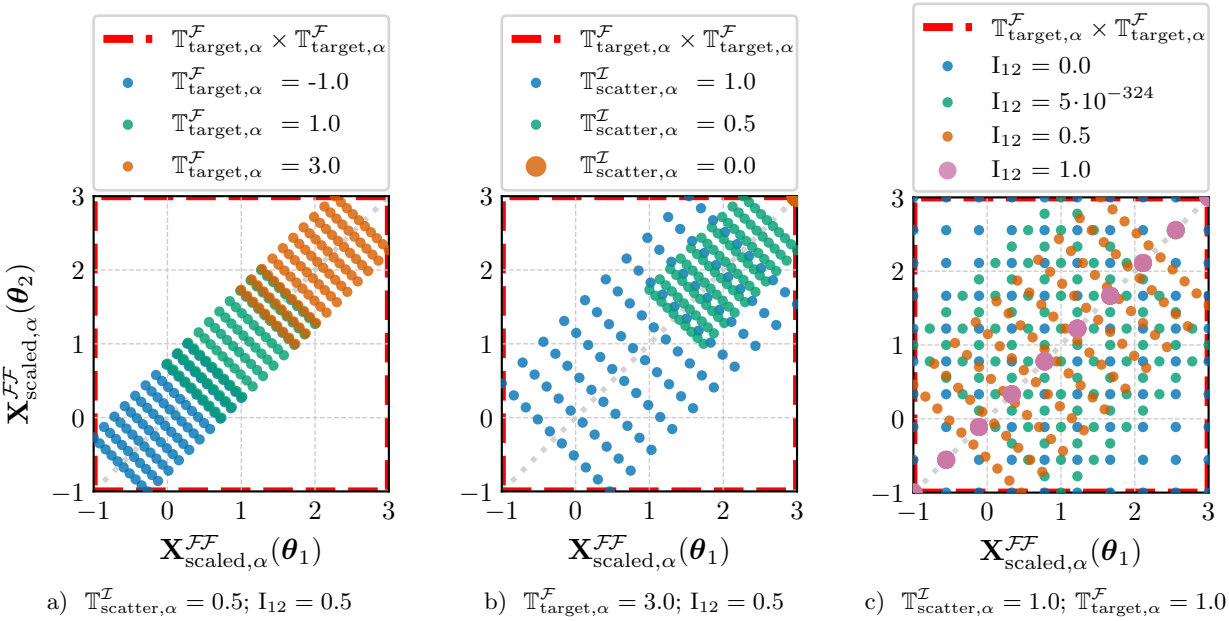
Due to identity of the two fuzzy quantities $\mathbb{T}^{\mathcal{F}}_{\text{target}}$ in Eq. (11), and recalling that $\mathbb{T}^{\mathcal{I}}_{\text{scatter}} = [0,\, 1]$,

$$\begin{aligned} \mathbf{X}^{\mathcal{FF}}_{\text{scaled},\alpha=1}\left(\mathbb{T}^{\mathcal{I}}_{\text{scatter}}\right) &\subseteq \mathbf{X}^{\mathcal{FF}}_{\text{scaled},\alpha=1}\left(\mathbb{T}^{\mathcal{I}}_{\text{scatter}}{}^{\star} = 0\right) \\ &\subseteq \mathbb{T}^{\mathcal{F}}_{\text{target},\alpha=1} + 0 \cdot \left(\begin{bmatrix} 0 \\ \vdots \\ 0 \end{bmatrix} + \mathbb{T}^{\mathcal{F}}_{\text{target},\alpha=1,\mathrm{L}} - \mathbb{T}^{\mathcal{F}}_{\text{target},\alpha=1} \right) = \begin{bmatrix} \mathbb{T}^{\mathcal{F}}_{\text{target},\alpha=1} \\ \vdots \\ \mathbb{T}^{\mathcal{F}}_{\text{target},\alpha=1} \end{bmatrix} \end{aligned} \tag{12}$$

shows redundancy. Hence, the target fuzzy quantity $\mathbb{T}^{\mathcal{F}}_{\text{target},\alpha=1}$ at all observation points is already parametrized by $\mathbb{T}^{\mathcal{I}}_{\text{scatter}} = 0$ at $\alpha = 1$ and redundant realizations are simulated for $\mathbb{T}^{\mathcal{I}}_{\text{scatter}} =]0, 1]$.

Discussion of the Method's Interaction Characteristics

Finally, an unintentional characteristic of the method from (Götz et al., 2016) is investigated, leading to a discontinuity at transition from case of low interaction to the marginal case of no interaction.



a) $\mathbb{T}^{\mathcal{I}}_{\text{scatter},\alpha} = 0.5$; $\mathrm{I}_{12} = 0.5$ b) $\mathbb{T}^{\mathcal{F}}_{\text{target},\alpha} = 3.0$; $\mathrm{I}_{12} = 0.5$ c) $\mathbb{T}^{\mathcal{I}}_{\text{scatter},\alpha} = 1.0$; $\mathbb{T}^{\mathcal{F}}_{\text{target},\alpha} = 1.0$

Figure 1. Influence of the parameters on the auto-interaction between two observation points $\boldsymbol{\theta}_1$ and $\boldsymbol{\theta}_2$ at a specific α-level, where $\mathbb{T}^{\mathcal{F}}_{\text{target},\alpha} = [-1, 3]$, with $\mathbb{T}^{\mathcal{F}}_{\text{scale},\alpha,i} = [-1, 1]$ for each $i \in \{1, 2\}$ discretized by 10 samples and all $n_\lambda = 2$ eigenmodes in Python implementation. Starred parameters $\bullet^*$ indicate interval quantities fixed to deterministic values.

Therefore, the marginal membership functions at two discrete observation points $\mathbb{T}^{\mathcal{F}}_{\text{target}}(\boldsymbol{\theta}_1)$ and $\mathbb{T}^{\mathcal{F}}_{\text{target}}(\boldsymbol{\theta}_2)$ of a fuzzy field are considered. Fuzzy field realizations with interactions by Eq. (5) are restricted to a subset of the α-level cuts' Cartesian products $\mathcal{C}^{\mathcal{F}}_\alpha = \mathbb{T}^{\mathcal{F}}_{\text{target},\alpha}(\boldsymbol{\theta}_1) \times \mathbb{T}^{\mathcal{F}}_{\text{target},\alpha}(\boldsymbol{\theta}_1)$, as shown in Figure 1.

For $\mathrm{I}_{12} = 1$, all realizations of fully interacted intervals are expected to be on the diagonal spanned by $\left(\mathbb{T}^{\mathcal{F}}_{\text{target},\alpha,\mathrm{L}}(\boldsymbol{\theta}_1), \mathbb{T}^{\mathcal{F}}_{\text{target},\alpha,\mathrm{L}}(\boldsymbol{\theta}_2)\right)$ and $\left(\mathbb{T}^{\mathcal{F}}_{\text{target},\alpha,\mathrm{R}}(\boldsymbol{\theta}_1), \mathbb{T}^{\mathcal{F}}_{\text{target},\alpha,\mathrm{R}}(\boldsymbol{\theta}_2)\right)$. If $\mathrm{I}_{12} = 0$, the non-interacted intervals' sampling should reach every point in $\mathcal{C}^{\mathcal{F}}_\alpha$. These bounding cases are both enabled by the method and a validation is provided in Figure 1c). Additionally, it would be desired that the interaction models influence on the condition of the resulting α-level optimization problem is negligible for all subsets of the problem, but doubts about this are already noted in Eq. (9).

With Eq. (4), the interaction is expanded by normalized fuzzy quantities and a linear transformation is applied by Eq. (5) to match the bounds of the marginal membership function. Therefore, the desired interaction characteristics apply to arbitrary marginal membership functions.

In Figure 1, the influence of a fuzzy field's input quantities (1a and 1b) and of the interaction parameter (1c) on the auto-interaction is displayed. For each sample, Eq. (4) is evaluated with different parameters described in the respective subplot. The investigation of three parameter combinations for $\mathbb{T}^{\mathcal{F}}_{\text{target},\alpha}$, with fixed $\mathrm{I}_{12} = 0.5$ and $\mathbb{T}^{\mathcal{I}}_{\text{scatter},\alpha} = 0.5$, in Figure 1a), shows that several subsets of identical realizations, disadvantageous for optimization algorithms, exist. In Figure 1b), $\mathbb{T}^{\mathcal{F}}_{\text{target},\alpha} = 3.0$ is fixed, while the interaction is as in a) and the influence of $\mathbb{T}^{\mathcal{I}}_{\text{scatter},\alpha}$ is investigated.

It is shown that the interaction model relies on the width of $\mathbb{T}^{\mathcal{I}}_{\text{scatter},\alpha}$ to reach the diagonal corners of $\mathcal{C}^{\mathcal{F}}_{\alpha}$. However, this parameter also leads to the same problem of overlapping subsets

In Figure 1c), the influence of the auto-interaction parameter on the scaling of the subspace of the Cartesian product is shown. The cases $\mathrm{I}_{12} = 0$ and $\mathrm{I}_{12} = 1$ are expected, as noted before, and all points within $\mathcal{C}^{\mathcal{F}}_{\alpha}$ are reachable for them. Contrarily, for any $\mathrm{I}_{12} > 0$, the domain gets restricted. This is validated by the double precision machine epsilon > 0, as LAPACK routines are used for eigenvector computation, which is $\mathrm{I}_{12} = 5{\cdot}10^{-324}$, see Figure 1c). The restricted domain is defined by the rays parallel to the diagonal that connect the centroids $\mathbb{T}^{\mathcal{F}}_{\text{target},\alpha,\mathrm{C}}$ of the α-level of the marginal membership function. This undesired discontinuity is due to the orthogonal expansion of Eq. (4), which results in unit base vectors for the eigenvectors in case of $\mathbf{I} = \operatorname{diag}(1, \cdots, 1)$, the identity matrix. However, as soon as $\mathbf{I}_{ij} > 0$ the coordinate transformation, by 45° in Figure 1, takes place.

In result to this discontinuity, only fractions of the Cartesian product ($\frac{3}{4}$ area in two-dimensional case) are represented, limiting the applicability to realistic interactions. Especially, application for distance dependent auto-interactions as in Eq. (3) is questionable, since it is anticipated that $\lim_{\mathrm{d}(\boldsymbol{\theta}_i,\boldsymbol{\theta}_j)\to\infty}(I_{ij}) = 0$, and accordingly, far distanced observation points should be fully independent.

Conclusions and Improvement Suggestions for the Method
Based on observations in Eqs. (10)–(12), the following modifications are suggested:

a) To avoid resulting observation points unintentionally being fully auto-interacted at $\alpha = 1$, it is suggested to redefine the scale parameters by $\mathbb{T}^{\mathcal{I}\,\text{redef.}}_{\text{scale},i} := [-1, 1]$ as interval quantities. By this redefinition, it is ensured that the normalization to unit-hyperrectangle and scaling to the bounds of the marginal membership function are defined respectively for all α-levels.

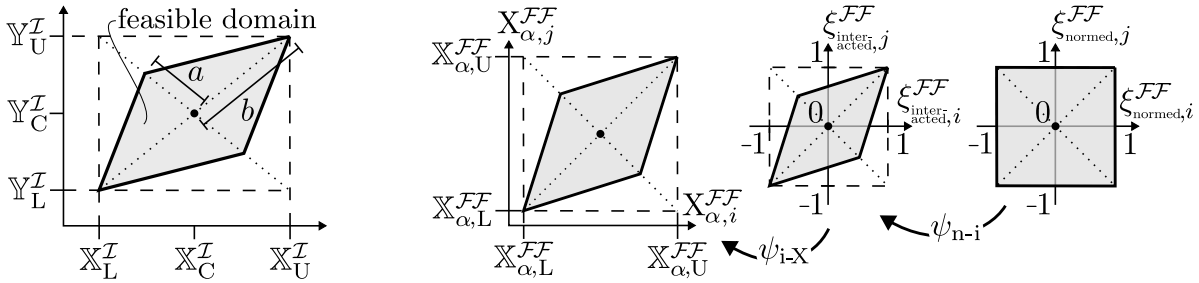
b) Contrarily, if constant realizations of the fuzzy field (fully interacted over all observation points) are actually intended as additional case, it is still suggested to redefine $\mathbb{T}^{\mathcal{I}\,\text{redef.}}_{\text{scale},i} := [-1, 1]$ as in a) and, additionally, $\mathbb{T}^{\mathcal{I}\,\text{fully-interacted}}_{\text{scale},i} := 0$ for all i and $\mathbb{T}^{\mathcal{I}\,\text{fully-interacted}}_{\text{scatter}} := 0$ can be set in a separate simulation, to enable an efficient fuzzy analysis without the redundancies of Eq. (12).

In conclusion, the numerical effort of over-parametrization with $n_{\text{input}} > n_\theta$ (all eigenmodes considered), the resulting ill-conditioning of the optimization problem and the non-physical discontinuity at transition case to zero interaction remain as disadvantages of the proposed method.

2.3. Dependency Model for Interval and Fuzzy Quantities – Interaction by a Multidimensional Parallelepiped

The multidimensional parallelepiped (MP) model for interval interaction is defined in several concepts by the same authors e.g. in (Jiang et al., 2015b) and specifically for interval arithmetic based uncertainty quantification formulated in (Jiang et al., 2015a). Therein, the MP model definition is founded on a dependency coefficient $\mathrm{i}^{\text{MP}}(\mathbb{X}^{\mathcal{I}}, \mathbb{Y}^{\mathcal{I}}) = (b-a)/(b+a)$, defined for the two-dimensional interaction between intervals $\mathbb{X}^{\mathcal{I}}$ and $\mathbb{Y}^{\mathcal{I}}$. Therein, the parameters a and b are defined by the parallelogram, describing the feasible area of interacted samples of the two intervals, and fixed to the diagonals as displayed in Fig. 2a). Based on this idea, the multidimensional interaction matrix $\mathbf{I}^{\text{MP}}$ for interactions between all intervals $\mathbb{X}_i$ and $\mathbb{X}_j$ is defined as symmetric matrix with entries

$$\mathrm{I}^{\text{MP}}_{ij} = \mathrm{I}^{\text{MP}}_{ji} = i^{\text{MP}}(\mathbb{X}^{\mathcal{I}}_i, \mathbb{X}^{\mathcal{I}}_j). \tag{13}$$



a) Parallelogram defining the dependency coefficient of the MP model in 2-dim.

b) Mapping scheme for α-level of MP fuzzy field – though it is noted that effective projections of n-dim. MPs are *not* parallelograms.

Figure 2. Multidimensional parallelepiped (MP) as interaction for interval interaction and fuzzy fields.

The MP for the n-dimensional interval interaction is defined by the feasible domain

$$\left|\mathbf{I}^{\text{MP}\,-1}\,\mathbf{T}^{-1}\,\mathbf{R}^{-1}\,(\mathbf{X}^{\mathcal{I}}-\mathrm{C}\,([\mathbf{X}^{\mathcal{I}}]))\right|\leq\mathbf{1}. \tag{14}$$

Therein, the norm denotes entry-wise absolute values, $\mathbf{1}=[1\ \cdots\ 1]^{\intercal}$ is the all-ones vector and

$$\mathbf{T}=\mathrm{diag}\,(w_1,\ldots,w_n),\qquad w_i=1/\sum_{j=1}^{n}|\mathrm{I}_{ij}|,\qquad \mathbf{R}=\mathrm{diag}\,(\mathrm{R}(\mathbb{X}_1^{\mathcal{I}}),\ldots,\mathrm{R}(\mathbb{X}_n^{\mathcal{I}})), \tag{15}$$

by applying the interval radius $\mathrm{R}(\bullet)$ and (entry-wise) centroid $\mathrm{C}([\bullet])$, see Section 2.1.

Although it is stated in (Jiang et al., 2015a) that the MP model is solely based on the bounds and mutual interactions of the intervals, it has to be noted that projections of an MP to the (i,j)-coordinate planes are not generally parallelograms, in contrast to the two-dimensional case, see Figure 2a). Moreover, in (Jiang et al., 2015a) an argumentation for the modeling of interaction coefficients for the multidimensional examples is omitted and in (Jiang et al., 2015b) data-based modeling of parallelograms in (i,j)-coordinate planes is shown, but the deviation to the geometry of the resulting parallelepiped is not quantified. Nevertheless, the idea of the MP is promising for characterization of multidimensional interval interactions and will be extended in Section 2.4, but the constituting assumption of a parallelogram with i^{MP} is not followed further.

2.4. Development of a Fuzzy Field Method by Modification and Extension of the Multidimensional Parallelepiped Interval Dependency

Based on the investigation of some non-negligible disadvantages in the existing fuzzy field approach, pointed out in Section 2.2, a novel definition of fuzzy fields is presented in this section. Therefore, it is recalled that fuzzy fields in α-level discretized representation can be interpreted as nested interval field models. Hence, the idea of an MP model of Section 2.3 is modified to an auto-interaction formulation for interval fields and, accordingly, extended to auto-interacted fuzzy fields.

Most importantly, it is shown at the end of this section that the modified MP model can be represented by an orthogonal series expansion, allowing for an eigenvalue decomposition that can be

excited by a reduced number of orthogonal base variables. Hence, the numerical feasibility in fuzzy analyses of fuzzy fields of many observation points is enabled by the proposed method.

Definition of the Modification and Extension to Fuzzy Fields
For a sampling oriented definition of MP-based fuzzy fields, based on α-level discretization, the optimization design space of a discrete α-level can be interpreted as centered unit-hypercube $[-1,1]^{n_\theta}$, noted as vector of independent normed base intervals $\boldsymbol{\xi}^{\mathcal{FF}}_{\text{normed},\alpha} = ([-1,1] \ \cdots \ [-1,1])^\intercal$, with n_θ entries corresponding to the number of observation points in the fuzzy field. Their transformation to interacted intervals, forming an MP in analogy with Eq. (14), is defined by

$$\psi_{\text{n-i}} : \ \boldsymbol{\xi}^{\mathcal{FF}}_{\text{normed},\alpha} \mapsto \boldsymbol{\xi}^{\mathcal{FF}}_{\text{interacted},\alpha}, \quad \boldsymbol{\xi}^{\mathcal{FF}}_{\text{interacted},\alpha} = \mathcal{S}^{\pm}(\mathbf{I})\, \boldsymbol{\xi}^{\mathcal{FF}}_{\text{normed},\alpha}, \tag{16}$$

where $\mathbf{I}$ is the interaction matrix constituted by Eq. (3), characterizing the fuzzy field's distance-dependent auto-interaction. In (Jiang et al., 2015a), a normalized interaction matrix, denoted as shape matrix, is proposed for the transformation to the MP, by the row-wise normalization matrix of Eq. (15), to enforce the bounds of the centered unit-hypercube $[-1,1]^{n_\theta}$ for the transformed $\boldsymbol{\xi}^{\mathcal{FF}}_{\text{interacted},\alpha}$. This shape matrix is not necessarily symmetric, and therefore, an orthogonal basis spanned by its eigenvectors in $\mathbb{R}^{n_\theta}$ is not guaranteed. It is noted that this fact is not obvious in the examples of (Jiang et al., 2015a, Eqs. (26, 31, 38, 46, 49, 52, 56)), since only interaction matrices – mostly two-dimensional – with a priori identical row and column sums are presented therein.

In this contribution, an MP model modification is proposed by incorporating the Sinkhorn-Knopp algorithm, to achieve a doubly stochastic matrix form of the interaction matrix, see (Sinkhorn and Knopp, 1967). The algorithm is implemented in an adopted form to retain the entry signs in the matrix, since negative interactions are possible. By this, for Eq. (16), the component $\mathcal{S}^{\pm}(\mathbf{I})$ is referred to as the signed Sinkhorn form of the interaction matrix. It constitutes the mathematical precondition for the proper orthogonal decomposition, as shown at the end of this section.

As final step in the mapping chain, which in total is visualized in Figure 2b),

$$\psi_{\text{i-X}} : \ \boldsymbol{\xi}^{\mathcal{FF}}_{\text{interacted},\alpha} \mapsto \mathbf{X}^{\mathcal{FF}}_{\alpha}, \quad \mathbf{X}^{\mathcal{FF}}_{\alpha} = \mathbf{R}\, \boldsymbol{\xi}^{\mathcal{FF}}_{\text{interacted},\alpha} + \mathrm{C}([\mathbf{X}^{\mathcal{FF}}_{\alpha}]) \tag{17}$$

is defined, equivalent to Eq. (14), to scale the MP to the desired bounds of the marginal membership. The vector $\mathbf{X}^{\mathcal{FF}}_{\alpha}$ of auto-interacted intervals, corresponding to the observation points of the fuzzy field, is achieved. For a homogeneous fuzzy field, the same marginal membership function $\mu_{\mathbb{X}^{\mathcal{F}}}$, of the field-constituting fuzzy quantity $\mathbb{X}^{\mathcal{F}}$, is defined for all observation points, as in Section 2.2. Hence, the radii and centroids of all entries of $\mathbf{X}^{\mathcal{FF}}_{\alpha}$ are all identical with the field-constituting fuzzy quantity, with $\mathrm{R}\,(\mathrm{X}^{\mathcal{FF}}_{\alpha,i}) = \mathbb{X}^{\mathcal{F}}_{\mathrm{R}}$ and $\mathrm{C}\,(\mathrm{X}^{\mathcal{FF}}_{\alpha,i}) = \mathbb{X}^{\mathcal{F}}_{\mathrm{C}}$, respectively, for $i \in 1, \ldots, n_\theta$.

Orthogonal Decomposition and Reduced Basis Expansion
To enable numerically efficient fuzzy analyses, a reduced expansion is proposed for the MP-based fuzzy field method. Therefore, it is recalled that the interaction matrix is represented by its signed Sinkhorn form $\mathcal{S}^{\pm}(\mathbf{I})$ in Eq. (16). Eigenvectors of a Sinkhorn matrix are orthogonal (due to symmetry) and the largest (first if ordered) eigenvalue is $\lambda_1 = 1$. The same properties are also assumed to hold for the signed Sinkhorn form. Hence, the first eigenvector $\boldsymbol{\phi}_1$ of $\mathcal{S}^{\pm}(\mathbf{I})$ is oriented in direction of the largest diagonal of the multidimensional parallelepiped.

By all eigenvalues λ_i and eigenvectors $\boldsymbol{\phi}_i$ with $i \in 1, \dots, n_\lambda$ of $\mathcal{S}^{\pm}(\mathbf{I})$ and $\boldsymbol{\Lambda} = \operatorname{diag}(\lambda_1, \dots, \lambda_{n_\lambda})$, the orthogonal expansion is

$$\mathcal{S}^{\pm}(\mathbf{I}) = \boldsymbol{\Phi}\ \boldsymbol{\Lambda}\ \boldsymbol{\Phi}^{\intercal}, \qquad \text{where} \quad \boldsymbol{\Phi} = \begin{bmatrix} | & & | \\ \boldsymbol{\phi}_1 & \cdots & \boldsymbol{\phi}_{n_\lambda} \\ | & & | \end{bmatrix}_{n_\lambda \times n_\theta}, \tag{18}$$

with respectively sorted eigenvalues $\lambda_i > \lambda_j : i < j$ and normed eigenvectors upright in the matrix.

Instead of the n_θ interval quantities in Eq. (16), it is desired to excite the eigenmodes by a reduced number n_λ of base intervals, with α-level notation in the vector $\boldsymbol{\zeta}_\alpha$, and postulated that

$$\psi_{\zeta\text{-i}} : \ \boldsymbol{\zeta}_\alpha \mapsto \boldsymbol{\xi}^{\mathcal{FF}}_{\text{interacted},\alpha}, \quad \boldsymbol{\xi}^{\mathcal{FF}}_{\text{interacted},\alpha} = \boldsymbol{\Phi}\ \boldsymbol{\Lambda}\ \boldsymbol{\zeta}_\alpha \quad \text{if } n_\lambda = n_\theta. \tag{19}$$

It is requested that this is an equivalent reducible basis orthogonal representation of the mapping $\psi_{\text{n-i}}$ to the multidimensional parallelepiped in the centered unit-hypercube, with

$$\begin{aligned} \psi_{\zeta\text{-i}} \overset{!}{=} \psi_{\text{n-i}} \quad \Leftrightarrow \quad \boldsymbol{\Phi}\ \boldsymbol{\Lambda}\ \boldsymbol{\zeta}_\alpha &= \mathcal{S}^{\pm}(\mathbf{I})\, \boldsymbol{\xi}^{\mathcal{FF}}_{\text{normed},\alpha} && (20) \\ &= \boldsymbol{\Phi}\ \boldsymbol{\Lambda}\ \boldsymbol{\Phi}^{\intercal}\ \boldsymbol{\xi}^{\mathcal{FF}}_{\text{normed},\alpha}, \qquad \text{by Eq. (18), and hence,} \\ \Leftrightarrow\ \boldsymbol{\zeta}_\alpha &= \boldsymbol{\Phi}^{\intercal}\ \boldsymbol{\xi}^{\mathcal{FF}}_{\text{normed},\alpha}. && (21) \end{aligned}$$

Accordingly with $n_\lambda < n_\theta$, an approximation of the fuzzy field is achieved by incorporating a reduced orthogonal basis in Eq. (19). The mapping, explicitly noting the matching matrix dimensions, reads

$$\psi_{\zeta\text{-i,red}} : \ \boldsymbol{\zeta}^{\text{red}}_\alpha \mapsto \boldsymbol{\xi}^{\mathcal{FF},\text{approx}}_{\text{interacted},\alpha}, \quad \left[\boldsymbol{\xi}^{\mathcal{FF},\text{approx}}_{\text{interacted},\alpha}\right]_{n_\theta} = \left[\boldsymbol{\Phi}^{\text{red}}\right]_{n_\theta \times n_\lambda} \left[\boldsymbol{\Lambda}^{\text{red}}\right]_{n_\lambda \times n_\lambda} \left[\boldsymbol{\zeta}^{\text{red}}_\alpha\right]_{n_\lambda}, \tag{22}$$

where $\boldsymbol{\Phi}^{\text{red}}$ and $\boldsymbol{\Lambda}^{\text{red}}$ are the reduced matrices of n_λ eigenvectors and eigenvalues, respectively. Therefore, the base intervals in $\boldsymbol{\zeta}^{\text{red}}$ define the design variables of the α-level optimization by a reduced n_θ-dimensional optimization problem. However, a challenge remains in the sampling of $\boldsymbol{\zeta}^{\text{red}}$, which requires to be compliant with Eq. (21). This equivalence is accounted for by incorporating the constraints of the centered unit-hypercube $-1 \leq [\boldsymbol{\xi}^{\mathcal{FF}}_{\text{normed},\alpha}]_i \leq 1$, for all components noted

$$\mathbf{S}\ \boldsymbol{\xi}^{\mathcal{FF}}_{\text{normed},\alpha} \leq \mathbf{1} \quad \Leftrightarrow \quad \mathbf{S}\ \boldsymbol{\Phi}\ \boldsymbol{\zeta}_\alpha \leq \mathbf{1} \quad \text{with} \quad \mathbf{S} = \begin{bmatrix} 1 & 0 & \cdots \\ -1 & 0 & \cdots \\ 0 & 1 & \cdots \\ 0 & -1 & \cdots \\ \vdots & \vdots & \ddots \end{bmatrix}_{2n_\theta \times n_\theta} \quad \text{and} \quad \boldsymbol{\Phi}^{-1} = \boldsymbol{\Phi}^{\intercal}. \tag{23}$$

Accordingly, $2 \cdot n_\theta$ constraints have to be considered for the reduced basis in $[\mathbf{S}^{\text{red}}]_{2n_\theta \times n_\lambda}$. The component-wise design bounds of $\boldsymbol{\zeta}_\alpha$ can be computed, e.g. by the corresponding linear programming problem, by investigation of all diagonals of the MP – attained by evaluating Eq. (21) for all $2^{n_\theta - 1}$ corners of the centered unit-hypercube – or by reasonably estimating bounds. It is noted that the component-wise bounds of $\boldsymbol{\zeta}^{\text{red}}_\alpha$ in Eq. (23) are tighter, since MP diagonals are not all reachable in reduced expansions. However, since the eigenvectors are normed, the half diagonals of the centered unit-hypercube in orthogonal basis are general bounds $\left|[\boldsymbol{\zeta}^{\mathcal{FF}}_\alpha]_i\right| \leq \sqrt{n_\theta}$ per component.

In analogy to the decompositions in (Sudret and Der Kiureghian, 2000; Götz et al., 2016), the fraction $q = \sum_{i=1}^{n_\lambda} \lambda_i \,/\, \sum_{j=1}^{n_\theta} \lambda_j$ is an indicator for the ignorance of uncertainty in the approximated input space, sufficient for trade-off decisions between numerical effort and approximation quality. Finally, it is noted that, based on the affine interval transformations, the demonstrated mapping chain $\mathbb{X}^{\mathcal{I}} = \psi_{\text{i-X}}(\psi_{\zeta\text{-i,red}}(\zeta^{\text{red}}))$ is bijective. Hence, in contrast to the adverse sampling of the method investigated in Section 2.2, the novel MP-based fuzzy fields provide a uniqueness in sampling.

3. Numerical Example

Two numerical examples are presented to show the applicability of the novel method and for validation with documented results. The developed approach of Section 2.4 is implemented in Python and all numerical optimization tasks are performed with the optimization framework Pymoo (v0.6.1.6) of (Blank and Deb, 2020). For comparibility, the common evolutionary strategy is applied (single objective optimization), although the implementation is modified to enable brief hyper-parameter optimization via the Pymoo interface to the Optuna tools of (Akiba et al., 2019).

Example 1 – Validation by an MP-based Interval Field Problem
With (Jiang et al., 2015a, "Numerical Example 3") as reference, the polynomial interval function

$$\mathbb{G}^{\mathcal{I},\text{E1}}(\mathbf{X}^{\mathcal{I}}) = -10\,\mathbb{X}_1^{\mathcal{I}} + 4\,\mathbb{X}_2^{\mathcal{I}} - 12\,\mathbb{X}_3^{\mathcal{I}} + \mathbb{X}_1^{\mathcal{I}} \cdot \mathbb{X}_2^{\mathcal{I}} + 2\,\mathbb{X}_1^{\mathcal{I}} \cdot \mathbb{X}_3^{\mathcal{I}} + \mathbb{X}_2^{\mathcal{I}} \cdot \mathbb{X}_3^{\mathcal{I}} + 10 \tag{24}$$

is defined as basic solution for the uncertainty quantification. Additionally, the parameters are

$$\mathbf{I} = \begin{bmatrix} 1.0 & -0.4 & 0.4 \\ & 1.0 & -0.4 \\ \text{sym.} & & 1.0 \end{bmatrix}, \qquad \mathbb{X}_i^{\mathcal{I}} = [0,\, 8],\; i \in \{1, 2, 3\}, \tag{25}$$

where the matrix of interactions is according to Eq. (13) and all intervals have the same bounds.

The method definitions of the reference and the proposed method (see Section 2.4) differ in the transformation to the interacted intervals (cp. Eqs. (14) and (16)). However, Eq. (25) already has identical sums of row and column absolute values, and therefore, leads to a signed Sinkhorn form with Eq. (15). Hence, the methods are equivalent in the transformation.

The reference results are achieved by interval arithmetic with analytical interaction transformation of the intervals. The overestimation due to inherent interval dependency (wrapping effect) is mentioned in passing, but accepted without effort in (Jiang et al., 2015a). It is shown there that

$$\begin{aligned} \mathbb{G}^{\mathcal{I},\text{E1b}}_{\text{interacted}}(\boldsymbol{\xi}^{\mathcal{I}}) = 1.1851\,{\xi_1^{\mathcal{I}}}^2 - 2.3703\,{\xi_2^{\mathcal{I}}}^2 + 1.1851\,{\xi_3^{\mathcal{I}}}^2 + 2.9629\,\xi_1^{\mathcal{I}}\,\xi_2^{\mathcal{I}} + 5.9259\,\xi_1^{\mathcal{I}}\,\xi_3^{\mathcal{I}} \\ +2.9629\,\xi_2^{\mathcal{I}}\,\xi_3^{\mathcal{I}} - 0.8888\,\xi_1^{\mathcal{I}} + 7.1111\,\xi_2^{\mathcal{I}} - 1.7777\,\xi_3^{\mathcal{I}} - 30 \end{aligned} \tag{26}$$

results from the analytical interaction transformation. Due to interval wrapping, the equivalent is

$$\mathbb{G}^{\mathcal{I},\text{E1c}}_{\substack{\text{interacted} \\ \text{wrapping}}}(\boldsymbol{\xi}^{\mathcal{I}}_{\text{equiv.}}) = 1.1851\xi_1^{\mathcal{I}}\xi_2^{\mathcal{I}} - 2.3703\,\xi_3^{\mathcal{I}}\xi_4^{\mathcal{I}} + \cdots - 1.7777\,\xi_{15}^{\mathcal{I}} - 30. \tag{27}$$

Table I. Results of numerical example 1 with reference solutions of (Jiang et al., 2015a).

setup	*uncertainty quantification method*	*interaction method*	*wrapping avoided*	*basic solution*	*input bounds*	*resulting interval*	*relative radius*
E1a) reference	interval arithmetic	non-interacted	⊖	Eq. (24)	$[0, 8]^3$	$[-198, 266]$	100.0 %
E1b) reference	interval arithmetic	Sec. 2.3, analytical	⊖	Eq. (26)	$[-1, 1]^3$	$[-56.37, -3.63]$	11.4 %
E1c) validation	analytical bounds	Sec. 2.3, analytical	⊖	Eq. (27)	$[-1, 1]^{15}$	$[-56.3698, -3.6302]$	11.4 %
E1d) computed	α-level optimized	Sec. 2.3 $\widehat{=}$ 2.4, full	✓	Eq. (24)	$[0, 8]^3$	$[-45.7037, -11.9259]$	7.3 %
E1e) computed	α-level optimized	Sec. 2.4, reduced ev.	✓	Eq. (24)	$[-1, 1]^2$	$[-37.74, -22.05]$	3.4 %

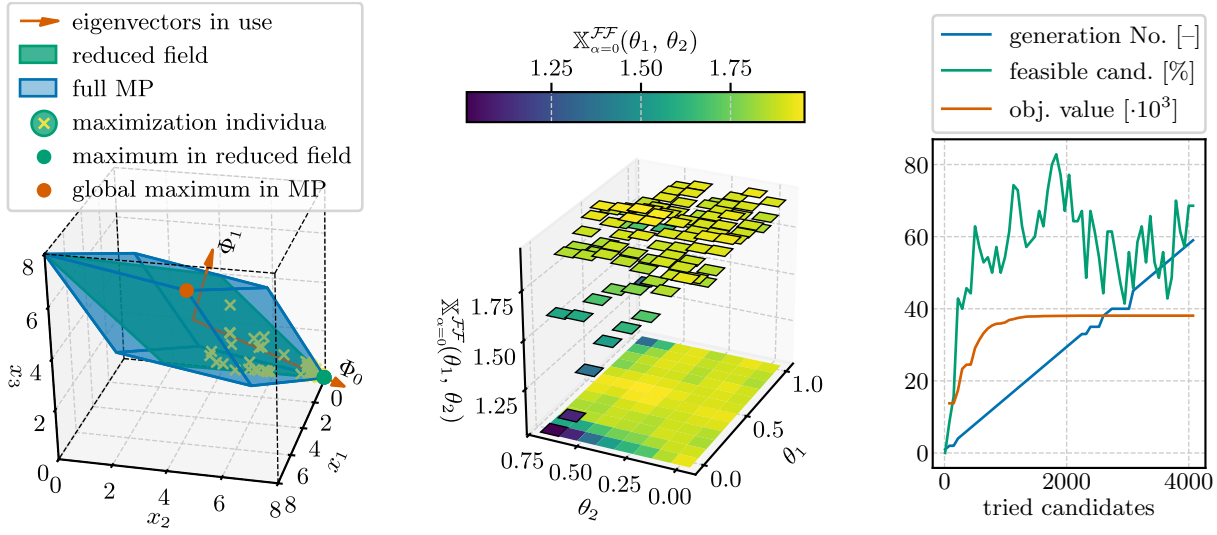
The numerical experiment setups and computed results are listed in Table I. The results of (Jiang et al., 2015a) are taken as references, denoted as setups E1a) and b). In validation setup E1c), the interval wrapping is tracked by interval optimization with the expanded form of the problem. The reference is successfully reproduced, although it is noted that the optima of Eq. (27) are analytically found at such bounds of the fifteen-dimensional input space, where variable combinations trivially satisfy positive/negative signs of all equation parts for maximization/minimization, respectively.

The proposed interaction method of MP-based fuzzy fields is demonstrated in E1d) and e). Therefore, the fuzzy field is viewed as an interval field (single α-level investigation) with predefined interaction matrix. In this specific case, as stated before, the proposed method and the reference method are equivalent and fully comparable. However, E1d) shows that the wrapping effect is avoidable by interval optimization. The full consideration of all interval dependencies results in a tight interval, contrarily to the overestimation in the interval arithmetic approach of E1b).

Finally, setup E1e) is performed with a reduced two-dimensional basis, applying the proposed orthogonal expansion. For this, the maximization individua are visualized in Figure 3. The global maximum in the MP (green volume) is at a vertex (orange point) that is not included in the reduced field (blue plane), spanned by the two eigenvectors (orange arrows) that correspond to the two largest eigenvalues. By this, it is emphasized that the proposed reduced orthogonal expansion is numerically advantageous, due to the reduced basis. The full MP is covered by the two-dimensional sub-space, based on the eigenvalues' weighting of the most pronounced extent of the MP. However, if the global maximum is not included in the reduced sub-space, as it is the case in E1e) shown in Figure 3a), the uncertainty quantification is prone to underestimation of the resulting interval. In conclusion, the reduction with E1e) covers less than half of the result of E1d), while the number of effective basic solution evaluations is 108|96 for hyper-parameter optimization and 101|242 for the min.|max. to reach 10 % tolerance in the objective function over the last 5 optimization generations.

Example 2 – MP-based Fuzzy Field evaluated at the Rosenbrock benchmark function
The Rosenbrock function, according to (Blank and Deb, 2020), is investigated as basic solution by

$$\mathbb{G}^{\mathcal{F},\mathrm{E2}}_{\mathrm{Rosenbrock}}\left(\mathbf{X}^{\mathcal{FF}}\right) = \sum_{i=1}^{n_\theta - 1} \Big(100 \cdot \left(\mathbf{X}^{\mathcal{FF}}(\boldsymbol{\theta}_{i+1}) - \mathbf{X}^{\mathcal{FF}}(\boldsymbol{\theta}_i)^2\right)^2 + \left(1 - \mathbf{X}^{\mathcal{FF}}(\boldsymbol{\theta}_i)^2\right) . \tag{28}$$



a) Maximization individua of E1e) on reduced orthogonal expansion (plane), enveloped by full MP.

b) Exemplary realization of MP-based 2-dim. spatially interacting fuzzy field at local maximum of E2a) in $\alpha = 0$.

c) Optimization characteristics for maximization task E2b) – feasibility due to constraints.

Figure 3. Results and characteristics of the optimization tasks for the numerical examples.

Table II. Results of numerical example 2, by 96-dim. Rosenbrock function (Blank and Deb, 2020) as basic solution.

setup	*uncertainty quantification method*	*MP-based fuzzy field*	*basic solution*	*input quantities*	*resulting fuzzy quantity*	*relative radius at* $\alpha = 0$
E2a)	α-level optimized	full	Eq. (28)	$\langle 0.5, 1.5, 2.0\rangle^{96}$	$\langle 55.7, 5367.5, 25268.1\rangle$	66.2 %
E2b)	α-level optimized	reduced ev.	Eq. (28)	$[-1, 1]^3$	$\langle 3{\cdot}10^{-5}, 5367.5, 38089.4\rangle$	100.0 %

Therein, $\mathbf{X}^{\mathcal{FF}}$ is simulated as stationary MP-based fuzzy field, as defined in Section 2.4. The field constituting marginal fuzzy quantity is $\mathbb{X}^{\mathcal{F}} = \langle 0.5, 1.5, 2.0\rangle$ and the observation points are defined in a two-dimensional equidistant 12×8 grid, as shown in Figure 3b). A spatial auto-interaction by squared exponential kernel, see (Schietzold et al., 2019), is defined with interaction length parameter $\theta_\mathrm{d} = 0.1$, allowing for a high scattering in the field realizations. The results of both setups for this numerical example are listed in Table II. For the fuzzy analyses, α-level optimization for support $\alpha = 0$ is performed in addition to a single computation of the core $\alpha = 1$. The full MP-based fuzzy field with 96 base variables, one for each observation point, is simulated in E2a). In contrast, a reduced orthogonal basis is applied for E2b), by 3 eigenvectors ($q_\mathrm{E2b)} = \sum_{i=1}^{3}\lambda_i \,/\, \sum_{j=1}^{96}\lambda_j = 9.6\,\%$).

Based on 5800|5800 evaluations in hyper-parameter optimizations and 5820|15130 evaluations in the optimizations of min|max, E2a) gets stuck in local optima, terminating with less than 10 % objective function change in the last 10 generations. With the same optimization setup, E2b) converges after only 5730|4163 hyper-parameter optimization evaluations and further 1331|2326

calls, outperforming E2a) by $\approx 50\,\%$ increased result radius at $\alpha = 0$. Hence, the reduced expansion enables finding the optima at all. In Figure 3c), optimization characteristics of E2b) are plotted, where the fraction of feasible candidates fluctuates over generations, emphasizing the importance of efficient constraint implementation for the design variables (orthogonal bases), see Eq. (23).

4. Conclusions and Outlook

Realistic system safety assessment with spatially and temporally dependent uncertainty under severe lack of knowledge requires epistemic uncertain field formulations. Mathematical models and uncertainty quantification for such fields are discussed in this contribution. Especially, an existing fuzzy field method, defined by orthogonal decomposition, is investigated. Although, improvement suggestions for this method are provided, disadvantages still remain. Hence, a novel fuzzy field method, based on the existing concept of multidimensional parallelepipeds (MP) for interval interactions, is developed. The disadvantages of the existing method are eliminated in the novel approach. The developments enable a consistent distance-based auto-interaction structure, with free choice of an interaction kernel, where corners of the hyperrectangle of interval input spaces are bounding and reachable in contrast to ellipsoidal convex interaction models. Moreover, the proposed MP-based fuzzy fields allow for the development of orthogonal decomposition and reduced basis expansion, developed for efficient fuzzy analysis. The orthogonal expansion method enables to select a desired approximation quality of a fuzzy field by number of α-level optimization design variables, while still covering the most significant extents of the MP in a low-dimensional representation.

The demonstrated methods can straightforward be applied for engineering tasks, e.g. in structural analysis with basic solutions by FE simulations. The dimensionality of the fuzzy field formulation can be defined for systems with arbitrary n_θ-dimensional spatially and temporally dependent uncertainty. As limitation of the proposed MP-based fuzzy field method, it is noted that projections of an MP in the (i, j)-coordinate planes are not parallelograms and, especially, dependent on the number of observation points, which is required to be recognized in the generalization of data-based uncertainty modeling for auto-interaction structures. In conclusion, it is therefore noted that there is potential for further research into the development of additional fuzzy field interaction models.

Acknowledgements

The authors express their sincere thanks to Nicolas Winkler, whose project thesis 'Efficient Simulation of Fuzzy Fields in Uncertainty Analyses' (Institute for Structural Analysis, Technische Universität Dresden, 2024) supported to understand the fuzzy field approach of Section 2.2. Special thanks go to Vladik Kreinovich (University of Texas at El Paso), whose contribution to the discussion of intermediate results at the 'Workshop on Recent Advancements in Uncertainty Quantification and Propagation' (Leibniz Universität Hannover, 2024) greatly inspired the developments.

The demonstrated results and research activities arise from Projects 310979960 (KA 1163/38) and 310979960 (GR 1504/11, KA 1163/37) of the DFG Priority Program SPP 1886 (Project 273721697) and of Subproject D3 of the Research Training Group GRK 2868 D^3 (Project 493401063). The funding by the German Research Foundation (DFG) is gratefully acknowledged.

References

Akiba, T., S. Sano, T. Yanase, T. Ohta, and M. Koyama: 2019, 'Optuna: A Next-generation Hyperparameter Optimization Framework'. In: *Proceedings of the 25th ACM SIGKDD*. Anchorage, AK, USA, pp. 2623–2631.

Beer, M., S. Ferson, and V. Kreinovich: 2013, 'Imprecise probabilities in engineering analyses'. *Mechanical Systems and Signal Processing* **37**, 4–29.

Blank, J. and K. Deb: 2020, 'Pymoo: Multi-Objective Optimization in Python'. *IEEE Access* **8**, 89497–89509.

Do, D. M., W. Gao, and C. Song: 2016, 'Stochastic finite element analysis of structures in the presence of multiple imprecise random field parameters'. *Computer Methods in Applied Mechanics and Engineering* **300**, 657–688.

Faes, M. and D. Moens: 2017, 'Identification and quantification of spatial interval uncertainty in numerical models'. *Computers and Structures* **192**, 16–33.

Faes, M. and D. Moens: 2019, 'Recent Trends in the Modeling and Quantification of Non-probabilistic Uncertainty'. *Archives of Computational Methods in Engineering* **27**, 633–671.

Fina, M., W. Wagner, and W. Graf: 2023, 'On polymorphic uncertainty modeling in shell buckling'. *Computer-Aided Civil and Infrastructure Engineering* **38**, 2632–2647.

Götz, M.: 2017, *Numerische Entwurfsmethoden Unter Berücksichtigung Polymorpher Unschärfe*. Dissertationsschrift, Technische Universität Dresden, Publications of the Institute for Structural Analysis, Issue 32.

Graf, W., M. Götz, and M. Kaliske: 2015, 'Analysis of dynamical processes under consideration of polymorphic uncertainty'. *Structural Safety* **52**, 194–201.

Götz, M., W. Graf, and M. Kaliske: 2016, 'Structural analysis with spatial varying polymorphic uncertain parameters – fuzzy fields using spectral decomposition'. In: H. Huang, J. Li, J. Zhang, and J. Chen (eds.): *6th Asian-Pacific Symposium on Structural Reliability and its Applications (APSSRA6)*. Shanghai, China.

Hanss, M.: 2005, *Applied Fuzzy Arithmetic*. Heidelberg: Springer.

Harazin, F., J. Platen, F. N. Schietzold, W. Graf, and M. Kaliske: 2026, 'Multiscale polymorphic uncertainty quantification based on physics-augmented neural networks'. *Computer Methods in Applied Mechanics and Engineering* **452**, 118726.

Jiang, C., C.-M. Fu, B.-Y. Ni, and X. Han: 2015a, 'Interval arithmetic operations for uncertainty analysis with correlated interval variables'. *Acta Mechanica Sinica* **32**, 743–752.

Jiang, C., Q. F. Zhang, X. Han, J. Liu, and D. A. Hu: 2015b, 'Multidimensional parallelepiped model – a new type of non-probabilistic convex model for structural uncertainty analysis'. *International Journal for Numerical Methods in Engineering* **103**, 31–59.

Luo, Y., J. Zhan, J. Xing, and Z. Kang: 2019, 'Non-probabilistic uncertainty quantification and response analysis of structures with a bounded field model'. *Computer Methods in Applied Mechanics and Engineering* **347**, 663–678.

Möller, B. and M. Beer: 2004, *Fuzzy Randomness: Uncertainty in Civil Engineering and Computational Mechanics*. Springer, Heidelberg.

Möller, B., W. Graf, and M. Beer: 2000, 'Fuzzy structural analysis using α-level optimization'. *Computational Mechanics* **26**, 547–565.

Pannier, S., M. Waurick, W. Graf, and M. Kaliske: 2013, 'Solutions to problems with imprecise data – An engineering perspective to generalized uncertainty models'. *Mechanical Systems and Signal Processing* **37**, 105–120.

Richter, B., F. N. Schietzold, W. Graf, and M. Kaliske: 2025, 'Intermediately discretized extended α-level-optimization – An advanced fuzzy analysis approach'. *Advances in Engineering Software* **202**, 103865.

Schietzold, F. N., W. Graf, and M. Kaliske: 2024, 'Establishing Polymorphic Uncertainty as a Generalized Data Concept in Engineering Analyses'. *GAMM Rundbrief* **1/2024**.

Schietzold, F. N., A. Schmidt, M. M. Dannert, A. Fau, R. M. N. Fleury, W. Graf, M. Kaliske, C. Könke, T. Lahmer, and U. Nackenhorst: 2019, 'Development of fuzzy probability based random fields for the numerical structural design'. *Surveys for Applied Mathematics and Mechanics* **42**, e201900004.

Sinkhorn, R. D. and P. J. Knopp: 1967, 'Concerning Nonnegative Matrices and Doubly Stochastic Matrices'. *Pacific Journal of Mathematics* **21**, 343–348.

Sudret, B. and A. Der Kiureghian: 2000, 'Stochastic Finite Element – Methods and Reliability – A State-of-the-Art Report'. Technical Report UCB/SEMM-2000/08, University of California, Berkeley.

Zadeh, L. A.: 1965, 'Fuzzy Sets'. *Information and Control* **8**, 338–353.

Surrogate Modeling Strategy for Random Fields with Uncertain Correlation Lengths

Emily Zeller, Maximilian Schweizer, Marc Fina, Werner Wagner and Steffen Freitag
Institute for Structural Analysis, Karlsruhe Institute of Technology, Karlsruhe 76131, Germany,
emily.zeller@kit.edu

Abstract. Thin-walled shell structures achieve high load-bearing capacities with low material consumption. However, they are highly susceptible to stability issues caused by geometric imperfections. To account for these imperfections, random fields are incorporated into finite element (FE) models, and the structural response is evaluated with Monte Carlo simulations. Time-consuming FE analyses can be replaced by an artificial neural network (ANN) surrogate model. When applying the Karhunen-Loève expansion (KLE), the shape of the random field is determined by a correlation length, which may be affected by epistemic uncertainty. Consequently, the random field is modeled using fuzzy correlation lengths, leading to a further increase in computation time. To reduce this effort, an interpolation-based surrogate modeling strategy is proposed and compared with the conventional approach of solving the KLE eigenvalue problem. Within a multilevel surrogate modeling framework, the ANN is combined with least-squares polynomials to perform a structural optimization including fuzzy stochastic analysis. The introduced model is then applied to a fiber composite plate to optimize its thickness and fiber orientation angle. Therefore, both single-objective constrained and multi-objective unconstrained optimization are conducted.

Keywords: multilevel surrogate modeling, fuzzy stochastic analysis, polymorphic uncertainty, uncertain correlation length, Karhunen-Loève expansion, artificial neural network, structural design optimization

1. Introduction

The design of structures commonly involves an optimization process aiming to achieve high load-bearing capacities with minimal material consumption. Consequently, thin-walled shell structures are widely employed. In practice, however, their behavior is strongly influenced by geometric imperfections (Donnell and Wan, 1950). Deviations from the perfect geometry increase the susceptibility to stability problems, which can lead to a significant reduction in load-bearing capacity. In finite element (FE) analyses, geometric imperfections are incorporated by applying correlated random fields (Yang et al., 2022).

One approach to generate random fields is the Karhunen-Loève expansion (KLE), in which the spatial characteristics of the imperfections are primarily determined by the so-called correlation length ℓ_c (Schenk and Schuëller, 2007; Lauterbach et al., 2018). To obtain a realistic model, the correlation length can be derived from measurements of real structures, see (Fina et al., 2020; Fina et al., 2023). Due to the limited amount of available data, the correlation length is affected by

© 2026 by the author(s). This work is licensed under the Creative Commons Attribution 4.0 International License (CC BY 4.0), which permits unrestricted use, distribution, and reproduction in any medium, provided the original author and source are credited.

epistemic uncertainty. The performance of a fuzzy stochastic analysis (Schweizer et al., 2025b) allows the consideration of uncertainty within numerical simulations. However, the integrated Monte Carlo simulation (MCS) requires a large number of FE evaluations, entailing a substantial computational cost. This effort can be reduced by employing an artificial neural network (ANN) as a surrogate model for the FE buckling calculation, see (Schweizer et al., 2025a; Schweizer et al., 2025b). If the correlation length is treated as an uncertain input parameter, the eigenvalue problem of the KLE has to be solved separately for each correlation length, which increases the computation time for generating the ANN training data. Therefore, an interpolation-based strategy is introduced, replacing the conventional solution of the KLE eigenvalue problem.

In this contribution, the fuzzy stochastic analysis is combined with an optimization loop in order to design robust and high-performing shell structures with low material usage. Thus, an ANN surrogate model is developed in which the design variables for the optimization process are incorporated as additional input variables alongside the uncertain a priori parameters. Therefore, the ANN proposed in (Schweizer et al., 2025b) is extended to account for uncertain correlation lengths. Moreover, least-squares (LSQ) polynomials complement the ANN within a multilevel surrogate modeling approach. This computational framework is used for both single-objective constrained and multi-objective unconstrained optimization to determine the optimal structural design of a fiber composite plate.

2. Optimization of Geometrically Imperfect Structures under Polymorphic Uncertainty

Apart from theoretical considerations, real-world structures are commonly affected by several kinds of uncertainty. According to (Götz et al., 2015; Der Kiureghian and Ditlevsen, 2009), it can be distinguished between aleatory and epistemic uncertainty. While aleatory uncertainty describes inherent natural variability, epistemic uncertainty results from incomplete information and imprecisions. The combination of both types is referred to as polymorphic uncertainty, also known as mixed or hybrid uncertainty. In the following, this concept is incorporated into structural design optimization.

2.1. Modeling of Geometric Imperfections

Geometric imperfections are modeled by applying a correlated random field to the FE model of the investigated structure, representing deviations of the surface geometry in the normal direction. In this contribution, the random fields are generated using the KLE, which is briefly summarized based on (Sudret and Der Kiureghian, 2000), (Vanmarcke, 2010) and (Zhang and Ellingwood, 1994).

In general, a random field

$$w(\boldsymbol{x}, \theta) = \{X(\boldsymbol{x}, \theta) \mid \boldsymbol{x} \in \Omega, \theta \in \Theta\} \tag{1}$$

assigns a random variable to each spatial point $\boldsymbol{x}$ and each event θ, where Ω denotes the surface of the structure and Θ represents the set of all possible events. Within the KLE framework, the

random field is discretized at the n FE nodes and the autocorrelation matrix

$$\boldsymbol{\rho} = \begin{bmatrix} \rho(\boldsymbol{x}_1, \boldsymbol{x}_1) & \cdots & \rho(\boldsymbol{x}_1, \boldsymbol{x}_n) \\ \vdots & \ddots & \vdots \\ \rho(\boldsymbol{x}_n, \boldsymbol{x}_1) & \cdots & \rho(\boldsymbol{x}_n, \boldsymbol{x}_n) \end{bmatrix} \tag{2}$$

is employed, which is symmetric and positive definite. For generating the random field, the eigenvalue problem of the KLE

$$\boldsymbol{\rho} \cdot \boldsymbol{\varphi} = \lambda \cdot \boldsymbol{\varphi} \tag{3}$$

has to be solved, where $\boldsymbol{\varphi}$ and λ denote the eigenvectors and eigenvalues, respectively. Thus, the discrete random field is defined by

$$\hat{w}(\boldsymbol{x}, \theta) = \sum_{i=1}^{n} \xi_i(\theta) \sqrt{\lambda_i}\, \varphi_i(\boldsymbol{x}) \tag{4}$$

with the standard normally distributed random variables $\xi_i(\theta) \sim \mathcal{N}(0, 1)$.

If the structure is discretized with a large number of FE nodes n, many terms are required to construct the series given in Eq. (4). Hence, it is reasonable to truncate the series by discarding terms associated with small eigenvalues, which, therefore, have a negligible influence on the resulting random field. This truncation is performed using the quality index Q

$$\sum_{i=1}^{\tilde{n}} \lambda_i \geq Q \cdot \sum_{i=1}^{n} \lambda_i \tag{5}$$

after sorting the eigenvalues in descending order, thereby reducing the number of retained terms from n to $\tilde{n}$. Following (Brenner, 1995), a quality index of $Q = 99\,\%$ is adopted.

The entries of the autocorrelation matrix $\boldsymbol{\rho}$, introduced in Eq. (2), are specified through the autocorrelation function. Here, the squared exponential function

$$\rho(\boldsymbol{x}_i, \boldsymbol{x}_j) = \exp\left[-\frac{d^2(\boldsymbol{x}_i, \boldsymbol{x}_j)}{\ell_c^2}\right] \tag{6}$$

is employed, depending on the distance between the FE nodes $d(\boldsymbol{x}_i, \boldsymbol{x}_j)$ and the correlation length ℓ_c.

By varying ℓ_c, the spatial characteristics of the random field can be controlled systematically. Large values of ℓ_c correspond to highly correlated, smooth fields, whereas small values lead to more irregular realizations. This relationship is illustrated in Figure 1, where three different correlation lengths are used to generate a random field based on the same set of random variables $\boldsymbol{\xi}$. The correlation length ℓ_c can be obtained from measurements of structural surfaces, as demonstrated in (Fina et al., 2023).

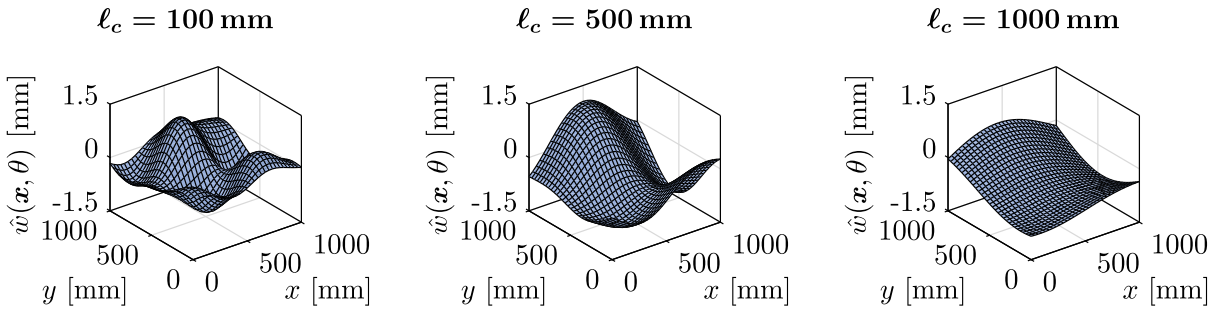


Figure 1. Influence of the correlation length on the random field of a square plate with the lateral dimension $L = 1000\,\mathrm{mm}$ and a discretization with $m = 30 \times 30 = 900$ elements

Since the available data are usually limited, ℓ_c is treated as an epistemically uncertain input parameter. The membership of the element ℓ_c to a set is rated gradually between $\mu(\ell_c) = 0$ and $\mu(\ell_c) = 1$ using the membership function $\mu(\ell_c)$. Consequently, the normalized fuzzy variable

$$\tilde{\ell}_c = \{(\ell_c, \mu(\ell_c)) \mid \ell_c \in \mathbb{R}\}, \quad \mu(\ell_c) : \mathbb{R} \to [0, 1] \tag{7}$$

can be introduced, see (Möller and Beer, 2004). If $\mu(\ell_c)$ is defined as a piecewise linear function that increases monotonically to its maximum $\mu(\ell_c) = 1$ and decreases monotonically thereafter, $\tilde{\ell}_c = \langle \ell_{c,1}, \ell_{c,2}, \ell_{c,3} \rangle$ is referred to as a convex fuzzy triangular variable, fully defined by its lower bound $\ell_{c,1}$, trend value $\ell_{c,2}$ and upper bound $\ell_{c,3}$.

By incorporating this fuzzy variable, Eq. (4) yields a so-called fuzzy probability-based random (fp-r) field, see (Schietzold et al., 2019). This field assigns an fp-r variable to each spatial point $\boldsymbol{x}$ and each event θ and is defined on the fuzzy probability space $(\Omega, \Sigma, \hat{P})$. The fuzzy probability $\hat{P} = (\hat{P}_\alpha)_{\alpha \in [0,1]}$ associates each α-level with an interval-valued probability measure

$$\hat{P}_\alpha = [\hat{P}^l_\alpha(\ell_c), \hat{P}^r_\alpha(\ell_c)], \quad 0 \leq \hat{P}^l_\alpha(\ell_c) \leq \hat{P}^r_\alpha(\ell_c) \leq 1 \quad . \tag{8}$$

2.2. Numerical Buckling Analysis

In this contribution, the load-bearing capacities of geometrically imperfect systems are investigated. Deviations from the reference geometry can limit the structural performance significantly. In general, slender structures subjected to compressive loading tend to fail due to stability phenomena. After the stability point is reached, large deformations occur, which are commonly referred to as buckling. In the following, a brief introduction to numerical buckling analysis is given based on (Wagner, 1995).

Reaching the stability point corresponds to an indifferent equilibrium state, which is numerically characterized by a singular tangential stiffness matrix $\boldsymbol{K}_T$. This critical point can be determined by performing either a linear or nonlinear buckling analysis. Linear buckling analysis neglects a possible nonlinear pre-buckling behavior, but, in those cases, provides sufficiently accurate results. This approach involves the decomposition of the tangential stiffness matrix

$$\boldsymbol{K}_T = \boldsymbol{K}_L + \boldsymbol{K}_{NL} \tag{9}$$

into the linear stiffness matrix $\boldsymbol{K}_L$ and the nonlinear stiffness matrix $\boldsymbol{K}_{NL}$. First, the linear solution at the origin of the load-displacement curve

$$\boldsymbol{K}_L \boldsymbol{u}_0 = \boldsymbol{P} \quad \Longleftrightarrow \quad \boldsymbol{u}_0 = \boldsymbol{K}_L^{-1} \boldsymbol{P} \tag{10}$$

is computed. Subsequently, the linear buckling analysis

$$[\boldsymbol{K}_L + \Lambda \boldsymbol{K}_{NL}(\boldsymbol{u}_0)]\boldsymbol{\varphi} = \boldsymbol{0} \tag{11}$$

can be performed, and the critical buckling load $\boldsymbol{P}_{\mathrm{cr,perf}} = \Lambda \boldsymbol{P}$ as well as the associated critical displacement $\boldsymbol{u}_{\mathrm{cr}} = \Lambda \boldsymbol{u}_0$ are obtained.

As a numerical example, an axially loaded composite plate is investigated. For this structure, the presence of geometric imperfections transforms the stability problem into a stress problem, since $\boldsymbol{K}_T$ no longer becomes singular. Therefore, no classical buckling analysis can be applied to determine the critical load. Following (Schweizer et al., 2025b), the critical load of the geometric imperfect structure is defined as the load corresponding to the critical displacement of the plate without imperfections, given by $P_{\mathrm{cr}} = P(u_{\mathrm{cr}})$. This concept is shown in Figure 2 for a square plate subjected to a distributed load p, resulting in a total load $P = p \cdot L$, where L denotes the lateral dimension.

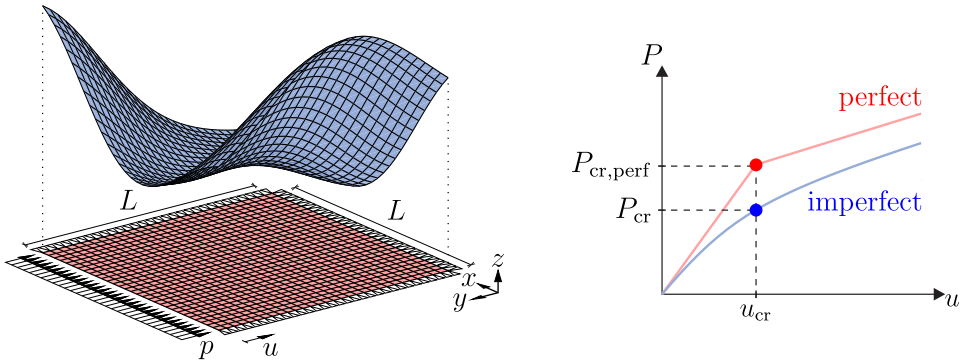


Figure 2. Influence of geometric imperfections on the load-displacement curve of an axially loaded plate

Moreover, geometric imperfections lead to a nonlinear response prior to reaching the critical displacement. A displacement-controlled arc-length method (Batoz and Dhatt, 1979; Wagner and Wriggers, 1988) is employed to generate the load-displacement curves and evaluate the critical load. To account for uncertain geometric imperfections, an MCS is performed, in which for each realization one random field is applied to the structure and the corresponding critical load P_{cr} is computed. Based on the MCS, an α-level optimization (Möller et al., 2000) is performed, in which the minimum and maximum stochastic responses are identified at discrete α-levels α_k. This procedure yields the fuzzy stochastic quantities of interest and the fuzzy cumulative distribution function (CDF) of the critical load P_{cr}. In this contribution, the mean value $E(P_{\mathrm{cr}})$, the coefficient of variation $CV(P_{\mathrm{cr}})$ and the 5% quantile $q_{0.05}(P_{\mathrm{cr}})$ are evaluated. To render the fuzzy stochastic quantities suitable for the subsequent optimization, they have to be transformed into deterministic values by means of information reduction measures (Böttcher et al., 2023). As suggested in (Schweizer et al., 2025b), the centroids of these quantities are adopted (indicated by the index c).

2.3. Structural Design Optimization

Mathematically, an optimization problem is formulated as a minimization problem

$$\min[z(\boldsymbol{x}_d)], \quad \boldsymbol{x}_d \in \mathcal{D} \quad , \tag{12}$$

in which the objective function $z(\boldsymbol{x}_d)$ is minimized with respect to the design variables $\boldsymbol{x}_d$, see (Boyd and Vandenberghe, 2004). Both single-objective constrained and multi-objective unconstrained optimization are investigated and therefore introduced in the following.

In structural design, the aim is to achieve a high load-bearing capacity with a low dead load and, consequently, low material consumption by adjusting the design variables, e.g., thickness and fiber orientation. For structures with constant density, minimizing the dead load is equivalent to minimizing the volume. Accordingly, in the single-objective constrained approach, the volume is selected as the objective function $z(\boldsymbol{x}_d)$ to be minimized. To ensure sufficient load-bearing behavior, a threshold value P_{tr} is imposed. A high level of resistance is assessed by characterizing the load-bearing capacity through the 5% quantile of the critical load $q_{0.05,c}(P_{\mathrm{cr}}(\boldsymbol{x}_d))$. Thus, for constrained optimization, Eq. (12) is extended to

$$\min[z(\boldsymbol{x}_d)] \quad \text{subject to}: \quad q_{0.05,c}(P_{\mathrm{cr}}(\boldsymbol{x}_d)) \geq P_{\mathrm{tr}} \quad . \tag{13}$$

To account for this constraint, a modified objective function

$$\tilde{z}(\boldsymbol{x}_d) = z(\boldsymbol{x}_d) + \beta \cdot \underbrace{\max\{0,\, P_{\mathrm{tr}} - q_{0.05,c}(P_{\mathrm{cr}}(\boldsymbol{x}_d))\}}_{g(\boldsymbol{x}_d)} \tag{14}$$

is employed, incorporating the penalty function $g(\boldsymbol{x}_d)$ and the penalty factor β. Particle swarm optimization (PSO) is adopted as the numerical optimization algorithm, see, e.g., (Siarry, 2016).

Furthermore, a multi-objective unconstrained formulation is examined. To design a robust and high-performing system, two objective functions

$$z_1(\boldsymbol{x}_d) = CV_c(P_{\mathrm{cr}}(\boldsymbol{x}_d)), \quad z_2(\boldsymbol{x}_d) = -E_c(P_{\mathrm{cr}}(\boldsymbol{x}_d)) \tag{15}$$

are defined. The coefficient of variation $CV_c(P_{\mathrm{cr}}(\boldsymbol{x}_d))$ and the mean value $E_c(P_{\mathrm{cr}}(\boldsymbol{x}_d))$ represent robustness and performance, respectively. Since a large mean value is desirable, a negative sign is introduced to maintain the minimization framework. Moreover, a min-max normalization

$$z_i^*(\boldsymbol{x}_d) = \frac{z_i(\boldsymbol{x}_d) - z_{i,\min}}{z_{i,\max} - z_{i,\min}}, \quad 0 \leq z_i^*(\boldsymbol{x}_d) \leq 1, \quad i = 1, 2 \tag{16}$$

is applied to bring the objective functions onto comparable scales, using the minimum $z_{i,\min}$ and maximum $z_{i,\max}$ of each objective function within the design space, see (Miler et al., 2025). Analogously to the constrained approach, a PSO is employed. Because its standard formulation is restricted to single-criterion problems, the two normalized objectives are combined into a modified function based on Chebyshev scalarization

$$\tilde{z}(\boldsymbol{x}_d) = \max\{w_1 \cdot |z_1^*(\boldsymbol{x}_d)|;\; w_2 \cdot |z_2^*(\boldsymbol{x}_d)|\}, \quad 0 \leq w_1, w_2 \leq 1, \quad w_1 + w_2 = 1 \tag{17}$$

with weight factors w_1, w_2, see (Lin et al., 2024).

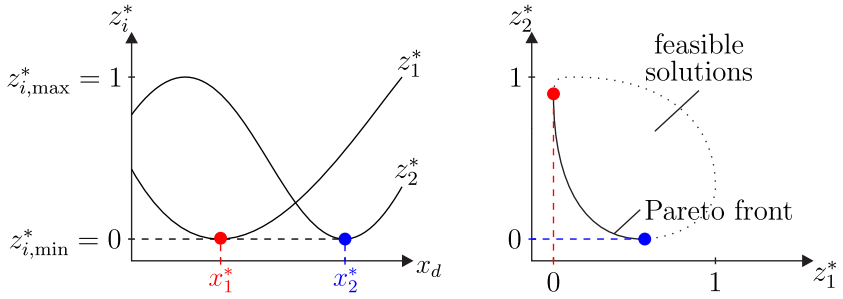


Figure 3. Determination of the Pareto front for two objective functions in a one-dimensional design space

In multi-objective optimization, a conflict of targets arises when the minima of the different objectives correspond to distinct design variable sets. In that case, no unique optimum exists. Instead, Pareto-optimal solutions can be identified, for which none of the objectives can be improved without deteriorating at least one of the others. These compromise solutions form the so-called Pareto front, as illustrated in Figure 3.

3. Computational Framework

The computational framework is divided into the fuzzy stochastic analysis and an structural optimization stage. First, the design variables $\boldsymbol{x}_d$ are introduced, which are subject to optimization. Within the design space, N_O uniformly distributed optimization sample points are selected. At each of these points, a fuzzy stochastic analysis is conducted. The correlation length is employed as a fuzzy triangular input variable $\tilde{\ell}_c = \langle \ell_{c,1}, \ell_{c,2}, \ell_{c,3} \rangle$ and is discretized into $N_\alpha = 11$ α-levels. At the lowest level $\mu(\ell_c) = 0$, N_F equidistant fuzzy sample points are defined. For each of them, an MCS is carried out to evaluate P_{cr} for N_{MCS} realizations with different geometric imperfections. In total, $N_O \times N_F \times N_{MCS}$ realizations are required.

To reduce the computational cost, an ANN is employed as a surrogate model $\hat{\mathcal{M}}_1(\ell_c, \boldsymbol{x}_d, \boldsymbol{\xi})$ for the time-consuming FE calculations. Based on (Schweizer et al., 2025a), the ANN is implemented as a feed-forward multilayer perceptron, comprising three hidden layers with ten neurons each. As proposed in (Schweizer et al., 2025b), the design variables $\boldsymbol{x}_d$ and the standard normally distributed random variables $\boldsymbol{\xi} = (\xi_1, \ldots, \xi_M)$ serve as input to the ANN. To incorporate fuzzy correlation lengths, the ANN input vector is extended by adding the correlation length ℓ_c.

The number M of the standard normally distributed random variables corresponds to the required terms of the KLE, which is reduced from n to $\tilde{n}$ by applying the quality index Q, given in Eq. (5). Since $\tilde{n}$ varies with ℓ_c, the maximum value $\tilde{n}_{\max}$, occurring for the smallest correlation length $\ell_{c,1}$, is determined in advance. Thus, $M = \tilde{n}_{\max}$ random variables are used as ANN inputs to maintain a constant network architecture. Consequently, for each correlation length $\tilde{n} = \tilde{n}_{\max}$ terms are retained when constructing the KLE.

For the following α-level optimization, an LSQ polynomial surrogate model $\hat{\mathcal{M}}_2(\ell_c)$ is employed. This procedure yields the fuzzy stochastic output, from which the corresponding centroids $E_c(P_{\mathrm{cr}})$, $CV_c(P_{\mathrm{cr}})$ and $q_{0.05,c}(P_{\mathrm{cr}})$ are evaluated. The same process is repeated for all optimization sample

points. Subsequently, additional LSQ polynomial surrogate models $\hat{\mathcal{M}}_3(\boldsymbol{x}_d)$ are constructed to represent the dependence of these quantities on the design variables. On this basis, the structural optimization is carried out and the optimal design within the admissible domain is determined. Figure 4 provides an overview of the adopted computational framework.

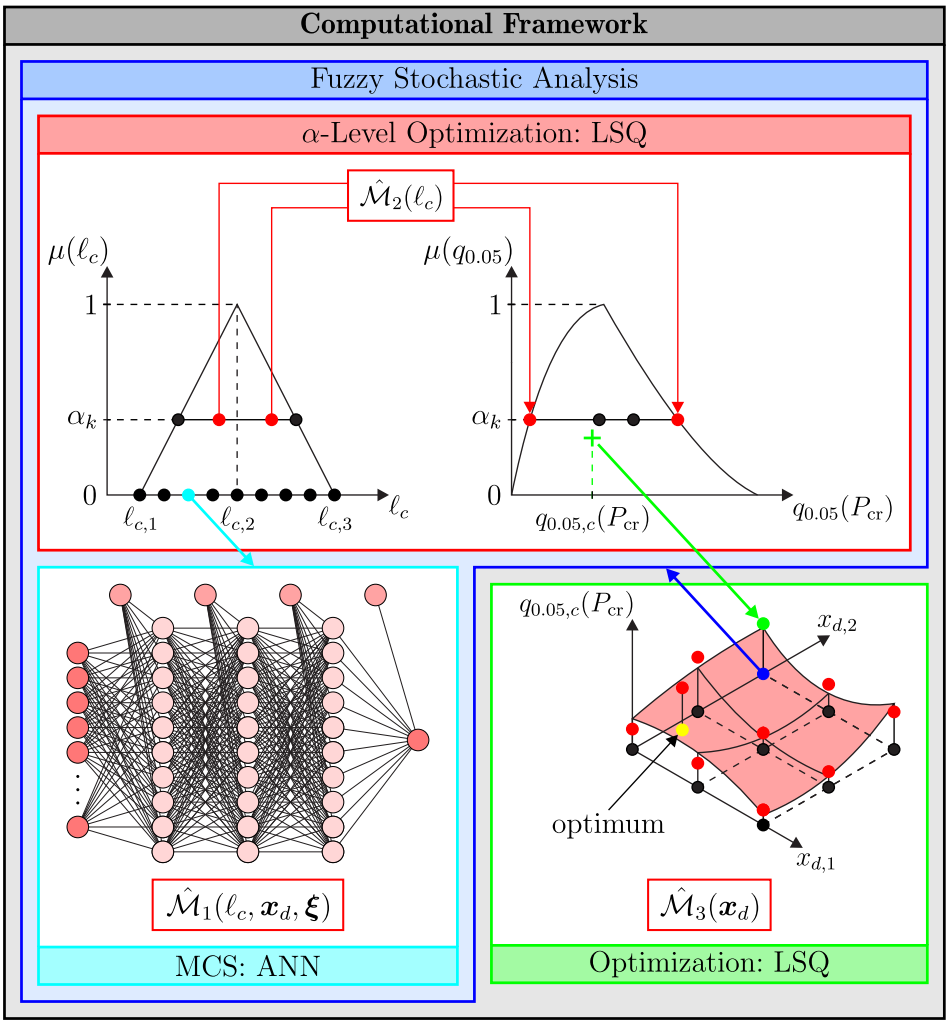


Figure 4. Procedure of the structural optimization including fuzzy stochastic analysis using three surrogate models for a two-dimensional design space, shown for the 5% quantile $q_{0.05}(P_{\mathrm{cr}})$

4. Numerical Example

The previously introduced framework is applied to a fiber composite plate that has been investigated in (Gürdal et al., 2008; Fina and Bisagni, 2025; Schweizer et al., 2025b). The plate has a lateral

dimension of 1000 mm and is subjected to an axial load along the free edge with the resulting load $P = p \cdot 1000\,\text{mm}$. In the direction of thickness, the structure consists of twelve plies with different fiber orientation angles. A symmetric laminate configuration $[\pm\alpha]_{3s}$ is adopted, as illustrated in Figure 5. Moreover, transversely isotropic material behavior is assumed, and the corresponding properties are provided therein.

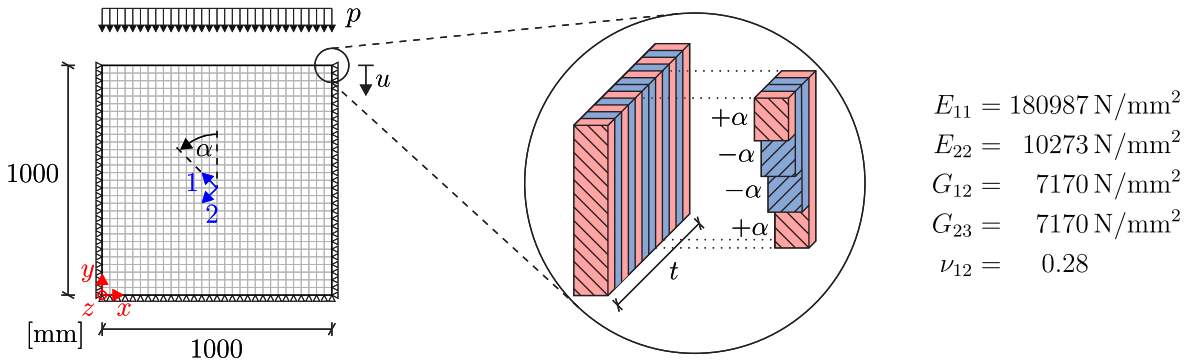


Figure 5. FE model and material properties of the investigated fiber composite plate

For FE calculations, the system is discretized with $m = 30 \times 30 = 900$ nonlinear four-node shell elements with moderate rotations and internal stacking (Wagner and Gruttmann, 1994; Wagner and Gruttmann, 2005; Gruttmann and Wagner, 2006), resulting in a total of $n = 961$ nodes. The correlation length is introduced as the fuzzy triangular variable $\tilde{\ell}_c = \langle 500, 750, 1000 \rangle\,\text{mm}$, which leads to a truncation of the KLE from $n = 961$ to $\tilde{n}_{\max} = 13$ terms. The thickness $t = [1, 2]\,\text{mm}$ and the fiber orientation angle $\alpha = [0, 90]^\circ$ are selected as design variables. With respect to the adopted sampling scheme, $N_O \times N_F \times N_{MCS} = 361 \times 5 \times 10^4 = 1.8 \times 10^7$ realizations are required.

4.1. ANN Training and Testing

Due to the large number of realizations, employing an ANN as a surrogate model for the FE calculations is reasonable. The network is trained using $N_{\text{train}} = 10^4$ training samples, each characterized by a different correlation length as well as different design variables and random variables. A major challenge results from the fact that variations in ℓ_c lead to changes in both the eigenvalues λ and eigenvectors $\boldsymbol{\varphi}$. Consequently, the KLE eigenvalue problem from Eq. (3) has to be solved $N_{\text{train}} = 10^4$ times. For finely discretized models with n FE nodes, solving the eigenvalue problem of an $n \times n$ matrix corresponds to a high computation time. Therefore, an alternative strategy is developed to determine the eigenvalues and eigenvectors with respect to ℓ_c.

Numerically, the scaling factor of an eigenvector is not uniquely determined. While its magnitude is fixed by the applied solver, its sign is arbitrary. To ensure consistency of the eigenvectors corresponding to different correlation lengths, the smallest considered value $\ell_c = 500\,\text{mm}$ is chosen as a reference and all other eigenvectors are adjusted accordingly by enforcing a consistent sign convention. In addition, repeated eigenvalues require special treatment, since no fixed ordering of the associated eigenvectors is guaranteed. Therefore, the eigenpairs are sorted with respect to the reference eigenvectors. After sign-alignment and sorting, the eigenvectors of different correlation

lengths exhibit only minor variations while preserving their overall spatial characteristics. Figure 6 presents the first eigenvector for several correlation lengths, both along the sequence of nodes and over the two-dimensional structural domain.

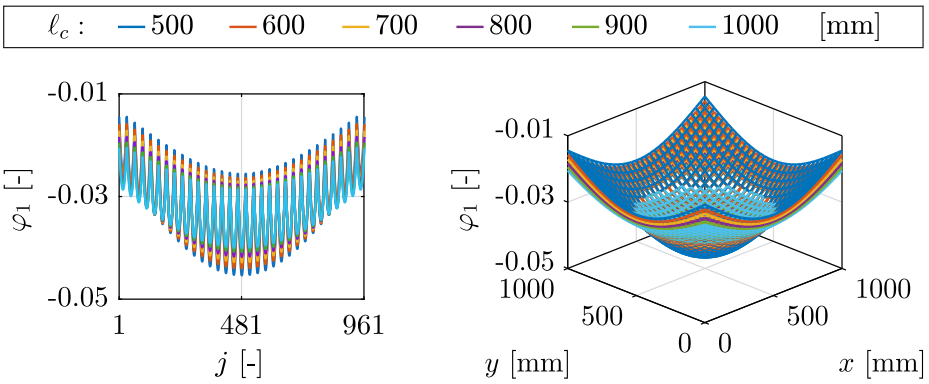


Figure 6. First eigenvector $\boldsymbol{\varphi}_1$ for $\ell_c = \{500, 600, \ldots, 1000\}$ mm, shown along the nodal index j and across the two-dimensional structure (x, y)

Motivated by this similar behavior, the eigenvector φ_i corresponding to an arbitrary value of ℓ_c is obtained by linear interpolation between the results for neighboring correlation lengths. The same procedure is applied to the eigenvalues λ. Thus, the eigenvalue problem of the KLE is solved once beforehand at discrete sampling points $\ell_c = \{500, 550, 600, \ldots, 1000\}$ mm instead of $N_{\text{train}} = 10^4$ times for each new ℓ_c during ANN training. In the following, this interpolation-based approach is denoted by *Int*, whereas the conventional solution of the KLE eigenvalue problem is referred to as *EVP*. The Int method is illustrated in Figure 7 for the first eigenvector of a one-dimensional structure and the complete set of eigenvalues.

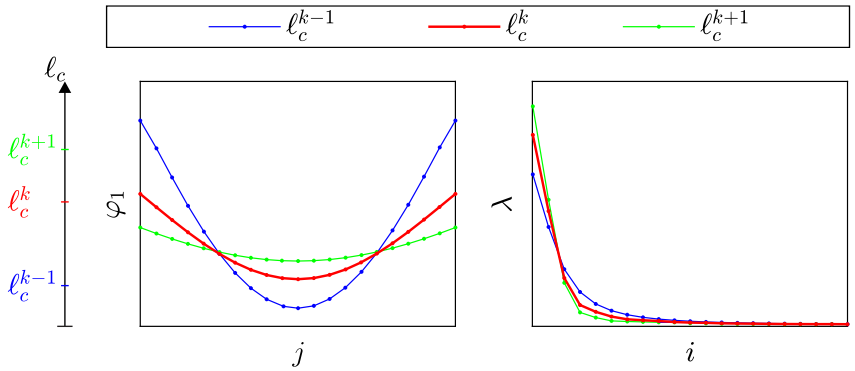


Figure 7. Scheme of the proposed interpolation-based method (Int) for a one-dimensional structure

To evaluate the efficiency of the proposed interpolation-based strategy, the ANN training is performed for different discretizations from $m = 10 \times 10 = 100$ to $m = 70 \times 70 = 4900$ elements and compared with the conventional solution of the eigenvalue problem. The 10^4 training samples are generated in a parallel loop with 12 processing cores operating at 4.70 GHz and 32 GB of

RAM under Windows 11. The resulting computation times for this environment are presented in Figure 8. For reference, the computation time of the EVP method using a discretization with $m = 100$ elements is normalized to 1, and all other efforts are expressed as a relative time factor.

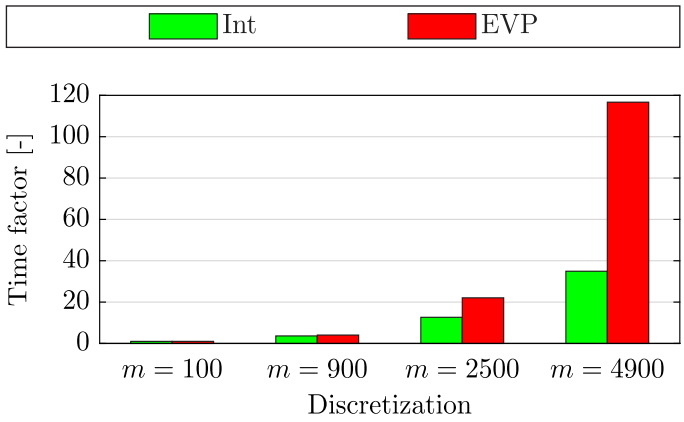


Figure 8. Normalized computation time to generate $N_{\text{train}} = 10^4$ training samples in a parallel loop using the Int and EVP methods for different discretizations with m elements

For coarse discretizations, the Int and EVP methods exhibit comparable computational costs. However, as the number of elements m increases, the Int approach becomes progressively more efficient than the EVP method. To assess the suitability of the interpolation-based strategy, ANN surrogate models are trained for both methods Int and EVP. The predictive accuracy of these neural networks is evaluated using regression diagrams. As shown in Figure 9, the ANN-predicted critical loads $P_{\text{cr,ANN}}$ exhibit only minor deviations from the corresponding FE results $P_{\text{cr,FE}}$.

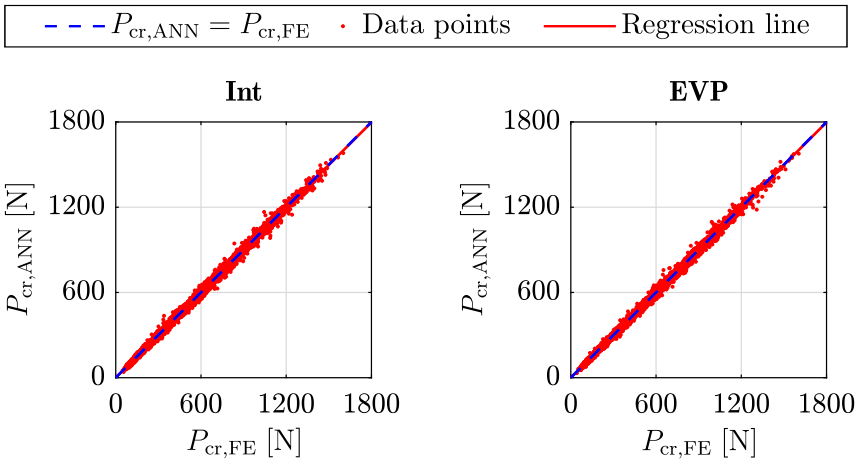


Figure 9. Regression diagrams of ANN training using the Int and EVP methods with $N_{\text{train}} = 10^4$

The high prediction quality is further confirmed through independent ANN plausibility testing. For this purpose, the correlation length is fixed at $\ell_c = 750\,\text{mm}$ and the random vector is set to

$\boldsymbol{\xi} = \mathbf{1}$. Moreover, one of the design variables is held constant at $t = 1.5\,\text{mm}$ or $\alpha = 45\,°$, while the other design variable is varied equidistantly across the design space using $N_{\text{test}} = 19$ sampling points. In Figure 10, the resulting ANN predictions are compared with the FE solutions.

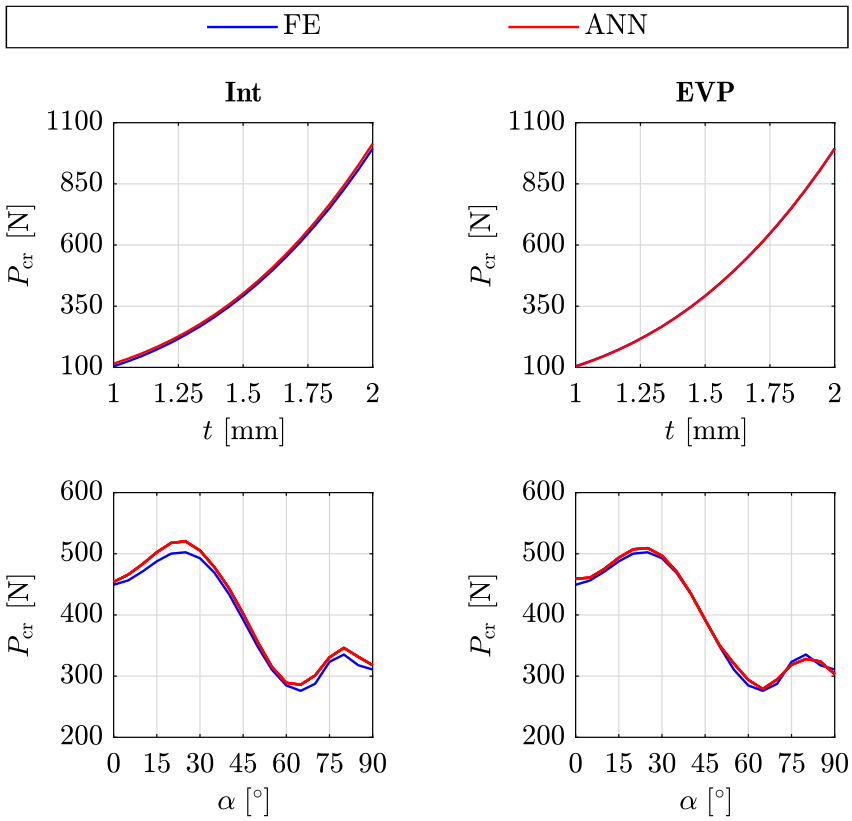


Figure 10. ANN testing using the Int and EVP methods for $t = [1, 2]\,\text{mm}$ (top) and $\alpha = [0, 90]\,°$ (bottom) with $N_{\text{test}} = 19$

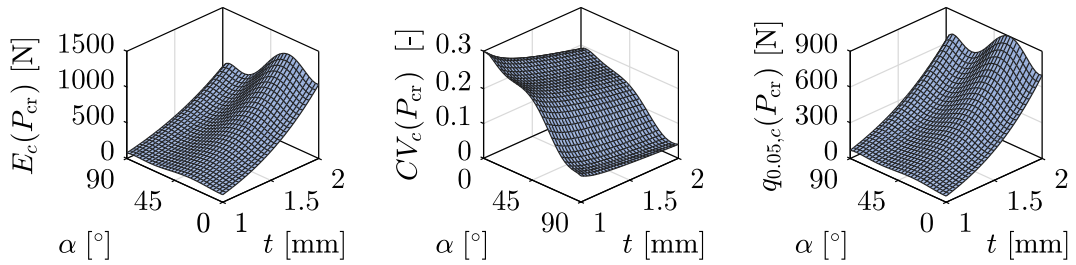


Figure 11. Predictions of the LSQ surrogate models for the mean value $E_c(P_{\text{cr}})$, coefficient of variation $CV_c(P_{\text{cr}})$ and 5% quantile $q_{0.05,c}(P_{\text{cr}})$ using the ANN EVP method with $N_O = 19 \times 19 = 361$

For both methods, the variation of P_{cr} with respect to the design variable is captured accurately by the neural networks. These results demonstrate that the ANN surrogate models are sufficiently

reliable for the subsequent optimization studies. In the following, the two models are denoted by *ANN Int* and *ANN EVP* and used to construct separate LSQ surrogate models for the optimization stage. The results of the surrogate models generated by the ANN EVP method are presented in Figure 11.

4.2. Single-Objective Constrained Optimization

For the single-objective constrained optimization, the threshold value of the 5% quantile is prescribed as $P_{\mathrm{tr}} = 500\,\mathrm{N}$. To guarantee satisfaction of the constraint, a comparatively large penalty factor of $\beta = 10^4$ is adopted. Figure 12 illustrates the constraint of the 5% quantile $q_{0.05,c}(P_{\mathrm{cr}})$ and the modified objective function $\tilde{z}$, see Eq. (14), over the design space, shown for the ANN EVP strategy. In addition, the corresponding optimum $(t_{\mathrm{opt}}, \alpha_{\mathrm{opt}})$ is indicated.

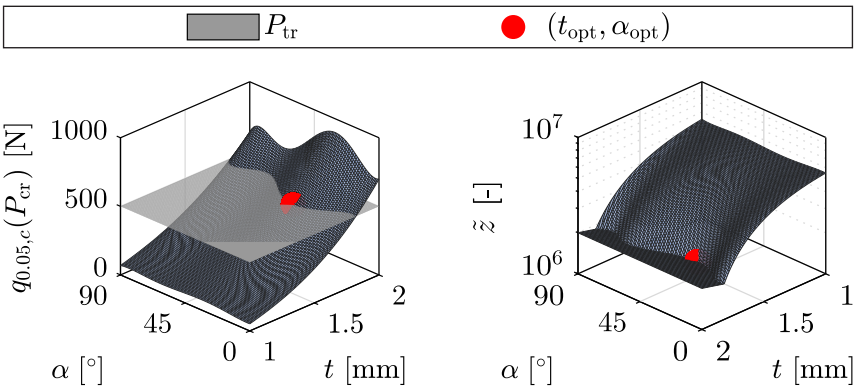


Figure 12. Determination of the optimum $(t_{\mathrm{opt}}, \alpha_{\mathrm{opt}})$ for the single-objective constrained optimization using the ANN EVP method, shown for the constraint $q_{0.05,c}(P_{\mathrm{cr}})$ (left) and the modified objective function $\tilde{z}$ (right)

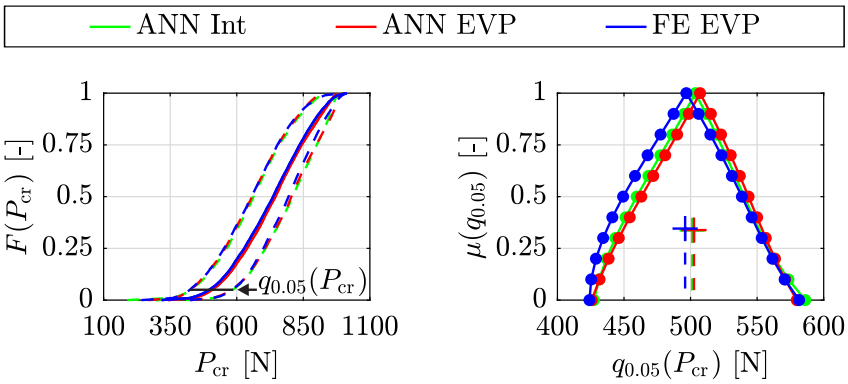


Figure 13. Fuzzy CDF and fuzzy 5% quantile $q_{0.05}(P_{\mathrm{cr}})$ for the optimum $(1.68\,\mathrm{mm}, 31.0\,°)$ of the single-objective constrained optimization using the ANN Int, ANN EVP and FE EVP methods with $N_{\mathrm{MCS}} = 10^4$ and $N_F = 5$

Both methods identify similar optimal points $(1.685\,\mathrm{mm}, 30.66\,°)$ and $(1.684\,\mathrm{mm}, 31.21\,°)$. To derive the fuzzy stochastic output, the optimum is rounded to $(1.68\,\mathrm{mm}, 31\,°)$. For validation

purposes, a FE reference analysis is performed, in which the eigenvalue problem of the KLE is solved conventionally. The fuzzy CDF and the fuzzy 5% quantile of the critical load obtained with the methods ANN Int, ANN EVP and FE EVP are compared in Figure 13. To compute the fuzzy CDF, the probability $F(P_{\mathrm{cr}})$ is discretized with 100 quantile values. Overall, the close agreement among all approaches demonstrates the adequacy of the constructed ANN surrogate models in the constrained optimization setting.

4.3. Multi-Objective Unconstrained Optimization

According to the predictions of the surrogate models shown in Figure 11, the mean value of the critical load $E_c(P_{\mathrm{cr}})$ increases for larger thickness values t, whereas the coefficient of variation $CV_c(P_{\mathrm{cr}})$ decreases. Consequently, the multi-objective unconstrained optimum for maximizing $E_c(P_{\mathrm{cr}})$ and minimizing $CV_c(P_{\mathrm{cr}})$ is attained at the upper bound $t = 2\,\mathrm{mm}$, such that the optimization problem effectively reduces to one design variable α. The discrete weight factors of Chebyshev scaling in Eq. (17) are chosen as $w_1 = \{0, 0.05, 0.1, \ldots, 1\}$ with $w_2 = 1 - w_1$. Figure 14 presents the resulting Pareto fronts generated using the ANN Int and ANN EVP approaches in both the normalized and original objective spaces. In addition, the optimal fiber orientation α_{opt} is shown with respect to the weight factor w_1.

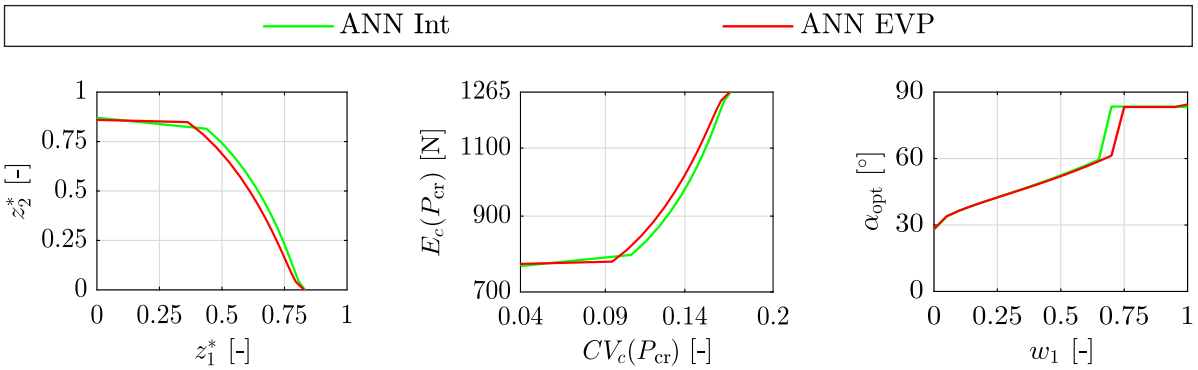


Figure 14. Results of the multi-objective unconstrained optimization using the ANN Int and ANN EVP methods: Pareto fronts in the normalized objective space (left) and original objective space (middle), and the corresponding optimum α_{opt} as a function of the weight factor w_1 (right)

Both methods produce closely matching results, confirming the suitability of the developed ANN surrogate models. With respect to the coefficient of variation, the minimum and, thus, the highest robustness are attained at $\alpha \approx 84\,°$, whereas the mean value reaches its maximum at $\alpha \approx 28\,°$, corresponding to the highest structural performance. In contrast to the single-objective constrained optimization with a unique optimum, a trade-off between robustness and performance is required to determine the final design. According to the individual preferences, the structural configuration can be selected from the set of Pareto-optimal solutions.

5. Conclusions

In this paper, a structural optimization framework incorporating fuzzy stochastic analysis was introduced. Therefore, random fields were generated within an MCS to represent aleatory uncertainty, while the correlation length of the KLE was treated as an epistemically uncertain input parameter. Structural optimization under polymorphic uncertainty substantially increases the computational effort because a large number of samples is required. Consequently, the use of efficient surrogate models becomes indispensable. Surrogate modeling was employed at three different stages. First, an ANN replaced FE calculations within the MCS. Moreover, an LSQ polynomial surrogate model was used for the α-level optimization and additional LSQ models were constructed to conduct the structural optimization within the design space.

Introducing the correlation length as a fuzzy variable further increases the computational cost, since the eigenvalue problem of the KLE has to be solved for each considered value of ℓ_c, which is particularly time-consuming for fine spatial discretizations. To mitigate this expense, an interpolation-based strategy was proposed and assessed against the conventional solution of the KLE eigenvalue problem. Separate neural networks were trained for both approaches and subsequently applied in two optimization settings. The single-objective constrained formulation targeted a reduction in structural mass while maintaining sufficient load-bearing capacity, resulting in a distinct optimum. In contrast, the multi-objective unconstrained formulation yielded a set of Pareto-optimal solutions, balancing structural performance and robustness.

Overall, both ANNs produced closely matching results. Thus, the proposed interpolation-based method constitutes an efficient alternative to repeatedly solving the eigenvalue problem of the KLE. In future studies, the correlation length could be derived from experimental surface measurements. The epistemic uncertainty caused by the limited amount of available data can be naturally incorporated into the developed computational framework. Additionally, alternative surrogate modeling techniques may be explored. For instance, convolutional neural networks can be used to predict the structural load-bearing capacity based on representations of geometric imperfections. Extending such approaches to account for epistemically uncertain correlation lengths that influence the spatial characteristics of the generated random fields represents a promising direction for further research.

References

Batoz, J.-L. and G. Dhatt: 1979, 'Incremental Displacement Algorithms for Nonlinear Problems'. *International Journal for Numerical Methods in Engineering* **14**(8), 1262–1267.

Böttcher, M., W. Graf, and M. Kaliske: 2023, 'Designing Structures with Polymorphic Uncertainty: Enhanced Decision Making Using Information Reduction Measures to Quantify Robustness'. *PAMM* **23**(4), e202300289.

Boyd, S. P. and L. Vandenberghe: 2004, *Convex Optimization*. Cambridge University Press.

Brenner, C.: 1995, 'Ein Beitrag Zur Zuverlässigkeitsanalyse von Strukturen Unter Berücksichtigung von Systemuntersuchungen Mit Hilfe Der Methode Der Stochastischen Finiten Elemente'. Ph.D. thesis, Fakultät für Bauingenieurwesen und Architektur, Universität Innsbruck.

Der Kiureghian, A. and O. Ditlevsen: 2009, 'Aleatory or Epistemic? Does It Matter?'. *Structural Safety* **31**(2), 105–112.

Donnell, L. H. and C. C. Wan: 1950, 'Effect of Imperfections on Buckling of Thin Cylinders and Columns Under Axial Compression'. *Journal of Applied Mechanics* **17**(1), 73–83.

Fina, M. and C. Bisagni: 2025, 'Buckling Design Optimization of Tow-Steered Composite Panels and Cylindrical Shells Considering Aleatory and Epistemic Uncertainties'. *Computational Mechanics* **76**(1), 59–92.

Fina, M., W. Wagner, and W. Graf: 2023, 'On Polymorphic Uncertainty Modeling in Shell Buckling'. *Computer-Aided Civil and Infrastructure Engineering* **38**(18), 2632–2647.

Fina, M., P. Weber, and W. Wagner: 2020, 'Polymorphic Uncertainty Modeling for the Simulation of Geometric Imperfections in Probabilistic Design of Cylindrical Shells'. *Structural Safety* **82**, 101894.

Götz, M., W. Graf, and M. Kaliske: 2015, 'Structural Design with Polymorphic Uncertainty Models'. *International Journal of Reliability and Safety* **9**(2/3), 112–131.

Gruttmann, F. and W. Wagner: 2006, 'Structural Analysis of Composite Laminates Using a Mixed Hybrid Shell Element'. *Computational Mechanics* **37**(6), 479–497.

Gürdal, Z., B. F. Tatting, and C. K. Wu: 2008, 'Variable Stiffness Composite Panels: Effects of Stiffness Variation on the in-Plane and Buckling Response'. *Composites Part A: Applied Science and Manufacturing* **39**(5), 911–922.

Lauterbach, S., M. Fina, and W. Wagner: 2018, 'Influence of Stochastic Geometric Imperfections on the Load-Carrying Behaviour of Thin-Walled Structures Using Constrained Random Fields'. *Computational Mechanics* **62**(5), 1107–1125.

Lin, X., X. Zhang, Z. Yang, F. Liu, Z. Wang, and Q. Zhang: 2024, 'Smooth Tchebycheff Scalarization for Multi-Objective Optimization'. *Proceedings of the 41th International Conference on Machine Learning*.

Miler, D., M. Hoić, R. Tomić, A. Jokić, and R. Mašović: 2025, 'Simultaneous Multi-Objective and Topology Optimization: Effect of Mesh Refinement and Number of Iterations on Computational Cost'. *Computation* **13**(7), 168.

Möller, B. and M. Beer: 2004, *Fuzzy Randomness*. Berlin, Heidelberg: Springer.

Möller, B., W. Graf, and M. Beer: 2000, 'Fuzzy Structural Analysis Using α-Level Optimization'. *Computational Mechanics* **26**(6), 547–565.

Schenk, C. A. and G. I. Schuëller: 2007, 'Buckling Analysis of Cylindrical Shells with Cutouts Including Random Boundary and Geometric Imperfections'. *Computer Methods in Applied Mechanics and Engineering* **196**(35), 3424–3434.

Schietzold, F. N., A. Schmidt, M. M. Dannert, A. Fau, R. M. N. Fleury, W. Graf, M. Kaliske, C. Könke, T. Lahmer, and U. Nackenhorst: 2019, 'Development of Fuzzy Probability Based Random Fields for the Numerical Structural Design'. *GAMM-Mitteilungen* **42**(1), e201900004.

Schweizer, M., M. Fina, W. Wagner, and S. Freitag: 2025a, 'Artificial Neural Networks for Random Fields to Predict the Buckling Load of Geometrically Imperfect Structures'. *Computational Mechanics* **76**(1), 181–204.

Schweizer, M., M. Fina, W. Wagner, and S. Freitag: 2025b, 'Optimization of Shell Structures with Fuzzy Probability-Based Random Fields Using Artificial Neural Networks'. *PAMM* **25**(4), e70038.

Siarry, P. (ed.): 2016, *Metaheuristics*. Cham: Springer International Publishing.

Sudret, B. and A. Der Kiureghian: 2000, *Stochastic Finite Element Methods and Reliability: A State-of-the-Art Report*. Departement of Civil & Environmental Engineering, University of California, Berkeley.

Vanmarcke, E.: 2010, *Random Fields: Analysis and Synthesis*. Singapore: World Scientific Publishing Co. Pte. Ltd., revised and expanded new edition.

Wagner, W.: 1995, 'A Note on FEM Buckling Analysis'. *Communications in Numerical Methods in Engineering* **11**(2), 149–158.

Wagner, W. and F. Gruttmann: 1994, 'A Simple Finite Rotation Formulation for Composite Shell Elements'. *Engineering Computations* **11**(2), 145–176.

Wagner, W. and F. Gruttmann: 2005, 'A Robust Non-Linear Mixed Hybrid Quadrilateral Shell Element'. *International Journal for Numerical Methods in Engineering* **64**(5), 635–666.

Wagner, W. and P. Wriggers: 1988, 'A Simple Method for the Calculation of Postcritical Branches'. *Engineering Computations* **5**(2), 103–109.

Yang, H., S. Feng, P. Hao, X. Ma, B. Wang, W. Xu, and Q. Gao: 2022, 'Uncertainty Quantification for Initial Geometric Imperfections of Cylindrical Shells: A Novel Bi-Stage Random Field Parameter Estimation Method'. *Aerospace Science and Technology* **124**, 107554.

Zhang, J. and B. Ellingwood: 1994, 'Orthogonal Series Expansions of Random Fields in Reliability Analysis'. *Journal of Engineering Mechanics* **120**(12), 2660–2677.

Random field modeling approach for uncertainty quantification of reused concrete elements

Luigi Schiano[1], Marc Fina[1], Razhan S. Ahmed[2], Oleksandr Al-Shboul[3], David Ringeloth[4], Vladislav Gudžulić[2], Stefanie Schoen[2], Jelena Bijeljic[4,5], Ernst Niederleithinger[4], Iurie Curoșu[3], Gerrit E. Neu[2], Steffen Freitag[1]

[1] *Institute for Structural Analysis, Karlsruhe Institute of Technology, 76131 Karlsruhe, Germany; luigi.schiano@kit.edu, marc.fina@kit.edu, steffen.freitag@kit.edu*

[2] *Institute for Structural Mechanics, Ruhr University Bochum, 44801 Bochum, Germany; razhan.ahmed@rub.de, vladislav.gudzulic@rub.de, stefanie.m.schoen@rub.de, gerrit.neu@rub.de*

[3] *Chair of Construction Materials, Ruhr University Bochum, 44801 Bochum, Germany; Oleksandr.Al-Shboul@rub.de, iurie.curosu@rub.de*

[4] *Division 8.2 NDT Methods for Civil Engineering, Bundesanstalt für Materialforschung und -prüfung, 12205 Berlin, Germany; david.ringeloth@bam.de, Ernst.Niederleithinger@bam.de*

[5] *University of Niš, Faculty of Civil Engineering and Architecture, 18000 Niš, Serbia; jelena.bijeljic@gaf.ni.ac.rs*

Abstract. Global sustainability goals require the reduction of waste and CO_2 emissions, motivating the reuse of reinforced concrete elements on a structural level. Assessing the structural reliability of such reused elements is particularly challenging, as their performance varies due to aging processes and exposure to environmental influences. In order to take these variabilities into account when performing structural analyses, the appropriate representation of uncertainty is crucial, see e.g. (Schoen, 2025). This contribution focuses on the generation of random fields for uncertainty quantification of spatially variable material properties of reused concrete elements, see (Botte et al., 2025). Correlation properties, such as correlation functions and lengths, are determined from measurement data (see e.g. (Fina et al., 2020)) of removed concrete elements obtained through destructive and non-destructive testing. The generated random fields are integrated into a nonlinear computational model of a reinforced concrete structure. Comprehensive probabilistic analyses are performed to show the influence of different random field approaches on the stochastic load-bearing capacity.

Keywords: Random fields, Uncertainty quantification, Reused concrete elements, Measurement data.

1. Introduction

Limited resources require a circular economy in which materials are continuously reused and recycled. Nonetheless, in structural engineering, the majority of buildings are typically still demolished, which often triggers a fatal downcycling process. However, the lack of reuse is not due to capacity deficits, but rather to utilization limits and construction regulations (Mark et al., 2025). In order

© 2026 by the author(s). This work is licensed under the Creative Commons Attribution 4.0 International License (CC BY 4.0), which permits unrestricted use, distribution, and reproduction in any medium, provided the original author and source are credited.

to reuse structural elements, a controlled demolition process and a comprehensive assessment of their condition are required. This should be done in a fast and economical, but reliable and representative manner (Curoșu et al., 2025). Especially ensuring the reliability, which is the central task in structural design, becomes more difficult with reused elements, as geometric and material properties are not or only imprecisely known. Therefore, uncertainties have to be identified and quantified from measurements, preferably obtained from non-destructive testing, and the impact on the load bearing capacity has to be analyzed using simulation models.

Some material and geometric parameters, such as Young's modulus, strength, thickness, the position of the reinforcement, and deviations from the reference geometry (geometric imperfections), can vary spatially. Therefore, defining these parameters as uncorrelated random variables is no longer meaningful. The spatial variability of the parameters can be quantified using random fields. Structural responses, such as displacements or load-bearing capacities, can depend on the correlation properties of the random field, which are characterized by its auto-correlation function and correlation length. Several works in the literature address the definition of correlation properties. For example, (Faes et al., 2022) explore the properties of the auto-correlation function and illustrate the need for its finite differentiability. Eliáš et al. (Eliáš et al., 2015) model the material parameters of a concrete beam using auto-correlated random fields and analyze the influence of the correlation length on peak load, energy dissipation, and crack location. Lauterbach et al. (Lauterbach et al., 2018) quantitatively investigate the influence of the correlation length of random geometric imperfection fields on the stochastic buckling response of shell structures using the Karhunen-Loève Expansion (KLE). The correlation structure of the random field can be identified from experimental data, as demonstrated by Schenk et al. (Schenk and Schuëller, 2003), who employed a spectral decomposition of the covariance matrix estimated from imperfection measurements. Alternatively, Broggi and Schuëller (Broggi and Schuëller, 2011) and Papadopoulos et al. (Papadopoulos et al., 2009) use evolutionary spectra to generate random imperfections of cylindrical shells. Often, assumptions of Gaussian random fields and homogeneity are made to estimate the covariance structure. To account for the spatial non-homogeneity of geometric imperfections due to the manufacturing process, Fina et al. (Fina et al., 2026) present a non-homogeneous random field approach for the probabilistic buckling analysis of suction bucket foundations for offshore wind turbines.

A random field describes the inherent natural variability of a spatially varying quantity, i.e., the aleatory uncertainty. However, when only a limited number of measurements are available, accurately determining its correlation properties becomes challenging. This introduces an additional source of uncertainty, namely epistemic uncertainty, which results from the limited amount of available data. Consequently, both aleatory and epistemic uncertainties must be considered when characterizing the correlation structure of the random field. An overview of epistemic extensions to the aleatoric approach of random fields is given in (Schietzold et al., 2019). Dannert et al. (Dannert et al., 2021) describe extended random fields, so-called imprecise random fields, for nonlinear concrete damage analysis, where the correlation length is treated as an interval. In (Schweizer et al., 2025; Fina and Bisagni, 2026), imprecise random fields are defined to model epistemic uncertainty in shell imperfections. A fuzzy correlation model to extract correlation lengths from shell imperfection measurements, considering the limited amount of data, is introduced in (Fina

et al., 2020). A sensitivity analysis of the extracted correlation length on the buckling behavior of shells is shown in (Fina et al., 2021).

In this paper, a reinforced concrete beam is investigated, which was extracted in a controlled manner from a campus building at Ruhr University Bochum. Measurements from rebound hammer testing, used as a non-destructive indicator of the compressive strength, show spatially variable material properties; see (Al-Shboul et al., 2026b). The focus of this paper lies on the estimation of correlation properties from such measurements of a reused concrete element. The random field realizations of the compressive strength are then integrated into a nonlinear computational model of the tested concrete beam. Comprehensive probabilistic analyzes are performed to demonstrate the influence of different correlation structures on the stochastic load-bearing capacity.

2. Random Fields

In this paper, variations of material parameters are modeled as correlated random fields. The basic theory is therefore briefly explained, based on (Sudret and Der Kureghian, 2000). For a given domain $\Omega \subseteq \mathbb{R}^d$ a random field $H(\mathbf{x}, \theta)$ is a collection of random variables that are assigned to each location vector $\mathbf{x} \in \Omega$ in the domain. Consequently, for a fixed $\mathbf{x}_0$, $H(\mathbf{x}_0, \theta)$ describes a random variable, with $\theta \in \Theta$ denoting the outcome, where Θ is a set of all possible outcomes. On the other hand, for a fixed outcome θ_0, $H(\mathbf{x}, \theta_0)$ describes a realization of the random field, as illustrated in Fig. 1.

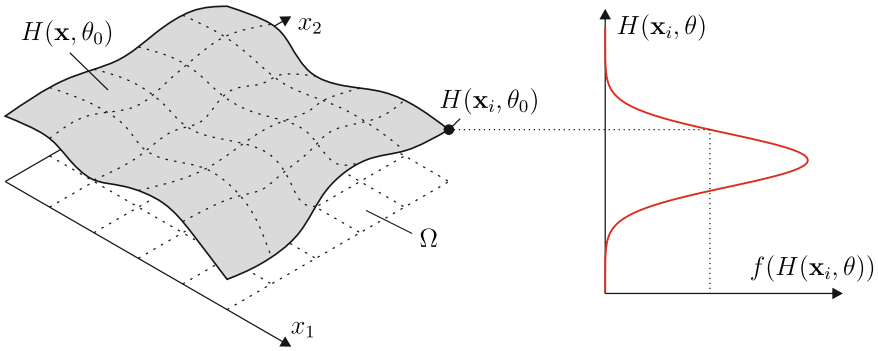


Figure 1. Realization of a random field

For the numerical implementation in a finite element model, the random field has to be discretized according to the finite element nodes. This can be done with various methods; here the so-called Karhunen-Loève expansion (KLE), see e.g. (Zhang and Ellingwood, 1994), is used. It is based on the spectral decomposition of the autocovariance function

$$C(\mathbf{x}_i, \mathbf{x}_j) = \sigma^2 \, \rho(\mathbf{x}_i, \mathbf{x}_j) \quad , \tag{1}$$

with the variance σ^2 and the autocorrelation function $\rho(\mathbf{x}_i, \mathbf{x}_j)$. The deterministic functions over which the random field is expanded then follow from the eigenvalue problem

$$\mathbf{C}\,\boldsymbol{\varphi}_i = \lambda_i\,\boldsymbol{\varphi}_i \quad \text{with} \quad \mathbf{C} = \sigma^2 \begin{bmatrix} \rho(\mathbf{x}_1, \mathbf{x}_1) & \dots & \rho(\mathbf{x}_1, \mathbf{x}_N) \\ \vdots & \ddots & \vdots \\ \rho(\mathbf{x}_N, \mathbf{x}_1) & \dots & \rho(\mathbf{x}_N, \mathbf{x}_N) \end{bmatrix} \;, \tag{2}$$

where the autocovariance matrix $\mathbf{C}$ is obtained by evaluating the autocorrelation function for every pair $(\mathbf{x}_i, \mathbf{x}_j)$ of the N finite element nodes. With the eigenvalues λ_i and eigenvectors $\boldsymbol{\varphi}_i$ the KLE can be written as

$$\hat{H}(\mathbf{x}, \theta) = \mu + \sum_{i=1}^{M} \sqrt{\lambda_i}\,\xi_i(\theta)\,\varphi_i(\mathbf{x}) \;, \tag{3}$$

where μ denotes the mean value and $\xi_i(\theta)$ a set of random variables. In the case of a Gaussian random field – that is, every vector $\{H(\mathbf{x}_1), \dots, H(\mathbf{x}_n)\}$ is gaussian – the $\xi_i(\theta)$ form a set of uncorrelated standard normal variables $\xi_i(\theta) \sim \mathcal{N}(0, 1)$. In this paper, for the autocorrelation function a quadratic exponential function is used

$$\rho(\mathbf{x}_i, \mathbf{x}_j) = \exp\left[-\frac{d(\mathbf{x}_i, \mathbf{x}_j)^2}{\ell_c^2}\right] \quad \text{with} \quad d(\mathbf{x}_i, \mathbf{x}_j) = |\mathbf{x}_i - \mathbf{x}_j| \;, \tag{4}$$

which depends only on the correlation length ℓ_c and the distance $d(\mathbf{x}_i, \mathbf{x}_j)$ of the considered finite element nodes, see Fig. 2.

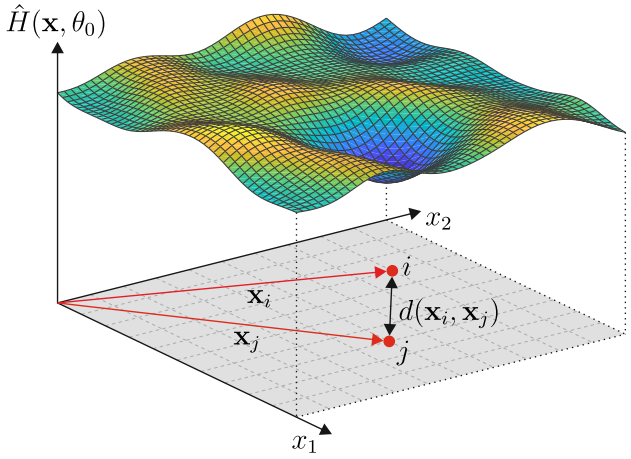


Figure 2. Realization of the Karhunen-Loêve-Expansion of a random field

The correlation length is a parameter that controls the distance in which points correlate with each other. For example, if $\ell_c \to \infty$ then all points fully correlate and every realization is a constant value. If $\ell_c \to 0$ then every point is independent and a realization of the random field is highly fluctuating. In this paper, the mean value and the variance are constant values, and the correlation

function is, as already mentioned, only dependent on the distance. In this case the random field is called homogeneous.

3. Estimation of Correlation Parameters

In order to generate random fields for the uncertainty quantification of material parameters, correlation parameters such as the correlation length or the appropriate correlation function have to be determined from experimental data. In a first step, the sample mean value and variance can be estimated according to the following formulas

$$\bar{\mu}(\mathbf{x}_i) = \frac{1}{n_{smp}} \sum_{n=1}^{n_{smp}} H(\mathbf{x}_{i,n}) \ , \quad \bar{\sigma}^2(\mathbf{x}_i) = \frac{1}{n_{smp}-1} \sum_{n=1}^{n_{smp}} (H(\mathbf{x}_{i,n}) - \mu(\mathbf{x}_i))^2 \ , \tag{5}$$

where n_{smp} denotes the number of samples. For the variance, the unbiased estimator is used, as indicated by the denominator $n_{smp}-1$. The covariance between two random variables is defined as

$$C(\mathbf{x}_i, \mathbf{x}_j) = \mathbb{E}\left[(H(\mathbf{x}_i) - \mu(\mathbf{x}_i))(H(\mathbf{x}_j) - \mu(\mathbf{x}_j))\right] \tag{6}$$

and can be estimated analogously by

$$\bar{C}(\mathbf{x}_i, \mathbf{x}_j) = \frac{1}{n_{smp}-1} \sum_{n=1}^{n_{smp}} (H(\mathbf{x}_{i,n}) - \bar{\mu}(\mathbf{x}_i))(H(\mathbf{x}_{j,n}) - \bar{\mu}(\mathbf{x}_j))) \ . \tag{7}$$

In Fig. 3, a covariance matrix C with a quadratic exponential function and a variance $\sigma^2 = 1$ is illustrated, as well as the estimation of the covariance matrix $\bar{C}$ from 100 realizations of the KLE of the corresponding random field.

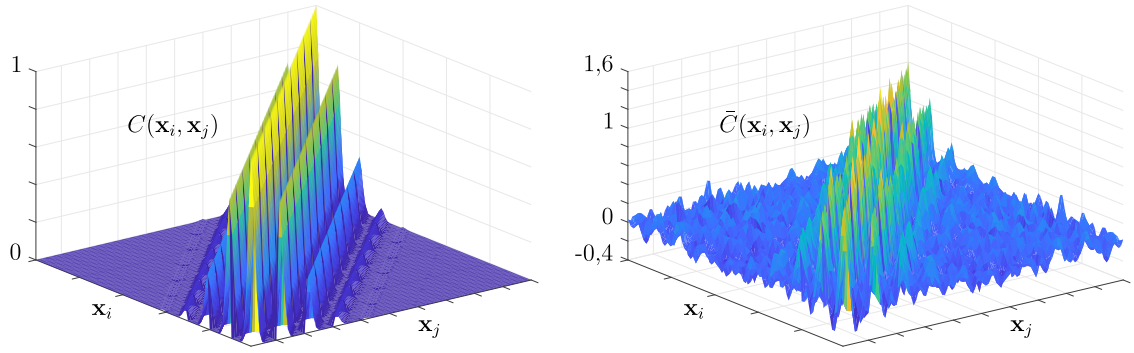


Figure 3. Covariance matrix C with quadratic exponential correlation function and variance $\sigma^2 = 1$ (left) and its estimation $\bar{C}$ from $n_{smp} = 100$ Samples (right)

Of course, the quality of the estimation directly depends on the number of samples used and according to the law of large numbers for $n_{smp} \to \infty$ it has to follow that $\bar{C} \to C$.

For the determination of the correlation length, in the next step, the autocorrelation function has to be estimated. As the goal of future work is to model the correlation length as a epistemic uncertain parameter, that is, as an interval or fuzzy variable, it has to be determined sample-wise. This can be achieved by computing the covariance matrix for each sample according to Eq. (7) and then – as the correlation function depends on the distance – sorting the covariances by the distance of the node pairs. All correlation values for one distance are finally averaged in order to obtain the correlation function for one sample. This is illustrated in Fig. 4 for one realization of a one dimensional random field with a length of 10 and a discretization with 50 nodal points.

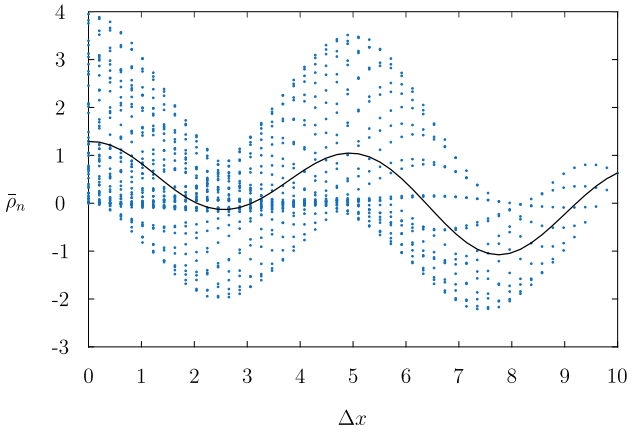


Figure 4. Correlation function $\bar{\rho}_n$ for one realization of a one dimensional random field with length of 10 and 50 nodal points, computed by averaging the correlations for each distance Δx

This approach can be expressed for the one-dimensional case with the following formula

$$\bar{\rho}_n(\xi\,\Delta x_0) = \frac{1}{N-\xi}\sum_{i=1}^{N-\xi}\frac{\left[H(x_{i,n}+\xi\,\Delta x_0)-\bar{\mu}(x_i+\xi\,\Delta x_0)\right]\left[H(x_{i,n})-\bar{\mu}(x_i)\right]}{\bar{\sigma}(x_i+\xi\,\Delta x_0)\,\bar{\sigma}(x_i)}\ , \tag{8}$$

where the correlation function $\bar{\rho}_n$ is calculated for every multiple ξ of the distance Δx_0. Here, all correlations for one fixed distance are directly computed and averaged. Obviously, the grid has to be uniform in this case. If the random field is two-dimensional, the correlation function can either be estimated separately for each direction or together for both directions. In the latter case, also diagonal distances are taken into account when computing the correlation function. Finally, the correlation length follows from a least squares fit with a chosen correlation function, for example the quadratic exponential correlation function defined in Eq. (4).

4. Numerical Model

In order to investigate the influence of the spatial variability of concrete properties on the structural response of reused reinforced concrete elements, a material-nonlinear finite element framework is employed. To make reliable predictions regarding the load-bearing capacity and fracture behavior,

a modeling approach based on the discrete representation of cracks using zero-thickness cohesive interface elements is adopted. All material nonlinearities associated with concrete cracking under tension are described by a cohesive-frictional traction–separation relationship of the interface elements, which are inserted between the solid finite elements. Reinforcement bars are explicitly modeled using beam elements with an elastic-plastic constitutive law to account for yielding of the reinforcement. The bond-slip mechanism between the concrete and the reinforcement is represented by a bond-slip law that couples the beam element nodes to the surrounding concrete matrix according to the fib Model Code. Further details regarding the modeling approach and extensive validations can be found in (Gudžulić, 2024; Neu, 2023).

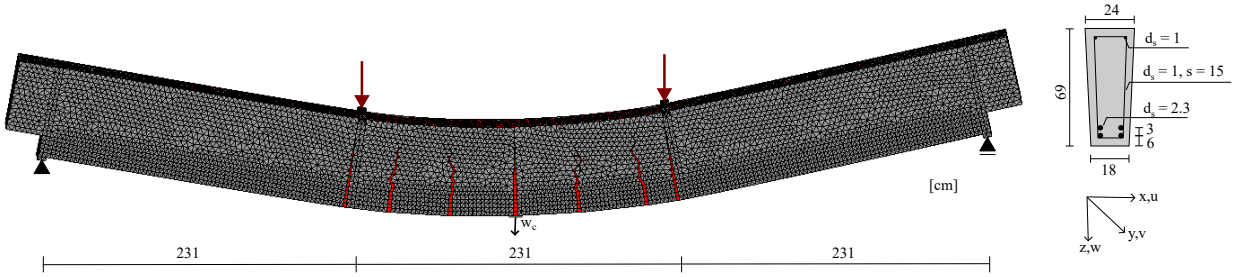


Figure 5. Numerical model of the extracted beam to predict its load-bearing capacity

The finite element model of the investigated beam is shown in Fig. 5. The beam is discretized using 177410 three-dimensional tetrahedral elements with characteristic element sizes ranging between 30 and 70 mm. The applied loading is introduced in a displacement-controlled manner to ensure a stable tracing of the structural response up to failure. The beam is supported from below at its outer edges and loaded at the quarter points in a four-point bending test.

To account for the material heterogeneity commonly observed in existing concrete structures, the concrete compressive strength is represented by a spatially correlated random field. The statistical properties of the random field are derived from the experimental measurements presented in section 5. For each realization, the random field is generated on a structured three-dimensional rectangular grid consisting of 72 072 grid points, which fully encloses the finite element model. The generated field is subsequently mapped onto the finite element mesh according to the spatial coordinates of the integration points.

Since the adopted discrete crack formulation is governed by interface properties rather than the compressive strength directly, the local compressive strength values are converted into the corresponding tensile strength and fracture energy using the empirical relationships given in Eurocode 2 (DIN, 2011) and the CEB-FIP Model Code (fib – fédération internationale du béton, 2013). The tensile strength is determined as

$$f_t = \begin{cases} 0.30\, f_c^{2/3}, & f_c \leq 50 \text{ MPa}, \\ 2.12 \ln\left(1 + \dfrac{f_c + 8}{10}\right), & f_c > 50 \text{ MPa}, \end{cases} \tag{9}$$

while the mode-I fracture energy is calculated according to

$$G_F = G_{F0} \left(\frac{f_c + 8}{10} \right)^{0.7}, \tag{10}$$

where $G_{F0} = 0.030$ N/mm corresponds to a maximum aggregate size of 16 mm. Consequently, both the tensile strength and fracture energy vary spatially according to the generated compressive strength field and directly govern crack initiation and propagation through the cohesive interface elements. In contrast, Young's modulus is kept constant for all realizations, such that the elastic stiffness and stress field remain deterministic, while the spatial variability is introduced exclusively through the fracture-related material properties.

5. Example

In the following, measurement data for the compressive strength from rebound hammer testing are analyzed. The data were obtained by the Chair of Construction Materials within the framework of the collaborative research center 1683. The broader non-destructive and destructive testing measurement campaign on the investigated elements from Ruhr University Bochum is reported in (Al-Shboul et al., 2026a). With the rebound hammer values, the surface hardness can be determined and consequently the compressive strength of the concrete can be estimated. The test was performed on several reference concrete elements, that were dismantled on the campus of Ruhr University in Bochum. In this section, data from one reinforced concrete beam with a length of 747 cm and a trapezoidal cross section with a height of 69 cm and a width of 24 cm at the top and 18 cm at the bottom (see Fig. 6), are examined regarding the generation of random fields. Fig. 6 shows a photo of the beam after cutting its edges.



Figure 6. Extracted reinforced concrete beam with cutted edges and testing areas marked in red, from (Al-Shboul et al., 2026b)

The red areas mark where the rebound hammer values were taken. Each of the 18 areas contains 11 values, resulting in a total of 198 values. Looking at the histogram of all rebound hammer values in Fig. 7, it can be seen that the data are approximately normally distributed. That is why in the following a Gaussian random field is assumed.

Although the 11 values in one area are not measured in the exact same position, they are given the same coordinate. Then, the 11 values can be treated as realizations of random variables at these locations. Furthermore, combinations of the values over all 18 spots represent realizations of

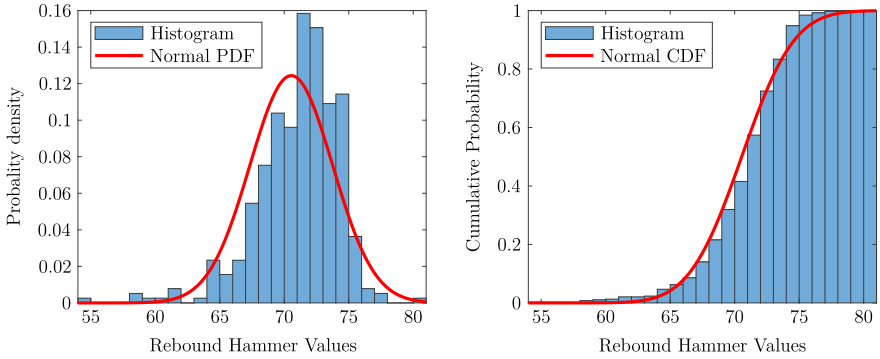


Figure 7. Histogram of rebound hammer data and fit of normal probability density function (left) and normal cumulative distribution function (right)

a random field and therefore serve as samples for the estimation of the correlation length. In total, there are 11^{18} possible combinations of all values. Out of these samples, the correlation function can be estimated and then fitted in order to obtain the correlation length. Fig. 8 shows the correlation function obtained as the mean of all correlation functions in red and the least squares fit in black. It can be seen that in the x-direction the fit closely matches the data, whereas in the z-direction the quadratic exponential function cannot exactly represent the wavy behavior of the correlation function. The determined mean values for the correlation length show, that the behavior of the random field is anisotropic, as the correlation lengths in x- and z-directions differ significantly from one another. This cannot be captured with one single correlation length in both directions and, therefore, in the following only the separate correlation lengths $\ell_{c,x}$ and $\ell_{c,z}$ are considered.

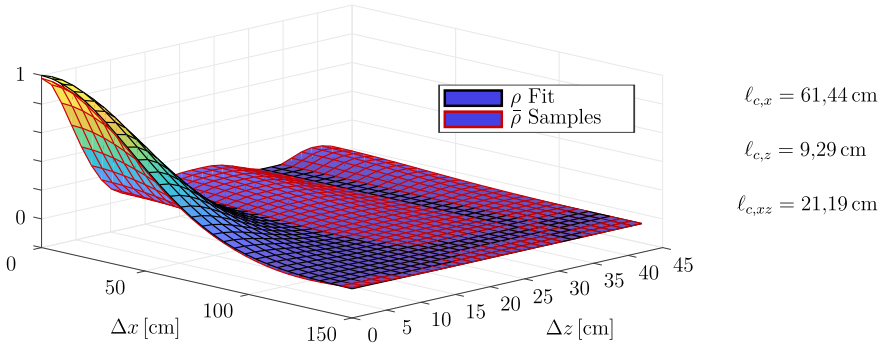


Figure 8. Mean correlation function and least squares fit for the rebound hammer measurements

Fig. 9 shows the histograms of the two correlation lengths with the minimum, maximum, and mean values. The frequency is especially high between zero and the mean value, whereas in the higher areas the values spread more and there are some outliers.

For the analysis with the numerical presented in Section 4, only the minimum, mean, and maximal values of the correlation lengths, shown in Fig. 9 are used, as the calculation is time-consuming. For the same reason, for each set of correlation lengths, only 10 realizations of the KLE of the corresponding random field are used, in order to get a first estimation of the influence of the

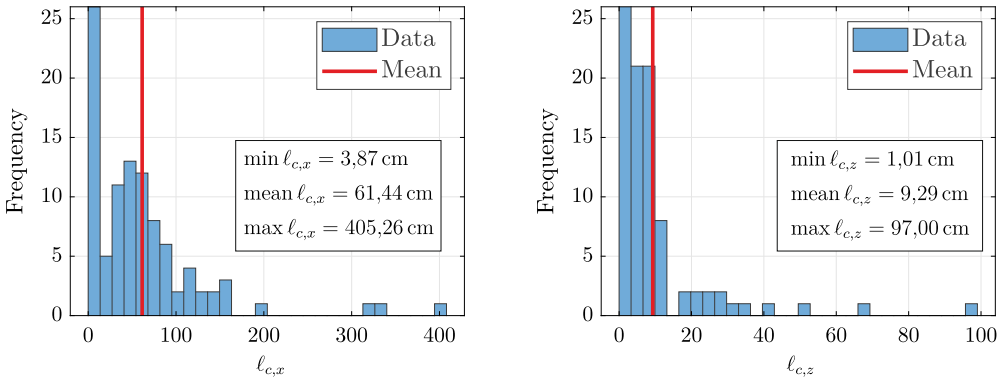


Figure 9. Histogram of the correlation lengths in x- and z-direction determined from 100 Samples

rebound hammer values on the load-bearing capacity. In total, 30 realizations of the three random fields are being computed. One realization for the mean correlation lengths $\ell_{c,x} = 61{,}44\,\text{cm}$ and $\ell_{c,z} = 9{,}29\,\text{cm}$ is shown in Fig. 10.

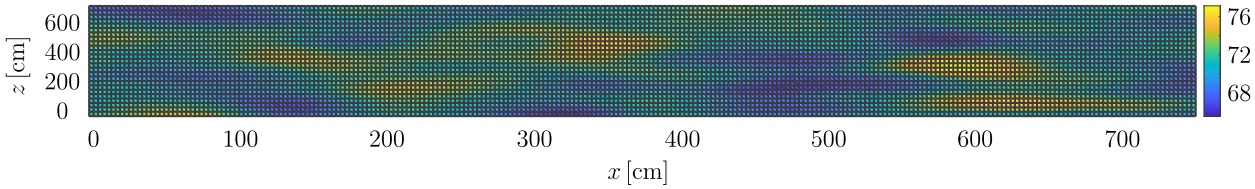


Figure 10. Realization of the KLE of the random Field of the rebound hammer values with correlation lengths $\ell_{c,x} = 61{,}44\,\text{cm}$ and $\ell_{c,z} = 9{,}29\,\text{cm}$

Fig. 11 presents the resulting bending moment-deflection curves of the numerical model for the three different sets of correlation lengths investigated. The colored curves represent the results from the realizations of the random fields of compressive strength. It can be seen that the random fields of the compressive strength have no significant effect on the load-bearing capacity in this investigated problem.

However, it was observed that the different random fields do have an influence on the crack pattern of the beam. This is illustrated in Fig. 12, where two crack patterns and the corresponding realizations of the random fields of the compressive strength are shown. The top one belongs to the set of minimal correlation lengths, and the bottom one corresponds to the set of maximal correlation lengths. For the realization with the maximum correlation lengths, fewer but larger cracks can be observed with a maximum crack width of 6,76 mm, whereas for the realization with the minimum correlation lengths, more but smaller cracks appear with a maximum crack width of 5,54 mm.

Further analysis on the effect of rebar corrosion in (Al-Shboul et al., 2026b) has shown that the problem is very sensitive to the rebar diameter. In the analysis the rebar diameter of the bottom longitudinal rebar was reduced from 23 to 20 mm, which should simulate corrosion of the rebar. However, it can also be interpreted as an inaccuracy in the detection of the rebar diameter. The high sensitivity indicates that the load-bearing capacity depends primarily on the rebar. The bending

moment-deflection curve with rebar corrosion is also shown in Fig. 11 and has a significantly lower maximum bending moment. Therefore, in further investigations the effect of random field modeling of the rebar diameter or the tensile strength of the rebar will be examined.

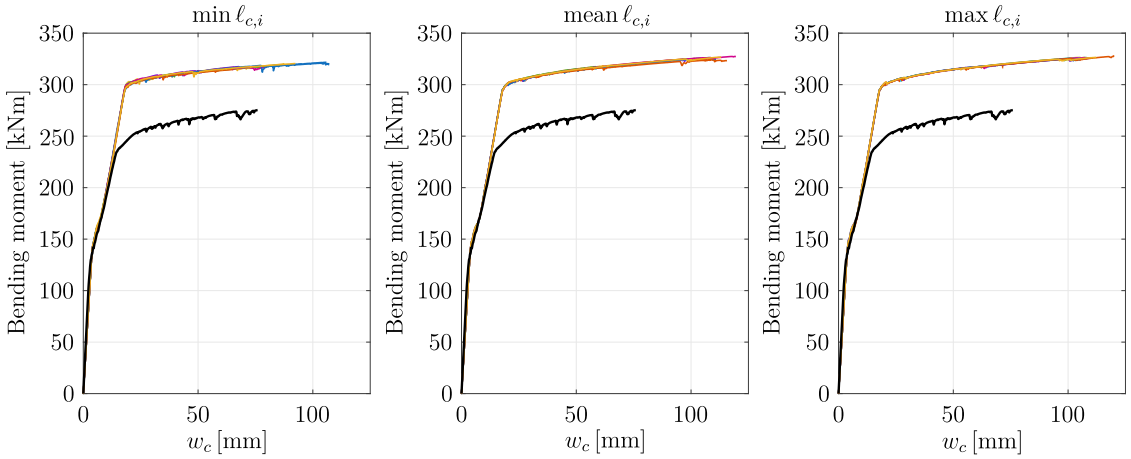


Figure 11. Bending moment-deflection curves for the three investigated sets of correlation lengths; Realizations of the random field of compressive strength are the colored curves, the effect of rebar corrosion is shown in the black curve

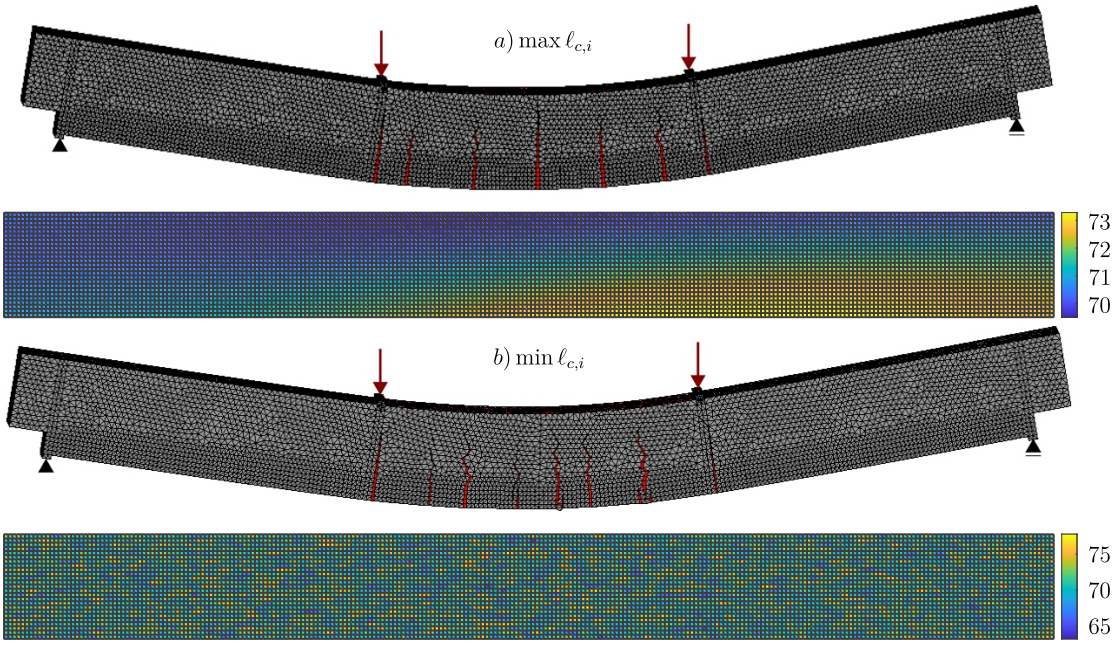


Figure 12. Crack patterns of the investigated beam and corresponding realizations of the random field of the compressive strength with a) the maximum set of correlation lengths max $\ell_{c,i}$ and b) the minimum set of correlation lengths min $\ell_{c,i}$

6. Conclusion

This study presents a way to estimate correlation parameters, such as the correlation length, out of measurement data for the modeling of material or geometric parameters as random fields. This was shown examplarily for rebound hammer measurements at an extracted reinforced concrete beam from Ruhr University Bochum. For each combination of measurements, the correlation function was determined. The correlation length for each sample was obtained by fitting the correlation function to an assumed quadratic exponential function. With the minimum, maximum and mean values of the correlation lengths, random fields were generated with the Karhunen-Loève Expansion and integrated into a nonlinear computational model of the beam. Results show that in this investigated case, the load-bearing capacity of the beam is not very sensitive to the variation of the compressive strength. In contrast, the rebar diameter to be detected has a significantly higher influence on the maximum load-bearing capacity. Therefore, in future work the influence of random field modeling of the rebar properties, such as the diameter, Young´s modulus and yield stress is investigated. Furthermore, different random field approaches, such as non-homogeneous random fields and different correlation functions will be examined.

References

Al-Shboul, O., S. Abdul-Hafiz, D. Ringeloth, N. Roumia, E. Niederleithinger, W. Z. Taffese, S. Freitag, and I. Curoşu: 2026a, 'Prediction of the Chloride Ingress Resistance of Concrete Based on Non-Destructive Tests in the Context of Structural Reuse'. *Beton- und Stahlbetonbau* pp. 1–11.

Al-Shboul, O., R. Ahmed, S. Schoen, L. Schiano, D. Ringeloth, M. Fina, J. Bijeljic, G. E. Neu, E. Niederleithinger, S. Freitag, and I. Curoşu: 2026b, 'Quantification of Spatial Variability of Concrete Parameters for the Reliability Assessment of Reused Concrete Elements'. 16th fib International PhD Symposium in Civil Engineering, accepted.

Botte, W., E. Vereecken, and R. Caspeele: 2025, 'Random Field Modelling of Spatial Variability in Concrete – a Review'. *Structure and Infrastructure Engineering* **21**(6), 1047–1060.

Broggi, M. and G. Schuëller: 2011, 'Efficient modeling of imperfections for buckling analysis of composite cylindrical shells'. *Engineering Structures* **33**(5), 1796–1806.

Curoşu, I., D. Balzani, S. Freitag, G. E. Neu, E. Niederleithinger, S. Simon, and S. Weber: 2025, 'Methoden zur Bewertung abgebauter Stahlbetonelemente für deren Wiederverwendung'. *Bautechnik* **102**(8), 483–492.

Dannert, M., M. Faes, R. Fleury, A. Fau, U. Nackenhorst, and D. Moens: 2021, 'Imprecise random field analysis for non-linear concrete damage analysis'. *Mechanical Systems and Signal Processing* **150**, 107343.

DIN: 2011, 'Eurocode 2: Design of Concrete Structures – Part 1-1: General Rules and Rules for Buildings'. DIN EN 1992-1-1:2011-01.

Eliáš, J., M. Vořechovský, J. Skoček, and Z. Bažant: 2015, 'Stochastic discrete meso-scale simulations of concrete fracture: Comparison to experimental data'. *Engineering Fracture Mechanics* **135**, 1–16.

Faes, M. G., M. Broggi, P. D. Spanos, and M. Beer: 2022, 'Elucidating appealing features of differentiable auto-correlation functions: A study on the modified exponential kernel'. *Probabilistic Engineering Mechanics* **69**, 103269.

fib – fédération internationale du béton: 2013, *fib Model Code for Concrete Structures 2010*. Berlin, Germany: Ernst & Sohn.

Fina, M. and C. Bisagni: 2026, 'Neural Network-Based Structural Optimization of Tow-Steered Composite Panels accounting for Polymorphic Uncertainty'. *Composite Structures* **387**, 120323.

Fina, M., M. Böhm, S. Freitag, P. Schaumann, and E. Ghafoori: 2026, 'Probabilistic buckling analysis of suction bucket foundations for offshore wind turbines using non-homogeneous random fields'. *Journal of Constructional Steel Research* **245**, 110531.

Fina, M., L. Panther, P. Weber, and W. Wagner: 2021, 'Shell buckling with polymorphic uncertain surface imperfections and sensitivity analysis'. *ASCE-ASME Journal of Risk and Uncertainty in Engineering Systems Part B: Mechanical Engineering* **7**(2).

Fina, M., P. Weber, and W. Wagner: 2020, 'Polymorphic Uncertainty Modeling for the Simulation of Geometric Imperfections in Probabilistic Design of Cylindrical Shells'. *Structural Safety* **82**, 101894.

Gudžulić, V.: 2024, 'Virtual Lab for Mechanical Testing of Steel and Steel-Fiber Reinforced Concrete'. Ph.D. thesis, Ruhr University Bochum.

Lauterbach, S., M. Fina, and W. Wagner: 2018, 'Influence of stochastic geometric imperfections on the load-carrying behaviour of thin-walled structures using constrained random fields'. *Computational Mechanics* **62**(5), 1107–1125.

Mark, P., D. Sanio, D. Balzani, I. Curoșu, A. Hafner, M. König, B. Kuhlenkötter, M. Thewes, W. Baille, K. Hackl, P. Hagedorn, G. Meschke, T. Nestorović, G. E. Neu, R. Sauer, M. Tafili, A. Vogel, S. Weber, M. Wichern, T. Wichtmann, E. Niederleithinger, S. Freitag, A. Menges, and S. Simon: 2025, 'Modulares Wiederverwenden von Bestandstragwerken'. *Bautechnik* **102**(8), 424–435.

Neu, G. E.: 2023, 'Computational Approaches to a Robust Segmental Lining Design in Mechanized Tunneling'. Ph.D. thesis, Ruhr University Bochum.

Papadopoulos, V., G. Stefanou, and M. Papadrakakis: 2009, 'Buckling analysis of imperfect shells with stochastic non-Gaussian material and thickness properties'. *International Journal of Solids and Structures* **46**(14), 2800–2808.

Schenk, C. and G. Schuëller: 2003, 'Buckling analysis of cylindrical shells with random geometric imperfections'. *International Journal of Non-Linear Mechanics* **38**(7), 1119–1132.

Schietzold, F., A. Schmidt, M. Dannert, A. Fau, R. Fleury, W. Graf, M. Kaliske, C. Könke, T. Lahmer, and U. Nackenhorst: 2019, 'Development of fuzzy probability based random fields for the numerical structural design'. *GAMM-Mitteilungen* **42**(1), e201900004.

Schoen, S. M.: 2025, 'Reliability Analysis and Design of RC and SFRC Structures Considering Polymorphic Uncertainties'. Ph.D. thesis, Ruhr University Bochum.

Schweizer, M., M. Fina, W. Wagner, and S. Freitag: 2025, 'Optimization of shell structures with fuzzy probability-based random fields using artificial neural networks'. *Proceedings in Applied Mathematics and Mechanics (PAMM)* **25**(4), e70038.

Sudret, B. and A. Der Kureghian: 2000, 'Stochastic Finite Element Methods and Reliability A State-of-the-Art Report'. Technical report, Department of Civil & Environmental Engineering, University of California, Berkeley.

Zhang, J. and B. Ellingwood: 1994, 'Orthogonal Series Expansions of Random Fields in Reliability Analysis'. *Journal of Engineering Mechanics* **120**(12), 2660–2677.

Three-Dimensional Multivariable Non-Gaussian Random Field Modeling and Simulation of Concrete Constitutive Law

Jia-Hui Fu
Institute for Risk & Reliability, Leibniz University Hannover, Hannover 30167, Germany
School of Civil Engineering, Hefei University of Technology, Hefei 230009, China
Email: jiahui.fu@irz.uni-hannover.de

Yi Luo
Institute for Risk & Reliability, Leibniz University Hannover, Hannover 30167, Germany
Email: yi.luo@irz.uni-hannover.de

Meng-Ze Lyu
Institute for Risk & Reliability, Leibniz University Hannover, Hannover 30167, Germany
Email: mengze.lyu@irz.uni-hannover.de

Michael Beer
Institute for Risk & Reliability, Leibniz University Hannover, Hannover 30167, Germany
Department of Civil & Environmental Engineering, University of Liverpool, Liverpool L69 3GH, UK
International Joint Research Center for Engineering Reliability & Stochastic Mechanics & International Joint Research Center for Resilient Infrastructure, Tongji University, Shanghai 200092, China
Email: beer@irz.uni-hannover.de

Abstract: The constitutive behavior of concrete exhibits significant randomness and spatial variability, which necessitates a probabilistic description for accurate mechanical analysis. In this study, a comprehensive framework is developed for the unified representation and simulation of four key constitutive parameters (including elastic modulus, compressive strengths, peak compressive strains, and compressive shape parameters) using three-dimensional (3D) multivariate non-Gaussian random fields. The uncertainties are represented at three hierarchical levels: variable randomness (modeled via marginal distributions), inter-variable dependence (modeled via copulas), and spatial variability (captured by correlation functions). To achieve this, two novel concepts, i.e., the bridge function and the transformed correlation function, are introduced, enabling the generation of random fields that rigorously satisfy prescribed marginal distributions, cross-dependencies, and spatial correlations. For efficient simulation, the parsimonious stochastic harmonic function (SHF) is employed. Within this framework, the three-dimensional wavenumber domain is partitioned using a Voronoi tessellation scheme, enabling the spectrum-dependent random wavenumbers to be represented with a significantly reduced number of basic random variables. In addition, a starting-time phase evolution strategy is introduced to further minimize the number of random variables required for characterizing the random phases. As a result, only 28 basic random variables are sufficient to generate high-fidelity realizations of the four-variable dependent fields. The proposed approach provides a practical and computationally efficient tool for stochastic finite element analysis of concrete structures, enabling rigorous assessment of structural performance under material uncertainties.

© 2026 by the author(s). This work is licensed under the Creative Commons Attribution 4.0 International License (CC BY 4.0), which permits unrestricted use, distribution, and reproduction in any medium, provided the original author and source are credited.

Keywords: Concrete constitutive law; 3D multivariate non-Gaussian random fields; Vine copula; Probabilistic dependency; Spatial variability.

1. Introduction

Concrete is one of the most widely used construction materials in civil infrastructure, and the majority of existing engineering structures are constructed from concrete (Chen et al., 2025). Throughout their service life, these structures are subjected to various loading conditions (Ghanem and Spanos, 2003; Li and Chen, 2009), making the accurate assessment of their mechanical behavior and load-carrying capacity of paramount importance. However, uncertainties are inherently present in both materials and loading environments and therefore cannot be neglected in structural analysis and design (Lyu et al., 2024a, 2025b).

As demonstrated by Tao et al. (2020; 2023), concrete constitutive parameters are characterized by substantial randomness, spatial variability, and complex inter-parameter dependence. These three levels of uncertainty must be properly considered to achieve reliable predictions of structural performance and safety. Random fields provide an effective probabilistic framework for characterizing both the inherent randomness and spatial variability of material properties, and have therefore been widely employed for uncertainty modeling in engineering applications (Ghanem and Spanos, 2003; Li and Chen, 2009). However, most concrete constitutive parameters exhibit distinctly non-Gaussian behavior (Tao et al., 2020), rendering Gaussian random field models inadequate for accurate characterization. Moreover, practical concrete structures are inherently three-dimensional, while different constitutive parameters are often statistically dependent (Tao et al., 2020). Therefore, a realistic probabilistic description of concrete material properties necessitates the development of three-dimensional multivariate non-Gaussian random field models capable of simultaneously capturing marginal non-Gaussianity, spatial correlation, and inter-variable dependence.

Random field modeling plays a fundamental role in uncertainty quantification and propagation for concrete structures and serves as a prerequisite for random field simulation. In general, the randomness of individual variables is characterized by their marginal probability distributions (Benjamin and Cornell, 2014), spatial variability is described by autocorrelation functions in the physical domain or power spectral density functions in the frequency domain (Ghanem and Spanos, 2003), and probabilistic dependence among variables is commonly represented using copulas or vine copulas (Tao et al., 2020; Lyu et al., 2024b). Owing to their ability to decouple a multivariate joint probability density function into marginal distributions and copula density functions, copula-based approaches provide a flexible and efficient framework for modeling complex dependence structures (Lyu et al., 2024c).

However, for multivariate non-Gaussian random fields, these three probabilistic descriptions, i.e, marginal distributions, spatial correlations, and inter-variable dependence, are generally incompatible (Liu et al., 2026; Fu et al., 2026). Consequently, conventional simulation methods often require iterative procedures (Liu and Der Kiureghian, 1986; Phoon et al., 2005; Zheng et al., 2023) or auxiliary transformations, such as Hermite polynomial models (Li and Xu, 2024) and the S-transform (Huang and Xu, 2021), to approximately satisfy the prescribed statistical characteristics. To address these challenges, several studies have focused on

correlation-based approaches. Lyu et al. (2025a) proposed the bridge function, which establishes a probabilistic relationship among the autocorrelation functions of the target field, the dependent field, and an independent standard Gaussian field. Within this framework, the dependent field can be constructed from the main field and an independent Gaussian field, thereby resolving the incompatibility between prescribed marginal distributions and copula- or vine-copula-based dependence structures. Furthermore, Liu et al. (2026) developed the transformed correlation function, which enables the direct generation of non-Gaussian random fields from standard Gaussian fields while exactly preserving the target marginal distributions and spatial correlations without iterative procedures. Building upon these developments, the present study adopts both the bridge function and the transformed correlation function to establish a probability-compatible framework for the modeling of three-dimensional multivariate non-Gaussian random fields representing concrete constitutive parameters.

Once the probabilistic modeling is completed, the next step is the simulation of random fields based on the established uncertainty models. However, many widely used simulation techniques, such as the spectral representation method (Shinozuka and Deodatis, 1996), require a large number of basic random variables to accurately reproduce the target stochastic characteristics. This limitation becomes particularly severe for three-dimensional random fields, resulting in substantial computational costs and a pronounced curse-of-dimensionality problem.

To address this challenge, a parsimonious stochastic harmonic function (SHF) representation is adopted in this study. The proposed approach incorporates Voronoi wavenumber partitioning (Song et al., 2019), spectrum-dependent random wavenumbers (Chen et al., 2020), and the concept of phase-evolution starting points (Li et al., 2013) into the SHF framework (Chen et al., 2013, 2017). As a result, a three-dimensional random field can be represented with high accuracy using only seven basic random variables, leading to a dramatic reduction in stochastic dimensionality and computational effort. Therefore, once the transformed correlation function corresponding to the target non-Gaussian field is obtained, the parsimonious SHF representation is employed to generate the underlying standard Gaussian field. Subsequently, three-dimensional non-Gaussian random fields of the concrete constitutive parameters are constructed using the proposed probability-compatible transformation framework. The bridge function is employed to establish the probabilistic dependence among the parameter fields.

The remainder of this paper is organized as follows. Section 2 presents the probability-compatible modeling framework for the concrete constitutive parameters. Section 0 introduces the parsimonious SHF representation and the corresponding simulation procedure, followed by numerical investigations to validate the accuracy and efficiency of the proposed approach. Finally, conclusions are drawn in Section 4.

2. Probabilistic Modeling of Three-Dimensional Random Fields for Concrete Constitutive Parameters

In this section, the constitutive parameter fields of concrete, including the elastic modulus $E(\boldsymbol{x})$, compressive strength $f_c(\boldsymbol{x})$, peak strain $\varepsilon_c(\boldsymbol{x})$, and the parameter governing the descending branch $\alpha_c(\boldsymbol{x})$, are modeled as three-dimensional random fields. Here, $\boldsymbol{x} = (x_1, x_2, x_3)^{\mathrm{T}}$ denotes the spatial coordinate vector.

2.1. Probabilistic Characterization of Three Sources of Uncertainty

The three levels of uncertainty, namely parameter randomness, spatial variability, and inter-parameter dependence, are characterized probabilistically in this study.

First, the marginal distributions of the constitutive parameters are specified based on available experimental data. The elastic modulus E and compressive strength f_c are modeled using lognormal distributions, whereas the peak strain ε_c and the descending-branch parameter α_c are represented by Γ and shifted-Γ Gamma distributions, respectively. The corresponding probability density functions (PDFs) are given as follows:

$$\begin{cases} p_E(w) = \dfrac{1}{\sqrt{2\pi}\,\sigma_E w} e^{-\frac{1}{2\sigma_E^2}\ln^2\frac{w}{r_E}}, & \text{for } w \geqslant 0, \\ p_f(x) = \dfrac{1}{\sqrt{2\pi}\,\sigma_f x} e^{-\frac{1}{2\sigma_f^2}\ln^2\frac{x}{r_f}}, & \text{for } x \geqslant 0, \\ p_\varepsilon(y) = \dfrac{y^{k_\varepsilon-1}e^{-\frac{y}{\theta_\varepsilon}}}{\Gamma(k_\varepsilon)\theta_\varepsilon^{k_\varepsilon}}, & \text{for } y \geqslant 0, \\ p_\alpha(z) = \dfrac{(z-r_\alpha)^{k_\alpha-1}e^{-\frac{z-r_\alpha}{\theta_\alpha}}}{\Gamma(k_\alpha)\theta_\alpha^{k_\alpha}}, & \text{for } z \geqslant r_\alpha, \end{cases} \tag{1}$$

where r_E, σ_E, r_f, σ_f, θ_ε, k_ε, r_α, θ_α, and k_α denote the distribution parameters; $\Gamma(\cdot)$ is the Γ function.

Based on the study of Tao et al. (2020), probabilistic dependence exists among the parameters f_c, ε_c and α_c.To accurately characterize their joint behavior, the probabilistic dependence among $f_c(\boldsymbol{x})$, $\varepsilon_c(\boldsymbol{x})$, and $\alpha_c(\boldsymbol{x})$ must be explicitly modeled. The joint probability density function (PDF) at an arbitrary spatial location $\boldsymbol{x}$ is constructed using a vine copula (Tao et al., 2020), i.e.,

$$\begin{aligned} p_{f\varepsilon\alpha}(x,y,z) = c_{f\varepsilon|\alpha}\{C_{f|\alpha}[F_{f_c}(x)\,|F_\alpha(z)\,]C_{\varepsilon|\alpha}[F_\varepsilon(y)\,|F_\alpha(z)\,]\}\\ \cdot c_{f\alpha}[F_f(x),F_\alpha(z)]c_{\varepsilon\alpha}[F_\varepsilon(y),F_\alpha(z)]p_f(x)p_\varepsilon(y)p_\alpha(z), \end{aligned} \tag{2}$$

According to Tao et al. (2020), the dependence structures represented by $c_{f\alpha}(\cdot,\cdot)$, $c_{\varepsilon\alpha}(\cdot,\cdot)$, and $c_{f\varepsilon|\alpha}(\cdot,\cdot)$ are best described by the Frank copula, Gaussian copula, and 90° Clayton copula, respectively. The corresponding copula density functions are expressed as follows

$$\begin{cases} c_{f\alpha}(u,v) = \dfrac{-\theta_{f\alpha}(e^{-\theta_{f\alpha}}-1)e^{-\theta_{f\alpha}(u+v)}}{[e^{-\theta_{f\alpha}}-1+(e^{-\theta_{f\alpha}u}-1)(e^{-\theta_{f\alpha}v}-1)]^2}, \\ c_{\varepsilon\alpha}(u,v) = \dfrac{1}{\sqrt{1-\varrho_{\varepsilon\alpha}^2}} e^{-\frac{\varrho_{\varepsilon\alpha}^2[\Phi^{-1}(u)]^2-2\varrho_{\varepsilon\alpha}\Phi^{-1}(u)\Phi^{-1}(v)+\varrho_{\varepsilon\alpha}^2[\Phi^{-1}(v)]^2}{2(1-\varrho_{\varepsilon\alpha}^2)}}, \\ c_{f\varepsilon|\alpha}(u,v) = \dfrac{1+\theta_{f\varepsilon}}{(uv)^{1+\theta_{f\varepsilon}}\left(\frac{1}{u^{\theta_{f\varepsilon}}}+\frac{1}{v^{\theta_{f\varepsilon}}}-1\right)^{2+\frac{1}{\theta_{f\varepsilon}}}}, \end{cases} \tag{3}$$

where $\theta_{f\alpha}$, $\varrho_{\varepsilon\alpha}$, and $\theta_{f\varepsilon}$ denote the copula parameters.

The spatial variability of the constitutive parameters is characterized by the exponential correlation

model (Tao and Chen, 2023), i.e.,

$$\rho_E(\boldsymbol{\xi}) = e^{-\frac{|\boldsymbol{\xi}|}{l_E}},\ \rho_f(\boldsymbol{\xi}) = e^{-\frac{|\boldsymbol{\xi}|}{l_f}},\ \rho_\varepsilon(\boldsymbol{\xi}) = e^{-\frac{|\boldsymbol{\xi}|}{l_\varepsilon}},\ \text{and}\ \rho_\alpha(\boldsymbol{\xi}) = e^{-\frac{|\boldsymbol{\xi}|}{l_\alpha}}, \tag{4}$$

where l_E, l_f, l_ε, and l_α denote the correlation lengths. The target statistical parameters for the uncertainty model are summarized in Table I Table I and Table II. With the marginal distributions, copula-based dependence structure, and correlation functions fully specified, the three levels of uncertainty are completely characterized.

Table I. Marginal distribution models and statistical parameters of concrete constitutive parameters.

Constitutive parameters	Distribution	Parameters of distribution	Mean	COV	Correlation length
E_c	Log-normal	$r_E = 3.66\times10^{10}\,\text{Pa},\ \sigma_E = 0.149$	$3.7\times10^{10}\,\text{Pa}$	0.15	$l_E = 0.18$ m
f_c	Log-normal	$r_f = 2.27\times10^{7}\,\text{Pa},\ \sigma_E = 0.149$	$2.3\times10^{7}\,\text{Pa}$	0.15	$l_f = 0.32$ m
ε_c	Γ	$\theta_\varepsilon = 2.25\times10^{-5}, k_\varepsilon = 44.44$	1.0×10^{-3}	0.15	$l_\varepsilon = 0.40$ m
α_c	Shifted Γ	$r_\alpha = 0.3, \theta_\alpha = 0.25, k_\alpha = 0.79$	0.5	0.45	$l_\alpha = 0.17$ m

Table II. Vine copula model for concrete constitutive parameters.

Constitutive parameters	Copula	Copula parameters
$f_c,\ \alpha_c$	Frank	$\theta_{f\alpha} = 4.4$
$\varepsilon_c,\ \alpha_c$	Gauss	$\varrho_{\varepsilon\alpha} = 0.69$
$f_c, \varepsilon_c \vert \alpha_c$	90 ◦Clayton	$\theta_{f\varepsilon} = 0.51$

2.2. Probability-Compatible Modeling

As discussed in Section 2.1, the probabilistic descriptions of marginal distributions, spatial variability, and inter-parameter dependence are generally incompatible for multivariate non-Gaussian random fields. Therefore, it is

necessary to characterize these three sources of uncertainty within a probability-compatible framework. In this subsection, a correlation-function-based probability-compatible modeling approach is adopted.

To resolve the incompatibility between the marginal distributions and the spatial variability of non-Gaussian random fields, the *transformed correlation function* (Liu et al., 2026) is employed. This function represents the correlation structure of an underlying standard Gaussian field that can be directly transformed into the target non-Gaussian field while exactly preserving the prescribed marginal distribution and spatial correlation, without requiring any iterative procedure. The relationship between the target correlation function and the transformed correlation function is expressed as (Liu et al., 2026)

$$\rho = \frac{1}{\sigma^2}\left[\iint_0^1 F^{-1}(u_1)F^{-1}(u_2)c_{\mathrm{G}}\left(u_1,u_2;\tilde{\rho}\right)\mathrm{d}u_1\mathrm{d}u_2 - \mu^2\right]. \tag{5}$$

where $F(\cdot)$ denotes the marginal distribution of the target non-Gaussian field, $c_{\mathrm{G}}(\cdot)$ is the Gaussian copula density function, $\tilde{\rho}$ represents the transformed correlation function, and ρ is the target correlation function of the non-Gaussian field. Equation (5) can be solved numerically to establish the relationship between $\rho(\boldsymbol{\xi})$ and $\tilde{\rho}(\boldsymbol{\xi})$, $\boldsymbol{\xi} = (\xi_1,\xi_2,\xi_3)^{\mathrm{T}}$ is the spatial lag vector.

Once the transformed correlation function $\tilde{\rho}(\boldsymbol{\xi})$ is obtained, it can be employed to generate an underlying standard Gaussian random field using any suitable random field simulation technique. Subsequently, the generated Gaussian field can be directly transformed into the target non-Gaussian field while preserving the prescribed marginal distribution and spatial correlation structure. This transformation forms the basis for the probability-compatible simulation of the concrete constitutive parameter fields considered in this study.

The probabilistic dependence of multivariate non-Gaussian random fields should also be characterized in a probability-compatible manner. Since the dependence structure among different variables is described using copula functions, the incompatibility between prescribed marginal distributions and copula-based dependence models must be properly addressed (Lyu et al., 2025a; Liu et al., 2026). To this end, a target non-Gaussian field can be constructed from a main dependent field and an independent standard Gaussian field through the bridge-function framework. Specifically,

$$Y_2(\boldsymbol{x}) = F_2^{-1}\left(C_{2|1}^{-1}\{\Phi[Z_{\mathrm{b}}(\boldsymbol{x})]|F_1[Y_1(\boldsymbol{x})]\}\right), \tag{6}$$

where $C_{2|1}^{-1}(\cdot)$ denotes the inverse conditional copula function, $Z_{\mathrm{b}}(\boldsymbol{x})$ represents the standard Gaussian bridge field with correlation function $\rho_{\mathrm{b}}(\boldsymbol{\xi})$, $Y_1(\boldsymbol{x})$ is the main non-Gaussian field, and $Y_2(\boldsymbol{x})$ denotes the dependent non-Gaussian field. According to Eq. (6), the dependent field is generated from the main field and the Gaussian bridge field. Consequently, a relationship exists among the correlation functions of the main field, the dependent field, and the Gaussian bridge field. To characterize this relationship, Lyu et al. (2025b) introduced the *bridge function* for multivariate Gaussian random fields, which was subsequently generalized to dependent non-Gaussian random fields by Liu et al. (2026). The resulting bridge function can be expressed as

$$\begin{aligned}\tilde{\rho}_2 &= r_{\mathrm{b}}\left(\rho_{\mathrm{b}}|\tilde{\rho}_1\right)\\ &= \iiiint_{[0,1]^4} \Phi^{-1}[C_{2|1}^{-1}(u_{\mathrm{b}}|u_1)]\Phi^{-1}[C_{2|1}^{-1}(u_{\mathrm{b}}'|u_1')]c_{\mathrm{G}}(u_{\mathrm{b}},u_{\mathrm{b}}';\rho_{\mathrm{b}})c_{\mathrm{G}}\left(u_1,u_1';\tilde{\rho}_1\right)\mathrm{d}u_1\mathrm{d}u_{\mathrm{b}}\mathrm{d}u_1'\mathrm{d}u_{\mathrm{b}}'.\end{aligned} \tag{7}$$

3. Numerically simulating three-dimensional random fields of concrete constitutive parameters

Uncertainty simulation is the indispensable computational counterpart to uncertainty modeling. Once the uncertainty modeling is finished, the uncertainty simulation can be carried out. This section presents the simulation procedure for the three-dimensional random fields of concrete constitutive parameters using the parsimonious stochastic harmonic function.

3.1. Parsimonious Stochastic Harmonic Function Representation

Conventional random field simulation methods, such as the spectral representation method (Shinozuka and Deodatis, 1996) and the Karhunen–Loève expansion (Phoon et al., 2005; Zheng et al., 2023), generally require a large number of basic random variables and considerable storage resources to accurately reproduce the target stochastic characteristics. This limitation becomes particularly severe for three-dimensional random fields, leading to high computational costs and reduced efficiency. To address this challenge, a parsimonious stochastic harmonic function (SHF) representation is employed in this study. The proposed approach incorporates Voronoi wavenumber partitioning (Song et al., 2019), spectrum-dependent random wavenumbers (Chen et al., 2020), and the concept of phase-evolution starting points (Li et al., 2013) into the SHF framework, thereby enabling an accurate and computationally efficient representation of three-dimensional random fields with only a small number of basic random variables. The parsimonious SHF representation is expressed as

$$\widetilde{Z}_{\mathrm{Voro}}^{\mathrm{SHF}}(\boldsymbol{x})=\sum_{q=1}^{N}\sqrt{4S(\widetilde{\boldsymbol{\kappa}}_q)\,\mathrm{Vol}(\Omega_q)}\sum_{m=1}^{4}\cos\left[(\boldsymbol{s}_m\odot\widetilde{\boldsymbol{\kappa}}_q)^{\mathrm{T}}\boldsymbol{x}+\widetilde{\phi}_q^{(m)}\right], \tag{8}$$

where $\mathrm{Vol}(\Omega_q)$ denotes the volume of the Voronoi cell Ω_q, $\boldsymbol{s}_1=[1,1,1]^{\mathrm{T}}$, $\boldsymbol{s}_2=[1,1,-1]^{\mathrm{T}}$, $\boldsymbol{s}_3=[1,-1,1]^{\mathrm{T}}$, $\boldsymbol{s}_4=[1,-1,-1]^{\mathrm{T}}$ are sign vectors used to generate different directional combinations of the wavenumbers, and the operator $\odot$ denotes the Hadamard (element-wise) product (Horn and Johnson, 2012); $\widetilde{\boldsymbol{\kappa}}_q=(\widetilde{\kappa}_{q,1},\widetilde{\kappa}_{q,2},\widetilde{\kappa}_{q,3})^{\mathrm{T}}$ are the spectrum-dependent wavenumbers generated by

$$\begin{cases}\widetilde{\kappa}_{q,1}=(\kappa_{q,1}^{\mathrm{U}}-\kappa_{q,1}^{\mathrm{L}})\vartheta_1\\ \widetilde{\kappa}_{q,2}=(\kappa_{q,2}^{\mathrm{U}}-\kappa_{q,2}^{\mathrm{L}})\vartheta_2\\ \widetilde{\kappa}_{q,3}=(\kappa_{q,3}^{\mathrm{U}}-\kappa_{q,3}^{\mathrm{L}})\vartheta_3\end{cases}, \tag{9}$$

where ϑ_1, ϑ_2, and ϑ_3 are three independent random variables uniformly distributed over $[0,1]$ (Chen et al., 2020); $\widetilde{\phi}_q^{(m)}$ are the random phase angles generated by

$$\widetilde{\phi}_q^{(m)}=\mathrm{mod}\left[|\widetilde{\boldsymbol{\kappa}}_q|\sqrt{4S(\widetilde{\boldsymbol{\kappa}}_q)\,\mathrm{Vol}(\Omega_q)}\,\varpi_m,2\pi\right], \tag{10}$$

where ϖ_m, m=1,2,3,4, are four independent Γ - distributed random variables with shape parameter $k_\varpi=1.1$ and scale parameter $s_\varpi=8.2\times10^8$ (Li et al., 2013). Together with the three spectrum-dependent random wavenumbers, the proposed parsimonious SHF representation requires only seven basic random variables to simulate a three-dimensional random field.

3.2. Parsimonious Simulation of Three-Dimensional Multivariate Constitutive Parameter Fields

First, the three dependent random fields, $f_c(\boldsymbol{x})$, $\alpha_c(\boldsymbol{x})$, and $\varepsilon_c(\boldsymbol{x})$, are generated. The simulation procedure starts with the specification of the target marginal distributions, the transformed correlation functions of $f_c(\boldsymbol{x})$, $\alpha_c(\boldsymbol{x})$, and $\varepsilon_c(\boldsymbol{x})$, as well as the vine-copula dependence structure among these constitutive parameters. Subsequently, the correlation functions of the Gaussian bridge fields $Z_{b1}(\boldsymbol{x})$ and $Z_{b3}(\boldsymbol{x})$ are determined using the bridge-function framework. Based on the obtained correlation functions, the bridge fields $Z_{b1}(\boldsymbol{x})$, $Z_{b3}(\boldsymbol{x})$, and the underlying Gaussian field $Z_{\alpha_c}(\boldsymbol{x})$ are efficiently generated using the parsimonious SHF representation.

The generated Gaussian fields are then transformed into the target non-Gaussian constitutive parameter fields through the probability-compatible transformation framework described in Section 2. As a result, the simulated fields simultaneously preserve the prescribed marginal distributions, spatial correlation structures, and vine-copula-based dependence characteristics. The field $\alpha_c(\boldsymbol{x})$ is first obtained through the marginal transformation of $Z_{\alpha_c}(\boldsymbol{x})$. Subsequently, the prescribed dependence structure is incorporated sequentially according to the vine-copula hierarchy. The bridge field $Z_{b2}(\boldsymbol{x})$ is generated conditionally on $Z_{b1}(\boldsymbol{x})$ and $Z_{b3}(\boldsymbol{x})$. Based on $\alpha_c(\boldsymbol{x})$ and $Z_{b1}(\boldsymbol{x})$, the compressive strength field $f_c(\boldsymbol{x})$ is obtained through the inverse pair-copula transformation. Finally, the strain field $\varepsilon_c(\boldsymbol{x})$ is constructed from $\alpha_c(\boldsymbol{x})$ and $Z_{b2}(\boldsymbol{x})$ using the inverse conditional-copula transformation.

Through this recursive construction procedure, the resulting fields $\alpha_c(\boldsymbol{x})$, $f_c(\boldsymbol{x})$, and $\varepsilon_c(\boldsymbol{x})$ simultaneously satisfy the prescribed marginal distributions, spatial correlation structures, and nonlinear probabilistic dependence relationships. Owing to the parsimonious SHF representation, only seven basic random variables are required for each three-dimensional random field. Consequently, the entire trivariate constitutive-parameter model can be represented using only 21 basic random variables, including those associated with the bridge fields. Representative points in the resulting stochastic space are generated using the generalized F-discrepancy method. The overall simulation procedure is illustrated in Figure 1.

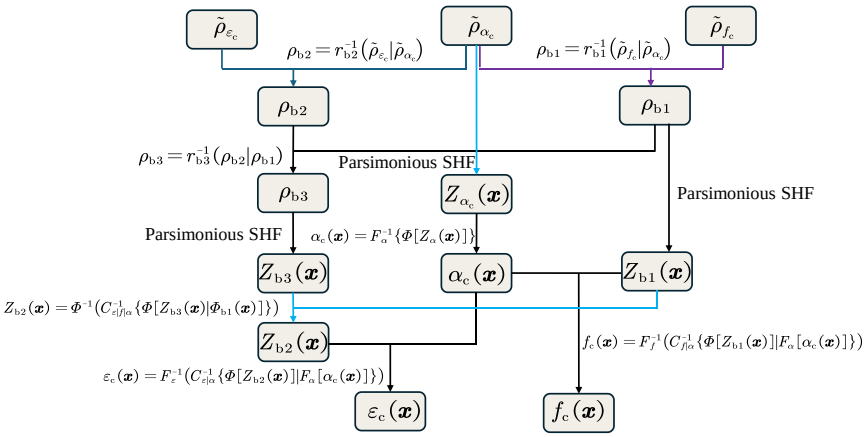
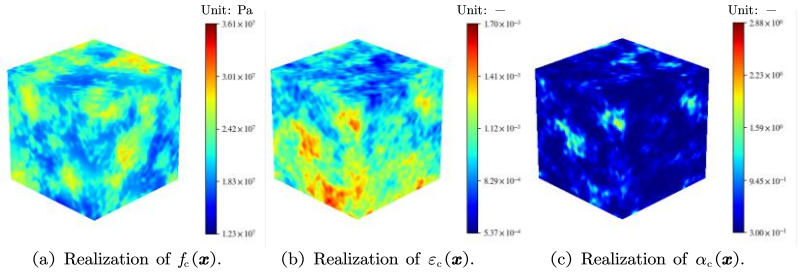


Figure 1. Simulation procedure for the dependent concrete constitutive parameter fields $\alpha_c(\boldsymbol{x})$, $f_c(\boldsymbol{x})$, and $\varepsilon(\boldsymbol{x})$.

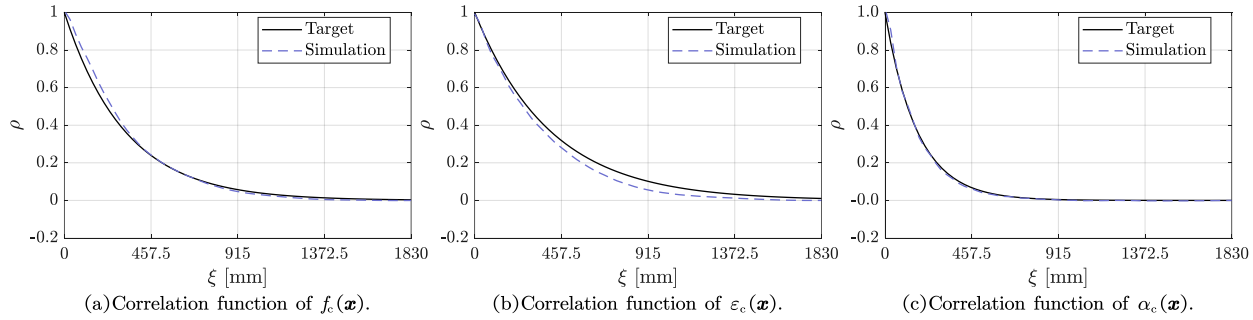
Figure 2 presents representative realizations of the generated trivariate random fields, showing realistic spatial variability for $f_c(\boldsymbol{x})$, $\varepsilon_c(\boldsymbol{x})$, and $\alpha_c(\boldsymbol{x})$. As shown in Figure 3, the simulated correlation functions agree closely with the target correlation functions, demonstrating that the prescribed spatial correlation

structures are accurately reproduced. The comparisons of the target and simulated marginal probability density functions in Figure 4 indicate excellent agreement for all three variables. Furthermore, Figure 5 shows that the simulated samples closely follow the target joint probability distributions, confirming the ability of the proposed vine-copula-based framework to reproduce the prescribed nonlinear dependence structure. Overall, the results verify that the proposed method simultaneously preserves marginal distributions, spatial correlations, and probabilistic dependence while maintaining a highly parsimonious stochastic representation.



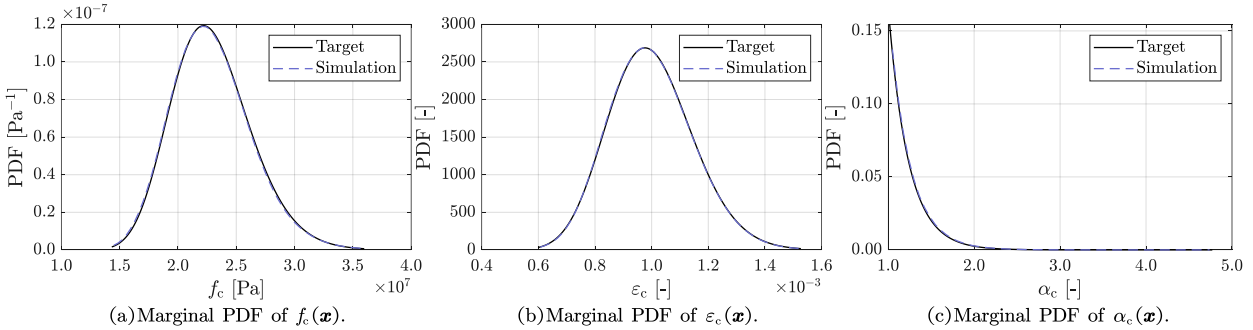
(a) Realization of $f_c(\boldsymbol{x})$. (b) Realization of $\varepsilon_c(\boldsymbol{x})$. (c) Realization of $\alpha_c(\boldsymbol{x})$.

Figure 2. Representative realizations of the generated trivariate random fields $\alpha_c(\boldsymbol{x})$, $f_c(\boldsymbol{x})$, and $\varepsilon(\boldsymbol{x})$.



(a)Correlation function of $f_c(\boldsymbol{x})$. (b)Correlation function of $\varepsilon_c(\boldsymbol{x})$. (c)Correlation function of $\alpha_c(\boldsymbol{x})$.

Figure 3. Comparison of the target and simulated correlation functions.



(a)Marginal PDF of $f_c(\boldsymbol{x})$. (b)Marginal PDF of $\varepsilon_c(\boldsymbol{x})$. (c)Marginal PDF of $\alpha_c(\boldsymbol{x})$.

Figure 4. Comparison of the target marginal PDFs and the simulated results.

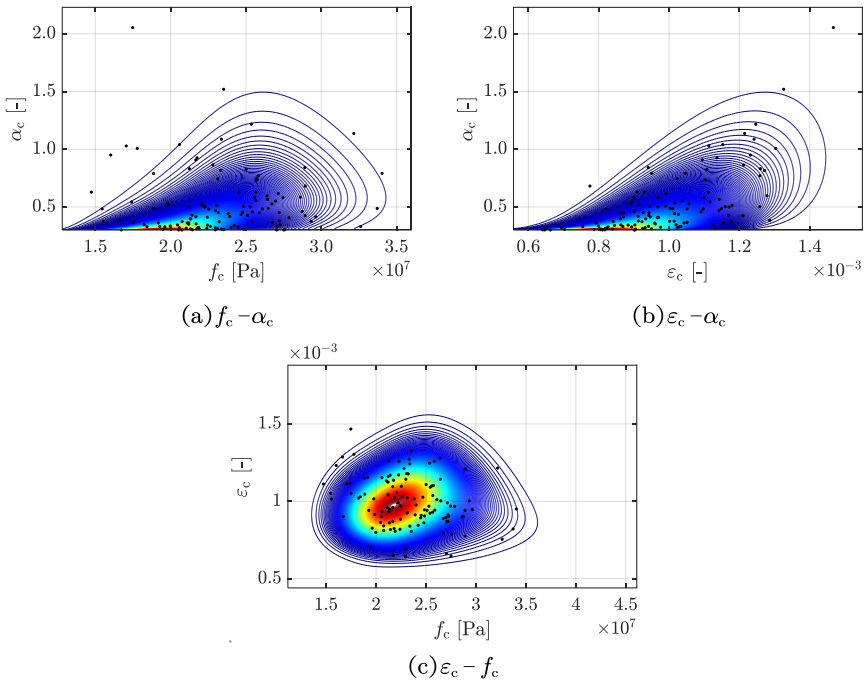


Figure 5. Generated sample points obtained by the proposed method together with the target joint PDF contours.

The independent field $E(\boldsymbol{x})$ can be generated directly from its transformed correlation function. However, to ensure consistency with Drucker's postulate (Wan et al., 2020), the realizations of $E(\boldsymbol{x})$ are adjusted accordingly. The resulting realizations, together with comparisons between the target and simulated correlation functions and marginal probability density functions, are presented in Figure 6.

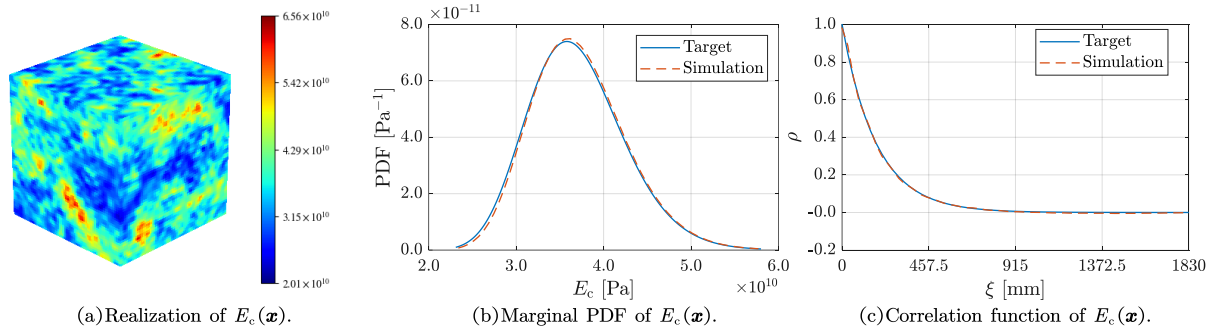


Figure 6. Representative realization of $E(\boldsymbol{x})$ and comparisons of the marginal PDF and correlation function between target and simulated results.

4. Concluding remarks

In this paper, a probability-compatible and computationally efficient framework is proposed for the simulation of three-dimensional multivariate non-Gaussian random fields. The framework integrates the transformed correlation function, the bridge function, the vine-copula-based dependence model, and the parsimonious SHF representation into a unified modeling and simulation procedure. As a result, the generated random fields simultaneously and accurately reproduce the prescribed marginal distributions, spatial correlation structures, and nonlinear probabilistic dependence relationships.

Numerical investigations demonstrate that the proposed approach accurately reproduces the prescribed statistical characteristics, including the target marginal distributions, spatial correlation structures, and probabilistic dependence relationships. Furthermore, owing to the parsimonious SHF representation, only seven basic random variables are required for each three-dimensional random field, resulting in a substantial reduction in stochastic dimensionality and computational cost compared with conventional simulation techniques. Consequently, the four concrete constitutive parameter fields considered in this study can be represented using only 28 basic random variables in total, providing an efficient framework for large-scale uncertainty quantification and stochastic finite element analysis.

The proposed framework therefore provides a rigorous and efficient tool for the modeling and simulation of multivariate heterogeneous random media. Its ability to preserve complex probabilistic characteristics while maintaining high computational efficiency makes it particularly attractive for uncertainty quantification, reliability analysis, and stochastic finite element modeling of engineering materials and structures.

Acknowledgements

Financial supports from German Research Foundation (DFG) (Grant No. 562994444), the National Natural Science Foundation of China (Grant No. 12302037), and China Scholarship Council (CSC) are highly appreciated.

References

Benjamin, J.R., Cornell, C.A., 2014. Probability, statistics, and decision for civil engineers. Courier Corporation.

Chen, J., Comerford, L., Peng, Y., Beer, M., Li, J., 2020. Reduction of random variables in the Stochastic Harmonic Function representation via spectrum-relative dependent random frequencies. Mechanical Systems and Signal Processing 141, 106718.

Chen, J., Kong, F., Peng, Y., 2017. A stochastic harmonic function representation for non-stationary stochastic processes. Mechanical Systems and Signal Processing 96, 31–44.

Chen, J., Ren, X., Feng, D.-C., Kohler, J., Sørensen, J.D., Wu, J.-Y., Le, J.-L., Caspeele, R., 2025. Recent developments in mechanical and uncertainty modelling of concrete. Structural Safety 113, 102526.

Chen, J., Sun, W., Li, J., Xu, J., 2013. Stochastic harmonic function representation of stochastic processes. Journal of Applied Mechanics 80, 011001.

Fu, J.-H., Luo, Y., Wei, X.-L., Lyu, M.-Z., Beer, M., 2026. Probability-compatible modeling and efficient stochastic harmonic function representation of three-dimensional multivariate non-Gaussian random fields with nonlinear dependences. International Journal of Non-Linear Mechanics 189, 105402.

Ghanem, R.G., Spanos, P.D., 2003. Stochastic finite elements: a spectral approach. Courier Corporation.

Horn, R.A., Johnson, C.R., 2012. Matrix analysis. Cambridge university press.

Huang, Z., Xu, Y.-L., 2021. A multi-taper S-transform method for spectral estimation of stationary processes. IEEE Transactions on Signal Processing 69, 1452–1467.

Li, J., Chen, J., 2009. Stochastic dynamics of structures. John Wiley & Sons.

Li, J., Peng, Y., Yan, Q., 2013. Modeling and simulation of fluctuating wind speeds using evolutionary phasespectrum. Probabilistic Engineering Mechanics 32, 48–55.

Li, Y., Xu, J., 2024. Novel Hermite Polynomial Model Based on Probability-Weighted Moments for Simulating Non-Gaussian Stochastic Processes. J. Eng. Mech. 150, 04024006.

Liu, P.-L., Der Kiureghian, A., 1986. Multivariate distribution models with prescribed marginals and covariances. Probabilistic engineering mechanics 1, 105–112.

Liu, Y.-Y., Lyu, M.-Z., Chen, J.-B., Zhang, S., 2026. A new model for the multivariate non-Gaussian random fields involving between-variable nonlinear correlation. ASCE-ASME Journal of Risk and Uncertainty in Engineering Systems, Part A: Civil Engineering.

Lyu, M., Feng, D., Cao, X., Beer, M., 2024a. A full-probabilistic cloud analysis for structural seismic fragility via decoupled M-PDEM. Earthq Engng Struct Dyn 53, 1863–1881.

Lyu, M.-Z., Fei, Z.-J., Feng, D.-C., 2024b. Copula-based cloud analysis for seismic fragility and its application to nuclear power plant structures. Engineering Structures 305, 117754.

Lyu, M.-Z., Fei, Z.-J., Feng, D.-C., 2024c. Vine-copula-based multi-dimensional fragility analysis of nuclear power plant under sequential earthquakes. Structural Safety 110, 102494.

Lyu, M.-Z., Liu, Y.-Y., Chen, J.-B., 2025a. A novel model and simulation method for multivariate Gaussian fields involving nonlinear probabilistic dependencies and different variable-wise spatial variabilities. Reliability Engineering & System Safety 260, 110963.

Lyu, M.-Z., Yang, J.-S., Chen, J.-B., Li, J., 2025b. High-efficient non-iterative reliability-based design optimization based on the design space virtually conditionalized reliability evaluation method. Reliability Engineering & System Safety 254, 110646.

Phoon, K.K., Huang, H.W., Quek, S.T., 2005. Simulation of strongly non-Gaussian processes using Karhunen–Loeve expansion. Probabilistic Engineering Mechanics 20, 188–198.

Shinozuka, M., Deodatis, G., 1996. Simulation of Multi-Dimensional Gaussian Stochastic Fields by Spectral Representation. Appl. Mech. Rev 49, 29–53.

Song, Y., Chen, J., Beer, M., Comerford, L., 2019. Wind Speed Field Simulation via Stochastic Harmonic Function Representation Based on Wavenumber–Frequency Spectrum. J. Eng. Mech. 145, 04019086.

Tao, J., Chen, J., 2023. Experimental Study on the Spatial Variability of Concrete by the Core Test and Rebound Hammer Test. ASCE-ASME J. Risk Uncertainty Eng. Syst., Part A: Civ. Eng. 9, 04023029.

Tao, J., Chen, J., Ren, X., 2020. Copula-Based Quantification of Probabilistic Dependence Configurations of Material Parameters in Damage Constitutive Modeling of Concrete. J. Struct. Eng. 146, 04020194.

Wan, Z., Chen, J., Li, J., 2020. Probability density evolution analysis of stochastic seismic response of structures with dependent random parameters. Probabilistic Engineering Mechanics 59, 103032.

Zheng, Z., Beer, M., Nackenhorst, U., 2023. An iterative multi-fidelity scheme for simulating multi-dimensional non-Gaussian random fields. Mechanical Systems and Signal Processing 200, 110643.

Spectrally Consistent Upscaling of Wind Speed Time Series Data

Marius Bittner[1,*], Parth Tambat[1], Marco Behrendt[2], and Michael Beer[1,3,4]
[1]*Institute for Risk and Reliability, Leibniz University Hannover, 30167 Hannover, Germany*
[*]*Corresponding author: bittner@irz.uni-hannover.de*
[2]*Department of Civil and Environmental Engineering, Rice University, Houston, USA*
[3]*Institute for Risk and Uncertainty, University of Liverpool, Liverpool, UK*
[4]*International Joint Research Center for Engineering Reliability and Stochastic Mechanics, Tongji University, Shanghai, China*

Abstract. As the share of wind energy grows, reliable engineering computations for wind speed modeling become critical for forecasting, stability assessment, and risk-informed design. A central challenge is that available wind records are often limited to coarse time averages, such as 10-minute or hourly means, which suffice for energy yield estimates but miss the high-frequency variability needed for reliability analysis, fatigue assessment, and extreme-event studies.

Building on the Temporal Enhanced Fourier Transform (TEFT), we develop an integrated storm-hazard reliability framework that transforms coarse storm wind histories into high-resolution structural loading scenarios. The approach estimates the spectrum implied by averaged data, corrects for attenuation due to temporal averaging, and reconstructs a finer time grid by adjusting Fourier coefficients under consistency constraints. These constraints enforce agreement with observed moments and marginal distributions, while stochastic sampling generates ensembles that reflect uncertainty. The procedure avoids direct reliance on measured high-rate data, yet maintains realistic maxima, means, variance, distributional fit, and spectral slope.

Results show that the generated high-resolution series align with observed characteristics and support reliability computations. The method enables more faithful storm-to-structure simulations for grid stability, structural reliability of onshore and offshore assets, and extreme-event risk analysis, thereby strengthening the reliability and reproducibility of engineering decisions for critical infrastructure systems.

Keywords: wind speed modeling, risk assessment in wind energy, stochastic wind simulation, high-resolution wind data, environmental processes

1. Introduction

High-frequency wind fluctuations can dominate short-duration structural demand, fatigue accumulation, and threshold exceedances, but many environmental wind archives are distributed only as time-averaged records. TEFT was introduced to reconstruct high-resolution wind-speed histories from coarse measurements while preserving statistical and spectral properties (Tambat et al., 2026). The resulting scale gap is especially relevant for tropical-cyclone and severe-storm scenarios, where a slowly varying storm envelope can coexist with reliability-relevant turbulent fluctuations.

© 2026 by the author(s). This work is licensed under the Creative Commons Attribution 4.0 International License (CC BY 4.0), which permits unrestricted use, distribution, and reproduction in any medium, provided the original author and source are credited.

Hybrid parametric and background-wind models have already been used to connect typhoon wind fields with port disruption and regional economic losses (Zhang et al., 2020; Tian et al., 2023). Artificial storm-track generation has likewise been used to construct targeted rare-event scenarios for coastal risk studies (Sun et al., 2022). The present work redirects these ideas toward structural reliability by coupling the storm wind-field layer with TEFT-based temporal refinement and OpenSees dynamic response analysis (McKenna et al., 2010).

The paper is organized around a modular hazard-to-response workflow. The methodology is summarized in Section 2, followed by a controlled fixed-storm TEFT benchmark and a stochastic storm-to-structure reliability example.

2. Methodology

The proposed framework couples tropical-cyclone wind-field simulation, spectrally consistent temporal upscaling, structural load generation, and dynamic reliability analysis. The workflow starts from best-track-like storm information, computes a coarse wind-speed history at the structure location, reconstructs a high-resolution wind signal using TEFT (Tambat et al., 2026), and propagates the resulting wind loads through a unit-consistent finite-element model. This structure keeps the hazard model, temporal refinement, and structural response model modular, so that deterministic storm scenarios and stochastic storm ensembles can be treated within the same computational pipeline at the desired level of modeling detail.

2.1. Storm Representation and Wind-Field Model

Each storm event is represented by a best-track-like table

$$\mathcal{B} = \{t_i, \phi_i, \lambda_i, p_{c,i}, V_{\max,i}, R_{\max,i}, u_{b,i}, v_{b,i}\}_{i=1}^{N}, \tag{1}$$

where t_i is time, ϕ_i and λ_i are the cyclone-center latitude and longitude, $p_{c,i}$ is central pressure, $V_{\max,i}$ is maximum wind speed, $R_{\max,i}$ is the radius of maximum wind speed, and $(u_{b,i}, v_{b,i})$ denotes the eastward and northward components of the background wind vector at the site. For deterministic examples, this table is prescribed. For stochastic examples, the table is generated from a small set of physically interpretable random variables. The current Monte Carlo results use random track geometry, central pressure, maximum intensity, background wind, and TEFT realization seed. $R_{\max}$ is not sampled independently in these Monte Carlo runs; it is computed inside the parametric wind model from central pressure, latitude, and translation speed. A separate stochastic one-shot prototype additionally samples $R_{\max}$ explicitly, but that variant is not the source of the reliability numbers reported in Section 3. This extends targeted artificial-track ideas used for synthetic superstorm studies (Sun et al., 2022) by randomizing a richer set of best-track and wind-field variables.

The stochastic modelling of tropical cyclones uses a quadratic-Bezier track generator in a local east–north coordinate system centered at the structure site. Let $\mathbf{e}(\alpha) = (\cos\alpha, \sin\alpha)^\top$ be the along-track unit vector for heading α, and $\mathbf{n}(\alpha) = (-\sin\alpha, \cos\alpha)^\top$ its left-normal direction. For each sample, the heading H, along-track extent L, closest-approach control distance D_c, curvature

control κ, minimum pressure $p_{\min}$, maximum intensity cap $V_{\max}^{\mathrm{cap}}$, background-wind speed U_b, and background-wind direction Θ_b are drawn independently from bounded uniform distributions:

$$\begin{array}{ll} H \sim \mathrm{Unif}(150^\circ, 205^\circ), & L \sim \mathrm{Unif}(1900, 3000)\ \mathrm{km}, \\ D_c \sim \mathrm{Unif}(35, 140)\ \mathrm{km}, & \kappa \sim \mathrm{Unif}(0, 520)\ \mathrm{km}, \\ p_{\min} \sim \mathrm{Unif}(910, 945)\ \mathrm{hPa}, & V_{\max}^{\mathrm{cap}} \sim \mathrm{Unif}(54, 68)\ \mathrm{m/s}, \\ U_b \sim \mathrm{Unif}(2, 10)\ \mathrm{m/s}, & \Theta_b \sim \mathrm{Unif}(-120^\circ, 40^\circ). \end{array} \tag{2}$$

All angles are measured counterclockwise from east. A common ocean-side genesis region is imposed through the reference heading $H_{\mathrm{ref}} = 160^\circ$ and start distance $D_0 = 1050$ km:

$$\mathbf{P}_0 = -D_0 \mathbf{e}(H_{\mathrm{ref}}), \qquad \mathbf{P}_2 = \mathbf{P}_0 + L\mathbf{e}(H). \tag{3}$$

The quadratic Bezier control point is then chosen as

$$\mathbf{P}_1 = 2D_c \mathbf{n}(H) - \frac{1}{2}\left(\mathbf{P}_0 + \mathbf{P}_2\right) + \kappa \mathbf{n}(H), \tag{4}$$

and the storm centerline is

$$\mathbf{P}(\tau) = (1-\tau)^2 \mathbf{P}_0 + 2(1-\tau)\tau \mathbf{P}_1 + \tau^2 \mathbf{P}_2, \qquad 0 \le \tau \le 1. \tag{5}$$

The $N = 21$ best-track rows are evaluated at $\tau_i = (i-1)/(N-1)$, using 6 h spacing. The local coordinates $\mathbf{P}(\tau_i)$ are converted to latitude and longitude by a local geodetic offset. The parameter D_c should be interpreted as a closest-approach control rather than an exact realized minimum distance: the curvature term shifts the mid-track point to $(D_c + \kappa/2)\mathbf{n}(H)$, and the actual minimum site distance follows from the full sampled curve.

The pressure and intensity histories are smooth functions of the normalized track coordinate $u = 2\tau - 1$:

$$p_c(\tau) = p_{\mathrm{outer}} - (p_{\mathrm{outer}} - p_{\min}) \exp(-3u^2), \tag{6}$$

with $p_{\mathrm{outer}} = 1000$ hPa in the reported runs. The maximum wind speed parameter is linked to the pressure deficit by

$$V_{\max}(\tau) = V_{\min} + \eta(\tau)^{0.65}\left(V_{\max}^{\mathrm{cap}} - V_{\min}\right), \qquad \eta(\tau) = \frac{p_{\mathrm{env}} - p_c(\tau)}{p_{\mathrm{env}} - p_{\min}}, \tag{7}$$

where $V_{\min} = 18$ m/s and $p_{\mathrm{env}} = 1010$ hPa. The background wind is constant within one sample, $(u_b, v_b) = U_b(\cos\Theta_b, \sin\Theta_b)$, but varies between samples.

At each time step, the wind vector at a site is obtained from a hybrid parametric cyclone model. Following the broad structure used in typhoon-induced port-disruption studies (Zhang et al., 2020; Tian et al., 2023), the storm-relative wind is decomposed into a moving component and a rotating component, and then blended with the background wind:

$$\mathbf{v}(t) = (1 - e(r))\,\mathbf{v}_{tc}(t) + e(r)\mathbf{v}_b(t), \tag{8}$$

with

$$e(r) = \frac{c^4}{1 + c^4}, \qquad c = \frac{r}{nR_{\max}}. \tag{9}$$

Here r is the distance from the cyclone center to the site and n controls the transition from cyclone-dominated to background-dominated flow. The vector $\mathbf{v}_{tc}(t)$ is the sum of the storm translation and rotating cyclone components, $\mathbf{v}_b(t) = (u_b(t), v_b(t))^\top$ is the background wind, c is the radius normalized by $nR_{\max}$, and $e(r)$ is the corresponding hybrid blending weight. In the current Monte Carlo runs, the radius of maximum wind is derived as

$$R_{\max} = \left[a_R \tanh\{b_R(\phi - 28)\} + c_R \exp\left(\frac{p_{\text{env}} - p_c}{33.86}\right) + d_R V_{\text{tr}} + e_R \right] 1000, \tag{10}$$

where ϕ is storm-center latitude, V_{tr} is translation speed. The coefficients are

$$(a_R, b_R, c_R, d_R, e_R) = (28.52, 0.0873, 12.22, 0.2, 37.22). \tag{11}$$

The bracketed value is in kilometres and is converted to metres before evaluating the wind field. The resulting coarse wind-speed history is the Euclidean norm

$$U_c(t_k) = \|\mathbf{v}(t_k)\|_2 , \tag{12}$$

evaluated on a regular time grid, here using 10-minute spacing.

2.2. Threshold-Triggered TEFT Upscaling

The high-frequency wind content is reconstructed only during dynamically relevant storm periods. A TEFT window is triggered when the coarse site wind speed exceeds a prescribed threshold U_{thr}. Padding is added before and after the triggered interval so that the upscaling captures the surrounding storm envelope.

Let $U_c(t_k)$ denote the coarse wind-speed samples with time step ΔT. The coarse signal is separated into a slowly varying trend and a fluctuating component,

$$U_c(t_k) = m_c(t_k) + u'_c(t_k). \tag{13}$$

The Fourier amplitudes of u'_c are estimated from the coarse record. Because coarse samples represent time-averaged wind speeds, the resolved spectrum is corrected for attenuation by the temporal averaging operation. The unresolved high-frequency Fourier coefficients are then extrapolated according to the estimated spectral decay, while the total variance is constrained to match a target turbulence level.

A fine-grid fluctuation $u'_f(t)$ is synthesized by combining the corrected and extrapolated Fourier amplitudes with stochastic phases. An iterative amplitude adjusted Fourier transform step is used to preserve the target marginal distribution and moment constraints. The final high-resolution wind history is constructed as

$$U_f(t) = m_f(t) + a(t)u'_f(t), \tag{14}$$

where $m_f(t)$ is the interpolated storm-scale trend and $a(t)$ is a time-varying turbulence envelope derived from the coarse storm history. In the implementation, a preliminary envelope is computed from the interpolated trend relative to the coarse-window mean,

$$\tilde{a}(t) = \max\left(\frac{m_f(t)}{\overline{U}_c}, a_{\min}\right), \tag{15}$$

where $a_{\min}$ is an envelope floor. The envelope is then RMS-normalized,

$$a(t) = \frac{\tilde{a}(t)}{\left(\frac{1}{|\mathcal{T}|}\int_{\mathcal{T}} \tilde{a}^2(\tau)\, d\tau\right)^{1/2}}, \tag{16}$$

so that it redistributes the target turbulent standard deviation over time without changing its window-scale energy. This gives a separable evolutionary spectral representation,

$$S(t, f) = a^2(t) S_{\mathrm{TEFT}}(f), \tag{17}$$

where $S_{\mathrm{TEFT}}(f)$ is the one-sided spectrum implied by the corrected and extrapolated TEFT Fourier amplitudes of the stationary fluctuation $u'_f(t)$. This preserves the non-stationary cyclone envelope while restoring high-frequency variability relevant for structural response.

2.3. Wind Load Generation and Structural Response

The refined wind-speed history is converted to nodal wind loads for the finite-element model. For each loaded structural node j, the wind load is computed from the local wind speed using a Eurocode-style aerodynamic load model (European Committee for Standardization, 2005), including height-dependent exposure and force coefficients:

$$F_j(t) = \frac{1}{2}\rho C_j A_j U_j^2(t). \tag{18}$$

The resulting load histories are written as OpenSees input files and applied to the structural model as time-dependent nodal loads.

The structural model used in the numerical examples is a 50 m steel lattice tower idealized as a cantilever truss-type structure in OpenSees (McKenna et al., 2010). The tower is discretized by 17 nodes and 16 beam-column elements, as shown schematically in panel (a) of Figure 1. Nodes 1–16 correspond to the wind-loaded tower sections, while Node 17 is fixed at the base. Section-dependent aerodynamic areas, enclosed areas, reference heights, and lumped masses are assigned according to the tower documentation. The lumped mass distribution follows the enclosed-area allocation

$$m_i = M_{\mathrm{tot}} \frac{A_i^{\mathrm{enc}}}{\sum_k A_k^{\mathrm{enc}}}, \qquad M_{\mathrm{tot}} = 13\,172 \text{ kg}. \tag{19}$$

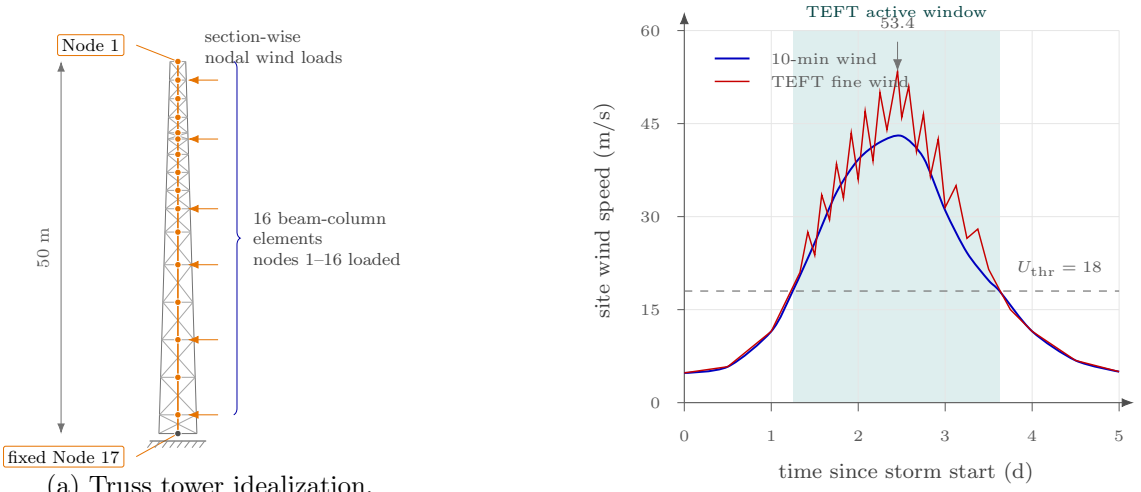
The section stiffnesses are derived from the lattice-support approximation

$$I_{\mathrm{eff}} = 0.5 h_0^2 A_{\mathrm{ch}}, \tag{20}$$

where h_0 is the section width and A_{ch} is the total cross-sectional area of the main chord members. In the present numerical examples the nominal Young's modulus is $E = 2.1 \cdot 10^8$ kN/m^2.

The structural response is evaluated by solving the dynamic equilibrium equation

$$\mathbf{M}\ddot{\mathbf{q}}(t) + \mathbf{C}\dot{\mathbf{q}}(t) + \mathbf{K}\mathbf{q}(t) = \mathbf{F}(t), \tag{21}$$



(a) Truss tower idealization.

(b) Threshold-triggered storm wind history.

Figure 1. Coupled structural and wind-loading representation used in the numerical examples. The tower idealization defines the nodal load application points, while the site wind-speed history illustrates the threshold-triggered TEFT refinement that supplies high-resolution dynamic loading during the storm core.

where $\mathbf{q}(t)$ contains the structural degrees of freedom and $\mathbf{F}(t)$ is the vector of wind-induced nodal loads. The present numerical examples extract response histories and peak nodal displacements after each OpenSees simulation. To avoid evaluating the initial transient caused by sudden load application, peak displacement metrics are computed only after the first 20 s of simulated response.

2.4. Reliability Formulation

For stochastic analyses, the random input vector X may include storm-track parameters, pressure deficit, maximum wind speed, $R_{\max}$, background wind, TEFT phase realization, turbulence intensity, and structural parameters. The performance function is defined in terms of the maximum absolute top-node displacement:

$$g(X) = d_{\mathrm{cap}} - \max_{t} |d_{\mathrm{top}}(t; X)|. \tag{22}$$

Failure occurs when $g(X) \leq 0$, and the failure probability is estimated by Monte Carlo simulation as

$$\hat{P}_f = \frac{1}{N_s} \sum_{s=1}^{N_s} \mathbf{1}\left[g(X_s) \leq 0\right]. \tag{23}$$

This formulation allows the same framework to support deterministic one-shot demonstrations, stochastic best-track scenarios, and full storm-to-structure reliability simulations.

2.5. Computational Implementation

The computational workflow is implemented as a Julia package `StormHazards` (Bittner, 2026; Bezanson et al., 2017). It couples parametric storm simulation, TEFT upscaling, load generation, and reliability orchestration, and uses OpenSees for dynamic structural response (McKenna et al., 2010). Monte Carlo sampling and external-model execution are managed through UncertaintyQuantification.jl (Behrensdorf et al., 2023; Behrensdorf et al., 2026), with SLURM scripts used for cluster-scale runs. Each module exchanges explicit tabular data products, including best-track tables, wind histories, load histories, response histories, and figure-ready CSV files. This makes the framework practical and modular: the storm generator, temporal-upscaling method, structural solver, or reliability estimator can be replaced without changing the complete pipeline.

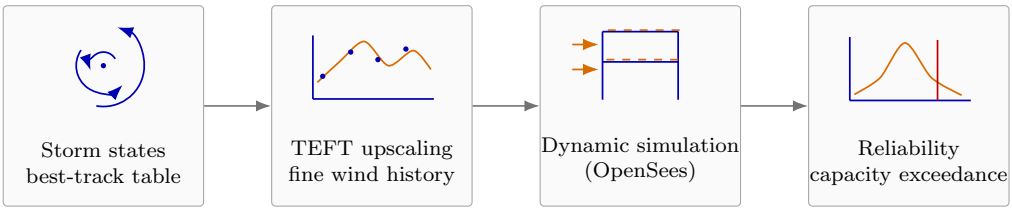


Figure 2. Modular storm-to-reliability workflow. The implementation keeps the storm description, temporal reconstruction, structural analysis, and reliability calculation as separate exchangeable stages connected by auditable data files.

3. Numerical Results

Two $N = 1000$ truss-tower simulations are used to separate the effect of temporal wind upscaling from the effect of storm-to-storm variability. The first run, denoted here as the controlled TEFT benchmark, keeps the single synthetic storm history, background wind, structural model, and capacity fixed, and samples only the unresolved TEFT-EPSD wind realization. The second run samples the artificial best-track geometry, intensity parameters, background-wind vector, and TEFT realization before propagating each event through the same OpenSees tower model. Both runs use a demonstration site near Kowloon Bay, Hong Kong, $(22.3°\text{N}, 114.2°\text{E})$, a 10-minute coarse wind record, a 10 s refined time step, an 18 m/s trigger threshold, and the illustrative top-displacement capacity $d_{\text{cap}} = 0.25$ m.

Table I summarizes the two experiments. In the controlled benchmark, the maximum coarse site wind speed is 43.47 m/s. After TEFT-EPSD refinement, the sample-wise maximum wind speed has mean 52.14 m/s and reaches 66.95 m/s. The mean maximum absolute top-node displacement is 0.182 m, with 95th and 99th percentiles of 0.264 m and 0.288 m, respectively. At the selected capacity, 93 of 1000 samples fail, giving $\hat{P}_f = 0.093$ with Monte Carlo standard error 0.0092. This run is therefore best interpreted as a controlled check of the TEFT-to-structure coupling: the storm envelope is fixed, but the unresolved temporal variability alone is sufficient to move part of the response distribution into the failure domain.

The stochastic storm ensemble adds storm-to-storm variability to the same OpenSees structural calculation. The random-variable definitions and ranges are given in Section 2.1, and Figure 3

Table I. Summary of the two 1000-sample truss-tower reliability runs. Wind maxima refer to sample-wise TEFT-refined maxima; displacement statistics refer to the maximum absolute top-node displacement.

Run	Main random variables	$\overline{U}_{\max}$ (m/s)	$U_{\max}$ (m/s)	d_{95} (m)	d_{99} (m)	$d_{\max}$ (m)	$\hat{P}_f$
Controlled TEFT benchmark	TEFT-EPSD realization	52.14	66.95	0.264	0.288	0.292	0.093
Stochastic storm ensemble	Track, intensity, background wind, TEFT-EPSD realization	47.82	77.87	0.274	0.321	0.395	0.093

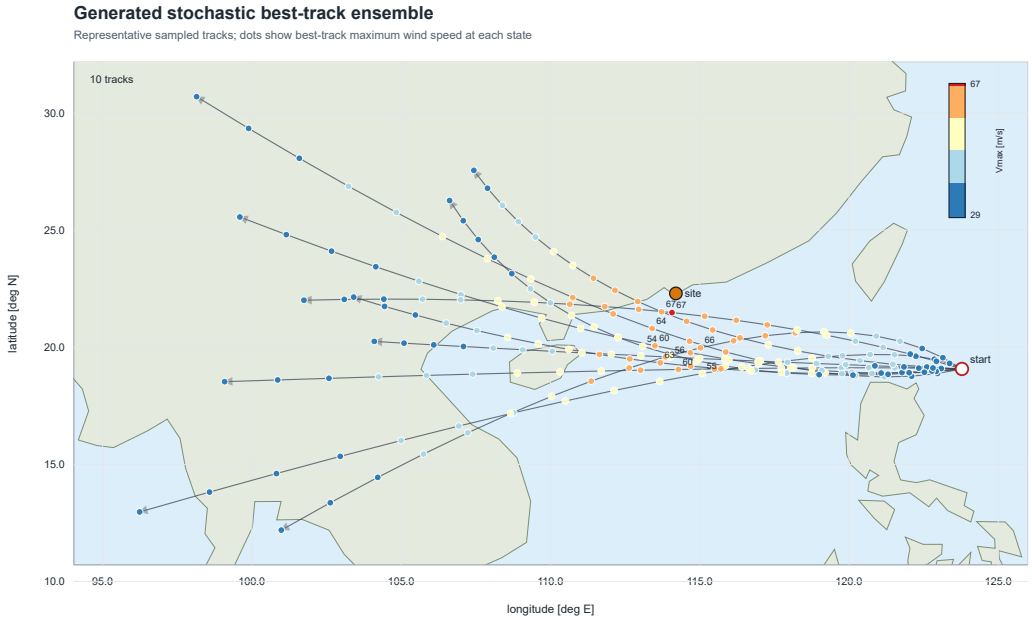


Figure 3. Generated stochastic best-track ensemble used as hazard input for the storm-to-structure simulations. The curves show representative sampled quadratic-Bezier storm tracks, while the colored best-track states indicate the evolving maximum wind-speed parameter along each artificial event. The figure documents the stochastic storm geometry before temporal upscaling and structural propagation.

visualizes representative sampled quadratic-Bezier best tracks before temporal upscaling and structural propagation. In the present 1000-sample run, the sampled coarse-wind ensemble has mean maximum speed 42.90 m/s and reaches 54.29 m/s; after TEFT-EPSD refinement the corresponding sample-wise wind maxima have mean 47.82 m/s and reach 77.87 m/s.

Figure 4 summarizes the wind input and the resulting top-node demand for the stochastic storm ensemble. The reliability calculation itself is evaluated from the maximum absolute top-node displacement defined in Eq. (22). In the wind diagnostic, the deterministic fixed-storm preview

remains visible as a reference, while the sampled coarse-wind mean and the TEFT-refined ensemble describe the stochastic run.

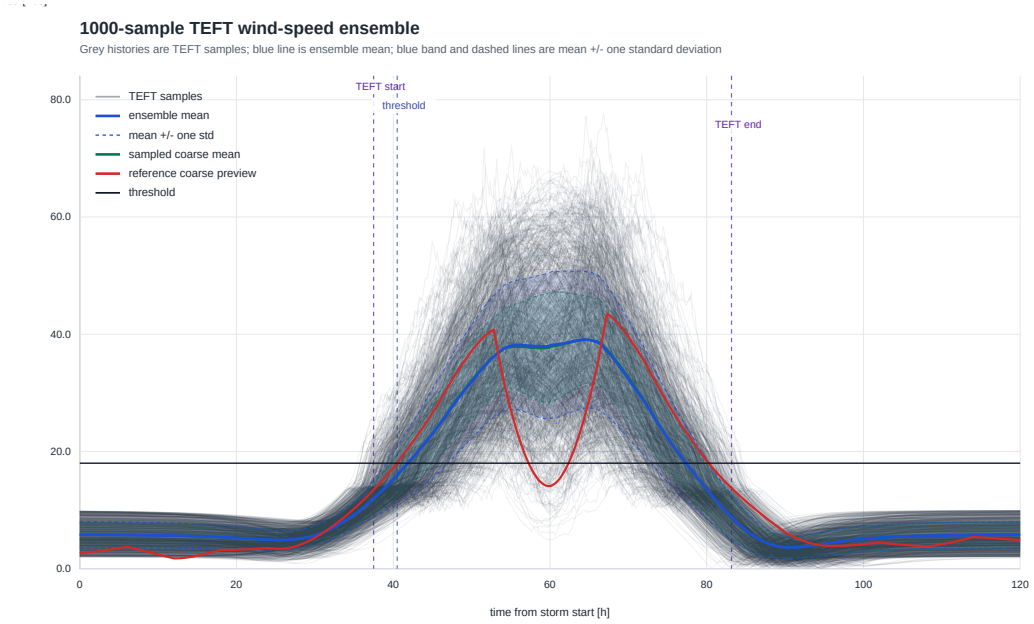
The stochastic run produces a mean maximum absolute top-node displacement of 0.157 m and a median of 0.147 m, both below the corresponding controlled-run values of 0.182 m and 0.184 m. This decrease in central demand is expected because many sampled storms pass less unfavorably than the fixed benchmark track. The main difference appears in the upper tail: the 95th percentile increases from 0.264 m to 0.274 m, the 99th percentile increases from 0.288 m to 0.321 m, and the maximum observed top-node displacement increases from 0.292 m to 0.395 m. At $d_{\mathrm{cap}} = 0.25$ m, 93 of 1000 stochastic storm samples fail, giving $\hat{P}_f = 0.093$ with Monte Carlo standard error 0.0092. Thus, at the selected illustrative capacity, the two experiments give the same exceedance estimate, with both values obtained directly from the exported sample tables. They reach this estimate through different demand distributions: the stochastic storm ensemble has a lower center and a heavier extreme tail.

The height-wise displacement profile in Figure 5 shows that the largest responses occur at the upper tower nodes and decrease toward the base, as expected for the cantilever-type idealization. Across both runs, the top response node is also the critical node for the reported capacity exceedance. In the controlled benchmark the estimated exceedance probability drops to zero once the capacity exceeds 0.295 m. In the stochastic storm run, a nonzero exceedance tail remains up to the largest inspected capacity of 0.35 m, where 3 of 1000 samples still exceed the limit. This comparison is the clearest reliability effect of the second example: even when the probability at 0.25 m is unchanged, storm-parameter uncertainty controls the high-capacity tail.

The Fourier-coefficient and PSD diagnostics generated with the runs are retained as traceability outputs, but they are not all reproduced here. Their role is to verify the same TEFT steps described by Tambat et al. (Tambat et al., 2026): the resolved low-frequency body is inferred from the coarse record, the high-frequency tail is extrapolated, and the spectrum is rescaled to match the target turbulent standard deviation. The present framework differs by applying that reconstruction only inside the storm-triggered active window and by embedding it in the separable TEFT-EPSD representation $S(t, f) = a^2(t) S_{\mathrm{TEFT}}(f)$. Figure 6 shows this time-frequency construction. The diagnostic highlights that the spectral shape $S_{\mathrm{TEFT}}(f)$ is retained while the nonstationary storm envelope modulates the local spectral energy over time.

4. Conclusions

The first numerical results support the intended role of the framework as a bridge between coarse storm-wind information and structural reliability analysis. In the fixed-storm benchmark, TEFT-EPSD sampling restores unresolved short-duration wind peaks and produces a non-negligible displacement exceedance probability for the OpenSees tower model. In the stochastic storm example, the central top-node demand decreases because many sampled tracks are less severe than the fixed benchmark, but the upper response tail becomes substantially larger once storm-track, intensity, curvature, and background-wind variables are sampled together with the TEFT realization. At the illustrative 0.25 m displacement capacity, both 1000-sample experiments give the same exceedance estimate, while the stochastic storm ensemble retains nonzero exceedance probability at

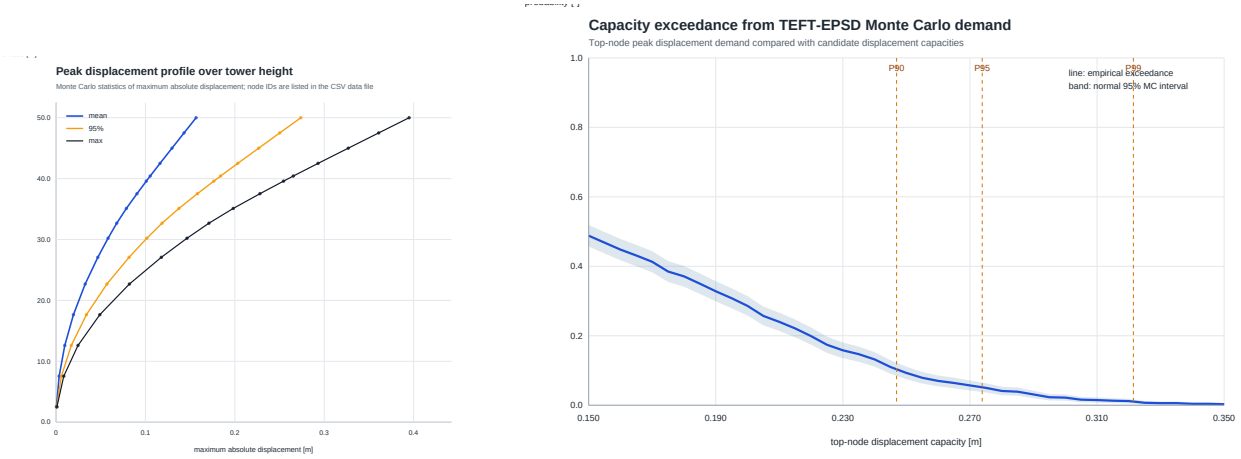


(a) Stochastic wind-speed ensemble.



(b) Signed top-node displacement histories.

Figure 4. Wind input and structural response diagnostics for the 1000-sample stochastic tower run. The wind histories retain the threshold-triggered storm envelope, while the response histories show the signed OpenSees top-node displacement before extracting maximum absolute demand for the reliability calculation.



(a) Node-wise peak displacement profile. (b) Capacity exceedance curve.

Figure 5. Structural reliability diagnostics for the stochastic tower run. Panel (a) reports Monte Carlo statistics over height, while panel (b) reports the estimated exceedance probability as a function of displacement capacity. The vertical marker indicates the 0.25 m capacity used for the main reliability estimate.

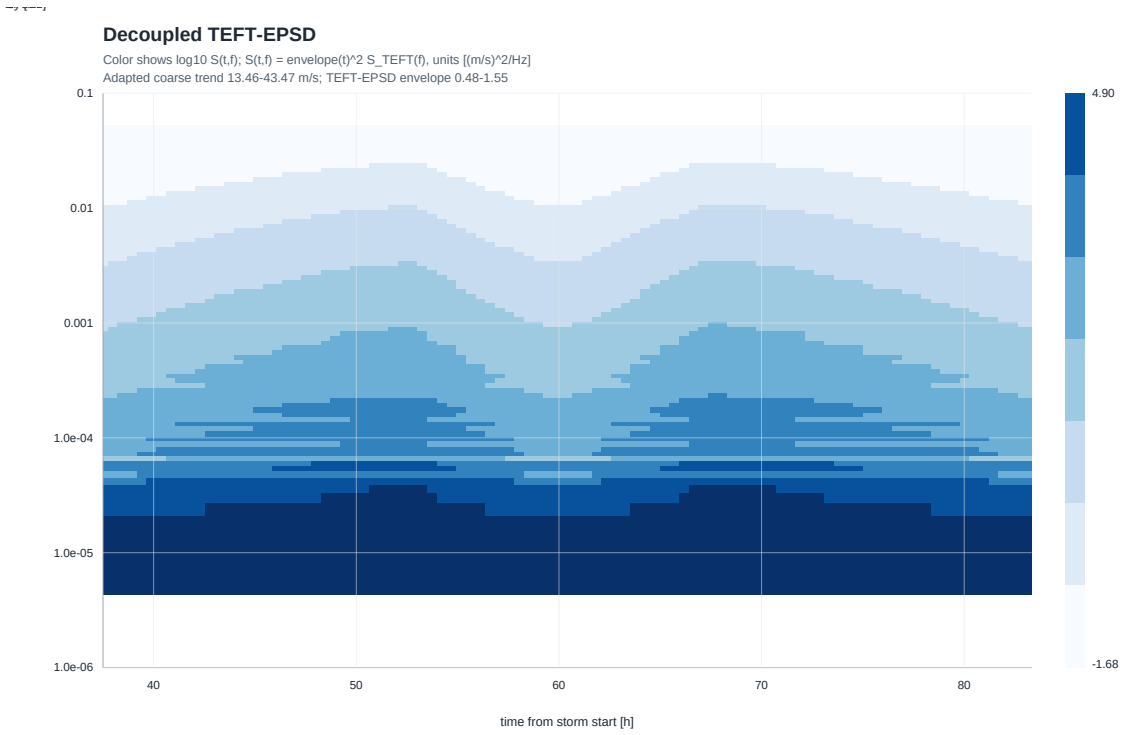


Figure 6. TEFT-EPSD heat map for the stochastic tower run. Color represents $\log_{10} S(t, f)$, illustrating how the stationary TEFT spectrum is modulated by the storm-scale envelope during the active window.

larger capacities. This redistribution of demand toward a rarer but more severe tail is the central reliability-relevant effect observed so far.

The present results should be interpreted as proof-of-concept demonstration cases rather than site-specific design values. The storm-variable ranges are bounded synthetic inputs, the displacement capacity is illustrative, and the final rare-event calculations are still being extended. Nevertheless, the computed response statistics show that the modular TEFT–storm–OpenSees workflow can produce traceable demand distributions, capacity-exceedance curves, and spectral diagnostics from coarse wind histories in a practical manner.

Acknowledgements

Marco Behrendt acknowledges financial support from the Alexander von Humboldt Foundation through a Feodor Lynen Research Fellowship. Marius Bittner acknowledges funding by dtec.bw - Digitalization and Technology, Research Center of the Bundeswehr. dtec.bw is funded by the European Union - NextGenerationEU.

References

Behrensdorf, J., Gray, A., Broggi, M., and Beer, M. (2023). UncertaintyQuantification.jl: A new framework for uncertainty quantification in julia. In *Proceedings of the 5th International Conference on Uncertainty Quantification in Computational Sciences and Engineering*, pages 419–436. doi: 10.7712/120223.10347.19810.

Behrensdorf, J., Gray, A., Perin, A., Grashorn, J., Luttmann, M., Fritsch, L., Belik, F., Schmidt, M., Broggi, M., Agarwal, G., Mett, F., Bittner, M., and Knipper, L. (2026). Juliauq/uncertaintyquantification.jl: v0.14.0. Software, Zenodo. `https://doi.org/10.5281/zenodo.18415973`.

Bezanson, J., Edelman, A., Karpinski, S., and Shah, V. B. (2017). Julia: A fresh approach to numerical computing. *SIAM Review*, 59(1):65–98. doi: 10.1137/141000671.

Bittner, M. (2026). Storm hazards simulation framework.

European Committee for Standardization (2005). EN 1991-1-4: Eurocode 1: Actions on structures – part 1-4: General actions – wind actions. Technical report, European Committee for Standardization, Brussels.

McKenna, F., Scott, M. H., and Fenves, G. L. (2010). Nonlinear finite-element analysis software architecture using object composition. *Journal of Computing in Civil Engineering*, 24(1):95–107. doi: 10.1061/(ASCE)CP.1943-5487.0000002.

Sun, Y., Bittner, M., Zhang, Y., and Beer, M. (2022). Simulation and risk evaluation of possible superstorms hitting europe's north sea coast. In Beer, M., Zio, E., Phoon, K.-K., and Ayyub, B. M., editors, *Proceedings of the 8th International Symposium on Reliability Engineering and Risk Management, ISRERM 2022*, pages 629–634, Singapore. Research Publishing Services. doi: 10.3850/978-981-18-5184-1_MS-19-105-cd.

Tambat, P., Bittner, M., Behrendt, M., and Beer, M. (2026). Data-driven modeling of synthetic wind speed signals with adaptive temporal resolution. SSRN preprint. Temporal Enhanced Fourier Transform (TEFT) manuscript; doi: 10.2139/ssrn.6531666; available at https://ssrn.com/abstract=6531666.

Tian, Z., Zhang, Y., Udo, K., and Lu, X. (2023). Regional economic losses of china's coastline due to typhoon-induced port disruptions. *Ocean and Coastal Management*, 237:106533. doi: 10.1016/j.ocecoaman.2023.106533.

Zhang, Y., Wei, K., Shen, Z., Bai, X., Lu, X., and Guedes Soares, C. (2020). Economic impact of typhoon-induced wind disasters on port operations: A case study of ports in china. *International Journal of Disaster Risk Reduction*, 50:101719. doi: 10.1016/j.ijdrr.2020.101719.

SESSION 5

Bayesian Inference, Active Learning and Surrogates

Papers in this session

1. Probability-box propagation with interval prediction models: a reproducible Python workflow
2. Multivariate Active Learning for Polynomial Chaos Expansion
3. Probabilistic Fatigue Life Modelling of Additively Manufactured Aluminum Alloys via Bayesian Inference
4. Combining Bayesian active learning and stratified sampling for bounding small failure probability under hybrid uncertainties
5. PINN-Accelerated Diffusion Models for Amortized Bayesian Inversion of Chloride Transport in Concrete
6. Bayesian Calibration of Resistance Spot Welding Models Using Temporal Process Features and Streamlined Active Learning

Probability-box propagation with interval prediction models: a reproducible Python workflow

Juntao Hu[1], Yu Chen[2], and Edoardo Patelli[1]
[1]*Department of Civil and Environmental Engineering, University of Strathclyde, Glasgow, UK*
juntao.hu@strath.ac.uk, edoardo.patelli@strath.ac.uk
[2]*Mechanical and Aerospace Engineering, University of Liverpool, Liverpool, UK*
yu.chen2@liverpool.ac.uk

Abstract. Probability boxes, or p-boxes, provide a useful representation of uncertainty when a precise probability distribution cannot be justified from the available information. Although p-box propagation is well established theoretically, its practical implementation remains challenging for users who require transparent and reproducible computational workflows. This paper presents a tutorial-style Python workflow for constructing and propagating p-boxes and for approximating propagated response bounds using Interval Prediction Models via a newly developed Python package `PyUncertainNumber`. The aim is not to introduce a new propagation theory, but to clarify how p-box inputs can be defined, propagated through nonlinear models, extracted as probability-level-dependent response intervals, and represented by a compact interval model. The workflow is first demonstrated using the Rosenbrock function, which provides a simple nonlinear benchmark. It is then extended to an excavation-induced tunnel displacement problem, where a first-level Interval Prediction Model is used as a surrogate of numerical simulation data and soil-parameter uncertainty is propagated to tunnel displacement predictions. The results show how p-box propagation and interval modelling can be combined into a reproducible workflow for conservative engineering response assessment. The paper is intended as a practical guide for researchers and engineers implementing imprecise-probability propagation in software-based uncertainty analysis.

Keywords: Probability box; Uncertain number; Interval Prediction Model; Tutorial

1. Introduction

Engineering systems are commonly affected by multiple sources of uncertainty, including natural variability, limited experimental data, measurement errors, model-form simplifications, and incomplete knowledge of the physical system. In reliability analysis and risk-informed decision-making, these uncertainties must be propagated through computational models in order to assess the possible range of system responses. This task becomes particularly important when the predicted response is used for safety evaluation, design verification, or failure probability estimation, see e.g. (Nuttall et al., 2025). In many engineering applications, uncertainty is traditionally represented using precise probabilistic models. However, sufficient data are not always available to justify a precise distributional assumption. In such cases, assigning a specific probability distribution may lead to overconfident predictions.

© 2026 by the author(s). This work is licensed under the Creative Commons Attribution 4.0 International License (CC BY 4.0), which permits unrestricted use, distribution, and reproduction in any medium, provided the original author and source are credited.

To address this issue, imprecise probability models have been developed to represent uncertainty under limited or incomplete information (Faes et al., 2021). Probability boxes, or P-boxes, provide a flexible representation of imprecise probabilistic information. Instead of defining a single cumulative distribution function, a P-box describes a family of admissible distributions bounded by lower and upper cumulative distribution functions. This allows aleatory variability and epistemic uncertainty to be considered simultaneously. P-boxes have therefore been widely used in engineering analysis when probability distributions are only partially known, when data are sparse, or when multiple sources of uncertain information must be combined (Lye et al., 2022; Zhang et al., 2023; Chen and Ferson, 2025).

The propagation of P-boxes through computational models remains a challenging task. Compared with conventional probabilistic uncertainty propagation, P-box propagation often requires the evaluation of response bounds over a family of possible input distributions. Direct approaches, such as double-loop sampling, interval Monte Carlo, or repeated optimisation, can become computationally demanding, especially when the model is nonlinear, high-dimensional, or expensive to evaluate. This difficulty is particularly relevant for engineering problems involving high-fidelity numerical models, where each model evaluation may require considerable computational resources.

Several efficient methods have been proposed to reduce the computational cost of P-box propagation (Patelli et al., 2015). Sparse polynomial chaos expansions have been used to propagate P-box uncertainty through complex computational models with a reduced number of model evaluations (Schöbi and Sudret, 2017). Sparse-decomposition-based polynomial chaos expansions have also been developed for parameterized P-boxes, aiming to obtain probability bounds and statistical moment bounds more efficiently (Liu et al., 2020). For dependent uncertain inputs, copula-based methods have been introduced to propagate correlated parametric P-boxes in structural models (Liu et al., 2021). More recently, meta-model-based strategies, such as active-learning Kriging, have been proposed for uncertainty propagation involving non-parameterized P-boxes (Zhang et al., 2023). These studies demonstrate the importance of surrogate-assisted P-box propagation, but most existing approaches are primarily designed to approximate response functions or response distributions rather than to construct conservative interval response envelopes directly.

Interval Predictor Models provide a data-driven framework for constructing response bounds from available data (Sadeghi et al., 2018). Unlike conventional regression or surrogate models that aim to approximate a single deterministic response or a conditional mean, an Interval Predictor Model seeks to enclose observed responses within lower and upper prediction functions. The original formulation of interval predictor models with linear parameter dependency provides a basis for constructing bounded response predictions under uncertainty (Crespo et al., 2016). This interval-valued structure makes IPMs particularly attractive for engineering applications where conservative lower and upper response envelopes are more informative than a single best-estimate prediction. The use of Interval Predictor Models for P-box propagation has been investigated as a robust strategy for propagating imprecise probabilistic information through computational models (Sadeghi et al., 2020). In this setting, the IPM acts as an interval-based surrogate that maps uncertain inputs to lower and upper response bounds. Compared with point-valued surrogate models, this is particularly useful when the objective is not only to approximate the model response, but also to retain conservative response bounds throughout the uncertainty propagation process. However, further development is required to extend this idea to multidimensional uncertain input spaces and to

clarify its role as an efficient surrogate framework for engineering applications involving limited data and expensive numerical simulations.

The contribution of this paper is therefore practical rather than theoretical. It provides: (i) a reproducible Python workflow for constructing parametric p-boxes and propagating them through nonlinear models; (ii) a clear distinction between a first-level IPM used as a surrogate of an engineering model and a second-layer IPM used to approximate a propagated output p-box; (iii) a tutorial benchmark based on the Rosenbrock function; and (iv) an engineering demonstration involving excavation-induced tunnel displacement, where uncertainty in soil parameters is propagated through an IPM surrogate. The paper is intended to help users implement p-box propagation in a transparent and auditable way, rather than to propose a new propagation algorithm.

2. P-box propagation and IPM approximation workflow

This section defines the methodological and software workflow used in the remainder of the paper. The aim is not to provide a complete theoretical review of probability boxes or Interval Prediction Models, but to introduce the concepts required to implement the proposed tutorial. The workflow combines three components: p-box representation of imprecise probabilistic inputs, propagation through a model or surrogate, and interval approximation of the propagated output p-box.

A central distinction in this paper is between two different uses of Interval Prediction Models. A first-level IPM may be used as a surrogate of an expensive engineering model. In contrast, a second-layer IPM is used after p-box propagation to approximate the extracted output p-box bounds as functions of probability level. These two uses are conceptually different and should not be interpreted as the same modelling task.

2.1. Probability boxes

A probability box, or p-box, represents uncertainty by bounding a family of cumulative distribution functions. Instead of assuming one precise cumulative distribution function $F_X(x)$, a p-box is defined by lower and upper cumulative probability bounds:

$$\underline{F}_X(x) \leq F_X(x) \leq \overline{F}_X(x), \tag{1}$$

where $\underline{F}_X(x)$ and $\overline{F}_X(x)$ denote the lower and upper cumulative distribution bounds, respectively. This representation is useful when the available information is insufficient to identify a unique probability distribution, but sufficient to constrain a family of admissible distributions.

In this paper, p-boxes are mainly used to represent uncertain input variables whose distributional parameters are not precisely known. For example, a normally distributed variable with uncertain mean and uncertain standard deviation can be expressed as

$$X \sim \mathcal{N}(\mu, \sigma^2), \qquad \mu \in [\underline{\mu}, \overline{\mu}], \qquad \sigma \in [\underline{\sigma}, \overline{\sigma}]. \tag{2}$$

and the corresponding p-box encloses the cumulative distribution functions associated with this distribution family.

2.1.1. *P-box propagation*

The propagation stage takes uncertain inputs represented as p-boxes

$$\mathbf{X}_{\text{pbox}} = [X_{1,\text{pbox}}, X_{2,\text{pbox}}, \ldots, X_{d,\text{pbox}}]\,. \tag{3}$$

and propagates them through model

$$\mathbf{X}_{\text{pbox}} \to g(\mathbf{X}) \to Y_{\text{pbox}}. \tag{4}$$

The output Y_{pbox} describes the imprecise probabilistic uncertainty in the model response induced by the input p-boxes. In practice, the propagation of p-boxes is often perfomed using the slicing methods that propagates a p-box by discretising its probability axis into a finite number of probability levels. For each probability level α_i, the input p-box is represented by an interval of admissible quantile values,

$$X_{\alpha_i} = [\underline{x}(\alpha_i), \overline{x}(\alpha_i)]\,, \qquad i = 1, \ldots, M. \tag{5}$$

For multiple uncertain inputs, each input p-box is sliced in the same way. At probability level α_i, the corresponding uncertain input domain is therefore

$$\mathcal{X}_{\alpha_i} = X_{1,\alpha_i} \times X_{2,\alpha_i} \times \cdots \times X_{d,\alpha_i}. \tag{6}$$

The response interval associated with this probability level is obtained by bounding the model response over the sliced input domain:

$$\underline{y}(\alpha_i) = \min_{\mathbf{x} \in \mathcal{X}_{\alpha_i}} g(\mathbf{x}), \qquad \overline{y}(\alpha_i) = \max_{\mathbf{x} \in \mathcal{X}_{\alpha_i}} g(\mathbf{x}). \tag{7}$$

Repeating this operation for all probability levels gives a discrete representation of the propagated output p-box:

$$Y_{\text{pbox}} = \left\{\alpha_i, \underline{y}(\alpha_i), \overline{y}(\alpha_i)\right\}_{i=1}^{M}. \tag{8}$$

Thus, the slicing procedure converts p-box propagation into a sequence of interval propagation problems. The probability levels preserve the probabilistic ordering of the input uncertainty, while the interval bounds at each level account for the epistemic uncertainty associated with the admissible family of input distributions. For nonlinear or non-monotonic models, the lower and upper response bounds should be obtained using an interval-bounding or optimisation strategy rather than by evaluating only the interval endpoints.

2.2. Interval Prediction Models

An Interval Prediction Model is a data-driven model that constructs lower and upper response bounds from input–output data. IPMs are used because their interval-valued structure is consistent with the objective of conservative response prediction under uncertainty. However, it is important to distinguish between two different use of IPM in the workflow, see Table I. The first-level IPM is a surrogate of a physical, numerical, or mathematical model. The second-layer IPM is a compact approximation of the p-box bounds obtained after uncertainty propagation through a model.

Table I. IPM roles in the proposed workflow.

Component	Input-Output	Purpose
First-level IPM	Measurements or model inputs-outputs	Regression analysis or surrogate of an expensive computational model
Second-layer IPM	Probability level α and corresponding response	Compact approximation of the propagated output p-box

2.2.1. *First-level IPM construction*

A first-level IPM is constructed from input–output data obtained from experimental values or from a computational model that maps input variables to a response quantity. The input samples may be generated using a deterministic design of experiments, random sampling, Latin Hypercube Sampling, or user-defined engineering scenariosn obtained a dataset:

$$\mathcal{D} = \{\mathbf{x}_i, y_i\}_{i=1}^{N}, \tag{9}$$

. An IPM learns lower and upper prediction functions:

$$\mathrm{IPM}_1(\mathbf{x}) = [y_L(\mathbf{x}), y_R(\mathbf{x})], \tag{10}$$

where $y_L(\mathbf{x})$ and $y_R(\mathbf{x})$ denote the lower and upper bounds of the interval prediction. A fitted IPM is normally required to enclose the training responses,

$$y_L(\mathbf{x}_i) \le y_i \le y_R(\mathbf{x}_i), \qquad i = 1, \ldots, N, \tag{11}$$

while keeping the prediction interval as compact as possible.

Once trained, the first-level IPM can be evaluated more efficiently than the original model and can therefore be used during the p-box propagation stage.

2.2.2. *Second-layer IPM approximation of the output p-box*

The second-layer IPM is obtained from the propagation of the uncertainty in a form of p-box through a computational model (or surrogate). An interval-valued mapping from probability level to response bounds:

$$\alpha_i \to [Y_L(\alpha_i), Y_R(\alpha_i)]. \tag{12}$$

and a IPM is then fitted to provide a bounded functional approximation of the p-box envelope:

$$\mathrm{IPM}_2 : \alpha \to \left[\widehat{Y}_L(\alpha), \widehat{Y}_R(\alpha)\right]. \tag{13}$$

The second-layer IPM is not the only possible approximation strategy. Alternative approaches, such as interpolation, spline approximation, monotone regression, or direct storage of the extracted p-box bounds, could also be used. The IPM is adopted because it provides an interval-valued representation consistent with the broader interval-modelling framework used in this paper.

2.3. Software components

Two uncertainty-related Python libraries are used. `pyuncertainnumber` (Chen and Ferson, 2025) is used to construct and propagate p-boxes. `PyIPM` (Sadeghi, 2020) is used to construct the first-level and second-layer Interval Prediction Models. `PyIPM` is a Python implementation of the Interval Predictor Model toolbox originally developed in the OpenCOSSAN uncertainty quantification framework (Patelli et al., 2017). Alternative implementations also exist, including OpenCOSSAN in MATLAB (Patelli et al., 2014) and ProbabilityBoundsAnalysis.jl in Julia (Gray et al., 2021).

The p-box and IPM components are connected through data transformations rather than treated as a single algorithm. First, uncertain inputs are defined either directly as p-boxes, as in the Rosenbrock tutorial, or through physical parameters, as in the excavation-induced tunnel displacement demonstration. The model response is then propagated through either an explicit mathematical function, a numerical model, or a first-level IPM surrogate. The resulting probability-level-dependent response bounds are finally reformulated as an interval dataset for the second-layer IPM approximation.

3. Tutorial example: Rosenbrock function

This section provides an executable tutorial example to demonstrate how input p-boxes are constructed, propagated through a nonlinear model, extracted as probability-level-dependent response bounds, and approximated using a second-layer IPM. The Rosenbrock function is used because it is simple to evaluate while still sufficiently nonlinear to produce an informative output p-box. Since the Rosenbrock function can be evaluated directly, no first-level IPM is required in this tutorial example.

3.1. Model definition

The two-dimensional Rosenbrock function is defined as

$$g(x_1, x_2) = (1 - x_1)^2 + 100(x_2 - x_1^2)^2. \tag{14}$$

It is treated as a generic black-box model with uncertain input variables X_1 and X_2. Listing 1 gives the Python implementation used in the propagation.

```python
def rosenbrock_model(*args):
    """ Rosenbrock function.
    It can accept either rosenbrock_model([x1, x2]) or rosenbrock_model(x1, x2). """
    if len(args) == 1:
        x1, x2 = args[0][0], args[0][1]
    elif len(args) == 2:
        x1, x2 = args
    else:
        raise ValueError("Rosenbrock model expects one or two input variables.")

    return (1 - x1)**2 + 100 * (x2 - x1**2)**2
```

Listing 1: Definition of the Rosenbrock benchmark function.

3.2. Input p-box construction

The two input variables are represented as parametric p-boxes. Each variable is assumed to follow a normal distribution with uncertain mean and uncertain standard deviation:

$$X_1 \sim \mathcal{N}(\mu_1, \sigma_1^2), \qquad \mu_1 \in [-1.2, -0.8], \qquad \sigma_1 \in [0.10, 0.20], \tag{15}$$

and

$$X_2 \sim \mathcal{N}(\mu_2, \sigma_2^2), \qquad \mu_2 \in [0.8, 1.2], \qquad \sigma_2 \in [0.10, 0.20]. \tag{16}$$

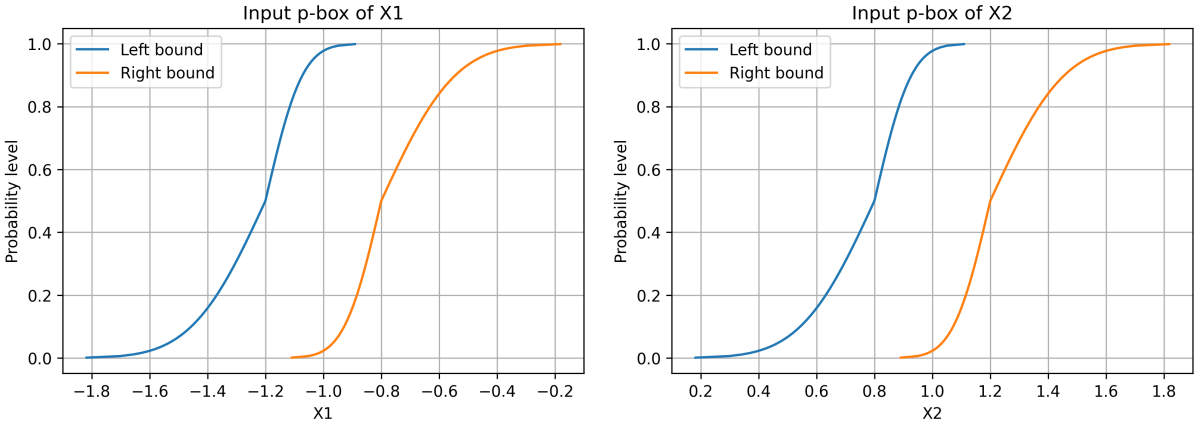
The corresponding p-boxes are constructed using `PyUncertainNumber`, as shown in Listing 2.

```
from pyuncertainnumber import pba
from pyuncertainnumber import slicing

# Construct normal p-boxes with interval-valued parameters
x1_pbox = pba.normal([-1.2, -0.8], [0.10, 0.20])
x2_pbox = pba.normal([0.8, 1.2], [0.10, 0.20])
```

Listing 2: Construction of input p-boxes using PyUncertainNumber.

The resulting input p-boxes are shown in Figure 1.



(a) X_1 (b) X_2

Figure 1. Input p-boxes for the Rosenbrock example.

3.3. Direct p-box propagation

The input p-boxes are propagated through the Rosenbrock function using the slicing-based procedure introduced in Section 2.1.1. The corresponding implementation is shown in Listing 3, and the directly propagated output p-box is shown in Figure 2.

```
# Run slicing-based p-box propagation
y_pbox = slicing(vars=[x1_pbox, x2_pbox],func=rosenbrock_model,
    interval_strategy="direct", n_slices=20, outer_discretisation=True)
```

Listing 3: Propagation of input p-boxes through the Rosenbrock function.

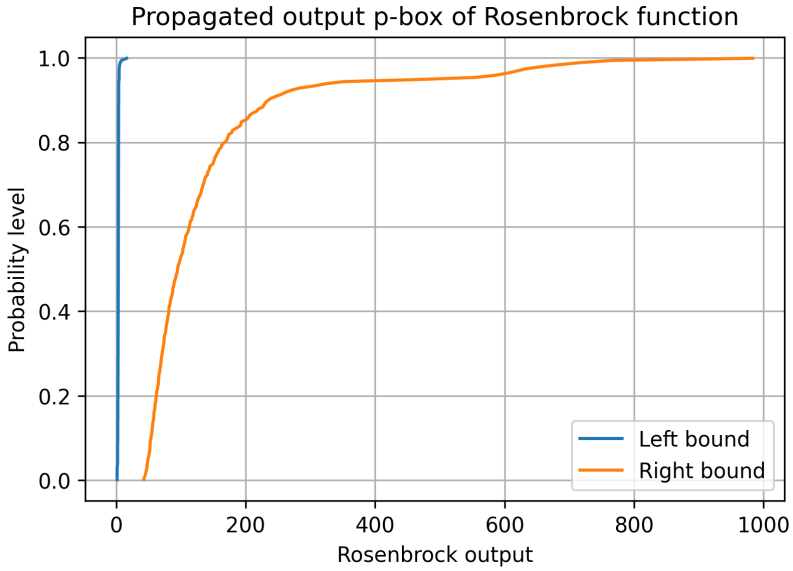


Figure 2. Output p-box of the Rosenbrock response propagated using `PyUncertainNumber`.

The spread between the left and right cumulative bounds reflects the epistemic uncertainty associated with the interval-valued distribution parameters of the inputs. The nonlinear form of the Rosenbrock function also induces an asymmetric response structure, which is visible in the large range of the propagated output bounds.

3.4. Extraction of output p-box bounds

Following Section 2.2.2, the propagated output p-box is extracted into arrays of probability levels and corresponding left and right response bounds. These arrays form the training data for the second-layer IPM. The extraction uses only public attributes of the `Pbox` object, as shown in Listing 3.

```
def extract_pbox_bounds(pbox):
    """Extract probability levels and p-box bounds using public attributes.
    No private attributes such as _construct, _left, or _right are used."""
    alpha = np.asarray(pbox.p_values).reshape(-1, 1)
    y_left = np.asarray(pbox.left)
    y_right = np.asarray(pbox.right)
    return alpha, y_left, y_right

alpha, y_left, y_right = extract_pbox_bounds(y_pbox)
```

Listing 3: Extraction of output p-box probability levels and response bounds.

3.5. Second-layer IPM approximation

The second-layer IPM follows the mapping defined in Section 2.2.2 and it is used fit the Rosenbrock output p-box bounds. The Rosenbrock's response has a long right tail, therefore a log scale of

the output space is used to fit the IPM. Since the logarithmic transformation is monotonic for positive responses, the ordering of the lower and upper response bounds is preserved after back-transformation. The implementation is shown in Listing 4.

```
import PyIPM
# Avoid log(0) before applying the logarithmic transformation
eps = 1e-12
y_left_safe = np.maximum(y_left, eps)
y_right_safe = np.maximum(y_right, eps)

# Stack the lower and upper propagated bounds as training responses
alpha_train = np.vstack([alpha, alpha])
log_y_train = np.concatenate([np.log(y_left_safe),np.log(y_right_safe)])

# Fit a quadratic second-layer IPM
model_ipm2 = PyIPM.IPM(polynomial_degree=2)
model_ipm2.fit(alpha_train, log_y_train)

# Predict second-layer IPM bounds at the extracted probability levels
log_upper_pred, log_lower_pred = model_ipm2.predict(alpha)
log_upper_pred = np.asarray(log_upper_pred).ravel()
log_lower_pred = np.asarray(log_lower_pred).ravel()

# Transform the fitted bounds back to the original response scale
y_upper_ipm = np.exp(log_upper_pred)
y_lower_ipm = np.exp(log_lower_pred)
```

Listing 4: Second-layer IPM approximation of the extracted output p-box using PyIPM.

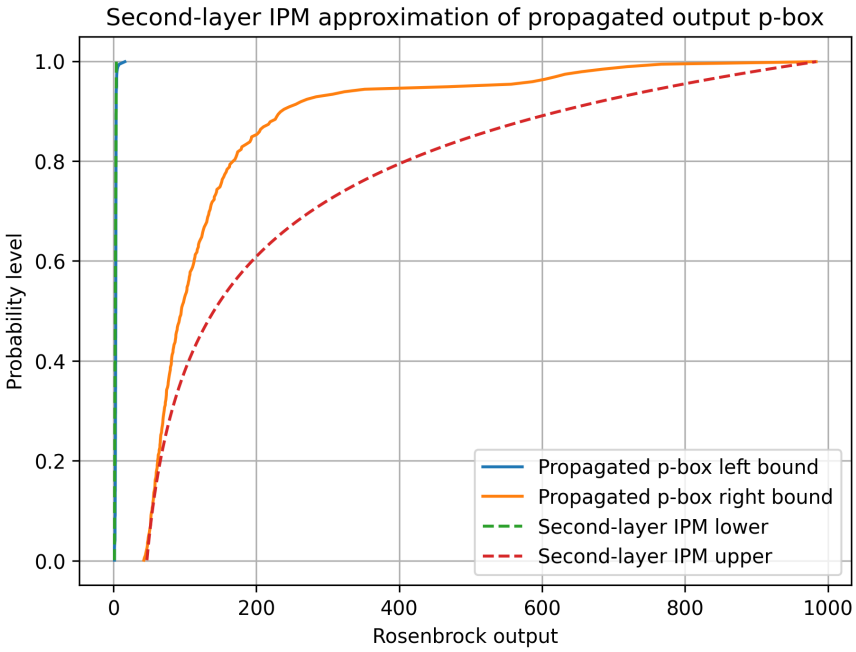


Figure 3. Second-layer IPM approximation of the Rosenbrock output p-box.

In this implementation, the extracted lower and upper response bounds are stacked into a single training set. The same probability levels are used for both sets of response values. The fitted bounds are then transformed back to the original response scale for visualisation. The resulting second-layer IPM approximation is shown in Figure 3.

The second-layer IPM should not be interpreted as an exact reconstruction of the propagated p-box. It is a compact interval approximation fitted to the extracted probability-level-dependent bounds. In this tutorial, a quadratic polynomial basis is deliberately used to keep the implementation simple and interpretable. The purpose is to demonstrate the computational connection between p-box propagation and interval approximation, rather than to optimise the approximation accuracy. If higher approximation accuracy were required, a higher-order basis or a more flexible approximation scheme could be used.

4. Engineering demonstration: excavation-induced tunnel displacement

This section demonstrates how the Rosenbrock tutorial workflow can be transferred to an engineering problem involving excavation-induced tunnel displacement. The purpose is not to present a complete site-specific reliability assessment, but to show how p-box propagation can be coupled with a first-level IPM surrogate trained from numerical simulation data. The excavation model, simulation dataset, and calibration procedure are reported in detail in the submitted journal paper (Hu et al., 2026). Therefore, this section focuses only on using the trained excavation IPM surrogate within the p-box propagation workflow.

The demonstration considers the horizontal displacement of an existing tunnel affected by a nearby excavation, a common urban geotechnical problem where ground movements may affect adjacent underground infrastructure.

4.1. First-level excavation IPM surrogate

The first-level IPM surrogate is trained from an excavation simulation dataset. The input vector is defined as

$$\mathbf{x} = \left[B, EI_{\text{ratio}}, \frac{s_u}{\sigma'_v}, \frac{E_{ur}}{\sigma'_v}, D_h, \frac{D_v}{H} \right], \tag{17}$$

where B is the excavation width, EI_{ratio} is the retaining system stiffness ratio, s_u/σ'_v is the undrained shear strength ratio, E_{ur}/σ'_v is the unloading stiffness ratio, D_h is the horizontal distance between the excavation and the tunnel, and D_v/H is the normalised tunnel depth. The response variable considered in this demonstration is the horizontal tunnel displacement u_x.

The first-level IPM maps the excavation input vector to lower and upper displacement predictions:

$$\text{IPM}_1(\mathbf{x}) = \left[u_{x,L}(\mathbf{x}), u_{x,R}(\mathbf{x}) \right]. \tag{18}$$

In the present demonstration, the upper bound $u_{x,R}(\mathbf{x})$ is used as the conservative response for the subsequent p-box propagation:

$$U_x = u_{x,R}(\mathbf{x}). \tag{19}$$

This means that the propagation is performed through the upper envelope of the surrogate, rather than through a single deterministic best-estimate model.

The training performance of the first-level IPM surrogate is summarised in Table II. The reported lower-bound and upper-bound violations are close to numerical precision, indicating that the fitted IPM encloses the training responses.

Table II. Summary of the first-level IPM training results for horizontal tunnel displacement.

Item	Value
Number of training samples	1000
Number of input variables	6
Output variable	Horizontal displacement, u_x
Maximum lower-bound violation	2.65×10^{-12}
Maximum upper-bound violation	1.46×10^{-12}
Average interval width	0.6675
Minimum interval width	0.0507
Maximum interval width	3.2939

Table II confirms that the first-level IPM provides an enclosing surrogate over the training dataset. However, this training enclosure should not be interpreted as a complete validation of predictive accuracy outside the sampled domain. The surrogate is used here only within the range represented by the simulation data.

4.2. Soil-parameter uncertainty model

The input uncertainty is introduced through physically meaningful soil parameters rather than by directly prescribing uncertainty on the surrogate descriptors s_u/σ'_v and E_{ur}/σ'_v. Specifically, uncertainty is assigned to cohesion c, friction angle ϕ, and a stiffness multiplier λ. These parameters are then transformed into the strength and stiffness descriptors required by the first-level IPM.

The undrained shear strength ratio is computed as

$$\frac{s_u}{\sigma'_v} = \frac{c\cos\phi}{\sigma'_v} + \frac{1}{2}(1 + K_0)\sin\phi, \tag{20}$$

where σ'_v is the effective vertical stress and K_0 is the earth pressure coefficient at rest. The unloading stiffness ratio is then obtained from

$$\frac{E_{ur}}{\sigma'_v} = \lambda\frac{s_u}{\sigma'_v}, \tag{21}$$

where λ is an uncertain multiplicative coefficient. This transformation preserves the dependency between the strength and stiffness descriptors and avoids physically inconsistent strength–stiffness combinations. The remaining engineering variables are fixed at representative values to isolate the effect of soil-parameter uncertainty.

4.3. P-box propagation through the excavation surrogate

The p-box propagation is performed through the conservative upper response of the first-level IPM surrogate. At each probability slice, the uncertain soil parameters define admissible intervals for c, ϕ, and λ. These intervals are transformed through Equations (20) and (21) to obtain corresponding intervals for s_u/σ'_v and E_{ur}/σ'_v. The resulting uncertain engineering descriptors are then propagated through the first-level IPM using the conservative response defined in Equation (19).

Repeating this process over all probability levels gives the output p-box of the conservative horizontal displacement response. The propagated output p-box is shown in Figure 4. The vertical dashed line indicates a 20 mm displacement threshold used here as an illustrative engineering control limit.

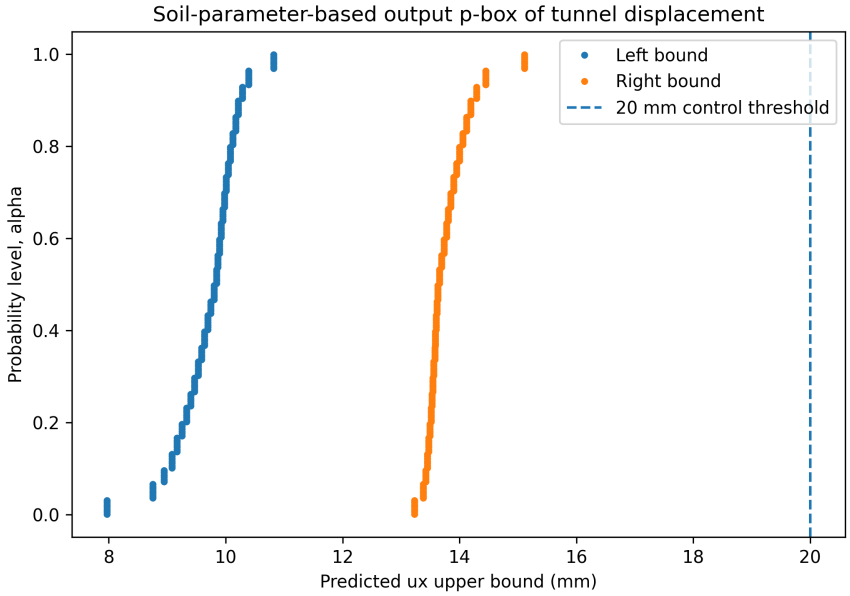


Figure 4. Soil-parameter-based output p-box of conservative horizontal tunnel displacement.

The output p-box provides more information than a deterministic displacement prediction. It shows the range of cumulative response behaviour induced by imprecise soil-parameter uncertainty. If the upper response bound remains below the 20 mm threshold over the relevant probability range, the scenario can be interpreted as conservatively acceptable under the specified uncertainty assumptions. If part of the upper response bound crosses the threshold, the result indicates that the uncertainty model admits soil conditions that may require additional design review, monitoring, or more detailed numerical analysis.

4.4. Second-layer approximation of the engineering output p-box

The same procedure introduced in Section 2.2.2 is used here to compute the bounds of the conservative horizontal displacement response obtained from the first-level excavation IPM surrogate.

The second-layer approximation is shown in Figure 5. The markers denote the propagated p-box bounds, while the fitted curves provide a compact interval representation of the same result.

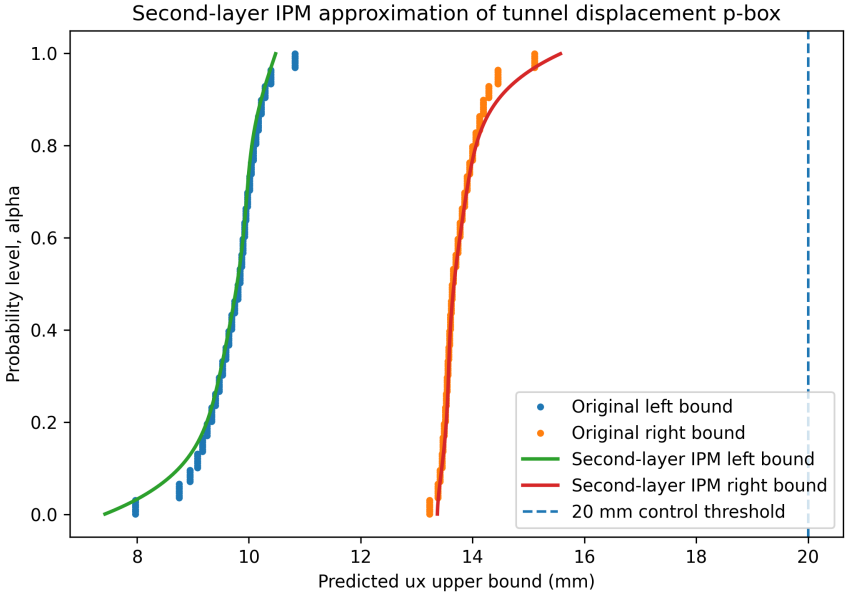


Figure 5. Second-layer IPM approximation of the soil-parameter-based output p-box.

This second-layer approximation is optional but useful when a compact functional representation of the propagated p-box is needed for storage, comparison, or subsequent calculations. However, it should be interpreted as an approximation of the already propagated p-box, not as a replacement for the first-level excavation surrogate or the original numerical simulation model.

4.5. Discussion and limitations of the engineering demonstration

The engineering demonstration shows how the tutorial workflow can be transferred from an analytical benchmark to a surrogate-based geotechnical problem. The uncertainty is introduced through physically interpretable soil parameters, while the expensive model response is replaced by an interval-valued surrogate. This makes it possible to combine p-box propagation with conservative response prediction in a computationally efficient way.

The demonstration also highlights the importance of preserving physical dependencies between derived inputs. In the present case, the strength and stiffness descriptors are both computed from the same underlying soil parameters. This avoids the physically inconsistent combinations that could arise if the two descriptors were treated as independent uncertain inputs.

Several limitations should be noted. First, the example is intended as a demonstration of the workflow, not as a complete site-specific reliability analysis. Only selected soil parameters are treated as uncertain, while other engineering variables are fixed at representative values. Second, the first-level IPM is used within the range of the simulation data from which it was trained. Its

reliability outside this range is not assessed here. Third, the training enclosure reported in Table II demonstrates consistency with the training data, but it does not replace independent validation. Finally, the 20 mm threshold is used as an illustrative control limit; a real assessment would require a project-specific serviceability or damage criterion.

Future engineering applications should therefore include a broader uncertainty model, explicit treatment of dependency between geotechnical parameters, validation of the first-level IPM against independent simulations, and sensitivity analysis of the p-box propagation settings. Despite these limitations, the example demonstrates the practical role of the proposed workflow as a transparent bridge between imprecise soil-parameter uncertainty and conservative displacement assessment.

5. Conclusions

This paper presented a reproducible workflow for propagating probability boxes using a Python library called `pyuncertainnumber` and approximating the propagated output bounds using Interval Prediction Models. The contribution is practical rather than theoretical: the paper clarifies how p-box inputs can be constructed, propagated, extracted as probability-level-dependent response intervals, and represented by a compact second-layer IPM.

The Rosenbrock example showed the complete workflow in a controlled nonlinear setting. Two normal p-box inputs with interval-valued means and standard deviations were propagated through the Rosenbrock function using slicing-based propagation. The resulting output p-box was then extracted as pairs of lower and upper response bounds at discrete probability levels. A quadratic second-layer IPM, fitted in logarithmic response space, provided a compact approximation of this propagated p-box.

The excavation-induced tunnel displacement example showed how the same workflow can be used when the original model is replaced by a first-level IPM surrogate. In this case, uncertainty was introduced through cohesion, friction angle, and a stiffness multiplier, then transformed into the strength and stiffness descriptors required by the excavation surrogate. This avoided assigning independent uncertainty directly to derived variables and preserved a clearer physical link between soil uncertainty and tunnel displacement.

The main technical distinction is that the two IPMs have different roles. The first-level IPM is a surrogate of the engineering model. The second-layer IPM is not a model surrogate; it is an approximation of the propagated output p-box. This distinction is essential for interpreting the workflow correctly.

The results indicate that the proposed workflow is useful for tutorial and engineering-screening purposes, especially when users need an auditable connection between imprecise input distributions, p-box propagation, and conservative response bounds. The results indicate that the proposed workflow is useful for tutorial and engineering-screening purposes, especially when users need an auditable connection between imprecise input distributions, p-box propagation, and conservative response bounds. Future work should focus on broader uncertainty modelling, independent validation of the first-level IPM, and sensitivity analysis of the propagation settings.

References

Chen, Y. and S. Ferson: 2025, 'Imprecise uncertainty management with uncertain numbers to facilitate trustworthy computations'. In: *SciPy Proceedings*.

Crespo, L. G., S. P. Kenny, and D. P. Giesy: 2016, 'Interval predictor models with a linear parameter dependency'. *Journal of Verification, Validation and Uncertainty Quantification* **1**(2), 021007.

Faes, M., M. Daub, S. Marelli, E. Patelli, and M. Beer: 2021, 'Engineering analysis with probability boxes: A review on computational methods'. *Structural Safety* **93**, 102092.

Gray, A., S. Ferson, and E. Patelli: 2021, 'ProbabilityBoundsAnalysis.jl: Arithmetic with sets of distributions'. *Proceedings of the JuliaCon Conferences*.

Hu, J., E. Patelli, Y. Chen, and M. De Angelis: 2026, 'A Robust Data-Driven Interval Prediction of Tunnel Displacement Induced by Urban Excavation'. Manuscript submitted for publication.

Liu, H., M. Chen, C. Du, J. Tang, C. Fu, and G. She: 2021, 'A copula-based uncertainty propagation method for structures with correlated parametric p-boxes'. *International Journal of Approximate Reasoning* **138**, 89–104.

Liu, H. B., C. Jiang, and Z. Xiao: 2020, 'Efficient uncertainty propagation for parameterized p-box using sparse-decomposition-based polynomial chaos expansion'. *Mechanical Systems and Signal Processing* **138**, 106589.

Lye, A., M. Kitahara, M. Broggi, and E. Patelli: 2022, 'Robust Optimization of a Dynamic Black-box System under Severe Uncertainty: A Distribution-Free Framework'. *Mechanical Systems and Signal Processing* **167**, 108522.

Nuttall, W., E. Patelli, E. Smith, D. Webbe-Wood, and S. Middleburgh: 2025, *Perspectives on Engineering Uncertainty: Civil Nuclear Energy Safety and Efficiency*. Springer Nature. Accepted: 2025-05-13T08:23:33Z.

Patelli, E., D. A. Alvarez, M. Broggi, and M. d. Angelis: 2015, 'Uncertainty management in multidisciplinary design of critical safety systems'. *Journal of Aerospace Information Systems* **12**(1), 140–169.

Patelli, E., M. Broggi, M. d. Angelis, and M. Beer: 2014, 'OpenCossan: An Efficient Open Tool for Dealing with Epistemic and Aleatory Uncertainties'. In: *Vulnerability, Uncertainty, and Risk*. pp. 2564–2573, American Society of Civil Engineers.

Patelli, E., M. Broggi, S. Tolo, and J. Sadeghi: 2017, 'Cossan Software: A Multidisciplinary and Collaborative Software for Uncertainty Quantification'. In: *Proceedings of the 2nd ECCOMAS Thematic Conference on Uncertainty Quantification in Computational Sciences and Engineering*. Rhodes Island, Greece.

Sadeghi, J., M. D. Angelis, and E. Patelli: 2018, 'Frequentist history matching with interval predictor models'. *Applied Mathematical Modelling* **61**, 29–48.

Sadeghi, J., M. De Angelis, and E. Patelli: 2020, 'Robust propagation of probability boxes by interval predictor models'. *Structural Safety* **82**, 101889.

Sadeghi, J. C.: 2020, 'PyIPM: Interval Predictor Models in Python'. `https://github.com/JCSadeghi/PyIPM`. Python package, version 2.0.

Schöbi, R. and B. Sudret: 2017, 'Uncertainty propagation of p-boxes using sparse polynomial chaos expansions'. *Journal of Computational Physics* **339**, 307–327.

Zhang, K., N. Chen, J. Liu, S. Yin, and M. Beer: 2023, 'An efficient meta-model-based method for uncertainty propagation problems involving non-parameterized probability-boxes'. *Reliability Engineering & System Safety* **238**, 109477.

Multivariate Active Learning for Polynomial Chaos Expansion

Qitian Lu, Miroslav Vořechovský, Lukáš Novák
Faculty of Civil Engineering, Brno University of Technology, Brno 602 00, Czechia,
Lukas.Novak4@vut.cz

Abstract. The paper extends the active learning strategy of (Novák et al., 2021), which was originally designed for scalar-output polynomial chaos expansion surrogate models, to the case of vector-valued quantities of interest. Physical systems simulated by mathematical models typically contain multiple outputs (e.g., extrema in stress fields), and thus it is often necessary to construct several surrogate models for subsequent uncertainty quantification of each output. While the construction of surrogate models one-by-one for a single one-shot experimental design generated by various techniques (e.g., Latin Hypercube Sampling) is straightforward, an active learning methodology for multiple outputs remains an open research question. The proposed method combines the adaptivity of a polynomial chaos expansion with sequential sampling, enabling a one-by-one extension of the experimental design. The iterative process of sequential sampling selects points from a large pool of candidates by attempting to cover the design domain proportionally to their local variance contribution. The proposed criterion for sample selection balances between exploitation of the surrogate model and exploration of the design domain, while accounting for the different contributions of each output to the total criterion. The obtained numerical results confirm its superiority over standard non-sequential approaches in terms of surrogate model accuracy and estimation of output variance, especially with respect to extreme values.

Keywords: Uncertainty Quantification, Active Learning, Polynomial Chaos Expansion

1. Motivation

Uncertainty quantification of the quantity of interest (QoI), the outcome of a physical system represented by a complex mathematical model, is typically computationally costly; thus, it is often necessary to construct a surrogate model. One of the most suitable surrogate models for UQ is polynomial chaos expansion (PCE), which allows for analytical estimation of statistical moments and sensitivity analysis (Novák, 2022; Sudret, 2008). However, the quality of the approximation is governed by the quality of the experimental design (ED) used for the construction of non-intrusive PCE. On the one hand, it would be optimal to use a very large set of samples for ED, but on the other hand, each sample brings an additional significant computational burden (e.g., nonlinear finite element method); thus, it is necessary to reduce the number of model evaluations as much as possible in the process of training the surrogate model while maintaining the accuracy of the approximation. This challenge is commonly addressed by advanced sampling strategies (Shields et al., 2015; Fajraoui et al., 2017; Hadigol and Doostan, 2018). Moreover, active learning approaches provide a more targeted strategy, iteratively enriching the experimental design based on prescribed

© 2026 by the author(s). This work is licensed under the Creative Commons Attribution 4.0 International License (CC BY 4.0), which permits unrestricted use, distribution, and reproduction in any medium, provided the original author and source are credited.

criteria (Jones et al., 1998; Marelli and Sudret, 2018). Recently, Novák et al. (Novák et al., 2021) proposed Θ criterion based on simple idea of combining exploration aspect with variance density obtained directly from PCE, thereby achieving a balance between space-filling and variance-based model refinement. This strategy has been demonstrated to improve surrogate accuracy and provide more reliable estimation of the output variance compared to standard non-sequential sampling approaches while introducing only negligible additional computational cost.

Despite these merits, the original Θ criterion is formulated for single-output problems. This restriction may be limiting in many engineering applications, where one simulation simultaneously produces several outputs and all of them must be approximated under a limited and shared computational budget. The straightforward single-output criterion is generally unsatisfactory for several reasons. First, using different ED for each of the outputs may make it difficult to maintain consistency across the surrogate construction, which is undesirable when multiple responses are to be approximated jointly in a unified multi-output setting. Second, the repeated sampling procedure for different training sets may become computationally inefficient when the underlying model is expensive. Third, different outputs may exhibit different levels of variability, smoothness, and approximation difficulty, so that a sample selected as informative for one output may be much less informative for other outputs. Therefore, the extension from single-output to multi-output criterion is not merely a formal generalization but a necessary step toward an efficient sampling strategy for practical multi-output problems.

Motivated by this limitation, this paper proposes a multi-output Θ criterion for the adaptive sequential sampling for non-intrusive PCE. The proposed approach aggregates variance and distance information from multiple outputs into a unified criterion, so that each additional sample is selected to maximize the overall improvement of the surrogate model. The proposed method is verified through several numerical examples. The results show that the proposed method provides an effective and efficient sampling strategy for multi-output PCE surrogate models.

2. Non-intrusive Polynomial Chaos Expansion

Let $Y = g(\boldsymbol{X})$ represent a computational model, where $\boldsymbol{X} = (X_1, X_2, \ldots, X_M)$ is a set of M independent random inputs. Under the Wiener-Askey framework (Xiu and Karniadakis, 2002), the input variables are transformed into a series of standardized germs $\boldsymbol{\xi} = (\xi_1, \xi_2, ..., \xi_M)$, with respect to which an orthonormal polynomial basis can be constructed. The model response is then approximated by a truncated expansion in terms of these basis functions, ensuring a finite representation suitable for practical computation, as

$$Y \approx \sum_{\alpha \in \mathcal{A}} \beta_\alpha \Psi_\alpha(\boldsymbol{\xi})$$

where $\alpha \in \mathbb{N}^M$ denotes a multi-index specifying the polynomial degree associated with each germ dimension ξ_i, $\mathcal{A}$ is the truncated multi-index set, β_α are the corresponding expansion coefficients, and $\Psi_\alpha(\boldsymbol{\xi})$ are multivariate orthonormal polynomial bases constructed from a tensor product of

univariate orthonormal polynomials

$$\Psi_\alpha(\boldsymbol{\xi}) = \prod_{i=1}^{M} \psi_{\alpha_i}(\xi_i).$$

The coefficients β_α can be estimated using regression techniques (Blatman and Sudret, 2011). Owing to the orthonormality of the basis functions, the variance of the response σ_Y^2 can be directly obtained, given by

$$\sigma_Y^2 = \sum_{\substack{\alpha \in \mathcal{A} \\ \alpha \neq 0}} \beta_\alpha^2.$$

The variance can be regarded as an integral of local contributions over the input space. Based on the PCE representation, a local variance measure can therefore be defined to quantify the contribution of a given point ξ to the total variance. In particular, the local variance is expressed as

$$\sigma_{\mathcal{A}}^2(\boldsymbol{\xi}) = \left[\sum_{\substack{\alpha \in \mathcal{A} \\ \alpha \neq 0}} \beta_\alpha \, \Psi_\alpha(\boldsymbol{\xi}) \right]^2 p_{\boldsymbol{\xi}}(\boldsymbol{\xi})$$

where $p_{\boldsymbol{\xi}}(\boldsymbol{\xi})$ represents the probability density function of the standardized germs. A large local variance indicates that the surrogate carries greater uncertainty in the corresponding region, and is therefore of higher importance for sampling.

3. Adaptive Sequential Sampling

3.1. Extension of Variance-based Sequential Sampling

Once the PCE surrogate is constructed, it can be exploited to guide the selection of new samples in an adaptive manner. In particular, the experimental design is iteratively enriched by selecting new points according to a variance-based criterion derived from the surrogate model. For the single-output case, the Θ criterion is defined as (Novák et al., 2021)

$$\Theta(\boldsymbol{\xi}^{(c)}) \equiv \Theta_c = \underbrace{\sqrt{\sigma_c^2 \cdot \sigma_s^2}}_{\text{ave. var. density}} \underbrace{l_{c,s}^M}_{\text{vol.}}$$

where σ_c^2 and σ_s^2 are the local variance $\sigma_{\mathcal{A}}$ evaluated at the candidate point $\boldsymbol{\xi}^{(c)}$ and its nearest neighbor $\boldsymbol{\xi}^{(s)}$, respectively, and $l_{c,s}$ is the distance between these two points in the input space. The first term reflects the local contribution to the response variability, while the second term indicates spatial exploration of the design domain. The combination of these two terms ensures a balance between refining regions of high variability and maintaining a proper coverage of the input space.

In the multi-output setting, the local variance must be extended to account for multiple quantities of interest, as they may differ significantly in scale, leading to disproportionate contributions

to the overall variability. For this purpose, a unified variance measure is constructed by aggregating the contributions from all outputs. The general form of multi-output Θ criterion is formulated as

$$\Theta_c = \underbrace{\sqrt{\left(\sum_{i=1}^{N_\mathrm{e}} w_{c,i}\lambda_{c,i}\right)\cdot\left(\sum_{i=1}^{N_\mathrm{e}} w_{s,i}\lambda_{s,i}\right)}}_{\text{ave. var. density}}\ \underbrace{l_{c,s}^{M}}_{\text{vol.}}$$

where $w_{c,i}$ and $w_{s,i}$ are weight factors of the ith eigenvalue (PCE function) for the candidate point and the nearest selected point, respectively, introduced to prevent dominance of large-scale outputs and other complicating factors. To obtain equal weights for individual eigenmodes (PCEs), one can select $w_{c,i} = \max_D \lambda_{c,i}$ and $w_{s,i} = \max_D \lambda_{s,i}$. Moreover, in case the individual models (PCEs) are independent (uncorrelated), the eigenvalue $\lambda_{c,i}$ are equal to the local variance density $\sigma^2_{c,i}$ of PCE_i at the location of candidate c. In this case, the multi-output Θ criterion can be written as

$$\Theta_c = \sqrt{\left(\sum_{i=1}^{N_\mathrm{PCE}} \frac{\sigma^2_{c,i}}{\max_D \sigma^2_{c,i}}\right)\cdot\left(\sum_{i=1}^{N_\mathrm{PCE}} \frac{\sigma^2_{s,i}}{\max_D \sigma^2_{s,i}}\right)}\, l_{c,s}^{M}.$$

In this work, no truncation is applied, and N_e equals N_PCE. It is worth noting that, when all eigenvalues are equally weighted (i.e., $w = 1$) and outputs are correlated, using only the sum of the eigenvalues of the covariance matrix leads to a result equivalent to that obtained under the assumption of independent outputs. This is because the sum of eigenvalues equals the trace of the covariance matrix, which corresponds to the sum of marginal variances and does not capture cross-correlations between outputs. Therefore, to account for correlations among outputs, additional weighting strategies are required. In this context, the correlation matrix provides a natural reference for constructing such weights, enabling the aggregation to reflect the dependency relationship between different quantities of interest. However, in our practice, although the coupling may influence the specific selection of samples during the sequential process, the overall advantage of the Θ-criterion over non-sequential sampling strategies generally remains robust. As the number of added samples increases, the selected sample set tends to progressively approach a similar global distribution.

4. Numerical Experiments

4.1. Illustrative 2D Example

To illustrate the effectiveness of the proposed multi-output Θ criterion, we consider a 2D line-singularity function defined over the unit square $(X_1, X_2) \in [0,1]^2$, which exhibits point symmetry with respect to the center $(0.5, 0.5)$. The model is given by

$$f(X_1, X_2) = \frac{1}{|0.3 - X_1^2 - X_2^2| + \delta} - \frac{1}{|0.3 - (1-X_1)^2 - (1-X_2)^2| + \delta}, \qquad (X_1, X_2) \in [0,1]^2.$$

The singular behavior occurs along circular curves where the denominators of two terms approach equal to δ, a regularization parameter to control the sharpness of the singular regions, leading to sharply localized gradients confined to narrow regions. Such localized features pose a challenge for PCE, particularly when the parameter δ is small. In this study, we consider $\delta = 0.1$, for which the response variance is approximately $\sigma_Y^2 \approx 13.070\,477$. Due to the concentration of variability in limited regions, conventional space-filling designs may fail to allocate sufficient samples near the singular peak, resulting in reduced surrogate accuracy. Moreover, to transform the problem into a multi-output case, we introduce a partition of the input domain along the diagonal (see Figure 1), thereby defining two complementary mathematical models:

$$Y_1(X_1, X_2) = \begin{cases} f(X_1, X_2), & X_1 \geq X_2, \\ 0, & X_1 < X_2, \end{cases} \qquad Y_2(X_1, X_2) = \begin{cases} 0, & X_1 > X_2, \\ f(X_1, X_2), & X_1 \leq X_2. \end{cases}$$

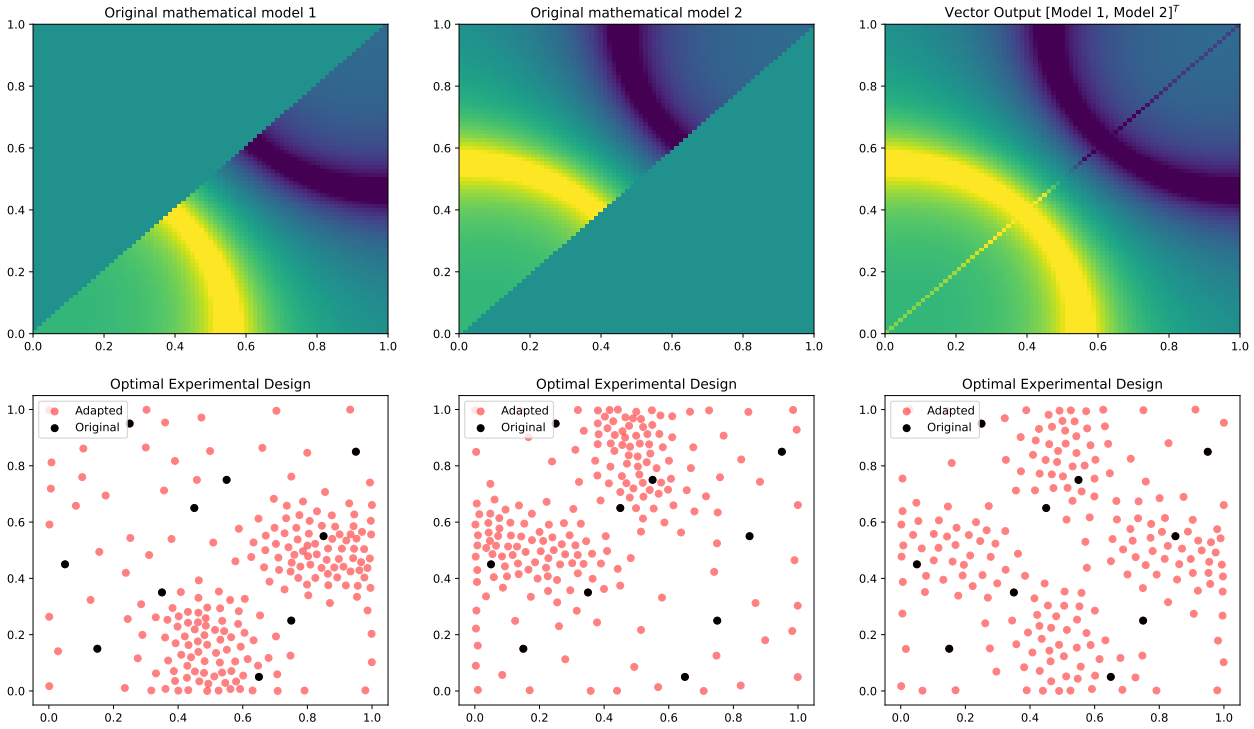


Figure 1. 2D line-singularity function and corresponding multi-output formulation with optimal experimental designs.

As a baseline sampling strategy, Latin Hypercube Sampling (LHS) is considered due to its widespread use in uncertainty quantification (Choi et al., 2004). Figure 2 summarizes the performance over 100 independent runs in terms of the mean and standard deviation of the log-transformed maximum absolute error (MaxAE), mean absolute error (MAE), relative absolute error of variance, and leave-one-out (LOO) error. As illustrated in Figure 2(a), the Θ criterion achieves a noticeably faster reduction in MaxAE at early stages and maintains lower error throughout the

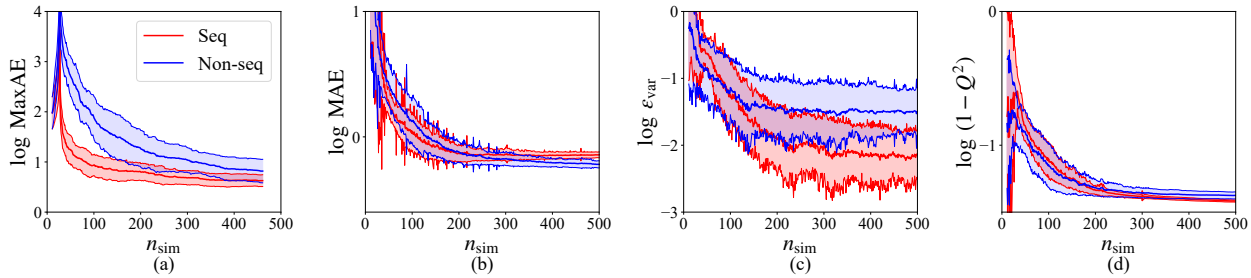


Figure 2. 2D line-singularity function: comparison of Θ criterion and LHS for PCE surrogate model construction: mean and standard deviation of (a) MaxAE, (b) MAE, (c) relative variance error, and (d) LOO error.

whole sampling process compared to the LHS. Although the gap gradually becomes narrow as the sample size increases, the Θ criterion consistently exhibits a tighter standard deviation region, indicating better robustness in the worst-case prediction. For MAE shown in Figure 2(b), a similar trend can be observed at the early stage. When n_{sim} reaches around 250, the performance of two strategies becomes comparable. After this point, the Θ-based method exhibits a slight increase in MAE, however, it still retains a narrower spread, reflecting more stable performance across repeats. In terms of the relative variance error in Figure 2(c), the advantage of the Θ-based strategy becomes more pronounced. The variance error decreases faster and converges to a consistently lower level than that of non-sequential LHS. This behavior suggests that the multi-output Θ criterion accounts for the local variance contributions from both outputs, which effectively improves the estimation of second-order statistics in the surrogate for the complete model. For the LOO error in Figure 2(d), both methods show a similar overall decreasing trend, but finally the Θ criterion achieves a relatively lower error and significantly lower variability.

4.2. Metaball function – complicated topology

The second example is a metaball function (Vořechovský, 2022), which consists of a superposition of two smooth components and can be naturally reformulated as a multi-output problem by treating the two components as separate outputs. The interaction between these components produces a highly nonlinear and non-convex failure surface, with multiple regions of important influence, making it challenging for surrogate modeling and adaptive sampling, given by

$$g\left(x_1, x_2\right) = \frac{30}{\left(\frac{4(x_1+2)^2}{9} + \frac{x_2^2}{25}\right)^2 + 1} + \frac{20}{\left(\frac{(x_1-2.5)^2}{4} + \frac{(x_2-0.5)^2}{25}\right)^2 + 1} - 5. \tag{1}$$

As shown in Fig. 3, the sequential design based on the multi-output Θ criterion shows a better performance than the non-sequential approach across both components and the complete model. From the perspective of surrogate accuracy, the Θ criterion effectively controls extreme errors while maintaining comparable levels of MAE and relative variance error for both individual components and the complete model. In particular, both MaxAE and MAE exhibit narrower standard deviation regions in the later stages, indicating that the samples selected by the Θ criterion are less sensitive to

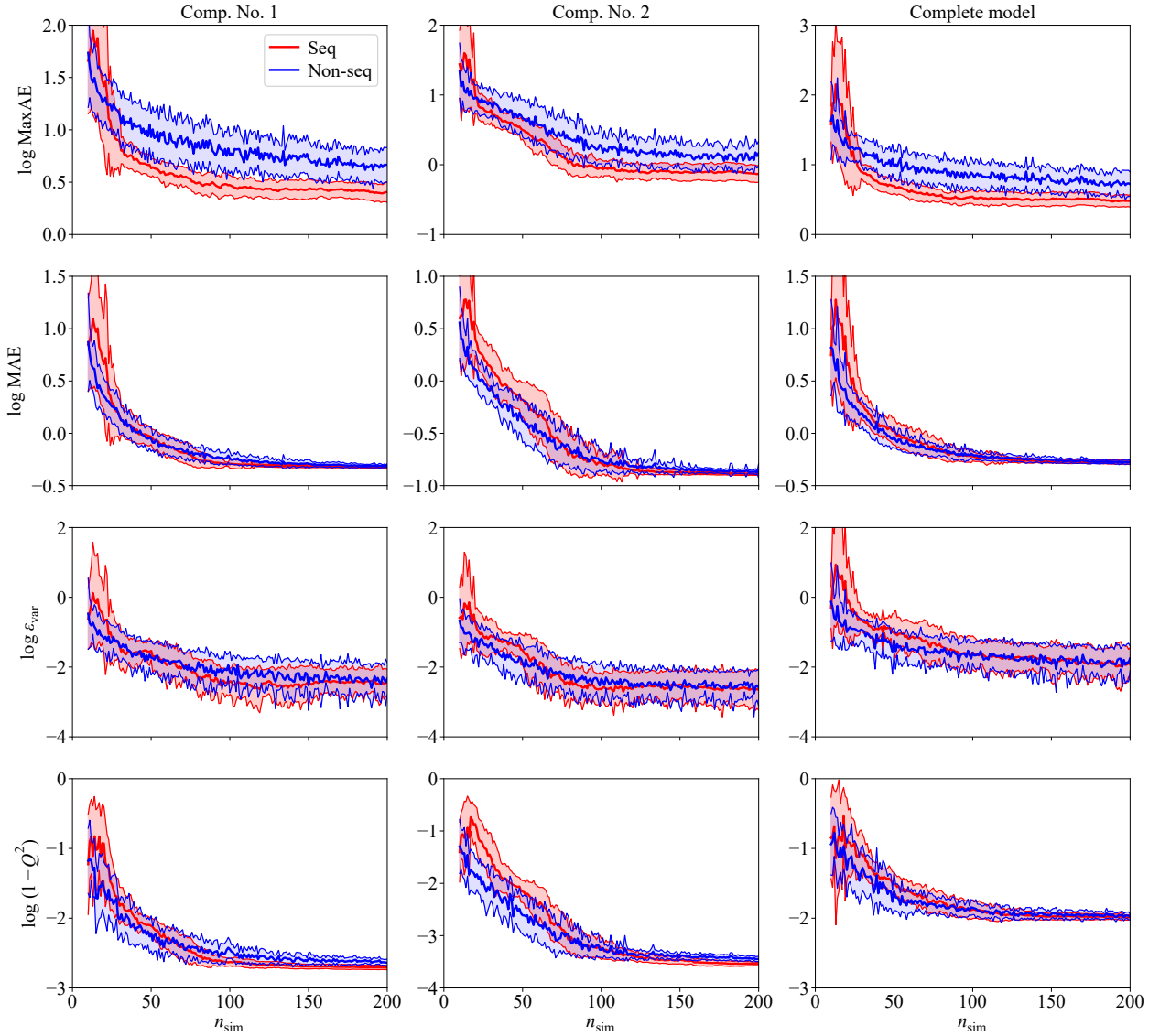


Figure 3. Metaball function: comparison of Θ criterion and LHS for PCE surrogate model construction: mean and standard deviation of MaxAE, MAE, relative variance error, and LOO error

randomness in repeated runs. From the perspective of surrogate stability, the model using samples selected by the Θ criterion shows a slight advantage for the individual components, with lower mean LOO errors and narrower standard deviation bands. For the full model, the Θ criterion maintains a level of stability comparable to that of the non-sequential LHS.

4.3. Four Branches problem

The last example in this paper is a 2D Four Branches function (Borri and Speranzini, 1997), which is a common benchmark problem in reliability analyses; see, e.g., studies with various parameter settings (Schueremans and Gemert, 2005; Echard et al., 2011; Papaioannou et al., 2016; Schöbi et al., 2017). The function describes the failure of a series system, expressed as

$$g_1(x_1, x_2) = \min \begin{cases} 3 + 0.1(x_1 - x_2)^2 - (x_1 + x_2)/\sqrt{2} \\ 3 + 0.1(x_1 - x_2)^2 + (x_1 + x_2)/\sqrt{2} \end{cases} \tag{2}$$

$$g_2(x_1, x_2) = \min \begin{cases} x_1 - x_2 + 7/\sqrt{2} \\ x_2 - x_1 + 7/\sqrt{2} \end{cases}. \tag{3}$$

In this formulation, the system can be interpreted as consisting of two failure modes, represented by g_1 and g_2, corresponding to nonlinear and linear branches of the failure surface, respectively. To investigate the performance of the proposed multi-output Θ criterion, two separate PCE surrogate models are constructed for g_1 and g_2 while sharing the same experimental design. The combined performance function is defined as $g = \min\{g_1, g_2\}$, and failure occurs when $g(x_1, x_2) \leq 0$. Due to the symmetry of the problem, both outputs exhibit similar behavior.

This case is more challenging for PCE than the previous smooth examples, because both component functions and the complete model are defined through minimum operators. These operators introduce non-smooth switching regions, where the active branch changes. Such piecewise behavior cannot be represented efficiently by a global polynomial basis, and therefore may lead to slower and less stable convergence of the PCE approximation. Despite this difficulty, the sequential design based on the multi-output Θ criterion remains effective (see Figure 4). For MaxAE, the multi-output Θ criterion shows a clear reduction for each component and the complete model, which is consistent with the previous two examples. For MAE, the two strategies show comparable overall performance. For the first component, the Θ criterion exhibits larger fluctuations in the intermediate stages, but its performance becomes comparable to LHS near the end. Notably, for the complete model, the Θ criterion shows a certain advantage over the non-sequential approach, indicating that the adaptively selected samples can still be beneficial when the component functions are combined. For the relative variance error, the trend is different. In the complete model, the Θ criterion leads to a larger relative variance error than the non-sequential LHS, although it exhibits a narrower error band. The reason for this phenomenon is that, unlike the previous two examples, where the complete models are formed by combining outputs with different input-domain characteristics, the minimum operator applied to g_1 and g_2 generates additional narrow regions with high local variance near the switching boundaries. These regions are not explicitly emphasized by the Θ criterion and may therefore be overlooked during the sequential selection process, whereas the space-filling nature of LHS makes it more likely to have a small number of samples in these regions. For the first component, the Θ criterion still performs relatively well. Regarding model stability, the results are consistent with the previous examples, i.e. the surrogate model using the samples from the Θ criterion exhibits better stability than that based on LHS.

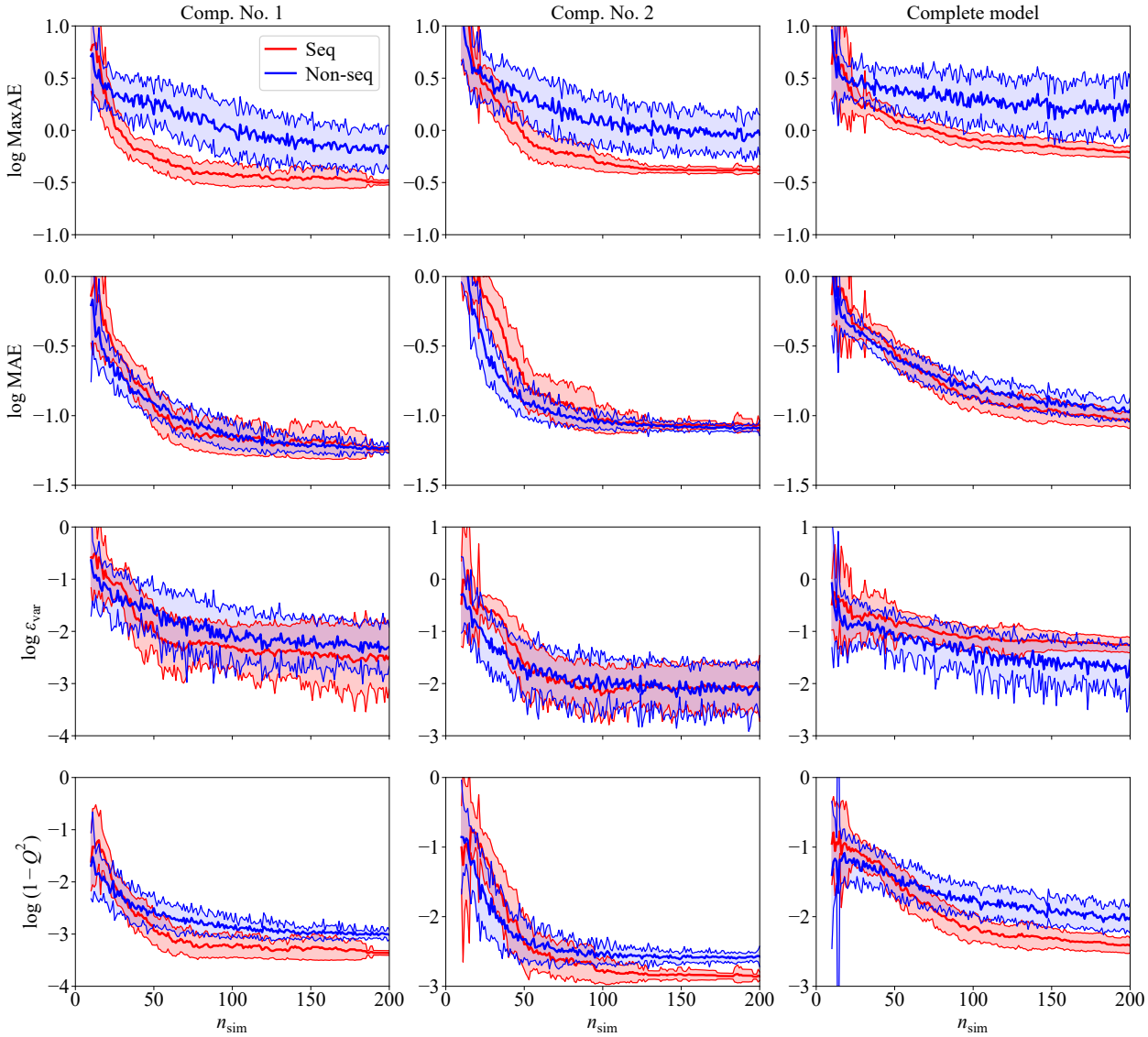


Figure 4. 2D Four Branches function: comparison of Θ criterion and LHS for PCE surrogate model construction: mean and standard deviation of MaxAE, MAE, relative variance error, and LOO error

5. Conclusion

This work extends the variance-based Θ criterion to a multi-output setting for the adaptive sampling of PCE surrogates. By aggregating the local variance contributions of multiple quantities of interest into a unified criterion, the proposed multi-output Θ criterion enables a robust and reliable sequential enrichment of a single experimental design shared across all outputs. The numerical results show that the proposed criterion consistently outperforms non-sequential sampling strategies across all

examples, achieving higher accuracy and improved robustness in various metrics. In particular, it provides more reliable estimation in worst-case scenarios (measured by maximum absolute error), suggesting its potential for reducing sampling costs in multi-output engineering problems where the extreme value is of primary concern.

It should be noted that the present study assumes independence among the surrogate models associated with different outputs. In practice, however, correlations between quantities of interest are often present and may influence the effect of sampling strategy. As discussed in Section 3, the incorporation of weighting parameters provides a potential way to account for such dependencies, with the correlation matrix serving as a natural reference. Another possibility is to apply a direct decorrelation to the surrogate outputs, for instance, based on the covariance structure of surrogate prediction at each iteration, i.e. transforming the correlated surrogate outputs into uncorrelated linear combinations for the evaluation of the sampling criterion. Further investigation in this direction will be pursued in future work.

Acknowledgements

This work was supported by the Czech Science Foundation under project No. 26-20456S. The development of theoretical background was supported by the Ministry of Education, Youth and Sports of the Czech Republic under project No. LUAUS24260.

References

Blatman, G. and B. Sudret: 2011, 'Adaptive sparse polynomial chaos expansion based on least angle regression'. *Journal of Computational Physics* **230**(6), 2345–2367.

Borri, A. and E. Speranzini: 1997, 'Structural reliability analysis using a standard deterministic finite element code'. *Structural Safety* **19**(4), 361–382.

Choi, S.-K., R. V. Grandhi, R. A. Canfield, and C. L. Pettit: 2004, 'Polynomial Chaos Expansion with Latin Hypercube Sampling for Estimating Response Variability'. *AIAA Journal* **42**(6), 1191–1198.

Echard, B., N. Gayton, and M. Lemaire: 2011, 'AK-MCS: An active learning reliability method combining Kriging and Monte Carlo Simulation'. *Structural Safety* **33**(2), 145–154.

Fajraoui, N., S. Marelli, and B. Sudret: 2017, 'Sequential Design of Experiment for Sparse Polynomial Chaos Expansions'. *SIAM/ASA Journal on Uncertainty Quantification* **5**(1), 1061–1085.

Hadigol, M. and A. Doostan: 2018, 'Least squares polynomial chaos expansion: A review of sampling strategies'. *Computer methods in Applied Mechanics and Engineering* **332**, 382–407.

Jones, D. R., M. Schonlau, and W. J. Welch: 1998, 'Efficient global optimization of expensive black-box functions'. *Journal of Global optimization* **13**(4), 455–492.

Marelli, S. and B. Sudret: 2018, 'An active-learning algorithm that combines sparse polynomial chaos expansions and bootstrap for structural reliability analysis'. *Structural Safety* **75**, 67–74.

Novák, L.: 2022, 'On distribution-based global sensitivity analysis by polynomial chaos expansion'. *Computers & Structures* **267**, 106808.

Novák, L., M. Vořechovský, V. Sadílek, and M. D. Shields: 2021, 'Variance-based adaptive sequential sampling for Polynomial Chaos Expansion'. *Computer Methods in Applied Mechanics and Engineering* **386**, 114105.

Papaioannou, I., C. Papadimitriou, and D. Straub: 2016, 'Sequential importance sampling for structural reliability analysis'. *Structural Safety* **62**, 66–75.

Schöbi, R., B. Sudret, and S. Marelli: 2017, 'Rare Event Estimation Using Polynomial-Chaos Kriging'. *ASCE-ASME Journal of Risk and Uncertainty in Engineering Systems, Part A: Civil Engineering* **3**(2).

Schueremans, L. and D. V. Gemert: 2005, 'Benefit of splines and neural networks in simulation based structural reliability analysis'. *Structural Safety* **27**(3), 246–261.

Shields, M. D., K. Teferra, A. Hapij, and R. P. Daddazio: 2015, 'Refined stratified sampling for efficient Monte Carlo based uncertainty quantification'. *Reliability Engineering & System Safety* **142**, 310–325.

Sudret, B.: 2008, 'Global sensitivity analysis using polynomial chaos expansions'. *Reliability Engineering & System Safety* **93**(7), 964–979.

Vořechovský, M.: 2022, 'Reliability analysis of discrete-state performance functions via adaptive sequential sampling with detection of failure surfaces'. *Computer Methods in Applied Mechanics and Engineering* **401**, 115606.

Xiu, D. and G. E. Karniadakis: 2002, 'The Wiener–Askey Polynomial Chaos for Stochastic Differential Equations'. *SIAM Journal on Scientific Computing* **24**(2), 619–644.

Probabilistic Fatigue Life Modelling of Additively Manufactured Aluminum Alloys via Bayesian Inference

Zhanhua Liang[1)], Jingwen Song[2)]
1) School of Mechanical Engineering, Northwestern Polytechnical University, 710072 Xi'an, China, zhanhualiang@mail.nwpu.edu.cn
2) School of Mechanical Engineering, Northwestern Polytechnical University, 710072 Xi'an, China, jingwensong@nwpu.edu.cn

Abstract: Metal additive manufacturing (AM) of aluminum alloys has shown great potential in high-performance lightweight manufacturing industries, where the undesirable fatigue failure remains a critical challenge for reliable design. This paper focuses on probabilistic fatigue life prediction of AM aluminum alloys by considering the inherent variations in fatigue process and the uncertainties in limited fatigue data. A Bayesian inference-based uncertainty quantification framework for fatigue life prediction is proposed in this paper. Fatigue experiments are conducted with AlSi10Mg alloy specimens fabricated via Laser Powder Bed Fusion (LPBF) under two building direction (BD), generating the original experimental dataset. Four candidate models—the Coffin-Manson-Basquin, Morrow, Ostergren, and Kohout-Věchet models—are adopted for fatigue life prediction. Using the valid but scarce fatigue data, the corresponding uncertain model parameters are inferred via a sampling-based Bayesian updating technique. The results demonstrate that the 95% confidence intervals of the fatigue life models updated via Bayesian inference effectively encompass most of the experimental data.

Keywords: Additively manufactured aluminum alloys, Low-cycle fatigue, Uncertainty quantification

1. Introduction

Additive Manufacturing (AM), also known as 3D printing, offers significant advantages such as integrated forming, shortened manufacturing cycles, reduced part counts, and notable improvements in structural stiffness and weight reduction. These characteristics make it particularly suitable for the rapid manufacturing of complex structures (Zhu, 2021). Among various metal AM techniques, Laser Powder Bed Fusion (LPBF) shows considerable popularity and attracted extensive attention in the production of complex structures for aerospace applications (Blakey-Milner, 2021). A wide range of metal alloys have been successfully processed via LPBF (DebRoy, 2018). As one of the most widely used lightweight metallic materials, aluminum alloys play a significant role in weight reduction due to their excellent specific strength, good corrosion resistance, high thermal and electrical conductivity, and relatively low cost (Kotadia,2021).

Despite the considerable potential of AM aluminum alloys in the fabrication of complex geometries and rapid prototyping, it still faces numerous challenges in practical applications, particularly regarding fatigue performance (Liu, 2019). Process-induced defects such as porosity, microstructural inhomogeneity, and residual stress significantly impact the fatigue life of AM aluminum components (Sanaei,2021). Although

© 2026 by the author(s). This work is licensed under the Creative Commons Attribution 4.0 International License (CC BY 4.0), which permits unrestricted use, distribution, and reproduction in any medium, provided the original author and source are credited.

post-processing treatments (e.g., mechanical peening and heat treatment) can partially improve performance, the additional cost and the limitations for complex structures with internal features bring new problems. Therefore, fatigue damage susceptibility has become one of the primary bottlenecks limiting the high-reliability application of aluminum alloys in additive manufacturing (Yi, 2024).

To overcome the fatigue performance limitations of additively manufactured aluminum alloys and enhance the service reliability of critical components, accurate prediction of fatigue life is essential. Numerous researchers have investigated and developed various fatigue life prediction models for additively manufactured materials. Fatigue life prediction models based on stress and strain variables have been widely adopted. For instance, Zhou et al. integrated the Basquin equation with the Goodman criterion to significantly extend fatigue life by optimizing stress distribution through adjusted scanning strategies (Zhou, 2022). Ramirez et al. employed the Basquin relationship to study the correlation between process parameters and fatigue life (Ramirez, 2024). Another widely used category of models is based on the theory of Strain Energy Density (Liao, 2023). This approach offers the advantage of comprehensively reflecting stress-strain responses and their interactions, demonstrating unique potential in characterizing fatigue damage. In response to diverse engineering requirements, SED-based fatigue theories continue to be refined, with recent studies extending to complex conditions such as different loading types and temperature ranges (Sarkar, 2017; Liao, 2021).

Although the aforementioned fatigue life prediction models can provide valuable estimates under specific conditions, an unavoidable challenge severely limits their reliability when applied to AM aluminum alloys: fatigue life data for these materials commonly exhibit significant variations, even under strictly controlled nominal test conditions (Leonetti, 2018; Zhao, 2019). Given this inherent variability, parameter calibration for traditional fatigue life models typically relies on deterministic regression analysis to establish life relationships. Such approaches suffer from two major limitations: First, they assume that data fluctuate within a narrow range around the mean—a premise that is difficult to uphold in the face of AM's significant dispersion. Second, their parameter calibration depends on large volumes of experimental data to achieve statistical significance, which poses a considerable challenge for AM research characterized by high experimental costs and limited sample sizes.

In fact, the unavoidable variations in AM materials does not stem from flaws in experimental design, but rather directly reflects the uncertainty of the additive manufacturing process itself. These uncertainties primarily stem from three sources: uncertainty in experimental measurement error, uncertainty in model parameters due to material property variability, and model form uncertainty arising from simplifications in the modeling approach.

Therefore, to effectively characterize the fatigue behavior of AM aluminum alloys under uncertain conditions and establish reliable predictive models, it is imperative to move beyond deterministic mean-value analyses. The theory of Uncertainty Quantification (UQ) provides a powerful framework to address this challenge. UQ aims to explicitly characterize, propagate, and quantify the multiple sources of uncertainty mentioned above. It is particularly adept at constructing probabilistic predictive models using limited experimental data, thereby enabling more robust estimation of fatigue life and its confidence interval. Within the UQ framework, experimental error uncertainty and model parameter uncertainty can be quantitatively assessed through Bayesian updating theory. This approach incorporates prior knowledge and experimental data to probabilistically correct and update model parameters (Beck, 1998), effectively quantifying the effects of material variability and experimental errors on model predictions (Bi, 2023). Several researchers have applied Bayesian updating theory to fatigue life prediction of additively manufactured materials. For instance, Wang et al. proposed a reliability framework integrated with uncertainty quantification to predict the low-

cycle fatigue (LCF) life of turbine disks (Wang, 2017). He et al. developed an efficient Bayesian neural network model for uncertainty quantification in multiaxial fatigue life prediction (He, 2024). These studies demonstrate that Bayesian updating, as a key tool within UQ, provides essential methodological support for achieving highly reliable fatigue life predictions of AM aluminum alloys and other materials in uncertain environments.

The present research focuses on incorporating the abovementioned model parameter uncertainties and model form uncertainties into fatigue life prediction models of AM aluminum alloys. For selected candidate fatigue life models, the Bayesian updating methodology is applied to calibrate model parameters using limited fatigue data. This approach can provide point estimates (e.g., posterior mean) of the parameters but also quantifies their posterior uncertainty. The parameter uncertainties are subsequently propagated to obtain the probability distribution of the predicted fatigue life. Furthermore, through comparative analysis of model predictions under different building direction, the influence of building direction on the fatigue performance of the additively manufactured aluminum alloy is systematically revealed.

2. AM specimens of aluminum alloys and experiments

The material used in this research was AlSi10Mg alloy, with spherical powder employed for the LPBF fabrication process. The main chemical composition and particle size distribution are presented in Table I.

Table I. The main chemical composition and particle size distribution

Composition (wt%)	Al	Si	Mg	Fe	Cu	Zn	Ti	Mn
	Bal.	9.0-11.0	0.20-0.45	≤0.50	≤0.03	≤0.10	≤0.15	≤0.40
Particle size distribution (%)	D10 μm 15-30	/ /	D50 μm 30-50	/ /	/ /	D90μm 55-75	/ /	/ /

The LPBF process was conducted on a BLT-S400 metal additive manufacturing system using optimized parameters provided by the manufacturer. Key process parameters included a laser spot size of 80 μm, a laser power of 500 W, and a powder layer thickness of 30 μm. To enhance densification, particular attention was paid to the rotation of the scanning direction between successive layers. Owing to the continuous rotation of the scan direction across layers, the material can be considered transversely isotropic relative to the building direction (i.e., the direction of layer-by-layer material deposition in laser powder bed fusion). A series of specimens were fabricated for microstructural and mechanical characterization. All specimens underwent heat treatment after the LPBF process to improve their mechanical properties.

For the cyclic tension-compression tests, two sets of $\phi 13\,\mathrm{mm} \times 110\,\mathrm{mm}$ cylindrical bars were printed. One set was printed parallel to the building direction, and the other perpendicular to it. Each set consisted of ten cylindrical rods, which were subsequently machined into standardized specimens for cyclic testing. The strain-controlled cyclic tension-compression tests were conducted on an MTS servo-hydraulic testing system in compliance with the standard specifications of GB/T 15248-2008. A strain ratio $R_\varepsilon = -1$ and a loading frequency $f = 0.1\,\mathrm{Hz}$ were applied. Throughout the tests, the longitudinal strain was measured and controlled using an MTS extensometer with a 12 mm gauge length.

The building direction and geometry of the specimens used in the cyclic tests are illustrated in Figure 1. global coordinate system was established to facilitate specimen identification, with the x-axis parallel to the building direction and the y–z plane perpendicular to it. All specimens were labeled according to their building direction. For instance, specimens subjected to cyclic tension-compression parallel to the building

direction are designated as S followed by the specimen number, while those loaded perpendicular to the building direction are labeled H followed by the specimen number.

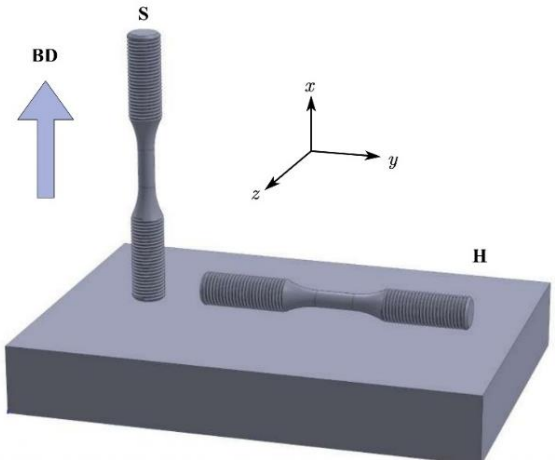


Figure 1. Specimens for cyclic tension-compression experiments.

The strain-fatigue life data for the two building direction are presented in Figure 2, along with their corresponding fitted strain-life curves. Based on the fitted curves, when the strain amplitude exceeds 0.4, specimens subjected to cyclic loading perpendicular to the building direction exhibit higher fatigue lives than those loaded parallel to the building direction. Conversely, at strain amplitudes below 0.4, specimens loaded parallel to the building direction demonstrate relatively longer fatigue lives.

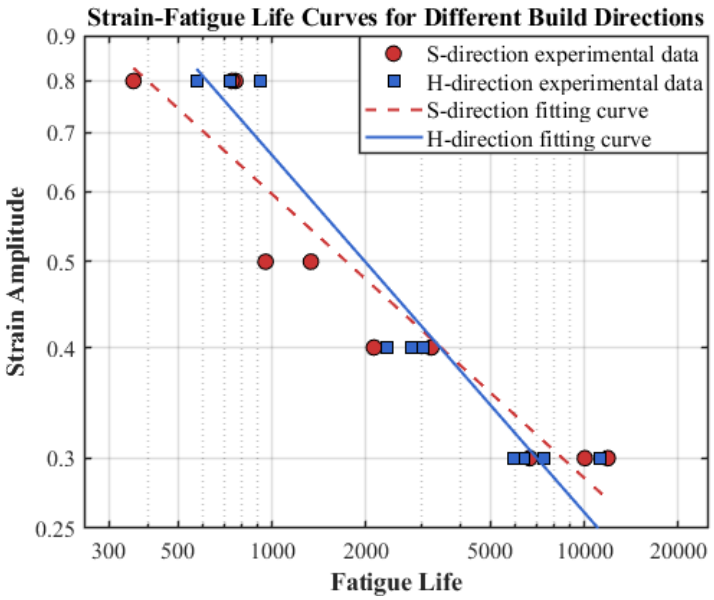


Figure 2. Strain–Fatigue Life Behavior under Different Building direction.

3. Bayesian inference of candidate Fatigue Life Model Parameters

3.1. BAYESIAN UPDATING THEORY

The Bayesian updating process is based on the well-known Bayes' theorem, which is generally expressed as:

$$P(\boldsymbol{\theta} \mid \boldsymbol{Y}_{\text{obs}}) = \frac{L(\boldsymbol{\theta} \mid \boldsymbol{Y}_{\text{obs}})P(\boldsymbol{\theta})}{\int L(\boldsymbol{\theta} \mid \boldsymbol{Y}_{\text{obs}})P(\boldsymbol{\theta})d\boldsymbol{\theta}}, \tag{1}$$

where $\boldsymbol{\theta}$ represents the variables to be updated (e.g., model parameters), and $\boldsymbol{Y}_{\text{obs}}$ denotes the observed data of model responses. The term $P(\boldsymbol{\theta}|\boldsymbol{Y}_{\text{obs}})$ is the posterior probability density function (PDF) of the variables conditional on the observations; $L(\boldsymbol{\theta}|\boldsymbol{Y}_{\text{obs}}) = P(\boldsymbol{Y}_{\text{obs}}|\boldsymbol{\theta})$ is the likelihood function, indicating the probability of observing the data $\boldsymbol{Y}_{\text{obs}}$ given the variables $\boldsymbol{\theta}$; and $P(\boldsymbol{\theta})$ is the prior PDF, representing pre-existing knowledge about the variables before updating. The multidimensional integral $c_E = \int L(\boldsymbol{\theta}|\boldsymbol{Y}_{\text{obs}})\,P(\boldsymbol{\theta})\,\mathrm{d}\boldsymbol{\theta}$, known as the model evidence, serves as a normalization constant ensuring that the posterior PDF integrates to unity.

The posterior PDF quantifies the joint probability distribution of the parameters by inference from the observed data. This indicates that the objective of Bayesian updating is not to determine specific parameter values corresponding to individual observations, but rather to infer the overall probability distribution of the parameters. A key advantage of this approach lies in its ability to integrate prior knowledge with observed data, thereby yielding more accurate estimates of unknown variables while quantifying the uncertainty associated with these estimates.

Within the Bayesian framework, initial knowledge regarding unknown adjustable parameters—such as information derived from prior studies or expert judgment—is represented through the prior PDF. When the upper and lower bounds of a parameter are known, a uniform distribution is often adopted as a suitable prior. Conversely, if the mean value and relative error of a parameter are available, a Gaussian distribution may serve as an appropriate prior.

The likelihood function provides a measure of the discrepancy between the available experimental data $\boldsymbol{Y}_{\text{obs}}$ and the corresponding model predictions $\boldsymbol{Y}_{\text{pre}}$. In this study, this discrepancy is conventionally modeled as a Gaussian distribution with zero mean and a covariance matrix Σ. Under the assumption that the observations are mutually independent, the covariance matrix Σ reduces to a diagonal matrix. Correspondingly, the likelihood function is expressed as:

$$L\left(\boldsymbol{\theta} \mid \boldsymbol{Y}_{\text{obs}}\right) = \left(2\pi\right)^{-n/2} |\Sigma|^{-1/2} \exp\left(-\frac{1}{2}\left(\boldsymbol{Y}_{\text{obs}} - \boldsymbol{Y}_{\text{pre}}\right)^{\mathrm{T}} \Sigma^{-1} \left(\boldsymbol{Y}_{\text{obs}} - \boldsymbol{Y}_{\text{pre}}\right)\right) \tag{2}$$

where $\boldsymbol{\theta}$ denotes the parameters to be updated, and n denotes the dimension of the observed data $\boldsymbol{Y}_{\text{obs}}$.

Special attention must be paid to the definition of the likelihood function. Different choices of likelihood functions can lead to substantially different accuracy and efficiency in the updating procedure; therefore, the selection should be made carefully. The use of an inappropriate likelihood function may result in posterior

distributions that deviate significantly from the prior, failing to incorporate meaningful information from the data.

The principles of Bayesian updating provide a rigorous theoretical framework for the uncertainty quantification of model parameters. To efficiently implement this Bayesian inference process in practical applications, this chapter employs two computational methods: the Bayesian Updating with Structural reliability methods (BUS) and the Particle Filter (PF) method. The BUS method reformulates the Bayesian updating problem as a structural reliability problem, leveraging well-established and efficient algorithms from that field. The PF method, on the other hand, is a sequential Monte Carlo sampling technique particularly suited for parameter estimation problems. It is worth noting that Bayesian updating techniques continue to evolve, with emerging advanced methods offering alternatives for complex updating scenarios. For instance, sampling-based adaptive Bayesian quadrature provides novel solutions for model updating, serving as a reference for methodologies beyond the scope of this study (Song, 2025).

3.2. Bayesian Updating of Model Parameters

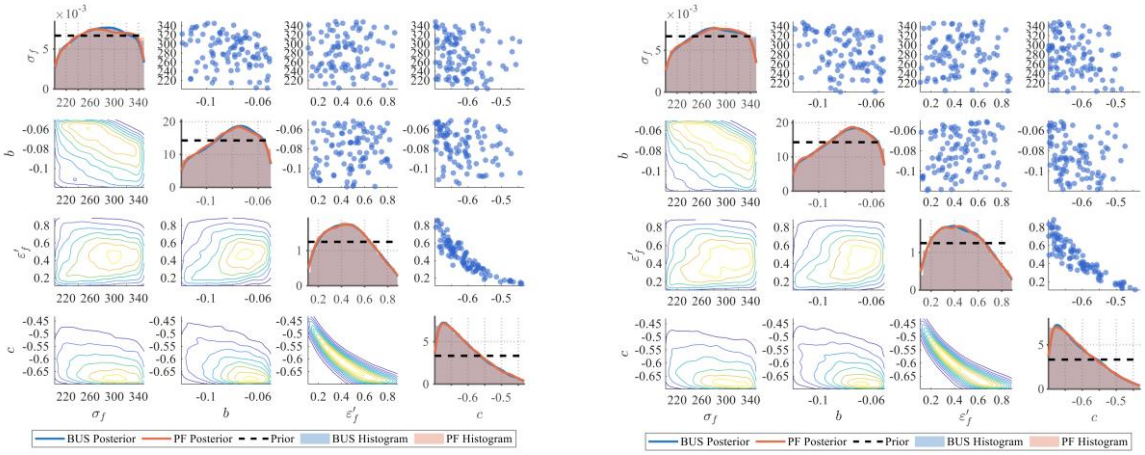
3.2.1. *Inference for Coffin–Manson–Basquin Model Parameters*

The Coffin–Manson–Basquin model represents a landmark theory in fatigue life prediction, founded through seminal contributions by Basquin , Coffin and Manson, and later integrated into a unified framework. Basquin first established the power-law relationship between stress and life in high-cycle fatigue, revealing failure mechanisms dominated by cyclic elastic deformation (OH, 1910). Independently, Manson and Coffin proposed a plastic strain–life equation for low-cycle fatigue, highlighting the critical role of cumulative plastic damage (Manson, 1953; Coffin, 1954). The integration of these approaches resulted in a total strain–life model that unified fatigue life prediction from short to long lifetimes. The mathematical expression of the model is given as follows:

$$\varepsilon_a = \frac{\sigma_f^{'}}{E}\left(2N_f\right)^b + \varepsilon_f^{'}\left(2N_f\right)^c \tag{3}$$

where ε_a denotes the stress amplitude, σ_f' denotes the fatigue strength coefficient, E denotes the Young's modulus, b denotes the fatigue strength exponent, ε_f' denotes the fatigue ductility coefficient, and c denotes the fatigue ductility exponent.

The fatigue strength coefficient σ_f', fatigue strength exponent b, fatigue ductility coefficient ε_f', and fatigue ductility exponent c were treated as the model parameters to be updated. Figure 3 displays the PDF curves of the updated model parameters. As can be observed, there is no significant difference between the marginal posterior PDF obtained using the BUS and PF methods. Compared to the uniform prior distributions, the fatigue ductility coefficient ε_f' and the fatigue ductility exponent c exhibit noticeable updating effects, whereas the updates for the fatigue strength coefficient σ_f' is less pronounced. This discrepancy arises because σ_f' and b primarily govern the elastic strain component in the model, while ε_f' and c control the plastic strain component. In low-cycle fatigue of aluminum alloys, the behavior is dominated more significantly by plastic strain than by elastic strain. Consequently, the parameters controlling elastic strain (σ_f' and b) cannot be effectively updated using only low-cycle fatigue data.



(a) (b)

Figure 3. Posterior PDF and Posterior Samples for the Coffin–Manson–Basquin Model: (a)Posterior PDF and Posterior Samples in the S direction; (b)Posterior PDF and Posterior Samples in the H direction

The lower triangular section of the figure shows contour plots of the joint posterior PDF for pairs of parameters, enabling analysis of correlations between them. It can be observed that the updated parameters ε_f' and c exhibit a clear correlation. The upper triangular section presents scatter plots of samples drawn from the joint posterior PDF, illustrating the spatial distribution of the parameter samples.

3.2.2. *Inference for Morrow Model Parameters*

The energy-based approach is an well-established method for predicting fatigue life. Morrow proposed that fatigue damage can be considered as a continuous and irreversible process of strain energy accumulation (Morrow, 1965).Theoretically, the plastic strain energy absorbed in a complete cycle can be obtained by integrating the area enclosed by the hysteresis loop, denoted as ΔW_p. The relationship between the plastic strain energy density ΔW_p and the fatigue life N_f is expressed as follows:

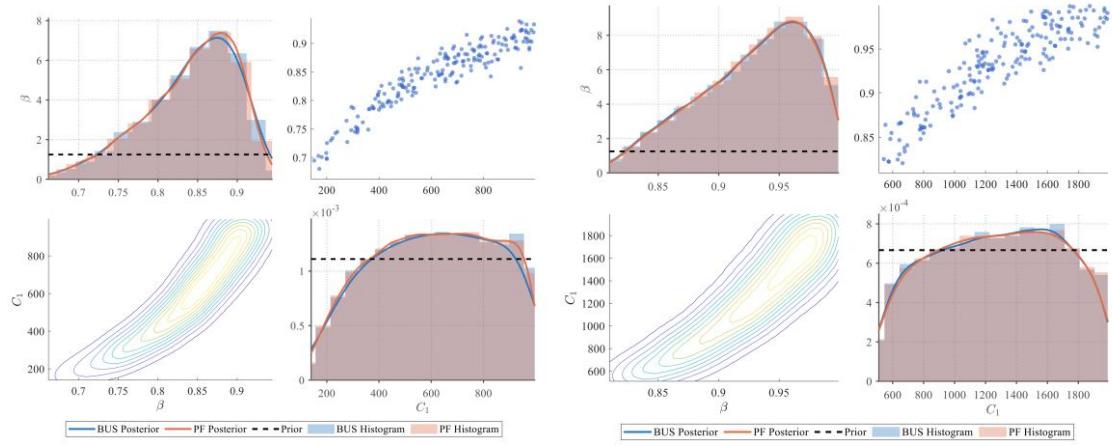
$$\Delta W_p N_f^{\beta} = C_1 \tag{4}$$

where both β and C_1 are material constants.

The plastic strain energy density ΔW_p was determined by calculations of the area of hysteresis loop at the half-life cycle of each specimen during testing. The material constants β and C_1 were updated using both the BUS and PF methods. Note that the prior distributions of the parameters to be updated were appropriately adjusted and are not identical for the two building directions. The posterior results obtained from the PF and BUS methods show good agreement. Furthermore, the posterior means of both β and C_1 in the H direction were higher than those in the S direction.

Figure 4 shows the PDF curves of the updated model parameters. It can be observed that the marginal posterior PDF obtained by the BUS and PF methods show no significant differences. The parameter updating effects are notable for both building direction.

The lower triangular section displays contour plots of the joint posterior PDF for parameter pairs, allowing analysis of correlations between parameters. The figure indicates a clear correlation between the updated parameters β and C_1. The upper triangular section presents scatter plots of samples drawn from the joint posterior PDF, illustrating the spatial distribution of the samples.



(a) (b)

Figure 4. Posterior PDF and Posterior Samples for the Morrow Model: (a) Posterior PDF and Posterior Samples in the S direction; (b) Posterior PDF and Posterior Samples in the H direction.

3.2.3. *Inference for Ostergren Model Parameters*

Ostergren proposed a strain energy damage function model analogous to the material toughness equation (Ostergren, 1976). The strain energy damage function, denoted as ΔW_s, is approximated by the product of the inelastic strain range $\Delta\varepsilon_{in}$ and the maximum tensile stress $\sigma_{\max}$:

$$\Delta W_s = \Delta\varepsilon_{in}\sigma_{\max} \tag{5}$$

where the inelastic strain range $\Delta\varepsilon_{in}$ can be substituted by the plastic strain range $\Delta\varepsilon_p$ under pure fatigue conditions. The relationship between the strain energy damage function and fatigue life N_f can be expressed as:

$$\Delta W_s N_f^m = C_2 \tag{6}$$

The maximum tensile stress $\sigma_{\max}$ was obtained directly from experimental data, and the plastic strain range $\Delta\varepsilon_p$ was derived from processed experimental data, allowing the calculation of the strain energy

damage function ΔW_s for each specimen. Using the observed data of ΔW_s, the material constants m and C_2 were updated.

The PDF curves of the updated model parameters are shown in Figure 5. It can be observed that the marginal PDFs shows good consistencies between BUS and PF methods. The parameter updating effects are notable for both building direction.

The lower triangular section of the figure displays contour plots of the joint posterior PDF for parameter pairs, allowing analysis of correlations between the parameters. The upper triangular section presents scatter plots of samples drawn from the joint posterior PDF, illustrating the dependencies of spatial distribution among the samples. It indicates that the two model parameters m and C_2 has significant positive correlation effects, where the case of H direction shows a stronger linear correlation than that of S direction. The correlations would inevitably influence the accuracies of subsequent fatigue life predictions.

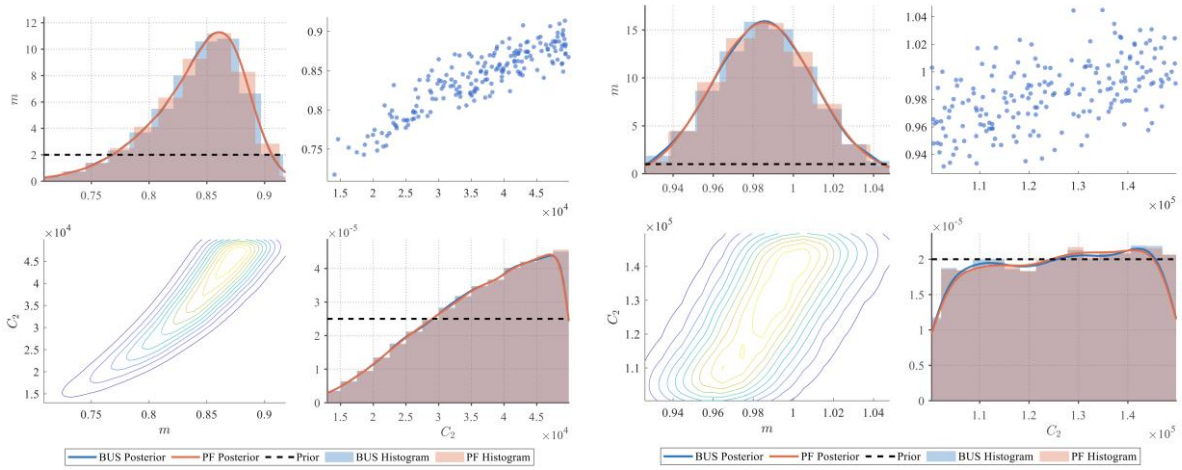


Figure 5. Posterior PDF and Posterior Samples for the Ostergren Model: (a) Posterior PDF and Posterior Samples in the S direction; (b) Posterior PDF and Posterior Samples in the H direction.

3.2.4. *Inference for Kohout-Věchet (K-V) Model Parameters*

Kohout and Věchet proposed a fatigue life model based on a stress-based damage parameter (Kohout, 2001). This model describes fatigue life behavior by adjusting the geometry of the S–N curve, namely its slope and position. This model enables prediction of the fatigue life of metallic materials in both the low-cycle fatigue (LCF) and high-cycle fatigue (HCF) regimes, as given in Equation (8):

$$\sigma_{max} = \sigma_{\mathrm{UTS}} \left(\frac{1+\dfrac{N_f}{B}}{1+\dfrac{N_f}{C}} \right)^{b} \tag{7}$$

where $\sigma_{\max}$ denotes the maximum tensile stress, σ_{UTS} denotes the ultimate tensile strength, and B, C, and b are material constants. Here, B represents the number of cycles at the intersection of the finite-life region

tangent and the asymptote at the ultimate tensile strength level, while C denotes the number of cycles at the intersection of the finite-life region tangent and the asymptote at the fatigue limit level.

The maximum tensile stress $\sigma_{\max}$ was obtained directly from experimental data. The parameters of the model were updated by BUS and PF methods. The PDF curves of the updated model parameters are shown in Figure 6. It can be observed that the marginal posterior PDF functions derived by the BUS and PF methods exhibit no significant differences. The updating effects are notable for parameters σ_{UTS} and b, while the updates for parameters B and C are less pronounced. This is due to the lack of observational data in the regions near the asymptotes of the ultimate tensile strength and the fatigue limit.

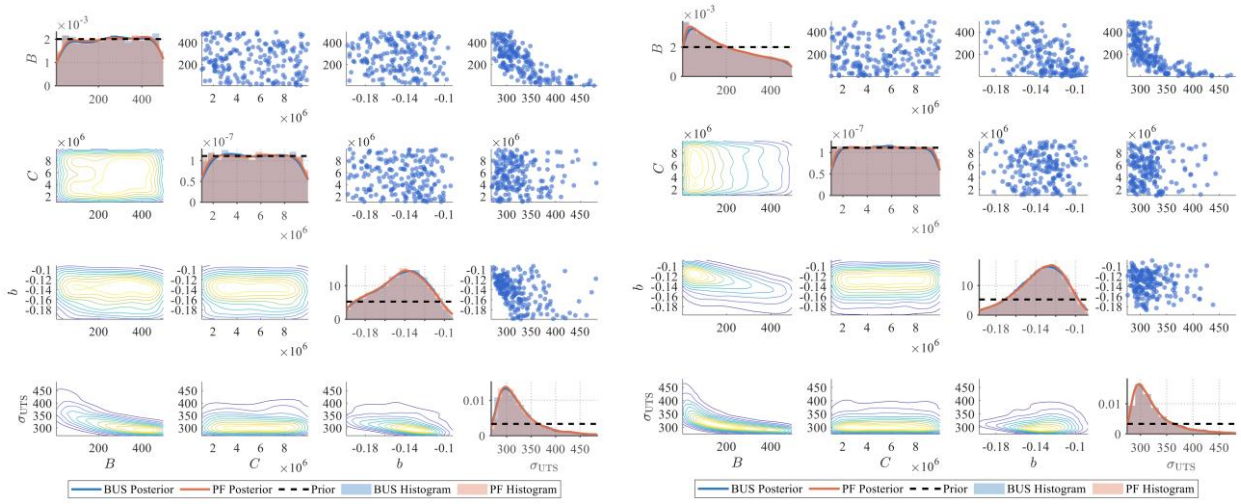


Figure 6. Posterior PDF and Posterior Samples for the K-V Model: (a)Posterior PDF and Posterior Samples in the S direction; (b) Posterior PDF and Posterior Samples in the H direction

3.3. Propagation of Uncertainty in Model Predictions

In Bayesian updating, we infer the posterior distribution of model parameters conditional on observed fatigue life data. By treating fatigue life as the output, parameter uncertainty can be consistently propagated into a predictive distribution for fatigue life, thereby providing a common benchmark for all models. In practical engineering, designers are more concerned with the service life of structural components under given loading conditions and the confidence level of this prediction. The presentation method in this paper directly addresses this question, with the provided life confidence intervals better serving reliability design and risk assessment than traditional single curves.

Model predictions were generated using the updated parameters, with the associated parameter uncertainties propagated to the output to produce 95% confidence intervals for the predictions. A comparison of the predictions from all four models is presented in Figure 7. The confidence intervals of all four models encompass the majority of the experimental data, demonstrating the accuracy of the probabilistic predictions.

It is noteworthy that the prediction confidence intervals of the K-V model exhibit the poorest coverage capability for experimental data. As a stress-based model, the K-V model's complex parameters require joint

constraints from both high-cycle and low-cycle fatigue data. The limited low-cycle data available in this study could not effectively update its high-cycle parameters, resulting in high posterior uncertainty for these parameters. This ultimately caused the predicted fatigue life distribution to deviate from the observed data.

Furthermore, comparative observations reveal that at lower fatigue life cycles and under identical strain amplitudes, specimens built in the S direction are more susceptible to fatigue failure, while those in the H direction exhibit superior fatigue performance. This behavior can be attributed to the fact that in S-oriented specimens, the longitudinal axis is parallel to the building direction, causing interlayer interfaces to be perpendicular to the loading direction. This orientation may result in weaker interlayer bonding, facilitating crack propagation along the interfaces and thus reducing fatigue life. In contrast, H-oriented specimens likely possess a more uniform defect distribution, with interlayer interfaces parallel to the loading direction, thereby minimizing the influence of interlayer bonding on fatigue performance and contributing to higher fatigue strength.

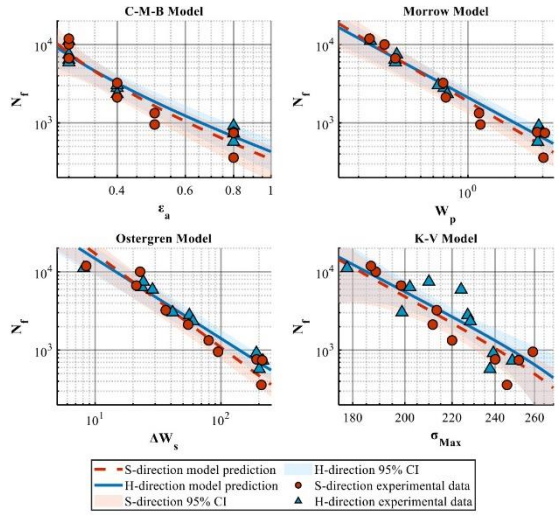


Figure 7. Comparison of Predicted Results from Different Models.

Acknowledgements

This work is supported by the National Natural Science Foundation of China under grant number 12202358 and the Foundation of National Key Laboratory of Strength and Structural Integrity with grant number LSSIKFJJ202402011. The second author is also supported by the National Key R&D Program of China with grant number 2023YFB3407103.

References

Beck, J. L. and Katafygiotis, L. S. Updating models and their uncertainties. I: Bayesian statistical framework. Journal of Engineering Mechanics, 124(4): 455-461, 1998.

Bi, S., Beer, M., Cogan, S., et al. Stochastic model updating with uncertainty quantification: an overview and tutorial. Mechanical Systems and Signal Processing, 204: 110784, 2023.

Blakey-Milner, B., Gradl, P., Snedden, G., et al. Metal additive manufacturing in aerospace: a review. Materials & Design, 209: 110008, 2021.

Coffin, L. F., Jr. A study of the effects of cyclic thermal stresses on a ductile metal. Transactions of the American Society of Mechanical Engineers, 76(6): 931-949, 1954.
DebRoy, T., Wei, H. L., Zuback, J. S., et al. Additive manufacturing of metallic components--process, structure and properties. Progress in materials science, 92: 112-224, 2018.
He, G. Y., Zhao, Y. X., and Yan, C. L. Uncertainty quantification in multiaxial fatigue life prediction using Bayesian neural networks. Engineering Fracture Mechanics, 298: 109961, 2024.
Kohout, J. and Vechet, S. A new function for fatigue curves characterization and its multiple merits. International Journal of Fatigue, 23(2): 175-183, 2001.
Kotadia, H. R., Gibbons, G., Das, A., et al. A review of laser powder bed fusion additive manufacturing of aluminium alloys: microstructure and properties. Additive Manufacturing, 46: 102155, 2021.
Leonetti, D., Maljaars, J., and Snijder, H. H. Uncertainty analysis of constant amplitude fatigue test data employing the six parameters random fatigue limit model. In MATEC Web of Conferences, 165: 10016, 2018.
Liao, D., Zhu, S. P., Gao, J. W., et al. Generalized strain energy density-based fatigue indicator parameter. International Journal of Mechanical Sciences, 254: 108427, 2023.
Liao, X., Wang, Y., Feng, L., et al. Fatigue crack initiation and energy-based life analysis for Q345qD bridge steel at low temperatures. Journal of Constructional Steel Research, 180: 106571, 2021.
Liu, S. and Shin, Y. C. Additive manufacturing of Ti6Al4V alloy: a review. Materials & Design, 164: 107552, 2019.
Manson, S. S. Behavior of materials under conditions of thermal stress. National Advisory Committee for Aeronautics, 1953.
Morrow, J. D. Cyclic plastic strain energy and fatigue of metals. ASTM International, West Conshohocken, PA, 1965.
Oh, B. The exponential law of endurance tests. In Proceedings of the American Society for Testing Materials, 10: 625-630, 1910.
Ostergren, W. J. A damage function and associated failure equations for predicting hold time and frequency effects in elevated temperature, low cycle fatigue. Journal of Testing and Evaluation, 4(5): 327-339, 1976.
Ramirez, B., Banuelos, C., De La Cruz, A., et al. Effects of process parameters and process defects on the flexural fatigue life of Ti-6Al-4V fabricated by laser powder bed fusion. Materials, 17(18): 4548, 2024.
Sanaei, N. and Fatemi, A. Defects in additive manufactured metals and their effect on fatigue performance: a state-of-the-art review. Progress in Materials Science, 117: 100724, 2021.
Sarkar, P. P., De, P. S., Dhua, S. K., et al. Strain energy based low cycle fatigue damage analysis in a plain C-Mn rail steel. Materials Science and Engineering: A, 707: 125-135, 2017.
Song, J., Liang, Z., Wei, P., et al. Sampling-based adaptive Bayesian quadrature for probabilistic model updating. Computer Methods in Applied Mechanics and Engineering, 433: 117467, 2025.
Wang, R., Liu, X., Hu, D., et al. Zone-based reliability analysis on fatigue life of GH720Li turbine disk concerning uncertainty quantification. Aerospace Science and Technology, 70: 300-309, 2017.
Yi, M., Tang, W., Zhu, Y., et al. A holistic review on fatigue properties of additively manufactured metals. Journal of Materials Processing Technology, 118425, 2024.
Zhao, B., Xie, L., Song, J., et al. Prediction of multiaxial fatigue life for complex three‐dimensional stress state considering effect of additional hardening. Fatigue & Fracture of Engineering Materials & Structures, 42(11): 2558-2578, 2019.
Zhou, J., Barrett, R. A., and Leen, S. B. Three-dimensional finite element modelling for additive manufacturing of Ti-6Al-4V components: effect of scanning strategies on temperature history and residual stress. Journal of Advanced Joining Processes, 5: 100106, 2022.
Zhu, J. H. A review of topology optimization for additive manufacturing: status and challenges. Chinese Journal of Aeronautics, 34(1): 91-110, 2021.

Combining Bayesian active learning and stratified sampling for bounding small failure probability under hybrid uncertainties

X. Y. Zhu[1)], Y. F. Cui[1)] and P. F. Wei[1)]
[1)]*School of Power and Energy, Northwestern Polytechnical University*
Xi'an 710072, China, zhuxinyu@mail.nwpu.edu.cn

Abstract: Forward uncertainty propagation of hybrid uncertainties from inputs to the outputs, and estimating the resultant bounds of failure probability under insufficient information is a critical issue for the safety and reliability assessment. The two curses—namely the double-loop structure and the extremely small failure probability—pose challenges to the numerical efficiency and global convergence of existing methods when solving this problem. The recently developed Collaborative and Adaptive Bayesian Optimization (CABO) has been recognized as an appealing scheme for breaking the double-loop curse. Under this methodology framework, this work presents a novel algorithm, named combining Bayesian active learning and stratified sampling (BAL-SS), for efficiently estimating the bounds of small failure probability. Specifically, a new learning function, with the aim of adaptive balance of exploration and exploitation, is developed for implementing Bayesian optimization during the marginal space of epistemic uncertainty, and then develops a Bayesian quadrature rule that combines active learning and stratified sampling to estimate the target small failure probabilities. The proposed BAL-SS algorithm is devised by collaborative implementation of the above two key procedures, in the marginal supports of epistemic and aleatory uncertainties, to sequentially approach the global optima and estimate the corresponding failure probabilities with desired accuracy. Effectiveness of the proposed method is ultimately demonstrated with numerical benchmark study and practical engineering applications.

Keywords: Hybrid uncertainty propagation; Small failure probability; Bayesian active learning; Stratified sampling; Gaussian process regression.

1. Introduction

Estimating the small failure probability is a critical issue for the safety assessment of critical structures in many engineering fields, such as civil and aerospace engineering. However, the standard mathematical formulation of this problem requires precise probability models of the random input variables. This requirement often renders state-of-the-art developments inapplicable to real-world engineering applications, as precise probability models are generally inaccessible due to a lack of or poor quality of information (Beer, 2013). Under this situation, imprecise probability models, like the probability box (p-box) models (Crespo, 2013), the fuzzy probability models (Stein, 2013; Blair 2001), the evidence theory (Agarwal, 2004; McGill, 2008) and the hierarchical probability models (Zhang, 2018) have been developed. These frameworks are all capable of separately modeling the two types of uncertainties owning to the hierarchical model structures, but also bring a great challenge for propagating the uncertainties, which is the so-called "double-loop curse". This challenge becomes even more severe when estimating the bounds of extremely small failure probabilities, a common requirement in structural reliability analysis.

© 2026 by the author(s). This work is licensed under the Creative Commons Attribution 4.0 International License (CC BY 4.0), which permits unrestricted use, distribution, and reproduction in any medium, provided the original author and source are credited.

In case of hybrid uncertainties, some attempts have been presented for addressing the double-loop curse challenge. The standard implementation follows a double-loop structure: the outer loop performs probabilistic analysis with Monte Carlo simulation (MCS) over aleatory variables, while the inner loop conducts an interval analysis for each realization to determine the bounds of the model response by using either intrusive method like interval finite element analysis or non-intrusive method like particle swarm optimization (PSO). This approach, known as interval Monte Carlo Simulation (IMCS), is intrusive due to its reliance on repeated interval finite element analyses (Zhang, 2010; Zhang, 2013; Zhao, 2024). Building upon this double-loop algorithm and aiming for greater efficiency, the interval importance sampling method represents a significant improvement (Zhang, 2012; Alvarez, 2018). While the double-loop method is conceptually simple and arguably requires less subjective information, it remains difficult to directly incorporate the effect of interval parameters into structural reliability assessments, as it necessitates evaluating the families of all candidate probability distributions within the interval bounds.

To break the nested loops, single-loop methods have been extensively developed, including Extended Monte Carlo Simulation (EMCS) (Wei, 2014), Non-intrusive Imprecise Stochastic Simulation (NISS) (Wei, 2019; Wei, 2019; Song 2020), the operator norm method (Faes, 2021), and Collaborative and Adaptive Bayesian Optimization (CABO) (Hong, 2024; Hong, 2023; Wei, 2021). The implementation of single-loop methods for resolving double-loop problems primarily follows two strategic directions: decoupling the nested procedural structure and adopting non-intrusive computational techniques. The former strategy addresses the inherent randomness of the input by discretizing any random fields or processes into a finite set of random variables. This is typically achieved through methods such as the expansion optimal linear estimation (EOLE) (Li, 1993), Karhunen–Loève (KL) expansion (Huang, 2007), stochastic Harmonic function representation (SHFR) (Chen, 2017), or sparse Gaussian process (GP) based on simulation (Wilson, 2020; Vakili, 2021). While this discretization is a essential prerequisite for decoupling, it can itself introduce a significant computational burden. The latter strategy, employing non-intrusive techniques, leverages the model as a black box, requiring only input-output evaluations without the need for surrogate modeling of the limit state function. This approach offers great flexibility. However, a key limitation arises when dealing with high-dimensional epistemic inputs, as the estimation of bounds for model response moments and failure probabilities can become inefficient or intractable.

The task of this work is to extend our previous work CABO (Wei, 2021) for estimating the bounds of failure probability functions under hybrid uncertainties. In this work, we propose a novel reliability analysis framework, named Bayesian active learning with stratified sampling (BAL-SS), designed for efficiently bounding failure probability with hybrid uncertainties. By strategically integrating an improved Upper Confidence Bound (UCB) learning function, BAL-SS is designed to efficiently overcome high-dimensional bottlenecks and precisely bound failure probabilities with complex hybrid uncertainties.

2. Problem Statement

Define $\boldsymbol{y} = g(\boldsymbol{x})$ as the limit state function (LSF) and $\boldsymbol{y}$ refers to the univariate model output. The uncertainty in $\boldsymbol{y}$ originates from the uncertainty $\boldsymbol{x}$. In this paper, we consider the case that the input variables are characterized by three types of uncertainty characteristic models, which are referred to as the $[\boldsymbol{x}_{\mathrm{I}}, \boldsymbol{x}_{\mathrm{II}}, \boldsymbol{x}_{\mathrm{III}}]$ hereinafter. Let $\boldsymbol{x}_{\mathrm{I}} = [\boldsymbol{x}_{\mathrm{I}}^1, \boldsymbol{x}_{\mathrm{I}}^2, ..., \boldsymbol{x}_{\mathrm{I}}^{n_{\mathrm{I}}}]^{\mathrm{T}}$ represent n_{I}-dimensional random variables with aleatory uncertainty, characterized by a precise probability density function (PDF) $f_{\mathrm{I}}(\boldsymbol{x}_{\mathrm{I}})$. Then define $\boldsymbol{x}_{\mathrm{II}} = [\boldsymbol{x}_{\mathrm{II}}^1, \boldsymbol{x}_{\mathrm{II}}^2, ..., \boldsymbol{x}_{\mathrm{II}}^{n_{\mathrm{II}}}]^{\mathrm{T}}$ as a n_{II}-dimensional random variables incorporating both aleatory uncertainty and epistemic uncertainty,

represented by the p-box model $f_{\mathrm{II}}(\boldsymbol{x}_{\mathrm{II}}|\boldsymbol{\theta})$. The epistemic uncertainty of $\boldsymbol{x}_{\mathrm{II}}$ is associated with the non-deterministic distribution parameters $\boldsymbol{\theta}$, which are characterized by hyper-rectangular $[\boldsymbol{\theta}^{\mathrm{L}},\boldsymbol{\theta}^{\mathrm{U}}]$. Finally, let $\boldsymbol{x}_{\mathrm{III}}=[\boldsymbol{x}_{\mathrm{III}}^{1},\boldsymbol{x}_{\mathrm{III}}^{2},...,\boldsymbol{x}_{\mathrm{III}}^{n_{\mathrm{III}}}]^{\mathrm{T}}$ denote n_{III}-dimensional random variables with epistemic uncertainty quantified by the hyper-rectangular $[\boldsymbol{x}_{\mathrm{III}}^{\mathrm{L}},\boldsymbol{x}_{\mathrm{III}}^{\mathrm{U}}]$. Assuming all these three types of inputs are independent, and the joint PDF of $\boldsymbol{x}_{\mathrm{I}}$ and $\boldsymbol{x}_{\mathrm{II}}$ can be formulated as $f_{\mathrm{I}}(\boldsymbol{x}_{\mathrm{I}})=\prod_{i=1}^{n_{\mathrm{I}}}f_{\mathrm{I}}^{i}(x_{\mathrm{I}}^{i})$ and $f_{\mathrm{II}}(\boldsymbol{x}_{\mathrm{II}}|\boldsymbol{\theta})=\prod_{i=1}^{n_{\mathrm{II}}}f_{\mathrm{II}}^{i}(x_{\mathrm{II}}^{i}|\theta^{i})$. In summary, the aleatory uncertainties are derived from $\boldsymbol{x}_{\mathrm{I}}$ and $\boldsymbol{x}_{\mathrm{II}}$ with PDF of $f_{\mathrm{I}}(\boldsymbol{x}_{\mathrm{I}})$ and $f_{\mathrm{II}}(\boldsymbol{x}_{\mathrm{II}}|\boldsymbol{\theta})$, and the epistemic uncertainties are derived from deterministic interval variables $\boldsymbol{x}_{\mathrm{III}}$ and $\boldsymbol{\theta}$. For reliability analysis, assume $\boldsymbol{y}<0$ means structure failure and failure domain is denoted as $F=\{(\boldsymbol{x}_{\mathrm{I}},\boldsymbol{x}_{\mathrm{II}},\boldsymbol{x}_{\mathrm{III}}):g(\boldsymbol{x}_{\mathrm{I}},\boldsymbol{x}_{\mathrm{II}},\boldsymbol{x}_{\mathrm{III}})<0\}$. The indicate function $I_F(\boldsymbol{x}_{\mathrm{I}},\boldsymbol{x}_{\mathrm{II}},\boldsymbol{x}_{\mathrm{III}})$ of failure domain is defined as $I_F(\boldsymbol{x}_{\mathrm{I}},\boldsymbol{x}_{\mathrm{II}},\boldsymbol{x}_{\mathrm{III}})=1$ when $(\boldsymbol{x}_{\mathrm{I}},\boldsymbol{x}_{\mathrm{II}},\boldsymbol{x}_{\mathrm{III}})\in F$ and $I_F(\boldsymbol{x}_{\mathrm{I}},\boldsymbol{x}_{\mathrm{II}},\boldsymbol{x}_{\mathrm{III}})=0$ when $(\boldsymbol{x}_{\mathrm{I}},\boldsymbol{x}_{\mathrm{II}},\boldsymbol{x}_{\mathrm{III}})\notin F$. Based on the above settings, the failure probability is estimated by integrating out aleatory parameters $\boldsymbol{x}_{\mathrm{I}}$ and $\boldsymbol{x}_{\mathrm{II}}$:

$$P_f(\boldsymbol{x}_{\mathrm{III}},\boldsymbol{\theta})=\int_{R^{n_{\mathrm{I}}+n_{\mathrm{II}}}}I_F(\boldsymbol{x}_{\mathrm{I}},\boldsymbol{x}_{\mathrm{II}},\boldsymbol{x}_{\mathrm{III}},\boldsymbol{\theta})f(\boldsymbol{x}_{\mathrm{I}})f_{\mathrm{II}}(\boldsymbol{x}_{\mathrm{II}}|\boldsymbol{\theta})d\boldsymbol{x}_{\mathrm{I}}d\boldsymbol{x}_{\mathrm{II}}. \tag{1}$$

The main objective of this work is to quantify the bounds of the failure probability parameterized by epistemic uncertainty variables. The lower bound and upper bound of failure probability are separately defined as:

$$P_{f,\mathrm{L}}=\min_{\boldsymbol{x}_{\mathrm{III}}\in[\boldsymbol{x}_{\mathrm{III}}^{\mathrm{L}},\boldsymbol{x}_{\mathrm{III}}^{\mathrm{U}}],\boldsymbol{\theta}\in[\boldsymbol{\theta}^{\mathrm{L}},\boldsymbol{\theta}^{\mathrm{U}}]}P_f(\boldsymbol{x}_{\mathrm{III}},\boldsymbol{\theta}), \tag{2a}$$

$$P_{f,\mathrm{U}}=\max_{\boldsymbol{x}_{\mathrm{III}}\in[\boldsymbol{x}_{\mathrm{III}}^{\mathrm{L}},\boldsymbol{x}_{\mathrm{III}}^{\mathrm{U}}],\boldsymbol{\theta}\in[\boldsymbol{\theta}^{\mathrm{L}},\boldsymbol{\theta}^{\mathrm{U}}]}P_f(\boldsymbol{x}_{\mathrm{III}},\boldsymbol{\theta}). \tag{2b}$$

It is seen that Eqs.(2a) and (2b) involve a double-loop structure. In the inner-loop, aleatory uncertainties are addressed and Bayesian integration is performed to estimate the failure probability, where the propagation of the aleatory uncertainty has to be conducted for each realization during the search for epistemic parameters. While in the outer-loop, Bayesian optimization is performed to search for the global optima.

3. Bayesian active learning with stratified sampling for bounding failure probability

3.1. Gaussian Process Regression

Before reporting the main procedure of Bayesian integration, the isoprobabilistic transformation is used to decouple $\boldsymbol{x}_{\mathrm{II}}$, as $\boldsymbol{x}_{\mathrm{II}}$ represent the variable with the mixture of epistemic uncertainty and aleatory uncertainty. Assume $F_{\mathrm{II}}(\boldsymbol{x}_{\mathrm{II}}|\boldsymbol{\theta})$ denotes the cumulative distribution function (CDF) of $\boldsymbol{x}_{\mathrm{II}}$. It is known that CDF of any variable follows a uniform distribution in interval [0,1]. Let $\boldsymbol{u}=(u^{1},u^{2},...,u^{n_{\mathrm{II}}})$ with each element being independent of each other and let $u^{i}=F_{\mathrm{II}}^{i}(x_{\mathrm{II}}^{i}|\theta^{i})$, the inverse transformation can be expressed as $x_{\mathrm{II}}^{i}=F_{\mathrm{II}}^{i-1}(u^{i}|\theta^{i})$. Then the LSF with arguments $\boldsymbol{\omega}=(\boldsymbol{x}_{\mathrm{I}},\boldsymbol{u},\boldsymbol{x}_{\mathrm{III}},\boldsymbol{\theta})$ is denoted by $\boldsymbol{y}=g(\boldsymbol{\omega})$. After that, it is required to transform $\boldsymbol{x}_{\mathrm{I}}$ and $\boldsymbol{u}$ into variables with normal standard distribution.

Assume $g(\boldsymbol{\omega})$ is characterized by a Gaussian distribution, represented as $\hat{g}(\boldsymbol{\omega})\sim\mathcal{GP}(m(\boldsymbol{\omega}),\kappa(\boldsymbol{\omega},\boldsymbol{\omega}'))$, where $\boldsymbol{\omega}=[\boldsymbol{x}_{\mathrm{I}},\boldsymbol{u},\boldsymbol{x}_{\mathrm{III}},\boldsymbol{\theta}]$. $m(\boldsymbol{\omega})$ is the prior mean function, which can be set as 0, constant and polynomial.

$\boldsymbol{\kappa}(\boldsymbol{\omega},\boldsymbol{\omega}')$ is prior covariance and can measure the prior covariance of correlation $g(\boldsymbol{\omega})$ at site $\boldsymbol{\omega}$ and site $\boldsymbol{\omega}'$. Here the square kernel function serves as the covariance kernel function, and is formulated as:

$$\boldsymbol{\kappa}(\boldsymbol{\omega},\boldsymbol{\omega}')=\sigma_0^2\exp\left(-\frac{1}{2}(\boldsymbol{\omega}-\boldsymbol{\omega}')\Sigma^{-1}(\boldsymbol{\omega}-\boldsymbol{\omega}')^{\mathrm{T}}\right), \tag{3}$$

where σ_0^2 and Σ are hyper parameters of covariance function.

Then define the N_0 -dimension training data vector $\boldsymbol{D}=(\boldsymbol{W},\boldsymbol{Y})$, where $\boldsymbol{W}=[\boldsymbol{\omega}_1;\boldsymbol{\omega}_2;...;\boldsymbol{\omega}_{N_0}]$ are the randomly generated training sample points and $\boldsymbol{Y}=\hat{\mathcal{G}}(\boldsymbol{W})$. The likelihood function is defined as the joint probability density function of Gaussian random vectors, formulated as:

$$\mathcal{L}(\boldsymbol{D})=\frac{1}{(2\pi)^{\frac{N_0}{2}}|\boldsymbol{K}|^{\frac{1}{2}}}\exp\left(-\frac{1}{2}(\boldsymbol{Y}-m(\boldsymbol{W}))^{\mathrm{T}}\boldsymbol{K}^{-1}(\boldsymbol{Y}-m(\boldsymbol{W}))\right), \tag{4}$$

where $\boldsymbol{K}=\boldsymbol{\kappa}(\boldsymbol{W},\boldsymbol{W})$ is the covariance matrix of $\boldsymbol{\omega}$.

The posterior distribution of the prediction $\hat{g}(\boldsymbol{\omega})$ at $\boldsymbol{\omega}$ is estimated with the hyper parameters of Gaussian process. The posterior distribution can be represented as $\hat{g}(\boldsymbol{\omega})\sim\mathcal{GP}(\mu_g(\boldsymbol{\omega}),\mathrm{cov}_g(\boldsymbol{\omega},\boldsymbol{\omega}'))$, where $\mu_g(\boldsymbol{\omega})$ is the posterior mean function of $\hat{g}(\boldsymbol{\omega})$. The variance σ_g^2 and posterior covariance $\mathrm{cov}_g(\boldsymbol{\omega},\boldsymbol{\omega}')$ are indicated as:

$$\mu_g(\boldsymbol{\omega})=m(\boldsymbol{\omega})+\boldsymbol{\kappa}(\boldsymbol{W},\boldsymbol{\omega})^{\mathrm{T}}\boldsymbol{K}^{-1}(Y-m(\boldsymbol{W})), \tag{5}$$

$$\sigma_g^2(\boldsymbol{\omega})=\sigma_0^2-\boldsymbol{\kappa}(\boldsymbol{W},\boldsymbol{\omega})^{\mathrm{T}}\boldsymbol{K}^{-1}\boldsymbol{\kappa}(\boldsymbol{W},\boldsymbol{\omega}), \tag{6}$$

$$\mathrm{cov}_g(\boldsymbol{\omega},\boldsymbol{\omega}')=\boldsymbol{\kappa}(\boldsymbol{\omega},\boldsymbol{\omega}')-\boldsymbol{\kappa}(\boldsymbol{W},\boldsymbol{\omega})^{\mathrm{T}}\boldsymbol{K}^{-1}\boldsymbol{\kappa}(\boldsymbol{W},\boldsymbol{\omega}'), \tag{7}$$

where posterior variance $\sigma_g^2(\boldsymbol{\omega})=\mathrm{cov}_g(\boldsymbol{\omega},\boldsymbol{\omega})$ and measures the prediction error at $\boldsymbol{\omega}$ based on posterior GPR model.

Once the GPR model is trained, the induced failure probability function follows a random process with unknown distribution parameters as failure probability function defined in Eq.(1) is not a linear map of LSF $g(\boldsymbol{x}_{\mathrm{I}},\boldsymbol{u},\boldsymbol{x}_{\mathrm{III}},\boldsymbol{\theta})$. The bounds of prediction based on posterior GPR model, denoted as $\mu_g^{\mathrm{L}}(\boldsymbol{x}_{\mathrm{I}},\boldsymbol{u},\boldsymbol{x}_{\mathrm{III}},\boldsymbol{\theta})$ and $\mu_g^{\mathrm{U}}(\boldsymbol{x}_{\mathrm{I}},\boldsymbol{u},\boldsymbol{x}_{\mathrm{III}},\boldsymbol{\theta})$ are then defined by incorporating the posterior standard deviation as a measure of epistemic uncertainty. Let a be a scaling factor that quantifies the uncertainty magnitude, the bounds of prediction can be expressed as:

$$\mu_g^{\mathrm{U}}(\boldsymbol{x}_{\mathrm{I}},\boldsymbol{u},\boldsymbol{x}_{\mathrm{III}},\boldsymbol{\theta})=\mu_g(\boldsymbol{x}_{\mathrm{I}},\boldsymbol{u},\boldsymbol{x}_{\mathrm{III}},\boldsymbol{\theta})+a\sigma_g(\boldsymbol{x}_{\mathrm{I}},\boldsymbol{u},\boldsymbol{x}_{\mathrm{III}},\boldsymbol{\theta}), \tag{8a}$$

$$\mu_g^{\mathrm{L}}(\boldsymbol{x}_{\mathrm{I}},\boldsymbol{u},\boldsymbol{x}_{\mathrm{III}},\boldsymbol{\theta})=\mu_g(\boldsymbol{x}_{\mathrm{I}},\boldsymbol{u},\boldsymbol{x}_{\mathrm{III}},\boldsymbol{\theta})-a\sigma_g(\boldsymbol{x}_{\mathrm{I}},\boldsymbol{u},\boldsymbol{x}_{\mathrm{III}},\boldsymbol{\theta}), \tag{8b}$$

where a is a constant parameter and typically set to $a=1$ by default.

Then the bounds of failure probability $\overline{P}_f(a,\boldsymbol{x}_{\mathrm{III}},\boldsymbol{\theta})$ and $\underline{P}_f(a,\boldsymbol{x}_{\mathrm{III}},\boldsymbol{\theta})$ are formulated as Eq.(9), and the failure probability function is negatively correlated with prediction of GPR model.

$$\begin{aligned}\overline{P}_f(a,\boldsymbol{x}_{\mathrm{III}},\boldsymbol{\theta})&=\Pr(\mu_g(\boldsymbol{X}_{\mathrm{I}},\boldsymbol{U},\boldsymbol{x}_{\mathrm{III}},\boldsymbol{\theta})-a\sigma_g(\boldsymbol{X}_{\mathrm{I}},\boldsymbol{U},\boldsymbol{x}_{\mathrm{III}},\boldsymbol{\theta})<0)\\&=\int I(\mu_g(\boldsymbol{x}_{\mathrm{I}},\boldsymbol{u},\boldsymbol{x}_{\mathrm{III}},\boldsymbol{\theta})-a\sigma_g(\boldsymbol{x}_{\mathrm{I}},\boldsymbol{u},\boldsymbol{x}_{\mathrm{III}},\boldsymbol{\theta})<0)f(\boldsymbol{x}_{\mathrm{I}})f(\boldsymbol{u})d\boldsymbol{x}_{\mathrm{I}}d\boldsymbol{u},\end{aligned} \tag{9a}$$

$$\begin{aligned}\underline{P}_f(a,\boldsymbol{x}_{\mathrm{III}},\boldsymbol{\theta})&=\Pr(\mu_g(\boldsymbol{X}_{\mathrm{I}},\boldsymbol{U},\boldsymbol{x}_{\mathrm{III}},\boldsymbol{\theta})+a\sigma_g(\boldsymbol{X}_{\mathrm{I}},\boldsymbol{U},\boldsymbol{x}_{\mathrm{III}},\boldsymbol{\theta})<0)\\&=\int I(\mu_g(\boldsymbol{x}_{\mathrm{I}},\boldsymbol{u},\boldsymbol{x}_{\mathrm{III}},\boldsymbol{\theta})+a\sigma_g(\boldsymbol{x}_{\mathrm{I}},\boldsymbol{u},\boldsymbol{x}_{\mathrm{III}},\boldsymbol{\theta})<0)f(\boldsymbol{x}_{\mathrm{I}})f(\boldsymbol{u})d\boldsymbol{x}_{\mathrm{I}}d\boldsymbol{u},\end{aligned} \tag{9b}$$

where $\overline{P}_f(a,\boldsymbol{x}_{\mathrm{III}},\boldsymbol{\theta})$ and $\underline{P}_f(a,\boldsymbol{x}_{\mathrm{III}},\boldsymbol{\theta})$ measure the range of uncertainty of the estimated failure probability function value at the point $(\boldsymbol{x}_{\mathrm{III}},\boldsymbol{\theta})$ based on current GPR model for better optimization in the next steps, $\boldsymbol{X}_{\mathrm{I}}$ and $\boldsymbol{U}$ are MCS sample set of random input $\boldsymbol{x}_{\mathrm{I}}$ and $\boldsymbol{u}$ respectively. Under the epistemic uncertainty generated from GPR model, the true value of the failure probability function lies within the range delimited by the upper and lower bounds.

For characterizing the random process of failure probability function, the posterior mean $\mu_g(\boldsymbol{x}_{\mathrm{I}},\boldsymbol{u},\boldsymbol{x}_{\mathrm{III}},\boldsymbol{\theta})$, and its bounds $\mu_g^{\mathrm{L}}(\boldsymbol{x}_{\mathrm{I}},\boldsymbol{u},\boldsymbol{x}_{\mathrm{III}},\boldsymbol{\theta})$ and $\mu_g^{\mathrm{U}}(\boldsymbol{x}_{\mathrm{I}},\boldsymbol{u},\boldsymbol{x}_{\mathrm{III}},\boldsymbol{\theta})$ are mapped to failure probability function by MCS. In this case, the upper and lower bound of failure probability based on current GPR model can be inferred as follows:

$$\overline{P}_f(a,\boldsymbol{x}_{\mathrm{III}},\boldsymbol{\theta})=\frac{1}{N}\sum_{j=1}^{N}I\left(\mu_g(\boldsymbol{X}_{\mathrm{I}}^j,\boldsymbol{U}^j,\boldsymbol{x}_{\mathrm{III}},\boldsymbol{\theta})-a\sigma_g(\boldsymbol{X}_{\mathrm{I}}^j,\boldsymbol{U}^j,\boldsymbol{x}_{\mathrm{III}},\boldsymbol{\theta})\right) \tag{10a}$$

$$\underline{P}_f(a,\boldsymbol{x}_{\mathrm{III}},\boldsymbol{\theta})=\frac{1}{N}\sum_{j=1}^{N}I\left(\mu_g(\boldsymbol{X}_{\mathrm{I}}^j,\boldsymbol{U}^j,\boldsymbol{x}_{\mathrm{III}},\boldsymbol{\theta})+a\sigma_g(\boldsymbol{X}_{\mathrm{I}}^j,\boldsymbol{U}^j,\boldsymbol{x}_{\mathrm{III}},\boldsymbol{\theta})\right) \tag{10b}$$

where $\underline{P}_f(a,\boldsymbol{x}_{\mathrm{III}},\boldsymbol{\theta})\leqslant P_f(a,\boldsymbol{x}_{\mathrm{III}},\boldsymbol{\theta})\leqslant\overline{P}_f(a,\boldsymbol{x}_{\mathrm{III}},\boldsymbol{\theta})$, and N is the size of sample pool.

3.2. Combination With Stratified Sampling

The MCS method is widely employed for failure probability estimation. However, for reliability analysis involving rare events with a failure probability on the order of 10^{-k}, the required sample set must be at least 10^{k+1} to ensure the statistically significant verification. Such a large sample set will lead to substantial computational cost, especially in the context of Bayesian integration. To overcome this challenge, the stratified sampling (SS) method is adopted, which inherits the advantages of the MCS method while improving its efficiency in estimating failure probability in the rare events.

First, transform the aleatory variable $\boldsymbol{x}_{\mathrm{I}}$ into the standard normal space. Then both $\boldsymbol{x}_{\mathrm{I}}$ and $\boldsymbol{u}$ serve as random inputs within the epistemic uncertainty space. They are combined into a composite vector of random variables $\boldsymbol{z}=[\boldsymbol{x}_{\mathrm{I}},\boldsymbol{u}]$ which jointly follows standard normal distribution. The process begins with a set of initial samples $\boldsymbol{z}=(z_1,z_2,...,z_{n_z})$ with n_z-dimensional independent standard normal variables. Subsequently generate a set of independent samples $\boldsymbol{Z}$ with size of N_z, and divide these samples into s stratified subdomains $(\beta_1^2\leqslant\|z_1\|\leqslant\beta_2^2,\beta_2^2\leqslant\|z_2\|\leqslant\beta_3^2,...,\beta_s^2\leqslant\|z_s\|\leqslant\beta_{s+1}^2)$ with $\beta_i(0=\beta_1<\beta_2<...<\beta_s<\beta_{s+1}=\infty)$. The value of the radius β is chosen with Eq.(11).

$$\beta_i=\sqrt{(\chi_{n_z}^2)^{-1}(1-p_0^i)}, \tag{11}$$

where $\chi_{n_z}^2(\beta_i^2)$ is the CDF of chi-square distribution with n_z degrees of freedom and $(\chi_{n_z}^2)^{-1}$ is the inverse function of $\chi_{n_z}^2(\beta_i^2)$, the value of failure probability parameter p_0 is chosen as 0.1. The probability density function (PDF) of truncated samples in i-th truncated subdomain is expressed as:

$$f_{\boldsymbol{Z}}^{\mathrm{tr}(i)}(\boldsymbol{z})=\begin{cases}\dfrac{1}{\chi_{n_z}^2(\beta_{i+1}^2)-\chi_{n_z}^2(\beta_i^2)}f_{\boldsymbol{Z}}(\boldsymbol{z}),\ \text{if}\ \beta_i^2\leqslant\|\boldsymbol{z}_i\|^2\leqslant\beta_{i+1}^2\\ 0,\ \text{otherwise}\end{cases}, \tag{12}$$

where $f_{\boldsymbol{Z}}^{\mathrm{tr}(i)}(\boldsymbol{z})$ satisfy $\int_{\beta_i^2 \leqslant \|\boldsymbol{z}_i\|^2 \leqslant \beta_{i+1}^2} f_{\boldsymbol{Z}}^{\mathrm{tr}(i)}(\boldsymbol{z}) = 1$.

Then define the random inputs $\boldsymbol{z}$ with $\boldsymbol{z} = r \cdot \boldsymbol{\alpha}$, where r and $\boldsymbol{\alpha}$ are the length and direction of $\boldsymbol{z}$ respectively. The direction vector $\boldsymbol{\alpha}$ can be obtained by $\boldsymbol{\alpha}_j = \dfrac{\boldsymbol{z}_j}{\|\boldsymbol{z}_j\|^2}$, while the length vector r^2 satisfies the chi-square distribution with n_z degree of freedom, thus generate N_z samples with:

$$r_j^{(i)} = \sqrt{(\chi_{n_z}^2)^{-1}([\chi_{n_z}^2(\beta_{i+1}^2) - \chi_{n_z}^2(\beta_i^2)] \cdot v_j^{(i)} + \chi_{n_z}^2(\beta_i^2))} \tag{13}$$

where $v_j^{(i)}$ follows uniform distribution of interval [0,1] and $r_j^{(i)}$ represents the length of i-th part of j-th direction of sampling. Then generate samples by using $\boldsymbol{z}_j^{(i)} = r_j^{(i)} \cdot \boldsymbol{\alpha}_j$. Here an example with two-dimensional random inputs is used to illustrate the sampling principle of SS in Figure 1. As is shown in Figure 1, the whole aleatory space is divided into seven parts with β_i and samples in each subdomain are independent of samples in other subdomains.

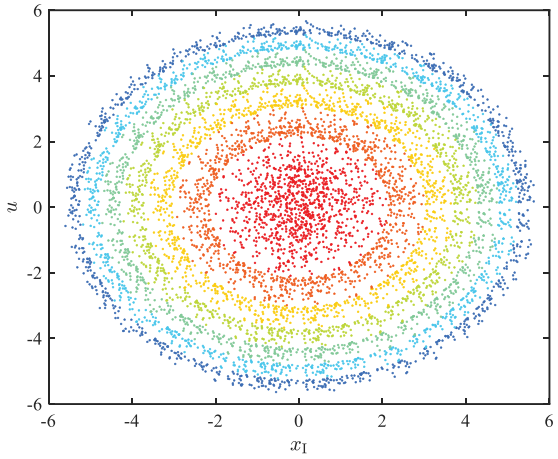


Figure 1. The generated samples of two-dimensional random inputs by SS.

The failure probability of the whole aleatory sphere at fixed $(\boldsymbol{x}_{\mathrm{III}}, \boldsymbol{\theta})$ can be formulated as Eq.(14) through the total probability formula:

$$\begin{aligned} P_f(\boldsymbol{x}_{\mathrm{III}}, \boldsymbol{\theta}) &= \Pr\{g(\boldsymbol{z}, \boldsymbol{x}_{\mathrm{III}}, \boldsymbol{\theta}) \leqslant 0 \,|\boldsymbol{z} \in F\} \\ &= \sum_{i=1}^{s} \Pr\{g(\boldsymbol{z}, \boldsymbol{x}_{\mathrm{III}}, \boldsymbol{\theta}) \leqslant 0 \,|\beta_i^2 \leqslant \|\boldsymbol{z}_i\|^2 \leqslant \beta_{i+1}^2\} \Pr\{\beta_i^2 \leqslant \|\boldsymbol{z}_i\|^2 \leqslant \beta_{i+1}^2\} \\ &= \sum_{i=1}^{s} \Pr\{g(\boldsymbol{z}, \boldsymbol{x}_{\mathrm{III}}, \boldsymbol{\theta}) \leqslant 0 \,|\beta_i^2 \leqslant \|\boldsymbol{z}_i\|^2 \leqslant \beta_{i+1}^2\} [\chi_{n_z}^2(\beta_{i+1}^2) - \chi_{n_z}^2(\beta_i^2)] \end{aligned} \tag{14}$$

where $\|\boldsymbol{z}_i\|^2 = \sum_{j=1}^{n_z} z_{i,j}^2$ denotes the distance between $\boldsymbol{z}_i$ and original point and is distributed as chi-square distribution, $\Pr(\cdot)$ represents the probability of $g(\boldsymbol{z}, \boldsymbol{x}_{\mathrm{III}}, \boldsymbol{\theta}) \leqslant 0$.

The first term in Eq.(14) can be easily obtained by MCS sampling in the sphere:

$$P_f^{(i)}(\boldsymbol{x}_{\mathrm{III}},\boldsymbol{\theta})=\int I_F(\boldsymbol{z},\boldsymbol{x}_{\mathrm{III}},\boldsymbol{\theta})f_{\boldsymbol{Z}}^{\mathrm{tr}(i)}(\boldsymbol{z})d\boldsymbol{z}$$
$$=\frac{1}{N_z}\sum_{j=1}^{N_z}I_F(\boldsymbol{z}_j^{(i)},\boldsymbol{x}_{\mathrm{III}},\boldsymbol{\theta}) \tag{15}$$

So based on MCS sampling method, Eq.(14) can be expressed as is shown in Eq.(16):

$$P_f(\boldsymbol{x}_{\mathrm{III}},\boldsymbol{\theta})=\sum_{i=1}^{s}\{[\chi^2_{n_z}(\beta^2_{i+1})-\chi^2_{n_z}(\beta^2_i)]P_f^{(i)}(\boldsymbol{x}_{\mathrm{III}},\boldsymbol{\theta})\}$$
$$=\sum_{i=1}^{s}\left\{[\chi^2_{n_z}(\beta^2_{i+1})-\chi^2_{n_z}(\beta^2_i)]\frac{1}{N_z}\sum_{j=1}^{N_z}I_F(\boldsymbol{z}_j^{(i)},\boldsymbol{x}_{\mathrm{III}},\boldsymbol{\theta})\right\} \tag{16}$$

Calculate the expectation on both sides of Eq.(16):

$$E[P_f(\boldsymbol{x}_{\mathrm{III}},\boldsymbol{\theta})]=E\left\{\sum_{i=1}^{s}\left[[\chi^2_{n_z}(\beta^2_i)-\chi^2_{n_z}(\beta^2_{i+1})]\cdot\frac{1}{N_z}\sum_{j=1}^{N_z}I_F(\boldsymbol{z}_j^{(i)},\boldsymbol{x}_{\mathrm{III}},\boldsymbol{\theta})\right]\right\}$$
$$=\sum_{i=1}^{s}\left\{[\chi^2_{n_z}(\beta^2_i)-\chi^2_{n_z}(\beta^2_{i+1})]\cdot E\left[\frac{1}{N_z}\sum_{j=1}^{N_z}I_F(\boldsymbol{z}_j^{(i)},\boldsymbol{x}_{\mathrm{III}},\boldsymbol{\theta})\right]\right\} \tag{17}$$
$$=P_f$$

The estimation of failure probability based on stratified beta-sphere sampling technique is unbiased which is equal to the expectation. Then calculate the variance on both sides of the Eq.(16):

$$\mathrm{Var}[P_f(\boldsymbol{x}_{\mathrm{III}},\boldsymbol{\theta})]=\sum_{i=1}^{s}\left[[\chi^2_{n_z}(\beta^2_{i+1})-\chi^2_{n_z}(\beta^2_i)]^2\cdot\frac{[P_f^{(i)}(\boldsymbol{x}_{\mathrm{III}},\boldsymbol{\theta})-(P_f^{(i)}(\boldsymbol{x}_{\mathrm{III}},\boldsymbol{\theta}))^2]}{N_z}\right]. \tag{18}$$

And the COV of this method can be achieved by Eq.(19):

$$\mathrm{COV}[P_f(\boldsymbol{x}_{\mathrm{III}},\boldsymbol{\theta})]=\frac{\sqrt{\mathrm{Var}[P_f(\boldsymbol{x}_{\mathrm{III}},\boldsymbol{\theta})]}}{P_f(\boldsymbol{x}_{\mathrm{III}},\boldsymbol{\theta})}. \tag{19}$$

Based on above assumptions, the expectation and variance are the functions of failure probability estimation, which inherit the accuracy of MCS. The failure probability within each subdomain can be evaluated in parallel, therefore reduces time consumption and improves computational efficiency.

Thus, the failure probability bounds are obtained as shown in Eq.(20) using the general framework defined in Eqs.(10a) and (10b).

$$\overline{P}_f(a,\boldsymbol{x}_{\mathrm{III}},\boldsymbol{\theta})=\sum_{i=1}^{s}\left\{[\chi^2_{n_z}(\beta^2_{i+1})-\chi^2_{n_z}(\beta^2_i)]\cdot\left[\frac{1}{N_z}\sum_{j=1}^{N_z}I_F(\mu_g(\boldsymbol{Z}^j,\boldsymbol{x}_{\mathrm{III}},\boldsymbol{\theta})-a\cdot\sigma_g(\boldsymbol{Z}^j,\boldsymbol{x}_{\mathrm{III}},\boldsymbol{\theta}))\right]\right\}, \tag{20a}$$

$$\underline{P}_f(a,\boldsymbol{x}_{\mathrm{III}},\boldsymbol{\theta})=\sum_{i=1}^{s}\left\{[\chi^2_{n_z}(\beta^2_{i+1})-\chi^2_{n_z}(\beta^2_i)]\cdot\left[\frac{1}{N_z}\sum_{j=1}^{N_z}I_F(\mu_g(\boldsymbol{Z}^j,\boldsymbol{x}_{\mathrm{III}},\boldsymbol{\theta})+a\cdot\sigma_g(\boldsymbol{Z}^j,\boldsymbol{x}_{\mathrm{III}},\boldsymbol{\theta}))\right]\right\}. \tag{20b}$$

3.3. Bayesian Optimization In Epistemic Uncertainty Space

The SS method is integrated with the GPR model and active learning strategy: the aleatory uncertainty space is first divided into multiple subdomains from which a sample pool is generated. The GPR model is then trained with initial training samples selected from sample pool. With all the above information settled, the

UCB function of Bayesian optimization for maximizing or minimizing the objective $P_f(a,\boldsymbol{x}_{\mathrm{III}},\boldsymbol{\theta})$ can be formulated as:

$$\mathcal{L}_{P_{f,\mathrm{L}}}(a,b,\boldsymbol{x}_{\mathrm{III}},\boldsymbol{\theta})=P_f(a,\boldsymbol{x}_{\mathrm{III}},\boldsymbol{\theta})-b\Big(\overline{P}_f(a,\boldsymbol{x}_{\mathrm{III}},\boldsymbol{\theta})-\underline{P}_f(a,\boldsymbol{x}_{\mathrm{III}},\boldsymbol{\theta})\Big), \tag{21a}$$

$$\mathcal{L}_{P_{f,\mathrm{U}}}(a,b,\boldsymbol{x}_{\mathrm{III}},\boldsymbol{\theta})=P_f(a,\boldsymbol{x}_{\mathrm{III}},\boldsymbol{\theta})+b\Big(\overline{P}_f(a,\boldsymbol{x}_{\mathrm{III}},\boldsymbol{\theta})-\underline{P}_f(a,\boldsymbol{x}_{\mathrm{III}},\boldsymbol{\theta})\Big), \tag{21b}$$

where coefficient b scales the predicted covariance of the failure probability estimated by the GPR model $\hat{g}(\boldsymbol{x}_{\mathrm{I}},\boldsymbol{x}_{\mathrm{II}},\boldsymbol{x}_{\mathrm{III}},\boldsymbol{\theta})$. This parameter b governs the trade-off between exploration and exploitation during the Bayesian optimization process.

By setting the learning functions as objective functions which are presented in Eqs.(22a) and (22b), the particle swarm optimization (PSO) method is suggested to search the point with highest or lowest value of learning functions straightforwardly.

$$(\boldsymbol{x}_{\mathrm{III}}^{+},\boldsymbol{\theta}^{+})=\arg\min_{\boldsymbol{x}_{\mathrm{III}}\in[\boldsymbol{x}_{\mathrm{III}}^{\mathrm{L}},\boldsymbol{x}_{\mathrm{III}}^{\mathrm{U}}],\boldsymbol{\theta}\in[\boldsymbol{\theta}^{\mathrm{L}},\boldsymbol{\theta}^{\mathrm{U}}]}\mathcal{L}_{P_{f,\mathrm{L}}}(a,b,\boldsymbol{x}_{\mathrm{III}},\boldsymbol{\theta}), \tag{22a}$$

$$(\boldsymbol{x}_{\mathrm{III}}^{+},\boldsymbol{\theta}^{+})=\arg\max_{\boldsymbol{x}_{\mathrm{III}}\in[\boldsymbol{x}_{\mathrm{III}}^{\mathrm{L}},\boldsymbol{x}_{\mathrm{III}}^{\mathrm{U}}],\boldsymbol{\theta}\in[\boldsymbol{\theta}^{\mathrm{L}},\boldsymbol{\theta}^{\mathrm{U}}]}\mathcal{L}_{P_{f,\mathrm{U}}}(a,b,\boldsymbol{x}_{\mathrm{III}},\boldsymbol{\theta}). \tag{22b}$$

If the values of learning functions $\mathcal{L}_{P_{f,\mathrm{U}}}(a,b,\boldsymbol{x}_{\mathrm{III}},\boldsymbol{\theta})$ and $\mathcal{L}_{P_{f,\mathrm{L}}}(a,b,\boldsymbol{x}_{\mathrm{III}},\boldsymbol{\theta})$ tend to converge, the values of the learning functions of next added point $[\boldsymbol{x}_{\mathrm{III}}^{+},\boldsymbol{\theta}^{+}]$ will be equal to that of the current optimal point $[\boldsymbol{x}_{\mathrm{III}}^{*},\boldsymbol{\theta}^{*}]$. And the search of outer-loop will end till the convergence criteria in Eqs.(23a) and (23b) are satisfied.

$$\frac{|\mathcal{L}_{P_{f,\mathrm{L}}}(a,b,\boldsymbol{x}_{\mathrm{III}}^{+},\boldsymbol{\theta}^{+})-\mathcal{L}_{P_{f,\mathrm{L}}}(a,b,\boldsymbol{x}_{\mathrm{III}}^{*},\boldsymbol{\theta}^{*})|}{|\mathcal{L}_{P_{f,\mathrm{L}}}(a,b,\boldsymbol{x}_{\mathrm{III}}^{*},\boldsymbol{\theta}^{*})|}\leqslant\varepsilon, \tag{23a}$$

$$\frac{|\mathcal{L}_{P_{f,\mathrm{U}}}(a,b,\boldsymbol{x}_{\mathrm{III}}^{+},\boldsymbol{\theta}^{+})-\mathcal{L}_{P_{f,\mathrm{U}}}(a,b,\boldsymbol{x}_{\mathrm{III}}^{*},\boldsymbol{\theta}^{*})|}{|\mathcal{L}_{P_{f,\mathrm{U}}}(a,b,\boldsymbol{x}_{\mathrm{III}}^{*},\boldsymbol{\theta}^{*})|}\leqslant\varepsilon \tag{23b}$$

where ε is a user-defined error tolerance. The value of the error tolerance is governed by the required precision for locating the maxima and minima, and typically falls within the range of 10^{-3} to 10^{-2}.

3.4. Bayesian Integration In Aleatory Uncertainty Space

Once the current best guess $(\boldsymbol{x}_{\mathrm{III}},\boldsymbol{\theta})$ is estimated by solving Eq.(23), it is required to estimate the failure probability at fixed $(\boldsymbol{x}_{\mathrm{III}},\boldsymbol{\theta})$. Based on the principle of MCS, the sign judgment of the probability is vital for failure probability estimation. To improve the accuracy of the GPR surrogate model in characterizing LSF, the points with a high potential risk of nearing the predicted LSF are added to the training process to update the GPR model and then evaluate the failure probability of LSF. These points mainly contain three characteristics: to be with high distribution density because it has high variance and aleatory uncertainty, to be close to LSF with high risk of misjudgment or both at the same time. Currently, the most widely used learning functions are U function (Echard, 2011), expected feasibility function (Bichon, 2008) and H function (Lv, 2015). The U function is applied to this work for its performance on the variance of posterior GPR model and the distance between the predicted and actual LSF value. U function is presented as:

$$U(\boldsymbol{x}_{\mathrm{I}},\boldsymbol{u})=\frac{|\mu_g(\boldsymbol{x}_{\mathrm{I}},\boldsymbol{u},\boldsymbol{x}_{\mathrm{III}}^{+},\boldsymbol{\theta}^{+})|}{\sigma_g(\boldsymbol{x}_{\mathrm{I}},\boldsymbol{u},\boldsymbol{x}_{\mathrm{III}}^{+},\boldsymbol{\theta}^{+})}, \tag{24}$$

and the CDF of the U function $\Phi(U(\boldsymbol{x}_{\mathrm{I}},\boldsymbol{u}))$ is used to represent the probability of making a mistake on the sign of $\hat{g}(\boldsymbol{x}_{\mathrm{I}},\boldsymbol{u},\boldsymbol{x}_{\mathrm{III}},\boldsymbol{\theta})$ at fixed $(\boldsymbol{x}_{\mathrm{III}}^{+},\boldsymbol{\theta}^{+})$. Adding the point and the response of LSF with minimum value of $U(\boldsymbol{x}_{\mathrm{I}},\boldsymbol{u})$ to the training process, the aleatory uncertainty of failure probability based on posterior GPR model will be reduced, which is formulated as:

$$(\boldsymbol{x}_{\mathrm{I}}^{+},\boldsymbol{u}^{+})=\arg\min_{\boldsymbol{x}_{\mathrm{I}}\in\boldsymbol{X}_{\mathrm{I}},\boldsymbol{u}\in\boldsymbol{U}}[U(\boldsymbol{x}_{\mathrm{I}},\boldsymbol{u})]. \tag{25}$$

And the stopping condition is set as $\min(U(\boldsymbol{x}_{\mathrm{I}},\boldsymbol{u}))\geqslant 2$ for $(\boldsymbol{x}_{\mathrm{I}},\boldsymbol{u})\in(\boldsymbol{X}_{\mathrm{I}},\boldsymbol{U})$. The U function equal to 2 corresponds to a probability of misjudging on the sign of $\Phi(-2)=0.023$. As is mentioned in Ref[43], such a stopping criterion guarantees the accuracy of GPR model. In the inner-loop of Bayesian integration in aleatory uncertainty space, U function is used to make GPR model more reliable under current best guess $(\boldsymbol{x}_{\mathrm{III}}{}^{+},\boldsymbol{\theta}^{+})$ by adding the pair $(\boldsymbol{x}_{\mathrm{I}}^{+},\boldsymbol{u}^{+})$. In the outer-loop of Bayesian optimization in epistemic uncertainty space, newly developed learning function is used to search for the bounds of failure probability with minimum or maximum value of $\mathcal{L}_{P_{f,\mathrm{L}}}(a,b,\boldsymbol{x}_{\mathrm{III}},\boldsymbol{\theta})$ and $\mathcal{L}_{P_{f,\mathrm{U}}}(a,b,\boldsymbol{x}_{\mathrm{III}},\boldsymbol{\theta})$. Then the double-loop procedure will end until the convergence criteria for two learning functions are both satisfied.

3.5. SUMMARY OF THE PROPOSED BAL-SS

As we introduced in subsection 3.1, 3.2, 3.3 and 3.4, the aim of this subsection is to present the details for computational process. The basic framework is illustrated in Figure 2.

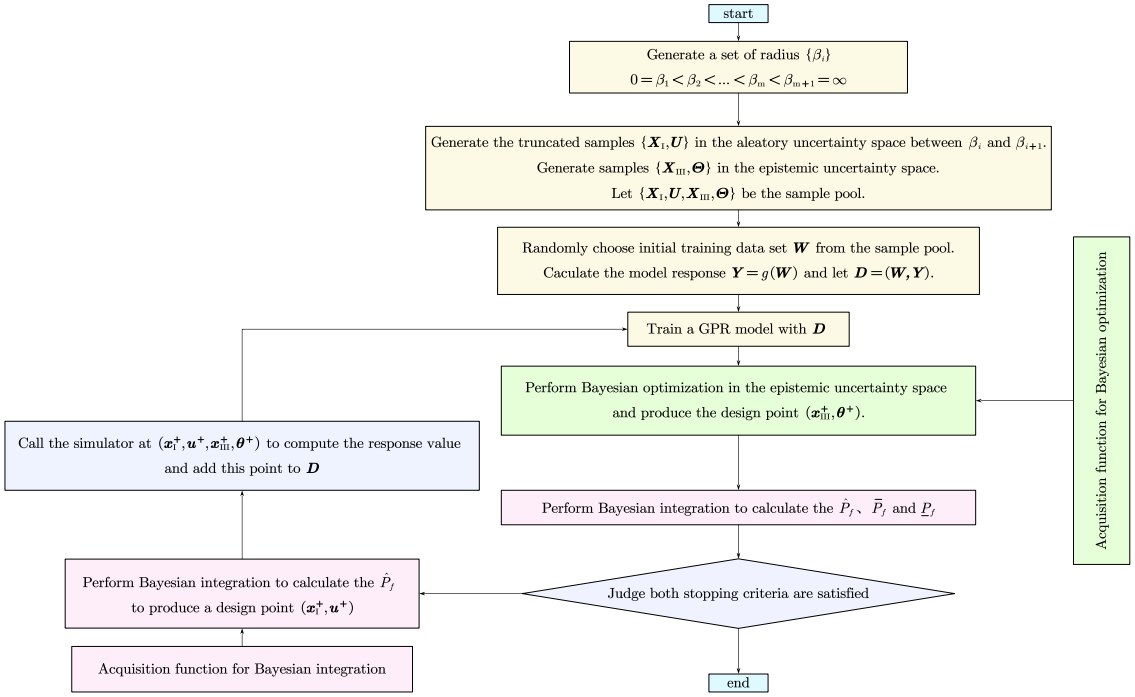


Figure 2. The process of the BAL-SS method.

Firstly, generate a training data set $\boldsymbol{D}$ in the augmented aleatory uncertainty space and epistemic uncertainty space. Train a GPR model with initial training samples. Then solve the outer-loop optimization by Bayesian optimization in the epistemic uncertainty to search for the bounds of failure probability. Solve the inner-loop integral by Bayesian integration to reduce the aleatory uncertainty. In the Bayesian optimization process, developed learning functions are utilized to create the design point $(\boldsymbol{x}_{\mathrm{III}}^{+}, \boldsymbol{\theta}^{+})$. In the Bayesian integration process, U function is applied to generate the experiment design point $(\boldsymbol{x}_{\mathrm{I}}^{+}, \boldsymbol{u}^{+})$ and accelerate the convergence process. At last, with newly added point $(\boldsymbol{x}_{\mathrm{I}}^{+}, \boldsymbol{u}^{+}, \boldsymbol{x}_{\mathrm{III}}^{+}, \boldsymbol{\theta}^{+})$ in the joint probability space, the algorithm will end when both optimization and integration satisfy convergence criteria, which have been reported respectively in subsection 3.3 and 3.4. And the global optimization points will be achieved. Based on different selections of the learning function, the corresponding upper and lower bound of the failure probability can be achieved respectively.

4. Benchmark Studies

4.1. A Three-Dimensional Numerical Example

We consider three-dimensional numerical examples:

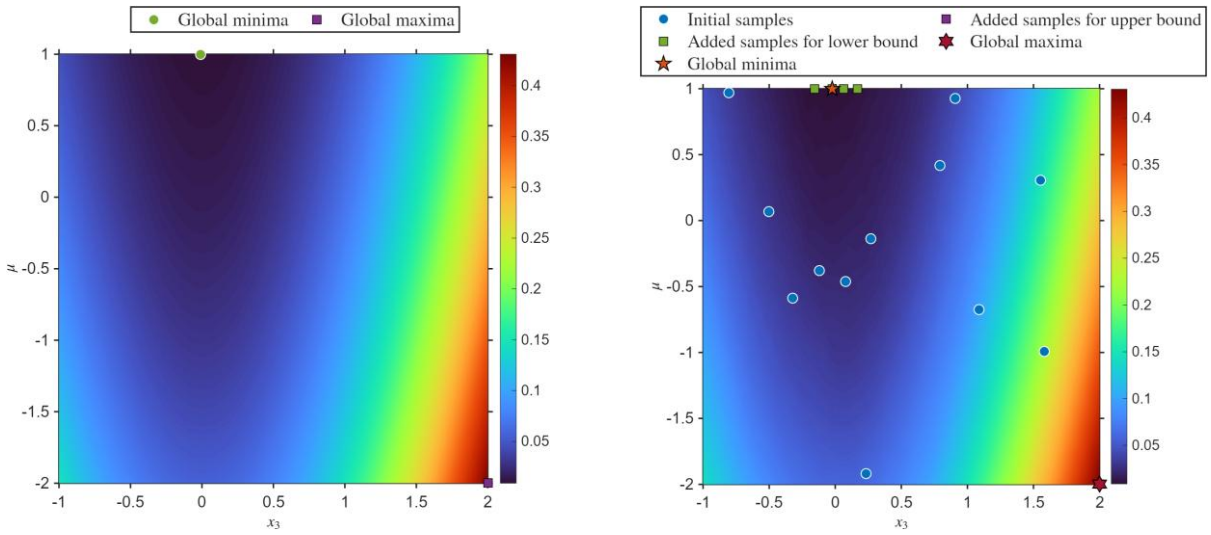
$$g_1(x) = 7 - (x_1 + x_3)^2 + x_2 \tag{26}$$

and

$$g_2(x) = 20 - (x_1 + x_3)^2 + x_2 \tag{27}$$

where x_1 is stochastic variable following standard normal distribution, x_2 follows normal distribution of $\mathcal{N}(\mu, 2)$ with $\mu \in [-2, 1]$, and x_3 is the deterministic variable following uniform distribution of $x_3 \in [-1, 2]$. We perform CABO and BAL method to estimate the bounds of failure probability. Initially we set the number of sampling pool with the size of N_z as 10000, the number of training samples as 12, and the error tolerance of learning functions as 10^{-3}. The reference and the estimation results of $g_1(x)$ are displayed in Figure 2. and Table 1. As is shown in Table 1, evaluating the lower bound using BAL consumed only 45.34s, compared to the 438.88s required by CABO. This drastic reduction in computational time is achieved because BAL completely avoids the KL expansion used in CABO framework. CABO requires the spectral decomposition of a large covariance matrix to directly sample from the posterior GPR model, which becomes computationally prohibitive and impractical for the rare events. In contrast, the proposed BAL method utilizes pointwise UCB criteria to evaluate epistemic uncertain-ty independently at each candidate point, thereby bypassing the time-consuming KL expansion altogether. Consequently, the computational overhead is greatly reduced while successfully reaching the global optimal points as the convergence condition is satisfied, as evidenced by the convergence condition shown in Figure 3.

For g_2-function, we estimate the failure probability of rare events and set the initial number as is mentioned above. As can be seen in Table 2, estimating the lower bound of the failure probability required only 8 additional simulator calls for the BAL-SS. The SS methods is capable of estimating failure probability of rare events with limited sample size, whereas the MCS method fails to achieve comparable efficiency within the double-loop framework. The SS method fundamentally overcomes this limitation by systematically stratifying the aleatory space, ensuring that extreme tail regions are adequately represented without the need for brute-force massive sampling.



(a) The reference result of $g_1(x)$. (b) The estimation result of $g_1(x)$.

Figure 3. The training details of calculating design point of the bounds of three-dimensional case1.

Table I. Results of reliability analysis for g_1-function.

Method	*Sampling Method*	*Bounds*	P_f	*Optima of* (x_{III},θ)	*COV*	*Number of Calls*	*Time(s)*
CABO	*MCS*	Lower	0.0076	(-0.0420,1)	0.1601	12+4+9	428.88
		Upper	0.4322	(-2,2)	0.0114		169.39
BAL		Lower	0.0089	(-0.0353,1)	0.0052	12+8+4	45.23
		Upper	0.4322	(-2,2)	0.0041		115.48
Reference		Lower	0.0088	(-0.0264,1)	--	--	--
		Upper	0.4308	(-2,2)			

Table II. Results of reliability analysis for g_2-function.

Method	*Sampling Method*	*Bounds*	P_f	*Optima of* (x_{III},θ)	*COV*	*Number of Calls*
BAL	*MCS*	*Lower*	--	--	--	--
		Upper	0.0147	(2,-2)	0.0082	12+6
	SS	*Lower*	7.783×10^{-6}	(-0.0039,1)	0.0267	12+8+11
		Upper	0.0150	(2,-2)	0.0208	

The results reported in Table I and II indicate that the both bounds of failure probability are accurately estimated with BAL-SS as the values of bounds match well with different sampling methods and the posterior COVs are sufficiently small. It is evident that the posterior COVs of the lower bound is higher than that of the upper bound, that's because the lower bound of failure probability is significantly smaller than the upper bound and is influenced by the significant aleatory uncertainties of inputs which makes it hard to estimate accurately.

4.2. Operating State Analysis Of Satellite

We consider a more detailed and realistic example. As is shown in Figure 4, the model calibration consists of a 7146-DOF generic communication satellite FE model with 1191 nodes and 1262 elements. It is assumed that the Young's moduli of different components of the satellite are characterized by different uncertainty 447 models given in Table III. Let random variables $\boldsymbol{x}_{\mathrm{I}}=(E_1,E_2)$ obey log-normal distribution with means 5.8×10^8 and variance 2.9×10^7. The imprecise random variables $\boldsymbol{x}_{\mathrm{II}}=E_3$ satisfy log-normal distribution where means are interval variables of $[2.4,3.6]\times10^5$ and variance are also interval variables of $[0.45,0.9]\times10^5$, let $\theta=(\mu_E,\sigma_E)$. The interval random variables $\boldsymbol{x}_{\mathrm{III}}=(E_4,E_5)$ are suggested as uniform distribution of interval $[6.4,9.6]\times10^{10}$.

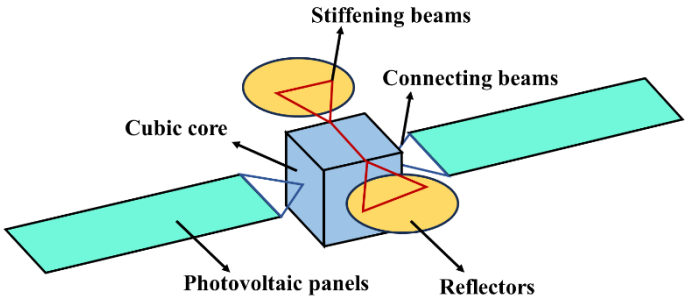


Figure 4. The structure of satellite.

In this structure of the satellite, the cubic core is fixed with reflectors and photovoltaic panels by the connecting beams and stiffening beams. It is important for the first natural frequency to ensure the safety of satellite. Based on the above assumption, we suppose that the satellite will fail if the first natural frequency is less than the given threshold. Therefore, the LSF of the first natural frequency is formulated as:

$$g(\boldsymbol{x})=d_A(\boldsymbol{x})-0.16 \tag{28}$$

Table III. Distribution information of Young's modulus of the satellite.

Parameters	*Distribution Type*	*Means*	*Std*	*Range*
E_1 *(cubic core,* Pa*)*	*Log-normal*	5.8×10^8	2.9×10^7	
E_2 *(photovoltaic panels,* Pa*)*	*Log-normal*	5.8×10^8	2.9×10^7	
E_3 *(reflectors,* Pa*)*	*Log-normal*	$\mu_{E_3}\in[2.4,3.6]\times10^5$	$\sigma_{E_3}\in[0.45,0.9]\times10^5$	
E_4 *(connecting beams,* Pa*)*	*Uniform*			$[6.4,9.6]\times10^{10}$
E_5 *(stiffening beams,* Pa*)*	*Uniform*			$[6.4,9.6]\times10^{10}$

To estimate the bounds of the failure probability, the initial number $Ntrain$ of training samples is set as 30, the number of subdomains for BAL-SS method is set as 7 and the number of samples in each subdomain is set as 1000. While the convergence criterion ε is defined as 10^{-2}, the parameters a and b are defined as 1 and 1.5 to speed up the convergence rate. The results shown in Table IV indicate that the estimations failure probability bounds are accurate and efficient because the COVs are less than 5% and the number of calls of the whole procedure is adequately small.

Table IV. Results of reliability analysis for satellite.

Method	*Bounds*	P_f	*Optima of* $(E_4, E_5, \mu_{E_5}, \sigma_{E_5})$	*COV*	*Number of Calls*
CABO	Lower	--	--	--	30+33
	Upper	0.4914	$(6.4000\times10^{10}, 6.4000\times10^{10})$ $(2.4000\times10^{5}, 0.9000\times10^{5})$	0.0051	
BAL-SS	Lower	6×10^{-4}	$(8.3120\times10^{10}, 8.7216\times10^{10})$ $(2.8251\times10^{5}, 0.4500\times10^{5})$	0.0408	30+43+18
	Upper	0.4914	$(6.4000\times10^{10}, 6.4000\times10^{10})$ $(2.4000\times10^{5}, 0.9000\times10^{5})$	0.0102	

5. Conclusions

This work presents a computationally efficient algorithm for reliability analysis called BAL-SS, to effectively estimate the bounds of small failure probability under hybrid aleatory and epistemic uncertainties. Before applying the procedure of BAL-SS, we characterize the input variables by three models respectively, which are precise probabilistic model, non-probabilistic model and imprecise probabilistic model. It is suggested to transform those input variables to independent uniform distributional inputs and interval epistemic parameters. Then we implement adaptive Bayesian optimization scheme to update the GPR model in the epistemic uncertainty space. Specifically, we develop a new learning function to propagate epistemic uncertainties especially non-parametric uncertainties caused by GPR model and search the optimal points in epistemic uncertainty space of failure probability boundary. U function is applied to produce optimal points in aleatory uncertainty space and infer the posterior distribution of failure probability at deterministic sites specified by PSO algorithm. The two learning functions generate a set of new training points to update the GPR model until the process of optimizing and updating is convergent. By integrate the proposed Bayesian active learning function with a stratified sampling method, the framework effectively overcomes the double-loop computational curse and the challenges associated with rare event.

Acknowledgements

This work is supported by the National Natural Science Foundation of China under grant number 52475164.

References

Beer M., Ferson S. and Kreinovich V. Imprecise probabilities in engineering analyses. *Mechanical Systems and Signal Processing* 37:4–29, 2013.

Crespo, L. G., Kenny, S. P., Giesy, D. P. Reliability Analysis of Polynomial Systems Subject to P-Box Uncertainties. *Mechanical System and Signal Processing*, 37:121–136, 2013.

Stein, M., Beer, M., Kreinovich, V. Bayesian Approach for Inconsistent Information. *Information Sciences*, 245:96–111, 2013.

Blair, A. N., Ayyub, B. M., Bender, W. J. Fuzzy Stochastic Risk-Based Decision Analysis with the Mobile Offshore Base as a Case Study. *Marine Structures*, 14:69–88, 2001.

Agarwal, H., Renaud, J. E., Preston, E. L., et al. Uncertainty Quantification Using Evidence Theory in Multidisciplinary Design Optimization. *Reliability Engineering & System Safety*, 85(1/3):281–294, 2004.

McGill, W. L., Ayyub, B. M. Estimating Parameter Distributions in Structural Reliability Assessment Using the Transferable Belief Model. *Computers & Structures*, 86(10–11):1052–1060, 2008.

Zhang, J. X., Shields, M. D. On the Quantification and Efficient Propagation of Imprecise Probabilities Resulting from Small Datasets. *Mechanical Systems and Signal Processing*, 98:465–483, 2018.
Zhang, H., Mullen, R. L., Muhanna, R. L. Interval Monte Carlo Methods for Structural Reliability. *Structural Safety*, 32(3):183–190, 2010.
Zhang, H., Dai, H., Beer, M., et al. Structural Reliability Analysis on the Basis of Small Samples: An Interval Quasi-Monte Carlo Method. *Mechanical Systems and Signal Processing*, 37(1–2):137–151, 2013.
Zhao, Z., Lu, Z. H., Zhao, Y. G., et al. A Novel Random-Interval Hybrid Reliability Analysis Method Combining Active Learning Kriging and Two-Phase Subset Simulation. *Structures*, 63:106383, 2024.
Zhang, H. Interval Importance Sampling Method for Finite Element-Based Structural Reliability Assessment Under Parameter Uncertainties. *Structural Safety*, 38:1–10, 2012.
Alvarez, D. A., Uribe, F., Hurtado, J. E. Estimation of the Lower and Upper Bounds on the Probability of Failure Using Subset Simulation and Random Set Theory. *Mechanical Systems and Signal Processing*, 100:782–801, 2018.
Wei, P. F., Lu, Z. Z. and Song, J. W. Extended Monte Carlo Simulation for Parametric Global Sensitivity Analysis and Optimization. *AIAA Journal*, 52:867-878, 2014.
Wei, P. F., Song, J. W., Bi, S. F., et al. Non-Intrusive Stochastic Analysis with Parameterized Imprecise Probability Models: I. Performance Estimation. *Mechanical Systems and Signal Processing*, 124:349-368, 2019.
Wei, P. F., Song, J. W., Bi, S. F., et al. Non-Intrusive Stochastic Analysis with Parameterized Imprecise Probability Models: II. Reliability and Rare Events Analysis. *Mechanical Systems and Signal Processing*, 126:227-247, 2019.
Song, J. W., Valdebenito, M., Wei, P. F., et al. Non-Intrusive Imprecise Stochastic Simulation by Line Sampling. *Structural Safety*, 84:101936, 2020.
Faes, M. G., Valdebenito, M. A., Moens, D., et al. Operator Norm Theory as an Efficient Tool to Propagate Hybrid Uncertainties and Calculate Imprecise Probabilities. *Mechanical Systems and Signal Processing*, 152:107482, 2021.
Hong, F. Q., Wei, P. F., Fu, J. F., et al. A Sequential Sampling-Based Bayesian Numerical Method for Reliability-Based Design Optimization. *Reliability Engineering & System Safety*, 244:109939, 2024.
Hong, F. Q., Wei, P. F., Song, J. W., et al. Collaborative and Adaptive Bayesian Optimization for Bounding Variances and Probabilities Under Hybrid Uncertainties. *Computer Methods in Applied Mechanics and Engineering*, 417:116410, 2023.
Wei, P. F., Hong, F. Q., Phoon, K. K., et al. Bounds Optimization of Model Response Moments: A Twin-Engine Bayesian Active Learning Method. *Computational Mechanics*, 67:1273-1292, 2021.
Li, C. C., Der Kiureghian, A. Optimal Discretization of Random Fields. *Journal of Engineering Mechanics*, 119(6):1136-1154, 1993.
Huang, S., Mahadevan, S., Rebba, R. Collocation-Based Stochastic Finite Element Analysis for Random Field Problems. *Probabilistic Engineering Mechanics*, 22(2):194-205, 2007.
Chen, J., Kong, F., Peng, Y. A Stochastic Harmonic Function Representation for Non-Stationary Stochastic Processes. *Mechanical Systems and Signal Processing*, 96:31-44, 2017.
Wilson, J., Borovitskiy, V., Terenin, A., et al. Efficiently Sampling Functions from Gaussian Process Posteriors. *International Conference on Machine Learning*. PMLR, 10292-10302, 2020.
Vakili, S., Moss, H., Artemev, A., et al. Scalable Thompson Sampling Using Sparse Gaussian Process Models. *Advances in Neural Information Processing Systems*, 34:5631-5643, 2021.
Echard, B., Gayton, N., Lemaire, M. AK-MCS: An Active Learning Reliability Method Combining Kriging and Monte Carlo Simulation. *Structural Safety*, 33(2):145-154, 2011.
Bichon, B. J., Eldred, M., Swiler, L. P., et al. Efficient Global Reliability Analysis for Nonlinear Implicit Performance Functions. *AIAA Journal*, 46:2459-2468, 2008.
Lv, Z. Y., Lu, Z. Z., Wang, P. A New Learning Function for Kriging and Its Applications to Solve Reliability Problems in Engineering. *Computers & Mathematics with Applications*, 70(5):1182-1197, 2015.

PINN-Accelerated Diffusion Models for Amortized Bayesian Inversion of Chloride Transport in Concrete

Xuanyi Zhao[1)], Weiping Zhang[1)*]
[1)] *Department of Structural Engineering, College of Civil Engineering, Tongji University, 1239 Siping Road, Shanghai 200092, P.R. China; Email: 2430629@tongji.edu.cn*

Abstract: Accurate estimation of chloride transport parameters is critical for predicting chloride penetration and the residual service life of marine concrete structures. In-situ continuous monitoring using embedded solid-state chloride sensors (e.g., Ag/AgCl ion-selective electrodes) enables rich spatiotemporal observations at multiple cover depths over the entire service life; however, the resulting data streams are inevitably corrupted by sensor drift, temperature-induced potential shifts, and electromagnetic interference, making the inversion ill-conditioned. This study proposes a PINN-accelerated conditional score-based diffusion (PINN-Diff) framework that (i) trains a conditional Physics-Informed Neural Network (PINN) surrogate once over the full prior parameter space to serve simultaneously as a millisecond-scale forward solver and a high-throughput training data-generator, and (ii) performs amortized posterior sampling via a conditional score-based diffusion model equipped with Classifier-Free Guidance (CFG) and Feature-wise Linear Modulation (FiLM) conditioning, thereby enabling real-time Bayesian inference for any new observation without retraining. On synthetic benchmarks with noise levels $\sigma \in \{0.5\%, 1\%, 2\%, 5\%, 10\%\}$ across 20 test cases with 10 repetitions each, PINN-Diff achieves 26% lower posterior mean absolute error than MCMC-PINN (normalized MAE 0.040 vs. 0.054 at $\sigma = 2\%$) and over 50× faster inference (0.08 s vs. 4.2 s per 1,000 posterior samples), while maintaining well-calibrated 90% credible intervals ($Coverage_{90} = 88 - 91\%$). Ablation studies on the noise schedule, observation sparsity, and PINN surrogate capacity confirm the robustness of the framework across a broad range of design choices.

Keywords: Bayesian inversion, Chloride transport, Diffusion model, PINN surrogate, Uncertainty quantification

1. Introduction

Reinforced concrete (RC) structures exposed to marine environments—including cross-sea bridges, port wharves, offshore wind foundations, and coastal revetments—face the persistent risk of chloride-induced steel corrosion. Chloride ions diffuse inward from the concrete surface, and when the free chloride concentration at the reinforcement depth exceeds a critical threshold ($C_{\text{crit}} \approx 0.3 - 0.5\%$ by concrete mass), the protective passive film undergoes depassivation, marking the onset of accelerated deterioration (Angst et al., 2009).

With the advent of embeddable solid-state Ag/AgCl ion-selective electrodes (ISEs) and all-solid-state chloride sensors (Zhang et al., 2020; Jin et al., 2024), it has become feasible to deploy multi-depth sensor arrays at cover depths of 10–50 mm in newly constructed marine concrete structures, continuously recording free chloride concentrations over the entire service life. Combined with the extended Fick's second law incorporating time-dependent diffusivity and Langmuir nonlinear binding, three core transport parameters can be identified from these monitoring records: the reference diffusion coefficient D_{ref} , the time decay

© 2026 by the author(s). This work is licensed under the Creative Commons Attribution 4.0 International License (CC BY 4.0), which permits unrestricted use, distribution, and reproduction in any medium, provided the original author and source are credited.

exponent m, and the asymptotic surface concentration $C_{s,\infty}$. These parameters serve as fundamental inputs for probabilistic service-life prediction under the fib Bulletin 34 framework (fib, 2006) and, more broadly, for the dynamic calibration of digital twin models that mirror the evolving durability state of the structure (Červenka et al., 2023).

However, embedded sensor data are subject to compound uncertainties at three distinct levels: (i) systematic drift of the Ag/AgCl electrode potential due to gradual dissolution and morphological degradation of the AgCl film in the high-pH concrete pore environment, with reported deviations of 25–70% from reference concentrations over multi-year exposures (Zhang et al., 2020); (ii) spatial random fluctuations attributable to concrete heterogeneity, with coefficients of variation (COV) commonly exceeding 15% between adjacent sensor locations even in nominally identical structural elements; and (iii) transient measurement noise arising from temperature-induced potential shifts, environmental electromagnetic interference, and analog-to-digital conversion quantization, with composite noise levels estimated at 2–15% of the measured values. Together, these factors make the parameter inversion ill-conditioned and motivate a Bayesian treatment that can quantify posterior uncertainty.

Current approaches for Bayesian inversion of chloride transport parameters can be categorized into three classes. (1) Traditional Markov chain Monte Carlo (MCMC) methods: Metropolis–Hastings sampling algorithms are classical tools for Bayesian structural parameter identification (Beck and Au, 2002); however, each sampling step requires a call to a numerical PDE solver, and complete inversion typically demands on the order of 10^5 forward evaluations, with acceptance rates declining sharply under high-noise conditions. This computational bottleneck becomes particularly prohibitive when sensor arrays transmit updated observations at hourly to daily intervals, requiring the inference engine to keep pace with the streaming data rate for real-time durability assessment. (2) Pure data-driven methods: simulation-based inference approaches using normalizing flows or neural posterior estimation achieve rapid online inference through offline training (Cranmer et al., 2020), yet their generalization capability depends heavily on training data coverage, and they lack explicit incorporation of physical constraints. (3) Physics-informed neural network (PINN) methods: Raissi et al. (2019) introduced PINNs that embed governing PDEs directly into the training loss, enabling mesh-free forward and inverse solutions. In the chloride domain, Shaban et al. (2023) applied a physics-informed deep neural network to predict chloride diffusion profiles, demonstrating improved forward accuracy over purely data-driven models; however, their work did not address the inverse parameter estimation problem. More broadly, existing PINN-based inversions typically yield only maximum a posteriori (MAP) point estimates through gradient-based optimization, without providing full posterior distributions or uncertainty bounds. How to couple the physical consistency of PINNs with a flexible generative model that captures the complete posterior remains an open question.

Recent progress in generative modeling suggests a potential solution. Score-based diffusion models, originally developed for image generation, (Ho et al., 2020; Song et al., 2021a), learn target distribution score functions through forward noising and neural-network-guided reverse denoising processes. In the context of scientific inverse problems, Chung et al. (2023) proposed the Diffusion Posterior Sampling (DPS) framework, which injects observation likelihood gradients at each reverse diffusion step. Baldassari et al. (2024) extended conditional score-based diffusion to infinite-dimensional Bayesian inverse problems. However, none of these methods have been applied to chloride transport, where strong nonlinearity and time-varying coefficients pose additional challenges.

This paper proposes the PINN-Diff framework, which integrates a conditional PINN surrogate model with a conditional score-based diffusion network to achieve fast and robust Bayesian inversion of chloride transport parameters in concrete. The specific contributions are as follows:

1. Conditional PINN surrogate as training oracle. A residual neural network surrogate is constructed with normalized parameters $\widetilde{\boldsymbol{\theta}} \in [0,1]^3$ as conditional input through two-stage training (Adam optimizer 2×10^4 steps followed by L-BFGS, 500 steps), covering the entire prior parameter space with $R^2 > 0.981$ on 5,000 random test points and a single-evaluation time below 1 ms on GPU. The PINN serves as a high-throughput data generator, producing 200,000 $(\boldsymbol{\theta}, \mathbf{y})$ training pairs for the diffusion model at a fraction of the cost of finite difference solvers.
2. Amortized conditional score-based diffusion. A conditional denoising diffusion probabilistic model (DDPM) score network is trained on offline-generated $(\boldsymbol{\theta}, \mathbf{y}_{obs})$ pairs using Classifier-Free Guidance (CFG) with 10% unconditional masking during training and a guidance scale $w = 1.0$ during inference. Feature-wise Linear Modulation (FiLM) layers enable expressive observation conditioning. Inference via 50-step DDIM generates 1,000 posterior samples in approximately 0.08 seconds on GPU, achieving amortized inference whereby the same trained model serves any new observation without retraining.
3. Comprehensive experimental validation toward sensor-informed digital twins. Systematic comparisons are conducted across 20 test cases × 10 repetitions at noise levels representative of embedded sensor conditions ($\sigma \in \{2\%, 10\%\}$) against two primary baselines (MCMC-PINN and PINN-MAP), with a finite-difference-based MH-MCMC reference establishing the computational infeasibility of direct PDE-solver sampling (33,313 s per case). The proposed PINN-Diff achieves the lowest posterior MAE and the best-calibrated credible intervals, with an inference time of 0.08 s per 1,000 posterior samples—over 50× faster than MCMC-based methods—making it suitable as a real-time update engine for structural digital twins that receive streaming sensor data.

The remainder of this paper is organized as follows: Section 2 establishes the mathematical model and details the framework architecture; Section 3 reports experimental results; Section 4 presents ablation studies and discusses limitations; Section 5 draws conclusions.

2. Methodology

The PINN-Diff framework consists of two functionally independent modules: (1) a conditional PINN surrogate (Module 1, offline training), and (2) a conditional score-based diffusion network (Module 2, offline training and online inference). Both offline modules need only be trained once for a given specific concrete system; thereafter, the online inference module can be repeatedly invoked for any observation sample from the same structural system.

2.1. MATHEMATICAL MODEL

2.1.1. *Chloride Transport Forward Problem*

Consider the following one-dimensional nonlinear partial differential equation governing the transport of free chloride concentration $C(x,t)$ (expressed as a percentage of concrete mass) in a bounded domain $x \in [0, L], L = 100\text{mm}$:

$$R_K(C) \cdot \frac{\partial C}{\partial t} = \frac{\partial}{\partial x}\left[D(t;\boldsymbol{\theta}) \cdot \frac{\partial C}{\partial x}\right] \tag{1}$$

The time-varying diffusion coefficient D(t; θ) follows the power-law decay model proposed by Tang and Nilsson (1992):

$$D(t;\boldsymbol{\theta}) = D_{\mathrm{ref}} \cdot \left(\frac{t_{\mathrm{ref}}}{t}\right)^{m}, t_{\mathrm{ref}} = 2.419 \times 10^{6}\mathrm{s}\ (28\mathrm{days}) \quad (2)$$

where $D_{\mathrm{ref}} \in [1,8] \times 10^{-12}\mathrm{m}^2/\mathrm{s}$ is the reference diffusion coefficient at 28 days, and $m \in [0.15,0.50]$ is the time decay exponent that reflects the physical mechanism whereby hydration products progressively fill the capillary pore network.

The nonlinear binding capacity factor R_K(C) is described by the Langmuir binding isotherm (Tang, 1996):

$$R_K(C) = 1 + \frac{\chi}{(1+\beta C)^2}, \chi = 11.8, \beta = \frac{400}{n_{\mathrm{cm}}} \approx 2352.94 \quad (3)$$

where n_cm = 0.17 is the cement mortar volume fraction. The boundary and initial conditions are specified as:

$$C(0,t) = C_{s,\infty}\left(1 - e^{-t/t_c}\right), \left.\frac{\partial C}{\partial x}\right|_{x=L} = 0, C(x,0) = 0 \quad (4)$$

where $C_{s,\infty} \in [0.6,2.0]\%$ is the asymptotic surface chloride concentration, $t_c = 1.577 \times 10^{7}\mathrm{s}(\approx 0.5\mathrm{year})$. The parameter vector to be inverted is $\boldsymbol{\theta} = (D_{\mathrm{ref}}, m, C_{s,\infty}) \in \mathbb{R}^3$, with a simulation duration of T = 70 years and a critical corrosion concentration of $C_{\mathrm{crit}} = 0.5\%$.

2.1.2. *Bayesian Inversion Problem Formulation*

Consider a sensor array comprising five embedded Ag/AgCl ISEs installed at cover depths $x_i \in \{10,20,30,40,50\}mm$during construction. Each sensor records the local free chloride concentration at nine monitoring epochs $t_j \in \{1,2,5,10,15,20,30,50,70\}$ years, yielding $N_{\mathrm{obs}} = 45$ noisy observations with additive Gaussian noise representing the composite effect of sensor drift, thermal fluctuation, and electronic interference:

$$y_{ij} = C(x_i, t_j; \boldsymbol{\theta}) + \varepsilon_{ij}, \varepsilon_{ij} \sim \mathcal{N}(0, \sigma_{\mathrm{obs}}^2) \quad (5)$$

The raw sensor potential readings (mV) are assumed to have been converted to free chloride concentrations via the Nernst equation and site-specific calibration curves prior to inversion; the additive Gaussian noise term ε_{ij} therefore subsumes both the intrinsic sensor noise and the calibration transfer uncertainty.

The Bayesian inversion target is to compute the parameter posterior distribution:

$$p(\boldsymbol{\theta} \mid \mathbf{y}) \propto p(\mathbf{y} \mid \boldsymbol{\theta}) \cdot p(\boldsymbol{\theta}) \quad (6)$$

The likelihood function takes the standard Gaussian form:

$$\log p(\mathbf{y} \mid \boldsymbol{\theta}) = -\frac{1}{2\sigma_{\mathrm{obs}}^2} \left\| \mathbf{y} - F_{\varphi}(\boldsymbol{\theta}) \right\|^2 \quad (7)$$

where $F_{\varphi}(\boldsymbol{\theta}) \in \mathbb{R}^{N_{\mathrm{obs}}}$ is the PINN surrogate forward prediction vector. The prior distribution assigns uniform distributions to all three parameters:

$$p(\boldsymbol{\theta}) = \mathcal{U}(D_{\mathrm{ref}}; 10^{-12}, 8 \times 10^{-12}) \times \mathcal{U}(m; 0.15,0.50) \times \mathcal{U}(C_{s,\infty}; 0.6,2.0) \quad (8)$$

The inference target is to obtain M = 1,000 approximately independent posterior samples for computing the posterior mean, standard deviation, 90% credible intervals, and corrosion initiation time distributions.

2.2. MODULE 1: CONDITIONAL PINN SURROGATE

The conditional PINN surrogate $F_\varphi: (\tilde{x}, \tilde{t}, \tilde{\boldsymbol{\theta}}) \mapsto \tilde{C}$ takes normalized coordinates ($\tilde{x} = x/L, \tilde{t} = t/T$) and normalized parameters ($\tilde{\boldsymbol{\theta}} \in [0,1]^3$) as input, predicting normalized concentration ($\tilde{C} = C/C_{\text{scale}}$, where $C_{\text{scale}} = 2.2\%$).

2.2.1. *Network architecture*

The architecture comprises three components: an input projection layer (Linear(5 → 128) with SiLU activation) that embeds the five-dimensional input into a 128-dimensional hidden space; four residual blocks, each consisting of FC(128 → 128), SiLU activation, FC(128 → 128), an identity skip connection, and LayerNorm; and an output layer (Linear(128 → 1) with Sigmoid activation) that ensures the physically bounded output $\tilde{C} \in [0,1]$. The total number of trainable parameters is approximately 99,713.

2.2.2. *PINN Loss Function*

The PINN training loss comprises four weighted terms:

$$\mathcal{L}_{\text{PINN}} = w_{\text{pde}}\mathcal{L}_{\text{pde}} + w_{\text{bc}}\mathcal{L}_{\text{bc}} + w_{\text{nb}}\mathcal{L}_{\text{nb}} + w_{\text{ic}}\mathcal{L}_{\text{ic}} \tag{9}$$

where L_pde is the PDE interior residual at N_int = 8,000 collocation points; L_bc is the surface boundary condition MSE at N_bc = 800 points; L_nb is the Neumann condition at $\tilde{x} = 1$; L_ic is the initial condition at $\tilde{t} = 0$. Loss weights: $w_{\text{pde}} = 1, w_{\text{bc}} = 20, w_{\text{nb}} = 2, w_{\text{ic}} = 20$, following the gradient balancing principle of Wang et al. (2021).

2.2.3. *Training Strategy*

Training employs a two-stage strategy: Stage 1 (Adam, 2×10^4 steps, initial learning rate 5×10^{-4} with cosine annealing) provides fast initial convergence; Stage 2 (L-BFGS optimizer, 500 steps) leverages full-batch second-order information to compress PDE residuals to approximately 10^{-5}. Validation on 5,000 independent random parameter test points yields $R^2 = 0.981, \text{MAE} = 0.035\%$, and $\text{RMSE} = 0.054\%$, with single GPU evaluation time under 1 ms.

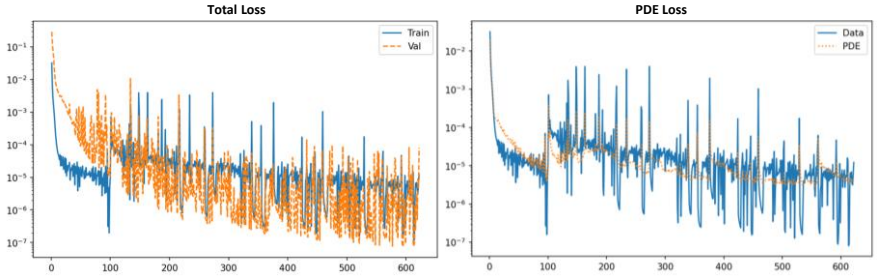


Figure 1. PINN surrogate training curves for the base (4-block) architecture: total loss convergence (left), data/PDE loss decomposition (right).

Beyond serving as a fast forward solver, the PINN surrogate also serves as a training data generator. By efficiently producing 200,000 $(\boldsymbol{\theta}, \mathbf{y})$ pairs covering the entire prior parameter space, it eliminates the computational bottleneck that would otherwise require days of finite difference simulations.

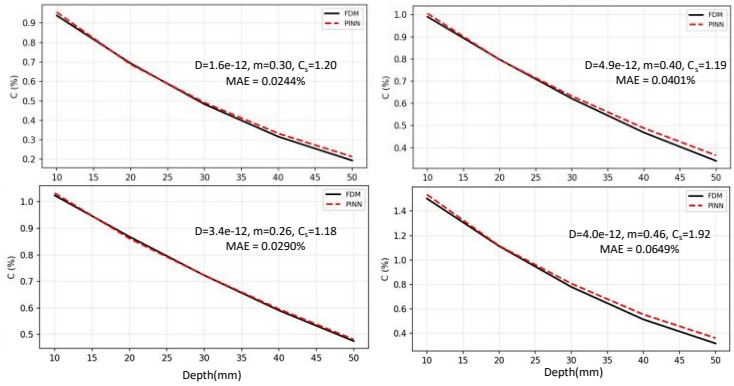


Figure 2. PINN validation: concentration profiles at t = 70 yr for four representative parameter combinations compared against finite difference method (FDM) reference solutions. Maximum MAE = 0.065%.

2.3. MODULE 2 : CONDITIONAL SCORE-BASED DIFFUSION NETWORK

The diffusion model operates in the normalized parameter space$\boldsymbol{\theta} \in [0,1]^3 \subset R^3$, learning the conditional posterior distribution $p(\boldsymbol{\theta} \mid \mathbf{y})$ through a conditional denoising process.

2.3.1. *Noise Schedule and Forward Process*

A cosine schedule (Nichol and Dhariwal, 2021) with $T_{\text{diff}} = 1{,}000$ total diffusion steps is adopted:

$$\bar{\alpha}_k = \frac{\cos^2\left[\frac{\pi\left(\frac{k}{T_{\text{diff}}} + s\right)}{2(1+s)}\right]}{\bar{\alpha}_0}, s = 0.008 \tag{10}$$

The cosine schedule provides smoother signal-to-noise ratio (SNR) transitions at low diffusion steps (k $\approx$ 0), which is crucial for preserving the physics-dictated negative correlation between D_ref and m—a structural feature of chloride diffusion where higher initial diffusivity compensates for slower time decay, and vice versa. Single-step noise coefficients are derived as $\beta_k = 1 - \frac{\bar{\alpha}_k}{\bar{\alpha}_{k-1}}$, clipped to $[10^{-4}, 0.9999]$. The forward process follows: $q(\tilde{\theta}_k|\tilde{\theta}_0) = \mathcal{N}(\sqrt{\bar{a}_k} \cdot \tilde{\theta}_0, (1-\bar{a}_k)I)$.

2.3.2. *Score Network Architecture*

The score network $\boldsymbol{\epsilon}_\psi(\widetilde{\boldsymbol{\theta}}_k, k, \mathbf{y})$ employs a conditional residual architecture with 6 ConditionalResBlocks with a hidden dimension of 256. Conditioning information is derived from two independent encoders: a time embedding module that produces $\mathbf{c}_t \in \mathbb{R}^{128}$ via sinusoidal positional encoding followed by a two-layer MLP (128→128, GELU activation); and an observation embedding module that compresses y $\in \mathbb{R}^{45}$ to $\mathbf{c}_y \in \mathbb{R}^{128}$ via three-layer MLP (45→128, 128→128 (with residual), 128→128 (with residual)), GELU activation with residual connections and LayerNorm). The concatenated condition vector $\mathbf{c} = [\mathbf{c}_t; \mathbf{c}_y] \in \mathbb{R}^{256}$ modulates each residual block through Feature-wise Linear Modulation (FiLM) (Perez et al., 2018):

$$\mathbf{h}_{\text{out}} = \boldsymbol{\gamma}(\mathbf{c}) \odot \mathbf{h} + \boldsymbol{\beta}(\mathbf{c}) \tag{11}$$

where γ, β are learned affine parameters. The FiLM layers are initialized with $\gamma_{\text{bias}} = 1$, $\beta_{\text{bias}} = 0$, $\gamma_{\text{weight}} = 0$, and $\beta_{\text{weight}} = 0$, ensuring identity mapping at training onset so that the FiLM layers do not corrupt the residual signal during early training stages.

2.3.3. *Classifier-Free Guidance (CFG)*

During training, the observation condition y is replaced by a zero vector with probability $p_{\text{uncond}} = 0.10$, training the network to perform both conditional and unconditional score estimation. At inference time, the guided noise prediction amplifies the conditional information (Ho and Salimans, 2022):

$$\boldsymbol{\epsilon}_{\text{guided}} = (1 + w)\boldsymbol{\epsilon}_{\psi}(\tilde{\boldsymbol{\theta}}_t, t, \mathbf{y}) - w\boldsymbol{\epsilon}_{\psi}(\tilde{\boldsymbol{\theta}}_t, t, 0), w = 1.0 \quad (12)$$

2.3.4. *Training*

The ε-prediction denoising score matching loss (Vincent, 2011) is minimized:

$$\mathcal{L}_{\text{diff}} = \mathbb{E}_{k,\tilde{\boldsymbol{\theta}}_0,\boldsymbol{\epsilon}} \left\| \boldsymbol{\epsilon} - \boldsymbol{\epsilon}_{\psi}\left(\sqrt{\bar{\alpha}_k}\tilde{\boldsymbol{\theta}}_0 + \sqrt{1 - \bar{\alpha}_k}\boldsymbol{\epsilon}, k, \mathbf{y}\right) \right\|^2 \quad (13)$$

The training set consists of: 200,000 $(\tilde{\boldsymbol{\theta}}, \mathbf{y})$ pairs where $\tilde{\boldsymbol{\theta}} \sim \text{Uniform}[0,1]^3$ and y is generated by the PINN surrogate with added Gaussian noise (σ uniformly sampled from $[0.5\%, 15\%]$ per sample, providing noise-level diversity). The training configuration is as follows: Adam optimizer (learning rate 2×10^{-4}, weight decay 0.01, batch size 512, 2,000 epochs). Exponential Moving Average (EMA) with a decay factor of 0.9999 is maintained throughout training; inference employs the EMA weights to mitigate the effects of late-stage loss oscillation.

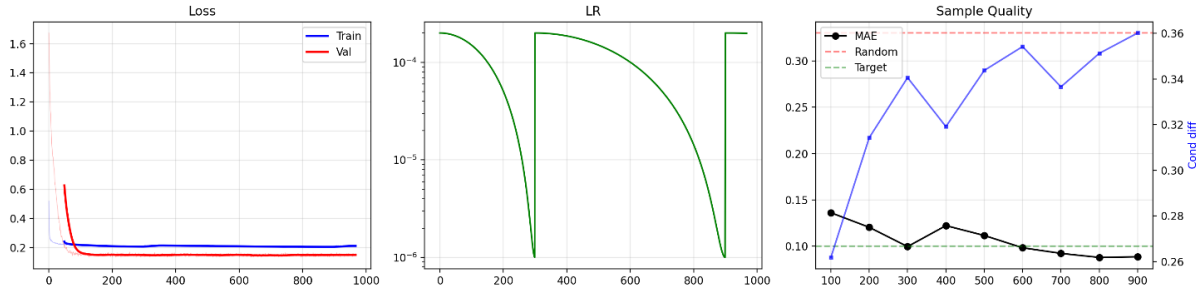


Figure 3. Diffusion model training diagnostics: loss convergence (left), learning rate schedule with warm restarts (center), and sample quality evolution showing MAE approaching target while conditional difference metric stabilizes (right).

2.4. DDIM INFERENCE

The inference stage employs deterministic Denoising Diffusion Implicit Model (DDIM) (Song et al., 2021b) reverse sampling with N_steps = 50 steps spanning all 1,000 diffusion steps, achieving approximately 20× speedup over standard DDPM sampling.

Algorithm 1: PINN-Diff Inference.

Require: observation y, $N_{\text{samples}} = 1000$, $N_{\text{steps}} = 50$, CFG scale $w = 1.0$

Ensure: posterior samples $\{\tilde{\theta}^{(i)}\}$, mapped to physical parameters via prior bounds

1: **for** $i = 1$ to N_{samples} (parallelized on GPU) **do**

2: Sample initial noise: $\tilde{\theta}_T \sim \mathcal{N}(0, I)$

3: **for** $k = 0,1,\ldots,49$ (diffusion steps t from $999 \rightarrow 0$) **do**

4: **(a)** Compute predictions:

$$\hat{\varepsilon}_{\text{cond}} = \varepsilon_\psi(\tilde{\theta}_t, t, y)$$

$$\hat{\varepsilon}_{\text{uncond}} = \varepsilon_\psi(\tilde{\theta}_t, t, 0)$$

(b) Classifier-Free Guidance (CFG) combination:

$$\hat{\varepsilon} = (1 + w) \cdot \hat{\varepsilon}_{\text{cond}} - w \cdot \hat{\varepsilon}_{\text{uncond}}$$

(c) Reconstruct sample from noise prediction, clipped to $[0,1]^3$:

$$\hat{\tilde{\theta}}_0 = \frac{\tilde{\theta}_t - \sqrt{1 - \bar{a}_t} \cdot \hat{\varepsilon}}{\sqrt{\bar{a}_t}}$$

(d)

$$\tilde{\theta}_{t_{\text{prev}}} = \sqrt{\bar{a}_{t_{\text{prev}}}} \cdot \hat{\tilde{\theta}}_0 + \sqrt{1 - \bar{a}_{t_{\text{prev}}}} \cdot \hat{\varepsilon}$$

end for

Output posterior sample: $\tilde{\theta}^{(i)}$

end for

The entire inference procedure requires only forward passes through the score network—no PDE solving and no gradient computation—with GPU batch processing completing 1,000 posterior samples in approximately 0.08 s. This is the key benefit of amortized inference: once trained, the model provides instant posterior estimates for any new observation, rendering the probabilistic assessment of hundreds of structural elements computationally feasible.

3. Inversion Performance

3.1. EXPERIMENTAL SETUP

3.1.1. *Synthetic data generation*

Twenty normalized true parameter vectors $\boldsymbol{\theta}_{\text{true}}$ are drawn from the uniform prior $\mathcal{U}([0,1]^3)$ with a fixed random seed (seed = 42), corresponding to the physical ranges $D_{\text{ref}} \in [1,8] \times 10^{-12}\text{m}^2/\text{s}$, $m \in [0.15,0.50]$, $C_{s,\infty} \in [0.6,2.0]\%$. For each $\boldsymbol{\theta}_{\text{true}}$, reference concentration profiles are generated using a high-accuracy finite difference solver (spatial step $\Delta x = 0.5\text{mm}$, adaptive Runge-Kutta time integration, tolerance 10^{-8}) at 45 observation nodes (5 depths × 9 time points), with independent Gaussian noise added at levels $\sigma \in \{2\%, 10\%\}$, representing the lower and upper bounds of composite sensor noise expected from well-calibrated and degraded Ag/AgCl ISEs, respectively (Zhang et al., 2020). Each parameter-noise combination generates 10 independent noisy observation vectors, yielding 20 × 2 × 10 = 400 independent inversion experiments. All experiments are conducted on an NVIDIA RTX 4070Ti SUPER GPU with PyTorch 2.1, Python 3.10, and CUDA 11.8.

3.1.2. *Baseline methods*

Three baselines are established: (1) MCMC-PINN: Metropolis-Hastings MCMC with the trained PINN surrogate as the forward model (GPU batch evaluation), n_{burnin} = 2,000, n_{thin} = 5, target $n_{samples}$ = 1,000, and an adaptive proposal scheme targeting an acceptance rate of 23.4%. (2) PINN-MAP: Adam optimization (learning rate 10^{-3}, 2,000 steps) minimizing the negative log-posterior, producing only a MAP point estimate. (3) MH-MCMC: Metropolis-Hastings with a finite difference forward solver. A single inversion run required 33,313 s (≈9.3 hours) to generate 1,000 posterior samples, rendering the full 400-case benchmark (estimated at >3,700 hours of sequential computation) infeasible within the allocated computational budget. This

baseline is therefore excluded from Tables 1–2 but serves to contextualize the computational advantage of PINN-accelerated approaches.

3.1.3. *Evaluation metrics*

Six metrics are adopted: (1) Normalized MAE: $|\widehat{\boldsymbol{\theta}} - \boldsymbol{\theta}_{\text{true}}|$ in [0,1] space (0 = perfect, 1/3 ≈ random guess); (2) Physical-space relative MAE (%); (3) $Coverage_{90}$: proportion of true values falling within the 5th–95th percentile credible interval (ideal = 0.90); (4) CI_{width}: credible interval width; (5) Inference time $T_{infer(s)}$ and (6) Effective sample size (ESS).

3.2. MAIN BENCHMARK RESULTS

Table 1 presents the main benchmark comparison. The proposed PINN-Diff achieves the lowest average normalized MAE at both noise levels: 0.040 ($\sigma = 2\%$) and 0.119 ($\sigma = 10\%$), outperforming MCMC-PINN (0.054 and 0.123), and PINN-MAP (0.054 and 0.128).

Table 1 Main benchmark: normalized MAE in [0,1] space (0 = perfect, 0.33 ≈ random). Bold indicates best result.

Method	D_ref	m	C_s,∞	Mean	Cov_{90}	CI_w	T(s)
$\sigma = 2\%$							
MCMC-PINN	0.071	0.081	0.011	0.054	0.82	0.154	4.20
PINN-Diff (Ours)	**0.050**	**0.053**	**0.016**	**0.040**	**0.88**	**0.158**	**0.075**
PINN-MAP	0.070	0.072	0.020	0.054	—	—	3.62
$\sigma = 10\%$							
MCMC-PINN	0.136	0.158	0.074	0.123	0.90	0.475	3.40
PINN-Diff (Ours)	**0.135**	**0.150**	**0.072**	**0.119**	**0.91**	**0.487**	**0.076**
PINN-MAP	0.151	0.166	0.069	0.128	—	—	3.62

The per-parameter breakdown reveals that PINN-Diff is particularly strong on D_ref (normalized MAE 0.050 vs. MCMC-PINN's 0.071 at σ = 2%) and m (0.053 vs. 0.081), while all methods perform comparably well on C_s,∞, which is strongly constrained by the surface observations.

Table 2 Physical-space relative error (%) and effective sample size (ESS).

Method	D_ref%	m%	C_s%	Mean%	ESS
$\sigma = 2\%$					
MCMC-PINN	11.31	9.25	1.27	7.27	43
PINN-Diff (Ours)	**8.03**	**5.83**	**1.87**	**5.24**	**916**
PINN-MAP	10.61	7.82	2.36	6.93	—
$\sigma = 10\%$					
MCMC-PINN	23.19	17.15	7.76	16.03	70
PINN-Diff (Ours)	**21.83**	**16.86**	**8.96**	**15.88**	**923**
PINN-MAP	23.52	18.56	7.86	16.65	—

The accuracy advantage of PINN-Diff is noise-dependent. At σ = 2%, it achieves a 26% MAE reduction over MCMC-PINN, with gains most pronounced for D_{ref} (30%) and m (35%). At σ = 10%, the gap narrows to 3.3% (0.119 vs. 0.123). This is expected: at high noise the posterior is dominated by the prior (CI width

expands from 0.158 to 0.487), and all methods are constrained by the same observation information content. The value of PINN-Diff at high noise is therefore not superior accuracy but equivalent accuracy at near-zero marginal cost.

In terms of uncertainty quantification, PINN-Diff provides well-calibrated credible intervals with $Coverage_{90}$ = 0.88 (σ =2%) and 0.91 (σ =10%), close to the nominal value of 0.90. The slight undercoverage at low noise is due to three factors: (a) the PINN surrogate's systematic error (MAE $\approx$ 0.035%) becomes non-negligible relative to the observation noise, biasing the effective likelihood; (b) the deterministic DDIM sampler (η = 0) may underrepresent tail probabilities when the posterior is very narrow; and (c) Classifier-Free Guidance (w = 1.0) tends to sharpen the predicted distribution under low-noise conditions. Despite this, PINN-Diff outperforms MCMC-PINN ($Coverage_{90}$ = 0.82 at σ = 2%), whose undercoverage stems from insufficient chain mixing at ESS = 43.

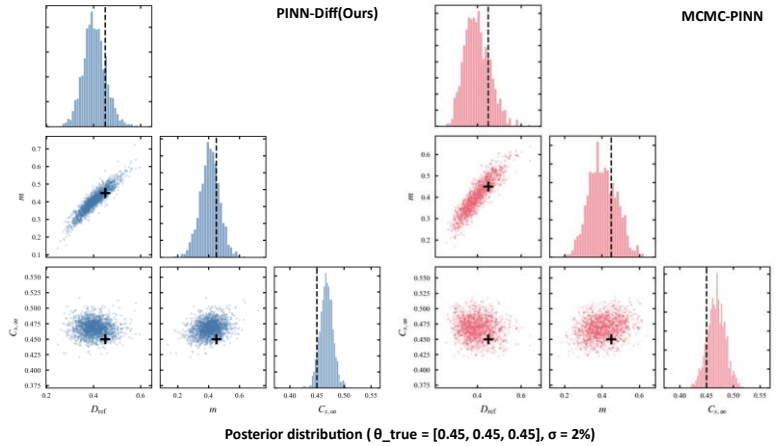


Figure 4. Posterior distributions for a representative test case (θ_{true} = [0.45, 0.45, 0.45], σ = 2%). Left (blue): PINN-Diff (Ours). Right (pink): MCMC-PINN. Dashed lines indicate true values; crosses mark posterior means. PINN-Diff produces well-localized posteriors with the characteristic $D_{ref}-m$ negative correlation correctly captured.

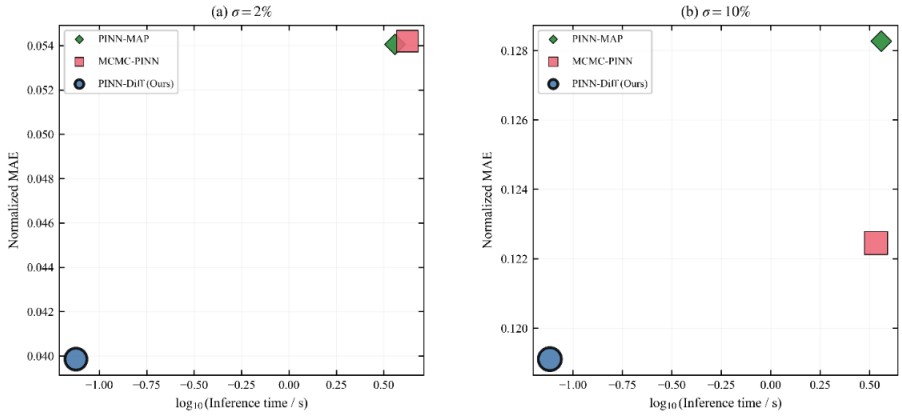


Figure 5. Efficiency–accuracy Pareto front: (a) σ = 2%, (b) σ = 10%. PINN-Diff (circle) occupies the ideal lower-left region (fast + accurate), clearly dominating all baselines.

3.3. NOISE ROBUSTNESS

Figure 6 presents the performance of PINN-Diff and MCMC-PINN across five noise levels $\sigma \in \{0.5\%, 1\%, 2\%, 5\%, 10\%\}$. Each data point is based on 20 cases × 10 repetitions = 200 independent inversions.

PINN-Diff consistently outperforms MCMC-PINN across all noise levels, with the advantage most pronounced at low-to-moderate noise (σ ≤ 2%), where posterior concentration amplifies the benefit of the diffusion model's expressive capacity (e.g., 26% MAE reduction at σ = 2%). At higher noise (σ ≥ 5%), the gap narrows as the posterior is increasingly dominated by the prior, limiting the recoverable information content for all methods (CI width expands from 0.158 to 0.487).

The per-parameter trends in Figure 6a reveal that D_{ref} and m are consistently the most difficult parameters to recover, with relative MAE rising steeply from approximately 5–6% at σ = 0.5% to over 20% at σ = 10%. In contrast, $C_{s,\infty}$ remains well-constrained across all noise levels (relative MAE < 9% even at σ = 10%), because the surface boundary observations directly inform this parameter with minimal coupling to D_{ref} or m. This separation suggests that, in practice, surface chloride concentration can be reliably estimated even from degraded sensor arrays, whereas accurate recovery of the diffusion–decay pair (D_{ref}, m) demands either low-noise sensors or dense temporal coverage.

Figure 6b shows that both methods approach the nominal 90% coverage at higher noise levels, where the broadened posterior naturally encompasses the true value. At low noise, however, PINN-Diff maintains $\text{Coverage}_{90} \approx 0.88$–$0.91$ while MCMC-PINN drops to 0.78–0.82, reflecting the latter's insufficient mixing (ESS = 43). This coverage gap closes at σ ≥ 5% as the wider posterior compensates for MCMC's mixing limitations.

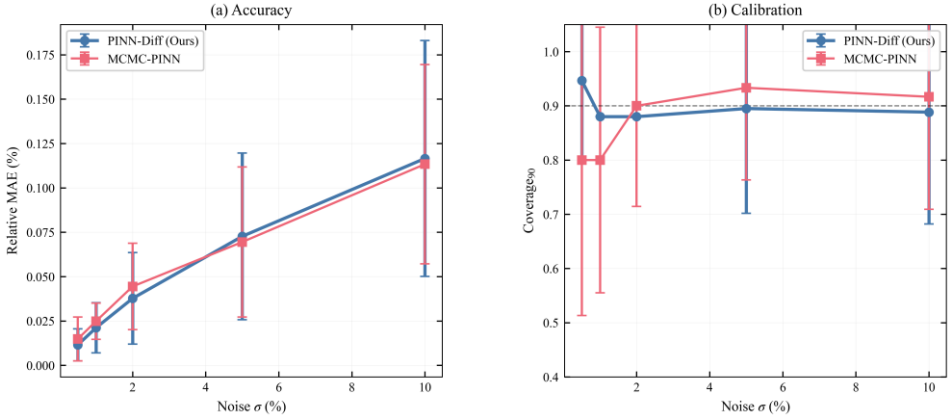


Figure 6. Noise robustness across five noise levels: (a) Relative MAE (%) vs. noise level σ, (b) Coverage_{90} vs. noise level σ. Dashed line in (b) indicates nominal 90% coverage.

3.4. COMPUTATIONAL EFFICIENCY

Table 1 and 2 report the inference time and effective sample size (ESS) for each method. PINN-Diff generates 1,000 posterior samples in 0.075 s (σ = 2%) and 0.076 s (σ = 10%), compared to 4.2 s for MCMC-PINN and 3.6 s for PINN-MAP. The ESS further highlights a structural difference in sampling mechanisms: PINN-Diff achieves ESS = 916–923 (near-independence) because each sample is drawn from an independent initial noise vector, while MCMC-PINN yields ESS = 43–70 due to the inherent serial correlation of Markov chains.

In terms of effective samples per second, PINN-Diff achieves approximately 12,200 versus 10 for MCMC-PINN.

For a coastal bridge with 200 sensor-equipped elements, full Bayesian parameter estimation shifts from ≈14 hours (MCMC-PINN) or 77 days (MH-MCMC) to under 16 seconds, enabling the digital twin to assimilate each sensor update within the acquisition cycle. The total offline training cost—approximately 30 minutes (PINN) plus 3 hours (diffusion model)—is amortized from the first batch of inversion tasks.

It should be noted that MCMC is asymptotically exact given sufficient samples, whereas the diffusion model produces independent draws from a learned approximate posterior. Any systematic bias in the learned distribution affects all samples uniformly. This tradeoff between asymptotic exactness and amortized efficiency is inherent to the framework.

4. ABLATION STUDIES

To quantify the contribution of individual design decisions, three ablation experiments are conducted at both σ = 2% and σ = 10%, using the same 20 test cases (seed = 42). Results are summarized in Figure 7 and Table 3.

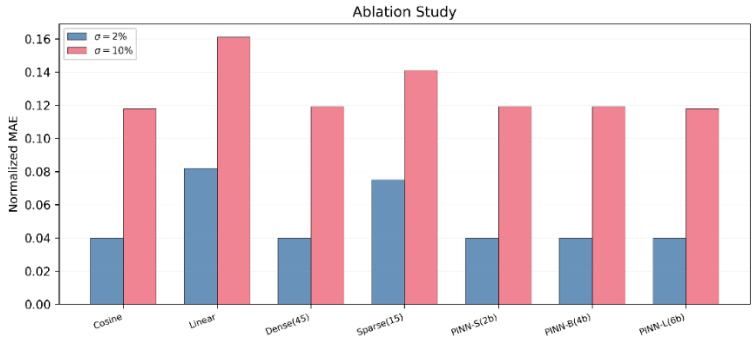


Figure 7. Ablation study summary: normalized MAE for all variants at $\sigma = 2\%$ (blue) and $\sigma = 10\%$ (pink). Sparse observations produce the largest degradation.

Table 3 Ablation study summary: normalized MAE.

Ablation	Variant	σ = 2%	σ = 10%
A1: Schedule	cosine (default)	0.040	0.118
	Linear	0.082	0.161
A2: Observations	Dense (45 obs)	0.040	0.119
	Sparse (15 obs)	0.075	0.141
A3: PINN Capacity	Small (2 blocks)	0.040	0.119
	Base (4 blocks)	0.040	0.119
	Large (6 blocks)	0.040	0.118

4.1. EFFECT OF NOISE SCHEDULE

The cosine schedule achieves notably lower MAE (0.040 vs. 0.082 at $\sigma = 2\%$; 0.118 vs. 0.161 at $\sigma = 10\%$) compared to the linear schedule, confirming that smoother SNR transitions are essential for capturing fine-

grained posterior correlations. Specifically, the cosine schedule preserves the strong $D_{ref}-m$ negative correlation (median ρ at σ = 2%) whereas the linear schedule produces substantially weaker correlation.

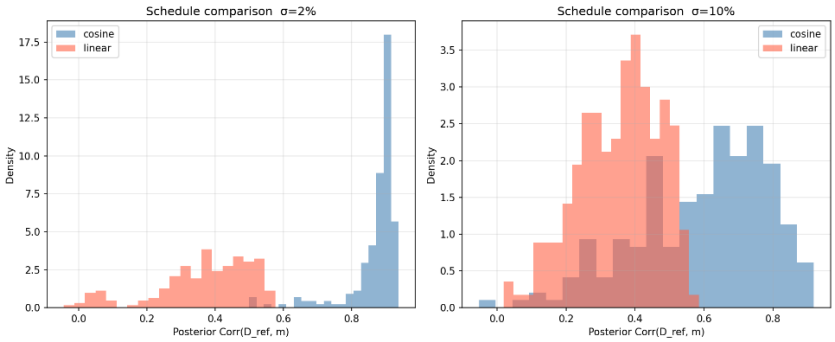


Figure 8. Ablation A1: posterior $Corr(D_{ref}, m)$distributions for cosine vs. linear schedule at $\sigma = 2\%$ (left) and $\sigma = 10\%$ (right).

4.2. EFFECT OF OBSERVATION SPARSITY

The dense configuration (45 obs, observation-to-parameter ratio 15:1) consistently outperforms the sparse configuration (15 obs, ratio 5:1), with normalized MAE of 0.040 vs. 0.075 at $\sigma = 2\%$ and 0.119 vs. 0.141 at $\sigma = 10\%$. The degradation is more pronounced under low noise (1.9× increase) than under high noise (1.2×), indicating that when observation noise is already the dominant source of posterior uncertainty, reducing the number of sensors has a comparatively modest additional effect. Conversely, at low noise where data are highly informative, the loss of 30 observation points substantially weakens the constraints on D_{ref} and m, whose posterior correlation structure relies on dense temporal coverage.

These results carry practical implications for sensor array deployment: dense temporal coverage ($\geqslant$9 epochs) is essential under well-calibrated sensor conditions ($\sigma \leqslant 2\%$), while a reduced 15-sensor array may suffice under degraded conditions where observation noise already dominates the uncertainty budget.

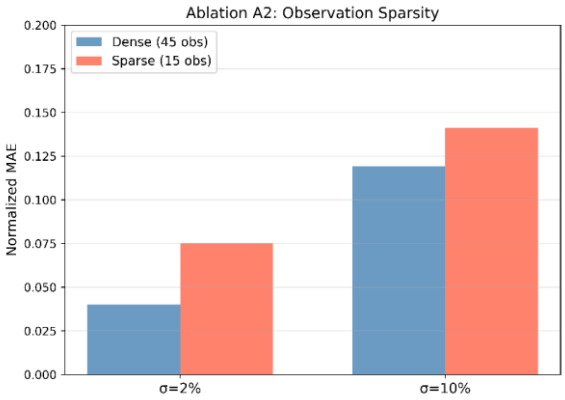


Figure 9. Ablation A2: Normalized MAE for dense (45 obs) vs. sparse (15 obs) configurations.

4.3. EFFECT OF PINN SURROGATE CAPACITY

Three PINN architectures are compared: Small (2 blocks, ~38K params), Base (4 blocks, ~100K params), and Large (6 blocks, ~163K params). All three achieve comparable normalized MAE (~0.040 at $\sigma = 2\%$ and ~0.119 at $\sigma = 10\%$) with overlapping error bars, suggesting the Base architecture already provides sufficient forward model fidelity for the downstream diffusion model.

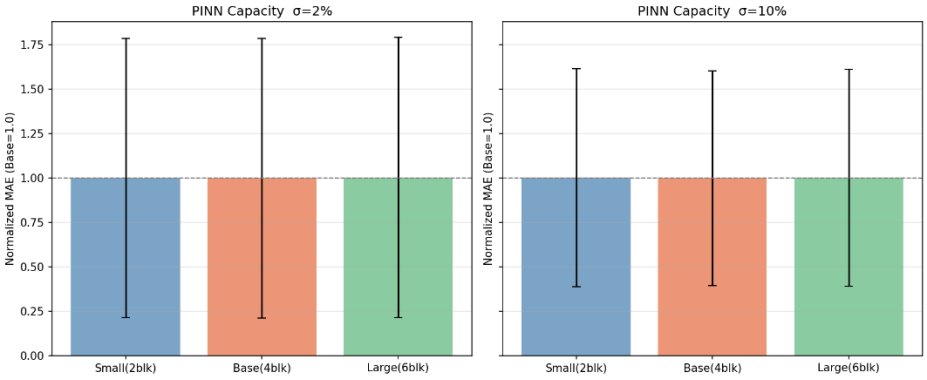


Figure 10. Ablation A3: Normalized MAE (base = 1.0) for Small/Base/Large PINN architectures.

4.4. LIMITATIONS AND FUTURE WORK

Several limitations should be acknowledged. (1) The framework assumes spatially uniform parameters; extension to spatially varying fields would require more expressive generative architectures. (2) The observation noise level σ is not provided to the diffusion model at inference time; the network must implicitly infer it from the observation vector. While the diverse training noise range ($\sigma \in [0.5\%, 15\%]$) enables implicit adaptation, the framework's behavior under noise distributions that deviate substantially from the training range (e.g., non-Gaussian sensor artifacts) has not been evaluated. (3) Validation relies on synthetic data from the same PDE model, creating a potential inverse crime; field validation with real sensor data is essential. (4) Current Ag/AgCl sensors have operational lifetimes of 5–20 years (Zhang et al., 2020); the assumed observation epochs extending to 70 years may not be fully achievable, and the framework's accuracy under truncated observation windows has not been systematically evaluated. (5) $Coverage_{90} = 0.88$ at σ = 2% indicates slight overconfidence that may be mitigated through stochastic DDPM sampling or calibration-aware training.

5. Conclusion

This paper proposed PINN-Diff, a framework integrating conditional PINN surrogates with conditional score-based diffusion models for amortized Bayesian inversion of chloride transport parameters $\theta = (D_{ref}, m, C_{s,\infty})$ in marine concrete. The key idea is to decouple forward modeling from inference: the PINN is trained once as a millisecond-scale oracle, and the diffusion model learns to map any observation to a full posterior via a single forward pass.

Systematic evaluation across 400 independent inversion experiments demonstrates that PINN-Diff achieves the lowest posterior MAE among all compared methods, with well-calibrated credible intervals ($Coverage_{90}$ = 88–91%) and near-independent samples (ESS > 900). The inference time of 0.075 s per 1,000 posterior samples—yielding approximately 12,200 effective samples per second versus 10 for MCMC-PINN—makes real-time Bayesian parameter updating feasible for sensor-instrumented structures. Ablation studies confirm that the cosine noise schedule and dense temporal observations are the most influential design choices, while the framework is insensitive to PINN surrogate capacity beyond the Base architecture.

PINN-Diff can therefore serve as a real-time parameter update engine for service-life digital twins, where embedded sensor arrays provide continuous observations and amortized inference delivers instantaneous posterior estimates to support proactive maintenance decisions. Future work will focus on field sensor validation, spatially heterogeneous parameter fields, and comparison with flow-based amortized alternatives.

6. References

Angst, U., B. Elsener, C. K. Larsen, and Ø. Vennesland. Critical chloride content in reinforced concrete—a review. Cement and Concrete Research, 39(12):1122–1138, 2009.

Baldassari, L., A. Siahkoohi, J. Garnier, K. Solna, and M. V. de Hoop. Conditional score-based diffusion models for Bayesian inference in infinite dimensions. Advances in Neural Information Processing Systems, 36, 2023.

Beck, J. L. and S. K. Au. Bayesian updating of structural models and reliability using Markov chain Monte Carlo simulation. Journal of Engineering Mechanics, 128(4):380–391, 2002.

Červenka, J., J. Rymes, L. Jendele, and R. Pukl. Digital twins for reinforced concrete structures. In A. Ilki et al. (eds.), Building for the Future: Durable, Sustainable, Resilient, fib Symposium 2023, Lecture Notes in Civil Engineering, vol. 349, pp. 1619–1627. Springer, 2023.

Chung, H., J. Kim, M. T. Mccann, M. L. Klasky, and J. C. Ye. Diffusion posterior sampling for general noisy inverse problems. International Conference on Learning Representations, 2023.

Cranmer, K., J. Brehmer, and G. Louppe. The frontier of simulation-based inference. Proceedings of the National Academy of Sciences, 117(48):30055–30062, 2020.

fib. fib Bulletin 34: Model Code for Service Life Design. International Federation for Structural Concrete, 2006.

Ho, J., A. Jain, and P. Abbeel. Denoising diffusion probabilistic models. Advances in Neural Information Processing Systems, 33:6840–6851, 2020.

Ho, J. and T. Salimans. Classifier-free diffusion guidance. NeurIPS 2021 Workshop on Deep Generative Models and Downstream Applications, 2022.

Jin, Z., M. Zhang, H. Fu, L. Tian, Z. Du, and P. Wang. Embeddable chloride sensor for monitoring chloride penetration into cement mortar. Sensors, 24(7):2149, 2024.

Nichol, A. and P. Dhariwal. Improved denoising diffusion probabilistic models. International Conference on Machine Learning, pp. 8162–8171, 2021.

Perez, E., F. Strub, H. de Vries, V. Dumoulin, and A. Courville. FiLM: Visual reasoning with a general conditioning layer. AAAI Conference on Artificial Intelligence, 32(1), 2018.

Raissi, M., P. Perdikaris, and G. E. Karniadakis. Physics-informed neural networks: A deep learning framework for solving forward and inverse problems involving nonlinear partial differential equations. Journal of Computational Physics, 378:686–707, 2019.

Shaban, W. M., K. Elbaz, A. Zhou, and S.-L. Shen. Physics-informed deep neural network for modeling the chloride diffusion in concrete. Engineering Applications of Artificial Intelligence, 125:106691, 2023.

Song, Y., J. Sohl-Dickstein, D. P. Kingma, A. Kumar, S. Ermon, and B. Poole. Score-based generative modeling through stochastic differential equations. International Conference on Learning Representations, 2021a.

Song, J., C. Meng, and S. Ermon. Denoising diffusion implicit models. International Conference on Learning Representations, 2021b.

Tang, L. and L.-O. Nilsson. Chloride diffusivity in high strength concrete at different ages. Nordic Concrete Research, 11(1):162–171, 1992.

Tang, L. Chloride transport in concrete—measurement and prediction. PhD thesis, Chalmers University of Technology, 1996.

Vincent, P. A connection between score matching and denoising autoencoders. Neural Computation, 23(7):1661–1674, 2011.

Wang, S., Y. Teng, and P. Perdikaris. Understanding and mitigating gradient flow pathologies in physics-informed neural networks. SIAM Journal on Scientific Computing, 43(5):A3055–A3081, 2021.

Zhang, Z., J. Hu, Y. Ma, Y. Wang, H. Huang, Z. Zhang, J. Wei, S. Yin, and Q. Yu. A state-of-the-art review on Ag/AgCl ion-selective electrode used for non-destructive chloride detection in concrete. Composites Part B: Engineering, 200:108289, 2020.

Bayesian Calibration of Resistance Spot Welding Models Using Temporal Process Features and Streamlined Active Learning

B. Verkens[1,2*], P. Li[3], L. Bogaerts[1,2], M. Faes[4,5], P. Van Rymenant[1] and D. Moens[1,2]
[1)] *KU Leuven, Department of Mechanical Engineering*
Jan Pieter de Nayerlaan 5, 2860 Sint-Katelijne-Waver, Belgium
email: {bouwe.verkens, patrick.vanrymenant, david.moens}@kuleuven.be
[2)] *FlandersMake@KU Leuven, Belgium*
[3] *Key Laboratory of Urban Security and Disaster Engineering of Ministry of Education, Beijing University of Technology, Beijing 100124, China*
email: li.peipei@bjut.edu.cn
[4)] *TU Dortmund, Chair for Reliability Engineering*
Leonhard-Euler-Strasse 5, 44227 Dortmund, Germany
email: matthias.faes@tu-dortmund.de
[5)] *Tongji University, International Joint Research Center for Engineering Reliability and Stochastic Mechanics, Shanghai 200092, China*

Abstract. Accurate multi-physics finite element modelling of resistance spot welding (RSW) remains challenging due to the uncertainties in contact and material parameters that shape the coupled thermal–electrical–mechanical process. This study introduces a Bayesian calibration framework, in contrast to the deterministic parameter optimisation approaches commonly adopted in existing RSW literature, which neglect the inherent variability of the welding process. The proposed framework performs calibration using multivariate model outputs, combining weld nugget geometry with geometrical and temporal attributes (El Ouafi et al., 2012) extracted from process signals such as dynamic resistance and electrode displacement. These features provide physically interpretable information on process evolution while reducing redundancy and correlation relative to full time-series data, enabling more effective parameter identifiability than nugget-only calibration. The methodology is applied to a 2D axisymmetric finite element model of RSW implemented in Simufact. In addition to the electrical and thermal contact parameters, a modified thermal conductivity formulation is introduced and treated as an unknown parameter to be inferred. Bayesian inference is performed using the Streamlined Bayesian Active Learning Cubature (SBALC) method (Li et al., 2025), with experimental multi-physics data (including nugget diameter and height, as well as process signals) used to infer posterior distributions for key modelling input variables.

Keywords: Resistance spot welding; Bayesian calibration; parameter inference

© 2026 by the author(s). This work is licensed under the Creative Commons Attribution 4.0 International License (CC BY 4.0), which permits unrestricted use, distribution, and reproduction in any medium, provided the original author and source are credited.

1. Introduction

Resistance spot welding (RSW) is a joining process process in which coupled thermal, electrical, and mechanical fields interact to form a fusion nugget between multiple metal sheets in milliseconds. To ensure structural reliability of the joints, there is an increasing demand for real-time quality monitoring of the welds. Modern monitoring algorithms rely on data-driven techniques that require large, diverse and well-labeled datasets (Xia et al., 2025). However, experimental data aquisition (process signal collection and quality metrics) is costly and time-consuming, resulting in machine-learning models that struggle to generalize to new materials, stack-ups, or production environments. At the same time, multi-physics finite element (FE) models of RSW have advanced considerably. Recent research approximate molten metal convection without explicitly modelling the flow field by introducing an enhanced thermal conductivity (Xia et al., 2023). A simultaneous simulation of nugget growth and process signals such as dynamic resistance and electrode displacement is achieved. Building on this, Lv et al. incorporate servo-gun dynamics and propose a rapid model generalization strategy across different steel grades and stack-up configurations through recalibration of contact parameters.

The accuracy of these FE models remains strongly dependent on uncertain model parameters, such as electrical and thermal contact properties between the plates and electrodes, whose true values may vary from weld to weld (Xia et al., 2023; Verkens et al., 2024). Traditional calibration techniques rely on tuning these unknown parameters by evaluating model output against measured nugget geometry and/or time-series data. Although this approach is widely applied, it inherently treats the modelling process as deterministic, which neglects the industrial variability and epistemic uncertainty present in RSW. Moreover, the resulting inverse problem is often ill-posed, admitting multiple parameter combinations that fit the data comparably well, and gradient-based solvers can become trapped in local minima. This motivates a calibration framework that is robust to modeling error, delivers uncertainty on inferred parameters and predictions, and remains computationally feasible for multi-physics FE models.

Bayesian calibration offers a framework for this problem (Kennedy and O'Hagan, 2001). Rather than producing a single point estimate, it yields a posterior probability distribution over the uncertain parameters, fully quantifying the remaining uncertainty given the available data. The main challenge to applying traditional Bayesian calibration techniques to high-fidelity RSW models is it's computational cost, since each forward model evaluation is expensive (Bogaerts et al., 2024). Recent research in these techniques has provided an elegant solution for this by modelling the likelihood function directly and reducing the amount of forward model evaluations substantially (Li et al., 2025).

A comprehensive calibration of the multi-physical RSW model necessitates the use of both weld quality measures, such as nugget diameter and thickness, as well as the characteristic process signals, such as dynamic resistance and electrode force, recorded during welding. These signals contain valuable information about the evolution of the weld across different physical fields (El Ouafi et al., 2012; American Welding Society et al., 2023), yet directly using full time-series data would lead to a very high-dimensional calibration problem. Moreover, as process measurements such as dynamic resistance and electrode force are long time series with high autocorrelation, treating the full time series as the calibration target introduces numerical difficulties in likelihood construction

and Gaussian process (GP) surrogate modelling. To overcome these difficulties, this paper proposes compressing the time-series model outputs into a small set of physically motivated scalar features prior to calibration. This reduces the dimensionality of the calibration target, tackles the numerical issues associated with high autocorrelation in likelihood construction and GP surrogate modelling, while maintaining the physical information carried by these process signals.

The remainder of this paper is structured as follows. Section 2 describes the RSW finite element model, the uncertain parameters, and the extraction of scalar calibration features from the model outputs. A global sensitivity analysis identifies which parameters most strongly influence which features, and the selected features are used to define the calibration target. Section 3 reports the results of a preliminary parameter study, the sensitivity analysis, and a first application of SBALC to the RSW model. Section 4 discusses the findings and outlines directions for future work.

2. Methodology

2.1. Restistance spot welding model

The RSW process is modelled as a 2D axisymmetric coupled thermal–electrical–mechanical finite element model, implemented in Simufact Forming 2026.1. The forward model is denoted $\mathcal{M}(\mathbf{x}, \theta)$, where $\mathbf{x}$ are the known process parameters (welding current, welding time, electrode force) and $\theta \in \mathbb{R}^d$ are the uncertain model parameters to be inferred. In this work, $\mathbf{x}$ is fixed to a single welding schedule, so that $\mathcal{M}(\mathbf{x}, \theta)$ reduces to $\mathcal{M}(\theta)$ for the remainder of the paper.

The stack-up consists of two 1 mm thick DP1200 steel sheets. The electrode caps are truncated-cone copper electrodes with a cap diameter of 15.8 mm, a face diameter of 5.5 mm, and a tip radius of curvature of 30 mm, following the geometry used in (Verkens et al., 2024). The welding schedule applies an electrode force of 3 kN, followed by a welding current of 8 kA for 150 ms with a 10 ms ramp-up and 10 ms ramp-down. The simulation terminates 10 ms after the current reaches zero; the hold phase is not modelled.

The mesh uses quadtree elements with a base edge length of 0.25 mm. A level-2 refinement is applied within a bounding box around the weld zone, yielding a minimum element size of approximately 0.0625 mm in the contact region.

2.1.1. *Contact model*

The electrical contact resistance (ECR) at the electrode/sheet (E/S) and sheet/sheet (S/S) interfaces is modelled using the Bay-Wanheim formulation implemented in Simufact. The contact resistivity ρ is computed as:

$$\rho = 3 \cdot \frac{\sigma_{\text{soft}}}{\sigma_n} \cdot \frac{\rho_1 + \rho_2}{2} + \rho_c \,, \tag{1}$$

where σ_{soft} is the flow stress of the softer contact material, σ_n is the contact normal stress, ρ_1 and ρ_2 are the bulk resistivities of the two contact materials, and ρ_c is the coating resistivity. The electrical contact conductance is then obtained by dividing by the film thickness t_f. Two parameters per interface (E/S and S/S) are treated as uncertain: the film thickness t_f and the coating resistivity ρ_c.

The thermal contact resistance (TCR) is computed using a Simufact-specific formulation:

$$\mathrm{HTC} = P_1 \left(\frac{c_1 + c_2}{2} \right) \frac{1}{P_2} \left(1 - e^{-P_3 \left(\frac{F_n}{\sigma_d} + P_3 \right)} \right)^{P_4}, \tag{2}$$

where c_1 and c_2 are the thermal conductivities of the contact pair, F_n is the contact normal stress, σ_d is the yield stress, and P_1, P_2, P_3, P_4 are constants. The constants P_2, P_3, and P_4 are fixed at their Simufact default values; only P_1 is treated as an uncertain parameter. The value of P_1 directly influences the temperature difference across the interfaces and consequently affects the nugget shape and process signals (Lv et al., 2025).

2.1.2. *Modified thermal conductivity*

Standard FE formulations of RSW neglect fluid flow in the molten weld pool (Li et al., 2011), leading to unrealistically high predicted peak temperatures. Following Lv et al. (Lv et al., 2025), the thermal conductivity of the DP1200 steel is set to an elevated value λ_m above the melting temperature:

$$\lambda(T) = \begin{cases} \lambda_(T), & T < T_{\mathrm{melting}}, \\ \lambda_m, & T \geq T_{\mathrm{melting}}, \end{cases} \tag{3}$$

where $\lambda_(T)$ is the temperature-dependent thermal conductivity from the material database and $T_{\mathrm{melting}} = 1507\,^{\circ}\mathrm{C}$ is the melting point of DP1200. The elevated value λ_m approximates the enhanced heat transport due to convective mixing in the weld pool.

2.1.3. *Uncertain parameters*

Six uncertain model parameters are considered for calibration, collected in the vector $\theta \in \mathbb{R}^6$. Due to the symmetric stack-up, the lower electrode/lower plate contact is assumed to share the same parameters as the upper electrode/upper plate contact. The prior distributions and bounds are summarised in Table I. For parameters spanning several orders of magnitude (t_f, ρ_c, and P_1), the prior is defined as uniform in $\log_{10}$-space, ensuring equal prior weight per order of magnitude. The modified thermal conductivity λ_m is assigned a uniform prior in physical space.

Table I. Unknown model parameters with prior distributions and bounds.

#	Symbol	Description	Unit	Prior bounds
1	$t_{f,\mathrm{S/S}}$	Film thickness, S/S interface	mm	$[1 \times 10^{-4},\ 5 \times 10^{-1}]^*$
2	$\rho_{c,\mathrm{S/S}}$	Coating resistivity, S/S interface	$\Omega \cdot \mathrm{m}$	$[5 \times 10^{-7},\ 5 \times 10^{-5}]^*$
3	$t_{f,\mathrm{E/S}}$	Film thickness, E/S interface	mm	$[1 \times 10^{-4},\ 5 \times 10^{-1}]^*$
4	$\rho_{c,\mathrm{E/S}}$	Coating resistivity, E/S interface	$\Omega \cdot \mathrm{m}$	$[5 \times 10^{-7},\ 5 \times 10^{-5}]^*$
5	P_1	HTC scaling constant	–	$[1 \times 10^{-3},\ 1 \times 10^{-1}]^*$
6	λ_m	Thermal conductivity above melting	W/(m·K)	[35, 200]

* Prior is uniform in $\log_{10}$-space.

Parameters 1–4 govern the electrical contact interactions at the two interface types through Equation 1. Parameter P_1 scales the heat transfer from the sheets to the electrodes via Equation 2,

and λ_m governs the heat redistribution within the molten nugget. Uninformative uniform priors are assigned to all parameters:

$$\theta_i \sim \mathcal{U}(\theta_i^{\min}, \theta_i^{\max}), \quad i = 1, \ldots, 6. \tag{4}$$

2.2. Calibration targets: feature extraction from model outputs

The forward model $\mathcal{M}(\theta)$ produces both scalar outputs (nugget geometry) and time-series signals (dynamic resistance, temperature history, electrode displacement). Using full time-series data as calibration targets is problematic for surrogate-based Bayesian methods. Process signals such as dynamic resistance are generated by a system of coupled partial differential equations driven by a time-varying current input. Therefore successive samples carry almost identical information about θ. Treating m such samples as independent under a diagonal covariance $\Sigma = \mathrm{diag}(\sigma_1^2, \ldots, \sigma_m^2)$ amounts to counting the same physical discrepancy m times, resulting in a sharper log-likelihood surface, which produces an overconfident posterior. A peaked log-likelihood surface causes two numerical failures in the SBALC framework: the GP surrogate requires an extremely short kernel length scale to fit the narrow likelihood and the active learning loop clusters new evaluation points in a shrinking neighbourhood of the optimum causing the GP covariance matrix to be ill-conditioned and Cholesky factorisation can fail.

The solution adopted in this work is to extract a small set of physically motivated scalar features from the time-series outputs prior to calibration. This reduces the residual dimension from m to $p \ll m$, broadens the likelihood surface by eliminating the pseudo-replication effect, and avoids the numerical fragility described above. As the resulting features are scalar quantities with distinct physical origins, a diagonal covariance $\Sigma \in \mathbb{R}^{p \times p}$ is an appropriate noise model. In this work the following features extracted from the RSW FE model are used:

Nugget geometry. The FE model produces a set of geometric metrics describing the weld nugget and contact zone, including nugget height and width (at both liquidus and solidus isotherms), joint penetration depth into each sheet, electrode/sheet contact width, indentation depth, and minimum remaining solid sheet thickness.

Dynamic resistance features The dynamic resistance (DR) curve is a time-varying signal that reflects the evolution of electrical resistance during the welding stage. Rather than using the full DR signal, scalar features are extracted following the geometrical characterisation approach of El Ouafi et al. (El Ouafi et al., 2012). Candidate features include: the resistance values at the first inflection point (R_α), the peak (R_β), and the final value (R_γ); the corresponding times (t_α, t_β, t_γ); the slopes before and after the peak (m_1, m_2); the mean resistance (R_m); and the resistance drops $dR_1 = R_\beta - R_\alpha$ and $dR_2 = R_\gamma - R_\beta$.

The peak resistance R_β is primarily driven by the bilinear relationship between sheet resistivity and temperature, while the post-peak resistance drop is dominated by the increase of the electrode/sheet contact diameter (American Welding Society et al., 2023).

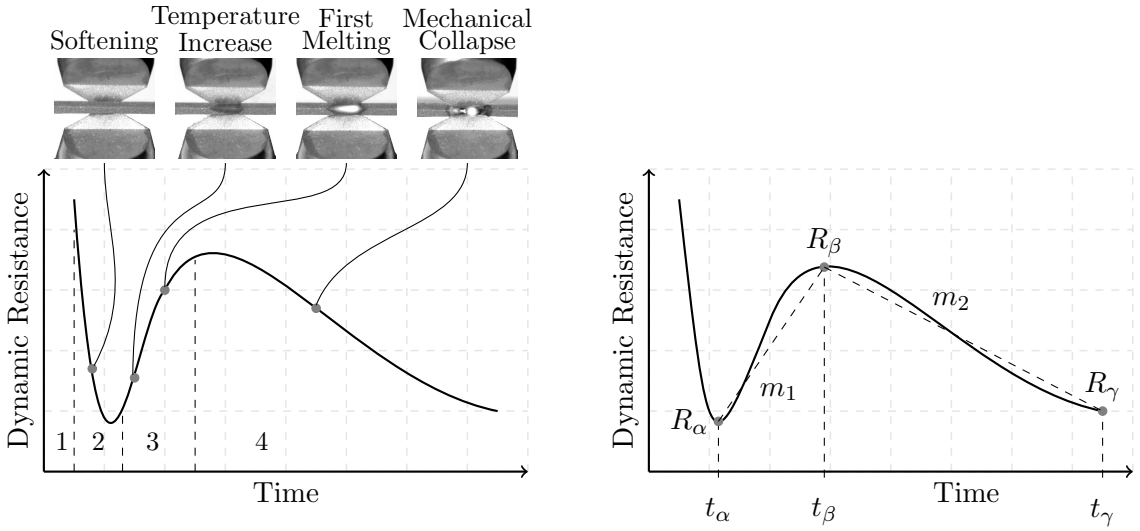


Figure 1. Schematic representation of dynamic resistance features. (Left) Theoretical dynamic resistance curve with weld nugget evolution stages, adapted from Dickinson et al. (Dickinson et al., 2013). The upper images illustrate the nugget evolution captured by a Phantom VEO 640 high-speed camera (Bogaerts et al., 2023). (Right) Selected geometrical features extracted from the dynamic resistance curve, adapted from El Ouafi et al. (El Ouafi et al., 2012).

Maximum sheet temperature The peak temperature in the upper and lower sheets during welding. This quantity is directly sensitive to λ_m (higher λ_m reduces the peak temperature) and P_1 (which controls the heat transfer at the interfaces).

Electrode displacement features. The electrode displacement signal records the relative motion of the upper electrode during welding. While welding, the the upper electrode moves due to thermal expansion of the heated sheets and nugget growth. Four scalar features are extracted from the displacement signal $S(t)$, with a 2 ms margin trimmed from the start of the welding stage to exclude the initial settling transient. Let S_0 denote the displacement at the start of the trimmed interval and S_{peak} the maximum displacement reached. The peak expansion $\Delta S_P = S_{\text{peak}} - S_0$ captures the total thermal expansion during nugget growth. The end-of-welding displacement S_{end} and the net displacement $\Delta S_{\text{net}} = S_{\text{end}} - S_0$ reflect the residual deformation after current shut-off and partial cooling. The expansion rate $\dot{S}_{\text{exp}}$ is obtained as the slope of a linear fit to $S(t)$ from the start of welding to the time of peak displacement, providing a measure of the nugget growth rate.

For $d = 6$ unknown parameters, at least $p \geq 6$ features with approximately linearly independent sensitivities are required to ensure identifiability. The sensitivity analysis in Section 2.3 is used to select the most informative subset.

2.3. Global sensitivity analysis

To quantify the influence of each uncertain parameter on the model outputs and to guide feature selection for calibration, a variance-based global sensitivity analysis is performed using Sobol indices

(Sobol, 2001). A Design of Experiments (DoE) of 90 samples is generated from the six-dimensional prior distribution using a Latin Hypercube design. Each sample requires a full forward model evaluation in Simufact. One simulation failed to converge, leaving 88 successful runs. From each simulation, 18 scalar output features are extracted, grouped into four categories:

- *Dynamic resistance* (3 features): peak resistance R_β, end-of-welding resistance R_γ, and mean resistance R_m. These are extracted from a Savitzky–Golay-smoothed DR signal (3rd-order polynomial, window size 11), with a 2 ms margin trimmed from both ends of the welding stage to avoid transient artefacts.
- *Electrode displacement* (4 features): peak expansion $\Delta S_P = S_{\text{peak}} - S_0$, end-of-welding displacement S_{end}, net displacement $\Delta S_{\text{net}} = S_{\text{end}} - S_0$, and expansion rate $\dot{S}_{\text{exp}}$ (slope of a linear fit to the displacement signal from the start of welding to the peak).
- *Sheet temperature* (4 features): maximum temperature across both sheets $T_{\max}$, time to reach peak temperature $t(T_{\max})$, end-of-simulation temperature T_{end}, and cooling rate $\dot{T}_{\text{cool}}$ (computed as the slope from $T_{\max}$ to T_{end}).
- *Nugget geometry* (7 features): nugget width and height at the liquidus isotherm ($d_{\text{n,liq}}$, $h_{\text{n,liq}}$) and solidus isotherm ($d_{\text{n,sol}}$, $h_{\text{n,sol}}$), electrode/sheet contact width w_{elec}, indentation depth d_{indent}, and minimum remaining unmolten sheet thickness t_{unmolt}.

A Polynomial Chaos Expansion (PCE) surrogate is fitted to the 88 successful runs using the Least Angle Regression Sparse (LARS) algorithm (Blatman and Sudret, 2011) with candidate polynomial degrees 1 through 5, as implemented in UQLab (Marelli and Sudret, 2014). The leave-one-out (LOO) cross-validation error is used to assess the quality of the surrogate for each output. First-order and total-order Sobol indices are then computed analytically from the PCE coefficients at no additional computational cost. The first-order Sobol index of parameter θ_i on output Y is:

$$S_i = \frac{\text{Var}[\mathbb{E}(Y \mid \theta_i)]}{\text{Var}(Y)}, \tag{5}$$

and the total-order index, which includes all interaction effects, is:

$$S_{T_i} = 1 - \frac{\text{Var}[\mathbb{E}(Y \mid \boldsymbol{\theta}_{\sim i})]}{\text{Var}(Y)}, \tag{6}$$

where $\boldsymbol{\theta}_{\sim i}$ denotes all parameters except θ_i. Second-order interaction indices are also computed to identify parameter pairs with coupled effects on specific outputs. The results of this analysis are presented and discussed in Section 3.2.

2.4. Bayesian model calibration

The calibration framework follows the Bayesian approach described in (Kennedy and O'Hagan, 2001). Given observations Y_{obs}, Bayes' theorem updates the prior distribution $f(\theta)$ to the posterior:

$$f(\theta \mid Y_{\text{obs}}) = \frac{L(Y_{\text{obs}} \mid \theta)\, f(\theta)}{c}, \tag{7}$$

where $L(Y_{\text{obs}} \mid \theta)$ is the likelihood function and $c = \int L(Y_{\text{obs}} \mid \theta)\, f(\theta)\, \mathrm{d}\theta$ is the model evidence. Assuming Gaussian measurement error with zero mean and covariance Σ, the log-liklihood for N_{obs} independent observation replicates is:

$$\ln L(\theta) = \mathscr{L}(\theta) = -\frac{1}{2} \sum_{k=1}^{N_{\text{obs}}} r_k(\theta)^\top \Sigma^{-1} r_k(\theta) + \text{const}, \tag{8}$$

where $r_k(\theta) = Y_{\text{obs}}^{(k)} - \mathcal{M}(\theta)$ is the residual between the k-th observation and the model response. As the calibration targets are scalar features with distinct physical origins rather than successive datapoints from an autocorrelated signal, a diagonal covariance Σ is appropriate and no full covariance estimation is required.

2.5. Streamlined Bayesian Active Learning Cubature (SBALC)

The posterior distribution in Equation 7 is evaluated using the SBALC method (Li et al., 2025), which fits a Gaussian Process (GP) surrogate directly to the log-likelihood function $\mathscr{L}(\theta)$ and uses active learning to minimise the number of forward model evaluations. The model evidence is estimated as:

$$\hat{c} = \mathbb{E}_\theta[\exp(\hat{m}_{\mathscr{L}_n}(\theta))]\,, \tag{9}$$

where $\hat{m}_{\mathscr{L}_n}$ is the GP posterior mean after n evaluations, with the expectation approximated by Monte Carlo over $N_M = 2 \times 10^4$ prior samples. At each iteration, the next evaluation point is selected by maximising the learning function:

$$\mathrm{LF}(\theta) = \sigma^2_{\mathscr{L}_n}(\theta) \cdot \left(e^{m_{\mathscr{L}_n}(\theta) + b\,\sigma_{\mathscr{L}_n}(\theta)} - e^{m_{\mathscr{L}_n}(\theta) - b\,\sigma_{\mathscr{L}_n}(\theta)} \right), \tag{10}$$

with $b = 1$. Iterations stop when the convergence ratio $|c_{\text{upper}} - c_{\text{lower}}|/\hat{c} < 0.1$ holds over two consecutive iterations. Posterior samples are generated via Sampling-Importance-Resampling (SIR) (Rubin and Rubin, 1988). A detailed derivation of the method is provided by Li et al..

3. Results

3.1. Preliminary parameter study

To confirm the expected physical influence of the parameters P_1 and λ_m and to verify consistency with the findings reported by Lv et al. (Lv et al., 2025), a preliminary one-at-a-time parameter study was performed. Five simulations were run with varying values of $P_1 \in [0.0005,\ 0.0025]$ (at fixed $\lambda_m = 35$ W/(m·K)) and eight with varying values of $\lambda_m \in [0,\ 200]$ W/(m·K) (at fixed $P_1 = 0.0005$). All contact parameters were held at their nominal values: $t_{f,\mathrm{S/S}} = t_{f,\mathrm{E/S}} = 10^{-5}$ mm and $\rho_{c,\mathrm{S/S}} = \rho_{c,\mathrm{E/S}} = 2.1 \times 10^{-6}$ Ω·m.

3.1.1. *Effect of thermal conductivity at melting λ_m.*

Figure 2 summarises the influence of λ_m on the peak resistance, the maximum sheet temperature, and the nugget geometry at the solidus isotherm. The peak resistance R_β is virtually unaffected

by λ_m, which is expected since the DR signal is governed by the bulk and contact resistivities rather than by the thermal field inside the nugget. In contrast, the maximum sheet temperature decreases substantially with increasing λ_m. The elevated thermal conductivity redistributes heat within the molten pool, suppressing unrealistic temperature peaks. The nugget geometry responds accordingly: both the solidus diameter d_n and height h_n increase with λ_m as the thermal energy is spread more uniformly. The effect saturates for $\lambda_m \gtrsim 100$ W/(m·K), consistent with the findings of Lv et al. (Lv et al., 2025).

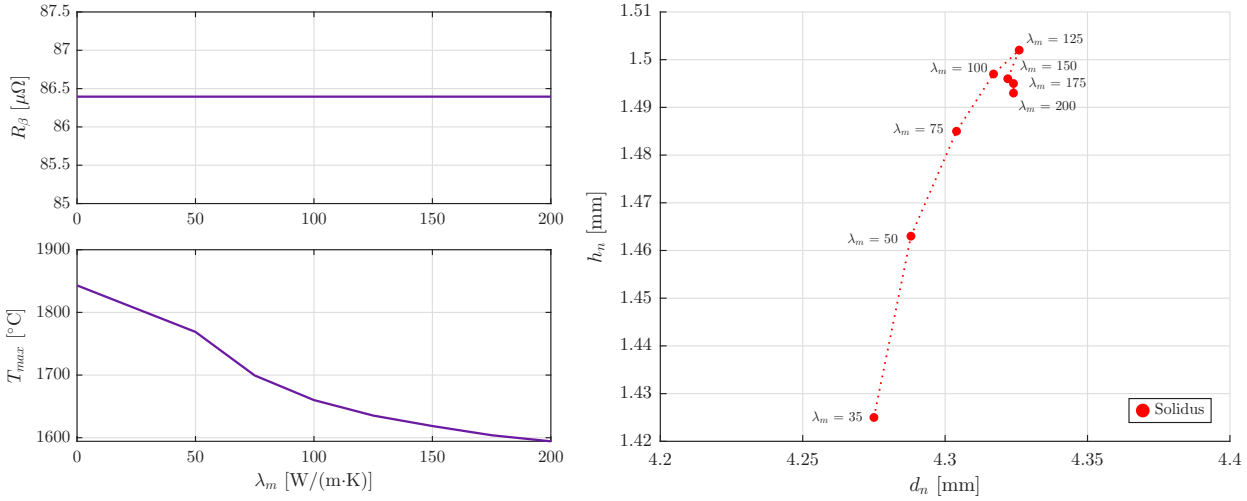


Figure 2. Influence of λ_m on peak resistance R_β (top left), maximum sheet temperature $T_{\max}$ (bottom left), and nugget geometry at the solidus isotherm (right).

3.1.2. *Effect of heat transfer coefficient scaling constant* P_1.
Figure 3 shows the influence of P_1 on the peak resistance, the peak displacemnt of the upper electrode, and the nugget geometry at both the liquidus and solidus isotherms. Increasing P_1 enhances the thermal contact conductance at the E/S interface, allowing more heat to flow from the sheets into the electrodes. This produces a moderate decrease in the peak resistance R_β and a reduction in the peak electrode expansion ΔS_P, both consistent with a cooler sheet surface. The effect on the nugget geometry is pronounced: as P_1 increases from 0.0005 to 0.0025, the nugget diameter d_n decreases while the nugget height h_n is reduced substantially (from approximately 2.1 mm to 1.5 mm at the liquidus isotherm). Physically, a higher HTC draws heat away from the weld zone through the electrodes, resulting in a smaller and flatter nugget.

These results confirm the findings of Lv et al. (Lv et al., 2025) and demonstrate that P_1 and λ_m have distinct and significant effects on the model outputs, motivating their inclusion as uncertain parameters in the Bayesian calibration. Notably, λ_m primarily affects the thermal field and nugget geometry while leaving the DR signal unchanged, whereas P_1 influences both the process signals and the nugget shape. This complementary sensitivity structure suggests that including both DR features and nugget geometry in the calibration target will aid in distinguishing the two parameters.

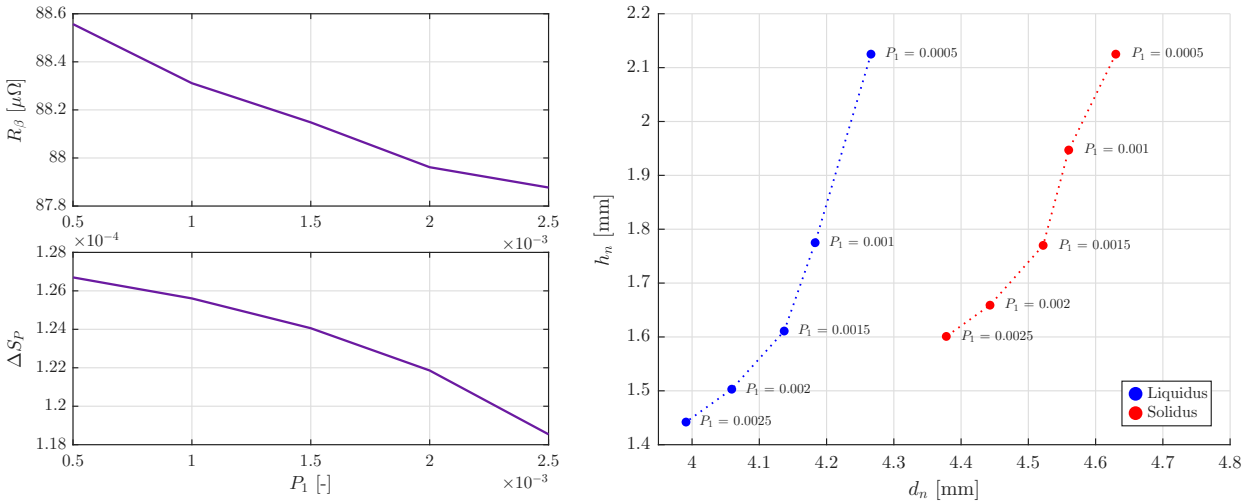


Figure 3. Influence of P_1 on peak resistance R_β (top left), peak electrode expansion ΔS_P (bottom left), and nugget geometry at the liquidus and solidus isotherms (right).

3.2. Global sensitivity analysis

Figure 4 and 5 present the first-order and total-order Sobol indices for all 18 output features with respect to the six uncertain parameters.

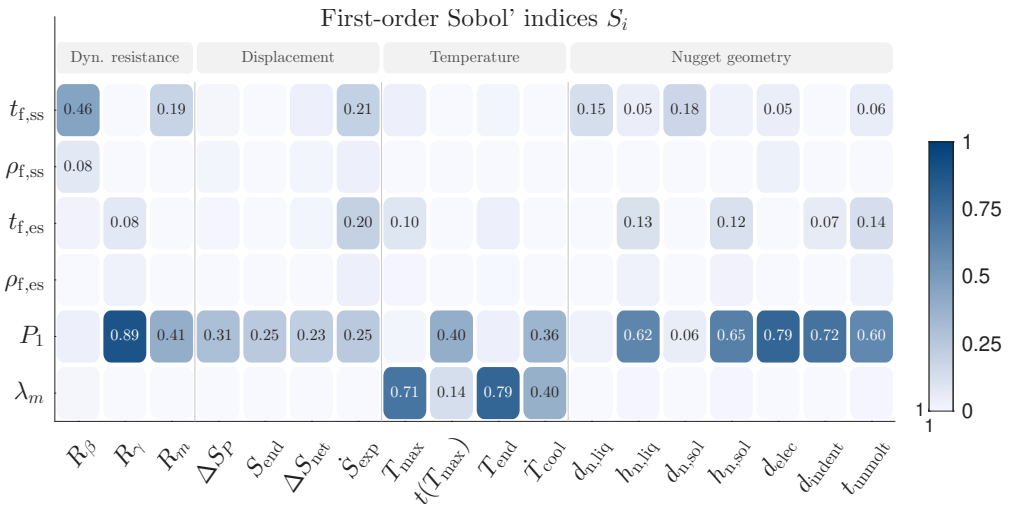


Figure 4. First-order Sobol indices for each output feature and uncertain parameter. Values below 0.05 are omitted for clarity.

The results show how each input parameter contributes to the variance of the features in the four output categories. Each parameter influences a distinct subset of output features, suggesting that the features provide complementary information for identifying the input parameters. The

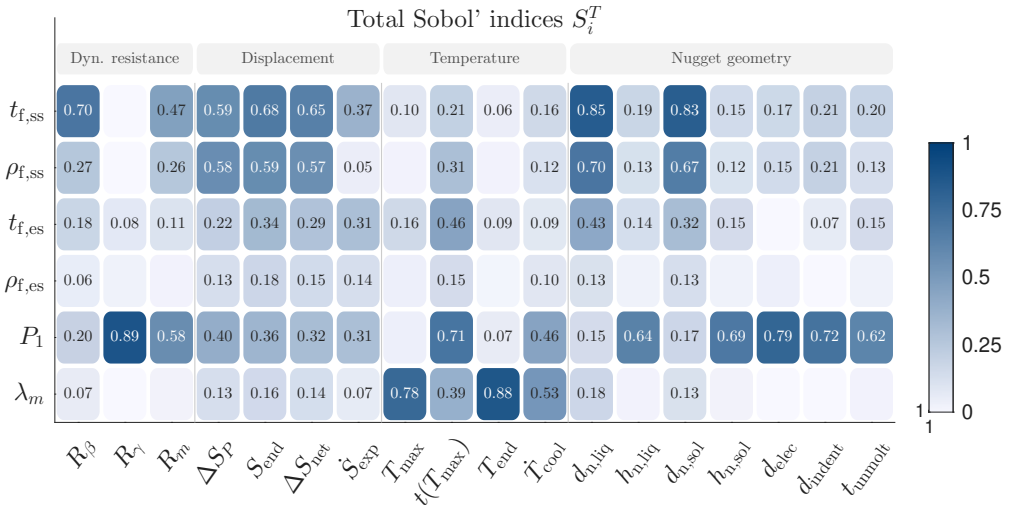


Figure 5. Total-order Sobol indices S_i^T for each output feature and uncertain parameter. Values below 0.05 are omitted for clarity.

parameter P_1 is the single most influential parameter overall. In the dynamic resistance features it dominates R_γ with a first order index of $S_i = 0.89$ and has a moderate influence on R_m. Its influence is spanning accros the other four output categories and is affecting the displacement features ($S_i = 0.25 - 0.31$), the temperature features ($S_i = 0.36 - 0.79$), and the nugget geometry, where the first-order indices range from 0.6 to 0.79. This is consistent with the physical role of P_1 as the HTC scaling constant, which controls the heat extraction through the electrodes.

The modified thermal conductivity λ_m has a complementary sensitivity pattern, with its influence concentrated on the temperature features ($S_1 = 0.71$ for $T_{\max}$ and 0.79 for $t(T_{\text{end}})$). This confirms the observation from the preliminary parameter study (Section 3.1), as λ_m redistributes heat within the molten pool without affecting the electrical and mechanical response. The total-order indices for λ_m are larger than the first-order values, reaching $S_i^T = 0.78$ for $T_{\max}$ and 0.88 for $t(T_{\text{end}})$, indicating interaction effects with other parameters on the temperature outputs.

The S/S film thickness $t_{f,\text{S/S}}$ is the most influential contact parameter, with $S_1 = 0.46$ for the peak resistance R_β and smaller direct contributions to the liquidus nugget diameter $d_{n,\text{liq}}$ ($S_i = 0.15$), the solidus nugget diameter $d_{n,\text{sol}}$ ($S_i = 0.18$), and the expansion rate $\dot{S}_{\text{exp}}$ ($S_i = 0.21$). However, its total-order indices are substantially larger across nearly all outputs, indicating that $t_{f,\text{S/S}}$ acts heavily through interaction effects. The remaining S/S parameter $\rho_{c,\text{S/S}}$ shows weak sensitivity overall, with only minor total-order contribution to the displacement peak resistance. Nevertheless, its total-order indices reveal substantial interaction contributions as well.

The E/S film thickness $t_{f,\text{E/S}}$ has only small direct effects, with its largest contributions on $\dot{S}_{\text{exp}}$, $T_{\max}$, and hn, liq. Its higher total-order indices indicate that its influence is mainly through interactions with other parameters. In contrast, the E/S coating resistivity $\rho_{f,\text{E/S}}$ shows negligible sensitivity across all outputs ($S_i^T < 0.18$), suggesting that it has little effect and is difficult to identify from the data.

Feature selection for calibration. Based on the sensitivity analysis, ten features are selected for the calibration target vector $Y \in \mathbb{R}^{10}$: the peak resistance R_β, the peak electrode expansion ΔS_P, the maximum and end-of-simulation sheet temperatures $T_{\max}$ and T_{end}, the nugget width and height at both liquidus and solidus isotherms ($d_{\text{n,liq}}$, $h_{\text{n,liq}}$, $d_{\text{n,sol}}$, $h_{\text{n,sol}}$), the electrode contact width w_{elec}, and the indentation depth d_{indent}. Time-dependent features (t_α, t_β, $t(T_{\max})$) are excluded as the discrete time stepping of the FE solver introduces artificial quantisation that would degrade the smoothness of the likelihood surface. The selected features span all four output categories and collectively provide sensitivity to five parameters, with R_β and ΔS_P primarily targeting P_1 and the contact parameters, $T_{\max}$ and T_{end} targeting λ_m, and the nugget geometry features providing information on all parameters simultaneously.

3.3. Bayesian calibration

As a first step towards a full Bayesian calibration of all six unknown parameters, a single-parameter calibration is performed. Based on the Sobol analysis in Section 3.2, P_1 is selected as calibration parameter. The SBALC algorithm is applied with $P_1 \sim \mathcal{U}(0.0001, 0.1)$ as only unknown parameter, where R_γ is used as calibration feature. The initial design consists of $n_0 = 5$ Hammersley points and the convergence threshold is chosen as $b_{\text{cr}} = 0.1$.

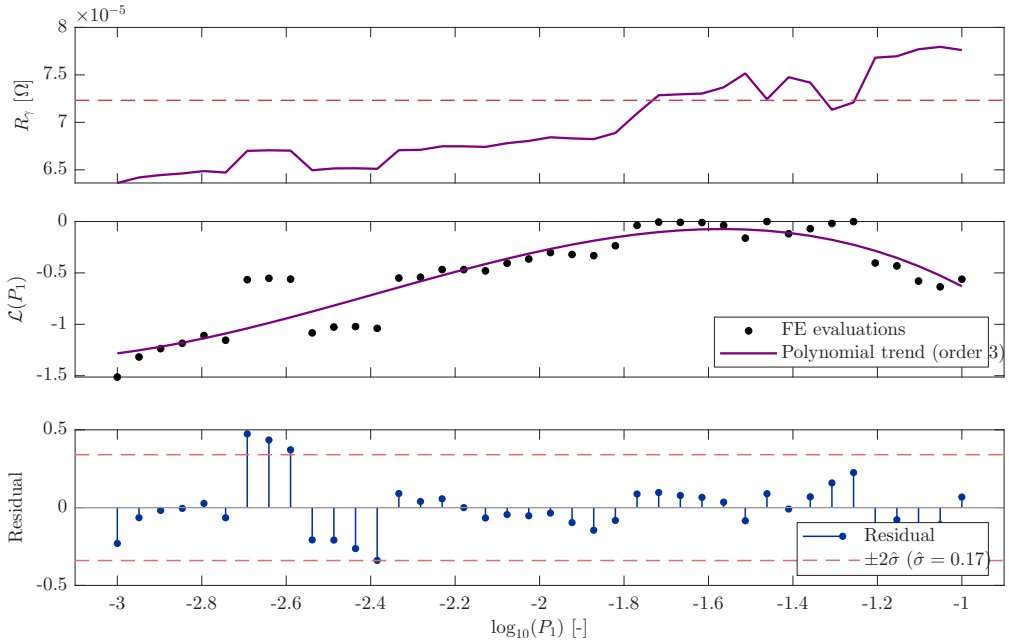


Figure 6. Diagnostic sweep over $\log_{10}(P_1)$. Top: model response R_γ with Y_{obs} (dashed). Middle: log-likelihood $\mathscr{L}(P_1)$ evaluated at each model response point. Bottom: residuals after detrending.

However, when SBALC is directly applied to the RSW FE model, no satisfactory convergence is reached. To investigate the cause of this behaviour, the log-likelihood is evaluated at 40 points over the prior range of P_1. The results are shown in Figure 6. In here we see that the log-likelihood follows

a global trend, similar to the one observed in Section 3.1. On top of this trend, small deviations can be observed. These deviations correspond to deterministic numerical noise, which originates from mesh discretisation and adaptive time stepping in the FE model. Repeated evaluation at the same parameter values yields identical results, which indicates that the noise is not stochastic and cannot be reduced by averaging. It is an inherent artefact of the numerical discretisation.

This behaviour is problematic for SBALC, as the method uses a GP surrogate of the log-likelihood and assumes sufficient smoothness for accurate interpolation between a limited number of training points. If no noise model is included in the GP, the GP interpolates exactly through all training points, including the noise. As a result, the GP is overfitting, which influences both the learning function used to select new evaluation points and the convergence criterion based on the upper and lower bounds of the model evidence estimate. Li et al. acknowledge this limitation, noting that SBALC is restricted to likelihood-functions of moderate smoothness.

Resolving this issue requires modifying the GP fitting procedure to account for the deterministic noise, for instance by introducing a fixed nugget term in the GP covariance and separating the resulting epistemic and aleatoric contributions to the predictive variance. This extension is the subject of ongoing work and will be reported in a future publication.

4. Discussion and conclusions

This paper presents a Bayesian calibration framework for a 2D axisymmetric resistance spot welding finite element model with six uncertain parameters. This contrasts the current deterministic optimization approaches commonly used in RSW calibration. A key element of the approach presented here is the use of physical motivated features extracted from process signals, rather than using the full-time series. While full time-series would carry more information, the high autocorrelation of these signals (such as dynamic resistance and electrode displacement) leads to an narrow log-likelihood and numerical instabilities in the GP surrogate.

A preliminary parameter study confirmed that P_1 and λ_m have distinct and complementary effects on the model outputs. The parameter P_1 primarily governs the nugget geometry and process signals through its control of heat extraction at the electrode/sheet interface, whereas λ_m affects the temperature field and nugget dimensions without changing the dynamic resistance signal.

A global sensitivity analysis over all six model parameters revealed that P_1 influences most output features, while λ_m mostly influences the temperature response. The S/S interface is more influential than the E/S interface, with the film thickness $t_{f,\mathrm{S/S}}$ emerging as the most influential contact parameter contributing to both the resistance and nugget diameter. The E/S film thickness $t_{f,\mathrm{E/S}}$ showed negligible first-order sensitivity but substantial total-order indices on selected features, indicating that it acts through parameter interactions. Based on these results, ten calibration features are selected to use in further work.

A first application of SBALC to a single parameter calibration (P_1) revealed that deterministic numerical noise from mesh discretisation and adaptive time stepping in the FE model prevents convergence of the method. This noise is reproducible and cannot be reduced by repeated forward model evaluations, which distinguishes it from stochastic measurement noise. Addressing this limitation requires modifying the GP fitting to account for the deterministic noise, for instance by

introducing a nugget term in the GP covariance. This extension, along with the full six-parameter calibration, is the subject of ongoing work.

Acknowledgements

The authors gratefully acknowledge the support of the Research Foundation – Flanders (FWO) under grant 1SE1423N, the internal funding of KU Leuven grant C24E/21/026 and the support of the Flemish Government through the Flanders Make.

References

American Welding Society, Y.-J. Xia, T.-L. Lv, Y.-B. Li, H. Ghassemi-Armaki, and B. E. Carlson: 2023, 'Quantitative Interpretation of Dynamic Resistance Signal in Resistance Spot Welding'. *Welding Journal* **102**(4), 69–87.

Blatman, G. and B. Sudret: 2011, 'Adaptive sparse polynomial chaos expansion based on *least angle regression*'. *Journal of Computational Physics* **230**(6), 2345–2367.

Bogaerts, L., A. Dejans, M. G. R. Faes, and D. Moens: 2023, 'A machine learning approach for efficient and robust resistance spot welding monitoring'. *Welding in the World*.

Bogaerts, L., M. G. Faes, and D. Moens: 2024, 'A Data Driven Black Box Approach for the Inverse Quantification of Set-Theoretical Uncertainty'. *ASCE-ASME J Risk and Uncert in Engrg Sys Part B Mech Engrg* **11**(031201).

Dickinson, D. W., J. E. Franklin, and A. Stanya: 2013, 'Characterization of Spot Welding Behavior by Dynamic Electrical Parameter'.

El Ouafi, A., R. Belanger, and M. Guillot: 2012, 'Dynamic Resistance Based Model for On-Line Resistance Spot Welding Quality Assessment'. *Materials Science Forum* **706-709**, 2925–2930.

Kennedy, M. C. and A. O'Hagan: 2001, 'Bayesian Calibration of Computer Models'. *Journal of the Royal Statistical Society Series B: Statistical Methodology* **63**(3), 425–464.

Li, P.-P., C. Dang, C. H. Acevedo, M. A. Valdebenito, and M. G. R. Faes: 2025, 'Bayesian model updating via streamlined Bayesian active learning cubature'. arXiv:2509.11204 [stat].

Li, Y. B., Z. Q. Lin, Q. Shen, and X. M. Lai: 2011, 'Numerical analysis of transport phenomena in resistance spot welding process'. *Journal of Manufacturing Science and Engineering, Transactions of the ASME* **133**(3), 1–8. Number: 3.

Lv, T.-L., Y.-J. Xia, S. P. Murugan, F. Okigami, H. Ghassemi-Armaki, B. E. Carlson, and Y. Li: 2025, 'Multi-physical process simulation of resistance spot welding available for synthetic data generation'. *Journal of Manufacturing Processes* **141**, 709–724.

Marelli, S. and B. Sudret: 2014, 'UQLab: A Framework for Uncertainty Quantification in Matlab'. pp. 2554–2563. Publisher: American Society of Civil Engineers.

Rubin, D. and D. Rubin: 1988, 'Using the SIR algorithm to simulate posterior distributions'.

Sobol, I.: 2001, 'Global sensitivity indices for nonlinear mathematical models and their Monte Carlo estimates'. *Mathematics and Computers in Simulation* **55**(1-3), 271–280.

Verkens, B., M. Faes, P. Van Rymenant, and D. Moens: 2024, 'Towards industrial relevance: Uncertainty in numerical resistance spot welding models'. In: *9th European Congress on Computational Methods in Applied Sciences and Engineering*. CIMNE.

Xia, Y.-J., T.-L. Lv, H. Ghassemi-Armaki, Y.-B. Li, and B. E. Carlson: 2023, 'Collaborative Simulation of Nugget Growth and Process Signals for Resistance Spot Welding'. *Welding in the World* **67**(6), 1377–1392. Company: Springer Distributor: Springer Institution: Springer Label: Springer Number: 6 Publisher: Springer Berlin Heidelberg.

Xia, Y.-J., Q. Song, B. Yi, T. Lyu, Z. Sun, and Y. Li: 2025, 'Improving out-of-distribution generalization for online weld expulsion inspection using physics-informed neural networks'. *Welding in the World* **69**(5), 1309–1322.

SESSION 6

Engineering Applications and Monitoring

Papers in this session

1. Stability Analysis of Concrete Gravity Dams under Uncertainty
2. Probabilistic Assessment of Multiphysics-Driven Stochastic Corrosion for the Safety Evaluation of Nuclear Waste Canisters
3. Probabilistic reliability evaluation of autonomous navigation for firefighting robots in uncertain environments
4. Integrating Deterministic and Stochastic Uncertainty in Terrestrial Laser Scanner-based Deformation Monitoring
5. A Holistic Approach to the Life Cycle Assessment of a Propeller System

Stability Analysis of Concrete Gravity Dams under Uncertainty

***Binod K. Yadav*[1)] *and Rafi L. Muhanna*[2)]**

[1)]*Federal Energy Regulatory Commission, Atlanta, GA USA, binod.yadav@ferc.gov*

[2)]*Department of Civil and Environmental Engineering, Georgia Institute of Technology, North Avenue, Atlanta, Georgia, 30332, USA, rafi.muhanna@gatech.edu*

Abstract: The stability analysis of concrete gravity dams is challenging due to uncertainties in shear strength parameters and external loads. Conventional crack-based Limit Equilibrium Methods (LEM), which rely on the linear Mohr–Coulomb (MC) shear strength model, often yield conservative results because they neglect nonlinear strength gain from joint roughness and dilation. Probabilistic approaches, such as Monte Carlo Simulation (MCS), provide useful statistical insight but require extensive site-specific data and probability distributions that are rarely available for existing old dams.

This work presents an Interval Finite Element Method (IFEM) framework for sliding stability assessment under parameter uncertainty. The method integrates interval arithmetic with the nonlinear Barton–Choubey (BC) shear strength model, an element-by-element assembly strategy to reduce dependency effects, and an interval crack initiation and propagation criterion driven by tensile- and shear-stress conditions. External load (uplift pressure) and boundary conditions are updated iteratively as the crack propagates. All uncertain parameters, including Young's modulus, density, Barton-Choubey shear strength parameters, are expressed as intervals and incorporated into the IFEM framework.

The framework is validated through a concrete gravity dam case study using laboratory data, historical temperature records, and construction photographs. Results show that the dam remains stable with interval safety factors consistently above unity and crack lengths closely matching Monte Carlo Simulation (MCS) predictions, while avoiding the excessive safety margins characteristic of LEM. The proposed IFEM approach provides reliable, computationally feasible, and data-efficient safety bounds suitable for dams with limited site information.

Keywords: Concrete gravity dams, Stability, Mohr-Coulomb, Barton-Choubey, Rock joint shear strength, Uncertainty, Interval Finite Element Method, Crack-Based Limit Equilibrium Method, Monte Carlo Simulation, Dam Safety

1. Introduction

Concrete gravity dams resist hydrostatic, uplift, hydrodynamic, silt, thermal, and seismic loads primarily through self-weight and shear resistance mobilized along the concrete–foundation rock interface. Sliding stability along the base represents one of the governing limit states evaluated in dam safety assessments (FERC, 2016; USACE, 2005). Reliable evaluation of sliding resistance requires realistic modeling of interface shear strength and explicit treatment of uncertainty in material properties and loading conditions.

Traditional crack-based Limit Equilibrium Methods (LEM) typically employ linear Mohr–Coulomb (MC) shear strength assumptions. However, laboratory and field investigations demonstrate that rock joint shear strength is nonlinear and stress-dependent due to surface roughness and dilation effects (Barton and Choubey, 1977). Linear MC models may therefore misrepresent sliding resistance, particularly when cracking and uplift redistribution reduce effective normal stress.

Probabilistic approaches such as Monte Carlo Simulation (MCS) propagate uncertainty through repeated sampling of random variables. Although statistically rigorous, these methods require defensible probability distributions, which are rarely available for aging dams. Interval analysis provides an alternative uncertainty framework that does not require probability distributions (Moore, 1979; Muhanna and Mullen, 2001). The Interval Finite Element Method (IFEM) computes guaranteed bounds on structural response under bounded epistemic uncertainty (Muhanna et al., 2007; Yadav, 2025).

© 2026 by the author(s). This work is licensed under the Creative Commons Attribution 4.0 International License (CC BY 4.0), which permits unrestricted use, distribution, and reproduction in any medium, provided the original author and source are credited.

This study presents an application-focused comparison of deterministic LEM, Monte Carlo Simulation, and IFEM for sliding stability assessment of a concrete gravity dam under parameter uncertainty. Unlike previous applications of IFEM that assume uniform interval material properties, The present work integrates the nonlinear Barton–Choubey (BC) shear strength model into a two-dimensional interval finite element framework, with a spatially varying elastic modulus that accounts for moisture-dependent stiffness variations. The formulation further couples uplift redistribution and crack propagation, enabling guaranteed safety bounds without assuming probability distributions or relying on resultant-force simplifications inherent in LEM.

2. Methodology

This section presents the governing formulations and computational procedures adopted in the deterministic crack-based Limit Equilibrium Method (LEM), Monte Carlo Simulation (MCS), and Interval Finite Element Method (IFEM) frameworks for sliding stability assessment of concrete gravity dams under parameter uncertainty. While LEM employs the linear Mohr–Coulomb (MC) shear strength model, both MCS and IFEM utilize the nonlinear Barton–Choubey (BC) model to represent the concrete–foundation rock interface behavior. The factor of safety against sliding (FSS) is evaluated in each framework along the sliding interface. The resulting formulations establish the basis for the numerical implementation in Section 3 and the comparative evaluation presented in Section 4.

2.1 Deterministic Crack-Based Limit Equilibrium Method

The deterministic sliding stability assessment follows the crack-based Limit Equilibrium Method formulation presented in Yadav (2025), consistent with current dam safety practice (FERC, 2016; USACE, 2005). The overall analysis procedures are presented below.

2.1.1 External Loads

The governing external loads considered in this study are dead load (self-weight), hydrostatic forces acting on the upstream and downstream faces, and uplift pressure along the sliding interface. Although concrete gravity dams may be subjected to additional loads such as silt loads, hydrodynamic loads, thermal loads, and seismic forces, the overall analytical procedure remains the same as presented in this paper.

The dead load or self-weight is a major stabilizing force and acts vertically downward through the centroid of the dam cross-section (U.S. Army Corps of Engineers 2005, Federal Energy Regulatory Commission 2016). It is computed as:

$$F_D = V_c \gamma_c \tag{1}$$

where F_D is the dead load or self-weight of dam, V_c is the volume of concrete, and γ_c is the unit weight of concrete.

Hydrostatic pressure acts perpendicular to the dam face and increases linearly with depth, producing a triangular pressure distribution (De Sazilly 1853, United State Bureau of Reclamation 1987, White 2011). For a vertical surface, the resultant hydrostatic force is given by:

$$F_h = \frac{1}{2}\gamma_w h^2 \tag{2}$$

where F_h is the hydrostatic force, γ_w is the unit weight of water, and h is the depth of water.

The unit weight of water is taken as $\gamma_w = 9.81\ \mathrm{kN/m^3}$ ($62.4\ \mathrm{lbf/ft^3}$), in accordance with standard engineering practice(United State Bureau of Reclamation 1987, White 2011). The resultant force acts at one-third of the water height measured from the base. Figure 1 and 2 illustrates the dead load acting through C.G, the hydrostatic pressure distribution and corresponding resultant force locations for both upstream and downstream faces.

Uplift pressure is a critical vertical force that reduces the effective compressive normal stress along the concrete–foundation rock interface and directly influences sliding stability (U.S. Army Corps of Engineers 2005, Federal Energy Regulatory Commission 2016, Nallanathel, Ramesh et al. 2018). For an uncracked interface, uplift pressure is commonly assumed to vary linearly from the heel to the toe (Federal Energy Regulatory Commission 2016), as depicted in Figure 1. When cracking occurs, the uplift pressure is assumed to remain constant from the heel to the crack tip and is taken as equal to the headwater pressure, since water

can freely enter the crack, followed by a linear decrease to the toe (Federal Energy Regulatory Commission 2016), as depicted in Figure 2.

Because the uplift distribution depends on crack length, and crack length itself depends on the applied loads and resulting stress state, crack-based LEM requires an iterative uplift–crack coupling procedure to obtain a consistent solution (Federal Energy Regulatory Commission 2016).

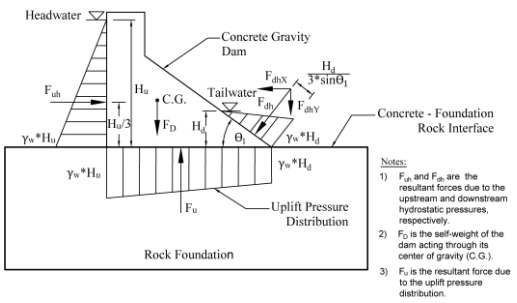


Figure 1: Uplift pressure distribution for an uncracked interface

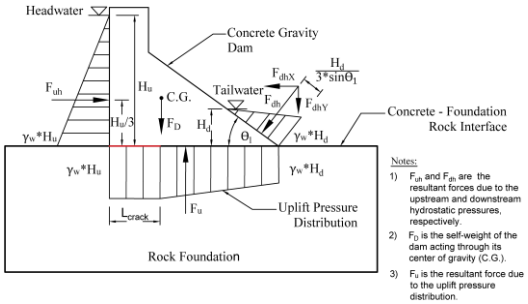


Figure 2: Uplift pressure distribution for a cracked interface

2.1.2 Failure Criterion Utilized in Limit Equilibrium Method (LEM)

In dam stability analysis, establishing a failure criterion is fundamental. The Limit Equilibrium Method (LEM) evaluates stability by assuming the dam is at a limit state, i.e., on the verge of failure (Ali, Alam et al. 2012). At this state, the system satisfies static equilibrium under applied loads, meaning driving and resisting forces and moments are balanced. The term "Limit" denotes the condition immediately preceding failure, while "Equilibrium" implies that all external forces and moments are in balance (Ali, Alam et al. 2012). The dam is treated as a rigid body without deformation, and equilibrium equations are used to compute the factor of safety against sliding (FSS).

A key step in LEM is estimating the shear strength parameters along the concrete–foundation rock interface, namely the friction angle (ϕ) and cohesion (c). For practical application, LEM adopts the linear Mohr–Coulomb (MC) shear strength model, assuming a smooth failure surface. The shear strength is expressed as (Weijermars 1997, Fell, MacGregor et al. 2015):

$$\tau_s = c + \sigma_n \tan\phi \tag{3}$$

where τ_s is the shear strength, c is cohesion, σ_n is the effective compressive normal stress on the sliding plane, and ϕ is the available friction angle.

Based on the known external forces and shear strength parameters, the factor of safety against sliding (FSS) is computed as (Fell, MacGregor et al. 2015):

$$\mathrm{FSS} = \frac{cA_C + A_c\sigma_n \tan\phi}{F_s} \tag{4}$$

where A_C is uncracked area under compression along the concrete-foundation rock interface and F_s is total driving or sliding force along the interface, typically taken as the horizontal component of the resultant load vector.

Due to uncertainty in cohesion, particularly at concrete–rock interfaces, the Federal Energy Regulatory Commission recommends either neglecting cohesion or applying a higher factor of safety (Federal Energy Regulatory Commission 2016). If cohesion is neglected, Equation (4) reduces to:

$$\mathrm{FSS} = \frac{A_c\sigma_n \tan\phi}{F_s} = \frac{\tan\phi}{\frac{F_s}{A_c\sigma_n}} = \frac{\tan\phi}{\tan\alpha_r} \tag{5}$$

where α_r is required friction angle, defined as angle between the resultant load vector and the normal to the sliding plane.

2.1.3. Crack Initiation and Propagation Criteria. In conventional crack-based Limit Equilibrium Method (LEM), the concrete–foundation rock interface is assumed to have zero tensile strength (Federal Energy Regulatory Commission 2016). Any portion of the interface subjected to tensile normal stress is therefore considered cracked.

For illustration, consider the case shown in Figure 3. The base length of the dam is B_0 and B_1 the location of the resultant force measured from the toe. If the resultant lies within the middle third of the base length i.e., between $\frac{B_0}{3}$ and $\frac{2B_0}{3}$, the entire interface remains in compression and no cracking occurs. If the resultant lies outside the middle third, tensile stress develops at the heel and cracking initiates (Federal Energy Regulatory Commission 2016).

For a unit width of the dam section, the normal stresses at the heel and toe are expressed as

$$\sigma_{toe/heel} = \frac{F_{RY}}{B_0} \pm \frac{6F_{RY}e}{{B_0}^2} \tag{6}$$

where F_{RY} is the vertical component of the resultant force and e is the eccentricity measured from the centerline of the base.

When tensile stress develops at the heel, the portion of the interface remaining in compression extends a distance $3B_1$ from the toe, consistent with the triangular stress distribution. The crack length for the first iteration is therefore will be $B_0 - 3B_1$. Figure 3 illustrates the stress distribution corresponding crack length definition along the base interface.

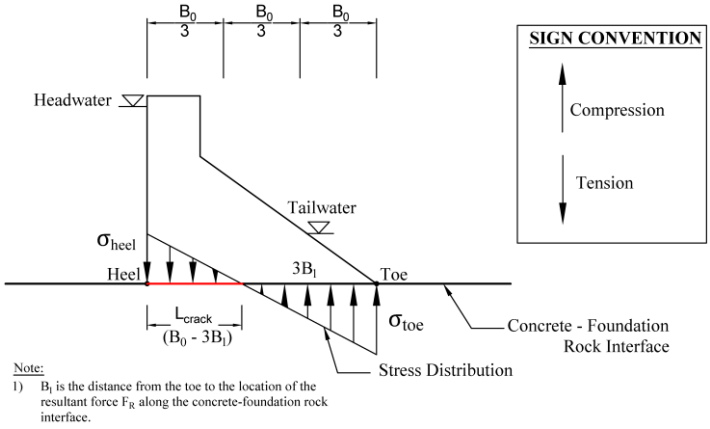


Figure 3: Tension at the heel when resultant force (F_R) is located within the outer third of base length

2.1.4. Iterative Crack–based Solution Procedure

Because the uplift pressure is directly influenced by the extent of cracking, and the crack length is in turn controlled by the applied external loads, its evaluation requires an iterative procedure. This interdependence forms the basis of the crack–based LEM(Federal Energy Regulatory Commission 2016). Accordingly, crack–based LEM requires determining the crack length along the sliding interface, followed by an evaluation of stability against sliding.

2.1.4.1 Crack Length Determination

The determination of crack length follows these steps:

a) **Initial Assumption:** The interface has zero tensile strength. Assume no initial crack and apply the uplift pressure distribution for a non-cracked base, as discussed in Section 2.1.3.

b) **Determine Resultant Force Location:** Find the location of the resultant force by taking moments about the heel or toe. Let B_0, be the base length of dam and B_1 be the resultant force location from the toe.

c) **Compute Compression Zone:** The portion of base under compression will be $3B_1$ from the toe.

d) **Check the Compression Condition:**

- If $3B_1 \geq B_0$, the entire base is in compression. Hence there will be no cracking. Assumed uplift pressure distribution is correct and proceed to factor of safety against sliding (FSS) computation as described in Section 2.1.5.

- If $3B_1 < B_0$, the entire base is not in compression. Hence there will be cracking, and the new crack length will be $Lc = B_0 - 3B_1$.

e) **Re-apply uplift pressure:** If there is cracking, update the uplift pressure distribution for the cracked base, based on the calculated crack length, as discussed in Section 2.1.3.

f) **Recalculate Resultant Force Location:** Determine the new location of resultant force, B_1, from the toe by taking moments about the heel or toe.

g) **Update Crack Length:** Compute the new crack length: $Lc_new = B_0 - 3B_1$.

h) **Iterate Until Convergence:** Repeat steps e to g until the crack length converges or until the entire base is cracked. If the entire base is cracked, the dam is considered unstable and will undergo sliding unless the sufficient anchoring measures are implemented to satisfy current engineering guidelines. If the entire base is not cracked, proceed with steps outlined in Section 2.1.5.

2.1.5 Factor of Safety against Sliding (FSS)

Once the crack length and corresponding uplift forces are determined, the magnitude and location of the new resultant force (F_R) along the sliding interface are calculated by taking moments about the heel or toe of the dam. From the components of the resultant force, the required friction angle (α_r) with respect to the normal to the sliding plane is obtained as:

$$\alpha_r = \tan^{-1}\left|\frac{F_{RX}}{F_{RY}}\right| \quad (7)$$

where F_{RX} and F_{RY} are the horizontal and vertical components of the resultant force, respectively.

The available friction angle (ϕ) is selected based on the foundation rock type. The factor of safety against sliding (FSS) is then computed using Equation (5).

Sliding stability is satisfied when $FSS \geq 1$, i.e., when the available friction angle (ϕ) exceeds or equals the required friction angle (α_r). If $FSS < 1$, the dam is considered unstable with respect to sliding and may require anchoring or other stabilization measures to meet current engineering guidelines.

2.2 Failure Criterion Utilized in Monte Carlo Simulation (MCS) and Interval Finite Element Method (IFEM)

In the 1970s, Barton introduced his initial non-linear shear strength criterion for rock joints, utilizing the basic friction angle (ϕ_b), derived from an analysis of joint strength data available in the literature. Later, Barton and Choubey (1977) refined this equation based on their direct shear test results conducted on 130 samples of rock joints with varying degrees of weathering, leading to a revised formulation as shown in Equation (8).

$$\tau_s = \sigma_n \tan\left(\phi_r + JRC \log_{10}\left(\frac{JCS}{\sigma_n}\right)\right) \quad (8)$$

where ϕ_r is residual friction angle in degree, JRC is the joint roughness coefficient and JCS is the join wall compressive strength.

2.3 Monte Carlo Simulation (MCS)

The Monte Carlo simulation (MCS) is implemented to evaluate variability in sliding stability due to uncertain parameters. The uncertain parameters include the density of concrete, the unit weight of water, the joint roughness coefficient (JRC), the joint wall compressive strength (JCS), and the residual friction angle (ϕ_r).. These parameters are defined using the same interval bounds adopted in IFEM to ensure consistency. Sampling is performed using scaled Beta distributions, bounded on the interval $[\underline{X}, \overline{X}]$. The mean value ($X_{mean}$) is taken as the midpoint of the interval, and the shape parameters of the scaled Beta distribution are obtained as:

$$\alpha_{MCS} = \mu_{MCS}\kappa, \qquad \beta_{MCS} = (1 - \mu_{MCS})\kappa \quad (9)$$

$$\mu_{MCS} = \frac{(X_{mean} - \underline{X})}{(\overline{X} - \underline{X})} \quad (10)$$

where α_{MCS} and β_{MCS} are the Beta shape parameters, μ_{MCS} defines the scaled location of the mean within the interval, and κ is the concentration factor controlling the spread of the realizations around the mean.

The probability density function of the Beta distribution used for sampling is expressed as:

$$f(x) = \frac{x^{\alpha_{MCS}-1}(1-x)^{\beta_{MCS}-1}}{Beta(\alpha_{MCS}, \beta_{MCS})} \quad (11) \qquad Beta(\alpha_{MCS}, \beta_{MCS}) = \int_0^1 n^{\alpha_{MCS}-1}(1-n)^{\beta_{MCS}-1} dn \quad (12)$$

where x is the sampled random variable and n is a dummy integration variable.

A concentration factor (κ) is selected based on the expected variability of each uncertain parameter. Higher κ values (e.g., for densities) yield narrower distributions around the mean, whereas moderate κ values (e.g., for JRC, JCS and ϕ_r) allow a broader spread across the full interval of each parameter. The resulting realizations are then propagated through the uplift–crack coupling formulation to compute the crack length and factor of safety for each simulation.

The severity of cracking is coupled to the Barton–Choubey shear strength model. First, the uplift distribution assuming no crack is taken as a trapezoid:

$$F_{u0} = \frac{1}{2}(\gamma_w H_u + \gamma_w H_d)B_0 \tag{13}$$

where F_{u0} is the uplift force, H_u is the headwater depth, H_d is the tailwater depth, B_0 is the dam base length and γ_w is the unit weight of water.

The effective pre-crack normal stress is calculated as:

$$\sigma_0 = \max\left(\frac{F_D - F_{u0}}{B_0}, 0\right) \tag{14}$$

where F_D is the self-weight of dam and the corresponding mobilized friction angle was given by:

$$\phi_{BC} = \phi_r + JRC \log_{10}\left(\frac{JCS}{\sigma_0}\right) \tag{15}$$

A severity index (s_0) is then defined as:

$$s_0 = \frac{F_s}{F_s + \tan\phi_{BC} \max(F_D - F_{u0}, 1)} \tag{16}$$

where F_s is the sliding force.

A severity index (s_0) links crack length to the balance between sliding force and mobilized BC shear resistance. When the sliding force dominates, s_0 is larger and longer cracks are promoted, whereas when resistance is higher, s_0 is smaller and the crack is shorter. This coupling ensures that the crack length distribution is not imposed arbitrarily but responds directly to the mobilized shear strength. The actual crack length (Lc) was sampled from a Beta distribution whose mean was tied to s_0 as:

$$Lc = B_0\left(\text{Beta}\left(1 + \lambda_{LC}s_0, 1 + \lambda_{LC}(1 - s_0)\right)\right) \tag{17}$$

where beta concentration factor (λ_{LC}) is set above 20 to maintain concentration around the mean. The adopted Beta-based crack length sampling is not imposed arbitrarily; rather, its mean is tied to severity index (s_0) ensuring that crack propagation responds directly to the mobilized shear strength and applied sliding demand.

Uplift after cracking is taken as:

$$F_u = \gamma_w H_u Lc + \frac{1}{2}(\gamma_w H_u + \gamma_w H_d)(B_0 - Lc) \tag{18}$$

The normal compressive stress on the bonded portion is calculated as:

$$\sigma_1 = \max\left(\frac{F_D - F_{u0}}{B_0 - Lc}, \sigma_{floor}\right) \tag{19}$$

where σ_{floor} is set to 1 Pa for numerical safeguard.

The Barton–Choubey friction angle is then re-evaluated at the bonded interface as:

$$\phi_{BC} = \phi_r + JRC \log_{10}\left(\frac{JCS}{\sigma_1}\right) \tag{20}$$

Since MCS does not discretize the interface, shear strength is evaluated through angle comparison. The resultant of the sliding and vertical forces makes an angle, α_r, :with respect to the normal to the sliding plane and can be determined as:

$$\alpha_r = \tan^{-1}\left|\frac{F_S}{F_D - F_{u0}}\right| \tag{21}$$

The factor of safety against sliding (FSS) is computed as:

$$FSS = \frac{\tan\phi_{BC}}{\tan\alpha_r} \tag{22}$$

This expression tests whether the mobilized Barton–Choubey shear strength is sufficient to resist the resultant action without making assumptions about the stress distribution along the interface. Unlike IFEM, which integrates the shear strength distribution, the MCS compares mobilized and resultant angles, providing a lumped yet computationally efficient estimate of the factor of safety.

2.4 Interval Finite Element Method (IFEM)

The Interval Finite Element Method (IFEM) is adopted to rigorously propagate uncertainty in material properties, geometry, and external loads through the structural equilibrium equations. Uncertain parameters are represented as interval variables, and the computed solution provides guaranteed bounds that enclose the true structural response. It should be noted that the resulting uncertainty bounds are mesh-dependent, as they are influenced by the level of discretization and the associated approximation of the structural domain. An introduction to interval arithmetic, with relevant discussions can be found in (Moore 1966, Kulisch 1981, Alefeld 1983, Neumaier 1990), along with an overview of the main computational challenges such as dependency and overestimation.

Hereafter, boldface font is used to denote interval quantities.

The structural equilibrium is defined through the interval linear system:

$$\mathbf{K}\mathbf{u} = \mathbf{f} \tag{23}$$

where $\mathbf{K}$ is the interval global stiffness matrix, $\mathbf{u}$ is the interval nodal displacement vector, and $\mathbf{f}$ is the interval equivalent nodal load vector.

Derived quantities are obtained as:

$$\boldsymbol{\varepsilon} = \mathrm{B}\mathbf{u}, \qquad \boldsymbol{\sigma} = \mathbf{S}\mathbf{u} \tag{24}$$

where B is the strain–displacement matrix and $\mathbf{S}$ is the stress–displacement matrix.

2.4.1 Decomposition of the Stiffness and Stress Matrices

To minimize dependency-induced overestimation in interval arithmetic, the stiffness matrix is decomposed as:

$$\mathbf{K} = \mathrm{A}\,\mathrm{diag}(\Lambda\boldsymbol{\alpha})\mathrm{A}^{\mathrm{T}} \tag{25}$$

where A and Λ are deterministic matrices, $\boldsymbol{\alpha}$ is the interval parameter vector.

For an 8-node rectangular isoparametric element under plane stress or strain conditions, the Young's modulus ($\mathbf{E}$) is represented as an interval. The corresponding stiffness matrix is then calculated as:

$$\mathbf{K_e} = \int_{\Omega} \mathrm{B}_{\mathrm{e}}^{\mathrm{T}}(\xi)\mathbf{E_e}(\xi)\mathrm{B}_{\mathrm{e}}(\xi)\mathrm{t}(\xi)\mathrm{d}\Omega \tag{26}$$

where t is the thickness and B_{e} is the strain-displacement matrix.

The integral in Equation (26) is typically evaluated using a 3×3 Gaussian quadrature rule:

$$\mathbf{K_e} = \sum_{\mathrm{j}=1}^{9} \mathrm{B}_{\mathrm{e}}^{\mathrm{T}}(\xi_{\mathrm{j}})\mathbf{E_e}(\xi_{\mathrm{j}})\mathrm{B}_{\mathrm{e}}(\xi_{\mathrm{j}})\mathrm{w}_{\mathrm{j}}\mathrm{J}(\xi_{\mathrm{j}})\mathrm{t}(\xi) \tag{29}$$

where, w_{j} are weights at the integration points, ξ_{j} is the integration coordinate, and J is the determinant of the Jacobian matrix for the transformation from local to global coordinates. This numerical integration transforms the modulus field into a smoother interval representation.

The constitutive matrix $\mathbf{E_e}(\xi_{\mathrm{j}})$ in Equation (29) can be expressed as:

$$\mathbf{E_e}(\xi_{\mathrm{j}}) = \Phi_{\mathrm{e}}\,\mathrm{diag}\{\phi_e\mathbf{E}_{\mathrm{j}}\}\Phi_{\mathrm{e}}^{\mathrm{T}} \tag{30}$$

where Φ_{e} is a 3×3 deterministic matrix whose columns are eigenvectors ϕ_e is a 3×1 vector whose rows are eigenvalues. Both Φ_{e} and ϕ_e depends on Poisson's ratio (ν), and $\mathbf{E}_{\mathrm{j}}$ is the Young's modulus at j-th integration point ξ_{j}. Using this, Equation (29) becomes:

$$\begin{aligned}\mathbf{K_e} &= \sum_{\mathrm{j}=1}^{9} \mathrm{B}_{\mathrm{e}}^{\mathrm{T}}(\xi_{\mathrm{j}})\Phi_{\mathrm{e}}\,\mathrm{diag}\{\phi_e\mathbf{E}_{\mathrm{j}}\}\Phi_{\mathrm{e}}^{\mathrm{T}}\mathrm{B}_{\mathrm{e}}(\xi_{\mathrm{j}})\mathrm{w}_{\mathrm{j}}\mathrm{J}(\xi_{\mathrm{j}})\mathrm{t}(\xi) \\ &= \{\mathrm{B}_{\mathrm{e}}^{\mathrm{T}}(\xi_1)\Phi_{\mathrm{e}} \ldots\ldots\ldots\ldots \mathrm{B}_{\mathrm{e}}^{\mathrm{T}}(\xi_9)\Phi_{\mathrm{e}}\}\end{aligned} \tag{31}$$

$$\begin{Bmatrix} (w_1 J_1 t_1)\mathrm{diag}(\phi_e)\mathbf{E_1} & & \\ & \ddots & \\ & & (w_9 J_9 t_9)\mathrm{diag}(\phi_e)\mathbf{E_9} \end{Bmatrix} \begin{Bmatrix} \Phi_e^T B_e(\xi_1) \\ \vdots \\ \Phi_e^T B_e(\xi_9) \end{Bmatrix}$$

where the subscripts j denotes quantities at the j-th integration point. The deterministic matrices A_e and Λ_e are obtained as:

$$A_e = \{B_e^T(\xi_1)\Phi_e \dots\dots\dots\dots B_e^T(\xi_9)\Phi_e\};$$

$$\Lambda_e = \begin{Bmatrix} (w_1 J_1 t_1)\mathrm{diag}(\phi_e) & & \\ & \ddots & \\ & & (w_9 J_9 t_9)\mathrm{diag}(\phi_e) \end{Bmatrix}, \qquad \boldsymbol{\alpha_e} = \begin{Bmatrix} \mathbf{E_1} \\ \vdots \\ \mathbf{E_9} \end{Bmatrix} \tag{32}$$

This decomposition of the diagonal matrix, $\mathrm{diag}(\Lambda_e \boldsymbol{\alpha_e})$, effectively reduces redundant interval terms and plays a critical role in reducing overestimation in interval due to dependency.

The element stress-displacement matrix ($\mathbf{S_e}$) depends linearly on the stiffness parameter vector $\boldsymbol{\alpha_e}$. Just like the stiffness matrix $\mathbf{K_e}$, this matrix ($\mathbf{S_e}$) can also be expressed in a simplified and structured form. The matrix $\mathbf{S_e}$ is written as:

$$\mathbf{S_e} = \Phi_{se}\mathrm{diag}(\Lambda_{se}\boldsymbol{\alpha_e})A_{se}^T \tag{33}$$

For example, at any location within 8-node rectangular isoparametric element, the stress $\boldsymbol{\sigma_e}$ can be obtained either by interpolating or extrapolating the stresses calculated at the integration (Gauss) points. This procedure is described by:

$$\boldsymbol{\sigma_e} = \sum_{j=1}^{9} \upsilon_j \boldsymbol{\sigma_e}(\xi_j) = \sum_{j=1}^{9} \upsilon_j \, \mathbf{E_e}(\xi_j) B_e(\xi_j)\mathbf{u_e} \tag{34}$$

where ξ_j represents the coordinates of the numerical integration points, υ_j are the corresponding interpolation or extrapolation weights, and $\mathbf{u_e}$ is the nodal displacement vector of the element. By factoring out $\mathbf{u_e}$, the stress-displacement matrix $\mathbf{S_e}$ takes a simplified form:

$$\mathbf{S_e} = \sum_{j=1}^{9} \upsilon_j \mathbf{E_e}(\xi_j) B_e(\xi_j) \tag{35}$$

Substituting $\mathbf{E_e}(\xi_j) = \Phi_e \mathrm{diag}\{\phi_e \mathbf{E}_j\}\Phi_e^T$ into Equation (35):

$$\mathbf{S_e} = \sum_{j=1}^{9} \upsilon_j \, \Phi_e \mathrm{diag}\{\phi_e \mathbf{E}_j\}\Phi_e^T B_e(\xi_j)$$

$$= \{\Phi_e \ \cdots \ \Phi_e\} \begin{Bmatrix} \upsilon_1 \mathrm{diag}(\phi_e)\mathbf{E_1} & & \\ & \ddots & \\ & & \upsilon_9 \mathrm{diag}(\phi_e)\mathbf{E_9} \end{Bmatrix} \begin{Bmatrix} \Phi_e^T B_e(\xi_1) \\ \vdots \\ \Phi_e^T B_e(\xi_9) \end{Bmatrix} \tag{36}$$

The deterministic matrices Φ_{se}, Λ_{se} and A_{se} are obtained as:

$$\Phi_{se} = \{\Phi_e \ \cdots \ \Phi_e\}, \qquad \Lambda_{se} = \begin{Bmatrix} \upsilon_1 \mathrm{diag}(\phi_e) & & \\ & \ddots & \\ & & \upsilon_9 \mathrm{diag}(\phi_e) \end{Bmatrix};$$

$$A_{se} = \{B_e{}^T(\xi_1)\Phi_e \quad \dots \quad B_e{}^T(\xi_9)\Phi_e\} \tag{37}$$

These decompositions are performed at the element level before global assembly using an Element-by-Element (EBE) strategy.

2.4.2 Decomposition of Equivalent Nodal Load Vector

For an element subjected to concentrated, body, and line loads, the uncertain load vector is expressed as:

$$\boldsymbol{\delta} = [\mathbf{P_c} \quad \mathbf{P_s} \quad \mathbf{P_l}]^T \tag{38}$$

The equivalent nodal load vector becomes:

$$\mathbf{f} = F\boldsymbol{\delta} \tag{39}$$

where F is a deterministic matrix constructed from shape functions and Jacobian terms.

2.4.3 Matrix Assembly – Element–by–Element (EBE)

After determining the element-level matrices, $\mathbf{K}_e$ (stiffness matrix), $\mathbf{f}_e$ (nodal load vector), $\mathbf{S}_e$ (stress–displacement matrix), and B_e (strain–displacement matrix), these must be assembled to form their global counterparts: **K**, **f**, **S**, and B.

This is accomplished using the Element-by-Element (EBE) approach, which assembles each matrix in a block-by-block manner (Muhanna, Zhang et al. 2007, Mallella, Mullen et al. 2011, Muhanna, Mallela et al. 2013, Xiao 2015). In this method, the entire structure is modeled as a collection of separate elements connected by shared nodes. The global displacement vector $\mathbf{u}$ is formed by combining all local element displacement vectors $\mathbf{u}_e$, with $\mathbf{u}_n$ representing the displacement vector of the common (shared) nodes. Consequently, the global stiffness matrix **K** and global nodal load vector **f** are assembled from their element counterparts as shown in Equation (40):

$$\mathbf{u} = \begin{Bmatrix} \mathbf{u_e} \\ \vdots \\ \mathbf{u_e} \\ \mathbf{u_n} \end{Bmatrix}, \qquad \mathbf{K} = \begin{Bmatrix} \mathbf{K_e} & & \\ & \ddots & \\ & & \mathbf{K_e} \\ 0 & & 0 \end{Bmatrix}, \qquad \mathbf{f} = \begin{Bmatrix} \mathbf{f_e} \\ \vdots \\ \mathbf{f_e} \\ \mathbf{f_n} \end{Bmatrix} \tag{40}$$

where $\mathbf{f}_n$ represents the concentrated loads directly applied to the common nodes. Unlike standard FEM assembly, where the global matrices are formed in a single step, the EBE method constructs **K** and **f** by stacking individual $\mathbf{K}_e$ and $\mathbf{f}_e$ blocks. One key point to note is that the global stiffness matrix **K** is initially singular since it does not yet incorporate constraints such as boundary conditions.

To reduce overestimation due to dependency from repeated interval variables, the matrices **K** and **f** are further decomposed using interval decomposition techniques $\mathbf{K} = A\mathrm{diag}(\Lambda\alpha)A^T$, $\mathbf{f} = F\delta$, as follows:

$$\boldsymbol{\alpha_e} = L_\alpha \boldsymbol{\alpha}, \quad \boldsymbol{\delta}_e = L_\delta \boldsymbol{\delta} \tag{41}$$

In this representation, $\boldsymbol{\alpha}_e$ and $\boldsymbol{\delta}_e$ (element-level interval vectors) are either selected directly from, or interpolated from, the global interval vectors $\boldsymbol{\alpha}$ and $\boldsymbol{\delta}$. These element-level vectors are related to the global ones through mapping relations:

The global matrices A, Λ, and F are assembled in a way similar to **K** and **f**, again using a block-by-block strategy:

$$A = \begin{Bmatrix} A_e & & \\ & \ddots & \\ & & A_e \\ 0 & & 0 \end{Bmatrix}, \qquad \Lambda = \begin{Bmatrix} \Lambda_e L_\alpha \\ \vdots \\ \Lambda_e L_\alpha \end{Bmatrix}, \qquad F = \begin{Bmatrix} F_e L_\delta \\ \vdots \\ F_e L_\delta \\ F_n \end{Bmatrix} \tag{42}$$

where $\mathbf{f}_n = F_n\boldsymbol{\delta}$ is the decomposition of $\mathbf{f}_n$. If any interval components in $\boldsymbol{\alpha}$ or $\boldsymbol{\delta}$ refer to the same variable, the corresponding columns in Λ or F must be summed. Similarly, if certain components in $\boldsymbol{\delta}$ are zero, the associated columns in F are removed to avoid redundancy.

The global strain vector $\boldsymbol{\varepsilon}$ is assembled by combining all the element-level strain vectors $\boldsymbol{\varepsilon}_e$. The global strain-displacement matrix B is also constructed in block using each element matrix B_e. This assembly procedure ensures that all local contributions are consistently represented in the global system, preparing it for further analysis:

$$\boldsymbol{\varepsilon} = \begin{Bmatrix} \boldsymbol{\varepsilon}_e \\ \vdots \\ \boldsymbol{\varepsilon}_e \end{Bmatrix}, \qquad B = \begin{Bmatrix} B_e & & 0 \\ & \ddots & \vdots \\ & B_e & 0 \end{Bmatrix} \tag{43}$$

$$\boldsymbol{\sigma} = \begin{Bmatrix} \boldsymbol{\sigma}_e \\ \vdots \\ \boldsymbol{\sigma}_e \end{Bmatrix}, \qquad \mathbf{S} = \begin{Bmatrix} \mathbf{S_e} & & 0 \\ & \ddots & \vdots \\ & \mathbf{S_e} & 0 \end{Bmatrix} \tag{44}$$

Finally, the deterministic matrices Φ_s, Λ_s and A_s are assembled as:

$$\Phi_s = \begin{Bmatrix} \Phi_{se} & & \\ & \ddots & \\ & & \Phi_{se} \end{Bmatrix}, \qquad \Lambda_s = \begin{Bmatrix} \Lambda_{se} L_\alpha \\ \vdots \\ \Lambda_{se} L_\alpha \end{Bmatrix}, \qquad A_s = \begin{Bmatrix} A_{se} & & \\ & \ddots & \\ & & A_{se} \\ 0 & \dots & 0 \end{Bmatrix} \tag{45}$$

2.4.4 Calculation of reactions and derived variables ($\boldsymbol{\varepsilon}$ and $\boldsymbol{\sigma}$)

After the global stiffness matrix **K** is assembled using the EBE strategy, it remains singular. This occurs because, at this stage, the model does not yet include connections between shared nodes of adjacent elements, nor are essential boundary conditions applied. As a result, the assembled system lacks the necessary constraints to produce a unique solution.

To resolve this, both compatibility requirements and essential boundary conditions must be enforced. These constraints are expressed in the form of a matrix equation $\mathbf{Cu} = 0$, where C is a constraint matrix that enforces physical conditions, such as continuity between nodes and essential boundary conditions. Once these conditions are imposed, the singularity of the stiffness matrix is eliminated, and the system becomes fully solvable.

As an example, consider an 8-node rectangular isoparametric element, where each node has two degrees of freedom. To enforce compatibility between an element node (with two DOFs) and a corresponding common node using a constraint matrix C, the two rows of C can be defined as in Eq. (46) (Mallella, Mullen et al. 2011, Xiao 2015):

$$\begin{matrix} & \text{Element node DOF} & & & & \text{Common node DOF} & & \\ \mathrm{C} = & \cdots & \cdots & \cdots & \cdots & \cdots & \cdots & \cdots \\ & \cdots & 1 & 0 & \cdots & -1 & 0 & \cdots \\ & \cdots & 0 & 1 & \cdots & 0 & -1 & \cdots \\ & \cdots & \cdots & \cdots & \cdots & \cdots & \cdots & \cdots \end{matrix} \quad (46)$$

$$\begin{matrix} & \text{Element node DOF} & & & & \text{Common node DOF} & & \\ \mathrm{C} = & \cdots & \cdots & \cdots & \cdots & \cdots & \cdots & \cdots \\ & \cdots & 0 & 0 & \cdots & 1 & 0 & \cdots \\ & \cdots & 0 & 0 & \cdots & 0 & 1 & \cdots \\ & \cdots & \cdots & \cdots & \cdots & \cdots & \cdots & \cdots \end{matrix} \quad (47)$$

To apply essential boundary conditions, specific entries in the constraint matrix C are assigned a value of 1, while other entries in the same row are set to zero as in Eq. (47) (Mallella, Mullen et al. 2011, Xiao 2015).

To enforce these compatibility conditions and maintain equilibrium, a Lagrange multiplier $\boldsymbol{\lambda}$ is introduced. The system's energy functional, $\boldsymbol{\Pi}$, is given by:

$$\boldsymbol{\Pi} = \frac{1}{2}\mathbf{u}^{\mathrm{T}}\mathbf{K}\mathbf{u} - \mathbf{u}^{\mathrm{T}}\mathbf{f} + \boldsymbol{\lambda}^{\mathrm{T}}\mathrm{C}\mathbf{u} \quad (48)$$

By minimizing $\boldsymbol{\Pi}$ with respect to $\mathbf{u}$ and $\boldsymbol{\lambda}$, the interval-based governing equation is obtained:

$$\begin{Bmatrix} \mathbf{K} & \mathrm{C}^{\mathrm{T}} \\ \mathrm{C} & 0 \end{Bmatrix} \begin{Bmatrix} \mathbf{u} \\ \boldsymbol{\lambda} \end{Bmatrix} = \begin{Bmatrix} \mathbf{f} \\ 0 \end{Bmatrix} \quad (49)$$

To reduce overestimation, the stiffness matrix $\mathbf{K}$ and load vector $\mathbf{f}$ are decomposed as previously described in Equation (25) and (39) respectively. In this formulation, Equation (49) is expressed as (Muhanna, Mallela et al. 2013, Xiao 2015):

$$\begin{Bmatrix} \mathrm{A} \\ 0 \end{Bmatrix} \mathrm{diag}(\Lambda\Delta\boldsymbol{\alpha}) \begin{Bmatrix} \mathrm{A}^{\mathrm{T}} & 0 \end{Bmatrix} + \begin{Bmatrix} \mathrm{K}_0 & \mathrm{C}^{\mathrm{T}} \\ \mathrm{C} & 0 \end{Bmatrix} \begin{Bmatrix} \mathbf{u} \\ \boldsymbol{\lambda} \end{Bmatrix} = \begin{Bmatrix} \mathrm{F} \\ 0 \end{Bmatrix} \boldsymbol{\delta} \quad (50)$$

where $\Delta\boldsymbol{\alpha}$ represents the difference between the interval vector $\boldsymbol{\alpha}$ and its reference value α_0, i.e. $\Delta\boldsymbol{\alpha} = \boldsymbol{\alpha} - \alpha_0$, with $\alpha_0 = \mathrm{mid}(\boldsymbol{\alpha})$ being the midpoint value of the interval, and $\mathrm{K}_0 = \mathrm{A}\mathrm{diag}(\Lambda\alpha_0)\mathrm{A}^{\mathrm{T}}$.

The Lagrange multiplier $\boldsymbol{\lambda}$ has physical meaning in this context: it represents internal forces between element nodes and common nodes when compatibility is enforced, and reaction forces at supports when essential boundary conditions are applied. Thus, internal forces and support reactions can be directly obtained as by-products of solving the constraint equation $\mathbf{Cu} = 0$ (Xiao 2015).

Additional derived quantities such as generalized strain ($\boldsymbol{\varepsilon}$) and stress ($\boldsymbol{\sigma}$) in Equation (24) can also be computed. To avoid intermediate interval steps and further overestimation, these variables ($\mathbf{u}, \boldsymbol{\varepsilon}$, and $\boldsymbol{\sigma}$) are solved simultaneously by introducing additional Lagrange multipliers $\boldsymbol{\mu_1}$ and $\boldsymbol{\mu_2}$, corresponding to the relations $\boldsymbol{\varepsilon} = \mathrm{B}\mathbf{u}$ and $\boldsymbol{\sigma} = \mathbf{S}\mathbf{u}$, respectively. The modified energy functional is then expressed as:

$$\boldsymbol{\Pi} = \frac{1}{2}\mathbf{u}^{\mathrm{T}}\mathbf{K}\mathbf{u} - \mathbf{u}^{\mathrm{T}}\mathbf{f} + \boldsymbol{\lambda}^{\mathrm{T}}\mathrm{C}\mathbf{u} + \mu_1^{\mathrm{T}}(\boldsymbol{\varepsilon} - \mathrm{B}\mathbf{u}) + \mu_2^{\mathrm{T}}(\boldsymbol{\sigma} - \mathbf{S}\mathbf{u}) \quad (51)$$

Above formulation includes six unknowns: $\mathbf{u}, \boldsymbol{\lambda}, \boldsymbol{\mu_1}, \boldsymbol{\mu_2}, \boldsymbol{\varepsilon}$, and $\boldsymbol{\sigma}$. Taking the first variation of this energy functional yields:

$$\begin{Bmatrix} \mathbf{K} & \mathrm{C}^{\mathrm{T}} & \mathrm{B}^{\mathrm{T}} & \mathbf{S}^{\mathrm{T}} & 0 & 0 \\ \mathrm{C} & 0 & 0 & 0 & 0 & 0 \\ \mathrm{B} & 0 & 0 & 0 & -I & 0 \\ \mathbf{S} & 0 & 0 & 0 & 0 & -I \\ 0 & 0 & -I & 0 & 0 & 0 \\ 0 & 0 & 0 & -I & 0 & 0 \end{Bmatrix} \begin{Bmatrix} \mathbf{u} \\ \boldsymbol{\lambda} \\ \boldsymbol{\mu_1} \\ \boldsymbol{\mu_2} \\ \boldsymbol{\varepsilon} \\ \boldsymbol{\sigma} \end{Bmatrix} = \begin{Bmatrix} \mathbf{f} \\ 0 \\ 0 \\ 0 \\ 0 \\ 0 \end{Bmatrix} \quad (52)$$

From the last two rows of Equation (52), it can be inferred that $\mu_1 = 0$ and $\mu_2 = 0$ Substituting these trivial solutions back into Equation (52) yields a simplified, asymmetric form:

$$\begin{Bmatrix} \mathbf{K} & \mathrm{C}^{\mathrm{T}} & 0 & 0 \\ \mathrm{C} & 0 & 0 & 0 \\ \mathrm{B} & 0 & -I & 0 \\ \mathbf{S} & 0 & 0 & -I \end{Bmatrix} \begin{Bmatrix} \mathbf{u} \\ \boldsymbol{\lambda} \\ \boldsymbol{\varepsilon} \\ \boldsymbol{\sigma} \end{Bmatrix} = \begin{Bmatrix} \mathbf{f} \\ 0 \\ 0 \\ 0 \end{Bmatrix} \tag{53}$$

While this results in a smaller stiffness matrix, it is no longer symmetric (Xiao 2015). Considering the previous decomposition of **K** and **f**, the governing equation can finally be written as (Muhanna, Mallela et al. 2013, Xiao 2015):

$$\begin{Bmatrix} \mathrm{A} & 0 \\ 0 & 0 \\ 0 & 0 \\ 0 & \Phi_{\mathrm{s}} \end{Bmatrix} \mathrm{diag}\left(\begin{Bmatrix} \Lambda \\ \Lambda_{\mathrm{s}} \end{Bmatrix} \Delta\boldsymbol{\alpha} \right) \begin{Bmatrix} \mathrm{A}^{\mathrm{T}} & 0 & 0 & 0 \\ \mathrm{A}_{\mathrm{S}}^{\mathrm{T}} & 0 & 0 & 0 \end{Bmatrix} + \begin{Bmatrix} \mathrm{K}_0 & \mathrm{C}^{\mathrm{T}} & 0 & 0 \\ \mathrm{C} & 0 & 0 & 0 \\ \mathrm{B} & 0 & -I & 0 \\ \mathrm{S}_0 & 0 & 0 & -I \end{Bmatrix} \begin{Bmatrix} \mathbf{u} \\ \boldsymbol{\lambda} \\ \boldsymbol{\varepsilon} \\ \boldsymbol{\sigma} \end{Bmatrix} = \begin{Bmatrix} \mathrm{F} \\ 0 \\ 0 \\ 0 \end{Bmatrix} \boldsymbol{\delta} \tag{54}$$

where $\Delta\boldsymbol{\alpha}$ and K_0 have the same definitions as in Equation (50), and S_0 denotes the generalized stress-displacement matrix as defined earlier, i.e., $\mathrm{S}_0 = \Phi_{\mathrm{s}}\mathrm{diag}(\Lambda_{\mathrm{s}}\alpha_0)\mathrm{A}_{\mathrm{s}}^{\mathrm{T}}$

Equation (54) can be expressed in a generalized form as:

$$\left\{\mathrm{A}_{\mathrm{g}}\mathrm{diag}\left(\Lambda_{\mathrm{g}}\Delta\boldsymbol{\alpha}\right)\mathrm{B}_{\mathrm{g}} + \mathrm{K}_{\mathrm{g}}\right\}\mathbf{u_g} = \mathrm{F}_{\mathrm{g}}\boldsymbol{\delta} \tag{55}$$

where $\mathrm{A}_{\mathrm{g}}, \Lambda_{\mathrm{g}}, \mathrm{B}_{\mathrm{g}}, \mathrm{K}_{\mathrm{g}}, \mathrm{F}_{\mathrm{g}}$ are deterministic matrices, while $\Delta\boldsymbol{\alpha}$ and $\boldsymbol{\delta}$ are interval vectors.

Equations (50) and (54) are the equilibrium equations to be solved. The generalized form of these equations are given in Equation (55). Any interval solver can be employed to solve this general equation. In this paper, a new version of the iterative enclosure method introduced by Xiao (2015) is utilized, which applies an expanding strategy that begins with a simple initial guess and progressively refines the solution.

2.4.5 Piecewise Approach to Reduce Dependency in the Barton–Choubey (BC) Shear Strength Model

Since the BC shear strength model involves uncertain parameters, such as joint roughness coefficient (JRC), joint wall compressive strength (JCS), and residual friction angle (ϕ_{r}), arising from natural geological variability and site characterization, dependency-induced overestimation can occur in interval computations. To mitigate this effect, this research adopts the piecewise (partition) strategy. The method works as follows:

1) Partition the original uncertain interval **X** into N subintervals:

$$\mathbf{X} = \cup\, \mathbf{X}^{(\mathrm{i})}\ , \quad \mathbf{X}^{(\mathrm{i})} = \left[\, \underline{\mathrm{X}}^{(\mathrm{i})}, \overline{\mathrm{X}}^{(\mathrm{i})} \,\right], \qquad \mathrm{i} = 1 \ldots . \mathrm{N} \tag{56}$$

2) Evaluate the interval function $\mathrm{f}\left(\mathbf{X}^{(\mathrm{i})}\right)$ of the function $\mathrm{f}(\mathbf{X})$ over each subinterval.
3) Take the hull of the union of the results. The hull operator ensures that the result remains a single interval, even when individual images from subintervals are disjoint.

$$\mathrm{f}(\mathbf{X}) \subseteq \Diamond \left(\cup\, \mathrm{f}\left(\mathbf{X}^{(\mathrm{i})}\right) \right) \tag{57}$$

4) Refine iteratively: as N increases, dependency within each subinterval is reduced, and the enclosure contracts toward the true image of the function.

The convergence of piecewise interval evaluation is guaranteed for continuous functions; in the limit, the hull converges to the exact range (Yadav 2025), although for finite N it generally provides an enclosure. This strategy can also be used in validating numeric and interval finite element formulations, where dependency problems otherwise lead to meaningless results.

2.4.6 Step-by-step procedure in IFEM

1. Start / collect all existing information including:
   - Dam geometry and foundation profile
   - External loading conditions (dead load, hydrostatic pressure, uplift pressure, thermal loads, seismic loads if applicable)
   - Material properties (**E**, ν)
   - Shear strength parameters ($\boldsymbol{\phi_{\mathrm{r}}}$, **JRC**, **JCS**)
   - Represent uncertain parameters in interval form
2. Assume an uncracked interface (i.e., crack length, $\mathrm{Lc} = 0$).

3. Calculate all external loads in interval form. Note: Uplift pressure distribution along the interface depends on crack length.
4. Define geometry, discretize the domain using appropriate finite element types and mesh sizes, and assign interval material properties.
5. Apply external loads.

Iterative crack update and uplift/Boundary Conditions (BCs) update

6. Apply BCs: restrain translation in both global X and Y directions at the boundary (concrete–foundation rock interface).
7. Solve using IFEM.
8. Check tensile condition: Is the interface under tension?
   If YES:
   a) Calculate the new crack length Lc (length of tensile zone or segment where shear strength < shear stress at the interface).
   b) Update and apply uplift pressure along the interface based on the current crack length Lc.
   c) Update BCs of the cracked interface:
   - Release translation in global X direction in all cases.
   - If tension: allow separation (release in global Y direction).
   - If compression: enforce no penetration (keep restraint in global Y direction).

   d) Go back to Step 7.
   If NO (i.e., no tension): continue to Step 9.
9. Calculate shear strength using compressive stress at the interface and the Barton–Choubey Shear Strength model.
10. Check shear crack criterion: Is computed shear strength < shear stress at the interface?
    If YES: Go back to Step 8a (update Lc, then uplift/BCs, then re-solve).
    If NO (i.e., crack length is converged): proceed to next step.
11. Check for the rigid body motion: Is entire interface in cracked?
    If $Lc \geq B_0$, the entire interface is cracked. Hence, the dam transforms into a rigid body motion, and the sliding factor of safety is taken as zero. The further computation ends here.
    If $Lc < B_0$, the entire interface is not cracked. Hence, the dam does not transform into a rigid body motion. Proceed to step 12 to compute **FSS**.

Post-convergence (sliding demand vs resistance and FSS calculation)

12. Obtain sliding force from interface reactions (or equivalently from applied external loads).
13. Calculate shear strength of the uncracked interface from compressive stress using the Barton–Choubey model.
14. Calculate resisting force by integrating shear strength over the uncracked portion of the interface.
15. Compute interval factor of safety against sliding (**FSS**) by comparing sliding and resisting forces.
16. End.

2. Case Study

The numerical illustration considers a concrete gravity dam constructed in 1962 within the Carolina Slate Belt, a northeast-trending geologic province composed of low-grade metamorphic, volcanic, and sedimentary rocks extending from southwestern Virginia to central Georgia. The dam geometry is shown in Figure 4, and the principal dimensions are summarized in Table 2. Sliding is evaluated along the concrete–foundation rock interface. The foundation consists primarily of basaltic tuffs from the Upper Volcanic Sequence and mafic tuffaceous argillite from the Volcanic Sedimentary Sequence.

A comprehensive site investigation conducted in 1993 provided the material parameters required for stability assessment. The program included exploratory drilling and core logging, laboratory testing of concrete samples to determine density and compressive strength, compressive strength testing of foundation rock, and direct shear testing to characterize joint shear strength. The resulting material properties adopted in the deterministic, Monte Carlo, and IFEM analyses are summarized in Table 1.

Table 1: Material Properties utilized in LEM, MCS and IFEM Analyses

Parameters	LEM	Mean value (X_{mean}) for PDF for MCS	IFEM
(γ_c), N/m^3	24,082.363	24,082.363	[23,480.304, 24,684.423]
(γ_w), N/m^3	9,745.953	9,745.953	[9,732.386 , 9,759.519]
$\tau_s = c + \sigma_n \tan\phi_p$ (MPa)	$\tau_s = 0.0235 + \sigma_n \tan 52.66°$	N/A	N/A
JRC	N/A	11.5	[10.925, 12.075]
JCS (MPa)	N/A	57.5	[56.062, 58.938]
ϕ_r	39.62°	39.62°,	[38.63°, 40.61°]
E_{avg} (MPa)	N/A	N/A	28,222.316
Poisson's ratio (ν)	N/A	N/A	0.2

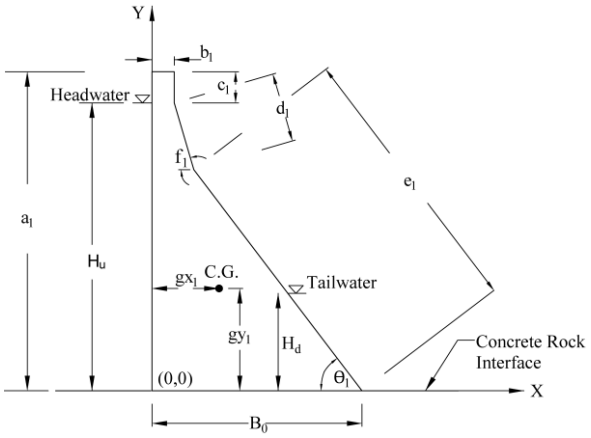


Figure 4: Geometry of the concrete gravity dam section under consideration

Segment	**Length**
a_1	26.18 m (85.9 ft)
b_1	1.83 m (6 ft)
c_1	2.56 m (8.4 ft)
d_1	5.71 m (18.73 ft)
e_1	22.71 m (74.50 ft)
B_0	17.22 m (56.5 ft)
Slope	**Angle**
f_1	74°
θ_1	53°

Table 2: Dimensions of dam geometry under consideration

Spatial variability of the modulus of elasticity (E) is particularly relevant in hydraulic structures due to long-term moisture exposure, especially near the upstream face. Previous studies (Sokolov and Rasskazchikov, 1986) documented moisture penetration depths of 4–6 m from the upstream face, with moisture content varying from approximately 1.5% at the heel to 0.1% near the downstream toe. These variations significantly influence stiffness and stress distribution along the concrete–rock interface.

Based on these observations, a linear spatial variation of moisture content $M_c(X, Y)$ is adopted, ranging from 0.1% at the water surface and toe to 1.5% at the heel. Following Liu et al. (2014), the Young's modulus is expressed as:

$$E(X, Y) = 1982.3M_c(X, Y) + E_{avg} \quad (58)$$

where E_{avg} is the average elastic modulus in MPa.

To reduce overestimation, the following stepwise approach is used. First, the deterministic Young's modulus is computed at each nodal coordinate using Equation (58). Then, the nodal values are interpolated to integration (Gauss) points using standard shape functions:

$$E_{Int_pts} = N(\xi, \eta) \times E_{Nodal_Coordinates} \quad (59)$$

where $N(\xi, \eta)$ denotes the matrix of shape functions in local co-ordinates, and $E_{Nodal_Coordinates}$ represents the vector of elastic moduli at the element nodes.

To incorporate uncertainty, a variation of $\pm 2.5\%$ is applied on E_{Int_pts}, giving a total variation of 5%. Accordingly, the modulus of elasticity in interval form at the integration points is expressed as

$$\mathbf{E}_{Int_pts} = E_{Int_pts}[0.975, 1.025] \quad (60)$$

This formulation enables consistent comparison of deterministic, probabilistic, and interval-based stability assessments while explicitly accounting for spatial stiffness variation.

3. Results and Discussion

The dam section was discretized using 108 eight-node quadrilateral isoparametric elements (Figure 5). Spatial variability of Young's modulus, derived from moisture-dependent stiffness, is shown in Figure 6 using mid-interval values. External loads included self-weight, hydrostatic pressures, and uplift. The initial hydrostatic and uplift distributions (zero crack length assumption) are presented in Figure 7.

Crack initiation was evaluated based on tensile stress and shear stress exceeding interface shear strength. As cracking developed, boundary conditions and uplift distribution were iteratively updated within the IFEM framework. The converged uplift profile and crack configuration are shown in Figure 8. Convergence was achieved in three iterations.

The final crack length was 3.1309 m (18.18% of the 17.22 m base). The computed interval sliding factor of safety was $\mathbf{FSS} = [3.104, 4.938]$, indicating stability for all admissible parameter bounds. Stress distributions on the deformed configuration are shown in Figures 9 through 11. Cracked segments under tension provide no shear resistance, while uncracked compressive regions maintain shear strength exceeding the applied shear stress.

In contrast, the crack-based LEM predicted a crack length of 16.564 m (96.19% of the base) with $\mathrm{FSS} = 0.086$, indicating instability. This discrepancy stems from the linear Mohr–Coulomb assumption and simplified crack initiation and propagation criterion in LEM. Even when peak Mohr–Coulomb strength parameters from laboratory tests were adopted, LEM predicted nearly full-base cracking and $\mathrm{FSS} < 1$. The predicated instability becomes more pronounced when residual friction angle and zero cohesion are used, as commonly assumed in practice.

The Monte Carlo simulation with 2×10^6 realizations yields factor of safety at the $5\mathrm{th}$, $50\mathrm{th}$, and $95\mathrm{th}$ percentiles of $\mathrm{P}_5 = 1.49, \mathrm{P}_{50} = 1.83$ and $\mathrm{P}_{95} = 2.16$, respectively, while the probability of failure ($\mathrm{P}(\mathrm{FSS} < 1)$) is zero. The Monte Carlo simulation predicted a mean crack length of 3.11 m, corresponding to the $95\mathrm{th}$ percentile, which differs from the IFEM result (3.13 m) by about 0.64%. This close agreement in crack length indicates that the IFEM has efficiently captured the uplift–crack coupling, resulting in a more realistic prediction of crack propagation. By comparison, the interval finite element method produces a factor of safety enclosure of $[3.104, 4.938]$. The factor of safety is lower in the Monte Carlo simulation because the formulation compares lumped angles. In contrast, IFEM integrates the stress-dependent BC shear strength distribution along the uncracked interface, leading to a resistance evaluation consistent with local stress states rather than a single resultant-based comparison. Since the interval **FSS** is entirely greater than unity, no admissible parameter realization within defined bounds results in sliding failure. IFEM therefore provides a guaranteed safety bound, while the MCS offers probabilistic insight into the most likely outcomes under the same interval bounds. Together, the two approaches confirm that the structure remains stable under the full range of interval-defined uncertainty, whereas the limit equilibrium method (LEM) predicts almost the entire base to be cracked and the dam to be unstable. This contrast highlights the importance of the IFEM approach proposed in this paper, as it provides a more realistic and reliable assessment of dam stability.

4. Conclusions

This study presented a comparative evaluation of deterministic crack-based Limit Equilibrium Method (LEM), Monte Carlo Simulation (MCS), and an Interval Finite Element Method (IFEM) for sliding stability analysis of concrete gravity dams, incorporating iterative uplift–crack coupling through boundary-condition updates. The conventional LEM, based on linear Mohr–Coulomb strength and resultant-force-based crack estimation, predicted extensive cracking and a factor of safety below unity for the considered parameter set. The Monte Carlo framework provided realistic percentile-based safety factors but required extensive sampling and probabilistic input assumptions.

The proposed IFEM integrates the nonlinear Barton–Choubey shear strength model, interval representation of uncertain parameters, piecewise treatment to control overestimation, element-by-element assembly, and iterative crack–uplift coupling. The method captured tensile and shear cracking mechanisms while consistently updating uplift redistribution. For the case study, IFEM predicted limited cracking and an

interval factor of safety entirely greater than unity, consistent with Monte Carlo results and observed dam performance.

Unlike LEM, IFEM does not rely on simplified resultant-force assumptions, and unlike MCS, it does not require probability density functions. Instead, it provides mathematically guaranteed safety bounds using only upper and lower parameter limits, offering a computationally efficient and reliable framework for sliding stability assessment under bounded uncertainty.

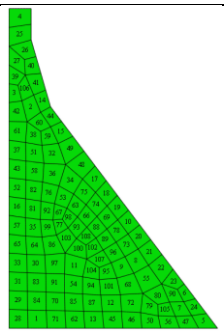


Figure 5: Finite element mesh of dam geometry (8-node quadrilateral isoparametric elements)

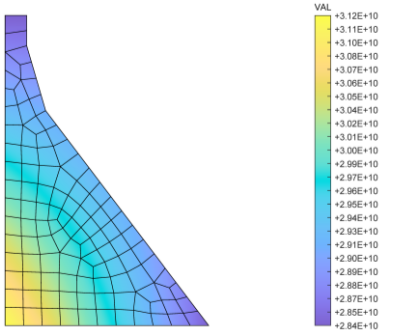


Figure 6: Spatial variation of modulus of elasticity (E) within the dam body due to moisture content, plotted using mid-interval values

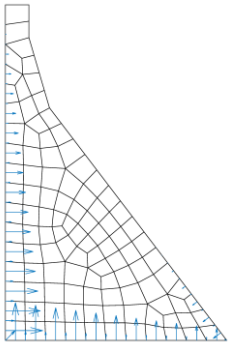


Figure 7: Hydrostatic and uplift pressure distributions for the first iteration with zero crack length

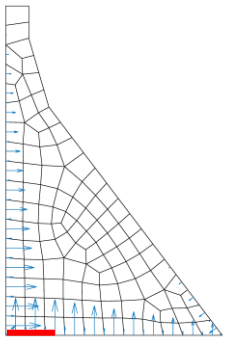


Figure 8 Hydrostatic and updated uplift pressure distributions under the converged crack state. Note the uniform uplift pressure along the cracked interface shown in red

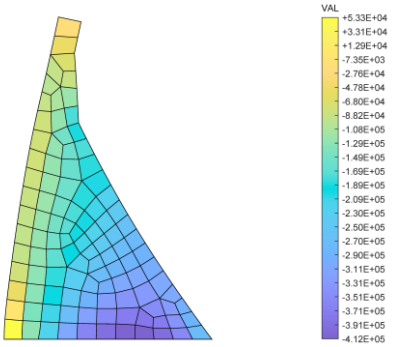


Figure 9: Distribution of σ_{YY} (normal stress in Y-direction) on the deformed dam shape, plotted using mid-interval values

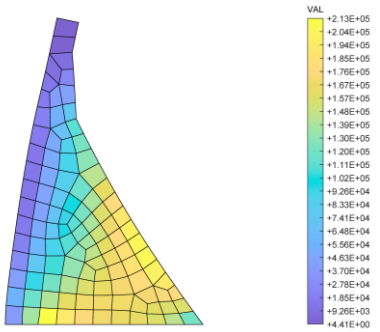


Figure 10: Distribution of τ (shear stress) on the deformed dam shape, plotted using mid-interval values

References

Alefeld, G. and J. Herzberger (1983). Introduction to Interval Computations. New York, Academic Press.

Ali, M. H., M. R. Alam, M. N. Haque and M. J. Alam (2012). "Comparison of Design and Analysis of Concrete Gravity Dam." Natural Resources 3(1): 30–36.

Barton, N. (1973). "Review of a new shear-strength criterion for rock joints." Engineering Geology 7(4): 287–332.

Barton, N. (1974). A review of the shear strength of filled discontinuities in rock. Norwegian Geotechnical Institute. Bergmekanikk, Oslo.
Barton, N. (1976). "The shear strength of rock and rock joints." International Journal of Rock Mechanics and Mining Sciences & Geomechanics Abstracts 13(9): 255–279.
Barton, N. (2013). "Shear strength criteria for rock, rock joints, rockfill and rock masses: Problems and some solutions." Journal of Rock Mechanics and Geotechnical Engineering 5(4): 249–261.
Barton, N. (2016). "Non-linear shear strength for rock, rock joints, rockfill and interfaces." Innovative Infrastructure Solutions 1(1): 30.
Barton, N. and S. Bandis (1982). "Effect of block size on the shear behavior of jointed rocks." Proceedings - Symposium on Rock Mechanics: 739–760.
Barton, N. and V. Choubey (1977). "The shear strength of rock joints in theory and practice." Rock Mechanics Felsmechanik Mecanique des Roches 10(1-2): 1–54.
Barton, N., C. Wang and R. Yong (2023). "Advances in joint roughness coefficient (JRC) and its engineering applications." Journal of Rock Mechanics and Geotechnical Engineering 15(12): 3352–3379.
Barton, N. R. and S. C. Bandis (1990). Review of predictive capabilities of JRC-JCS model in engineering practice. Rock Joints. N. Barton and O. Stephansson. Rotterdam, Balkema.
De Sazilly, J. A. T. (1853). "Note sur un type de profil d'égale résistance, proposé pour les murs de réservoirs d'eau (Note on a profile of equal resistance proposed for water reservoir walls)." Journal: Annales des ponts et chaussées **6**(2e semestre): 191–222.
Federal Energy Regulatory Commission (2015). Chapter 1 - General Requirements of Engineering Guidelines for the Evaluation of Hydropower Projects. Washington, DC, Federal Energy Regulatory Commission (FERC).
Federal Energy Regulatory Commission (2016). Chapter 3 – Gravity Dams of Engineering Guidelines for the Evaluation of Hydropower Projects. Washington, DC, Federal Energy Regulatory Commission (FERC).
Fell, R., P. MacGregor, D. Stapledon, G. Bell and M. Foster (2015). Goetechnial Engineering of Dams. Boca Raton, FL, CRC Press.
Kulisch, U. W. and W. L. Miranker (1981). INTERVAL ARITHMETIC. Computer Arithmetic in Theory and Practice, Elsevier: 84–151.
Liu, B. D., W. J. Lv, L. Li and P. F. Li (2014). "Effect of moisture content on static compressive elasticity modulus of concrete." Construction and Building Materials 69: 133–142.
Mallela, V. R. R., R. L. Mullen and R. L. Muhanna (2011). "A new interval finite element formulation with the same accuracy in primary and derived variables." International Journal of Reliability and Safety 5(4): 347–360.
Moore, R. E. (1966). Interval Analysis. Englewood Cliffs, NJ, Prentice Hall.
Moore, R. E. (1979). Methods and Applications of Interval Analysis. Philadelphia, SIAM.
Muhanna, R., V. R. R. Mallela and R. Mullen (2013). "Advances in Interval Finite Element Modelling of Structures." 2: 15–22.
Muhanna, R. L. and R. L. Mullen (2001). "Uncertainty in Mechanics Problems—Interval–Based Approach." Journal of Engineering Mechanics 127(6): 557–566.
Muhanna, R. L., H. Zhang and R. L. Mullen (2007). "Combined Axial and Bending Stiffness in Interval Finite-Element Methods." Journal of Structural Engineering 133(12): 1700–1709.
Muhanna, R. L., H. Zhang and R. L. Mullen (2007). "Interval Finite Elements as a Basis for Generalized Models of Uncertainty in Engineering Mechanics." Reliable Computing 13(2): 173–194.
Nallanathel, M., B. Ramesh and P. K. A. Raju (2018). "Stability Analysis of Concrete Gravity Dam Using STAAD Pro." International Journal of Pure and Applied Mathematics 119(17): 297–310.
Neumaier, A. (1990). Interval Methods for Systems of Equations, Cambridge University Press.
Rao, M. V. R., R. L. Mullen and R. L. Muhanna (2011). "A new interval finite element formulation with the same accuracy in primary and derived variables." International Journal of Reliability and Safety 5(3/4): 336.
Rump, S. M. (1999). "Fast and Parallel Interval Arithmetic." BIT Numerical Mathematics 39(3): 534–554.
Rump, S. M. (1999). INTLAB - Interval Laboratory. Developments in Reliable Computing. Dordrecht, Netherlands, Kluwer Academic Publishers: 77–104.
Sokolov, I. B. and V. A. Rasskazchikov (1986). "Consideration of moisture effects on the upstream face of concrete dams." Hydrotechnical Construction 20(3): 193–198.
U.S. Army Corps of Engineers (2005). Stability Analysis of Concrete Structures. Washington, D.C.
United States Bureau of Reclamation (1987). Design of Small Dams. Denver, CO, United States Department of the Interior, Bureau of Reclamation.
Weijermars, R. (1997). Principles of Rock Mechanics, Alboran Science Publishing.
White, F. M. (2011). Fluid Mechanics. New York, NY, McGraw-Hill.
Xiao, N. (2015). Interval Finite Element Approach for Inverse Problem under Uncertainty. PhD Thesis, Georgia Institute of Technology.
Xiao, N., F. Fedele and R. Muhanna (2016). "Interval-based parameter identification for structural static problems." 23: 47–72.
Xiao, N., R. Muhanna, F. Fedele and R. Mullen (2015). "Interval Finite Element Analysis of Structural Dynamic Problems." SAE International Journal of Materials and Manufacturing 8.
Yadav, B. (2025). Interval Finite Element Approach for Stability Analysis of Concrete Gravity Dams under Uncertainties. PhD Thesis, Georgia Institute of Technology.

Probabilistic Assessment of Multiphysics-Driven Stochastic Corrosion for the Safety Evaluation of Nuclear Waste Canisters

Shenghao Piao
Institute for Risk and Reliability, Leibniz University Hannover, Hannover 30167, shenghao.piao@irz.uni-hannover.de

Zhibao Zheng
Institute for Risk and Reliability, Leibniz University Hannover, Hannover 30167, zhibao.zheng@ibnm.uni-hannover.de

Michael Beer
Institute for Risk and Reliability, Leibniz University Hannover, Hannover 30167, beer@irz.uni-hannover.de

Abstract. Ensuring the long-term safety of deep geological disposal systems requires reliable prediction of corrosion in nuclear waste canisters. Their interfacial corrosion is governed by coupled thermal-hydro-chemical (THC) processes and is strongly affected by uncertainties arising from heterogeneous materials, spatially variable conditions and environmental parameters. However, existing numerical approaches face substantial challenges when addressing large computational domains, high-dimensional random inputs, and long-term simulations required to represent geological time scales. This study presents an efficient stochastic finite element framework for quantifying the probabilistic evolution of corrosion depth at canister interfaces. The framework solves coupled stochastic THC PDEs and models the interface recession as an evolving random field. Uncertainty in initial conditions, material-environment interaction coefficients and corrosion mechanisms is represented through structured high-dimensional random inputs. The proposed method separates the spatial, temporal and random components of the solution space, which enables scalable and computationally efficient simulations while maintaining accuracy in estimating probability distributions and ensemble statistics of corrosion progression. The resulting stochastic solutions further facilitate reliability evaluation, sensitivity analysis and inverse identification of key corrosion parameters for safety assessment.

Keywords: Stochastic corrosion, Nuclear waste canister, Stochastic multiphysics coupling, Stochastic finite element method, Uncertainty quantification

1. Introduction

Deep geological disposal (DGD) is widely recognized as one of the most promising strategies for the long-term management of high-level radioactive waste (Liu et al., 2025). In a DGD system, nuclear waste canisters are emplaced hundreds of meters below the ground surface and are protected by a multi-barrier system consisting of engineered barriers and surrounding geological formations. As

© 2026 by the author(s). This work is licensed under the Creative Commons Attribution 4.0 International License (CC BY 4.0), which permits unrestricted use, distribution, and reproduction in any medium, provided the original author and source are credited.

illustrated in Figure 1, the canister constitutes the primary engineered barrier and is responsible for isolating radioactive materials from the environment over time scales ranging from thousands to hundreds of thousands of years. Consequently, the long-term integrity of the canister plays a crucial role in the overall safety assessment of geological repositories.

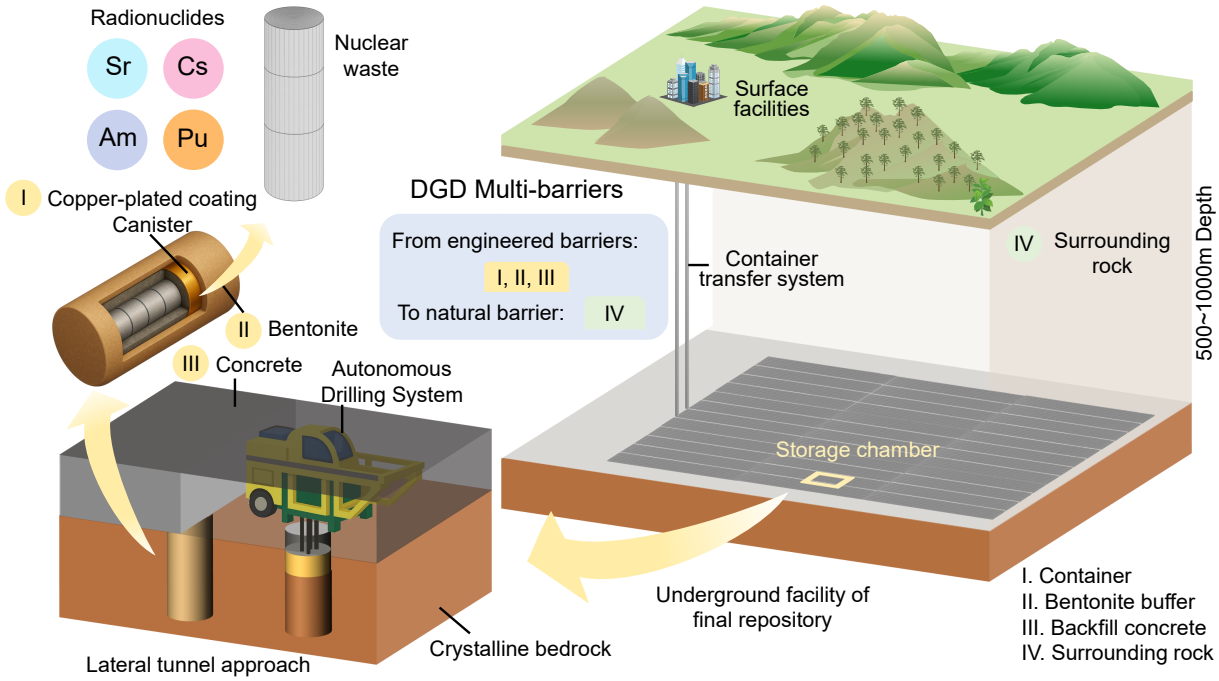


Figure 1. Schematic illustration of the deep geological disposal system for high-level radioactive waste. The multi-barrier concept consists of engineered barriers, including the waste form, canister, and buffer materials, together with the surrounding geological formation. Long-term safety relies on the integrity of the canister and its resistance to corrosion-induced degradation under coupled environmental conditions.

Despite the favorable environmental conditions provided by deep geological formations, the canister remains exposed to complex thermal-hydro-chemical (THC) processes throughout its service life. Decay heat generated by radioactive waste induces transient thermal fields, which in turn influence moisture migration, oxygen transport, condensation, evaporation, and various electrochemical reactions. These coupled processes affect the evolution of corrosion products and lead to progressive degradation of the canister surface (Frankel et al., 2021). Figure 2 schematically illustrates the corrosion process occurring at the copper–steel interface, where interactions among temperature, moisture, oxygen, and material properties govern the long-term recession of the protective coating and the underlying substrate (Guo et al., 2020).

Reliable prediction of corrosion evolution remains a challenging task because of the significant uncertainties involved (Järvine et al., 2019; Kurgyis et al., 2024). Material properties of engineered barriers exhibit spatial variability due to manufacturing tolerances and heterogeneity. Environmental conditions, including temperature, humidity, oxygen availability, and transport coefficients, are inherently uncertain and may evolve over long geological periods. Furthermore, corrosion mecha-

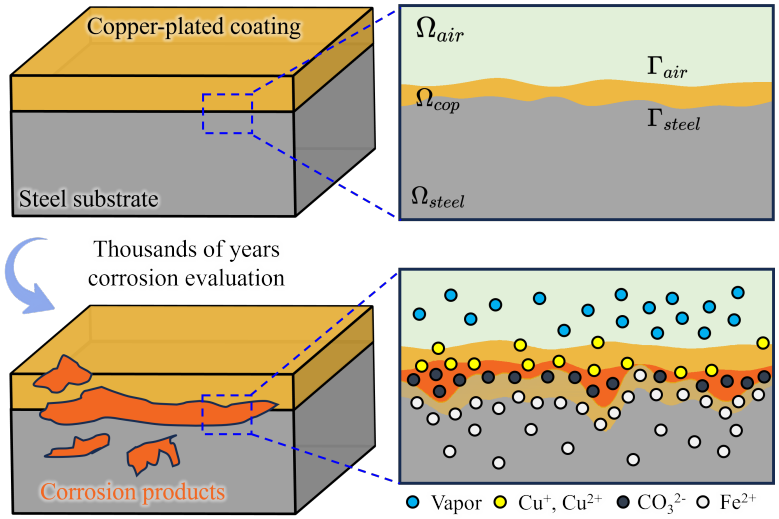


Figure 2. Schematic representation of interfacial corrosion at the copper–steel canister system. Coupled thermal, moisture, oxygen, and electrochemical processes drive the progressive degradation of the copper coating and the formation of corrosion products at the material interface during long-term repository operation.

nisms are influenced by coupled multiphysics interactions whose governing parameters are often difficult to characterize experimentally. As a result, deterministic simulations may not adequately represent the variability and uncertainty associated with long-term canister degradation.

The present work focuses on spatially varying but macroscopically uniform interfacial corrosion occurring at the copper–steel interface. The main contributions of this work are summarized as follows: (a) A coupled stochastic THC model is formulated for the long-term corrosion analysis of nuclear waste canisters. (b) An efficient stochastic finite element framework is developed to handle high-dimensional uncertainties associated with material properties, environmental conditions, and corrosion parameters. (c) The probabilistic evolution of corrosion depth is quantified through probability distributions, ensemble statistics, and spatial corrosion fields.

2. Physical Problem and Multiphysics Corrosion Model

2.1. Physical Problem

The present study considers the long-term corrosion behavior of a copper-coated steel canister used for the geological disposal of high-level radioactive waste. As shown in Figure 2, the computational domain consists of three subdomains corresponding to the surrounding air environment, the copper coating, and the steel substrate, denoted by Ω_{air}, Ω_{cop}, and Ω_{steel}, respectively.

The copper-steel and air-copper interfaces are assumed to exhibit small geometric irregularities representing surface roughness generated during manufacturing and long-term degradation processes. The canister is subjected to coupled THC processes driven by the decay heat generated by the radioactive waste and the surrounding environmental conditions. Heat transfer affects moisture

migration and oxygen transport, while the availability of oxygen and moisture governs the corrosion reactions occurring at the material interfaces. In the present work, corrosion is assumed to occur primarily as spatially varying interfacial corrosion. Localized pitting corrosion and microbiologically influenced corrosion are neglected in order to focus on the probabilistic evolution of large-scale corrosion damage (King et al., 2021).

The principal quantity of interest is the corrosion depth $D(\mathbf{x}, t, \boldsymbol{\theta})$, which is treated as a stochastic field depending on spatial position $\mathbf{x}$, time t, and a set of random variables $\boldsymbol{\theta}$ representing uncertain material properties, environmental parameters, and corrosion coefficients.

2.2. Coupled THC equations

The thermal field is described by a transient heat conduction equation

$$\rho c_p \frac{\partial T}{\partial t} = \nabla \cdot (\lambda \nabla T), \tag{1}$$

where ρ, c_p, and λ denote the density, specific heat capacity, and thermal conductivity, respectively. Water vapor transport is described by

$$\frac{\partial C_{H_2O}}{\partial t} = \nabla \cdot (D_{H_2O} \nabla C_{H_2O}), \tag{2a}$$

$$-D_{H_2O} (\nabla C_{H_2O}) \cdot n = F_{ev/cn} \quad \text{on} \quad \Gamma_{air}, \tag{2b}$$

where C_{H_2O} is the vapor concentration and D_{H_2O} is the effective diffusion coefficient, and $F_{ev/cn}$ is the evaporation–condensation flux. The oxygen concentration field is governed by

$$\frac{\partial C_{O_2}}{\partial t} = \nabla \cdot (D_{O_2} \nabla C_{O_2}), \tag{3a}$$

$$-D_{O_2} (\nabla C_{O_2}) \cdot n = \Phi (C_{O_2}, D_{O_2}) \quad \text{on} \quad \Gamma_{air}, \tag{3b}$$

where C_{O_2} and D_{O_2} denote the oxygen concentration and oxygen diffusivity, respectively. Φ denotes the reduction-controlled oxygen consumption rate. At the corrosion interface, oxygen is consumed through electrochemical reactions. The corrosion process is assumed to be controlled by the local thermal-hydro-chemical conditions. Accordingly, the corrosion depth D evolution is expressed as

$$\frac{\partial D}{\partial t} = \eta_c \Phi (C_{O_2}, T)\, g(s). \tag{4}$$

where η_c is an effective corrosion coefficient and s denotes the film thickness.

2.3. Stochastic Representation and Solution Framework

The coupled THC model contains multiple uncertain parameters associated with thermal properties, diffusion coefficients, environmental conditions, and corrosion kinetics. These uncertainties are represented as random fields. For a generic stochastic parameter $k(\mathbf{x}, \theta)$, the spatial variability is described through the Karhunen–Loève (KL) expansion

$$k(\boldsymbol{x}, \theta) = \bar{k}(\boldsymbol{x}) + \sum_{n=1}^{M} \sqrt{\lambda_n} \phi_n(\boldsymbol{x}) \xi_n(\theta), \tag{5}$$

where $k(\boldsymbol{x})$ denotes the mean value, λ_n and $\phi_n(\boldsymbol{x})$ are the eigenvalue and eigenfunction of the covariance the covariance kernel, respectively (Zheng et al., 2025). ξ_n are mutually independent random variables. The truncation order M determines the dimension of the stochastic space. Using the KL expansion, the uncertain thermal conductivity, moisture diffusivity, oxygen diffusivity, and corrosion parameters are transformed into a finite set of random variables. Consequently, the governing fields become stochastic quantities.

The spatial discretization of the coupled THC equations is performed using the finite element method (Arregui-Mena et al., 2016). After finite element discretization, the governing equations can be expressed into a global system

$$\mathbf{M}(\boldsymbol{\xi})\,\dot{\mathbf{u}} + \mathbf{K}(\boldsymbol{\xi})\,\mathbf{u} = \mathbf{F}(\mathbf{u}, t, \boldsymbol{\xi}), \tag{6}$$

where $\mathbf{u}$contains the nodal temperature, moisture, oxygen concentration and corrosion-depth unknowns (Hughes et al., 2022). The stochastic system is solved for each realization generated from the truncated KL expansion, and the resulting ensemble is used to evaluate the probabilistic evolution of corrosion.

The stochastic finite element system is advanced incrementally in time according to the solution procedure illustrated in Figure 3 (Nahed et al., 2024). For each time step $t_n \rightarrow t_{n+1}$, a realization

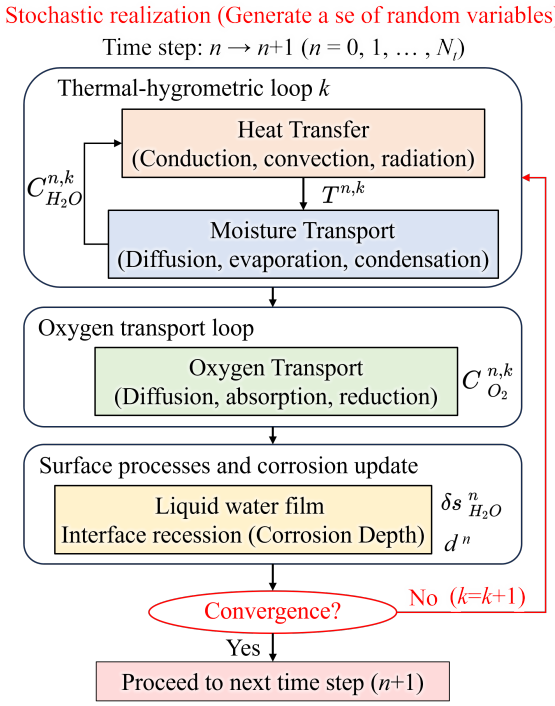


Figure 3. Stochastic finite element solution procedure for the coupled thermo-hydro-chemical corrosion model. At each time step, random realizations generated from the truncated KL expansion are propagated through the heat-transfer, moisture-transport, oxygen-transport, and corrosion-update loops until convergence is achieved.

of the stochastic parameters is first generated from the truncated KL expansion. The coupled THC equations are then solved through a sequential iterative procedure. The thermal-hygrometric loop is considered converged when the relative changes of temperature and moisture concentration between two successive iterations fall below a prescribed tolerance ε. Subsequently, the oxygen transport equation is solved and the corrosion depth is updated. The iterative procedure continues until the relative variation of all primary field variables satisfies the convergence criterion

$$\frac{||\mathbf{u}^{k+1} - \mathbf{u}^k||}{\mathbf{u}^k} < \varepsilon. \tag{7}$$

Once convergence is achieved, the solution is accepted and the algorithm proceeds to the next time step. This staggered stochastic finite element strategy enables efficient simulation of long-term corrosion evolution while preserving the coupling among thermal, moisture, oxygen, and corrosion processes.

3. Numerical result illustration

3.1. Computational Setup

To demonstrate the proposed framework, we considered a 3D local interface segment is considered to investigate stochastic corrosion evolution. The computaional geometry is illustrated in Figure 4. Small interface irregularities are introduced to represent the geometric roughness of the material surfaces. The thermal conductivity, moisture diffusivity, oxygen diffusivity, and corrosion coefficient are treated as uncertain parameters and represented through truncated KL expansions. The resulting stochastic model is solved using the solution procedure described in Figure 3. Simulations are performed over a time horizon ranging from 10^{-1} to 10^4 years to investigate the long term probabilistic evolution of corrosion.

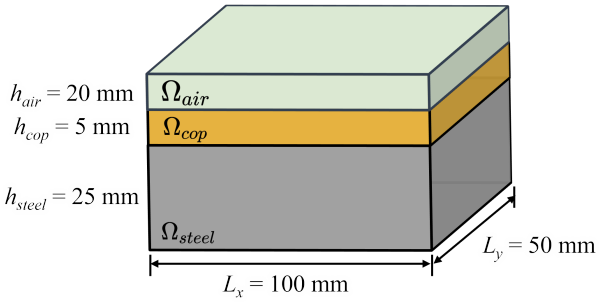


Figure 4. Computational geometry adopted for the stochastic corrosion analysis, including geometrical dimensions and interface roughness.

3.2. Probabilistic Corrosion Evolution

The probabilistic evolution of corrosion depth predicted by the proposed framework is shown in Figure 5. The mean corrosion depth increases continuously over time, while the uncertainty band expands as the stochastic effects accumulate during long-term degradation. At early times, corrosion growth remains relatively slow and the associated uncertainty is limited. As the exposure period increases, the coupled THC processes progressively amplify the influence of uncertain environmental and material parameters, resulting in a broader distribution of possible corrosion depths. The inset Probability density functions (PDFs) further illustrate the evolution of uncertainty. At short exposure times, the probability density is concentrated around small corrosion depths, indicating limited degradation. As time increases, the distribution shifts toward larger corrosion depths and becomes progressively wider, reflecting increased variability in corrosion progression. These results demonstrate the capability of the proposed stochastic framework to capture not only the mean corrosion trend but also the associated uncertainty throughout the repository lifetime.

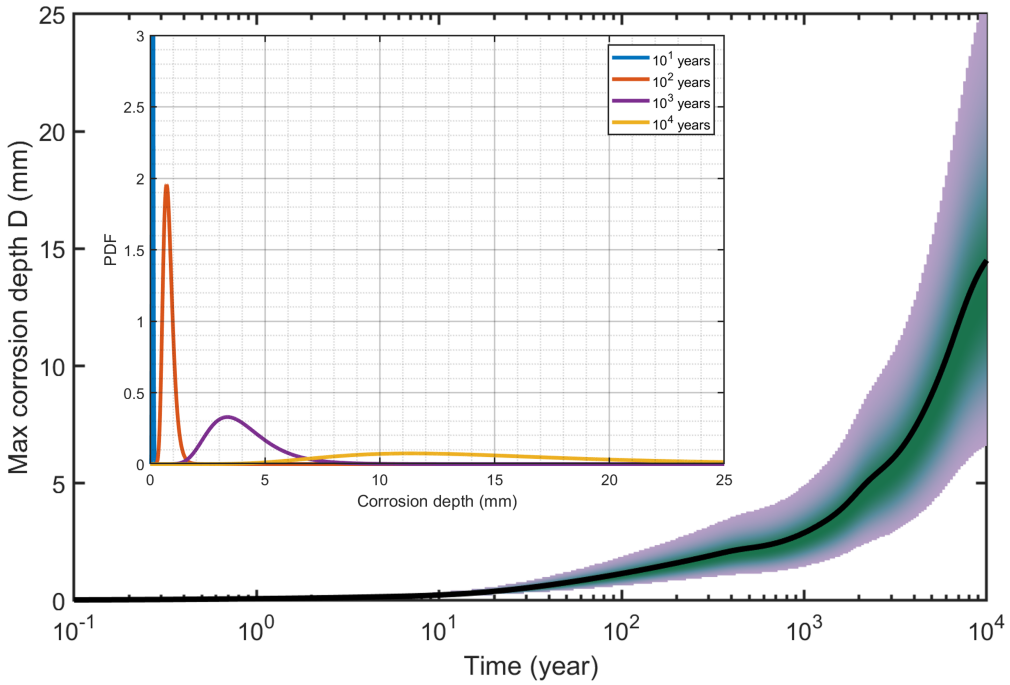


Figure 5. Probabilistic evolution of corrosion depth over geological time scales. The solid curve denotes the mean corrosion depth, while the shaded region represents the uncertainty envelope. The inset shows the evolution of the corresponding probability density functions at selected times.

3.3. Spatial Evolution of Multiphysics Fields

Figure 6 presents the spatial evolution of the temperature field, oxygen concentration field, and interfacial corrosion damage field at 10^2, 10^3, and 10^4 years. The temperature field gradually approaches thermal equilibrium as the decay heat generated by the waste decreases over time. Consequently, thermal gradients become less pronounced during long-term repository operation. A significant depletion of oxygen is observed as corrosion reactions consume the available oxygen near the interface. At later times, the system evolves toward predominantly anoxic conditions, which substantially influences the corrosion kinetics. The interfacial corrosion field exhibits progressive degradation concentrated near the material interfaces. As time increases, the corrosion zone expands and the maximum corrosion depth increases significantly. The spatial variability observed in the corrosion field is a direct consequence of the uncertain material properties and environmental conditions represented in the stochastic model. Overall, the results indicate that uncertainty propagation through the coupled THC processes can lead to substantial variability in long-term corrosion predictions, highlighting the importance of probabilistic assessment for repository safety evaluation.

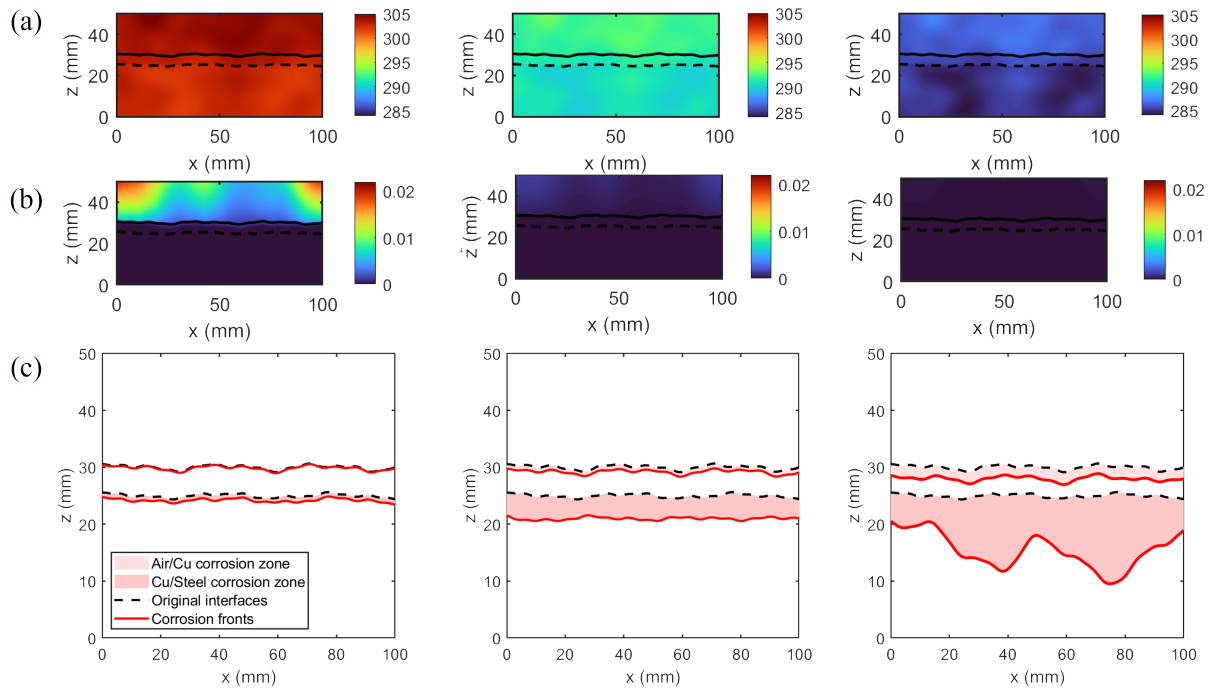


Figure 6. Spatial evolution of temperature (a), oxygen concentration (b), and interfacial corrosion fields (c) at $L_y = 0$ (left for $t = 10^2$, middle for $t = 10^3$, right for $t = 10^4$). The results illustrate the coupled influence of thermal transport, oxygen depletion, and corrosion progression during long-term repository operation.

4. Conclusion

This study presented a stochastic finite element framework for the probabilistic assessment of multiphysics-driven corrosion in nuclear waste canisters. The proposed approach combines coupled THC processes with stochastic representations of uncertain material and environmental parameters, enabling efficient simulation of long-term corrosion evolution under repository conditions. Numerical examples demonstrated the capability of the proposed framework to predict both the mean evolution and the uncertainty of corrosion depth over geological time scales. The probabilistic results showed a continuous increase in corrosion depth accompanied by a progressive expansion of uncertainty. The spatial distributions of temperature, oxygen concentration, and corrosion damage further illustrated the strong interactions among the coupled THC processes and their influence on long-term canister degradation. The resulting stochastic solutions provide direct access to PDFs, ensemble statistics, and spatial distributions of corrosion damage. These probabilistic outputs establish a foundation for subsequent reliability evaluation, global sensitivity analysis, and inverse identification of uncertain corrosion-related parameters, thereby supporting risk-informed safety assessment of deep geological repositories.

The present work focused on spatially varying interfacial corrosion and did not explicitly consider localized pitting corrosion or microbiologically influenced corrosion. Nevertheless, the proposed framework provides an efficient and flexible foundation for uncertainty quantification in corrosion analysis and safety assessment of deep geological disposal systems. Future work will incorporate more detailed corrosion mechanisms, including localized corrosion phenomena and additional chemical reactions, as well as experimental calibration and validation of the stochastic model parameters for realistic repository environments.

References

Arregui-Mena, J. D., L. Margetts, and P. M. Mummery: 2016, 'Practical application of the stochastic finite element method'. *Archives of computational methods in engineering* **23**(1), 171–190.

Frankel, G. S., J. D. Vienna, J. Lian, X. Guo, S. Gin, S. H. Kim, J. Du, J. V. Ryan, J. Wang, W. Windl, et al.: 2021, 'Recent advances in corrosion science applicable to disposal of high-level nuclear waste'. *Chemical reviews* **121**(20), 12327–12383.

Guo, X., S. Gin, P. Lei, T. Yao, H. Liu, D. K. Schreiber, D. Ngo, G. Viswanathan, T. Li, S. H. Kim, et al.: 2020, 'Self-accelerated corrosion of nuclear waste forms at material interfaces'. *Nature materials* **19**(3), 310–316.

Hughes, T. J., M. Papadrakakis, and T. Zohdi: 2022, 'Of computer methods in applied mechanics and engineering'. *Computer Methods in Applied Mechanics and Engineering* **397**, 115206.

Järvine, A. K., A. G. Murchison, P. G. Keech, and M. D. Pandey: 2019, 'A probabilistic model for estimating the life expectancy of used nuclear fuel containers in a Canadian geological repository: Baseline model'. *Nuclear Engineering and Design* **352**, 110202.

King, F., M. Kolář, I. Puigdomenech, P. Pitkänen, and C. Lilja: 2021, 'Modeling microbial sulfate reduction and the consequences for corrosion of copper canisters'. *Materials and Corrosion* **72**(1-2), 339–347.

Kurgyis, K., P. Achtziger-Zupančič, M. Bjorge, M. S. Boxberg, M. Broggi, J. Buchwald, O. G. Ernst, J. Flügge, A. Ganopolski, T. Graf, et al.: 2024, 'Uncertainties and robustness with regard to the safety of a repository for high-level radioactive waste: introduction of a research initiative'. *Environmental Earth Sciences* **83**(2), 82.

Liu, J., C. Yang, R. Song, Q. Wanyan, A. Nakayama, and J. Xiong: 2025, 'Advances of Geological Storage Engineering and Technology'. *GeoStorage* **1**(1), 1–26.

Nahed, C., J. de Lamare, and A. Pasteau: 2024, 'Errors in model development; the verification of a thermo-hygro-corrosive model for radioactive waste storage applications'. In: *16ème Colloque National en Calcul de Structures (CSMA 2024)*.

Zheng, Z., X. Wang, J. Flügge, and T. Nagel: 2025, 'A stochastic modeling framework for radionuclide migration from deep geological repositories considering spatial variability'. *Advances in Water Resources* **203**, 105003.

Probabilistic reliability evaluation of autonomous navigation for firefighting robots in uncertain environments

Zhaowei Zhou[1)], Ruikun Li[1)], Fang Cong[1)], and Wei Shi[1, *)]
1) Shanghai fire research institute of MEM, Shanghai 200032, China, zhouzhaowei0206 @sina.com; ruikunli@sina.com; congfang@sina.com
**) Corresponding author, shiwei11005@sina.com (W.S.)*

Abstract: Autonomous navigation is a mission-critical capability for firefighting robots operating in hazardous, unstructured, and highly uncertain environments. However, existing evaluation approaches are largely based on deterministic performance metrics and provide limited support for quantifying navigation reliability under uncertainty. This limitation hinders objective benchmarking and standardized assessment across different robotic platforms and operating conditions. This paper proposes an uncertainty-aware reliability assessment framework for autonomous navigation of firefighting robots. The framework integrates multi-source sensing, trajectory reconstruction, deviation analysis, and probabilistic performance evaluation into a unified pipeline. A nearest-neighbor-based trajectory matching method is employed to quantify discrepancies between reference and executed trajectories under asynchronous and non-uniform sampling conditions. To move beyond deterministic evaluation, key performance indicators, including trajectory deviation, completion time, and obstacle avoidance success rate, are modeled as stochastic variables, from which probabilistic reliability measures are derived. Experimental studies were conducted in controlled environments with static, dynamic, and complex obstacle configurations. The results show that the proposed framework effectively captures both navigation accuracy and performance variability across scenarios. In particular, the reliability metrics provide a more informative assessment than conventional threshold-based indicators by explicitly reflecting the probability of satisfying navigation requirements under uncertainty. The proposed framework offers a systematic and quantitative approach for reliability assessment of autonomous navigation systems and provides practical value for performance benchmarking, system validation, and algorithm improvement in firefighting robotics and related mobile robotic applications.

Keywords: firefighting robot; autonomous navigation; reliability assessment; trajectory deviation

1. Introduction

Firefighting robots are increasingly deployed in hazardous environments such as industrial facilities, underground infrastructures, and disaster-response sites, where high temperatures, dense smoke, toxic gases, unstable structures, and cluttered terrain pose substantial risks to human responders. In such scenarios, autonomous navigation is a prerequisite for effective task execution, including environment exploration, obstacle avoidance, target localization, and continuous mobility under limited visibility or restricted communication conditions. Reliable navigation capability improves operational efficiency and reduces human exposure to life-threatening conditions (Al Mahmud et al., 2024; Liu et al., 2024; Usinskis et al., 2025; Waga et al., 2025).

Recent advances in sensing, path planning, and motion control have significantly improved the navigation performance of mobile robots in complex environments. Existing studies have mainly focused on obstacle detection, sensor fusion, path planning algorithms, and online replanning strategies (AlAli and Alabady, 2022; Ghauri et al., 2024; Dong et al., 2025; Deng et al., 2026). While these developments have enhanced the

© 2026 by the author. This work is licensed under the Creative Commons Attribution 4.0 International License (CC BY 4.0).

autonomy of robotic systems, the evaluation of navigation performance remains comparatively underdeveloped. In many cases, performance is assessed using deterministic indicators such as trajectory deviation, completion time, collision count, or task success rate. These metrics are useful at a basic level, but they are often scenario-specific, insufficiently standardized, and not explicitly linked to uncertainty (Kim et al., 2024; Raoufi et al., 2025).

This limitation is particularly critical for firefighting robots. Their operating environments are inherently uncertain due to sensing noise, communication disturbances, environmental variability, and control imperfections. As a result, navigation performance cannot be fully characterized by single deterministic values alone. Two systems may exhibit similar average trajectory errors while having substantially different levels of robustness and failure risk under dynamic obstacles or changing terrain conditions. Therefore, a meaningful evaluation framework should not only measure navigation accuracy but also quantify the likelihood that the system satisfies required performance thresholds under uncertainty (Stephens et al., 2024; Chen and Xiao, 2025; Rado et al., 2025).

The same trend is visible in localization and SLAM research. Multi-sensor fusion methods based on UWB, IMU, wheel odometry, LiDAR, and camera sensing have significantly improved the resilience of mobile robot localization, but they also make evaluation more complex because uncertainty propagates across sensing, estimation, and control stages (Ji et al., 2024; Deng et al., 2025; Cao et al., 2025; Fan et al., 2025). Foundational surveys on motion planning and SLAM remain highly relevant here because they show that performance should be discussed jointly in terms of path quality, localization consistency, and robustness to environmental variation (Paden et al., 2016; Cadena et al., 2016).

In reliability engineering, mixed uncertainties, cross-stage error propagation, and system-level risk aggregation have been addressed through probabilistic and evidence-based modeling frameworks (Mi et al., 2022; Bensaci et al., 2023; Pan et al., 2024). These ideas are highly relevant to mobile robots, yet a unified reliability-oriented framework for evaluating firefighting robot navigation remains underdeveloped. Existing robotic studies typically focus on algorithmic improvement, while standardized and uncertainty-aware evaluation frameworks are still rare (Nrioui et al., 2019). A recent digital-twin-based navigation evaluation study underscores this gap by explicitly calling for multi-metric and uncertainty-aware validation in robotics (Bergs et al., 2025).

To address these challenges, this paper proposes an uncertainty-aware reliability assessment framework for autonomous navigation of firefighting robots. The main contributions are threefold. First, a unified evaluation framework is established by integrating scenario configuration, trajectory generation, data acquisition, and probabilistic performance analysis into a closed-loop pipeline. Second, a nearest-neighbor-based trajectory deviation quantification method is developed for asynchronous and non-uniform sampling conditions. Third, a probabilistic reliability metric system is introduced to estimate the likelihood that predefined navigation requirements are satisfied under uncertainty.

2. Methodology

2.1 Problem Formulation

2.1.1 *Trajectory Representation*

In an autonomous navigation task, the motion of a firefighting robot can be represented as a trajectory in a two-dimensional workspace. Let the reference trajectory generated by the planning module be denoted by Eq. (1).

$$\Gamma^* = \left\{ \mathbf{p}^*(t) = (x^*(t), y^*(t)) \mid t \in [0, T_f] \right\} \tag{1}$$

Let the actual executed trajectory be Eq. (2).

$$\Gamma = \{\mathbf{p}(t) = (x(t), y(t)) \mid t \in [0, T_f]\} \tag{2}$$

In practice, the reference trajectory is typically available as a continuous curve or a densely sampled sequence, whereas the executed trajectory is reconstructed from discrete measurements acquired by the sensing system. Therefore, the actual trajectory is expressed as Eq. (3).

$$\Gamma = \{\mathbf{p}_i = (x_i, y_i)\}_{i=1}^{N} \tag{3}$$

2.1.2 *Trajectory Deviation Definition*

To quantify the discrepancy between the reference trajectory and the actual executed trajectory, a nearest-neighbor matching strategy is adopted. For each sampled point pi on the executed trajectory, the closest point on the reference trajectory is determined by Eq. (4).

$$\mathbf{p}_i^* = \arg \min_{\mathbf{q} \in \Gamma^*} \| \mathbf{p}_i - \mathbf{q} \| \tag{4}$$

The point-wise trajectory deviation is then defined as Eq. (5).

$$e_i = \| \mathbf{p}_i - \mathbf{p}_i^* \| \tag{5}$$

Based on the matched point pairs, the root mean square (RMS) trajectory error is computed as Eq. (6).

$$e_{\mathrm{RMS}} = \sqrt{\frac{1}{N} \sum_{i=1}^{N} e_i^2} \tag{6}$$

In addition to the RMS error, the maximum deviation and deviation variance are also considered to capture the magnitude and variability of path-tracking errors.

To further characterize deviation behavior, the maximum trajectory deviation, mean trajectory deviation, and deviation variance are defined as Eqs. (7) - (9).

$$E_{max} = \max_{1 \le i \le N} e_i \tag{7}$$

$$\mu_E = \frac{1}{N} \sum_{i=1}^{N} e_i \tag{8}$$

$$\sigma_E^2 = \frac{1}{N} \sum_{i=1}^{N} (e_i - \mu_E)^2 \tag{9}$$

These metrics jointly reflect the overall magnitude, worst-case behavior, and fluctuations in trajectory-tracking errors.

2.1.3 *Performance Variables under Uncertainty*

To characterize navigation performance, several key variables are introduced: trajectory deviation *E*, task completion time T_c, travel distance *D*, and obstacle avoidance success indicator *S*. In this study, *E* denotes a trajectory-deviation-related performance variable, which can be instantiated by metrics such as e_{RMS}, μ_E, or E_{max}, depending on the evaluation objective.

In realistic firefighting environments, these variables are influenced by multiple uncertainty sources, including measurement noise, obstacle dynamics, environmental disturbances, and actuation errors. Consequently, they are modeled as random variables rather than fixed deterministic quantities. This probabilistic formulation provides the basis for reliability-oriented performance assessment. Instead of merely reporting whether a metric exceeds a threshold in a single trial, the objective is to estimate the probability that a navigation system satisfies predefined requirements over repeated trials or uncertain operating conditions (Stephens et al., 2024; Lind et al., 2024; Pan et al., 2024).

2.2 RELIABILITY ASSESSMENT METHODOLOGY

2.2.1 *Evaluation Framework*

The proposed framework consists of four tightly coupled components: scenario configuration, multi-source sensing and data acquisition, trajectory reconstruction and deviation analysis, and probabilistic reliability evaluation.

First, the testing environment is configured by defining the workspace geometry, obstacle layout, start and target positions, and scenario-specific constraints. The framework supports both static and dynamic

obstacle settings, allowing the navigation system to be examined under different levels of environmental complexity. Second, multi-source data are collected during task execution. The experimental platform integrates ultra-wideband (UWB) positioning and inertial measurement unit (IMU) sensing to obtain robot position, motion state, and temporal information. The UWB system provides the global positioning reference, while the IMU contributes short-term motion dynamics and improves trajectory reconstruction consistency. All data streams are time-synchronized and recorded for subsequent analysis. Third, the executed trajectory is reconstructed from the measured data and compared with the reference trajectory. Deviation metrics are computed through nearest-neighbor matching, enabling robust trajectory comparison under asynchronous and non-uniform sampling conditions. Finally, the obtained performance indicators are analyzed statistically and transformed into probabilistic reliability measures. This step allows the framework to move beyond deterministic threshold checking and to explicitly quantify the likelihood that navigation requirements are satisfied (Liu et al., 2024; Usinskis et al., 2025; Bergs et al., 2025). The overall framework forms a closed-loop assessment pipeline, from controlled experimentation to quantitative reliability characterization, and supports repeatable comparison across different scenarios and robotic platforms. The reliability assessment framework for autonomous navigation of firefighting robots is shown in Figure 1.

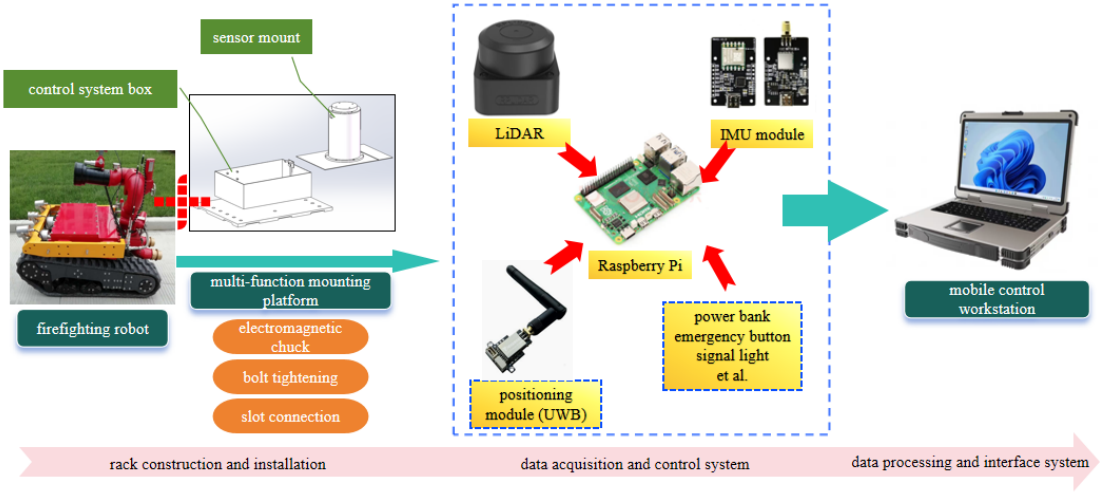


Figure 1. Reliability assessment framework for autonomous navigation of firefighting robots.

2.2.2 *Trajectory Deviation Analysis*

2.2.2.1 *Nearest-Neighbor Matching*

Trajectory comparison is complicated by the fact that the reference and executed trajectories often have different point densities and non-uniform time sampling. Direct one-to-one point correspondence is therefore generally unavailable. To address this issue, nearest-neighbor matching is employed to associate each measured point on the executed trajectory with the closest point on the reference trajectory. Compared with strict time-based alignment, this strategy is less sensitive to local speed variations and irregular sampling intervals. It provides a geometrically meaningful measure of deviation and is particularly suitable for autonomous navigation tasks in which the executed path may deviate locally due to obstacle avoidance or replanning (Xu et al., 2025; Xu, 2024).

2.2.2.2 *Statistical Characterization of Deviation*

Trajectory deviation is not fully represented by a single error metric. For this reason, the framework characterizes deviation using multiple statistical descriptors, including the mean deviation μ_E, RMS deviation e_{RMS}, maximum deviation Emax, and deviation variance σ_E^2. These indicators reflect different aspects of

performance. The mean deviation represents the average path-tracking quality, the RMS deviation reflects the overall error magnitude, the maximum deviation captures the local worst-case behavior, and the deviation variance characterizes stability and fluctuation. Together, these metrics provide a richer description of navigation performance than any single error measure alone. (Katona et al., 2024; Bergs et al., 2025; Tran et Ryoo, 2025).

2.2.2.3 *Segment-Wise Analysis*

Navigation tasks often consist of several motion phases, such as straight-line travel, turning, obstacle avoidance, and path recovery. The same robot may perform well during nominal tracking but exhibit larger errors during maneuvering or dynamic obstacle interaction. To identify such localized performance variations, the trajectory can be segmented into different motion phases, and deviation metrics can be calculated separately for each segment. Segment-wise analysis improves interpretability and helps identify the specific navigation stages that contribute most strongly to performance degradation. This is particularly useful for diagnosing the impact of obstacle interactions and environmental complexity.

2.2.3 *Probabilistic Reliability Modeling*

2.2.3.1 *Uncertainty Sources*

Navigation performance variability arises from multiple sources of uncertainty. In the present framework, these sources are grouped into three categories. The first category is measurement uncertainty, including UWB positioning noise, IMU drift, packet loss, and timestamp mismatch. These effects influence trajectory reconstruction accuracy and therefore affect all downstream deviation metrics. The second category is environmental uncertainty, including changes in obstacle position, dynamic obstacle motion, terrain variation, and disturbances caused by cluttered surroundings. These factors increase task difficulty and alter the motion response of the robot. The third category is control uncertainty, including path-tracking errors, actuation delay, wheel slip, and controller response variation. These uncertainties directly influence the difference between the reference path and the executed path. The combined effect of these uncertainty sources results in variability of the measured navigation performance across repeated trials (Al Mahmud et al., 2024; Xu et al., 2025).

2.2.3.2 *Reliability Metrics*

To quantify navigation reliability, deterministic thresholds are extended to probabilistic indicators. Let δ_E denote the acceptable threshold for trajectory deviation. The reliability associated with deviation is defined as Eq. (10).

$$R_E = P(E \leq \delta_E) \tag{10}$$

This metric expresses the likelihood that the trajectory deviation remains within the acceptable range. Similarly, if δ_T is the maximum acceptable completion time, the time-related reliability is defined as Eq. (11).

$$R_T = P(T_c \leq \delta_T) \tag{11}$$

For obstacle avoidance success, the corresponding reliability can be defined as Eq. (12).

$$R_S = P(S = 1) \tag{12}$$

Where S=1 indicates successful completion of the obstacle avoidance task without collision or task failure, and S=0 indicates failure. These definitions transform conventional threshold-based performance evaluation into a reliability-oriented interpretation.

2.2.3.3 *Composite Reliability Index*

In practical applications, autonomous navigation performance depends on multiple criteria rather than a single metric. To aggregate different aspects of performance into a single interpretable indicator, a composite reliability index is introduced in Eq. (13) – (14) (Mi et al., 2022; Bensaci et al., 2023; Pan et al., 2024).

$$R = w_1 R_E + w_2 R_T + w_3 R_S \tag{13}$$

Zhaowei Zhou, Ruikun Li, Fang Cong and Wei Shi

$$w_1 + w_2 + w_3 = 1 \qquad w_1, w_2, w_3 \geq 0 \tag{14}$$

The weighting factors can be adjusted according to mission requirements. For example, in time-critical rescue missions, completion time may be assigned a higher weight, whereas in high-risk environments, avoidance success and trajectory control may receive greater emphasis.

2.2.3.4 *Distribution Estimation*

The proposed framework adopts a data-driven strategy for reliability estimation. Rather than assuming a specific parametric distribution for each performance variable, empirical distributions are constructed from repeated experimental trials. Based on these empirical samples, probabilities of satisfying performance thresholds are estimated directly. This approach is advantageous for experimental robotic systems because the underlying distributions may deviate from standard Gaussian assumptions, especially in the presence of nonlinear path replanning, intermittent disturbances, or heterogeneous obstacle interactions. In addition to empirical probabilities, conventional statistical descriptors such as sample mean, variance, and confidence intervals can also be reported to support interpretation (Lind et al., 2024; Bergs et al., 2025).

3. Experimental Validation and Results

3.1 Experimental Setup

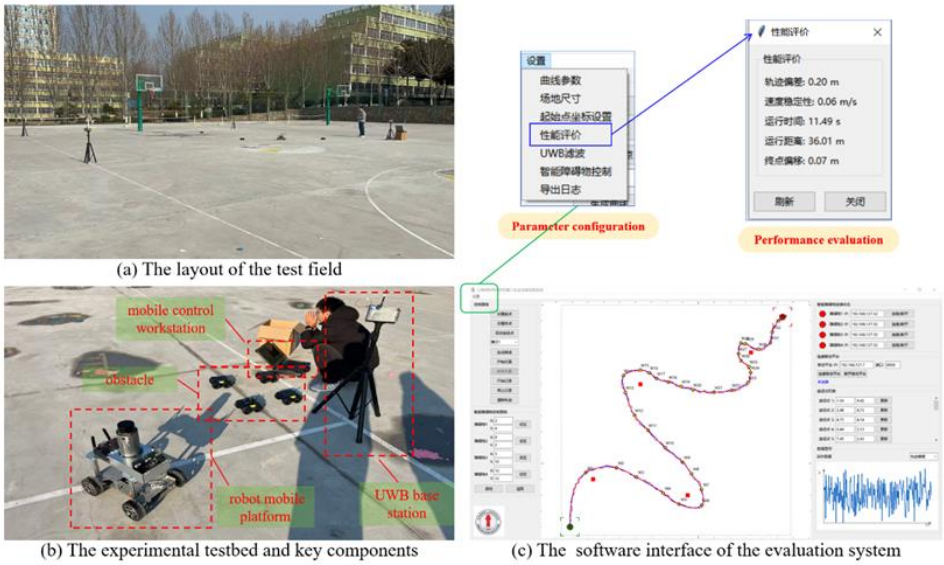


Figure 2. Layout of the test field.

The experimental platform was constructed in a controlled outdoor environment to evaluate the proposed framework under representative navigation conditions. A rectangular test field of approximately 15 m × 15 m was established, and different obstacle configurations were deployed to create static, dynamic, and complex scenarios. The robot was equipped with a multi-sensor measurement module integrating UWB positioning and IMU sensing. The UWB system provided a global spatial reference with centimeter-level positioning capability, while the IMU supplied motion-state information to improve consistency in trajectory reconstruction (Ji et al., 2024; Deng et al., 2025; Tran and Ryoo, 2025; Cao et al., 2025). A workstation was used for scenario configuration, task execution control, data acquisition, and real-time monitoring. All sensor streams were synchronized and stored for offline analysis. The position data were sampled at a sufficiently high rate to support trajectory reconstruction and statistical deviation analysis. Figure 1 presents the standardized layout of the test field, including the start point, target point, and representative obstacle configuration.

3.2 Test Scenarios

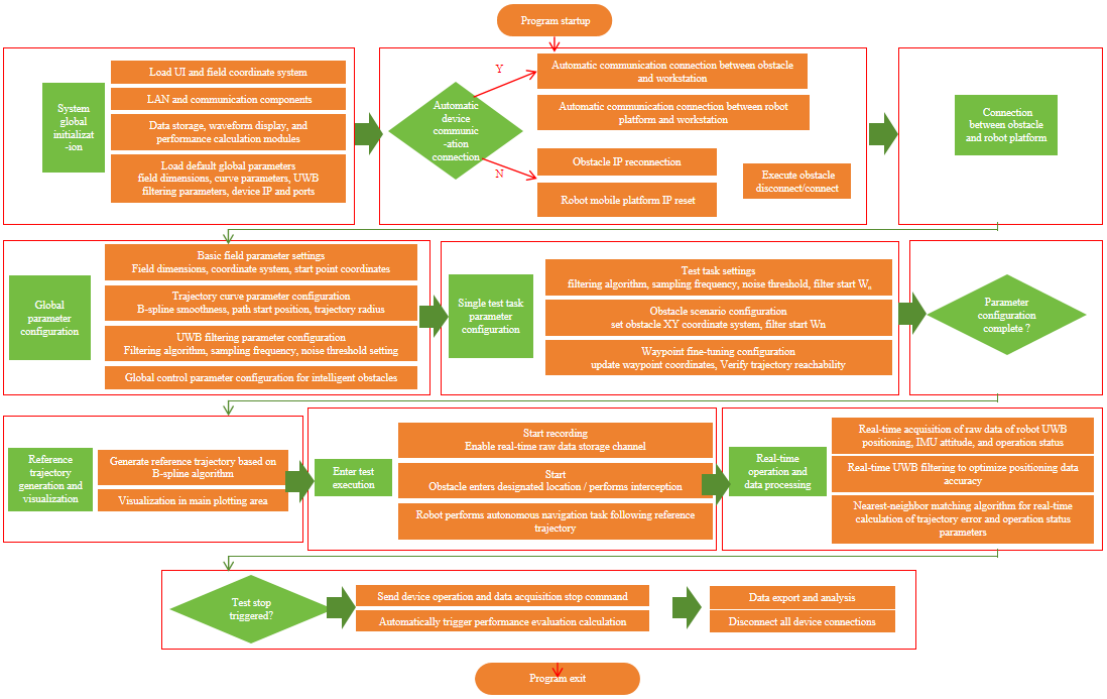


Figure 3. Flowchart of the main program.

Three types of scenarios were considered in the experiments. In the static obstacle scenario, fixed obstacles were placed along or near the planned path. The robot was required to navigate from the start point to the target while autonomously avoiding collisions. This scenario evaluates baseline path-tracking accuracy and obstacle avoidance capability in a relatively stable environment. In the dynamic obstacle scenario, moving obstacles were introduced to simulate unexpected disturbances during navigation. The robot was required to respond online to changes in obstacle position and to modify its path accordingly. This scenario emphasizes responsiveness, replanning robustness, and performance degradation under dynamic interference. In the complex path scenario, multiple obstacles were arranged in a denser and less regular pattern, generating narrow passages and multiple turning regions. This setting increases geometric constraints and better reflects cluttered or partially unstructured environments. It is intended to evaluate navigation behavior under higher environmental complexity (Chen and Xiao, 2025; Rado et al., 2025; Deng et al., 2026). For each scenario, repeated trials were conducted to obtain statistically meaningful results. These three scenarios are implemented using the software shown in Figure 2(c), and the program flowchart is presented in Figure 3.

3.3 Performance Metrics

The following performance indicators were evaluated: RMS trajectory error e_{RMS}, maximum trajectory deviation Emax, task completion time T_c, obstacle avoidance success indicator S and its empirical success probability, probabilistic reliability measures R_E, R_T, and R_S, and composite reliability index R. The deviation-related threshold δ_E and the time-related threshold δ_T were predefined according to the navigation performance requirements of the test task. These thresholds enable the estimation of probabilistic reliability from repeated trials (Bergs et al., 2025).

3.4 Results and Reliability Analysis

Zhaowei Zhou, Ruikun Li, Fang Cong and Wei Shi

3.4.1 *Trajectory Comparison*

The trajectory tracking performance in static and dynamic obstacle scenarios can be quantitatively distinguished by the maximum trajectory deviation and the locations of critical deviations. In the static scenario, the system achieves an average maximum trajectory deviation of 0.098 m, which occurs only at path turning points, indicating good overall tracking consistency. In the dynamic scenario, due to obstacle interaction and online path adjustment, the average maximum trajectory deviation increases to 0.365 m and is concentrated in key regions of obstacle interaction, where local deviations become significantly larger. These results suggest that visual inspection of a single trajectory is insufficient for rigorous evaluation; instead, statistical characterization from repeated trials is necessary to effectively identify performance variability and quantify system reliability.

3.4.2 *Statistical Performance Comparison*

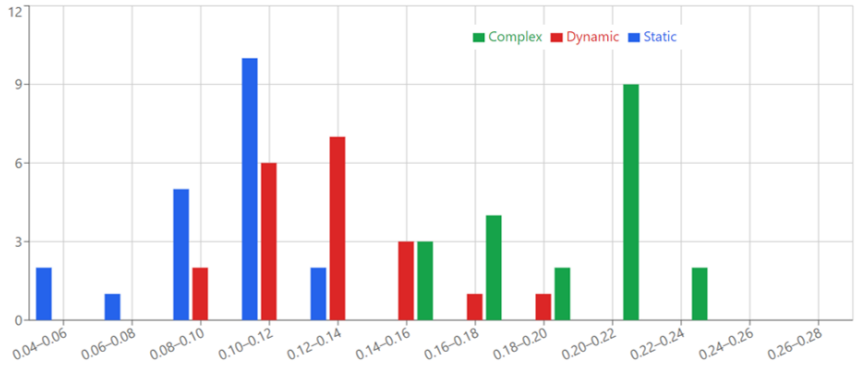
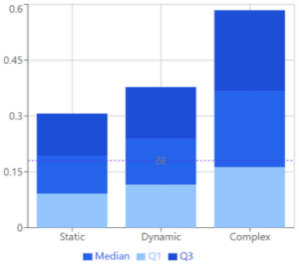
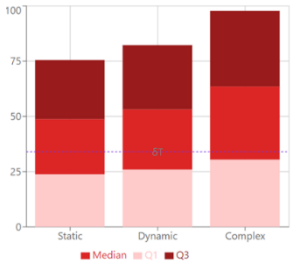


Figure 4. Empirical distribution of e_{RMS}.



(a). Box summaries of e_{RMS}



(b). Box summaries of T_c

Figure 5. Boxplots of RMS error and task completion time under different scenarios.

Figure 4 shows the empirical distribution of the RMS trajectory error *e*RMS for the three tested scenarios. The static scenario exhibited the smallest deviation and the narrowest distribution, indicating relatively stable tracking performance. The dynamic scenario showed larger deviation and higher variability, reflecting the influence of moving obstacles and replanning behavior. The complex scenario exhibited the broadest distribution, suggesting that environmental complexity substantially increases the uncertainty of navigation performance. Figure 5 compares the RMS error and completion time across scenarios using boxplots. Both the median value and dispersion increased from static to dynamic and complex settings. This trend indicates that the navigation task becomes progressively more difficult as obstacle interaction and geometric constraints increase. These observations are consistent with the expected effect of uncertainty and environmental complexity. They also demonstrate that repeated-trial statistics provide more informative evidence than single-trial deterministic measurements.

3.4.3 *Reliability Evaluation*

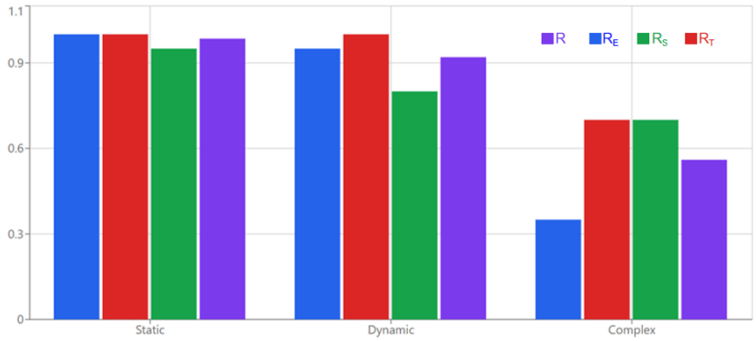


Figure 6. Reliability metrics comparison.

Based on repeated trials, probabilistic reliability measures were estimated for each scenario. The deviation-related reliability RE reflects the probability that trajectory deviation remains below the acceptable threshold. The time-related reliability RT reflects the probability that task completion time satisfies the required upper bound, and RS represents the empirical success probability of obstacle avoidance. Figure 5 compares the reliability metrics across scenarios. The static scenario achieved the highest reliability values, while both the dynamic and complex scenarios showed reduced reliability, particularly in deviation-related performance. The composite reliability index also decreased with increasing environmental complexity.

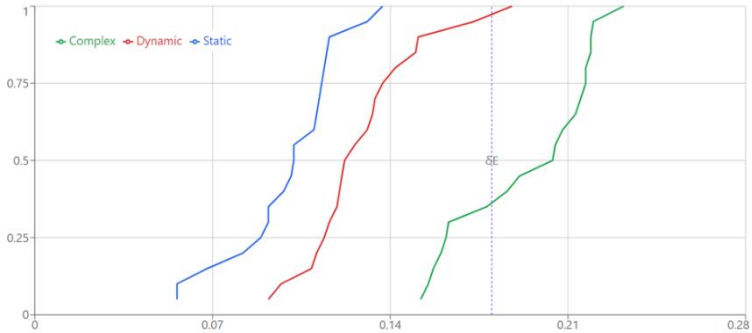


Figure 7. ECDF of e_{RMS}.

To further explain the deviation-related reliability, Figure 6 presents the empirical cumulative distribution functions (ECDFs) of the RMS trajectory error e_{RMS} under different scenarios. In correspondence with the bar-chart results shown in Figure 5, Figure 6 provides a direct visualization of the cumulative probability that $e_{RMS} \leqslant \delta_E$ for a given deviation threshold δ_E. The static scenario exhibits the leftmost and steepest cumulative curve, indicating smaller overall deviation and the highest probability of satisfying the threshold. The dynamic scenario shows intermediate behavior, whereas the complex scenario is shifted to the right, implying larger errors, stronger dispersion, and a substantially lower probability of meeting the same requirement. This distribution-level evidence further confirms the comparative results of R_E shown in Figure 5. In this sense, the ECDF provides a graphical interpretation of the deviation-related reliability R_E.

These results demonstrate that the proposed reliability formulation captures not only average performance but also performance consistency under uncertainty. In particular, two scenarios with similar mean values may still differ substantially in reliability if one scenario exhibits a larger spread or more frequent threshold violations. The distributional evidence provided by Figure 6 further illustrates that, compared with conventional deterministic evaluation, probabilistic reliability measures offer a more informative characterization of navigation performance under uncertainty.

4. Discussion

The experimental results demonstrate that autonomous navigation performance cannot be adequately described by deterministic metrics alone. Although trajectory-related indicators such as e_{RMS}, Emax, and T_c are useful baseline measures, they do not directly reveal the consistency of performance across repeated trials or the likelihood of satisfying operational requirements under uncertainty. The proposed framework addresses this limitation by transforming key performance indicators into probabilistic reliability measures.

Another important observation is that environmental complexity has a clear and systematic influence on navigation reliability. As the task environment changes from static to dynamic and complex obstacle configurations, both performance variability and threshold violation frequency increase. This result is consistent with the practical challenges encountered by firefighting robots in real applications, where sensing noise, local disturbances, and unstructured surroundings interact in a non-negligible manner (Pan et al., 2024; Bensaci et al., 2023).

The present study has several limitations. The experiments were conducted in controlled test conditions and therefore do not yet include all factors present in real fireground environments, such as dense smoke, severe thermal interference, uneven surfaces, or reduced sensor visibility. The current reliability estimation is based on empirical repeated-trial statistics, which are appropriate for data-driven evaluation but could be further enhanced by more advanced uncertainty quantification techniques. The experiments focused primarily on trajectory-level performance and did not explicitly model semantic perception reliability or mission-level task success (AlAli and Alabady, 2022; Dong et al., 2025; Kilic et al., 2025).

Despite these limitations, the proposed framework provides a practical and extensible basis for standardized performance evaluation of firefighting robot navigation. It is particularly suitable for benchmarking, iterative algorithm testing, and comparative assessment under controlled scenario variations.

5. Conclusion

This study proposed an uncertainty-aware reliability assessment framework for autonomous navigation of firefighting robots. By integrating nearest-neighbor-based trajectory deviation analysis with probabilistic reliability modeling, the framework extends conventional deterministic evaluation into a quantitative uncertainty-aware assessment scheme.

Experimental results from static, dynamic, and complex obstacle scenarios show that the proposed method captures both navigation accuracy and reliability degradation under increasing environmental complexity. The results also demonstrate that probabilistic reliability metrics provide a more informative characterization than conventional deterministic indicators.

Future work will focus on more realistic fireground conditions, including smoke interference, uneven terrain, and multi-robot cooperation, as well as on advanced uncertainty quantification and learning-based reliability modeling.

Acknowledgements

This work was supported by the National key research and development program project under Grant 2023YFC3011005.

End Notes

Table I. Nomenclature

symbol	Definition	Unit / Type	Remarks
Γ^*	Reference trajectory	Trajectory set	
Γ	Executed trajectory	Trajectory set	

$p^*(t)$	Point on the reference trajectory at time t	Position vector	
$p(t)$	Point on the executed trajectory at time t	Position vector	
$x^*(t)$	x-coordinate of the reference trajectory	m	
$y^*(t)$	y-coordinate of the reference trajectory	m	
$x(t)$	x-coordinate of the executed trajectory	m	
$y(t)$	y-coordinate of the executed trajectory	m	
t	Time	s	
T_f	End time of the navigation task	s	
p_i	i-th sampled point on the executed trajectory	Position vector	$p_i = (x_i, y_i)$
x_i	x-coordinate of the i-th sampled point	m	
y_i	y-coordinate of the i-th sampled point	m	
i	Sample index	Integer	i=1, 2,…
N	Number of sampled trajectory points	Count	
p_i^*	Nearest matched point on the reference trajectory for p_i	Position vector	
q	Candidate point on the reference trajectory	Position vector	
$\|\| \bullet \|\|$	Euclidean norm	Operator	Used to compute point-to-point distance
e_i	Point-wise trajectory deviation	m	Distance between pi and pi∗
e_{RMS}	Root mean square trajectory error	m	
E_{max}	Maximum trajectory deviation	m	
μ_E	Mean trajectory deviation	m	
σ_E^2	Variance of trajectory deviation	m^2	
E	Trajectory deviation performance variable	Random variable	
T_c	Task completion time	s	
D	Travel distance	m	
S	Obstacle avoidance success indicator	Binary / random variable	S=1 for successful task completion
δ_E	Acceptable deviation threshold	m	
δ_T	Acceptable time threshold	s	
$P(\cdot)$	Probability operator	Operator	
R_E	Deviation-related reliability	Probability	
R_T	Time-related reliability	Probability	
R_S	Success-related reliability	Probability	
R	Composite reliability index	Dimensionless	
w_1	Weight for deviation-related reliability	Dimensionless	
w_2	Weight for time-related reliability	Dimensionless	
w_3	Weight for success-related reliability	Dimensionless	

References

Al Mahmud, S., Kamarulariffin, A., Ibrahim, A. M., and Mohideen, A. J. H. Advancements and Challenges in Mobile Robot Navigation: A Comprehensive Review of Algorithms and Potential for Self-Learning Approaches. *Journal of Intelligent & Robotic Systems*, 110:120, 2024.

AlAli, Z. T., and Alabady, S. A. A survey of disaster management and SAR operations using sensors and supporting techniques. *International Journal of Disaster Risk Reduction*, 82:103295, 2022.

Zhaowei Zhou, Ruikun Li, Fang Cong and Wei Shi

Bensaci, C., Zennir, Y., Pomorski, D., Innal, F., and Lundteigen, M. A. Collision hazard modeling and analysis in a multi-mobile robots system transportation task with STPA and SPN. *Reliability Engineering & System Safety*, 234:109138, 2023.

Bergs, L., Huber, M., Moriz, A., Göppert, A. M. R., Schmitt, R. H., Chan, F. K. S., Law, Y. N., Pan, X., and Drescher, B. Evaluating mobile robot navigation behavior in flexible assembly systems through digital twin and real-world experiments. *Discover Robotics*, 1:10, 2025.

Cadena, C., Carlone, L., Carrillo, H., Latif, Y., Scaramuzza, D., Neira, J., Reid, I., and Leonard, J. J. Past, Present, and Future of Simultaneous Localization and Mapping: Toward the Robust-Perception Age. *IEEE Transactions on Robotics*, 32(6):1309-1332, 2016.

Cao, Y., Usai, A., Gu, W., and Rizzo, A. Localization Handover for Mobile Robots: A Seamless Indoor-Outdoor Approach. *Journal of Intelligent & Robotic Systems*, 111:82, 2025.

Chen, Y., and Xiao, J. Target Search and Navigation in Heterogeneous Robot Systems with Deep Reinforcement Learning. *Machine Intelligence Research*, 22:79-90, 2025.

Deng, R., Ding, S., Ding, Y., Wang, M., Huang, X., and Usmani, A. S. Autonomous navigation of non-perception firefighting robot through CCTV-informed vision sharing. *Expert Systems with Applications*, 296(Pt D):129210, 2026.

Deng, Z., Zhang, S., Chen, X., and co-authors. Fusion-Based Localization System Integrating UWB, IMU, and VIO. *Applied Sciences*, 15(12):6501, 2025.

Dong, D., Wang, Z., Guan, J., Xiao, Y., and Wang, Y. Research on key technology and application progress of rescue robot in nuclear accident emergency situation. *Nuclear Engineering and Technology*, 57:103457, 2025.

Fan, Z., Zhang, Z., Deng, F., and co-authors. LiDAR, IMU, and camera fusion for simultaneous localization and mapping: a systematic review. *Artificial Intelligence Review*, 58, 174, 2025.

Ghauri, S. A., Sarfraz, M., Qamar, R. A., Sohail, M. F., and Khan, S. A. A Review of Multi-UAV Task Allocation Algorithms for a Search and Rescue Scenario. *Journal of Sensor and Actuator Networks*, 13(5):47, 2024.

Ji, P., Duan, Z., and Xu, W. A Combined UWB/IMU Localization Method with Improved CKF. *Sensors*, 24(10):3165, 2024.

Katona, K., Neamah, H. A., and Korondi, P. Obstacle Avoidance and Path Planning Methods for Autonomous Navigation of Mobile Robot. *Sensors*, 24(11):3573, 2024.

Kilic, K. I., Samir Maity, and co-authors. Challenges and AI-driven solutions in maritime search and rescue planning: A comprehensive literature review. *Marine Policy*, 178:106692, 2025.

Kim, Y.-J., Kim, H., Ha, B., and Kim, W.-T. Advanced fire emergency management based on potential fire risk assessment with informative digital twins. *Automation in Construction*, 167:105722, 2024.

Kristoffersson Lind, S., Xiong, Z., Forssen, P.-E., and Kruger, V. Uncertainty quantification metrics for deep regression. *Pattern Recognition Letters*, 186:91-97, 2024.

Lee, D., Jung, M., and Kim, A. LiDAR odometry survey: recent advancements and remaining challenges. *Intelligent Service Robotics*, 17:531-558, 2024.

Liu, Y., Wang, S., Xie, Y., Xiong, T., and Wu, M. A Review of Sensing Technologies for Indoor Autonomous Mobile Robots. *Sensors*, 24(4):1222, 2024.

Mi, J., Lu, N., Li, Y.-F., Huang, H.-Z., and Kang, R. An evidential network-based hierarchical method for system reliability analysis with common cause failures and mixed uncertainties. *Reliability Engineering & System Safety*, 220:108295, 2022.

Niroui, F., Zhang, K., Kashino, Z., and Nejat, G. Deep reinforcement learning robot for search and rescue applications: Exploration in unknown cluttered environments. *IEEE Robotics and Automation Letters*, 4(2):610-617, 2019.

Paden, B., Cap, M., Yong, S. Z., Yershov, D., and Frazzoli, E. A Survey of Motion Planning and Control Techniques for Self-Driving Urban Vehicles. *IEEE Transactions on Intelligent Vehicles*, 1(1):33-55, 2016.

Pan, F., Zhang, Y., Liu, J., Head, L., Elli, M., and Alvarez, I. Reliability modeling for perception systems in autonomous vehicles: A recursive event-triggering point process approach. *Transportation Research Part C: Emerging Technologies*, 169:104868, 2024.

Raoufi, M., Telikani, A., Zhang, T., and Shen, J. Fire front path planning and tracking control of Uncrewed Aerial Vehicles using deep reinforcement learning. *Robotics and Autonomous Systems*, 186:105076, 2025.

Stephens, A., Budd, M., Staniaszek, M., Casseau, B., Duckworth, P., Fallon, M., Hawes, N., and Lacerda, B. Planning under uncertainty for safe robot exploration using Gaussian process prediction. *Autonomous Robots*, 48(7):18, 2024.

Tran, Q.-K., and Ryoo, Y.-J. Multi-Sensor Fusion Framework for Reliable Localization and Trajectory Tracking of Mobile Robot by Integrating UWB, Odometry, and AHRS. *Biomimetics*, 10(7):478, 2025.

Usinskis, V., Nowicki, M., Dzedzickis, A., and Bucinskas, V. Sensor-Fusion Based Navigation for Autonomous Mobile Robot. *Sensors*, 25(4):1248, 2025.

Waga, A., Benhlima, S., Bekri, A., Abdouni, J., and Saber, F. Z. A survey on autonomous navigation for mobile robots: From traditional techniques to deep learning and large language models. *Journal of King Saud University Computer and Information Sciences*, 37:198, 2025.

Xu, N., Guan, M., and Wen, C. A survey on Ultra Wide Band based localization for mobile autonomous machines. *Journal of Automation and Intelligence*, 4(2):82-97, 2025.
Xu, T. Recent advances in Rapidly-exploring random tree: A review. *Heliyon*, 10(11):e32451, 2024.

Integrating Deterministic and Stochastic Uncertainty in Terrestrial Laser Scanner-based Deformation Monitoring

Reza Naeimaei and Steffen Schön
Institut für Erdmessung (IfE), Leibniz Universität Hannover, Hannover, Germany
naeimaei@ife.uni-hannover.de; schoen@ife.uni-hannover.de

Elisabeth Ötsch and Hans Neuner
Research Group Engineering Geodesy, Geodesy and Geoinformation, TU Vienna, Vienna, Austria
elisabeth.oetsch@geo.tuwien.ac.at; hans.neuner@geo.tuwien.ac.at

Abstract. Terrestrial laser scanning (TLS) is widely used for deformation monitoring, where decisions about structural safety depend on a reliable description of measurement uncertainty. Classical congruency tests typically treat this uncertainty in a purely stochastic manner. However, remaining systematic effects from instrumental, atmospheric, and modelling sources may still influence the estimated deformation field. This becomes critical when the expected deformation is close to the magnitude of these unmodeled effects, as apparent displacements could be caused either by actual structural change or by systematic influences. In such situations of uncertainty, forcing a purely binary test decision may be difficult to justify.

To address this, this contribution introduces an interval-extended uncertainty propagation framework for TLS-based deformation monitoring. The uncertainty budget is separated into two components: stochastic variability, represented by random variables, and remaining systematic effects, represented as unknown-but-bounded intervals. Using sensitivity analysis of the TLS correction and measurement models, these bounded effects are propagated from physical influence parameters to the control-point (CP) domain of a B-spline surface model, and subsequently to the derived surface points (SP). This establishes a transparent link between physically interpretable TLS influence parameters and their impact on the final deformation decision.

The resulting congruency test extends the classical binary approach with a ternary decision structure: strict acceptance, ambiguity, and strict rejection. In the CP domain, the method utilizes a correlation-aware localization procedure based on the Schur complement. Conversely, in the SP domain, the propagated results are interpreted strictly as a pointwise diagnostic map. This distinction is essential because dense surface points are derived evaluations of the underlying CP deformation field; treating them as independent estimated parameters would be mathematically singular.

The results demonstrate that bounded systematic effects can significantly alter classical deformation decisions, and the interval-extended formulation makes this influence explicit. Rather than forcing uncertain cases into overconfident binary classifications, the proposed framework identifies regions where the deformation signal cannot be reliably separated from systematic uncertainty, providing a more cautious, transparent, and structurally safe basis for TLS-based deformation interpretation.

Keywords: Terrestrial Laser Scanning, Deformation Monitoring, Interval Analysis, Influence Parameters, Congruency Tests

© 2026 by the author(s). This work is licensed under the Creative Commons Attribution 4.0 International License (CC BY 4.0), which permits unrestricted use, distribution, and reproduction in any medium, provided the original author and source are credited.

1. Introduction

Terrestrial Laser Scanning (TLS) has fundamentally advanced geodetic deformation monitoring over recent decades, driven by significant progress in sensor technology and high-resolution data analysis methods (Niemeier, 2025). State-of-the-art applications now routinely achieve dense 3D displacement estimates for structural health monitoring, yet quantifying and reducing the complex uncertainty associated with these point clouds remains a critical challenge (Shi et al., 2025; Meyer et al., 2025). Classical deformation analysis relies heavily on rigorous statistical testing to identify structural movements over time (Caspary, 1987; Heunecke et al., 2013). However, millimetre-level deformation monitoring with TLS is often limited by systematic effects that remain even after applying sophisticated correction models.

Classical stochastic models describe random variability under standard distributional assumptions but do not provide rigorous bounds for these persistent systematic contributions. In uncertainty-modelling terms, this implies that random variability is accompanied by systematic effects: part of the uncertainty can be described stochastically, whereas another part is only available as bounded or admissible ranges (Beer et al., 2013). Building on recent advancements that integrate bounded systematic errors into TLS observation models (Naeimaei and Schön, 2025), this contribution extends these concepts to continuous surface monitoring. Here, remaining systematic effects are represented as bounded deviations and propagated as intervals through the estimation of B-spline surfaces.

The primary goal is to detect deformation reliably by comparing control-point (CP) coordinates between two measurement epochs while explicitly accounting for the correlation structure induced by the B-spline model. Specifically, this study aims to answer how bounded remaining systematic effects alter congruency decisions, and whether a ternary decision model is preferable to a forced binary one in uncertainty-dominated cases. The proposed workflow does not replace the classical stochastic test but complements it with a robust decision layer for scenarios in which the remaining systematics cannot be justified by a precise probability model.

The remainder of the paper is structured as follows. Section 2 introduces the mathematical framework for joint uncertainty modelling, including B-spline surface parameterisation and interval propagation. Section 3 describes the synthetic surface dataset, epoch configurations, and the Monte Carlo simulation design. Section 4 presents the classical congruency test and evaluates its empirical performance and limitations. Section 5 introduces the interval-extended framework and compares its diagnostic performance against the classical baseline. Finally, Section 7 draws conclusions and outlines directions for future research.

2. Mathematical Framework for Joint Uncertainty Modelling

To rigorously evaluate deformations at the millimetre level, it is essential to trace the impact of both random noise and residual systematic effects from the raw observations to the final deformation decision. This section formalizes the functional and stochastic models of the TLS measurements and introduces the framework for propagating bounded deterministic uncertainties.

2.1. B-spline surface parameterization and adjustment

The object surface is represented by a tensor-product B-spline surface (Piegl and Tiller, 1997):

$$\boldsymbol{S}(u,v) = \sum_{i=0}^{n}\sum_{j=0}^{m} N_{i,p}(u)\, N_{j,q}(v)\, \boldsymbol{P}_{i,j}, \tag{1}$$

with control points $\boldsymbol{P}_{i,j} \in \mathbb{R}^3$ and basis functions $N_{i,p}$ and $N_{j,q}$ of degrees p and q, respectively. In TLS-based surface modelling, tensor-product B-splines are attractive because they combine smoothness, local support, and a compact control-point representation that can be used directly for deformation analysis and stochastic modelling (Harmening, 2020; Kermarrec et al., 2020).

Using Cartesian coordinates observations $\boldsymbol{l}$, the approximation is formulated in a linearized Gauss–Markov model (Ötsch et al., 2025):

$$\boldsymbol{l} = \boldsymbol{A}\boldsymbol{x} + \boldsymbol{e}, \qquad \mathbb{E}[\boldsymbol{e}] = \boldsymbol{0}, \;\; \mathrm{Cov}(\boldsymbol{e}) = \boldsymbol{\Sigma}_{ll}, \tag{2}$$

where $\boldsymbol{x}$ stacks all control-point coordinates and $\boldsymbol{A}$ is the design matrix. The stochastic model $\boldsymbol{\Sigma}_{ll}$ summarizes the precision and correlation assumptions of the TLS observations. Weighted least squares uses $\boldsymbol{P} = \boldsymbol{\Sigma}_{ll}^{-1}$ and the normal matrix $\boldsymbol{N} = \boldsymbol{A}^{\mathsf{T}}\boldsymbol{P}\boldsymbol{A}$.

Since the B-spline model is linear in the control-point coefficients, the functional model can be written as

$$\hat{\boldsymbol{x}} = \boldsymbol{x}_0 + \boldsymbol{K}\,(\boldsymbol{l} - \boldsymbol{A}\boldsymbol{x}_0), \tag{3}$$

where $\boldsymbol{x}_0$ denotes a linearization point and the observation-to-parameter mapping $\boldsymbol{K}$ is defined as:

$$\boldsymbol{K} \;=\; (\boldsymbol{A}^{\mathsf{T}}\boldsymbol{P}\boldsymbol{A})^{-1}\boldsymbol{A}^{\mathsf{T}}\boldsymbol{P} \;=\; \boldsymbol{N}^{-1}\boldsymbol{A}^{\mathsf{T}}\boldsymbol{P}. \tag{4}$$

Introducing the reduced observation vector $\tilde{\boldsymbol{l}} := \boldsymbol{l} - \boldsymbol{A}\boldsymbol{x}_0$, the estimated increment relative to the linearization point is $\delta\hat{\boldsymbol{x}} = \boldsymbol{K}\,\tilde{\boldsymbol{l}}$. The adjustment provides the covariance matrix $\boldsymbol{\Sigma}_{\hat{x}}$ through:

$$\boldsymbol{\Sigma}_{\hat{x}} = \hat{\sigma}_0^2\,\boldsymbol{Q}_{\hat{x}\hat{x}}, \qquad \boldsymbol{Q}_{\hat{x}\hat{x}} = (\boldsymbol{A}^{\top}\boldsymbol{P}\boldsymbol{A})^{-1}. \tag{5}$$

2.2. TLS measurement and bounded correction model

Cartesian coordinates are computed from TLS polar measurements (range r, horizontal angle φ, vertical angle θ) and correction functions $(C_r, C_\varphi, C_\theta)$:

$$\boldsymbol{p} = \begin{bmatrix} x \\ y \\ z \end{bmatrix} = \begin{bmatrix} (r + C_r)\sin(\theta + C_\theta)\sin(\varphi + C_\varphi) \\ (r + C_r)\sin(\theta + C_\theta)\cos(\varphi + C_\varphi) \\ (r + C_r)\cos(\theta + C_\theta) \end{bmatrix}. \tag{6}$$

Following the correction model in Medić et al. (2019), the polar corrections are parameterized as

$$C_r(r, \theta; \boldsymbol{s}) \;=\; x_2 \sin\theta + x_{10}, \tag{7}$$

$$C_\varphi(r, \theta; \boldsymbol{s}) \;=\; \frac{x_{1z}}{r\tan\theta} + \frac{x_3}{r\sin\theta} + \frac{x_{5z} - x_7}{\tan\theta} + \frac{2x_6}{\sin\theta} + \frac{x_{1n}}{r}, \tag{8}$$

$$C_\theta(r, \theta; \boldsymbol{s}) \;=\; \frac{x_{1n}\cos\theta}{r} + \frac{x_2\cos\theta}{r} + x_4 + x_{5n}\cos\theta - \frac{x_{1z}\sin\theta}{r} - x_{5z}\sin\theta, \tag{9}$$

where $\boldsymbol{s} = \{x_{1n}, x_{1z}, x_2, x_3, x_{10}, x_4, x_{5n}, x_{5z}, x_6, x_7\}^{\mathsf{T}}$ collects the influential calibration parameters. Each influential parameter is treated as an unknown-but-bounded deviation,

$$s_k \in \left[s_k^* - \Delta s_k, \;\; s_k^* + \Delta s_k\right].$$

This formulation is consistent with the interval-based treatment of systematic effects proposed by Naeimaei and Schön (2025), where remaining calibration uncertainties are modeled as admissible bounded deviations. In this paper, the interval radius Δs_k is derived from the simulated calibration sets in Table I as half of the observed range,

$$\Delta s_k \;=\; 0.5 \cdot \left|\max s_k - \min s_k\right|, \tag{10}$$

Table I. Instrument error-source parameters used in the synthetic dataset. Sets 1 through 4 represent different calibration states across simulated epochs. The interval radius Δs_k is derived as half the maximum range across all four sets.

Parameter	Description	Set 1	Set 2	Set 3	Set 4	Radius Δs_k
x_{1n} [mm]	Horizontal beam offset	0.07	0.08	0.05	0.05	0.015
x_{1z} [mm]	Vertical beam offset	0.08	0.31	0.21	0.14	0.115
x_2 [mm]	Horizontal axis offset	−0.12	−0.11	−0.12	−0.14	0.015
x_3 [mm]	Mirror offset	−0.02	0.00	−0.06	−0.03	0.030
x_{10} [mm]	Rangefinder offset	−0.16	0.03	0.01	−0.03	0.095
x_4 [arcsec]	Vertical index offset	4.20	5.10	5.17	4.51	0.485
x_{5n} [arcsec]	Horizontal beam tilt	4.50	4.67	5.62	5.38	0.560
x_{5z} [arcsec]	Vertical beam tilt	−12.00	−14.71	−14.33	−16.78	2.390
x_6 [arcsec]	Mirror tilt	4.19	3.59	4.11	3.41	0.390
x_7 [arcsec]	Horizontal axis error	−22.35	−25.38	−26.31	−33.50	5.575

which yields symmetric intervals around nominal values s_k^*. The parameterization and magnitude levels in Table I are based on the calibration model proposed by Medić et al. (2019).

2.3. Sensitivity analysis and interval propagation

To evaluate the impact of these bounded systematic errors on the estimated control points, we apply an interval-extended least-squares adjustment (IELSA). Sensitivity analysis quantifies how small changes in model inputs affect the model output (Kutterer, 1999; Naeimaei and Schön, 2025).

Let a model output $f(\boldsymbol{s})$ depend on influence parameters $\boldsymbol{s}$. The first-order differential is $\mathrm{d}f = \boldsymbol{F}\,\mathrm{d}\boldsymbol{s}$, with Jacobian row vector $\boldsymbol{F}$. If the influence parameters are bounded by intervals $\boldsymbol{\Delta}_s$, the corresponding first-order interval radius is:

$$\Delta f = \sum_{i=1}^{n} \left| \frac{\partial f(\boldsymbol{s}^*)}{\partial s_i} \right| \Delta s_i \;=\; |\boldsymbol{F}|\,\boldsymbol{\Delta}_s. \tag{11}$$

Applying Eq. (11) to the TLS correction model—where the notation $|\cdot|$ applied to a matrix denotes the element-wise absolute value—yields observation-level interval radii $\boldsymbol{\Delta}_l = |\boldsymbol{F}|\,\boldsymbol{\Delta}_s$. Propagating these bounds through the linearized least-squares estimator (using the mapping matrix $\boldsymbol{K}$ from Eq. 4) yields the parameter-level enclosure for the control points:

$$\boldsymbol{\Delta}_{\hat{x}} = |\boldsymbol{K}\boldsymbol{F}|\,\boldsymbol{\Delta}_s. \tag{12}$$

This formulation is typically tighter than the two-step bound $|\boldsymbol{K}|\,|\boldsymbol{F}|\,\boldsymbol{\Delta}_s$ because possible cancellations are preserved before taking absolute values.

3. Experimental Dataset and Preprocessing

3.1. Monte Carlo simulation of noise and bounded systematics

To rigorously evaluate the congruency testing framework, a controlled Monte Carlo simulation environment is established. The evaluation relies on generating 1000 Monte Carlo realizations per

configuration to adequately capture stochastic variability. Given a predefined scan station coordinate, true Cartesian coordinates of the SP are first transformed into polar pseudo-observations (r, φ, θ). For each realization, these observations are then corrupted by two distinct uncertainty components:

1. **Stochastic Noise:** Zero-mean Gaussian noise is added independently to each polar component with standard deviations

$$\sigma_r = 1\,\text{mm}, \qquad \sigma_\varphi = \sigma_\theta = 4.44\,\text{mgon}\ (= 0.004^\circ). \tag{13}$$

2. **Deterministic Bias:** Using the correction model established in Eq. (6), specific calibration parameter sets (Table I) are injected. Set 1 is applied to the reference state, and Set 4 to the subsequent comparison states. This intentional mismatch simulates realistic, unmodeled calibration inconsistencies between measurement campaigns.

This general simulation pipeline provides a foundation for generating specific structural deformation scenarios with known ground truth.

3.2. Synthetic surface and deformation scenarios

Applying the Monte Carlo framework described above, an experimental dataset is constructed consisting of a reference epoch $\mathcal{E}_{\text{ref}}$ and a comparison epoch $\mathcal{E}_{\text{comp}}$. The monitored object is modeled as a tensor-product B-spline surface with a fixed parameterization across epochs, enabling direct epoch differencing in the CP domain without remeshing.

To simulate localized deformations, specific CPs in $\mathcal{E}_{\text{comp}}$ are displaced by 10 mm and 20 mm along the y-direction (Figure 1). Because B-spline surfaces possess local support, these discrete CP movements do not translate the entire surface; instead, they induce a continuous, smoothly tapering deformation. The surface displacement peaks within the region of maximum basis-function influence but remains strictly bounded by the CP displacement magnitudes. Consequently, while CP ground truth is defined by the discrete displacement vector, surface ground truth is determined by a *region-of-influence* mask, effectively partitioning the surface into stable and deformed regions based on whether a point's local support includes a displaced CP.

The 10 mm and 20 mm magnitudes represent realistic macro-deformations and were deliberately chosen to lie safely above the TLS stochastic noise floor ($\sigma \approx 2$ mm) and the theoretical Minimum Detectable Deformation (MDD). Enforcing this high signal-to-noise ratio ensures that any false alarms or missed detections observed during testing are strictly driven by unmodeled systematic biases, spatial correlations, or B-spline topology, rather than simple stochastic noise limits.

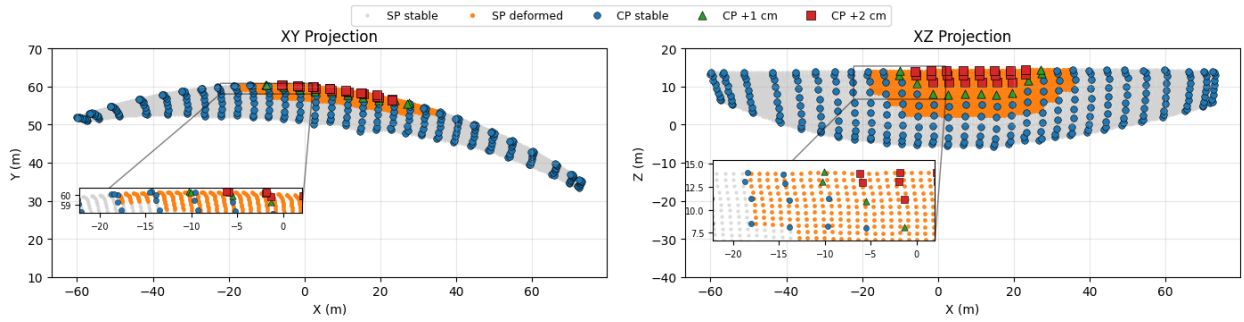


Figure 1. Visualization of the synthetic deformation scenario. (a) Nominal B-spline surface and control-point network ($\mathcal{E}_{\text{ref}}$). (b) Deformed surface ($\mathcal{E}_{\text{comp}}$). (c) Injected 1 cm and 2 cm displacements in the discrete CP domain. (d) Resulting continuous deformation in the SP domain, illustrating the spatial influence of the B-spline local support.

4. Classical congruency test

This section presents classical two-epoch congruency tests in the control-point (CP) domain and on the reconstructed surface. All tests are formulated with the full variance–covariance matrix of the estimated control points within each epoch; hence both intra-point XYZ correlations and inter-point correlations are retained.

4.1. Global test in the Control points domain

Let $\hat{\boldsymbol{x}}_1, \hat{\boldsymbol{x}}_2 \in \mathbb{R}^{3n_{\mathrm{cp}}}$ be the stacked CP coordinate vectors estimated in Epoch 1 and Epoch 2, ordered as $[x_1, y_1, z_1, \ldots, x_{n_{\mathrm{cp}}}, y_{n_{\mathrm{cp}}}, z_{n_{\mathrm{cp}}}]^\top$. The epoch difference is

$$\hat{\boldsymbol{d}} = \hat{\boldsymbol{x}}_2 - \hat{\boldsymbol{x}}_1. \tag{14}$$

Neglecting cross-covariances between the two epoch solutions, the covariance of $\hat{\boldsymbol{d}}$ is

$$\boldsymbol{\Sigma}_{\hat{d}\hat{d}} = \boldsymbol{\Sigma}_{\hat{x}_1} + \boldsymbol{\Sigma}_{\hat{x}_2}, \tag{15}$$

where $\boldsymbol{\Sigma}_{\hat{x}_k} = \hat{\sigma}^2_{0,k}\, \boldsymbol{Q}_{\hat{x}_k\hat{x}_k}$ for Epoch $k \in \{1, 2\}$.

4.1.1. *Measurement model for the epoch differences*

In the classical test, the estimated difference vector is modelled as

$$\hat{\boldsymbol{d}} = \boldsymbol{\mu} + \boldsymbol{e}, \qquad \mathbb{E}[\boldsymbol{e}] = \boldsymbol{0}, \qquad \mathrm{Cov}(\boldsymbol{e}) = \boldsymbol{\Sigma}_{dd}, \tag{16}$$

where $\boldsymbol{\mu}$ denotes the unknown true displacement vector and $\boldsymbol{e}$ collects stochastic estimation errors. The hypotheses are

$$H_0 : \ \boldsymbol{\mu} = \boldsymbol{0}, \qquad H_1 : \ \boldsymbol{\mu} \neq \boldsymbol{0}. \tag{17}$$

4.1.2. *Compatibility of variance factors and pooled scale*

Before combining epochs, the compatibility of the a posteriori variance factors $\hat{\sigma}^2_{0,1}$ and $\hat{\sigma}^2_{0,2}$ is verified via an F-test (Caspary, 1987; Heunecke et al., 2013). Across all simulated realizations, they remain statistically compatible. Because both epochs share identical measurement configurations and parameterizations ($f_1 = f_2$), the pooled variance simplifies to their arithmetic mean:

$$\hat{\sigma}^2_0 = \frac{\hat{\sigma}^2_{0,1} + \hat{\sigma}^2_{0,2}}{2}, \tag{18}$$

where the total redundancy is defined as $f := f_1 + f_2$.

4.1.3. *Global test statistic*

Using the cofactor matrix $\boldsymbol{Q}_{\hat{d}\hat{d}} = \boldsymbol{Q}_{\hat{x}_1\hat{x}_1} + \boldsymbol{Q}_{\hat{x}_2\hat{x}_2}$ and $\boldsymbol{\Sigma}_{\hat{d}\hat{d}} = \hat{\sigma}^2_0 \boldsymbol{Q}_{\hat{d}\hat{d}}$, the global congruency quadratic form is based on:

$$R_{\mathrm{glob}} = \hat{\boldsymbol{d}}^{\mathsf{T}}\, \boldsymbol{Q}^{-1}_{\hat{\boldsymbol{d}}\hat{\boldsymbol{d}}}\, \hat{\boldsymbol{d}}, \tag{19}$$

With $h = \mathrm{rank}(\boldsymbol{Q}_{\hat{d}\hat{d}})$, the normalized statistic is

$$T_{\mathrm{glob}} = \frac{(R_{\mathrm{glob}}/h)}{\hat{\sigma}^2_0}. \tag{20}$$

Under H_0,

$$T_{\mathrm{glob}} \sim F(h, f), \qquad k_\alpha := F_{h,f;\,1-\alpha}, \qquad T_{\mathrm{glob}} \geq k_\alpha \ \Rightarrow \ \text{reject } H_0. \tag{21}$$

4.2. Local test in the control point domain

Following a global rejection, local diagnosis aims to identify specific control points contributing to the deformation signal. Due to the inherent stochastic correlations among the estimated points, we apply the successive decomposition of the global quadratic form, a standard multiple-testing procedure established by Caspary (1987) and further detailed by Heunecke et al. (2013). The vector $\hat{\boldsymbol{d}}$ and cofactor matrix $\boldsymbol{Q}_{\hat{d}\hat{d}}$ are partitioned into the target point p and the remaining points n:

$$\hat{\boldsymbol{d}} = \begin{pmatrix} \hat{\boldsymbol{d}}_n \\ \hat{\boldsymbol{d}}_p \end{pmatrix}, \qquad \boldsymbol{Q}_{\hat{d}\hat{d}} = \begin{pmatrix} \boldsymbol{Q}_{nn} & \boldsymbol{Q}_{np} \\ \boldsymbol{Q}_{pn} & \boldsymbol{Q}_{pp} \end{pmatrix}. \tag{22}$$

To account for cross-covariances, the conditional displacement $\bar{\boldsymbol{d}}_p$ and its associated cofactor matrix (Schur complement) $\boldsymbol{Q}_{p|n}$ are computed as:

$$\bar{\boldsymbol{d}}_p = \hat{\boldsymbol{d}}_p - \boldsymbol{Q}_{pn}\,\boldsymbol{Q}_{nn}^{-1}\,\hat{\boldsymbol{d}}_n, \qquad \boldsymbol{Q}_{p|n} = \boldsymbol{Q}_{pp} - \boldsymbol{Q}_{pn}\,\boldsymbol{Q}_{nn}^{-1}\,\boldsymbol{Q}_{np}. \tag{23}$$

The local quadratic contribution is $R_p = \bar{\boldsymbol{d}}_p^{\top}\,\boldsymbol{Q}_{p|n}^{-1}\,\bar{\boldsymbol{d}}_p$. For a 3D point, the normalized statistic $T_p = (R_p/3)/\hat{\sigma}_0^2$ is compared against the threshold $F_{3,f;\,1-\alpha}$.

Localization is an iterative elimination process: the point maximizing T_p is removed, and the system is recomputed until the remaining set passes a global congruency test, ensuring a statistically consistent reference frame. Throughout this decomposition, the initial pooled variance factor $\hat{\sigma}_0^2$ is strictly retained to prevent masking effects and maintain consistent test power.

4.3. Pointwise diagnostic map in the surface domain

After a global rejection in the CP domain, the deformation field is evaluated on the reconstructed surface. Since the surface is a deterministic linear mapping of the estimated control points, the SP displacements do not represent an independent set of estimated parameters. Therefore, the SP analysis is not used as a second rigorous localization procedure equivalent to the CP-domain Schur-complement localization. Instead, it is used as a pointwise diagnostic evaluation to visualize how the CP-domain deformation field is expressed over the continuous surface.

The displacement of a surface point at parameter location (u, v) is calculated as:

$$\hat{\boldsymbol{d}}_S(u,v) = \boldsymbol{B}(u,v)\hat{\boldsymbol{d}}. \tag{24}$$

Here, $\boldsymbol{B}(u,v) \in \mathbb{R}^{3\times 3n_{\mathrm{cp}}}$ collects the tensor-product basis functions $N_{i,p}(u)N_{j,q}(v)$ associated with the local support. By linear propagation of the full CP-domain covariance, the associated surface cofactor matrix is:

$$\boldsymbol{Q}_{\hat{d}_S\hat{d}_S}(u,v) = \boldsymbol{B}(u,v)\,\boldsymbol{Q}_{\hat{d}\hat{d}}\,\boldsymbol{B}(u,v)^{\top}. \tag{25}$$

The normalized surface statistic is formulated analogously to the local CP test:

$$T_{\mathrm{surf}}(u,v) = \frac{(\hat{\boldsymbol{d}}_S^{\top}\,\boldsymbol{Q}_{\hat{d}_S\hat{d}_S}^{-1}\,\hat{\boldsymbol{d}}_S/3)}{\hat{\sigma}_0^2}, \tag{26}$$

where $T_{\mathrm{surf}}(u,v) \sim F(3,f)$ under H_0. A surface location is flagged as deformed if $T_{\mathrm{surf}}(u,v) \geq F_{3,f;\,1-\alpha}$.

Unlike the CP domain, rigorous successive elimination (Eq. 23) is omitted in the SP domain. Because dense surface points are strictly derived evaluations rather than independent estimated parameters, their covariance matrix is highly rank-deficient. This makes local Schur-complement

steps mathematically singular. Consequently, the pointwise surface statistic (T_{surf}) serves strictly as a diagnostic map. This necessary simplification inherently neglects spatial cross-covariances between adjacent surface points.

4.4. Empirical performance and limitations of the classical test

The classical congruency tests are executed at $\alpha = 0.05$. Because the CP domain utilizes rigorous successive elimination while the SP domain relies on a pointwise diagnostic map, their performances must be evaluated separately.

Table II. Averaged classical confusion matrix evaluated in the CP domain across 1000 Monte Carlo realizations (rigorous successive elimination).

Ground Truth	Total	Pred. Stable	Pred. Deformed
Stable	266	TN: 250.4 (94.1%)	FP: 15.6 (5.9%)
Deformed	34	FN: 0.2 (0.6%)	TP: 33.8 (99.4%)

Table II summarizes the CP domain performance. The false-alarm rate (5.9%) slightly exceeds the nominal level, indicating that remaining systematic biases influence the test statistics despite rigorous correlation handling.

Table III. Averaged classical confusion matrix evaluated in the SP domain across 1000 Monte Carlo realizations (pointwise diagnostic map).

Ground Truth	Total	Pred. Stable	Pred. Deformed
Stable	3609	TN: 3097.5 (85.8%)	FP: 511.5 (14.2%)
Deformed	891	FN: 292.9 (32.9%)	TP: 598.1 (67.1%)

In the dense SP domain (Table III), 14.2% of physically stable surface points are flagged as deformed by the pointwise diagnostic evaluation. This value should not be interpreted in the same way as the CP-domain false-alarm rate, because the SP map consists of many spatially dependent derived evaluations and no multiple-testing correction is applied. The result nevertheless illustrates an important practical issue: when the continuous surface is evaluated pointwise, remaining systematic effects and strong spatial dependence can produce extended regions of apparent deformation. The SP map is therefore useful as a diagnostic visualization, but not as a fully correlation-aware statistical localization procedure.

To interpret the high CP detection rates, we perform a detectability analysis. Under H_1, the local 3D CP statistic follows a non-central F-distribution with non-centrality parameter:

$$\lambda = \frac{\boldsymbol{\mu}_{\text{true}}^{\mathsf{T}}\, \boldsymbol{Q}_{p|n}^{-1}\, \boldsymbol{\mu}_{\text{true}}}{\hat{\sigma}_0^2}, \tag{27}$$

where $\boldsymbol{\mu}_{\text{true}}$ is the true displacement and $\boldsymbol{Q}_{p|n}$ is the Schur-complement cofactor (Eq. 23). Figure 2 shows that both displacement groups lie far above their 80% detectability thresholds (2.71 mm and 3.13 mm). Thus, the near-unit true-positive rate in the CP domain is theoretically expected and should not be overinterpreted as a general method strength.

Classically termed *minimum detectable bias* (Baarda, 1967), we refer to this as *minimum detectable deformation* (MDD) to avoid confusion with the bounded systematic biases (Section 5). For a unit

direction $\boldsymbol{u}$, the directional MDD is:

$$\mathrm{MDD}(\boldsymbol{u}) = \sqrt{\lambda_{\mathrm{MDD}}\, \boldsymbol{u}^{\mathsf{T}}\, \hat{\sigma}_0^2\, \boldsymbol{Q}_{p|n}\, \boldsymbol{u}}, \tag{28}$$

where λ_{MDD} is derived from the target power $P(F(3, f, \lambda_{\mathrm{MDD}}) \geq F_{3,f;\,1-\alpha}) = 1 - \beta$. Therefore, Figure 2 depicts directional MDD_{80} values, not universal thresholds.

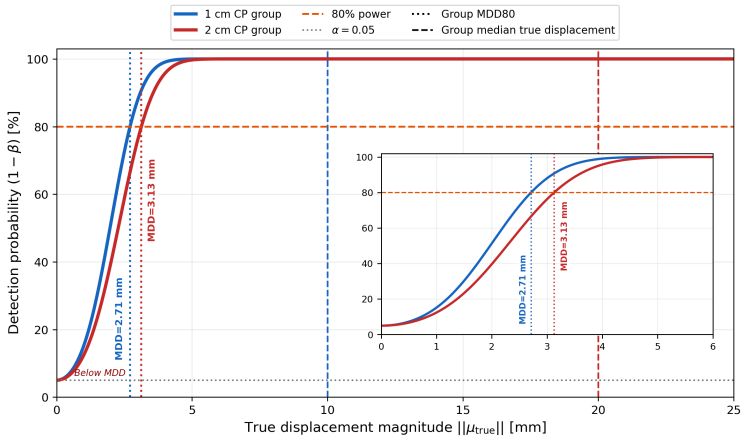


Figure 2. Analytical power curves of the local 3D CP congruency test. Both displacement groups (10 mm, 20 mm) lie far above the corresponding MDD thresholds.

Importantly, CP-based detectability does not guarantee uniform SP detectability. Surface displacements taper across the B-spline support, so edge deformations often fall below the MDD, increasing SP missed detections (Figure 3). Ultimately, the elevated SP false-alarm rate reveals a fundamental limit in purely stochastic monitoring: when rigorous correlation handling becomes mathematically inaccessible on dense surfaces, the resulting necessary simplifications force overconfident binary decisions. This specific limitation—the inability to safely absorb the uncertainty caused by methodological simplifications and unmodeled biases—directly motivates the interval-extended framework in Section 5.

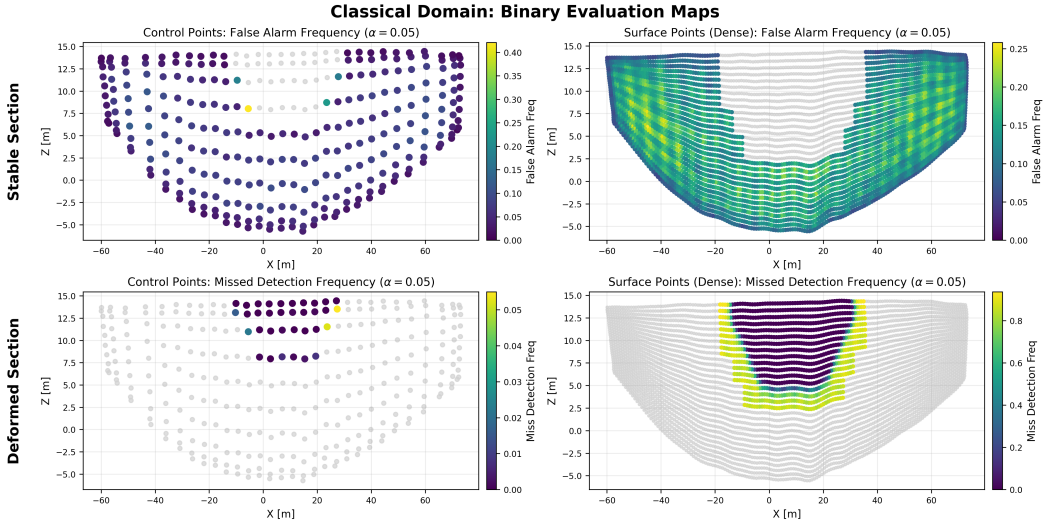


Figure 3. Spatial distribution of empirical error frequencies across 1000 Monte Carlo realizations ($\alpha = 0.05$). Left: missed-detection frequency on the deformed subset. Right: false-alarm frequency on the stable subset.

5. Interval-extended congruency test

This section extends the classical congruency test by explicitly accounting for remaining systematic effects in the epoch differences. In addition to stochastic estimation noise, the epoch-difference vector is affected by an unknown but bounded systematic contribution. The resulting decision is therefore ternary rather than binary.

5.1. Global test in the CP domain

5.1.1. *Measurement model for the epoch differences*

Let $\hat{\boldsymbol{d}}$ denote the CP epoch-difference vector introduced in Section 4, with covariance $\boldsymbol{\Sigma}_{dd} = \hat{\sigma}_0^2\, \boldsymbol{Q}_{dd}$. In the interval-extended model, the observation equation is written as

$$\hat{\boldsymbol{d}} = \boldsymbol{\mu} + \boldsymbol{b} + \boldsymbol{e}, \qquad \mathbb{E}[\boldsymbol{e}] = \boldsymbol{0}, \qquad \mathrm{Cov}(\boldsymbol{e}) = \boldsymbol{\Sigma}_{dd}, \qquad \boldsymbol{b} \in \mathcal{B}, \tag{29}$$

where $\boldsymbol{b}$ is an additional systematic contribution bounded by an admissible set $\mathcal{B}$ (Naeimaei and Schön, 2026). The hypotheses remain $H_0 : \boldsymbol{\mu} = \boldsymbol{0}, \qquad H_1 : \boldsymbol{\mu} \neq \boldsymbol{0}$.

5.1.2. *Bias set representation (error box)*

To obtain a simple and transparent uncertainty model, the systematic contribution is enclosed by an axis-aligned box in CP-difference space:

$$\mathcal{B}_{\square} = [-\Delta_{\boldsymbol{d}},\, +\Delta_{\boldsymbol{d}}] = \left\{ \boldsymbol{b} \in \mathbb{R}^{3n_{\mathrm{cp}}} :\; -\Delta_{\boldsymbol{d}} \leq \boldsymbol{b} \leq +\Delta_{\boldsymbol{d}} \right\}, \tag{30}$$

where $\Delta_{\boldsymbol{d}}$ denotes the componentwise radius of the admissible systematic bias.

5.1.3. *Partial cancellation of systematic effects*

While some systematic effects may partially cancel during epoch differencing, perfect cancellation is rare in practice because station setups, geometry, and calibration conditions easily vary between measurements. Therefore, the influence parameters are partitioned into two groups: parameters assumed to remain consistent across epochs (C) and parameters that may vary between epochs (E).

In this study, only the rangefinder offset x_{10} and the vertical index offset x_4 are assumed to vary between epochs, while all other parameters are assumed stable. The corresponding CP-domain bias radius is modeled as:

$$\Delta_{\boldsymbol{d}} = |(\boldsymbol{K}\boldsymbol{F}_2 - \boldsymbol{K}\boldsymbol{F}_1)|_{(:,C)}\; \Delta_{\boldsymbol{s}_C} + (|\boldsymbol{K}\boldsymbol{F}_2| + |\boldsymbol{K}\boldsymbol{F}_1|)_{(:,E)}\, \Delta_{\boldsymbol{s}_E}. \tag{31}$$

As a result, stable contributions are partially reduced by differencing, whereas epoch-dependent contributions are conservatively accumulated.

5.1.4. *Global ternary decision*

Using the same quadratic form as the classical global test, but corrected by an admissible bias vector, the interval-dependent statistic is

$$T_{\mathrm{glob}}(\boldsymbol{b}) = \frac{1}{h\hat{\sigma}_0^2} (\hat{\boldsymbol{d}} - \boldsymbol{b})^{\mathsf{T}} \boldsymbol{Q}_{dd}^{-1} (\hat{\boldsymbol{d}} - \boldsymbol{b}), \qquad \boldsymbol{b} \in \mathcal{B}_{\square}, \tag{32}$$

with $h = \mathrm{rank}(\boldsymbol{Q}_{dd})$. Since the exact bias realization is unknown, the decision is based on the extremal values

$$T_{\mathrm{glob,min}} = \min_{\boldsymbol{b} \in \mathcal{B}_{\square}} \left(T_{\mathrm{glob}}(\boldsymbol{b}) \right), \qquad T_{\mathrm{glob,max}} = \max_{\boldsymbol{b} \in \mathcal{B}_{\square}} \left(T_{\mathrm{glob}}(\boldsymbol{b}) \right). \tag{33}$$

Note that while calculating $T_{\text{glob,min}}$ is a standard convex quadratic program solvable in polynomial time, computing the exact $T_{\text{glob,max}}$ over a high-dimensional box is an NP-hard optimization problem. However, for the global diagnostic decision, evaluating $T_{\text{glob,min}}$ is strictly sufficient to determine if the local diagnosis must be triggered. With the same critical value $k_\alpha = F_{h,f;1-\alpha}$ as in the classical test, the decision rule becomes

$$\text{strict accept } H_0 \quad \text{if } T_{\text{glob,max}} < k_\alpha, \qquad \text{strict reject } H_0 \quad \text{if } T_{\text{glob,min}} > k_\alpha, \quad \text{ambiguous} \quad \text{otherwise.} \tag{34}$$

Hence, congruency is accepted only if all admissible biases support H_0, and rejected only if all admissible biases contradict it.

5.2. Local test in the CP domain

If the global test rejects H_0 or remains ambiguous, local diagnosis is performed for individual CPs. As in the classical approach, the test is based on correlation-aware single-point diagnosis, but now under bounded systematic bias. Partition the epoch-difference vector, the admissible bias vector, and the cofactor matrix into the target point p and all remaining points n:

$$\hat{\boldsymbol{d}} = \begin{pmatrix} \hat{\boldsymbol{d}}_n \\ \hat{\boldsymbol{d}}_p \end{pmatrix}, \qquad \boldsymbol{b} = \begin{pmatrix} \boldsymbol{b}_n \\ \boldsymbol{b}_p \end{pmatrix}, \qquad \boldsymbol{Q}_{dd} = \begin{pmatrix} \boldsymbol{Q}_{nn} & \boldsymbol{Q}_{np} \\ \boldsymbol{Q}_{pn} & \boldsymbol{Q}_{pp} \end{pmatrix}, \tag{35}$$

with $\hat{\boldsymbol{d}}_p, \boldsymbol{b}_p \in \mathbb{R}^3$ and $\boldsymbol{Q}_{pp} \in \mathbb{R}^{3\times 3}$. Analogous to the classical case, the correlation-aware local displacement of point p, conditional on the remaining points, is:

$$\bar{\boldsymbol{d}}_p(\boldsymbol{b}) = (\hat{\boldsymbol{d}}_p - \boldsymbol{b}_p) - \boldsymbol{Q}_{pn}\boldsymbol{Q}_{nn}^{-1}(\hat{\boldsymbol{d}}_n - \boldsymbol{b}_n), \tag{36}$$

with the same Schur-complement cofactor matrix $\boldsymbol{Q}_{p|n}$ as in the classical case. This expression can be written in affine form as:

$$\bar{\boldsymbol{d}}_p(\boldsymbol{b}) = \bar{\boldsymbol{d}}_p - \boldsymbol{M}_p\boldsymbol{b}, \qquad \boldsymbol{M}_p = [-\boldsymbol{Q}_{pn}\boldsymbol{Q}_{nn}^{-1} \quad \boldsymbol{I}_3] \tag{37}$$

where $\bar{\boldsymbol{d}}_p$ is the conditional displacement and $\boldsymbol{M}_p$ is the corresponding bias mapping.

5.2.1. *Local bounding and ternary decision*

To avoid repeated optimization in the full CP space, the global bias set is projected into a local 3D uncertainty set for each control point. This set is conservatively approximated by an axis-aligned bounding box, enabling efficient evaluation of the local test statistic:

$$\boldsymbol{u}_p \in [-\Delta_{\bar{\boldsymbol{d}}_p}, +\Delta_{\bar{\boldsymbol{d}}_p}], \qquad \Delta_{\bar{\boldsymbol{d}}_p} = |\boldsymbol{M}_p|\Delta_{\boldsymbol{d}}. \tag{38}$$

For any admissible local bias $\boldsymbol{u}_p$, the test statistic is:

$$T_p(\boldsymbol{u}_p) = \frac{1}{3\hat{\sigma}_0^2}(\bar{\boldsymbol{d}}_p - \boldsymbol{u}_p)^{\mathsf{T}}\boldsymbol{Q}_{p|n}^{-1}(\bar{\boldsymbol{d}}_p - \boldsymbol{u}_p). \tag{39}$$

Since the exact bias realization is unknown, the extremal values within this bounding box are evaluated:

$$T_{p,\text{min}} = \min_{\boldsymbol{u}_p}\left(T_p(\boldsymbol{u}_p)\right), \qquad T_{p,\text{max}} = \max_{\boldsymbol{u}_p}\left(T_p(\boldsymbol{u}_p)\right). \tag{40}$$

The local ternary decision is obtained analogously to the global case using the critical value $k_\alpha = F_{3,f;1-\alpha}$:

$$\begin{aligned} &\text{strict accept } H_0 \text{ for CP } p \quad \text{if } T_{p,\text{max}} < k_\alpha, \\ &\text{strict reject } H_0 \text{ for CP } p \quad \text{if } T_{p,\text{min}} > k_\alpha, \\ &\text{ambiguous} \qquad\qquad\qquad\quad \text{otherwise.} \end{aligned} \tag{41}$$

5.2.2. *Iterative localization and stopping criterion*

In classical diagnosis, localization stops when the remaining network passes a global congruency test. In the interval framework, this criterion can be overly conservative because bounded systematic effects accumulate over the network and may lead to artificial rejection of stable points.

Therefore, the extended framework uses a local stopping criterion. Control points classified as *strictly deformed* ($T_{p,\min} > k_\alpha$) are removed iteratively until no point exceeds the local threshold. Ambiguous points are retained in the reference frame, so that unresolved systematic uncertainty is not converted into false structural alarms.

5.3. Local test in the surface domain

As established in Section 4.3, the nominal surface displacement $\hat{\boldsymbol{d}}_S(u,v)$ and its stochastic cofactor matrix $\boldsymbol{Q}_{d_S d_S}(u,v)$ are obtained via linear propagation through the B-spline basis matrix $\boldsymbol{B}(u,v)$.

Under the interval framework, the induced systematic surface bias is similarly bounded by projecting the global CP bounds ($\Delta_{\boldsymbol{d}}$) through the absolute basis functions:

$$\Delta_{\boldsymbol{b}_S(u,v)} = |\boldsymbol{B}(u,v)|\,\Delta_{\boldsymbol{d}}. \tag{42}$$

Because the tensor-product B-spline basis functions are strictly non-negative and sum to one (satisfying the convex hull property), this propagation effectively maps the exact systematic bounds to the continuous surface without introducing any artificial interval overestimation.

For any admissible surface bias $\boldsymbol{b}_S \in [-\Delta_{\boldsymbol{b}_S(u,v)}, +\Delta_{\boldsymbol{b}_S(u,v)}]$, the normalized test statistic $T_S(\boldsymbol{b}_S)$ is formulated analogously to the classical surface test (Eq. 26). The extremal values $T_{S,\min}$ and $T_{S,\max}$ are then evaluated over this bounded set, and the final surface diagnosis follows the identical ternary decision rule (Eq. 41).

5.4. Empirical validation and diagnostic results

The interval-extended procedure was applied to 1000 Monte Carlo realizations at $\alpha = 0.05$. As in the classical analysis, CP and SP results are reported separately: the CP domain uses correlation-aware local diagnosis with a local stopping criterion, whereas the SP domain provides a pointwise diagnostic map of the propagated surface deformation field. In contrast to the classical test, which forced an

Table IV. Averaged extended 2×3 confusion matrix evaluated in the CP domain. The ambiguous state absorbs points whose true status is obscured by systematic uncertainty.

Ground Truth	Total	Strictly Stable	Ambiguous	Strictly Deformed
Stable	266	212.0 (79.7%)	44.5 (16.7%)	9.5 (3.6%)
Deformed	34	0.0 (0.0%)	0.1 (0.3%)	33.9 (99.7%)

overconfident binary choice, the extended test utilizes the *ambiguous* classification as a mathematical buffer. As seen in the physically stable CP subset (Table IV), the ambiguous state (16.7%) draws from both former true negatives and former false positives. The strict false-alarm rate drops from 5.9% in the classical model to just 3.6% (9.5 points), safely below the nominal 5% expectation. Most importantly, the strictly stable misclassification on the deformed subset drops to exactly 0.0%, eradicating critical non-detections.

The spatial distribution of these decisions across the CP domain is visualized in Figure 4. The top row demonstrates how systematic noise in the stable section is largely intercepted by the ambiguous

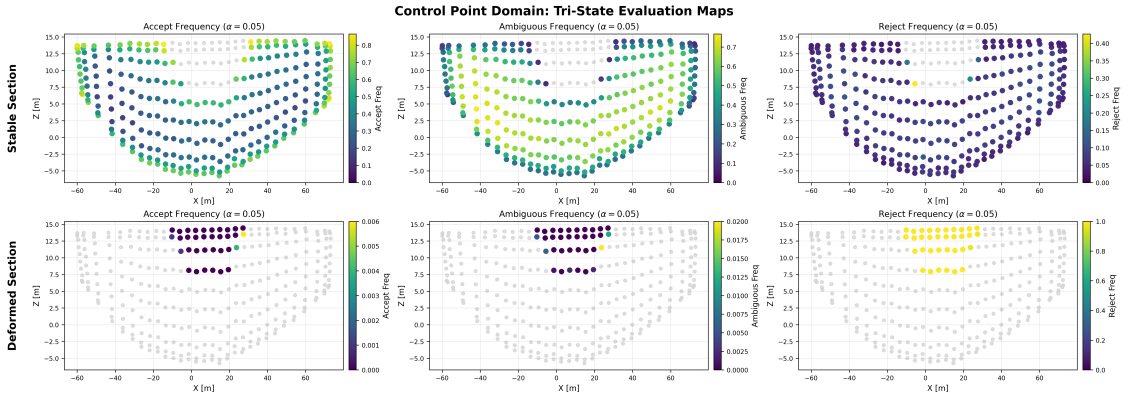


Figure 4. Spatial distribution of the extended ternary decisions in the control point domain ($\alpha = 0.05$). Top row: Evaluation frequencies on the physically stable section. Bottom row: Evaluation frequencies on the physically deformed section.

buffer. Conversely, the bottom row confirms that true deformations are never incorrectly accepted as stable.

5.4.1. *Diagnostic performance in the dense surface domain*

The protective effect of the interval framework serves its most critical role in the dense surface domain. As established in Section 4.4, because exact stochastic correlation handling is mathematically singular on the continuous surface, the required pointwise simplification leaves the diagnosis vulnerable to systematic biases.

Table V. Averaged extended 2×3 confusion matrix evaluated in the dense SP domain.

Ground Truth	**Total**	**Strictly Stable**	**Ambiguous**	**Strictly Deformed**
Stable	3609	2531.8 (70.2%)	822.6 (22.8%)	254.7 (7.1%)
Deformed	891	231.0 (25.9%)	101.2 (11.4%)	558.8 (62.7%)

The interval-extended surface test (Table V) mitigates this vulnerability by introducing the explicit ambiguous class. On the physically deformed surface, 62.7% of the points are strictly classified as deformed, while 11.4% are transferred to the ambiguous class. It must be noted that 25.9% of the true deformations are still missed (classified as strictly stable). As established in Section 4.4, this is an unavoidable physical consequence of the deformation tapering off at the boundaries of the B-spline support, where the theoretical non-centrality parameter λ drops below the Minimum Detectable Deformation threshold.

Both the classical and the interval-extended tests inherently face this exact same physical detection limit at the deformation edges. However, their behavior diverges crucially on the physically stable surface. While the classical test suffered from a cascade of false alarms (14.2%) due to unmodeled biases, the interval framework acts as a protective buffer. By assigning 22.8% of the stable points to the ambiguous class, the strict false-alarm rate is halved to 7.1%. This demonstrates the primary advantage of the extended framework: even though it cannot bypass the physical limits of detecting microscopic tapering deformations, it successfully suppresses the false positive cascade that plagues classical testing under systematic uncertainty.

The power of this ternary classification becomes particularly evident when considering sub-MDD deformations, such as a 5 mm displacement. In such a scenario, the classical test would yield a highly

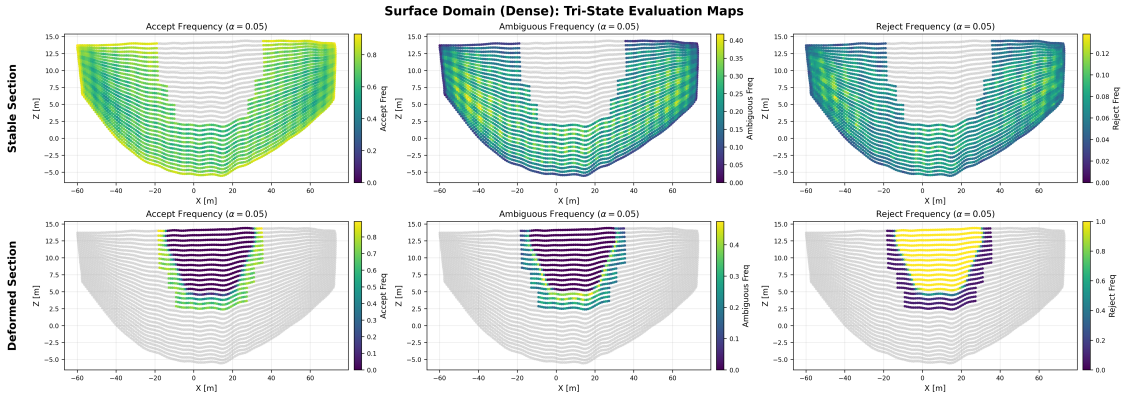


Figure 5. Spatial distribution of the extended ternary decisions in the dense surface domain ($\alpha = 0.05$). The ambiguous state absorbs regions where the decision is dominated by bounded systematic uncertainty.

unreliable mix of stochastic missed detections and systematic false alarms. The interval-extended framework, however, would correctly classify these sub-threshold movements as ambiguous. This safely informs the monitoring engineer that while a deviation exists, it cannot be rigorously separated from the system's calibration uncertainty, thereby preventing unwarranted structural alarms while maintaining continuous observation.

6. Discussion

The interval-extended congruency test changes not only the numerical outcome of the analysis, but also the interpretation of the final decision. In practical monitoring, a binary statement is often required, although the proposed framework yields a ternary outcome. In fuzzy-interval approaches, this transition is handled through a continuous rejectability measure (Neumann and Kutterer, 2009; Kutterer and Neumann, 2008). The present method uses simple interval bounds instead, so the ambiguous class defines a bounded decision space: a conservative interpretation merges ambiguity with the stable class to minimise false alarms, whereas a safety-first interpretation merges it with the deformed class to minimise missed detections. To formalise this transition, let $\alpha_{\text{strict}} = P(\text{strictly deformed} \mid H_0)$, $\beta_{\text{strict}} = P(\text{strictly stable} \mid H_1)$, $\gamma_0 = P(\text{ambiguous} \mid H_0)$, and $\gamma_1 = P(\text{ambiguous} \mid H_1)$. The empirical error rates after binary collapse are then

$$\begin{aligned} \text{Conservative:} \quad & \alpha_{\text{cons}} = \alpha_{\text{strict}}, \\ & \beta_{\text{cons}} = \beta_{\text{strict}} + \gamma_1, \end{aligned} \qquad \begin{aligned} \text{Safety-first:} \quad & \alpha_{\text{safe}} = \alpha_{\text{strict}} + \gamma_0, \\ & \beta_{\text{safe}} = \beta_{\text{strict}}. \end{aligned} \tag{43}$$

Figure 6 summarises the main effect of this transition. In the CP domain, the conservative interpretation reduces the Type I error from 5.9% to 3.6% and the Type II error from 0.6% to 0.3%; the safety-first interpretation eliminates missed detections entirely (Type II = 0.0%) at the cost of a higher false-alarm rate (Type I = 20.3%). In the SP domain the trade-off is more pronounced: the conservative interpretation reduces the Type I error from 14.2% to 7.1% while the Type II error rises to 37.3%, whereas the safety-first interpretation reduces the Type II error to 25.9% while the Type I error rises to 29.9%.

The interval-extended framework therefore does not define a single unique binary improvement over the classical test. Rather, it makes the underlying risk trade-off explicit and converts part of the classical binary misclassification into explicit uncertainty. The ambiguous class marks regions where the signal-to-bias ratio is insufficient for a reliable hard decision, allowing the final interpretation

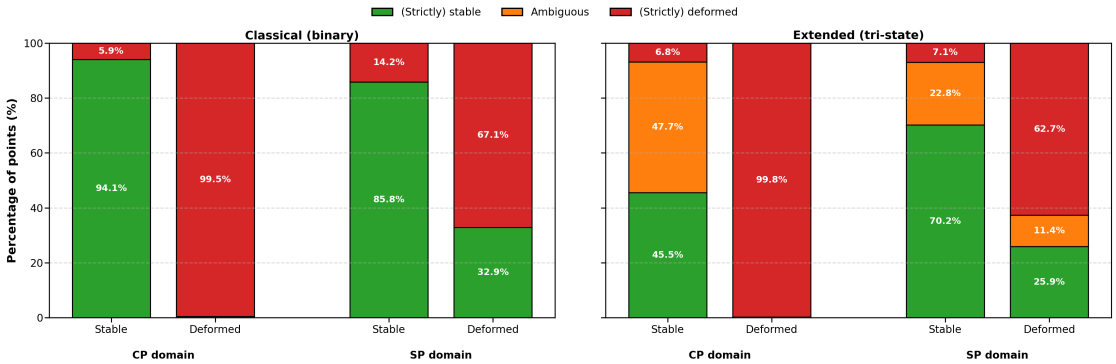


Figure 6. Comparison of the decision distribution between the classical binary approach and the interval-extended ternary approach at $\alpha = 0.05$ in the CP and SP domains.

to be aligned with the monitoring objective. From an engineering perspective, this is preferable to hiding uncertainty inside overconfident binary classifications.

7. Conclusion

Reliable TLS-based deformation monitoring requires an uncertainty model that accounts not only for stochastic measurement noise, but also for remaining systematic effects that cannot be represented confidently by a precise probability model. This study introduced an interval-extended congruency framework in which such effects are represented as unknown-but-bounded quantities and propagated from TLS influence parameters through the B-spline adjustment to the final deformation decision.

The proposed framework extends the classical binary congruency test by a ternary decision structure consisting of strict acceptance, ambiguity, and strict rejection. In the CP domain, the method is combined with a correlation-aware Schur-complement localization procedure. The results show that part of the classical binary decision can be transferred into an explicit ambiguous class, making the influence of remaining systematic uncertainty visible instead of hiding it inside a forced stable/deformed classification.

For the SP domain, the results must be interpreted more cautiously. Surface points are derived evaluations of the same CP deformation field and are not independent estimated parameters. Therefore, the SP-domain analysis was used as a pointwise diagnostic map, not as a fully correlation-aware localization procedure. The corresponding percentages should be read as descriptive indicators of the spatial expression of the deformation field, especially in the presence of remaining systematic effects and multiple pointwise tests.

Overall, the interval-extended approach does not replace the classical stochastic congruency test. Rather, it complements it by identifying cases where the available uncertainty information is insufficient for a defensible binary decision. This is particularly relevant for TLS-based monitoring scenarios in which small deformation signals, spatial dependence, and residual systematic effects occur simultaneously.

References

Baarda, W.: 1967, 'Statistical concepts in geodesy, volume 2 (4) of Publications on Geodesy'. *New Series. Netherlands Geodetic Commission, Delft, Netherlands.*

Beer, M., S. Ferson, and V. Kreinovich: 2013, 'Imprecise probabilities in engineering analyses'. *Mechanical Systems and Signal Processing* **37**(1–2), 4–29.

Caspary, W. F.: 1987, *Concepts of Network and Deformation Analysis*, No. 11 in Monograph. Kensington, N.S.W., Australia: School of Surveying, The University of New South Wales.

Harmening, C.: 2020, 'Spatio-temporal deformation analysis using enhanced B-spline models of laser scanning point clouds'. Ph.D. thesis, Technische Universität Wien.

Heunecke, O., H. Kuhlmann, W. Welsch, A. Eichhorn, and H. Neuner: 2013, *Handbuch Ingenieurgeodäsie: Auswertung geodätischer Überwachungsmessungen*. Neu bearbeitete und erweiterte auflage edition.

Kermarrec, G., B. Kargoll, and H. Alkhatib: 2020, 'Deformation analysis using B-spline surface with correlated terrestrial laser scanner observations—A bridge under load'. *Remote Sensing* **12**(5), 829.

Kutterer, H.: 1999, 'On the sensitivity of the results of least-squares adjustments concerning the stochastic model'. *Journal of Geodesy* **73**, 350–361.

Kutterer, H. and I. Neumann: 2008, 'Multidimensional Statistical Tests for Imprecise Data'. In: P. Xu, J. Liu, and A. Dermanis (eds.): *VI Hotine-Marussi Symposium on Theoretical and Computational Geodesy*. Berlin, Heidelberg, pp. 232–237, Springer Berlin Heidelberg.

Medić, T., H. Kuhlmann, and C. Holst: 2019, 'Designing and evaluating a user-oriented calibration field for the target-based self-calibration of panoramic terrestrial laser scanners'. *Remote Sensing* **12**(1), 15.

Meyer, N., T. Medic, E. Friedli, R. Senti, and A. Wieser: 2025, 'Investigation of different registration methods for TLS-based deformation analysis of hydroelectric dams – A case study'. Technical report.

Naeimaei, R. and S. Schön: 2026, 'Beyond a Pure Stochastic Treatment: Integrating Remaining Systematics into Congruency Tests'. In: *Ingenieurvermessung*.

Naeimaei, R. and S. Schön: 2025, 'Deterministic uncertainty for terrestrial laser scanning observations based on intervals'. *Journal of Applied Geodesy* **19**(3), 385–394.

Neumann, I. and H. Kutterer: 2009, 'The probability of type I and type II errors in imprecise hypothesis testing with an application to geodetic deformation analysis'. *International Journal of Reliability and Safety* **3**(1-3), 286–306.

Niemeier, W.: 2025, '50 Years of Deformation Monitoring - What has been achieved?'. Technical report.

Ötsch, E., C. Harmening, and H. Neuner: 2025, 'Employing variance component estimation for point cloud based geometric surface representation by B-splines'. *Journal of Applied Geodesy* **19**(3), 377–384.

Piegl, L. and W. Tiller: 1997, *The NURBS Book*. Berlin: Springer.

Shi, N., T. Medic, N. Meyer, A. Voordendag, and A. Wieser: 2025, 'Quantifying and Reducing the Uncertainty of 3D Displacement Estimates from Terrestrial Laser Scanner Point Clouds: A Case Study in Alpine Geomonitoring'. Technical report.

A Holistic Approach to the Life Cycle Assessment of a Propeller System

Paulo Lucas Figueiredo[1)2)], José Torres Farinha[1)], Hugo Raposo[1)], António J. Marques Cardoso[2)], Alice do Carmo Duarte Rodrigues[3)], Paula Gonçalves[4)5)]

[1)]RCM2+, ISEC, 3030-199 Coimbra, Portugal, paulofigueiredoo@hotmail.com, hugo.raposo@isec.pt, tfarinha@isec.pt

[2)]CISE, UBI, 6201-001 Covilhã, Portugal, ajmcardoso@ieee.org

[3)]DEP, 2614-506 Amadora, acduarte@emfa.gov.pt

[4)]CIAFA, Lisboa 2715-311, pagoncalves@academiafa.edu.pt

[5)]CIDIUM, Lisboa 1449-027

Abstract: This study aims to demonstrate the value of life cycle analysis in legacy aircraft based on data fusion from asset usage and respective monitoring parameters to support management decisions across all operational levels, being the extend of the useful life of assets or the configuration management. The research includes a case study focused on the propeller system, which serves as a reference for applying the methodology to the entire aircraft and its components.

The proposed analysis integrates state-of-the-art models covering three dimensions: Life Cycle Investment, Sustainability-Oriented Life Cycle Assessment, and Operational Risk Analysis. These models are interconnected to identify cause-and-effect relationships across the different spectra, providing a holistic view of asset performance and degradation.

The methodology considers all operational and maintenance activities, from acquisition to decommissioning, with the objective of increasing asset availability, optimizing resource allocation, reducing component cannibalization, and extending Remaining Useful Life (RUL).

A key feature of the approach is real-time data updating, enabling continuous and accurate information refreshment. This dynamic data environment supports the development of machine learning models and the integration of Generative Artificial Intelligence (GenAI), enhancing predictive and prescriptive capabilities, increasing reliability, and improving risk analysis and forecasting.

Keywords: Life Cycle Analysis; Reliability; Propeller System; Aircraft

© 2026 by the author(s). This work is licensed under the Creative Commons Attribution 4.0 International License (CC BY 4.0), which permits unrestricted use, distribution, and reproduction in any medium, provided the original author and source are credited.

1. Introduction

The need for combining engineering expertise with financial insights is driven by the exponential pace of technological advancement, the geopolitical context and today's socio-economic challenges. This article stems from a collaborative project between the Defence and Academic Sectors in Industrial Engineering field. The main objective of this research is to develop an innovative tool to aid high-level decision-making, involving the entire chain of command. The parameters considered to achieve the desired results involve all operational staff, from the workshop floor to the accounts department. The aim is to apply the methodology to all aircraft and their respective fleets, starting with proof of concept in Propeller Systems. This methodology will provide an overview of all flows and KPIs for an asset within the organization. In addition to this general overview, it will also provide a detailed assessment of any component of any subsystem, considering the basis of its structure. All necessary data will be collected to measure the performance of these assets. As well as all data relating to Life Cycle Cost (LCC) and Life Cycle Assessment (LCA). Moreover, the financial information, it will provide operational KPIs and details on all risks associated with the acquisition and operation of assets, as well as assessments from a sustainability perspective.
This methodology aims to provide immediate insights into the current assets performance. As it is developed and implemented, Deep Neural Networks (DNN) will be employed, including Generative AI (GenAI), enabling the mapping of various distinct pathways based on the organization's objectives. This will correct potential deviations, given the risk analysis and the need for adjustments.

2. State of the art

During the preliminary stages of this research, it became evident that there are several gaps in the literature, which underpins and justifies the efforts that will be undertaken throughout this research to address them. This article highlights some specific examples of these gaps.

Although topics, such as Life Cycle Assessment (LCA), Life Cycle Cost (LCC) and Reliability, Availability, Maintainability and Safety (RAMS) Engineering have become increasingly relevant to the industry, it is quite challenging to identify comprehensive medium and long term studies that directly link these concepts at an operational level. Muazu *et al*. (2021), through a study they conducted, related LCA to Environmental Risk Assessment (ERA), the authors concluded that both complemented each other. However, despite this complementarity, some barriers to the integration of LCA and ERA were identified, namely "the lack of data (e.g., on toxicity) and differences in model structure of LCA and ERA. Most of the proposed approaches presented in the reviewed studies are inclined towards LCA or ERA, resulting in the omission of important components from the other, and leading to the inability of these approaches to address properly the needs of both LCA and ERA simultaneously. There is no clarity on the available information or data required to progress in this area and a clear pathway for practitioners to follow when integrating LCA and ERA is also lacking. Holwerda *et al*. (2021) directly address the gap that this work aims to fill by the end of the research. They discuss several possible life cycle analyses that can be performed, known as Life Cycle Thinking (LCT). The authors state that "a large majority of existent literature focuses on LCT methodologies and case studies. At best, assumptions are made – implicitly or explicitly – about the adoption of LCT methodologies to support sustainable practice. However, empirical research on the practical application of LCT outcomes in decision-making is scarce". The authors also conclude that greater assistance is needed to operationalise LCT results to achieve sustainable policies and operations. This research has the potential of enabling that LCT can be operationalised and monitored in the medium to long term.

As more research is conducted on projects of this scale and complexity, the existing gap becomes clearer: the need to reach conclusions that relate the results obtained in studies of the various types of life cycle of the same asset in a specific and simultaneous way. In other words, there is a necessity to develop a method that relates the various types of life cycles and to identify the cause-and-effect relationships. Saraswat & Yadava (2008), through their work aimed to provide an overview of RAMS engineering in industry, and concluded that despite the variety of work carried out in these four areas, there are few conclusions that link the obtained results. Several key issues are raised in the NATO document "Methods and Models for Life Cycle Cost Calculation" TREATY (2007) on LCC analysis. The authors point out that "Life cycle costing should not be considered as a one-off task but should be recognised as an ongoing activity throughout the life cycle to evaluate all programme changes and exploit cost saving opportunities. Although this report focuses on the importance of conducting life cycle cost analysis, it should be recognised that there are limitations of such analysis. Some of the limitations are Life cycle costing is not an exact science. A life cycle cost analysis does not provide an exact number of the costs; it merely gives an insight in the major cost factors and an insight into the magnitude of the costs:

- The life cycle cost estimate is inherently uncertain; its accuracy depends on the quality of the inputs, which are often themselves estimates or based on expert judgment.;
- Life cycle cost models require large volumes of data; however, only limited data are typically available at the time of estimation. Therefore, multiple assumptions must be made, and the resulting cost estimate is highly dependent on those assumptions—any change in them may significantly affect the outcome.;
- Life cycle cost results are used for multiple purposes and are not always directly comparable; for example, estimates developed for comparative or trade-off analyses may not be suitable for budgeting purposes.

These limitations should be carefully considered when conducting a life cycle cost analysis.

The authors highlight important limitations in the analysis of life cycle costs. One of them, which is the methodology presented in this paper that aims to overcome, is the widespread use of generalised costs, since one of the objectives is to create an adaptable model that seeks to consider all costs related to the activity of assets, such as their systems and their respective components. The second is the uncertainty in forecasting future costs. In this case, the research proposes a risk analysis in the projection of values, considering the history of the components and the constant updating of the data considered. In addition to this factor, this is where DNN with GenAI, come in. In other words, the introduction of GenAI will help to overcome the problem of black swam events, because the deep dive in working orders historic permits to identify the events outside the PdM tools. Based on historical data and other variables that may constitute the AI tool, a probabilistic study can be developed to enable projections for future values. However, this method is often contested because, although historical data can be used to predict the future behaviour of equipment in specific scenarios, there is always the chance of unique operational circumstances arise. This may occur exclusively at that moment of the life cycle, wich makes it difficult to identify outlier events.

To better understand the problem, a practical and simple example can be used to extrapolate. Considering risk and history as a probabilistic basis for estimating future costs, a direct comparison can be made with the algorithms used in Condition Based Maintenance (CBM) and AI tools in Predictive Maintenance (PdM). On the one hand, because the cost of maintenance interventions directly enters the life cycle analysis of the asset

in question; On the other hand, because the methodologies can be transposed and replicated. In this way, similar mathematical gaps can be found.

In fact, by viewing life cycle analysis as a holistic management task, it will be possible to build much more accurate physical asset management systems. The emerging need to integrate asset management with technology and data management for system optimisation leads to an evolution in the quality of KPIs chosen to provide data that feeds algorithms to aid decision-making. Ferreira & Gonçalves (2022) emphasise the need for monitoring for PdM to predict the Remaining Useful Life (RUL) of equipment. RUL is a clear example of an indicator that has become increasingly reliable due to advances in technology and more reliable analysis and decision-making methods. It is a direct part of CBM and PdM and, as such, asset management.

Since this project will be developed with military physical assets, it is important to note the research conducted by Scott *et al*. (2022), which emphasise the need and urgency to implement sensorisation and accept the credibility of the data collected; this subject is equally relevant in non military assets. The evolution of the reliability of these sensors (which is already happening) is important, since pilots are being removed from aircraft and the world is moving towards a future where autonomous vehicles predominantly operate. The quality of the data collected ensures that these aircraft can operate autonomously. But more than that, with the accuracy and quality of the sensors that enable data collection from these vehicles, increasingly more opportunities are arising for expert monitoring of the asset life cycle. Also, in the study of Scott *et al*. (2022), the authors state that "military and civil domains may see benefit from greater cross-collaboration, enabling a dual-use case for PdM technologies, while also providing higher returns on funding and resources". Byington *et al*. (2002) evaluate the adjacent possibilities between the failures diagnosis and prognosis. Referring to the ability to predict the future condition of an asset, the authors emphasised that an "advanced prognostic capability is desired because the ability to forecast this future condition enables a higher level of CBM for optimally managing total LCC". The authors also conclude that the "ability to predict the time to conditional or mechanical failure (on a real-time basis) is of enormous benefit and health management systems that can effectively implement the capabilities presented here offer a great opportunity in terms of reducing the overall LCC of operating systems as well as decreasing the operations/maintenance logistics footprint". All these mentioned gaps and facts are based on the predominant matter of physical asset management, with the analysis of the various life cycles being a key point for real and effective management. The way in which the terms are perceived can influence how investments are conceived and how profits are derived from these actions. When interpreting the data collected, issues of mindset and how each one views the life cycle can determine whether or not good decisions are made.

In line with this reasoning, Farinha (2018) highlights an important point, noting that "regarding management itself, the introduction and certification of many organizations by ISO 55000 will be a revolution when compared with the current vision of asset management. The word "cost" will be replaced by the asset's fixed initial investment and the variable asset investment over time". The author mentions some of the times and stages that must be met during the life cycle of an asset:

- t1- Acquisition decision
- t2 - Terms of reference
- t3 - Market consultation
- t4 - Acquisition

- t5 - Commissioning
- t6 - Starting production/maintenance
- t7 - Economic/lifespan issues
- t8 - Renewal/withdrawal

In another study, Farinha (2024) demonstrates the optimisation potential that the implementation of maintenance policies and standards can offer to an organisation, considering the quantitative support for decision-making.

Considering all these broad themes, it is possible to assess the importance that the proposed methodology could have and the impact it could cause on organizations and the scientific community.

3. Methodology

3.1 SCIENTIFIC APPROACH

In order to contribute to the sharing of knowledge and scientific innovation, efforts will be made to improve the application and integration of the various existing LCA and LCA models. Not from the theoretical perspective of mathematical formulation, as these have already proven to be robust, but rather in the acquisition of the data that feeds them, by establishing a direct link with data collected via sensors used, for example, in maintenance. Furthermore, innovation is sought in data processing and the predictive analysis of maintenance costs with the aid of maintenance algorithms. Thus, in addition to optimising all investments related to the acquisition and operation of the assets under study, it will also be possible to improve the efficiency of the associated maintenance and maximise its lifecycle. Finally, by analysing the models applied, it will be possible to support and inform decision-making regarding whether and when to renew or replace this equipment. Figure 1 is a diagram that provides a simplified illustration of the data analysis, learning and managing process throughout a typical life cycle, from the acquisition decision to disposal.

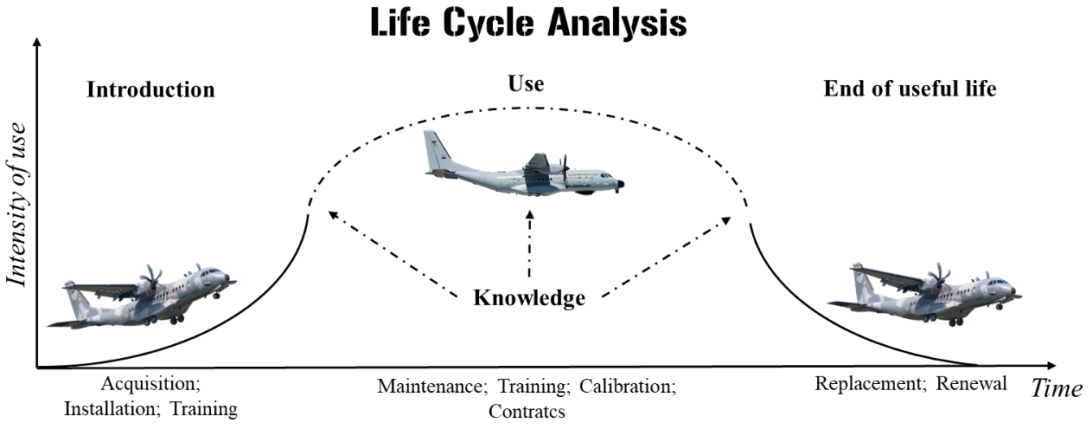


Figure 1 - Life cycle analysis

This research consist of five main phases:

- State-of-the-art research with an in-depth bibliographic analysis;
- Data collection and processing;
- Models' preparation and application with the parameters considered most appropriate, based on processed data;
- Analysis of the correlation among variables and models;
- DNN training and application of AI tools.

A review of the literature also played a major role in the choice of this approach. It was a topic that had been discussed and on which an intuitive consensus had been reached within the organisation. This fact demonstrates and underscores its suitability. Thus, it is possible to structure in advance what is expected to be the outcome and the development of this method. The social constraint was taken into account, since the asset is managed by an organisation and its management can be unique and decisive in achieving results. The sampling process is characteristic of the qualitative method, as the process is non-probabilistic. It will be selected using specific indicators of the asset under study. These indicators are in line with the study's requirements, as the life-cycle models applied take them into account. This may be considered a purposive (judgmental) sample, where participants are intentionally selected based on their knowledge of the models being applied. The information collected will enable the interpretation of the relationship among multiple variables, in terms of the asset's performance and the transformation of its life cycle. Ideally, these variables will be exploratory data and may be considered to originate from secondary sources of empirical information. It is the organisation that collects them directly and provides them to the researcher. The sources of evidence expected to be used in this study will be observations, documents and records, and physical artefacts. Observations will be made regarding the condition of the equipment and how it operates. The documents and records will provide access to the equipment's operational history. Physical artefacts, on the other hand, will allow for the verification of the results of potential deterioration, which has been recorded and studied by the organisation. These will also provide for the adoption of precautions and considerations in the approach to maintenance management. Once again, the mixed nature of qualitative and quantitative research methods is demonstrated. One of the main goals of the study's conclusion is to identify the most appropriate point in the life cycle for renewing or replacing the asset by a new equivalent. This involves determining the most suitable life cycle model for the asset, in line with the manager's objectives. Once the model has been determined, the objective is to design a decision-support tool that can be applied to other physical assets. It is also hoped that, by obtaining maintenance data, patterns will be identified that allow maintenance costs to be optimised and clearer forecasts of future costs to be made. Thus, equipment availability will be maximised and it will be possible to meet the Defence Sector's need for a tool that helps optimise investment in its assets.

3.2 METHODOLOGY IMPLEMENTATION

Given that the first stage was more theoretical, involving a survey of the state of the art with an in-depth bibliographic analysis, this second step involves data collection and processing. Although all other stages are important, this specific stage of the project will be decisive and will determine the quality of the results obtained. It addresses the gaps that have been identified. There is a wealth of data and numerous types of data available. However, much of it is raw data. Considering the practical work carried out in partnership with the Defence Sector, the purpose is to identify KPIs to assess the life cycle and the ideal replacement period. These indicators must be interpreted to enable the information to be processed so, they are introduced into the

models. The models to be applied are the following (de Almeida Pais *et al*., 2021; Farinha *et al*., 2023; Mendes *et al*., 2023; Raposo *et al*., 2019):

- Uniform Annual Income (UAI);
- Minimization of Total Average Cost with (MTAC) with and without Reduction to Present Value (MTAC-RPV);
- Life Cycle Recovery (LCR);
- Life Cycle Investment (LCI);
- Life Cycle Investment Assessment Method (LCIAM).

To apply these models, several parameters must be addressed:

- Time period (*j=1, 2, 3,…,n*);
- Acquisition cost (*CA*);
- Cessation value (*VC*);
- Lifetime corresponding to *VCn* (*N*);
- Exploration value (*CE*);
  - Operating Cost (*CO*);
  - Maintenance Cost (*CM*).
- Apparent rate (*iA*).
- Average Availability (*A*);
- Benefits value (*B*);
- Non-production costs (*NP*).

The UAI calculation methodology is represented in equation (1).

$$UAI_n = \frac{i_A \times (1+i_A)^j}{(1+i_A)^j - 1} \times (CA + \sum_{j=0}^{n} \frac{CM_j + CO_j}{(1+i_A)^j} - \frac{V_n}{(1+i_A)^j}) \quad (1)$$

The MTAC method is obtained from equations (2), (3) and (4).

$$Cn' = \frac{\sum_{j=0}^{n} CM_j + CO_j}{n} \quad (2)$$

$$Cn'' = \frac{CA - Vn}{n} \quad (3)$$

$$MTAC = Cn' + Cn'' \quad (4)$$

The MTAC-RPV method is based on the equations (5), (6) and (7).

$$Cn' = \frac{1}{n} \times \frac{\sum_{j=1}^{n} CM_j + CO_j}{(1 + i_A)^j} \tag{5}$$

$$Cn'' = \frac{CA - \frac{V_n}{(1 + i_A)^j}}{n} \tag{6}$$

$$MTAC - RPV = Cn' + Cn'' \tag{7}$$

The LCI method includes profits derived from the assets, as well as fees and expenses. The LCI method can therefore be calculated using equation (8) (already modified to include non-production costs).

$$GR_n = \sum_{j=0}^{n} \frac{B_j}{(1 + i_A)^j} - \sum_{j=0}^{n} \frac{CO_j}{(1 + i_A)^j} - \sum_{j=0}^{n} \frac{CM_j}{(1 + i_A)^j} - \sum_{j=0}^{n} \frac{NP_j}{(1 + i_A)^j} \tag{8}$$

The LCR method, on the other hand, not only considers the depreciation of the asset that was acquired or will be acquired based on the rates, but also the value of a new equivalent at the same rates. This way, in addition to organizations being able to consider the costs of renovating and maintaining assets, it is easier to find the best time to replace them, based on the variation in the market value of the new asset. Equation (9) relates the Apparent Rate to the depreciation of the physical asset, where C_{0D}^{t} represents the value of the asset in period *t* and C_{0D}^{t-1} represents the value of the asset in the previous period.

$$C_{0D}^{t} = C_{0D}^{t-1} \times i_A C_{0D}^{t} = C_{0D}^{t-1} \times i_A \tag{9}$$

Equation (10) represents the same relationship, but this time from the point of view of acquiring equivalent new equipment, where C_{0N}^{t} represents the value of the new physical asset at time *t* and $C_{0N}^{t-1}$the value of the new physical asset at time *t-1*.

$$C_{0N}^{t} = C_{0N}^{t-1} \times i_A \tag{10}$$

The total net present value, considering the devaluation of physical assets (NPV_{TD}), depends on the net present value of the movement in financial production (NPV_{FpD}) and the net present value of the financial expenses movement (NPV_{Fe}), as can be seen in eq. (11).

$$NPV_{TD} = NPV_{FpD} + NPV_{Fe} - C_{0D}^{t} \tag{11}$$

Similarly, equation (12) presents the total net present value considering a new physical asset (NPV_{TN}), where NPV_{FpN} represents the net present value of the financial production movement considering the acquisition of the equivalent new equipment. NPV_{Fe} is calculated using equation (13).

$$NPV_{TN} = NPV_{FpN} + NPV_{Fe} - C_{0N}^{t} \tag{12}$$

$$NPV_{Fe} = -\sum_{j=0}^{n} \frac{F_j}{(1+i_A)^j} - \sum_{j=0}^{n} \frac{M_j}{(1+i_A)^j} \quad (13)$$

All these models can be integrated into the LCIAM assessment, if the current Net Asset Value (*NPV*) is modified to the Integrated Net Present Value (*INPV*). The current *NPV* formula is expressed in equation (14).

$$NPV_n = CA + \sum_{j=0}^{n} \frac{CM_j + CO_j}{(1+i_A)^j} - \frac{V_n}{(1+i_A)^j} \quad (14)$$

On the other hand, the *INPV* method includes the following parameters:

- Investment in technological upgrade (*IUT*);
- Technological depreciation (*DT*);
- Sustainability depreciation (*DS*);
- Residual Value of the upgraded part (*R*).

INPV is presented in equation (15).

$$INPV_n = CA + \sum_{j=0}^{n} \frac{CM_j + CO_j + IUT_j + DT_j + DS_j}{(1+i_A)^j} - \frac{V_n + \sum_{j=0}^{n} R_j}{(1+i_A)^j} \quad (15)$$

However, it is certain that there will be a need to modify and introduce new types of data to ensure its complementarity. At this point of the research will seek to fill one of the biggest gaps in literature, which is the possibility of finding points of interconnection between the various types of life cycle analysis of physical assets, thereby making this assessment permanent and simultaneous. For example, to understand the environmental impact of operations involving the studied assets, it is necessary to include the sustainability depreciation parameter. Or even to reflect changes (improvements) that have been implemented to the assets since its acquisition, technological upgrades will be included as parameters. When selected, these indicators must cover all parameters of sustainability, availability, operation, maintenance, technological updates and more. It will also be crucial to understand the parameters that characterize the need for cannibalization and stock calculation. Rationalization will be the key, and effective stock rationalization will only be possible by applying lean principles and striving to implement a Just In Time (JIT) methodology, without compromising the availability of components and aircraft. In addition to all the models and parameters indicated so far, many others will also be included, where applicable. These are, among others, the Mean Time to Repair (MTTR), the Mean Time Before Failure (MTBF), the Availability, and the Mean Time to Failure (MTTF) for consumable or irreparable damage. It will presumably be necessary to find additional applicable parameters as understanding of the asset's operation increases. Particularly because many of the performance parameters are measured differently, since flight hours predominate (and this is where there is greater deterioration of the equipment), but operating hours and component age must also be considered. Another calculation that will have to go hand in hand with the methodology and all life cycle models will be the Return on the Investment (ROI). Given the type of asset, the return on investment will also be required to reflect the political and social return that could also present a challenge to overcome, and which is expected to add value to the

current state of the art. Nevertheless, once again, such steps will only be possible if the appropriate indicators are carefully selected, processed, and interpreted. In addition to the link between the various possibilities for analyzing an asset's life cycle, a platform will be made available where managers can select a specific life cycle analysis. If the user wants to find out the minimum average cost of an asset's operation, this can be found in the MTAC-RPV. If the user wants to find out about the environmental impact, it is possible to analyze the modified models with the inclusion of the sustainability depreciation parameter (INPV). Everyone involved must be able to answer these three questions about the collected data:

- Why is it being collected?
- How is it being collected?
- What is it being collected for?

This procedure will be extremely important, as it will keep everyone aware of their role and how it can impact the proper functioning of the system. In addition, this deep understanding of the entire process will lead to a reduction in errors caused by human interpretation. Discrepancies in interpretation among different users will be reduced by standardizing the process and minimizing subjective assessments. The quantitative and qualitative features that define the work to be performed and that will allow the data to be interpreted and processed, suggest that the approach to data processing is considered the most appropriate. The data is obtained through the history of all components (cannibalization, availability, maintenance, flight hours, lifetime, end of life due to irreparable defects, among others).

The methodology presented in this paper, part of Predictive Life Cycle Analysis for Aircraft Navigation Equipment (PLANE) project, is an innovative methodology that uses the variables of the asset’s life cycle, namely Operational KPIs, including Maintenance, Economic, Spare Parts, Risk, and maintenance historic.

Figure 2 provides a simplistic diagram of the methodology to be applied.

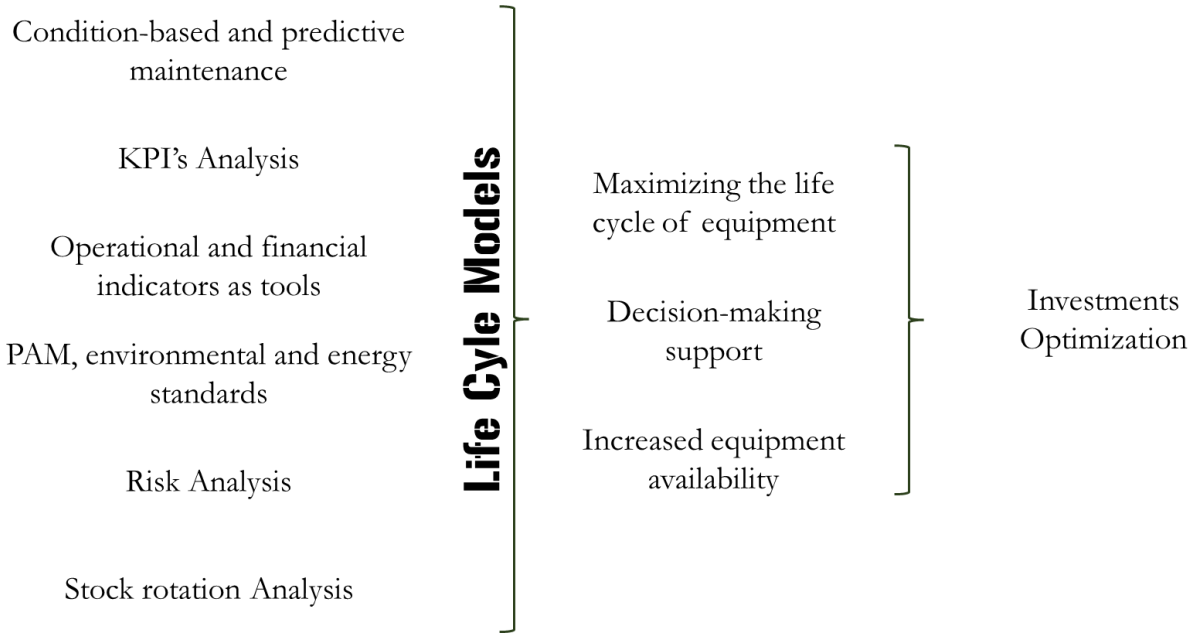


Figure 2 - Simplistic diagram of PLANE methodology.

Integrating AI into PLANE will primarily target increasing efficiency and improving hypothesis formulation. By training DNNs, like Long Short Term Memory (LSTM), Gated Recurrent Units (GRU) among others, the goal is to develop predictive models capable of understanding both trends and potential variations in the parameters of life-cycle models during asset operation. It will also be important to help visualize potential relationships between them through asset performance. The application of these tools, such as GenAI, will enable the creation of new models and combinations based on Large Language Models (LLMs) training, because in near past these resources were not available, including the hardware processing. This means that, until recent days, those approaches were not possible to be implemented because the lack of processing means.

The goal is to assist users in interpreting data, reformulating logistics strategies and specifications as needed. This could involve, for example, simulating potential combinations of different aircraft part serial numbers to optimize operations—whether to minimize costs, reduce environmental impact, maximize availability, mitigate risk, or even suggest the best approach to achieve the most efficient performance across all these areas simultaneously. The possibilities are endless and will enable managers to optimize resources, boost efficiency, and anticipate hypothetical scenarios.

4. Conclusions

This paper presents not only the state of art of life cycle analysis but presents proposals to help to manage physical assets, namely propeller systems of aeronautical assets. Through this study, knowledge about life-cycle analysis will be deepened, but, above all, it will be established as a standard tool that can be replicated and adapted to any asset in any sector. The implementation of best practices, the rationalization of resources and investment analysis can take any organization to a new level of management. This project aims to deepen

knowledge of life cycle analysis, but above all, to establish it as a standard tool that can be replicated and adapted to any asset in any sector. The implementation of best practices, the rationalization of resources and investment analysis can elevate any organization to a higher level of management, thereby contributing to a more sustainable management of physical assets.

References

Byington, C. S., Roemer, M. I., & Galie, T. (2002). *Prognostic Enhancements to Diagnostic Systems for Improved Condition-Based Maintenance*. IEEE.

de Almeida Pais, J., Raposo, H. D. N., Farinha, J., Cardoso, A. J. M., & Marques, P. A. (2021). Optimizing the life cycle of physical assets through an integrated life cycle assessment method. *Energies*, *14*(19). https://doi.org/10.3390/en14196128

Farinha, J. M. T. (2018). *Asset Maintenance Engineering Methodologies*.

Farinha, J. T., Raposo, H. D. N., de-Almeida-e-Pais, J. E., & Mendes, M. (2023). Physical Asset Life Cycle Evaluation Models—A Comparative Analysis towards Sustainability. *Sustainability*, *15*(22). https://doi.org/10.3390/su152215754

Ferreira, C., & Gonçalves, G. (2022). Remaining Useful Life prediction and challenges: A literature review on the use of Machine Learning Methods. In *Journal of Manufacturing Systems* (Vol. 63, pp. 550–562). Elsevier B.V. https://doi.org/10.1016/j.jmsy.2022.05.010

Holwerda, H., Haanstra, W., Braaksma, J., Coenen, T., & Santos, J. (2021). Application of Life Cycle Assessment and similar methodologies in Asset Management: A multiple case study. *Proceedings of the The 10th International Conference on Through-Life Engineering Services*.

J. M. T. Farinha. (2024). *Physical Asset Management for a Sustainable World*.

Mendes, C., Raposo, H., Ferraz, R., & Farinha, J. T. (2023). The Economic Management of Physical Assets: The Practical Case of an Urban Passenger Transport Company in Portugal. *Sustainability (Switzerland)*, *15*(15). https://doi.org/10.3390/su151511492

Muazu, R. I., Rothman, R., & Maltby, L. (2021). Integrating life cycle assessment and environmental risk assessment: A critical review. *Journal of Cleaner Production*, *293*, 126120.

Nogueira Raposo, H. D., Farinha, J. M. T., Ferreira, L. A., & Galar, D. (2019). Reserve fleet indexed to exogenous cost variables. *Transport*, *34*(4), 437–454. https://doi.org/10.3846/transport.2019.11079

Saraswat, S., & Yadava, G. S. (2008). An overview on reliability, availability, maintainability and supportability (RAMS) engineering. *International Journal of Quality & Reliability Management*, *25*(3), 330–344.

Scott, M. J., Verhagen, W. J. C., Bieber, M. T., & Marzocca, P. (2022). A Systematic Literature Review of Predictive Maintenance for Defence Fixed-Wing Aircraft Sustainment and Operations. In *Sensors* (Vol. 22, Number 18). MDPI. https://doi.org/10.3390/s22187070

TREATY, N. A. (2007). *Methods and Models for Life Cycle Costing*.

SESSION 7

Stochastic Dynamics and Computational Methods

Papers in this session

1. A generalized autoregressive model for time-variant dynamical systems
2. Stochastic contact analysis and its applications
3. A Continuous-Time Markovian Framework for Performance-Based Earthquake Engineering: Integrated Seismic Risk and Resilience Assessment
4. Neural network-driven uncertainty qualification analysis of printed circuit heat exchangers
5. Towards a Set-Based IVP Solver for ODEs on the GPU
6. Efficient Probabilistic Response Analysis of Large-Scale Engineering Structures under Stochastic Excitation via the DR-PDEE Incorporating an Auxiliary Diffusion Process
7. A Regression-Tree-Based Method for Structural Reliability Assessment
8. Probabilistic Resilience Analysis of Urban Road Network Considering Wind Damage to Street Trees via Dimension-Reduced Probability Density Evolution Equation (DR-PDEE)

A generalized autoregressive model for time-variant dynamical systems

Styfen Schär[(1*)], Chiara Nardin[(1,2)], Stefano Marelli[(1)] and Bruno Sudret[(1)]
[(1)] *Chair of Risk, Safety and Uncertainty Quantification,ETH Zurich, 8093 Zurich, Switzerland - {schaers,cnardin,marellis,sudretb}@ethz.ch*

[(2)] *Department of Civil, Environmental and Mechanical Engineering, University of Trento, 38132 Trento, Italy - {chiara.nardin}@unitn.it*

Abstract. Surrogate models are a staple tool for the reliability analysis of complex engineering systems, because they enable the use of otherwise computationally prohibitive algorithms, such as Monte-Carlo simulation. Their prevalence in the context of nonlinear dynamic engineering systems, however, is significantly lower, because approximating their time-dependent response is generally considered more challenging than for their static counterparts. A powerful class of surrogate models is provided by autoregressive with exogenous input models, but their use is mostly limited to system identification tasks, as they tend to underperform in pure prediction tasks. Recent advances in data-driven autoregressive modeling, have vastly improved their prediction capabilities for engineering applications, but they still rely on the assumption of time-invariant dynamics at the core of NARX. In this contribution we demonstrate how the mNARX$^+$ framework can efficiently handle time-variant dynamical systems, such as, e.g., civil or mechanical structures subject to plastic damage or fatigue accumulation, making it an ideal tool for their reliability assessment.

Keywords: Surrogate Modeling, Time-Variant Dynamical Systems, Autoregressive Modeling, mNARX, Uncertainty Quantification

1. Introduction

Structural reliability analysis has reached a high level of maturity, providing rigorous frameworks to assess the safety of engineering systems under uncertainty. When the underlying computational models are highly complex, direct simulation methods such as Monte Carlo Simulation (MCS) become computationally intractable, necessitating the use of fast-to-evaluate surrogate models (Moustapha et al., 2022).

For time-invariant problems, where the quantity of interest is a scalar or a low-dimensional vector, classical surrogate modeling techniques have become standard tools. Methods such as sparse polynomial chaos expansions (PCE) (Blatman and Sudret, 2011; Lüthen et al., 2021) and Kriging (Santner et al., 2003) allow for the accurate approximation of the input-to-output map with a limited computational budget. These techniques effectively replace the expensive solver within the reliability loop, enabling efficient estimation of failure probabilities, especially when paired with

creative commons © 2026 by the author(s). This work is licensed under the Creative Commons Attribution 4.0 International License (CC BY 4.0), which permits unrestricted use, distribution, and reproduction in any medium, provided the original author and source are credited.

active learning paradigms borrowed from the machine learning literature (Echard et al., 2011; Marelli and Sudret, 2018; Moustapha et al., 2022).

However, many critical engineering systems are inherently dynamical, *e.g.* offshore wind turbines, vehicle suspensions, or structures evolving under highly variable external loads, such as seismic excitations. In such cases, the model output is a time-dependent vector field or trajectory defined over a specific time domain. Rather than learning the global map directly, it can be significantly more effective to emulate the discrete-time evolution of the system, switching to a more state-space-like approach. This leads naturally to the class of Nonlinear AutoRegressive with eXogenous inputs (NARX) models (Billings, 2013).

By learning the recursive law governing the system, rather than the full trajectory, NARX models construct predictions based on the immediate past history of the input and the output, thereby naturally enforcing causality. Despite their utility, classical standard NARX formulations struggle heavily with the selection of optimal time lags and the processing of high-dimensional inputs, which often leads to instability over long time periods (Billings, 2013). Highly complex systems, such as wind turbines operating under turbulent winds or tall buildings subject to seismic loads, introduce additional challenges due to active control systems, uncertain structural parameters, etc.

To overcome these limitations, advanced surrogate models based on modified autoregressive approaches have recently been proposed, notably the manifold-NARX (mNARX) (Schär et al., 2024) and functional-NARX ($\mathcal{F}$-NARX) (Schär et al., 2025) frameworks. The mNARX approach constructs surrogates on a reduced-dimensionality manifold of auxiliary state variables, that can handle both high-dimensionality exogenous inputs, and highly nonlinear system responses. This is achieved by embedding expert knowledge into the regression formulation, by introducing a sequence of auxiliary NARX models of intermediate response quantities that are informative w.r.t. the desired quantity of interest (Schär et al., 2024). Conversely, $\mathcal{F}$-NARX mitigates the arbitrary nature of lag selection, long-memory effects and dependence on sampling rate, by extracting functional temporal features from continuous time windows (Schär et al., 2025). More recently, the mNARX$^+$ framework (Schär et al., 2026) was introduced to bridge these methods, automating the construction of the auxiliary manifold through data-driven feature selection, thereby removing the previous reliance on domain expertise.

In this paper, we capitalize on the mNARX methodology to handle the case of non-time-invariant engineering systems, by introducing auxiliary response variables that can track the state of the system over time. This allows us create an autoregressive manifold that can naturally account for time-varying states, e.g. due to progressive damage accumulation. The proposed approach ensures accurate trajectory predictions even after the structural integrity of the system has been partially compromised, an essential ingredient for efficiently quantifying their reliability and resilience.

2. Methodology

To model time-variant engineering systems undergoing progressive change, we need a robust mathematical framework that can capture and keep track of complex, nonlinear and time-dependent behaviors. This section outlines the theoretical foundations of autoregressive modeling, detailing the

mNARX and $\mathcal{F}$-NARX frameworks before establishing the theoretical basis for our damage-tracking approach.

2.1. Standard NARX Framework

Consider a computational model of a dynamical system denoted by $\mathcal{M}$, that models some response quantity of interest $y(t)$. The system is subjected to a time-dependent, multi-dimensional exogenous excitation vector $\boldsymbol{x}(t)$. The model output over a time axis $\mathcal{T}$ is then given by:

$$y(t) = \mathcal{M}(\boldsymbol{x}(\mathcal{T} \leq t)). \tag{1}$$

Within this section, we also assume that the time axis $\mathcal{T} \in [0, T]$ is discretized regularly with a sampling interval $\delta t \ll T$.

A standard NARX model assumes that the current output $y(t)$ depends on its own past values (autoregressive terms) and the current and past values of the exogenous input. This discrete-time relationship is formally expressed as:

$$y(t) = \mathcal{H}\Big(y(t-\delta t), \ldots, y(t-n_y\delta t), \boldsymbol{x}(t), \boldsymbol{x}(t-\delta t), \ldots, \boldsymbol{x}(t-n_x\delta t)\Big) + e(t) \tag{2}$$

where n_x and n_y represent the maximum time lags for the exogenous inputs and system responses, respectively, $\mathcal{H}$ is a nonlinear mapping function, and $e(t)$ represents the residual error. In systems with high-dimensional exogenous inputs or those requiring long-term memory, the input space for $\mathcal{H}$ grows exponentially, exacerbating the curse of dimensionality and severely complicating surrogate training (Billings, 2013).

2.2. Functional Feature-based NARX ($\mathcal{F}$-NARX)

To overcome the limitations of classical discrete-time NARX models, the authors introduced the $\mathcal{F}$-NARX approach (Schär et al., 2025). It represents a major step away from discrete time steps by exploiting the functional nature of system trajectories over continuous time windows.

In a typical $\mathcal{F}$-NARX implementation, principal component analysis (PCA) is used to project historical time windows of the exogenous inputs and past outputs onto a set of orthogonal basis functions. The corresponding set of coefficients $\boldsymbol{\xi}(t)$ are then used instead of the input lags in an autoregressive setting (Schär et al., 2025).

In other words, Eq. (1) is rewritten as:

$$y(t) \approx \widehat{\mathcal{M}}(\boldsymbol{\xi}(\mathcal{T} \leq t)). \tag{3}$$

The model in Eq. (3) is then approximated with a standard NARX approach, as in Eq. (2).

This approach successfully maps continuous trajectory segments to interpretable time-dependent features, rather than isolated discrete points in time, fundamentally mitigating the numerical instabilities associated with very small time steps and long memory limits (Schär et al., 2025).

2.3. Manifold-NARX (mNARX)

To efficiently approximate the response of complex dynamical systems over extended time periods, the mNARX approach further constructs the surrogate on a problem-specific, reduced-order manifold of auxiliary state variables $\boldsymbol{\zeta}(t)$ (Schär et al., 2024).

By leveraging the underlying physics of the system as well as prior expert knowledge, mNARX decomposes the full problem into a hierarchical sequence of smaller sub-problems, which are then combined to form an input manifold $\boldsymbol{\zeta}(t)$ suitable for autoregressive modeling. More in detail, the manifold $\boldsymbol{\zeta}(t) = \{\tilde{\boldsymbol{x}}(t), \hat{\boldsymbol{z}}(t)\}$ is formed by two components: $\tilde{\boldsymbol{x}}(t)$, a set of features extracted from the input excitation $\boldsymbol{x}(t)$, e.g. through dimensionality reduction or spectral decomposition, and $\hat{\boldsymbol{z}}(t)$, a set of auxiliary quantities of interest that may be related to the output quantity of interest (QoI) $y(t)$, such as auxiliary quantities, or even quantities post-processed from the model response $y(\mathcal{T} < t)$. In general, the latter are not directly available from the input excitation, but need to be treated as additional model responses, and therefore modeled themselves as autoregressive surrogates:

$$\hat{z}_k(t) \approx \widehat{\mathcal{M}}_k \left(\tilde{\boldsymbol{x}}(\mathcal{T} \leq t), \hat{z}_1(\mathcal{T} < t), \ldots, \hat{z}_{k-1}(\mathcal{T} < t)\right). \tag{4}$$

Once the complete input manifold is available, the output QoI can be modeled autoregressively:

$$\hat{y}(t) = \widehat{\mathcal{M}}_y\Big(\boldsymbol{\zeta}(\mathcal{T} \leq t), \hat{y}(\mathcal{T} < t)\Big). \tag{5}$$

As demonstrated in Schär et al. (2024), this approach enables the efficient and accurate surrogate modeling of complex dynamical systems, even in the presence of high dimensional random inputs and active control systems. Further extensions to this algorithm include fully data-driven automatic construction of the input manifold (Schär et al., 2026), and long term functional output prediction, including estimation of epistemic error (Song et al., 2026).

2.4. Using mNARX to track damage in time-variant systems

In their native formulation (Eq. (2)), NARX models implicitly rely on the time-invariant nature of the underlying system. This is what allows them to accurately predict future states based on a finite model memory. In many real situations, however, dynamical systems vary over time, e.g. due to progressive damage accumulation, thus requiring autoregressive models to deal with potentially infinite memory. The same limitation also applies to the $\mathcal{F}$-NARX and mNARX models presented in the previous sections.

However, one of key features of the mNARX approach is that it can encode expert information about the system state directly in the input manifold $\boldsymbol{\zeta}(t)$, and use it to improve its prediction capability. If we can define one or more suitable *system-state trackers* $\boldsymbol{D}(t)$, that either represent or correlate to some indicator of the current state of the system, they can be included into the auxiliary manifold components $\hat{\boldsymbol{z}}(t)$ to keep track of the system state outside of its autoregressive window. Examples of such trackers include cumulative damage indices in structural systems, such as the Park–Ang damage index for earthquake-excited structures (Park and Ang, 1985); rainflow counting in fatigue (ASTM, 2017); effective stiffness degradation inferred from force-displacement hysteresis in nonlinear systems (Ibarra et al., 2005); or shifts in dominant response frequencies

associated with stiffness loss (Lieven et al., 2001; Fassois and Sakellariou, 2006). Depending on the application, these indicators may be directly available as additional simulator outputs or may need to be estimated through post-processing of the system response

The resulting augmented manifold then becomes:

$$\tilde{\boldsymbol{\zeta}}(t) = \{\tilde{\boldsymbol{x}}(t), \hat{\boldsymbol{z}}^*(t)\}, \quad \hat{\boldsymbol{z}}^*(t) = \left\{\hat{\boldsymbol{z}}(t), \hat{\boldsymbol{D}}(t)\right\}, \tag{6}$$

where $\hat{\boldsymbol{D}}(t)$ is an autoregressive approximation of the chosen damage trackers $\boldsymbol{D}(t)$. This formulation ensures that the surrogate model explicitly parametrizes the state trackers $\boldsymbol{D}(t)$, continuously updating its internal representation of the system. In other words, the framework dynamically adapts, providing stable predictions across different system states, without the need to modify the overall formulation of the mNARX methodology.

3. Application: portal frame subject to high amplitude seismic excitation

3.1. Computational Model

The model adopted is based on, and slightly modified from, the reinforced concrete (RC) portal frame example provided in the OpenSeesPy manual (see the RCFrameEarthquake example in OpenSeesPy documentation (OpenSeesPy, 2024)).

More specifically, a one-bay, base-fixed RC portal frame with dimensions 144 in $\times$ 366 in and rectangular cross-sections (16 in $\times$ 25 in) was implemented as a two-dimensional nonlinear finite element model within the OpenSeesPy framework (OpenSeesPy Development Team, 2024). The columns were modeled using `forceBeamColumn` elements to capture both material and geometric nonlinearities, including P-Δ effects. A Gauss–Lobatto integration scheme with nine integration points per element was employed. The cross-sections were discretized into fiber components, consisting of: (i) confined concrete core ($f'_c = -6.0$ ksi); (ii) unconfined cover concrete ($f'_c = -5.0$ ksi); and (iii) longitudinal reinforcing steel ($f_y = 60$ ksi). Concrete behavior was represented using the `Concrete01` (Kent–Scott–Park) model, while reinforcing steel was modeled with the `Steel02` material with elastic modulus $E = 30000$ ksi, strain-hardening ratio $b = 0.02$, and standard transition parameters $R_0 = 18.0$, $c_{R1} = 0.925$, and $c_{R2} = 0.15$, as illustrated in Figure 1. Instead, the beam was modeled as a linear elastic `elasticBeamColumn` element. Constant axial loads of $P = 180$ kips were applied at both column tops through preliminary static analysis.

Differently from the reference example, the damping model was implemented using Rayleigh damping, calibrated to provide approximately 5% critical damping in the first two modes, following standard recommendations for RC structures, see (Chopra, 2007).

Finally, the dynamic response of the system is evaluated by imposing seismic excitation as a `UniformExcitation` load pattern, through transient analysis.

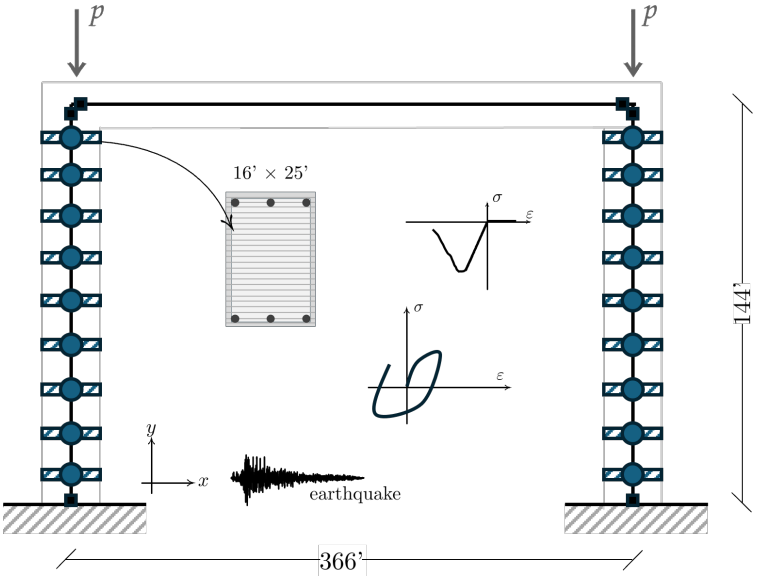


Figure 1. RC portal frame model and column fiber section, including Gauss–Lobatto integration (9 points) and material models for confined/unconfined concrete and steel.

3.2. Synthetic input ground motions

To assess the validity of the proposed framework, an ensemble of synthetically generated ground motions was employed as time-varying input. Specifically, synthetic accelerograms were generated using the site-based stochastic ground motion model (SGMM) proposed in (Su, 2025)[1]. This approach enables the generation of statistically compatible ground motions by fitting a stochastic model to a dataset of recorded motions representative of the seismic hazard of interest.

To construct the reference dataset, 50 real ground motions were selected following the methodology proposed by Baker and Lee (2018)[2], using the Pacific Earthquake Engineering Research Center (PEER) NGA-West2 database. The objective Baker's selection algorithm is to identify a subset of recorded ground motions whose response spectra optimally match a prescribed target distribution. This is achieved through an optimization procedure that minimizes the error between the spectra of the selected records and the target spectrum over a broad period range (0.1 s to 10 s), thereby ensuring both spectral compatibility and statistical representativeness. The selection was refined through a weighted optimization process ($w_{mean} = 1.0, w_{std} = 2.0, w_{skew} = 0.3$), prioritizing the match of the target standard deviation to better focus on capturing the inherent record-to-record variability.

The overall procedure consisted of a two-stage filtering approach. First, a target median response spectrum was defined based on a reference rupture scenario characterized by moment magnitude $M_w = 6.5$, Joyner-Boore distance $R_{jb} = 11$ km, and site condition $V_{s30} = 800$ m/s. Second, metadata-based constraints were imposed to ensure physical consistency of the selected motions.

[1] Available at the corresponding GitHub repository: `https://github.com/MaijiaSu/Toolbox_Site_based_GMMs`
[2] Available at the corresponding GitHub repository: `https://github.com/bakerjw/CS_Selection`

In particular, records were restricted to magnitudes between 6.0 and 8.2 and rupture distances between 10 and 50 km. This procedure ensures that the selected records are consistent with the seismological characteristics of the target scenario.

Once the dataset was defined, the SGMM was calibrated using the selected 50 records, allowing the joint probability distribution of the key ground motion parameters to be characterized, *i.e.* Arias intensity $\log(I_a)$, effective durations D_{0-5}, D_{5-30}, D_{30-45}, D_{45-75}, D_{75-95}, D_{95-100}, dominant frequency $\omega(t_{mid})$, rate of change of the filter frequency $\omega'(t_{mid})$, filter bandwidth $\zeta(t_{mid})$, and corner frequency fc. Subsequently, synthetic ground motion time histories were sampled from the resulting model, resulting in an ensemble of 10,000 synthetic records.

3.3. Problem setup

In this case study, we construct an mNARX surrogate model to predict the strain in the upper steel reinforcement bars at the base section (see Figure 1), denoted by $\varepsilon(t)$ and hereafter referred to as *steel top strain*. The input excitation is given by the ground motion acceleration introduced in Section 3.2, denoted by $x(t)$.

Based on the quantity of interest $\varepsilon(t)$, we define a damage indicator $D(t)$ that quantifies exceedance of a threshold strain value ε_{th}. Specifically, we consider a cumulative damage measure defined as

$$D(t) = \int_0^t \left(\varepsilon^+(\tau)\right)^2 \, d\tau, \tag{7}$$

where $\varepsilon^+(t)$ denotes the strain exceeding the threshold:

$$\varepsilon^+(t) = \max\big(|\varepsilon(t)| - \varepsilon_{\text{th}},\, 0\big). \tag{8}$$

The threshold $\varepsilon_{\text{th}} = 0.2\%$, below which strain excursions are assumed elastic and non-damaging, is inspired by the implicit yield threshold of Park and Ang (Park and Ang, 1985). The continuous-time integral formulation, which avoids cycle counting, follows the spirit of continuum damage mechanics (Lemaitre and Chaboche, 1990).

A visual illustration of this damage indicator is provided in Figure 2, which shows the steel top strain together with the corresponding accumulated damage. The latter can be interpreted as the squared area (highlighted in grey) outside the threshold bounds $\pm\varepsilon_{\text{th}}$.

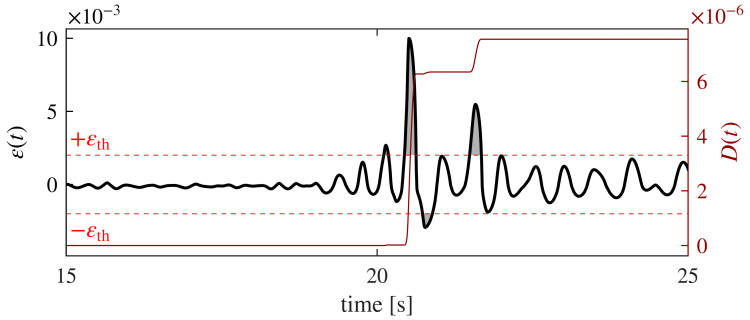


Figure 2. Example strain response and corresponding accumulated damage.

The experimental design consists of 100 simulated ground motion records and their corresponding strain responses and damage histories, which are used to train the surrogate model. For validation, an independent out-of-sample dataset comprising 10,000 ground motion records and corresponding strain responses is employed. Note that during validation the surrogate does not have access to the true underlying damage values.

3.4. Surrogate construction

Within the mNARX framework from Section 2.3, we employ an $\mathcal{F}$-NARX model as introduced in Section 2.2, using a multilayer perceptron (MLP) as the underlying function approximator for the mapping $\widehat{\mathcal{M}}$ in Eq. (3). The MLP consists of two hidden layers with 256 neurons each and ReLU activation functions.

The memory length of the $\mathcal{F}$-NARX model is set to 0.5 seconds (corresponding to $n = 50$ time steps). Temporal features are extracted using principal component analysis (PCA), following Schär et al., with a target explained variance of 90%. This results in 12 features for the exogenous input $\boldsymbol{\xi}_x(t)$ and 3 features for the autoregressive component $\boldsymbol{\xi}_\varepsilon(t)$.

In addition, the surrogate incorporates the cumulative damage $D(t)$ as defined in Section 3.3. During training, the $\mathcal{F}$-NARX model $\widehat{\mathcal{M}}$ learns the mapping

$$\varepsilon(t) \approx \widehat{\varepsilon}(t) = \widehat{\mathcal{M}}\big(\boldsymbol{\xi}_x(t), \boldsymbol{\xi}_\varepsilon(t), D(t-\delta t)\big), \tag{9}$$

with

$$\boldsymbol{\xi}_x(t) = \mathcal{K}_x\left(x(t), x(t-\delta t), \ldots, x(t-n\delta t)\right), \tag{10}$$

$$\boldsymbol{\xi}_\varepsilon(t) = \mathcal{K}_\varepsilon\left(\varepsilon(t-\delta t), \varepsilon(t-2\delta t), \ldots, \varepsilon(t-n\delta t)\right), \tag{11}$$

where $\mathcal{K}_x(\cdot)$ and $\mathcal{K}_\varepsilon(\cdot)$ denote feature extraction operators applied to the exogenous input and autoregressive histories, respectively. In this work, both operators are implemented using PCA as mentioned above. Note that the true strain and damage values are provided during training.

In contrast, when predicting the system output for new excitations, the damage is iteratively calculated on the fly from Eq. (7), using the predicted strain $\hat{\varepsilon}(t)$:

$$\varepsilon(t) \approx \widehat{\varepsilon}(t) = \widehat{\mathcal{M}}\big(\boldsymbol{\xi}_x(t), \boldsymbol{\xi}_{\widehat{\varepsilon}}(t), \widehat{D}(t-\delta t)\big), \tag{12}$$

with

$$\boldsymbol{\xi}_{\widehat{\varepsilon}}(t) = \mathcal{K}_\varepsilon\left(\widehat{\varepsilon}(t-\delta t), \widehat{\varepsilon}(t-2\delta t), \ldots, \widehat{\varepsilon}(t-n\delta t)\right), \tag{13}$$

and

$$\widehat{D}(t) = \sum_{k=0}^{\frac{t}{\delta t}-1} \left(\widehat{\varepsilon}^{+}(k\delta t)\right)^2 \delta t, \quad \widehat{\varepsilon}^{+}(t) = \max\big(|\widehat{\varepsilon}(t)| - \varepsilon_{\mathrm{th}},\, 0\big). \tag{14}$$

To train the model in Eq. (9), we use an 80/20 train–test split of approximately 500,000 regression samples (corresponding to 100 simulations with an average length of 5,000 time steps). The model parameters are optimized using the Adam optimizer with a learning rate of 0.001 and a batch size of 512. Training is continued until convergence of the mean absolute error (MAE), which is assumed

when the validation error does not decrease for 50 consecutive epochs. Based on this criterion, convergence is reached after approximately 400 epochs.

For comparison, we also train a baseline $\mathcal{F}$-NARX model with identical architecture but without the damage input. This allows us to highlight the limitations of finite-memory autoregressive models when applied to time-variant systems, and to demonstrate the benefit of mNARX with explicit damage tracking in such scenarios. Using the same training procedure as with the mNARX model, the baseline model converges after approximately 450 epochs.

3.5. Results

The overall performance of the mNARX model with damage tracking and baseline model without damage tracking on the out-of-sample validation dataset is shown in Figure 3.

Figure 3 (left) presents the distribution of the normalized mean squared error (NMSE) on a logarithmic scale. The NMSE for the i-th realization is defined as

$$\mathrm{NMSE}^{(i)} = \frac{1}{N_t^{(i)} \operatorname{Var}(\boldsymbol{\varepsilon}^{(i)})} \sum_{k=0}^{N_t^{(i)}-1} \left(\varepsilon^{(i)}(k\delta t) - \widehat{\varepsilon}^{(i)}(k\delta t) \right)^2, \tag{15}$$

where $N_t^{(i)}$ denotes the number of time steps and $\operatorname{Var}(\boldsymbol{\varepsilon}^{(i)})$ the variance of the time-series $\boldsymbol{\varepsilon}^{(i)}$.

Figure 3 (right) compares the predicted and true peak absolute strain values $\max(|\varepsilon(t)|)$ on logarithmic axes.

The surrogate model incorporating damage tracking significantly outperforms the baseline model without damage tracking. Most realizations exhibit NMSE values below 0.5, with a median of 0.07, whereas the baseline model yields substantially larger errors, with a median NMSE of 2.6 and many realizations exceeding 10.

This improvement is also evident in the peak strain predictions. The damage-aware surrogate closely follows the diagonal, indicating accurate reconstruction of extreme responses, while the baseline model shows a systematic deviation. Interestingly, the benefit of damage tracking is most pronounced for peak strains below approximately 5%, whereas both models exhibit comparable performance at higher strain levels.

We interpret this overall improvement at lower ground motion amplitudes as a direct consequence of the lack of damage tracking: the baseline surrogate effectively learns an "average" system response between undamaged and damaged systems, corresponding to an "effective" intermediate damage state. Consequently, it performs poorly when the true system is either undamaged or strongly damaged. On the contrary, the availability of a damage indicator in the input manifold allows the damage-aware surrogate to effectively separate the different system operational regimes, resulting in significantly improved model expressivity and accuracy.

The reduced accuracy at high strain levels for both models can be attributed to the limited representation of this regime in the training data: only three simulations exhibit peak strains above 5%, and only approximately 1.7% of all time steps in the experimental design show such high strains.

These trends are further illustrated by individual time histories shown in Figure 4. The top panels correspond to cases without accumulated damage, while the bottom panels show strongly

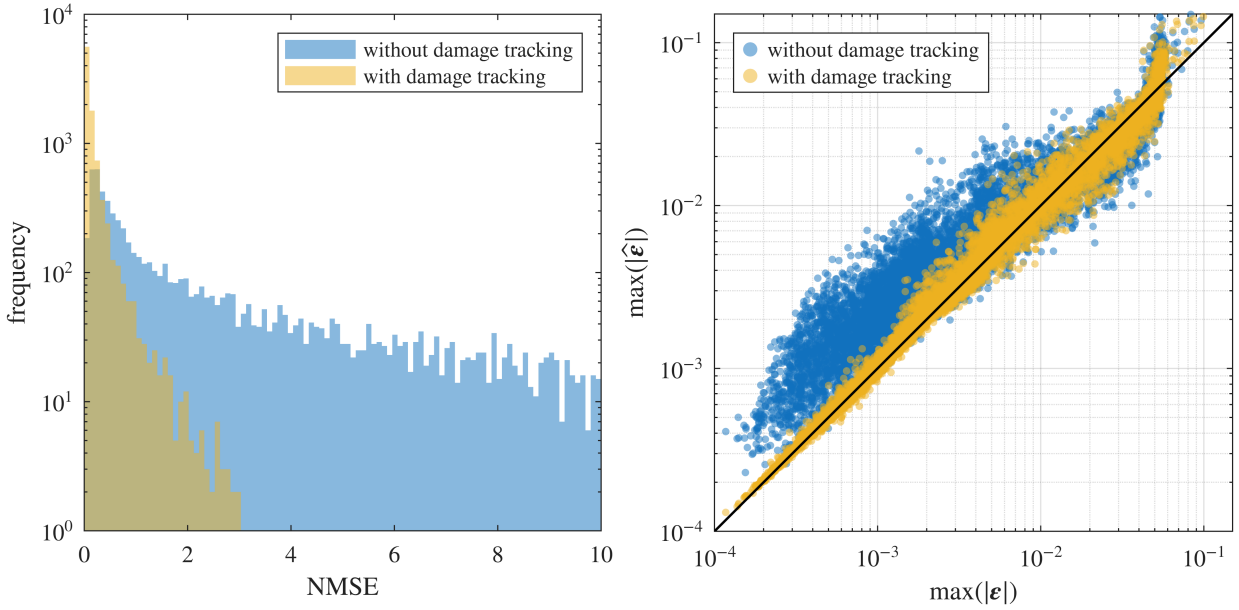


Figure 3. Distribution of the normalized mean squared error (NMSE) on the out-of-sample validation dataset (left), and comparison of predicted versus true peak absolute strain (right) for the surrogate model with and without damage tracking. The histogram (left) uses a logarithmic y-axis, while the scatter plot (right) uses logarithmic scaling on both axes.

damaged systems. The NMSE for these four representative simulations, for both the surrogate with and without damage tracking, are provided in Table I.

Table I. NMSE, as defined in Eq. (3.5), corresponding to the traces shown in Figure 4.

	Top left	Top right	Bottom left	Bottom right
With damage tracking	0.0066	0.0210	0.1444	0.3357
Without damage tracking	6.0327	1.9077	0.2937	0.9130

In the undamaged case, both models accurately follow the ground truth at early time instants; however, the baseline surrogate gradually deviates over time, whereas the damage-aware model remains accurate throughout the entire duration of the simulations. In the damaged case in the bottom right panel, the baseline model fails to represent the accumulation of residual strain, as it effectively approximates an averaged system response and therefore reverts toward zero-mean behavior. In contrast, the damage-tracking surrogate captures both the transient response and the evolving permanent deformation.

These observations confirm that incorporating damage tracking enables the surrogate to adapt to structural state changes, which leads to significantly improved predictive accuracy across a wide range of conditions.

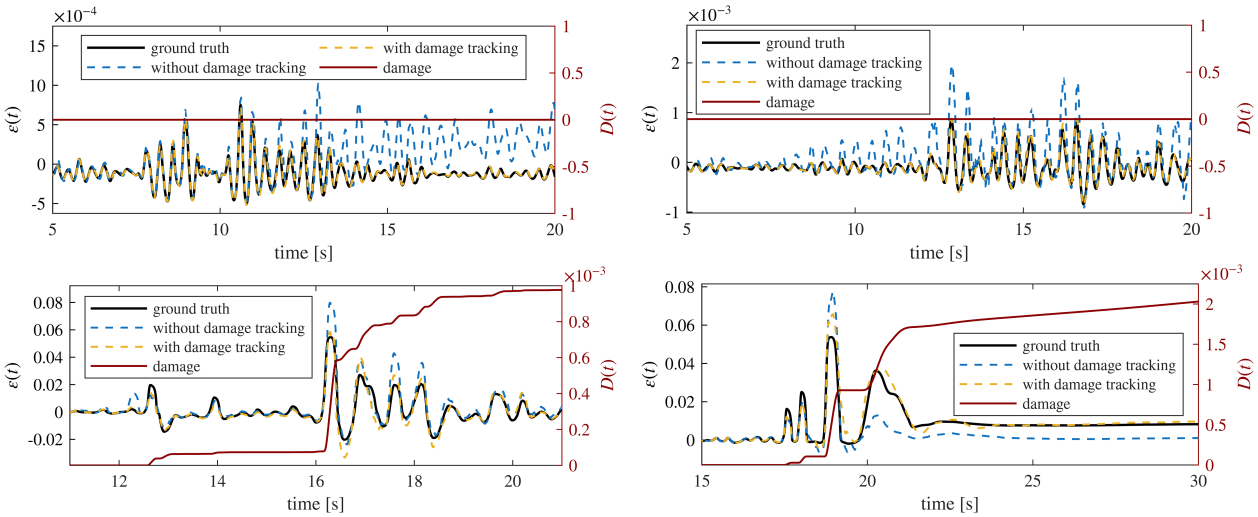


Figure 4. Example time histories. Top: simulations without accumulated damage. Bottom: simulations with significant damage. The ground truth is shown in black, the surrogate without damage tracking in blue, and the surrogate with damage tracking in yellow. The damage tracker $D(t)$ is shown in red.

3.6. Discussion and conclusion

In this paper, we introduced a generalized framework that enables the use of finite-memory autoregressive models to represent time-variant dynamical systems. Building upon the mNARX (Schär et al., 2024) and $\mathcal{F}$-NARX (Schär et al., 2025) methodologies, the proposed approach augments the autoregressive structure with auxiliary state-tracking variables that capture the evolving properties of the system.

The effectiveness of the method is demonstrated on a reinforced concrete portal frame subjected to severe, realistic ground motion excitations. In this context, we compared a baseline $\mathcal{F}$-NARX model without state tracking to an mNARX model incorporating a damage-based tracking variable. The results clearly show that the baseline model struggles to generalize across different structural states, performing poorly in both undamaged and highly damaged regimes. In contrast, the damage-aware surrogate is able to accurately capture the system response across the full range of conditions.

These findings indicate that augmenting a NARX-type model with appropriate state-tracking variables provides a practical and effective means of extending finite-memory autoregressive models to time-variant systems, which would otherwise require infinite memory.

Future work will focus on exploring more advanced and potentially multiple tracking variables, as well as automated strategies for their selection, leveraging already available information to extract other quantities of interest, such as displacements or forces, in order to improve robustness and generalization capabilities of the final surrogate.

Acknowledgements

This research is supported by the Marie-Sklodowska Curie program and the REACTIS project, GA no. 101147351. Views and opinions expressed are however those of the authors only and do not necessarily reflect those of the European Union, or REA or any sponsor. Neither the European Union nor the granting authority can be held responsible for them.

References

ASTM: 2017, 'Standard practices for cycle counting in fatigue analysis'. (E1049-85).

Baker, J. W. and C. Lee: 2018, 'An improved algorithm for selecting ground motions to match a conditional spectrum'. *Journal of Earthquake Engineering* **22**(4), 708–723.

Billings, S. A.: 2013, *Nonlinear system identification: NARMAX methods in the time, frequency, and spatio-temporal domains*. Chichester, West Sussex, United Kingdom: John Wiley & Sons, Inc.

Blatman, G. and B. Sudret: 2011, 'Adaptive sparse polynomial chaos expansion based on least angle regression'. *J. Comput. Phys.* **230**(6), 2345–2367.

Chopra, A. K.: 2007, *Dynamics of structures: theory and applications to earthquake engineering*. Pearson Prentice Hall, 3 edition.

Echard, B., N. Gayton, and M. Lemaire: 2011, 'AK-MCS: An active learning reliability method combining Kriging and Monte Carlo Simulation'. *Structural Safety* **33**(2), 145–154.

Fassois, S. D. and J. S. Sakellariou: 2006, 'Time-series methods for fault detection and identification in vibrating structures'. *Philosophical Transactions of the Royal Society A: Mathematical, Physical and Engineering Sciences* **365**(1851), 411–448.

Ibarra, L. F., R. A. Medina, and H. Krawinkler: 2005, 'Hysteretic models that incorporate strength and stiffness deterioration'. *Earthquake Engineering & Structural Dynamics* **34**(12), 1489–1511.

Lemaitre, J. and J. Chaboche: 1990, *Mechanics of solid materials*. Cambridge University Press.

Lieven, N. A. J., D. J. Ewins, C. R. Farrar, S. W. Doebling, and D. A. Nix: 2001, 'Vibration–based structural damage identification'. *Philosophical Transactions of the Royal Society A: Mathematical, Physical and Engineering Sciences* **359**(1778), 131–149.

Lüthen, N., S. Marelli, and B. Sudret: 2021, 'Sparse polynomial chaos expansions: Literature survey and benchmark'. *SIAM/ASA Journal on Uncertainty Quantification* **9**(2), 593–649.

Marelli, S. and B. Sudret: 2018, 'An active-learning algorithm that combines sparse polynomial chaos expansions and bootstrap for structural reliability analysis'. *Structural Safety* **75**, 67–74.

Moustapha, M., S. Marelli, and B. Sudret: 2022, 'Active learning for structural reliability: Survey, general framework and benchmark'. *Structural Safety* **96**, 102174.

OpenSeesPy: 2024, 'Reinforced concrete frame earthquake analysis example'. OpenSeesPy Documentation, accessed March 19, 2026.

OpenSeesPy Development Team: 2024, 'OpenSeesPy: Python interface for OpenSees'. `https://openseespydoc.readthedocs.io`. Accessed: 2026-03-19.

Park, Y. and A. Ang: 1985, 'Mechanistic seismic damage model for reinforced concrete'. *Journal of Structural Engineering* **111**(4), 722–739.

Santner, T. J., B. J. Williams, and W. I. Notz: 2003, *The design and analysis of computer experiments*. Springer, New York.

Schär, S., S. Marelli, and B. Sudret: 2024, 'Emulating the dynamics of complex systems using autoregressive models on manifolds (mNARX)'. *Mechanical Systems and Signal Processing* **208**, 110956.

Schär, S., S. Marelli, and B. Sudret: 2025, 'Surrogate modeling with functional nonlinear autoregressive models (F-NARX)'. *Reliability Engineering & System Safety* p. 111276.

Schär, S., S. Marelli, and B. Sudret: 2026, 'mNARX+: A surrogate model for complex dynamical systems using manifold-NARX and automatic feature selection'. *Computer Methods in Applied Mechanics and Engineering* **449**, 118550.

Schär, S., S. Marelli, and B. Sudret: 2026, 'mNARX+: A surrogate model for complex dynamical systems using manifold-NARX and automatic feature selection'. *Computer Methods in Applied Mechanics and Engineering* **449**, 118550.

Song, Z., M. A. Valdebenito, S. Schär, S. Marelli, B. Sudret, and M. G. R. Faes: 2026, 'Probabilistic function-on-function nonlinear autoregressive model for emulation and reliability analysis of dynamical systems'. arXiv preprint.

Su, M.: 2025, 'Stochastic ground motion models for uncertainty quantification in earthquake engineering'. Phd thesis, University of Trento, Trento, Italy. Repository: `https://github.com/MaijiaSu/Toolbox_Site_based_GMMs`.

Stochastic contact analysis and its applications

Zhibao Zheng
Leibniz University Hannover, Institute for Risk and Reliability, 30167 Hannover, Germany
Email: zhibao.zheng@irz.uni-hannover.de

Abstract. Stochastic contact problems (SCPs) arise in many engineering applications where uncertainties in material properties, geometry or loading conditions affect contact behavior. Compared with deterministic contact analysis, the coupling of contact mechanics and randomness dramatically increases the computational complexity. In particular, stochastic contact nodes whose probability density functions can be strongly discontinuous or even singular render SCPs highly sensitive to uncertain inputs and computationally demanding. To address these challenges, a unified framework is presented for solving SCPs. It integrates Lagrange multiplier, penalty or augmented Lagrange multiplier formulations with semi-reduced-order approximations. In this framework, stochastic solutions are approximated as sums of products of random variables and deterministic vectors, thereby transforming high-dimensional SCPs into deterministic problems coupled with low-dimensional stochastic algebraic systems. Semi-reduced-order equations further combine smooth reduced-order solutions with full-order nonsmooth components to reduce computational cost without sacrificing accuracy. In addition, the framework is extended to rolling SCPs via the development of a stochastic arbitrary Lagrangian–Eulerian (ALE) formulation, which enables efficient analysis of rolling interfaces with uncertainties. Numerical results on high-dimensional SCP benchmarks and engineering-level cases such as rolling tires demonstrate that the proposed framework is both efficient and scalable. It accurately captures stochastic contact nodes while also significantly reducing computational cost. This framework provides a powerful tool for robust design and reliability assessment of engineering contact systems under uncertainty.

Keywords: Stochastic contact; Stochastic Lagrangian multiplier/penalty methods; Rolling contact analysis; Stochastic arbitrary Lagrangian–Eulerian method.

1. Introduction

Contact problems play a critical role in engineering practice (Wriggers and Laursen, 2006). As uncertainties are unavoidable in many problems, the consideration of uncertainties in system behavior has become an essential part of the analysis and design of engineering applications. However, there is limited experience in the treatment of SCPs. This article focuses on two-body contact problems with random parameters, e.g., random material properties and external forces. Currently, there are several methods for solving SCPs. The Monte Carlo (MC) method and its extensions such as the multilevel Monte Carlo (MLMC) method and the adaptive MLMC method (Chevalier et al., 2005; Bierig and Chernov, 2015; Rey et al., 2019) have been applied to SCPs. Although MC-type methods can be readily implemented using existing deterministic codes, a large

creative commons © 2026 by the author(s). This work is licensed under the Creative Commons Attribution 4.0 International License (CC BY 4.0), which permits unrestricted use, distribution, and reproduction in any medium, provided the original author and source are credited.

number of deterministic contact problems must be solved to achieve high-accuracy solutions, which is prohibitively expensive for large-scale problems in practice.

Another approach is the polynomial chaos (PC)-based method (Ghanem and Spanos, 2003; Xiu and Karniadakis, 2002). In this method, the stochastic solution is projected onto a stochastic space spanned by (generalized) PC basis, and the stochastic Galerkin projection is used to transform the original stochastic problem into a deterministic equation that is much larger than the original stochastic problem. However, its accuracy and efficiency still need improvement. On one hand, the classical PC method cannot accurately capture discontinuous stochastic contact solutions. Hence it usually works in conjunction with other methods such as the stochastic collocation method (Forster and Kornhuber, 2010; Arnst and Ghanem, 2012). On the other hand, because the computational effort increases sharply with the number of random variables and the expansion order, the PC method suffers from the so-called curse of dimensionality (Arnst and Ghanem, 2012), which is prohibitively expensive for large-scale and high-dimensional cases. Furthermore, other methods have also been proposed to solve contact-related problems, for example, within the framework of stochastic variational inequality problems (Jiang and Xu, 2008; Garreis and Ulbrich, 2017).

To solve SCPs efficiently and accurately, a unified framework is proposed to integrate Lagrange multiplier, penalty and augmented Lagrange multiplier formulations with semi-reduced-order approximations. The stochastic solutions are approximated as sums of products of random variables and deterministic vectors, thereby transforming high-dimensional SCPs into deterministic problems coupled with low-dimensional stochastic algebraic systems. They are then computed in their individual spaces. The deterministic problems are solved by existing finite element methods. The stochastic algebraic equations are solved by a sampling method, and the computational cost does not increase dramatically with the stochastic dimension. Hence, the curse of dimensionality in high-dimensional stochastic spaces is effectively circumvented. The effectiveness of the proposed approaches is demonstrated on numerical examples of up to 100 dimensions. The full-reduced-order equations directly constructed from the reduced basis cannot adequately capture the nonsmooth solutions of stochastic contact problems. Therefore, semi-reduced-order equations are used to combine smooth reduced-order solutions with full-order nonsmooth components, reducing computational cost without sacrificing accuracy. The size of the semi-reduced-order equation is small since the possible contact region is small compared to the whole domain in many applications. In addition, the framework is extended to rolling SCPs by developing a stochastic ALE formulation, which enables efficient analysis of rolling interfaces with uncertainties.

2. Stochastic Lagrange multiplier method and stochastic penalty method

For the treatment of randomness in structural parameters, e.g., material properties or potential contact points within the framework of the finite element method (FEM), we propose reduced-order computational schemes for both the Lagrange multiplier (LM) method and the penalty method (PM) to enforce the contact constraints (Zheng and Nackenhorst, 2023). In order to reduce the computational effort, in particular for high-dimensional stochastic problems, e.g., random fields for material properties, we suggest splitting the solution into pure deterministic computation and

an iterative scheme to solve the stochastic problem. Both schemes will be compared to the native Monte Carlo (MC) method with regard to accuracy and computational effort.

For the LM approach we split the solution into pure deterministic vectors and random variables

$$\mathbf{u}_k(\theta) = \mathbf{u}_{k-1} + \lambda_k(\theta)\,\mathbf{d}_k, \tag{1}$$

where $\mathbf{d}_k$ are solutions of the designed deterministic contact problems and $\lambda_k(\theta)$ are associated random variables. As given in (Zheng and Nackenhorst, 2023), the solution is obtained by an iterative scheme solving for $\mathbf{d}_k$ and $\lambda_k(\theta)$ in a staggered way. By doing so, the possibly high-dimensional problem is decomposed into solutions of deterministic contact problems and one-dimensional stochastic solutions, and the latter can be efficiently solved using sampling processes, even for very high-dimensional random inputs.

Because of the non-smoothness of the solutions, particularly for contact problems, we have observed that the accuracy of the solution can be improved by a semi-reduced model order reduction approach. Reduced-order modeling is applied only to non-contact nodes. Thus, the degrees of freedom of the active contact nodes are retained for solving the original finite element problem.

Unfortunately, the previously outlined approach does not work for the PM approach, because the typically large penalty parameter numerically deteriorates the update loop for the random variables. Here, an alternative scheme is proposed using the incremental solution

$$\mathbf{u}_k(\theta) = \mathbf{u}_{k-1}(\theta) + \Delta\mathbf{u}_k(\theta), \tag{2}$$

where the stochastic increment $\Delta\mathbf{u}_k(\theta) = [\lambda_{k,1}(\theta)\,\mathbf{Z}_1 + \lambda_{k,2}(\theta)\,\mathbf{Z}_2]\,\mathbf{d}_k$, $\lambda_{k,1}(\theta)$ and $\lambda_{k,2}(\theta)$ are scalar random variables, and $\mathbf{d}_k$ is the solution vector of the designed deterministic contact problems. Similar to the semi-reduced approach for the LM-based technique, the matrices $\mathbf{Z}_1$ and $\mathbf{Z}_2$ are index matrices, which split the finite element matrix into non-contact and contact nodes. A staggered iterative scheme is developed to solve $\lambda_{k,1}(\theta)$, $\lambda_{k,2}(\theta)$ and $\mathbf{d}_k$.

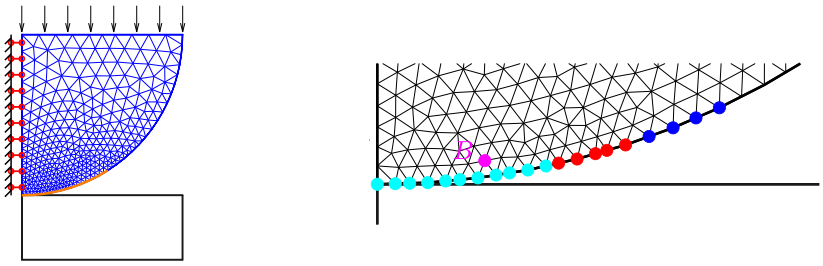


Figure 1. Model and its finite element mesh (left) and nodes on the possible contact interface (right).

The proposed methods are tested using a stochastic contact problem between a hemisphere and a rigid body as shown in Figure 1 (left). The Young's modulus is modeled as a random field that is approximated by Karhunen-Loève expansion with 10 and 100 random variables. As shown in Figure 1 (right), there are three types of characteristic nodes on the possible contact interface, including the contact nodes (cyan points), the possible contact nodes (red points), and the non-contact nodes (blue points), where the possible contact nodes are the nodes that are in contact

states for some samples of random parameters and in non-contact states for other samples, and they are thus referred to as "possible" (or stochastic) contact nodes.

Probability density functions (PDFs) of a possible contact node and the reference point B not on the contact interface (shown in Figure 1 (right)) calculated via the LM, PM and native MC approaches are shown in Figure 2 (left), (center) and (right), respectively. Both the LM and PM methods can capture strongly discontinuous and singular PDFs and achieve comparable accuracy to the native MC method. Computational times for stochastic dimensions of 10 and 100 are listed in Table I. The proposed methods can solve both low- and high-dimensional stochastic contact problems at low cost and are much more efficient than the MC method.

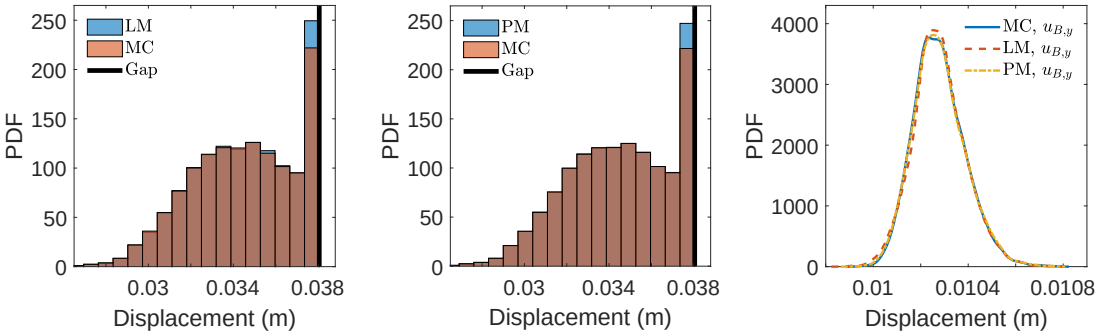


Figure 2. PDFs of a possible contact node obtained by MC, LM (left) and PM (mid) methods and PDFs of the vertical displacement of the reference point B (right).

Table I. Computational costs (seconds) for stochastic dimensions of 10 and 100.

Dimension	LM	PM	MCS
10	51	37	1742
100	241	269	2004

3. Stochastic augmented Lagrange multiplier method

As is well known in deterministic contact analysis, the augmented Lagrange multiplier method offers better robustness and convenience. Following this, we extend the stochastic Lagrange multiplier method and the stochastic penalty method presented above to stochastic augmented Lagrange multiplier methods. To this end, we still employ the stochastic approximation (2). New stochastic Uzawa-type algorithms are proposed to solve SCPs, and they also provide new insights into SCPs through the so-called stochastic contact interface systems (Zheng and Nackenhorst, 2025b).

Analogous to the deterministic Uzawa approach (Wriggers and Laursen, 2006; Laborde and Renard, 2008), stochastic contact constraints are imposed by weak penalties and stochastic Lagrange multipliers. Based on the stochastic solution approximation described above, a stochastic Uzawa algorithm and a generalized stochastic Uzawa algorithm are presented to solve for the stochastic Lagrange multipliers and each pair of random variable and deterministic vector in a greedy manner. In the stochastic Uzawa algorithm, the stochastic Lagrange multipliers are updated through a randomized Uzawa approach based on the known pair of random variable and deterministic vector (or given by initial values). Based on the obtained stochastic Lagrange multipliers, each pair of random variable and deterministic vector is then solved using a local alternating iteration. In the local alternating iteration, the original SCP is transformed into deterministic problems and two-dimensional stochastic algebraic equations. The deterministic problems can be solved by existing numerical solvers, and the two-dimensional stochastic equations are solved by a non-intrusive sampling method. Since the sampling method is not sensitive to stochastic dimensions, the proposed method can be applied to high-dimensional SCPs without further modifications. The generalized stochastic Uzawa algorithm avoids the local alternating iteration and only requires a three-component alternating iteration. One component of the random variable, the deterministic vector, or the stochastic Lagrange multipliers is solved by assuming the other two are known, where the stochastic Lagrange multipliers are updated through a randomized Uzawa approach, and the random variable and the deterministic vector are solved using two-dimensional stochastic algebraic equations and deterministic problems that are obtained in a manner similar to the local alternating iteration described above.

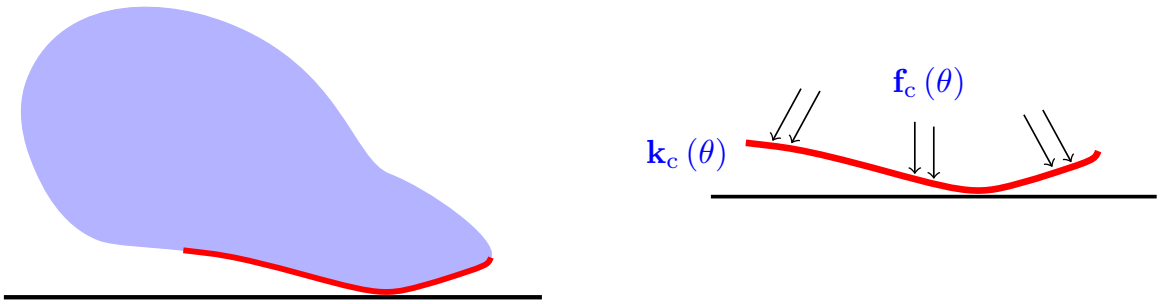


Figure 3. The flexible-rigid stochastic contact problem (left) and the corresponding SCI system (right).

To further improve the accuracy, the stochastic solution is recalculated by an equivalent stochastic contact interface system, which is generated by representing the non-contact stochastic solution of the original SCP using the contact stochastic solution and the obtained deterministic vectors, as illustrated in Figure 3. The stochastic contact interface system involves only the contact stochastic solution. Its size is much smaller than that of the original SCP, since the possible contact region is usually small compared to the whole domain in most cases. In this way, the SCP is solved only on the contact interface. Therefore, good convergence and high accuracy can be achieved.

As a test, we consider a 1D Euler–Bernoulli beam fixed on the left and constrained by a rigid block on the right, as shown in Figure 4. Both the SU and GSU methods are used to solve this example. The iterative errors of the SU and GSU methods are shown in Figure 5 (left). Three retained

terms are sufficient for both methods, which demonstrates the good convergence of the proposed methods. In this case, the SU and GSU methods have very similar convergence properties. To check the computational accuracy of the proposed method, the PDFs of the vertical displacements of the contact node obtained by the SU method and MC simulations are compared in Figure 5 (right). Note that the PDF is discontinuous at the boundaries 0.01 and 0.015 of the random gap. As can be seen from Figure 5, the proposed method captures the discontinuities very well. The computational times of the two methods are listed in Table II. It can be seen that both methods are much more efficient than MC simulations. Since the GSU method avoids the local alternating iteration used in the SU method, its iteration time is lower than that of the SU method. Furthermore, the same number of deterministic vectors results in similar recalculation times for the two methods.

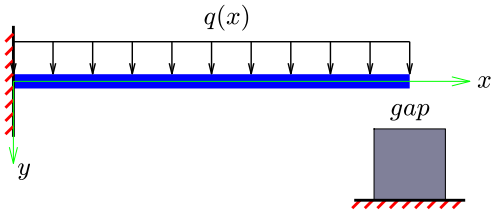


Figure 4. Euler–Bernoulli beam supported by a rigid block with a random gap.

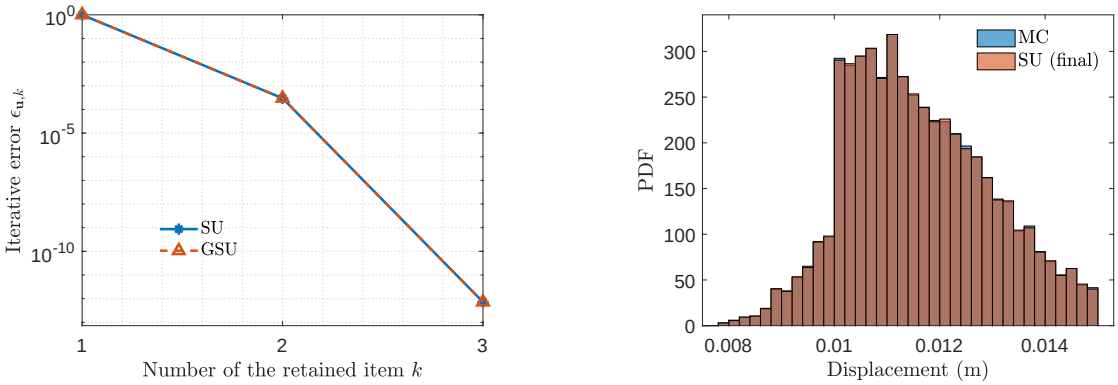


Figure 5. Iterative errors of different retained terms (left) and the PDFs of the contact point (right).

Table II. Computational times (seconds) of the SU and GSU methods.

Method	Iteration time	Recalculation time	Total time	MCS
SU	0.52	0.89	1.41	23.51
GSU	0.09	0.94	1.03	

4. Stochastic rolling contact analysis

In this part, we consider rolling contact on a rigid surface, which occurs widely in situations such as tire rolling contact. Following the idea of the deterministic ALE method for rolling contact analysis (Nackenhorst, 2004), the stochastic rolling motion is decomposed into pure rigid body motion and its stochastic deformation. As shown in Figure 6, the initial configuration is Ω_0, and the reference and current configurations are given by Ω_χ and Ω_φ, respectively. With these, we present a stochastic ALE method to handle rolling contact with uncertain inputs (Zheng and Nackenhorst, 2025a), e.g., material properties, velocity and external forces. The following stochastic finite element equation is thus generated

$$\left[\mathbf{K}_0(\theta) - \mathbf{W}(\theta) + \alpha\mathbf{K}_\mathrm{p}(\theta)\right]\mathbf{u}(\theta) = \mathbf{F}(\theta) + \alpha\mathbf{F}_\mathrm{p}(\theta), \tag{3}$$

where the stochastic global stiffness matrix $\mathbf{K}_0(\theta)$, the stochastic global inertia matrix $\mathbf{W}(\theta)$ (including the contribution of the stochastic flux term), the stochastic global contact stiffness matrix $\mathbf{K}_\mathrm{p}(\theta)$, the stochastic global force vector $\mathbf{F}(\theta)$, and the stochastic global contact force vector $\mathbf{F}_\mathrm{p}(\theta)$ are assembled using their element matrices and vectors (Nackenhorst, 2004; Zheng and Nackenhorst, 2025a). For efficient solutions, we use the stochastic penalty method and still employ the stochastic approximation (2).

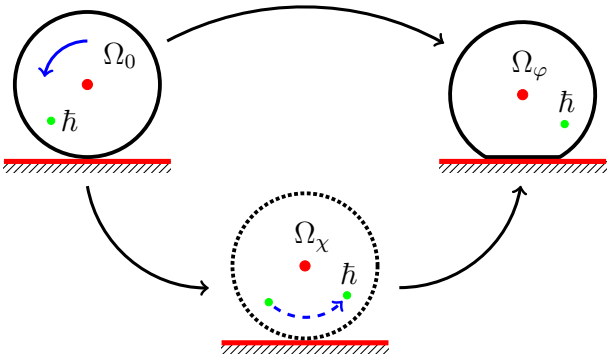


Figure 6. SALE framework for stochastic rolling contact.

A 2D rolling model with material and velocity uncertainties is used to illustrate the proposed method, as shown in Figure 7. The PDFs of stochastic contact nodes are shown in Figure 8 and are compared with MC simulations, demonstrating good accuracy in capturing discontinuous PDFs.

5. Conclusion and discussion

This paper presents a framework to handle SCPs by integrating Lagrange multiplier, penalty and augmented Lagrange multiplier formulations with semi-reduced-order approaches. In this framework, SCPs are decoupled into deterministic problems and low-dimensional stochastic algebraic systems. Semi-reduced-order equations further reduce computational cost by combining smooth reduced-order solutions with full-order nonsmooth components. Numerical results demonstrate the

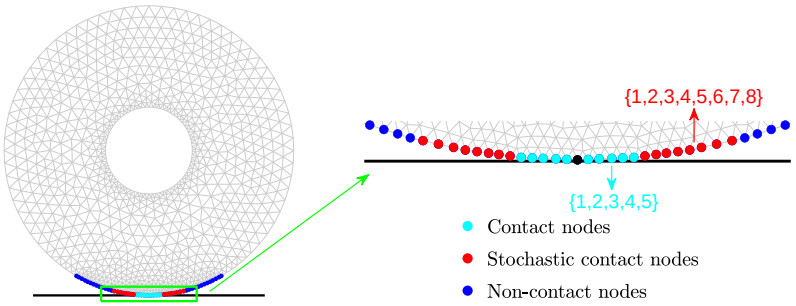


Figure 7. Contact nodes, stochastic contact nodes and non-contact nodes.

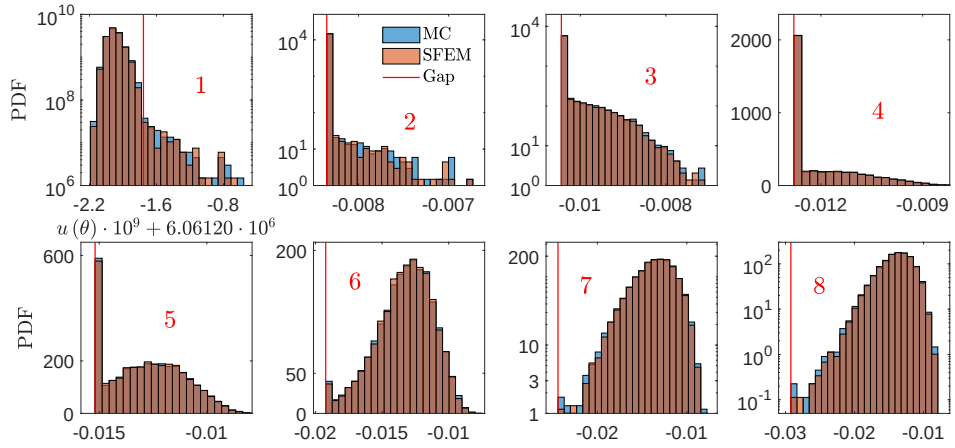


Figure 8. PDFs of the stochastic displacements in the y direction of the stochastic contact nodes.

promising performance of the proposed framework. It can accurately capture discontinuous PDFs of stochastic contact nodes. Although the framework is general-purpose, it still requires further investigation to extend the method to more complex stochastic contact analysis, such as stochastic contact with large deformation and plasticity.

Acknowledgements

The author is grateful to the German Research Foundation (DFG) projects (grant numbers 527222589 and 575372789), the Alexander von Humboldt Foundation, and the Ministry of Science and Culture of Lower Saxony, Germany.

References

Arnst, M. and R. Ghanem: 2012, 'A variational-inequality approach to stochastic boundary value problems with inequality constraints and its application to contact and elastoplasticity'. *International Journal for Numerical Methods in Engineering* **89**(13), 1665–1690.

Bierig, C. and A. Chernov: 2015, 'Convergence analysis of multilevel Monte Carlo variance estimators and application for random obstacle problems'. *Numerische Mathematik* **130**(4), 579–613.

Chevalier, L., S. Cloupet, and C. Soize: 2005, 'Probabilistic model for random uncertainties in steady state rolling contact'. *Wear* **258**(10), 1543–1554.

Forster, R. and R. Kornhuber: 2010, 'A polynomial chaos approach to stochastic variational inequalities.'. *Journal of Numerical Mathematics* **18**(4).

Garreis, S. and M. Ulbrich: 2017, 'Constrained optimization with low-rank tensors and applications to parametric problems with PDEs'. *SIAM Journal on Scientific Computing* **39**(1), A25–A54.

Ghanem, R. G. and P. D. Spanos: 2003, *Stochastic finite elements: a spectral approach*. Courier Corporation.

Jiang, H. and H. Xu: 2008, 'Stochastic approximation approaches to the stochastic variational inequality problem'. *IEEE Transactions on Automatic Control* **53**(6), 1462–1475.

Laborde, P. and Y. Renard: 2008, 'Fixed point strategies for elastostatic frictional contact problems'. *Mathematical Methods in the Applied Sciences* **31**(4), 415–441.

Nackenhorst, U.: 2004, 'The ALE-formulation of bodies in rolling contact: Theoretical foundations and finite element approach'. *Computer Methods in Applied Mechanics and Engineering* **193**(39-41), 4299–4322.

Rey, V., S. Krumscheid, and F. Nobile: 2019, 'Quantifying uncertainties in contact mechanics of rough surfaces using the multilevel Monte Carlo method'. *International Journal of Engineering Science* **138**, 50–64.

Wriggers, P. and T. A. Laursen: 2006, *Computational contact mechanics*. Springer.

Xiu, D. and G. E. Karniadakis: 2002, 'The Wiener–Askey polynomial chaos for stochastic differential equations'. *SIAM Journal on Scientific Computing* **24**(2), 619–644.

Zheng, Z. and U. Nackenhorst: 2023, 'Semi-reduced order stochastic finite element methods for solving contact problems with uncertainties'. *Computational Mechanics* **72**(5), 991–1008.

Zheng, Z. and U. Nackenhorst: 2025a, 'Stochastic arbitrary Lagrangian–Eulerian formalism for stochastic rolling contact analysis'. *Computational Mechanics* **76**(5), 1285–1302.

Zheng, Z. and U. Nackenhorst: 2025b, 'Stochastic augmented Lagrangian multiplier methods for stochastic contact analysis'. *Computer Methods in Applied Mechanics and Engineering* **435**, 117661.

A Continuous-Time Markovian Framework for Performance-Based Earthquake Engineering: Integrated Seismic Risk and Resilience Assessment

Chiara Nardin, Stefano Marelli, Bruno Sudret and Marco Broccardo
[1)] *Department of Civil, Environmental and Mechanical Engineering, University of Trento, 38132 Trento, Italy - {chiara.nardin, marco.broccardo}@unitn.it*

[2)] *Chair of Risk, Safety and Uncertainty Quantification,ETH Zurich, 8093 Zurich, Switzerland - {cnardin,marellis,sudretb}@ethz.ch*

Abstract. Assessing the seismic reliability of structural systems increasingly requires models that jointly represent damage evolution and recovery. Yet, the traditional PEER PBEE formulation does not capture the temporal dynamics of post-event repair, and modern reliability analyses often rely on scarce or uncertain recovery data, motivating the need for tractable methods.

We reformulate the PEER PBEE framework using a continuous time Markov Chain (CTMC) Monte Carlo approach, which naturally models probabilistic transitions among damage and recovery states under time-invariant seismic hazards. Transition rates incorporate metamodel-based state-dependent fragility functions, as well as recovery processes, yielding a unified representation of hazard effects and system evolution. Leveraging the analytical properties of CTMCs, we compute steady-state performance statistics, such as mean time to failure and time spent in degraded states, and define a resilience index adapted from the classical reliability index β.

The approach is tested on a simple yet representative example, showing that the CTMC-enhanced PBEE framework captures the temporal progression from damage to recovery in a computationally efficient and data-flexible manner.

Keywords: PEER PBEE framework, seismic reliability, recovery, CTMC

1. Introduction

The PEER performance-based earthquake engineering (PBEE) framework has revolutionized seismic risk quantification by decomposing performance assessment into hazard, structural response, damage, and loss. Despite its success, the framework's foundational assumptions, formalized in the seminal works of (Cornell and Krawinkler, 2000) and (Moehle and Deierlein, 2004), feature specific limitations regarding temporal dynamics, as noted by (Der Kiureghian, 2005). Two critical gaps persist:

– probability-based vs. rate-based assessment: traditional PBEE evaluates risk through conditional probabilities of damage given an intensity measure. However, reliability is intrinsically

© 2026 by the author(s). This work is licensed under the Creative Commons Attribution 4.0 International License (CC BY 4.0), which permits unrestricted use, distribution, and reproduction in any medium, provided the original author and source are credited.

rate-based. By focusing on event-based probabilities, the framework often misses the underlying temporal dynamics, specifically the transition rates that govern system evolution over time.

– absence of renewal mechanisms: real-world systems are not static; they degrade and recover. While standard PBEE typically evaluates structures on a per-event basis, it lacks an intrinsic renewal mechanism to account for the stochastic interplay between damage accumulation and restoration.

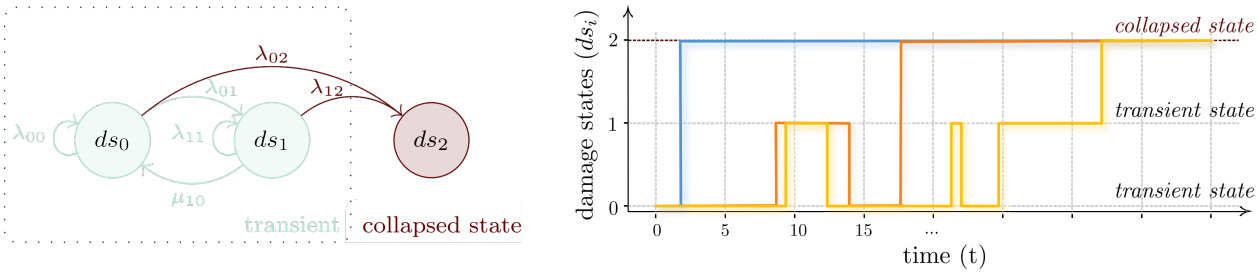
Significant research has sought to address the first point by modeling seismic damage accumulation. Several researchers (Guida and Pulcini, 2011; Iervolino et al., 2015a; Iervolino et al., 2015b) proposed state-dependent Markov models to capture cumulative path-dependence, while (Andriotis and Papakonstantinou, 2018) developed generalized frameworks for complex damage interactions. While these models represent a major step forward, they remain largely probabilistic in terms of damage exceedance. They do not explicitly represent the infinitesimal transition rates required to seamlessly couple damage accumulation and recovery within a single, time-dependent stochastic engine. Recent work by (Nardin et al., 2025; Nardin et al., 2026) bridged this gap by formulating damage accumulation via transition rates λ_{ij}, directly derived from surrogate model-based state-dependent PBEE fragility curves.

In parallel to these developments, the engineering community has prioritized the treatment of recovery processes, shifting from a risk perspective to a resilience one. Thus, the research on modeling recovery processes, registered a substantial progress over the past decade, not only in conceptual and probabilistic frameworks, but also in developing widely available engineering software that can embed recovery into seismic loss assessment. Indeed, many community- or regional-scale resilience studies rely on recovery functions to be included into classical loss and damage assessment procedure. A prominent example is the FEMA HAZUS model and manual (Federal Emergency Management Agency (FEMA), 2020), which provides a national database of generalized damage, loss, and recovery curves for use in large-scale planning and risk assessment (native to U.S. practice). Similar examples include the P-58 project (Federal Emergency Management Agency (FEMA), 2018a; Federal Emergency Management Agency (FEMA), 2018b), carried out by FEMA, and the ongoing ATC-138 project (Applied Technology Council, 2021), that provides recovery-based design tools and guidelines for modern buildings.

Nevertheless, a gap still remains: most existing formulations treat recovery as a post-event *add-on* rather than a competing mechanism between degradation and repair interventions. Hence, a unified framework capable of representing the continuous-time evolution of system performance under the simultaneous mechanisms of hazard-driven degradation and repair-driven renewal is still missing.

1.1. Contribution

Based on these premises, in this paper, we address these challenges by generalizing the PEER PBEE framework to a continuous-time Markov chain (CTMC) environment. We adopt a twofold strategy: we first propose a unified stochastic dynamics approach, where we represent both damage and recovery as stochastic state transitions, allowing for a rigorous treatment of system performance



(a) (b)

Figure 1. (a) State transition diagram for the 3-state CTMC model, and (b) example of possible CTMC trajectories simulating transitions from undamaged -0- to damaged -1- and collapse -2- states, along with the recovery path from state -1- to -0-.

over any decision horizon. We then shift to a rate-based approach, by showing that hazard effects can be embedded through state-dependent transition rates rather than static probabilities.

Under this generalized framework, structural collapse emerges naturally as an absorbing state, while repair actions introduce a renewal mechanism that provides a formal basis for resilience metrics. We conclude by validating these analytical CTMC solutions using Monte Carlo simulation, demonstrating the flexibility of the framework for complex engineering applications.

2. Methodological Framework

Classical PEER-PBEE evaluates performance through exceedance probabilities derived under Poissonian assumptions. While computationally efficient, this formulation implicitly enforces renewability and memorylessness: after each event, the structure is assumed to return to its original condition. Such assumptions hinder the consistent representation of cumulative damage, irreversible failure, and recovery dynamics over long service horizons.

To overcome these limitations, we propose a generalization of the PEER PBEE within a continuous-time Markov chain (CTMC) framework. The key conceptual shift is from probabilities of system damage/deterioration to rates of full stochastic dynamic evolution considering both damage/deterioration and recovery processes. Structural performance is represented as a stochastic process evolving among discrete damage states, thereby embedding degradation and recovery directly into the system dynamics.

Let $\mathcal{D} = \{ds_0, ds_1, \ldots, ds_C\}$ denote the finite set of possible structural damage states, ordered by increasing damage severity. Here, ds_0 represents the fully operational state, $ds_1, \ldots, ds_{C-1}$ denote progressively degraded conditions, and ds_C represents collapse. In the CTMC context, collapse is modeled as an absorbing state, representing an irreversible terminal condition.

The structural condition at time t is described by the stochastic variable $DS(t)$, with corresponding state probabilities

$$\pi_i(t) = P(DS(t) = ds_i), \qquad \boldsymbol{\pi}(t) = [\pi_0(t), \ldots, \pi_C(t)],$$

satisfying $\sum_{i=0}^{C} \pi_i(t) = 1$ at each time instant. In this framework, the evolution of the system depends solely on its current state, thus replacing the renewal assumption with a physically consistent memory of accumulated damage.

The CTMC is defined by its infinitesimal generator matrix $\boldsymbol{Q} = \{Q_{ij}\}$. For $i \neq j$, Q_{ij} represents the transition rate from state ds_i to state ds_j, while diagonal entries satisfy

$$Q_{ii} = -\sum_{j \neq i} Q_{ij}. \tag{1}$$

The time evolution of the state probability vector follows the Kolmogorov forward equation (see (Ross, 2014; Trivedi and Bobbio, 2017; Brémaud, 2020)):

$$\dot{\boldsymbol{\pi}}(t) = \boldsymbol{\pi}(t)\boldsymbol{Q}, \qquad \boldsymbol{\pi}(0) = \boldsymbol{\pi}_0, \tag{2}$$

the solution of which is available in closed form through the matrix exponential

$$\boldsymbol{\pi}(t) = \boldsymbol{\pi}_0 e^{\boldsymbol{Q}t}, \tag{3}$$

providing the exact transient occupancy probability of each damage state at any time.

One notable property of the generator matrix is its direct physical interpretation. Indeed, we can see it as a composition of a *damage* (the upper triangular of the matrix) and *recovery* contributions (the lower triangular). To exemplify, consider the 3-state system depicted in Fig. 1. Its generator matrix reads:

$$\boldsymbol{Q} = \boldsymbol{Q}_{\text{dam}} + \boldsymbol{Q}_{\text{rec}} = \begin{bmatrix} -\sum_{j>0}^{j=\text{C}} \lambda_{0j} & \lambda_{01} & \lambda_{0,\text{C}} \\ \mu_{10} & -\left(\mu_{10} + \sum_{j>1}^{j=\text{C}} \lambda_{1j}\right) & \lambda_{1\text{C}} \\ 0 & 0 & 0 \end{bmatrix}. \tag{4}$$

Damage transitions move the system toward more severe damage states; hence $\boldsymbol{Q}_{\text{dam}}$ is upper-triangular and characterized by transition rates λ_{ij} for $j > i$. These rates incorporate state-dependent fragility functions and the seismic hazard, as derived in (Nardin et al., 2025):

$$\lambda_{ij} = \int_{IM} \mathbb{P}(DS = ds_j \mid DS = ds_i, im)\, |d\lambda(im)|, \tag{5}$$

where $\lambda(im)$ denotes the hazard curve and the conditional probability $\mathbb{P}(DS = ds_j \mid DS = ds_i, im)$ represents the fragility conditioned on the current structural state and the hazard. This formulation generalizes PEER-PBEE by replacing exceedance probabilities with transition intensities and by explicitly conditioning on the instantaneous damage state. In the limiting case involving only ds_0 and ds_C, the classical two-state Poisson collapse model is recovered.

Recovery transitions, represented by $\boldsymbol{Q}_{\text{rec}}$, return the structure from more severe to less severe states. These transitions populate the lower-triangular portion of the generator matrix and are

governed by the corresponding recovery rates μ_{ij} for $i > j$. Although constant rates are used here for computational tractability, the framework can in principle accommodate more complex time-dependent or even stochastic recovery models if required.

Moreover, leveraging the structure of the generator matrix, we can partition it into the contribution of transient states and absorbing states:

$$\boldsymbol{Q} = \begin{bmatrix} \boldsymbol{Q}_T & \boldsymbol{a} \\ \mathbf{0} & 0 \end{bmatrix}, \tag{6}$$

where $\boldsymbol{Q}_T$ corresponds to transitions among the non-collapse states ds_0, ds_1, and $\boldsymbol{a} = (\lambda_{0C}, \lambda_{1C})^\intercal$ to the transitions towards the absorbed state ds_C.

Let $\mathcal{T}$ be the random variable describing the first time instant when the system collapses, and $F_\mathcal{T}$ its cumulative distribution function (CDF). Then, the probability of the system entering the absorbing collapse state by time t is derived from the missing probability mass in the transient sub-generator $\boldsymbol{Q}_T$:

$$F_\mathcal{T}(t) = \mathbb{P}(\mathcal{T} \leq t) = 1 - S_\mathcal{T}(t) = 1 - \sum_{i \in \mathcal{D}_T} \pi_i(t) = 1 - \boldsymbol{\pi}_T(0) \cdot e^{\boldsymbol{Q}_T t} \cdot \mathbf{1}_T, \tag{7}$$

where $\mathcal{D}_T = [ds_0, ds_1]$ and $S_\mathcal{T}$ is the survival function. The product $\boldsymbol{\pi}_T(0) \cdot e^{\boldsymbol{Q}_T t}$ gives the probability distribution over all "safe" (i.e., non-collapsed) states at time t, and multiplication by the column vector of ones $\mathbf{1}_T$ sums these probabilities. This formulation highlights an important structural property of the transient sub-generator $\boldsymbol{Q}_T$: its rows do not sum to zero. In a standard generator matrix $\boldsymbol{Q}$, each row sums to zero because total probability is conserved. In contrast, the rows of $\boldsymbol{Q}_T$ sum to strictly negative values. The "missing" probability mass corresponds exactly to the rate at which probability flows out of the transient state space and into the absorbing collapse state (through the coupling vector $\boldsymbol{a}$).

Following standard structural reliability jargon (Ditlevsen, 1979), we consider transition to the absorbing state as failure, and therefore $F_\mathcal{T}(t)$ in Eq. (7) as a time-dependent probability of failure. We can therefore map this failure probability to a time-dependent reliability index β_t:

$$\beta_t = -\Phi^{-1}(F_\mathcal{T}(t)), \tag{8}$$

where Φ is the standard normal CDF.

Thus, the reliability index β_t, derived from the transient subgenerator $\boldsymbol{Q}_T$, measures the probability of no collapse by time t, but ignores how the system degrades beforehand. This limitation motivates a shift to structural resilience, which emphasizes sustained performance over time. Accordingly, in a structural resilience perspective, the focus moves from the time-to-collapse $\mathcal{T}$ to the occupation time of the undamaged state ds_0.

First consider the occupation time of the undamaged state ds_0 over the interval $[0, t]$, defined as

$$A_0(t) := \int_0^t \mathbf{1}_{\{DS(s)=ds_0\}}\, ds, \tag{9}$$

where $\mathbf{1}_{\{\cdot\}}$ is the indicator function. The random variable $A_0(t)$ represents the total time spent in the undamaged state during $[0, t]$.

The expected occupation time admits a closed-form expression in terms of the transient sub-generator $\boldsymbol{Q}_T$. Indeed, recalling that the mean of an indicator function equals the corresponding probability, one obtains

$$\mathbb{E}[A_0(t)] = \int_0^t \mathbb{E}[\mathbf{1}_{\{DS(s)=ds_0\}}]\, ds, = \int_0^t \mathbb{P}(DS(s) = ds_0)\, ds = \int_0^t \left[e^{\boldsymbol{Q}_T s}\right]_{00} ds, \tag{10}$$

where $\mathbb{P}(DS(s) = ds_0)$ is the unconditional probability of being in the undamaged state ds_0 at time s. One recognizes that this quantity coincides with the $(0,0)$ entry of the truncated fundamental matrix

$$\boldsymbol{N}(t) = \int_0^t e^{\boldsymbol{Q}_T s}\, ds = \boldsymbol{Q}_T^{-1}\left(e^{\boldsymbol{Q}_T t} - \boldsymbol{I}\right), \tag{11}$$

so that $\mathbb{E}[A_0(t)] = n_{00}(t)$, where $n_{ij}(t)$ denotes the (i,j) entry of $\boldsymbol{N}(t)$ and represents the expected total time spent in state ds_j, starting from state ds_i, over the interval $[0,t]$. As $t \to \infty$, the truncated fundamental matrix converges to the well-known fundamental matrix (see (Ross, 2014; Trivedi and Bobbio, 2017)) $\boldsymbol{N} = -\boldsymbol{Q}_T^{-1}$, whose (i,j) entry n_{ij} represents the expected total time spent in state ds_j before absorption, starting from state ds_i.

We now define the unconditional metric $\mathcal{R}_0^{\text{unc}}$ as the expected fraction of the horizon T_{hor} during which the system does not remain in the undamaged state ds_0, starting from ds_0:

$$\mathcal{R}_0^{\text{unc}} = 1 - \frac{n_{00}(T_{\text{hor}})}{T_{\text{hor}}}, \tag{12}$$

where $n_{00}(T_{\text{hor}}) = [\boldsymbol{N}(T_{\text{hor}})]_{00}$ is the $(0,0)$ entry of the truncated fundamental matrix evaluated at T_{hor}. This metric is unconditional in the sense that the expectation is taken over all possible trajectories, including those that reach the collapse state before T_{hor}. Equivalently, $\mathcal{R}_0^{\text{unc}}$ admits the probabilistic interpretation

$$\mathcal{R}_0^{\text{unc}} = \mathbb{P}(DS(U) \neq ds_0), \qquad U \sim \mathcal{U}(0, T_{\text{hor}}), \tag{13}$$

that is, the probability that a time instant U drawn uniformly at random from $[0, T_{\text{hor}}]$ falls within a period during which the system is not in the undamaged state, without conditioning on survival. Consequently, a high value of $\mathcal{R}_0^{\text{unc}}$ indicates a higher likelihood of sustained or progressive damage or early collapse, while a lower value reflects the system spends most of its time undamaged.

To maintain consistency with the reliability index β, we introduce the resilience index ρ^{unc} as

$$\rho^{\text{unc}} = -\Phi^{-1}(\mathcal{R}_0^{\text{unc}}), \tag{14}$$

where $\mathcal{R}_0 \in [0,1]$ ensures that ρ^{unc} is well defined. Since $\mathcal{R}_0^{\text{unc}}$ is the expected fraction of time spent in damaged states, the index ρ^{unc} provides a one-to-one transformation of the resilience metric into the standard normal space, directly comparable to β_t.

Interestingly, both the reliability and the resilience indices are fully consistent with the underlying damage accumulation and recovery mechanisms encoded in the generator matrix $\mathbf{Q}$. The latter provides therefore a unified basis for comparing alternative structural configurations, retrofitting strategies, or recovery policies within a single probabilistic framework.

Moreover, since both indices are directly from $\mathbf{Q}_T$, their estimation does not require costly Monte Carlo simulations, but they can be obtained directly by integrating Eq. (11). This makes the approach particularly suitable for long-time horizon assessments, where repeated simulation of event sequences would otherwise be computationally demanding.

3. A Simple Example: time evolution of a 3-state System

3.1. System Configuration and Parameters

To demonstrate the capabilities of the CTMC-generalized PBEE framework, we analyze a 3-state example that captures the fundamental competition between hazard-driven degradation and repair-driven recovery. This system allows for a clear visualization of how infinitesimal transition rates govern long-term structural performance.

As shown in Fig. 1, we consider a 3-state space $\mathcal{D} = \{0, 1, 2\}$, where state $c = 2$ represents structural collapse. The transition rates within the generator matrix $\boldsymbol{Q}$ are defined as:

$$\lambda_{01} = 0.02, \quad \lambda_{02} = 0.0001, \quad \lambda_{12} = 0.005. \tag{15}$$

and a time horizon T_{hor} of 50 years. These values are selected to reflect a physically consistent engineering scenario: the rate of direct collapse from an undamaged state (λ_{02}) is significantly lower than the rate of recoverable-damage from a pristine initial condition state (λ_{01}), capturing the general desired structural behavior.

Nevertheless, we let μ_{10}, i.e., the only recovery rate of the system, to range in the interval 10^{-3} to 10^{1} [years^{-1}], corresponding to a mean recovery time that varies from months to over a century. Fig. 2 illustrates the time-dependent occupancy probabilities over a 50-year horizon (T_{hor}) for two extreme scenarios: a low-recovery case ($\mu_{10} = 10^{-3}$) and a high-recovery case ($\mu_{10} = 10^{1}$). In panel (a), the near absence of recovery means that the system evolves in only one direction: probability mass gradually shifts from the undamaged state ds_0 to the damaged state ds_1, and eventually to collapse ds_2. This behavior closely reflects the implicit assumption of classical PEER-PBEE, where each seismic event affects a structure that is not repaired between events. As a result, long-term performance is governed almost entirely by the damage rates λ_{ij}. In this limit, the CTMC reproduces the traditional formulation, providing a useful consistency check.

Panel (b) shows a fundamentally different regime which can not be captured by the classical framework. When the recovery rate μ_{10} becomes comparable to the damage rate λ_{01}, damage and repair compete with each other and reach a balance. Instead of continuously degrading, the probability of being in the undamaged state ds_0 remains relatively high over time, reflecting ongoing repair. The probability of being in the damaged state ds_1 stays limited, and the rate of collapse is significantly reduced. This type of behavior cannot be described using event-based exceedance probabilities alone; it requires accounting for the transition rates between states in both directions, which is what the generator matrix $\mathbf{Q}$ represents.

Taken together, these panels highlight the main advantage of the CTMC reformulation. In the PEER-PBEE framework, hazard, fragility, and loss are evaluated separately for each event. In contrast, the CTMC approach models damage and recovery together as a continuous process over

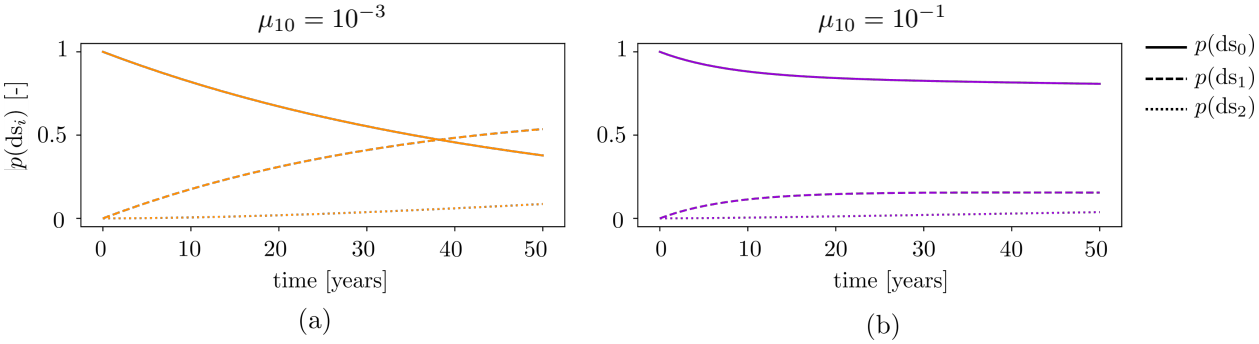


Figure 2. Time-dependent occupancy probabilities for transient states (0, 1) and the absorbing collapse state (2) over a 50-year horizon, comparing (a) negligible recovery ($\mu_{10} = 10^{-3}$), and (b) normal recovery ($\mu_{10} = 10^{-1}$).

time, so that the proportion of time spent in each damage state reflects the combined effect of these competing mechanisms. This shifts the focus from the probability of exceeding a damage threshold in a single event to the expected fraction of time the structure spends in each performance state over its lifetime, which is a more informative and practical measure for lifecycle management, retrofit prioritization, and recovery planning.

3.2. Verification and Performance Metrics

Next, we evaluate the reliability and resilience of the system using the metrics derived in Section 2: the first-passage probability to collapse $F_{\mathcal{T}}(T_{\mathrm{hor}})$ (Eq. (7)) and the expected damaged fraction of lifetime $\mathcal{R}_0^{\mathrm{unc}}$ (Eq. (12)). Analytically, both quantities are computed from the sub-generator $\boldsymbol{Q}_T$ of the transient states via matrix exponentiation and the truncated fundamental matrix $\boldsymbol{N}(T_{\mathrm{hor}})$, as described in Section 2. To verify these predictions, we generate $N_{\mathrm{sim}} = 10^5$ independent sample trajectories of the CTMC using the full generator $\boldsymbol{Q}$: holding times are drawn as $\Delta t \sim \mathrm{Exp}(-Q_{ii})$ and the next state j is sampled with probability $Q_{ij}/(-Q_{ii})$, censoring each path at T_{hor}. A trajectory contributes to the MCS estimate $\hat{F}(T_{\mathrm{hor}})$ if it reaches the absorbing state within the horizon, while $\mathcal{R}_0$ is estimated as the average fraction of $[0, T_{\mathrm{hor}}]$ over which damage accumulates across all trajectories. The agreement between analytical and MCS results confirms the correctness of both the theoretical expressions and their numerical implementation.

Figure 3 shows near-perfect agreement between the analytical predictions and the Monte Carlo estimates across the full range of recovery rates μ_{10}. The results confirm that $F_{\mathcal{T}}$ and $\mathcal{R}_0^{\mathrm{unc}}$ are smooth, monotone functions of μ_{10}, and that even a modest increase in recovery rate produces a substantial reduction in collapse probability and a marked increase in the fraction of time spent in the operational state. This sensitivity is not a numerical artifact: it reflects the physical competition between damage and recovery encoded in $\boldsymbol{Q}$, and it is precisely what the CTMC paradigm makes quantitatively accessible. In the classical PEER-PBEE setting, such a sensitivity curve cannot be so easily constructed, because recovery has no direct representation in the framework.

The convergence of the MC estimates is examined in Fig. 4. In the case of $\mu_{10} = 10^{-2}$/years, the running mean stabilizes well before the 10^5 trajectory limit and confidence interval consistently narrows, confirming the reliability of the simulation baseline. The analytical solution via $\boldsymbol{Q}_T$ reaches

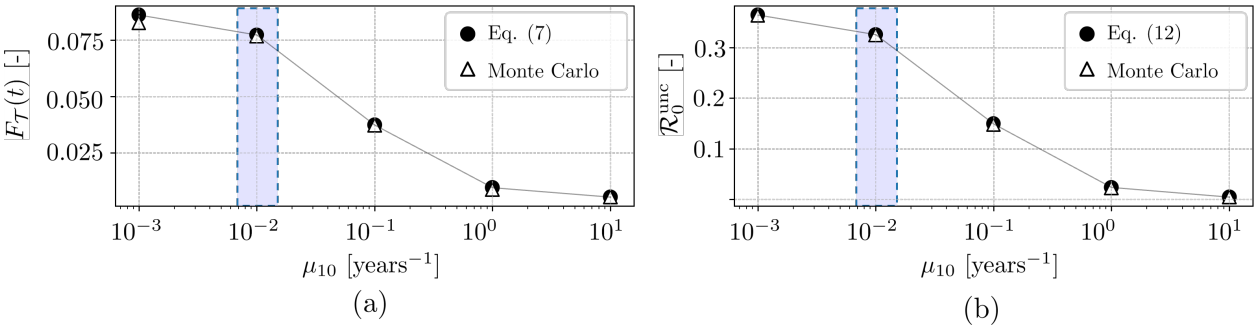


Figure 3. Comparison of (a) first-passage probability $F_{\mathcal{T}}(\cdot)$ and (b) resilience metric $\mathcal{R}_0^{\text{unc}}$ calculated via analytical CTMC estimation and Monte Carlo simulation across a range of recovery rates. The colored box indicates the region zoomed in Fig. 4 to illustrate Monte Carlo convergence.

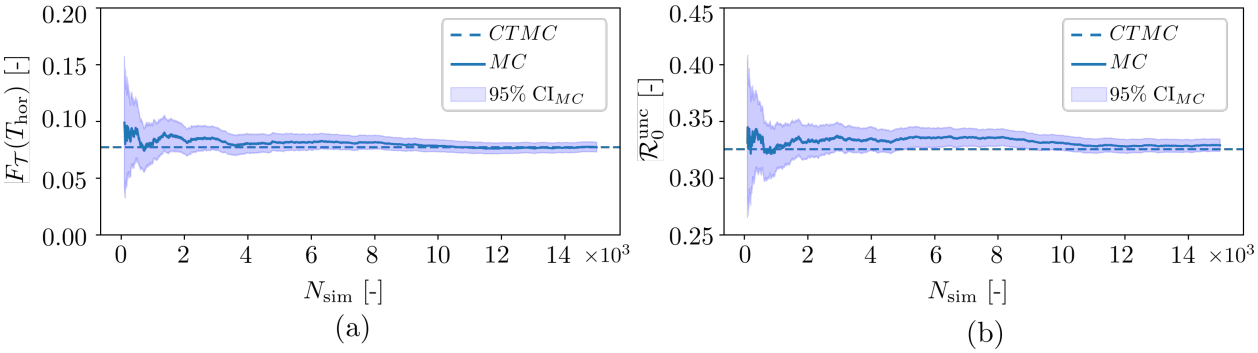


Figure 4. Monte Carlo convergence analysis showing the running mean and standard error for (a) the first-passage probability $F_{\mathcal{T}}(T_{\text{hor}})$ and (b) resilience metric $\mathcal{R}_0^{\text{unc}}$ as a function of the number of simulations N_{sim}.

the same result instantaneously, which is a practical bonus for long-horizon assessments. More importantly, both routes agree, lending credibility to the CTMC model itself as a representation of the underlying engineering problem.

Finally, Fig. 5 maps the system performance onto the β–ρ^{unc} plane as μ_{10} varies across several orders of magnitude. Grey-filled markers correspond to the specific values of μ_{10} adopted in Fig. 3, providing a direct link between the two figures. The green-shaded region identifies the high-performance quadrant, defined by $\beta \geq 2$ and $\rho \geq 2$, which represents configurations where the system is simultaneously highly reliable and highly resilient; this threshold can be used as a practical design target. The various points concretely illustrates how recovery capacity shapes overall performance: systems with negligible repair rates cluster in the low-reliability, low-resilience corner, while faster recovery pushes the system into the desirable quadrant.

One can also observe a positive correlation between β and ρ^{unc} along the trajectory. This is not incidental: by construction, ρ^{unc} is defined through $\mathcal{R}_0^{\text{unc}}$, which accounts for the fraction of lifetime spent in damaged states across all trajectories, including those that reach collapse. For low values of μ_{10}, collapse events are more frequent, meaning a larger share of trajectories contributes damaged

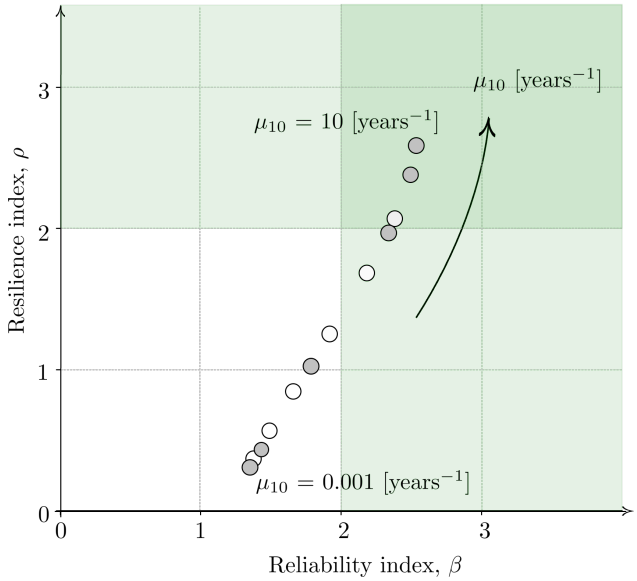


Figure 5. System performance trajectory in the resilience (ρ^{unc}) vs. reliability (β) domain, illustrating how increasing recovery rates move the system into the high-performance quadrant.

time up to absorption, which simultaneously depresses both β and ρ^{unc}. As recovery rates increase, fewer trajectories reach collapse, damage accumulation is curtailed, and both indices rise together.

Crucially, this entire mapmap is a direct output of the CTMC formulation and does not require re-running a full probabilistic analysis for each configuration: it naturally follows from varying a single entry of the generator matrix $\boldsymbol{Q}$. This makes the β–ρ^{unc} map a practical design and decision tool, allowing an engineer to read off, for a target reliability or resilience level, the minimum recovery rate that must be achieved through repair policies or structural intervention.

4. Conclusions

This paper presents a generalization of the PEER-PBEE framework that addresses two fundamental limitations in contemporary seismic risk assessment: the implicit Poissonian renewal hypothesis and the exclusion of recovery dynamics from the structural evolution. By adopting a continuous-time Markov chain (CTMC) approach, we have established a framework that naturally integrates hazard-driven damage accumulation and restoration processes under a unified stochastic engine.

Several key findings emerge from this work. First, we demonstrate that structural reliability and resilience are not merely secondary outputs, but are directly encoded within the system's infinitesimal generator matrix $\mathbf{Q}$. This mathematical coupling allows for the simultaneous evaluation of state-dependent deterioration and recovery mechanisms. Such a formulation provides a rigorous

basis for comparing alternative structural configurations, retrofitting strategies, and post-disaster recovery policies within a single, consistent probabilistic environment.

Second, the analytical solutions derived for first-passage times and state occupancy were validated through extensive Monte Carlo simulations. The convergence between these methods highlights the computational efficiency of the CTMC approach; by utilizing analytical matrix exponentials, the framework enables long-horizon performance assessments that would otherwise be computationally prohibitive or statistically unstable using simulation alone.

The elegant, modular nature of this framework paves the way for several future research directions. The current time-invariant hazard assumption can be extended to incorporate time-variant phenomena, such as seismic aftershock sequences or climate-induced degradation. Furthermore, the rate-based formulation is flexible enough to accommodate diverse recovery models, ranging from linear restoration to complex, resource-constrained logistical functions.

Acknowledgements

This research is supported by the Marie-Sklodowska Curie program and the REACTIS project, GA no. 101147351. Views and opinions expressed are however those of the authors only and do not necessarily reflect those of the European Union, or REA or any sponsor. Neither the European Union nor the granting authority can be held responsible for them.

References

Andriotis, C. P. and K. G. Papakonstantinou: 2018, 'Extended and generalized fragility functions'. *Journal of Engineering Mechanics* **144**(9).

Applied Technology Council: 2021, 'ATC-138: Seismic Performance Assessment of Buildings. Volume 8: Methodology for Assessment of Functional Recovery Time'. Federal Emergency Management Agency (FEMA). https://femap58.atcouncil.org/documents/fema-p-58/34-atc-138-3-volume-8-methodology-for-assessment-of-functional-recovery-time/file.

Brémaud, P.: 2020, *Probability Theory and Stochastic Processes*, Universitext. Cham: Springer Nature Switzerland.

Cornell, C. A. and H. Krawinkler: 2000, 'Progress and Challenges in Seismic Performance Assessment'. PEER Center News. Spring issue.

Der Kiureghian, A.: 2005, 'Non-ergodicity and PEER's framework formula'. *Earthquake Engineering & Structural Dynamics* **34**(13), 1643–1652.

Ditlevsen, O.: 1979, 'Generalized Second Moment Reliability Index'. *Journal of Structural Mechanics* **7**, 435–451.

Federal Emergency Management Agency (FEMA): 2018a, 'FEMA P-58-1: Seismic Performance Assessment of Buildings, Volume 1 – Methodology'. https://femap58.atcouncil.org/documents/fema-p-58/24-fema-p-58-volume-1-methodology-second-edition/file.

Federal Emergency Management Agency (FEMA): 2018b, 'FEMA P-58-2: Seismic Performance Assessment of Buildings, Volume 2 – Implementation Guide, Appendix C: PACT Software'. https://femap58.atcouncil.org/documents/fema-p-58/25-fema-p-58-volume-2-implementation-second-edition/file.

Federal Emergency Management Agency (FEMA): 2020, 'HAZUS Earthquake Model 4.2.'. https://www.fema.gov/sites/default/files/2020-10/fema_hazus_earthquake_technical_manual_4-2.pdf.

Guida, M. and G. Pulcini: 2011, '"A Continuous-State Markov Model for Age- and State-Dependent Degradation Processes"'. *Structural Safety* **33**(6), 354–366.

Iervolino, I., M. Giorgio, and E. Chioccarelli: 2015a, ‘“Age- and State-Dependent Seismic Reliability of Structures”’. In: *12th International Conference on Applications of Statistics and Probability in Civil Engineering (ICASP12)*. Vancouver, Canada.

Iervolino, I., M. Giorgio, and E. Chioccarelli: 2015b, ‘“Markov Chain Modeling of Seismic Damage Accumulation”’. *Earthquake Engineering & Structural Dynamics* **44**(7), 1015–1032.

Moehle, J. and G. G. Deierlein: 2004, ‘A Framework Methodology for Performance-Based Earthquake Engineering’. In: *Proceedings of the 13th World Conference on Earthquake Engineering*. Vancouver, Canada.

Nardin, C., S. Marelli, O. S. Bursi, B. Sudret, and M. Broccardo: 2025, ‘“UQ state-dependent framework for seismic fragility assessment of industrial components”’. *Reliability Engineering & System Safety* p. 111067.

Nardin, C., S. Marelli, B. Sudret, and M. Broccardo: 2026, ‘“A Generalized Framework for Performance-Based Earthquake Engineering: Integrated Seismic Risk and Resilience Assessment”’. *”In preparation”* pp. –.

Ross, S. M.: 2014, *“Introduction to Probability Models”*. Boston: Academic Press, 11th edition.

Trivedi, K. S. and A. Bobbio: 2017, *“Reliability and Availability Engineering: Modeling, Analysis, and Applications”*. Cambridge: Cambridge University Press.

Neural network-driven uncertainty qualification analysis of printed circuit heat exchangers

Hanshu Chen[1)], Yanzhao Gu[2)] Zhuojia Fu[3)], Guohai Chen[4)], Dixiong Yang[5)]

[1)]College of Mechanics and Engineering Science, Hohai University, Nanjing, Jiangsu, 211100, China. E-mail: chenhanshu@163.com

2)College of Mechanics and Engineering Science, Hohai University, Nanjing, Jiangsu, 211100, China. E-mail: 15253418257@163.com

3)College of Mechanics and Engineering Science, Hohai University, Nanjing, Jiangsu, 211100, China. E-mail: 20130010@hhu.edu.cn

4)Department of Engineering Mechanics, International Research Center for Computational Mechanics, Dalian University of Technology, Dalian 116024, China, E-mail: chenguohai_382@126.com

5)Department of Engineering Mechanics, International Research Center for Computational Mechanics, Dalian University of Technology, Dalian 116024, China, E-mail: yangdx@dlut.edu.cn

Abstract: The randomness in structural parameters of printed circuit heat exchangers (PCHEs) is unavoidable and can significantly impact shakedown limit and reliability. However, studies on the influence of random structural parameters are limited due to the expensive computation burden. Therefore, this paper aims to achieve efficient stochastic shakedown and reliability analyses of PCHEs with multiple random structural parameters. First, the Linear Matching Method (LMM) is utilized to perform the shakedown analysis. Then, to account for the influence of random structural parameters, the Direct Probability Integral Method (DPIM), as an efficient non-intrusive stochastic analysis method, is introduced. By exploiting the advantages of LMM and DPIM, a novel LMM-DPIM is proposed for the uncertainty qualification analysis of PCHEs. Furthermore, the data-driven neural network model is implemented to improve the computational efficiency. As a result, an LMM-DPIM-based neural network (LMM-DPIM-NN) model is established. Finally, the high accuracy and efficiency of the proposed model are verified through comparisons with Monte Carlo simulation. Moreover, the results of uncertainty qualification analysis reveal the effects of different random structural parameters on the shakedown limit and reliability of PCHE. Particularly, the fillet radius at the corner of channels significantly influences the shakedown limit, leading to a huge reduction in reliability.

Keywords: printed circuit heat exchangers; stochastic shakedown and reliability analyses; linear matching method; direct probability integral method; neural network model.

1. Introduction

Printed circuit heat exchangers are compact micro-channel devices widely used in chemical, aerospace, and energy applications owing to their high thermal efficiency and structural compactness [1, 2]. In service, PCHEs are subjected to cyclic thermo-mechanical loads arising from alternating hot and cold fluid channels joined by diffusion bonding. Shakedown analysis is therefore essential for structural integrity assessment [3]: within the shakedown boundary the structure develops limited plastic strain after initial cycles, whereas loads beyond the boundary may lead to low-cycle fatigue or incremental collapse. Although the ASME and R5 codes recommend Bree-diagram-based rule-based methods [4-6], these are restricted to standard geometries;

© 2026 by the author(s). This work is licensed under the Creative Commons Attribution 4.0 International License (CC BY 4.0), which permits unrestricted use, distribution, and reproduction in any medium, provided the original author and source are credited.

cycle-by-cycle inelastic finite element analysis, while general, incurs prohibitive computational cost. Several direct methods have been developed for efficient shakedown and limit analysis of engineering structures [7-9]. The Linear Matching Method, grounded in Koiter's kinematic shakedown theorem, has emerged as an accurate and efficient direct method for non-standard components [10-13], and has been successfully applied to deterministic shakedown assessment of PCHEs [14, 15]. However, geometric and material uncertainties inherent in manufacturing—such as channel radius, fillet radius, and temperature dependent yield stress can significantly affect shakedown limits, motivating stochastic analysis as the foundation for reliability-based design.

To quantify these uncertainties, the Direct Probability Integral Method offers a non-invasive framework based on a probability density integral equation that separates the probability evaluation from the physical model [16-18]. Compared with Monte Carlo simulation, DPIM requires far fewer model evaluations and avoids random convergence issues [19]. Nevertheless, when the structural response is strongly nonlinear—as in PCHE shakedown under multiple random parameters—the repeated LMM evaluations needed by DPIM remain costly. Data-driven surrogate models, particularly back-propagation neural networks, can approximate this nonlinear mapping efficiently [20-22] and have shown success in creep-fatigue and ratcheting reliability assessments of pressurized components.

This paper presents an LMM-DPIM-NN framework for stochastic shakedown and reliability analysis of PCHEs. The contributions are: (1) combining LMM with DPIM for the first time and building a neural-network surrogate for PCHEs with multiple random parameters; (2) efficiently obtaining probabilistic shakedown limit information under limited data; and (3) revealing that the fillet radius at the channel corner exerts the strongest influence on the shakedown limit and can trigger stochastic P-bifurcation, with reliability decreasing by up to 19.43 % as the fillet radius increases.

2. Methodology

2.1 Modified LMM for stochastic shakedown analysis

The LMM iteratively updates the shear modulus to match the yield condition based on the plastic strain-rate history, computing the shakedown multiplier λ via Koiter's kinematic theorem. In deterministic analysis, the thermo-mechanical load ratio is fixed and the shakedown multiplier is scaled along a radial line in load space; repeating for different ratios constructs the classical Bree diagram. For stochastic analysis, the load ratio and structural parameters become random variables, and the shakedown boundary transforms from a curve to a surface in the thermo-mechanical load space. The total elastic stress field is decomposed as

$$\sigma_{ij}^{E}(x,t) = \alpha_T \sigma_{ij}^{T}(x,t) + \alpha_P \sigma_{ij}^{P}(x,t) \tag{1}$$

where α_T and α_P are initial multipliers for the construction of various loading combinations, and σ_{ij}^{T} and σ_{ij}^{P} mean the corresponding linear elastic solution. The cyclic stress history is expressed as

$$\Delta\sigma_{ij}(x,t) = \lambda\Delta\sigma_{ij}^{E}(x,t) + \bar{\rho}_{ij}(x,t) + \bar{\rho}_{ij}(x,t) \tag{2}$$

in which $\overline{\rho}_{ij}$ indicates constant residual stress field, λ means the shakedown multiplier to solve, ρ_{ij} is the varying residual stress field of shakedown problems. By introducing Koiter's shakedown theorem, the shakedown multiplier is evaluated by

$$\lambda = \frac{\int_V \sigma_y(T)\Delta\epsilon_{eq}^{p*} dV}{\int_V \Delta\sigma_{ij}^{E}\Delta\epsilon_{ij}^{p*} dV} \tag{3}$$

where $\sigma_y(T)$ is the temperature-dependent yield stress and $\Delta\epsilon_{ij}^{p*}$ is the kinematically admissible plastic strain-rate cycle. By introducing random variables, the deterministic Bree diagram is extended to a two-dimensional Probability Density Function (PDF) surface representing the stochastic shakedown limit, bounded by a 95 %-probability variation envelope.

2.2 LMM-DPIM-based neural network model

DPIM is based on the probability density integral equation (PDIE), derived from the probability conservation principle, where the PDF of response can be obtained by

$$p_{Y_l}(y_l) = \int_{\Omega_\Theta} p_{Y_l|\Theta}(y_l|\theta)\, p_\Theta(\theta)\, d\theta \tag{4}$$

where Θ denotes the random variable vector, Y_l the response of interest, and $p_\Theta(\theta)$ the joint PDF of the inputs. For numerical evaluation, the probability space is partitioned into representative points $\{\theta_q\}$ with assigned probabilities $\{P_q\}$, and the Dirac delta function is replaced by an adaptive Gaussian kernel:

$$p_{Y_l}(y_l) \approx \sum_{q=1}^{N} P_q \cdot \frac{1}{\eta\sqrt{2\pi}} \exp\left[-\frac{\left(y_l - \lambda_l(\theta_q)\right)^2}{2\eta^2}\right] \tag{5}$$

where N is the total number of representative points and η is the smoothing parameter determined adaptively. Reliability is evaluated by introducing the Heaviside function: $R = \sum_{q=1}^{N} P_q \cdot \mathcal{H}\left[\lambda_S(\theta_q) - B\right]$, where B is the prescribed threshold.

The LMM-DPIM-based neural network model (LMM-DPIM-NN) workflow, as illustrated in Figure 1, proceeds in five steps:

• **Step 1.** Partition the probability space to obtain representative points and assigned probabilities as input random variables.

• **Step 2.** Perform LMM-based shakedown analysis for each representative point under varying load ratios to obtain the shakedown multiplier λ.

• **Step 3.** Train a fully connected BPNN to map input random variables to the shakedown multiplier, using training, validation, and test subsets.

• **Step 4.** Solve the PDIE using the trained NN to obtain the PDF of the shakedown multiplier.

• **Step 5.** Conduct reliability analysis based on the shakedown limit threshold and the reliability equation.

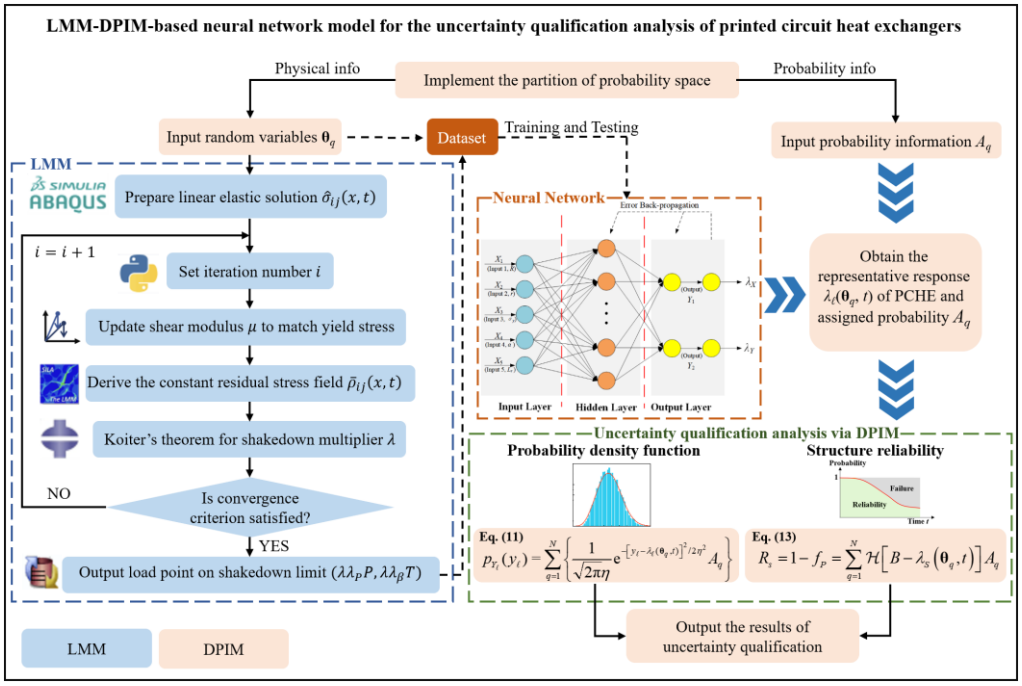


Figure 1. LMM-DPIM-based neural network model for stochastic shakedown and reliability analyses.

3. Numerical example

3.1 PCHE model and random variables

A typical PCHE with semi-circular channels is considered. The hot and cold channel pairs form a unit-cell model. A 2D plane-strain FE model is constructed with symmetric boundary conditions on the symmetry planes and coupled normal displacements on the top and left edges to simulate the repeating channel pattern. The hot channel inner surface is subjected to pressure $P_H = 25$ MPa and temperature $T_H = 50\,^{\circ}\text{C}$, while the cold channel inner surface carries $P_C = 10$ MPa and $T_C = 20\,^{\circ}\text{C}$. The FE model is meshed in Abaqus/CAE with 5367 elements.

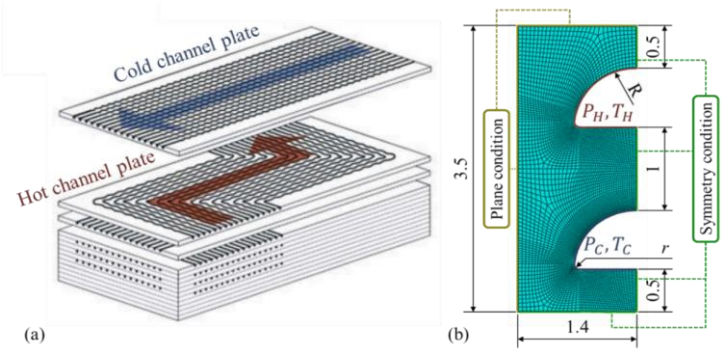


Figure 2. (a) Stacked and bonded plates in a PCHE core; (b) a unitary cell model [14].

The random variables are listed in Table I. Six temperature-dependent yield stresses, channel radius R, fillet radius r, thermal expansion coefficient α, and load ratio L_r are treated as random variables with normal or uniform distributions. Elastic modulus, Poisson's ratio, and thermal conductivity are held constant.

Table I. Random variables with distribution types and ranges.

Design parameter	Temperature [°C]	Mean value (μ_M)	Distribution type	Variation range
Load ratio L_r	—	5	Uniform	[μ_M−5, μ_M+5]
Channel radius R [mm]	—	0.75	Normal	[μ_M−0.1, μ_M+0.25]
Fillet radius r [mm]	—	0.045	Normal	[μ_M−0.08, μ_M+0]
Yield stress σ_y [MPa]	20	241	Normal	[μ_M−12, μ_M+12]
Yield stressσ_y [MPa]	100	212	Normal	[μ_M−12, μ_M+12]
Yield stress σ_y [MPa]	200	188	Normal	[μ_M−12, μ_M+12]
Yield stress σ_y [MPa]	300	174	Normal	[μ_M−12, μ_M+12]
Yield stress σ_y [MPa]	400	166	Normal	[μ_M−12,μ_M+12]
Yield stress σ_y [MPa]	500	162	Normal	[μ_M−12, μ_M+12]
Thermal expansion α [10^{-5}/°C]	—	1.83	Normal	[μ_M−0.183, μ_M+0.183]
Young's modulus E [10^3 MPa]	—	159	Constant	—
Poisson's ratio	—	0.3	Constant	—
Thermal conductivity [W/(m·K)]	—	0.02149	Constant	—

3.2 Verification and uncertainty qualification analysis results

Deterministic solution. With all design parameters set to their mean values, the deterministic shakedown limit (Bree diagram) is computed. The upper boundary corresponds to the reverse plasticity limit and the lower boundary to the ratchet limit. Three load points near the shakedown limit are selected for verification by step-by-step analysis in Abaqus with 50 loading–unloading cycles to ensure steady-state cyclic behavior. The PEMAG evolution agrees well with the LMM prediction, confirming the accuracy of the deterministic shakedown limit.

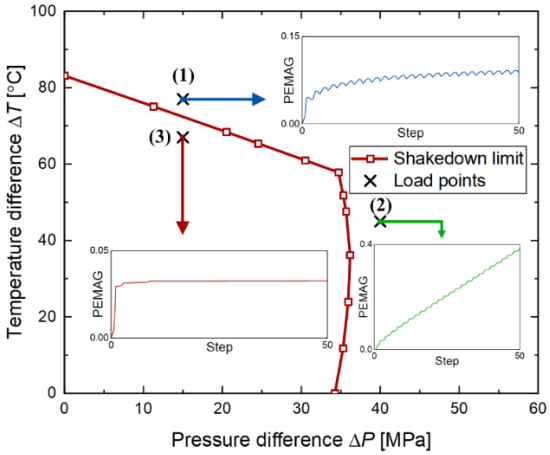


Figure 3. The cyclic behaviour of load points near the deterministic shakedown limit.

LMM-DPIM vs. MCS. Table II compares the LMM-DPIM and MCS results for the stochastic shakedown analysis. The relative error for the CoV of the pressure difference decreases from 268.13% with 100 representative points to 0.43% with 1500 representative points. To guarantee the accuracy of stochastic shakedown analysis, 1500 representative points are selected for LMM-DPIM in this case. Compared with MCS using 1×10^4 samples, LMM-DPIM greatly reduces the CPU time while maintaining good accuracy.

Table II. LMM-DPIM vs. MCS comparison — CoV, relative error, CPU time.

Method	Sampling size	Cov of pressure difference	Relative error	Cov of temperature difference	Relative error	CPU Time
MCS	1×10^4	0.1415	–	0.1127	–	449518.55
LMM-DPIM	100	0.5209	268.13%	0.4514	301.77%	4623.88
LMM-DPIM	500	0.2237	58.09%	0.1823	63.00%	23136.06
LMM-DPIM	1000	0.1460	3.18%	0.1142	1.33%	45921.90
LMM-DPIM	1500	0.1421	0.43%	0.1123	0.35%	69191.72

Stochastic shakedown analysis. Five random parameters (σ_y, R, r, α, L_r) are considered in the Stochastic shakedown analysis via LMM-DPIM with 1500 representative points. Moreover, LMM-DPIM-NN model is established to reproduce the LMM-DPIM results with high accuracy, while reducing CPU time from approximately 68 800 s to 10.7 s. The results of stochastic shakedown are illustrated in Figure 4, 95%-probability shakedown limit variation boundary is indicated by the red line, and the most probable variation range is shown in yellow.

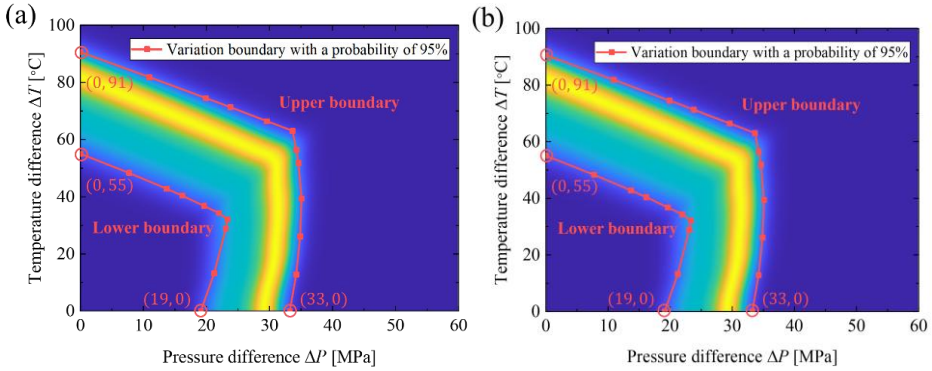


Figure 4. PDF surface for the stochastic shakedown limit obtained by (a) LMM-DPIM-NN model; (b) LMM-DPIM.

Influence of random parameters. The stochastic shakedown analysis results of PCHE structure under different random parameters are presented in Figure 5. The results shows that the fillet radius r at the channel corner exerts the most significant influence, in which its variation range induces a bimodal PDF and triggers stochastic P-bifurcation. The channel radius R also substantially affects the shakedown limit, while the thermal expansion coefficient α has the least influence.

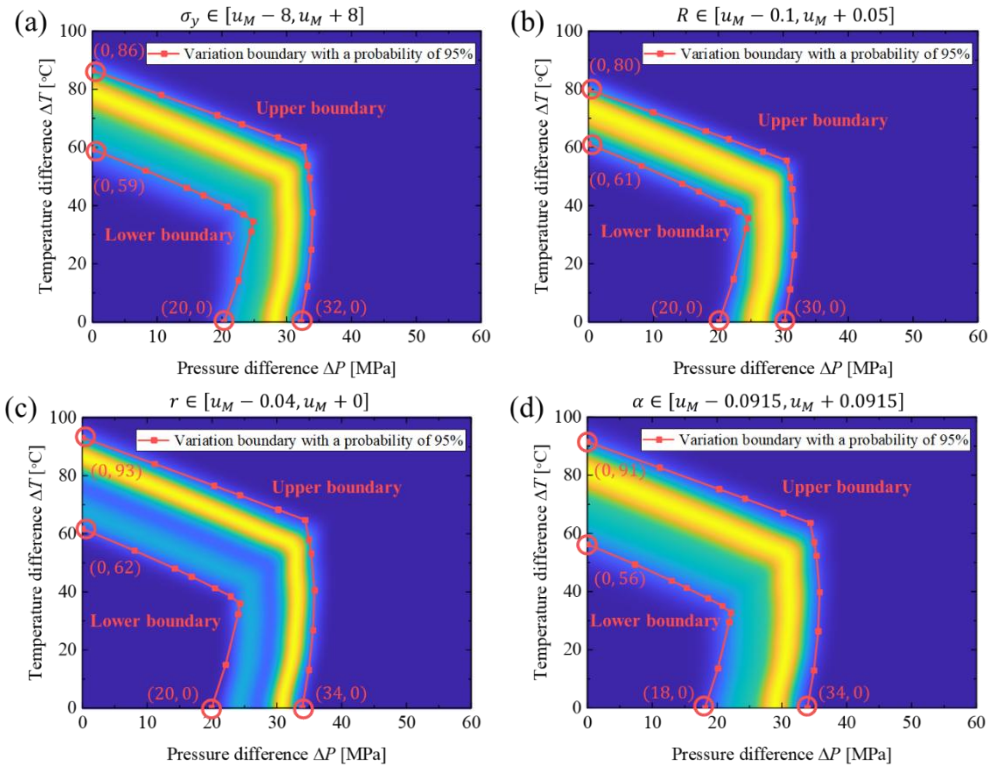
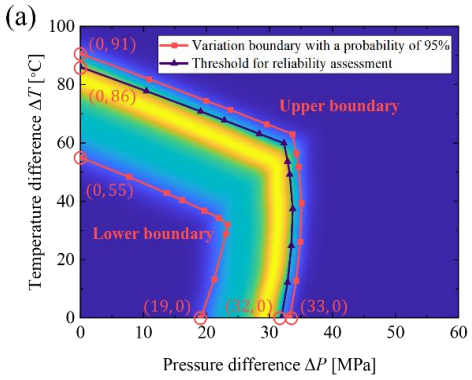


Figure 5. PDF surface for the stochastic shakedown limit for PCHE structure after the variations of different random parameters: (a) yield stress σ_y changed from [u_M–12, u_M+12] to [u_M–8, u_M+8]; (b) channel radius R changed from [u_M–0.1, u_M+0.25] to [u_M–0.1, u_M+0.05]; (c) fillet radius r changed from [u_M–0.08, u_M+0] to [u_M–0.04, u_M+0]; (d) thermal expansion α changed from [u_M–0.183, u_M+0.183] to [u_M–0.0915, u_M+0.0915].

Reliability analysis. Reliability curves are evaluated based on the shakedown limit threshold, as shown in Figure 6. Both R and r significantly affect reliability. The fillet radius r has the strongest impact: reliability decreases by 19.43% as r increases. The LMM-DPIM-NN reliability results agree well with MCS, validating the proposed framework for efficient stochastic reliability assessment.



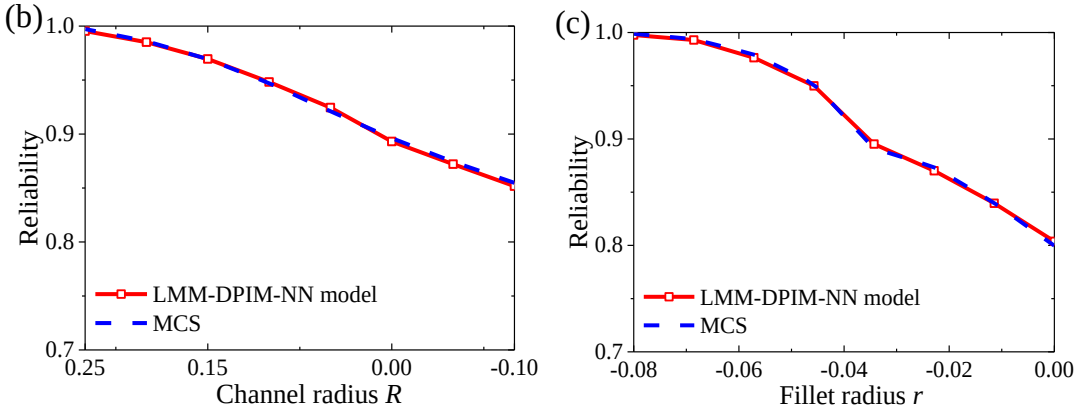


Figure 6. (a) Threshold for reliability assessment of PCHE structure; (b) reliability curve under different channel radius R; (c) reliability curve under different fillet radius r.

4. Conclusions

1. The LMM was combined with DPIM for the first time, and an LMM-DPIM-NN model was established for uncertainty qualification analysis of PCHEs with multiple random parameters. Verification against Monte Carlo simulation confirmed the accuracy of proposed method.

2. The LMM-DPIM-NN model achieves high accuracy comparable to LMM-DPIM while reducing CPU time, providing an efficient tool for stochastic shakedown analysis of PCHEs.

3. The fillet radius at the channel corner is the most influential random variable: it can induce stochastic P-bifurcation and causes reliability to decrease by up to 19.43 % as it increases, highlighting the importance of manufacturing tolerance control for this geometric parameter.

References

[1] Chen, M.H., X.D. Sun, R.N. Christensen, I. Skavdahl, V. Utgikar and P. Sabharwall. Pressure drop and heat transfer characteristics of a high-temperature printed circuit heat exchanger. *Applied Thermal Engineering*, 108: 1409–1417, 2016.

[2] Torre, R. de la., J. L. François and C. X. Lin. Assessment of the design effects on the structural performance of the Printed Circuit Heat Exchanger under very high temperature condition. *Nuclear Engineering and Design*, 365: 110713, 2020.

[3] Pham, D.C. Shakedown theory for elastic plastic kinematic hardening bodies. *International Journal of Plasticity*, 23: 1240–1259, 2007.

[4] *ASME Boiler and Pressure Vessel Code, Section III, Division 1—Subsection NH, in, The American Society of Mechanical Engineers*. New York, 2013.

[5] *R5: Assessment Procedure for the High Temperature Response of Structures*, in, EDF Energy.

[6] Bree, J. Elastic-plastic behaviour of thin tubes subjected to internal pressure and intermittent high-heat fluxes with application to fast-nuclear-reactor fuel elements, *Journal of strain analysis*, 2: 226–238, 1967.

[7] Polizzotto, C. On the conditions to prevent plastic shakedown of structures: Part I—Theory. *Journal of applied mechanics*, 60: 15–19, 1993.
[8] Peng, H., Y.H. Liu and H.F. Chen. A numerical formulation and algorithm for limit and shakedown analysis of large-scale elastoplastic structures. *Computational Mechanics*, 63: 1–22, 2019.
[9] Peng, H., Y.H. Liu, H.F. Chen and J. Shen, Shakedown analysis of engineering structures under multiple variable mechanical and thermal loads using the stress compensation method. *International Journal of Mechanical Sciences*, 140: 361–375, 2018.
[10] Chen, H.F., and A.R.S. Ponter. Shakedown and limit analyses for 3-D structures using the linear matching method. *International Journal of Pressure Vessels and Piping*, 78: 443–451, 2001.
[11] Chen, H.F., and A.R.S. Ponter. A method for the evaluation of a ratchet limit and the amplitude of plastic strain for bodies subjected to cyclic loading. *European Journal of Mechanics-A/Solids*, 20: 555–571, 2001.
[12] Koiter, W. T. *General theorems for elastic plastic solids*. Progress of Solid Mechanics, 1960.
[13] Barbera, D., H. Chen, Y. Liu, and F. Xuan. Recent developments of the linear matching method framework for structural integrity assessment. *Journal of Pressure Vessel Technology*, 139.5: 051101, 2017.
[14] Ma, Z.Y., Z.J. Fu, H.F. Chen and X.X. Wang. Shakedown and creep rupture analysis of printed circuit heat exchangers based on the linear matching method framework. *Finite Elements in Analysis and Design*, 233: 104127, 2024.
[15] Shen, J., Z.Y. Ma and H.F. Chen. Shakedown and ratcheting analysis of Printed Circuit Heat Exchangers under multiple cyclic mechanical and thermal loads. *International Journal of Pressure Vessels and Piping*, 199: 104723, 2022.
[16] Li, J. Probability density evolution method: background, significance and recent developments. *Probabilistic Engineering Mechanics*, 44: 111–117, 2016.
[17] Chen, G.H. and D.X. Yang. Direct probability integral method for stochastic response analysis of static and dynamic structural systems. *Computer Methods in Applied Mechanics and Engineering*, 357: 112612, 2019.
[18] Chen, H.S., Y.X. Gao, D.X. Yang, Z. Meng and Z.J. Fu. A novel weight index-based uniform partition technique of multi-dimensional probability space for structural uncertainty quantification. *Computer Methods in Applied Mechanics and Engineering*, 431: 117297, 2024.
[19] Wang, X.X., H.F. Chen and F.Z. Xuan. Direct method-based probabilistic shakedown analysis for the structure under multiple uncertain design conditions. *Ocean Engineering*, 280: 114653, 2023.
[20] Wang, R. Z., H. H. Gu, S. P. Zhu, K. S. Li, J. Wang, X. W. Wang and S. T. Tu. A data-driven roadmap for creep-fatigue reliability assessment and its implementation in low-pressure turbine disk at elevated temperatures. *Reliability Engineering & System Safety*, 225: 108523, 2022.
[21] Wang, X.X., J. Yang, H.F. Chen and F.Z. Xuan. Physics-based neural network for probabilistic low cycle fatigue and ratcheting assessments of pressurized elbow pipe component. *International Journal of Fatigue*, 172: 107598, 2023.
[22] Sepasdar, R., A. Karpatne and M. Shakiba. A data-driven approach to full-field nonlinear stress distribution and failure pattern prediction in composites using deep learning. *Computer Methods in Applied Mechanics and Engineering*, 397: 115126, 2022.

Towards a Set-Based IVP Solver for ODEs on the GPU

Ekaterina Auer
University of Applied Sciences Wismar, ekaterina.auer@hs-wismar.de
Lorenz Gillner
University of Applied Sciences Wismar, lorenz.gillner@hs-wismar.de
Julien Alexandre dit Sandretto
ENSTA, Institut Polytechnique de Paris, julien.alexandre-dit-sandretto@ensta.fr

Abstract. Reachability analysis is a key component of (formal) verification techniques for cyber-physical systems subject to uncertainty, as it enables the computation of sets of states that the system can reach over time. However, such methods are often computationally expensive, making algorithmic and implementation-level optimizations essential. In this paper, we propose a verified interval-based ODE solver for reachability analysis, based on the classical fourth-order Runge–Kutta scheme and designed to execute entirely within a single GPU kernel. This enables efficient subdivision strategies to mitigate overestimation while supporting the parallel propagation of a large number of subboxes. Using the Van der Pol oscillator as a benchmark, we demonstrate the applicability of the proposed approach and compare its performance with non-verified GPU-based uncertainty propagation techniques derived from Müller-type theorems, as well as with the CPU-based reference tool DynIbex.

Keywords: result verification, ODE, Runge-Kutta schemes, GPU

1. Introduction

Verification and uncertainty quantification play a central role in ensuring the reliability of computational models. However, these processes can be very time-consuming, especially for computationally demanding problems. One natural way to accelerate computations is through high-performance computing or parallelization.

GPUs are highly specialized programmable units which are widely used in parallel scientific computing today. They offer an affordable alternative to supercomputers—provided that the problem fits the stream processing model, where the same kernel is applied to different data to produce independent results. Since GPU architectures differ significantly from CPUs, existing CPU-oriented software generally cannot be ported to GPUs without substantial redesign.

In (Auer et al., 2025b), we investigated GPU-based acceleration for parameter identification using least squares and global optimization:

$$F(\mathbf{p}) = \sum_{k=T_b}^{T_e} \sum_{j=1}^{n_m} \left(y_j(t_k, \mathbf{p}) - y_{j,m}(t_k)\right)^2 \overset{\mathbf{p}\in[\mathbf{p}]}{\longrightarrow} \min \ ,$$

© 2026 by the author(s). This work is licensed under the Creative Commons Attribution 4.0 International License (CC BY 4.0), which permits unrestricted use, distribution, and reproduction in any medium, provided the original author and source are credited.

where $t \in [T_b, T_e]$, $y_j(t_k, \mathbf{p})$ denotes, at time t_k, the j-th component of the solution to the initial value problem (IVP) for the ordinary differential equations (ODE) of the form

$$\dot{\mathbf{y}} = \mathbf{f}(\mathbf{y}(t)) \tag{1}$$

with $\mathbf{y}(t_0) \in [\mathbf{y}_0] \in \mathbb{IR}^{n_y}$, and $y_{j,m}(t_k)$ the corresponding measured value among n_m measurements[1]. The aim is to enclose parameter values $\mathbf{p}$ that achieve the global minimum of $F(\mathbf{p})$ over the search space $[\mathbf{p}]$. Once $[\mathbf{p}]$ is subdivided into subdomains $[\mathbf{p_1}], \ldots, [\mathbf{p}_\kappa]$, the problem exhibits massive data parallelism suitable for GPU evaluation.

When such properties as cooperativity (Hirsch and Smith, 2005) cannot be exploited or a mathematical formula for the exact solution does not exist, computing enclosures of $\mathbf{y}(t, \mathbf{p})$ requires a set-based IVP solver on the GPU. In (Auer et al., 2017), we introduced a method for computing a rough (a priori) enclosure on the GPU, a necessary first step toward a full set-based solver as explained in Section 2.

Our goal in this paper is therefore to develop a verified ODE solver that operates entirely within a single GPU kernel. Such a solver is particularly well suited for parameter identification in dynamical models via brute-force global optimization. It also offers an effective way to reduce overestimation: bounded uncertainties in the initial conditions $[\mathbf{y}_0]$ or in other parameters can be subdivided into smaller interval boxes, whose flows under Eq. (1) are computed in parallel on the GPU. Taking the hull of these flows then yields a tighter enclosure of the solution, as illustrated in Section 4.

The paper is structured as follows. Section 2 reviews the theoretical foundations of verified solution methods for IVPs and summarizes Müller-type theorems for bounding the corresponding ODE flow. Section 2.2 is of particular importance, as it introduces the proposed GPU-based verified method. It is built upon the classical fourth-order Runge–Kutta scheme, with local truncation errors rigorously estimated using the Butcher series expansion. In Section 3, we briefly review the tools required for guaranteed computations, in particular for interval arithmetic and for its use with automatic differentiation. These components are essential prerequisites for a verified GPU implementation. In Section 4, we present a comparative evaluation of the proposed solver using the Van der Pol oscillator as a benchmark. We compare the performance of its different GPU implementations against non-verified GPU-based uncertainty propagation techniques based on Müller-type theorems and against the established verified CPU-based tool DynIbex (Alexandre dit Sandretto and Chapoutot, 2016). Finally, Section 5 summarizes the main results and outlines directions for future research.

2. Verifying the Flow of an Initial Value Problem

ODEs of the form in Eq. (1) are among the most classical continuous differential equations. They possess a unique solution $\mathbf{y}(t)$ provided certain conditions are satisfied, for example, if $\mathbf{f}$ is Lipschitz continuous. In general, closed-form solutions are not available, so that numerical integration schemes must be used to approximate the state of the system over time starting from the initial condition

[1] In the following, we assume that $t_0 = 0$

$\mathbf{y}(0) = \mathbf{y}_0$. The integral formulation

$$\mathbf{y}(t) = \mathbf{y}_0 + \int_0^t \mathbf{f}(\mathbf{y}(s))\, ds, \tag{2}$$

does not in fact represent a solution but a true reformulation because the unknown function $\mathbf{y}(\cdot)$ appears both on the left-hand side and inside the integral on the right-hand side.

A widely used class of numerical integrators for ODEs is given by Runge–Kutta schemes, which can be selected according to the characteristics of the problem and the desired level of accuracy. However, when uncertainty must be handled rigorously or result guarantees are required, standard numerical approximations are insufficient.

To address this, a number of verified IVP solvers have been developed for CPUs over the past decades, including VNODE (Nedialkov et al., 1999) and DynIbex (Alexandre dit Sandretto and Chapoutot, 2016). Although these solvers rely on different underlying techniques, they share a common approach to verification, which we outline in Subsection 2.1. We then present the verified fourth-order Runge–Kutta scheme implemented on the GPU (Subsection 2.2), and finally discuss non-verified approaches capable of handling uncertainty (Subsection 2.3).

2.1. General Verification Scheme

The main approach to verifying a numerical integration method, as described in (Nedialkov et al., 1999), is to structure each step of the integration scheme into two phases.

Phase 1: Compute an *a priori* enclosure $[\tilde{\mathbf{y}}_j]$ of the solution such that

- $\mathbf{y}(t; [\mathbf{y}_j])$ is guaranteed to exist for all $t \in [t_j, t_{j+1}]$, that is, over the whole time interval at the current step, and for all $\mathbf{y}_j \in [\mathbf{y}_j]$;
- $\mathbf{y}(t; [\mathbf{y}_j]) \subseteq [\tilde{\mathbf{y}}_j]$ for all $t \in [t_j, t_{j+1}]$.

If adaptive step-size control is employed, the step size $h_j = t_{j+1} - t_j > 0$ is chosen as large as possible while preserving both the existence guarantee and the desired enclosure tightness. Alternatively, for a fixed step size h_j, the algorithm terminates if no suitable interval $[\tilde{\mathbf{y}}_j]$ can be found.

Phase 2: Compute a tighter enclosure of $[\mathbf{y}_{j+1}]$ at time t_{j+1} such that $\mathbf{y}(t_{j+1}, [\mathbf{y}_j]) \subseteq [\mathbf{y}_{j+1}]$.

2.1.1. *A priori enclosure*

Consider the space of continuously differentiable functions $\mathcal{C}^1([t_j, t_{j+1}], \mathbb{R}^n)$ and the Picard-Lindelöf operator

$$\mathbf{p}_\mathbf{f}(\mathbf{y}) = t \mapsto \mathbf{y}_j + \int_{t_j}^t \mathbf{f}(\mathbf{y}(s)) ds \ , \tag{3}$$

where $\mathbf{y}_j$ is the true solution $\mathbf{y}(t_j)$ at time t_j. We can define a simple enclosure function for the right-hand side of the mapping in Eq. (3) such that

$$[\mathbf{p}_\mathbf{f}]([\mathbf{r}]) \overset{\text{def}}{=} [\mathbf{y}_j] + [0, h_j] \cdot \mathbf{f}([\mathbf{r}]) \ . \tag{4}$$

Consequently, if one can find an interval $[\mathbf{r}]$ such that $[\mathbf{p_f}]([\mathbf{r}]) \subseteq [\mathbf{r}]$, then $[\tilde{\mathbf{y}}_j] \subseteq [\mathbf{r}]$ by the Banach fixed-point theorem. That is, we want to find such h_{max}, ρ_{min} and $[\mathbf{r}] := [\mathbf{y}_j - \rho_{min}, \mathbf{y}_j + \rho_{min}]$ that

$$[\mathbf{p_f}]([\mathbf{r}]) = [\mathbf{y}_j] + [0, h_{max}] \cdot \mathbf{f}([\mathbf{r}]) \subseteq [\mathbf{r}] \ . \tag{5}$$

This enclosure is rather coarse, as the true solution is generally not constant over the interval $[t_j, t_j + h_{max}]$. Moreover, when the enclosures $[\tilde{\mathbf{y}}_{j+1}]$, $[\tilde{\mathbf{y}}_{j+2}]$, ... are computed successively from $[\tilde{\mathbf{y}}_j]$, $[\tilde{\mathbf{y}}_{j+1}]$, ... using Eqs. (4)–(5), their widths typically grow monotonically, irrespective of the true behavior of the solution. Higher-order schemes (e.g., those based on Taylor series decomposition) can mitigate this effect to some extent, but they cannot eliminate the resulting overestimation completely.

2.1.2. *Tighter enclosure*
After Phase 1, the a priori enclosure $[\tilde{\mathbf{y}}_j]$ is obtained such that

$$\mathbf{y}(t; [\mathbf{y}_j]) \subset [\tilde{\mathbf{y}}_j] \quad \forall t \in [t_j, t_{j+1}] \ .$$

In particular, we have $\mathbf{y}(t_{j+1}; [\mathbf{y}_j]) \subset [\tilde{\mathbf{y}}_j]$. The goal of Phase 2 is now to compute a tighter enclosure $[\mathbf{y}_{j+1}]$ at time t_{j+1} such that

$$\mathbf{y}(t_{j+1}; [\mathbf{y}_j]) \subset [\mathbf{y}_{j+1}] \subseteq [\tilde{\mathbf{y}}_j] \ .$$

Any formula for improving the a priori enclosure can be seen as consisting of two parts:

- the *approximation part* $\Phi(t, [\mathbf{y}_j]) \approx \mathbf{y}(t; [\mathbf{y}_j])$. It usually follows a formula for a traditional numerical integration method such as Runge-Kutta or a direct Taylor series decomposition.
- the *local truncation error part* $\mathrm{LTE}_\Phi(t, \mathbf{y}, [\mathbf{y}_j])$. It is intended to provide the formula for the distance (enclosure) between the exact solution and the approximate solution produced by the approximation part:

$$\mathrm{LTE}_\Phi(t, \mathbf{y}, [\mathbf{y}_j]) \stackrel{\text{def}}{=} \mathbf{y}(t; [\mathbf{y}_j]) - \Phi(t, [\mathbf{y}_j]) \ . \tag{6}$$

A verified numerical integration method has the following property:

$$\begin{aligned} \exists \xi \in]t_j, t_{j+1}[, \quad \mathbf{y}(t_{j+1}; [\mathbf{y}_j]) \ &= \ \Phi(t_{j+1}, [\mathbf{y}_j]) + \mathrm{LTE}_\Phi(\xi, \mathbf{y}, [\mathbf{y}_j]) \\ &\subset \ \Phi(t_{j+1}, [\mathbf{y}_j]) + \mathrm{LTE}_\Phi([t_j, t_{j+1}], [\tilde{\mathbf{y}}_j], [\mathbf{y}_j]) \ \subset \ [\tilde{\mathbf{y}}_j] \ . \end{aligned}$$

Consequently, the tight enclosure is obtained by evaluating the approximation part at time t_{j+1} and combining it with bounds on the local truncation error derived from the a priori enclosure $[\tilde{\mathbf{y}}_j]$.

2.2. A Verified Runge-Kutta Scheme for a Tighter Enclosure

Let us consider the well-known and widely used fourth-order method from the Runge–Kutta family of explicit integration schemes. It provides an accurate and computationally efficient approximation of the solution of an IVP to an ODE by evaluating the vector field at several intermediate stages within each time step. The method achieves fourth-order accuracy, meaning that the local truncation error scales as $\mathcal{O}(h^5)$ and the global error as $\mathcal{O}(h^4)$ for a step size h. The scheme is defined by

the Butcher tableau given below on the left, which specifies the intermediate stage coefficients and the weights used to combine them into the final update. Eq. (7) on the right shows how the stage values are computed for a current state $\mathbf{y}_n \approx \mathbf{y}(t_n)$ and step size h. The next approximation of the solution is then obtained by the weighted combination in Eq. (8).

$$\begin{array}{c|cccc} 0 & 0 & 0 & 0 & 0 \\ 1/2 & 1/2 & 0 & 0 & 0 \\ 1/2 & 0 & 1/2 & 0 & 0 \\ 1 & 0 & 0 & 1 & 0 \\ \hline & 1/6 & 1/3 & 1/3 & 1/6 \end{array} \qquad \begin{aligned} \mathbf{k}_1 &= \mathbf{f}(\mathbf{y}_n), \\ \mathbf{k}_2 &= \mathbf{f}\big(\mathbf{y}_n + \tfrac{h}{2}\mathbf{k}_1\big), \\ \mathbf{k}_3 &= \mathbf{f}\big(\mathbf{y}_n + \tfrac{h}{2}\mathbf{k}_2\big), \\ \mathbf{k}_4 &= \mathbf{f}(\mathbf{y}_n + h\mathbf{k}_3). \end{aligned} \tag{7}$$

$$\begin{aligned} \mathbf{y}_{n+1} &= \Phi_4(t_{n+1}, \mathbf{y}_n) \\ &= \mathbf{y}_n + \frac{h}{6}\Big(\mathbf{k}_1 + 2\mathbf{k}_2 + 2\mathbf{k}_3 + \mathbf{k}_4\Big) \end{aligned} \tag{8}$$

The LTE of the this Runge-Kutta scheme can be obtained by comparing the Butcher-series representation of the exact solution with that of the numerical method, as developed in (Butcher, 2021) via the associated rooted-tree formalism. We use the following multilinear derivative notation:

- $f'(\mathbf{y}) \in \mathbb{R}^{n_y \times n_y}$ denotes the Jacobian of $\mathbf{f}$ at $\mathbf{y}$.
- $f''(\mathbf{y})[\mathbf{u}, \mathbf{v}]$ denotes the bilinear application of the Hessian tensor.
- $f^{(k)}(\mathbf{y})[\mathbf{v}_1, \ldots, \mathbf{v}_k]$ denotes the k-th order Fréchet derivative.

Here, $f'(\mathbf{y})\,\mathbf{v} := J_f(\mathbf{y}) \cdot \mathbf{v}$, $f''(\mathbf{y})[\mathbf{u}, \mathbf{v}] := \sum_{i,j} \dfrac{\partial^2 \mathbf{f}}{\partial y_i \partial y_j}(\mathbf{y})\, u_i v_j$. Expressions such as $f' \cdot [f' \cdot [f' \cdot \mathbf{f}]]$ are interpreted as repeated Jacobian-vector products: $J_f(\mathbf{y})(J_f(\mathbf{y})(J_f(\mathbf{y})\,\mathbf{f}(\mathbf{y})))$. Similarly, $f''[\mathbf{f}, \mathbf{f}]$ denotes a Hessian contraction in two identical directions: $f''(\mathbf{y})[\mathbf{f}(\mathbf{y}), \mathbf{f}(\mathbf{y})]$.

The LTE can be written as a linear combination of rooted-tree (Butcher) contributions. For the specific method from this section, this linear combination becomes (with $h = t_{n+1} - t_n$)

$$\begin{aligned} &\mathrm{LTE}_4([t_n, t_{n+1}], [\tilde{\mathbf{y}}_n], [\mathbf{y}_n]) := \\ &h^5 \Big(-\tfrac{1}{120} f' \cdot [f' \cdot [f' \cdot [f' \cdot \mathbf{f}]]] + \tfrac{1}{480} f' \cdot \Big[f' \cdot \Big[f'' \cdot [\mathbf{f}, \mathbf{f}] \Big] \Big] \\ &-\tfrac{1}{240} f' \cdot \Big[f'' \cdot [f' \cdot \mathbf{f},\, \mathbf{f}] \Big] + \tfrac{1}{120} f'' \cdot \Big[f' \cdot [f' \cdot [f' \cdot \mathbf{f}]],\, \mathbf{f} \Big] \\ &-\tfrac{1}{720} f' \cdot [f^{(3)} \cdot [\mathbf{f}, \mathbf{f}, \mathbf{f}]] - \tfrac{1}{480} f'' \cdot [f'' \cdot [\mathbf{f}, \mathbf{f}],\, \mathbf{f}] + \tfrac{1}{160} f'' \cdot \Big[f' \cdot \mathbf{f},\, f' \cdot \mathbf{f} \Big] \\ &+\tfrac{1}{480} f^{(3)} \cdot \Big[f' \cdot \mathbf{f},\, \mathbf{f},\, \mathbf{f} \Big] + \tfrac{1}{2880} f^{(4)} \cdot \Big[\mathbf{f},\, \mathbf{f},\, \mathbf{f},\, \mathbf{f} \Big] \Big) \quad . \end{aligned} \tag{9}$$

Although the formula is written as a nested expression, it should not be evaluated in a naive manner. Instead, it corresponds to a directed acyclic graph (DAG) of tensor contractions (Mullier et al., 2018), where the nodes represent intermediate quantities such as $\mathbf{f}$, $f' \cdot \mathbf{f}$, $f'' \cdot [\mathbf{f}, \mathbf{f}]$, ...; the edges represent dependency relations between contractions. Thus, an efficient algorithm is necessary to compute subexpressions only once and to reuse them (*common subexpression elimination*, CSE).

Direct evaluation of nested expressions in Eq. (9) leads to repeated computation of identical Jacobian and Hessian contractions. Moreover, we cannot represent tensors (especially higher-order derivatives) in their "natural" explicit form as multidimensional arrays on the GPU since this would be expensive in both storage and access cost. Even if we consider flat vectors only, storing all

intermediate results simultaneously may reduce GPU occupancy. Another challenge is the computation of Fréchet derivatives up to fourth order, ideally via automatic differentiation (AD). While AD techniques based on repeated application of the chain rule have been studied extensively (Griewank and Walther, 2000), tracing-based methods commonly used in verified IVP solvers are difficult to implement efficiently on GPUs due to memory and control-flow constraints (cf. Section 3.2). In particular, forward-mode tracing (e.g., FADBAD++ (Bendsten and Stauning, 1996)) can compute Fréchet derivatives implicitly, but may introduce overhead compared to optimized contraction sequences. Instead of runtime evaluation, possibly with AD, it is therefore preferable to transform the expression at compile time into an optimized sequence of tensor contractions. In this work, we present a basic GPU implementation of this approach for the LTE, while extending it to AD remains future work. Automatic code generation for the LTE has been demonstrated on CPUs (Alexandre dit Sandretto, 2025), but without GPU-specific optimizations, and extending such methods to GPUs remains challenging due to differences in execution and memory models.

The final (naive) verified Runge-Kutta method (denoted by RK4) relies on the following formula:

$$[\mathbf{y}_{n+1}] := \Phi_4(t_{n+1}, [\mathbf{y}_n]) + \mathrm{LTE}_4([t_n, t_{n+1}], [\tilde{\mathbf{y}}_n], [\mathbf{y}_n]) \ . \tag{10}$$

When using conventional interval arithmetic (as opposed to, e.g., affine arithmetic as implemented in DynIbex), the method becomes more susceptible to the wrapping effect. Various strategies have been proposed in the CPU context to mitigate this issue, including approaches based on the mean value theorem (MVT) and coordinate transformations such as QR decomposition (Nedialkov et al., 1999). To reduce the wrapping effect while maintaining efficiency on GPUs, one must balance its mitigation against the computational cost of additional work (AD and coordinate transformations). In the our implementation, we incorporate a basic MVT-based step for Φ_4:

$$[\mathbf{y}_{n+1}] := \Phi_4(t_{n+1}, \hat{\mathbf{y}}_n) + J_{\Phi_4}([\mathbf{y}_n])([\mathbf{y}_n] - \hat{\mathbf{y}}_n) + \mathrm{LTE}_4([t_n, t_{n+1}], [\tilde{\mathbf{y}}_n], [\mathbf{y}_n]) \ , \tag{11}$$

with $\hat{\mathbf{y}}_n$ chosen as the midpoint of $[\mathbf{y}_n]$ and J_{Φ_4} being the Jacobean of Φ_4, which we compute using our GPU version of FADBAD++ (cf. Section 3.2). We denote this method by MRK4 in the following.

Note that any of the described methods can be naturally combined with a subdivision strategy on the GPU. A classical branch-and-bound (brute-force) approach proceeds as follows:

1. **Subdivide:** Decompose the parameter box $[\mathbf{p}]$ into subboxes $[\mathbf{p}] = \bigcup_{j=1}^{\ell} [\mathbf{p}_j]$, where $[\mathbf{p}]$ represents an interval vector of model parameters (CPU or GPU execution).
2. **Evaluate:** For each subbox $[\mathbf{p}_j]$, integrate the system in Eq. (1) from t_0 to t_{end} using a suitable method (e.g., RK4 or MRK4), running all ℓ subproblems in parallel on the GPU.
3. **Combine:** Compute an enclosure of the reachable set by taking the interval hull of the results, $\mathrm{hull}\left(\bigcup_{j=1}^{\ell} [\mathbf{y}_{end,j}]\right)$, which can be carried out on either the CPU or GPU.

2.3. Cooperative Systems and Monotone Inclusions

If the objective is to propagate uncertainty in the initial conditions or other parameters through a dynamical system in a reliable manner, a non-verified solver may be combined with suitable monotonicity properties of the system. The property of *cooperativity* (or *competitivity*) holds for the system in Eq. (1) if

$$\frac{\partial f_i}{\partial y_j} \geq 0 \ \left(\text{or } \frac{\partial f_i}{\partial y_j} \leq 0\right) \text{ for all } i \neq j,\ i,j = 1 \dots n_y \ . \tag{12}$$

Müller's theorem (Meslem and Ramdani, 2011), combined with the first property in Eq. (12) and positivity of y_j, yields Smith's theorem (Hirsch and Smith, 2005). It shows that the uncertainty in a cooperative system can be quantified by solving two systems with crisp parameters instead of one system with uncertain parameters:

$$\mathbf{y}'_{\text{lb}} = \underline{\mathbf{f}}(\mathbf{y}_{\text{lb}}) \quad \text{and} \quad \mathbf{y}'_{\text{ub}} = \overline{\mathbf{f}}(\mathbf{y}_{\text{ub}}) \tag{13}$$

(two bracketing systems). For cooperative (or competitive) systems, these are decoupled and can be solved in parallel. If the system is not monotone, both $\underline{\mathbf{f}}$ and $\overline{\mathbf{f}}$ may depend on $\mathbf{y}_{\text{lb}}$ and $\mathbf{y}_{\text{ub}}$, leading to a coupled system of dimension $2n_y$:

$$\mathbf{y}'_{\text{lb}} = \underline{\mathbf{f}}(\mathbf{y}_{\text{lb}}, \mathbf{y}_{\text{ub}}) \quad \text{and} \quad \mathbf{y}'_{\text{ub}} = \overline{\mathbf{f}}(\mathbf{y}_{\text{lb}}, \mathbf{y}_{\text{ub}}) \tag{14}$$

The bounding functions $\underline{\mathbf{f}}$ and $\overline{\mathbf{f}}$ can be obtained via interval arithmetic, though often conservatively. A tighter alternative is to compute global extrema of the right-hand side of (1), which is generally difficult due to nonlinear optimization.

The true solution $\mathbf{y}(t)$ lies in the interval $[\underline{\mathbf{y}}_{\text{lb}}(t), \overline{\mathbf{y}}_{\text{ub}}(t)]$. Evaluating such enclosures at each grid point t_k yields a verified flow of (1). A practical approximation is given by $\mathbf{y}_{\text{lb}}^{(k)}$, $\mathbf{y}_{\text{ub}}^{(k)}$ obtained from (13) or (14) using standard floating point arithmetic with sufficiently small step sizes. This captures most of the output uncertainty but is not fully verified; we use monotone inclusions as a baseline for comparison with the verified solver from Section 2.2.

3. Methods with Result Verification on the GPU

As shown in Section 2.2, set-based arithmetics and exact derivatives are required to verify Runge–Kutta schemes. In this section, we describe existing software for performing interval computations on NVIDIA GPUs using CUDA (NVIDIA, 2026). We then review available approaches to AD on GPUs, with particular attention to those compatible with interval arithmetic.

3.1. Interval Analysis on the GPU

Interval arithmetic is well supported on CPUs, where mature libraries such as Boost.Interval (Boost C++ Libraries, 2026) and INTLAB-style systems (Rump, 2026) provide good implementations. In

contrast, GPU support remains limited and is largely driven by research rather than production-ready libraries. Modern NVIDIA GPUs offer IEEE-754 compliant floating point arithmetic and support directed rounding via hardware intrinsics, which are essential for interval methods.

Early CUDA-based interval arithmetic was developed in academic work by Collange et al. (Collange et al., 2011), demonstrating the feasibility of Boost-style approaches on GPUs. However, these efforts have not resulted in currently maintained library. In practice, a common approach is to rely on established CPU interval libraries while adapting them for GPU use through compatible interfaces. For example, Boost.Interval can be employed with policy specializations that enable using the same library on the CPU and the GPU, see our implementation at `https://github.com/lorenzgillner/boost-interval`.

We reuse a simple GPU-based algorithm for a priori enclosure computation from (Auer et al., 2017) in a slightly modified form. While the original method employs adaptive step sizes (cf. Section 2.1.1), we restrict ourselves to constant step sizes to avoid branching and reduce thread divergence. Nevertheless, adaptive strategies may still improve performance by allowing larger steps in regions with mild dynamics. Moreover, we developed a GPU-based global optimization solver for parameter identification problems described in the Introduction, with such applications as for cooperative solid oxide fuel cell systems (Auer et al., 2025b). This problem class has received significant attention in both historically and recently; see, for instance, (Sanders, 2022).

3.2. Automatic Differentiation on the GPU

Recent developments in machine learning have strongly promoted both GPU computing and AD. As a consequence, there are more and more AD tools for the GPU. For successful use on the GPU, AD methods must be fast and fit the synchronous kernel execution. Symbolic computations, especially at runtime, are often not suitable, as they may introduce overhead or irregular execution patterns. Ideally, an AD algorithm should be able to provide the n-th derivative or all derivatives up to order n without requiring n to be fixed in advance. Two major approaches to AD are:

Source code transformation (SCT): Derivatives are generated by manipulating the program code itself. The original source code is analyzed and transformed into new code that explicitly computes the derivatives.

Tracing: Derivatives are computed at runtime using special data structures. The program execution is recorded, and derivative information is propagated according to the chain rule. This approach usually offers somewhat more flexibility with respect to derivative order.

3.2.1. *Source Code Transformation Versus Tracing on the GPU*

The decisive distinction between SCT and tracing in the context of GPU computing concerns the stage at which derivative information is generated and how it is integrated into the execution model. In SCT, derivatives are computed ahead of time, typically during compilation. The source code is transformed to generate additional derivative code, which is then compiled together with the original program. The resulting executable is deployed to the GPU, where multiple worker threads execute it. Since the derivative logic is already embedded, each worker can evaluate derivatives

Table I. Different AD tools based on SCT

Tool	Type	Intermediate rep.	CUDA	Interval support	Reference
Clad	Compiler plugin	Clang AST	yes	no	(Ifrim et al., 2023)
Enzyme	Compiler plugin	LLVM IR	yes	no	(Moses et al., 2022)
Tapenade	Preprocessor	IL Syntax Tree	manual transfer to GPU		(Hascoet and Pascual, 2013)
OpenAD	Preprocessor	Xaif	manual transfer to GPU		(Utke et al., 2008)

immediately at launch without additional runtime construction. Thus, derivative computation is effectively shifted to the compilation phase.

Tracing follows a fundamentally different approach. The source code is compiled without explicitly generating separate derivative functions. During execution on the GPU, derivatives are computed dynamically. Special data structures record operations and propagate derivative information via the chain rule, so each worker both evaluates the function and propagates its derivative at runtime.

Using SCT, derivative routines are embedded directly into the compiled program. Since NVIDIA GPU programming is typically performed in C++ variants (e.g., CUDA) compiled into GPU-specific assembly, transformation mechanisms can be integrated into the compilation pipeline. Compiler toolchains may be extended via preprocessors or plugins that support SCT, enabling derivative generation at compile time. This requires a suitable intermediate representation for symbolic manipulation. However, current tools (cf. Table I) are limited in scope and usually support only basic data types such as integers, floats, and doubles.

3.2.2. *Tracing on the GPU*

When tracing is used on the GPU, derivatives are computed during program execution, introducing computational overhead but offering greater flexibility. In particular, AD can be implemented with custom data types using C++ templates, making tracing-based approaches easily adaptable to intervals. A central challenge for tracing on GPUs is memory usage. Stack memory is limited but fast, whereas heap allocations reside in slower global memory. Since tracing often relies on dynamically allocated structures, it may lead to performance decrease. In this setting, forward mode is generally preferred, as it better fits the limited fast local memory of GPU threads.

These aspects become evident when porting AD libraries from the CPU to the GPU. The C++ library FADBAD++, originally designed for CPUs, offers a choice between stack and heap memory usage in forward mode, while the backwards mode and the Taylor coefficients computation rely solely on heap allocations. Although our GPU implementation of FADBAD++, available at `https://github.com/lorenzgillner/FADBAD-NG`, supports higher-order derivatives in principle, it is not optimized for GPU architectures. As a result, execution is slow and resource-intensive, particularly in heap mode (Auer et al., 2025a).

To address these limitations, we developed a GPU-optimized proof-of-concept implementation called TADA (available at `https://github.com/lorenzgillner/tada`). This approach follows a

generic design tailored to GPU execution. It currently supports first- and second-order derivatives, but not arbitrary orders. An additional advantage is its architectural flexibility: it runs on both CPUs and GPUs and works out of the box with interval data types.

AD on GPUs is currently limited in efficiency and scalability for higher-order derivatives, particularly when interval-valued data types are used. Consequently, in our LTE implementation, we do not employ AD for the involved tensors. The only use of AD in our framework is for the implementation of the MRK4 scheme in Eq. (11), where we utilize our GPU-based version of FADBAD++ in forward mode with a stack-based memory model.

4. Illustration: Van der Pol Equation

The ODE form of the Van der Pol equation (VDP) is given by

$$\left[\begin{array}{c} \dot{y}_1 = y_2 \\ \dot{y}_2 = -y_1 + \mu y_2 \left(1 - y_1^2\right) \end{array}\right] \tag{15}$$

It is a well-known example that describes a non-conservative oscillator with non-linear damping, which can become stiff for large values of μ. The system is neither cooperative nor competitive.

In this section, we illustrate possibilities available for set-based solving of IVPs on the GPU using the VDP example with $\mu = 1$. In Subsection 4.1, the options provided by monotone inclusions are highlighted and compared to a CPU-based verified solver DynIbex. In Subsection 4.2, a DynIbex-like implementation of RK4 along with MRK4 for VDP on the GPU is investigated. We conduct all GPU-related tests and simulations in this section using an Intel® Core™ i7-9700 CPU (3.00 GHz) and an NVIDIA GeForce GTX TITAN Black GPU, running on Ubuntu 22.04.5 LTS.

4.1. Monotone Inclusions for the Van der Pol Equation

Müller's theorem allows one to construct order-preserving bounding systems even when the original system is not monotonic (cf. Section 2.3). We can apply Müller's theorem to VDP as given by Eq. (15). Suppose $y_1 \in [\underline{y}_1, \overline{y}_1]$, $y_2 \in [\underline{y}_2, \overline{y}_2]$. The flow of VDP can be bounded by considering the following system:

$$\left[\begin{array}{c} \dot{\underline{y}}_1 = \underline{y}_2 \\ \dot{\overline{y}}_1 = \overline{y}_2 \\ \dot{\underline{y}}_2 = -\overline{y}_1 + \underline{y}_2 - \overline{P} \\ \dot{\overline{y}}_2 = -\underline{y}_1 + \overline{y}_2 - \underline{P} \end{array}\right] \tag{16}$$

where $[\underline{P}, \overline{P}] = [\min P, \max P]$ with $P = \{m\underline{y}_2, m\overline{y}_2, M\underline{y}_2, M\overline{y}_2\}$ and

$$M = \max(\underline{y}_1^2, \overline{y}_1^2), \quad m = \left\{\begin{array}{cc} 0, & 0 \in [\underline{y}_1, \overline{y}_1] \\ \min(\underline{y}_1^2, \overline{y}_1^2), & \text{otherwise} \end{array}\right. \tag{17}$$

A tighter construction is possible if we use the two-dimensional VDP form given by Liénard's theorem and find the bounding system for it. The Liénard's form is given below

$$\left[\begin{array}{c} \dot{y}_1 = y_1 - \frac{1}{3}y_1^3 - y_2 \\ \dot{y}_2 = y_1 \end{array}\right] , \tag{18}$$

with the bounding system given by

$$\left[\begin{array}{c} \dot{\underline{y}}_1 = -\overline{y}_2 + \min\left(\underline{y}_1 - \frac{1}{3}\underline{y}_1^3, \overline{y}_1 - \frac{1}{3}\overline{y}_1^3, -\frac{2}{3}\right) \\ \dot{\overline{y}}_1 = -\underline{y}_2 + \max\left(\underline{y}_1 - \frac{1}{3}\underline{y}_1^3, \overline{y}_1 - \frac{1}{3}\overline{y}_1^3, \frac{2}{3}\right) \\ \dot{\underline{y}}_2 = \underline{y}_1 \\ \dot{\overline{y}}_2 = \overline{y}_1 \end{array}\right] \tag{19}$$

because local extrema of $y_1 - \frac{1}{3}y_1^3$ occur at ± 1. Note that the notation above means that the value $-2/3$ is taken into account for the minimum only if $-1 \in [\underline{y}_1, \overline{y}_1]$, and, analogously, the value $2/3$ is considered for the maximum only if $1 \in [\underline{y}_1, \overline{y}_1]$. Furthermore, using the exact extrema of the right-hand side via min and max does not violate the assumptions of Müller's theorem. Indeed, the resulting right-hand side remains locally Lipschitz continuous, which guarantees that the solutions remain well defined and unique.

The simulation results for the VPD system, obtained by monotone inclusions using Thrust and a floating point IVP solver from the Boost library[2] as described in (Auer et al., 2025b), are shown in Figure 1. Only the state y_1 is displayed, as it represents the oscillator flow and is identical in both forms (15) and (18). For comparison, we also show the solution computed on the CPU using DynIbex relying on the verified Runge-Kutta method of order 4 (yellow line) with the VDP form in (18). The initial conditions are $y_1(0) \in [1.9, 2.1]$ and $y_2(0) = 0$ when using (15), and $y_2(0) = -2/3$ when using (18), ensuring that y_1 is the same in both forms. In all cases, the precision of 10^{-11} was used. The blue lines represent solutions obtained for sampled crisp initial conditions within the interval $[1.9, 2.1]$ using the same Boost IVP solver.

We observe that applying subdivision to the first initial condition on the GPU considerably reduces overestimation, particularly when the Liénard form as given by Eq. (19) is used (red line). In this respect, the CPU-based solution provided by DynIbex for the Liénard form in Eq. (18) also yields tight enclosures (yellow line). In contrast, when Müller's theorem is applied directly with interval arithmetic without subdivision, the enclosure grows rapidly, as illustrated by the black line. Even if used with subdivision, interval arithmetic alone does not provide very viable lower and upper bracketing systems (green and orange lines); cf. also Table II.

Note that we report the wall-clock time for DynIbex in Table II only as a reference, since it runs entirely on the CPU, in cases 4 and 5 without parallelization; therefore, a direct comparison of runtimes would not be meaningful. Nevertheless, the results show that the fully verified solver DynIbex performs substantially better for the VDP formulation in Eq. (18) than the approaches based on monotone inclusions with respect to the break-down time, that is, the time t after which the flow enclosure becomes too conservative. Increasing the number of subintervals in the subdivision

[2] the Dormand-Prince method of order 5 with adaptive step size (DP5)

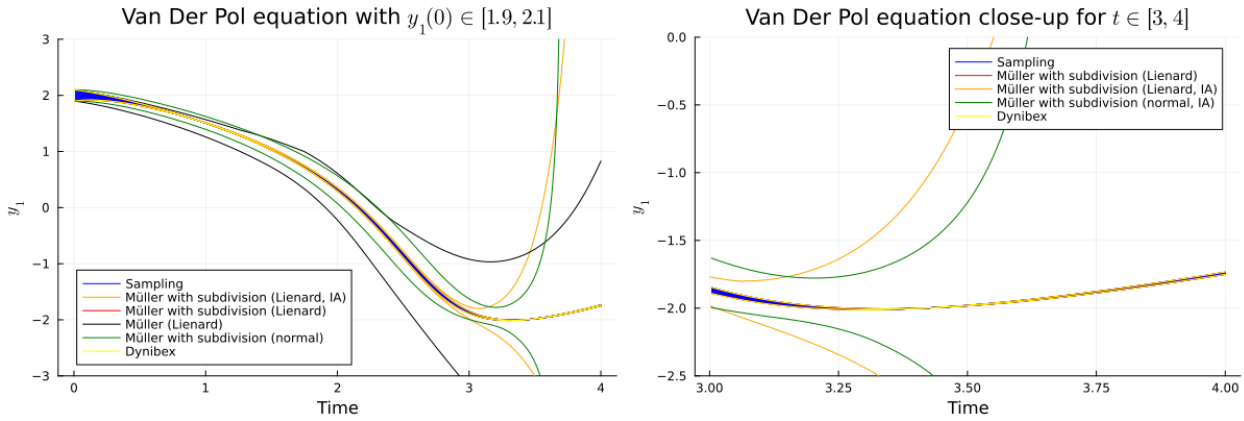


Figure 1. Different types of monotone inclusions for VDP on the GPU in comparison to DynIbex (CPU).

Table II. Subdivision on the GPU (2^{14} boxes) for different types of monotone inclusions for VDP in comparison to DynIbex on the CPU (adaptive step size for all).

		Variant	Kernel (GPU) or real (CPU) time in ms ($t \in [0, 3]$)	Break-down t	Break-down w($[y_1]$)
GPU	1	(19)	85	13.2	≈ 20
	2	(18) + IA for bracketing systems	78	3.79	≈ 13
	3	(15) + IA for bracketing systems	338	3.70	≈ 20
CPU	4	(18) + DynIbex	214,688	> 40	≈ 0.25
	4′	+ parallelization (16 boxes, 8 cores)	64,462	> 40	$\approx 10^{-5}$
	5	(15) + DynIbex	387,869	3.43	≈ 54
	5′	+ parallelization (16 boxes, 8 cores)	114,804	18.22	≈ 56

strategy on the GPU has only a limited effect since the initial uncertainty is relatively small. For example, considering variant 2 from Table II with 2^{20} boxes instead of 2^{14} reduces the width of $[y_1]$ in $t = 3$ from 0.22 to 0.05. However, this improvement comes at a significant computational cost, as the runtime increases to 1312 ms, which is mainly due to the specific block-thread structure of the employed GPU. This suggests that a well-designed verified implementation using techniques for enclosure tightening can outperform monotone inclusions for uncertainty propagation, especially if the system is not cooperative or competitive. This observation motivates our effort to develop such a verified solver for the GPU.

4.2. RK4 and MRK4 Algorithms for VDP

In this subsection, we apply the approach from Section 2.2 to the Liénard form of VDP in Eq. (18). For comparison with variant 5 in Table II, we also report results for the formulation in (15), cf. Table III. Due to the lack of efficient interval-based AD tools, verifying the IVP flow on the GPU currently requires external generation of derivative tensor code, in particular for third- and fourth-

order terms. The first derivative required for MRK4 is obtained via tracing on the GPU using our version of FADBAD++. We further employ the same uniform linear subdivision of the first initial condition as in the previous subsection.

For LTE computation, we consider three options. First, we use the hand-optimized formula in Eq. (9) together with manually precomputed tensors evaluated at runtime (OP1). The DAG of the LTE expression is optimized once since it remains unchanged. All tensors are stored in flat arrays on the GPU with local memory allocations, and common subexpressions are evaluated only once. The second option follows (Alexandre dit Sandretto, 2025) (OP2). Symbolic evaluation of Eq. (9), including tensors and their products, yields the following expression (pre-generated on the CPU) for the Liénard form of VDP:

$$
\begin{aligned}
LTE_{4,y_1} &= h^5 \Bigg(-\frac{y_1^2 \left(-\frac{y_1^3}{3} + y_1 - y_2\right)^3}{120} + \frac{y_1(1-y_1^2)\left(-y_1 + (1-y_1^2)\left(-\frac{y_1^3}{3} + y_1 - y_2\right)\right)\left(-\frac{y_1^3}{3} + y_1 - y_2\right)}{120} \\
&- \frac{y_1\left(-y_1 + (1-y_1^2)\left(-\frac{y_1^3}{3} + y_1 - y_2\right)\right)^2}{80} \\
&- \frac{y_1\left(-\frac{y_1^3}{3} + y_1 - y_2\right)\left(\frac{y_1^3}{3} - y_1 + y_2 + (1-y_1^2)\left(-y_1 + (1-y_1^2)\left(-\frac{y_1^3}{3} + y_1 - y_2\right)\right)\right)}{60} \\
&- \frac{(1-y_1^2)\left(-\frac{y_1^3}{3} + y_1 - y_2\right)^2\left(\frac{2y_1^3}{3} - 2y_1 + 2y_2\right)}{720} \\
&+ \frac{\left(2y_1 - 2(1-y_1^2)\left(-\frac{y_1^3}{3} + y_1 - y_2\right)\right)\left(-\frac{y_1^3}{3} + y_1 - y_2\right)^2}{480} \\
&+ \frac{\left(-2y_1(1-y_1^2)^2\left(-\frac{y_1^3}{3} + y_1 - y_2\right)^2 + 2y_1\left(-\frac{y_1^3}{3} + y_1 - y_2\right)^2\right)}{480} \\
&- \frac{1}{120}\Bigg[-\frac{y_1^3}{3} + y_1 - y_2 - (1-y_1^2)\left(-y_1 + (1-y_1^2)\left(-\frac{y_1^3}{3} + y_1 - y_2\right)\right) + (1-y_1^2)\Bigg(y_1 \\
&- (1-y_1^2)\left(-\frac{y_1^3}{3} + y_1 - y_2\right) + (1-y_1^2)\left(\frac{y_1^3}{3} - y_1 + y_2 + (1-y_1^2)\left(-y_1 + (1-y_1^2)\left(-\frac{y_1^3}{3} + y_1 - y_2\right)\right)\right)\Bigg)\Bigg]\Bigg) \\
LTE_{4,y_2} &= h^5 \Bigg(-\frac{h^5 y_1(1-y_1^2)\left(-\frac{y_1^3}{3} + y_1 - y_2\right)^2}{240} + \frac{h^5 y_1\left(-y_1 + (1-y_1^2)\left(-\frac{y_1^3}{3} + y_1 - y_2\right)\right)\left(-\frac{y_1^3}{3} + y_1 - y_2\right)}{120} \\
&- \frac{h^5\left(y_1 - (1-y_1^2)\left(-\frac{y_1^3}{3} + y_1 - y_2\right) + (1-y_1^2)\left(\frac{y_1^3}{3} - y_1 + y_2 + (1-y_1^2)\left(-y_1 + (1-y_1^2)\left(-\frac{y_1^3}{3} + y_1 - y_2\right)\right)\right)\right)}{120} \\
&- \frac{h^5\left(-\frac{y_1^3}{3} + y_1 - y_2\right)^2\left(\frac{2y_1^3}{3} - 2y_1 + 2y_2\right)}{720}\Bigg)
\end{aligned}
$$

The code generator from (Alexandre dit Sandretto, 2025) is not specifically optimized for RK4 and can produce LTE formulas for arbitrary Runge-Kutta methods and ODE models. Although

the generated LTE expressions are optimized via subexpression factorization, further manual reformulation with GPU-specific considerations can improve efficiency. In particular, restructuring the expressions to reuse common subexpressions, enhance memory coalescing, and enable fused operations can better exploit the GPU architecture and accelerate execution. The workflow of OP2 is more involved than OP1: code is first generated on the CPU and then manually transferred to the GPU. Its advantage is that no matrix–vector multiplications are required within the GPU kernel.

Option OP1 can be implemented more efficiently if the LTE expression is constructed using a compile-time expression template system[3] (OP3). VDP is represented as a function object, and symbolic operators such as the Jacobian are composed into expression trees at compile time. These trees encode repeated derivative applications without numerical evaluation during construction; computation is deferred to runtime, where the expressions are evaluated for a given state stored in a computational context object. At runtime, the evaluator traverses the tree and computes intermediate results using preallocated buffers, allowing for efficient GPU execution.

The results are presented in Table III and Figure 2. In contrast to monotone inclusions and DynIbex, both RK4 and MRK4 are evaluated with a fixed step size $h = 0.01$, which affects both enclosure quality and computational cost. Since OP1, OP2, and OP3 implement essentially the same formula and thus yield identical solution flows, only OP2 for Eq. (18) and OP1 for Eq. (15) are shown in the figure, while the table reports performance data for all options.

The naive RK4 implementation based on Eq. (10) is more susceptible to the wrapping effect than MRK4 in Eq. (11), but achieves lower runtimes. Both approaches yield weaker enclosure quality for Eq. (18) than the CPU-based DynIbex (cf. Table II), although they are significantly faster. Compared to the monotone inclusion methods in Table II (Variants 1 and 2), MRK4 provides tighter enclosures while remaining almost fully verified. The only non-verified component is the subdivision, which is currently non-overlapping and may contain gaps of up to 2 ULP.

Notably, improved enclosure quality is achieved even for the reduced number of subdivisions, as reflected in the last two columns of Table III as compared to Table II, which decreases kernel runtimes. For a fixed number of subdivisions, however, MRK4 is slower than the monotone inclusion methods, mainly due to the use of AD. Furthermore, the monotone approaches are implemented using Thrust, benefiting from optimized memory handling, whereas our RK4 and MRK4 implementations rely on a yet unoptimized CUDA design. OP1/OP3 produce slightly wider intervals than OP2 for both RK4 and MRK4. Since the fourth-order tensor for VDP is zero and not used, OP1 achieves slightly better computation times than OP2. In the case of OP3, the runtime of RK4 is reduced by approximately a factor of two compared to OP1, since no AD is applied. For MRK4, however, the performance gain is less pronounced, as FADBAD++ performs derivative computations at runtime.

5. Conclusions

As far as we know, this is the first implementation of a verified IVP solver for tight enclosure of ODE flows on a GPU. While its performance does not yet match that of established CPU-based approaches, particularly when additional subdivision is used on the CPU, it already yields

[3] The same is true for our FADBAD++ implementation for the GPU, but this is left for future work

Table III. Solving VPD using subdivision (2^{12} and 2^{14} boxes) on the GPU for RK4 and MRK4 with different implementation options (constant step size 0.01).

	Variant	Kernel time in ms ($t \in [0,3]$)		Break-down using 2^{12} boxes	
		2^{12}	2^{14}	t	$w([y_1])$
6	(18) + RK4 + OP1	22	71	4.92	≈ 14.6
6′	(18) + RK4 + OP2	27	90	4.92	≈ 14.3
6″	(18) + RK4 + OP3	12	35		same as OP1
7	(18) + MRK4 + OP1	56	166	16.78	≈ 9.95
7′	(18) + MRK4 + OP2	59	184	16.78	≈ 9.88
7″	(18) + MRK4 + OP3	45	142		same as OP1
8	(15) + MRK4 + OP1	54	166	10.12	≈ 3.92

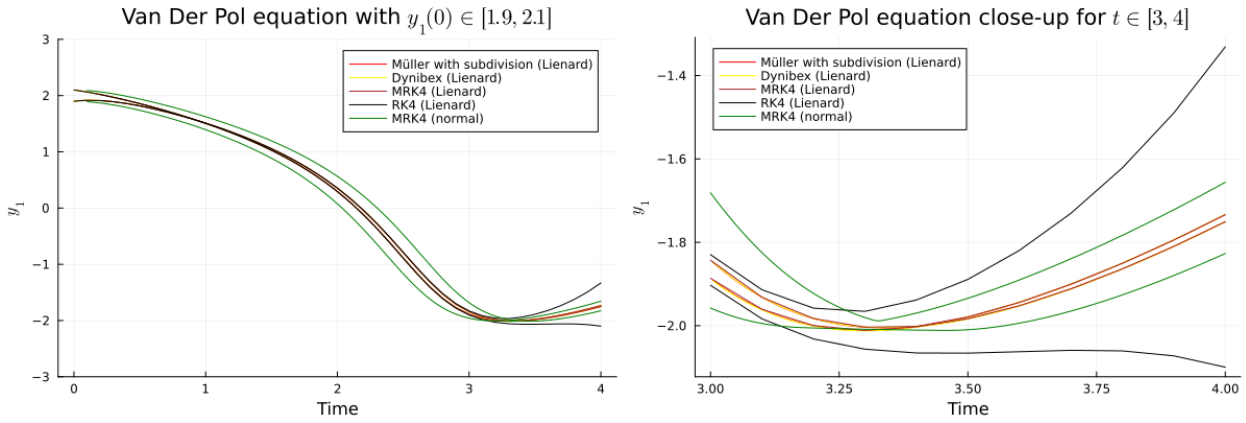


Figure 2. VDP in the Liénard form in Eq. (18) compared with VDP form in Eq. (15) on the GPU as well as DynIbex (CPU) and monotone inclusions (GPU, variant 1 from Table II)

significantly improved enclosure quality for the Liénard form of the Van der Pol oscillator compared to purely a priori enclosure techniques. Moreover, all variants of our MRK4 implementation produce tighter enclosures than monotone inclusion methods while requiring fewer subdivisions, thereby also reducing runtime.

Future work will include more extensive numerical testing, as well as a more efficient workflow for automatic differentiation to compute higher-order derivative tensors (up to order four) within a unified GPU framework. In addition, implementing interval-aware automatic differentiation at compile time appears promising for further reducing computational cost. Finally, improved subdivision strategies remain an important direction for future research.

References

Alexandre dit Sandretto, J.: 2025, 'Symbolic-Numeric Pipeline for Reachability Analysis of Differential Equations with B-Series'. *ACM Communications in Computer Algebra* **59**(3), 57–63. Publisher Copyright: © 2025 Copyright is held by the owner/author(s).

Alexandre dit Sandretto, J. and A. Chapoutot: 2016, 'Validated Explicit and Implicit Runge–Kutta Methods'. *Reliable Computing* **22**(1), 79–103.

Auer, E., A. Ahrens, and L. Gillner: 2025a, 'GPU-Based Interval Optimization in the Context of Optical MIMO Systems'. In: R. Wyrzykowski, J. Dongarra, E. Deelman, and K. Karczewski (eds.): *Parallel Processing and Applied Mathematics*. Cham, pp. 360–374, Springer Nature Switzerland.

Auer, E., S. Kiel, and A. Rauh: 2017, 'Towards a Verified ODE Solver for GPU-Based Parameter Identification'. In: *Proceedings of ICOSSAR 2017*. pp. 2039–2049, CRC Press / Taylor & Francis.

Auer, E., A. Rauh, and L. Gillner: 2025b, 'Parameter Identification for Cooperative SOFC Models on the GPU'. In: T. N. Dinh, A. Rauh, S. Z. Yong, and Z. Wang (eds.): *Set-Valued Approaches to Control and Estimation of Uncertain Systems*, Mathematical Engineering. Springer Cham, pp. 211–238.

Bendsten, C. and O. Stauning: 1996, 'FADBAD, a flexible C++ package for automatic differentiation using the forward and backward methods'. Technical Report 1996-x5-94, Technical University of Denmark, Lyngby.

Boost C++ Libraries: 2026, 'Boost Interval Arithmetic Library'. `https://www.boost.org/doc/libs/release/libs/numeric/interval/doc/interval.htm`. Accessed: 2026-04-29.

Butcher, J. C.: 2021, *B-series and Runge–Kutta methods*, pp. 177–209. Cham: Springer International Publishing.

Collange, C., M. Daumas, and D. Defour: 2011, 'Interval Arithmetic in CUDA'. In: W. mei W. Hwu (ed.): *GPU Computing Gems Jade Edition*, No. 978-0-12-385963-1. Morgan Kaufmann, pp. 99–107.

Griewank, A. and A. Walther: 2000, 'Evaluating derivatives - principles and techniques of algorithmic differentiation, Second Edition'. In: *Frontiers in applied mathematics*.

Hascoet, L. and V. Pascual: 2013, 'The Tapenade automatic differentiation tool: principles, model, and specification'. *ACM Transactions on Mathematical Software (TOMS)* **39**(3), 1–43.

Hirsch, W. M. and H. L. Smith: 2005, *Monotone Dynamical Systems*, Vol. 2, Chapt. 4 of Ordinary Differential Equations, pp. 239–357. Elsevier.

Ifrim, I., V. Vassilev, and D. J. Lange: 2023, 'GPU Accelerated Automatic Differentiation With Clad'. *Journal of Physics: Conference Series* **2438**(1), 012043.

Meslem, N. and N. Ramdani: 2011, 'Interval observer design based on nonlinear hybridization and practical stability analysis'. *International Journal of Adaptive Control and Signal Processing* **25**(3), 228–248.

Moses, W. S., S. H. K. Narayanan, L. Paehler, V. Churavy, M. Schanen, J. Hückelheim, J. Doerfert, and P. Hovland: 2022, 'Scalable Automatic Differentiation of Multiple Parallel Paradigms through Compiler Augmentation'. In: *Proceedings of the International Conference on High Performance Computing, Networking, Storage and Analysis*. IEEE Press.

Mullier, O., A. Chapoutot, and J. A. dit Sandretto: 2018, 'Validated computation of the local truncation error of Runge–Kutta methods with automatic differentiation'. *Optimization Methods and Software* **33**(4-6), 718–728.

Nedialkov, N. S., K. Jackson, and G. Corliss: 1999, 'Validated solutions of initial value problems for ordinary differential equations'. *Appl. Math. and Comp.* **105**(1), 21 – 68.

NVIDIA: 2026, 'CUDA Toolkit Documentation: CUDA C++ Programming Guide'. `https://docs.nvidia.com/cuda/`. Accessed: 2026-04-29.

Rump, S. M.: 2026, 'INTLAB — Interval Laboratory, Version 11'. `http://www.ti3.tu-harburg.de/rump/intlab/`. Accessed: 2026-04-29.

Sanders, D. P.: 2022, 'Global optimization and interval constraint programming using Julia: Symbolics, code generation, GPU'.

Utke, J., U. Naumann, M. Fagan, N. Tallent, M. Strout, P. Heimbach, C. Hill, and C. Wunsch: 2008, 'OpenAD/F: A modular open-source tool for automatic differentiation of Fortran codes'. *ACM Transactions on Mathematical Software (TOMS)* **34**(4), 1–36.

Efficient Probabilistic Response Analysis of Large-Scale Engineering Structures under Stochastic Excitation via the DR-PDEE Incorporating an Auxiliary Diffusion Process

Tingting Sun[1)] and Jianbing Chen[2)]
[1)] *State key laboratory of disaster reduction in Civil Engineering and College of Civil Engineering, Tongji University, Shanghai 200092, China; suntingting@tongji.edu.cn;*
[2)] *State key laboratory of disaster reduction in Civil Engineering and College of Civil Engineering, Tongji University, Shanghai 200092, China; chenjb@tongji.edu.cn*

Abstract. Probabilistic response analysis of engineering structures under stochastic excitation remains a critical and long-standing challenge. The main difficulties arise from the high dimensionality of structural systems, nonlinear material behavior, and uncertainties in both system parameters and external excitations. To address these challenges, an efficient framework is developed based on the dimension-reduced probability density evolution equation (DR-PDEE) incorporating an auxiliary diffusion process. The DR-PDEE is a low-dimensional partial differential equation (PDE) governing the instantaneous probability density function (PDF) of a path-continuous response of interest in a high-dimensional dynamical system. However, under non-white stochastic excitation, the intrinsic diffusion function of the response generally vanishes. This zero-diffusion issue complicates the numerical solution of the DR-PDEE. To overcome this difficulty, white noise statistically correlated with the original non-white excitation is constructed and applied to a simple stochastic system. The system output is then selected as the auxiliary diffusion process. Consequently, a two-dimensional DR-PDEE with nonzero diffusion is formulated for the joint process of the response of interest and the auxiliary variable. This formulation avoids the construction of an equivalent linear filter and provides high flexibility for complex non-white excitations. The proposed method is applied to a high-rise reinforced concrete (RC) frame-core tube structure subjected to stochastic near-field seismic excitation. Nonlinear constitutive behavior of both reinforcing steel and concrete is considered, together with uncertainties in the concrete material properties. The proposed method accurately captures the pronounced nonstationary and non-Gaussian features of the response PDFs. The results demonstrate its applicability and efficiency for probabilistic response analysis of large-scale nonlinear structures under complex non-white stochastic excitations.

Keywords: Nonlinear engineering structure, Non-white excitation, Stochastic response analysis, DR-PDEE, Auxiliary diffusion process.

1. Introduction

Engineering structures are frequently subjected to environmental dynamic actions with inherent randomness. In particular, these dynamic actions, such as seismic ground motions, turbulent winds,

© 2026 by the author(s). This work is licensed under the Creative Commons Attribution 4.0 International License (CC BY 4.0), which permits unrestricted use, distribution, and reproduction in any medium, provided the original author and source are credited.

and ocean waves, often exhibit pronounced non-white and non-stationary characteristics (Rezaeian and Der Kiureghian, 2008; Li and Chen, 2009). Meanwhile, uncertainties in structural properties, such as material parameters, may significantly affect structural responses (Schuëller, 2007). Probabilistic response analysis is therefore essential for quantifying structural responses under stochastic excitation.

Despite extensive efforts, probabilistic response analysis of high-dimensional nonlinear engineering systems remains highly challenging. Simulation-based methods, such as Monte Carlo simulation (MCS), require numerous deterministic analyses and may become computationally prohibitive (Li and Wang, 2023). Even with advanced sampling strategies and surrogate models, these methods remain costly for large-scale engineering structures, as a single nonlinear time-history analysis may require substantial computational resources and be highly time-consuming (Moustapha et al., 2022). Another class of methods directly solves equations governing the evolution of response probability density functions (PDFs), such as the Fokker–Planck–Kolmogorov (FPK) equation (Gardiner, 1985). However, the classical FPK equation generally applies to Markov systems driven by white-noise excitation and typically becomes high-dimensional for engineering structures (Gardiner, 1985). Similar dimensionality issues arise in other classical PDF evolution equations, such as the Liouville equation (Soong, 1973) and the Dostupov–Pugachev equation (Dostupov and Pugachev, 1957). Analytical solutions to these equations are rarely available (Zhu et al., 1990), while their direct numerical solution is generally impractical for large-scale systems. Approximate methods, including stochastic linearization (Roberts and Spanos, 1990) and moment-closure techniques (Zhang et al., 2020), may lose accuracy for strongly nonlinear systems. The dimensionality problem therefore remains a central obstacle in stochastic analysis of nonlinear engineering structures.

Further, the non-white and non-stationary nature of stochastic excitations makes the stochastic response analysis more challenging. For example, applying the FPK equation to systems under non-white excitation generally requires filters to represent the excitation, which augment the system state and increase the equation dimensionality. Stochastic averaging can also be applied to certain non-white excitation problems, but it generally relies on restrictive assumptions regarding system damping and excitation bandwidth (Roberts and Spanos, 1986).

Moreover, simultaneous consideration of stochastic excitation and uncertain system parameters complicates the analysis. Such problems are commonly reformulated as stochastic structural analyses. One approach is to represent the stochastic excitation using a finite set of random variables. Alternatively, the conditional random vibration problem is first solved for fixed system parameters, and the parameter uncertainty is then propagated through the resulting conditional solutions. For high-dimensional nonlinear systems, however, both approaches generally lead to higher-dimensional or more complex stochastic analyses.

In this regard, the dimension-reduced probability density evolution equation (DR-PDEE) provides an efficient alternative for stochastic response analysis of high-dimensional nonlinear systems (Lyu and Chen, 2022). It governs the PDF of general path-continuous response processes and does not require these processes to be Markovian (Lyu and Chen, 2022; Luo et al., 2022b). Therefore, a low-dimensional DR-PDEE can be established for the path-continuous response process of interest, irrespective of the dimension of the original structural system and whether the system parameters are deterministic or random (Chen and Lyu, 2022).

The DR-PDEE also applies to structural responses under non-white excitation. However, when the non-white excitation has no singular component in its autocorrelation function, the intrinsic diffusion coefficient of the structural response vanishes. This results in a Liouville-type equation and complicates the numerical solution. Previous studies addressed this issue by representing the non-white excitation using a linear filter driven by white noise (Lyu and Chen, 2022; Chen et al., 2024; Luo et al., 2022a). The two-dimensional DR-PDEE was then formulated for the joint process consisting of the response of interest and one filter output. However, constructing such filters can be difficult, particularly for complex excitations without rational power spectral density (PSD) functions or with fully non-stationary characteristics (Luo et al., 2022b; Chen et al., 2024).

To overcome this limitation, this study introduces an auxiliary diffusion process method that avoids filter construction. The approach first constructs a white-noise process statistically correlated with the non-white excitation and uses it to drive a simple low-dimensional stochastic system. The resulting output serves as the auxiliary diffusion process. By combining the structural response of interest with this auxiliary process, a two-dimensional DR-PDEE can be established, and a non-zero diffusion term is retained in the equation. The response PDF can therefore be obtained without constructing an equivalent linear filter. To demonstrate the applicability of the proposed method to large-scale engineering structures, a reinforced concrete (RC) frame–core tube structure subjected to stochastic near-field pulse-type ground motions is investigated. Its probabilistic responses are obtained using the proposed method.

The remainder of this paper is organized as follows. The proposed DR-PDEE method incorporating an auxiliary diffusion process and its numerical procedure are introduced in Section 2. An application of the method to the stochastic response analysis of a high-rise RC structure under stochastic seismic excitation is presented in Section 3. Finally, concluding remarks are provided in Section 4.

2. DR-PDEE-based stochastic response analysis by incorporating an auxiliary diffusion process

2.1. Problem statement

Generally, engineering structures subjected to stochastic excitation can be modeled as multi-degree-of-freedom (MDOF) systems after spatial discretization by the finite element method (FEM). Therefore, an n-degree-of-freedom (n-DOF) structural system is considered here. Its equation of motion reads

$$\boldsymbol{M}(\boldsymbol{\Theta})\ddot{\boldsymbol{X}}(t)+\boldsymbol{C}\left(\boldsymbol{X}(t),\dot{\boldsymbol{X}}(t),t;\boldsymbol{\Theta}\right)\dot{\boldsymbol{X}}(t)+\boldsymbol{f}\left(\boldsymbol{X}(t),\dot{\boldsymbol{X}}(t),t;\boldsymbol{\Theta}\right)=\boldsymbol{L}\boldsymbol{\xi}(t), \tag{1}$$

where $\boldsymbol{X}(t)$, $\dot{\boldsymbol{X}}(t)$, and $\ddot{\boldsymbol{X}}(t)\in\mathbb{R}^n$ denote the displacement, velocity, and acceleration vectors, respectively. The matrix $\boldsymbol{M}\in\mathbb{R}^{n\times n}$ denotes the mass matrix, while $\boldsymbol{C}\in\mathbb{R}^{n\times n}$ denotes the damping matrix. The vector $\boldsymbol{f}\in\mathbb{R}^n$ represents the nonlinear restoring force. The stochastic excitation is denoted by $\boldsymbol{\xi}(t)\in\mathbb{R}^r$, and $\boldsymbol{L}\in\mathbb{R}^{n\times r}$ is the corresponding load-location matrix. The random vector $\boldsymbol{\Theta}\in\mathbb{R}^s$ characterizes uncertainty in the structural parameters. Consequently, $\boldsymbol{M}$, $\boldsymbol{C}$, and $\boldsymbol{f}$ may depend on $\boldsymbol{\Theta}$. In this study, $\boldsymbol{\xi}(t)$ is considered to be a non-white stochastic process.

Denote $\dot{\boldsymbol{X}}(t)$ by $\boldsymbol{V}(t)$. The state vector is introduced as $\boldsymbol{Z}(t) = \left(\boldsymbol{X}^{\top}(t), \boldsymbol{V}^{\top}(t)\right)^{\top} \in \mathbb{R}^m$, where $m = 2n$. For simplicity, the mass matrix $\boldsymbol{M}$ is assumed to be deterministic. Eq. (1) can then be rewritten in the state-space form as

$$\mathrm{d}\boldsymbol{Z}(t) = \boldsymbol{a}(\boldsymbol{Z}(t), t; \boldsymbol{\Theta})\,\mathrm{d}t + \boldsymbol{B}\boldsymbol{\xi}(t)\,\mathrm{d}t, \tag{2}$$

where

$$\boldsymbol{a}(\boldsymbol{Z}(t), t; \boldsymbol{\Theta}) = \begin{pmatrix} \boldsymbol{V}(t) \\ -\boldsymbol{M}^{-1}\left[\boldsymbol{C}(\boldsymbol{X}(t), \boldsymbol{V}(t), t; \boldsymbol{\Theta})\,\boldsymbol{V}(t) + \boldsymbol{f}(\boldsymbol{X}(t), \boldsymbol{V}(t), t; \boldsymbol{\Theta})\right] \end{pmatrix}, \tag{3}$$

and

$$\boldsymbol{B} = \begin{bmatrix} \boldsymbol{0}_{n\times r} \\ \boldsymbol{M}^{-1}\boldsymbol{L} \end{bmatrix}. \tag{4}$$

Here, $\boldsymbol{0}n \times r$ denotes the $n \times r$ zero matrix. Only additive excitation is considered in this study; namely, $\boldsymbol{L}$ is independent of $\boldsymbol{X}(t)$ and $\dot{\boldsymbol{X}}(t)$. Therefore, different interpretations of stochastic integration with respect to $\boldsymbol{\xi}(t)$ need not be distinguished (Gardiner, 1985).

Accurate assessment of structural safety requires reliable estimation of the instantaneous PDFs of system responses. This is the main objective of this study.

2.2. DR-PDEE for the response of interest and the zero-diffusion issue

Determining the probabilistic response of the nonlinear system governed by Eq. (2) is challenging, particularly when the instantaneous PDF of a response of interest is required. The difficulty becomes especially severe for systems with a large number of DOFs n or a high-dimensional state space of dimension m. Nevertheless, the DR-PDEE provides an efficient tool for addressing this problem. In this subsection, the DR-PDEE for a general path-continuous process is first introduced, followed by its formulation for a response component of the state vector of Eq. (2). The zero-diffusion issue arising from non-white excitation is then discussed.

2.2.1. *DR-PDEE for general path-continuous processes*

First, consider a one-dimensional stochastic process, denoted by $Y(t) \in \mathbb{R}$. Assume that $Y(t)$ satisfies the Dynkin–Kinney condition (Dynkin, 1952; Kinney, 1953); namely, for any $\varepsilon > 0$,

$$\lim_{\Delta t \to 0} \frac{1}{\Delta t} \int_{|z-y|>\varepsilon} p_Y(z, t+\Delta t \mid y, t)\,\mathrm{d}z = 0 \tag{5}$$

holds uniformly for all y and t. The Dynkin–Kinney condition, also known as the path-continuity condition (Seregin, 1961), implies that the sample paths of $Y(t)$ are continuous in t with probability one.

According to Ref. (Lyu and Chen, 2022), the instantaneous PDF of $Y(t)$ satisfying the Dynkin–Kinney condition is governed by

$$\frac{\partial p_Y(y,t)}{\partial t} = -\frac{\partial a_Y^{\mathrm{int}}(y,t)\,p_Y(y,t)}{\partial y} + \frac{1}{2}\frac{\partial^2 b_Y^{\mathrm{int}}(y,t)\,p_Y(y,t)}{\partial y^2}. \tag{6}$$

Eq. (6) is referred to as the dimension-reduced probability density evolution equation (DR-PDEE) for the path-continuous stochastic process $Y(t)$. Here, $a_Y^{\text{int}}(y,t)$ and $b_Y^{\text{int}}(y,t)$ denote the intrinsic drift and diffusion functions of $Y(t)$, respectively. They are defined as the first- and second-order conditional derivate moments of $Y(t)$ (Lyu and Chen, 2022; Gardiner, 1985):

$$\begin{cases} a_Y^{\text{int}}(y,t) = \lim\limits_{\Delta t\to 0}\dfrac{1}{\Delta t}\mathbb{E}\left(Y(t+\Delta t)-Y(t)\middle|\, Y(t)=y\right), \\ b_Y^{\text{int}}(y,t) = \lim\limits_{\Delta t\to 0}\dfrac{1}{\Delta t}\mathbb{E}\left\{\left[Y(t+\Delta t)-Y(t)\right]^2\middle|\, Y(t)=y\right\}. \end{cases} \tag{7}$$

In Eq. (7), $\mathbb{E}$ denotes mathematical expectation.

The DR-PDEE for the multidimensional case takes a similar form. Consider a d-dimensional stochastic process $\boldsymbol{Y}(t)\in\mathbb{R}^d$. Assume that $\boldsymbol{Y}$ also satisfies the Dynkin–Kinney condition (Dynkin, 1952; Kinney, 1953). Specifically, for any $\varepsilon>0$,

$$\lim_{\Delta t\to 0}\frac{1}{\Delta t}\int_{\|\boldsymbol{z}-\boldsymbol{y}\|>\varepsilon} p_{\boldsymbol{Y}}(\boldsymbol{z},t+\Delta t\mid \boldsymbol{y},t)\,\mathrm{d}\boldsymbol{z}=0 \tag{8}$$

holds uniformly for all $\boldsymbol{y}$ and t, where $\|\cdot\|$ denotes the Euclidean norm. Under this condition, the instantaneous PDF of $\boldsymbol{Y}(t)$, denoted by $p_{\boldsymbol{Y}}(\boldsymbol{y},t)$, is governed by the following DR-PDEE (Lyu and Chen, 2022):

$$\frac{\partial p_{\boldsymbol{Y}}(\boldsymbol{y},t)}{\partial t} = -\sum_{i=1}^{d}\frac{\partial a_{\boldsymbol{Y},i}^{\text{int}}(\boldsymbol{y},t)\,p_{\boldsymbol{Y}}(\boldsymbol{y},t)}{\partial y_i} + \frac{1}{2}\sum_{i=1}^{d}\sum_{j=1}^{d}\frac{\partial^2 b_{\boldsymbol{Y},ij}^{\text{int}}(\boldsymbol{y},t)\,p_{\boldsymbol{Y}}(\boldsymbol{y},t)}{\partial y_i\partial y_j}, \tag{9}$$

where

$$\begin{cases} a_{\boldsymbol{Y},i}^{\text{int}}(\boldsymbol{y},t) = \lim\limits_{\Delta t\to 0}\dfrac{1}{\Delta t}\mathbb{E}\left(Y_i(t+\Delta t)-Y_i(t)\middle|\,\boldsymbol{Y}(t)=\boldsymbol{y}\right), \\ b_{\boldsymbol{Y},ij}^{\text{int}}(\boldsymbol{y},t) = \lim\limits_{\Delta t\to 0}\dfrac{1}{\Delta t}\mathbb{E}\left\{\left[Y_i(t+\Delta t)-Y_i(t)\right]\left[Y_j(t+\Delta t)-Y_j(t)\right]\middle|\,\boldsymbol{Y}(t)=\boldsymbol{y}\right\}. \end{cases} \tag{10}$$

Note that the DR-PDEEs in Eqs. (6) and (9) do not require $Y(t)$ and $\boldsymbol{Y}(t)$, respectively, to be Markovian (Lyu and Chen, 2022; Chen and Lyu, 2022; Luo et al., 2022b).

2.2.2. *DR-PDEE for path-continuous response processes under non-white excitation*

Next, consider the state response process governed by Eq. (2). Since the DR-PDEE applies to general path-continuous processes regardless of whether they are Markovian, a low-dimensional DR-PDEE can be established for any response component of interest.

For example, let the ℓ-th component of $\boldsymbol{Z}(t)$ in Eq. (2) be the response of interest, denoted by $Z_\ell(t)$. By setting $Y(t)=Z_\ell(t)$, the corresponding one-dimensional DR-PDEE governing its PDF $p_{Z_\ell}(z_\ell,t)$ takes the form of Eq. (6). The intrinsic drift and diffusion functions of $Z_\ell(t)$ are examined below. According to Eq. (2), the increment of $Z_\ell(t)$ over a small time interval Δt is expressed as

$$\Delta Z_\ell(t) = Z_\ell(t+\Delta t)-Z_\ell(t) = \int_t^{t+\Delta t} a_\ell\left(\boldsymbol{Z}(\tau),\tau;\boldsymbol{\Theta}\right)\mathrm{d}\tau + \int_t^{t+\Delta t}\left[\boldsymbol{B}\boldsymbol{\xi}(\tau)\right]_\ell\mathrm{d}\tau. \tag{11}$$

Further, define the integral process of the non-white excitation $\boldsymbol{\xi}(t)$ as $\boldsymbol{\Xi}(t) = \int_0^t \boldsymbol{\xi}(\tau)\,\mathrm{d}\tau$. Assume that $\boldsymbol{\Xi}(t)$ is mean-square continuous. This assumption is satisfied when the autocorrelation function of $\boldsymbol{\xi}(t)$, denoted by $\boldsymbol{R}_{\boldsymbol{\xi}}(t_1,t_2) = \mathbb{E}\left(\boldsymbol{\xi}(t_1)\boldsymbol{\xi}^{\top}(t_2)\right)$, contains no Dirac-$\delta$-type singularity at $t_1 = t_2$, unlike that of white noise. This condition is generally satisfied by physical random excitations. For example, wind loads, ocean waves, and realistic earthquake ground motions are non-white processes with finite mean-square values, and their autocorrelation functions contain no such Dirac-δ-type singularity. Therefore, the integral processes of these excitations are generally mean-square continuous.

Under this condition, substituting Eq. (11) into the definitions of the intrinsic drift and diffusion functions yields (Lyu, 2022)

$$\begin{cases} a_{Z_\ell}^{\mathrm{int}}(z_\ell,t) = \lim\limits_{\Delta t\to 0}\dfrac{1}{\Delta t}\mathbb{E}\left(\Delta Z_\ell(t)\middle|\, Z_\ell(t)=z_\ell\right) = \mathbb{E}\left(a_\ell\left(\boldsymbol{Z}(t),t;\boldsymbol{\Theta}\right) + \left[\boldsymbol{B}\boldsymbol{\xi}(t)\right]_\ell\middle|\, Z_\ell(t)=z_\ell\right), \\ b_{Z_\ell}^{\mathrm{int}}(z_\ell,t) = \lim\limits_{\Delta t\to 0}\dfrac{1}{\Delta t}\mathbb{E}\left\{\left[\Delta Z_\ell(t)\right]^2\middle|\, Z_\ell(t)=z_\ell\right\} = 0. \end{cases} \tag{12}$$

It follows that the intrinsic diffusion function degenerates to zero when $\left[\boldsymbol{B}\boldsymbol{R}_{\boldsymbol{\xi}}(t_1,t_2)\boldsymbol{B}^{\top}\right]_{\ell\ell}$ contains no Dirac-δ-type singularity at $t_1 = t_2$. In this case, the excitation-induced response increment is of order Δt, and its second-order conditional moment is therefore of order $(\Delta t)^2$. Dividing this moment by Δt and taking the limit as $\Delta t \to 0$ consequently gives zero. Accordingly, the DR-PDEE for $Z_\ell(t)$ reduces to the following Liouville-type PDE:

$$\frac{\partial p_{Z_\ell}(z_\ell,t)}{\partial t} = -\frac{\partial a_{Z_\ell}^{\mathrm{int}}(z_\ell,t)\,p_{Z_\ell}(z_\ell,t)}{\partial z_\ell}. \tag{13}$$

In principle, Eq. (13) can still be solved numerically. However, the tails of the resulting PDF are sensitive to the diffusion term (Lyu, 2022). When the intrinsic diffusion function vanishes, the numerical solution may be less robust than that of an equation with nonzero diffusion. This issue is particularly evident when the DR-PDEE is solved using the path integral solution (PIS) technique, because the zero diffusion term makes construction of the short-time transition PDF less straightforward (Yu et al., 1997). Similar difficulties may also arise in other numerical schemes. Therefore, a key objective of this study is to formulate a low-dimensional DR-PDEE with a nonzero intrinsic diffusion function. The auxiliary diffusion process introduced in the next subsection is constructed for this purpose.

2.3. The DR-PDEE for the state response of interest incorporating an auxiliary diffusion process

2.3.1. *Constructing white noise correlated with the non-white excitation*

The auxiliary diffusion process is introduced to retain a nonzero intrinsic diffusion function. In previous studies, a possible approach is to represent the non-white excitation $\boldsymbol{\xi}(t)$ using a linear filter driven by white noise. The filter parameters are selected such that its output reproduces the statistical properties of $\boldsymbol{\xi}(t)$ (Luo et al., 2022b; Chen et al., 2024). However, this approach becomes difficult to apply to excitations with irrational PSDs or fully non-stationary characteristics, both of which are commonly encountered in practical engineering problems.

A more flexible method is developed based on the spectral representation of the non-white excitation. The desired white noise is then constructed by modifying the spectral amplitudes while retaining the same random phases. For simplicity, a one-dimensional non-white excitation $\xi_{\mathrm{nw}}(t)$ is considered first. It can be represented using the classical spectral representation (Shinozuka, 1971) method as

$$\xi_{\mathrm{nw}}(t) \approx \sum_{i=1}^{N} A_i \cos(\omega_i t + \Phi_i), \tag{14}$$

where $\{\Phi_i\}_{i=1}^{N}$ are independent random phase angles uniformly distributed over $[0, 2\pi]$. For a stationary excitation, the spectral amplitude is given by (Shinozuka, 1971)

$$A_i(\omega) = \sqrt{\frac{2S_{\mathrm{nw}}(\omega_i)\,\Delta\omega_i}{\pi}}, \tag{15}$$

where $S_{\mathrm{nw}}(\omega)$ denotes the PSD of $\xi_{\mathrm{nw}}(t)$.

The key idea here is to retain the same random phase angles $\{\Phi_i\}_{i=1}^{N}$ while replacing the spectral amplitudes $A_i(\omega)$ or $A_i(\omega, t)$ with those corresponding to a constant white-noise spectrum. In this way, an approximate white noise process, denoted by $\xi_{\mathrm{w}}(t)$, can be constructed as

$$\xi_{\mathrm{w}}(t) \approx \sum_{i=1}^{N} \sqrt{\frac{2D_0\Delta\omega_i}{\pi}} \cos(\omega_i t + \Phi_i), \tag{16}$$

where D_0 denotes the intensity of the white noise $\xi_{\mathrm{w}}(t)$. Because Eqs. (14) and (16) share the same random phase angles, the constructed white noise is statistically correlated with the original non-white excitation.

The above spectral representations are discrete approximations. In a formal continuous form, the non-white excitation can be expressed through the white noise by

$$\xi_{\mathrm{nw}}(t) = \mathcal{F}^{-1}\left[\sqrt{\frac{S_{\mathrm{nw}}(\omega)}{D_0}}\mathcal{F}(\xi_{\mathrm{w}}(t))\right], \tag{17}$$

where $\mathcal{F}$ denotes the Fourier transform. In the classical sense, the Fourier transform is defined for absolutely integrable functions, whereas white noise does not possess a classical Fourier transform. Therefore, Eq. (17) should be interpreted in the generalized-function sense, under which the symbolic operation remains consistent with its classical counterpart.

Since $\xi_{\mathrm{nw}}(t)$ and $\xi_{\mathrm{w}}(t)$ share the same random phases, they are correlated. For stationary cases, their cross-correlation function is

$$\mathbb{E}[\xi_{\mathrm{nw}}(t_1)\,\xi_{\mathrm{w}}(t_2)] = \frac{1}{\pi}\int_0^{\infty} \sqrt{S_{\mathrm{nw}}(\omega)\,D_0}\cos(\omega(t_1 - t_2))\,\mathrm{d}\omega. \tag{18}$$

For a non-stationary excitation characterized by the evolutionary PSD $S_{\mathrm{nw}}(\omega, t)$, the above representation retains the same form, whereas the spectral amplitude becomes time-dependent as (Liang et al., 2007)

$$A_i(\omega, t) = \sqrt{\frac{2S_{\mathrm{nw}}(\omega_i, t)\,\Delta\omega_i}{\pi}}. \tag{19}$$

2.3.2. *Constructing the auxiliary diffusion process from the correlated white noise*
Next, the constructed white noise $\xi_{\mathrm{w}}(t)$ is taken as the input to a simple stochastic system, yielding the Itô stochastic differential equation (SDE) governing the auxiliary diffusion process:

$$\mathrm{d}\boldsymbol{U}(t) = -\boldsymbol{\alpha}(\boldsymbol{U}(t))\,\mathrm{d}t + \boldsymbol{\beta}\mathrm{d}W_0(t), \tag{20}$$

where $\boldsymbol{U}(t), \boldsymbol{\alpha}, \boldsymbol{\beta} \in \mathbb{R}^{n_U}$, and $W_0(t) = \int_0^t \xi_{\mathrm{w}}(\tau)\,\mathrm{d}\tau$. As long as $\boldsymbol{\beta}$ is not identically zero, at least one component of $\boldsymbol{U}(t)$ is a diffusion process with a nonzero intrinsic diffusion function. This component can therefore be selected as the desired auxiliary diffusion process.

2.3.3. *DR-PDEE for the response of interest combined with the auxiliary diffusion process*
Further, the original state equation in Eq. (2) is combined with Eq. (20), together with the transformation between the white noise $\xi_{\mathrm{w}}(t)$ and non-white excitations $\xi_{\mathrm{nw}}(t)$. The resulting augmented system is

$$\begin{cases} \mathrm{d}\boldsymbol{Z}(t) = \boldsymbol{a}(\boldsymbol{Z}(t), t; \boldsymbol{\Theta})\,\mathrm{d}t + \boldsymbol{B}\xi_{\mathrm{nw}}(t)\,\mathrm{d}t, \\ \xi_{\mathrm{nw}}(t) = \mathcal{G}(\xi_{\mathrm{w}}(t)) \\ \mathrm{d}\boldsymbol{U}(t) = -\boldsymbol{\alpha}(\boldsymbol{U}(t))\,\mathrm{d}t + \boldsymbol{\beta}\mathrm{d}W_0(t). \end{cases} \tag{21}$$

In Eq. (21), the operator $\mathcal{G}$ represents the transformation in Eq. (17). Although the augmented system in Eq. (21) involves white noise, it is generally non-Markovian because the non-white excitation $\xi_{\mathrm{nw}}(t)$ depends on the history of $\xi_{\mathrm{w}}(t)$ through the transformation $\mathcal{G}$. It should also be noted that the state equations governing $\boldsymbol{Z}(t)$ and $\boldsymbol{U}(t)$ are dynamically decoupled. Nevertheless, the processes $\boldsymbol{Z}(t)$ and $\boldsymbol{U}(t)$ are statistically correlated because their respective excitations, $\xi_{\mathrm{nw}}(t)$ and $\xi_{\mathrm{w}}(t)$, are correlated.

Based on the above formulation, the response of interest $Z_\ell(t)$ is combined with one component of $\boldsymbol{U}(t)$, denoted by $U_\kappa(t)$, where $\kappa \in \{1, \ldots, n_{\boldsymbol{U}}\}$. The process $U_\kappa(t)$ is selected as the auxiliary diffusion process and must satisfy $\beta_\kappa \neq 0$. Here, β_κ is the κ-th component of $\boldsymbol{\beta}$.

By taking $\boldsymbol{Y}(t)$ in Eq. (9) as the joint process $(Z_\ell(t), U_\kappa(t))^{\mathrm{T}}$, the DR-PDEE governing its instantaneous joint PDF $p_{Z_\ell U_\kappa}(z_\ell, u_\kappa, t)$ is formulated as

$$\begin{aligned} \frac{\partial p_{Z_\ell U_\kappa}(z_\ell, u_\kappa, t)}{\partial t} = &-\frac{\partial a^{\mathrm{int}}_{Z_\ell U_\kappa, 1} p_{Z_\ell U_\kappa}(z_\ell, u_\kappa, t)}{\partial z_\ell} - \frac{\partial a^{\mathrm{int}}_{Z_\ell U_\kappa, 2} p_{Z_\ell U_\kappa}(z_\ell, u_\kappa, t)}{\partial u_\kappa} \\ &+ \frac{1}{2}\frac{\partial^2 \left[\beta_\kappa^2 D_0\right] p_{Z_\ell U_\kappa}(z_\ell, u_\kappa, t)}{\partial {u_\kappa}^2}. \end{aligned} \tag{22}$$

In Eq. (22), the intrinsic drift functions are

$$\begin{cases} a^{\mathrm{int}}_{Z_\ell U_\kappa, 1} = \mathbb{E}\left\{ a_\ell(\boldsymbol{Z}(t), t; \boldsymbol{\Theta}) + B_\ell \xi_{\mathrm{nw}}(t) \middle| Z_\ell(t) = z_\ell, U_\kappa(t) = u_\kappa \right\}, \\ a^{\mathrm{int}}_{Z_\ell U_\kappa, 2} = \mathbb{E}\left\{ -\alpha_\kappa(\boldsymbol{U}(t)) \middle| Z_\ell(t) = z_\ell, U_\kappa(t) = u_\kappa \right\} \\ \qquad\qquad + \beta_\kappa \lim_{\Delta t \to 0} \frac{1}{\Delta t}\mathbb{E}\left\{ \int_t^{t+\Delta t} \xi_{\mathrm{w}}(\tau)\,\mathrm{d}\tau \middle| Z_\ell(t) = z_\ell, U_\kappa(t) = u_\kappa \right\}. \end{cases} \tag{23}$$

The diagonal intrinsic diffusion coefficients are $b^{\mathrm{int}}_{Z_\ell U_\kappa, 11} = 0$ and $b^{\mathrm{int}}_{Z_\ell U_\kappa, 22} = \beta_\kappa^2 D_0$. The cross intrinsic diffusion coefficient $b^{\mathrm{int}}_{Z_\ell U_\kappa, 12}$ is given by

$$b^{\mathrm{int}}_{Z_\ell U_\kappa, 12} = B_\ell \beta_\kappa \lim_{\Delta t \to 0} \frac{1}{\Delta t} \int_t^{t+\Delta t} \int_t^{t+\Delta t} \mathbb{E}\left\{ \xi_{\mathrm{nw}}(\tau_1)\, \xi_{\mathrm{w}}(\tau_2) \middle| Z_\ell(t) = z_\ell, U_\kappa(t) = u_\kappa \right\} \mathrm{d}\tau_1 \mathrm{d}\tau_2 \tag{24}$$

If the ℓ-th row of $\boldsymbol{B}$ is zero, i.e., $B_\ell = 0$, the cross intrinsic diffusion term becomes $b^{\text{int}}_{Z_\ell U_\kappa,12} = 0$. Otherwise, the cross term should be examined. A sufficient condition is

$$\int_t^{t+\Delta t}\int_t^{t+\Delta t} \mathbb{E}\left\{\xi_{\text{nw}}\left(\tau_1\right)\xi_{\text{w}}\left(\tau_2\right)\middle|\, Z_\ell\left(t\right)=z_\ell, U_\kappa\left(t\right)=u_\kappa\right\}\mathrm{d}\tau_1\mathrm{d}\tau_2 = o\left(\Delta t\right), \tag{25}$$

where $o\left(\Delta t\right)$ denotes a higher-order term than Δt. Under this condition, the cross intrinsic diffusion term also vanishes after division by Δt and taking the limit $\Delta t \to 0$.

Thus, a two-dimensional DR-PDEE is established for $Z_\ell\left(t\right)$ and $U_\kappa\left(t\right)$. The auxiliary process introduces the nonzero intrinsic diffusion coefficient $\beta_\kappa^2 D_0$ and prevents complete degeneration of the diffusion term. Solving Eq. (22) yields the joint PDF of $\left(Z_\ell\left(t\right), U_\kappa\left(t\right)\right)^\top$. The PDF of $Z_\ell\left(t\right)$ is then obtained by

$$p_{Z_\ell}\left(z_\ell, t\right) = \int_{-\infty}^{\infty} p_{Z_\ell U_\kappa}\left(z_\ell, u_\kappa, t\right)\mathrm{d}u_\kappa. \tag{26}$$

2.3.4. *SDE governing the auxiliary diffusion process*

The above derivation allows some flexibility in selecting the SDE for the auxiliary diffusion process. In particular, the functions $\boldsymbol{\alpha}$ and $\boldsymbol{\beta}$ in Eq. (20) can be chosen according to the following guidelines:

- Eq. (20) should be as simple as possible to limit the additional computational cost.
- The auxiliary process should facilitate accurate estimation of the intrinsic drift functions while retaining a nonzero intrinsic diffusion coefficient.

The second guideline can be understood from Eq. (23). The first component of the intrinsic drift function, $a^{\text{int}}_{Z_\ell U_\kappa,1}$, depends on the statistical dependence among $Z_\ell\left(t\right)$, $U_\kappa\left(t\right)$, and $a_\ell\left(\boldsymbol{Z}\left(t\right), t; \boldsymbol{\Theta}\right) + B_\ell\xi_{\text{nw}}\left(t\right)$, where the last quantity represents the instantaneous velocity of $Z_\ell\left(t\right)$. Therefore, the governing equation for $\boldsymbol{U}\left(t\right)$ should be selected such that $U_\kappa\left(t\right)$ is strongly correlated with this velocity. This correlation reduces the scatter of the samples used to estimate the conditional expectation. Consequently, $a^{\text{int}}_{Z_\ell U_\kappa,1}$ can be estimated more accurately with a limited number of deterministic analyses.

Following these guidelines, a simple choice is the one-dimensional Ornstein–Uhlenbeck-type Itô SDE (Sun et al., 2025)

$$\mathrm{d}U\left(t\right) = -\alpha_0 U\left(t\right)\mathrm{d}t + \beta\mathrm{d}W_0\left(t\right). \tag{27}$$

In this case, $U\left(t\right)$ itself serves as the auxiliary diffusion process. Another choice is a linear single-degree-of-freedom system governed by

$$\begin{cases}\mathrm{d}U_1\left(t\right) = U_2\left(t\right)\mathrm{d}t \\ \mathrm{d}U_2\left(t\right) = -\left[\omega_0^2 U_1\left(t\right) + 2\zeta_0\omega_0 U_2\left(t\right)\right]\mathrm{d}t + \beta_2\mathrm{d}W_0\left(t\right).\end{cases} \tag{28}$$

Here, $U_2\left(t\right)$ is selected as the auxiliary diffusion process.

To satisfy the second guideline, the parameters α_0, ω_0, and ζ_0 may be selected with reference to the characteristic time scale or dominant frequency of the original system in Eq. (2).

2.4. Numerical Procedure

The proposed method determines the PDF of the response of interest under non-white excitation through the following four steps:

1. Generate N_{smp} samples of $\boldsymbol{\Theta}$ and N_{smp} paired trajectories of $\xi_{\text{nw}}(t)$ and $\xi_{\text{w}}(t)$ using Eqs. (14) and (16). The same random phase angles are used for each pair.

2. For each sample, numerically integrate the augmented system in Eq. (21). Record the trajectories of $Z_\ell(t)$ and $U_\kappa(t)$, together with the quantities required to evaluate the intrinsic drift functions.

3. Estimate the intrinsic drift functions of $(Z_\ell(t), U_\kappa(t))^\top$ in Eq. (23) from the N_{smp} response trajectories at each time step. Various estimators of conditional expectation can be used. In this study, locally weighted least-squares regression (LOWESS) is adopted (Cleveland and Devlin, 1988).

4. Substitute the estimated intrinsic drift functions into Eq. (22) and solve the two-dimensional DR-PDEE numerically. The PIS technique is used in this study (Yu et al., 1997). The PDF of $Z_\ell(t)$ is then obtained by evaluating the integral in Eq. (26).

Note that, when estimating the intrinsic drift functions in Eq. (23), the conditional expectations must first be evaluated prior to numerical differentiation for estimating the time derivatives. A detailed numerical scheme can be found in Ref. (Sun et al., 2025).

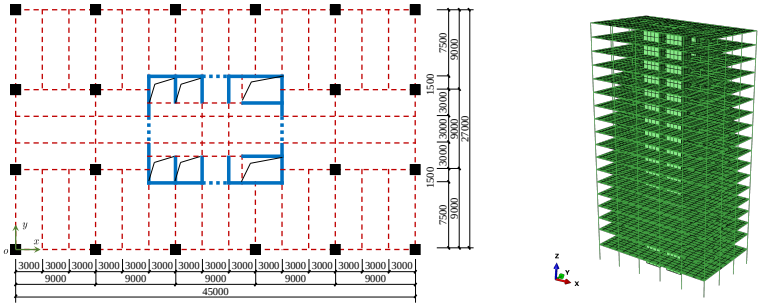
3. Engineering application: High-rise RC frame–core tube structure subjected to near-field seismic excitation

To demonstrate the proposed method in an engineering application, a high-rise RC frame–core tube structure subjected to stochastic near-field seismic excitation is considered. The uncertainties in both the material properties and seismic excitation are taken into account. The structural model is first introduced, followed by the probabilistic response using the proposed method.

3.1. Finite element model

The case study considers an 18-story high-rise RC frame–core tube structure. The total structural height is 84.0 m. The first two stories are 6.0 m high, while each of the remaining stories is 4.5 m high. The slab thickness is 120 mm. The structural plan layout is shown in Fig. (1a). The finite element (FE) model is shown in Fig. (1b). In this model, beams and columns are modeled using Timoshenko beam elements, whereas shear walls and slabs are modeled using layered shell elements. The FE model consists of 29312 elements, including 16856 beam elements and 12456 layered shell elements. It contains 13412 nodes and 80472 unconstrained DOFs.

Gravity loads, slab live loads, and curtain-wall loads are considered in the structural design. The slab live load is 3.5 kN/m^2, and the curtain-wall load is 3.5 kN/m along the perimeter of



(a) Structural plan layout. (b) FE model.

Figure 1. High-rise RC frame–core tube structure considered in the case study.

the structural plan. The stochastic seismic excitation is then applied to evaluate the probabilistic dynamic response of the structure.

3.2. Structural material properties and their probabilistic model

The structure consists of reinforcing steel and concrete. The reinforcing steel is treated as deterministic owing to its relatively low variability. It follows a bilinear elastic–plastic constitutive law, with its density, initial Young's modulus, yield strength, and ultimate strength taken as 7800 kg/m^3, 205 GPa, 335 MPa, and 470 MPa, respectively.

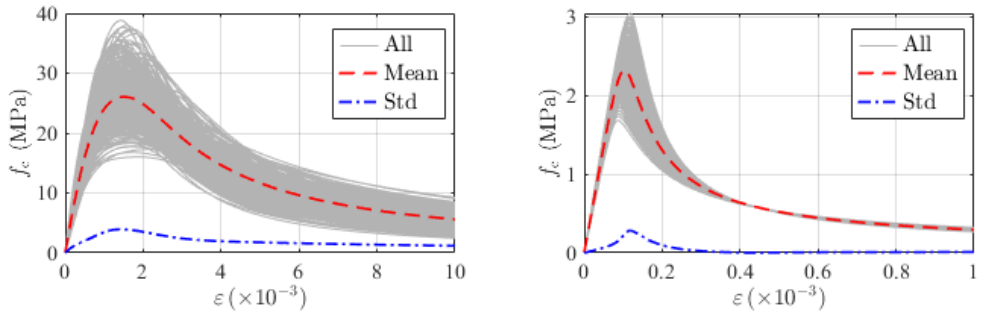
In contrast, concrete is considered as a random material because of the pronounced variability observed in its constitutive behavior (Li et al., 2014). In this structure, the concrete strength grade is C40 for walls and columns and C30 for beams and slabs. The constitutive behavior of concrete is described by the bi-scalar elastoplastic damage model (Li et al., 2014). This model characterizes the multiaxial nonlinear behavior of concrete and its parameters need to be calibrated using uniaxial compressive and tensile stress–strain relations.

In this study, the uniaxial compressive and tensile stress–strain relationships of concrete follow the constitutive model recommended by the Chinese Code for Design of Concrete Structures (GB 50010–2015) (Ministry of Housing and Urban-Rural Development of the People's Republic of China, 2015). The compressive stress–strain curve is governed by four parameters: the initial Young's modulus E_c, the compressive strength f_{cu}, the compressive peak strain ε_{cu}, and the shape parameter governing its descending stage α_c. Similarly, the tensile stress–strain curve is governed by E_c, the tensile strength f_{tu}, the tensile peak strain ε_{tu}, and the corresponding shape parameter for its descending regime α_t. Thus, the constitutive model involves seven material parameters in total.

The probabilistic model of $(E_c, f_{cu}, \varepsilon_{cu}, \alpha_c)$ proposed by Refs. (Tao et al., 2020; Tao et al., 2021) is adopted. The marginal distribution of α_c follows the original model. For E_c, f_{cu}, and ε_{cu}, the coefficients of variation are assumed to be independent of the concrete strength grade. Their distribution parameters are slightly adjusted to match the strength levels specified in the Chinese Code for Design of Concrete Structures (Ministry of Housing and Urban-Rural Development of the People's Republic of China, 2015). Their dependence structure also follows Ref. (Tao et al., 2020) where copulas are employed.

The tensile constitutive parameters $(f_{\mathrm{tu}}, \varepsilon_{\mathrm{tu}}, \alpha_t)$ follow the empirical relationships in Ref. (Guo et al., 1982) where they are expressed as deterministic functions of f_{tu}.

Based on the probabilistic model described above, 500 samples of the four compressive constitutive parameters are generated. The corresponding uniaxial compressive and tensile stress–strain curves for C30 concrete are shown in Fig. 2 for illustration. The remaining concrete properties, namely Poisson's ratio, biaxial strength factor, plastic hardening coefficient, and density, are taken as 0.2, 1.16, 0.1, and 2500 $\mathrm{kg/m^3}$, respectively.



(a) Compressive. (b) Tensile.

Figure 2. Samples of the uniaxial compressive and tensile stress–strain curves for C30 concrete.

3.3. Near-field seismic excitation

The structure is assumed to be subjected to seismic excitation acting along the Y-axis. The ground motion is modeled using a seismic ground motion model involving near-fault pulse-like ground motion. In this model, the acceleration, denoted by $\xi_{\mathrm{g}}(t)$, is described by (Jensen et al., 2012)

$$\xi_{\mathrm{g}}(t) = \mathcal{F}^{-1}\left\{\left[\left|\mathcal{F}\left(\xi_{\mathrm{g}}^{\mathrm{H}}(t)\right)\right| - \left|\mathcal{F}\left(\xi_{\mathrm{g}}^{\mathrm{L}}(t)\right)\right|\right] \exp\left(\mathrm{i}\cdot\arg\left\{\mathcal{F}\left[\xi_{\mathrm{g}}^{\mathrm{H}}(t)\right]\right\}\right)\right\} + \xi_{\mathrm{g}}^{\mathrm{L}}(t), \tag{29}$$

where $\xi_{\mathrm{g}}^{\mathrm{H}}(t)$ and $\xi_{\mathrm{g}}^{\mathrm{L}}(t)$ denote the high-frequency and low-frequency pulse-like components, respectively.

The high-frequency component $\xi_{\mathrm{g}}^{\mathrm{H}}(t)$ is generated by modulating a standard white noise $\xi_{\mathrm{w}}(t)$:

$$\xi_{\mathrm{g}}^{\mathrm{H}}(t) = \mathcal{F}^{-1}\left\{A(\omega; M, r)\,\frac{\mathcal{F}\{\psi(t; M, r)\cdot\xi_{\mathrm{w}}(t)\}}{\sqrt{\frac{1}{2\pi}\int_{-\infty}^{\infty}\left|\mathcal{F}\{\psi(t; M, r)\}\right|^2 \mathrm{d}\omega}}\right\}, \tag{30}$$

where $\psi(t; M, r)$ and $A(\omega; M, r)$ denote the modulation function in the time and frequency domain, respectively. Both depend on the moment magnitude M and epicentral distance r. Further details of this relationship can be found in Ref. (Boore, 2003). The pulse-like component is described by

the model proposed in Ref. (Mavroeidis and Papageorgiou, 2003)

$$\xi_{\mathrm{g}}^{\mathrm{L}}(t) = I\left\{t \in \left(t_{\mathrm{p}} - \frac{\gamma_{\mathrm{p}}}{2f_{\mathrm{p}}},\, t_{\mathrm{p}} + \frac{\gamma_{\mathrm{p}}}{2f_{\mathrm{p}}}\right)\right\} \cdot \; A_{\mathrm{p}}\left\{\sin\left[\frac{2\pi f_{\mathrm{p}}}{\gamma_{\mathrm{p}}}(t-t_{\mathrm{p}})\right]\cos\left[\frac{2\pi f_{\mathrm{p}}}{\gamma_{\mathrm{p}}}(t-t_{\mathrm{p}})+\nu_{\mathrm{p}}\right] + \frac{2\pi f_{\mathrm{p}}}{\gamma_{\mathrm{p}}}\sin\left[\frac{2\pi f_{\mathrm{p}}}{\gamma_{\mathrm{p}}}(t-t_{\mathrm{p}})+\nu_{\mathrm{p}}\right]\left[1+\cos\left(\frac{2\pi f_{\mathrm{p}}}{\gamma_{\mathrm{p}}}(t-t_{\mathrm{p}})\right)\right]\right\}. \tag{31}$$

In this case, the moment magnitude M is set to 7.25. The epicentral distance r is considered as random. The parameters of the pulse model are also treated as random variables and their distributions are adopted from Ref. (Jensen et al., 2012).

Based on the probabilistic model described above, 500 samples of the pulse model are generated with a total duration of 25 s and a time step of 0.005 s. Owing to the variability of the epicentral distance r, the peak ground acceleration (PGA) also exhibits variability with a mean value of 2.81 m/s^2 and a coefficient of variation of 0.26.

3.4. Probabilistic response of the structure under seismic ground motion

The proposed method is applied to determine the probabilistic response of the structure under the prescribed stochastic seismic excitation. The equation of motion of the FE model is given by Eq. (1), where n = 80,472, and $\boldsymbol{X}(t)$, $\dot{\boldsymbol{X}}(t)$, and $\ddot{\boldsymbol{X}}(t)$ denote the nodal displacement, velocity, and acceleration vectors, respectively. The excitation is taken as the stochastic ground acceleration $\xi_{\mathrm{g}}(t)$ in Eq. (29).

The vector $\boldsymbol{\Theta}$ collects the random material parameters in the concrete constitutive model, i.e., $\boldsymbol{\Theta} = (E_{\mathrm{c}}, f_{\mathrm{cu}}, \alpha_{\mathrm{c}}, \varepsilon_{\mathrm{cu}}, f_{\mathrm{tu}}, \alpha_{\mathrm{t}}, \varepsilon_{\mathrm{tu}})^{\top}$. When material plasticity, hysteresis, and damage accumulation are considered, the nonlinear restoring force depends not only on the current displacement and velocity but also on the internal variable $\boldsymbol{\eta}(t)$, which represents the material history. Therefore, $\boldsymbol{f}\left(\boldsymbol{X}(t), \dot{\boldsymbol{X}}(t), \boldsymbol{\eta}(t), t; \boldsymbol{\Theta}\right)$ is generally a functional rather than an explicit function and is written in the compact form given in Eq. (1).

The interstory drift angle of the sixth floor is selected as the quantity of interest and denoted by $X_{\mathrm{qoi}}(t)$. Its corresponding velocity is denoted by $V_{\mathrm{qoi}}(t) = \dot{X}_{\mathrm{qoi}}(t)$. As discussed in Section 2.2.2, the intrinsic diffusion functions of $X_{\mathrm{qoi}}(t)$ and $V_{\mathrm{qoi}}(t)$ vanish according to the probabilistic model of $\xi_{\mathrm{g}}(t)$. Therefore, the equation governing the auxiliary process is introduced as

$$\begin{cases} \mathrm{d}U_1(t) = U_2(t)\,\mathrm{d}t \\ \mathrm{d}U_2(t) = -\left[\omega_0^2(\boldsymbol{\Theta})\,U_1(t) + 2\zeta_0\omega_0(\boldsymbol{\Theta})\,U_2(t)\right]\mathrm{d}t + \sqrt{D}\xi_{\mathrm{g}}^{\mathrm{L}}(t)\,\mathrm{d}t + \sqrt{D}\mathrm{d}W(t). \end{cases} \tag{32}$$

In the SDE, $\xi_{\mathrm{g}}^{\mathrm{L}}(t)$ denotes the low-frequency pulse component in Eq. (31). The Wiener process $W(t)$ corresponds to the standard white noise $\xi_{\mathrm{w}}(t)$ used in Eq. (30). Therefore, the transformation $\mathcal{G}$ in Eq. (21) is represented by the ground-motion model in Eq. (29). The natural circular frequency ω_0 is considered to depend on the random material properties and is specified as $\omega_0(\boldsymbol{\Theta}) = \omega_1(\boldsymbol{\Theta})/1.5$, where $\omega_1(\boldsymbol{\Theta})$ is the first natural circular frequency of the FE model. The damping ratio and diffusion intensity are set to $\zeta_0 = 0.05$ and $D = 0.1$, respectively. The process $U_2(t)$ is selected as the auxiliary diffusion process.

Next, the interstory drift angle of the sixth floor, $X_{\mathrm{qoi}}(t)$, is combined with the auxiliary diffusion process $U_2(t)$. The intrinsic drift functions of the joint process are estimated from 500 deterministic

analyses using the LOWESS technique. The resulting two-dimensional DR-PDEE is then solved by the PIS scheme. The PDFs of the interstory drift angle at representative time instants are shown in Fig. (3).

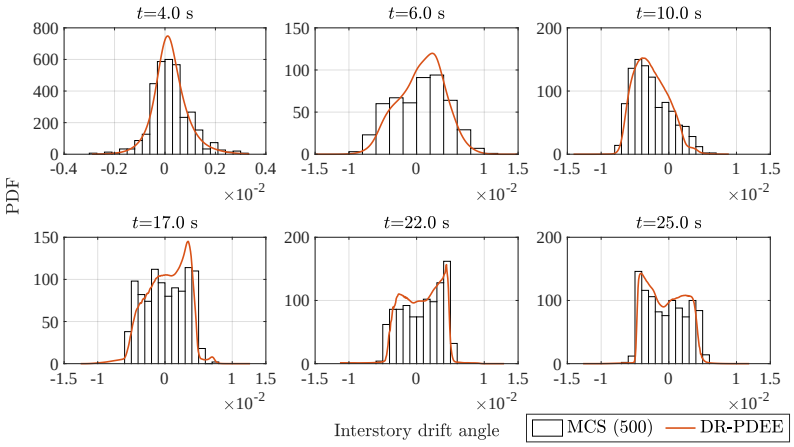


Figure 3. PDFs of the interstory drift angle of the structure at representative time instants.

The response distribution exhibits pronounced nonstationarity, skewness, and non-Gaussianity. Before the arrival of the low-frequency pulse, the PDF is unimodal. It gradually evolves into a bimodal distribution after the pulse. This evolution results from the combined effects of random material properties, structural nonlinearity, and uncertain excitation parameters. The bimodal feature becomes evident after the pulse peak, indicating an increasing influence of material nonlinearity. The proposed method captures this complex evolution. Despite the limited sample size imposed by the high cost of the deterministic analyses, the predicted PDFs agree well with the statistical estimates obtained from the 500 response samples.

4. Concluding Remarks

In this study, an efficient method is proposed for the stochastic response analysis of high-dimensional nonlinear systems under non-white excitation. The key idea is to formulate a low-dimensional DR-PDEE by incorporating an auxiliary diffusion process. A large-scale nonlinear RC structure subjected to pulse-like near-fault ground motions is investigated to demonstrate the effectiveness of the proposed method. The main conclusions are as follows:

1. By constructing the auxiliary diffusion process, a low-dimensional DR-PDEE with nonzero diffusion can be formulated without constructing a linear filter. This makes the DR-PDEE framework applicable to complex engineering excitations.

2. The auxiliary diffusion process can be constructed by generating white noise correlated with the original excitation and using it to drive a simple stochastic system. To improve the effectiveness

of the method, the selected auxiliary process should be strongly correlated with the velocity of the response of interest.

3. The engineering example demonstrates that the proposed method can quantitatively capture the time evolution of the response PDF of a large-scale nonlinear structure under stochastic near-fault ground motions. The method provides a theoretical basis for refined safety assessment of practical engineering structures.

Future work will focus on the optimal design of the governing equation for the auxiliary process and further develop the proposed method for reliability analysis.

Acknowledgements

The financial support from the National Natural Science Foundation of China (Grant Nos. 12472019 & 52494962) and the Chinesisch-Deutsches Zentrum für Wissenschaftsförderung (Grant No. M-0737) are highly appreciated.

References

Boore, D. M.: 2003, 'Simulation of Ground Motion Using the Stochastic Method'. *Pure and Applied Geophysics* **160**, 635–676.

Chen, J. B., J. H. Lyu, P. D. Spanos, and J. Li: 2024, 'Stochastic Response Analysis of a Spar-Type FOWT Subjected to Extreme Waves by a Novel Filter Wave Model and the DR-PDEE'. *Journal of Engineering Mechanics* **150**(4), 04024009.

Chen, J. B. and M. Z. Lyu: 2022, 'Globally-Evolving-Based Generalized Density Evolution Equation for Nonlinear Systems Involving Randomness from Both System Parameters and Excitations'. *Proceedings of the Royal Society A: Mathematical, Physical and Engineering Sciences* **478**(2264), 20220356.

Cleveland, W. S. and S. J. Devlin: 1988, 'Locally Weighted Regression: An Approach to Regression Analysis by Local Fitting'. *Journal of the American Statistical Association* **83**(403), 596–610.

Dostupov, B. G. and V. S. Pugachev: 1957, 'Equations Determining the Distribution Law of the Integral of a System of Ordinary Differential Equations with Random Parameters'. *Avtomatika i Telemekhanika* **18**, 620–630 (in Russian).

Dynkin, E. B.: 1952, 'Criteria of Continuity and of Absence of Discontinuities of the Second Kind for Trajectories of a Markov Random Process'. *Izvestiya Akademii Nauk SSSR. Seriya Matematicheskaya* **16**(6), 563–572 (in Russian).

Gardiner, C. W.: 1985, *Handbook of Stochastic Methods for Physics, Chemistry and the Natural Science*. Heidelberg: Springer-Verlag.

Guo, Z. H., X. Q. Zhang, D. C. Zhang, and R. Q. Wang: 1982, 'Experimental investigation of the full stress–strain curve of concrete (in Chinese)'. *Journal of Building Structures* **3**(1), 1–12.

Jensen, H., J. Sepulveda, and L. Becerra: 2012, 'Robust Stochastic Design of Base-Isolated Structural Systems'. *International Journal for Uncertainty Quantification* **2**(2), 95–110.

Kinney, J. R.: 1953, 'Continuity Properties of Sample Functions of Markov Processes'. *Transactions of the American Mathematical Society* **74**(2), 280–302.

Li, J. and J. B. Chen: 2009, *Stochastic Dynamics of Structures*. Singapore: John Wiley & Sons.

Li, J. and D. Wang: 2023, 'Comparison of PDEM and MCS: Accuracy and Efficiency'. *Probabilistic Engineering Mechanics* **71**, 103382.

Li, J., J. Y. Wu, and J. B. Chen: 2014, *Stochastic Damage Mechanics of Concrete (in Chinese)*. Beijing: Science Press.

Liang, J. W., S. R. Chaudhuri, and M. Shinozuka: 2007, 'Simulation of Non-Stationary Stochastic Processes by Spectral Representation'. *Journal of Engineering Mechanics* **133**(6), 616–627.

Luo, Y., J. B. Chen, and P. D. Spanos: 2022a, 'Determination of Monopile Offshore Structure Response to Stochastic Wave Loads via Analog Filter Approximation and GV-GDEE Procedure'. *Probabilistic Engineering Mechanics* **67**, 103197.

Luo, Y., P. D. Spanos, and J. B. Chen: 2022b, 'Stochastic Response Determination of Multi-Dimensional Nonlinear Systems Endowed with Fractional Derivative Elements by the GE-GDEE'. *International Journal of Non-Linear Mechanics* **147**, 104247.

Lyu, M. Z.: 2022, 'Globally-Evolving-Based Generalized Probability Density Evolution Equation for Response Determination and Reliability Evaluation of High-Dimensional Stochastic Dynamical Systems (in Chinese)'. Ph.D. thesis, Tongji University, Shanghai.

Lyu, M. Z. and J. B. Chen: 2022, 'A Unified Formalism of the GE-GDEE for Generic Continuous Responses and First-Passage Reliability Analysis of Multi-Dimensional Nonlinear Systems Subjected to Non-White-Noise Excitations'. *Structural Safety* **98**, 102233.

Mavroeidis, G. P. and A. S. Papageorgiou: 2003, 'A Mathematical Representation of Near-Fault Ground Motions'. *Bulletin of the Seismological Society of America* **93**(3), 1099–1131.

Ministry of Housing and Urban-Rural Development of the People's Republic of China: 2015, *Code for Design of Concrete Structures*. Beijing, China: China Architecture & Building Press.

Moustapha, M., S. Marelli, and B. Sudret: 2022, 'Active Learning for Structural Reliability: Survey, General Framework and Benchmark'. *Structural Safety* **96**, 102174.

Rezaeian, S. and A. Der Kiureghian: 2008, 'A Stochastic Ground Motion Model with Separable Temporal and Spectral Nonstationarities'. *Earthquake Engineering and Structural Dynamics* **37**(13), 1565–1584.

Roberts, J. B. and P. D. Spanos: 1986, 'Stochastic Averaging: An Approximate Method of Solving Random Vibration Problems'. *International Journal of Non-Linear Mechanics* **21**(2), 111–134.

Roberts, J. B. and P. D. Spanos: 1990, *Random Vibration and Statistical Linearization*. Chichester: John Wiley & Sons.

Schuëller, G. I.: 2007, 'On the Treatment of Uncertainties in Structural Mechanics and Analysis'. *Computers and Structures* **85**(5), 235–243.

Seregin, L. V.: 1961, 'Continuity Conditions for Stochastic Processes'. *Theory of Probability and Its Applications* **6**(1), 1–26.

Shinozuka, M.: 1971, 'Simulation of Multivariate and Multidimensional Random Processes'. *The Journal of the Acoustical Society of America* **49**(1B), 357–368.

Soong, T. T.: 1973, *Random Differential Equations in Science and Engineering*, Vol. 103 of *Mathematics in Science and Engineering*. New York: Academic Press.

Sun, T. T., J. B. Chen, Y. Luo, and J. H. Lyu: 2025, 'DR-PDEE-based Probabilistic Response Analysis for High-Dimensional Nonlinear Dynamical Systems under General Non-White and Non-Stationary Random Excitations via Constructing the Auxiliary Diffusion Process'. *Computer Methods in Applied Mechanics and Engineering* **442**, 118029.

Tao, J. J., J. B. Chen, and X. D. Ren: 2020, 'Copula-Based Quantification of Probabilistic Dependence Configurations of Material Parameters in Damage Constitutive Modeling of Concrete'. *Journal of Structural Engineering* **146**(9), 04020194.

Tao, J. J., X. D. Ren, and J. B. Chen: 2021, 'Random Transition of Failure Modes in Concrete Shear Walls with Constitutive Parameters Involving Spatial Variation'. *Engineering Structures* **242**, 112508.

Yu, J. S., G. Q. Cai, and Y. K. Lin: 1997, 'A New Path Integration Procedure Based on Gauss-Legendre Scheme'. *International Journal of Non-Linear Mechanics* **32**(4), 759–768.

Zhang, R. J., L. Li, and H. Z. Dai: 2020, 'A Copula-Based Gaussian Mixture Closure Method for Stochastic Response of Nonlinear Dynamic Systems'. *Probabilistic Engineering Mechanics* **59**, 103015.

Zhu, W. Q., G. Q. Cai, and Y. K. Lin: 1990, 'On Exact Stationary Solutions of Stochastically Perturbed Hamiltonian Systems'. *Probabilistic Engineering Mechanics* **5**(2), 84–87.

A Regression-Tree-Based Method for Structural Reliability Assessment

S. Russotto[1)], M. Di Paola[1)], and A. Pirrotta[1)]
[1)]*Engineering Department, Università degli Studi di Palermo, Palermo 90128, Italy,*
salvatore.russotto01@unipa.it mario.dipaola@unipa.it antonina.pirrotta@unipa.it

Abstract: Structural reliability plays a pivotal role in structural engineering, providing a quantitative basis for assessing safety, serviceability, and risk. Traditionally, the evaluation of a survival probability is carried out either through Monte Carlo simulations, which can be extremely computationally demanding, or through path integral approaches that account for absorbing barriers. However, for damped oscillators, path integral techniques typically require the probability density function (PDF) of the state variables, i.e., bi-dimensional PDF, which significantly increases both the mathematical complexity of the problem and the associated computational cost.
In this paper, a regression tree is specifically trained on a large dataset to estimate, within a fraction of a second, the survival probability of a damped oscillator at a given time instant when subjected to white noise excitation. The proposed method aims to retain the accuracy of reliability computations while drastically reducing runtime. The accuracy of the proposed method is validated by comparing its predictions against a Monte Carlo simulation, showing strong agreement and confirming the proposed approach as a fast and effective tool for structural reliability assessment.

Keywords: Structural Reliability, Regression Trees, Computational Efficiency.

1. Introduction

Structural reliability has long represented one of the fundamental pillars of modern structural engineering, because it provides a rational probabilistic framework for quantifying the safety, serviceability, and risk of structures in the presence of unavoidable uncertainties in loads, material properties, geometry, boundary conditions, deterioration mechanisms, and environmental actions (Cornell, 1969; Hasofer and Lind, 1974; Rackwitz, 2001; Ditlevsen and Madsen, 1996; Melchers and Beck, 2018; Pirrotta, 2007; Biondini and Frangopol, 2016; Chen and Li, 2007). In contrast with purely deterministic safety checks, reliability analysis explicitly recognizes that both resistance and demand are random quantities and that structural performance must therefore be evaluated in terms of the probability of violating a prescribed limit state. This viewpoint has profoundly influenced the development of probability-based design formats, reliability indices, and life-cycle performance assessment strategies for civil and mechanical systems (Cornell, 1969; Hasofer and Lind, 1974; Rackwitz, 2001; Ditlevsen and Madsen, 1996; Melchers and Beck, 2018; Biondini and Frangopol, 2016). In this sense, structural reliability is not merely a verification tool, but also a decision-support instrument for design, maintenance planning, optimization, and risk-informed management of engineering systems throughout their service life (Rackwitz, 2001; Ditlevsen and Madsen, 1996; Melchers and Beck, 2018; Biondini and Frangopol, 2016).

© 2026 by the author(s). This work is licensed under the Creative Commons Attribution 4.0 International License (CC BY 4.0), which permits unrestricted use, distribution, and reproduction in any medium, provided the original author and source are credited.

Despite its conceptual importance, structural reliability assessment remains computationally challenging, especially when the structural response is nonlinear. Over the years, a broad spectrum of methods has been developed, ranging from first-order and second-order reliability approximations to direct simulation methods and advanced rare-event strategies (Hasofer and Lind, 1974; Rackwitz, 2001; Ditlevsen and Madsen, 1996; Melchers and Beck, 2018; Doliński, 1983; Breitung, 1984; Der Kiureghian and De Stefano, 1991; Au and Beck, 2001; Spanos and Kougioumtzoglou, 2013; Bucher et al., 2016; Song and Kawai, 2023; Afshari et al., 2022). Classical first-order and second-order reliability approximations methodologies are attractive because of their analytical elegance and reduced computational cost, but their accuracy may deteriorate when the limit-state surface is strongly nonlinear or when multiple failure regions exist (Hasofer and Lind, 1974; Doliński, 1983; Breitung, 1984; Der Kiureghian and De Stefano, 1991). On the other hand, Monte Carlo simulation retains a nearly universal applicability and can be regarded as a benchmark method, yet it is notoriously computationally expensive when small failure probabilities must be estimated with adequate accuracy (Au and Beck, 2001; Song and Kawai, 2023). This issue becomes even more severe in stochastic dynamics and first-passage problems, where repeated time-domain simulations or repeated evaluations of transition probabilities are required (Au and Beck, 2001; Spanos and Kougioumtzoglou, 2013; Bucher et al., 2016; Song and Kawai, 2023). Recent reviews have in fact confirmed that Monte Carlo and related sampling procedures remain accurate but often computationally demanding, thereby motivating the search for faster surrogate-based alternatives (Song and Kawai, 2023; Afshari et al., 2022).

The above difficulty is particularly evident for nonlinear oscillatory systems under stochastic excitation. In such cases, reliability is often associated with a first-passage or survival probability, namely the probability that the response does not cross an assigned threshold up to a given time instant (Spanos and Kougioumtzoglou, 2013; Bucher et al., 2016). Path-integral formulations have proved to be powerful tools for this class of problems because they allow one to propagate the response probability density in time and, with suitable absorbing barriers, to evaluate first-passage quantities in a rigorous probabilistic setting (Spanos and Kougioumtzoglou, 2013; Bucher et al., 2016; Di Paola and Santoro, 2008; Pirrotta and Santoro, 2011; Kougioumtzoglou and Spanos, 2014; Kougioumtzoglou et al., 2015; Di Matteo et al., 2016; Kougioumtzoglou, 2017; Zhang et al., 2023). However, for dynamical systems excited by stochastic forces, these methods generally require the joint probability density of the state variables, typically displacement and velocity, which increases the dimensionality of the probabilistic problem and consequently the computational burden associated with discretization, numerical integration, and repeated evaluation in time (Spanos and Kougioumtzoglou, 2013; Bucher et al., 2016). Therefore, although path-integral approaches are mathematically sound and highly valuable, their practical implementation may still be onerous when many reliability evaluations are needed, for example in parametric analyses, sensitivity studies, optimization loops, or real-time decision environments.

For these reasons, the last decade has witnessed a growing interest in surrogate and machine-learning strategies for structural reliability analysis (Song and Kawai, 2023; Afshari et al., 2022). The central idea is to replace an expensive physical or numerical model, or even the reliability mapping itself, with an inexpensive predictor trained on representative data. In structural reliability, machine-learning methods have been employed to approximate limit-state functions, classify safe and failure domains, guide adaptive sampling, and accelerate Monte Carlo-based estimators (Song and Kawai, 2023; Afshari et al., 2022). Broadly speaking, the motivation is twofold: first, to preserve an acceptable level of accuracy; second, to reduce runtime to a level compatible with large-scale uncertainty propagation or near-real-time applications. In parallel, the broader structural-engineering literature has shown that machine learning is becoming increasingly relevant for nonlinear structural analysis, health monitoring, damage detection, resistance

prediction, and performance evaluation, especially when large datasets are available and repeated evaluations are required (Afshari et al., 2022; Thai, 2022).

Within the wide family of machine-learning methods, decision trees are especially appealing because they combine conceptual simplicity, interpretability, and low computational cost at inference time (Morgan and Sonquist, 1963; Friedman, 1977; Breiman et al., 1984; Quinlan, 1986; Kass, 1980; Loh and Shih, 1997; Quinlan, 1993; Frank et al., 1998; Breiman, 2001; Song and Ying, 2015). A decision tree organizes the prediction process through a hierarchical structure composed of a root node, internal decision nodes, branches, and terminal leaves. At each split, the dataset is partitioned according to a decision rule based on one predictor, with the objective of increasing the homogeneity of the resulting subsets. The final prediction is then associated with the terminal leaf reached by a given input pattern (Friedman, 1977; Breiman et al., 1984; Quinlan, 1986; Song and Ying, 2015). In decision trees, the terminal output is a class label or class probability, whereas in regression trees it is a continuous value, commonly represented by the mean response within the leaf or by a local predictive model (Breiman et al., 1984; Quinlan, 1986; Frank et al., 1998; Song and Ying, 2015). Owing to their nonparametric nature, trees can capture highly nonlinear relationships without imposing a global functional form, while still preserving a transparent rule-based structure that is generally easier to interpret than many black-box alternatives (Breiman et al., 1984; Quinlan, 1986; Song and Ying, 2015).

The historical development of tree-based methods is rich and diversified. Early roots can be traced back to Automatic Interaction Detection (AID), introduced by Morgan and Sonquist (Morgan and Sonquist, 1963), followed by recursive partitioning approaches for classification (Friedman, 1977). A decisive milestone was the Classification and Regression Trees (CART) proposed by Breiman, Friedman, Olshen, and Stone (Breiman et al., 1984), which established the modern formulation of classification and regression trees based on binary recursive splitting and pruning. Quinlan's Iterative Dichotomiser 3 (ID3) and later C4.5 algorithms extended tree induction through information-theoretic criteria and became particularly influential in the machine-learning community (Quinlan, 1986; Quinlan, 1993). Alternative families were subsequently proposed to address specific needs: Chi-squared Automatic Interaction Detection (CHAID) relies on chi-squared tests and naturally allows multiway splits (Kass, 1980); Quick Unbiased Efficient Statistical Tree (QUEST) was designed to reduce variable-selection bias and improve computational efficiency (Loh and Shih, 1997); model trees place local linear models at the leaves instead of constant predictions (Frank et al., 1998); and random forests extend single-tree predictors into an ensemble framework with improved generalization performance (Breiman, 2001). Accordingly, the literature now distinguishes, at least, between decision trees, regression trees, model trees, statistically driven multiway trees such as CHAID, unbiased split-selection trees such as QUEST, and ensemble tree methods (Breiman et al., 1984; Quinlan, 1986; Kass, 1980; Loh and Shih, 1997; Quinlan, 1993; Frank et al., 1998; Breiman, 2001; Song and Ying, 2015).

Beyond their methodological appeal, tree-based methods have already demonstrated their usefulness in several engineering domains. Model trees have been employed for hydrologic forecasting problems, where they showed the ability to provide accurate predictions together with an interpretable piecewise structure (Solomatine and Xue, 2004). In structural and civil engineering, decision-tree-based approaches have been used for seismic damage prediction of reinforced concrete buildings, preliminary vulnerability assessment, and vibration-based damage localization in structural health monitoring (Karbassi et al., 2014; Mariniello et al., 2021; Su and He, 2019). More generally, recent reviews on machine learning for structural engineering have emphasized that tree-based models and their ensemble variants now constitute a relevant class of predictors across structural analysis, monitoring, damage assessment, and material-property estimation tasks (Mariniello et al., 2021; Su and He, 2019; Thai, 2022). These applications are particularly significant because

they highlight two properties that are highly desirable also in structural reliability: fast evaluation and transparent partitioning of complex nonlinear input-output relationships (Mariniello et al., 2021; Su and He, 2019; Thai, 2022).

In the specific field of structural reliability, tree-based surrogates have already begun to attract attention. Keshtegar and Kisi (Keshtegar and Kisi, 2017) proposed an M5 model tree combined with Monte Carlo simulation for efficient structural reliability analysis, showing that a tree-based metamodel can significantly improve computational efficiency while maintaining satisfactory accuracy. The same authors later introduced the RM5Tree approach, in which the training strategy was refined to enhance the predictive capability of the model tree in reliability applications (Keshtegar and Kisi, 2018). These contributions clearly indicate that tree-based surrogates are not only conceptually attractive, but also practically competitive in reliability problems governed by complex and implicit performance functions (Keshtegar and Kisi, 2017; Keshtegar and Kisi, 2018). Nevertheless, much remains to be explored in the use of regression trees as standalone and accurate surrogate models for the estimation of time-dependent survival probabilities associated with dynamical systems excited by stochastic inputs.

Starting from this background, the present study proposes a regression-tree-based method for the rapid estimation of the survival probability of a damped oscillator subjected to white noise excitation. Rather than repeatedly solving the full reliability problem at each query point, the proposed approach trains a regression tree on a sufficiently large dataset so that, once learned, the mapping between the relevant input parameters and the corresponding survival probability can be evaluated in a fraction of a second. In this way, the method aims to retain the reliability information delivered by classical probabilistic analyses while drastically reducing computational time. The predictive capability of the proposed regression-tree-based method is then assessed against Monte Carlo simulations, which are taken as the reference solution for validation. Such a framework is particularly attractive for engineering scenarios in which reliability must be estimated many times under varying conditions, since it combines data-driven speed, limited inference cost, and a naturally interpretable model structure. From this perspective, the proposed method can be viewed as a bridge between rigorous stochastic reliability analysis and fast decision-oriented computational tools suitable for modern structural engineering applications.

2. Classical Structural Reliability Assessment via Monte Carlo Simulation

In this section, some preliminary concepts and definitions are introduced, including the classical method for the structural reliability assessment based on the Monte Carlo simulation.

Consider a damped oscillator, quiescent at $t=0$, excited by a zero-mean Gaussian white noise process. The governing equation of motion is

$$\begin{cases} \ddot{X}(t)+2\zeta_0\omega_0\dot{X}(t)+\omega_0^2X(t)=W(t) \\ X(0)=0 \quad \text{w.p.1} \\ \dot{X}(0)=0 \quad \text{w.p.1} \end{cases}, \tag{1}$$

in which $X(t)$, $\dot{X}(t)$ and $\ddot{X}(t)$ represent the stochastic response process in terms of displacement, velocity and acceleration, respectively, ω_0 is the natural frequency of the oscillator, ζ_0 is the damping ratio, and

$W(t)$ indicates the structural excitation: a zero-mean Gaussian white noise process. The latter is a delta-correlated stochastic process, fully described in probabilistic setting by the correlation function or, equivalently, by the power spectral density (PSD)

$$S_W(\omega) = S_0, \tag{2}$$

being $S_0 > 0$.

The first step of the Monte Carlo simulation consists in the generation of n samples of the input process, performed starting from the PSD by the Shinozuka's formula. Therefore, the *r*-th sample of the structural excitation, labeled as $W^{(r)}(t)$, is expressed in the form

$$W^{(r)}(t) = \sum_{k=1}^{m_c} \sqrt{4 S_W(\omega_k)\Delta\omega}\, \sin\left(\omega_k t + \theta_k^{(r)}\right) \tag{3}$$

in which $\Delta\omega$ is the frequency sampling step, $\omega_k = k\Delta\omega$, $\theta_k^{(r)}$ is the *r*-th realization of a random variable uniformly distributed in $(0, 2\pi)$, and $m_c = \omega_c / \Delta\omega$, being ω_c the sampling frequency.

Once the *r*-th sample of the structural excitation has been generated, the correspondent sample of the response process, labeled as $X^{(r)}(t)$, can be obtained by solving the following differential equation

$$\begin{cases} \ddot{X}^{(r)}(t) + 2\zeta_0\omega_0 \dot{X}^{(r)}(t) + \omega_0^2 X^{(r)}(t) = W^{(r)}(t) \\ X^{(r)}(0) = 0 \\ \dot{X}^{(r)}(0) = 0 \end{cases}. \tag{4}$$

To solve Eq.(4), different numerical techniques can be used. One of the most used is the explicit Runge-Kutta technique: a step-by-step integration that, by discretizing the time axis with a time sampling step Δt, allows to find the solution of Eq.(4) in terms of the state space variable $\mathbf{Y}^{(r)}(t) = \left[X^{(r)}(t) \quad \dot{X}^{(r)}(t)\right]^T$.

When all the n samples of the response process $X(t)$ have been calculated, the structural reliability assessment can be performed. To this end, first of all a value for the absorbing barrier, labeled as $x_{\lim}$, must be selected. Subsequently, for each time instant $t_j = j\Delta t$, examined sequentially from the earliest ($j = 0$) to the latest ($j = n_f$, being $t_{n_f} = n_f \Delta t$ the final time instant of the process), the samples that satisfy the condition

$$\left|X^{(r)}(t_j)\right| \geq x_{\lim} \tag{5}$$

are first identified and counted, and their number is denoted by n_j^{fail}. Once counted, all samples satisfying the condition in Eq.(5) are removed from the process before moving to the next time instant. Finally, the value of the survival probability in t_j, labeled as SP_j, is calculated, for each $j = 1, \ldots, n_f$, as

$$SP_j = 1 - \frac{1}{n}\sum_{u=0}^{j} n_u^{fail} \,. \tag{6}$$

Eq.(6) represents the survival probability in the time instant t_j, i.e. the probability that $\left|X\left(t\right)\right|$ does not exceed the barrier x_{lim} in $\left(0, t_j\right)$.

Although for high values of n the structural reliability assessment performed with the aid of the Monte Carlo simulation allows to obtain accurate results in terms of survival probability, it requires a very high computational burden. Therefore, in the next section, a novel and computationally efficient method for structural reliability assessment, based on regression tree models, is proposed.

3. Development of the Proposed Regression-Tree-Based Method for Structural Reliability Assessment

In order to drastically reduce the computational time required to perform a structural reliability assessment, a regression tree has been properly trained on a very large dataset.

A regression tree is a non-parametric supervised learning model for predicting a continuous response variable. The algorithm operates by recursively splitting the input feature space into smaller, non-overlapping regions. Each split is chosen by selecting the input feature and a threshold that best reduce the prediction error, while each terminal leaf is then associated with a constant prediction (output feature).

The proposed regression-tree-based method allows us to obtain in a fraction of a second, by providing ω_0, ζ_0, S_0, x_{lim}, and t_j as input features, the output feature SP_j.

To construct the dataset required for training the regression tree, a large number (N_{TR}) of different combinations of the input features must be considered, and the corresponding values of the output feature must be generated. To this end, the combinations of the input features have been generated as reported in Figure 1.

To obtain the structural response process necessary for the estimation of the survival probability, which is the output feature needed for training of the regression tree, the relationship

$$S_X\left(\omega\right) = \left|H\left(\omega\right)\right|^2 S_W\left(\omega\right) \tag{7}$$

has been initially used, in which $S_X\left(\omega\right)$ represents the PSD of the structural response process, while $H\left(\omega\right)$ is the frequency response function (FRF) of the structural system which can be evaluated in the form

$$H\left(\omega\right) = \frac{1}{\omega_0^2 - \omega^2 + 2i\zeta_0\omega_0\omega} \,. \tag{8}$$

Once the PSD of the structural response process has been obtained, the formula of Shinozuka can be used to directly generate samples of the structural response as

$$X^{(r)}\left(t_j\right) = \sum_{k=1}^{m_c} \sqrt{4S_X\left(\omega_k\right)\Delta\omega}\,\sin\left(\omega_k t_j + \theta_k^{(r)}\right) \,. \tag{9}$$

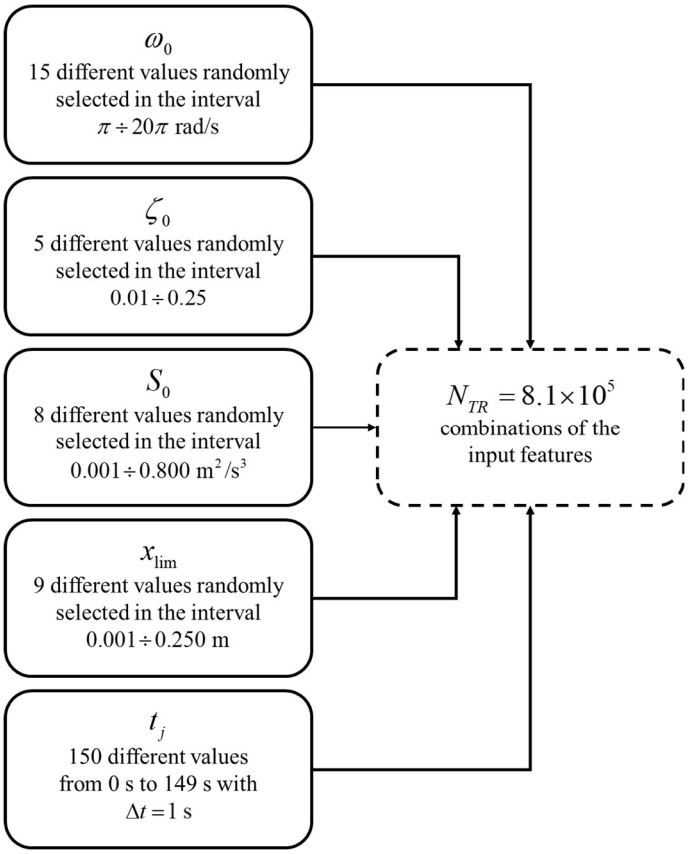


Figure 1. Selection of the input features.

For each value of ω_0, ζ_0, and S_0, a total of 10000 samples of the structural response have been generated with Eq.(9). Then, the survival probability has been evaluated, for each value of x_{lim} and for each value of t_j, as reported in Eq.(6). In this way, the 8.1×10^5 output features necessary to train the regression tree have been generated.

Before the training of the regression tree, the input features were organized into the matrix

$$\mathbf{F}_{IN} = \begin{bmatrix} \omega_0^{(1)} & \zeta_0^{(1)} & S_0^{(1)} & x_{\text{lim}}^{(1)} & t_j^{(1)} \\ \vdots & \vdots & \vdots & \vdots & \vdots \\ \omega_0^{(N_{TR})} & \zeta_0^{(N_{TR})} & S_0^{(N_{TR})} & x_{\text{lim}}^{(N_{TR})} & t_j^{(N_{TR})} \end{bmatrix}, \tag{10}$$

where the $\overline{q}$ -th row represents the $\overline{q}$ -th combination of the input features, being $\overline{q} = 1, \ldots, N_{TR}$. Similarly to the input features, the corresponding values of the output feature were organized into the vector

$$\mathbf{F}_{OUT} = \left[SP_j^{(1)} \quad \cdots \quad SP_j^{(N_{TR})} \right]^T, \tag{11}$$

in which the $\overline{q}$ -th value represents the survival probability associated with the $\overline{q}$ -th combination of the input features.

For the training of the regression tree, the regression learning tool of MATLAB has been used. Specifically, a "fine tree" was selected, with a minimum leaf size equal to four. During the training, both the principal component analysis (PCA) and the surrogate decision splits have been disabled.

After the training, to avoid values of the survival probability major than one or minor than zero, the following restriction has been added

$$SP_j = \begin{cases} 0 & \text{for} \quad SP_j < 0 \\ 1 & \text{for} \quad SP_j > 1 \end{cases}. \tag{12}$$

In the next section, the validation of the proposed regression-tree-based method for structural reliability assessment is reported.

4. Validation of the Proposed Regression-Tree-Based Method and results

In order to validate the proposed regression-tree-based method, $N_{VAL} = 50000$ different combinations of input features were randomly generated by considering the same intervals adopted for the training stage. For each validation combination $q = 1,\ldots,N_{VAL}$, the value of the survival probability was first predicted by the proposed model, thus obtaining $SP_{j(PM)}^{(q)}$. Then, the corresponding value $SP_{j(MC)}^{(q)}$ was evaluated by means of the classical Monte Carlo-based procedure described in Section 2. In this way, two sets of values for the survival probability were obtained and directly compared, over the whole validation set, in Figure 2.

In Figure 2, each point $P^{(q)} = \left(SP_{j(PM)}^{(q)}, SP_{j(MC)}^{(q)}\right)$ represents, simultaneously, the survival provability associated with the *q*-th validation combination of the input features obtained with the proposed method and that obtained from the Monte Carlo simulation. As for the continuous line in Figure 2, it is the least-squares regression line fitted to the points $P^{(q)}$. The slope of the latter represents the Pearson correlation coefficient, which is calculated as

$$\rho = \frac{\sum_{q=1}^{N_{VAL}} \left(SP_{j(PM)}^{(q)} - \mu_{SP_{j(PM)}}\right)\left(SP_{j(MC)}^{(q)} - \mu_{SP_{j(MC)}}\right)}{\sqrt{\sum_{q=1}^{N_{VAL}} \left(SP_{j(PM)}^{(q)} - \mu_{SP_{j(PM)}}\right)^2} \sqrt{\sum_{q=1}^{N_{VAL}} \left(SP_{j(MC)}^{(q)} - \mu_{SP_{j(MC)}}\right)^2}}, \tag{13}$$

being $\mu_{SP_{j(PM)}}$ and $\mu_{SP_{j(MC)}}$ the mean values over the whole validation set of $SP_{j(PM)}^{(q)}$ and $SP_{j(MC)}^{(q)}$, respectively.

In the present case, ρ is equal to 0.9992, thus indicating an almost perfect positive linear correlation between the survival probability estimated with the proposed method and those obtained from the Monte Carlo simulation, Moreover, it can be observed that the points are strongly concentrated around the least-squares regression line: a clear visual evidence of the high predictive accuracy of the proposed regression tree model.

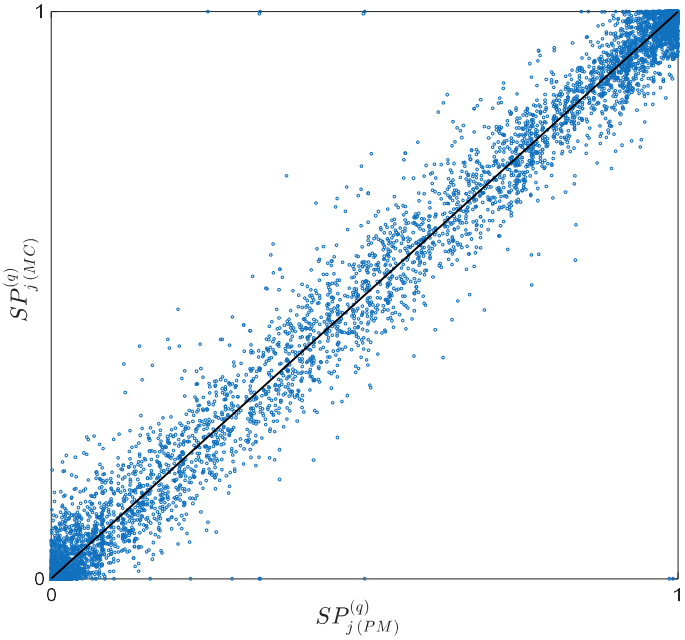


Figure 2. Graphical representation of the points $P^{(q)}$ (circular marker) and least-squares regression line fitted to the points $P^{(q)}$ (continuous line).

To quantify the accuracy, for each point $P^{(q)}$, the absolute difference between the value predicted by the proposed model and the corresponding benchmark value was computed as

$$D^{(q)} = \left| SP_{j(PM)}^{(q)} - SP_{j(MC)}^{(q)} \right|. \tag{14}$$

Then, the percentage of validation combinations for which $D^{(q)}$ is smaller than a selected threshold ε, denoted by P_ε, was evaluated as

$$P_\varepsilon = \frac{100}{N} \sum_{q=1}^{N_{VAL}} \mathbf{1}\left(D^{(q)} < \varepsilon \right), \tag{15}$$

in which

$$\mathbf{1}\left(D^{(q)} < \varepsilon \right) = \begin{cases} 1, & \text{if } D^{(q)} < \varepsilon \\ 0, & \text{if } D^{(q)} \geq \varepsilon \end{cases}. \tag{16}$$

The results obtained are reported in Figure 3.

From Figure 3, it can be observed that 89.89% of the validation combinations exhibit a value of $D^{(q)}$ smaller than 0.01, the 97.07% exhibit a value of $D^{(q)}$ lesser than 0.05, smaller than 0.05, while the 99.39% and the 99.91% exhibit a value of $D^{(q)}$ smaller than 0.1 and 0.2, respectively. These results indicate that the discrepancy between the proposed regression tree model and the benchmark Monte Carlo solution remains very limited for the overwhelming majority of the examined cases.

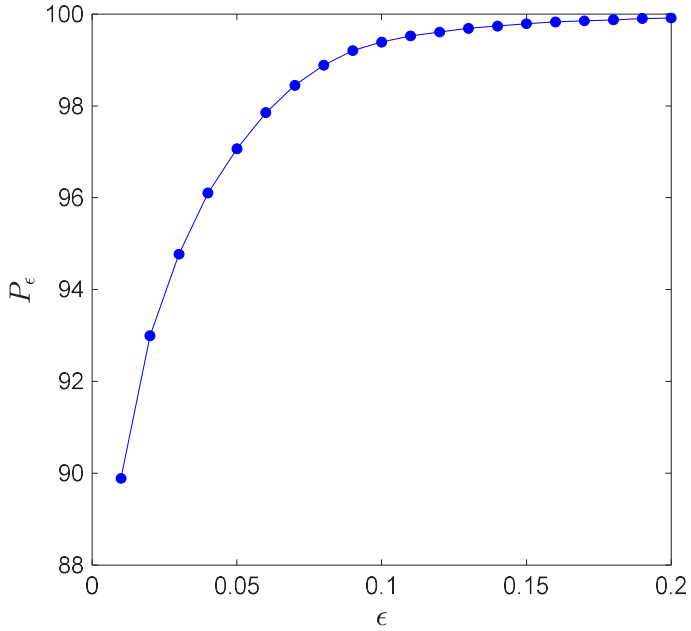


Figure 3. Evaluation of P_ε for different values of ε.

The joint evidence provided by the point concentration around the least-squares regression line in Figure 2, the Pearson correlation coefficient ρ equal to 0.9992, and the distribution of the absolute difference $D^{(q)}$ demonstrates that the proposed regression-tree-based method is capable of predicting the survival probability with high accuracy over the whole considered range of input features. Therefore, the proposed approach can be regarded as a reliable and computationally efficient surrogate tool for the structural reliability assessment of damped oscillators subjected to white noise excitation.

5. Concluding Remarks and Possible Future Developments

In this paper, a novel structural reliability assessment method based on a regression tree has been proposed for the rapid estimation of the survival probability of a damped oscillator subjected to white noise excitation. The main objective of the study was to develop a computationally efficient alternative to classical reliability assessment procedures, which are often associated with a significant computational burden, especially when repeated evaluations are required over a large number of input configurations. In this respect, the proposed approach has shown that, once properly trained, a regression tree can provide the value of the survival probability in a fraction of a second, thus making the estimation process extremely fast and suitable for applications in which computational speed is of primary importance.

The predictive capability of the proposed model has been assessed through a systematic comparison with results obtained by means of Monte Carlo simulation. The comparison has shown a very strong agreement between the predicted values and the reference ones, thereby confirming that the proposed method is able to

retain a high level of accuracy while drastically reducing the required computational effort. These results demonstrate that regression-tree-based models can represent a valid surrogate tool for structural reliability assessment and may constitute a promising bridge between rigorous stochastic analysis and fast engineering-oriented prediction.

Possible future developments may include an extension of the proposed methodology to more general classes of dynamical systems. In particular, a natural continuation of the present research consists in adapting the approach to the prediction of the survival probability of linear and nonlinear multi-degree-of-freedom structural systems subjected to seismic excitation.

References

Afshari, S. S., F. Enayatollahi, X. Xu, and X. Liang. Machine Learning-Based Methods in Structural Reliability Analysis: A Review. Reliability Engineering and System Safety, 219:108223, 2022.

Au, S. K. and J. L. Beck. Estimation of Small Failure Probabilities in High Dimensions by Subset Simulation. Probabilistic Engineering Mechanics, 16(4):263-277, 2001.

Biondini, F. and D. M. Frangopol. Life-Cycle Performance of Deteriorating Structural Systems Under Uncertainty: Review. Journal of Structural Engineering, 142(9):04016068, 2016.

Breiman, L., J. H. Friedman, R. A. Olshen, and C. J. Stone. Classification and Regression Trees. Wadsworth, Belmont, CA, 1984.

Breiman, L. Random Forests. Machine Learning, 45(1):5-32, 2001.

Breitung, K. Asymptotic Approximations for Multinormal Integrals. Journal of Engineering Mechanics, 110(3):357-366, 1984.

Bucher, C., A. Di Matteo, M. Di Paola, and A. Pirrotta. First-Passage Problem for Nonlinear Systems Under Lévy White Noise Through Path Integral Method. Nonlinear Dynamics, 85(3):1445-1456, 2016.

Chen, J. B. and J. Li. Development-Process-of-Nonlinearity-Based Reliability Evaluation of Structures. Probabilistic Engineering Mechanics, 22(3):267-275, 2007.

Cornell, C. A. A Probability-Based Structural Code. ACI Journal, 66:974-985, 1969.

Der Kiureghian, A. and M. De Stefano. Efficient Algorithm for Second-Order Reliability Analysis. Journal of Engineering Mechanics, 117(12):2904-2923, 1991.

Di Matteo, A., M. Di Paola, and A. Pirrotta. Path Integral Solution for Nonlinear Systems Under Parametric Poissonian White Noise Input. Probabilistic Engineering Mechanics, 44:89-98, 2016.

Di Paola, M. and R. Santoro. Non-Linear Systems Under Poisson White Noise Handled by Path Integral Solution. Journal of Vibration and Control, 14(1-2):35-49, 2008.

Ditlevsen, O. and H. O. Madsen. Structural Reliability Methods. John Wiley and Sons, Chichester, 1996.

Doliński, K. First-Order Second-Moment Approximation in Reliability of Structural Systems: Critical Review and Alternative Approach. Structural Safety, 1(3):211-231, 1983.

Frank, E., Y. Wang, S. Inglis, G. Holmes, and I. H. Witten. Using Model Trees for Classification. Machine Learning, 32(1):63-76, 1998.

Friedman, J. H. A Recursive Partitioning Decision Rule for Nonparametric Classification. IEEE Transactions on Computers, 26:404-408, 1977.

Hasofer, A. M. and N. C. Lind. Exact and Invariant Second-Moment Code Format. Journal of the Engineering Mechanics Division, ASCE, 100(1):111-121, 1974.

Karbassi, A., B. Mohebi, S. Rezaee, and P. Lestuzzi. Damage Prediction for Regular Reinforced Concrete Buildings Using the Decision Tree Algorithm. Computers and Structures, 130:46-56, 2014.

Kass, G. V. An Exploratory Technique for Investigating Large Quantities of Categorical Data. Applied Statistics, 29(2):119-127, 1980.

Keshtegar, B. and O. Kisi. M5 Model Tree and Monte Carlo Simulation for Efficient Structural Reliability Analysis. Applied Mathematical Modelling, 48:899-910, 2017.

Keshtegar, B. and O. Kisi. RM5Tree: Radial Basis M5 Model Tree for Accurate Structural Reliability Analysis. Reliability Engineering and System Safety, 180:49-61, 2018.

Kougioumtzoglou, I. A. A Wiener Path Integral Solution Treatment and Effective Material Properties of a Class of One-Dimensional Stochastic Mechanics Problems. Journal of Engineering Mechanics, 143:04017014, 2017.
Kougioumtzoglou, I. A. and P. D. Spanos. Nonstationary Stochastic Response Determination of Nonlinear Systems: A Wiener Path Integral Formalism. Journal of Engineering Mechanics, 140:04014064, 2014.
Kougioumtzoglou, I. A., A. Di Matteo, P. D. Spanos, A. Pirrotta, and M. Di Paola. An Efficient Wiener Path Integral Technique Formulation for Stochastic Response Determination of Nonlinear MDOF Systems. Journal of Applied Mechanics, 82:101005, 2015.
Loh, W. Y. and Y. S. Shih. Split Selection Methods for Classification Trees. Statistica Sinica, 7:815-840, 1997.
Mariniello, G., T. Pastore, C. Menna, P. Festa, and D. Asprone. Structural Damage Detection and Localization Using Decision Tree Ensemble and Vibration Data. Computer-Aided Civil and Infrastructure Engineering, 36(9):1129-1149, 2021.
Melchers, R. E. and A. T. Beck. Structural Reliability Analysis and Prediction. 3rd edition. John Wiley and Sons, Hoboken, NJ, 2018.
Morgan, J. N. and J. A. Sonquist. Problems in the Analysis of Survey Data, and a Proposal. Journal of the American Statistical Association, 58(302):415-434, 1963.
Pirrotta, A. Multiplicative cases from additive cases: Extension of Kolmogorov-Feller equation to parametric Poisson white noise processes. Probabilistic Engineering Mechanics, 22(2):127-135, 2007.
Pirrotta, A. and R. Santoro. Probabilistic Response of Nonlinear Systems Under Combined Normal and Poisson White Noise via Path Integral Method. Probabilistic Engineering Mechanics, 26(1):26-32, 2011.
Quinlan, J. R. Induction of Decision Trees. Machine Learning, 1:81-106, 1986.
Quinlan, J. R. C4.5: Programs for Machine Learning. Morgan Kaufmann, San Mateo, CA, 1993.
Rackwitz, R. Reliability Analysis: A Review and Some Perspectives. Structural Safety, 23(4):365-395, 2001.
Solomatine, D. P. and Y. Xue. M5 Model Trees and Neural Networks: Application to Flood Forecasting in the Upper Reach of the Huai River in China. Journal of Hydrologic Engineering, 9(6):491-501, 2004.
Song, C. and R. Kawai. Monte Carlo and Variance Reduction Methods for Structural Reliability Analysis: A Comprehensive Review. Probabilistic Engineering Mechanics, 73:103479, 2023.
Song, Y. Y. and L. Ying. Decision Tree Methods: Applications for Classification and Prediction. Shanghai Archives of Psychiatry, 27(2):130-135, 2015.
Spanos, P. D. and I. A. Kougioumtzoglou. Response and First-Passage Statistics of Nonlinear Oscillators via a Numerical Path Integral Approach. Journal of Engineering Mechanics, 139(9):1207-1217, 2013.
Su, L. and H. J. He. Decision Tree-Based Seismic Damage Prediction for Reinforcement Concrete Frame Buildings Considering Structural Micro-Characteristics. Advances in Structural Engineering, 22:2097-2109, 2019.
Thai, H. T. Machine Learning for Structural Engineering: A State-of-the-Art Review. Structures, 38:448-491, 2022.
Zhang, Y., I. A. Kougioumtzoglou, and F. Kong. A Wiener Path Integral Technique for Determining the Stochastic Response of Nonlinear Oscillators with Fractional Derivative Elements: A Constrained Variational Formulation with Free Boundaries. Probabilistic Engineering Mechanics, 71:103410, 2023

Probabilistic Resilience Analysis of Urban Road Network Considering Wind Damage to Street Trees via Dimension-Reduced Probability Density Evolution Equation (DR-PDEE)

Yi Luo
Institute for Risk & Reliability, Leibniz University Hannover, Hannover 30167, Germany
Email: yi.luo@irz.uni-hannover.de

De-Cheng Feng
School of Civil Engineering, Southeast University, Nanjing 211189, China
Email: dcfeng@seu.edu.cn

Xiao-Qiu Ai
Shanghai Institute of Disaster Prevention and Relief, Shanghai 200092, China
Email: aixiaoqiu@tongji.edu.cn

Michael Beer
Institute for Risk & Reliability, Leibniz University Hannover, Hannover 30167, Germany
Department of Civil & Environmental Engineering, University of Liverpool, Liverpool L69 3GH, UK
International Joint Research Center for Engineering Reliability & Stochastic Mechanics & International Joint Research Center for Resilient Infrastructure, Tongji University, Shanghai 200092, China
Email: beer@irz.uni-hannover.de

Abstract: A probabilistic framework to quantify the resilience of urban road networks considering the wind blowdown of urban trees is proposed. Various properties of street patterns, including length, speed class, and width, as well as the failure probability due to tree-blowdown are considered. The resilience is considered as the mean normalized efficiency during the reconstruction period, and a reconstruction strategy based on the edge betweenness and estimated edge recovering time is employed. The probability density function (PDF) of the estimated resilience under different wind speed is computed by using the dimension-reduced probability density evolution equation (DR-PDEE). The road network of the Inner-Ring area of Yangpu district, Shanghai, China is considered as an example.

Keywords: Probabilistic resilience; urban street network; wind risks; tree blowdown; Dimension-reduced probability density evolution equation (DR-PDEE).

1. Introduction

Estimation of the resilience of urban systems against various attacks has been a hotspot of research in recent years (Bruneau et al. 2003, Cavallaro et al. 2014, Gao et al. 2016). A key challenge in resilience assessment

© 2026 by the author(s). This work is licensed under the Creative Commons Attribution 4.0 International License (CC BY 4.0), which permits unrestricted use, distribution, and reproduction in any medium, provided the original author and source are credited.

of urban infrastructural systems is the presence of significant uncertainties. Hazard intensity, component vulnerability, post-disaster accessibility, resource availability, and restoration duration may all vary randomly. Accordingly, probabilistic resilience assessment has received increasing attention (Koliou et al. 2020). For example, Kameshwar et al. (2019) developed a probabilistic decision-support framework for community resilience by incorporating multi-hazard effects, infrastructure interdependencies, and resilience goals within a Bayesian-network formulation. Taghizadeh et al. (2023) proposed a probabilistic framework for evaluating transportation-system seismic resilience during emergency medical response by integrating hazard, risk, agent-based emergency response, and network congestion modules. Rincon and Padgett (2024) used probabilistic fragility models to propagate uncertainty from component-level damage to network-level resilience indicators for bridges and transportation-related infrastructure systems. Cao and Feng (2025) proposed probabilistic resilience assessment frameworks for engineering structures by explicitly incorporating uncertainties in functionality, recovery time, and recovery duration. These advances demonstrate the importance of representing resilience as a probabilistic quantity rather than a deterministic index.

In this study, we focus on the road network, one of the most important components of a city, and analyze its resilience considering the wind-blowdown of street trees. The road network of the Inner-Ring-area of Yangpu district, Shanghai city in China is used as an example to illustrate the methods and procedures. Specifically, the probability of road closure due to fallen trees are already given by a developed model (Luo & Ai 2022). The intention of this project is to quantify the resilience of streets in a city as a whole network after wind attacks. The classical definition of the resilience based on the network efficiency is employed (Bruneau et al. 2003). By taking into consideration the road width and speed limit, the transportation efficiency on the basis of travel-time budget is obtained. Then, the resilience of the network at a given damage state can be readily calculated with the assistance of a reconstruction strategy determined jointly by the edge betweenness and edge reconstruction time.

Since the wind damage of roads is a random event, the statistics of resilience are desired. In this context, the dimension-reduced probability density evolution equation (DR-PDEE) (Lyu & Chen 2022) is applied and developed for this problem by constructing a “resilience process”. The reliability and accuracy of the method is verified by pertinent Monte Carlo simulations. The probability density function (PDF) and other statistical quantities of network resilience under different wind speed are obtained and discussed.

2. Resilience of Street Network

2.1 BASIS INFORMATION OF THE NETWORK

A road network with 181 nodes and 298 links, as shown in Figure 1, is considered as an example to demonstrate the method and procedures proposed in this project. The inherent road information required for the network analysis including width (b_i), maximum speed (v_i), edge length (L_i), and node coordinates (x_i, y_i) are predefined according to the real situation, and assigned to each edge.

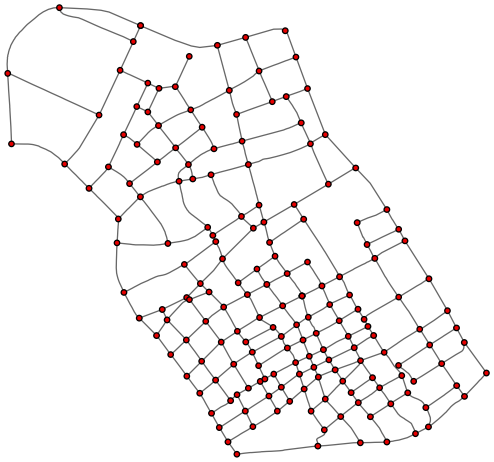


Figure 1. Network Topology.

The dominant tree species and tree height of each road should also be predetermined, but since the data is not available yet, the tree species and heights are assigned according to assumed distributions in this illustrative case study. Each edge is assumed to comprise only one tree species and one dominant tree height. Based on a wind fragility assessment model of trees, the failure probability of a single tree P_{T_i} can be obtained, and the edge failure probability is given by

$$P_i = 1 - \left(1 - P_{T_i}\right)^{N_i/N_c}. \tag{1}$$

In this equation, P_i is the failure probability of edge i; N_i is the number of trees in edge i, and is determined by $N_i = \left\{L_i/6.5\right\} \times 2$, where $\{\cdot\}$ denotes rounding-numbers, L_i is the length of the edge in meters; N_c is the number of trees whose performance are considered to be strongly connected. In this example, N_c is taken as 20.

A dangerous index (DI_i) is also allocated to each edge according to their dominant tree species and height. It is a number between 0 and 4, and will work as an essential factor for the reconstruction strategy in following calculation of network resilience.

2.2 TRAVEL-TIME BASED EFFICIENCY

Since in transportation networks, the travel time, instead of the physical distance, is a more logical measure for the "shortest path", with respect to human drivers' intuition (Lämmer et al. 2006), the global efficiency of a street network is determined based on the travel time budget. That is,

$$Eff = \frac{1}{N\left(N-1\right)} \sum_{i,j \in \aleph, i \neq j} \frac{\tau_{ij}^{\text{eucl}}}{\tau_{ij}}. \tag{2}$$

In this equation, N is the number of nodes; $\aleph$ denotes the set of all nodes. τ_{ij} denotes the shortest path between node i and j regarding the travel-time budget. The travel-time budget of each edge is calculated as

$$\tau_i = \frac{L_i}{\alpha_i v_i}, \tag{3}$$

where v_i is the speed limit, which takes value from $[40, 60, 70]$ km/h; α_i is a coefficient representing the influence of the street width to the travel speed, which is 0.7, 1, and 1.5 for narrow, medium, and wide street respectively. Note that the "travel-time budget" used here does not represent any "real" travel time, and it only makes sense in terms of relative value. τ_{ij}^{eucl} is a term to normalize pair-wise efficiency over all possible pairs of nodes, and it is defined as

$$\tau_{ij}^{\text{eucl}} = \frac{\sqrt{\left(x_i - x_j\right)^2 + \left(y_i - y_j\right)^2}}{70 \times 1.5}, \tag{4}$$

such that $\tau_{ij}^{\text{eucl}} / \tau_{ij}$ is always between 0 and 1.

2.3 MEASURE OF RESILIENCE

The classical definition of urban resilience is employed here, that is (Bruneau et al. 2003)

$$R = \frac{\int_{t_1}^{t_2} Y(t)\,\mathrm{d}t}{t_2 - t_1}, \tag{5}$$

where $Y(t)$ is the recovery function, t_1 and t_2 are respectively the starting time and completed time of the recovery process.

The recovery function $Y(t)$ is defined as the ratio between real-time efficiency $Eff(t)$ and the efficiency of the original network Eff_0, namely,

$$Y(t) = Eff(t) / Eff_0 . \tag{6}$$

If no damage occurs, the resilience R is set to be one. Notice that R depends on both the total damage and the reconstruction strategy. Because the intention of the project is not to compare the performance of different recovery strategies, but to assess the performance of the network subjected to different wind speed, only one reconstruction strategy is employed and will be soon introduced.

2.4 RECONSTRUCTION STRATEGY

In this project, a relative inflexible scheme is employed to simulate the reconstruction procedure for all the damaged networks. That is, the damaged edges are repaired one by one, and the sequence of the edges to be recovered has been pre-determined based on their relative "importance" and the order of difficulty to repair.

The "importance" is measured by travel-time-based edge betweenness, namely:

$$B_i = \sum_{s,t \in \mathbb{N}} \frac{n_{st}(i)}{N_{st}}, \tag{7}$$

where $n_{st}(i)$ is the number of shortest paths from node s to t that pass through edge i, N_{st} is the total number of shortest paths from node s to t.

The difficulty to repair is quantified by the estimated reconstruction time, which is a pseudo variable specifically constructed in this project. It is calculated as

$$RT_i = \ln\left(\frac{DI_i \cdot L_i}{100}+1\right)\Big/10\,. \tag{8}$$

Notice that similar as the travel-time budge τ_i, the reconstruction time RT_i only makes sense with respect to relative value, as well.

The order of edge reconstruction is determined by the order of B_i/RT_i, so that the edges of higher "importance" and with less reconstruction effort will be recovered earlier.

After determined the reconstruction strategy, the resilience can be calculated accordingly. However, since the total damage is a random event, the resilience at a given wind speed should be a random variable. Therefore, its statics, such as mean value, probability density function, and quantiles, are of concern. They will be analyzed in the next section.

3. Statistical Analysis of Resilience Based on DR-PDEE

In this section, the statistics of network resilience at different wind speed will be analyzed. Since the probability density function (PDF) is much more informative than statistical moments such as mean and standard deviation, it is the object we desired. However, using crude Monte Carlo Simulation to obtain the PDF is too time-consuming, even for the small network considered in this simple example. Therefore, the recently developed dimension-reduced probability density evolution equation (DR-PDEE) (Lyu & Chen 2022) technique is further developed to tackle the problem more efficiently.

3.1 FORMULATION OF DR-PDEE

For any one-dimensional continuous stochastic process $X(t)$ (the continuity of a stochastic process is defined by the Lindeberg's condition (Gardiner 2004)), its PDF $p_X(x,t)$ satisfies the following equation:

$$\frac{\partial p_X}{\partial t} = -\frac{\partial\left[a^{(\mathrm{int})}(x,t)\,p_X\right]}{\partial x}+\frac{1}{2}\frac{\partial^2\left[b^{(\mathrm{int})}(x,t)\,p_X\right]}{\partial x^2}, \tag{9}$$

where

$$a^{(\mathrm{int})}(x,t) = \lim_{\Delta t\to 0}\frac{1}{\Delta t}\mathrm{E}\left[\Delta X \middle| X(t)=x\right], \tag{10}$$

$$b^{(\mathrm{int})}(x,t) = \lim_{\Delta t\to 0}\frac{1}{\Delta t}\mathrm{E}\left[(\Delta X)^2 \middle| X(t)=x\right], \tag{11}$$

and $\Delta X = X(t+\Delta t)-X(t)$. Equation (9) is just the DR-PDEE for general continues random process (Lyu & Chen 2022). $a^{(\mathrm{int})}(x,t)$ and $b^{(\mathrm{int})}(x,t)$ is referred to as the intrinsic drift and diffusion coefficients, respectively.

3.2 DR-PDEE for determining the PDF of Resilience

The DR-PDEE is suitable for determine the time-varying probability of a stochastic process. The Resilience $R(\boldsymbol{\Theta})$, however, is a random variable determined by several random parameters $\boldsymbol{\Theta}$. Specifically, in this example, the random parameters are the performance of each edge, that is, $\boldsymbol{\Theta}=[\Theta_1,\Theta_2,\cdots,\Theta_m]$, where m is the total number of edges, and Θ_i, $i=1,\cdots,m$ are independent 0-1 variables. In this context, a process based on Equation (5) is constructed, that is

$$R(\boldsymbol{\Theta},t)=\begin{cases}\dfrac{\int_0^t Y(\boldsymbol{\Theta},\tau)\,\mathrm{d}\tau}{T_r(\boldsymbol{\Theta})}, & t<T_r(\boldsymbol{\Theta})\\ \dfrac{\int_0^{T_r(\Theta)} Y(\boldsymbol{\Theta},\tau)\,\mathrm{d}\tau}{T_r(\boldsymbol{\Theta})}, & t\geq T_r(\boldsymbol{\Theta})\end{cases}. \tag{12}$$

In this equation, $T_r(\boldsymbol{\Theta})$ denotes the total reconstruction time, and $R(\boldsymbol{\Theta},t)$ is defined as the resilience process.

Considering the DR-PDEE of $R(\boldsymbol{\Theta},t)$, one obtains

$$a^{(\mathrm{int})}(r,t)=\mathrm{E}\left[\dot{R}(t)\middle|R(t)=r\right], \tag{13}$$

$$b^{(\mathrm{int})}(r,t)=\lim_{\Delta t\to 0}O(\Delta t)=0, \tag{14}$$

and

$$\dot{R}(\boldsymbol{\Theta},t)=\begin{cases}\dfrac{Y(\boldsymbol{\Theta},\tau)}{T_r(\boldsymbol{\Theta})}, & t<RT(\boldsymbol{\Theta})\\ 0, & t\geq RT(\boldsymbol{\Theta})\end{cases}. \tag{15}$$

Consequently, the DR-PDEE in the form of equation (9) can be cast as

$$\frac{\partial p_R(r,t)}{\partial t}=-\frac{\partial\left[a^{(\mathrm{int})}(r,t)\,p_R(r,t)\right]}{\partial r}. \tag{16}$$

Equation (16) has a form similar to Liouville equation, and can be easily solved numerically. Notice that the intrinsic drift coefficient $a^{(\mathrm{int})}(r,t)$ is still implicit. Since its nature is the conditional mean function, it is estimated from samples at each time instant in the following analysis by using the locally weighted smoothing scatterplots (Lyu & Chen 2021). Figure 2 shows a typical example of the fitting result.

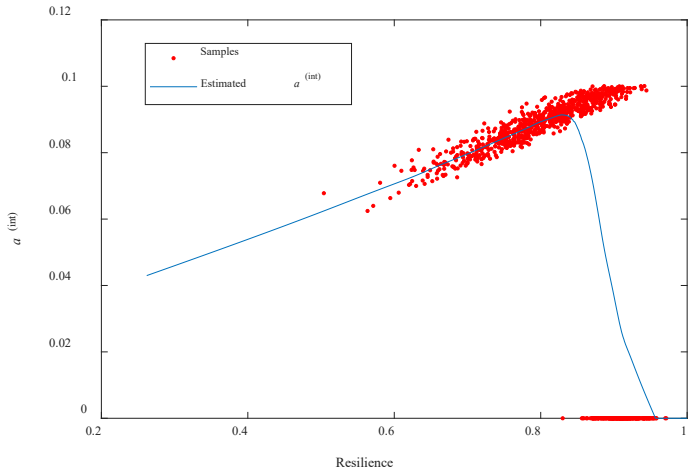


Figure 2. Typical fitting result of $a^{(\mathrm{int})}(r,t)$.

3.3 NUMERICAL RESULTS

In this section, the PDFs of resilience are solved by the DR-PDEE when the mean wind speed at 10m heigh U_{10} of the region considered is set to be 10 m/s, 15 m/s, 20 m/s, …, 40 m/s respectively.

Before proceeding to the final results, the reliability of the DR-PDEE is verified by comparing the PDF obtained by the DR-PDEE when $U_{10} = 20$ m/s with pertinent Monte Carlo simulations. The results are shown in Figure 3. 1000 samples are used for estimating the $a^{(\mathrm{int})}(r,t)$ of the DR-PDEE. It is obvious that the PDF obtained by the DR-PDEE agrees well with the results of MCS with 10^5 samples, and is much better than the PDF directly obtained from the 1000 samples.

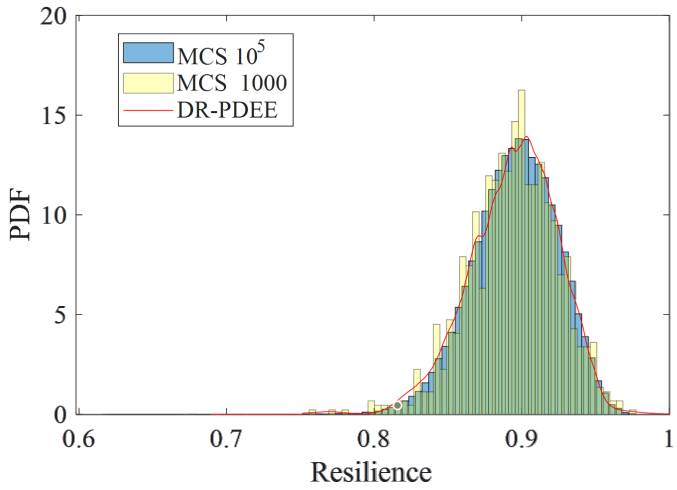


Figure 3. Comparison of the PDFs of resilience when $U_{10} = 20$ m/s .

Next, the PDFs under each wind condition are calculated by the DR-PDEE, see Figure 4 and Figure 5. Notice that the peak value of the PDF when $U_{10} = 10$ m/s is much higher than others, so it is plotted individually.

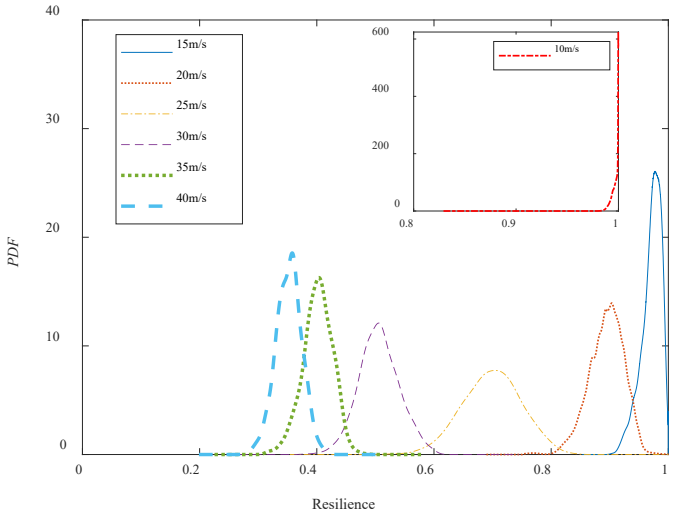


Figure 4. PDFs of resilience at different mean wind speeds.

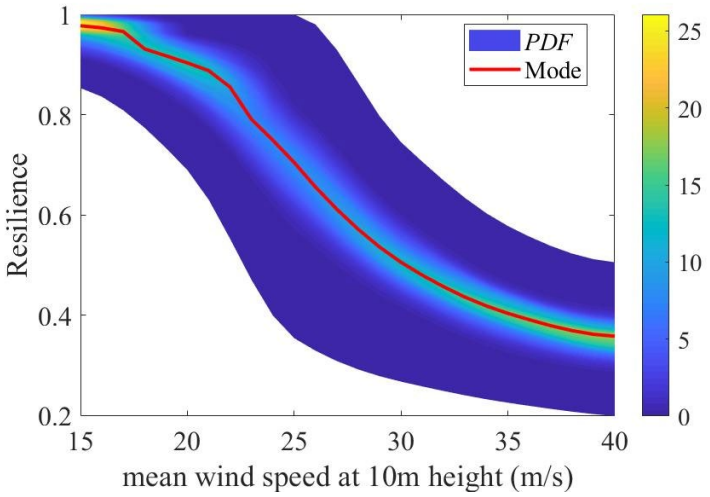


Figure 5. PDFs and modes of resilience at different mean wind speeds.

Except for the PDF results, the mean value and the quantiles may be more intuitive in engineering practice. For instance, the 10% quantile means that with a probability of 90%, or in other word, with a confidence level of 90%, the resilience of the network is higher than that value. Figure 6 shows the means and quantiles of the resilience under different mean wind speeds. It can be seen that the resilience approaches

to 1 at $U_{10} = 10$ m/s, and decreases with the increase of U_{10} in general. This is consistent with common sense. From Figure 4 and Figure 6, it is also obvious that the variability of the resilience is large for medium wind speed (around 25 m/s), and is small for very small or large wind.

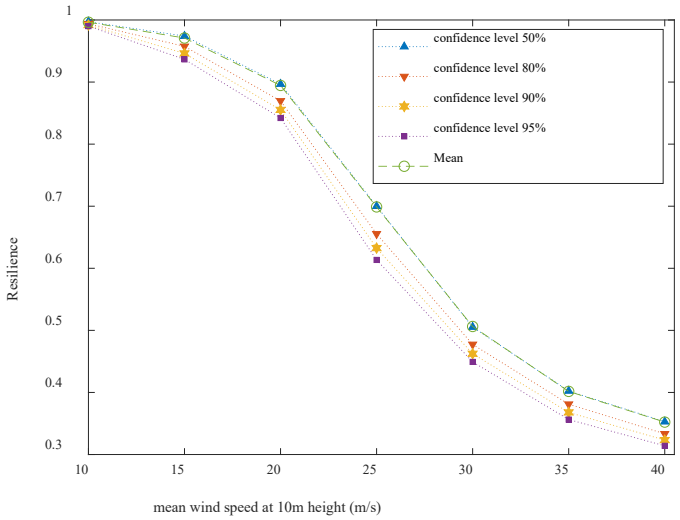


Figure 6. Means and quantiles of resilience at different mean wind speeds.

4. Concluding Remarks

In this study, a procedure to quantify the value and uncertainty of the resilience of urban road network considering the wind damage to street trees is proposed. Several steps have been taken.

(1) The classical definition of resilience is employed to quantify the resilience of the urban road network. When uncertainties of various input sources are considered, the statistics of the resilience indicator can be obtained.

(2) A method based on the dimension-reduced probability density is proposed to calculate various statistics of the resilience efficiently. Comparison with pertinent Monte Carlo simulations illustrates the reliability of the proposed method.

(3) The resilience under different wind speed is quantified and expressed by various means. Specially, the resilience values of different confidence level are obtained.

References

Der Kiureghian, A. & Dakessian, T. 1998. Multiple design points in first and second-order reliability. *Structural Safety* 20(1): 37-49.

Ditlevsen, O. & Madsen, H.O. 1996. *Structural Reliability Methods*. New York: John Wiley & Sons.

Bucher, C. 2009. Computational analysis of randomness in structural mechanics. In D.M. Frangopol (Ed.), *Structures and Infrastructures Book Series*, Vol. 3, London: Taylor & Francis, pp. xxx-xxx.

Bruneau, M. et al. 2003. A Framework to Quantitatively Assess and Enhance the Seismic Resilience of Communities. *Earthquake Spectra,* 19(4):733–752.

Cao, X. Y., & Feng, D. C. (2025). Probabilistic resilience assessment framework of structures considering the combined functionality-recovery-duration uncertainty. *Mechanical Systems and Signal Processing*, *223*, 111856.

Cavallaro, M. et al. 2014. Assessment of Urban Ecosystem Resilience through Hybrid Social-Physical Complex Networks. *Computer-Aided Civil and Infrastructure Engineering,* 29(8):608–625.

Gao, J. Barzel, B. & Barabási A.L. 2016. Universal Resilience Patterns in Complex Networks. *Nature,* 530(7590):307–312.

Gardiner, C.W. 2004. *Handbook of Stochastic Methods*. Berlin Heidelberg: Springer-Verlag.

Kameshwar, S., Cox, D. T., Barbosa, A. R., Farokhnia, K., Park, H., Alam, M. S., & van de Lindt, J. W. (2019). Probabilistic decision-support framework for community resilience: Incorporating multi-hazards, infrastructure interdependencies, and resilience goals in a Bayesian network. *Reliability Engineering & System Safety*, *191*, 106568.

Koliou, M., van de Lindt, J. W., McAllister, T. P., Ellingwood, B. R., Dillard, M., & Cutler, H. (2020). State of the research in community resilience: Progress and challenges. *Sustainable and resilient infrastructure*, *5*(3), 131-151.

Lämmer, S. Gehlsen, B. & Helbing, D. 2006. Scaling Laws in the Spatial Structure of Urban Road Networks. *Physica A: Statistical Mechanics and Its Applications,* 363(1):89–95.

Luo, Y., & Ai, X. (2022). Wind risk assessment of urban street trees based on wind-induced fragility. *Disaster Prevention and Resilience*, *1*(2), N-A.

Lyu, M.Z. & Chen J.B. 2021. First-Passage Reliability of High-Dimensional Nonlinear Systems under Additive Excitation by the Ensemble-Evolving-Based Generalized Density Evolution Equation. *Probabilistic Engineering Mechanics,* 63 (2021):103119

Lyu, M.Z. & Chen J.B. 2022. A unified formalism of the GE-GDEE for generic continuous responses and first-passage reliability analysis of high-dimensional nonlinear systems subjected to non-white noise excitations. *Structural Safety,* 98:102233.

Rincon, R., & Padgett, J. E. (2024). Fragility modeling practices and their implications on risk and resilience analysis: From the structure to the network scale. *Earthquake spectra*, *40*(1), 647-673.

Taghizadeh, M., Mahsuli, M., & Poorzahedy, H. (2023). Probabilistic framework for evaluating the seismic resilience of transportation systems during emergency medical response. *Reliability Engineering & System Safety*, *236*, 109255.

SESSION 8

Rare Events, Reliability and Optimization

Papers in this session

1. A computationally efficient framework for the propagation of interval-process uncertainty
2. A practical stratified importance sampling strategy for extremely rare event estimation in high dimensional systems
3. Uncertainty Analysis of Fatigue Failure Using a Fuzzy Approach
4. A Weighted Extreme Value Moment Method Using Adaptive Sparse Grids for Time-Variant Reliability-Based Design Optimization
5. Efficient robust topology optimization of large-scale continuum structures under load uncertainty
6. A Bayesian Framework for Modeling and Testing the Temperature-Dependent Residual Compressive Strength of Concrete
7. Optimal-Transport Flow Matching for Stochastic Model Updating: A Comparison with Transitional MCMC-based Bayesian Updating

A computationally efficient framework for the propagation of interval-process uncertainty

Rongyao Song, Changcong Zhou *
Department of Engineering Mechanics, Northwestern Polytechnical University, Xi'an 710129, China
E-mail: changcongzhou@nwpu.edu.cn

Abstract: Computing the lower and upper boundaries of a response interval process is essential for interval uncertainty propagation over a continuous evolution variable, but conventional discretization-optimization schemes require repeated inner extremum searches at many state points and are costly for complex models. This paper develops a dual-layer Bi-Extremum Alternating Surrogate (BEAS) framework. In the inner layer, the expected-improvement criteria for minimization and maximization are coupled within a shared Kriging-based Efficient Global Optimization framework, so the minimum and maximum responses at a fixed state point are found using one surrogate model and one training set. In the outer layer, an alternating strategy updates the two boundary surrogates in half-steps: the by-product extremum of every inner call is delivered to the opposite boundary and, subject to a distance-based screening rule, injected into its training set, with a buffer as a zero-cost fallback, so both extrema of each expensive call are exploited. On two analytical examples, BEAS reproduces the boundaries of conventional double-loop calculations while markedly reducing inner-layer calls and performance-function evaluations.
Keywords: Interval process, Bi-extremum optimization, boundary surrogate, alternating surrogate.

1. Introduction

In engineering systems, input parameters are often uncertain because of manufacturing errors and material variations (Wei et al., 2017). When data are insufficient to fix an exact probability distribution, interval models give a non-probabilistic description that needs only the parameter bounds, with no assumption on distribution type or statistical moments (Faes et al., 2017; Guo and Lu, 2015). They therefore suit cases such as manufacturing and assembly tolerances in moving mechanisms (Tang et al., 2021; Wu and Rao, 2007) and constraints in optimization design (Wang et al., 2021; Niu et al., 2024), and have become an effective tool for cognitive uncertainty.

To describe how the output evolves as one input varies continuously within its range, Chang et al. (2022) introduced the interval process: the other inputs are fixed as interval variables while the target input varies continuously, so the output becomes an evolving interval band rather than a static interval. Song et al. (2024) extended this to time-varying systems. In such a response interval process the upper and lower boundaries are the maximum and minimum of all possible outputs at each state point, and computing them efficiently remains an open problem.

The discretization-optimization method is the general framework for interval-process boundaries: the evolution domain is discretized into state points and a global optimizer is run at each point to obtain the minimum and maximum outputs. For finite-element and other expensive models the number of simulations becomes prohibitive, which motivates surrogate modeling. Kriging is widely used because it provides both a predictive mean and a variance (Kleijnen, 2009). Kriging-based efficient global optimization (EGO), with improved learning functions, has been applied successfully to expensive black-box minimization (Shahriari et al., 2016; Mockus, 2012; Forrester and Keane, 2009); at each iteration EGO adds the point of maximum expected improvement (EI), reaching the optimum with few evaluations.

The standard EGO still struggles on complex problems, and several improvements exist. Mohammadi et al. (2016) used a small-scale Kriging ensemble to adapt the sampling scale for parallel expensive optimization. Liu et al. (2023) modified the EI criterion with a balancing factor to escape local optima on multimodal objectives. For high-dimensional problems, KT-EGO (Wang et al., 2023) extends EGO beyond twenty dimensions through knowledge transfer, reducing calls to expensive simulations. These works broaden the applicability and efficiency of EGO in engineering.

Progress has also been made on interval uncertainty using surrogates and adaptive sampling. Yao et al. (2024) proposed an interval finite element method based on a bilevel Kriging model for structures with spatially uncertain parameters. Ni et al. (2020) combined the interval process with Kriging and a variance-

© 2026 by the author(s). This work is licensed under the Creative Commons Attribution 4.0 International License (CC BY 4.0), which permits unrestricted use, distribution, and reproduction in any medium, provided the original author and source are credited.

based adaptive sampling scheme, but updated the two boundaries independently using only prediction variance, ignoring the nature of extremum solving. Zhan and Xiao (2025) introduced an active-learning surrogate for time- and space-dependent reliability. These works mainly target failure probability rather than response boundaries. Two limitations thus remain: at the inner layer the two extrema are found by separate optimizations that duplicate expensive evaluations, and at the outer layer the two boundary surrogates are built independently, so extremum information for one boundary is not reused by the other.

To address these issues, this paper develops a dual-layer Bi-Extremum Alternating Surrogate (BEAS) method. The first contribution is an inner-layer bi-extremum strategy: within a Kriging-based EGO framework, the conventional EI criterion for minimization is paired with a directly formulated EI criterion for maximization, so both extrema at a state point are found from one surrogate and one training set. The second is an outer-layer alternating strategy: each iteration has two half-steps, one per boundary, in which state points are chosen by predictive variance and an inner call is spent only after absorbing the free by-product from the opposite half-step. Each by-product is injected into the opposite training set under a distance-based screening rule that protects the Kriging conditioning, with screened-out values buffered for later zero-cost retrieval. The two surrogates are refined alternately until both meet a normalized convergence criterion.

The remainder of this paper is organized as follows. Section 2 defines the response interval process and reviews existing boundary-evaluation frameworks. Section 3 formulates the inner-layer bi-extremum optimization strategy at a fixed state point. Section 4 develops the alternating boundary surrogate framework and assembles the complete BEAS method. Section 5 presents numerical examples and discussion, and Section 6 concludes the paper.

2. Response interval process and existing computational frameworks

This section defines the response interval process and reviews the main frameworks for its boundary evaluation. Here the term denotes an interval-valued response evolving with respect to a continuous independent variable, which may be physical time, spatial position, a design parameter, or the nominal value of an interval input; the formulation is thus not restricted to evolving systems.

2.1 Mathematical definition of the response interval process

A computational model is rigorously defined through a deterministic continuous real-valued function, with its mathematical formalism expressed as follows,

$$Y = f\left(\boldsymbol{X}, s\right), s \in \left[s_0, s_e\right] \tag{1}$$

where Y represents the response of interest in the model, $f\left(\boldsymbol{X}, s\right)$ is the performance function being analyzed. The vector $\boldsymbol{X} = \left(X_1, X_2, \cdots, X_n\right)^{\mathrm{T}}$ denotes the n-dimensional input variables, and the variable s denotes a continuous evolution variable. It is important to note that s and $\boldsymbol{X}$ are independent of each other.

Assuming that the model input $\boldsymbol{X}$ is uncertain and its available information is insufficient or incomplete, the input uncertainty can be quantified through the interval model. The uncertainty of an input X_i is represented as an interval variable as follows,

$$X_i^I = \left[X_i^l, X_i^u\right] = \left[X_i^c - X_i^r, X_i^c + X_i^r\right] \tag{2}$$

where the superscripts I, l and u denote the interval, lower bound and upper bound of X_i, respectively, and X_i^c is a nominal value of x_i within this interval. X_i^c is the midpoint of X_i^I, and X_i^r is the radius of X_i^I.

As shown in Fig. 1(a), when input uncertainty is represented using interval variables, the model response will also give rise to an interval at any given state point, i.e., $Y^I\left(s_j\right)$, which can be formulated as follows,

$$Y^I\left(s_j\right) = \left[Y^l\left(s_j\right), Y^u\left(s_j\right)\right] = \left[\min_{\boldsymbol{X} \in \boldsymbol{X}^I} f\left(\boldsymbol{X}, s_j\right), \max_{\boldsymbol{X} \in \boldsymbol{X}^I} f\left(\boldsymbol{X}, s_j\right)\right] \tag{3}$$

where $Y^l\left(s_j\right)$ and $Y^u\left(s_j\right)$ represent the minimum and maximum values of the output at the given state point s_j. Note that when the evolution variable s is fixed at a special state point s_j, the performance function depends solely on the vector $\boldsymbol{X}$.

Since the evolution variable s maintains continuity throughout the entire evolution process, the output uncertainty of the model is an interval process **Error! Reference source not found.**, which is shown in Fig. 1(b). The mathematical formula for this interval process is defined as follows,

$$Y^I(s)=\left[Y^l(s),Y^u(s)\right],s\in[s_0,s_e] \tag{4}$$

where $Y^l(s)$ is the lower boundary function, representing the minimum output of all possible outputs throughout the evolution process, $Y^u(s)$ is the upper boundary function, representing the maximum output of all possible outputs throughout the evolution process. As shown in Fig. 1(c), the interval process is surrounded by two consecutive boundary lines, representing that all possible outputs always fall within the region of the interval process.

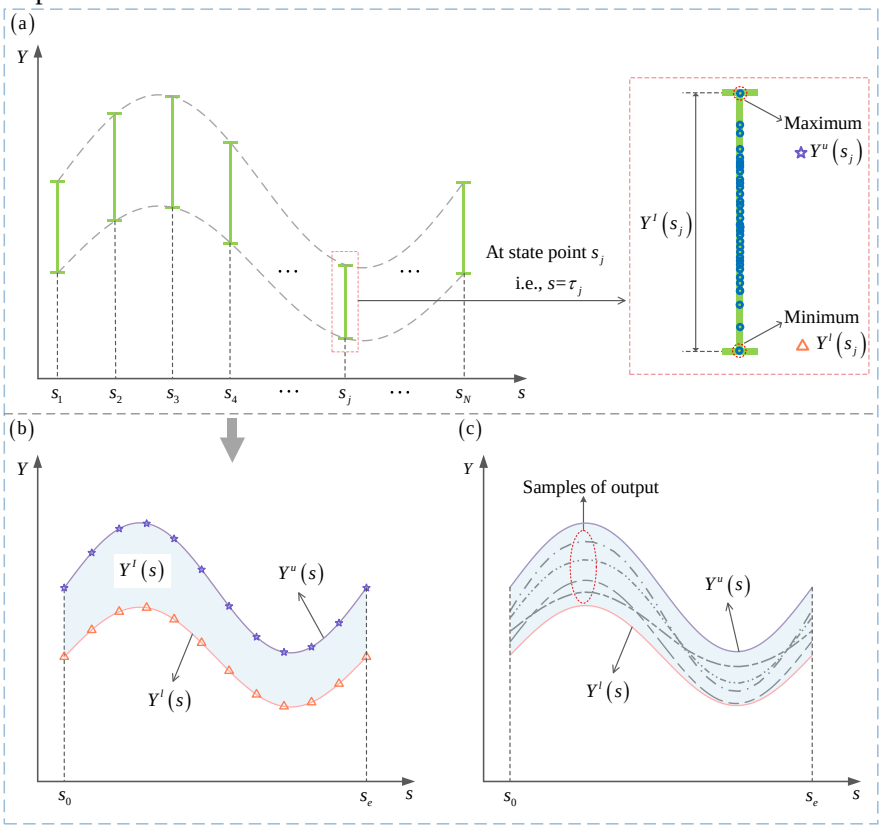


Fig. 1 Illustration of the response interval process

The response uncertainty is thus the region enclosed by the two boundaries. This interval process is related to the non-probabilistic convex model process (Jiang et al., 2014) for time-variant analysis, but here the focus is the interval process induced in the response rather than the correlation structure of interval inputs across states.

2.2 Discretization-optimization method

A direct way to compute the boundaries of a response interval process is the discretization-optimization method. This method discretizes the evolution domain into a set of state points and solves two static optimization problems at each state point to obtain the lower and upper response bounds.

Let the evolution domain $[s_0,s_e]$ be a closed and continuous interval. A finite set of state points is constructed via the discretization as follows,

$$\boldsymbol{S}=\left\{s_j\,\middle|\,s_j=s_0+(j-1)\Delta s,\ j=1,\cdots,N\right\},\Delta s=\frac{s_e-s_0}{N-1} \tag{5}$$

where N is the number of discretized state points, and Δs is the discretization step size. At each discretized state point s_j, two static optimization problems are solved to obtain the minimum value $Y^l(s_j)$ and the maximum value $Y^u(s_j)$ of the response, i.e.,

$$Y^l(s_j) = \min_{\boldsymbol{X} \in \boldsymbol{X}^I} f(\boldsymbol{X}, s_j) \tag{6}$$

and

$$Y^u(s_j) = \max_{\boldsymbol{X} \in \boldsymbol{X}^I} f(\boldsymbol{X}, s_j) \tag{7}$$

They can be solved by existing optimization algorithms (e.g., particle swarm optimization (PSO) **Error! Reference source not found.** or the genetic algorithm (GA) **Error! Reference source not found.**). As the discretization density increases, i.e., $m \to \infty$, the two sets of extrema asymptotically converge to the two boundaries, i.e.,

$$\lim_{m\to\infty} Y^l(s_j) = Y^l(s), \quad \lim_{m\to\infty} Y^u(s_j) = Y^u(s) \tag{8}$$

where $Y^l(s_j)$ and $Y^u(s_j)$ represent the values of the true lower boundary function $Y^l(s)$ and the true upper boundary function $Y^u(s)$ at the state point s_j. This methodology transforms the continuous boundary computation into $2m$ parameterized static optimization problems. Assuming that computing the minimum and maximum values at a single state point requires N_j^l and N_j^u evaluations of the performance function, the computational costs for determining the lower and upper boundaries are $N_l = \sum_{j=1}^{m} N_j^l$ and $N_u = \sum_{j=1}^{m} N_j^u$, respectively. However, in the context of engineering problems involving finite element analysis, each evaluation of the performance function may correspond to a time-consuming simulation, and the total number of evaluations required by the repeated inner optimizations quickly becomes unacceptable. To alleviate this computational burden, surrogate-based boundary approximation methods have been developed in recent studies, which are reviewed in the following subsection.

2.3 Surrogate-based boundary approximation

Although straightforward, the discretization-optimization method grows costly as the number of state points and the cost per inner optimization increase. Surrogate-based boundary approximation instead treats the lower and upper boundaries as unknown functions of the evolution variable and approximates them adaptively with surrogates such as Kriging (Kleijnen, 2009), radial basis functions (Buhmann, 2003), or neural networks (Hornik et al., 1989).

Building on the boundary function definitions given above, surrogate-based boundary approximation aims to learn the functional dependence of the two response boundaries on the evolution variable, rather than evaluating them at all discretized state points. Let $\hat{Y}^l(s)$ and $\hat{Y}^u(s)$ denote the surrogate models of the lower and upper response boundaries, respectively. They are constructed from two sets of boundary samples,

$$\boldsymbol{D}_l = \left\{\left(s_j^l, Y^l(s_j^l)\right)\right\}_{j=1}^{N_l}, \quad \boldsymbol{D}_u = \left\{\left(s_j^u, Y^u(s_j^u)\right)\right\}_{j=1}^{N_u} \tag{9}$$

and provide the approximations as follows.

$$Y^l(s) \approx \hat{Y}^l(s), \quad Y^u(s) \approx \hat{Y}^u(s), s \in \boldsymbol{S} \tag{10}$$

A typical framework is two-layered. In the inner layer, an optimizer searches the interval input space at a fixed state point for the lower or upper extremum; in the outer layer, the boundary surrogate is updated over the evolution domain, with new state points chosen by an adaptive criterion, commonly the predictive variance (Jones et al., 1998), and true boundary values supplied by the inner-layer optimization. For the two boundaries the adaptive enrichment selects a new state point by a learning function as follows,

$$s_{N_l+1}^l = \arg\max_{s \in \boldsymbol{S}_l} \alpha_l(s), \quad s_{N_u+1}^u = \arg\max_{s \in \boldsymbol{S}_u} \alpha_u(s) \tag{11}$$

where $\boldsymbol{S}_l$ and $\boldsymbol{S}_u$ are the candidate sets for the lower and upper boundary surrogates, $\alpha_l(s)$ and $\alpha_u(s)$ are the corresponding learning functions. In variance-based adaptive sampling, the learning functions are commonly defined from the predictive uncertainty of the surrogate model, i.e.,

$$\alpha_l(s) = \sigma_l^2(s), \quad \alpha_u(s) = \sigma_u^2(s) \tag{12}$$

where $\sigma_l^2(s)$ and $\sigma_u^2(s)$ denote the predictive variances of the two boundary surrogates. After a new state point is selected, the corresponding true boundary value is obtained by invoking the inner-layer optimization, and the sample is added to $\boldsymbol{D}_l$ or $\boldsymbol{D}_u$ for surrogate updating.

In most implementations the two boundary surrogates are built independently and sequentially (Fig. 2): one is refined to convergence, then the other, so their sample sets and updates are separated and the minimum and maximum searches are performed as two separate optimizations.

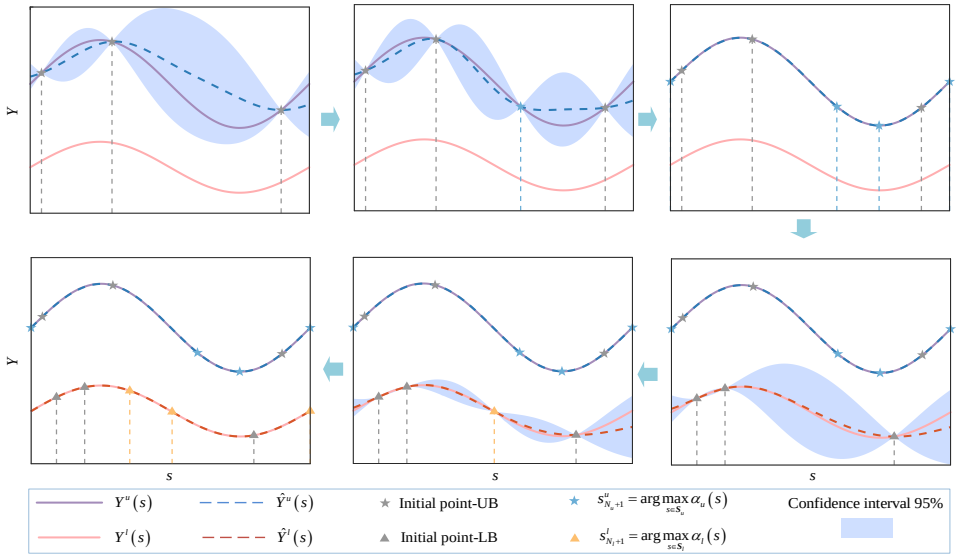


Fig. 2 Schematic of the independent sequential boundary surrogate strategy

In terms of computational cost, the surrogate models reduce the number of state points at which the inner optimization must be performed from the m grid points of section 2.2 to the adaptively selected ones, but each training sample of either boundary still requires one dedicated single-extremum optimization run. With N_0 initial state points per boundary, $N_{seq,l}$ and $N_{seq,u}$ adaptively added points, and $N_s^{(k)}$ performance-function evaluations consumed by the k-th run, the total cost of the sequential strategy is expressed as follows,

$$N_{eval}^{seq}=\sum_{k=1}^{2N_0+N_{seq,l}+N_{seq,u}} N_s^{(k)}=\left(2N_0+N_{seq,l}+N_{seq,u}\right)\times \bar{N}_{single} \tag{13}$$

where $\bar{N}_{single}$ denotes the average number of evaluations of one single-extremum run.

This sequential strategy is simple but ignores the coupling between the two boundaries. At a given state point both extrema come from the same model and input space, so extremum information from one boundary calculation is wasted by the other. These limitations motivate the two improvements below: a bi-extremum inner strategy (Section 3) and an alternating outer framework (Section 4) in which the two boundary models are kept separate but updated cooperatively over the whole evolution domain.

3. Bi-extremum optimization at a fixed state point

This section addresses the inner-layer problem. Once the evolution variable is fixed at a state point, the model reduces to a static mapping of the interval inputs, and the lower and upper bounds follow from a pair of static extremum searches.

3.1 Problem definition at a fixed state point

Let the evolution variable be fixed at a state point s_j. The model response then depends only on the interval input vector $\boldsymbol{X}$, and the reduced performance function is denoted as $f_j(\boldsymbol{X})\equiv f(\boldsymbol{X},s_j)$. The inner-layer task is to solve the following pair of optimization problems.

$$Y^l(s_j)=\min_{\boldsymbol{X}\in\boldsymbol{X}^I} f_j(\boldsymbol{X}),\quad Y^u(s_j)=\max_{\boldsymbol{X}\in\boldsymbol{X}^I} f_j(\boldsymbol{X}) \tag{14}$$

The two extrema correspond to one sample of the lower boundary and one sample of the upper boundary of the response interval process, respectively.

In this work, the two extrema are searched within a Kriging-based efficient global optimization (EGO) framework (Jones et al., 1998). The Kriging model (Sacks et al., 1989) is adopted because its predictive mean and variance naturally support expected-improvement type acquisition functions.

3.2 Expected improvement for minimization

The conventional expected improvement criterion, denoted as $EI_{\min}$ in this work, is used for the minimization problem. As the core acquisition function of the EGO algorithm, it evaluates the expected amount by which an untried point can improve the currently observed minimum, while accounting for the predictive uncertainty of the surrogate model.

Here, an untried point refers to a candidate input vector in the interval input space that has not yet been evaluated by the true model. At any such point $\boldsymbol{x} \in \boldsymbol{X}^I$, the Kriging model provides a Gaussian predictive distribution with mean $\hat{y}(\boldsymbol{x})$ and standard deviation $\sigma(\boldsymbol{x})$.

$$Y(\boldsymbol{x}) \sim N\left(\hat{y}(\boldsymbol{x}), \sigma^2(\boldsymbol{x})\right) \tag{15}$$

If the current best observed value is $f_{\min}$, the improvement of an untried point $\boldsymbol{x}$ with respect to $f_{\min}$ is a random variable.

$$I_{\min}(\boldsymbol{x}) = \max\left(0, f_{\min} - Y(\boldsymbol{x})\right) \tag{16}$$

The $EI_{\min}$ function is defined as the mathematical expectation of this improvement.

$$EI_{\min}(\boldsymbol{x}) = E\left[I_{\min}(\boldsymbol{x})\right] \tag{17}$$

Solving the above expectation yields the following closed-form expression. i.e.,

$$EI_{\min}(\boldsymbol{x}) = \left(f_{\min} - \hat{y}(\boldsymbol{x})\right)\Phi\left(\frac{\left(f_{\min} - \hat{y}(\boldsymbol{x})\right)}{\sigma(\boldsymbol{x})}\right) + \sigma(\boldsymbol{x})\phi\left(\frac{f_{\min} - \hat{y}(\boldsymbol{x})}{\sigma(\boldsymbol{x})}\right) \tag{18}$$

where $\Phi(\cdot)$ and $\phi(\cdot)$ denote the cumulative distribution function and probability density function of the standard normal distribution, respectively. The $EI_{\min}$ function can be understood as a nonlinear combination of exploitation and exploration. The first term of the $EI_{\min}$ function increases as $\hat{y}(\boldsymbol{x})$ decreases, which means it tends to select points with lower predicted response values, whereas the second term increases with $\sigma(\boldsymbol{x})$, encouraging exploration of regions with large predictive uncertainty.

At each iteration, the point maximizing $EI_{\min}$ over the interval input space is selected as the new training sample.

$$\boldsymbol{x}_{\min}^{*} = \arg\max_{\boldsymbol{X} \in \boldsymbol{X}^I} EI_{\min}(\boldsymbol{x}) \tag{19}$$

The $EI_{\min}$ function is continuous, equals zero at evaluated sample points, and is strictly positive elsewhere. Consequently, the point selected by maximizing $EI_{\min}$ never coincides with an existing sample. Under mild regularity conditions, the sequential infill strategy governed by the expected improvement criterion converges to the global optimum as the number of samples increases (Törn and Žilinskas, 1989). The stopping rule adopted in this work is defined in section 3.4.

3.3 Expected improvement for maximization

A maximization problem can be equivalently transformed into a minimization problem by changing the sign of the objective function, i.e., $\max_{\boldsymbol{x} \in \boldsymbol{X}^I} f_j(\boldsymbol{x}) \Leftrightarrow \min_{\boldsymbol{X} \in \boldsymbol{X}^I}\left(-f_j(\boldsymbol{x})\right)$. This transformation is mathematically precise and commonly used. However, in a conventional implementation, the minimization and maximization problems are addressed through two separate EGO runs. This means that two surrogate models are trained on distinct sample sets, and the costly model evaluations gathered during one search cannot be utilized by the other.

To enable the two searches to share a single Kriging model and a single training dataset, an expected improvement criterion for maximization, denoted as $EI_{\max}$, is formulated directly in the original response space as the counterpart of $EI_{\min}$.

Let $f_{\max}$ denote the currently observed maximum value. The improvement of an untried point $\boldsymbol{x}$ is defined as the amount by which its response exceeds $f_{\max}$.

$$I_{\max}(\boldsymbol{x}) = \max\left(0, Y(\boldsymbol{x}) - f_{\max}\right) \tag{20}$$

The $EI_{\max}$ function is defined as the mathematical expectation of this improvement.

$$EI_{\max}(\boldsymbol{x}) = E\left[I_{\max}(\boldsymbol{x})\right] \tag{21}$$

Evaluating the expectation gives the following expression.

$$EI_{\max}(\boldsymbol{x}) = \left(\hat{y}(\boldsymbol{x}) - f_{\max}\right)\Phi\left(\frac{\hat{y}(\boldsymbol{x}) - f_{\max}}{\sigma(\boldsymbol{x})}\right) + \sigma(\boldsymbol{x})\phi\left(\frac{\hat{y}(\boldsymbol{x}) - f_{\max}}{\sigma(\boldsymbol{x})}\right) \tag{22}$$

$EI_{\max}$ balances exploitation and exploration in the same manner as $EI_{\min}$, with the roles of the two terms mirrored for the maximization problem.

$$\boldsymbol{x}^*_{\max} = \arg\max_{\boldsymbol{X}\in\boldsymbol{X}^I} EI_{\max}(\boldsymbol{x}) \tag{23}$$

The characteristics of $EI_{\max}$ parallel function closely align with those of $EI_{\min}$ as it disappears at specific samples while remaining strictly positive in all other areas.

The $EI_{\max}$ criterion is mathematically equivalent to the conventional EI criterion applied to the sign-transformed objective. This equivalence guarantees that $EI_{\max}$ inherits the convergence properties of the standard expected improvement criterion, while keeping both the minimum and maximum searches formulated on the same surrogate model in the original response space, which is the prerequisite of the unified algorithm developed in the next subsection.

3.4 Unified bi-extremum optimization algorithm

The $EI_{\min}$ and $EI_{\max}$ criteria are coupled within a single EGO framework to search for the minimum and maximum responses at a fixed state point. Both searches share one Kriging model and one training dataset, rather than being performed by two isolated EGO runs. The algorithm consists of three stages, i.e., initialization, collaborative update, and separate refinement. The overall procedure is illustrated in Fig. 3.

To obtain a dimensionless stopping rule, the convergence indicators of the two searches are normalized by the currently observed interval width, i.e.,

$$Cr_{\min} = \frac{\max_{\boldsymbol{x}\in\boldsymbol{X}^I} EI_{\min}(\boldsymbol{x})}{f_{\max} - f_{\min}}, \quad Cr_{\max} = \frac{\max_{\boldsymbol{x}\in\boldsymbol{X}^I} EI_{\max}(\boldsymbol{x})}{f_{\max} - f_{\min}} \tag{24}$$

where $f_{\min}$ and $f_{\max}$ are the minimum and maximum observed responses in the current training dataset. A search is regarded as converged when its indicator falls below a prescribed threshold ε ($\varepsilon = 0.01$ in this work), i.e., the maximum expected improvement is less than 1% of the current interval width. To prevent premature termination caused by a transient underestimation of the expected improvement, the convergence condition is required to hold in two consecutive iterations. Note that this normalization is naturally available in the bi-extremum setting, since both extrema are tracked simultaneously; in addition, a maximum iteration number $N_{\max}$ is imposed as a safeguard.

1. Initialization stage

Step 1.1 Generate a candidate pool X_{pool} of N_{pool} points in the interval input space $\boldsymbol{X}^I$ by Latin hypercube sampling (LHS) (McKay et al., 1979), and randomly select N_0 initial training samples from the LHS portion of the pool.

Step 1.2 Evaluate the true responses of the initial samples, $y_i = f_j(\boldsymbol{x}_i)$ and form the initial training dataset $\boldsymbol{D} = \left\{\left(\boldsymbol{x}_i, y_i\right)\right\}, i = 1, \cdots, N_0$.

Step 1.3 Construct the initial Kriging model using $\boldsymbol{D}$, and set $f_{\min} = \min\left\{y_i\right\}$ and $f_{\max} = \max\left\{y_i\right\}$.

2. Collaborative update stage

Step 2.1 Evaluate $EI_{\min}(\boldsymbol{x})$ and $EI_{\max}(\boldsymbol{x})$ over the candidate pool and compute $Cr_{\min}$ and $Cr_{\max}$ by the convergence-indicator equation above. If $Cr_{\min} \le \varepsilon$ and $Cr_{\max} \le \varepsilon$, go to Step 4.1. If exactly one indicator satisfies its threshold, go to Step 3.1. Otherwise, continue with Step 2.2.

Step 2.2: Select $\boldsymbol{x}^*_{\min} = \arg\max_{\boldsymbol{X}\in\boldsymbol{X}^I} EI_{\min}(\boldsymbol{x})$ and $\boldsymbol{x}^*_{\max} = \arg\max_{\boldsymbol{X}\in\boldsymbol{X}^I} EI_{\max}(\boldsymbol{x})$ as the new samples for the minimum and maximum searches, respectively.

Step 2.3: Evaluate the true responses $f_j\left(\boldsymbol{x}^*_{\min}\right)$ and $f_j\left(\boldsymbol{x}^*_{\max}\right)$, and add both samples to $\boldsymbol{D}$. The two evaluations are independent and can be executed in parallel.

Step 2.4: Retrain the Kriging model with the updated $\boldsymbol{D}$, refresh $f_{\min}=\min\{y_i\}$ and $f_{\max}=\max\{y_i\}$, and return to Step 2.1.

3. Separate refinement stage

This stage is executed only for the extremum whose indicator has not yet converged. The procedure is stated for the minimum search, and the maximum search is refined in the mirrored manner using $EI_{\max}$ and $Cr_{\max}$.

Step 3.1: Select $\boldsymbol{x}^*_{\min}=\arg\max_{\boldsymbol{X}\in\boldsymbol{X}^I} EI_{\min}(\boldsymbol{x})$ as the new sample.

Step 3.2: Evaluate the true response $f_j(\boldsymbol{x}^*)$ and add it to $\boldsymbol{D}$.

Step 3.3: Retrain the Kriging model and refresh $f_{\min}=\min\{y_i\}$. Both $f_{\min}$ and $f_{\max}$ are refreshed, since a refinement sample may incidentally improve the other extremum.

Step 3.4: Recompute $Cr_{\min}$ by the convergence-indicator equation above. If $Cr_{\min}>\varepsilon$, return to Step 3.1. Otherwise, go to Step 4.1.

Output

Step 4.1: Return the observed extrema $Y^l(s_j)=f_{\min}$ and $Y^u(s_j)=f_{\max}$ as the lower and upper bounds at the state point s_j.

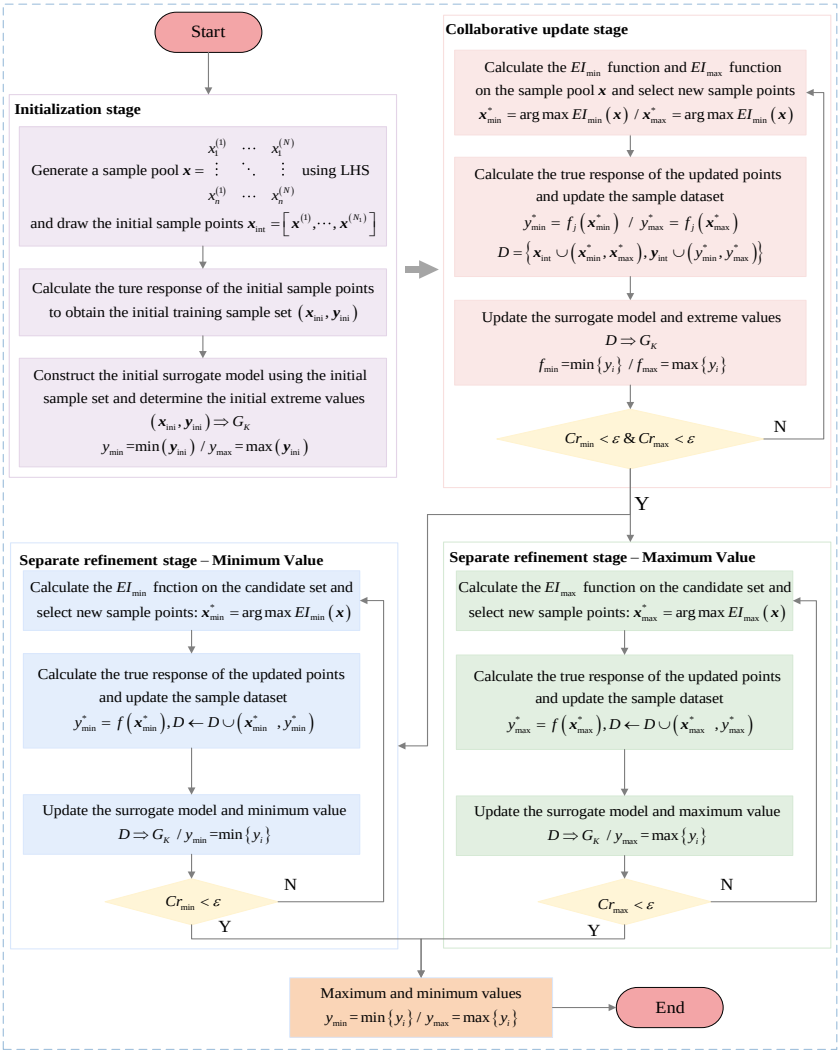


Fig. 3 Flowchart of the unified bi-extremum optimization algorithm at a fixed state point

The computational cost of the algorithm is dominated by the number of true model evaluations. Compared with two independent EGO runs, the unified strategy lets every evaluated sample inform both searches through the shared Kriging model, and the two evaluations in each collaborative-update iteration

can be executed in parallel, which further reduces the wall-clock time for expensive simulations. Moreover, since $f_{\min}$ and $f_{\max}$ are taken from evaluated samples, the returned interval $[f_{\min}, f_{\max}]$ is an inner estimate of the true response interval, and the residual normalized indicators bound the expected further widening: upon convergence, the expected underestimation of the interval width does not exceed ε times the current width. Finally, because the returned extrema are true model responses rather than surrogate predictions, they provide noise-free training data for the outer boundary surrogate framework developed in section 4.

4. Alternating surrogate modeling for response interval process boundaries

This section develops the outer layer. The bi-extremum algorithm of Section 3 returns both extrema at every visited state point, whereas the sequential strategy of Section 2.3 keeps only one and discards the other. The alternating strategy below ensures that both outputs of every inner-layer call enter the training data of the two boundary surrogates; the resulting method is termed the Bi-Extremum Alternating Surrogate (BEAS) method.

4.1 Alternating update strategy with conditional injection

The outer layer trains the two boundary surrogates $\hat{Y}^u(s)$ and $\hat{Y}^l(s)$ by adaptively adding samples to their training sets $\boldsymbol{D}_u$ and $\boldsymbol{D}_l$. Each boundary maintains a candidate pool, $\boldsymbol{S}_u$ and $\boldsymbol{S}_l$. Each boundary further maintains a buffer, $\boldsymbol{B}_u$ and $\boldsymbol{B}_l$, initially empty, which stores by-product values delivered to that boundary but not yet admitted into its training set.

The central mechanism of the strategy is the transfer of the by-product between successive half-steps. When a half-step evaluates *Ain* at a selected state point s^*, the operator returns both boundary values simultaneously. One of them is the primary sample requested by the active boundary and is added to its own training set. The other is a by-product, namely a true sample of the opposite boundary obtained without any additional execution of *Ain*, and is transferred to the opposite boundary. The transferred by-product serves as the update information with which the opposite boundary begins its own half-step. Successive half-steps are thereby linked into a chain, i.e., the upper-boundary half-step supplies a by-product that updates the lower boundary, the lower-boundary half-step supplies a by-product that updates the upper boundary, and so on in alternation.

Each outer iteration consists of two symmetric half-steps, one for each boundary. Taking the upper boundary as the active boundary, a half-step comprises the following five steps. The lower-boundary half-step is obtained by interchanging $u \leftrightarrow l$.

(i) **Step 1 (Injection and update)**. The by-product transferred from the preceding half-step, if admitted by the conditional injection rule as specified in case 1 below, is added to the active training set, and the active surrogate is refitted,

$$\boldsymbol{D}_u \leftarrow \boldsymbol{D}_u \cup \left\{s', Y^u(s')\right\}, \quad Y^u(s) \leftarrow GK\left(\boldsymbol{D}^u\right) \tag{25}$$

where s' is the state point of the transferred by-product and $GK(\cdot)$ denotes Kriging model fitting. The information carried by the by-product is thus incorporated before any decision of the current half-step is made.

(ii) **Step 2 (Convergence assessment)**. The normalized indicator is defined as follows,

$$Cr_u = \frac{\max_{s \in \boldsymbol{S}_u} \sigma_u(s)}{W}, W = \frac{1}{N_s} \sum_{s \in \boldsymbol{S}} \left(\hat{Y}^u(s) - \hat{Y}^l(s)\right) \tag{26}$$

where $\sigma_u(s)$ is the predictive standard deviation of $\hat{Y}^u(s)$. If $Cr_u \le \varepsilon_{\text{out}}$, the upper boundary is flagged converged and the half-step terminates without executing *Ain*. The algorithm stops when both boundaries are converged; a maximum iteration number $N_{\max}$ is imposed as a safeguard.

(iii) **Step 3 (State-point selection)**. The next state point is selected as the pool point of maximum predictive variance,

$$s^* = \arg\max_{s \in \boldsymbol{S}_u} \sigma_u^2(s) \tag{27}$$

(iv) **Step 4 (Inner-layer evaluation)**. If s^* coincides with a buffered state point of the active boundary, its stored value is admitted directly and no execution of A_{in} is performed, as specified in case 3 below. Otherwise, a single inner-layer execution is carried out, i.e.,

$$\left[Y^l\left(s^*\right), Y^u\left(s^*\right)\right] = Ain\left(s^*\right) \tag{28}$$

after which the primary sample is added to the active training set and the state point leaves the active pool.

$$\boldsymbol{D}_u \leftarrow \boldsymbol{D}_u \cup \left\{s^*, Y^u\left(s^*\right)\right\}, \quad \boldsymbol{S}_u \leftarrow \boldsymbol{S}_u \setminus \left\{s^*\right\} \tag{29}$$

(v) **Step 5 (By-product transfer)**. The by-product $\left(s^*, Y^u\left(s^*\right)\right)$ is transferred to the opposite boundary, where its destination is determined by the conditional injection rule based on its distance to the receiving training set.

$$d\left(s^*, \boldsymbol{D}_l\right) = \min_{s_j \in \boldsymbol{S}_l} \left|s^* - s_j\right| \tag{30}$$

The rule assigns the by-product to exactly one of three cases, and which is illustrated in Fig. 4.

(i) **Case 1 (Direct injection)**. If $d\left(s^*, \boldsymbol{D}_l\right) > d_{\min}$, the by-product is admitted into the lower training set and its state point leaves the lower pool.

$$\boldsymbol{D}_l \leftarrow \boldsymbol{D}_l \cup \left\{s^*, Y^l\left(s^*\right)\right\}, \quad \boldsymbol{S}_l \leftarrow \boldsymbol{S}_l \setminus \left\{s^*\right\} \tag{31}$$

(ii) **Case 2 (Screened buffering)**. If $d\left(s^*, \boldsymbol{D}_l\right) < d_{\min}$, the by-product is stored in the buffer and its state point is retained in the pool,

$$\boldsymbol{B}_l \leftarrow \boldsymbol{B}_l \cup \left\{s^*, Y^l\left(s^*\right)\right\}, \quad \boldsymbol{S}_l \leftarrow \boldsymbol{S}_l \tag{32}$$

Retaining s^* in $\boldsymbol{S}_l$ is essential that the lower-boundary value at s^* has not entered $\boldsymbol{D}_l$, so by the pool invariant the point remains a legitimate candidate for later selection. The threshold $d_{\min} = 1.5\Delta s$ is adopted in this work.

(iii) **Case 3 (Buffer retrieval)**. If a selection s^* made by operation (iii) of a later half-step coincides with a buffered state point, the stored value is admitted with no execution of *Ain*.

$$\boldsymbol{D}_l \leftarrow \boldsymbol{D}_l \cup \left\{s^*, Y^l\left(s^*\right)\right\}, \quad \boldsymbol{B}_l \leftarrow \boldsymbol{B}_l \cup \left\{s^*, Y^l\left(s^*\right)\right\}, \quad \boldsymbol{S}_l \leftarrow \boldsymbol{S}_l \setminus \left\{s^*\right\} \tag{33}$$

Delivery in case 1 or case 2 takes place even if the receiving boundary is already converged, since registering a by-product requires no execution of *Ain* and, by the variance-monotonicity property discussed below, never increases the predictive variance of the receiving surrogate.

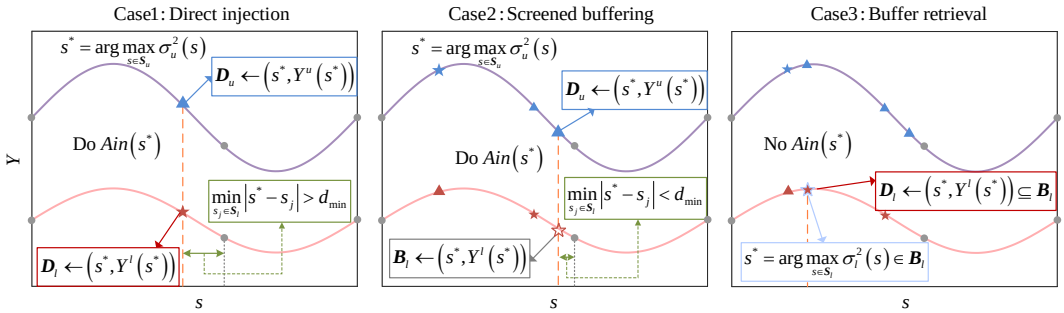


Fig. 4 Three by-product-handling cases in the alternating update strategy

Two properties of the Kriging predictive variance underlie the rule. The distance screening is applied only to a transferred by-product, because the predictive variance vanishes at every training point and the selection of step 3 is thereby kept away from existing samples, whereas a by-product is located by the opposite variance field and may fall arbitrarily close to a sample of the receiving set and render its correlation matrix ill-conditioned. Retrieval in case 3 is feasible because geometric distance and correlation distance differ, so that a by-product screened out as geometrically close may still carry a high predictive variance when its separation exceeds the correlation length and be selected in a later half-step. Retrieval is therefore governed by the ratio of $d_{\min}$ to the correlation length and does not occur under the default setting.

4.2 The complete BEAS procedure

The complete Bi-Extremum Alternating Surrogate (BEAS) method nests the bi-extremum inner-layer algorithm of section 3 within the alternating outer strategy of section 4.1. Following an initialization that executes *Ain* at N_0 uniformly spaced state points to form the two initial training sets and surrogates, the boundaries are updated in alternating half-steps of the five-step form of section 4.1. The first upper-boundary half-step starts from the initial surrogate with no by-product to incorporate, and every subsequent half-step incorporates the transferred by-product, assesses convergence, and, if not converged, selects the state point of maximum predictive variance and evaluates it by buffer retrieval or by one execution of *Ain*. The procedure terminates when both boundaries are converged or when $k > N_{\max}$. The complete procedure is summarized in Algorithm 1.

Algorithm 1: Alternating update with conditional injection (outer layer of BEAS)

Require: candidate grid $\boldsymbol{S}$ over the evolution domain, number of initial state points N_0, inner bi-extremum algorithm $Ain(\cdot)$, screening distance $d_{\min}$, threshold ε_{out}, maximum iterations $N_{\max}$.

Ensure: boundary surrogates $\hat{Y}^l(s)$ and $\hat{Y}^u(s)$

1: Select N_0 initial state points; call $Ain(\cdot)$ at each to obtain both extrema.
2: $\boldsymbol{D}_u, \boldsymbol{D}_l$ initial samples, $\boldsymbol{S}_u, \boldsymbol{S}_l$ initial points, $\boldsymbol{B}_u, \boldsymbol{B}_l \leftarrow \varnothing$, $conv_u, conv_l \leftarrow false$, $k = 1$.
3: while $conv_u = false \vee conv_l = false$ and $k \le N_{\max}$ do
4: for $side \in \{u, l\}$ do // two half-steps per iteration
5: if $conv_{side} = ture$ then continue
6: Retrain $\hat{Y}_{side}$ on $\boldsymbol{D}_{side}$ if $\boldsymbol{D}_{side}$ has changed. // absorbs injections
7: Compute Cr_{side}, if $Cr_{side} \le \varepsilon_{out}$ then $conv_{side} \leftarrow ture$, continue. // convergence gate
8: $s^* \leftarrow \arg\max_{s \in \boldsymbol{S}_{side}} \sigma^2_{side}(s)$.
9: if $s^* \in \boldsymbol{B}_{side}$ then // Case 3: retrieval, no inner call
10: Retrieve $Y^{side}(s^*)$ from $\boldsymbol{B}_{side}$, $\boldsymbol{B}_{side} \leftarrow \boldsymbol{B}_{side} \setminus \{s^*\}$.
11: else
12: $\left[Y^l(s^*), Y^u(s^*)\right] = Ain(s^*)$. // one inner call, both extrema
13: if $\min\left(d\left(s^*, \boldsymbol{D}_{other}\right)\right) \ge d_{\min}$ then // Case 1: injection
14: $\boldsymbol{D}_{other} \leftarrow \boldsymbol{D}_{other} \cup \left\{\left(s^*, Y^{other}(s^*)\right)\right\}$, $\boldsymbol{S}_{other} \leftarrow \boldsymbol{S}_{other} \setminus \{s^*\}$.
15: else $\boldsymbol{B}_{other} \leftarrow \boldsymbol{B}_{other} \cup \left\{\left(s^*, Y^{other}(s^*)\right)\right\}$. // Case 2: buffering
16: end if
17: $\boldsymbol{D}_{side} \leftarrow \boldsymbol{D}_{side} \cup \left\{\left(s^*, Y^{side}(s^*)\right)\right\}$, $\boldsymbol{S}_{side} \leftarrow \boldsymbol{S}_{side} \setminus \{s^*\}$.
18: end for
19: $k \to k+1$.
20: end while
21: Final retraining of both surrogates; return $\hat{Y}^l(s)$ and $\hat{Y}^u(s)$.

4.3 Computational cost analysis

The computational cost of BEAS is measured by the number of executions of the inner-layer algorithm *Ain* and by the resulting number of performance-function evaluations. For each boundary, the executions consumed by its own half-steps equal the number of adaptively added state points minus the number of buffer retrievals, since a retrieved point is admitted without executing *Ain*. These counts are $N_{new,u} - N_{ret,u}$ for the upper boundary and $N_{new,l} - N_{ret,l}$ for the lower boundary. Together with the N_0 initializing executions, the total number of inner-layer executions is expressed as follows.

$$N_{call} = N_0 + \left(N_{new,u} - N_{ret,u}\right) + \left(N_{new,l} - N_{ret,l}\right) \tag{34}$$

Denoting by N_{Ain}^k the number of performance-function evaluations consumed by the *k*-th execution, the total cost of the boundary evaluation is expressed as follows,

$$N_{eval}^{\mathrm{BEAS}} = \sum_{k=1}^{N_{call}} N_{Ain}^{(k)} = N_{call} \times \bar{N}_{bi} \tag{35}$$

where $\bar{N}_{bi}$ is the average cost of one bi-extremum execution.

Compared with the sequential strategy of section 2.3, whose cost is in the Eq. (13), BEAS reduces both factors of the product. The number of executions is reduced because every transferred by-product enters the training set of the receiving boundary without an execution of Ain, so the adaptive additions $N_{new,u}$ and $N_{new,l}$ required to resolve the two boundaries are fewer than the corresponding numbers of the sequential construction, and the buffer retrievals of case 3 remove further executions. The cost per execution satisfies $\bar{N}_{bi} < 2\bar{N}_{single}$, as established in section 3, because the two extremum searches share one surrogate model and one training dataset.

5. Examples and discussion

Two analytical examples validate the method. For each, the boundary iteration is shown for the proposed method, and efficiency is compared among three schemes: sequential single-boundary iteration with a PSO inner solver, the same with an EGO inner solver, and the proposed alternating-boundary iteration with the bi-extremum solver (BEAS). The total adaptively added state points, equal to the number of inner-layer executions, measures the outer-layer cost.

5.1 Experimental setup

Two analytical examples are used to evaluate the accuracy and efficiency of the proposed BEAS framework. Example 1 is a smooth double-boundary case that examines the baseline behavior of the algorithm, and its performance function is defined as follows,

$$\begin{aligned} f_1(\boldsymbol{X}, s) = X_1^2 + X_2^2 + X_3X_4 + X_1X_2\left(1.2\sin(s+0.8) + 0.3\sin(2s+1.5)\right) + \\ X_3X_4\left(0.9\cos(s-1.2) + 0.4\cos(1.5s-0.7)\right) + 0.25X_1X_3\sin(0.8s+2.1) \end{aligned} \tag{36}$$

where the interval input vector is $\boldsymbol{X}^I = \left(X_1^I, X_2^I, X_3^I, X_4^I\right)$ with $n = 4$ interval inputs. All inputs share the common midpoint $X_i^c = 0.5$ with radii $X_i^r = (0.07, 0.175, 0.35, 0.28)$, the evolution domain is $s \in [2,10]$. The harmonic terms of incommensurate frequencies produce smooth and slowly varying boundaries.

Example 2 augments the base function with an oscillatory term,

$$Y = f_2(\boldsymbol{X}, s) = f_1(\boldsymbol{X}, s) + 4(X_3 - 0.5)^2(1.5 + \sin 3s) \tag{37}$$

which is non-negative and vanishes at $X_3 = 0.5$ and oscillates for about 3.8 periods over the evolution domain. The upper boundary of Example 2 is therefore highly oscillatory while the lower boundary remains smooth, which produces an asymmetric sample demand between the two boundaries.

The reference boundaries are obtained by the discretization-optimization framework of section 2.2, with the inner optimization at each grid point replaced by an exhaustive evaluation over a fixed input set consisting of 10^5 uniformly distributed samples and the 2^n vertices of $\boldsymbol{X}^I$. At each grid point the reference boundaries are taken as the extrema of the performance function over this fixed set, $Y_{\mathrm{ref}}^l(s_j) = \min_{\boldsymbol{x} \in \boldsymbol{X}_{\mathrm{ref}}} f(\boldsymbol{x}, s_j)$ and $Y_{\mathrm{ref}}^u(s_j) = \max_{\boldsymbol{x} \in \boldsymbol{X}_{\mathrm{ref}}} f(\boldsymbol{x}, s_j)$, where $\boldsymbol{X}_{\mathrm{ref}}$ denotes the union of the sample set and the vertex set. The vertices are included because a finite random sample contains vertex-type extrema with probability zero, so purely random sampling would bias the reference interval inward. The reference thus realizes the discretization-optimization evaluation of section 2.2 with an exhaustive inner search and serves only for error assessment. All boundary errors are normalized by the reference mean interval width,

$$Err_u = \frac{\max_{s \in \boldsymbol{S}} \left|\hat{Y}^u(s) - Y_{\mathrm{ref}}^u(s)\right|}{\bar{W}_{\mathrm{ref}}}, \quad Err_l = \frac{\max_{s \in \boldsymbol{S}} \left|\hat{Y}^l(s) - Y_{\mathrm{ref}}^l(s)\right|}{\bar{W}_{\mathrm{ref}}} \tag{38}$$

where $\bar{W}_{\mathrm{ref}}$ is the mean width of the reference interval process, equal to 1.096 for Example 1 and 2.633 for Example 2. The parameters used in the experiments are listed in Table 1.

Table 1 Parameters used in the numerical experiments

Parameter	Value	Remark
Number of grid points N_s	500	Same for both examples
Initial state points N_0	4 (Example 1), 6 (Example 2)	Uniformly spaced
Screening distance $d_{\min}$	$1.5\Delta s$	Same for both examples
Outer threshold ε_{out}	0.01	Same for both examples
Inner candidate pool	10^5 LHS samples	Same for both examples
Inner threshold ε	0.01	Two consecutive iterations

5.2 Example 1 results

Fig. 6 shows the boundary iteration process of the sequential strategy for Example 1, and Fig. 7 shows that of the proposed alternating strategy.

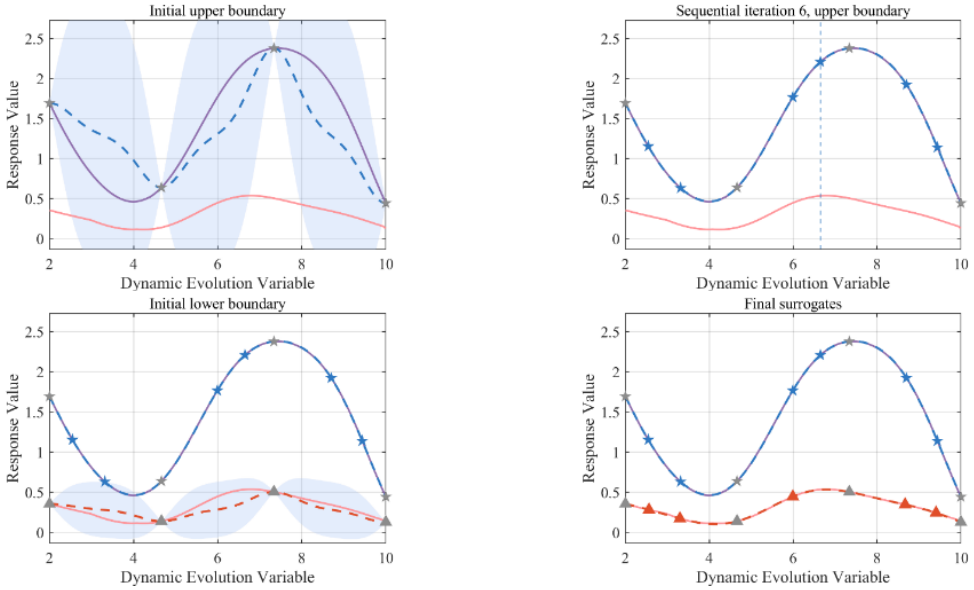


Fig. 6 Boundary iteration process of the sequential strategy for Example 1

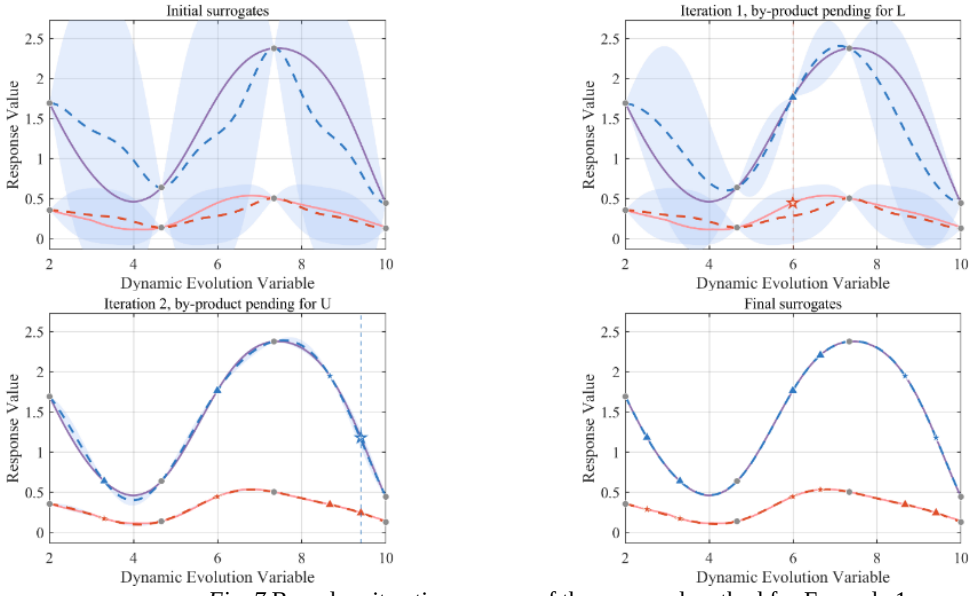


Fig. 7 Boundary iteration process of the proposed method for Example 1

The added state points in Table 2 are visible in the two figures. In Fig. 6 each colored marker is one of the 19 single-extremum runs of the sequential strategy; in Fig. 7 the stars mark the 10 bi-extremum executions of BEAS (4 for initialization) and the triangles are by-products obtained without any execution. The shrinking prediction bands and the matching final panels confirm the equal accuracy reported in Table 2.

Table 2 compares the three schemes for Example 1. For the sequential schemes the added state points are counted per state point at which an inner-layer optimization is executed, and the lower and upper responses are obtained by two separate single-extremum runs, whereas for the proposed method each added state point corresponds to a single bi-extremum execution that returns both responses; the by-products transferred between boundaries are reused without recomputation and are not counted.

Table 2 Efficiency and cost comparison for Example 1

Scheme	Outer strategy	Inner solver	Total state points	N_{eval}	Err_u (%)	Err_l (%)
S-PSO	sequential	PSO	19.0	16968.0	0.398	1.170
S-EGO	sequential	single-extremum EGO	19.0	325.6	0.398	1.177
BEAS	alternating	bi-extremum	10.0	191.0	0.391	1.201

The proposed method attains the same boundary accuracy as the two sequential baselines while reducing the cost on two independent levels. The upper- and lower-boundary errors of the three schemes are at the same level for both examples, so the cost comparison is made at equal accuracy.

The first level compares the two inner solvers. S-PSO and S-EGO share the sequential outer strategy and the same added state points, differing only in the inner solver. Since particle swarm optimization needs about a thousand evaluations per search, S-PSO costs roughly fifty times the evaluations of S-EGO, confirming the value of a Kriging surrogate in expensive-simulation settings.

The second level compares alternating reuse against sequential independent construction. S-EGO and BEAS use the same Kriging inner solver and differ only in the outer strategy. Because BEAS returns both extrema per execution and reuses the transferred by-product without recomputation, the inner-layer executions drop by about 47% and the evaluations by about 41%. This gain is independent of the inner solver and comes solely from by-product reuse.

5.3 Example 2 results

Fig. 8 shows the boundary iteration process of the sequential strategy for Example 2, and Fig. 9 shows that of the proposed alternating strategy in the representative run.

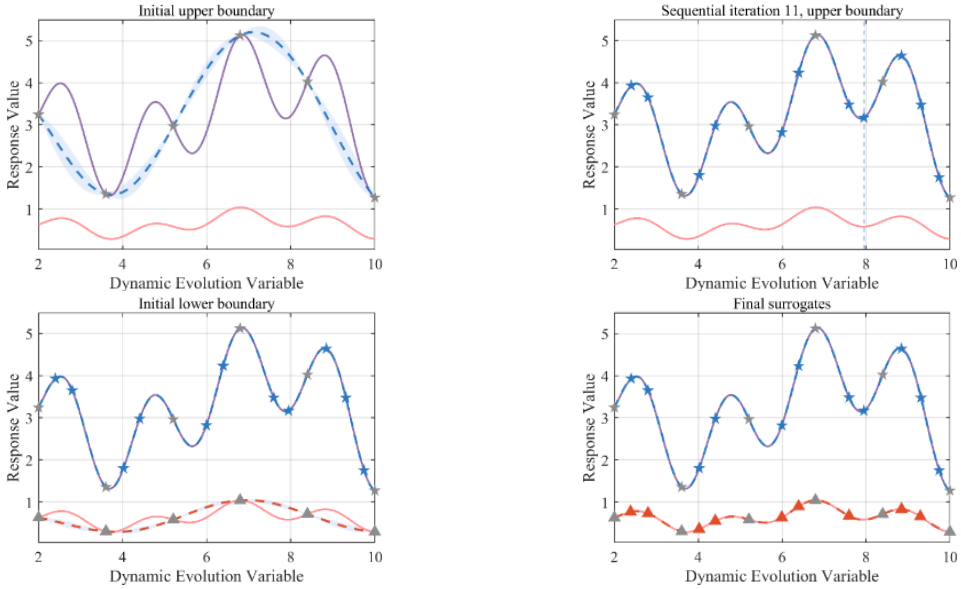


Fig. 8 Boundary iteration process of the sequential strategy for Example 2

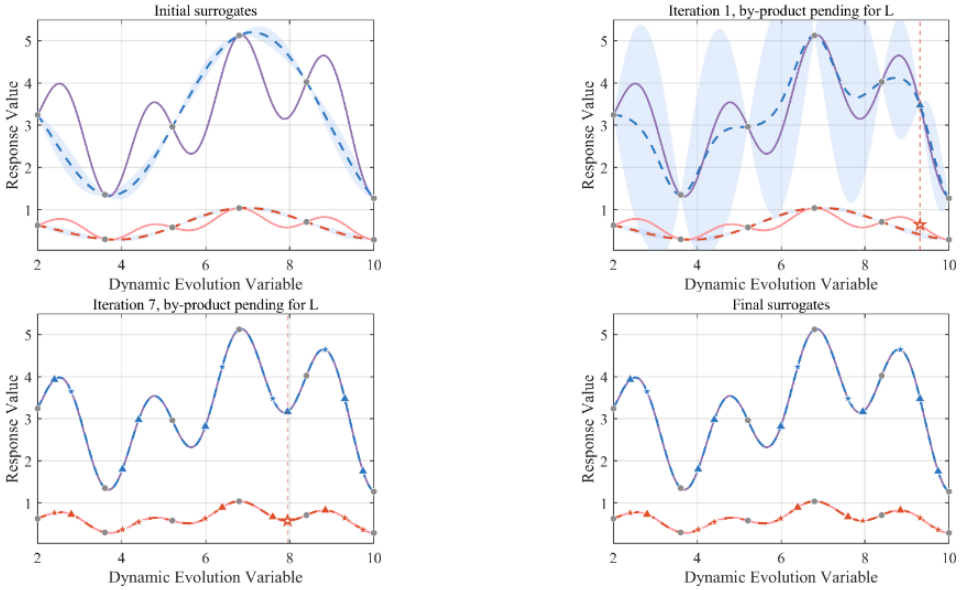


Fig. 9 Boundary iteration process of the proposed method for Example 2

The two figures make the outer-layer cost of Table 3 visible. In Fig. 8 every marker beyond the initial samples is one single-extremum run, with the oscillatory upper boundary consuming most of the 32 runs. In Fig. 9 the smooth lower boundary converges after its fourth half-step, while the remaining upper-boundary half-steps still deliver by-products to it. The eleven adaptive executions split seven to four between the boundaries and, with the six initial ones, give the seventeen added state points of Table 3. The triangles mark samples obtained without any inner execution, the source of the cost reduction.

Table 3 compares the three schemes for Example 2.

Table 3 Efficiency and cost comparison for Example 2

Scheme	Outer strategy	Inner solver	Total state points	N_{eval}	Err_u (%)	Err_l (%)
S-PSO	sequential	PSO	32.0	28568.0	0.310	0.288
S-EGO	sequential	single-extremum EGO	32.0	544.8	0.237	0.330
BEAS	alternating	bi-extremum	17.0	323.2	0.382	0.067

For Example 2 the same two-level reduction holds, with about 41% fewer performance-function evaluations than the single-extremum sequential scheme. Because the upper boundary is oscillatory and the lower one smooth, the added state points concentrate on the upper boundary and the absolute number of executions exceeds that of Example 1; yet the relative reduction of inner-layer executions is again about 47%. This cross-example consistency shows that the benefit of by-product reuse is insensitive to boundary symmetry.

6. Conclusion

This paper developed a dual-layer Bi-Extremum Alternating Surrogate (BEAS) method for the boundaries of a response interval process. At the inner layer, an EI criterion for maximization was formulated directly in the original response space and coupled with the minimization criterion in a single Kriging-based EGO framework, so both extrema at a state point are found from one surrogate and one training set, returning true, noise-free responses for the outer layer. At the outer layer, an alternating strategy updates the two boundary surrogates in half-steps: each inner call's by-product extremum is delivered to the opposite boundary and, under a distance-based screening rule protecting the Kriging conditioning, injected into its training set, with a buffer as a zero-cost retrieval path.

Two conclusions follow on cost. First, at equal accuracy BEAS reduces evaluations on two independent levels: replacing the population-based inner solver by the Kriging surrogate cuts evaluations by about fifty times, and replacing the sequential outer construction by alternating reuse cuts inner-layer executions by about 47% and evaluations by a further 41%. Second, this reduction is close for the smooth and oscillatory examples, so the benefit of by-product reuse is insensitive to boundary symmetry.

The main limitation is the common blind spot of variance-based sampling: boundary features narrower than the sample spacing may go undetected, and the outer indicator is a probabilistic rather than deterministic error measure. Future work includes applying BEAS to engineering problems with expensive simulations and extending the alternating framework to vector-valued responses and higher-dimensional evolution variables.

Acknowledgment

This work is supported by the National Natural Science Foundation of China (Grant No. NSFC52475283).

References

Buhmann, M. D. Radial Basis Functions: Theory and Implementations, Cambridge University Press, 2003.

Chang, Q., C. Zhou, M. A. Valdebenito, H. Liu, and Z. Yue. A novel sensitivity index for analyzing the response of numerical models with interval inputs, Comput. Methods Appl. Mech. Eng. 400 (2022) 115509.

Faes, M., J. Cerneels, D. Vandepitte, and D. Moens. Identification and quantification of multivariate interval uncertainty in finite element models, Comput. Methods Appl. Mech. Eng. 315 (2017) 896–920.

Forrester, A. I. J. and A. J. Keane. Recent advances in surrogate-based optimization, Prog. Aerosp. Sci. 45 (2009) 50–79.

Goldberg, D. E. Genetic Algorithms in Search, Optimization, and Machine Learning, Addison-Wesley, 1989.

Guo, S. X. and Z. Z. Lu. A non-probabilistic robust reliability method for analysis and design optimization of structures with uncertain-but-bounded parameters, Appl. Math. Model. 39 (2015) 1985–2002.

Hornik, K., M. Stinchcombe, and H. White. Multilayer feedforward networks are universal approximators, Neural Netw. 2 (1989) 359–366.

Jiang, C., X. Han, G. Y. Lu, J. Liu, Z. Zhang, and Y. C. Bai. Non-probabilistic convex model process: A new method of time-variant uncertainty analysis and its application to structural dynamic reliability problems, Comput. Methods Appl. Mech. Eng. 268 (2014) 656–676.

Jones, D. R., M. Schonlau, and W. J. Welch. Efficient global optimization of expensive black-box functions, J. Glob. Optim. 13 (1998) 455–492.

Kennedy, J. and R. Eberhart. Particle swarm optimization, in: Proceedings of ICNN'95 - International Conference on Neural Networks, 1995, pp. 1942–1948.

Kleijnen, J. P. C. Kriging metamodeling in simulation: A review, Eur. J. Oper. Res. 192 (2009) 707–716.

Liu, Z. C., H. Y. Huang, X. Y. Xu, M. Xiong, and Q. Z. Li. An efficient global optimization algorithm combining revised expectation improvement criteria and Kriging, Eng. Optim. 56 (2023) 608–624.

McKay, M. D., R. J. Beckman, and W. J. Conover. A comparison of three methods for selecting values of input variables in the analysis of output from a computer code, Technometrics 21 (1979) 239–245.

Mockus, J. Bayesian Approach to Global Optimization, Springer, 2012.

Mohammadi, H. and R. Le Riche. Small ensembles of Kriging models for optimization, arXiv preprint arXiv:1603.02638, 2016.

Ni, B. Y., C. Jiang, J. W. Li, and W. Y. Tian. Interval K-L expansion of interval process model for dynamic uncertainty analysis, J. Sound Vib. 474 (2020) 115254.

Niu, Z., C. Yan, and Y. Li. Non-probabilistic credible reliability analysis of the composite laminate, Aerosp. Sci. Technol. 144 (2024) 108774.

Sacks, J., W. J. Welch, T. J. Mitchell, and H. P. Wynn. Design and analysis of computer experiments, Stat. Sci. 4 (1989) 409–423.

Shahriari, B., K. Swersky, Z. Wang, R. P. Adams, and N. de Freitas. Taking the human out of the loop: A review of Bayesian optimization, Proc. IEEE 104 (2016) 148–175.

Song, R., C. Zhou, J. Rui, H. Li, and J. Li. A volume-ratio index for sensitivity analysis of time-dependent models with interval uncertainty inputs, Aerosp. Sci. Technol. 153 (2024) 109495.

Tang, T., H. Luo, Y. Song, H. Fang, and J. Zhang. Chebyshev inclusion function based interval kinetostatic modeling and parameter sensitivity analysis for Exechon-like parallel kinematic machines with parameter uncertainties, Mech. Mach. Theory 157 (2021) 104209.

Törn, A. and A. Žilinskas. Global Optimization, Springer, 1989.

Wang, L., Y. Liu, D. Liu, and Z. Wu. A novel dynamic reliability-based topology optimization (DRBTO) framework for continuum structures via interval-process collocation and the first-passage theories, Comput. Methods Appl. Mech. Eng. 386 (2021) 114107.

Wang, Q. N., L. M. Song, Y. Chen, G. J. Ma, Z. D. Guo, and J. Li. KT-EGO: a knowledge transfer assisted efficient global optimization algorithm for solving high-dimensional expensive black-box problems, Eng. Optim. 55 (2023) 2015–2033.

Wei, P., Y. Wang, and C. Tang. Time-variant global reliability sensitivity analysis of structures with both input random variables and stochastic processes, Struct. Multidisc. Optim. 55 (2017) 1883–1898.

Wu, W. and S. S. Rao. Uncertainty analysis and allocation of joint tolerances in robot manipulators based on interval analysis, Reliab. Eng. Syst. Saf. 92 (2007) 54–64.

Yao, Z. Y., S. H. Wang, P. G. Wu, B. Y. Ni, and C. Jiang. An interval finite element method based on bilevel Kriging model, Chin. J. Aeronaut. 37 (2024) 1–11.

Zhan, H. Y. and N. C. Xiao. A new active learning surrogate model for time- and space-dependent system reliability analysis, Reliab. Eng. Syst. Saf. (2025) 110536.

A practical stratified importance sampling strategy for extremely rare event estimation in high dimensional systems

Luyi Li[1,2] *, **Hao Wang**[1]

[1] *School of Aeronautics, Northwestern Polytechnical University, Xi'an 710072, China, luyili@nwpu.edu.cn*

[2] *National Key Laboratory of Aircraft Configuration Design, Xi'an 710072, China*

Abstract

Estimating extremely rare events in complex systems represents a significant and persistent challenge in reliability analysis. This difficulty is further compounded in high-dimensional settings, where the target probability mass becomes exceedingly difficult to capture, introducing new obstacles to accurate estimation. To address these challenges, this paper proposes a practical and adaptive stratified importance sampling (IS) strategy for reliability analysis involving high-dimensional inputs and extremely rare events. The proposed method makes several key contributions. First, it theoretically demonstrates that within existing stratified IS frameworks, the accuracy of estimating intermediate failure events does not impact the final rare-event probability estimate. Leveraging this insight, we design an adaptive stratified strategy that prioritizes rapid progression toward the failure domain over precise intermediate event estimation, thereby avoiding the computational inefficiency inherent in exhaustively exploring intermediate failure regions.

At the core of our approach is a novel sampling density construction. We develop a mixture IS density based on a bi-domain K-means clustering technique, integrated with variance-enlarged sampling. This design enables the method to not only converge efficiently toward the failure region but also accurately capture diverse and challenging failure modes, including discontinuous patterns and those with sharp gradient transitions. To mitigate the significant estimation errors that can arise from minor deviations in failure information in high-dimensional problems, an optimization mechanism is innovatively introduced in the final sampling layer. This allows for the accurate identification of the most probable failure information in high-dimensional space, leading to precise estimation of extremely rare events in high-dimensional systems. The effectiveness of the proposed method is validated through a series of benchmark problems in reliability analysis, encompassing high dimensionality, small failure probabilities, and complex failure domains. Results consistently show that our method outperforms existing approaches in both capturing varied failure modes and delivering efficient, high-precision estimates, particularly for high-dimensional systems.

Keywords: Rare event estimation; High dimensional system; Importance sampling.

Introduction

Structural reliability analysis aims to evaluate the probability that a structure fails under uncertainties associated with random loads, material properties, geometric dimensions, and environmental factors. It is a fundamental problem in structural safety assessment and reliability-based design (Cavalieri et al., 2017). For complex engineering structures, failure events typically correspond to small-probability regions in a high dimensional random input space. In particular, under high-reliability design requirements, the target failure probability often reaches the order of 10^{-6} or even lower (Cheng et al., 2022; Li et al., 2023). In such cases, failure samples are extremely rare under the original probability distribution. The high dimensional nature of the problem further exacerbates the curse of dimensionality, resulting in highly sparse effective samples and making the geometric characteristics of the failure domain difficult to characterize (Cheng et al., 2023).

© 2026 by the author(s). This work is licensed under the Creative Commons Attribution 4.0 International License (CC BY 4.0), which permits unrestricted use, distribution, and reproduction in any medium, provided the original author and source are credited.

Therefore, accurately and stably estimating small failure probabilities in high dimensional problems with limited performance function evaluations remains a key challenge in structural reliability analysis.

For subsequent methodological development, the basic mathematical formulation of a structural reliability problem is first introduced. Assume that the performance function of a structure is defined as：

$$Y = g(\boldsymbol{X}) = g(X_1, X_2, \cdots, X_n) \tag{1}$$

where $\boldsymbol{X} = \{X_1, X_2, \cdots, X_n\}^T$ is an n-dimensional random input variable. The limit-state equation $g(\boldsymbol{x}) = 0$ divides the input variable space into the failure domain $F = \{\boldsymbol{x} : g(\boldsymbol{x}) \le 0\}$ and the safe domain $S = \{\boldsymbol{x} : g(\boldsymbol{x}) > 0\}$. The structural failure probability can be expressed as

$$P_f = \int_F f_{\boldsymbol{X}}(\boldsymbol{x}) d\boldsymbol{x} \tag{2}$$

where $f_{\boldsymbol{X}}(\boldsymbol{x})$ is the joint probability density function (PDF) of $\boldsymbol{X}$. When the input variables are mutually independent $f_{\boldsymbol{X}}(\boldsymbol{x}) = \prod_{i=1}^{n} f_{X_i}(x_i)$,where $f_{X_i}(x_i)(i = 1, 2, \cdots, n)$ is the marginal PDF of the input variable X_i.

By introducing the failure-domain indicator function $I_F(\boldsymbol{x})$, the failure probability in Eq. (2) can be rewritten as:

$$P_f = \int_F f_{\boldsymbol{X}}(\boldsymbol{x}) d\boldsymbol{x} = \int_{R^n} I_F(\boldsymbol{x}) f_{\boldsymbol{X}}(\boldsymbol{x}) d\boldsymbol{x} = E[I_F(\boldsymbol{x})] \tag{3}$$

where,

$$I_F(\boldsymbol{x}) = \begin{cases} 1 & \boldsymbol{x} \in F \\ 0 & \boldsymbol{x} \notin F \end{cases} \tag{4}$$

Existing methods for structural reliability analysis can generally be classified into three categories: approximate analytical methods, numerical simulation methods, and surrogate-model-based methods. Approximate analytical methods mainly include the First-Order Reliability Method (FORM) (Hasofer, 1974) and the Second-Order Reliability Method (SORM) (Der Kiureghian et al., 1987). These methods usually perform first-order or second-order Taylor expansions of the performance function at the Most Probable Point (MPP), thereby replacing the actual limit-state surface with a local approximation. Because a large number of direct evaluations of the original performance function are avoided, these methods usually offer relatively high computational efficiency. However, when the limit-state surface is strongly nonlinear or implicit, or when multiple failure domains exist, local-expansion-based approximations may not accurately characterize the actual failure boundary, thereby affecting the accuracy of reliability estimates.

In contrast, numerical simulation methods have become important tools in structural reliability analysis because of their clear principles and broad applicability. The fundamental method is Monte Carlo Simulation (MCS). MCS does not require additional assumptions regarding the performance function and is theoretically applicable to reliability problems with arbitrary forms. However, when small failure probabilities are considered, it usually requires a very large number of samples and therefore incurs a high computational cost. For this reason, it is often used as a reference benchmark for other efficient algorithms (Song and Kawai, 2023). To improve the efficiency of numerical simulation, various methods have been developed, including Importance Sampling (IS) (Tabandeh et al., 2022), Subset Simulation (SuS) (Au and Beck, 2001; Papaioannou et al., 2015), Line Sampling (Pradlwarter et al., 2007), and Directional Sampling (Zhang et al., 2020).

The core idea of IS is to construct an importance sampling probability density function (IS-PDF), thereby enabling the sampling process to generate more samples with relatively large contributions to the failure probability. Classical IS often improves the occurrence probability of failure samples by shifting the

importance sampling center (ISC) toward the vicinity of the MPP. On this basis, various improved strategies, such as Meta-IS (Dubourg et al., 2013), have been developed. In contrast, SuS represents a small failure probability as the product of a series of conditional failure probabilities, thereby effectively avoiding the exponential increase in sample size as the failure probability decreases. SuS therefore exhibits relatively high efficiency in small failure probability analysis. According to the method used to generate conditional samples, SuS can be further classified into traditional SuS methods based on Markov chain Monte Carlo (MCMC) and SS-IS methods based on importance sampling (Song and Lu, 2008).

Although substantial progress has been achieved using existing methods, reliability analysis remains challenging when the focus is further narrowed to high dimensional problems involving extremely small failure probabilities. When the failure probability is extremely small, the failure domain is often far from the high-probability-mass region of the input random variables, resulting in an extremely limited number of failure samples. As the dimensionality further increases, the dispersion of samples in the high dimensional space significantly weakens the ability of conventional stochastic simulation methods to identify critical failure regions. To improve the efficiency and stability of estimating extremely small failure probabilities in high dimensional settings, researchers have proposed many specialized methods. Representative methods include generalized subset simulation (GSS), sequential importance sampling (SIS), sequential directional importance sampling (SDIS), subset adaptive importance sampling (SAIS), and AL-MRBF-iCE-m*.

GSS progressively relaxes the failure threshold and enlarges input variance to approach extremely rare failure regions; it further uses coordinate rotation in high-dimensional settings (Cheng et al., 2022). SIS constructs a sequence of intermediate distributions toward an IS-PDF and uses conditional-sampling MCMC to reduce dimension sensitivity (Papaioannou et al., 2014).

SDIS (Cheng et al., 2023) represents an extremely small failure probability as a sequence of auxiliary failure probabilities. At the first level, global exploration is conducted using MCS in Cartesian coordinates. At subsequent levels, directional importance sampling is performed in polar coordinates, and the sampling process gradually approaches the actual failure domain through sequential resampling and move mechanisms. SAIS (Helal and Elvira, 2026) further combines a multi-proposal mixture distribution, adaptive threshold updating, and a historical-sample recycling mechanism to improve coverage of complex failure domains, particularly multimodal failure domains. Meanwhile, for computationally expensive engineering black-box models, AL-MRBF-iCE-m* (Yang et al., 2025) combines active learning surrogate models with dimension-reduced cross-entropy importance sampling to estimate extremely small failure probabilities while reducing the number of true model evaluations.

Overall, existing methods for high dimensional and extremely small failure probability problems commonly employ sequential or stratified simulation, variance reduction, or a combination of both to rapidly and accurately approach the failure domain, and substantial progress has been made in improving sampling efficiency. However, the performance of these methods usually depends strongly on the quality of the constructed intermediate distributions, the effectiveness of proposal distribution updating, and the ability to identify critical failure regions. When the failure domain exhibits multimodal, nonlinear, or complex geometric characteristics, how to stably and comprehensively capture all important failure regions remains a central challenge in extremely small failure probability estimation.

Taking the classical sequential simulation method of MCMC-based SuS as an example, samples at each level are usually generated through Markov chains and may therefore exhibit strong autocorrelation, which affects sample quality and estimation efficiency. For SS-IS methods that combine sequential simulation and variance reduction, the existing designs usually emphasize the accurate estimation of the conditional failure probability at each level. Therefore, a relatively large number of samples is allocated to each intermediate

level to ensure statistical accuracy. However, from the estimation form of SS-IS, once the IS-PDF at the final level has been determined, the failure probability can be further expressed as a single-level importance sampling estimate with respect to this final-level density. This observation indicates that the role of the intermediate levels should not be understood solely as providing high-accuracy estimates of conditional probabilities at successive levels. More importantly, the intermediate levels provide an informational basis for constructing an effective final-level IS-PDF through sample screening, regional advancement, and sampling-center updating. In other words, if the accuracy requirement for estimating intermediate-level conditional failure probabilities can be appropriately relaxed, and more computational resources can be allocated to improving the quality of the final-level IS-PDF, the overall computational efficiency may be substantially improved without affecting the final failure probability estimate. Moreover, existing SS-IS methods often select ISC primarily based on PDF information without further correcting their relative positions with respect to the true limit-state surface. In high dimensional problems, the final IS-PDF is generally more sensitive to positional deviations of the ISCs. Even a slight shift of the center may weaken the ability of the IS-PDF to cover important failure regions and lead to reduced estimation stability and efficiency.

Based on the above analysis, this study focuses on high dimensional and extremely small failure probability problems. Starting from the SS-IS framework, it re-examines the distinct roles of the intermediate and final levels in failure probability estimation and accordingly develops a more efficient adaptive stratified importance sampling strategy. The central idea is to reduce the dependence on highly accurate estimates of intermediate-level conditional failure probabilities and shift the methodological focus toward the efficient construction of the final-level IS-PDF and the accurate identification of critical failure regions. In this way, the overall efficiency and robustness of extremely small failure probability estimation in high dimensional problems can be improved.

The remainder of this paper is organized as follows. The first part reveals, through an equivalent transformation of the failure probability estimator in SS-IS, that the estimation of failure probability in SS-IS can be expressed as an integral involving only the IS-PDF at the final level. The second part presents the underlying idea and detailed implementation procedure of the proposed method. The third part validates the accuracy, stability, and computational efficiency of the proposed method through three numerical examples involving complex failure domains, high dimensional linear problems with extremely small failure probabilities, and high dimensional nonlinear problems with extremely small failure probabilities.

1. Analysis for SS-IS method

The SuS method introduces a sequence of intermediate failure events $F_k = \{\boldsymbol{x} : g(\boldsymbol{x}) \le b_k\}(k = 1, 2, \cdots, m)$, where $b_1 > b_2 > \cdots > b_m = 0$ denotes a sequence of critical values. In this case, $F_1 \supset F_2 \supset \cdots \supset F_m = F$ and $F_k = \bigcap_{i=1}^{k} F_i$, and the final target failure probability is transformed into the product of a sequence of conditional failure probabilities. According to the multiplication theorem in probability theory and the inclusion relationship among the events, the formula shown in Eq. (5) can be obtained.

$$\begin{aligned} P_f &= P\{F\} = P\left\{\bigcap_{k=1}^{m} F_k\right\} = P\left\{F_m \mid \bigcap_{k=1}^{m-1} F_k\right\} \cdot P\left\{\bigcap_{k=1}^{m-1} F_k\right\} \\ &= P\{F_m \mid F_{m-1}\} \cdot P\left\{F_{m-1} \mid \bigcap_{k=1}^{m-2} F_k\right\} \cdot P\left\{\bigcap_{k=1}^{m-2} F_k\right\} \\ &\cdots\cdots \\ &= P\{F_1\} \cdot \prod_{k=2}^{m} P\{F_k \mid F_{k-1}\} \end{aligned} \tag{5}$$

For simplicity, let $P_1 = P\{F_1\}$ and $P_k = P\{F_k \mid F_{k-1}\}(k = 2,3,\cdots,m)$. Then the final failure probability can be expressed as:

$$P_f = \prod_{k=1}^{m} P_k \tag{6}$$

The term P_1 in Eq. (6) can be estimated by Eq. (7) as follows:

$$\hat{P}_1 = \hat{P}\{F_1\} = \frac{1}{N_1} \sum_{j=1}^{N_1} I_{F_1}(\boldsymbol{x}_j^1) \tag{7}$$

where $\{\boldsymbol{x}_j^1\}_{j=1}^{N_1}$ denotes the N_1 samples generated from the joint PDF $f_{\boldsymbol{X}}(\boldsymbol{x})$ of the input variables $\boldsymbol{X}$.

The conditional failure probability P_k in Eq. (6) can be estimated by Eq. (8) as follows:

$$\hat{P}_k = \hat{P}\{F_k \mid F_{k-1}\} = \frac{1}{N_k} \sum_{j=1}^{N_k} I_{F_k}(\boldsymbol{x}_j^k) \quad (k = 2,3,\cdots,m) \tag{8}$$

where $\{\boldsymbol{x}_j^k\}_{j=1}^{N_k}$ denotes the N_k samples generated from the conditional PDF $q_{\boldsymbol{X}}(\boldsymbol{x} \mid F_{k-1})$ of the input variables $\boldsymbol{X}$ shown in Eq. (9).

$$q_{\boldsymbol{X}}(\boldsymbol{x} \mid F_{k-1}) = \frac{I_{F_{k-1}}(\boldsymbol{x}) f_{\boldsymbol{X}}(\boldsymbol{x})}{P\{F_{k-1}\}} \quad (k = 2,3,\cdots,m) \tag{9}$$

Conditional samples following the conditional PDF $q_{\boldsymbol{X}}(\boldsymbol{x} \mid F_{k-1})$ can be generated directly by Monte Carlo sampling. However, this approach is inefficient. Therefore, the SuS method mainly uses MCMC to obtain conditional samples following $q_{\boldsymbol{X}}(\boldsymbol{x} \mid F_{k-1})$.

Although MCMC can effectively generate samples following $q_{\boldsymbol{X}}(\boldsymbol{x} \mid F_{k-1})$, the Markov-chain mechanism usually introduces a certain degree of correlation among the generated samples. To reduce sample correlation, the SS-IS method has been proposed (Song and Lu, 2008). This method efficiently obtains conditional failure samples through IS. Its basic procedure starts from the joint PDF of the input variables, sequentially constructs the IS-PDF function on each subset, estimates the corresponding conditional failure probability for each subset, and finally obtains the required estimate of the failure probability.

In SS-IS, P_1 is also estimated by Eq.(7), whereas the conditional failure probabilities $P_k = P\{F_k \mid F_{k-1}\}(k = 2,3,\cdots,m)$ is calculated using the IS method shown in Eq. (10):

$$P_k = \int_{R^n} I_{F_k}(\boldsymbol{x}) \cdot q_{\boldsymbol{X}}(\boldsymbol{x} \mid F_{k-1}) d\boldsymbol{x} = \int_{R^n} \frac{I_{F_k}(\boldsymbol{x}) \cdot q_{\boldsymbol{X}}(\boldsymbol{x} \mid F_{k-1})}{h_{\boldsymbol{X}}^k(\boldsymbol{x})} h_{\boldsymbol{X}}^k(\boldsymbol{x}) d\boldsymbol{x} = E\left[\frac{I_{F_k}(\boldsymbol{x}) \cdot q_{\boldsymbol{X}}(\boldsymbol{x} \mid F_{k-1})}{h_{\boldsymbol{X}}^k(\boldsymbol{x})}\right] \tag{10}$$

where $h_{\boldsymbol{X}}^k(\boldsymbol{x})$ is the IS-PDF of the k-th intermediate failure event. This IS-PDF takes the sample with the largest original PDF value among the conditional failure samples at level k-1 as the ISC and constructs its covariance matrix using the variance of the original PDF.

After drawing N_k samples $\{\boldsymbol{x}_j^k\}_{j=1}^{N_k}$ of the input variables from the IS-PDF $h_{\boldsymbol{X}}^k(\boldsymbol{x})$, the estimate $\hat{P}_k$ of the conditional failure probabilities P_k can be obtained as shown in Eq. (11).

$$\hat{P}_k = \frac{1}{N_k}\sum_{j=1}^{N_k}\frac{I_{F_k}(\boldsymbol{x}_j^k)q_{\boldsymbol{X}}(\boldsymbol{x}_j^k \mid F_{k-1})}{h_{\boldsymbol{X}}^k(\boldsymbol{x}_j^k)} \quad (k=2,3,\cdots,m) \tag{11}$$

According to Eq. (10), the conditional failure probability at the *m*-th level, namely the final level, can be expressed as Eq. (12):

$$P_m = \int_{R^n}\frac{I_{F_m}(\boldsymbol{x})\cdot q_{\boldsymbol{X}}(\boldsymbol{x} \mid F_{m-1})}{h_{\boldsymbol{X}}^m(\boldsymbol{x})}h_{\boldsymbol{X}}^m(\boldsymbol{x})d\boldsymbol{x} \tag{12}$$

If the conditional failure probability P_m at the *m*-th level is separated from Eq. (6) and the failure probability of the k-th intermediate failure event (k = 2,3,...,m) is considered, which can be expressed as:

$$P\{F_k\} = P\left\{\bigcap_{i=1}^{k}F_i\right\} = P\{F_k \mid F_{k-1}\}P\{F_{k-1} \mid F_{k-2}\}\cdots P\{F_2 \mid F_1\} = \prod_{i=1}^{k}P_i \tag{13}$$

Thus, the following expression can be obtained:

$$\begin{aligned} P_f &= \prod_{k=1}^{m}P_k = \prod_{k=1}^{m-1}P_k \times P_m \\ &= \prod_{k=1}^{m-1}P_k \times \int_{R^n}\frac{I_{F_m}(\boldsymbol{x})I_{F_{m-1}}(\boldsymbol{x})f_{\boldsymbol{X}}(\boldsymbol{x})}{P\{F_{m-1}\}h_{\boldsymbol{X}}^m(\boldsymbol{x})}h_{\boldsymbol{X}}^m(\boldsymbol{x})d\boldsymbol{x} \\ &= \frac{\prod_{k=1}^{m-1}P_k}{P\{F_{m-1}\}} \times \int_{R^n}\frac{I_{F_m}(\boldsymbol{x})I_{F_{m-1}}(\boldsymbol{x})f_{\boldsymbol{X}}(\boldsymbol{x})}{h_{\boldsymbol{X}}^m(\boldsymbol{x})}h_{\boldsymbol{X}}^m(\boldsymbol{x})d\boldsymbol{x} \\ &= \int_{R^n}\frac{I_{F_m}(\boldsymbol{x})f_{\boldsymbol{X}}(\boldsymbol{x})}{h_{\boldsymbol{X}}^m(\boldsymbol{x})}h_{\boldsymbol{X}}^m(\boldsymbol{x})d\boldsymbol{x} \end{aligned} \tag{14}$$

Eq. (14) shows that the failure probability P_f can be equivalently expressed as a single-level IS integral with respect to the *m*-th-level (final-level) IS-PDF $h_{\boldsymbol{X}}^m(\boldsymbol{x})$. Therefore, once the final-level IS-PDF $h_{\boldsymbol{X}}^m(\boldsymbol{x})$ is determined, the total failure probability can be estimated by a weighted integral under this PDF, and the estimator can be written as:

$$P_f = \frac{1}{N_m}\sum_{j=1}^{N_m}\frac{I_{F_m}(\boldsymbol{x}_j)f_{\boldsymbol{X}}(\boldsymbol{x}_j)}{h_{\boldsymbol{X}}^m(\boldsymbol{x}_j)} \tag{15}$$

where N_m denotes the number of samples used in the final-level importance sampling.

Therefore, in the SS-IS method, the accuracy of the final failure probability estimate actually depends only on the construction quality of the IS-PDF in the final-level and has no direct relationship with the construction of the intermediate-level IS-PDFs or the estimation accuracy of the conditional failure probabilities. This indicates that SS-IS does not need to accurately estimate the conditional failure probability at every intermediate level. Instead, it only needs to gradually approach the true limit-state surface through level-by-level advancement, sample screening, and sampling-center updating, and then construct a high-quality IS-PDF at the final level.

It should also be noted that although the intermediate levels do not directly affect the accuracy of the final failure probability estimate, they still indirectly influence the accuracy, variance, and stability of the final estimate by affecting the construction quality of the final-level IS-PDF. Therefore, compared with

traditional SS-IS, which emphasizes accurate level-by-level estimation of the intermediate conditional failure probabilities, this study focuses more on the role of intermediate levels in the process of approaching the limit-state surface, identifying potential important regions, and constructing a high-quality final IS-PDF. Based on the above derivation, this paper redesigns the construction strategy of the intermediate-level IS-PDF in SS-IS, so that intermediate samples can rapidly approach the limit-state surface, identify important failure regions, and support high-quality construction of the final-level IS-PDF.

2 A practical stratified IS strategy for extremely rare event estimation in high dimensional systems

To address the limitations of traditional SS-IS, namely that a single ISC cannot retain information from multiple potential important failure regions and that the traditional ISC updating strategy has limited stratified advancement efficiency, this paper proposes a practical stratified IS strategy. The strategy first enlarges the sampling variance of the first-level IS-PDF to enhance the initial exploration of potential failure regions. It then introduces K-means clustering to identify multiple candidate ISCs and construct a mixture IS-PDF for the intermediate levels. At the same time, a safe/failure bi-domain ISC screening mechanism, together with a corresponding stratified stopping criterion, is proposed to balance failure-region exploration and the efficiency of approaching the limit-state surface. Finally, in constructing the final-level IS-PDF, an optimization procedure is employed to obtain local optimal solutions to the maximization of the original PDF within failure domain. These local optimal solutions are then used as the ISCs for constructing the final-level IS-PDF, thereby improving the overall estimation accuracy and computational efficiency of the proposed method.

For ease of implementation, the proposed method is calculated in the standard normal space. For mutually independent non-standard normal random variables, marginal distribution transformation can be used. For correlated random variables, the Nataf transformation or Rosenblatt transformation can be adopted. To simplify the notation, this section directly assumes that all input variables $\boldsymbol{X}$ follow mutually independent standard normal distributions, and the corresponding performance function in the standard normal space is denoted by $g(\boldsymbol{X})$. The specific implementation steps of the proposed method are as follows:

Stage 1: Searching for potential important failure regions

1. **Initialization of the first-level IS-PDF and sample generation:** Determine the conditional failure sample ratio p_0 and the standard-deviation enlargement factor $\alpha = 3$ (Cheng et al., 2023) for the first level to obtain the first-level IS-PDF $h_{\boldsymbol{X}}^1(\boldsymbol{x}) = \prod_{r=1}^{n} \frac{1}{\alpha\sqrt{2\pi}} \exp(-\frac{x_r^2}{2\alpha^2})$. Then generate N_1 samples $\{\boldsymbol{x}_j^1\}_{j=1}^{N_1}$ following $h_{\boldsymbol{X}}^1(\boldsymbol{x})$ and set $k = 1$.
2. **Determination of the first-level conditional failure threshold:** Calculate the performance-function values $\{g(\boldsymbol{x}_j^1)\}_{j=1}^{N_1}$ of the N_1 samples. Sort these N_1 response values in descending order and denote the sorted results as $g(\boldsymbol{x}_{[1]}^1) > g(\boldsymbol{x}_{[2]}^1) > \cdots > g(\boldsymbol{x}_{[N_1]}^1)$, where $[\bullet]$ denotes the index after the response values are sorted in descending order, rather than the original sample index. The $\lceil (1-p_0)N_1 \rceil$-th response value is taken as the critical value b_1 of the intermediate failure event $F_1 = \{\boldsymbol{x} : g(\boldsymbol{x}) \le b_1\}$, where $b_1 = g(\boldsymbol{x}_{[\lceil (1-p_0)N_1 \rceil]}^1)$ and $\lceil \bullet \rceil$ denotes the upward rounding operator.
3. **Level-index update:** $k = k + 1$.
4. **Identification of potential important regions based on K-means:** Use K-means clustering to divide

the sample points $\{\boldsymbol{x}_j^{k-1}\}_{j=\lceil(1-p_0)N_{k-1}\rceil}^{[N_{k-1}]}$ falling into the intermediate failure domain F_{k-1} into K^* clusters, $\mathcal{C}_s^k, s=1,2,...,K^*$, where N_{k-1} denotes the number of samples at level k-1 and K^* denotes the number of clusters. Within each cluster, the conditional failure samples are further divided into two groups according to the indicator function $I_F(\boldsymbol{x})$ of the final failure domain, i.e., safe samples $\Omega_{KS,s}=\{\boldsymbol{x}\in\mathcal{C}_s^k \mid g(\boldsymbol{x})>0\}$ and failure samples $\Omega_{KF,s}=\{\boldsymbol{x}\in\mathcal{C}_s^k \mid g(\boldsymbol{x})\le 0\}$.

5. **Safe/failure bi-domain ISC screening:** If $\Omega_{KS,s}\neq\varnothing$, select the sample $\boldsymbol{x}_{KS,s}=\arg\min_{\boldsymbol{x}\in\Omega_{KS,s}}\phi_n(\boldsymbol{x})$ with the smallest PDF value $\phi_n(\boldsymbol{x})$ from $\Omega_{KS,s}$. If $\Omega_{KF,s}\neq\varnothing$, select the sample $\boldsymbol{x}_{KF,s}=\arg\max_{\boldsymbol{x}\in\Omega_{KF,s}}\phi_n(\boldsymbol{x})$ with the largest PDF value $\phi_n(\boldsymbol{x})$ from $\Omega_{KF,s}$, where $\phi_n(\boldsymbol{x})$ denotes the PDF of the standard normal distribution. By screening the K^* clusters of samples, the ISCs obtained from the safe samples can be represented as $\{\boldsymbol{x}_{KS,j}^k\}_{j=1}^{N_{KS}}$, where $N_{KS}\le K^*$ denotes the number of ISCs obtained from the K^* clusters of safe samples. The ISCs obtained from the failure samples can be represented as $\{\boldsymbol{x}_{KS,j}^k\}_{j=1}^{N_{KF}}$, where $N_{KF}\le K^*$ denotes the number of ISCs obtained from the K^* clusters of failure samples.

6. **Construction of the ISC set:** Merge $\{\boldsymbol{x}_{KS,j}^k\}_{j=1}^{N_{KS}}$ and $\{\boldsymbol{x}_{KS,j}^k\}_{j=1}^{N_{KF}}$ to obtain the ISC set $\{\boldsymbol{x}_{\mathrm{ISC}_k,j}^k\}_{j=1}^{N_{\mathrm{ISC}_k}}$ of level k, where $N_{\mathrm{ISC}_K}=N_{KS}+N_{KF}\le 2K^*$ is the number of ISCs.

7. **Judgment of the stratified stopping criterion:** Determine whether N_{KF} is equal to K^*. If $N_{KF}\neq K^*$, some of the K^* clusters contain no failure samples and therefore do not yield corresponding failure ISC. This suggests that some potential important regions identified by K-means may not yet have reached the true failure domain. In this case, the samples should be further advanced toward the limit-state surface, and the algorithm proceeds to Step 8 for the next-level search. If $N_{KF}=K^*$, each of the K^* clusters contains at least one failure sample and therefore yields a corresponding failure ISC. This indicates that all potential important regions represented by the current K-means clusters have reached the true failure domain. Consequently, the main potential failure regions are regarded as having been sufficiently explored under current condition. Therefore, set $m=k$, and $b_m=0$, and proceed to Step 12 to construct the final-level IS-PDF.

8. **Construction of the next-level IS-PDF and generation of importance samples:** For each ISC from $\{\boldsymbol{x}_{\mathrm{ISC},i}^k\}_{i=1}^{N_{\mathrm{ISC}_k}}$, construct a Gaussian distribution $h_{\boldsymbol{x}_{\mathrm{ISC},i}^k}^k(\boldsymbol{x})$ using $\boldsymbol{x}_{\mathrm{ISC},i}^k$ as the ISC and the identity covariance matrix as the covariance matrix. Then construct the k-th-level IS-PDF using an equally weighted Gaussian mixture strategy as follows,

$$h_{\boldsymbol{X}}^k(\boldsymbol{x})=\frac{1}{N_{\mathrm{ISC}_k}}\sum_{i=1}^{N_{\mathrm{ISC}_k}}h_{\boldsymbol{x}_{\mathrm{ISC},i}^k}^k(\boldsymbol{x}) \tag{16}$$

This is because that the main objective of the intermediate levels is to identify and advance multiple potential important regions rather than to directly estimate the final failure probability. At this stage, the relative contribution of each ISC to the final failure probability has not yet been determined. Therefore, an equally weighted mixture is adopted to prevent centers with large original PDF values from dominating the sampling process prematurely, thereby maintaining the exploration capability for low-probability potential failure regions.

Then draw the k-th-level importance samples from the density in Eq.(16). The detailed sampling

procedure is as follows. First, draw $\left\lceil \frac{N_k^*}{N_{\mathrm{ISC}_K}} \right\rceil$ samples following $h^k_{\boldsymbol{X}^k_{\mathrm{ISC},i}}(\boldsymbol{x})$. Traverse all ISCs to obtain $N_k = \left\lceil \frac{N_k^*}{N_{\mathrm{ISC}_K}} \right\rceil \times N_{\mathrm{ISC}_K}$ importance samples $\{\boldsymbol{x}_j^k\}_{j=1}^{N_k}$ and calculate their corresponding performance-function values $\{g(\boldsymbol{x}_j^k)\}_{j=1}^{N_k}$, where N_k^* denotes the preset sample size at level k and N_k denotes the actual sample size generated because of the rounding operation.

9. **Extraction of conditional failure samples:** According to the performance-function values $\{g(\boldsymbol{x}_j^k)\}_{j=1}^{N_k}$, identify the M_k sample points $\{\boldsymbol{x}_j^k\}_{j=1}^{M_k}$ falling into F_{k-1}, and denote their corresponding performance-function values by $\{g(\boldsymbol{x}_j^k)\}_{j=1}^{M_k}$.

10. **Update of the intermediate failure threshold:** Sort the above M_k response values in descending order and denote the sorted results as $g(\boldsymbol{x}^k_{[1]}) > g(\boldsymbol{x}^k_{[2]}) > \cdots > g(\boldsymbol{x}^k_{[M_k]})$. The $\lceil (1-p_0)M_k \rceil$-th response value is taken as the critical value b_k of the intermediate failure event $F_k = \{\boldsymbol{x} : g(\boldsymbol{x}) \le b_k\}$, and $b_k = g(\boldsymbol{x}^k_{[\lceil (1-p_0)M_k \rceil]})$.

11. **Proceed to the next-level search:** Return to Step 3 for the next-level search.

Stage 2: Construction of the final IS-PDF

12. **Failure-ISC optimization and ISC correction:** Taking the ISCs $\{\boldsymbol{x}^m_{ISC,i}\}_{i=1}^{N_{KF}}$ screened from the failure samples at level *m* as the initial iteration points, solve the following constrained optimization problem in the standard normal space using a local optimization method:

$$\min_{\boldsymbol{x}} \| \boldsymbol{x} \|, \quad s.t.\ g(\boldsymbol{x}) = 0 \tag{17}$$

This optimization process corrects each ISC onto the limit-state surface and moves ISC toward a position with a higher original probability density. This improves its representativeness as a final ISC. The optimized ISC set is denoted by $\{\boldsymbol{x}^{m,*}_{ISC,i}\}_{i=1}^{N_{KF}}$.

13. **Construction of the final-level IS-PDF and generation of importance samples:** First, the PDF value $\{\phi_n(\boldsymbol{x}^{m,*}_{ISC,i})\}_{i=1}^{N_{KF}}$ of each optimized ISC under the standard normal distribution is calculated, and the normalized weights $\gamma_i, i = 1,2,...,N_{KF}$ of all optimized ISCs are obtained from Eq. (18).

$$\gamma_i = \frac{\phi_n(\boldsymbol{x}^{m,*}_{ISC,i})}{\sum_{j=1}^{N_{KF}} \phi_n(\boldsymbol{x}^{m,*}_{ISC,j})}, i = 1,2,...,N_{KF} \tag{18}$$

Then, for each optimized ISC $\boldsymbol{x}^{m,*}_{\mathrm{ISC},i}$, construct a Gaussian component $h^m_{\boldsymbol{X}^{m,*}_{ISC,i}}(\boldsymbol{x})$ using $\boldsymbol{x}^{m,*}_{\mathrm{ISC},i}$ as the ISC and the identity covariance matrix as the covariance matrix. Based on these components, construct the final-level Gaussian-mixture IS-PDF.

$$h^m_{\boldsymbol{X}}(\boldsymbol{x}) = \sum_{i=1}^{N_{KF}} \gamma_i h^m_{\boldsymbol{X}^{m,*}_{\mathrm{ISC},i}}(\boldsymbol{x}) \tag{19}$$

Samples are then drawn from this density. The specific sampling process is as follows. According to the normalized weights $\{\gamma_i\}_{i=1}^{N_{KF}}$, the index of a Gaussian component is first randomly selected from the discrete distribution $Categorical(\gamma_1,...,\gamma_{N_{KF}})$. A sample is then generated from the corresponding Gaussian component.

Repeating this process N_m times yields N_m independent samples following the mixture density $h_X^m(\boldsymbol{x})$.

It is worth noting in this step that mixture weights proportional to their original PDF values is used in this step to construct the final IS-PDF. This is because that the optimized failure ISCs correspond to failure-boundary locations with relatively high probability density in different local failure regions. This strategy can improve the ability of the final IS-PDF to cover the main regions contributing to the failure probability.

Stage 3: Failure probability estimation

14. **Final failure probability estimation:** Based on the IS samples $\{\boldsymbol{x}_j^m\}_{j=1}^{N_m}$ obtained at level *m*, estimate the final failure probability using Eq. (21):

$$\hat{P}_f = \frac{1}{N_m}\sum_{j=1}^{N_m} I_F(\boldsymbol{x}_j^m)\frac{\phi_n(\boldsymbol{x}_j^m)}{h_{\boldsymbol{X}}^m(\boldsymbol{x}_j^m)} \tag{20}$$

In summary, the proposed method first enlarges the variance of the initial-level IS-PDF, enhancing the ability of early samples to explore potential failure regions far from the original high-probability area. This provides rich global exploration information for subsequent stratified searching. K-means clustering then partitions the conditional samples inside intermediate failure events into multiple candidate regions with distinct spatial distributions, overcoming the limitation of a single ISC in representing multimodal or widely separated failure regions. Within each cluster, a dual-domain ISC screening mechanism is applied: for safe samples, the one with a smaller original PDF value is chosen as the ISC to push next-level samples farther away from the high-probability region; for failure samples, the one with a larger original PDF value is retained to preserve failure information near the high-density region. By combining variance enlargement, clustering-based identification, and safe-domain ISC extrapolation, samples advance level by level toward the limit-state surface along multiple promising directions, enabling rapid approximation of the failure boundary. Furthermore, the algorithm checks whether failure samples appear in all clusters to determine if all potential important failure regions have been sufficiently explored, thereby deciding when to terminate the intermediate-level progression.

In the final IS-PDF construction stage, the screened failure ISCs serve as starting points for local optimization on the limit-state surface, shifting them to failure-boundary positions with relatively high probability density within their respective local failure regions. Mixture weights are then assigned based on the original PDF values of these optimized ISCs, yielding a weighted Gaussian-mixture IS-PDF. This procedure preserves information from multiple dominant failure regions while improving the quality of each individual ISC, ultimately constructing a high-quality final IS-PDF that enhances both the efficiency and robustness of rare-event failure probability estimation for complex systems.

3. Examples

This section uses three examples to test the accuracy and efficiency of the proposed method. The three examples examine, respectively, a complex failure-domain problem that is difficult for the classical SuS method, a linear high dimensional problem with extremely small failure probability, and a nonlinear high dimensional problem with extremely small failure probability. The proposed method is denoted as AS-IS (adaptive stratified importance sampling).

In the three test examples for failure probability estimation, the results obtained by MCS with a large sample size are used as reference solutions. The proposed method is compared with existing methods for high dimensional small failure probability problems, including SuS-aCS (Papaioannou et al., 2015), SIS (Papaioannou et al., 2014), and SDIS (Cheng et al., 2023). Five evaluation metrics are used for the comparison:

the mean failure probability $\bar{P}_f$ over 30 independent runs, the coefficient of variation *CoV* of the 30 failure probability estimates, the average relative error $\bar{\varepsilon}$ of the 30 independent failure probability estimates with respect to the reference solution, the relative error $\varepsilon_{\bar{P}_f}$ of the mean failure probability with respect to the reference solution, and the average number of performance-function calls *Ncall*. It should be noted that the comparison methods are selected according to the purpose of each example and the applicability conditions of the methods. In Example 3, because the failure probability decreases as the standard deviation of the input variables increases, SDIS, which constructs auxiliary failure probability sequences by variance enlargement, is not suitable and is therefore not included in the comparison for this example.

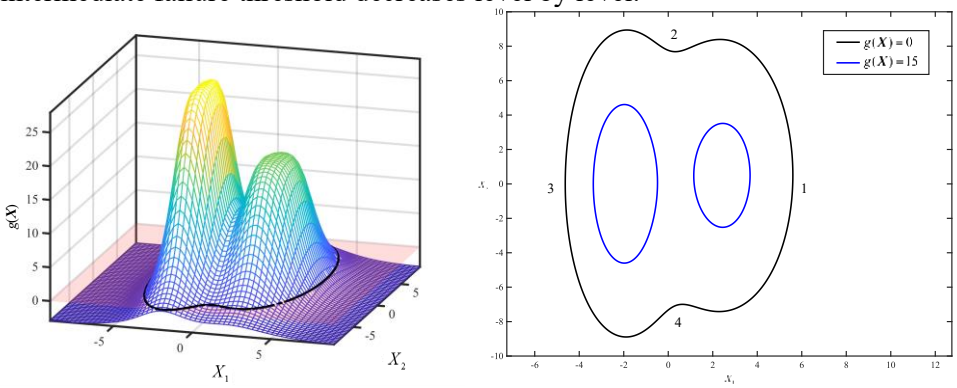
To ensure reproducibility of the comparison, the parameters of the comparison methods are set according to their corresponding references or the recommended settings in the publicly available source codes. Specifically, SuS-aCS uses 2000 conditional samples at each level, SIS uses 2000 IS samples at each level, and the SDIS parameters are set to NF = 100 and LEN = 5. For the proposed method, the sample size is selected so that the average number of performance-function calls is as close as possible to that of the most efficient comparison methods. This enables comparing the accuracy and efficiency of different methods under the similar computational cost.

Example 1

Example 1 selects the fourth representative example in (Breitung, 2019), which is difficult for the SuS method to solve effectively. This example mainly reflects the situation in which the main failure domains are blocked by high-performance-function regions and the topology of the failure domain changes during the level-by-level approximation process. The performance function can be expressed as follows.

$$g(X_1, X_2) = \frac{30}{\left(\frac{4(X_1+2)^2}{9} + \frac{X_2^2}{25}\right)^2 + 1} + \frac{20}{\left(\frac{(X_1-2.5)^2}{4} + \frac{(X_2-0.5)^2}{25}\right)^2 + 1} - 3 \tag{21}$$

As shown in Figure 1 (a), the performance function in this example has relatively complex geometric characteristics. At the same time, Figure 1 (b) shows that the contour shapes corresponding to $g(\boldsymbol{X})=15$ and $g(\boldsymbol{X})=0$ are clearly different, indicating that the geometry and connectivity of the conditional failure domain change as the intermediate failure threshold decreases level by level.



(a) (b)

Figure 1 Performance surface and contours of $g(\boldsymbol{X})=15$ and $g(\boldsymbol{X})=0$ for Example 1.

During this process, sequential simulation samples tend to advance along locally accessible directions of decreasing function values near the original sampling center and preferentially cluster toward failure

domains 2 and 4 in Figure 1 (b). And failure domains 1 and 3 contribute more to the final failure probability. Therefore, if samples fail to cross the local high-performance-function regions and enter these two domains, the dominant failure regions may not be adequately explored, leading to a substantial underestimation of the final failure probability.

Table 1 Failure probability estimates obtained by different methods for the problem in Example 1

	$\overline{P}_f$	CoV	$\overline{\varepsilon}$	$\varepsilon_{\overline{P}_f}$	$Ncall$
MCS	2.015×10^{-6}	0.0498	/	/	2×10^{8}
SuS-aCS	2.287×10^{-6}	1.9533	1.5485	0.1349	23400
SIS	1.938×10^{-6}	2.395	1.500	0.038	19133
SDIS	2.189×10^{-6}	0.1610	0.1538	0.0863	3229.2
AS-IS	2.031×10^{-6}	0.0797	0.0611	0.0081	3222.4

Table 1 and Figure 2 and Figure 3 compare the performance of SuS-aCS, SIS, and SDIS in Example 1. SuS-aCS yields a mean failure-probability estimate of 2.287×10^{-6}, but its relative error and CoV reach 0.1349 and 1.9533, respectively. As illustrated in Figure 2, its level-by-level samples tend to cluster in failure domains 2 and 4 and fail to adequately reach the dominant domains 1 and 3, leading to insufficient coverage and unstable estimates. SIS has a mean estimate of 1.938×10^{-6}, but its CoV remains as high as 2.395 and its average relative error is 1.500. Figure 3 shows that its final IS-PDF is likewise concentrated mainly in domains 2 and 4, indicating that sequential IS-PDF updating does not necessarily overcome the omission of important regions caused by performance-function barriers and topological changes. By comparison, SDIS provides a mean estimate of 2.189×10^{-6}, with a CoV of 0.1610 and an average of 3229.2 performance-function calls. Variance enlargement and directional sampling reduce the path dependence of local advancement; however, because its important directions are determined from randomly selected initial auxiliary failure samples, the coverage of the left and right dominant domains may still vary across runs, leaving its CoV higher than that of AS-IS.

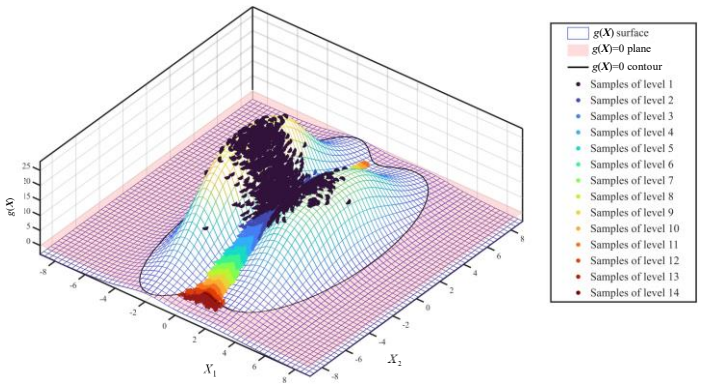


Figure 2 Sampling process of SuS-aCS method in the estimation of failure probability for the problem in Example 1

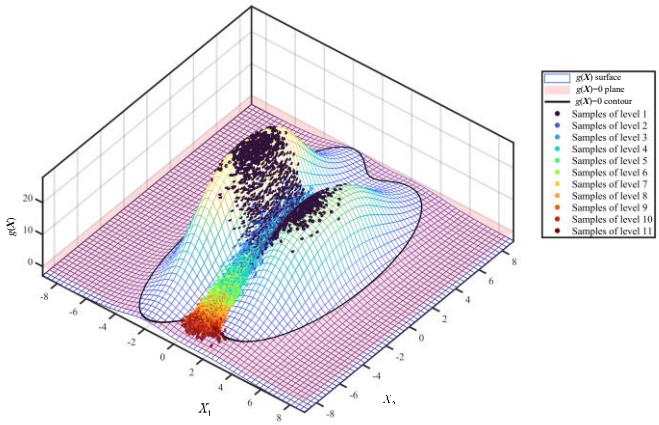


Figure 3 Sampling process of SIS method in the estimation of failure probability for the problem in Example 1

AS-IS exhibits better overall performance in this example. Its mean failure probability is 2.031×10^{-6}, which is highly consistent with the MCS reference value of 2.015×10^{-6}. The relative error of the mean is only 0.0081, and CoV is 0.0797, which is clearly lower than those of SuS-aCS, SIS, and SDIS. Its average number of performance-function calls is 3222.4, almost the same as the 3229.2 calls required by SDIS, but its estimation stability is higher. These results indicate that, under a similar or lower computational cost, AS-IS can more stably identify and cover the dominant failure regions on both sides and thus construct a more appropriate final IS-PDF.

Figure 4 illustrates the mechanism: variance enlargement supports early exploration, K-means identifies candidate regions, and local optimization moves screened ISCs toward the dominant failure domains. The resulting final IS-PDF covers the principal contributors simultaneously.

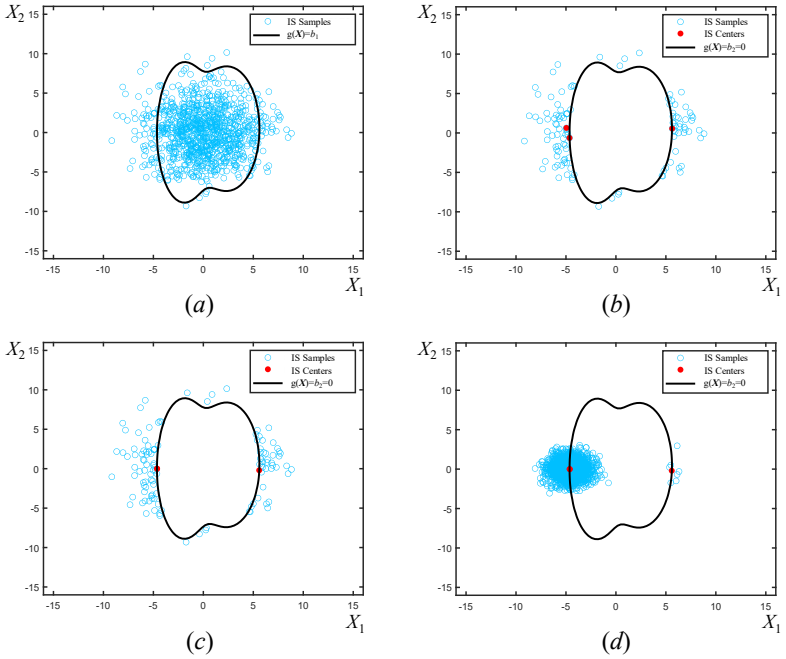


Figure 4 Sampling process of AS-IS method in the estimation of failure probability for the problem in Example 1

Therefore, the results of Example 1 show that when high-performance-function regions of the performance function obstruct the path between the original sampling center and important failure domains, the samples of SuS-aCS and SIS tend to extrapolate along locally accessible descent paths and consequently concentrate on non-dominant failure regions, while failing to sufficiently cover the truly important failure domains on the left and right sides. SDIS can alleviate this problem to some extent through variance enlargement and directional sampling, but its directional coverage is still affected by the randomness of the initial auxiliary failure samples. In contrast, AS-IS identifies potential important regions through K-means clustering and combines ISC optimization with multi-center Gaussian-mixture IS-PDF construction, enabling the ISCs to approach different dominant failure regions more stably and effectively. Therefore, AS-IS achieves the smallest relative error of the mean, a low CoV, and a number of performance-function calls comparable to that of SDIS in Example 1, demonstrating its advantages in accuracy, stability, and efficiency for problems with complex topological changes.

Example 2 A high dimensional linear example with an extremely small failure probability

Example 2 is mainly used to test the applicability of the proposed method to high dimensional problems with extremely small failure probability. For this purpose, the following high dimensional linear performance function is constructed:

$$g(\boldsymbol{X}) = 8 - \frac{1}{\sqrt{1000}} \sum_{i=1}^{1000} X_i \tag{22}$$

All random input variables follow standard normal distributions, and the theoretical solution of the failure probability is $P_f = \Phi(-8) \approx 6.221\times10^{-16}$. This example compares the proposed method with SuS-aCS, SIS, and SDIS. The solution results of different methods for Example 2 are shown in Table 2.

Table 2 Failure probability estimates obtained by different methods for the problem in Example 2

	$\overline{P}_f$	CoV	$\overline{\varepsilon}$	$\varepsilon_{\overline{P}_f}$	N_{call}
SuS-aCS	6.761×10^{-16}	1.1487	0.7309	0.0869	3.373×10^{4}
SIS	4.343×10^{-17}	1.9417	0.9302	0.9302	3.103×10^{4}
SDIS	7.445×10^{-16}	1.9629	1.4588	0.1968	4.296×10^{4}
AS-IS	6.235×10^{-16}	0.0499	0.0415	0.0023	3.041×10^{4}

As shown in Table 2, the estimated mean of AS-IS is 6.235×10^{-16}, which is highly consistent with the theoretical solution, and the relative error of the mean is only 0.0023. Meanwhile, its CoV is 0.0499 and the average relative error is 0.0415, indicating that the proposed method can maintain high estimation accuracy and good single-run stability in this high dimensional extremely small failure probability problem.

Overall, in this example, AS-IS outperforms SuS-aCS, SIS, and SDIS in estimation accuracy, single-run stability, and computational efficiency. This demonstrates that the proposed method can more stably construct a high-quality IS-PDF with sufficient coverage of the dominant failure region, thereby improving the accuracy and stability of failure probability estimation.

Example 3 A high dimensional nonlinear example with an extremely small failure probability

Example 3 is mainly used to test the applicability of the proposed method to high dimensional nonlinear performance functions. For this purpose, the following test performance function is constructed:

$$g(\boldsymbol{X}) = -760 + \sum_{i=1}^{100} X_i + \sum_{i=1}^{100} X_i^2 - \sum_{i=1}^{100} X_i^3$$

The random variables follow normal distributions with a mean of -2 and a standard deviation of 0.4, $X_i \sim N(-2, 0.4^2), i = 1, 2, ..., 100$. In the actual calculation, these non-standard normal variables are first standardized into independent standard normal variables, and the proposed algorithm is then implemented in the standard normal space.

Example 3 uses the MCS estimate as the reference solution and compares the proposed AS-IS method with SuS-aCS and SIS. Table 3 presents the solution results of different methods for Example 3.

Table 3 Failure probability estimates obtained by different methods for the problem in Example 3

	$\overline{P}_f$	CoV	$\overline{\varepsilon}$	$\varepsilon_{\overline{P}_f}$	N_{call}
MCS	3.681×10^{-10}	0.05	/	/	1.0868×10^{12}
SuS-aCS	4.135×10^{-10}	0.3153	0.2754	0.1235	4.4×10^{4}
SIS	4.341×10^{-10}	1.0705	0.8461	0.1795	4.5×10^{4}
AS-IS	3.675×10^{-10}	0.0463	0.0368	0.0014	4.2267×10^{4}

The third example mainly verifies the capability of the proposed method in handling high dimensional nonlinear performance functions. As shown in Table 3, the estimated mean of AS-IS is 3.675×10^{-10}, which is highly consistent with the MCS reference solution, and the relative error of the mean is only 0.0014. Meanwhile, its CoV is 0.0463 and the average relative error is 0.0368, both of which are the lowest among the three compared methods. The number of performance-function calls is only 4.2267×10^{4}, also the lowest among the three methods. These results indicate that the proposed method maintains high estimation accuracy while achieving good single-run stability and high computational efficiency.

4. Conclusion

This paper proposes a practical stratified importance sampling method to address the limitations of traditional stratified simulation methods in high dimensional small failure probability estimation, including sample correlation, insufficient identification of important failure regions, and limited construction quality of the final IS-PDF.

First, starting from the failure probability expression of SS-IS, this paper shows that when the final failure probability is evaluated by IS based on the final-level IS-PDF, the intermediate conditional failure probabilities no longer enter the final failure probability expression directly in a multiplicative form. Therefore, the primary role of the intermediate levels is not to accurately estimate the conditional failure probabilities level by level, but rather to progressively approach the limit-state surface, identify potential important failure regions, and provide effective information for constructing a high-quality final IS-PDF through sample screening, region advancement, and ISCs updating.

Based on this understanding, this paper constructs an adaptive stratified importance sampling strategy-AS-IS consisting of stratified search, ISC correction, and final-level IS estimation. The method first enlarges the sampling variance of the first-level IS-PDF to improve the initial exploration capability for potential important failure regions. It then uses K-means clustering to identify multiple candidate regions and screens safe ISCs and failure ISCs within each cluster. After failure samples are obtained in all current candidate regions, the failure ISCs are used as initial points and corrected by a local optimization method to positions

on the limit-state surface with relatively high original probability density. The final-level Gaussian-mixture IS-PDF is then constructed based on the optimized ISCs, and the failure probability estimation under high dimensional conditions is completed.

The three examples show that AS-IS more reliably covers dominant failure regions and achieves accurate, stable estimates at competitive computational cost. Future work will combine the final-level IS-PDF construction with surrogate models for more complex high-dimensional applications.

Acknowledgements

This work was supported by the National Natural Science Foundation of China (Grant No NSFC 52375156)

References

Cavalieri F, Franchin P, Gehl P, et al. Risk and reliability analysis: Theory and applications[J]. 2017.

Cheng K, Lu Z, Xiao S, et al. Estimation of small failure probability using generalized subset simulation[J]. Mechanical Systems and Signal Processing, 2022, 163: 108114.

Li G, Wang T, Chen Z, et al. RBIK-SS: A parallel adaptive structural reliability analysis method for rare failure events[J]. Reliability Engineering & System Safety, 2023, 239: 109513.

Cheng K, Papaioannou I, Lu Z, et al. Rare event estimation with sequential directional importance sampling[J]. Structural Safety, 2023, 100: 102291.

Hasofer A M. An exact and invarient first order reliability format[J]. J. Eng. Mech. Div., Proc. ASCE, 1974, 100(1): 111-121.

Der Kiureghian A, Lin H Z, Hwang S J. Second-order reliability approximations[J]. Journal of Engineering mechanics, 1987, 113(8): 1208-1225.

Song C, Kawai R. Monte Carlo and variance reduction methods for structural reliability analysis: A comprehensive review[J]. Probabilistic Engineering Mechanics, 2023, 73: 103479.

Tabandeh A, Jia G, Gardoni P. A review and assessment of importance sampling methods for reliability analysis[J]. Structural Safety, 2022, 97: 102216.

Au S K, Beck J L. Estimation of small failure probabilities in high dimensions by subset simulation[J]. Probabilistic engineering mechanics, 2001, 16(4): 263-277.

Papaioannou I, Betz W, Zwirglmaier K, et al. MCMC algorithms for subset simulation[J]. Probabilistic Engineering Mechanics, 2015, 41: 89-103.

Pradlwarter H J, Schueller G I, Koutsourelakis P S, et al. Application of line sampling simulation method to reliability benchmark problems[J]. Structural safety, 2007, 29(3): 208-221.

Zhang X, Lu Z, Cheng K, et al. A novel reliability sensitivity analysis method based on directional sampling and Monte Carlo simulation[J]. Proceedings of the Institution of Mechanical Engineers, Part O: Journal of Risk and Reliability, 2020, 234(4): 622-635.

Dubourg V, Sudret B, Deheeger F. Metamodel-based importance sampling for structural reliability analysis[J]. Probabilistic Engineering Mechanics, 2013, 33: 47-57.

Song S, Lu Z. Reliability sensitivity analysis based on subset simulation and importance sampling[J]. Chinese Journal of Theoretical and Applied Mechanics, 2008, 40(5): 654-662.

Papaioannou I, Papadimitriou C, Straub D. Sequential importance sampling for structural reliability[C]//Proc. 17th IFIP WG 7.5 Conference on Reliability and Optimization of Structural Systems, Huangshan, China. 2014.

Helal S, Elvira V. Efficient rare event estimation for multimodal and high dimensional system reliability via subset adaptive importance sampling[J]. Reliability Engineering & System Safety, 2026: 112473.

Yang X, Jiang W, Zhang Y, et al. An active learning method combining MRBF model and dimension-reduction importance sampling for reliability analysis with high dimensionality and very small failure probability[J]. Reliability Engineering & System Safety, 2025, 261: 111107.

Breitung K. The geometry of limit state function graphs and subset simulation: Counterexamples[J]. Reliability Engineering & System Safety, 2019, 182: 98-106.

Uncertainty Analysis of Fatigue Failure Using a Fuzzy Approach

Mansoureh Shahabi[1], Michael Desch[1], and Mehdi Modares[1*]

Department of Civil, Architectural and Environmental Engineering, Illinois Institute of Technology
**Corresponding author: mmodares@illinoistech.edu*

Abstract: Structural systems subjected to repeated or fluctuating loads are vulnerable to fatigue failure. This is because each cycle of loading causes damage to the system. Damage accumulates, causing cracks which reduce constituent member cross-sections, leading to an increased possibility of fracture. This can occur even when stresses remain below the yield limit. Fatigue failure is a multi-phase process that starts with a crack initiation phase and continues into a crack propagation phase.

In the conventional crack-initiation approach using Miner's rule, it is assumed that each cycle contributes a small increment of damage until failure occurs. This method relies on Stress–Life (S–N) curves derived from experiments. However, this approach is deterministic and does not reflect measurement imprecision or inherent uncertainties. These uncertainties derive from, material properties, geometry, fabrication quality, and cyclic loading. Uncertainty significantly affects the fatigue life of the system. Probabilistic and interval approaches have previously been used to enumerate these uncertainties. However, the former requires a well-defined distribution, whereas the latter requires exact bounds.

This work develops a new crack-initiation prediction method that uses a fuzzy approach for quantifying uncertainties in stress ranges as well as fatigue parameters. First, the fatigue coefficient and stress ranges are defined as fuzzy variables. These fuzzy variables are evaluated at multiple discrete levels of presumption, (α-cuts). Then, for each cut, the interval values of those variables are used to calculate the interval of damage and interval of fatigue life. Following that, the fuzzy values for interval damage and fatigue life are constructed. A numerical example is presented to demonstrate the applicability of the proposed method and it is compared with results obtained by Monte Carlo simulations. It is shown that obtaining fuzzy bounds on a system's fatigue life using this method does not require iterative methods.

Keywords: Fatigue, Damage, Uncertainty, Fuzzy

1. Introduction

Structural elements subject to repeated loading are susceptible to fatigue failure. This mode of failure can be attributed to the accumulation of damage at each cycle of loading. This damage accumulation over time can result in fracture even when stress levels remain below design limits. Fatigue failure is commonly described as a two-stage process which begins with crack initiation and followed by crack growth leading to final fracture. For analysis of these phases, a range of analytical methods has been developed to assess fatigue behavior and predict structural performance. For the first phase, the crack initiation method is widely used which is based on Miner's damage rule (Miner, 1945). This method assumes each load cycle contributes to the development of an infinitesimal amount of damage.

© 2026 by the author(s). This work is licensed under the Creative Commons Attribution 4.0 International License (CC BY 4.0), which permits unrestricted use, distribution, and reproduction in any medium, provided the original author and source are credited.

As the damage accumulates and reaches a critical value, fatigue failure occurs. Using this method, the fatigue life is estimated using the experimental relationships between the stress range and the number of cycles to failure. This is commonly expressed as an S–N curve (Basquin, 1910).

Conventional deterministic fatigue life prediction methods do not incorporate variations and uncertainty in the analysis of fatigue failure. These uncertainties can arise from numerous factors including scatter in laboratory fatigue data, variability in material and geometric properties, inaccuracies in field stress measurements, and modeling assumptions. The presence of these uncertainties may significantly affect predicted fatigue damage and remaining life, particularly when available data are limited. In order to incorporate the presence of uncertainties in the fatigue failure analysis, probabilistic approaches have been conventionally utilized (Ang and Munse, 1975; Sen, 2006; Kwon et al., 2012; Diekfuss and Foley, 2016). Furthermore, possibilistic approaches have been used that utilize interval analysis for fatigue life prediction (Desch and Modares, 2021**)** through which, uncertainties in fatigue parameters (from laboratory data) and stress ranges (from field measurements) are represented as interval variables. However, using probabilistic methods, the predicted fatigue analysis results are highly dependent on the assumption of the underlying probability distribution functions. On the other hand, possibilistic approaches, such as interval analysis, provide no information of the distribution of data.

In order to address the shortcomings of the aforementioned approaches, a fuzzy method can be utilized. Fuzzy set theory, first introduced by Zadeh (1965), provides a framework for representing imprecise information through membership functions. Fuzzy-based approaches are well suited for fatigue problems where limited data and modeling assumptions are major sources of uncertainty. Fuzzy approaches have been applied to fatigue analysis in which, imprecise information in the inputs is used to produce bounded predictions of fatigue damage, and fatigue life is represented without solely relying on probabilistic assumptions or possibilistic bounds. Muc and Kędziora (2001) used fuzzy sets to represent scatter in experimental fatigue and fracture data for composite materials. Tan et al. (2005) proposed a fuzzy reliability approach to predict the corrosion-fatigue life of aircraft structures. Zhang (2015) developed a fatigue life prediction model based on residual strength and cumulative damage concepts. However, work on fuzzy fatigue analysis has not yet produced a general framework to incorporate the uncertainties and variations from the experimental data level especially when limited data is available.

In this work, a new method is developed that is capable of determining the fatigue life of a structure using a fuzzy approach. In this method, fuzzy variables are utilized to quantify the uncertainties in the fatigue parameters (obtained from laboratory test data) as well as the stress ranges (obtained from field test data). Then, the fuzzy existing damage is determined, leading to a prediction of the structure's fuzzy remaining fatigue life. It is envisioned that the results obtained using this method can be used for reliability, safety, and management of aging infrastructure.

2. Background

This work is a symbiosis of two historically independent fields, fatigue life prediction and fuzzy analysis. In order to introduce the method, first, the background for both fields is presented.

2.1 FATIGUE LIFE PREDICTION

The fatigue behavior of a structural component is determined using laboratory fatigue test data. The relationship between the stress range S and the number of cycles to failure N is expressed by the S–N relation as (Basquin, 1910):

$$N = \frac{C}{S^m} \tag{1}$$

where C is the fatigue coefficient and m is the fatigue exponent. These parameters are determined experimentally. The value of N represents the number of cycles to failure when the component is subjected to a constant stress range S. As experiments for the S-N relationship possess considerable scatter, data regression is used to calculate values for the parameters C and m.

Eq. 1 is defined for a single stress range; however, in actual service conditions, structural components experience different stress ranges throughout their lifetime. To account for the existence of multiple stress ranges, a cumulative damage method can be applied. As such, each load cycle produces a small amount of damage and over time, these damages are accumulated. The cumulative damage relationship is expressed as (Miner, 1945):

$$D = \sum \frac{n_i}{N_i} \tag{2}$$

where, n_i is the number of cycles applied at stress range S_i, and N_i is the number of cycles to failure at that stress range. According to Miner's rule, fatigue failure occurs when the total accumulated damage reaches the critical value of unity ($D = 1$). Combining Eqs. 1 and 2, the accumulated fatigue damage is written as:

$$D = \frac{1}{C} \cdot \sum_i n_i \cdot S_i^m \tag{3}$$

In order to obtain the stress ranges from a measured stress-time history, a cycle counting method can be used. The rainflow-counting algorithm is one cycle counting methods that is widely used in fatigue analysis (Matsuishi and Endo, 1968).

2.1.1 REGRESSION OF S–N DATA

The fatigue parameters, C and m, are obtained from laboratory S-N data using regression analysis. First, both variables S and N are transformed into logarithmic space as $\ln S$ and $\ln N$ through which, this the nonlinear S–N relation becomes linear as:

$$\ln N = \ln C - m \ln S \tag{4}$$

Then, using least-squares regression, the fatigue coefficient and fatigue exponent are calculated as:

$$C = \exp\left(\frac{(\Sigma \ln N)(\Sigma (\ln S)^2) - (\Sigma \ln S)(\Sigma \ln S \ln N)}{p(\Sigma (\ln S)^2) - (\Sigma \ln S)^2}\right) \tag{5}$$

$$m = -\frac{p(\Sigma \ln S \ln N) - (\Sigma \ln S)(\Sigma \ln N)}{p(\Sigma (\ln S)^2) - (\Sigma \ln S)^2} \tag{6}$$

where, p is the number of data points. Moreover, using the least-squares method, the difference between the measured value and the predicted value for each data point, is expressed as:\

$$e_j = \ln N_j - \ln C + m \ln S_j \tag{7}$$

where, e_j is the residual value.

2.2 Uncertainty in Fatigue Life Prediction

These residual values obtained in Eq. 7 depict the scatter in experimental data which can be considered as indicatives of the presence of uncertainty in the estimated fatigue parameters. Since the uncertainties in the fatigue parameters are fully correlated (Ang and Munse, 1975), they can be represented through a single uncertain variable. Accordingly, the uncertainty can be solely considered in the fatigue parameter, *C*, while the fatigue exponent, *m*, is considered deterministic (Desch and Modares 2021).

2.3 Fuzzy Representation of Uncertainty

Fuzzy set theory is a possibilistic approach to quantify uncertainty. In fuzzy analysis, an uncertain parameter is described using a fuzzy variable. In this work, the fuzzy variables are depicted in bold.

2.3.1 Fuzzy Representation of Uncertainty

Considering *E* as a referential set, in an ordinary subset the characteristic function is:

$$\forall x \in E: \mu_A(x) \in \{0,1\} \tag{8}$$

In a fuzzy subset the characteristic function (membership function) is:

$$\forall x \in E: \mu_A(x) \in [0,1] \tag{9}$$

which allows for partial membership (Figure 1).

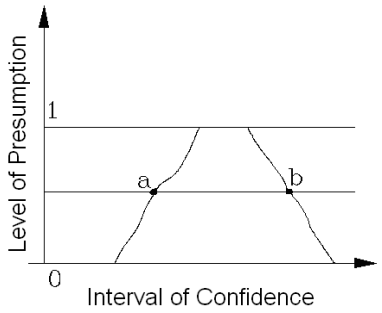


Figure 1. The membership function of a fuzzy variable

For each level of presumption (α-cut), there exists a corresponding level of confidence such that:

$$\forall \alpha_1, \alpha_2 \in [0,1], \alpha_1 < \alpha_2; [a^{\alpha_2}, b^{\alpha_2}] \subset [a^{\alpha_1}, b^{\alpha_1}] \tag{10}$$

2.3.2 Triangular Fuzzy Numbers

One of the most commonly used fuzzy numbers is the triangular fuzzy variable (Figure 2).

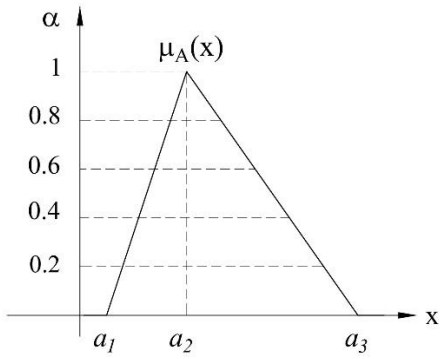


Figure 2. The membership function of a triangular fuzzy variable

A triangular fuzzy variable is defined using three values:

$$\boldsymbol{A} = (a_1,\ a_2,\ a_3) \tag{11}$$

where, a_1 is the lower bound, a_2 is the most likely value and a_3 is the upper bound. The α-cut of a triangular fuzzy variable is given by:

$$\boldsymbol{A_\alpha} = [a_1 + (a_2 - a_1)\alpha, a_3 - (a_3 - a_2)\alpha] \tag{12}$$

At $\alpha = 0$, the interval is $[a_1, a_3]$, representing the maximum uncertainty, whereas at $\alpha = 1$, the interval of confidence reduces to the single value a_2, representing the deterministic case.

2.3.3 Basic Operations on Fuzzy Variables

Considering two fuzzy variables $\boldsymbol{A}$ and $\boldsymbol{B}$ be represented at the α-cut level through their intervals of confidence as $\boldsymbol{A_\alpha} = [\underline{A_\alpha}, \overline{A_\alpha}]$ and $\boldsymbol{B_\alpha} = [\underline{B_\alpha}, \overline{B_\alpha}]$, respectively, the basic interval arithmetic operations are:

Addition:

$$\boldsymbol{A_\alpha} + \boldsymbol{B_\alpha} = \left[\underline{A_\alpha} + \underline{B_\alpha}, \overline{A_\alpha} + \overline{B_\alpha}\right] \tag{13}$$

Subtraction:

$$\boldsymbol{A_\alpha} - \boldsymbol{B_\alpha} = \left[\underline{A_\alpha} - \overline{B_\alpha}, \overline{A_\alpha} - \underline{B_\alpha}\right] \tag{14}$$

Multiplication:

$$\boldsymbol{A_\alpha} \times \boldsymbol{B_\alpha} = [\min(\{AB\}), \max(\{AB\})] \tag{15}$$

where:

$$AB = \left\{\left(\underline{A_\alpha} \cdot \underline{B_\alpha}\right), \left(\underline{A_\alpha} \cdot \overline{B_\alpha}\right), \left(\overline{A_\alpha} \cdot \underline{B_\alpha}\right), \left(\overline{A_\alpha} \cdot \overline{B_\alpha}\right)\right\} \tag{16}$$

Division:

$$\boldsymbol{A_\alpha} \div \boldsymbol{B_\alpha} = \left[\min\left(\left\{\frac{A}{B}\right\}\right), \max\left(\left\{\frac{A}{B}\right\}\right)\right] \tag{17}$$

where:

$$\frac{A}{B} = \left\{\left(\underline{A_\alpha}/\underline{B_\alpha}\right), \left(\underline{A_\alpha}/\overline{B_\alpha}\right), \left(\overline{A_\alpha}/\underline{B_\alpha}\right), \left(\overline{A_\alpha}/\overline{B_\alpha}\right)\right\} \tag{18}$$

and where, $0 \notin \boldsymbol{B_\alpha}$.

3. Methodology

3.1 Formulation of Fuzzy Fatigue Failure Analysis

The general algorithm and major steps for fuzzy fatigue failure analysis and fatigue life prediction are outlined as follows.

Step 1. Construct a Fuzzy S–N Relationship from laboratory test data

In this step, first, the fuzzy fatigue coefficient, $\boldsymbol{C}$, is constructed based on a triangular membership function. For α = 0, the laboratory test data is deterministically regressed and the corresponding interval of confidence for fuzzy fatigue coefficient $\boldsymbol{C}$ is:

$$\boldsymbol{C_{\alpha=0}} = \left[\underline{C}, \overline{C}\right] = C \cdot \left[\delta_{C_l}, \delta_{C_u}\right] \tag{19}$$

where, C is the deterministic fatigue coefficient and δ_{C_l} and δ_{C_u} are the lower and upper variations, respectively; obtained by an enveloping procedure as:

$$\delta_{C_l} = \exp\left(\min\left(e_j\right)\right) \tag{20}$$

$$\delta_{C_u} = \exp\left(\max\left(e_j\right)\right) \tag{21}$$

For α = 1, the deterministic fatigue coefficient C is considered as the most likely value. Then, the fuzzy fatigue coefficient is constructed through its triangular membership function as:

$$\boldsymbol{C} = \left\{0\ (c \le \underline{C}), \frac{c-\underline{C}}{C-\underline{C}}(\underline{C} \le c \le C), \frac{\overline{C}-c}{\overline{C}-C}(C \le c \le \overline{C}), 0\ (c \ge \overline{C})\right\} \tag{22}$$

where, the corresponding α-cut for the fuzzy fatigue coefficient is:

$$\boldsymbol{C_\alpha} = \left[\underline{C} + (C-\underline{C})\alpha, \overline{C} - (\overline{C}-C)\alpha\right] \tag{23}$$

Figure 3 depicts fuzzy fatigue coefficient schematically.

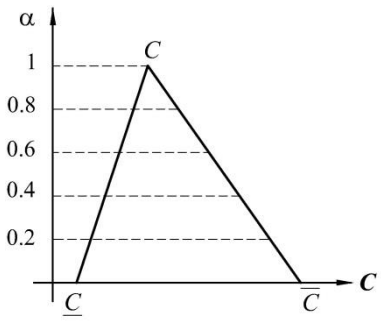


Figure 3. Fuzzy Fatigue Coefficient

By considering the fatigue exponent, *m*, as deterministic (i.e., the uncertainty is enumerated in fuzzy fatigue coefficient $\boldsymbol{C}$), the fuzzy S-N relationship can be constructed. Figure 4 depicts the interval of confidence for α = 0 of the fuzzy S-N relationship schematically.

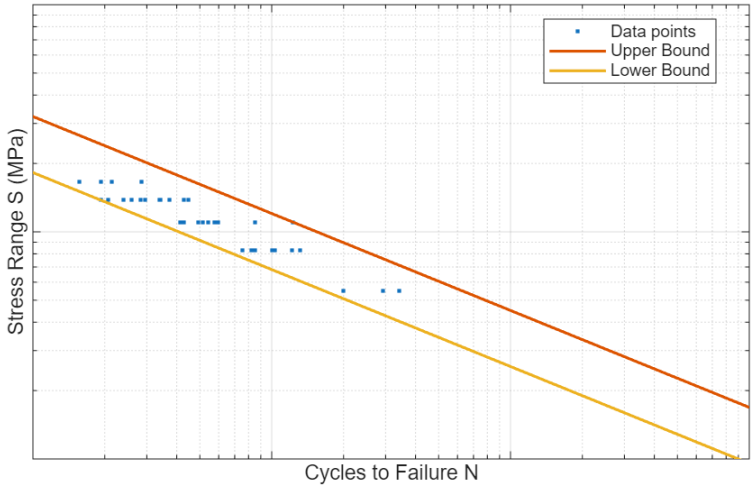


Figure 4. Interval of confidence for α = 0 of the fuzzy S-N relationship

Step 2. Determine Fuzzy Stress Ranges and Cycle Counts from Field Data

In this step, the fuzzy stress ranges are constructed using obtained field data followed by a cycle counting procedure. For α = 0 the interval of confidence for each stress range, i, is:

$$\boldsymbol{S_{i_{\alpha=0}}} = \left[\underline{S_i}, \overline{S_i}\right] = \left[S_i - \delta_{S_{i_l}}, S_i + \delta_{S_{i_u}}\right] \tag{24}$$

where, S_i is the deterministic stress range, $\underline{S_i}$ and $\overline{S_i}$ are the lower and upper bounds of the stress range, and $\delta_{S_{i_l}}$ and $\delta_{S_{i_u}}$ are the variation parameters for lower and upper bounds of the stress range, respectively. The variation parameters can be obtained by (a) the tolerance of sensors used in field data collection, (b) the level of rounding used in the cycle-counting process, and/or (c) engineering judgment or expert opinion. For α = 1, the deterministic stress range S_i is considered as most likely value.

Then, for each stress range, the fuzzy stress range is constructed through its triangular membership function as:

$$\boldsymbol{S_i} = \left\{0\ \left(s \le \underline{S_i}\right), \frac{s - \underline{S_i}}{S_i - \underline{S_i}}\left(\underline{S_i} \le s \le S_i\right), \frac{\overline{S_i} - s}{\overline{S_i} - S_i}\left(S_i\ \le s \le \overline{S_i}\right), 0\ \left(s \ge, \overline{S_i}\right)\right\} \tag{25}$$

The corresponding α-cut for the fuzzy stress range is:

$$\boldsymbol{S_{i_\alpha}} = \left[\underline{S_i} + \left(S_i - \underline{S_i}\right)\alpha, \overline{S_i} - \left(\overline{S_i} - S_i\right)\alpha\right] \tag{26}$$

Step 3. Determine the Fuzzy Damage Accumulated over the Duration of Field Data Collection

At a given level α, using the corresponding intervals of confidence for fuzzy fatigue coefficient $\boldsymbol{C_\alpha}$ and fuzzy stress ranges $\boldsymbol{S_{i_\alpha}}$, the interval of confidence for fuzzy accumulated damage over the duration of the field data collection, is calculated as:

$$\boldsymbol{D_{d_\alpha}} = \frac{1}{\boldsymbol{C_\alpha}} \sum_i n_i \left(\boldsymbol{S_{i_\alpha}}\right)^m \tag{27}$$

or equivalently:

$$\boldsymbol{D_{d_\alpha}} = \frac{1}{\left[\underline{C} + \left(C - \underline{C}\right)\alpha, \overline{C} - \left(\overline{C} - C\right)\alpha\right]} \sum_i n_i \left(\underline{S_i} + \left(S_i - \underline{S_i}\right)\alpha, \overline{S_i} - \left(\overline{S_i} - S_i\right)\alpha\right)^m \tag{28}$$

Then, using various α-cut levels, the fuzzy accumulated damage over the duration of the field data collection $\boldsymbol{D_d}$ is constructed.

Step 4. Calculation of Fuzzy Mean Damage Rate, Fuzzy Existing Damage, Fuzzy Fatigue Life, and Fuzzy Remaining Life

At a given level α:
1. The interval of confidence for fuzzy mean damage is calculated as:

$$\boldsymbol{D_{m_\alpha}} = \frac{\boldsymbol{D_{d_\alpha}}}{t_d} = \left[\frac{\underline{\boldsymbol{D_{d_\alpha}}}}{t_d}, \frac{\overline{\boldsymbol{D_{d_\alpha}}}}{t_d}\right] \tag{29}$$

where, t_d is the duration of field data collection.

2. The interval of confidence for fuzzy existing damage is calculated as:

$$\boldsymbol{D_{e_\alpha}} = \boldsymbol{D_{m_\alpha}}.t_a = \left[\underline{\boldsymbol{D_{m_\alpha}}}.t_a, \overline{\boldsymbol{D_{m_\alpha}}}.t_a\right] \tag{30}$$

where t_a is the current age of the structure.

3. The interval of confidence for fuzzy fatigue life is calculated as:

$$\boldsymbol{t_{l_\alpha}} = \frac{1}{\boldsymbol{D_{m_\alpha}}} = \left[\frac{1}{\overline{\boldsymbol{D_{m_\alpha}}}}, \frac{1}{\underline{\boldsymbol{D_{m_\alpha}}}}\right] \tag{31}$$

4. The interval of confidence for fuzzy remaining fatigue life calculated as:

$$\boldsymbol{t_{r_\alpha}} = \boldsymbol{t_{l_\alpha}} - t_a = \left[\underline{\boldsymbol{t_{l_\alpha}}} - t_a, \overline{\boldsymbol{t_{l_\alpha}}} - t_a\right] \tag{32}$$

Following that, using various α-cut levels, fuzzy mean damage $\boldsymbol{D_m}$, fuzzy existing damage $\boldsymbol{D_e}$, fuzzy fatigue life $\boldsymbol{t_l}$, and fuzzy remaining fatigue life $\boldsymbol{t_r}$ are constructed.

4. Numerical Example

4.1 Problem Definition

In this example, the developed method is applied to determine the existing damage and remaining fatigue life of a steel bridge component subjected to cyclic loading. Moreover, the main results are compared with 10^4 Monte Carlo simulation realizations using uniformly distributed random variables.

The age of the bridge under consideration is considered to be 20 years. The structure is fabricated from A514 structural steel. The most fatigue-critical details are identified as the cover plates attached to the bottom flanges of the deck girders, with un-welded ends, as shown in the original study (Figure 5). Laboratory fatigue test data for this detail and material combination are obtained from Fisher et al. (1969) (Table I).

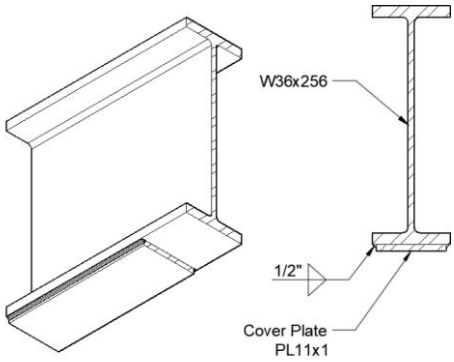


Figure 5. Cover plate detail, ends un-welded

Table I: Laboratory S-N data from Fisher et al. 1969												
S_i		N (load Cycles $\times 10^3$)										
MPa	ksi	Multiple tests										
55.16	8	1988.9	2916.2	3409.2								
82.74	12	1031.1	848.3	1310.9	821.7	1004.7	1220.0	755.2				
110.32	16	514.8	1227.8	854.9	428.5	542.2	598.5	429.9	412.5	589.6	578.0	
137.9	20	341.3	429.1	445.9	282.3	192.3	339.5	260.0	238.8	374.0	296.0	207.0
165.47	24	156.6	213.8	285.2	192.5							

Field stress range measurements and corresponding cycle counts for bridge #0160335 are obtained from monitoring data reported by Hahin et al. (1993) (table II). The cycle counts correspond to a 24-hour data collection period.

Table II: Stress range & cycle count data Hahin et al. 1993		
S_i		n_i
MPa	ksi	Cycles
6.89	1.0	2843
10.3	1.5	991.0
13.79	2.0	386
17.24	2.5	111
20.68	3.0	88
24.13	3.5	64
27.58	4.0	33
31.03	4.5	32
34.47	5.0	15
37.92	5.5	7

4.2 PROBLEM SOLUTION:

Step 1. In this step the fatigue parameters of the fuzzy S-N relationship is determined. First, the laboratory test data are regressed. Then, for the intervals of fuzzy fatigue coefficient for various α-levels are determined. Moreover, fatigue exponents are considered deterministic (Table III and Figure 6).

Table III: Fuzzy fatigue coefficient and fatigue exponent

α	Fuzzy Fatigue coefficient (***C***)		Fatigue Exponent (*m*)
	Mpa^m*10^{10}	ksi^m*10^8	
0	[1.976,7.481]	[2.148,8.132]	2.343
0.2	[2.231,6.635]	[2.424,7.211]	2.343
0.4	[2.485,5.788]	[2.701,6.291]	2.343
0.6	[2.739,4.941]	[2.977,5.371]	2.343
0.8	[2.993,4.094]	[3.253,4.450]	2.343
1	[3.247,3.247]	[3.530,3.530]	2.343

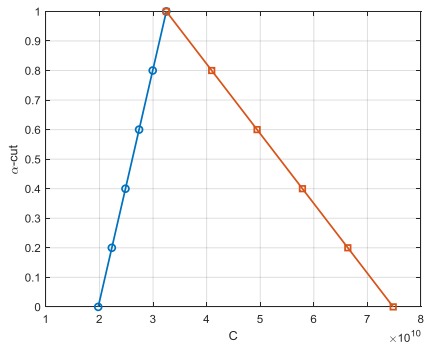


Figure 6. Fuzzy fatigue coefficient (***C***)

Step 2. In this step, the fuzzy stress ranges are determined. The stress ranges obtained from field monitoring are used to construct symmetric isosceles triangular membership functions. At α = 0, ±1% uncertainty is considered, while at α = 1 stress range S_i is considered deterministic. The results for various stress ranges are also obtained (Tables IV-a through IV-f.)

Table IV-a. Fuzzy stress range S_i, α=0	
MPa	ksi
[6.82,6.96]	[0.99,1.01]
[10.24,10.44]	[1.48,1.51]
[13.65,13.93]	[1.98,2.02]
[17.07,17.41]	[2.47,2.52]
[20.47,20.89]	[2.97,3.03]
[23.89,24.37]	[3.46,3.53]
[27.30,27.86]	[3.96,4.04]
[30.72,31.34]	[4.45,4.54]
[34.13,34.81]	[4.95,5.05]
[37.54,38.30]	[5.44,5.55]

Table IV-b. Fuzzy stress range S_i, α = 0.2	
Mpa	ksi
[6.835,6.945]	[0.991,1.007]
[10.257,10.423]	[1.487,1.511]
[13.680,13.900]	[1.984,2.016]
[17.102,17.378]	[2.480,2.520]
[20.515,20.845]	[2.975,3.023]
[23.937,24.323]	[3.471,3.527]
[27.359,27.801]	[3.967,4.031]
[30.782,31.278]	[4.463,4.535]
[34.194,34.746]	[4.958,5.038]
[37.617,38.223]	[5.454,5.542]

Table IV-c. Fuzzy stress range S_i, α = 0.4	
Mpa	Ksi
[6.849,6.931]	[0.993,1.005]
[10.278,10.402]	[1.490,1.508]
[13.707,13.873]	[1.988,2.0212]
[17.137,17.343]	[2.485,2.515]
[20.556,20.804]	[2.981,3.017]
[23.985,24.275]	[3.478,3.520]
[27.415,27.745]	[3.975,4.023]
[30.844,31.216]	[4.472,4.526]
[34.263,34.677]	[4.968,5.028]
[37.692,38.148]	[5.465,5.531]

Table IV-d. Fuzzy stress range S_i, α = 0.6	
Mpa	ksi
[6.862, 6.918]	[0.995,1.003]
[10.299, 10.381]	[1.493,1.505]
[13.735, 13.845]	[1.992,2.008]
[17.171, 17.309]	[2.490,2.510]
[20.597, 20.763]	[2.987,3.011]
[24.033, 24.227]	[3.485,3.513]
[27.470, 27.690]	[3.983,4.015]
[30.906, 31.154]	[4.481,4.517]
[34.332, 34.608]	[4.978,5.018]
[37.768, 38.072]	[5.476,5.520]

Table IV-e. Fuzzy stress range S_i, α = 0.8	
Mpa	Ksi
[6.876,6.904]	[0.997,1.001]
[10.319,10.361]	[1.496,1.502]
[13.762,13.818]	[1.996,2.004]
[17.206,17.274]	[2.495,2.505]
[20.639,20.721]	[2.996,3.005]
[24.082,24.178]	[3.492,3.506]
[27.525,27.635]	[3.991,4.007]
[30.968,31.092]	[4.490,4.508]
[34.401,34.539]	[4.988,5.008]
[37.844,38.996]	[5.487,5.509]

Table IV-f. Fuzzy stress range S_i, α = 1	
Mpa	ksi
6.890	0.999
10.340	1.499
13.790	2.000
17.240	2.500
20.680	2.999
24.130	3.499
27.580	3.999
31.030	4.499
34.470	4.998
37.920	5.498

Step 3. In this step, the accumulated fuzzy fatigue damage over the one-day field data collection period ($t_d = 1/365$ years) is determined and compared with Monte-Carlo simulation results (Table V and Figure 7).

Table V. Fuzzy damage during one day of data collection $\boldsymbol{D_d}$ ($\times 10^{-5}$)		
α	Fuzzy Results	MCS Results
0	[1.6384,6.499]	[1.7173,6.2900]
0.2	[1.856,5.732]	[1.9291,5.6090]
0.4	[2.138,5.122]	[2.2011,4.9954]
0.6	[2.516,4.625]	[2.5653,4.5543]
0.8	[3.051,4.212]	[3.0799,4.2030]
1	[3.865,3.865]	[3.8645,3.8645]

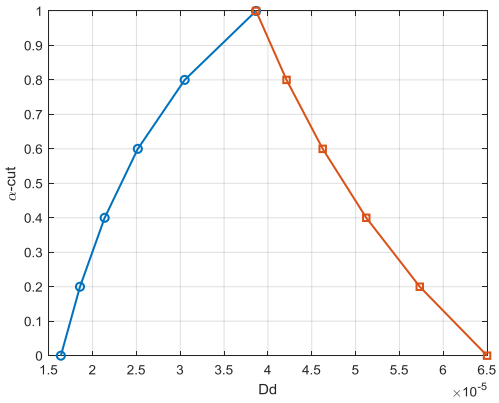


Figure 7. Fuzzy damage for one day of data collection

Step 4. In this step, the fuzzy mean damage rate, fuzzy existing damage ($t_a = 20$ years), fuzzy fatigue life, and fuzzy remaining life are determined (Tables VI-VIII and Figures 8-10).

Table VI: Existing Damage Results $\boldsymbol{D_e}$		
α	Fuzzy Results	MCS Results
0	[0.1196,0.47449	[0.12536,0.45917]
0.2	[0.13551,0.41846]	[0.14083,0.40946]
0.4	[0.15607,0.3739]	[0.16068,0.36466]
0.6	[0.18368,0.33762]	[0.18727,0.33246]
0.8	[0.22271,0.3075]	[0.22483,0.30682]
1	[0.28211,0.28211]	[0.28211,0.28211]

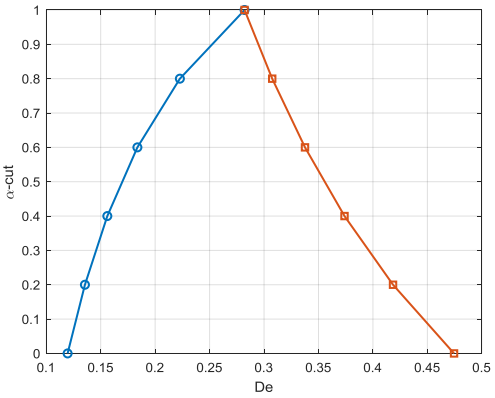


Figure 8. Fuzzy existing damage

Table VII: Fatigue Life Results t_l (Years)		
α	Fuzzy Results	MCS Results
0	[42.15,167.22]	[43.56,159.54]
0.2	[47.79,147.59]	[48.84,142.02]
0.4	[53.49,128.15]	[54.84,124.47]
0.6	[59.24,108.89]	[60.16,106.8]
0.8	[65.04,89.8]	[65.19,88.96]
1	[70.89,70.89]	[0.89,0.89]

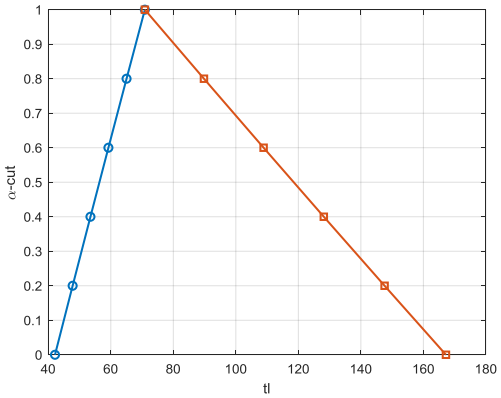


Figure 9. Fuzzy fatigue life t_l (years)

Table VIII: Remaining Life t_r (Years)		
α	Fuzzy Results	MCS Results
0	[22.15, 147.22]	[23.56,139.54]
0.2	[27.79, 127.59]	[28.84, 122.02]
0.4	[33.49, 108.15]	[34.84, 104.47]
0.6	[39.24, 88.89]	[40.16, 86.8]
0.8	[45.04, 69.8]	[45.19, 68.96]
1	50.89	50.89

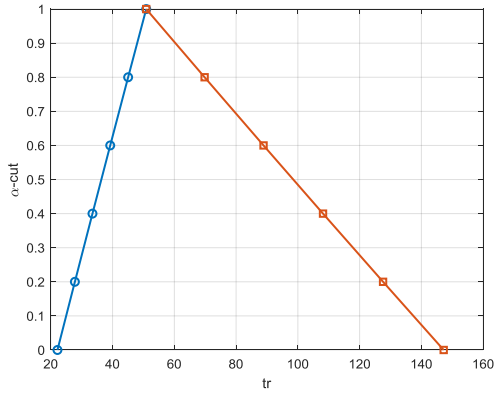


Figure 9. Fuzzy remaining fatigue t_r (years)

4.3 OBSERVATIONS

The results show that the predicted remaining fatigue life is strongly affected by the assumed level of uncertainty. For the lowest assumption level (α = 0), the remaining life varies widely, with a lower bound of 22.15 years and an upper bound of 147.22 years. This large range demonstrates the high sensitivity of fatigue life predictions to uncertainties in material properties, loading conditions, and field or laboratory measurements. As a result, greater uncertainty in input data leads to wider bounds in the estimated remaining life.

As anticipated, as the level of assumption decreases (i.e., with increasing α), uncertainty is reduced and the upper and lower bounds move closer to each other. This indicates increased confidence in the prediction. Additionally, the Monte Carlo simulation results for each α-cut are the inner bounds of the results by verifying the validity of the developed method.

5. Summary and Conclusions

In this paper, a new method for fatigue analysis of structures and determination of their fatigue life is developed that is capable of considering uncertainties using fuzzy analyses. This method includes uncertainties from both laboratory and field data, as well as uncertainties arising from the utilization of fuzzy variables and the construction of fuzzy functions. Due to the existence of various levels of presumption in the fuzzy approach it can produce results with more realistic consideration of uncertainties, when compared with an interval approach. The results are also compared with Monte Carlo simulations, which show the simulation results are inner bounds of the results obtained by the developed method. The simplicity and flexibility of this method, especially when data are limited, make it a useful tool for fatigue life prediction.

References

Ang, A. H.-S., and W. H. Munse. "Practical reliability basis for structural fatigue." Meeting preprint 2494, ASCE Annual National Structural Engineering Conference. New Orleans, April 1975: American Society of Civil Engineers. (1975).

Basquin, O.H. "The exponential law of endurance tests". American Society of Testing Materials, 10: 625-630. (1910).

Desch, M. and M. Modares. "Uncertainty Analysis of Fatigue Failure Using an Interval Approach". REC 2021, (2021).

Kwon, K., D.M. Frangopol, and M. Soliman. "Probabilistic Fatigue Life Estimation of Steel Bridges by Using a Bilinear S-N Approach". Journal of Bridge Engineering, 17(1): 58-70, (2012).

Miner, M.A. "Cumulative Damage in Fatigue". Journal of Applied Mechanics, 12: A159-A164. (1945).

Muc, A., & Kedziora, P. "A Fuzzy Set Analysis for Fracture and Fatigue Damage". *Composite Structures*, Vol. 54, No. 2–3, pp. 283–287, (2001).

Sen, T.K. "Probability of Fatigue Failure in Steel Catenary Risers in Deep Water". Journal of Engineering Mechanics, 132(9): 1001-1006, (2006).

Tan, X.M., Chen, Y.L., and Jin, P. "Corrosion Fatigue Life Prediction of Aircraft Structure Based on Fuzzy Reliability Approach". *Chinese Journal of Aeronautics*, 18(4): 346–351, (2005).

Zadeh, L.A. "Fuzzy Sets". Information and Control, 8: 338–353, (1965).

Zhang, Y. "A Fuzzy Residual Strength Based Fatigue Life Prediction Method". *Structural Engineering and Mechanics*, Vol. 56, No. 2, pp. 201–221, (2015).

A Weighted Extreme Value Moment Method Using Adaptive Sparse Grids for Time-Variant Reliability-Based Design Optimization

Hao-Ming Li, Pei-Pei Li*, and Yan-Gang Zhao
Department of Civil Engineering, Beijing University of Technology, Beijing 100124, China, lihaoming@emails.bjut.edu.cn
Department of Civil Engineering, Beijing University of Technology, Beijing 100124, China, li.peipei@bjut.edu.cn
Department of Civil Engineering, Beijing University of Technology, Beijing 100124, China, zhaoyg@bjut.edu.cn

Abstract. Time-variant reliability-based design optimization (t-RBDO) usually involves a nested-loop structure, in which repeated time-variant reliability analyses are required during design optimization. This paper proposes a weighted extreme value moment method using adaptive sparse grids for efficient t-RBDO. First, the extreme value method transforms the time-variant reliability constraints into equivalent reliability constraints based on extreme responses. The failure probability functions of the extreme responses are then constructed from their first three central moments using a three-parameter lognormal transformation. These central moment functions are obtained from raw extreme value moment functions. Next, a complete auxiliary density is introduced to express the raw moment functions as weighted integrals over the entire design domain, allowing evaluated extreme responses to be reused for different candidate designs. Subsequently, the weighted approach based on adaptive sparse grid collocation (WA-ASGC) evaluates the raw extreme value moment functions, with hierarchical surpluses guiding local refinement of the sparse grid. Finally, the resulting failure probability functions replace the time-variant probabilistic constraints, and the t-RBDO problem is solved through sequential deterministic optimization with reference point updating and local collocation point replenishment. The proposed method is non-intrusive and can be coupled with black-box numerical models. A nonlinear time-variant numerical example with two modified cases is presented to demonstrate its accuracy and efficiency.

Keywords: Time-Variant Reliability-Based Design Optimization; Extreme Value Moment; Complete Auxiliary Density; Failure Probability Function; Adaptive Sparse Grid Collocation

1. Introduction

Reliability-based design optimization (RBDO) provides a rational framework for obtaining economical designs that satisfy prescribed reliability requirements. Unlike deterministic optimization, it explicitly accounts for uncertainties in material properties, geometry, loads, and environmental actions (Valdebenito and Schueller, 2010). The most direct solution follows a double-loop structure: the outer loop searches for the optimal design, whereas the inner loop repeatedly evaluates reliability for each candidate design. Although this structure preserves the original problem formulation, a

© 2026 by the author(s). This work is licensed under the Creative Commons Attribution 4.0 International License (CC BY 4.0), which permits unrestricted use, distribution, and reproduction in any medium, provided the original author and source are credited.

new reliability analysis is required at nearly every optimization step. The resulting cost can be prohibitive when the limit state function is nonlinear, implicit, or evaluated by finite element simulations. For time-variant RBDO (t-RBDO), each inner analysis must additionally evaluate the failure event over the design lifetime, making repeated reliability evaluation an even greater computational burden.

According to the coupling between reliability analysis and optimization, existing RBDO methods can be classified as double-loop, single-loop, and decoupled approaches. Double-loop methods are the most direct strategy. The outer loop searches for the optimal design, while the inner loop evaluates the reliability of each candidate design. The reliability index approach and performance measure approach have been developed to reduce the cost of the inner analysis (Enevoldsen and Sørensen, 1994; Ting Lin et al., 2011; Youn et al., 2005). Although the double-loop approach preserves the original reliability formulation, a new reliability analysis is still required after each design update. Single-loop methods eliminate the explicit reliability loop through optimality conditions, probabilistic transformations, or local reliability approximations. Representative developments include the adaptive hybrid single-loop method of Jiang et al. (Jiang et al., 2017) and the adaptive sampling and Kriging strategy of Zhang et al. (Zhang et al., 2021). However, these methods may depend on approximation assumptions, gradient information, or local transformations. Their application to complex nonlinear or implicit reliability problems may therefore be limited. Decoupled methods instead construct an explicit reliability function. This separates reliability analysis from optimization and avoids repeated reliability analyses during optimization.

Within decoupled RBDO, a common strategy is to construct the reliability function using surrogate models. Response surface approximations were employed by Gasser and Schueller (Gasser and Schueller, 1997) and Rajasekhar and Ellingwood (Rajasekhar and Ellingwood, 1993). Kriging or Gaussian process regression formulations were studied by Kleijnen (Kleijnen, 2009) and Zhang et al. (Zhang et al., 2022). Neural networks and polynomial chaos expansions were adopted by Papadrakakis and Lagaros (Papadrakakis and Lagaros, 2002) and Zhou et al. (Zhou and Lu, 2019; Zhou et al., 2020). These models approximate reliability-related responses or reliability functions from analyses performed at a finite number of design points. Once constructed, they avoid repeated expensive reliability analyses during optimization. However, surrogate models are fitted to limited information. They may not fully represent the true reliability mapping and may introduce additional approximation errors. Their training cost may also increase rapidly with the number of design variables. Direct construction of the failure probability function (FPF) is therefore an important decoupling strategy for RBDO.

Another class of decoupled methods directly constructs the FPF using samples or integration points generated during reliability analysis. Zou and Mahadevan (Zou and Mahadevan, 2006) used reliability sensitivity information for direct decoupling. Ching and Hsieh (Ching and Hsieh, 2007) developed a three-step method based on subset simulation. Yuan and Lu (Yuan and Lu, 2014) expressed the FPF through weighted importance samples. Subsequent developments include simulation for highly nonlinear constraints (Rashki et al., 2014), augmented line sampling (Yuan et al., 2023), stochastic subset optimization (Tafazzolis and Beck, 2009), and Markov chain Monte Carlo based decoupling (Yuan et al., 2021; Jensen et al., 2020). These methods reuse samples or response evaluations for different candidate designs. Thus, they describe the relation between the design variables and failure probability without an additional surrogate fitting process. However, an

effective FPF representation over the entire design domain remains difficult, and its construction may still be computationally demanding.

More recently, two decoupled methods are particularly relevant to the present study. For t-RBDO, Zhao et al. (Zhao et al., 2023) combined an improved extreme value moment method with WA-SGNI to construct local extreme value moment and quantile functions. This approach improves the efficiency of time-variant reliability analysis. However, WA-SGNI uses a prescribed sparse grid accuracy level, and the functions are constructed in sequentially updated local design subregions. A unified representation over the entire design domain is therefore difficult to obtain. For structural RBDO, Yuan et al. (Yuan et al., 2024) proposed ASI-IS using augmented-space integration, importance sampling, subdomain updating, and sample reuse. This approach improves the efficiency of FPF estimation. However, its efficiency depends on the subdomain and sampling strategy. It also relies on failure indicators and sample weights, which may require many samples for small failure domains or strongly nonlinear limit state functions. Moreover, a common integration rule or sampling budget cannot automatically allocate computational effort according to the different refinement demands of multiple reliability constraints. Therefore, an efficient decoupled t-RBDO method that constructs the FPF over the entire design domain is still needed.

To address these issues, this paper proposes a weighted extreme value moment method using adaptive sparse grids for decoupled t-RBDO. First, the extreme value method transforms the time-variant reliability constraints into equivalent reliability constraints based on extreme responses. The failure probability functions of the extreme responses are then constructed from their first three central moments using a three-parameter lognormal transformation. These central moment functions are obtained from raw extreme value moment functions. Next, a complete auxiliary density is introduced to express the raw moment functions as weighted integrals over the entire design domain, allowing evaluated extreme responses to be reused for different candidate designs. Subsequently, WA-ASGC employs local hierarchical basis functions and surplus-guided refinement (Ma and Zabaras, 2009) to add collocation points according to the local behavior of each moment integrand. Finally, the resulting failure probability functions replace the time-variant probabilistic constraints. Sequential reference point updating and local collocation point replenishment then direct accuracy toward the candidate optimum and active reliability boundary without shrinking or relocating the prescribed design domain.

The remainder of this paper is organized as follows. Section 2 introduces the t-RBDO formulation. Section 3 presents the proposed t-RBDO methodology, including extreme value moment evaluation by WA-ASGC, moment-based failure probability transformation, and sequential deterministic optimization. Section 4 presents the numerical study, followed by the conclusions in Section 5.

2. Formulation of the t-RBDO Problem

The time-variant reliability-based design optimization (t-RBDO) problem considered in this study aims to minimize a general cost function under time-variant reliability constraints. Its formulation

is given by

$$\begin{aligned} &\text{minimize} && C(\theta) \\ &\text{subject to} && \Pr\{G_i[\mathbf{X},\mathbf{Y},\mathbf{Z}(t),t] \le 0,\ \exists t \in [0,T]\} \le P_{f_i}^t, \quad i = 1,2,\ldots,n_G, \\ & && h_j(\theta) \le 0, \quad j = 1,2,\ldots,n_h, \\ & && \underline{\theta} \le \theta \le \overline{\theta}. \end{aligned} \tag{1}$$

where $C(\cdot)$ is the cost function; $\mathbf{X}$ is the m-dimensional design random variable vector; $\theta = [\theta_1, \theta_2, \ldots, \theta_m]^T$ is the design variable vector and consists of selected distribution parameters of $\mathbf{X}$, such as its mean values or standard deviations; $\mathbf{Y}$ is the n-dimensional classical random variable vector; and $\mathbf{Z}(t)$ is the random process vector. In addition, $G_i[\mathbf{X},\mathbf{Y},\mathbf{Z}(t),t]$ is the ith time-dependent limit state function, $P_{f_i}^t$ is the corresponding target failure probability, T is the design lifetime, $h_j(\theta)$ is the jth deterministic constraint, and $\underline{\theta}$ and $\overline{\theta}$ denote the lower and upper bounds of θ, respectively.

Based on the equivalent extreme value event, the ith time-variant reliability constraint in Eq. (1) can be expressed as

$$\Pr\{G_{ie}(\mathbf{X},\mathbf{Y},\mathbf{Z}) \le 0\} \le P_{f_i}^t, \quad i = 1,2,\ldots,n_G, \tag{2}$$

where the extreme value limit state function is defined by

$$G_{ie}(\mathbf{X},\mathbf{Y},\mathbf{Z}) = \min_{t\in[0,T]} G_i[\mathbf{X},\mathbf{Y},\mathbf{Z}(t),t]. \tag{3}$$

The random process $\mathbf{Z}(t)$ can be represented by a finite set of basic random variables and deterministic functions of time, for example through the expansion optimal linear estimation method (Zhao et al., 2023). These additional random variables can be incorporated into $\mathbf{Y}$, reducing $G_{ie}(\mathbf{X},\mathbf{Y},\mathbf{Z})$ to $G_{ie}(\mathbf{X},\mathbf{Y})$. The t-RBDO problem can therefore be rewritten as

$$\begin{aligned} &\text{minimize} && C(\theta) \\ &\text{subject to} && \Pr\{G_{ie}(\mathbf{X},\mathbf{Y}) \le 0\} \le P_{f_i}^t, \quad i = 1,2,\ldots,n_G, \\ & && h_j(\theta) \le 0, \quad j = 1,2,\ldots,n_h, \\ & && \underline{\theta} \le \theta \le \overline{\theta}. \end{aligned} \tag{4}$$

For the following derivation, $\mathbf{x}$ and $\mathbf{y}$ denote realizations of $\mathbf{X}$ and $\mathbf{Y}$, respectively. The density of $\mathbf{X}$ under a given design is written as $f_{\mathbf{X}}(\mathbf{x}|\theta)$, and the density of $\mathbf{Y}$ is written as $f_{\mathbf{Y}}(\mathbf{y})$. The equivalent response $G_{ie}(\mathbf{X},\mathbf{Y})$ is the extreme value of the ith limit state function over the design lifetime. Therefore, the following method constructs raw moment functions of the extreme value G_{ie}. The same construction can be applied independently to multiple reliability constraints. For a time-independent problem, the time process and the extreme value operation are omitted, and G_{ie} reduces to the ordinary limit state response.

3. Proposed t-RBDO Methodology

Section 3.1 reformulates the raw moment functions of the extreme value using the complete auxiliary density. Section 3.2 presents their numerical evaluation by WA-ASGC. Section 3.3 transforms the extreme value moments into failure probability functions. Section 3.4 details the optimization strategy.

3.1. Complete Auxiliary Density Reformulation of Extreme Value Moments

Using the equivalent extreme value response defined in Eq. (3), the kth raw moment function of the extreme value of the ith limit state function is defined as

$$m^k_{G_{ie}}(\theta) = E\left\{[G_{ie}(\mathbf{X},\mathbf{Y})]^k \mid \theta\right\} = \int_{\Omega_\mathbf{x}}\int_{\Omega_\mathbf{y}} G_{ie}(\mathbf{x},\mathbf{y})^k f_\mathbf{X}(\mathbf{x}|\theta) f_\mathbf{Y}(\mathbf{y})\, d\mathbf{y}\, d\mathbf{x}, \qquad k=1,2,3. \tag{5}$$

Directly evaluating Eq. (5) at each candidate design point would still require repeated integrations over the random variable space. To obtain a reusable integral form, introduce a complete auxiliary density $h_A(\mathbf{x})$ for the design random variables (Liu et al., 2025b; Liu et al., 2025a). Multiplying and dividing the integrand in Eq. (5) by $h_A(\mathbf{x})$ gives

$$m^k_{G_{ie}}(\theta) = \int_{\Omega_\mathbf{x}}\int_{\Omega_\mathbf{y}} G_{ie}(\mathbf{x},\mathbf{y})^k \frac{f_\mathbf{X}(\mathbf{x}|\theta)}{h_A(\mathbf{x})} h_A(\mathbf{x}) f_\mathbf{Y}(\mathbf{y})\, d\mathbf{y}\, d\mathbf{x}, \qquad k=1,2,3. \tag{6}$$

The complete auxiliary density is constructed from the conditional densities of $\mathbf{X}$ over the entire design domain:

$$h_A(\mathbf{x}) = \frac{1}{|\Theta|}\int_\Theta f_\mathbf{X}(\mathbf{x}|\eta)\, d\eta, \tag{7}$$

where η is an auxiliary design variable in Θ and $|\Theta|$ is the volume of the design domain. Hence, $h_A(\mathbf{x})$ is a normalized density that incorporates the random variable regions induced by all admissible design parameters.

Equivalently,

$$m^k_{G_{ie}}(\theta) = E_{h_A f_\mathbf{Y}}\left[G_{ie}(\mathbf{x},\mathbf{y})^k \frac{f_\mathbf{X}(\mathbf{x}|\theta)}{h_A(\mathbf{x})}\right], \qquad k=1,2,3, \tag{8}$$

where $E_{h_A f_\mathbf{Y}}[\cdot]$ denotes expectation with respect to the product density $h_A(\mathbf{x}) f_\mathbf{Y}(\mathbf{y})$.

Eq. (6) expresses the raw moment function of the extreme value as a weighted integral under the complete auxiliary density. The extreme value response $G_{ie}(\mathbf{x},\mathbf{y})$ is evaluated at integration points governed by $h_A(\mathbf{x}) f_\mathbf{Y}(\mathbf{y})$, whereas the density ratio $f_\mathbf{X}(\mathbf{x}|\theta)/h_A(\mathbf{x})$ provides the weighting factor for each design. Thus, once these function values are available, the raw moment functions can be evaluated for different candidate designs without repeated limit state function evaluations.

3.2. WA-ASGC Evaluation of Extreme Value Moments

To evaluate Eq. (6), WA-ASGC maps the integration variable to a normalized sparse-grid space. Let $\mathbf{u} \in [-1,1]^{n_u}$ be the normalized collocation variable, and let $T(\mathbf{u}) = (\mathbf{x},\mathbf{y})$ be the corresponding

physical variables. For a fixed design vector θ, the integrand of the kth raw moment of the extreme value is defined as

$$\mathcal{G}_{k\theta}(\mathbf{u}) = G_{ie}(\mathbf{x},\mathbf{y})^k \frac{f_{\mathbf{X}}(\mathbf{x}|\theta)}{h_A(\mathbf{x})}. \tag{9}$$

Here $\mathcal{G}_{k\theta}(\mathbf{u})$ is the raw-moment integrand, $G_{ie}(\mathbf{x},\mathbf{y})$ is the extreme value response at the transformed collocation point, $f_{\mathbf{X}}(\mathbf{x}|\theta)$ is the conditional density for a given design, and $h_A(\mathbf{x})$ is the complete auxiliary density. The notation $\mathcal{G}_{k\theta}(\mathbf{u})$ emphasizes that $\mathbf{u}$ is the integration variable, while θ is a parameter of the integrand. Substituting Eq. (9) into Eq. (6) gives

$$m^k_{G_{ie}}(\theta) = \frac{1}{2^{n_u}} \int_{[-1,1]^{n_u}} \mathcal{G}_{k\theta}(\mathbf{u})\, d\mathbf{u}, \qquad k = 1,2,3. \tag{10}$$

where the factor $1/2^{n_u}$ corresponds to the uniform measure on $[-1,1]^{n_u}$.

The adaptive sparse-grid approximation is built with local hierarchical basis functions (Ma and Zabaras, 2009). The one-dimensional hat function is

$$\varphi(v) = \max(1 - |v|, 0). \tag{11}$$

For a collocation point $\mathbf{u}_p = (u_{p1}, \ldots, u_{pn_u})^T$, the corresponding multidimensional basis function is obtained by the tensor product

$$\phi_p(\mathbf{u}) = \prod_{r=1}^{n_u} \varphi\left(\frac{u_r - u_{pr}}{h_{pr}}\right). \tag{12}$$

where h_{pr} is the local support size of the basis function in the rth dimension.

Let $\mathcal{A}$ be the active sparse-grid point set. The hierarchical interpolant of $\mathcal{G}_{k\theta}$ is written as

$$A_{\mathcal{A}}(\mathcal{G}_{k\theta})(\mathbf{u}) = \sum_{p\in\mathcal{A}} c_p^{(k)}(\theta)\phi_p(\mathbf{u}). \tag{13}$$

In Eq. (13), $c_p^{(k)}(\theta)$ is the hierarchical surplus associated with point $\mathbf{u}_p$. It is defined as the difference between the actual integrand value and the previous-level prediction:

$$c_p^{(k)}(\theta) = \mathcal{G}_{k\theta}(\mathbf{u}_p) - A_{\ell_p-1}(\mathcal{G}_{k\theta})(\mathbf{u}_p). \tag{14}$$

where ℓ_p denotes the level of point $\mathbf{u}_p$, and A_{ℓ_p-1} denotes the interpolant before this point is activated.

After the interpolant is constructed, the raw moment of the extreme value is obtained by integrating the basis functions:

$$m^k_{G_{ie}}(\theta) \approx \sum_{p\in\mathcal{A}} c_p^{(k)}(\theta)\omega_p. \tag{15}$$

The coefficient ω_p in Eq. (15) is the integration weight of the basis function ϕ_p:

$$\omega_p = \frac{1}{2^{n_u}} \int_{[-1,1]^{n_u}} \phi_p(\mathbf{u})\, d\mathbf{u} = \frac{1}{2^{n_u}} \prod_{r=1}^{n_u} \int_{-1}^{1} \varphi\left(\frac{u_r - u_{pr}}{h_{pr}}\right) du_r. \tag{16}$$

The weight ω_p depends only on the sparse-grid point and the support of its basis function. The design dependence remains in $c_p^{(k)}(\theta)$ through the integrand in Eq. (9). At each collocation point, the extreme value response is evaluated once, and the values $G_{ie}(\mathbf{x},\mathbf{y})$, $G_{ie}(\mathbf{x},\mathbf{y})^2$, and $G_{ie}(\mathbf{x},\mathbf{y})^3$ are then used for the first three raw moments.

The same surplus idea is used to guide local refinement. Let $\mathcal{J}_{\theta_{\text{ref}}}(\mathbf{u})$ denote the reference integrand used for refinement at the current reference design θ_{ref}. The local refinement indicator is

$$\gamma_p = \mathcal{J}_{\theta_{\text{ref}}}(\mathbf{u}_p) - A_{\ell_p-1}(\mathcal{J}_{\theta_{\text{ref}}})(\mathbf{u}_p). \tag{17}$$

If this indicator is larger than the prescribed tolerance ε_s, admissible neighboring points are activated:

$$|\gamma_p| > \varepsilon_s \implies \mathcal{A} \leftarrow \mathcal{A} \cup \mathcal{S}(\mathbf{u}_p), \qquad |\mathcal{S}(\mathbf{u}_p)| \le 2n_u. \tag{18}$$

where $\mathcal{S}(\mathbf{u}_p)$ denotes the admissible neighboring points generated from $\mathbf{u}_p$. The refinement process stops when the maximum surplus over refinable active points satisfies

$$\max_{p\in\mathcal{A}_{\text{ref}}} |\gamma_p| \le \varepsilon_s. \tag{19}$$

where $\mathcal{A}_{\text{ref}}$ is the set of refinable active points. Thus, new collocation points are added only in regions where the reference integrand has strong local variation. The resulting point set is then used in Eq. (15) to compute the raw moment functions of the extreme value over the design domain.

3.3. Transformation of Extreme Value Moments to the Failure Probability Function

Once the first three raw moment functions of the extreme value are known, the first three central moment functions (i.e., mean, standard deviation, and skewness) can be computed as follows:

$$\mu_{G_{ie}}(\theta) = m^1_{G_{ie}}(\theta), \tag{20a}$$

$$\sigma_{G_{ie}}(\theta) = \left[m^2_{G_{ie}}(\theta) - \left(m^1_{G_{ie}}(\theta)\right)^2\right]^{1/2}, \tag{20b}$$

$$\alpha_{3G_{ie}}(\theta) = \frac{m^3_{G_{ie}}(\theta) - 3m^2_{G_{ie}}(\theta)m^1_{G_{ie}}(\theta) + 2\left(m^1_{G_{ie}}(\theta)\right)^3}{\sigma_{G_{ie}}(\theta)^3}. \tag{20c}$$

where $\mu_{G_{ie}}(\theta)$, $\sigma_{G_{ie}}(\theta)$, and $\alpha_{3G_{ie}}(\theta)$ denote the mean value, standard deviation, and skewness of the extreme value of the ith limit state function, respectively.

For the ith reliability constraint, let $Z_i = G_{ie}(\mathbf{X},\mathbf{Y})$, with G_{ie} defined by Eq. (3), denote the extreme value response under the design vector θ, and let $F_{Z_i|\theta}(\cdot)$ be its conditional cumulative distribution function. The failure probability is

$$P_{f_i}(\theta) = \Pr\{Z_i \le 0 \mid \theta\} = F_{Z_i|\theta}(0). \tag{21}$$

Based on the equivalent probability transformation, a response value z_i and its associated standard normal value u_i are related by equating their cumulative probabilities:

$$F_{Z_i|\theta}(z_i) = \Phi(u_i), \tag{22}$$

where $\Phi(\cdot)$ denotes the standard normal cumulative distribution function. Following the moment standardization idea, this probability-preserving relation can be written as the transformation function

$$u_i = S_i\left[z_i, \mu_{G_{ie}}(\theta), \sigma_{G_{ie}}(\theta), \alpha_{3G_{ie}}(\theta)\right]. \tag{23}$$

With the three-parameter (3P) lognormal moment transformation (Tichý, 1993), the function $S_i(\cdot)$ is written explicitly as

$$u_i = \frac{\operatorname{sign}\left[\alpha_{3G_{ie}}(\theta)\right]}{\left[\ln A(\theta)\right]^{1/2}} \ln\left\{[A(\theta)]^{1/2}\left[1 - \frac{z_i - \mu_{G_{ie}}(\theta)}{\sigma_{G_{ie}}(\theta) u_b(\theta)}\right]\right\}. \tag{24}$$

The auxiliary quantities are

$$A(\theta) = 1 + \frac{1}{u_b(\theta)^2}, \tag{25a}$$

$$u_b(\theta) = \left[a_L(\theta) + b_L(\theta)\right]^{1/3} + \left[a_L(\theta) - b_L(\theta)\right]^{1/3} - \frac{1}{\alpha_{3G_{ie}}(\theta)}, \tag{25b}$$

$$a_L(\theta) = -\frac{1}{\alpha_{3G_{ie}}(\theta)}\left[\frac{1}{2} + \frac{1}{\alpha_{3G_{ie}}(\theta)^2}\right], \qquad b_L(\theta) = \frac{\left[\alpha_{3G_{ie}}(\theta)^2 + 4\right]^{1/2}}{2\alpha_{3G_{ie}}(\theta)^2}. \tag{25c}$$

Substituting the failure boundary $z_i = 0$ into Eq. (24) gives the standard normal value associated with failure:

$$u_{Fi}(\theta) = \frac{\operatorname{sign}\left[\alpha_{3G_{ie}}(\theta)\right]}{\left[\ln A(\theta)\right]^{1/2}} \ln\left\{[A(\theta)]^{1/2}\left[1 + \frac{\mu_{G_{ie}}(\theta)}{\sigma_{G_{ie}}(\theta) u_b(\theta)}\right]\right\}. \tag{26}$$

The failure probability function is then obtained as

$$P_{f_i}(\theta) = \Phi\left[u_{Fi}(\theta)\right]. \tag{27}$$

For multiple reliability constraints, $P_{f_i}(\theta)$ denotes the moment-based failure probability function associated with the ith limit state function. Replacing the probabilistic constraints in Eq. (4) by Eq. (27) gives the following deterministic form:

$$\begin{aligned} &\text{minimize} && C(\theta) \\ &\text{subject to} && P_{f_i}(\theta) \le P_{f_i}^t, \quad i = 1, 2, \ldots, n_G, \\ &&& h_j(\theta) \le 0, \quad j = 1, 2, \ldots, n_h, \\ &&& \underline{\theta} \le \theta \le \overline{\theta}. \end{aligned} \tag{28}$$

Therefore, once the failure probability functions are constructed, the original reliability constraints are handled as deterministic functional constraints in the design space.

3.4. Sequential Optimization Strategy

Once the moment-based failure probability functions are available, the t-RBDO problem is solved as a sequence of deterministic optimization problems. At each iteration, after the reference point is

updated, WA-ASGC recomputes the hierarchical surpluses of the current active point set for the reference integrand. If the stopping criterion in Eq. (19) is not satisfied, only admissible neighboring points generated from surplus-exceeding points according to Eq. (18) are activated and evaluated. If the criterion is already satisfied, no additional extreme value response evaluations are required.

At the rth round, the current collocation information gives $P_{f_i}^{(r)}(\theta)$, and the deterministic optimization problem is

$$\begin{aligned} &\text{minimize} \quad C(\theta) \\ &\text{subject to} \quad P_{f_i}^{(r)}(\theta) \le P_{f_i}^{t}, \quad i = 1, 2, \ldots, n_G, \\ &\qquad\qquad h_j(\theta) \le 0, \quad j = 1, 2, \ldots, n_h, \\ &\qquad\qquad \underline{\theta} \le \theta \le \overline{\theta}. \end{aligned} \tag{29}$$

The candidate optimum obtained from Eq. (29) is used as the reference point in the next round:

$$\theta_{\text{ref}}^{(r+1)} = \theta_{\text{opt}}^{(r)}. \tag{30}$$

WA-ASGC then rechecks the surplus criterion at the updated reference point. Additional collocation points are introduced only when the current active set no longer satisfies Eq. (19). For multiple reliability constraints, each limit state function is refined separately.

The iteration stops when

$$\frac{\left\| \theta_{\text{opt}}^{(r)} - \theta_{\text{opt}}^{(r-1)} \right\|}{\left\| \theta_{\text{opt}}^{(r-1)} \right\|} \le \varepsilon_\theta. \tag{31}$$

The complete procedure is summarized as follows:

1) *Initialization:* Specify the design domain, initial reference point, objective function, constraints, target failure probabilities, and tolerances.

2) *Raw moment evaluation:* Recheck the WA-ASGC surplus criterion at the current reference point, add admissible neighboring points only when Eq. (19) is violated, and compute the first three raw moment functions of the extreme value for each limit state function.

3) *Failure probability evaluation:* Transform the extreme value moments into $P_{f_i}^{(r)}(\theta)$.

4) *Deterministic optimization:* Solve Eq. (29) to obtain $\theta_{\text{opt}}^{(r)}$.

5) *Reference point update:* Set $\theta_{\text{ref}}^{(r+1)} = \theta_{\text{opt}}^{(r)}$.

6) *Convergence check:* Stop if Eq. (31) is satisfied; otherwise, return to Step 2.

Throughout the optimization, the complete auxiliary density and all moment integrations are defined over the same design domain Θ; no domain reduction or domain updating is required. Existing collocation points and their extreme value response values are retained, and only new

points required by local refinement are added. The optimizer therefore uses deterministic failure probability functions, and any suitable optimization algorithm can be employed.

4. Numerical Study

A nonlinear time-variant numerical problem with multiple reliability constraints is used to examine the proposed method. In addition to the benchmark case, two modified cases are considered to test different feasible regions and optimum locations.

4.1. Nonlinear Time-Variant Problem

The example considers a mathematical design optimization problem adapted from the t-RBDO benchmark in (Zhao et al., 2023). It involves two normal random variables, $X_1 \sim N(\mu_1, 0.6)$ and $X_2 \sim N(\mu_2, 0.6)$, where the design variable vector is $\theta = [\mu_1, \mu_2]^T$. The t-RBDO problem is formulated as

$$\begin{aligned} &\text{minimize} \quad C(\theta) = \theta_1 + \theta_2 \\ &\text{subject to} \quad P\{G_i(X_1, X_2, t) \le 0,\ \exists t \in [0, T]\} \le P_{f_i}^t, \quad i = 1, 2, 3, \\ &\qquad\qquad 0 \le \theta_1, \theta_2 \le 10. \end{aligned} \tag{32}$$

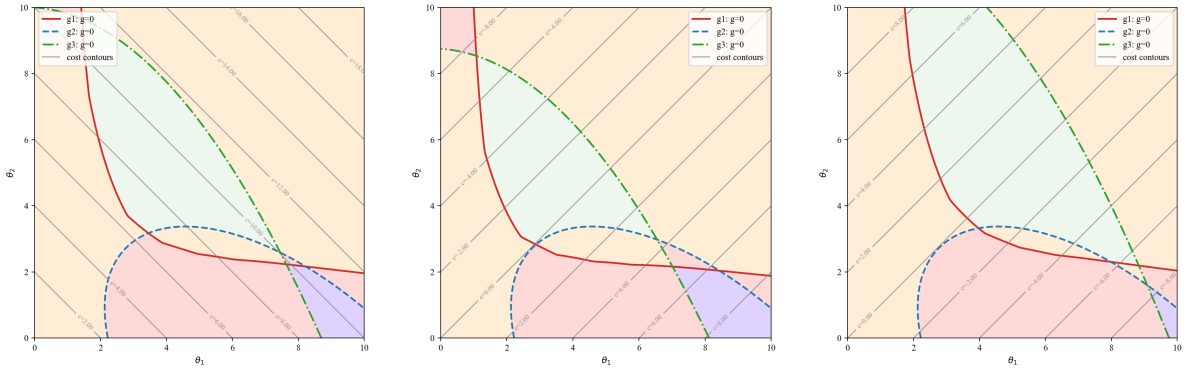
The target failure probability is set as $P_{f_i}^t = 0.1$ for all three limit state functions, and the time interval is $[0, T] = [0, 5]$. The three time-variant limit state functions are

$$\begin{aligned} G_1(X_1, X_2, t) &= X_1^2 X_2 - 5X_1 t + (X_2 + 1)t^2 - a, \\ G_2(X_1, X_2, t) &= \frac{(X_1 + X_2 - 0.1t - 5)^2}{b} + \frac{(X_1 - X_2 + 0.2t - 12)^2}{120} - 1, \\ G_3(X_1, X_2, t) &= \frac{c}{(X_1 + 0.05t)^2 + 8(X_2 + 0.1t) - \sin(t) + 5} - 1. \end{aligned} \tag{33}$$

For the benchmark problem, $[a, b, c] = [20, 30, 90]$. Two modified cases are also considered: $[a, b, c] = [10, 30, 80]$ with $C(\theta) = \theta_1 - \theta_2$, and $[a, b, c] = [30, 30, 110]$ with $C(\theta) = -\theta_1 + \theta_2$. Other settings remain unchanged.

Figure 1 shows the zero-level boundaries of the three limit state functions and the resulting feasible regions. Changing the constants and objective function moves the optimum to different parts of the fixed design domain. The benchmark and modified cases therefore test whether the proposed method can identify solutions governed by different active constraints and optimum locations.

Table I compares the optimization results for the benchmark case. The proposed method gives an optimal cost of 7.7768, differing from the DL-MCS reference by approximately 0.05%, and requires 901 limit state function evaluations over four iterations. The required number of evaluations is also lower than those of WA-SGNI and ASI-IS reported in the table. Moreover, the evaluations are distributed unevenly among the three constraints: 671 for G_1, 165 for G_2, and 65 for G_3. Because each limit state function is refined independently, WA-ASGC assigns more evaluations to the more demanding moment integrand and avoids applying the same computational effort to all constraints.



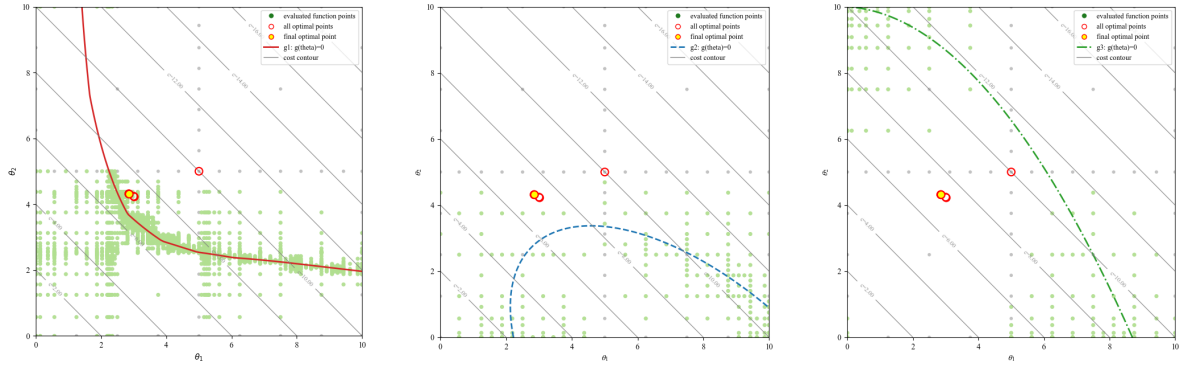
(a) Benchmark (b) Modified case 1 (c) Modified case 2

Figure 1. Limit state boundaries and optimal designs for the benchmark and modified nonlinear time-variant problems.

Table I. Results of the nonlinear time-variant problem.

Method	Optimal design point	Optimal cost	g-calls	Iterations
DL-MCS	$[3.7197, 4.0528]$	7.7726	9×10^6	9
WA-SGNI[a]	$[3.6886, 4.0836]$	7.7734	$3 \times 3 \times 135$	3
ASI-IS[b]	$[3.7834, 4.0771]$	7.8605	$4 \times (3 \times 3000)$	4
Proposed	$[3.7611, 4.0157]$	7.7768	$671 + 165 + 65$	4

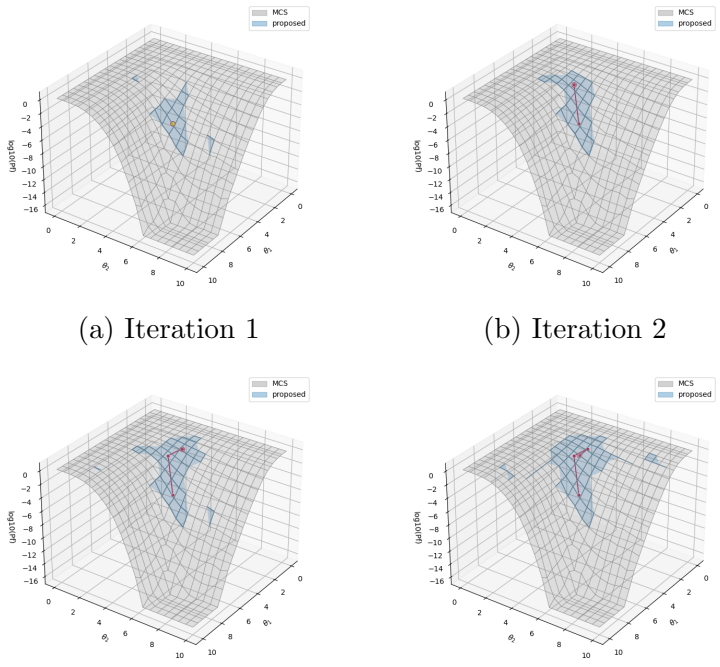
[a] Ref. (Zhao et al., 2023); [b] Ref. (Yuan et al., 2024).



(a) g_1 (b) g_2 (c) g_3

Figure 2. Adaptive sparse grid point distributions for the benchmark nonlinear time-variant problem.

The point distributions in Fig. 2 explain this difference in computational effort. The collocation points are enriched along the relevant portions of the limit state boundaries and around the sequence of candidate optima, whereas regions with little influence on the active constraints remain sparsely represented. The different refinement patterns for G_1, G_2, and G_3 are consistent with their different numbers of function evaluations in Table I.



(a) Iteration 1 (b) Iteration 2

(c) Iteration 3 (d) Iteration 4

Figure 3. Comparative results of failure probability estimates obtained by the proposed method and MCS for the benchmark nonlinear time-variant problem.

Figure 3 compares the failure probability estimates obtained by the proposed method and MCS during the sequential optimization. Although discrepancies may remain away from the current search region, the local estimate is progressively refined as the candidate optimum is updated. At the final iteration, the two results agree closely near the optimum and the active reliability boundary. This agreement is the relevant requirement for t-RBDO and confirms that the sequential strategy directs numerical accuracy toward the region controlling the optimization solution rather than seeking uniform accuracy over the entire design domain.

Table II summarizes the results for the two modified cases.

Table II. Results of the two modified nonlinear time-variant problems.

Method	Optimal design point	Optimal cost	g-calls	Iterations
Case 1: $[a, b, c] = [10, 30, 80]$, $C(\theta) = \theta_1 - \theta_2$				
DL-MCS	$[1.9469, 7.2308]$	-5.2839	12×10^6	12
WA-SGNI[a]	$[1.9491, 7.2365]$	-5.2874	$5 \times 3 \times 135$	5
ASI-IS[b]	$[1.9671, 7.422]$	-5.4549	$5 \times (3 \times 3000)$	5
Proposed	$[1.9418, 7.2106]$	-5.2687	$496 + 131 + 256$	5
Case 2: $[a, b, c] = [30, 30, 110]$, $C(\theta) = -\theta_1 + \theta_2$				
DL-MCS	$[8.1629, 3.0658]$	-5.0971	31×10^6	31
WA-SGNI[a]	$[8.1629, 3.0647]$	-5.0982	$5 \times 3 \times 135$	5
ASI-IS[b]	$[8.1092, 2.9989]$	-5.1103	$5 \times (3 \times 3000)$	5
Proposed	$[8.1562, 3.0564]$	-5.0997	$997 + 539 + 455$	5

[a] Ref. (Zhao et al., 2023); [b] Ref. (Yuan et al., 2024).

For Cases 1 and 2, the relative differences in optimal cost from the DL-MCS references are approximately 0.29% and 0.05%, respectively. The proposed method therefore retains its accuracy when both the feasible region and the location of the optimum change. The two solutions are obtained with 883 and 1991 limit state function evaluations, respectively, without shrinking or relocating the design domain. Together with Fig. 1, these results indicate that the method can follow different active constraints and locate optima in distinct parts of the prescribed design domain while maintaining substantially lower computational cost than DL-MCS.

5. Conclusions

This paper proposed an efficient decoupled t-RBDO method based on weighted extreme value moments and adaptive sparse grids. First, the extreme value method was used to convert the time-variant reliability constraints into equivalent reliability constraints based on extreme responses. The failure probability functions of the extreme responses were then constructed from their first three central moments using the three-parameter lognormal transformation. These central moment functions were obtained from raw extreme value moment functions. Next, a complete auxiliary density was introduced to decouple reliability analysis from optimization over the prescribed design domain. Finally, WA-ASGC evaluated the raw extreme value moment functions through local refinement guided by hierarchical surpluses, thereby enabling an efficient solution of the t-RBDO problem. Based on this formulation, the main conclusions are summarized as follows:

1. A complete auxiliary density is constructed to cover the entire design domain, thereby eliminating the need for iterative domain updates during optimization.

2. A weighted adaptive sparse grid integration strategy is proposed. Hierarchical surpluses guide local refinement, enabling efficient evaluation of the extreme value moment functions and improving computational resource allocation across multiple reliability constraints.

3. A complete t-RBDO solution procedure based on weighted extreme value moments and adaptive sparse grids is established. Its accuracy in reliability analysis, computational efficiency, and applicability to complex nonlinear problems are verified through numerical examples.

Although the proposed method is computationally efficient, it still has some limitations. The method has mainly been verified for low-dimensional problems, and its applicability to problems involving complex high-dimensional random variables and large-scale finite element models requires further study. In addition, constructing the complete auxiliary density over a wide design domain may introduce additional computational cost.

Acknowledgements

The authors gratefully acknowledge the support of the National Key R&D Program of China (2023YFC3009300, 2023YFC3009302).

References

Ching, J. and Y.-H. Hsieh: 2007, 'Approximate Reliability-Based Optimization Using a Three-Step Approach Based on Subset Simulation'. *Journal of Engineering Mechanics* **133**(4), 481–493.

Enevoldsen, I. and J. D. Sørensen: 1994, 'Reliability-Based Optimization in Structural Engineering'. *Structural Safety* **15**, 169–196.

Gasser, M. and G. I. Schueller: 1997, 'Reliability-Based Optimization of Structural Systems'. *Mathematical Methods of Operations Research* **46**, 287–307.

Jensen, H., D. Jerez, and M. A. Valdebenito: 2020, 'An Adaptive Scheme for Reliability-Based Global Design Optimization: A Markov Chain Monte Carlo Approach'. *Mechanical Systems and Signal Processing* **143**, 106836.

Jiang, C., H. Liu, L. Gao, X. Cai, and P. Li: 2017, 'An Adaptive Hybrid Single-Loop Method for Reliability-Based Design Optimization Using Iterative Control Strategy'. *Structural and Multidisciplinary Optimization* **56**, 1271–1286.

Kleijnen, J. P. C.: 2009, 'Kriging Metamodeling in Simulation: A Review'. *European Journal of Operational Research* **192**, 707–716.

Liu, J., M. A. Valdebenito, D. Yang, and M. G. R. Faes: 2025a, 'Adaptive Single-Loop Reweighted Numerical Integration for Estimating Response Moment Functions Under Hybrid Aleatory and Epistemic Uncertainties'. SSRN preprint.

Liu, J., D. Yang, C. Dang, M. A. Valdebenito, and M. G. R. Faes: 2025b, 'A Single-Loop Reweighted Numerical Integration Method for Failure Probability Function Estimation Under Parametric Probability Boxes'. SSRN preprint.

Ma, X. and N. Zabaras: 2009, 'An adaptive hierarchical sparse grid collocation algorithm for the solution of stochastic differential equations'. *Journal of Computational Physics* **228**(8), 3084–3113.

Papadrakakis, M. and N. D. Lagaros: 2002, 'Reliability-Based Structural Optimization Using Neural Networks and Monte Carlo Simulation'. *Computer Methods in Applied Mechanics and Engineering* **191**, 32, 3402, 3491–3507.

Rajasekhar, R. and B. R. Ellingwood: 1993, 'A New Look at the Response Surface Approach for Reliability Analysis'. *Structural Safety* **12**, 205–220.

Rashki, M., M. Miri, and M. A. Moghaddam: 2014, 'A Simulation-Based Method for Reliability Based Design Optimization Problems with Highly Nonlinear Constraints'. *Automation in Construction* **47**, 24–36.

Tafazzolis, A. A. and J. L. Beck: 2009, 'Stochastic Subset Optimization for Reliability Optimization and Sensitivity Analysis in System Design'. *Computers & Structures* **87**, 318–331.

Tichý, M.: 1993, *Applied Methods of Structural Reliability*. Dordrecht: Kluwer Academic Publishers.

Ting Lin, P., H. Chang Gea, and Y. Jaluria: 2011, 'A Modified Reliability Index Approach for Reliability-Based Design Optimization'. *Journal of Mechanical Design* **133**, 044501.

Valdebenito, M. A. and G. I. Schueller: 2010, 'A Survey on Approaches for Reliability-Based Optimization'. *Structural and Multidisciplinary Optimization* **42**(5), 645–663.

Youn, B. D., K. K. Choi, and L. Du: 2005, 'Enriched Performance Measure Approach for Reliability-Based Design Optimization'. *AIAA Journal* **43**, 874–884.

Yuan, X., S. Liu, M. A. Valdebenito, M. G. Faes, D. Jerez, H. A. Jensen, and M. Beer: 2021, 'Decoupled Reliability-Based Design Optimization Using Markov Chain Monte Carlo in Augmented Space'. *Advances in Engineering Software* **157**, 103020.

Yuan, X. and Z. Lu: 2014, 'Efficient Approach for Reliability-Based Optimization Based on Weighted Importance Sampling Approach'. *Reliability Engineering & System Safety* **134**, 107–114.

Yuan, X., M. A. Valdebenito, B. Zhang, M. Faes, and M. Beer: 2023, 'Efficient Decoupling Approach for Reliability-Based Optimization Based on Augmented Line Sampling and Combination Algorithm'. *Computers & Structures* **280**, 107003.

Yuan, X., S. Wang, Y. Dong, and C. Yin: 2024, 'Augmented Space Integral Approach for Structural Reliability-Based Optimization'. *AIAA Journal*.

Zhang, H., D. Auex, Lemosse, and E. S. de Curci: 2021, 'A Single-Loop Approach with Adaptive Sampling and Surrogate Kriging for Reliability-Based Design Optimization'. *Engineering Optimization* **53**(8), 1450–1466.

Zhang, H., C. Zhou, H. Zhao, and Z. Zhang: 2022, 'An Ensemble Model-Based Method for Estimating Failure Probability Function with Application in Reliability-Based Optimization'. *Applied Mathematical Modelling* **108**, 445–468.

Zhao, Z., Y.-G. Zhao, and P.-P. Li: 2023, 'A Novel Decoupled Time-Variant Reliability-Based Design Optimization Approach by Improved Extreme Value Moment Method'. *Reliability Engineering & System Safety* **229**, 108825.

Zhou, Y. and Z. Lu: 2019, 'Active Polynomial Chaos Expansion for Reliability-Based Design Optimization'. *AIAA Journal* **57**, 5431–5446.

Zhou, Y., Z. Lu, and W. Yun: 2020, 'Active Sparse Polynomial Chaos Expansion for System Reliability Analysis'. *Reliability Engineering & System Safety* **202**, 107025.

Zou, T. and S. Mahadevan: 2006, 'A Direct Decoupling Approach for Efficient Reliability-Based Design Optimization'. *Structural and Multidisciplinary Optimization* **31**, 190.

Efficient robust topology optimization of large-scale continuum structures under load uncertainty

Peihan Chen， Dixiong Yang
Department of Engineering Mechanics, Dalian University of Technology, Dalian 116024, China, chenpeihandut@163.com

Abstract: With the increasing complexity of structural design problems, robust topology optimization (RTO) faces increasingly severe computational efficiency challenges. The huge cost of large-scale structural analysis, compounded by repeated analyses required for uncertainty quantification, substantially increases the overall computational burden of RTO. To address this issue, this study proposes an efficient robust topology optimization framework based on discrete variable (RDVTO). The framework first applies direct probability integration (DPIM) with an iterative sequence sampling strategy to quantify uncertainties, enabling accurate statistics with minimal structural analyses. Subsequently, improvements are introduced to the multigrid preconditioned conjugate gradient method based on extended multiscale finite elements (EMsFEM-MGPCG), further enhancing structural analysis efficiency. For load uncertainty issues, the improved method employs matrix representation of load vectors, enabling the calculation of displacements for all representative points in a single computation. Finally, sequential approximate integer programming with trust region (SAIP-TR) is adopted to solve RDVTO problems, producing clear topology configurations. For 3D examples involving millions of degrees of freedom, the proposed method still achieves efficient solutions on a single computer, highlighting its strong potential for engineering applications.

Keywords: Robust topology optimization; EMsFEM-MGPCG acceleration; Large-scale structures; Direct probability integration method; Sequential approximate integer programming with trust region

1. Introduction

In continuum structural design, topology optimization provides an effective means of determining material distribution without relying on a predefined structural configuration. Although this capability has made topology optimization widely used, many existing formulations are still developed under deterministic assumptions, where material parameters, external loads, and boundary-related conditions are regarded as fixed inputs (Liu et al. 2020; Yang et al. 2022). Such assumptions are often inconsistent with practical engineering situations. In real applications, structural performance is inevitably affected by material dispersion, manufacturing imperfections, and stochastic loading environments (Lüthen et al. 2021; Wang and Dai, 2023). A design obtained by deterministic optimization may therefore exhibit reduced stiffness, degraded robustness, or insufficient reliability once these uncertainties appear in service. To improve the stability of optimized layouts against input perturbations, uncertainty effects should be embedded into the design process rather than treated as post-processing factors (Zhu et al. 2021). Among various uncertainty sources, load randomness is of particular significance, since it directly changes the structural response and thus exerts a notable effect on the global structural behavior (Jung and Cho, 2004). Robust topology optimization (RTO) provides a suitable framework for this purpose by describing uncertain parameters through statistical

© 2026 by the author(s). This work is licensed under the Creative Commons Attribution 4.0 International License (CC BY 4.0), which permits unrestricted use, distribution, and reproduction in any medium, provided the original author and source are credited.

quantities and including these quantities in the optimization model (Beyer and Sendhoff 2007; Li et al. 2023). Motivated by this consideration, this work focuses on RTO of continuum structures involving load uncertainty.

Despite its engineering significance, the application of RTO to large-scale structures remains computationally demanding. The difficulty is not caused by topology optimization alone, but by the coupling between large-scale finite element analysis and uncertainty quantification. On the one hand, each optimization iteration usually requires the assembly and solution of high-dimensional finite element equations, which becomes expensive as the design domain is refined (Baiges et al. 2019); (Herrero-Pérez et al. 2024). On the other hand, the evaluation of statistical responses under uncertainty often relies on repeated structural analyses, leading to a rapid increase in computational burden when accurate moment estimation is required (Martínez-Frutos and Herrero-Pérez, 2016). Therefore, an efficient RTO strategy should simultaneously reduce the number of structural evaluations required for uncertainty propagation and accelerate the solution of the finite element systems involved in each evaluation.

The multigrid preconditioned conjugate gradient method based on extended multiscale finite elements (EMsFEM-MGPCG) method has been demonstrated to be efficient for deterministic topology optimization (Liang, 2021); however, its direct extension to RTO does not fully remove the computational bottleneck. In the case of load uncertainty, numerous representative load samples may still have to be analyzed during each optimization iteration. As a result, repeated calls to the EMsFEM-MGPCG solver can dominate the total computational time, particularly for large-scale models. When the mesh size increases, this repeated reconstruction can become a major source of overhead and may even offset the acceleration gained from the multiscale solver.

To address these issues, this study develops an RTO framework that integrates direct probability integration method (DPIM) with an improved EMsFEM-MGPCG strategy. DPIM is adopted to evaluate the statistical moments of structural responses efficiently using a limited number of representative analyses (Chen and Yang, 2019). Based on the type of uncertainty considered, the EMsFEM-MGPCG procedure is further modified to reduce unnecessary repeated computations. For load uncertainty, the responses corresponding to multiple load cases are solved in a unified matrix form, thereby avoiding repeated solver calls within a single optimization iteration. The resulting robust discrete-variable topology optimization problem is solved using sequential approximate integer programming with trust region (SAIP-TR), enabling the direct generation of clear black-and-white structural layouts.

2. RDVTO Formulation

Typically, the objective function of RDVTO is a weighted sum of the mean and standard deviation for the structural response of interest, and the structural volume serves as the constraint. In this study, the formulation of robust topology optimization is defined as

$$\min_{\rho} \quad C_R(\rho) = \mathrm{E}[C(\rho)] + w\mathrm{Std}[C(\rho)]$$

$$\text{s.t.}: \begin{cases} \mathbf{K}(\boldsymbol{\rho},\boldsymbol{\Theta})\mathbf{U} = \mathbf{F}(\boldsymbol{\Theta}) \\ \sum_{i=1}^{N} \rho_i V_i \le \overline{V_f} V_0 \\ \rho_i \in \{0,1\} \ , \ i = 1,2,\ldots N \end{cases} \tag{1}$$

where the compliance C is expressed as $C(\rho) = \mathbf{F}^T\mathbf{U}$. E[$C(\rho)$] and Std[$C(\rho)$] are the mean and standard deviation of the compliance C, respectively. In this study, w is set to 3. $\boldsymbol{\rho}$ denotes the N-dimensional elemental density vector, and ρ_i is the density of the ith element, which takes the value of 0 or 1. $\boldsymbol{\Theta} = [\Theta_1, \Theta_2, ..., \Theta_n]$ is the n-dimensional random variable vector. $\mathbf{K}$ means the global stiffness matrix, $\mathbf{F}$ and $\mathbf{U}$ denote the external load vector and the global displacement vector. V_i indicates the volume of the ith element, V_0 is the volume of the structure when full of material, and $\overline{V_f}$ is the volume fraction. In this article, we use the discrete variable topology optimization method SAIP-TR to solve the optimization equation

In the SAIP-TR method, the objective and constraint functions of the programming subproblem are constructed using the first-order Taylor expansion. Specifically, a kth sequential integer programming subproblem of the SAIP-TR method is formulated by

$$\min_{\rho} \quad C_R(\rho) \approx C_R(\rho^k) + \sum_{i=1}^{N} \frac{\partial C(\rho^k)}{\partial \rho}(\rho - \rho^k)$$

$$\text{s.t.}: \begin{cases} \mathbf{K}(\boldsymbol{\rho}^k, \boldsymbol{\Theta})\mathbf{U} = \mathbf{F}(\boldsymbol{\Theta}) \\ \sum_{i=1}^{N} \rho_i^k V_i \le \overline{V_f} V_0 \\ \sum_{i=1}^{N} r_i \left(\rho_i - \rho_i^k\right) \le r_k \ , \ r_i = \{-1, 1\} \\ \rho_i = \{0, 1\} \ , \ i = 1, 2, \ldots N \end{cases} \tag{2}$$

where the penultimate constraint denotes the trust region, and the parameter r_k represents the radius of the trust region for the kth subproblem. Physically, it indicates the number of elements allowed to change density in each iteration, $\boldsymbol{\rho}^k$ represents the design variable vector of the kth iteration. Moreover, the above integer programming subproblems are solved by the canonical relaxation algorithm.

3. Uncertainty quantification for RDVTO

Calculation of statistical moments is crucial for RTO. However, there is no unified method for solving the high-dimensional random variables RTO problems efficiently and accurately. Therefore, the DPIM (Chen and Yang, 2019), a novel and efficient stochastic analysis method for stochastic static and dynamic systems, is employed to calculate the statistical moments of RTO problems herein.

In the RDVTO problems, the input random variables and the structural compliance response can be defined as the following mapping

$$Q: Y = C(\boldsymbol{\rho}, \boldsymbol{\Theta}) \tag{3}$$

According to the principle of probability conservation (Syski, 1967; Soong and Bogdanoff, 1973; Li and Chen, 2009), the probability measure determined by the random sources remains invariant in the propagation process of randomness from system input to output, i.e.

$$\int_{\boldsymbol{\Omega}_Y} p_Y(\mathbf{y}, t)\, \mathrm{d}\mathbf{y} = \int_{\boldsymbol{\Omega}_\Theta} p_{\boldsymbol{\Theta}}(\boldsymbol{\theta})\, \mathrm{d}\boldsymbol{\theta} \tag{4}$$

where $p_Y(\boldsymbol{y})$ and $p_{\boldsymbol{\Theta}}(\boldsymbol{\theta})$ denote the joint probability density function (PDF) of Y and $\boldsymbol{\Theta}$, respectively. $\boldsymbol{\Omega}_Y$ and $\boldsymbol{\Omega}_{\boldsymbol{\Theta}}$ denote the sample spaces of the input vector and output vector.

Based on the sifting properties of the Dirac δ function (Li and Chen, 2008) and Eq.(4), the relationship between the PDF of output response $Y=C(\boldsymbol{\rho}, \boldsymbol{\theta})$ and the input PDF (Li et al. 2021; Peng et al. 2024) is derived as

$$p_Y(y) = \int_{\Omega_\Theta} \delta\left(y - C(\boldsymbol{\rho},\boldsymbol{\theta})\right) p_\Theta(\boldsymbol{\theta}) \mathrm{d}\boldsymbol{\theta} \tag{5}$$

Eq. (3) is named as probability density integral equation of static system (Li and Chen, 2008). $\delta\left(y - C(\boldsymbol{\rho},\boldsymbol{\theta})\right)$ is a Dirac δ function, which is a linear functional and denotes the conditional PDF of stochastic response y given random input vector $\boldsymbol{\theta}$, i.e. $p_{Y|\Theta}(y \mid \boldsymbol{\theta}) = \delta(y - C(\boldsymbol{\rho},\boldsymbol{\theta}))$. Eq. (5) is a total probability formula of density form, namely

$$p_Y(y) = \int_{\Omega_\Theta} p_{Y|\Theta}(y \mid \boldsymbol{\theta}) p_\Theta(\boldsymbol{\theta}) \mathrm{d}\boldsymbol{\theta} = \int_{\Omega_\Theta} \delta\left(y - C(\boldsymbol{\rho},\boldsymbol{\theta})\right) p_\Theta(\boldsymbol{\theta}) \mathrm{d}\boldsymbol{\theta} \tag{6}$$

Meanwhile, Eq. (5) implies that the response PDF is the expectation of conditional PDF of response given random input $\boldsymbol{\theta}$ and the expectation of Dirac δ function, namely

$$p_Y(y) = \mathrm{E}\left[p_{Y|\Theta}(y \mid \boldsymbol{\theta}) \right] = \mathrm{E}\left[\delta\left(y - C(\boldsymbol{\rho},\boldsymbol{\theta})\right) \right] \tag{7}$$

The ith moment $m_i[Y]$ of the stochastic response Y is defined by

$$m_i[Y] = \mathrm{E}(Y^i) = \int_{\Omega_Y} y^i p_Y(y) \mathrm{d}y \tag{8}$$

In general, the response PDF $p_Y(y)$ in Eq. (11) is difficult to calculate. Thus, substituting in Eq. (5) into Eq. (8) yields

$$m_i[Y] = \int_{\Omega_Y} \int_{\Omega_\Theta} y^i \delta\left(y - C(\boldsymbol{\rho},\boldsymbol{\theta})\right) p_\Theta(\boldsymbol{\theta}) \mathrm{d}\boldsymbol{\theta} \mathrm{d}y = \int_{\Omega_\Theta} \left\{ \int_{\Omega_Y} y^i \delta\left(y - C(\boldsymbol{\rho},\boldsymbol{\theta})\right) dy \right\} p_\Theta(\boldsymbol{\theta}) \mathrm{d}\boldsymbol{\theta} \tag{9}$$

Using the sifting property of the Dirac function, the ith order origin moment of the stochastic response Y in input probability space is expressed as (Yang et al. 2025)

$$m_i[Y] = \int_{\Omega_\Theta} \left(C(\boldsymbol{\rho},\boldsymbol{\theta})\right)^i p_\Theta(\boldsymbol{\theta}) \mathrm{d}\boldsymbol{\theta} \tag{10}$$

Eq. (10) usually involves high-dimensional integrals and is hard to obtain an exact solution. Based on the representative point selection strategy of GF-discrepancy, DPIM is utilized to compute Eq. (10) by probability space partition, which is discretized as

$$m_i[Y] = \int_{\Omega_\Theta} \left(C(\boldsymbol{\rho},\boldsymbol{\theta})\right)^i p_\Theta(\boldsymbol{\theta}) \mathrm{d}\boldsymbol{\theta} = \sum_{q=1}^{M} \left(C(\boldsymbol{\rho},\boldsymbol{\theta}_q)\right)^i P_q \tag{11}$$

where M is the number of sample points required for structural analysis, and P_q denotes the assigned probability of the qth representative point $\boldsymbol{\theta}_q$ in the corresponding representative region (Chen et al. 2016). The number of sample points relates to the computation cost of structural analysis. In this paper, an iterative sampling strategy (Tao et al. 2022) is employed to efficiently determine the number of sample points.

In the iterative sampling strategy, the GF-discrepancy based point selection approach (Chen et al. 2016) is firstly used to obtain a pool of candidate sample points. Then, the sample points are gradually selected from the pool until the proposed stopping criterion is satisfied. In this study, the stopping criteria are defined below

$$N_u = tol_{N_u} \tag{12}$$

where

$$N_\mu = \sum_{i=1}^{n} I\left(\varepsilon_{\mu i} \le tol_{\varepsilon_\mu}\right);\ \varepsilon_\mu = \frac{\left\|\mu_i - \mu_{i-1}\right\|_2}{\left\|\mu_{i-1}\right\|_2} \tag{13}$$

where $I(x)$ is indicator function, $I = 1$ when x satisfies the requirement, otherwise $I = 0$. N_μ represent the total times when the error $\varepsilon_{\mu i}$ is less than the threshold tol_{ε_μ} in the first n iterations. In this study, the threshold is set to 1×10^{-3}. μ_i indicates the weighted sum of the mean and standard deviation of stochastic response. tol_{Nu} is a positive integer and the sampling process stops when Eq. (12) is satisfied. This strategy in DPIM can adaptively determine the number of samplings, which significantly enhances the efficiency. Interested readers can refer to Ref. (Tao et al. 2022) for details. According to Eq. (11), the first and second order origin moments are obtained by using DPIM

$$\mathrm{E}(Y) = \int_{\Omega_{\boldsymbol{\Theta}}} C(\boldsymbol{\rho},\boldsymbol{\theta}) p_{\boldsymbol{\Theta}}(\boldsymbol{\theta})\mathrm{d}\boldsymbol{\theta} = \sum_{q=1}^{M} C(\boldsymbol{\rho},\boldsymbol{\theta}_q) P_q \tag{14}$$

$$\mathrm{E}[Y^2] = \int_{\Omega_{\boldsymbol{\Theta}}} \left(C(\boldsymbol{\rho},\boldsymbol{\theta})\right)^2 p_{\boldsymbol{\Theta}}(\boldsymbol{\theta})\mathrm{d}\boldsymbol{\theta} = \sum_{q=1}^{M} \left(C(\boldsymbol{\rho},\boldsymbol{\theta}_q)\right)^2 P_q \tag{15}$$

The standard deviation of stochastic response Y can then be obtained by

$$\begin{aligned} \mathrm{Std}(Y) &= \sqrt{\int_{\Omega_{\boldsymbol{\Theta}}} \left(C(\boldsymbol{\rho},\boldsymbol{\theta})\right)^2 P_q \mathrm{d}\boldsymbol{\theta} - \left(\int_{\Omega_{\boldsymbol{\Theta}}} C(\boldsymbol{\rho},\boldsymbol{\theta}) P_q \mathrm{d}\boldsymbol{\theta}\right)^2} \\ &= \sqrt{\sum_{q=1}^{M} \left(C(\boldsymbol{\rho},\boldsymbol{\theta}_q)\right)^2 P_q - \left(\sum_{q=1}^{M} C(\boldsymbol{\rho},\boldsymbol{\theta}_q) P_q\right)^2} \end{aligned} \tag{16}$$

4. Improved EMsFEM-MGPCG

EMsFEM-MGPCG was originally incorporated into the SAIP-TR topology optimization scheme by Liang (2021), where it enabled high-resolution stiffness-oriented designs with low-order finite elements and small filtering radii. However, that work was mainly developed for deterministic optimization. Once uncertainties in external loads are introduced, the original implementation no longer fully reflects the potential efficiency of EMsFEM-MGPCG. Therefore, this section reformulates the method for RDVTO problems involving load uncertainty, with the goal of lowering the repeated analysis cost.

The main computational burden in RDVTO comes from the large number of finite element analyses required to evaluate statistical responses and their sensitivities. For load uncertainty, a conventional procedure performs an independent equilibrium analysis for each representative load at every design iteration, although these analyses use the same stiffness matrix within the current iteration. If EMsFEM-MGPCG is used in this manner, the solver still has to be called repeatedly for different representative points. To avoid this inefficiency, the proposed modification rewrites the problem in a multi-right-hand-side form. The load vectors associated with all representative points are grouped together, and the corresponding displacement solutions are obtained collectively under the shared stiffness matrix. By reusing the stiffness information across all load cases, the improved EMsFEM-MGPCG eliminates unnecessary repeated solves and substantially accelerates RDVTO under load uncertainty.

For M representative uncertainty points, the conventional independent finite element analysis is formulated as:

$$Ku_m = f_m \quad m = 1, 2, ..., M \tag{17}$$

Although these independent analyses share the exact same structural stiffness matrix K within the current iteration, a standard sequential solver executes M distinct linear solution pipelines. To resolve this inefficiency, the governing equations are rewritten into a compact multi-right-hand-side block matrix form:

$$KU = F \qquad U = [u_1, u_2, ..., u_M], \quad F = [f_1, f_2, ..., f_M] \tag{18}$$

In the EMsFEM paradigm, the global fine-mesh stiffness matrix is projected onto a downscaled coarse-mesh subspace via numerical basis functions: $K_c = \mathrm{P}^T K \mathrm{P}$. By utilizing the Eq. (18) formulation, the costly base-function calculation, fine-to-coarse projection, and multigrid preconditioning smoothers are executed exactly once per SAIP-TR optimization step. The block system is then solved collectively using parallelized MGPCG Krylov subspace projections, eliminating all redundant sub-meshing and assembly loops.

The solution framework is shown in Fig. 1.

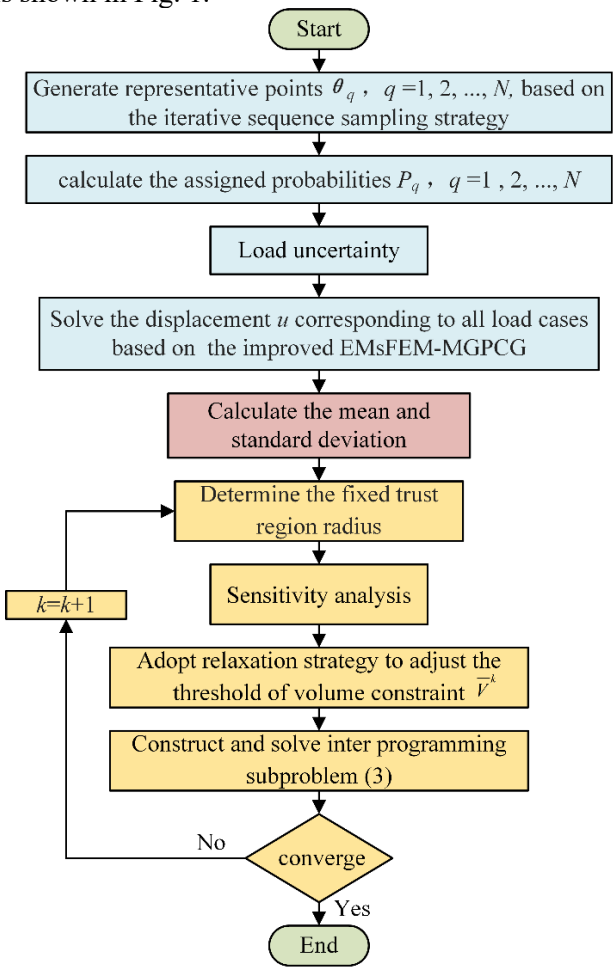


Fig. 1 Schematic diagram based on the proposed framework

5. Numerical examples

Engineering bridge structures are inherently three-dimensional, and their numerical models usually involve far more degrees of freedom than two-dimensional benchmarks. As the mesh resolution increases, the repeated structural analyses required in RTO become increasingly expensive. To examine the applicability of the proposed method to practical large-scale problems, a three-dimensional bridge model is therefore adopted as the test case.

The bridge deck is subjected to uncertain spatial loading, which may arise from variations in vehicle positions, traffic paths, snow or ice accumulation, and wind effects. The corresponding boundary conditions are shown in Fig. 2. The design domain is discretized by a 30 × 15 × 6 coarse mesh, and each coarse element is further resolved into 6 × 6 × 6 fine elements. The prescribed volume fraction is $V_f = 0.1$. A distributed load with random magnitude and direction is imposed on the non-design region marked in Fig. 2. The load magnitude is represented by a Gaussian random field constructed using EOLE, with a mean value of 1, a standard deviation of 0.1, and a correlation length of 30. Five truncation terms are retained, keeping the truncation error below 2%. The load direction follows a prescribed normal distribution, and 80 representative points selected by the iterative sequence sampling strategy are adopted.

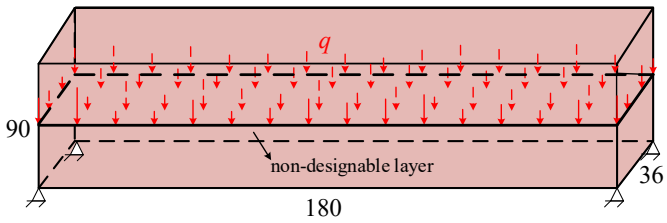


Fig. 2 3D bridge structure under random distributed loads with uncertain magnitude and direction

The three-dimensional bridge example involves 1,828,281 degrees of freedom, making it a typical million-scale RDVTO problem. The optimized layout in Fig. 3 captures the main load-carrying pattern of the real bridge shown in Fig. 4, while retaining fine structural details. Since SAIP-TR treats the design variables in a discrete manner, the final topology is directly obtained as a well-defined black-and-white configuration, without the need for filtering or post-processing. To assess the computational advantage of the proposed framework, the direct solver is used as a reference. Its cost is prohibitive: a single structural analysis iteration requires nearly 20 hours, so a complete optimization process would be impractical for engineering use. In comparison, the proposed framework reduces the structural analysis time per iteration to 82 s. The whole optimization process reaches convergence after 110 iterations and takes approximately 2.5 hours on a single workstation. These results suggest that the proposed method enables efficient and accurate topology optimization for million-DOF three-dimensional structures, and offers a practical computational strategy for large-scale engineering design.

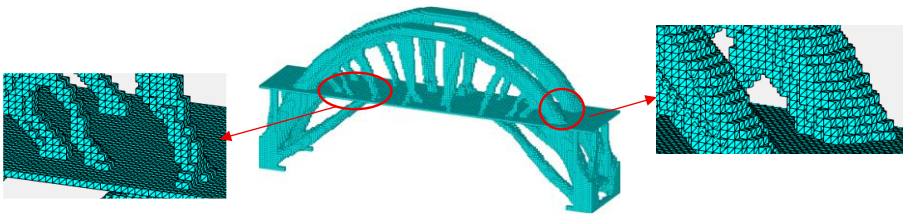


Fig. 3 Optimal topology configuration of the 3D bridge by RDVTO



Fig. 4 An existing through-arch bridge

6. Conclusions

This study develops an efficient RDVTO framework by improved EMsFEM-MGPCG and coupling it with DPIM and SAIP-TR. the modified solver reduces the cost of structural analysis under load uncertainty, while DPIM limits the number of analyses required for statistical moment estimation. For load uncertainty, the improved EMsFEM-MGPCG method enables simultaneous solution of all representative point displacements using a single right-hand-side matrix and one factorization of the global stiffness matrix K. For 3D RDVTO problems involving millions of degrees of freedom, the proposed framework reduces the structural analysis time per iteration from approximately 20 hours using traditional methods to just 82 s. This efficiency gain is primarily attributed to the improved EMSFEM-MGPCG's capability to solve multiple load cases simultaneously in matrix form, thereby eliminating redundant solver calls. Consequently, the framework achieves remarkable computational performance and demonstrates strong engineering applicability for large-scale structural optimization.

7. References

Baiges, J., J. Martínez-Frutos, D. Herrero-Pérez, et al. Large-scale stochastic topology optimization using adaptive mesh refinement and coarsening through a two-level parallelization scheme. Computer Methods in Applied Mechanics and Engineering, 343, pages 186–206, 2019.

Beyer, H. G., and B. Sendhoff. Robust optimization – A comprehensive survey. Computer Methods in Applied Mechanics and Engineering, 196, pages 3190–3218, 2007.

Chen, G. H., and D. X. Yang. Direct probability integral method for stochastic response analysis of static and dynamic structural systems. Computer Methods in Applied Mechanics and Engineering, 357, Article 112612, 2019.

Chen, J. B., J. Y. Yang, and J. Li. A GF-discrepancy for point selection in stochastic seismic response analysis of structures with uncertain parameters. Structural Safety, 59, pages 20–31, 2016.

Herrero-Pérez, D., S. G. Picó-Vicente, and H. Martínez-Barberá. Adaptive density-based robust topology optimization under uncertain loads using parallel computing. Engineering with Computers, 40, pages 21–43, 2024.

Jung, H. S., and S. Cho. Reliability-based topology optimization of geometrically nonlinear structures with loading and material uncertainties. Finite Elements in Analysis and Design, 41, pages 311–331, 2004.

Li, C. C., and A. Der Kiureghian. Optimal Discretization of Random Fields. Journal of Engineering Mechanics, 119, pages 1136–1154, 1993.

Li, J., and Chen, J. B. Stochastic Dynamics of Structures. John Wiley & Sons, Singapore, 2009.

Li, J., and Chen, J. B. The principle of preservation of probability and the generalized density evolution equation. Structural Safety, 30, pages 65–77, 2008.

Li, X. L., G. H. Chen, H. C. Cui, and D. X. Yang. Direct probability integral method for static and dynamic reliability analysis of structures with complicated performance functions. Computer Methods in Applied Mechanics and Engineering, 374, Article 113583, 2021.

Li, Z. S., L. Wang, and T. Q. Lv. Additive manufacturing-oriented concurrent robust topology optimization considering size control. International Journal of Mechanical Sciences, 250, Article 108269, 2023.

Liang, Y., General and high-performance discrete variable topology optimization method via sequential approximate integer

programming (SAIP), Ph.D. Dissertation, Dalian University of Technology, Dalian, China, 2021.
Liu, B. S., C. Jiang, G. Y. Li, and X. D. Huang. Topology optimization of structures considering local material uncertainties in additive manufacturing. Computer Methods in Applied Mechanics and Engineering, 360, Article 112786, 2020.
Lüthen, N., S. Marelli, and B. Sudret. Sparse Polynomial Chaos Expansions: Literature Survey and Benchmark. SIAM/ASA Journal on Uncertainty Quantification, 9, pages 593–649, 2021.
Martínez-Frutos, J., and D. Herrero-Pérez. Large-scale robust topology optimization using multi-GPU systems. Computer Methods in Applied Mechanics and Engineering, 311, pages 393–414, 2016.
Peng, H. J., F. J. Sun, F. Wu, and D. X. Yang. Dynamic reliability of mechanism based on direct probability integral method. International Journal of Mechanical Sciences, 270, Article 109105, 2024.
Soong, T. T., and J. L. Bogdanoff. Random Differential Equations in Science and Engineering. Academic Press, New York, 1973.
Syski, R. Stochastic Differential Equations. In: T. L. Saaty (Ed.), Modern Nonlinear Equations, Chapter 8. McGraw-Hill, New York, 1967.
Tao, T. Z., G. Z. Zhao, Y. Yu, et al. A fully adaptive method for structural stochastic response analysis based on direct probability integral method. Computer Methods in Applied Mechanics and Engineering, 396, Article 115066, 2022.
Wang, R. J., and H. Z. Dai. Stochastic analysis of structures under limited observations using kernel density estimation and arbitrary polynomial chaos expansion. Computer Methods in Applied Mechanics and Engineering, 403, Article 115689, 2023.
Yang, D. X., J. L. Liu, R. F. Yu, and G. H. Chen. Unified framework for stochastic dynamic responses and system reliability analysis of long-span cable-stayed bridges under near-fault ground motions. Engineering Structures, 322, Article 119061, 2025.
Yang, J. S., H. A. Jensen, and J. B. Chen. Structural optimization under dynamic reliability constraints utilizing probability density evolution method and metamodels in augmented input space. Structural and Multidisciplinary Optimization, 65, Article 107, 2022.
Zhu, J. H., H. Zhou, C. Wang, et al. A review of topology optimization for additive manufacturing: Status and challenges. Chinese Journal of Aeronautics, 34, pages 91–110, 2021.

A Bayesian Framework for Modeling and Testing the Temperature-Dependent Residual Compressive Strength of Concrete

Md Maidul Islam
Ghent University, Technologiepark-Zwijnaarde 60, Ghent 9052, Belgium, MdMaidul.Islam@UGent.be
Andrea Franchini
Ghent University, Technologiepark-Zwijnaarde 60, Ghent 9052, Belgium, Andrea.Franchini@UGent.be
Balsa Jovanovic
Ghent University, Technologiepark-Zwijnaarde 60, Ghent 9052, Belgium, Balsa.Jovanovic@UGent.be
Ruben Van Coile
Ghent University, Technologiepark-Zwijnaarde 60, Ghent 9052, Belgium, Ruben.VanCoile@UGent.be

Abstract: This study presents a novel Bayesian model for the temperature-dependent residual compressive strength of a concrete mix. The model consists of a lognormal distribution for the concrete strength retention factor k_{fc}, i.e., the ratio of the compressive strength after exposure to elevated temperature to the initial compressive strength at room temperature. The Bayesian conceptualization of the model enables straightforward updating of the k_{fc} model as new experimental data becomes available. Furthermore, a framework for pre-posterior analysis is presented to guide decision-making before actual data collection. Specifically, the concept of expected information gain (EIG) is adopted to optimize experimental design. This approach allows the identification of optimal measurement temperatures to reduce uncertainty in estimating k_{fc}. The analysis reveals that measuring at 600–900 °C yields a higher information gain than measuring at any other temperature. Comparative analyses illustrate the effectiveness of the EIG concept in guiding experimental planning.

Keywords: Bayesian updating; experimental design; uncertainty quantification.

1. Introduction

Concrete is one of the most widely used construction materials and is commonly considered to behave well under fire due to its low thermal conductivity (Gernay et al., 2021). Nonetheless, concrete structural elements may require post-fire repair due to the permanent degradation of material properties. Existing literature data on residual concrete strength however exhibit large variability (e.g., Al‐Jabri et al., 2016; Chen et al. 2014).

The residual concrete strength is commonly evaluated by specifying a concrete strength retention factor k_{fc}. This retention factor is defined as the residual compressive strength $f_{c,T}$ of a specimen having been exposed to a maximum temperature *T*, divided by the initial room-temperature strength $f_{c,20}$. (Shahraki et al., 2023) adopted the methodology from (Qureshi et al., 2020) to propose k_{fc} models for calcareous and siliceous concretes. The dataset used for the Shahraki models includes a wide range of concrete mixes, thereby representing the variability observed across all the different mixes. When a specific concrete building experiences a fire, adopting the Shahraki model is therefore likely to result in an overestimation of the uncertainty on residual k_{fc}. Moreover, this model does not provide a formal updating mechanism for

© 2026 by the author(s). This work is licensed under the Creative Commons Attribution 4.0 International License (CC BY 4.0), which permits unrestricted use, distribution, and reproduction in any medium, provided the original author and source are credited.

incorporating site-specific new data, which would allow the reduction of uncertainty in k_{fc} for specific buildings.

To address these limitations, a novel temperature-dependent model for the residual compressive strength of concrete is proposed in this paper. The model is developed by reevaluating the dataset presented in (Shahraki et al., 2023) and can be updated with new experimental data through Bayesian techniques (Gelman et al., 2021). These techniques also enable the design of optimal experimental protocols that maximize the expected utility of experiments, as outlined by recent research (Franchini and Van Coile, 2026). Sec. 2.1 of this paper develops the temperature-dependent Bayesian k_{fc} model. Next, Sec. 2.2 outlines the approach to update the model based on newly available information, while Sec. 2.3 presents a methodology to identify the measurement temperature that maximizes expected information gain on k_{fc}. Sec. 3 applies this methodology to determine optimal measurement temperatures for k_{fc} uncertainty reduction. Finally, Sec. 4 provides conclusions.

2. Methodology

2.1. MODEL SETUP

A considerable amount of experimental data on k_{fc} is available in the literature. This study utilizes the data sources outlined in (Shahraki et al., 2023). Because the Shahraki et al. dataset was not compiled in a mix-specific manner, the data sources are reanalyzed and the dataset reconstituted with an indication of the concrete mix. Furthermore, Shahraki et al. adopted an inclusion criterion whereby only samples with a retention time of at least 2 hours were incorporated into the dataset. This inclusion criterion has not been adopted here in order to obtain a larger number of data points. The reevaluated dataset contains data points for 248 different mixes of normal-strength concrete, where each mix is characterized by a temperature-dependent mean strength and standard deviation. This dataset defines the current state of knowledge (prior distribution) regarding k_{fc}.

The temperature-dependent k_{fc} for a particular concrete mix is assumed to be lognormally distributed as per Eq. (1) where μ_{kfc} is the mean and σ_{kfc} is the standard deviation. This assumption is motivated by the common usage of lognormal distributions to describe material strength properties (Holický and Sýkora, 2010) and the characteristic of the lognormal distribution in constraining results to positive values. The quantile levels of k_{fc} are considered to be perfectly correlated across exposure temperatures. For example, the 5th percentile (i.e., 0.05 quantile) of concrete retention factor at 100 °C will decay to a 5th percentile of retention factor at 900°C. The distribution parameters μ_{kfc} and σ_{kfc} (see Eq. (2)-(3)) are considered as uncertain and lognormally distributed with means and standard deviations denoted as μ_μ, σ_μ, μ_σ, and σ_σ.

$$k_{fc} \sim LN(\mu_{kfc}, \sigma_{kfc}^2) \tag{1}$$

$$\mu_{kfc} \sim LN(\mu_\mu, \sigma_\mu^2) \tag{2}$$

$$\sigma_{kfc} \sim LN(\mu_\sigma, \sigma_\sigma^2) \tag{3}$$

The value of k_{fc} at 20 °C is fixed to 1, consistent with its definition as a normalized ratio ($k_{fc} = f_{c,T}/f_{c,20}$). Furthermore, a simplifying assumption is adopted that no residual strength remains after exposure to 1000 °C, resulting in a k_{fc} equal to 0. At both these temperatures, k_{fc} is thus known and has no associated variability.

The variability among multiple mixes is quantified by first considering the mean $\mu_{z,T}$ and standard deviation $\sigma_{z,T}$ data for the z-th mix in the dataset. These statistics are evaluated at selected temperature levels $T \in T_{range} = \{100, 200, 300, 400, 500, 600, 700, 800, 900\}$ [°C], and the results are shown in Figure 1(a). Then, the mean and standard deviation of $\mu_{z,T}$ and $\sigma_{z,T}$ are calculated at each T. This results in 1 data point at each T across T_{range} for the model parameters μ_μ, σ_μ, μ_σ, and σ_σ (as shown in Figure 1(b)-(c)). Finally, polynomial regression is employed to obtain the best-fit curves for the 8 data points across T_{range} (see Eq. (4)-(7) and Figure 1(b)-(c)). The regression is carried out considering the following boundary conditions: $\mu_\mu(20°C) = 1$; $\mu_\mu(1000°C) = 0$; $\sigma_\mu(20°C) = 0$; $\sigma_\mu(1000°C) = 0$; $\mu_\sigma(20°C) = 0$; $\mu_\sigma(1000°C) = 0$; $\sigma_\sigma(20°C) = 0$; $\sigma_\sigma(1000°C) = 0$.

$$\mu_\mu(T) = 1.30 \times 10^{-12} \cdot T^4 - 2.61 \times 10^{-9} \cdot T^3 + 1.43 \times 10^{-6} \cdot T^2 - 1.14 \times 10^{-3} \cdot T + 1.022 \quad (4)$$

$$\sigma_\mu(T) = 2.52 \times 10^{-12} \cdot T^4 - 4.38 \times 10^{-9} \cdot T^3 + 1.17 \times 10^{-6} \cdot T^2 + 6.97 \times 10^{-4} \cdot T - 0.014 \quad (5)$$

$$\mu_\sigma(T) = -5.71 \times 10^{-13} \cdot T^4 + 1.84 \times 10^{-9} \cdot T^3 - 1.99 \times 10^{-6} \cdot T^2 + 7.29 \times 10^{-4} \cdot T - 0.014 \quad (6)$$

$$\sigma_\sigma(T) = -5.20 \times 10^{-13} \cdot T^4 + 1.64 \times 10^{-9} \cdot T^3 - 1.74 \times 10^{-6} \cdot T^2 + 6.27 \times 10^{-4} \cdot T - 0.012 \quad (7)$$

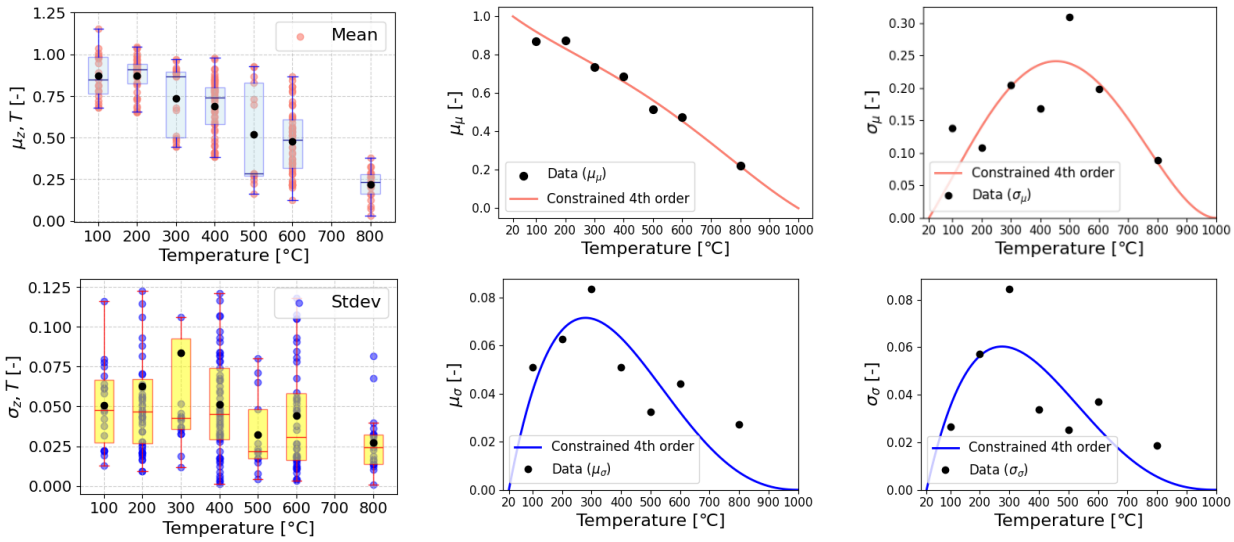


Figure 1. Regression analysis showing: (a) Data points representing 248 different mixes; (b) best-fit polynomials for μ_μ and μ_σ; and (c) best-fit polynomials for σ_μ and σ_σ.

The best-fit values from Eq. (4)-(7) define temperature-dependent distribution parameters for $\mu_{kfc}(T)$ and $\sigma_{kfc}(T)$. The quantile levels within these fixed lognormal distributions are denoted as q_μ and q_σ. For a given realization, the same quantile is assumed to occur at each temperature. Before considering site-specific data, all quantile levels are considered equally likely. Thus, q_μ and q_σ are described by uniform distributions between 0 and 1.

Realizations of k_{fc} are obtained as follows: **(i)** a set of quantile levels q_μ and q_σ is sampled from their uniform distributions using Monte Carlo Simulations (MCS); **(ii)** for each quantile-level pair, a realization pair of $\mu_{kfc}(T)$ and $\sigma_{kfc}(T)$ is obtained from the inverse cumulative lognormal distribution function; **(iii)** random realizations of k_{fc} are drawn at each temperature from the distributions defined by $\mu_{kfc}(T)$ and $\sigma_{kfc}(T)$; **(iv)** step (ii) and (iii) are repeated for each sampled quantile level. The obtained temperature-dependent distribution of k_{fc} is referred to as the "prior predictive distribution".

Figure 2 compares the obtained prior predictive distribution with the Shahraki model for siliceous concrete. Compared to the Shahraki model, the k_{fc} quantile values are closer to 1 after exposure to very low temperatures and closer to 0 at very high temperatures. This aligns with the boundary conditions specified for the model (constraints at 20°C and 1000°C). The proposed model exhibits more uncertainty between 200 and 800 °C than the Shahraki model because the Shahraki model does not consider the uncertainty on μ_{kfc} or σ_{kfc}. Also, a filtered dataset (data points with retaining time > 2 hr only) was used in their work, while all available data is used in this study, resulting in additional uncertainty in the proposed model.

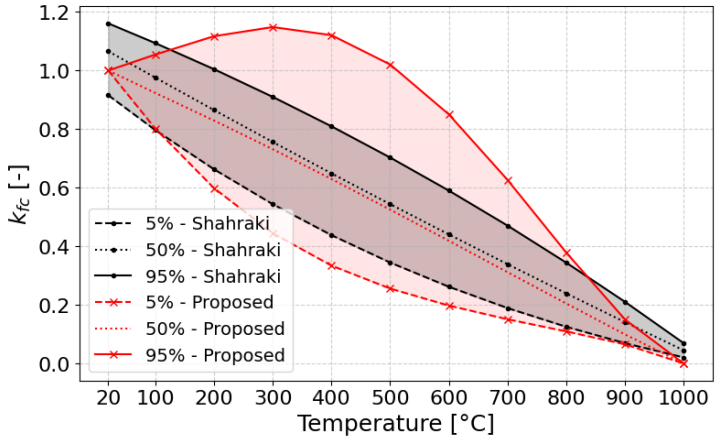


Figure 2. 5%, 50%, and 95% quantiles across T_{range} for the proposed model in comparison with the Shahraki model.

2.2. BAYESIAN MODEL UPDATING

The available knowledge on the parameters of interest $\boldsymbol{\theta}$ (here: q_μ and q_σ defined in Sec. 2.1) is represented through a prior joint probability distribution $p(\boldsymbol{\theta})$. In this paper, the two parameters of interest are assumed to be independent, with priors defined in Sec. 2.1. If an experiment is conducted and data $\boldsymbol{y}$ is observed (here: observations of k_{fc}), Bayes' theorem allows the updating of the prior distribution based on the obtained experimental outcome (Gelman et al., 2021):

$$p(\boldsymbol{\theta}|\boldsymbol{y}) = \frac{p(\boldsymbol{\theta}).\, p(\boldsymbol{y}|\boldsymbol{\theta})}{p(\boldsymbol{y})} \tag{8}$$

In this equation, $p(\boldsymbol{\theta}|\boldsymbol{y})$ is the posterior probability distribution; $p(\boldsymbol{y}|\boldsymbol{\theta})$ is the likelihood, which gives the probability of observing the data given $\boldsymbol{\theta}$; $p(\boldsymbol{y}) = \sum_{\theta} p(\boldsymbol{\theta})\, p(\boldsymbol{y}|\boldsymbol{\theta})$ is the total probability of observing the data y (also referred to as the marginal likelihood).

When measurements of residual compressive strength are obtained for a specific situation (e.g., post-fire analysis of a specific building), Bayesian analysis combines this data with the information in the prior model and enables updating prior knowledge on k_{fc}. The Markov Chain Monte Carlo (MCMC) method with the Metropolis algorithm (Gelman et al., 2021) can be adopted to solve Eq. (8) numerically and generate posterior samples for q_μ and q_σ. These samples can then be used to obtain the posterior predictive distribution of k_{fc}, following steps (i)-(iv) from Sec. 2.1.

2.3. OPTIMAL EXPERIMENTAL DESIGN APPROACH

When the goal is to inform decision-making on how to collect residual strength data (e.g., testing temperature, number of measurements), a pre-posterior Bayesian analysis can be carried out. To that end, this study implements the expected utility quantification framework by (Franchini and Van Coile, 2026) and focuses on the expected reduction of uncertainty in estimating the temperature-dependent k_{fc}.

To estimate this reduction, potential experimental observations are first sampled from the prior predictive distribution. Then, for each batch of measurements, Bayesian updating is performed to generate posterior distributions of q_μ and q_σ as outlined in Sec. 2.2. Finally, posterior predictive distributions of k_{fc} are obtained by following the steps (i)-(iv) described in Sec. 2.1, and information gain (IG) is calculated as the difference between prior and posterior predictive "entropy". Entropy is a measure of uncertainty in a random variable. EIG is the average information gain across all the simulated test batches. Thus, in pre-posterior analysis, if n denotes the number of simulated test batches, the EIG is given by:

$$EIG = \frac{1}{n}\sum_{i=1}^{n} IG_i \tag{9}$$

3. Example application

As an illustrative example, this section aims to identify the measurement temperature at which k_{fc} should be measured when the experimental campaign is limited to 3 measurements. This number of measurements aligns with the predominant sampling size reported in the literature. In this study, the 'evaluation temperature' T_e is defined as the temperature at which the k_{fc} is to be evaluated, which may differ from the temperature at which the experiments are conducted (i.e., the 'measurement temperature', T_m). First, 300 realizations of three potential experimental observations are sampled from the prior predictive

distributions (see Figure 3), resulting in an equivalent number of q_μ and q_σ realizations. Because each batch is independently drawn, adopting different pairs of q_μ and q_σ realizations, its corresponding batch-specific strength distribution differs across realizations. This variability represents the uncertainty between different test batches.

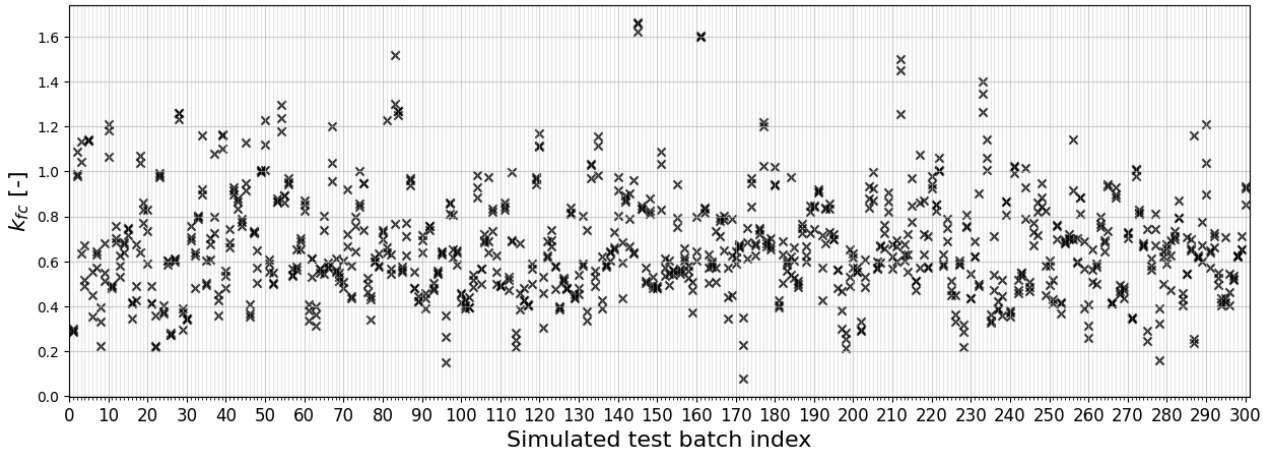
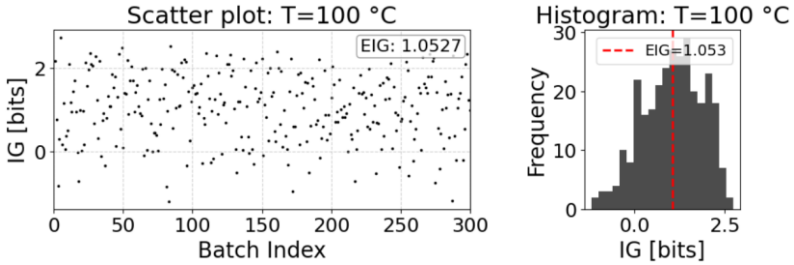
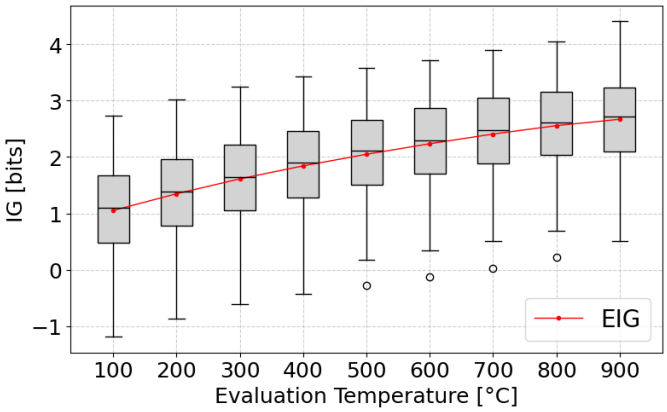


Figure 3. Example of 300 batches of simulated measurements (3 measurements at 400 °C).

For each simulated test batch, posterior distributions of q_μ and q_σ are generated by employing MCMC simulation. Depending on the convergence of the calculation, 4.5×10^5 to 6×10^5 MCMC simulation draws are generated and used to obtain posterior predictive distributions of k_{fc}. Then, IG values are calculated for each simulated test batch, and their average provides the EIG. The EIG is evaluated at each evaluation temperature $T_e \in T_{range}$. As an example, Figure 4(a) shows the pre-posterior IG and EIG values at T_e = 100 °C for 300 simulated test batches of 3 measurements at 400 °C (i.e., T_m = 400 °C). The black dots show IG values for each of the 300 batches, whereas the histogram shows the IG distribution with the mean value (red dashed line) representing the EIG. Figure 4(b) shows the boxplot indicating the mean and interquartile range of the IG across $T_e \in T_{range}$. The red dot at 100 °C corresponds to the red dashed line in Figure 4(a) and is the corresponding EIG value. EIG values at other T_e are obtained following the same procedure. The figure also indicates that EIG increases with an increase in evaluation temperature.



(a)



(b)

Figure 4. Plots for 3 measurements at 400 ℃ showing: (a) Pre-posterior information gain (IG) distributions and corresponding expected information gain (EIG); (b) Information gains (IGs) at evaluation temperatures and their interquartile range.

Figure 5 presents the EIG from three measurements as a function of the selected measurement temperature. Using this plot, a user can select an evaluation temperature and identify the measuring temperature where EIG is the highest. For example, if the estimation of k_{fc} is required at 500 ℃, from Figure 5 it can be concluded that measuring at 900 ℃ results in the highest EIG (approx. 2.37 bits). EIG values obtained for measurements at 600–900 °C are very similar for evaluation temperatures up to 400 ℃, indicating that testing within this temperature range provides comparable information gain. However, for evaluations in the 500–900 ℃ range, the marginal EIG resulting from testing at higher temperatures is notable. Measuring at 100-300 ℃ results in low EIG for any evaluation temperature. Assessing engineers can use this plot to optimize experimental data collection for the considered site-specific concrete structure.

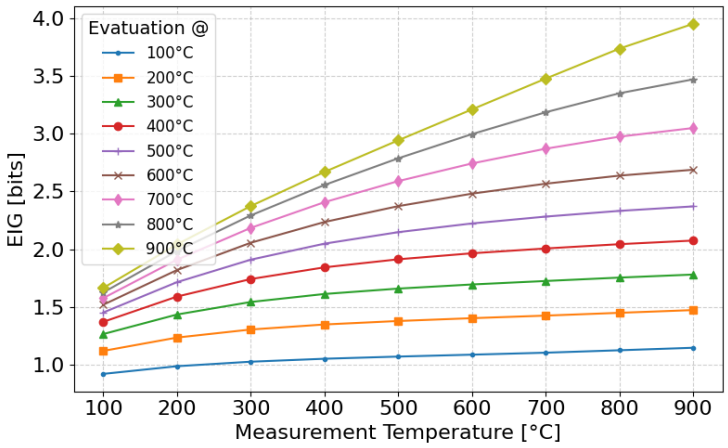


Figure 5. Expected information gain (EIG) across the selected evaluation and measurement temperatures for 3 measurements.

4. Conclusion

The main contributions and findings of this paper can be summarized as follows:

1. A Bayesian model is developed to characterize the temperature-dependent residual compressive strength retention factor for concrete k_{fc}. Unlike existing models, the proposed one captures the variability within a single mix.
2. Capturing the variability within a single mix is beneficial for post-fire assessment, where the goal is to assess a specific structure. The Bayesian formulation of the model allows the incorporation of site-specific experimental data when this becomes available.
3. The model is calibrated using a comprehensive dataset of 248 concrete mixes. To ensure physical consistency, the model enforces a residual retention factor of 1.0 at 20 °C and 0 at 1000°C. These fixed boundary conditions simplify the model specification and allow the variability at 20 °C to be treated independently from the temperature-dependent retention behavior.
4. A pre-posterior analysis is used to identify the most informative experimental protocol by using expected information gain (EIG) as the utility quantification metric. The analysis reveals that measurements within the 600–900 °C range yield significantly higher marginal information gain, highlighting more effective measurement temperatures for model updating and uncertainty reduction.

Acknowledgements

Funded by the European Union (ERC, AFireTest, 101075556). Views and opinions expressed are, however, those of the author(s) only and do not necessarily reflect those of the European Union or the European Research Council Executive Agency. Neither the European Union nor the granting authority can be held responsible for them.

The authors gratefully acknowledge the support of prof. Negar Elhami-Khorasani in providing access to the dataset adopted in (Shahraki et al. 2023).

References

Al-Jabri, Khalifa S., Muhammad Bilal Waris, and Abdullah H. Al-Saidy. 2016. “Effect of Aggregate and Water to Cement Ratio on Concrete Properties at Elevated Temperature.” *Fire and Materials* 40 (7): 913–25. https://doi.org/10.1002/fam.2351.

Chen, G. M., Y. H. He, H. Yang, J. F. Chen, and Y. C. Guo. 2014. “Compressive Behavior of Steel Fiber Reinforced Recycled Aggregate Concrete after Exposure to Elevated Temperatures.” *Construction and Building Materials* 71 (November): 1–15. https://doi.org/10.1016/j.conbuildmat.2014.08.012.

Franchini, Andrea, and Ruben Van Coile. 2026. “Quantifying the Expected Utility of Fire Tests and Experiments before Execution.” *Fire Safety Journal* 159 (January): 104538. https://doi.org/10.1016/j.firesaf.2025.104538.

Gelman, Andrew, John B. Carlin, Hal S. Stern, David B. Dunson, Aki Vehtari, and Donald B. Rubin. 2021. *Bayesian Data Analysis (BDA)*. 3rd ed. Electronic edition. https://sites.stat.columbia.edu/gelman/book/BDA3.pdf.

Gernay, Thomas, Venkatesh Kodur, Mohannad Z. Naser, Reza Imani, and Luke Bisby. 2021. “Concrete Structures.” In *International Handbook of Structural Fire Engineering*, edited by Kevin LaMalva and Danny Hopkin. Springer International Publishing. https://doi.org/10.1007/978-3-030-77123-2_6.

Holický, Milan, and Miroslav Sýkora. 2010. “Stochastic Models in Analysis of Structural Reliability.” *Proceedings of the International Symposium on Stochastic Models in Reliability Engineering, Life Sciences and Operation Management* (Beer Sheva, Israel).

Qureshi, Ramla, Shuna Ni, Negar Elhami Khorasani, Ruben Van Coile, Danny Hopkin, and Thomas Gernay. 2020. “Probabilistic Models for Temperature-Dependent Strength of Steel and Concrete.” *Journal of Structural Engineering* 146 (6): 04020102. https://doi.org/10.1061/(ASCE)ST.1943-541X.0002621.

Shahraki, Marzieh, Nan Hua, Negar Elhami-Khorasani, Anthony Tessari, and Maria Garlock. 2023. “Residual Compressive Strength of Concrete after Exposure to High Temperatures: A Review and Probabilistic Models.” *Fire Safety Journal* 135 (February): 103698. https://doi.org/10.1016/j.firesaf.2022.103698.

Optimal-Transport Flow Matching for Stochastic Model Updating: A Comparison with Transitional MCMC-based Bayesian Updating

Tairan Wang and Sifeng Bi
Department of Aeronautics and Astronautics Engineering, University of Southampton, Southampton, SO16 7QF, United Kingdom, tairan.wang@soton.ac.uk, sifeng.bi@soton.ac.uk

Abstract: Deep generative models have attracted considerable attention as inference engines for stochastic model updating. Among these deep generative models, conditional flow matching offers a particularly efficient formulation, in which a continuous transport map from a latent distribution to the posterior is learned by regression against optimal-transport probability paths, avoiding both the invertibility constraints of normalising flows and the iterative denoising of diffusion models. However, its performance in engineering model updating has not been examined against an established baseline such as the Bayesian updating framework under controlled conditions. In this work, conditional flow matching is therefore assessed against the Bayesian model updating approach with transitional Markov chain Monte Carlo, in which the Bhattacharyya distance provides the approximate likelihood for the Bayesian approach. The two methods are assessed with respect to posterior fidelity, evaluated by statistical distances against the known ground truth and computational expenditure in model evaluations, with the offline training budget reported separately from the inference cost of each subsequent conditioning. A 3-DOF spring–mass system with uncertain stiffness parameters serves as the benchmark. Since the calibrated posterior constitutes the input description upon which subsequent reliability assessment depends, the accuracy and the marginal cost of the updating step both bear directly on reliability computations. In addition, the amortised nature of the learned transport map is discussed in this work, as it permits the posterior to be re-evaluated under new observations at negligible cost, which is a property of practical relevance to reliability assessment under sequentially acquired monitoring data.

Keywords: Stochastic model updating, Flow matching, Bayesian inference, Uncertainty quantification.

1. Introduction

Numerical models of engineering structures invariably contain parameters that cannot be determined directly from design information, and whose values should instead be inferred from measured responses. In practice, these parameters are not merely unknown but genuinely variable. Manufacturing tolerances, material scatter and assembly conditions introduce aleatory variability across nominally identical specimens, while limited and imprecise observations leave the description of that variability itself epistemically uncertain. Stochastic model updating addresses this issue by treating the parameters as random variables and inferring the parameters of their distributions, rather than single deterministic values (Mares et al., 2006). The resulting distributional description is not an end in itself; it constitutes the input specification upon which any subsequent reliability computation is founded, so that both the fidelity and the cost of the updating step propagate directly into reliability practice (Sankararaman and Mahadevan, 2015).

© 2026 by the author(s). This work is licensed under the Creative Commons Attribution 4.0 International License (CC BY 4.0), which permits unrestricted use, distribution, and reproduction in any medium, provided the original author and source are credited.

The Bayesian model updating framework is recognised as the standard solution for the stochastic model updating problem. However, within the Bayesian formulation, the difficulty is that an explicit likelihood is rarely available (Beck and Katafygiotis, 1998, Bi et al., 2023). When the observations take the form of a scattered sample of responses rather than a single measurement, the comparison to be made is between two distributions, and the conventional geometric distance between two points is no longer appropriate. Approximate Bayesian computation circumvents this by replacing the likelihood with a kernel of a statistical distance between simulated and observed response sets. Among the candidate distances, the Bhattacharyya distance has been widely adopted in this context, since it measures the overlap of the two distributions across the full joint response space and thereby retains information on correlation that marginal comparisons discard (Bi et al., 2019a, Bi et al., 2019b, Kitahara et al., 2022). Sampling from the resulting posterior is most commonly performed by transitional Markov chain Monte Carlo (Ching and Chen, 2007), which traverses a sequence of tempered intermediate distributions and is robust to the flat and multimodal surfaces that distance-based likelihoods frequently exhibit. However, this cost cannot be amortised across datasets, because the tempering path is constructed for one specific set of observations and retains no reusable structure, each new measurement set requires the procedure to be executed in full, and the total computational expenditure therefore scales linearly with the number of updating instances.

Deep generative models redistribute this cost from inference to training. Rather than sampling a posterior that is specified implicitly, a conditional generative model is trained on simulated parameter–response pairs to represent the mapping from observations to posterior directly, and each subsequent update is obtained by integrating the learned generative model, which requires only inexpensive network evaluations and no further calls to the forward model. This is the perspective of simulation-based inference and neural posterior estimation, whose defining feature is amortisation, where the training cost is incurred only once, and after which any new observation is processed at negligible marginal cost (Papamakarios and Murray, 2016, Cranmer et al., 2020). Conditional normalising flows provide exact density amortised inference but require invertible architectures and tractable Jacobians, which constrain their expressivity (Papamakarios et al., 2021, Wang et al., 2025). Conditional denoising diffusion models remove these constraints and generate high-quality posteriors, but at the cost of integrating a reverse-time stochastic process over discrete steps (Ho et al., 2020, Song et al., 2020, Wang and Bi, 2026). Flow matching has more recently been proposed as a formulation that avoids the principal drawbacks of each: a continuous vector field transporting a reference distribution to the target is learned by regression against a prescribed conditional probability path (Lipman et al., 2022), so that training requires neither the invertible architectures and tractable Jacobians of normalising flows nor the long iterative denoising trajectories of diffusion models. When the probability path is chosen as the displacement interpolation between the coupled endpoints, the induced trajectories are close to straight, and accurate samples may be generated with a small number of integration steps (Liu et al., 2022, Tong et al., 2023).

Despite this progress, the relative merits of generative and sampling-based inference for stochastic model updating remain difficult to assess, as the two families have rarely been examined under comparable conditions. The present work addresses this gap by examining optimal-transport conditional flow matching against transitional Markov chain Monte Carlo on a common benchmark, in which the Bhattacharyya distance provides the approximate likelihood and the same distance is subsequently used as a common metric to quantify the posterior-predictive performance. The optimal-transport conditional flow matching is formulated for stochastic model updating in second-order form, so that the means and standard deviations of the uncertain parameters are calibrated jointly. The two methods are then assessed on equal terms with respect to posterior fidelity, measured against the known ground-truth uncertainty model and by cross-comparison of the two

posteriors, and with respect to computational expenditure, reported in both model evaluations and time consumption. The calibration performance is further quantified in the term of response prediction.

The remainder of the paper is organised as follows. Section 2 sets out the stochastic model updating problem and its Bayesian solution, comprising the Bhattacharyya-distance approximate likelihood and the transitional Markov chain Monte Carlo sampler. Section 3 develops the optimal-transport conditional flow matching framework, covering the conditional probability path, the training objective, and the resulting amortised updating procedure. Section 4 applies both methods to a three-degree-of-freedom spring–mass benchmark and compares them in terms of posterior fidelity and computational cost. Section 5 concludes the paper and outlines directions for future work.

2. Stochastic model updating and the Bayesian framework

2.1 Bayesian model updating problem

A physical system is represented by a numerical model $\mathbf{y}_{\text{sim}} = \mathcal{M}(\mathbf{x})$, in which $\mathbf{x} \in \mathbb{R}^{n_x}$ collects the physical input parameters and $\boldsymbol{y}_{\text{sim}} \in \mathbb{R}^{n_y}$ the output features. Under the multilevel formulation adopted here, the input parameters are aleatory and are governed entirely by a vector of hyperparameters $\boldsymbol{\theta}$ comprising the statistical moments of their assumed distribution family, i.e., $\mathbf{x} \sim p(\mathbf{x}|\boldsymbol{\theta})$,. The hyperparameters possess distinct but unknown values and thus carry the epistemic uncertainty of the problem, and they constitute the quantity to be calibrated. The observations form a sample set $\mathbf{Y_{obs}} \in \mathbb{R}^{N_{\text{obs}} \times n_y}$ rather than a single measurement, and the updating problem is to infer $\boldsymbol{\theta}$ such that the simulated feature set $\mathbf{Y_{sim}}(\boldsymbol{\theta}) \in \mathbb{R}^{N_{\text{sim}} \times n_y}$ reproduces the $\mathbf{Y_{obs}}$ in distribution. Following Bayes' theorem,

$$p(\boldsymbol{\theta}|\mathbf{Y_{obs}}) \propto P_L(\mathbf{Y_{obs}}|\boldsymbol{\theta}) p(\boldsymbol{\theta}) \tag{1}$$

with $p(\boldsymbol{\theta})$ a prior over the admissible intervals, $P_L(\mathbf{Y_{obs}}|\boldsymbol{\theta})$ refers to the likelihood, and $p(\boldsymbol{\theta}|\mathbf{Y_{obs}})$ is the posterior. Two routes to this posterior are contrasted in this work, including the classical Bayesian route, in which an approximate likelihood is constructed and sampled with the transitional Markov chain Monte Carlo (TMCMC), and the flow matching route developed in Section 3, in which the mapping from observations to posterior is learned directly.

2.2 Bhattacharyya distance-based approximate likelihood and transitional Markov chain Monte Carlo

Since the observations are scattered, the exact likelihood requires a density estimate for every candidate $\boldsymbol{\theta}$ and is prohibitive. Approximate Bayesian Computation (ABC) replaces it with a kernel of a statistical distance, for instance, the Bhattacharyya distance as illustrated in Eq. (2),

$$P_L(\mathbf{Y_{obs}}|\boldsymbol{\theta}) \propto \exp\left\{-\frac{d_{\text{BD}}^2\left(\mathbf{Y_{obs}}, \mathbf{Y_{sim}}(\boldsymbol{\theta})\right)}{\varepsilon^2}\right\} \tag{2}$$

in which ε is the width factor controlling the concentration of the posterior. The Bhattacharyya distance is adopted as the metric $d_{\text{BD}}(\cdot)$, evaluated by the binning algorithm in (Bi et al., 2019a, Bi et al., 2021) over a partition of the joint feature space common to both sample sets. It has been demonstrated that this metric measures the overlap of the two distributions and is therefore sensitive to dispersion and dependence as well as to location, whereas the Euclidean distance responds only to the centre of mass. An equally relevant

limitation is that the distance saturates when the two sample sets cease to overlap, so the surface is uninformative far from the solution.

Sampling from the resulting posterior is performed by transitional Markov chain Monte Carlo (TMCMC), which traverses a sequence of tempered intermediate distributions. The exponent β_j is increased adaptively so that the coefficient of variation of the plausibility weights remains bounded, with resampling and Metropolis–Hastings propagation at each stage. The tempering is what renders the flat distance surface tractable.

$$p_j(\boldsymbol{\theta}) \propto P_L(\mathbf{Y_{obs}}|\boldsymbol{\theta})^{\beta_j} p(\boldsymbol{\theta}), \qquad 0 = \beta_0 < \cdots < \beta_m = 1 \tag{3}$$

It is noted that each likelihood call requires N_{sim} evaluations of $\mathcal{M}(\cdot)$, so the cost of a single update is the product of the population size, the number of proposals per chain, and the number of tempering stages. And the tempering sequence is constructed for one dataset alone, which means a new set of observations requires the whole path to be traversed again, so the total cost grows in proportion to the number of updates performed.

3. Optimal-transport flow matching for stochastic model updating

3.1 Flow matching

The flow matching route bypasses the likelihood evaluation entirely. Instead of evaluating how well a candidate $\boldsymbol{\theta}$ reproduces the observations, a transformation is sought that carries a simple latent distribution onto the posterior itself, conditioned on the observed data. This is the principle underlying the flow-based approaches previously applied to model updating, where a conditional invertible network learns a bijection between the parameter space and a latent Gaussian (Wang et al., 2025).

Flow matching realises the same principle without requiring bijectivity. Rather than composing invertible layers with tractable Jacobians, a continuous-time velocity field is learned, and the transformation is obtained by integrating it. Let $\boldsymbol{\theta_0} \sim \mathcal{N}(0, \mathbf{I})$ denote a reference sample and $\boldsymbol{\theta_1}$ a sample of the target. A field $v_\phi(\boldsymbol{\theta_t}, t, \boldsymbol{s})$, conditioned on a summary $\boldsymbol{s}$ of the observations, defines the flow as in Eq. (4). Integrating this equation from $t = 0$ to $t = 1$ carries a sample drawn from the base distribution $\boldsymbol{\theta_0}$ to a sample of the posterior $p(\boldsymbol{\theta}|\boldsymbol{s})$. Neither an architectural constraint nor a Jacobian determinant is involved, and the change-of-variable rule is not evaluated at any point.

$$\frac{\mathrm{d}\boldsymbol{\theta_t}}{\mathrm{d}t} = v_\phi(\boldsymbol{\theta_t}, t, \boldsymbol{s}), \qquad t \in [0,1] \tag{4}$$

3.2 Conditional probability paths and training objective

Flow matching constructs the field by regression against a prescribed conditional probability path, which is a family of distributions interpolating, for a single target sample, between the reference and that sample. The conditional probability path adopted here is expressed as,

$$p_t(\boldsymbol{\theta}|\boldsymbol{\theta_1}) = \mathcal{N}(\boldsymbol{\theta}|t\boldsymbol{\theta_1}, (1-t)^2\mathbf{I}), \qquad t \in [0,1] \tag{5}$$

whose mean and standard deviation both vary linearly in t, so that p_0 is the standard Gaussian reference ($p_0 \sim \mathcal{N}(0, \mathbf{I})$) and p_1 concentrates on $\boldsymbol{\theta_1}$. This particular choice is the optimal-transport displacement interpolation between the two endpoints. Among all paths connecting them, it is the one along which the samples move in

straight lines at constant speed, which is what makes it the optimal-transport path. Samples of the path and the velocity generating it take the elementary form

$$\boldsymbol{\theta_t} = (1-t)\boldsymbol{\theta_0} + t\boldsymbol{\theta_1}, \qquad \mathbf{u_t}(\boldsymbol{\theta_t}|\boldsymbol{\theta_1}) = \boldsymbol{\theta_1} - \boldsymbol{\theta_0} \tag{6}$$

with $\boldsymbol{\theta_0} \sim \mathcal{N}(\mathbf{0}, \mathbf{I})$. The conditional velocity is constant in t, in contrast with the diffusion paths of denoising models, whose trajectories curve and whose velocity varies sharply near the endpoints.

The marginal field of interest is recovered by regressing against these conditional velocities. The parameters follow from the expectation being estimated by minibatch sampling over the training set and over t and $\boldsymbol{\theta_0}$, denoted in Eq. (7).

$$\mathcal{L}(\phi) = \mathbb{E}_{t\sim\mathcal{U}(0,1),(\boldsymbol{\theta_1},\boldsymbol{s}),\boldsymbol{\theta_0}\sim\mathcal{N}(\mathbf{0},\mathbf{I})}\left\|v_\phi(\boldsymbol{\theta_t}, t, \boldsymbol{s}) - (\boldsymbol{\theta_1} - \boldsymbol{\theta_0})\right\|^2 \tag{7}$$

Although the regression targets are defined conditionally on individual samples, the minimiser of this objective is the marginal field transporting the reference distribution onto the posterior, and the conditional construction serves only to render the target computable.

The objective is simulation-free that no trajectory is integrated at training time, and the loss is an ordinary least-squares regression, in contrast with the maximum-likelihood objective of invertible architectures, which requires the Jacobian log-determinant at every layer. And because the conditional paths are straight and traversed at constant speed, the learned marginal field is close to straight wherever the paths do not intersect, so that accurate samples are obtained by explicit integration with a modest number of steps.

3.3 Flow matching-based model updating framework

The proposed flow matching-based framework casts stochastic model updating as an amortised, simulation-based inference task. Rather than repeatedly evaluating a likelihood to explore the parameter space for every new set of measurements, a single conditional generative network is trained once on simulated data and can thereafter infer the updated parameters of any new dataset almost instantaneously. The framework comprises three stages, including the generation of training data, the training of the network, and the posterior inference.

In the first stage, the training data is generated entirely by simulation. Because the updating is second order, the parameters to be calibrated are the means and standard deviations of the uncertain parameters. Each training instance is formed by drawing one hyperparameter vector $\boldsymbol{\theta}$ from the prior distribution and $\boldsymbol{\theta}$ defines a distribution of the physical parameters $p(\mathbf{x}|\boldsymbol{\theta})$, from which a population of samples is drawn and propagated through the numerical model to yield the corresponding responses. The resulting responses are then condensed into a compact feature vector $\boldsymbol{s}$, their means, standard deviations and correlations, which forms the input paired with the hyperparameters $\boldsymbol{\theta}$ to form one training sample $(\boldsymbol{\theta}, \boldsymbol{s})$. Repeating this for many draws yields the training database, which is standardised before training.

In the second stage, the network is trained to reproduce the relationship between a population of responses and the hyperparameter vector $\boldsymbol{\theta}$ that generated it. The network gradually transforms samples drawn from a simple standard distribution into descriptor samples consistent with a given response feature, with that feature supplied as an additional input throughout the transformation. Since the response feature enters as a conditioning input rather than being fixed, one trained network applies to every possible dataset, and the cost of running the numerical model is incurred only once, during the construction of the training database.

In the third stage, the trained network performs the actual updating. For a given set of measured responses, the corresponding feature vector is formed and supplied to the network, which transforms a large number of samples from the base distribution into samples of the updated hyperparameter vector $\boldsymbol{\theta}$. Collecting these samples reconstructs the full posterior distribution, from which the updated means, the dispersions and the

joint dependence between parameters are obtained. As the numerical model is not called again at this stage, the updating of any new measurement is completed in a single, near-instantaneous pass of the trained network.

4. Case study: 3 DOF spring-mass system benchmark

4.1 Problem description

The benchmark is the classical three-degree-of-freedom spring–mass system shown in Figure 1. Three masses are connected to one another and to ground by six springs. The mass and stiffness matrices are illustrated as in Eq. (8) and Eq. (9).

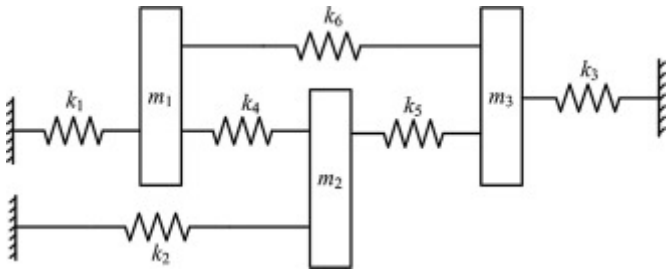


Figure 1. The 3 DOF spring-mass system.

$$\mathbf{M} = \mathrm{diag}(m_1, m_2, m_3) \tag{8}$$

and

$$\mathbf{K} = \begin{bmatrix} k_1 + k_4 + k_6 & -k_4 & -k_6 \\ -k_4 & k_2 + k_4 + k_5 & -k_5 \\ -k_6 & -k_5 & k_3 + k_5 + k_6 \end{bmatrix} \tag{9}$$

In the system, the masses and the three coupling stiffnesses are treated as known constants, $m_1 = 0.7$kg, $m_2 = 0.5$kg, $m_3 = 0.3$kg and $k_4 = k_5 = k_6 = 5.0$N/m, and require no updating. The remaining stiffnesses k_1, k_2, and k_3 are the uncertain input parameters, $\mathbf{x} = [k_1, k_2, k_3]^T$.

The output features are the three natural frequencies, obtained from the eigenproblem and collected in ascending order as $\mathbf{y} = [\omega_1, \omega_2, \omega_3]^T$.

$$|(\mathbf{K} - \omega_r^2 \mathbf{M})| = 0, \qquad r = 1,2,3 \tag{10}$$

The simulator $\mathcal{M}(\cdot)$ is thus a single eigensolution, and one model evaluation is defined throughout as one such solution for one realisation of $\mathbf{x}$. Its low cost is what allows both methods to be run at large simulation budgets without training a surrogate. Computational expenditure is accordingly reported primarily in the number of model evaluations and the time consumption.

4.2 Uncertainty characterisation and synthetic observations

The three uncertain stiffnesses are modelled as independent Gaussian random variables whose means and standard deviations are both unknown, so that the system involves aleatory and epistemic uncertainty. The

hyperparameter vector to be calibrated is accordingly six-dimensional, as shown in Eq. (11), with uniform priors $\mu_i \in [3.0,7.0]$ and $\sigma_i \in [0.0, 0.5], i = 1,2,3$.

$$\boldsymbol{\theta} = [\mu_1, \mu_2, \mu_3, \sigma_1, \sigma_2, \sigma_3]^T \tag{11}$$

The target values are $\mu_1 = 4.0$, $\mu_2 = 5.0$, $\mu_3 = 6.0$ and $\sigma_1 = 0.3$, $\sigma_2 = 0.1$, $\sigma_3 = 0.2$, as summarised in Table I.

Table I. Uncertainty characterisation with prior distributions and true target values.

Parameter	**Uncertainty characteristic**	**Target values**
k_1	Gaussian, $\mu_1 \in [3.0,7.0], \sigma_1 \in [0.0,0.5]$	$\mu_1 = 4.0, \sigma_1 = 0.3$
k_2	Gaussian, $\mu_2 \in [3.0,7.0], \sigma_2 \in [0.0,0.5]$	$\mu_2 = 5.0, \sigma_2 = 0.1$
k_3	Gaussian, $\mu_3 \in [3.0,7.0], \sigma_3 \in [0.0,0.5]$	$\mu_3 = 6.0, \sigma_3 = 0.2$
$k_4 - k_6$ $m_1 - m_3$	Constants with no updating needed.	

Updating the standard deviations alongside the means is what distinguishes stochastic from deterministic calibration, since the objective is no longer a single set of parameter values reproducing the observed value, but a set of distributions reproducing the observed scatter. It also makes the choice of likelihood metric consequential in Bayesian updating that a distance responding only to the centre of mass of the sample sets leaves the standard deviations essentially at their priors, whereas the Bhattacharyya distance is sensitive to the dispersion and the dependence of the features and can therefore identify all six hyperparameters within a single updating stage.

The observations are synthetic with a set of $N_{\text{obs}} = 100$ realisations of $\mathbf{x}$ drawn from the target distributions and propagated through $\mathcal{M}(\cdot)$, and each simulated frequency is then perturbed to represent experimental error, independently for every realisation and every mode, with $\delta = 0.1\%$.

$$\omega_r^{\text{obs}} = \omega_r\,(1 + \eta_r), \qquad \eta_r \sim \mathcal{N}(0, \delta^2) \tag{12}$$

The magnitude is chosen relative to the physical scatter of the responses that under the target input distributions the three frequencies exhibit coefficients of variation of approximately 1.5%, 0.3% and 0.5%, so that at 0.1% the measurement error is a visible but minority contribution to the total dispersion. This margin matters here since the standard deviations are inferred from precisely that dispersion and would be biased upwards were the perturbation comparable to it. The resulting sample set $\mathbf{Y_{obs}} \in \mathbb{R}^{100\times 3}$ is generated once and supplied unchanged to both methods, so that any difference in the inferred posteriors is attributable to the inference engine alone. The perturbation is applied to every synthetic dataset generated for training the velocity field, so that the vectors $\boldsymbol{s}$ seen in training and at inference arise from the same process. It is not applied within the sampling route, whose simulated sets are produced by the model alone, and the Bhattacharyya likelihood compares candidates against one another rather than in absolute terms, and a small unmodelled error component raises the attainable minimum of the distance without displacing its location.

4.3 Model updating implementations and results comparisons

The two frameworks are applied to the same second-order updating problem of the three-degree-of-freedom system, in which the stiffnesses are treated as independent Gaussian random variables and the six hyperparameters, the means and standard deviations $[\mu_1, \mu_2, \mu_3, \sigma_1, \sigma_2, \sigma_3]$, are to be calibrated. The synthetic

experimental data consists of $N_{\mathrm{obs}} = 100$ frequency observations generated from the target distribution $\mathcal{N}\left([4,5,6], \mathrm{diag}([0.3,0.1,0.2]^2)\right)$ and they are shared across the two methods.

For the Bayesian model updating framework, the six distribution hyperparameters are updated in a single stage by comparing the simulated and experimental frequency sample sets directly with the Bhattacharyya distance. The Bhattacharyya distance is evaluated by the binning algorithm with $n_{\mathrm{bin}} = 3$ per dimension over the joint (three-mode) frequency space, and $N_{\mathrm{sim}} = 1000$ realisations are propagated per likelihood evalutaion. The width factor is set to $\varepsilon = 0.01$. Transitional MCMC is run with a population of $N = 1000$, a proposal scaling of $\beta = 0.2$, and $n_{MH} = 13$ proposals (burn-in of 10 and thinning of 3) per chain per stage, with the tempering schedule advanced adaptively until the tempering parameter reaches unity.

For the flow matching method, the feature set of each dataset is reduced to the vector $\boldsymbol{s} \in R^9$ of the per-mode sample means, standard deviations and cross-correlations of the frequencies, standardised using the training-set statistics. The training set comprises $N_{\mathrm{train}} = 10^4$ pairs, corresponding to $N_{\mathrm{train}} \times N_{obs} = 10^6$ offline model evaluations, with $N_{\mathrm{obs}} = 100$ realisations propagated per pair. The velocity field is represented by a fully connected network of three hidden layers of 256 units with SiLU activations, taking $\boldsymbol{\theta_t}$, a sinusoidal embedding of t, and $\boldsymbol{s}$ as its input. Training uses the Adam optimiser with an initial learning rate of 2×10^{-4} under cosine decay and a batch size of 512, run for 600 epochs with the pairs split 80/10/10 into training, validation and test sets. At inference the flow is integrated by the explicit fourth-order Runge–Kutta scheme with 100 uniform steps, and 1000 posterior samples are drawn per conditioning.

Conditioned on the shared observation data, the two methods return closely consistent posteriors, as shown in Figure 2 and summarised in Table II. Transitional MCMC recovers posterior means of [3.98,5.01,5.98] for the stiffness means and [0.321,0.094,0.200] for the standard deviations, while flow matching recovers [3.96,5.03,5.99] and [0.312,0.092,0.203], respectively. The two solutions agree to within their posterior scatter and both enclose the ground truth. It is worth noting that both posteriors are displaced from the truth in the same direction, reflecting the empirical spread of the particular 100-sample record rather than a deficiency of either estimator, and the agreement of two independent methods on the same data is itself a consistency check. The flow-matching marginals are marginally broader, consistent with its reduction of each dataset to a nine-dimensional summary, whereas the Bhattacharyya likelihood exploits the full joint histogram of the frequency set. Additionally, Figure 3 shows that the per-stiffness joint posteriors from flow matching and TMCMC overlap closely and enclose the true values, confirming the two methods are in close agreement.

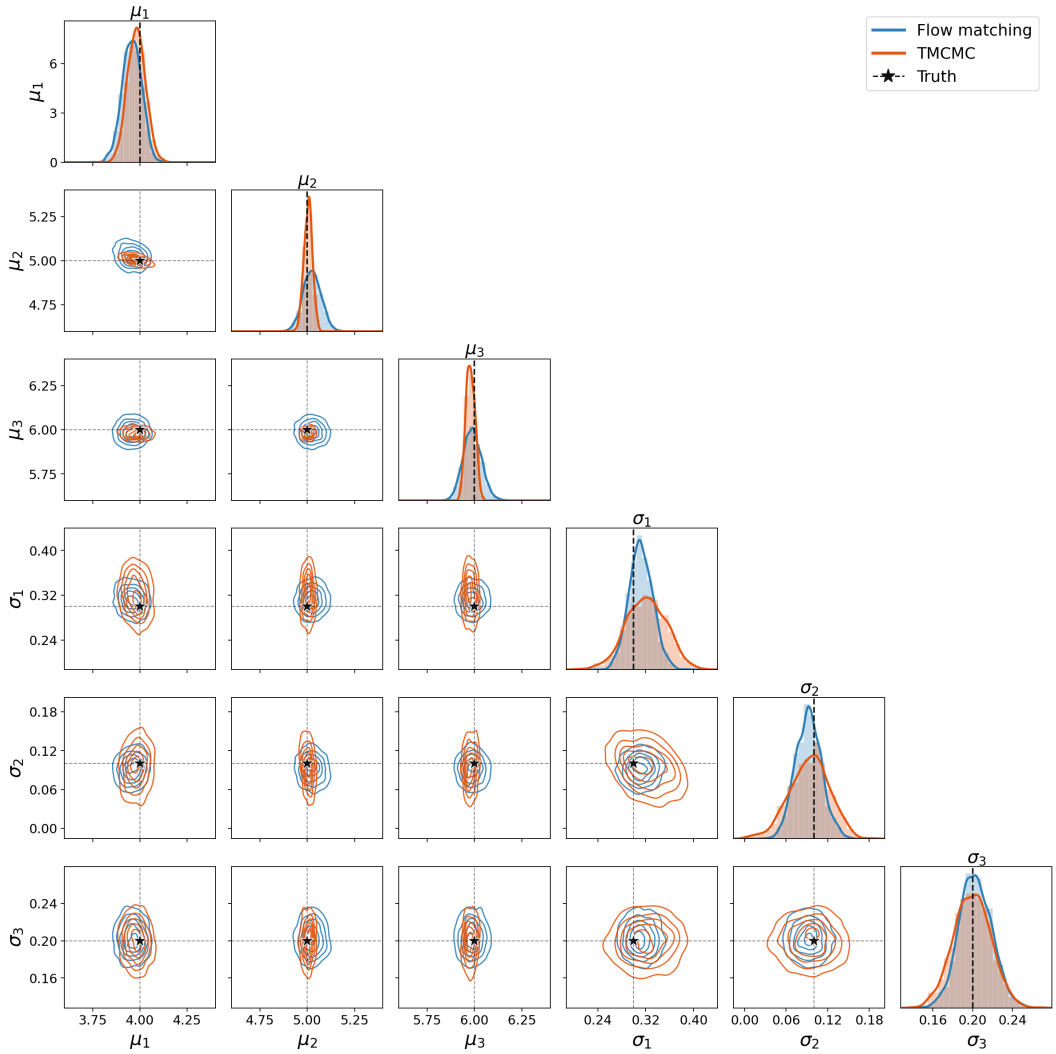


Figure 2. Posterior distributions over the six hyperparameters in comparison to the truth values.

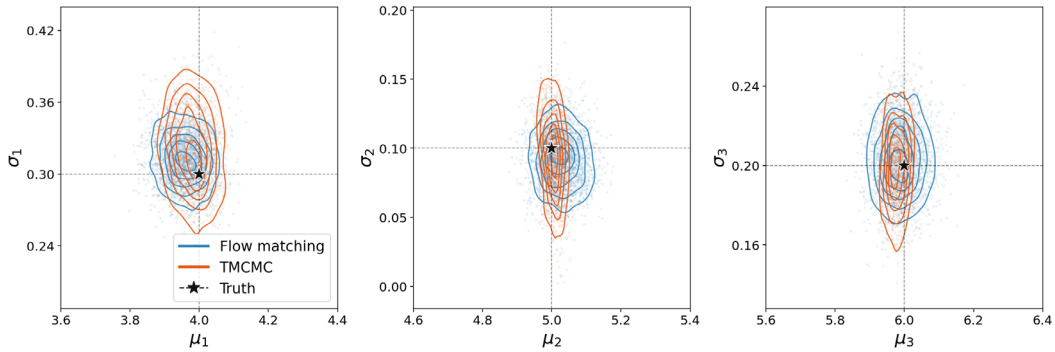


Figure 3. Joint posterior of the mean and standard deviation of each stiffness.

Table II. Calibrated uncertain parameters and computational cost comparison.		
Quantity	**Flow matching**	**Bayesian (with TMCMC)**
$[\mu_1, \mu_2, \mu_3]$	$[3.96, 5.03, 5.99]$	$[3.98, 5.01, 5.98]$
$[\sigma_1, \sigma_2, \sigma_3]$	[0.312,0.092,0.203]	$[0.321, 0.094, 0.200]$
Forward-model evaluations	10^6 (offline, one-off)	5.51×10^8 (per dataset)
Evaluations per new dataset	0	5.51×10^8
Time consumption	22.6s (Data generation: 0.77s; Training: 21.7s; Posterior inference: 0.17s)	140.5s

The essential difference between the two approaches is computational. The Bayesian scheme requires 5.51×10^8 forward-model evaluations and 140.5s of wall-clock time for this single dataset with a size of 100, and the entire procedure must be repeated for every new set of measurements. Flow matching instead spends its whole simulation budget of 10^6 evaluations once, during data generation (0.77 s). The network is then trained in a further 21.7s. For any observation dataset with the same size, it is updated in a single amortised pass of 0.17s without any further model evaluation and retraining, indicating a reduction of more than two orders of magnitude in both model calls and inference time.

To further validate the calibrated parameters at the observation level, each method's second-order posterior is propagated into a posterior-predictive response distribution. For every posterior sample of the hyperparameters, stiffness vectors are drawn from $\mathcal{N}\left(\mu, \mathrm{diag}(\sigma^2)\right)$ and propagated through the model, and the resulting frequencies are collected. This construction marginalises over the entire second-order posterior, thereby folding in the hyper-parameter uncertainty, rather than fixing a point estimate such as the posterior mean or MAP. The predictive distributions are compared with the 100 groups of synthetic observations (as shown in Figure 4). The Bhattacharyya distance is used for quantification of the discrepancies between the predictive distributions from the two methods and the target distribution with the results summarised in Table III. Both predictive distributions closely reproduce the observations, and the posterior-predictive Bhattacharyya distances to the target are 0.004 for flow matching and 0.003 for TMCMC, confirming that the recovered stiffness distributions are statistically indistinguishable from the target.

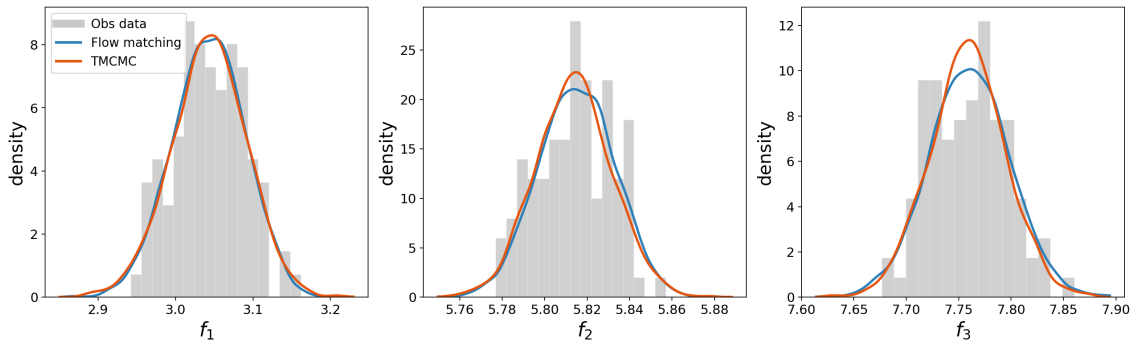


Figure 4. Posterior-predictive validation at the response level.

Table III. Posterior-predictive Bhattacharyya distance to the target observations.		
Metric	**Flow matching**	**Bayesian (with TMCMC)**
Bhattacharyya distance	0.004	0.003

5. Conclusion

This work has presented a controlled comparison between optimal-transport conditional flow matching and transitional Markov chain Monte Carlo for stochastic model updating, benchmarked on a three-degree-of-freedom spring–mass case study. The updating was posed in second-order form, in which the three stiffness means and standard deviations are calibrated jointly from a single shared set of frequency observations, so that any difference in the inferred posteriors is attributable to the inference engine alone.

Conditioned on identical data, the two methods returned closely consistent posteriors, where both recovered all six hyperparameters accurately and enclosed the ground truth, and the posterior-predictive response distributions reproduced the observed frequencies with Bhattacharyya distances to the target of 0.004 and 0.003 respectively. The flow-matching marginals were slightly broader, reflecting its reduction of each dataset to a fixed nine-dimensional summary, whereas the Bhattacharyya likelihood exploits the full joint response histogram.

The critical distinction lies in computational cost. The Bayesian framework required 5.5×10^{8} forward-model evaluations and over 140s of wall-clock time for a single dataset, and this cost recurs in full for every new set of measurements. Flow matching instead spent a one-off offline budget of 10^{6} evaluations and about 22 s of training, after which each new dataset was updated in a single amortised pass of 0.17 s with no further model calls, which is a reduction of more than two orders of magnitude in both model evaluations and inference time. The negligible cost of each subsequent update makes the framework especially suitable to time-sensitive or online tasks such as structural health monitoring, in which inference must be repeated as new data arrive and propagated into reliability assessment over the life of the structure.

Several extensions follow naturally from this study. The fixed summary statistic used here could be replaced by a conditioning network trained jointly with the velocity field, so that the informative features of the response are learned rather than prescribed and higher-order dependence is retained. The controlled comparison could then be broadened to higher-dimensional and experimentally measured structures, and to compare against conditional normalising-flow and diffusion posterior estimators evaluated under the same cost accounting so that the standing of optimal-transport flow matching among generative inference engines can be established more generally.

References

Beck, J. L. & Katafygiotis, L. S. 1998. Updating Models and Their Uncertainties. I: Bayesian Statistical Framework. *Journal of Engineering Mechanics,* 124**,** 455–461.

Bi, S., Beer, M., Cogan, S. & Mottershead, J. 2023. Stochastic Model Updating with Uncertainty Quantification: An Overview and Tutorial. *Mechanical Systems and Signal Processing,* 204.

Bi, S., Beer, M., Zhang, J., Yang, L. & He, K. 2021. Optimization or Bayesian Strategy? Performance of the Bhattacharyya Distance in Different Algorithms of Stochastic Model Updating. *ASCE-ASME J Risk and Uncert in Engrg Sys Part B Mech Engrg,* 7.

Bi, S., Broggi, M. & Beer, M. 2019a. The role of the Bhattacharyya distance in stochastic model updating. *Mechanical Systems and Signal Processing,* 117**,** 437–452.

Bi, S. F., Broggi, M., Wei, P. F. & Beer, M. 2019b. The Bhattacharyya distance: Enriching the P-box in stochastic sensitivity analysis. *Mechanical Systems and Signal Processing,* 129**,** 265–281.

Ching, J. Y. & Chen, Y. C. 2007. Transitional markov chain monte carlo method for Bayesian model updating, model class selection, and model averaging. *Journal of Engineering Mechanics,* 133**,** 816–832.

Cranmer, K., Brehmer, J., Louppe, G., Cranmer, K., Brehmer, J. & Louppe, G. 2020. The frontier of simulation-based inference. *Proceedings of the National Academy of Sciences,* 117.

Ho, J., Jain, A. & Abbeel, P. 2020. Denoising Diffusion Probabilistic Models. *Advances in neural information processing systems,* 33**,** pp.6840–6851.

Kitahara, M., Bi, S. F., Broggi, M. & Beer, M. 2022. Distribution-free stochastic model updating of dynamic systems with parameter dependencies. *Structural Safety,* 97.

Lipman, Y., Chen, R. T. Q., Ben-Hamu, H., Nickel, M. & Le, M. 2022. Flow Matching for Generative Modeling. *arXiv preprint arXiv:2210.02747*.

Liu, X., Gong, C. & Liu, Q. 2022. Flow Straight and Fast: Learning to Generate and Transfer Data with Rectified Flow. *arXiv preprint arXiv:2209.03003*.

Mares, C., Mottershead, J. E. & Friswell, M. I. 2006. Stochastic model updating: part 1—theory and simulated example. *Mechanical systems and signal processing,* 20**,** 1674–1695.

Papamakarios, G. & Murray, I. 2016. Fast ε-free Inference of Simulation Models with Bayesian Conditional Density Estimation. *Advances in Neural Information Processing Systems 29 (Nips 2016),* 29.

Papamakarios, G., Nalisnick, E., Rezende, D. J., Mohamed, S. & Lakshminarayanan, B. 2021. Normalizing Flows for Probabilistic Modeling and Inference. *Journal of Machine Learning Research,* 22.

Sankararaman, S. & Mahadevan, S. 2015. Integration of model verification, validation, and calibration for uncertainty quantification in engineering systems. *Reliability Engineering & System Safety,* 138.

Song, Y., Sohl-Dickstein, J., Kingma, D. P., Kumar, A., Ermon, S. & Poole, B. 2020. Score-Based Generative Modeling through Stochastic Differential Equations. *arXiv preprint arXiv:2011.13456*.

Tong, A., Fatras, K., Malkin, N., Huguet, G., Zhang, Y., Rector-Brooks, J., Wolf, G. & Bengio, Y. 2023. Improving and generalizing flow-based generative models with minibatch optimal transport. *arXiv preprint arXiv:2302.00482*.

Wang, T., Bi, S., Zhao, Y., Dinh, L. & Mottershead, J. 2025. Data-driven stochastic model updating and damage detection with deep generative model. *Mechanical Systems and Signal Processing,* 232.

Wang, T. R. & Bi, S. F. 2026. Stochastic model updating using conditional diffusion-based probabilistic generative models. *Mechanical Systems and Signal Processing,* 246.